

# 2018

# International Beam Instrumentation Conference

<https://indico.sinap.ac.cn/e/ibic2018>

SEP. 9-13, 2018

Shanghai, China

## Topics

- Overview and machine commissioning
- Beam charge and current monitors
- Beam loss monitors and machine protection
- Beam position monitors
- Longitudinal diagnostic and synchronization
- Transverse profiles and emittance monitors
- Data acquisition systems
- Feedback and beam stability
- Machine parameters measurements and others

## SPC Members

Yongbin Leng (Chair)	SINAP
Junhui Yue	IHEP
Baogeng Sun	USTC
Toshiyuki Mitsuhashi	KEK
Hirokazu Maesaka	RIKEN/SPRING-8
Changbum Kim	PAL
Prapong Klysubun	SLRI
Kuotung Hsu	NSRRC
Seadat Varnasseri	ESS-Bilbao
Ayhan Aydin	Ankara University
Guenther Rehm	DLS
Ubaldo Iriso	ALBA
Hermann Schmickler	CERN
Thibaut Lefevre	CERN
Kay Wittenburg	DESY
Andreas Jansson	ESS
Mario Ferianis	ELETTRA
Alan Fisher	SLAC
Sergio Marques	LNLS
Kevin Jordan	JLAB
David Gassner	BNL
Nicholas Sereno	APS
Steven Lidia	FRIB
Mark Boland	CLS

Organized by:

Shanghai Institute of Applied Physics, CAS (SINAP)



# 2018 International Beam Instrumentation Conference



SEP. 9-13, 2018 | Shanghai China

Organized by: Shanghai Institute of Applied Physics, CAS (SINAP)





Dear Colleagues,

The 7th International Beam Instrumentation Conference (IBIC 2018) was held in Shanghai (China) between September 9th and 13th 2018. It was held by Shanghai institute of applied physics (SINAP), which is the photon science center of China, operating two large scale facilities: SSRF and SXFEL. Like its predecessors, this conference is also dedicated to exploring the physics and engineering challenges of beam diagnostics and measurement techniques for charged particle beams.

Shanghai, located on China's central eastern coast at the mouth of the Yangtze River, is mainland China's center for commerce and finance. The city is also an emerging tourist destination renowned for its historical landmarks such as the Bund, Xintiandi, Yu Garden and the Oriental Pearl Tower. In addition, Shanghai is one of the leading technological centers of China, and a visit to the SSRF and SXFEL was organized.

The 3.5 day programme of the 2018 IBIC conference included 15 invited and 23 contributed talks, and 1 public lecture. Furthermore, 149 posters were presented in the 3 poster sessions, and a 3 day long vendor exhibition with 19 exhibitors could be visited during the conference. In total, 234 participants coming from 18 countries gather around during the 3.5 days of the conference. To all of them, the Organizing Committee is pleased to thank them for their enthusiastic participation.

Not only to the participants, we would like to explicitly express our gratitude to all those who have contributed to this conference: the Scientific Committee for forming a balanced and interesting programme, the Editorial Team for working hard to enable us to present these proceedings, and last but not least, the Local Organization Committee for turning this conference into reality.

Zhentang Zhao  
IBIC 2018 conference chair

Yongbin Leng  
IBIC 2018 Co-chair and PC chair



## COMMITTEES

### Conference Chairs

Zhentang Zhao, SINAP  
Yongbin Leng, SINAP

IBIC 2018 Conference Chair  
IBIC 2018 Co-chair and SPC Chair

### Scientific Program Committee

Yongbin Leng (Chair)	SINAP
Junhui Yue	IHEP
Baogeng Sun	USTC
Toshiyuki Mitsuhashi	KEK
Hirokazu Maesaka	RIKEN/SPring-8
Changbum Kim	PAL
Prapong Klysubun	SLRI
Kuotung Hsu	NSRRC
Seadat Varnasseri	ESS-Bilbao
Ayhan Aydin	Ankara University
Guenther Rehm	DLS
Ubaldo Iriso	ALBA
Hermann Schmickler	CERN
Thibaut Lefevre	CERN
Kay Wittenburg	DESY
Andreas Jansson	ESS
Mario Ferianis	ELETTRA
Alan Fisher	SLAC
Sergio Marques	LNLS
Kevin Jordan	JLAB
David Gassner	BNL
Nicholas Sereno	ANL
Steven Lidia	FRIB
Mark Boland	CLS

### Local Organizing Committee

Yongbin Leng, SINAP	Chair
Christine Petit-Jean-Genaz, CERN	Special adviser
Xin Han, SINAP	JACoW Coordinator
Yingbing Yan, SINAP	Oral and Poster manager
Longwei Lai, SINAP	Industrial Exhibition manager
Ning Zhang, SINAP	Registration and VISA manager
Weicheng Hu, SINAP	Social event manager

### JACoW Editors

Volker RW Schaa, GSI (Chief Editor)  
Christine Petit-Jean-Genaz, CERN  
Jan Chrin, PSI  
Johan Olander, ESS  
Zhichu Chen, SINAP



# Contents

<b>Preface</b>	<b>i</b>
Foreword . . . . .	iii
Committees . . . . .	iv
Contents . . . . .	v
<b>Papers</b>	<b>1</b>
MOOA02 – Noise in Radio/Optical Communications . . . . .	1
MOOB01 – Beam Commissioning of SuperKEKB Rings at Phase-2 . . . . .	6
MOOB03 – Upgrade and Status of Standard Diagnostic-Systems at FLASH and FLASHForward . . . . .	13
MOOB04 – Upgrade of the Machine Protection System Toward 1.3 MW Operation of the J-PARC Neutrino Beamline . . . . .	18
MOOC03 – The Removal of Interference Noise of ICT using the PCA Method . . . . .	22
MOPA01 – Status Overview of the HESR Beam Instrumentation . . . . .	26
MOPA02 – Beam Diagnostics for SuperKEKB Damping Ring in Phase-II Operation . . . . .	29
MOPA04 – The Beam Instruments for HIMM@IMP . . . . .	33
MOPA06 – Recent Advances in Beam Monitoring During SEE Testing on ISDE&JINR Heavy Ion Facilities . . . . .	36
MOPA07 – Beam Diagnostics and Instrumentation for Proton Irradiation Facility at INR RAS Linac . . . . .	40
MOPA09 – Overview of Beam Instrumentation and Commissioning Results from the Coherent Electron Cooling Experiment at BNL . . . . .	43
MOPA12 – The Design and Use of Faraday Cage in Linac Temporary Line of CSNS . . . . .	48
MOPA13 – Fast Luminosity Monitoring for the SuperKEKB Collider (LumiBelle2 Project) . . . . .	51
MOPA14 – Electron Spectrometer for a Low Charge Intermediate Energy LWFA Electron Beam Measurement . . . . .	57
MOPA16 – Design of a Compact Permanent Magnet Spectrometer for CILEX/APOLLON . . . . .	61
MOPA17 – Momentum Compaction Measurement Using Synchrotron Radiation . . . . .	66
MOPB02 – ARIES-ADA: An R&D Network for Advanced Diagnostics at Accelerators . . . . .	71
MOPB03 – High-Energy Scraper System for the S-DALINAC Extraction Beam Line - Commissioning Run . . . . .	75
MOPB04 – Progress in the Stripline Kicker for ELBE . . . . .	78
MOPB06 – DAΦNE Luminosity Monitor . . . . .	81
MOPB07 – Beam Parameter Measurements for the J-PARC High-Intensity Neutrino Extraction Beamline . . . . .	85
MOPB08 – Evaluation of the Transverse Impedance of Pf in-Vacuum Undulator Using Local Orbit Bump Method . . . . .	89
MOPB09 – Comparison Among Different Tune Measurement Schemes at HLS-II Storage Ring . . . . .	93
MOPB10 – A Study on the Influence of Bunch Longitudinal Distribution on the Cavity Bunch Length Measurement . . . . .	97
MOPB13 – Active Magnetic Field Compensation System for SRF Cavities . . . . .	101
MOPB14 – SSRF Beam Operation Stability Evaluation Using Bunch by Bunch Beam Position Method . . . . .	104
MOPB16 – Continuous Beam Energy Measurements at Diamond Light Source . . . . .	107
MOPB17 – Using a TE011 Cavity as a Magnetic Momentum Monitor . . . . .	111
MOPC02 – Identification of Faulty Beam Position Monitor Based Clustering by Fast Search and Find of Density Peaks . . . . .	114
MOPC03 – Precise Measurement of Small Currents at the MLS . . . . .	118
MOPC04 – Beam Charge Measurement and System Calibration in CSNS . . . . .	122
MOPC06 – Comparative Measurement and Characterisation of Three Cryogenic Current Comparators Based on Low-Temperature Superconductors . . . . .	126
MOPC08 – Beam Intensity Monitoring with nA Resolution - the Cryogenic Current Comparator (CCC) . . . . .	130
MOPC10 – Upgrade and Improvement of CT Based on TMR . . . . .	134
MOPC11 – Data Acquisition System for Beam Instrumentation of SXFEL and DCLS . . . . .	137
MOPC12 – The Radial Detector in the Cyclotron of HIMM . . . . .	140
MOPC14 – The Design of Dose Parameter Acquisition and Control System for a Pencil Beam Scanning System in HUST-PTF . . . . .	143
MOPC16 – The Development and Applications of Digital BPM Signal Processor on SSRF . . . . .	147
MOPC17 – On-line Crosstalk Measurement and Compensation Algorithm Study of SXFEL Digital BPM System . . . . .	150
MOPC18 – Development of an Expert System for the High Intensity Neutrino Beam Facility at J-PARC . . . . .	154
MOPC19 – Virtual Signal Spectrum Analyzer Development Based On RedPitaya and EPICS for Tune Measurement in BEPCII . . . . .	159
TUOA01 – The Diagnostic System at the European XFEL; Commissioning and First User Operation . . . . .	162
TUOA02 – Application of Machine Learning to Beam Diagnostics . . . . .	169



TUOB02 – Optics Measurements in Storage Rings: Simultaneous 3-Dimensional Beam Excitation and Novel Harmonic Analysis . . . . .	177
TUOB03 – Demonstration of a Newly Developed Pulse-by-pulse X-Ray Beam Position Monitor in SPring-8 . . .	182
TUOB04 – A Vertical Phase Space Beam Position and Emittance Monitor for Synchrotron Radiation . . . . .	186
TUOC01 – Integration of a Pilot-Tone Based BPM System Within the Global Orbit Feedback Environment of Elettra	190
TUOC03 – Commissioning of the Open Source Sirius BPM Electronics . . . . .	196
TUOC04 – Development of Beam Position Monitor for the SPring-8 Upgrade . . . . .	204
TUPA01 – Pin Diode in a Medical Accelerator - a Proof of Principle and Preliminary Measurements . . . . .	208
TUPA02 – A Micromegas Based Neutron Detector for the ESS Beam Loss Monitoring . . . . .	211
TUPA03 – Test of New Beam Loss Monitors for SOLEIL . . . . .	215
TUPA04 – Analysis of Interlocked Events based on Beam Instrumentation Data at J-PARC Linac and RCS . . .	219
TUPA07 – Collimator for Beam Position Measurement and Beam Collimation for Cyclotron . . . . .	224
TUPA08 – Arc Discharge Detectors for the CiADS Superconducting RF Cavities . . . . .	228
TUPA09 – The Monte Carlo Simulation for the Radiation Protection in a Nozzle of HUST-PTF . . . . .	232
TUPA14 – Beam Loss Monitoring in the ISIS Synchrotron Main Dipole Magnets . . . . .	236
TUPA15 – Adaptive Collimator Design for Future Particle Accelerators . . . . .	240
TUPA16 – Signal Processing for Beam Loss Monitor System at Jefferson Lab . . . . .	245
TUPA17 – Status of the BNL LEReC Machine Protection System . . . . .	249
TUPB01 – The Installation and Commissioning of the AWAKE Stripline BPM . . . . .	253
TUPB02 – Complete Test Results of New BPM Electronics for the ESRF New LE-Ring . . . . .	257
TUPB03 – Results of SPIRAL2 Beam Position Monitors on the Test Bench of the RFQ . . . . .	261
TUPB04 – Development of a New Button Beam-position Monitor for BESSY VSR . . . . .	265
TUPB05 – Design of a Cavity Beam Position Monitor for the ARES Accelerator at DESY . . . . .	269
TUPB07 – Stability Study of Beam Position Measurement Based on Higher Order Mode Signals at FLASH . .	273
TUPB09 – The Evaluation of Beam Inclination Angle on the Cavity BPM Position Measurement . . . . .	278
TUPB10 – Design and Simulation of Stripline BPM for HUST Proton Therapy Facility . . . . .	281
TUPB12 – Machine Studies with Libera Instruments at the SLAC Spear3 Accelerators . . . . .	284
TUPB13 – Stability Tests with Pilot-Tone Based Elettra BPM RF Front End and Libera Electronics . . . . .	289
TUPB14 – New Beam Position Monitors for the CERN LINAC3 to LEIR Ion Beam Transfer Line . . . . .	293
TUPC01 – Australian Synchrotron BPM Electronics Upgrade . . . . .	297
TUPC03 – Beam Quality Monitoring System in the HADES Experiment at GSI Using CVD Diamond Material . .	300
TUPC04 – BPM System Upgrade at COSY . . . . .	303
TUPC05 – Influence of Sampling Rate and Passband on the Performance of Stripline BPM . . . . .	307
TUPC07 – First Results of Button BPMs at FRIB . . . . .	311
TUPC09 – Initial Results from the LHC Multi-Band Instability Monitor . . . . .	314
TUPC10 – The Design of Scanning Control System for Proton Therapy Facility at CIAE . . . . .	319
TUPC11 – Design of an Ultrafast Stripline Kicker for Bunch-by-Bunch Feedback . . . . .	322
TUPC12 – Beam Transverse Quadrupole Oscillation Measurement in the Injection Stage for the HLS-II Storage Ring . . . . .	325
TUPC13 – Early Commissioning of the Luminosity Dither Feedback for SuperKEKB . . . . .	328
WEOA02 – Optical Investigation to Minimize the Electron Bunch Arrival-time Jitter Between Femtosecond Laser Pulses and Electron Bunches for Laser-Driven Plasma Wakefield Accelerators . . . . .	332
WEOA03 – First Electro-Optical Bunch Length Measurements from the European XFEL . . . . .	338
WEOA04 – The Application of Beam Arrival Time Measurement at SXFEL . . . . .	342
WEOB01 – New Beam Loss Detector System for EBS-ESRF . . . . .	346
WEOB02 – RadFET Dose Monitor System for SOLEIL . . . . .	353
WEOB03 – The European XFEL Beam Loss Monitor System . . . . .	357
WEOC02 – Review of Recent Status of Coded Aperture X-ray Monitors for Beam Size Measurement . . . . .	361
WEOC03 – A Simple Model to Describe Smoke Ring Shaped Beam Profile Measurements With Scintillating Screens at the European XFEL . . . . .	366
WEOC04 – Space Charge Effects Studies for the ESS Cold Linac Beam Profiler . . . . .	371
WEPA01 – A MicroTCA.4 Timing Receiver for the Sirius Timing System . . . . .	375
WEPA02 – Recent Progress of Bunch Resolved Beam Diagnostics for BESSY VSR . . . . .	379
WEPA06 – Thermal Coefficient of Delay Measurement of the New Phase Stable Optical Fiber . . . . .	383
WEPA07 – Beam Phase Measurement System in CSNS Linac . . . . .	386
WEPA09 – Long Term Beam Phase Monitoring Based on HOM Signals in SC Cavities at FLASH . . . . .	388

WEPA12 – Differential Evolution Genetic Algorithm for Beam Bunch Temporal Reconstruction . . . . .	392
WEPA13 – Electro-Optic Modulator Based Beam Arrival Time Monitor for SXFEL . . . . .	396
WEPA15 – Development of BAM Electronics in PAL-XFEL . . . . .	400
WEPA16 – Micro-Bunching Instability Monitor for X-ray Free Electron Laser . . . . .	404
WEPA17 – Development, Fabrication and Laboratory Tests of Bunch Shape Monitors for ESS Linac . . . . .	407
WEPA18 – Development of Longitudinal Beam Profile Diagnostics for Beam-beam Effects Study at VEPP-2000	410
WEPA19 – Results from the CERN LINAC4 Longitudinal Bunch Shape Monitor . . . . .	415
WEPA20 – First Results From the Bunch Arrival-Time Monitors at SwissFEL . . . . .	420
WEPB01 – Photon Beam Imager at SOLEIL . . . . .	425
WEPB02 – Development of a a YAG/OTR Monitor . . . . .	429
WEPB03 – First Prototype of a Coronagraph-based Halo Monitor for BERLinPro . . . . .	434
WEPB04 – Comparison of YAG Screens and LYSO Screens at PITZ . . . . .	438
WEPB06 – Time-Synchronous Measurements of Transient Beam Dynamics at SPEAR3 . . . . .	441
WEPB09 – Wire Scanner Measurements at the PAL-XFEL . . . . .	445
WEPB10 – Grating Scanner for Measurement of Micron-size Beam Profiles . . . . .	448
WEPB11 – Spatial Resolution Improvement of OTR Monitors by Off-axis Light Collection . . . . .	451
WEPB12 – Design and Implementation of Non-Invasive Profile Monitors for the ESS LEBT . . . . .	455
WEPB13 – Beam-Gas Imaging Measurements at LHCb . . . . .	459
WEPB14 – Recent Results on Non-invasive Beam Size Measurement Methods Based on Polarization Currents	464
WEPB15 – A Multipurpose Scintillating Fibre Beam Monitor for the Measurement of Secondary Beams at CERN	468
WEPB16 – Development of a Beam-Gas Curtain Profile Monitor for the High Luminosity Upgrade of the LHC .	472
WEPB18 – Performance of a Reflective Microscope Objective in an X-ray Pinhole Camera . . . . .	477
WEPB20 – Experimental Setup of Apodization Techniques for Beam Diagnostics Performed at ELBE . . . . .	482
WEPB21 – Transverse Beam Emittance Measurements with Multi-Slit and Moving-Slit Devices for LEReC . . .	486
WEPC02 – Synchrotron Emittance Analysis Procedure at MedAustron . . . . .	490
WEPC04 – Setup for Beam Profile Measurements using Optical Transition Radiation . . . . .	494
WEPC05 – The European XFEL Wire Scanner System . . . . .	498
WEPC06 – The New Diagnostic Suite for the Echo Enabled Harmonic Generation Experiment at FERMI . . . .	501
WEPC08 – Optical System of Beam Induced Fluorescence Monitor Toward MW Beam Power at the J-PARC Neutrino Beamline . . . . .	505
WEPC09 – Design and Test Results of a Double-Slit Emittance Meter at XiPAF . . . . .	509
WEPC15 – Machine Learning Applied to Predict Transverse Oscillation at SSRF . . . . .	512
WEPC16 – Design and Radiation Simulation of the Scintillating Screen Detector for Proton Therapy Facility . .	516
WEPC17 – X-ray Pinhole Camera in the Diagnostics Beamline BL7B at PLS-II . . . . .	519
WEPC19 – Selection of Wires for the New Generation of Fast Wire Scanners at CERN . . . . .	523
THOA01 – Low vs High Level Programming for FPGA . . . . .	527
THOA02 – High-Speed Direct Sampling FMC for Beam Diagnostic and Accelerator Protection Applications . . .	534
THOA03 – Progress on Transverse Beam Profile Measurement Using the Heterodyne Near Field Speckles Method at ALBA . . . . .	538
THOB01 – Injection Transient Study Using 6-Dimensional Bunch-by-bunch Diagnostic System at SSRF . . . .	542
THOB02 – Energy Loss Measurements with Streak Camera at ALBA . . . . .	548
THOB03 – Long Term Investigation of the Degradation of Coaxial Cables . . . . .	552
<b>Appendices</b> . . . . .	<b>557</b>
List of Authors . . . . .	557
Institutes List . . . . .	565





# NOISE IN RADIO/OPTICAL COMMUNICATIONS

M. Vidmar<sup>†</sup>, University of Ljubljana, FE, Tržaška 25, 1000 Ljubljana, Slovenia

## Abstract

Noise is a random signal that affects the performance of all electronic and/or optical devices. Although the sources of different kinds of noise have their backgrounds in physics, engineers dealing with noise use different methods and units to specify noise. The intention of this tutorial is to describe the main effects of noise in electronics up to optical frequencies while providing links between the physics and engineering worlds. In particular, noise is considered harmful while degrading the signal-to-noise ratio or broadening the spectrum of signal sources. On the other hand, noise can be itself a useful signal. Finally, artificially generated signals that exhibit many properties of random natural noise are sometimes required.

## NATURAL NOISE

Noise is a broadband signal. Therefore it makes sense to describe its intensity by the noise spectral density  $N_0$  or amount of noise power per unit bandwidth (see Fig. 1). In electronics the most important type of noise is thermal noise. Thermal noise adds to any signal. In optics the most important type of noise is shot noise. Shot noise is a property of any signal made from a discrete number of photons.

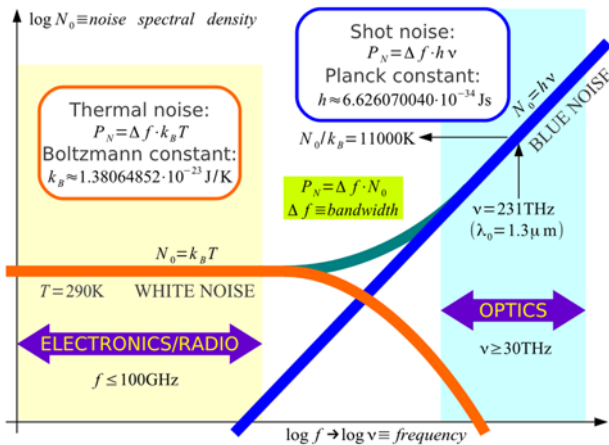


Figure 1: Noise spectral density.

Since the photon energy increases proportional with frequency, the higher the frequency the larger the shot noise spectral density. Such a noise is also called blue noise. Shot noise is unimportant in the radio-frequency range at room temperatures. Shot noise can only be observed at the highest end of the radio-frequency range at cryogenic temperatures.

Thermal noise is caused by thermal radiation. The Planck law (see Fig. 2) describes the spectral brightness  $B_f$  or radiated power per unit bandwidth, unit area and unit solid angle of a black

body. A black body with zero reflectivity  $\Gamma=0$  is the most efficient thermal radiator while a perfect mirror  $|\Gamma|=1$  does not radiate at all.

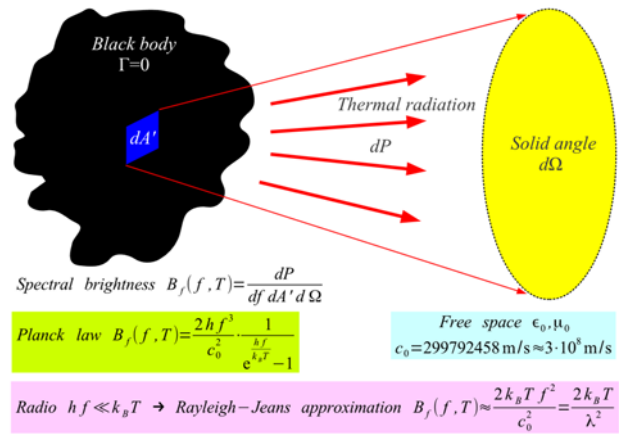


Figure 2: Black-body thermal radiation.

In the radio-frequency range it makes sense to use the Rayleigh-Jeans approximation of the Planck law to calculate the noise power collected by a lossless antenna. An antenna with an electrical connector (see Fig. 3) only collects half of the incident noise power on its effective area  $A_{eff}$ , the remaining half being orthogonally polarized.

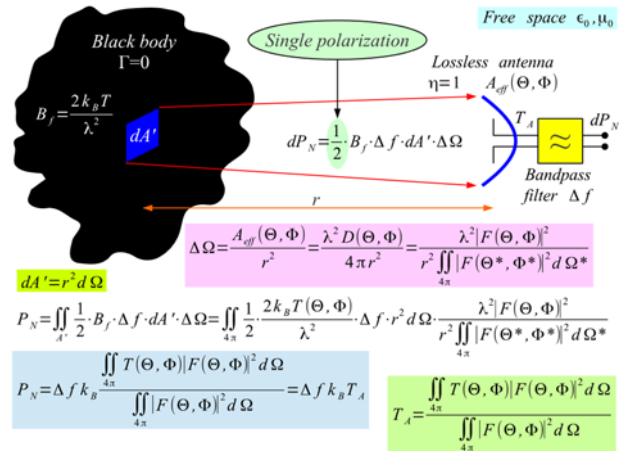


Figure 3: Received thermal-noise power.

In the radio-frequency range the noise spectral density is frequency independent. Thermal noise therefore behaves as white noise. Thermal noise spectral density is simply described by the black-body temperature  $T_A$  as observed by the radiation pattern  $F(\Theta, \Phi)$  of a lossless antenna ( $\eta=1$ ).

Above a certain frequency the thermal noise power begins decreasing when the complete Planck law applies. However, the sum of both noise spectral densities, thermal noise and shot noise, remains a monotonic function of

<sup>†</sup> email address: matjaz.vidmar@fe.uni-lj.si



Unfortunately, the active devices used in the oscillator generate additional flicker noise ( $1/f$  noise or pink noise) at small frequency offsets  $|\Delta f| < f_c$ . The flicker-noise corner frequency may be as high as  $f_c \approx 1$  MHz for surface devices like MOSFETs or HEMTs or as low as  $f_c \approx 1$  kHz for bulk devices like bipolar transistors or junction FETs.

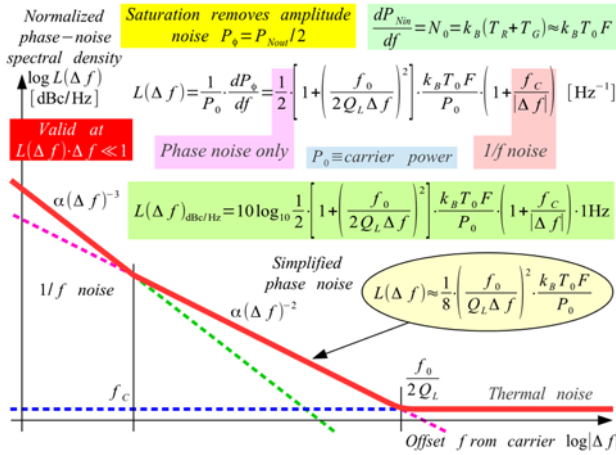


Figure 8: Leeson's equation.

The most important parameter of a good oscillator is the loaded quality  $Q_L$  of the resonator. An LC oscillator may achieve a  $Q_L \approx 100$ . A crystal oscillator may achieve a  $Q_L \approx 10^4$ . A HeNe laser may achieve a  $Q_L \approx 10^8$  but its signal usually can not be used directly. Additional requirements are low-noise devices (low  $F$  and low  $f_c$ ) operated at a high carrier power  $P_0$ .

The oscillator phase noise (see Fig. 9) has many detrimental effects: it increases the bit-error rate due to modulation constellation rotation, it adds residual FM in analog communications, it causes adjacent-channel interference and it causes clock timing jitter.

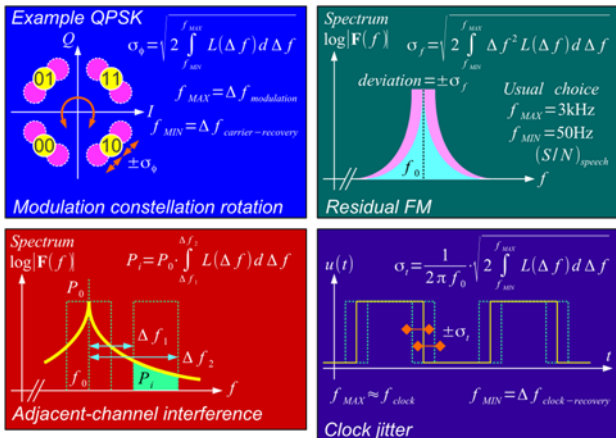


Figure 9: Effects of phase noise.

In all above case, the phase noise is integrated over a finite interval  $f_{MIN} < \Delta f < f_{MAX}$  where the Leeson's equation is accurate enough in almost all real-world engineering problems having a finite bandwidth  $f_{MAX} = \Delta f_{bandwidth}$  and fast-enough control loops  $f_{MIN} = \Delta f_{recovery}$ .

All of the above integrals give an infinite result both for  $f_{MIN} \rightarrow 0$  and/or for  $f_{MAX} \rightarrow \infty$ . Such an infinite result has no physical background and comes from the approximations used in the derivation of the Leeson's equation. The phase noise without approximations should include additional effects (see Fig. 10). The device  $f_{MAX}$  limits the bandwidth even more than the complete Planck law.

At the other end, at very small frequency offsets  $f_{MIN} \rightarrow 0$  the noise power is no longer small compared to the carrier power as assumed in the simple derivation. The spectrum of any real oscillator is a finite and continuous function with a rounded top at the central frequency  $f_0$ .

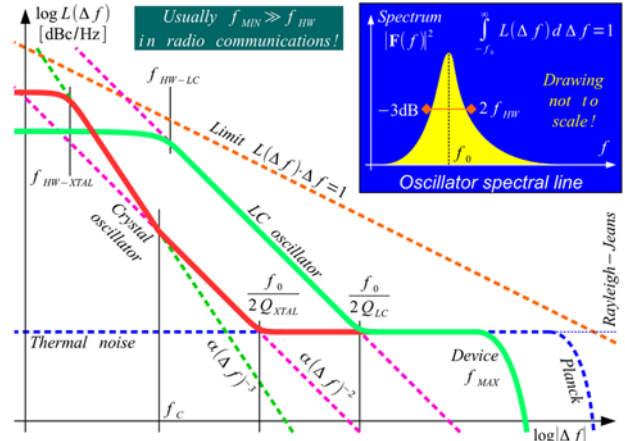


Figure 10: Phase noise without approximations.

When the flicker ( $1/f$ ) noise can be neglected, the simplified Leeson's equation evolves into a Lorentzian spectral line (see Fig. 11). The -3 dB spectral-line width of a rather poor ( $Q_L = 10$ ) electrical ( $f_0 = 3$  GHz) LC oscillator is just  $f_{FWHM} = 28 \text{ Hz} \approx 10^{-8} f_0$ .

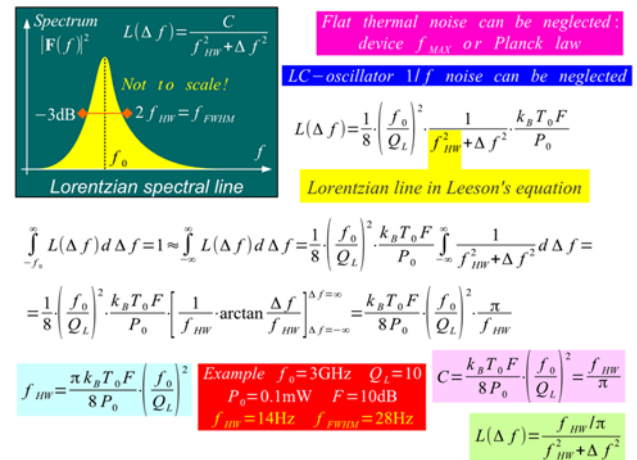


Figure 11: Lorentzian spectral-line width.

While both physicists and engineers observe the same effects, they look at different details. Physicists observe the line width  $f_{FWHM}$ . Engineers observe the phase-noise spectral density  $L(\Delta f)$  at much larger frequency offsets.



## FIBER-OPTICS NOISE

Although shot noise is the largest noise contribution at optical frequencies, other kinds of noise usually limit the performance of optical-fiber links (see Fig. 12). At low power levels in an optical-fiber link, the largest noise contribution is the thermal noise of the electrical amplifier following the photodiode due to impedance mismatch. At higher power levels both the intensity and phase noise of the laser are the largest noise contribution. Unwanted reflections (optical connectors etc) form interferometers that transform the laser phase noise into intensity noise.

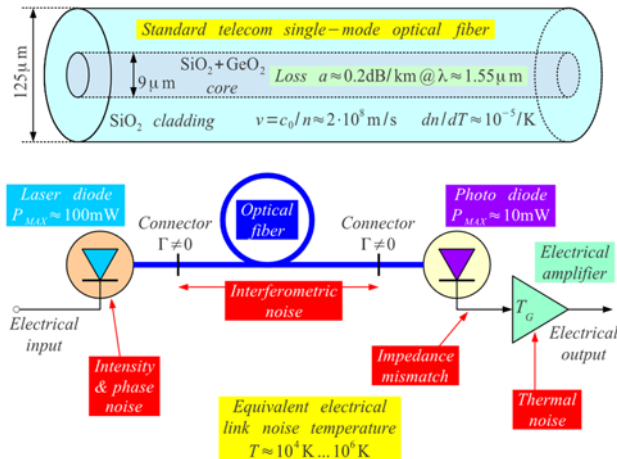


Figure 12: Optical-fiber link.

An electro-optical delay line could replace a very high  $Q_O > 10^6$  K resonator in an oscillator (see Fig. 13), but it is also very noisy  $T_R \gg 290$  K. Further it requires a mode-select electrical filter with a considerable  $Q_M \approx 10\% Q_O$ .

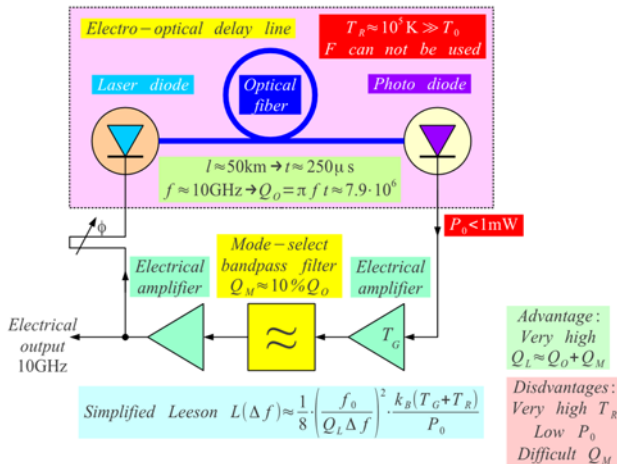


Figure 13: Opto-electronic oscillator.

A noisy electro-optical delay line allows more noise to be generated in the electrical circuits. In particular, an electrical Q multiplier (noisy circuit) can be used to achieve a high  $Q_M$  of the mode-select bandpass filter of an opto-electronic oscillator [2] to improve unwanted mode rejection while relatively contributing just a small fraction of the whole-oscillator loop noise.

## NOISE AS USEFUL SIGNAL

White noise can be used as a test signal in electronics exactly in the same way as white light is used as a test signal in optics. In electronics, white noise allows testing both linear and non-linear circuits (see Fig. 14). White noise allows measuring the transfer function  $H(\omega)$  of linear circuits. White noise is also useful to measure the intermodulation distortion (IMD) of non-linear circuits.

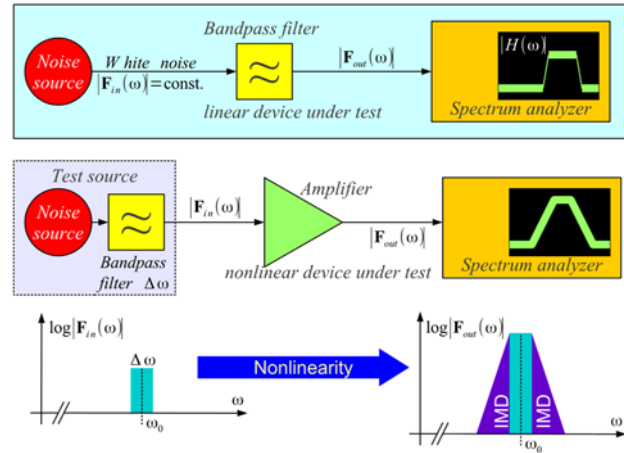


Figure 14: Noise as a test signal.

Truly random noise can also be used to generate secure cryptographic keys of any size. Carefully managing the signal-to-noise ratio in a low-loss communication link with strong forward-error correction (FEC) is the basis of noise (quantum) cryptography.

Finally, some circuits generate signals that are not random, but have many properties of random noise, like autocorrelation function, spectrum, sound or appearance. An  $m$ -stage binary polynomial divider with a carefully selected feedback (see Fig. 15) can generate such a pseudo-random sequence of the maximum length  $N = 2^m - 1$ . While useful for many purposes (synchronization, test signal etc), pseudo-random sequences have no cryptographic value.

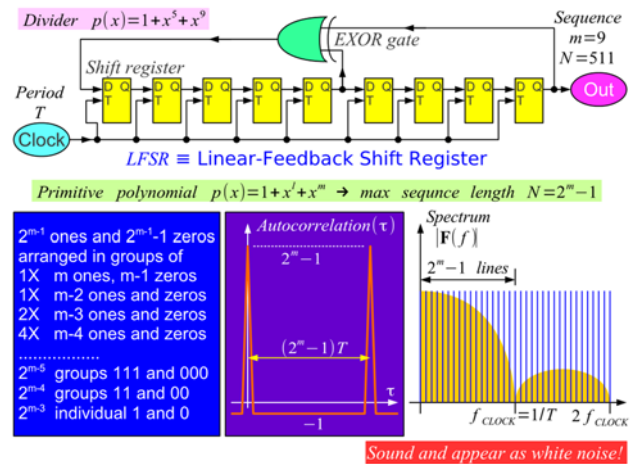


Figure 15: Linear-feedback shift register.



## REFERENCES

- [1] D.B. Leeson, “A simple model of feedback oscillator noise spectrum”, in *Proc. IEEE*, vol. 54, no. 2, pp. 329–330, Feb. 1966.
- [2] L. Bogataj, M. Vidmar, and B. Batagelj, “Opto-electronic oscillator with quality multiplier”, *IEEE Transactions on Microwave Theory and Techniques*, vol. 64, no. 2, pp. 663–668, Feb. 2016.

# BEAM COMMISSIONING OF SuperKEKB RINGS AT PHASE-2

M. Tobiyama\*, M. Arinaga, J. W. Flanagan, H. Fukuma, H. Ikeda, S. Iwabuchi, H. Ishii, G. Mistuka, K. Mori, E. Mulyani and M. Tejima, KEK Accelerator Laboratory, 1-1 Oho, Tsukuba 305-0801, Japan and also SOKENDAI, Japan  
G.S. Varner, U. Hawaii, Dept. Physics and Astronomy, 2505 Correa Rd., Honolulu HI 96822, USA  
G. Bonvicini, Wayne State U., 135 Physics Bldg., Detroit MI 4820, USA.

## Abstract

The Phase 2 commissioning of SuperKEKB rings with Belle II detector began in Feb. 2018. Staring the commissioning of positron damping ring (DR), the injection and storage of the main rings (HER and LER) smoothly continued in Apr. 2018. The first collision has been achieved on 26th Apr. with the detuned optics (200 mm x 8 mm). Performance of beam instrumentation systems and the difficulties encountered during commissioning time will be shown.

## INTRODUCTION

The KEKB collider has been upgraded to the SuperKEKB collider with a final target of 40 times higher luminosity than that of KEKB. It consists of a 7 GeV high energy ring (HER, electrons) and a 4 GeV low energy ring (LER, positrons). About 2500 bunches per ring will be stored at total beam currents of 2.6 A (HER) and 3.6 A (LER) in the final design goal. After the first stage of commissioning (Phase 1) without the Belle-II detector, which started in Feb. 2016 and continued until the end of June [1, 2], we have installed the superconducting final quadrupoles (QCS) and the Belle-II detector, without innermost detectors vertex detectors such as Pixel detectors nor Silicon Vertex Detectors (VXD).

The primary target of the Phase-2 operation in accelerator side was to verify the large crossing angle, nano-beam collision scheme by squeezing the  $\beta y^*$  smaller than the bunch length and to achieve high luminosity consistent to  $\beta y^*$ . There also required to achieve the following conditions to proceed to the phase-3 operation by the Belle II group:

- Achieve a machine luminosity of  $O(10^{34}/\text{cm}^2/\text{s})$  and see a clear path to further improvement.
- Examine the VXD background to verify that we can install the VXD at the start of phase 3 and then operate it for the initial first few years of phase 3.

The Phase-2 operation has started in Feb. 2018 with the commissioning of the positron damping ring (DR). The commissioning of HER and LER has started in late Mar. with detuned (non-collision) optics. After establishing the beam storage, we have jumped to the collision optics on 11th. Apr. The first collision has been observed on 26th. Apr with the IP parameter of ( $\beta x^*$ ,  $\beta y^*$  = 200 mm, 8 mm) [3, 4].

The beam instrumentation has played a very important role at each step of commissioning, such as establishing the

circulating orbit, finding the beam-beam kick, accumulating large beam currents, and so on.

In this paper we describe the results of the beam commissioning of phase 2 operation of SuperKEKB rings with the obtained performance of the beam instrumentations. The main parameters of the phase 2 operation of SuperKEKB HER/LER/DR and the types and number of main beam instrumentations are shown in Table 1.

Table 1: Main Parameters of SuperKEKB HER/LER/DR in Phase 2 Operation

	HER	LER	DR
Energy (GeV)	7	4	1.1
Circumference(m)	3016		135
Max. current (mA)	800	860	12
Bunch length (mm)	5	6	6.6
RF frequency (MHz)	508.887		
Harmonic number (h)	5120		230
Betatron tune(H/V)	44.54/ 46.56	45.54/ 43.56	8.24/ 7.17
Synchrotron tune	0.02	0.018	0.025
T. rad. damp time (ms)	58	43	12
x-y coupling (%)	0.27	0.28	10
Emittance (nm)	3.2	4.6	29
Peak luminosity	$5.5 \times 10^{33}/\text{cm}^2/\text{s}$		
Beam position monitor	486	444	83
Turn by turn monitor	69	70	83
Trans. FB system	2	2	1
Visible SR monitor	1	1	1
X-ray size monitor	1	1	0
Beta. tune monitor	1	1	1
DCCT	1	1	1
Bunch current mon.	1	1	1
Beam loss monitor	105(IC)/101(PIN)		34

\*✉ email address

makoto.tobiyama@kek.jp

## DAMPING RING COMMISSIONING

The commissioning of the positron damping ring has started on Feb. 8th, 2018 [5]. After the tuning of Linac to Ring beam transfer line (LTR), we have at first started to adjust the beam timing of the BPM detectors (18K11) [6]. We have used the turn-by-turn bpm detectors based on wideband Log-ratio method. As shown in Fig. 1 the main frequency divider creates the bunch revolution timing synchronized to the injection bunch timing. For each BPM

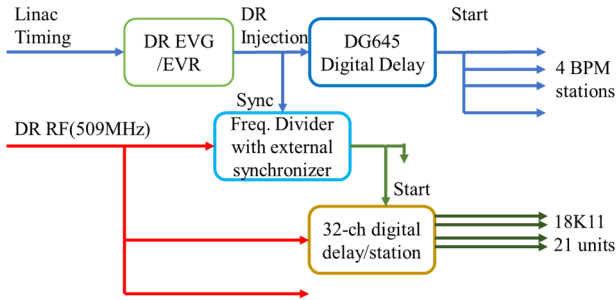


Figure 1: Block diagram of DR bpm timing system.

detectors, we have also prepared the 32-ch digital delay unit for each BPM station [7]. As we know the relative timing differences of BPMs from the measurements of cable lengths and from the BPM locations, we simply adjusted the station timing offset measured by the injected bunch at the most upstream electrode and added individual delays. With this method, all the BPM timing have been successfully adjusted within 2 hours after the first injection to the ring including the tuning of the beam orbit.

Though the 18K11 has more than 32k turns of memory for each channel, it took more than 4 seconds to calculate the beam position of the 32k turns of data due to extremely poor CPU power of MVME5500. We therefore limited the processing length of the BPM waveform upto 2k turns with the software, and also made other process such as evaluating the BPM consistency on a linux cpu. With this condition, we could repeat the position measurements less than 1 second cycle.

The BPM block positions relative to the quadrupole magnets have been surveyed using FARO 3D-ARM and the results been reflected to the beam position. The mean and standard deviation of the survey was  $0.07 \text{ mm} \pm 0.47 \text{ mm}$  and  $-0.25 \text{ mm} \pm 0.29 \text{ mm}$  for horizontal and vertical, respectively. The gain difference of each electrode has also been estimated by the beam-based gain mapping method [8]. It spreads roughly within 8%. The mean resolution of the BPM system with 2k sample for 1 nC/bunch beam have been estimated by the 3-BPM method to be about 2-3  $\mu\text{m}$ .

By detecting the 508 MHz components from a button electrode using a 4-tap FIR cable band pass filter, we have formed a CT like monitor. The monitor worked well to find the RF timing to capture the beam. Moreover, it showed mis-timing injecting beam which is far off phased from the majority of the beam.

The output of DCCT has been measured by the Keysight 34465A with roughly 5 ksps rate continuously without break due to data transfer. Figure 2 shows an example of

measured beam current in DR with accumulation time of 1 ms. Clearly it reflects imperfect step response of the DCCT circuit. The correction of the response using feed-forward method will be considered.

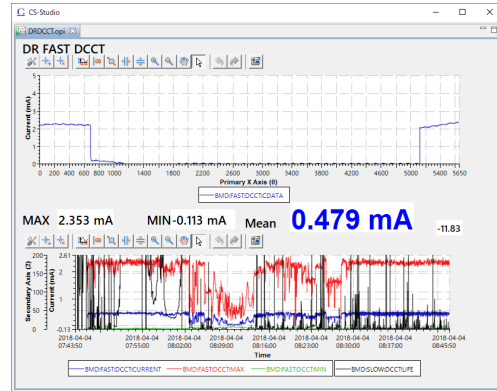


Figure 2: Example of DCCT data of DR with accumulation time of around 1 ms.

Though it is not needed to worry about the coupled-bunch instability (CBI) for DR, we have prepared a transverse bunch-by-bunch feedback system similar to the bunch feedback system to the main ring mainly to damp the residual kick of the injection and extraction kicker [9]. Using this FB system, we have also made a betatron tune measurement system. It showed enough response even with single bunch operation. The bunch current information is also measured using the FB detector and the memory board same as the MR with reduced ring memory size.

The longitudinal and transverse beam size from the injection to the extraction have been measured by a streak camera and a fast gated camera. Figure 3 shows an example of measured bunch length after the injection.

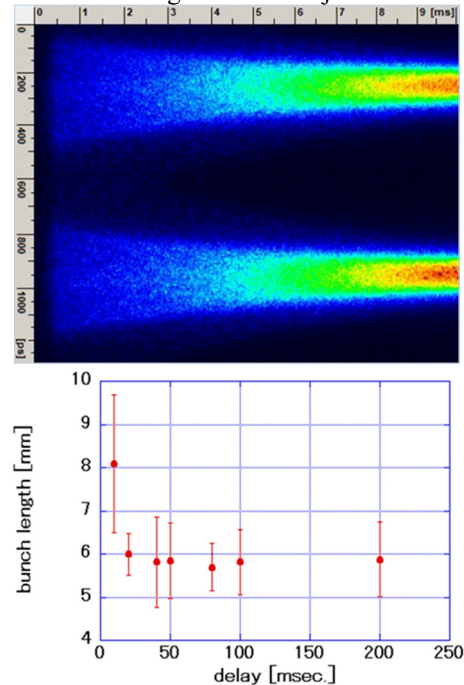


Figure 3: Measured bunch length of DR after injection.

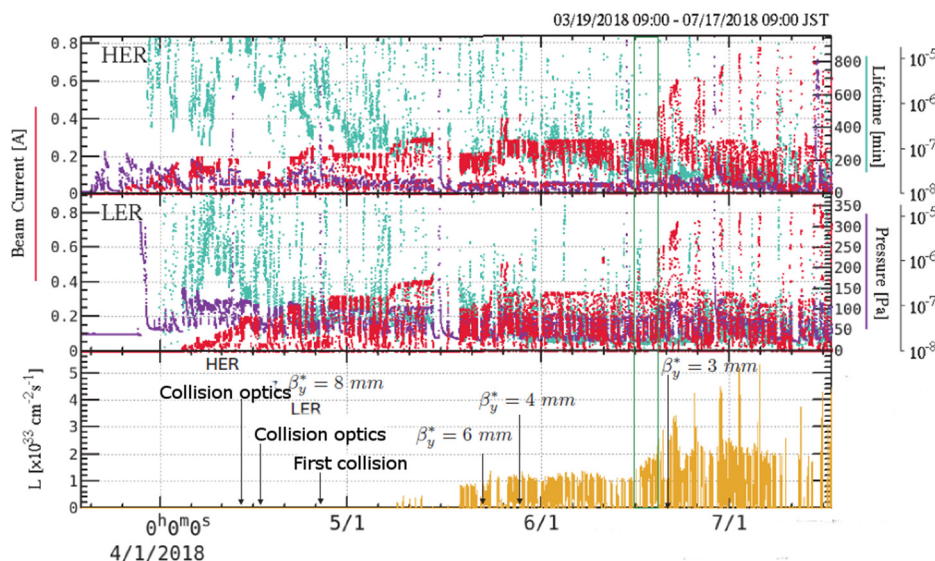


Figure 4: Beam currents and luminosity history of phase 2 operation of the SuperKEKB rings.

We have placed 34 ion chambers around the ring and the beam transport lines to measure the beam loss and also to stop the injection if the loss exceeds a threshold. The fast sample ADCs with digital peak hold circuit [10] have been used to monitor the integrated loss within 1 second.

Totally, the instruments prepared for the DR have worked pretty well during the phase 2 operation.

## HER/LER COMMISSIONING

Figure 4 shows the total history of the beam currents and luminosity of the phase 2 operation of the SuperKEKB rings. We have started the injection to HER and LER with detuned optics without local chromaticity correction section around the interaction point on late Mar. and early Apr., respectively. After establishing the beam storage, we have changed the optics to the detuned collision optics and enabled the local chromaticity corrections. This jump on beam optics needed enormous efforts such as measuring the beam optics and correcting it before establishing the stable orbit. Also, we have encountered many quenches on the superconducting coils in the final quads (QCSs). After the first collision on 26/Apr, we gradually tried to squeeze the betatron function to get the higher luminosity.

### Gated Turn-by-Turn Monitor

Though the beam timing (definition of the bucket 0) has been shifted wildly from the phase 1 mainly due to the insertion of the damping ring in the injection timing path, the gated turn-by-turn monitors (GTBT) with fully open-gated mode worked well to detect the injection beam orbit. Newly added 19 GTBTs in the ring, especially around the HER injection points and around the collision points have helped to pass through the beam smoothly.

After establishing the beam collision, we have re-adjusted the ADC and gate timing of the GTBTs using single bunch beam. Timing differences from phase 1 were about 920 ns and 880 ns for HER and LER, respectively.

We have newly included the offset and gain imbalance factors in the GTBTs position records. During the phase 2

operation, we have copied them from that of for the narrowband BPMs measured by employing beam based alignment (BBA) and beam based gain mapping (BBG).

The GTBTs have also routinely been used to reduce the residual kick of the injection kickers which helped to protect the QCS from the quench due to wild injection beam and to find the difficulties in the injection kickers such as mis-fire or timing error.

In SuperKEKB, normally the optical functions such as betatron functions, x-y couplings or dispersions have been measured by the single kick method using narrowband BPMs [11]. The GTBTs have also been used to measure the phase advances between the GTBTs, especially around the interaction point where either gain nor offsets relative to the superconducting quadrupoles are not so reliable due to fairly complexed structure and larger gain loss of the coaxial cables. Even though, for optics group the GTBTs are not so easy devices due to large size of the data. We plan to include data processing such as making FFTs, correction of one-turn delay, etc. in the IOCs for GTBTs.

The GTBTs have also used to check the orbit bump for IP dithering feedback [12]. It finds the horizontal beam offset or angle with lumosity peak at IP by slightly exciting the beam orbit with 60 to 80 Hz using air-cored magnets around IR. Figure 5 shows the measured normalized amplitude in the bump and out of the bump.

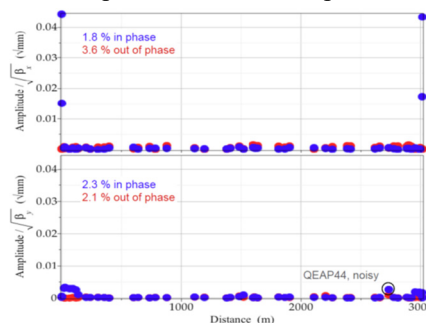


Figure 5: Normalized amplitude of dithering excitation with GTBTs. Blue dots show the in-phase components.



Clearly the dither system hardware including the timing and tuning knob have shown the good response as expected.

## IP Feedback Systems

In the nano-beam scheme, though the horizontal beam-beam kick is much lower than that of normal collider, the vertical beam-beam kick is estimated to be strong enough to find the center of the collision. We have prepared four BPM electrode set just outside the Belle II vertex chamber (QC1s). As the diameter of the vacuum chamber is only 20 mm there, we have developed special electrodes with the button diameter of 1.8 mm as shown in Fig. 6. Even with

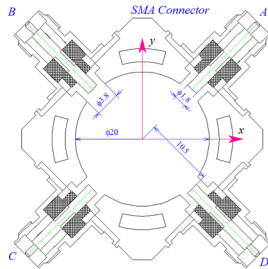


Figure 6: Special BPM electrodes for QC1.

this tiny electrode, the total power from the beam at maximum beam current is estimated to be the order of 10 W, which is similar level as that at the feedthrough of BPMs near IP in KEKB.

The vertical orbit shift at the BPMs is estimated to be several microns. A special wideband detector for the IP orbit feedback has been developed to measure the orbit at QC1s. Target performance of the detector is resolution less than 1  $\mu\text{m}$  with beam current larger than 1 A and the repetition rate from 5 kHz to 32 kHz. Schematic diagram of the detector is shown in Fig. 7.

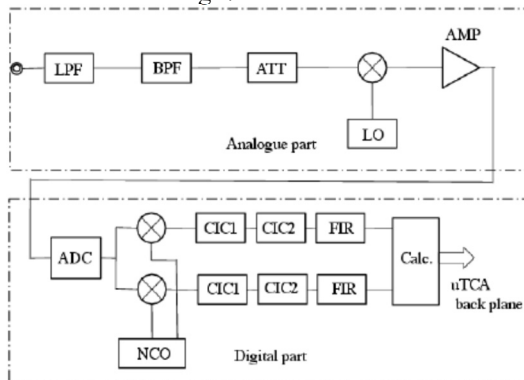


Figure 7: Block diagram of IP beam position detector.

The detector converts the 508 MHz component in BPM signal to an IF of 16.9 MHz with an analogue mixer. The IF signal is digitized by the 16-bit ADC on the mezzanine card of the microTCA card with Virtex5 FPGA (BPM unit) with the sampling frequency of 99.4 MHz, then process by a chain of digital filters (two CICs and a FIR). The cut-off frequency of the filter is 2 kHz.

The calculation of the kicks by the correctors is done by a FPGA (Virtex5) on the same microTCA shelf (DSP unit). The feedback algorithm (PID) has been designed and implemented using MATLAB/Simulink with system generator from Xilinx. Calculated kick angles for each fast steering magnets have been transferred from the DSP unit on the microTCA to the steering controller unit made of MTCA.4 through an optical fiber. The power supply controller also accepts the kick values through the network for slow correction. The BPM unit also works to output the mean beam position at QC1 as the EPICS record for COD correction and slow beam-beam kick feedback. Figure 8 shows an example of measured horizontal beam-beam kick using QC1 BPMs.

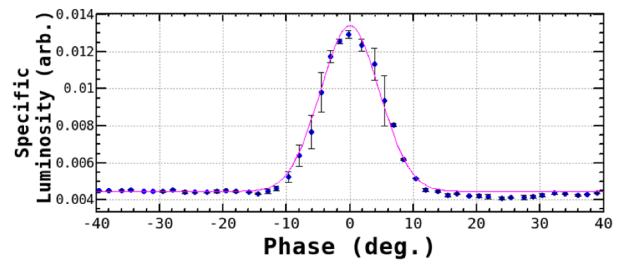
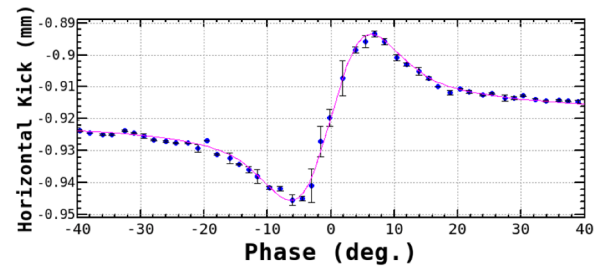


Figure 8: Example of horizontal beam-beam kick (upper) and the specific luminosity.

The resolution has been estimated by the beam to be around 5  $\mu\text{m}$  in left side (QC1LE, QC1LP), 2.5  $\mu\text{m}$  in right side (QC1RE, QC1RP) with beam current of 100 mA. The difference between left and right side comes from the signal loss due to longer cable path.

During phase 2 operation we have measured the beam based gain mapping several times. It was very strange that the gain imbalance in the QC1 BPMs were extremely larger than other BPMs, especially in QC1LP where the minimum gain coefficient was estimated to be 0.4. By the inspection and signal check during the phase 2 operation we could not find the cause of such large gain unbalance. After the phase 2 operation we will open the IP and replace the QC1 chamber assemblies and the bpm cables and try to find the cause of the gain imbalance.

Using the non-colliding and colliding beam, we have measured the slow beam vibration. Figure 9 shows an example of measured beam vibration up to 200 Hz with the beam current of around 140 mA. In the vertical plane there seem several amplitude peaks. The highest corresponds around 15 Hz with the IP converted amplitude of around 0.16  $\mu\text{m}$  which is smaller than 1/10 of vertical size at IP.

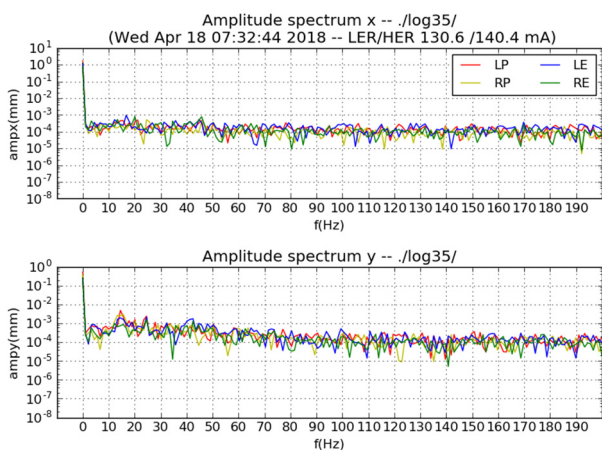


Figure 9: Measured beam vibration using QC1 BPMs with the beam current of LER/HER of 130 mA/140 mA.

We have also tried to close the vertical IP feedback and checked the beam behavior such as the beam oscillation components or luminosity by changing the gain (P) in the PID controller. Unfortunately due to overflow in a summing circuit in the controller caused by large offsets of beam position inputs it caused unexpectedly large canonical kick. There showed no obvious change either in the beam vibration spectrum nor luminosity. Nevertheless, the system did not go unstable even with larger gain. We will change the control circuit to escape the overflow. Also with the larger vertical beam size at IP it might not be easy to check the effect of fast IP feedback. We are considering to artificially excite the vertical beam position at IP to check the effect of IP feedback.

### Bunch Feedback Systems

Figure 10 shows the block diagram of the bunch-by-bunch feedback systems installed in SuperKEKB rings [9]. The system consists of position detection systems, high-speed digital signal processing systems with a base clock of 509 MHz (iGp12 [13]), and wide-band kickers fed by wide-band, high-power amplifiers.

Like the phase 1 operation, in the early stage of the commissioning of both rings we encountered very strong transverse coupled-bunch instabilities which limited the maximum beam currents. After the tuning of the timing and phase of the transverse feedback systems, we successfully suppressed the coupled-bunch instabilities up to the maximum beam current of around 800 mA with the minimum bunch separation of 4 ns.

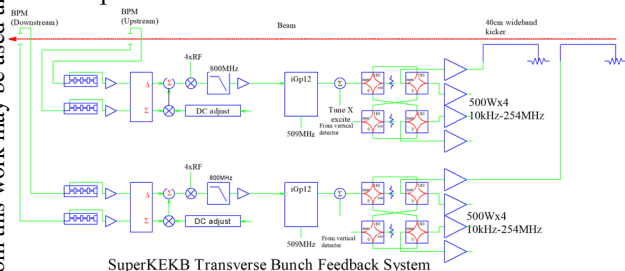


Figure 10: Block diagram of the transverse bunch feedback systems.

During the beam study of electron cloud effect (ECE) in LER we have obtained many transient domain data. Figure 11 shows an example of growing and damping transients with the 4 ns bunch separation with the beam current of 300 mA in the vertical plane. The distribution of the unstable modes and the growth time have changed drastically from the phase 1 time presumably due to the counter measure to suppress the cloud effect in the drift space.

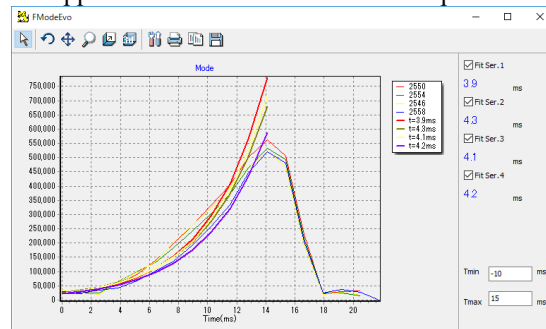


Figure 11: Evolution of vertical unstable modes with by-2 pattern in LER at a current of 300 mA. The growth time constant of mode 2550 was about 3.9 ms, which is much slower than that of obtained at phase 1. The damping time constant is estimated to be less than 1 ms, which is consistent with the phase 1 operation.

During the ECE study and the trial of high beam current at the very end of phase 2, we have encountered the longitudinal coupled-bunch instability in the LER. Though the threshold current for the nominal collision (3.06 spacing) has increased from 660 mA during the phase 1 to 800 mA, it still appeared with higher beam current. Also, the mode and threshold seemed to be affected by the setting of the head position of the vertical collimator nearest to the IP. Though we have the longitudinal bunch-by-bunch feedback systems in LER, we did not have time to tune the system. For phase 3, we will add two more longitudinal feedback cavities with 1 kW of wideband feedback amplifiers per each cavity. The longitudinal system should be tuned in the very early stage of the phase 3.

The bunch feedback related system such as the bunch current monitors, betatron tune monitors, bunch oscillation recorders have worked fine without difficulties. During the collision, we have measured the single bunch beam transfer function of a non-colliding bunch (pilot bunch) using the single bunch excitation function of the iGp12. Also, for the measurement of betatron phase advance between the GTBTs, we have excited the betatron frequency using the PLL excitation function of iGp12. Though it was not so difficult to simply excite the betatron oscillation of a pilot bunch, the beam lifetime of the bunch strongly reduced with a larger oscillation amplitude due to very narrow physical aperture in the ring. For phase 3, we are planning to implement burst beam excitation newly implemented to iGp12.

We have encountered several failures in the transverse wideband amplifiers with maximum power of 500 W due to breakdown of driver stage amplifiers. The failed amplifiers will be repaired soon. Though we have encountered

several failures of high power attenuators (1.5 kW) during phase 1 operation, all the attenuators have been confirmed to be healthy after phase 2 operation.

### Photon Monitors

X-ray monitors (XRM) are installed in both rings, primary for vertical beam size measurements [14, 15]. Since the deep-Si pixel detectors and the fast readout systems developed under the US-Japan collaboration were not in time, we have used the scintillator with a CCD camera, similar to phase 1. Though during phase 1 operation, the LER XRM have shown excellent agreement with the estimation from the optical measurement (X-Y coupling), the beam size from HER XRM was not consistent with the estimation from x-y coupling nor the beam lifetime measurement due to Touschek effect.

For phase 2 operation, we have exchanged the Be filter in the HER x-ray line from 16 mm to 0.2 mm to reduce the small angle scattering in the Be. Also, we have change the vertical betatron function at the light source point from 7.6 m to 28 m. By the measurement of point spread function of X-ray beam in HER in phase 2, the scattering has confirmed to be small enough. The estimated vertical beam size was consistent with that estimated from the x-y coupling measurements.

Figure 12 shows an example of measured vertical beam size at LER during the ECE study for various filling pattern.

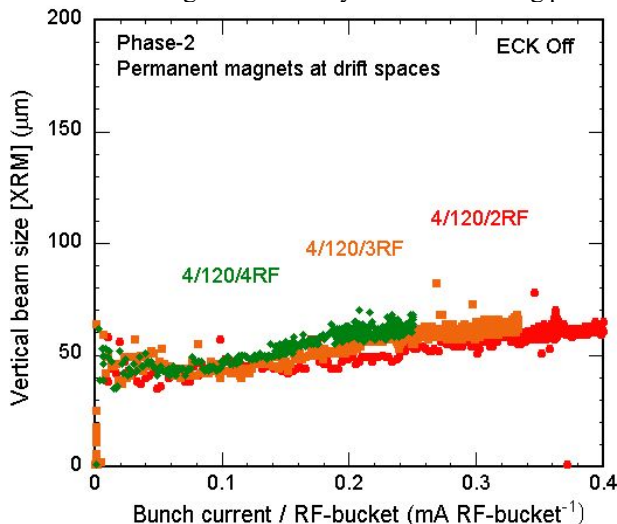


Figure 12: LER vertical beam size at ECE study.

We have also exchanged the diamond mirror in both rings for the visible SR line with 200% of larger aperture. To reduce the stray light in the visible SR line we have added baffles in the line and confirmed the effect using the laser light. With increased visible light we have tried to activate the interferometer for horizontal beam size measurements. Though in HER the system worked well, the SR spot seemed to be changed with the beam current in LER. We will open the mirror chamber to find the weak connection point around the mirror.

The bunch length has been measured using the streak camera for both rings. Figure 13 shows the measured bunch length for HER and LER.

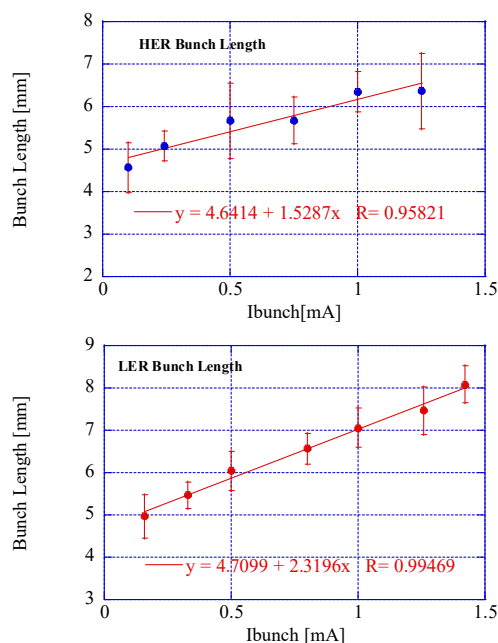


Figure 13: Measured bunch length of HER (upper) and LER (lower) with bunch current.

The bunch lengthening behaviour in HER is consistent with the KEKB because most of the vacuum chamber in arc and straight section have been re-used for SuperKEKB. Though the bunch lengthening in LER is moderated than that of measured in phase 1, it still shows unexpected larger lengthening with bunch current. We will need to find the impedance model to reproduce the behaviour.

The large angle beamstrahlung monitor (LABM) [16] installed just outside the QCS magnets have been commissioned during the phase 2 period. Though it seems still affected by large SR background, the analysis is in progress.

### Beam Loss Monitor

For phase 2 operation, we have replaced the damaged PIN-diode monitors and cables especially around the beam collimators. For newly installed collimators we have added PIN diode monitors both to protect the collimators and to monitor and optimize the beam loss at the collimator. By the requirement from the commissioning team and the Belle II group, we have tuned the gain and the threshold value of beam abort. The fine beam loss value before the beam abort has been recorded using multi-channel fast data loggers. After the suspicious beam abort such as QCS quench we have checked the beam loss behaviours with the change of the cavity voltages and the change of DCCT value to find the real cause of the abort [17].

To abort the beam when the orbit has excused wildly with high beam current operation to protect the vacuum chambers, we have prepared orbit abort system using Libera Brilliance+ in both rings with two BPM position per ring with the betatron phase advance around 90 deg. We have also recorded the post-mortem data of Libera (X, Y and intensity) when the beam position has changed to be out of the threshold value ( $\pm 2$  mm). Though during phase 2 operation we did not enable this abort, the post-mortem



data was useful also to confirm the beam orbit and the intensity just before the abort. As the current BPM for this abort has been selected in the dispersion free section, we plan to add the BPM with large dispersion to record the energy change just before the abort.

## SUMMARY

Beam instrumentation systems for SuperKEKB rings, especially in the positron damping ring, have been constructed and commissioned. All the system has shown excellent performance and helped to realize smooth beam commissioning of the rings. With the experience of phase 2 operation, we will improve the instrumentation to be much useful to realize the performance of the SuperKEKB collider.

The authors would like to express their sincere appreciation to the commissioning group of SuperKEKB for their help in the operation.

This work is partly supported by the US-Japan collaboration in High Energy Physics (R&D for SuperKEKB and the next generation high luminosity colliders).

## REFERENCES

- [1] Y. Funakoshi *et al.*, in *Proc. of IPAC'16*, Korea, Busan, 2016, paper TU0BA01.
- [2] M. Tobiyama *et al.*, in *Proc. of IBIC'16*, Spain, Barcelona, 2016, paper MOAL03.
- [3] Y. Onishi *et al.*, in *Proc. of IPAC'18*, 2018, Vancouver, BC, Canada.
- [4] A. Morita *et al.*, in *Proc of ICHEP'18*, Korea, Seoul, 2018, paper TU0BA01.
- [5] H. Ikeda *et al.*, presented at IBIC'18, China, Shanghai, paper MOPA02, this conference.
- [6] M. Tobiyama, in *Proc. of IBIC'14*, USA, CA, Monterey, USA, 2014.
- [7] M. Tobiyama *et al.*, in *Proc. of IBIC'17*, USA, MI, Grand Rapids, 2017, paper TUPCF09.
- [8] M. Tejima, in *Proc. of IBIC'15*, Australia, Melbourne, 2015, paper TUBLA01.
- [9] M. Tobiyama, *et al.*, in *Proc. of PASJ'16*, Japan, Chiba, 2016, paper TUOM06.
- [10] M. Tobiyama *et al.*, in *Proc. of IBIC'15*, Australia, Melbourne, 2015, paper MOPB018.
- [11] H. Sugimoto *et al.*, in *Proc. of IBIC'17*, USA, MI, Grand Rapids, 2017, paper TU3AB1.
- [12] M. Masuzawa, *et al.*, presented at IBIC'18, China, Shanghai, paper, this conference.
- [13] DimTel, <http://www.dimtel.com/>
- [14] E. Mulyani, *et al.*, Submitted to NIM A.
- [15] E. Mulyani, *et al.*, in *Proc of IPAC'18*, Canada, BC, Vancouver, 2018, paper THPWL074.
- [16] R. Ayad *et al.*, arXiv:1709.01608.
- [17] H. Ikeda *et al.*, in *Proc. of IBIC'16*, Spain, Barcelona, 2016, paper TUAL03.

# UPGRADE AND STATUS OF STANDARD DIAGNOSTIC-SYSTEMS AT FLASH AND FLASHFORWARD

N. Baboi\*, H.-T. Duhme, O. Hensler, G. Kube, T. Lensch, D. Lipka, B. Lorbeer, R. Neumann,  
P. Smirnov, T. Wamsat, M. Werner, DESY, 22607 Hamburg, Germany

## Abstract

Electron beam diagnostics plays a crucial role in the precise and reliable generation of ultra-short high brilliance XUV and soft X-ray beams at the Free Electron Laser in Hamburg (FLASH). Most diagnostic systems monitor each of up to typically 600 bunches per beam, with a frequency of up to 1 MHz, a typical charge between 0.1 and 1 nC and an energy of 350 to 1250 MeV.

The diagnostic monitors have recently undergone a major upgrade. This process started several years ago with the development of monitors fulfilling the requirements of the European XFEL and of the FLASH2 undulator beamline and it continued with their installation and commissioning. Later they have been further improved and an upgrade was made in the old part of the linac. Also the FLASHForward plasma-wakefield acceleration experiment has been installed in the third beamline.

This paper will give an overview of the upgrade of the BPM, Toroid and BLM systems, pointing out to their improved performance. Other systems underwent a partial upgrade, mainly by having their VME-based ADCs replaced with MTCA type. The overall status of the diagnostic will be reviewed.

## INTRODUCTION

FLASH [1] is self-amplified spontaneous-emission free electron laser (SASE-FEL) user facility. It generates high brilliance ultra-short XUV and soft X-ray pulses. It is also a test facility for various studies.

Figure 1 shows a schematic drawing of the facility. Seven TESLA accelerating modules accelerate the beam to an energy of 350 to 1250 MeV. Within each bunch train with a length of typically 400-600  $\mu$ s different lasers generate the sub-trains destined to the various beamlines. These can have different bunch frequency, up to 1 MHz, and bunch charge, typically between 0.1 and 1 nC. The train repetition rate is 10 Hz. During machine setup or special bunches may have a reduced rate of 1 Hz.

While the first 2 beamlines, FLASH1 and FLASH2, generate intense photon pulses for users, a plasma experiment, FLASHForward, was recently installed in the third beamline [2].

The FEL requires a precise control of the beam. The diagnostics system is essential for this, and therefore has to follow the increasing requirements over time.

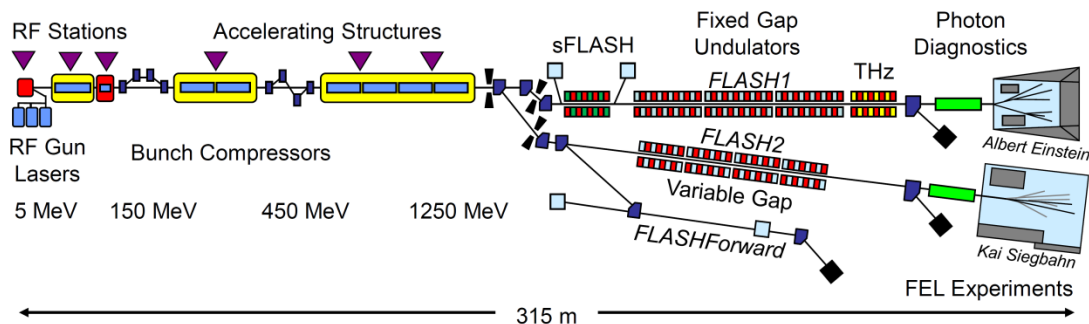


Figure 1: Schematic view of the FLASH facility [1].

This paper describes the recent upgrades that the various diagnostics systems underwent. After an overview of the diagnostics, the monitor types which underwent main upgrades are described, followed by the smaller work. The paper ends with a summary.

## Standard Diagnostics at FLASH

Many different kinds of diagnostics have been installed along the years in FLASH: toroids to monitor the individual bunch charge, beam position monitors (BPM) of various kinds, beam loss monitors (BLM), beam size moni-

tors, mainly OTR stations and wire scanners, dark current monitor etc. So-called special diagnostics has been developed mainly for longitudinal diagnostics, and is not the topic of this paper. Many of the systems deliver bunch-by-bunch information, and have to deal with the different bunch charge and pulse structure of the sub-trains for the various beamlines.

In recent years, many diagnostics systems have been developed for and installed in the European XFEL [3] and FLASH2 [4], which fulfil new requirements. The MTCA.4 standard [5] has been introduced for several systems. Besides the diagnostics, also LLRF and the timing system are based on this standard. Different systems

\* nicoleta.baboi@desy.de.

share crates and processing (CPU) resources, power supplies and remote management capabilities. This makes their maintenance easier, as failure detection and solving is spread over several systems and groups within the institute and abroad. Synergies in the form of hard- and firmware development can also be shared by different systems.

Since their installation in FLASH2, the newly developed diagnostics systems have been further improved and also installed and commissioned in the E-XFEL and FLASHForward. Some of the diagnostics in the old common and FLASH1 beamlines have been also fully or partially upgraded. The changes in the various standard diagnostics systems at FLASH as well as the status of the other monitors are reviewed in the next sections.

Table 1 gives an overview of the main standard diagnostics monitors in FLASH. The current status of the electronics is shown, including the most recent upgrades.

Table 1: Overview of Main Standard Diagnostics Systems at FLASH and Their Electronics Type

System	Electronics Type	#
Toroids	E-XFEL	19
Button BPM	FLASH	39
Stripline BPM	FLASH	34
Magnetic BPMs	FLASH	2
Cold cavity BPMs	TTF2	6
Cavity BPMs	E-XFEL	21
Screen stations	E-XFEL/TTF2	12/20
Wire Scanners	TTF2	7
BLMs	E-XFEL	162
Beam Halo Monitors	E-XFEL	2

### UPGRADED DIAGNOSTICS SYSTEMS

After the initial developments made for the E-XFEL and FLASH2 and their initial commissioning [4], many diagnostics systems have been further developed or improved.

While no standard diagnostics system has been fully exchanged, particularly the vacuum system remaining in general the same, major parts have been replaced for some monitor types. Particularly in the old FLASH1 and common beamlines, the old, VME-based systems, often named TTF2-type, have been replaced with MTCA ones, in order to eliminate some outdated monitors, and to have a unified system in the whole facility. Also, new systems have been installed in FLASHForward. The main upgrade work took place in the summer and winter of 2017.

#### Toroid Upgrade

Toroids, which are AC current transformers, are used for single bunch charge measurement [6]. The front end electronics and the MTCA Rear Transition Module (RTM) filters and dynamically amplifies the induced signal, before sending it to a SIS8300-L2D digitizer [7]. The system offers a high dynamic range, from ca. 0.2 pC to 2 nC.

This system has been installed in all beamlines, replacing the TTF2-type electronics, as well as the temporary solution initially installed at FLASH2 [4]. Figure 2 shows the resolution measured for the first bunch of the train for the FLASH1 and FLASH2 beamlines using a correlation method [8]. The bunch charge was 350 pC in FLASH1 and 60 pC in FLASH2. In both cases the resolution is ca. 0.2 pC rms. The second toroid still runs with the TTF2-type electronics, having a much higher noise.

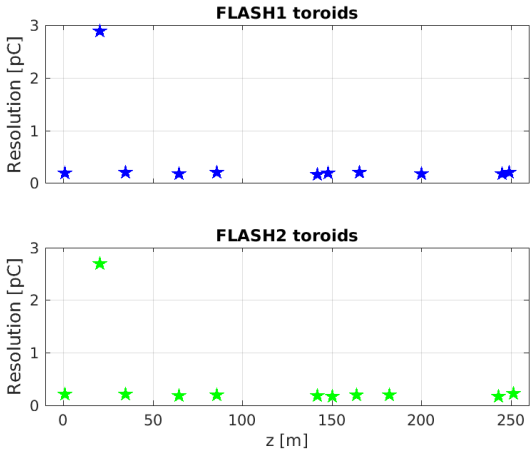


Figure 2: Toroid resolution in the FLASH1 (350 pC) and FLASH2 (60 pC).

In addition, the toroids are also used for transmission interlock. For this they compare the charge of pairs of toroids for the bunch train for each beamline. They monitor charge losses in individual bunches as well as in the integrated charge per train. Fast alarms are forwarded to the machine protection system (MPS). This function has replaced the old toroid protection system [9], which was designed for single beamlines.

For machine setup the toroid system implements a basic pulse detection (with lower accuracy) until the sampling phase is set correctly by the user. Once the toroids are configured in timing mode (full accuracy of ~0.2 pC, as seen in Figure 2) the system is able to detect gun-laser phase changes.

#### Stripline and Button BPM Upgrade

Most of the BPMs installed in FLASH are of stripline and button type. The initial VME-based TTF2 electronics has been developed for bunch charges of 1-3 nC. With the development of the FEL facility and the need for shorter and shorter bunches, the typical charge has been reduced to the order of hundreds of pC and lower. Therefore a new MTCA-based electronics has been developed and installed in the FLASH2 undulator beamline [10]. The signals from 2 opposite pickups are send on the same cable after each other with the help of a delay line. The 4 signals from each monitor are thus fed to 2 channels of a RTM.

The electronics was substantially improved since (Figure 3) [11]. Two BPMs (4 channels) can be connected now to one RTM. The firmware automatically adjusts itself to the signal peak. Other improvements include the



addition of on-board test circuit, the improvement of the sensitivity, of the signal integrity and channel separation, and the addition of the capability to externally discharge the peak detectors. The magnetic BPMs [12] installed after the dump vacuum window, are equipped with the same system. The same RTM is used also for the so-called energy BPMs at the E-XFEL, which consist of button arrays installed in the flat bunch compressor chambers.

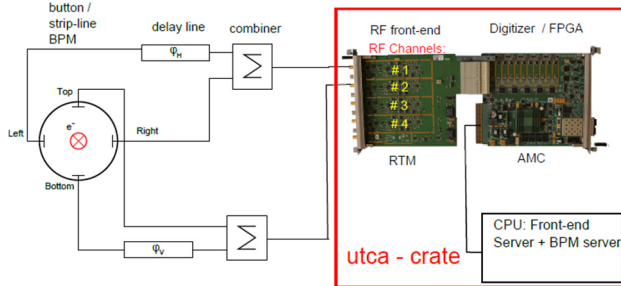


Figure 3: Upgraded stripline and button BPM electronics.

The performance has been evaluated with beam and compared to the old VME system. The charge range has been extended towards low charges, coming close to 10 pC. The resolution has been improved by ca. a factor 10 [11].

### BLM Upgrade

A MTCA-based system has been developed also for the BLM and BHM systems at the E-XFEL and FLASH [13,14].

Figure 4 shows the main parts of a BLM. The light produced by lost electrons or induced photons in the scintillators is sent to a photo-multiplier (PMT). The high voltage is produced locally in the detector front-end, which also pre-processes the signal which is then sent to an RTM connected to a DAMC2 [15].

While this system was installed initially in FLASH2, it is now installed in all 3 beamlines. In a few cases the old scintillators have been re-used, namely the ca. 2m long scintillator ‘paddles’ placed along the undulators in FLASH1.

Recent changes in the system include the so-called “LOLA masking”, for “special bunches”, distributed by the timing system. The BLM system marks these bunches which are rotated by a transverse deflecting structure and kicked to a special screen for longitudinal bunch profile monitoring, causing losses. As these losses should not cause cuts of the beam by the MPS, the BLM signal processing firmware ignores alarms at these bunch positions. The Beam Halo Monitors (BHM) [16], based on diamond and sapphire sensors, installed after the dump vacuum window at the end of each undulator beamline in FLASH1 and FLASH2, have meanwhile also been equipped with the same MTCA electronics as the BLMs. Only a small box including the HV generation and signal matching was specially developed to connect the BHMs to BLM electronics.

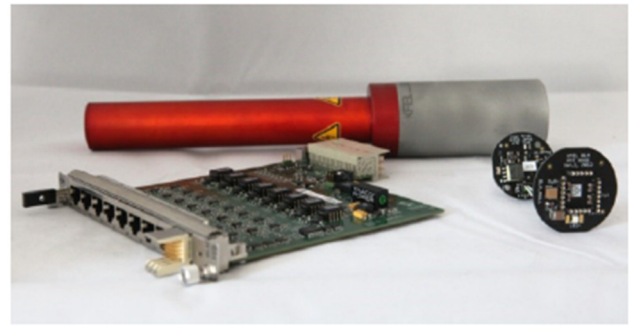


Figure 4: BLM detector with PMT, RTM and PMT base and high voltage generator.

### Other Upgraded Monitors

For several systems only the ADC reading has been upgraded to MTCA type in the summer 2018. The old VME-ADCs, which due to their age needed more and more maintenance work, has been replaced with SIS8300 [7]. This is the case for the cold cavity BPMs, the Faraday cups in the gun section and the ionization chamber briefly described in the following paragraphs. This exchange is relatively uncritical, presuming a re-installation of basically the same servers and re-calibration.

Cold cavity BPMs [17] are installed in the first 6 TESLA modules. These BPMs have been developed more than 20 years ago. They consist of a resonator working at 1.5 GHz and a I/Q mixer based electronics. For two accelerating modules planned to be exchanged, XFEL-type button BPMs are going to be installed. For the remaining cold cavity BPMs, a new electronics development is planned.

Also based on resonances induced in a resonator, the Dark Current Monitor (DCM or DaMon) [18] enables a non-destructive measurement of the dark current, mainly produced by the electron gun. It also delivers an additional monitor of the bunch charge.

Air filled Heliax cables are used as ionization chambers [19]. They are installed along the last 2 m of the beampipe, before the dump window.

Also the ADCs of the Higher Order Mode (HOM) based beam monitors installed at 1.3 GHz TESLA accelerating cavities [20,21] will be replaced with MTCA. They are used for beam alignment and position monitoring. The HOM-electronics for the 3.9 GHz cavities [22] already uses SIS8300 ADCs.

## STATUS OF OTHER MONITORS

In FLASH2 and FLASHForward screen stations developed for the E-XFEL have been installed [23,24]. They used LYSO:Ce screens mounted perpendicular to the beam axis. The light is observed under 45deg in order to suppress potential COTR radiation. The older OTR-screen stations in the common and FLASH1 beamlines [25] are based on 45deg CeYAG screens. It is planned to exchange them with the E-XFEL type on the occasion of a future major upgrade.

The CERN type of wire scanners [26] have been deactivated due to their old age and increased level of maintenance.

nance required. Another reason for this is the presence of screens at most locations where wire scanners are present. A replacement with XFEL type is being considered, in conjunction with the upgrade of the screen system. While also outdated, major maintenance work has been made on the so-called Zeuthen wire scanners [27] in the FLASH1 undulators, both in terms of hardware and small updates in the server. These scanners enable the matching of the beam in the undulator section. Their disassembly is planned in the process of replacing the undulators with variable gap ones.

Cavity BPMs, as developed for the E-XFEL have been installed in FLASH2 and FLASHForward [28]. They contain two resonators one monitoring a dipole mode for beam offset determination, the other a monopole mode, for charge normalization. Two types have been installed: for a beam pipe of 10 mm and respectively 40.5 mm in diameter. A resolution below 1  $\mu\text{m}$  rms has been observed in most cavity BPMs.

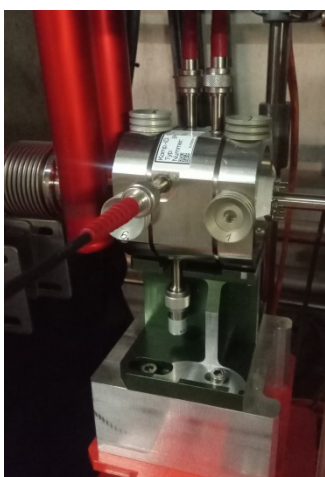


Figure 5: Cavity BPM in the FLASHForward beamline.

Last but not least are the Cherenkov fibres [29] installed at either side of both main undulator sections. They help reduce the losses in the permanent magnets of the undulators, which can cause magnetization loss. Not mentioned here are longitudinal profile monitors.

## SUMMARY AND OUTLOOK

Several diagnostics types have been developed for the E-XFEL and FLASH2, most based on the MTCA technology. Some of these monitors underwent further development and improvement. Further monitors have been installed at the new third beamline, hosting FLASHForward, while the old VME-based monitors in the old part of the linac have been partially replaced with the new system. The most significant changes were made in the button and stripline BPMs, the toroid and BLMs. Other systems underwent more minor changes, like the ADC upgrade for the cold cavity BPMs, ionization chambers and Faraday cups, while others were kept in the original state, like the cavity BPMs, the screen stations and the Cherenkov monitors.

Possible scenarios for future upgrades at FLASH are currently under investigation [30]. These will make upgrade work on the diagnostics system necessary, such as the replacement of the screen and wire scanner stations either with the E-XFEL type or with new design.

## ACKNOWLEDGEMENT

This paper is based on the work of many, many people who directly or indirectly contributed to the design, building and evaluation of the systems.

## REFERENCES

- [1] M. Vogt *et al.*, “Status of the Superconducting Soft X-Ray Free-Electron Laser FLASH at DESY”, in *Proc. IPAC’18*, Vancouver, BC, Canada, p. 1481, 2018.
- [2] A. Aschikhin *et al.*, “The FLASHForward Facility at DESY”, *Nucl. Instrum. & Methods in Phys. Research A*, 806, pp.175, 2016.
- [3] D. Nölle *et al.*, “The Diagnostic System at the European XFEL; Commissioning and First User Operation”, presented at IBIC’18, Shanghai, China, 2018, paper TUOA01, this conference.
- [4] N. Baboi and D. Nölle, “Commissioning of the FLASH2 Electron Beam Diagnostics in respect to its Use at the European XFEL”, in *Proc. of IBIC’14*, Monterey, CA, USA, p. 712, 2014.
- [5] MicroTCA.4, <http://mtca.desy.de/>
- [6] M. Werner *et al.*, “A Toroid based Bunch Charge Monitor System with Machine Protection Features for FLASH and XFEL”, in *Proc. of IBIC’14*, Monterey, CA, USA, p. 521, 2014.
- [7] <http://www.struck.de/sis8300.html>
- [8] N. Baboi *et al.*, “Resolution studies at beam position monitors at the FLASH facility at DESY”, *AIP Conf.Proc.* 868 (2006) 227-237.
- [9] A. Hamdi *et al.*, “Toroid Protection System for FLASH”, in *Proc. of DIPAC’07*, Venice, Italy, p. 349 (2007).
- [10] B. Lorbeer *et al.*, “Development Status and Performance Studies of the new MicroTCA based Button and Strip-line BPM Electronics at FLASH2”, in *Proc. of IBIC’15*, Melbourne, Australia, p. 335, 2015.
- [11] B. Lorbeer *et al.*, “High Resolution and Low Charge Button and Strip-Line Beam Position Monitor Electronics Upgrade at FLASH”, in *Proc. of IPAC’18*, Vancouver, BC, Canada, p. 1923.
- [12] N. Baboi *et al.*, “Magnetic Coupled Beam Position Monitor for the FLASH Dump Line”, in *Proc. of BIW’10*, Santa Fe, NM, USA, p. 214, 2010.
- [13] T. Wamsat *et al.*, “Status and Commissioning of the European XFEL Beam Loss Monitor System”, in *Proc. of IPAC’18*, Vancouver, BC, Canada, p. 1940, 2018.
- [14] T. Wamsat, “The European XFEL Beam Loss Monitor System”, presented at IBIC’18, Shanghai, China, 2018, paper WEOB03, this conference.
- [15] DESY Advanced Mezzanine Card, [http://fe.desy.de/fea/projects/tca\\_developments/damc2](http://fe.desy.de/fea/projects/tca_developments/damc2)
- [16] A. Ignatenko *et al.*, “Beam Halo Monitor for FLASH and the European XFEL”, in *Proc. of IPAC’12*, New Orleans, LA, USA, p. 816, 2012.

- [17] R. Lorenz *et al.*, “First Operating Experiences of Beam Position Monitors in the TESLA Test Facility Linac”, in *Proc. of PAC’97*, Vancouver, BC, Canada, p. 2137, 1997.
- [18] D. Lipka *et al.*, “Dark Current Monitor for the European XFEL”, in *Proc. of DIPAC’11*, Hamburg, Germany, p. 572, 2011.
- [19] N. Baboi *et al.*, “New Electron Beam Diagnostics in the FLASH Dump Line”, in *Proc. of BIW’10*, Santa Fe, NM, USA, p. 420, 2010.
- [20] S. Molloy *et al.*, “High Precision SC Cavity alignment Measurements with Higher Order Modes”, *Measur. Sci.Tech.* 18, pp. 2314-2319, 2007.
- [21] J. Wei *et al.*, “Stability Study of Beam Position Measurement based on Higher Order Mode Signals at FLASH”, TUPB07, presented at IBIC’18, Shanghai, China, 2018, this conference.
- [22] N. Baboi *et al.*, “Commissioning of the Electronics for HOM-based Beam Diagnostics at the 3.9 GHz Accelerating Module at FLASH”, in *Proc. of IBIC’14*, Monterey, CA, USA, p. 311, 2014.
- [23] C. Wiebers *et al.*, “Scintillating Screen Monitors for Transverse Electron Beam Profile Diagnostics at the European XFEL”, in *Proc. of IBIC’13*, Oxford, p. 807, 2013.
- [24] D. Lipka *et al.*, “First Experience with the Standard Diagnostics at the European XFEL Injector”, in *Proc. of IBIC’16*, Barcelona, Spain, p. 14, 2016.
- [25] K. Honkavaara *et al.*, “Design of OTR beam profile monitors for the TESLA Test Facility, phase 2 (TTF2)”, *Conf.Proc. C030512* (2003) 2476.
- [26] D. Nölle, “The Diagnostic System of TTF II”, in *Proc. of EPAC’02*, Paris, France, p. 242, 2002.
- [27] U. Hahn *et al.*, “Wire scanner system for FLASH at DESY”, *Nucl.Instrum.Meth. A592* (2008) 189-196.
- [28] D. Lipka *et al.*, “FLASH Undulator BPM Commissioning and Beam Characterization Results”, in *Proc. of IBIC’14*, Monterey, CA, USA, p. 315, 2014.
- [29] W. Goettmann *et al.*, “Beam Profile Measurement with Optical Fiber Sensors at FLASH”, in *Proc. of DIPAC’07*, Venice, Italy, p. 123, 2007.
- [30] M. Vogt *et al.*, “Possible Upgrades of FLASH — a View from the Accelerator-Perspective”, in *Proc. of IPAC’18*, Vancouver, BC, Canada, p. 1477, 2018.



# UPGRADE OF THE MACHINE PROTECTION SYSTEM TOWARD 1.3 MW OPERATION OF THE J-PARC NEUTRINO BEAMLINE

K. Sakashita\*, M.Friend, K.Nakayoshi, High Energy Accelerator Research  
Organization (KEK), Tsukuba, Japan

S. Yamasu, Y. Koshio, Okayama University, Okayama, Japan

## Abstract

The machine protection system (MPS) is one of the essential components to realize safe operation of the J-PARC neutrino beamline, where a high intensity neutrino beam for the T2K long baseline neutrino oscillation experiment is generated by striking 30 GeV protons on a graphite target. The proton beam is extracted from the J-PARC main ring proton synchrotron (MR) into the primary beamline. The beamline is currently operated with 485 kW MR beam power. The MR beam power is planned to be upgraded to 1.3 MW. The neutrino production target could be damaged if the high intensity beam hits off-centered on the target, due to non-uniform thermal stress. Therefore, in order to protect the target, it is important to immediately stop the beam when the beam orbit is shifted. A new FPGA-based interlock module, with which the beam profile is calculated in real time, was recently developed and commissioned. This module reads out signals from a titanium-strip-based secondary emission profile monitor (SSEM) which is placed in the primary beamline. An overview of the upgrade plan of the MPS system and the results of an initial evaluation test of the new interlock module will be discussed.

## INTRODUCTION

T2K(Tokai-to-Kamioka) is a long-baseline neutrino oscillation experiment. One of the main physics motivations is a search for CP (Charge-Parity symmetry) violation in neutrino oscillation. If CP is not conserved in neutrino oscillations, it may indicate a significant hint for the origin of our matter dominate universe. T2K can measure the CP asymmetry by comparing the oscillation probabilities between  $\nu_\mu \rightarrow \nu_e$  and  $\bar{\nu}_\mu \rightarrow \bar{\nu}_e$ . Since those probabilities are small, a high intensity neutrino beam is essential to measure the CP asymmetry. A high intensity muon neutrino beam is produced at the Japan Proton Accelerator Research Complex (J-PARC) at Tokai village, Ibaraki, Japan. The muon neutrino (anti-neutrino) beam is then directed to the Super-Kamiokande detector located 295 km away from J-PARC.

Recently, T2K operated stably with 485 kW of MR beam power. Figure 1 shows the accumulated protons on target (POT) and the beam power since 2010. T2K collected  $3.16 \times 10^{21}$  POT up to the end of May 2018. Based on the data collected until December 2017, T2K made a preliminary report that the CP conserving phase values ( $0, \pm\pi$ ) are outside of  $2\sigma$  region [1]. This result indicates a hint of neutrino CP violation, although the significance is still low.

---

\* kensh@post.kek.jp

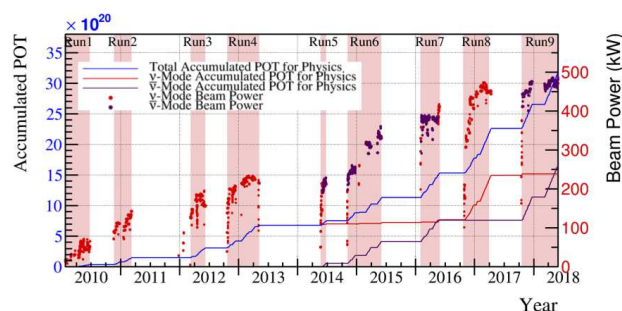


Figure 1: T2K accumulated protons on target (POT) and the beam power as a function of year.

In order to confirm the measurement of CP violation, T2K plans to collect more data up to  $2 \times 10^{22}$  POT by 2026 (T2K extension proposal, J-PARC E65 [2]). The expected sensitivity to CP violation with the exposure of  $2 \times 10^{22}$  POT is  $3\sigma$  assuming certain values of the oscillation parameters. In the T2K extension proposal, three upgrades are planned; (1) upgrade of the J-PARC MR beam power up to 1.3 MW, (2) increase of signal statistics by both hardware and analysis improvements, and (3) improvement of systematic uncertainties by upgrade of the T2K near detector.

The MR beam power will be upgraded up to 1.3 MW by both shortening the repetition time from 2.48 s to 1.16 s, and increasing the number of protons per pulse up to  $3.2 \times 10^{14}$  [3]. Table 1 shows the achieved and target values. For the shortened repetition time, the MR main magnet power supplies will be upgraded. Intensive development work on the new power supply design has been performed. Installation of these new power supplies will be completed by 2021. For the increase of the number of protons per pulse, intensive MR beam studies are in progress. So far, 520 kW with  $2.7 \times 10^{14}$  protons per pulse and 2.48 s repetition has been successfully performed. The total beam loss in the MR was estimated to be  $\sim 1$  kW. Although further beam loss reduction is necessary, this demonstrates that the MR has the capability of achieving  $\sim 1$  MW beam operation with 1.3 s of the repetition time.

Table 1: MR Operation Parameters for the Achieved and Target Beam Power.  $N_p$  represents the number of protons per pulse.

	Achieved	Target
Beam Power [MW]	0.49	1.3
$N_p$	$2.5 \times 10^{14}$	$3.2 \times 10^{14}$
Repetition Time [s]	2.48	1.16

## MACHINE PROTECTION SYSTEM AT J-PARC NEUTRINO BEAMLINE

Figure 2 shows an overview of the neutrino beamline at J-PARC. High intensity protons from the MR strike a graphite target and produce charged pions and kaons. Neutrinos (anti-neutrinos) can be produced from decays of positive (negative) charged pions in their flight in the decay volume. Either sign pions can be selected by flipping the horn electromagnet current direction. Toward 1.3 MW operation, some of the neutrino beamline equipment will be upgraded. For example, the cooling system of the horn and the target will be reinforced in order to remove the heat generated by the 1.3 MW beam. The horn power supplies and beamline data acquisition system will be upgraded to accept  $\sim 1$  Hz operation.

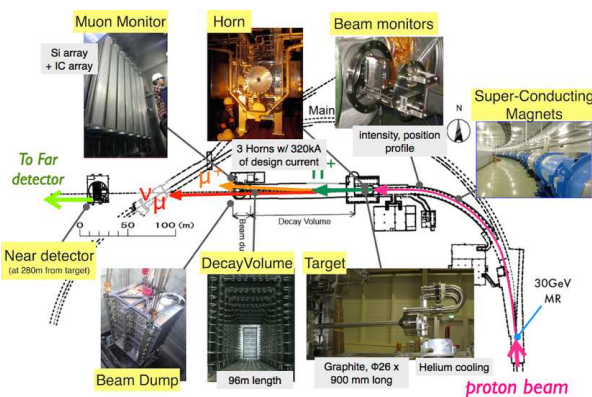


Figure 2: Overview of the neutrino beamline at J-PARC.

The machine protection system (MPS) at the neutrino beamline will be also upgraded in order to realize safe and stable operation with 1.3 MW beam. When any failure of beamline equipment and/or high beam loss in the primary beamline occur, then MPS immediately extracts the beam in the MR to the abort line and stops the next beam injection. The energy of single pulse at 1.3 MW operation (i.e.  $3.2 \times 10^{14}$  protons per pulse) corresponds to 1.6 MJ/pulse. There is a potential risk in such high intensity beam operation due to the high energy. For example, serious damage will occur when a high intensity beam pulse hits certain beamline equipment. As another example, serious damage to the target will occur if the high intensity beam pulse continuously hits off-centered at the target. In order to avoid these cases, an interim interlock system for the beam position and profile at the target is currently adopted.

## DEVELOPMENT OF BEAM POSITION AND PROFILE INTERLOCK MODULE

Figure 3 shows the present scheme of the beam position interlock. Signals from a beam profile monitor are digitized by readout electronics and those data are collected by a data acquisition (DAQ) system. One online monitor PC in the DAQ system performs a real-time calculation of the beam position and issues an MPS if the beam position on the target

is shifted by more than 1.5 mm in order to avoid the case that the beam continuously hits off-centered at the target. However, this scheme needs more than 1 second to issue the MPS after the beam is injected to the primary beamline, and therefore the next beam pulse is occasionally already injected to the MR. Cases like this will increase when the MR repetition time becomes short in the future. This situation is undesirable because the injected beam in the MR will be extracted to the abort line while the capacity of the abort dump is currently limited.

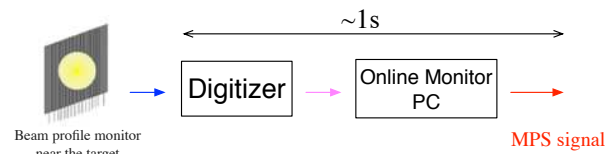


Figure 3: The present scheme of the beam position interlock.

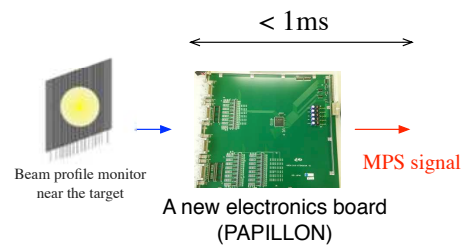


Figure 4: The new scheme of the beam position interlock using a newly developed electronics board, PAPILLON.

Figure 4 shows an idea of a new scheme for the beam position interlock. An electronics board named PAPILLON<sup>1</sup> is newly developed [4]. In the PAPILLON, signals from a beam profile monitor are digitized and sent to a FPGA which is embedded on the board. The FPGA can perform a real-time calculation of the beam position and generate the MPS signal if the calculated position is outside the pre-defined acceptable range. In this new scheme, the latency to issue the MPS signal can be significantly improved.

The PAPILLON board utilizes signals from a beam profile monitor located at the primary beamline, Segmented Secondary Emission Monitor (SSEM) [5]. There are 19 SSEMs along the beamline, as shown in Fig. 5. Figure 6 shows a schematic view of an SSEM. Twenty-four strips  $5 \mu\text{m}$  thick Ti foil in each plane (horizontal and vertical, total 48 strips) are used to measure the beam profile. Since each SSEM causes 0.005% beam loss, all of the SSEMs are only inserted in the beamline during beam tuning except for one (SSEM19), which is placed at the most downstream end of the primary beamline. SSEM19 is utilized to continuously monitor the beam position and profile in order to protect the target.

The analog signal from each strip of the SSEM is fed into the PAPILLON board and digitized by an 80 MHz sampling ADC. There are 24 analog input channels on the board. The digitized signal of all 24 channels are gathered by a FPGA

<sup>1</sup> PAPILLON stands for beam Position And Profile interLock mOdule for Neutrino experiment

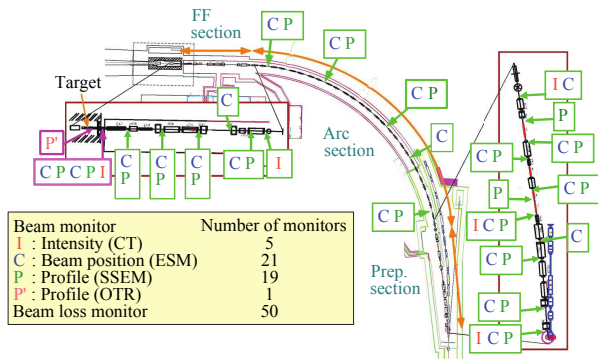


Figure 5: Beam monitors at the primary beamline.

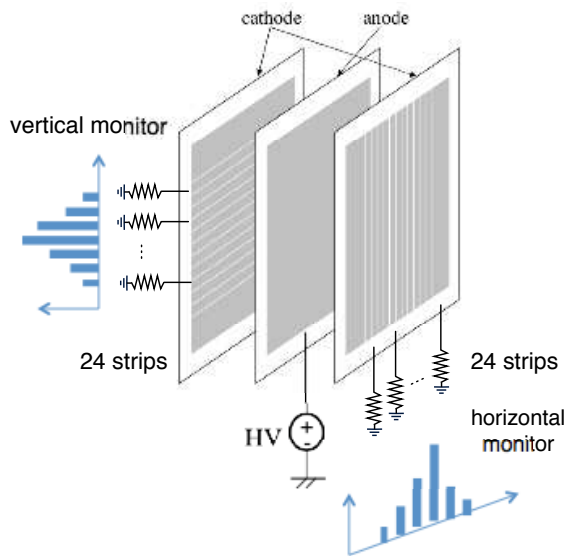


Figure 6: A schematic view of the SSEM.

(Xilinx Artix-7 families). An ethernet interface is adopted on the board in order to configure some of the parameters used in the PAPILLON and to transfer the data to a DAQ PC. In the FPGA, the beam position is calculated by the following procedures;

1. calculate an integrated ADC value for each strip (Fig. 7 (a)) over the single pulse beam duration,

$$Q_s = \sum_t^{t \leq 8\mu s} (p(t) - pedestal),$$

where  $p(t)$  is the ADC value at the time of  $t$  measured by the 80 MHz sampling ADC, and  $pedestal$  is the offset value of the strip signal,

2. calculate the beam position as the weighted mean of the profile of  $Q_s$ ,  $\frac{\sum_{s=0}^{23} Q_s \times x_s}{\sum_{s=0}^{23} Q_s}$ , where  $x_s$  is the center position of the strip  $s$  (Fig. 7 (b)).

Several verification tests were performed so far. In the latest verification test with actual beam, SSEM06, which is placed in the upstream section of the primary beamline, was utilized to evaluate the PAPILLON performance. The

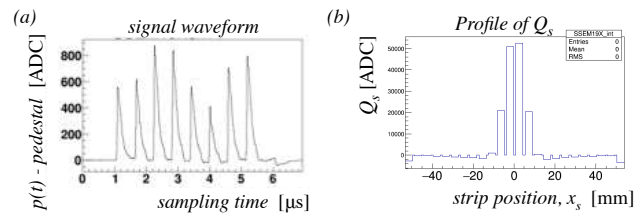


Figure 7: (a) shows an example of signal waveform after the pedestal subtraction,  $p(t) - pedestal$ . (b) shows an example of the profile of  $Q_s$ .

proton beam position at SSEM06 was intentionally changed by changing the upstream dipole and horizontal steering magnets while the beam power was set to 35 kW. The beam position was also calculated in the online monitor PC using a detailed off-line analysis method. Figure 8 shows the comparison between the beam position calculated in the FPGA and the online monitor PC. It is confirmed that the beam position calculation by the PAPILLON board was consistent with the one calculated by the online monitor PC. The latency of the MPS was also measured using the PAPILLON board. The measured value was 9  $\mu s$  which is fast enough to stop the next beam injection to the MR<sup>2</sup>.

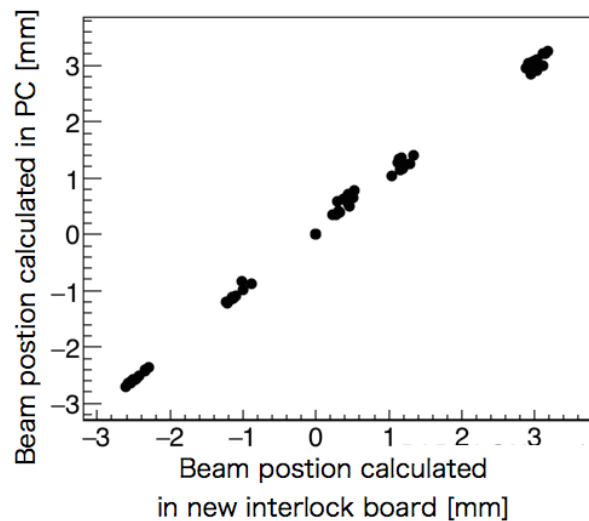


Figure 8: Comparison between the beam position calculated by the FPGA and the online monitor PC

## SUMMARY AND PROSPECT

The J-PARC neutrino beamline will be upgraded for 1.3 MW MR beam power toward the discovery of CP violation in neutrino oscillation. The machine protection system is one of the essential components to realize safe operation with such high intensity beam.

A new electronics board which will issue the beam position and profile interlock, PAPILLON, is under development.

<sup>2</sup> The expected time between the beam extraction to the neutrino primary line and the next beam injection to the MR is a few hundred millisecond.



The basic performance, including the beam position calculation by an FPGA has been verified using actual beam. Further verification tests are also planned to confirm its long-term stability and to check potential dependence of the calculated beam position on the beam intensity. Moreover, in addition to the beam position, the beam profile (width) measurement is also important. Development of FPGA firmware to calculate the beam width is in progress. We plan to install the PAPILLON and start its operation before the MR starts operation with a shortened repetition time.

## ACKNOWLEDGEMENTS

We'd like to thank the KEK IPNS electronics-system group and J-PARC neutrino facility group for their support of the PAPILLON development. This work is supported by the JSPS KAKENHI (Grant No. 16H06288).

## REFERENCES

- [1] "T2K Status, Results, and Plans" presented by M. Wascko at Neutrino 2018 conference, doi:10.5281/zenodo.1286751
- [2] K. Abe *et al.*, "Proposal for an Extended Run of T2K to  $20 \times 10^{21}$  POT," arXiv:1609.04111 [hep-ex].
- [3] T. Koseki, "Upgrade Plan of J-PARC MR - Toward 1.3 MW Beam Power," doi:10.18429/JACoW-IPAC2018-TUPAK005
- [4] [http://openit.kek.jp/project/beam\\_monitor\\_interlock/beam\\_monitor\\_interlock](http://openit.kek.jp/project/beam_monitor_interlock/beam_monitor_interlock)
- [5] M. Friend, "Beam Parameter Measurements for the J-PARC High-Intensity Neutrino Extraction Beamline", presented at IBIC'18, Shanghai, China, Sep. 2018, paper MOPB07, this conference.

# THE REMOVAL OF INTERFERENCE NOISE OF ICT USING PCA METHOD\*

J. Chen<sup>1</sup>, Y.B. Leng<sup>†</sup>, N. Zhang, L.Y. Yu

Shanghai Institute of Applied Physics, Chinese Academy of Science, 201204 Shanghai, China

<sup>1</sup>also at University of the Chinese Academy of Science, 100049 Beijing, China

## Abstract

The measurement of beam charge is a fundamental requirement to all particle accelerators facility. Shanghai soft X-ray free-electron laser (SXFEL) started construction in 2015 and is now in the commission phase. Although integrated current transformer (ICT) were installed in the entire FEL for the measurement of the absolute beam charge, the accurate measurement becomes difficult in the injector and the main accelerator section due to the noise interference from external factors such as klystron modulator. The evaluation of the source of noise signals and the procession of noise reduction using the principal component analysis (PCA) are proposed in this paper. Experiment results show that PCA method combing with polynomial fitting method can effectively remove the interference noise from the klystron modulator and it can also improve the resolution of the ICT system. Detailed experiment results and data analysis will be mentioned as well.

## INTRODUCTION

Beam charge is a fundamental parameter for the particle accelerator facility; therefore, the beam current detector is a very important diagnostic means. Beam charge measurement methods including intercepting measurements such as Faraday cup which often used for LINAC, transfer line and storage ring. Another brunch is the Non-intercepting measurements, DCCT often be used to measure the DC current and the beam lifetime in the booster and storage ring. But for the ultra-fast short pulse charge, since ICT has a time response of the order of ps to ns, it is widely used in LINAC and transfer line for the measurement of bunch charge.

For the ICT, typical usage is the use of Bergoz's ICT probe and BCM-IHR-E processor which can be seen in Fig. 1.

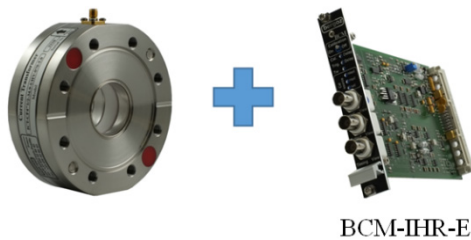


Figure 1: ICT and BCM processor.

The secondary coil of the transformer coupling electron

pulse signal and then be widened through the shaping network, and the integral area of the output pulse is proportional to the amount of charge. The diagram of Bergoz ICT is shown in Fig. 2.

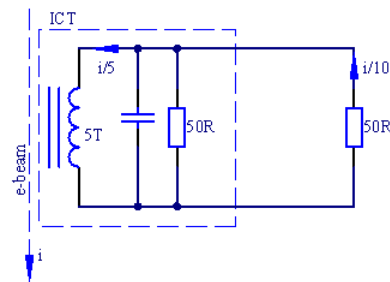


Figure 2: Diagram of Bergoz ICT.

If the input impedance of the external signal processing circuit is also 50 ohms, the Eq.(1) and Eq.(2)are satisfied between the beam charge  $Q$ , the bunch current  $i$ , and the voltage signal  $u_0$  detected by the signal processing circuit:

$$u_0 = \frac{i}{5} * \frac{1}{2} * 50\Omega. \quad (1)$$

$$Q = \int idt = \int \frac{5*2*u}{50\Omega} dt \quad (2)$$

Therefore, it is only necessary to measure the integral value of the output voltage pulse signal, the original beam charge can be calculated by combining the probe calibration coefficient. Typical signal processing method like BCM-IHR is to use an analog pulse integrator integrates the output pulse signal of ICT and a level signal which proportional to the integral value can be sampled and quantified by a slow ADC to calculate the beam charge.

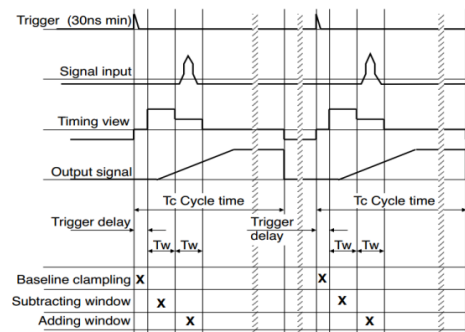


Figure 3: Timing of the BCM-IHR.

Figure 3 show the timing of the BCM-IHR processor. The signal processing is initiated by the external positive-going trigger pulse, then the timer creates three successive time windows: a trigger delay window and two integra-

\*Work supported by The National Key Research and Development Program of China (Grant No. 2016YFA0401903, 2016YFA0401900)

<sup>†</sup>lengyongbin@sinap.ac.cn

tion windows. One integrator integrates the pulse signal, the other integrates the input noise and baselineoffset. Then the pulse charge is obtained by summing the two integrators: the first with negativesign, the second with positive sign [1]. Since the integration window of BCM is in the order of us, if there is an interference signal of the order of MHz and the integration window is not on the integer period, it will easily lead to a large measurement error. So for the typical system, the advantage is that the requirement for DAQ is lower. However, the disadvantage is that the anti-interference ability is poor, external interference signals such as the AC signal comes from the grounded or the modulator noise will be simultaneously integrated and have a big effect on the beam charge measurement.

## SCHEME OF SSRF AND SXFEL

Taking into account the above situation, the design of the SSRF beam charge measurement system uses a digital sampling oscilloscope as a data acquisition device to directly quantize the original waveform of the ICT output. If there is an interference signal, it can be processed by the digital filtering algorithm or feed-forward baseline recovery algorithm remove the noise, and then numerical integration can be used to calculate the bunch charge.

For the acquisition of oscilloscope data, the embedded IOC software was developed. The scheme of ICT in SSRF and SXFEL is shown in Fig. 4.

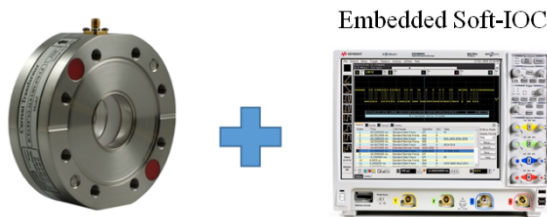


Figure 4: Scheme of ICT in SSRF and SXFEL.

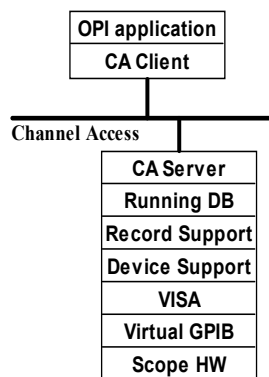


Figure 5: Diagram of embedded IOC.

Taking the oscilloscope as a standard IO device and using the CPU of oscilloscope as the IOC, write the driver to call the VISA Library interference of the machine to obtain the original data. The structure is shown in Fig. 5.

The OPI layer calls the channel access client function (CA Client) to send a data request. When the channel access server (CA Server) in the IOC receives the data

request, then using the form of the running database record to obtain the data. After evaluation and test, it can work well under the data refresh rate of 10 Hz [2].

With this scheme, when there is noise crosstalk coming in, it can be processed by digital signal processing algorithm, so the processing method of ICT noise signal needs to be studied.

## DATA PROCESSING FOR ICT

Multiple ICTs are used on the whole line of the SXFEL and straight line and transport line in SSRF, the layout can be seen in Fig. 6 and Fig. 7.

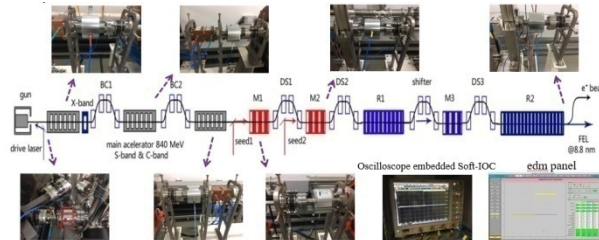


Figure 6: Sensors layout in SXFEL.

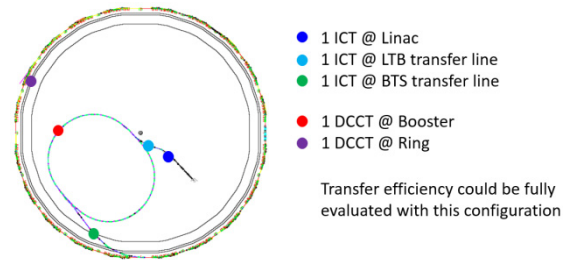


Figure 7: Sensors layout in SSRF.

For the ICTs in SXFEL, the characteristics of the waveform can be divided into three categories, one is only contains thermal noise, which can directly integrate the quantized ICT original waveform, as shown in Fig. 8.

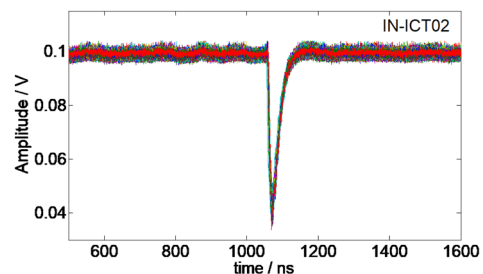


Figure 8: ICT waveform only contains thermal noise.

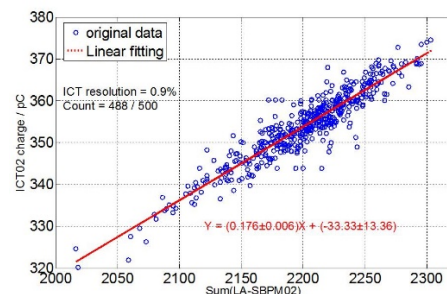


Figure 9: Bunch charge resolution of the ICT.



For this case, it is usually possible to integrate the quantized waveform directly to calculate the beam charge. But the application of the PCA method can separate the noise, improving the resolution of the ICT system to a certain degree especially under the low charge conditions [3].

The other case is that the ICT at the exit of the electron gun, the waveform of which is shown in Fig. 10. The reason that the waveform is concave due to the ICT is interfered by the dark current generated by the RF system. In addition, there is also have a modulation effect by high frequency signals. Fig. 11 show the waveform of the dark current when the driving laser is turn off.

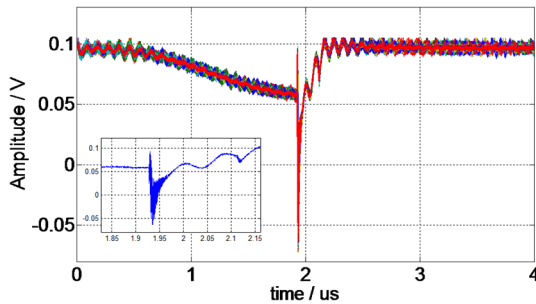


Figure 10: ICT waveform at the exit of the electron gun.

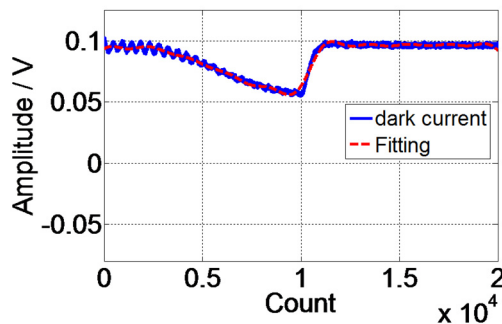


Figure 11: Waveform of dark current.

In this case, due to the existence of dark current, if we use analog integrator like BCM-IHR to set two windows to integrate the area, it will bring a large measurement error to the beam charge. Therefore, we can process the quantized ICT data in the digital domain to remove the effects of interfering signals.

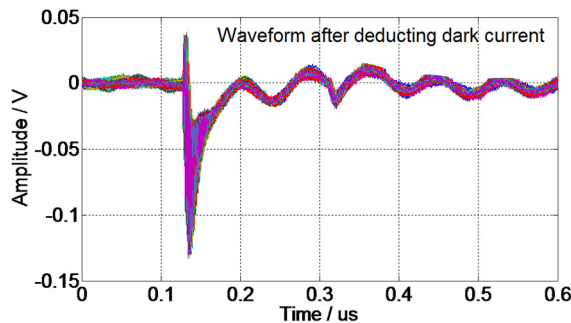


Figure 12: Waveform after subtracting dark current.

Fig.12 show the waveform after subtracting the dark current. But there is also have a modulation effect by high

frequency signals. Therefore, we use the PCA method to separate the noise patterns and analyze the noise sources based on the time domain waveform and spectra of the separated noise patterns[4].

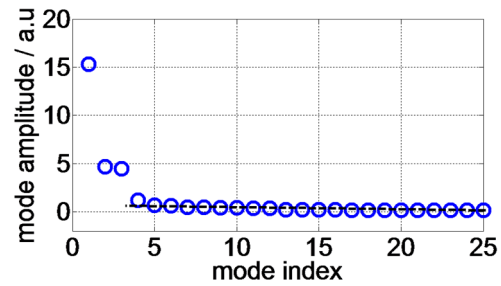


Figure 13: Singular value of IN-ICT01.

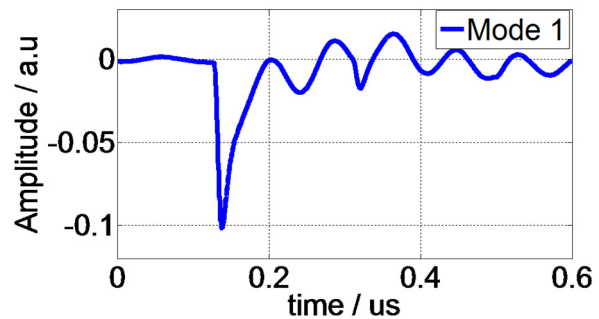


Figure 14: Waveform of model1.

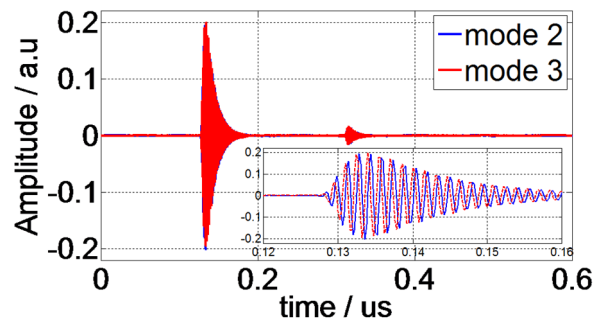


Figure 15: Waveform of mode2 and mode3.

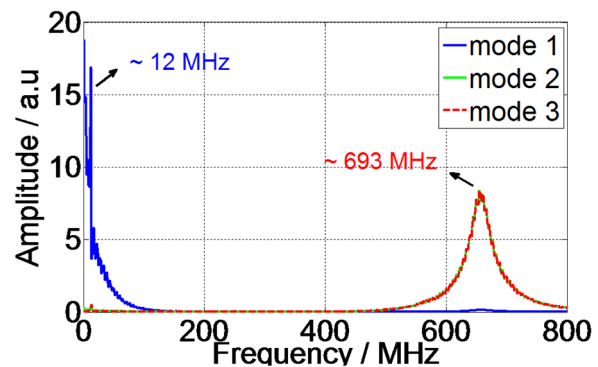


Figure 16: Spectrum of the first four modes.

From the Fig. 13, there has three modes were bigger than the others obviously, so we mainly analyse the first four modes. The waveform of the first mode can be seen in Fig. 14, combine the spectrum of Fig. 16, it can analyse that this is the main mode of the ICT but still have a low

frequency interference without separation. The waveform of mode2 and mode3 are shown in Fig. 15, it like a signal of a resonant cavity and the resonant frequency at 673 MHz but we have not analyzed the source of this signal now. In order to verify it comes from the algorithm rather than the actual physical quantity, we try to use the digital filtering algorithm to process the original data and the results verifies the conjecture we proposed.

Considering the main mode of the ICT, we only keep the first mode and remove the others mode and then convert back to real space. The waveform after PCA process can be seen in Fig. 17.

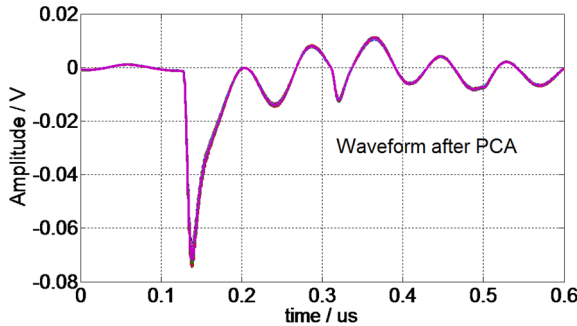


Figure 17: Waveform after PCA processing.

Although the high-frequency interference mode and noise mode are removed, the pattern related to the amount of beam charges still existed. For such interference, the polynomial fitting method is used to fit the interference signal and remove it. The fitting result is shown in Fig. 18.

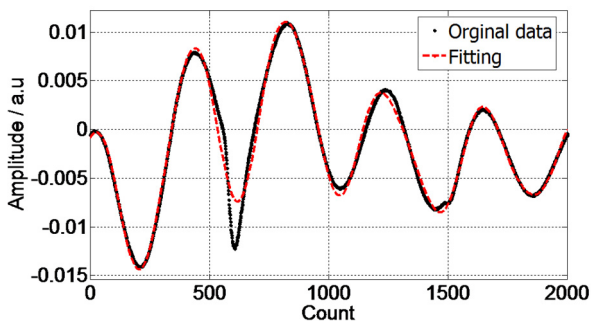


Figure 18: Polynomial fitting for the interference signal.

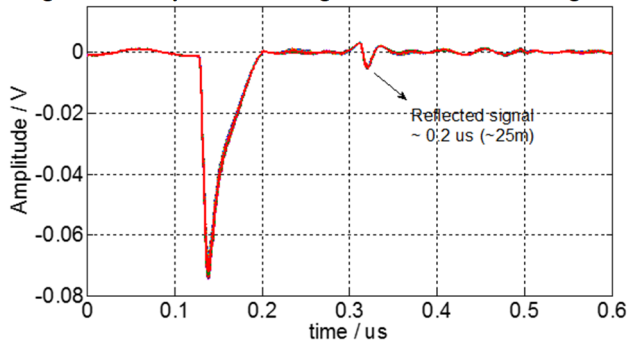


Figure 19: Waveform after deducting the fitting value.

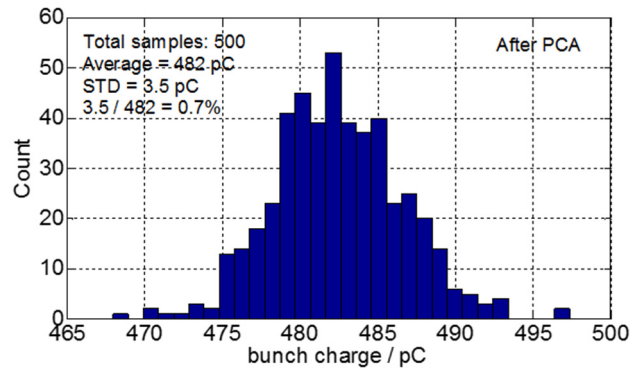


Figure 20: Charge resolution of the ICT.

After deducting the fitting value, the ICT waveform after processing through the digital domain was obtained which is shown in the Fig. 19. We can also find the phenomenon of signal reflection that may be caused by impedance mismatch. The charge resolution of the ICT about 0.7% after PCA method using two ICTs for correlation analysis.

## CONCLUSION

In this paper, we introduced the typical usage of ICT and analyzed the advantage of low requirement for DAQ. But it is also susceptible by noise and resulting in incorrect charge measurement. Based on this consideration, SSRF and SXFEL adopts the architecture based on digital oscilloscope and Soft-I/O. The benefit is that quantified ICT signals can be processed in the digital domain to remove the interference signal. Some experiments were performed in SXFEL, due to the presence of dark current and high frequency noise, signal processing can only be performed in the digital domain. The experimental results show that the PCA method combined with the polynomial fitting method can effectively remove the interference of multiple noises.

On the other hand, due to the in-air ICT be used and the external shield is designed by ourselves. There maybe reasons such as unsatisfactory process conditions, resulting in unsatisfactory shielding effect. In the next step, we will purchase in-flange ICT for testing.

## REFERENCES

- [1] *Beam charge Monitor Integrate-Hold-Reset User's Manual*, Bergoz Instrumentation, 01630 Saint Genis Pouilly, France, pp. 9-12, <http://www.bergoz.com/sites/www.bergoz.com/files/bcm-ihmanual13-0>
- [2] Y.B. Lenget *et al.*, "Scope-embedded IOC development in SSRF", in *Proc. ICALEPCS'07*, Knoxville, Tennessee, USA, Oct 2007, pp. 117-119
- [3] J. Irwin *et al.*, "Model-independent beam dynamics analysis", *Phys. Rev. Lett.*, vol. 82, pp. 1684-1687, Feb. 1997, doi:10.1103/PhysRevLett.82.1684
- [4] Y.B. Leng *et al.*, "Cavity BPM Performance Online Evaluation using PCA Method", in *Proc. IPAC'16*, Busan, Korea, May 2016, pp. 208-210, doi:10.18429/JACoW-IPAC2016-MOPMB051

# STATUS OVERVIEW OF THE HESR BEAM INSTRUMENTATION

C. Böhme, A. Halama, V. Kamerdzhev, F. Klehr, B. Klimczok, M. Maubach, S. Merzliakov,  
D. Prasuhn, R. Tölle, Forschungszentrum Jülich, Germany

## Abstract

The High Energy Storage Ring (HESR), within the Facility for Antiproton and Ion Research (FAIR), will provide proton and anti-proton beams for PANDA (Proton Antiproton Annihilation at Darmstadt) and heavy ion beams for SPARC (Stored Particles Atomic Physics Research Collaboration). With the beam instrumentation devices envisaged in larger quantities, e.g. BPM and BLM being in production, other BI instruments like Viewer, Scraper, or Ionization Beam Profile Monitor are in the mechanical design phase. An overview of the status is presented.

## INTRODUCTION

The HESR, part of the FAIR project in Darmstadt, Germany, is dedicated to the field of antiproton and heavy ion physics. The envisaged momentum range is 1.5 GeV/c to 15 GeV/c. The ring will be 574 m long in a racetrack shape. The planned beam instrumentation within the modularized start version is:

76	Diagonally Cut Beam Position Monitors (BPM)
118	Beam Loss Monitors (BLM)
2	Beam Current Transformers (BCT)
2	Ionization Beam Profile Monitor (IPM)
1	Wall Current Monitor (WCM)
1	Schottky Pick-up
1	Dynamical Tune-meter
1	Transverse Feedback System
5	Viewer
2	Scraper
73	Ion Clearing Chambers

## BPM SYSTEM

The pick-up design is based upon the COSY BPMs [1]. The length and diameter is shrunk by a common factor in order to keep the length to diameter ratio. Each BPM units consist of two diagonally cut pick-ups rotated by 90° around the beam axis in respect to each other. The setup is shown in Figure 1. The inner diameter of the pick-ups is 89 mm and the length 78 mm with a gap of 3 mm between the electrodes using an angle of 55.5°. The expected signal levels are depending on the capacitance of the pick-ups, the ion charge, the amount of ions, and the bunch length and can be calculated. The capacitance was calculated by means of COMSOL Multiphysics 5 simulations. This calculation resulted in a capacity to ground of 19 pF after optimization. For the lowest case, the first injection of antiprotons with 10<sup>8</sup> particles in the ring, the signal level was calculated to 0.5 mV. For the highest intensity case, with 10<sup>11</sup> antiprotons stored, the signal level is 390 mV.

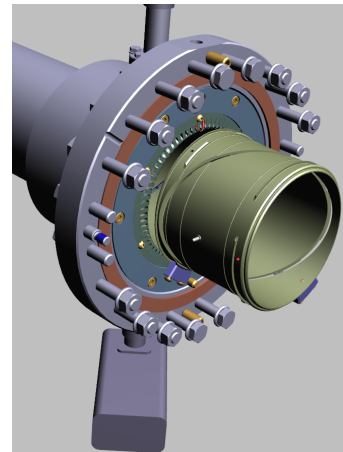


Figure 1: Schematic view on the BPM pick-up. Some parts of the assembly are not shown for better view on the pick-up.

## Signal Amplification

### Fixed Gain Head Amplifiers

Due to low amplitudes the HESR BPM signals require additional boosting prior to transmission over cables in order to achieve a better signal to noise ratio active head amplifiers with a high impedance low noise input were developed. At HESR the expected radiations levels are at a level an active solution could be taken into consideration. The amplifier itself is shown in Figure 2.

The specification of this amplifier is:

Amplification:	20 dB
Noise:	6 $\mu$ V at 50 pF input capacitance and 10 MHz bandwidth
Bandwidth:	10 MHz default, configurable up to 70 MHz
Input Impedance:	500 k $\Omega$
Power supply:	+8 V and -8 V
Output range:	$\pm$ 1.5 V at 50 $\Omega$

### Hadron Pre-Amplifier (HPA)

Within the FAIR project the decision was made early that a common amplifier solution should be found for all machines. Therefore the HPA was developed [2] in cooperation of the Gesellschaft für Schwerionenforschung (GSI) and Instrumentation Technologies, Slovenia.

The HPA amplifier has a gain range of +60 dB to -60 dB and is equipped with an overload protection which has been seen necessary especially for the SIS100. The HPA is equipped with a 50  $\Omega$  input.

For the above listed arguments the HESR deviated from this concept by introducing active head amplifiers instead of the passive impedance transformer. Still the HPA remains part of the signal chain, as the head amplifier will have a fixed



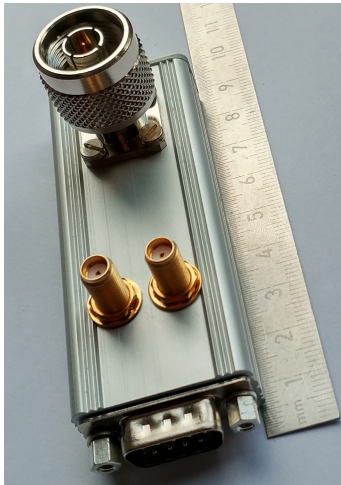


Figure 2: Picture of the head amplifier developed for the HESR BPM system. The N-type plug is main signal input. In SMA a calibration signal input and the signal output is visible. The power is connected through the D-Sub plug.

gain. An adjustable gain amplifier is seen necessary to adapt for different beam properties. The electric power needed for the head amplifiers will be supplied from the HPA, as the necessary voltages are available in the inside its chassis and therefore additional power supplies and cables from the power supply rooms are not needed. On the downside, the HPA has to be modified and will thus not longer be a standard FAIR item.

The HPA consists of two modules stacked after each other: First an attenuator stage and second an amplifier stage. For low input signal levels, the attenuator will be switched to a total attenuation of 0 dB, but still adding a noise to the signal. As the modified version of the HPA will be a non standard item anyway, the attenuator modules will be removed from the HPA in order to achieve a better signal to noise ratio.

## BEAM LOSS MONITOR

For machine commissioning, routine operation and further beam optimization detailed beam loss data is very valuable. Unlike other accelerators, the HESR BLM data will not be used for an automated machine protection, as the stored total beam energy will not be high enough to damage the machine. Along the ring 118 BLMs will be used. The BLM will consist of a BC-400 plastic scintillator and a Hamamatsu photomultiplier (PMT). This solution is favored over e.g. an ion chamber type loss monitor because of the low expected loss rates. A prototype is shown in Figure 3. It was developed by GSI and will be used in other parts of FAIR as well, e.g. the High Energy Beam Transport (HEBT).

For the readout of the BLMs a  $\mu$ TCA system is planned utilizing scaler SIS8800 and counter SIS8980 from Struck Innovative Systeme GmbH. Both cards are connected to each other via the  $\mu$ TCA backplane and provide 16 channels per card. The BPM photomultiplier will be powered individually utilizing a multichannel HV system in order to be able to



Figure 3: BLM prototype based on a scintillator and PMT setup during tests in the COSY synchrotron.

compensate for the properties of the individual BLM detector and the individual location.

## IONIZATION BEAM PROFILE MONITOR

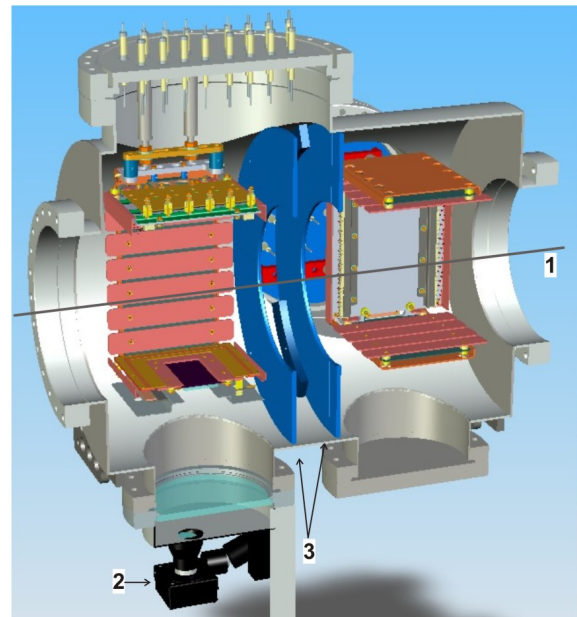


Figure 4: Drawing of the IPM prototype built together with the GSI [3]. The ion beam (1) ionizes residual gas which is accelerated towards a detector and read out by a standard GiGE camera (2). To minimize the effect of the electrical fields towards each other, shielding plates have been inserted between both devices.

An Ionization Beam Profile Monitor (IPM) (Figure 4) was built and tested in cooperation with the GSI in 2007 [4]. Since then it became a very valuable instrument in beam diagnostics at COSY and GSI [5]. Based on both experiences a similar device is under development for the

HESR. The HESR device will be a scaled down version, because of the smaller aperture. It is being designed in a size that would not only fit the HESR but also in the HEBT. Because of the delicate nature of the microchannel plates and the importance of the system, 2 systems will be installed, providing one backup system in case of failure. Together with the locations in the HEBT a FAIR wide number of 12 identical IPM installations is envisaged.

## VIEWER

There will be 5 viewers installed in the HESR. One at the beginning and end of each telescope and an additional one directly after the injection septum magnet. As shown in Figure 5, the viewer consists of a scintillation screen mounted at 45° and will be moved by a pneumatic drive. As a speciality, if the viewer is not used an RF cage will be moved into its place. This is done in order to minimize the overall impedance of the ring. If the RF cage is in it's place, a second pneumatic drive will move RF springs in their position to ensure an optimal electrical conduction. Before moving the RF cage out, these springs will be pulled back.

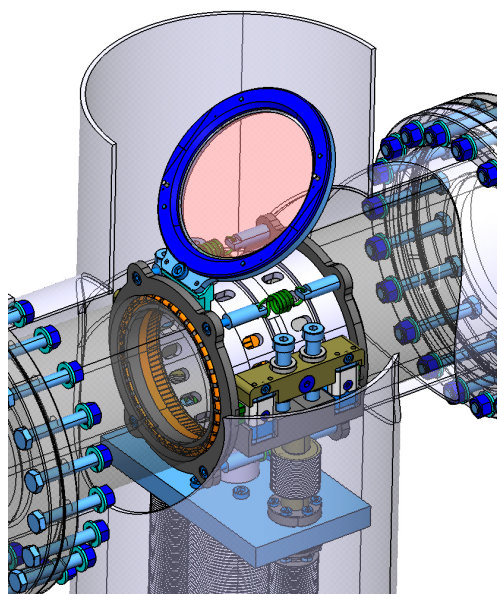


Figure 5: Drawing of the viewer. A scintillator screen is moved into the beam with 45°. While being moved out, a RF cage will be moved into it's position.

## SCRAPER

The scraper system is shown in Figure 6. There will be 2 scraper systems being installed in the HESR. Each system consists of 2 vertical and 2 horizontal jaws. Each jaw of 10 copper rods which are placed in an alternating manner and are each 25 mm in diameter. This layout assures a particle will be slowed down by at least 50 mm of material while the structure will have a minimal effect on the RF impedance while being on it's out position. Each jaw can move in farther than the middle of the beam pipe. As a safety measurement the jaws are therefore placed not directly facing

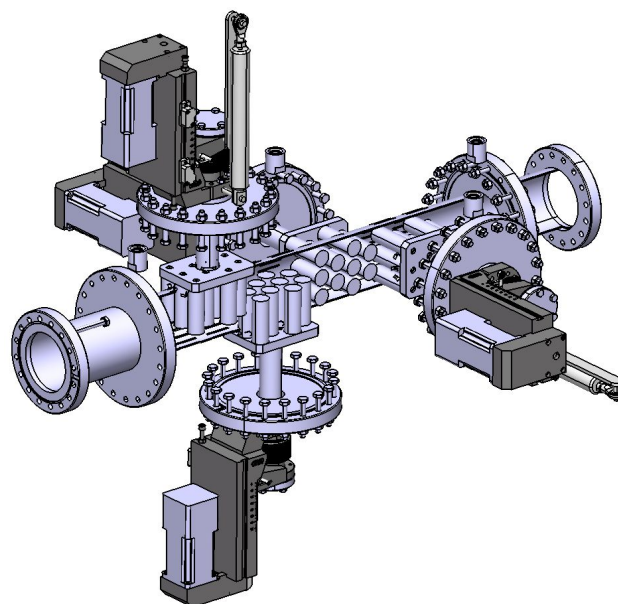


Figure 6: Drawing of the scraper. On each side of each plain the scraper consists of 10 rods of 25 mm diameter. The scraper can move in further than the middle of the beam pipe. To avoid damage opposing rods are moved in longitudinal position.

each other but longitudinally behind one another. If both jaws are moved in fully they will not touch each other and so not being damaged.

## OUTLOOK

At this point in time the BPM pick-ups are in the early production phase. The ion clearing system is currently in the bidding phase, so that both systems are considered being ready during 2019. The other presented systems, namely IPM, scraper and viewer are in the late design phase, so that the production will start within the next months. Other systems like the Wall Current Monitor, Schottky Pick-up, Dynamical Tune-meter, and Transverse Feedback System are in an early design phase, the design is envisaged to be finished within 2018.

## REFERENCES

- [1] R. Maier *et al.*, "Non-Beam Disturbing Diagnostics at COSY-Jülich," in *Proc. EPAC'90*, Nice, France, Jun. 1990, p. 800.
- [2] M. Schwickert *et al.*, "Status of Beam Diagnostics for SIS100," in *Proc. IPAC'17*, Copenhagen, Denmark, May 2017, pp.156–159. doi:10.18429/JACoW-IPAC2017MOPAB035
- [3] T. Giacomini, GSI Gesellschaft für Schwerionenforschung mbH, Darmstadt, Germany, private communication.
- [4] T. Giacomini *et al.*, "Ionization Profile Monitors - IPM @ GSI," in *Proc. DIPAC'11*, Hamburg, Germany, May 2011, paper TUPD51.
- [5] V. Kamerzhiev *et al.*, "Results of Electron Cooling Beam Studies at COSY," in *Proc. RuPAC'10*, Protvino, Russia, Sep.–Oct. 2010, paper WECHZ04.

# BEAM DIAGNOSTICS FOR SuperKEKB DAMPING RING IN PHASE-II OPERATION

H. Ikeda<sup>\*,A),B)</sup>, M. Arinaga<sup>A)</sup>, H. Ishii<sup>A)</sup>, S. Iwabuchi<sup>A)</sup>, M. Tejima<sup>A)</sup>, M. Tobiyama<sup>A),B)</sup>,  
H. Fukuma<sup>A)</sup>, J. W. Flanagan<sup>A),B)</sup>, G. Mitsuka<sup>A)</sup>, K. Mori<sup>A)</sup>,

<sup>A)</sup> High Energy Accelerator Research Organization (KEK) Ibaraki 305-0801, Japan

<sup>B)</sup> The Graduate University for Advanced Science (SOKENDAI)

## Abstract

The SuperKEKB damping ring (DR) commissioning started in February 2018, before main ring (MR) Phase-II operation. We constructed the DR in order to deliver a low-emittance positron beam. The design luminosity of SuperKEKB is 40 times larger than that of KEKB with high current and low emittance. A turn-by-turn beam position monitor (BPM), transverse feedback system, synchrotron radiation monitor (SRM), DCCT, loss monitor (LM) using ion chambers, bunch current monitor and tune meter have been installed for beam diagnostics at the DR. An overview of the instrumentation and its status will be presented.

## INTRODUCTION

SuperKEKB [1] is an electron-positron collider and started construction towards 40 times luminosity as large as KEKB in 2011. The beam energies are 4GeV and 7GeV for positron rings (LER) and electronic ring (HER). Phase-I was the test operation of the main ring (MR) for confirmation that there was no problem in accelerator from February 2016 through June [2]. We installed the Belle-II detector and remodeled injection region of an accelerator for Phase-II operation. The beam commissioning was from March 2018 to July [3,4]. It is necessary to squeeze the vertical beam size to nm level at the collision point to achieve design luminosity. We build the damping ring (DR) in order to achieve a low-emittance positron beam [5,6]. The present parameters of DR are shown in Table 1. DR tuning was started prior to MR commissioning at the beginning of February 2018. We performed the tuning of injection from the injection line (LTR) to DR and DR to extraction line (RTL) in approximately one month [7]. The DR monitor system adjustment including timing system and feedback system was smoothly advanced.

The monitor system of DR follows a system of the MR as shown in Table 2 [8]. Two button electrodes of BPM are attached to the top and down of the ante-chamber of 24mm height in 83 quadrupole magnets. The visible light from a bending magnet downstream of the extraction line is used for a synchrotron radiation monitor. The ion chambers are attached on the wall to cover all the tunnels to monitor beam loss. We installed a monitor chamber and a kicker chamber for bunch feedback, and a DCCT chamber for

beam current monitors just upstream of the injection point of DR.

Table 1: Damping Ring Parameters

Parameter		unit
Energy	1.1	GeV
No. of bunch trains/ bunches per train	2/2	
Circumference	135.5	m
Maximum stored current	12	mA
Damping time (h/v/z)	11.5/11.7/5.8	ms
Emittance(h/v)	29.2/1.5	nm
Energy spread	0.055	%
Bunch length	6.6	mm
Mom. compaction factor	0.01	
Cavity voltage	1.0	MV
RF frequency	509	MHz

Table 2: Beam Monitors in DR

System	Quantity
Beam position monitor	83
Synchrotron radiation monitor	1
Beam loss monitor	34
Transverse bunch by bunch feedback	1
DCCT	1
Bunch current monitor	1

## BEAM POSITION MONITOR

A button electrode with a diameter of 6 mm has been developed for the beam position monitor (BPM). Two button electrodes are attached in one flange due to narrow space for their installation as shown in Fig. 1. The detection circuit is VME 18K11 L/R which incorporates a logarithm amplifier. The signals of BPM are sent to four control racks which accommodate VME racks near cable holes on the ground to reduce a cable loss. 20 or 21 signals are sent to one rack and the converted signals are sent to the central control room through network.

\* email address: hitomi.ikeda@kek.jp

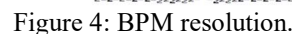




It is necessary to set timing of 83 BPM signals so that the measurement is completed before the next turn to measure the turn-by-turn beam position. Four electrode signals of single BPM have to be measured within 4 ns. Figure 2 is the flow of the timing signal. We divide the injection timing synchronized with bunch timing to the signal which synchronized with DR revolution using frequency divider and transmit to BPM station with a measurement-start-timing. We measured cable length from each BPM rack to an electrode (about 30m) using TDR and calculated the delay by the distance from an injection point to the BPM position before DR operation. We set total delay of every channel individually by a 32ch digital delay. The total delay is below around

For the confirmation of the installed position of each BPM block, we surveyed BPM block using FARO 3D-ARM [10] and obtained a result in Fig. 3. The measured result was put in EPICS record as an offset of BPM. After a startup, it was found that a BPM reported an abnormal position. This was because the assumed chamber shape was reversed in horizontal and vertical position. Other problems are not found on BPM system.

We estimated BPM resolution using the three BPM method. Vertical resolution is 2~3 $\mu\text{m}$  and horizontal resolution is 2~10 $\mu\text{m}$  as shown in Fig. 4.



The synchrotron radiation monitor (SRM) uses the light from a bending magnet with bending radius of 3.14m. The magnet is located just after beam extraction point of DR. The beryllium mirror is installed to 0.5m downstream of

the magnet to extract the light. Transfer mirrors are set in the pit under the tunnel floor to the SRM room which is in the same level as that of the tunnel. A streak camera and a gated camera are prepared for bunch length and transverse beam size measurement. The visible light was confirmed in the SRM room when the beam got longer lifetime and beam current became higher enough. The optical axis was adjusted to each camera.

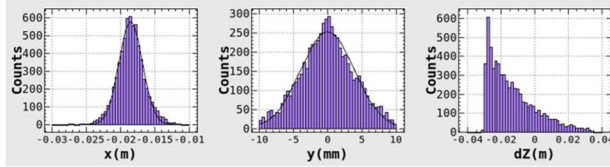


Figure 5: Bunch shape just after injection by a simulation.

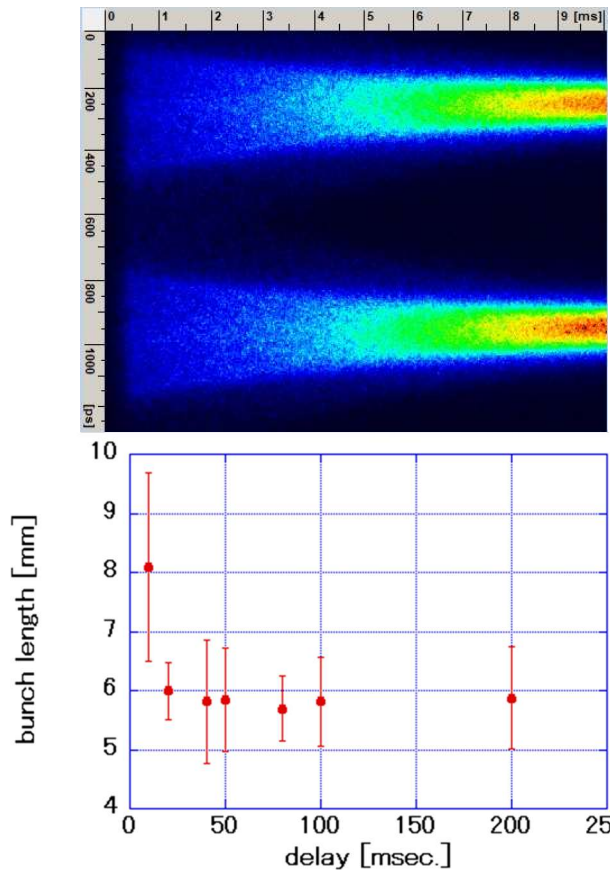


Figure 6: Measured bunch length after injection.

The bunch shape is distorted longitudinally just after injection according to a simulation as shown in Fig. 5. It is damped during accumulation and approaches Gaussian. Figure 6 shows that the bunch length gradually damped after injection and became 6.5mm of the design value in 20ms. As the measurement accuracy of the streak camera is 1ps, the measurement accuracy of the bunch length of 6.5mm is approximately 5%. Figure 7 shows the transverse beam size measured with a gated camera. As the calibration

of absolute value is not applied yet, there is an offset, but it is obvious that the size is almost damped after 50ms. We will calibrate the beam size in Phase-III and then compare it with the size measured by the wire scanner in RTL.

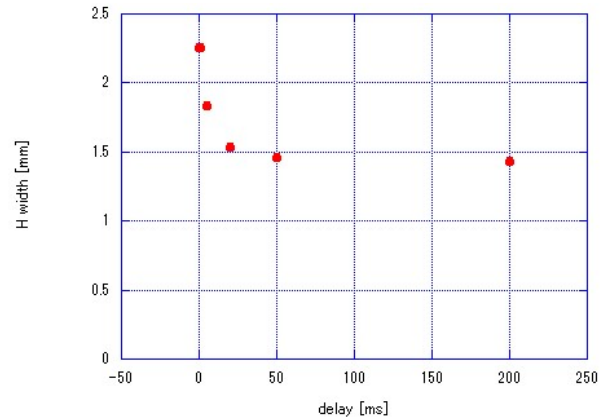


Figure 7: Measured horizontal beam size after injection.

## BEAM LOSS MONITOR

The purpose of the beam loss monitor (LM) is to prevent the damage of the hardware against unstable injected beam by stopping injection trigger. The sensors are ion chambers which are 9 m FC-20D co-axial cables and attached on the tunnel wall. The signals are sent to 8 channel integrators. An interlock level is adjusted by integration time (0.1,0.3,1ms) and gain (1,10,100,1,000). We can monitor the signal at each position in real time which helps injection tuning.

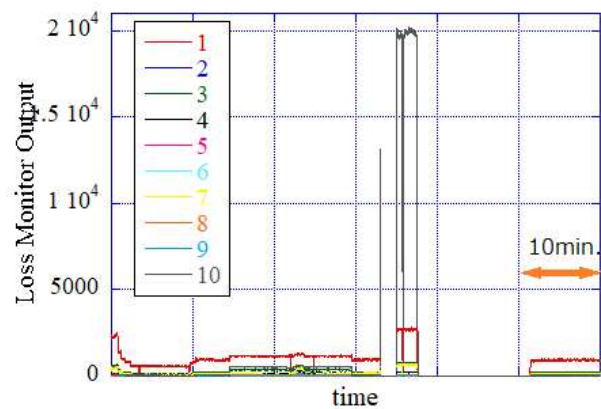


Figure 8: Loss monitor signals at the moment of the alarm from the radiation monitor.

There was an event that the radiation monitor which we attached to the SRM room issued an alarm in DR commissioning. Irradiation of neutron 15 $\mu$ Sv/h and gamma ray 12 $\mu$ Sv/h lasted several minutes, and it did not have any problem for a radiation management area at the time. Since it was an unexpected event, we checked the situation and found that 25Hz injection had continued with high bunch current although the high voltage of extraction septum

magnet had been off. As a result, the radiation level rose in the SRM room which is near to beam extraction region. The LM signal by the side of septum (which is shown in Fig. 8 No.10) showed 20 times larger value than normal level. Nevertheless, injection continued in six minutes because the level was lower than an interlock level. We made an interlock level severe after this event and added an 1m ion chamber to the direct down stream of both sides of septum to refine interlock system.

## BEAM CURRENT MONITOR

We use the detection circuit of MR which was modified to DR and a DCCT core which is reuse of MR as a beam current monitor. It is able to measure the current up to 200mA and the resolution is 30 $\mu$ A. The measurement rate is 5ksps. We always monitor the beam current as shown in Fig. 9. Current limit for the safety interlock is set to 17mA by software and injection is stopped if the current exceeds the limit level. A hardware current limiter will be constructed before Phase-III operation. We found the current level showed minus value after offset subtraction. This problem was caused by reverse installation of the chamber. The sign is reversed by software.

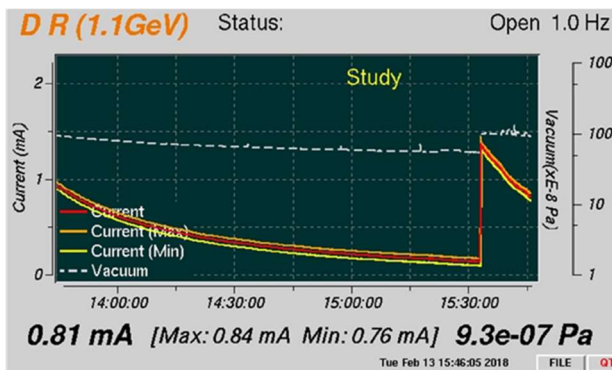


Figure 9: Beam current measurement by DCCT.

## BUNCH FEEDBACK SYSTEM

Bunch feedback system is installed to damp the residual bunch oscillation at injection and extraction. The detector uses 2GHz detection as same as that of MR. A digital filter is the iGp with firmware matched with DR. Power amps (250W x 4) are spares of KEKB. Four electrodes of 40cm in length which oriented 45 degree each other are used for a kicker. We adjusted the phase shift of iGp12 processors for both horizontal and vertical planes and successfully

excited betatron oscillation with stable amplitude using single-bunch PLL excitation function of iGp12.

As the bunch current monitor, the detection circuit that is same as that of MR and VME board (Digitex 18K10) which changed over the internal firmware are used. Injection is stopped if the bunch current exceeds the limit level for safety.

The tracking generator output of the spectrum analyzer is down converted and drives beam. The electrode output is observed directly with the spectrum analyzer for betatron tune measurement. The measurement system is working well.

## CONCLUSION

All the monitor systems of SuperKEKB DR were installed on schedule and finished initial tuning. We performed timing adjustment, phase adjustment, optical axis adjustment after DR injection started. System works smoothly after some alterations. We have plan to construct the beam current limiter, calibrate a gain of BPM, calibrate SRM and optimize the interlock level of LM before the high beam current operation at the Phase-III commissioning.

## REFERENCES

- [1] Y. Ohnishi *et al.*, "Accelerator design at SuperKEKB", *Prog. Theor. Exp. Phys.*, 2013, 03A011.
- [2] Y. Funakoshi, *Proceedings of IPAC'16*, Busan, Korea, May 2016, paper TUOBA01.
- [3] A. Morita *et al.*, to be published in *Proceedings of ICHEP2018*, Seoul, Korea, 2018, July, TUOBA01.
- [4] Y. Ohnishi *et al.*, *Proceedings of eeFACT'18*, Hong Kong, China, (2018).
- [5] M. Kikuchi *et al.*, *Proceedings of IPAC'10*, Kyoto, Japan, May 2010, paper TUPEB054, p. 1654.
- [6] N. Iida *et al.*, *Proceedings of IPAC'11*, San Sebastian, Spain, May 2011, paper THYA01, p. 2854.
- [7] N. Iida *et al.*, to be published in *Proceedings of eeFACT'18*, Hong Kong, China, 2018.
- [8] M. Tobiyama *et al.*, Presented at IBIC'18, Shanghai, China, Sep. 2018, paper MOOB01.
- [9] M. Tobiyama, H. Ikeda, in *Proc IBIC'17*, Grand Rapids, MI, USA, Aug. 2017, paper TUPCF09, pp. 221-224, <https://doi.org/10.18429/JACoW-IBIC2017-TUPCF09>, 2018.
- [10] <https://www.faro.com/ja-jp/products/factory-metrology/faroarm/>



# THE BEAM INSTRUMENTS FOR HIMM@IMP

T. C. Zhao<sup>†</sup>, R. S. Mao, X. C. Kang, M. Li, Y. C. Feng, Y. C. Chen, J. M. Dong, Z. L. Zhao, Z. G. Xu, K. Song, Y. Yan, W. N. Ma, Y. M. Wang, H. H. Song, W. L. Li, S. P. Li, K. Wei  
Insitute of Modern Physics, Lanzhou, China

## Abstract

The beam diagnostics(BD) devices for HIMM (Heavy Ion Medical Machine) are designed and produced by IMP BD department .An overview of the integrated devices is presented, and the common beam parameters in the different parts of the accelerator facility are reviewed including intensity measurement, beam profile, emittance, energy, beam loss and so on with the related detectors such as the View Screen, Faraday Cup, Radial Detector, Multi-wires, Phase Probe, Wire Scanner, DCCT, ICT, BPM, Schottky, Slit, Beam Stopper, Beam Halo Monitor, Multi-channel Ionization Chamber. Additionally, the RF-KO for beam extraction, the strip foil with automatic control system as well as the detectors for terminal therapy are described.

## INTRODUCTION

HIMM is a synchrotron based accelerator for cancer therapy in Wuwei city, China. It is composed of 2 ion sources, LEBT, cyclotron, MEBT, a synchrotron, HEBT and therapy terminals. The commissioning of HIMM is completed. The layout of the machine is shown in Fig. 1. At present, electrical safety, electromagnetic compatibility and performance testing of medical devices have been passed, and now enters the clinical tests phase.

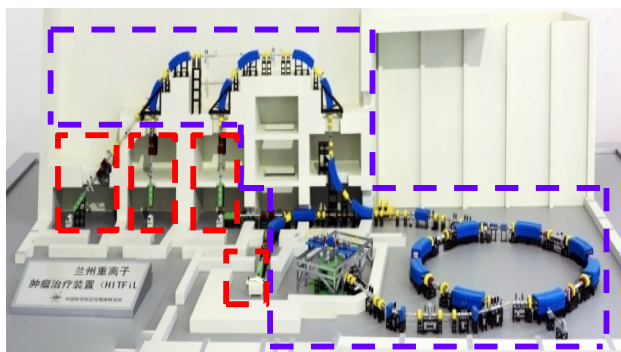


Figure 1: Layout of HIMM.

## RADIAL PROBE

HIMM selects a cyclotron as its primary accelerator. Two radial probes have been installed to measure the beam intensity in the central area of the cyclotron. The target includes integrating and differential figures shown in Fig.2 and the beam turn measurement is displayed in Fig.3. What's more, in order to obtain the intensity distribution of different radius, it is necessary to synchronize motion control and data acquisition.

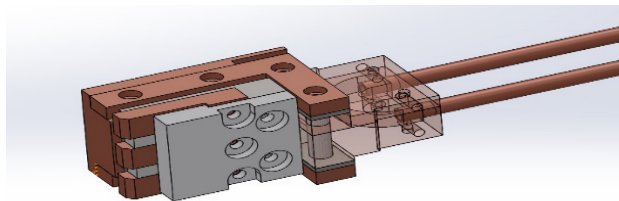


Figure 2: Target of radial probe.

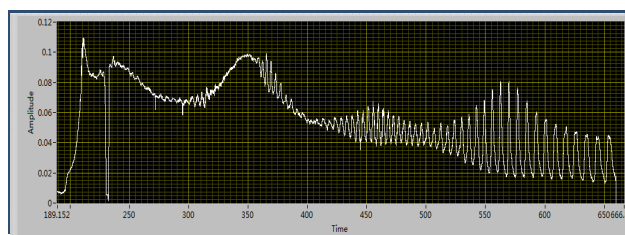


Figure 3: Intensity distribution of different radius.

## VIEW SCREENS

View Screen (VS) is a commonly used profile detector, especially in the early stage of the commissioning. 13 VS are installed in the MEBT, Synchrotron and MEBT. In order to measure the beam profile at different tracks, the servo motor is used, and the repeatability of positioning accuracy is better than 0.1mm comparing its mechanical installation precision which is less than 0.5mm. The signals from CCD are read in two ways, one is the release video transmitted on the internet after video compression, and the other is to use video capture card. After digitalization, the FWHM and the centre position of the beam are obtained through software analysis. The captured photos and its analysed profile information is displayed in Fig. 4.

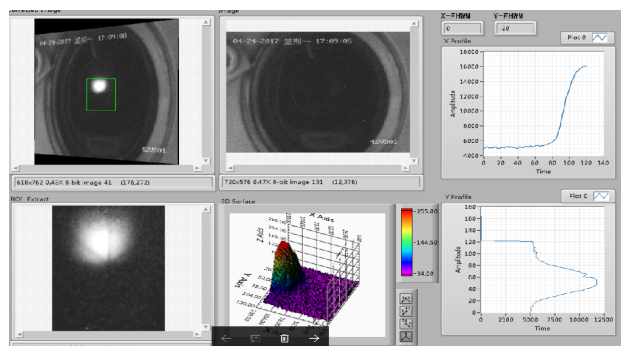


Figure 4: Beam profile and digital results.

## FARADAY CUP

Faraday Cup (FC) is a commonly used intensity detector. It is installed in the LEBT, MEBT and Synchrotron. We carried out the heating analysis, and optimized the cooling water and ceramic insulation structure. Pico ammeter is used for signal acquisition, data can be read directly through RS-232, or acquired with the data acquisition card, in which the sampling rate is much faster in order to monitor some rapid changes in the beam structure. The beam current measurement with FC by fast data acquisition system is shown in Fig. 5.

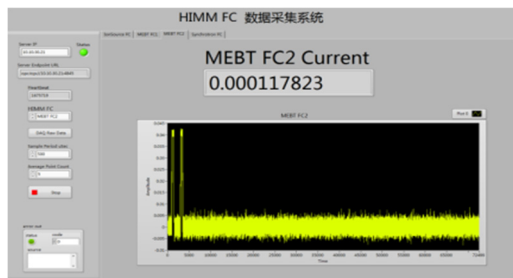


Figure 5: Beam intensity within 0.1ms.

## SEM-GRID

SEM-GRID is installed in MEBT to measure the beam profile. Electronics adopts integral gate control circuit and cyclic structure to realize weak current signal processing. The signal sampling period is adjustable from 200  $\mu$ s to 100ms, and its dead time is less than 50  $\mu$ s. The beam profile and its fitting profile at horizontal and vertical direction tested at MEBT are shown in Fig. 6.

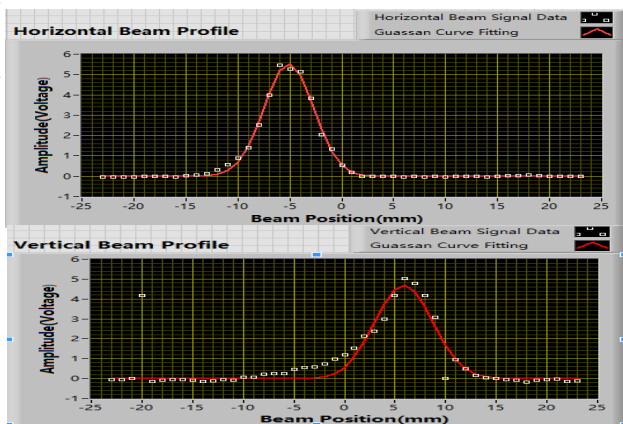


Figure 6: Beam profile measurement with SEM-GRID at MEBT.

## EMITTANCE

Emittance is an important parameter for characterizing beam quality. Slit-grid method, quadrupole variation method and three grid method are often used in beam lines [1, 2]. We use these three methods to measure the emittance of the cyclotron beams in MEBT illustrated in Figs. 7-9. In each of these three figures the right part of the figure shows the horizontal beam emittance while

the left part of which shows the vertical beam emittance. Furthermore, the three sets of beam emittance results are consistent.

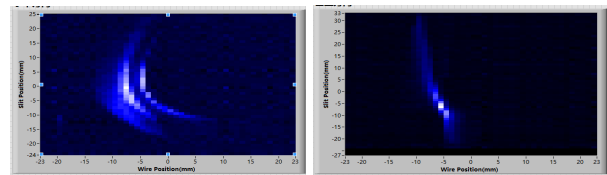


Figure 7: Slit-grid method, x:34.0mm.mrad, y:23.6 mm.mrad.

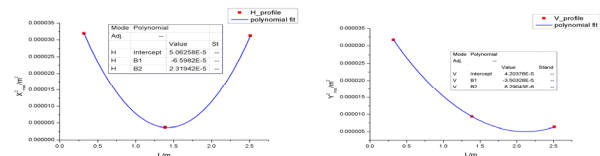


Figure 8: Three-grid method, x:37 mm.mrad, y:25.8 mm.mrad.

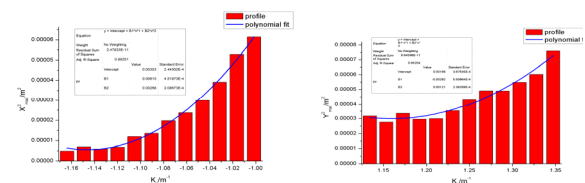


Figure 9: Quadrupole variation method, x: 33.5 mm.mrad, y: 21.2 mm.mrad.

## ICT

ICT is installed in MEBT as an on-line intensity monitor. The probe is bought from BERGOZ Instrumentation, and a lock-in amplifier is used with the RF signal from the cyclotron. The resolution is 10nA for continuous beam, and the shortest beam width can be measured is about 100 $\mu$ s. Fig.10 shows the detector and the beam current measurement at MEBT with ICT.

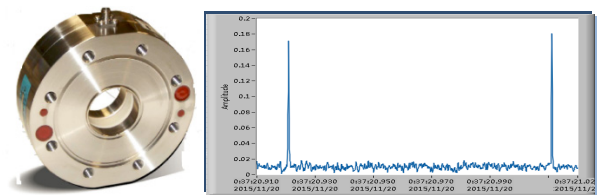


Figure 10: ICT probe and measuring result.

## PICK-UP

We use pick-up as on-line energy monitor in MEBT. The distance between the two detectors is accurately measured, and the electronics length of cables also needs precise measurement [1, 2]. According to Fig. 11 and the calculation, the beam energy extracted from the Cyclotron is 6.323 MeV/u.

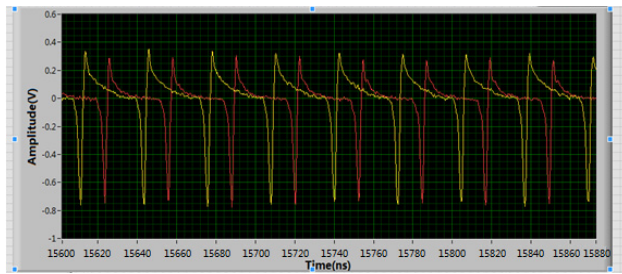


Figure 11: Energy measurement with pick-ups.

## STRIP FOIL

A carbon foil is used to change the charge state of the injected ions. The function of this device is to move the foil to the beam orbit, and the automatic foil exchange is necessary. We designed a four axis drive structure to achieve this goal. At present, it realizes automatic changing in vacuum and the mechanical design is shown in Fig.12.

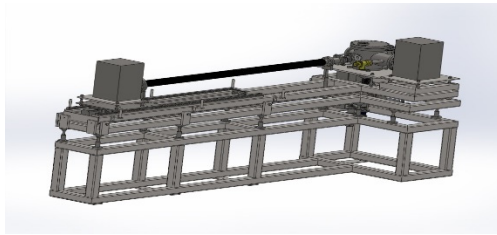


Figure 12: Mechanical of Strip foil.

## DCCT

A DCCT is installed in the synchrotron to measure the beam intensity. The resolution is  $0.5 \mu\text{A}/\sqrt{\text{Hz}}$  which is also purchased from the Bergoz Instrumentation. The detector and the beam current measured at Synchrotron is shown in Fig. 13

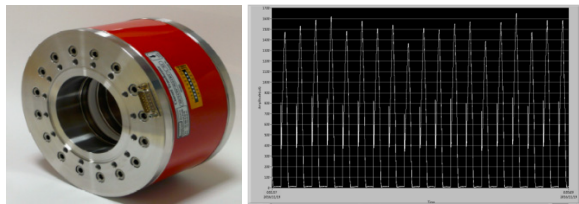


Figure 13: DCCT probe and measuring result.

## BPM

8 shoe-box type beam position monitors (BPM) is installed in the synchrotron which are used for orbit measurement, and the resolution is 0.2mm. Before the installation, calibration was carried out in the laboratory [3] shown in Fig. 14.

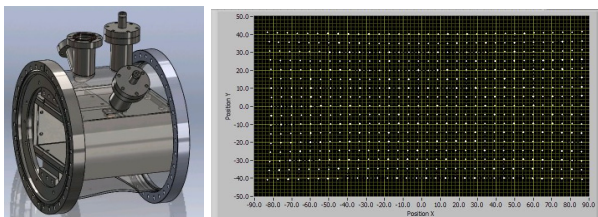


Figure 14: BPM probe and mapping result.

## RF-KO

HIMM adopts 1/3 resonance slow extraction, RF-KO provides a transverse extraction electric field. Amplitude and frequency modulation are used for the extraction signals. At the same time, a feedback system based on excitation and fast quadrupole is adopted. Through the above methods, the uniformity of beam extraction is greatly improved compared in Fig.15.

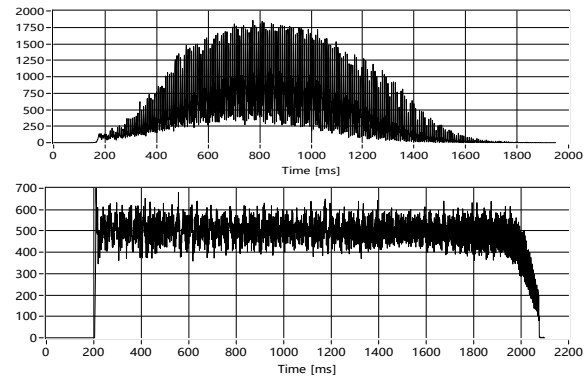


Figure 15: Beam structure improvement with RF-KO.

## MULTI-CHANNEL IONIZATION CHAMBER

For slow extracted beam from a synchrotron, the current is too low to be measured by a SEM-grid. As a result the Multi-channel Ionization Chamber (MIC) is designed to measure the profile in HEBT. The effective area of which is  $100 \text{ mm} \times 80 \text{ mm}$ , and the signal sampling period is adjustable from 1 ms to 100 ms. The beam profile measured at HEBT is displayed in Fig. 16 where the horizontal and vertical profile are displayed at the left and right part respectively.

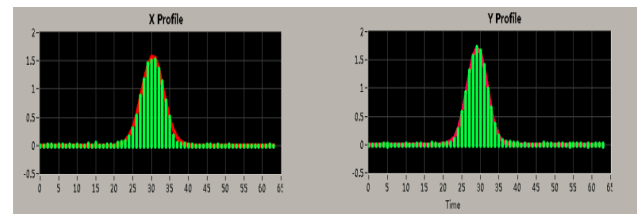


Figure 16: Profile measured by MIC.

## REFERENCES

- [1] Peter Strehl, *Beam Instrumentation and Diagnostics*, Springer
- [2] P. Forck, Lecture Note on Beam Instrumentation and Diagnostics, Joint University Accelerator School, 2016
- [3] P. Forck, P. Kowina, and D. Liakin, *Beam position monitors*, CERN Accelerator School, 2008



V. S. Anashin<sup>†</sup>, P. A. Chubunov, Branch of JSC United Rocket and Space Corporation - Institute of Space Device Engineering, Moscow, Russia  
S.V. Mitrofanov, A. T. Isatov, Joint Institute for Nuclear Research, Dubna, Russia

SEE testing of candidate electronic components for space applications is essential part of a spacecraft radiation hardness assurance process in terms of its operability in the harsh space radiation environment. The unique in Russia SEE test facilities have been created to provide SEE testing [1]. The existing facilities, including ion beam monitoring system have been presented at IBIC 2017[2]. However, this system has a number of shortcomings related to the lack of reliable online ion fluence measurement on the DUT, and inability to measure energies of the high-energy (15-60 MeV/nucleon) long-range (10-2000  $\mu\text{m}$ ) ions on the DUT. The paper presents the latest developments and their test results of the ISDE and JINR collaboration in the field of real-time flux monitoring (including, on the DUT) during tests using scintillation detectors, and ion energy measurement by total absorption method. The modernization of the standard beam monitoring procedure during testing is proposed.

This system is designed to monitor the stability and non-uniformity of the ion beams during heavy-ion testing on the low-energy test facilities. The system is based on an array of scintillation detectors consisting of 64 (8x8) sensors and designed for measuring such ion beam parameters as flux and integral fluence in real-time during heavy-ion testing, as well as non-uniformity. An important advantage of the system is the ability to obtain data without stopping the irradiation, i.e. in real time during testing, through the use of vacuum actuator installed in close proximity to the DUT.

Table 1 shows the technical features of the system, and Figures 1 and 2 show the appearance of the system after assembly and already mounted at the test facility.

Table 1: Technical features of the wide-angle complete-overlap ion beam profile monitoring system

Feature	Value	Unit
Ion species	Ne to Bi	
Energy range	3-6	MeV/nucleon
Fluxes	$1\text{-}10^5$	$\text{cm}^{-2}\text{*s}^{-1}$
Area	200x200	mm
Number of detectors	8x8	
Visualization system	Yes	
Input/output to/from the beam	In real-time	
Measurement and data output time	1	min
Ion flux determination error	Less than 10	%
Non-uniformity indication	Yes	



Figure 1: Wide-angle complete-overlap ion beam profile monitoring system (ready-assembled, before installation).

† npk1@niikp.org

Examples of measurement results visualization (software interface) are shown in Figs. 3 and 4. In addition to the instantaneous flux value for each of the 64 detectors, it is possible to calculate the average fluence over the entire irradiation area, as well as the non-uniformity.



Figure 2: Wide-angle complete-overlap ion beam profile monitoring system (installed in the beam channel).

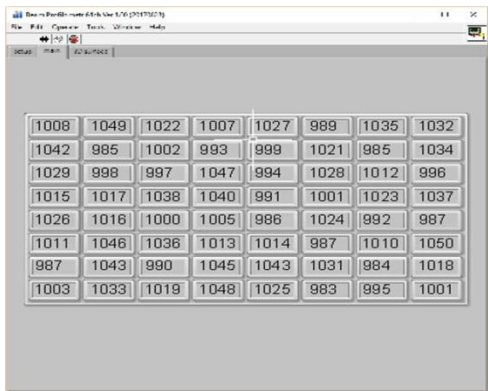


Figure 3: Software interface for the wide-angle complete-overlap ion beam profile monitoring system.

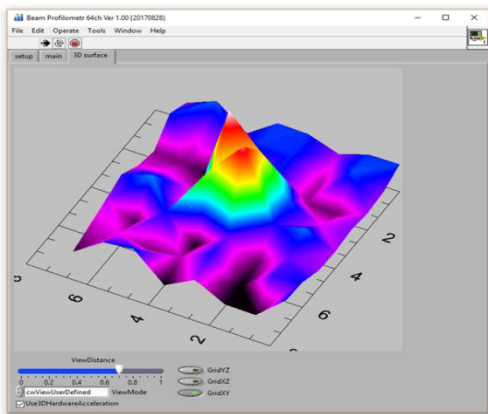


Figure 4: Example of measurement results visualization for wide-angle complete-overlap ion beam profile monitoring system.

A series of irradiation sessions was performed for the purpose of experimental testing of the system. The irradiation sessions were carried out at beam fluxes of 100000 and 50000 particles/cm<sup>2</sup>\*s by accelerated beam of Xe heavy ions with energy of 3.82 MeV/nucleon, and also at beam fluxes of 10000 and 1000 particles/cm<sup>2</sup>\*s by accelerated beam of Kr heavy ions with energy of 3.1 MeV/nucleon. During each session, the metrological certified track detectors were placed near each wide-angle complete-overlap ion beam profile monitoring system to compare the integral fluxes. The results coincided within the error margins.

15-CHANNEL BEAM PROFILE MONITORING SYSTEM

This system is equivalent to the previous one in terms of physical principles of ion flux registration. The system is used to monitor the beam of high-energy ions, which allows obtaining data on the spatial distribution of the ion beam uniformity in real time (during tuning the beam, pretest setup, etc.).

Table 2 shows the technical features of the system.

Table 2: Technical Features of the 15-channel Beam Profile Monitoring System

Feature	Value	Unit
<hr/>		
Ion species	Ne to Bi	
Energy range	15-60	MeV/nucleon
Fluxes	1-10 <sup>5</sup>	cm <sup>-2</sup> *s <sup>-1</sup>
Diameter	60	mm
Number of detectors	15	
Visualization system	Yes	
Input/output to/from the beam	In real-time	
Measurement and data output time	1	min
Ion flux determination error	Less than 10	%
Non-uniformity indication	Yes	

The design features are shown in Fig. 5.

Figure 6 shows the software interface. On the left side of the screen, the user can see the current value of ion flux per each detector, as well as average flux versus irradiation time plot. The right side of the screen displays the instantaneous flux and the integral fluence. At the bottom right, the required ion fluence is shown during the tests. For beam quality monitoring there is an option to display the non-uniformity.



Figure 5: Appearance of the 15-channel beam profile monitoring system.

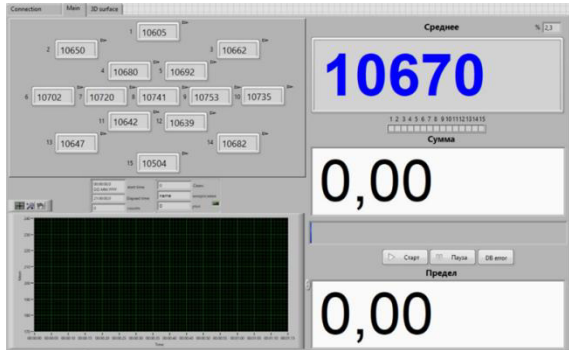


Figure 6: Software interface for the 15-channel beam profile monitoring system.

SCINTILLATION ONLINE DETECTORS  
SYSTEM FOR TEST SUPPORT

This system is designed for in-situ measurement of ion flux on the DUT during testing. In terms of design, the detector consists of a plastic scintillator, flexible WLS (wavelength shifting) fibres, and photomultiplier tube. The flexible structure allows the sensitive volume of the detector to be placed in close proximity to the DUT. Up to 8 such detectors can be placed in the test chamber simultaneously.

Table 3 shows the technical features of the system.

Table 3: Technical Features of the Scintillation Online Detectors System for Test Support		
Feature	Value	Unit
Active surface area	1	cm <sup>2</sup>
Ion species	Ne to Bi	
Energy range	3-60	MeV/nucleon
Fluxes	1-10 <sup>5</sup>	cm <sup>-2</sup> *s <sup>-1</sup>
Scintillator thickness	1-2 (for 3-10 MeV/nucleon) 5 (for 10-60 MeV/nucleon)	mm
Ion flux determination error	Less than 10	%
Non-uniformity indication	Yes	

Figure 7 shows an example of detectors positioning in the irradiation chamber.

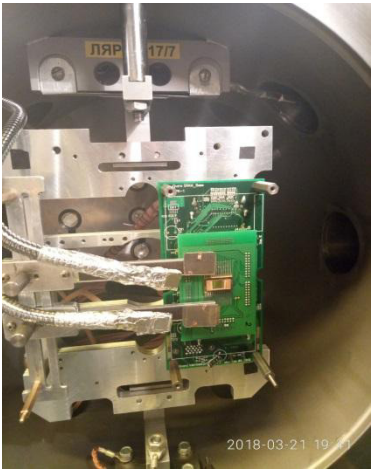


Figure 7: Positioning of scintillation online detectors system for test support on the DUT.

The software interface is similar to the previous one and is shown in Figure 8. The detectors can be turned off in order to ignore readings from unused sensors during calculation of the average flux.

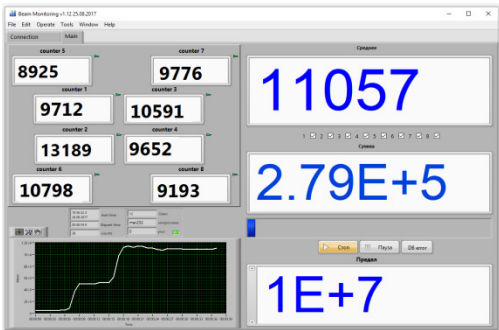


Figure 8: Software interface of scintillation online detectors system for test support.



## ION ENERGY MEASURING SYSTEM

This system is designed to measure the ion energies on the DUT surface. The system consists of semiconductor silicon detector (detector thickness – 500  $\mu\text{m}$ ) and charge sensitive preamplifier for Xe, Kr and Bi ions, as well as scintillation detector CsI (detector thickness – 5 mm), photomultiplier tube, and photon counter for lighter ions. When working with the system, it is necessary to calibrate the detector by taking the readings of amplitude spectra of the detector from the heavy ion beam at different energies (at least three; the energy is changed by placing aluminium foils of different thickness in the ion beam line) and comparing the results with the readings of time-of-flight detectors. After calibration, energy can be measured directly on the DUT.

During experimental testing of the system we obtained the amplitude spectra from accelerated heavy-ion beams of Xe with energies of 22.94, 19.28, 14.39 and 9.92 MeV/nucleon, Kr with energies of 25, 22.20, 18.49 and 15.19 MeV/nucleon, Ar with energies of 33.8, 24.68 and 12.17 MeV/nucleon, and Bi with energies of 12.12, 6.87 and 4.49 MeV/nucleon. Figure 9 shows an example of measurement results for Xe.

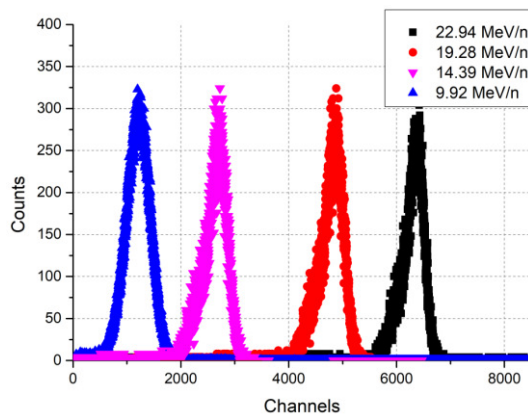


Figure 9: Amplitude spectra from accelerated heavy-ion beams of Xe with energies of 22.94, 19.28, 14.39 and 9.92 MeV/nucleon, obtained by silicon detector.

The calibration was followed by the ion energy measurements on the DUT. The measurement results of ion energies in the beam channel and on the DUT are presented in Table 4. We can see a close agreement of measurement results with estimated energies, especially for high energies.

Table 4: Results of ion energy measurements

Ion species	Ion energy in the beam channel, MeV/nucleon	Measured ion energy on the DUT, MeV/nucleon	Estimated ion energy on the DUT, MeV/nucleon
	n	n	n
Xe	22.94	20.39	20.53
Kr	25	23.09	23.15
Ar	33.8	32.78	32.93
Bi	12.12	9.65	8.74

## CONCLUSION

The paper presents the recent advances of ISDE & JINR collaboration in the field of beam parameters monitoring in the physical field of irradiation before and after the heavy-ion testing. Four systems have been developed that allow to monitor the ion beam fluxes, integral fluence and non-uniformity over the entire irradiation area for the low- and high-energy test facilities; to make real-time measurements of the ion fluxes, integral fluence directly on the DUT; to measure ion energy directly on the DUT. The introduction of the developed systems in a test process of candidate space electronics allows to increase the reliability of test data and to minimize errors in ion beam parameters determination.

## ACKNOWLEDGEMENTS

The authors thank Aleksey Konyukhov from ISDE for his participating in formatting and translating the article into English.

## REFERENCES

- [1] V. S. Anashin, P. A. Chubunov, S. A. Iakovlev, A. E. Koziukov, G. G. Gulbekyan, V. A. Skuratov, and S. V. Mitrofanov, "Typical Facilities and Procedure for Single Event Effects Testing in Roscosmos," *2015 15th European Conference on Radiation and Its Effects on Components and Systems (RADECS)*, Sep. 2015.
- [2] V.S. Anashin, P.A. Chubunov, S.V. Mitrofanov, G.A. Protopopov, V.A. Skuratov, and Yu.G. Teterev, "Estimation of Heavy Ion Beam Parameters During Single Event Effects Testing", in *Proc. 6th Int. Beam Instrumentation Conf. (IBIC'17)*, Grand Rapids, MI, USA, Aug. 2017, paper MOPCF10, pp. 94-97, ISBN: 978-3-95450-192-2, <https://doi.org/10.18429/JACoW-IBIC2017-MOPCF10>, 2018

# BEAM DIAGNOSTICS AND INSTRUMENTATION FOR PROTON IRRADIATION FACILITY AT INR RAS LINAC

S. Gavrilov<sup>†1,2</sup>, A. Melnikov<sup>1,2</sup>, A. Titov<sup>1,2</sup>

<sup>1</sup>Institute for Nuclear Research of the Russian Academy of Sciences, Troitsk, Moscow, Russia  
<sup>2</sup>Moscow Institute of Physics and Technology (State University), Moscow, Russia

## Abstract

A new proton irradiation facility to study radiation effects in electronics and other materials has been built in INR RAS linac. The range of the specified current from 10<sup>7</sup> to 10<sup>12</sup> protons per beam pulse is covered with three beam diagnostic instruments: current transformer, phosphor screen and multianode gas counter. Peculiarities of the joint use of the three instruments are described. Experimental results of beam parameters observations and adjustments are presented.

## INTRODUCTION

A proton irradiation facility (PIF) at INR RAS linac is intended to research on proton irradiation induced effects in different electronics, devices and materials. PIF is installed at the outlet of the linac, where bending magnet is used to deflect a beam for in air irradiation of targets. Beam energy at the PIF is adjusted in 20÷210 MeV range. Beam flux is defined by a combination of three parameters: pulse duration, pulse repetition rate and pulse current, which can be controlled in the range of 10<sup>7</sup>÷10<sup>12</sup> p/pulse by two collimators at the linac injection channel.

A general PIF layout is shown in Fig. 1. The main parts are: bending magnet with vacuum beam pipe, beam dump, target positioning system with energy degrader and beam diagnostic instrumentation.

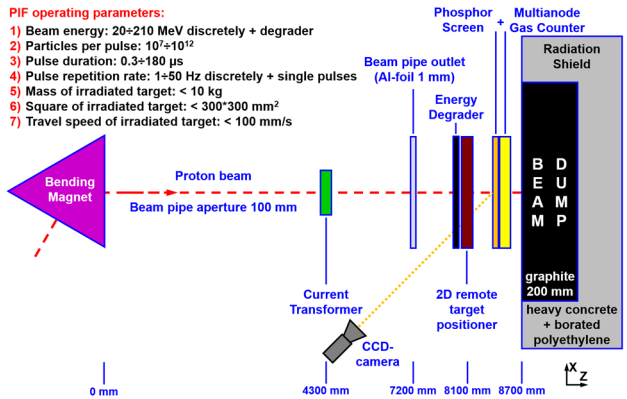


Figure 1: PIF layout.

The beam current transformer (BCT) is installed in the beam pipe about 3 m upstream the outlet window and provides absolute nondestructive measurements of beam pulse current with the amplitude > 25 μA, that corresponds to ~10<sup>10</sup> p/pulse with typical durations 50÷150 μs (full range is 0.3÷180 μs). For less intensive beams more sensitive diagnostic instruments are foreseen.

## MULTIANODE GAS COUNTER

A multianode gas counter (MGC) was proposed initially as the main detector for low intensity diagnostics at the PIF. MGC is a combination of ionization and proportional air chambers, formed by an array of five plates (Fig. 2), which are fabricated as a standard 5 accuracy class printed-circuit boards made of FR4 with 0.5 mm width. Electrodes consist of 18 μm nickel, plated with 0.5 μm immersive gold.

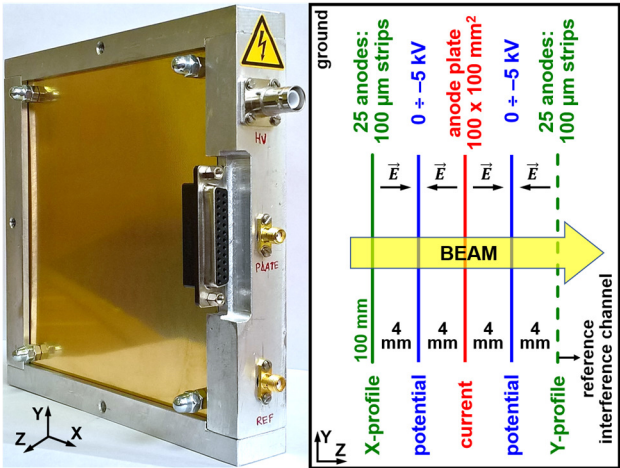


Figure 2: MGC photo and layout.

Central region operates as an ionization chamber to count particles in a beam pulse. A quasi-uniform electrostatic field is formed by two electrodes under negative potential and anode electrode under virtual ground of read-out electronics. All three electrodes have a duplex geometry, straddling the FR4 plate. Ionization electrons move to the current electrode from both sides, forming a relative beam intensity signal.

Lateral regions are proportional chambers for beam position and profile measurements. Each chamber is formed by the potential electrode and a multichannel structure, which consists of 25 anode stripes with 100 μm width, 100 mm length and 4 mm spacing. Strong non-uniform field around stripes (Fig. 3) leads to electron avalanches, increasing the desired signal.

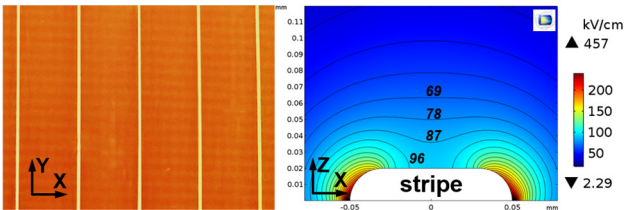


Figure 3: Photo of 100 μm stripes at the FR4 plate and distribution of electric field near a stripe at -4 kV potential.

## LUMINESCENT DIAGNOSTICS

A system of luminescent diagnostics was foreseen as alternative instrumentation to control beam position and profiles. It consists of a phosphor screen (PS) with 100 x 100 mm<sup>2</sup> operating area, fixed at the entrance plate of MGC (Fig. 4), and CCD-camera.

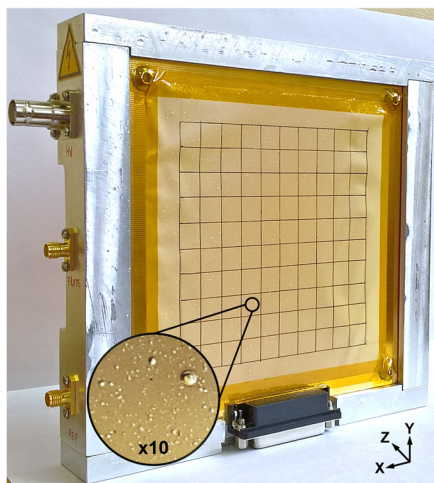


Figure 4: Phosphor screen fixed at MGC.

PS is made of P43 powder melted with polyimide – such process provides easy-to-use, but non-uniform luminescent film. However these nonuniformities of the powder are tens times smaller, than foreseen beam size.

The light emitted by PS is registered by monochrome CCD-camera Basler acA780-75gm in 12-bit mode. The lens (Azure 7524MM) and the CCD sensor (Sony ICX415) are sensitive to PS emission spectrum. The camera can be triggered by external sync pulse with beam pulse repetition rate as well as by an internal trigger with frequency up to 75 Hz. Data are transmitted to the control room in GigE standard by 130 m 6e-SFTP cable.

Besides measurements of spatial transverse parameters PS can be used as a pulse particle counter due to a high linearity of P43 light yield as a function of incident particles number [1]. Certainly, this type of intensity measurements, as well as MGC, demands a calibration by some absolute measurer, in our case – BCT.

The camera is located at a distance about 4 m and under an angle about 70° relative to PS plane, so registered image needs to be corrected (Fig. 5) and scaled. This procedure is realized with NI LabVIEW (IMAQ Vision module), which is used both for image capture and real-time postprocessing. In the actual PIF layout the reproduction PS scale is 2.2 pixel/mm.

Also, such software functions as background frame subtraction, frame summation and control of the camera parameters are implemented.

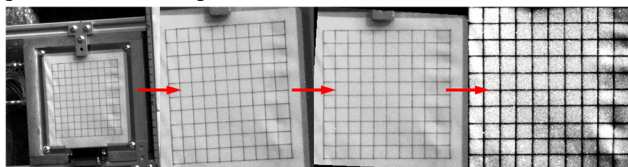


Figure 5: Image correction procedure in NI Vision.

## BEAM TEST RESULTS

Beam tests were done in the full range of PIF parameters. The current range  $10^{11}$ – $10^{12}$  p/pulse is totally covered by BCT for current measurements and partially covered by PS for position, but not for profile and current measurements. It was shown, that the beam density  $\sim 10^{10}$  p/cm<sup>2</sup> leads to PS light yield saturation (Fig. 6). Besides, at peak beam currents about  $10^{12}$  p/pulse and beam energies > 45 MeV, link through GigE interface was lost several times after 50–100 pulses with 1–10 Hz repetition rate. Also, after two week-long PIF runs a dark noise of the CCD-sensor increased three times. This small, but accumulative effect, induced by fluxes of  $\gamma$ -rays and neutrons from the irradiated target and the beam dump, deteriorates the sensitivity of the camera.

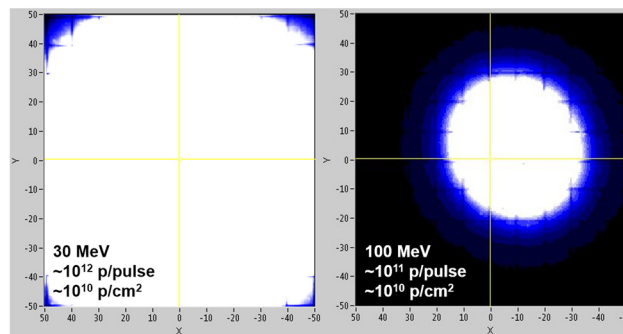


Figure 6: PS light yield saturation at different beam energies and currents, but with the same beam density.

MGC is also saturated in this current range and aging effects appear. The most important one is an irreversible decreasing of the signals from MGC stripes, which starts at beam density  $> 10^{10}$  p/cm<sup>2</sup>. At this density during beam tests the signals from the stripes started to decrease and disappeared totally at about  $10^{11}$  p/cm<sup>2</sup>. The main hypothesis about this effect is a sputtering of the gold from the nickel and following burning of the stripe in the avalanche due to O<sub>2</sub> molecular ions, that leads to a total stripe destruction and/or formation of dielectric oxide film on the stripe surface (Fig. 7), which blocks low energy ionization electrons. An obvious decision to resolve this problem is to use the air MGC with less intensive beams or to implement a gas-filled O<sub>2</sub>-free design of the counter for the full range of measurements.

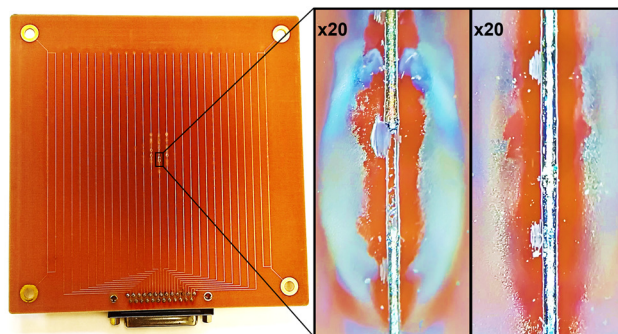


Figure 7: Aging effects at strips of proportional chamber: total stripe destruction and stripe oxidation – temper colors at the stripe nickel surface can be observed at the photos.



An initial procedure of calibration is started at about  $100\div150\text{ }\mu\text{A}$  pulse current ( $\sim10^{11}$  p/pulse), when BCT signal-to-noise ratio is still good enough, and MGC with PS operate already without saturation.

The front-end multichannel electronics of MGC operates with a maximum gain for each channel  $45\text{ mV/pC}$ . The currents of secondary electrons are integrated over a pulse at each channel simultaneously and then signals are transmitted by a multiplexer with the processing time  $24\text{ }\mu\text{s}$  per channel. The back-end electronics is NI USB-6003 DAQ module (ADC: 16-bit,  $100\text{ kS/s}$ ). The software is based on LabVIEW and provides MGC data acquisition, control of high-voltage supply and gain factor ( $1/10/100/1000$ ) as well as a manual procedure of the calibration by BCT.

The experimental operational range of MGC is  $10^7\div10^{11}$  p/pulse. An example of the experimental gain of MGC ionization and proportional chambers vs. applied potential for 94 MeV beam energy is shown in Fig. 8.

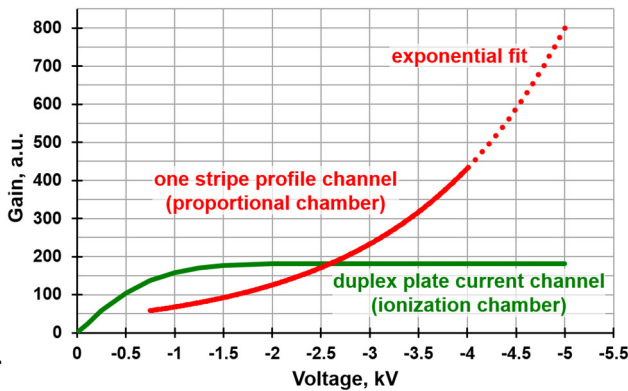


Figure 8: Experimental gain for the duplex plate current channel (green) and one stripe profile channel (red) at 94 MeV beam energy.

The finite thickness of MGC limits an energy of the incident beam to  $\sim21\text{ MeV}$ . At less energies the beam is stopped before the second profile plane due to ionization losses in MGC volume.

Beam profiles measurements with PS are routine. In this case, it is more precise instrument obviously, as provides  $\sim1\text{ mm}$  resolution vs.  $4\text{ mm}$  in MGC (Fig. 9).

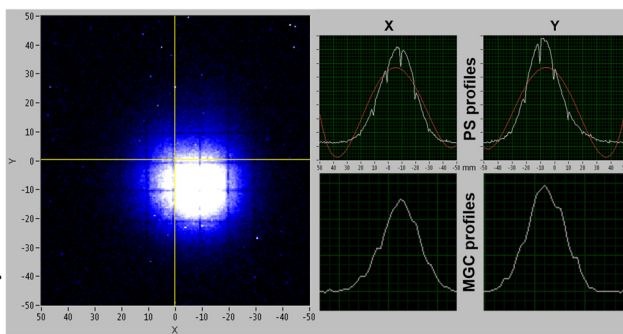


Figure 9: Beam cross-section at the PS and postprocessing profiles from the PS image and from MGC data.

Moreover, PS shows 2D beam cross sections and reveals images of irradiated targets with an ability to observe an internal density distribution (Fig. 10).

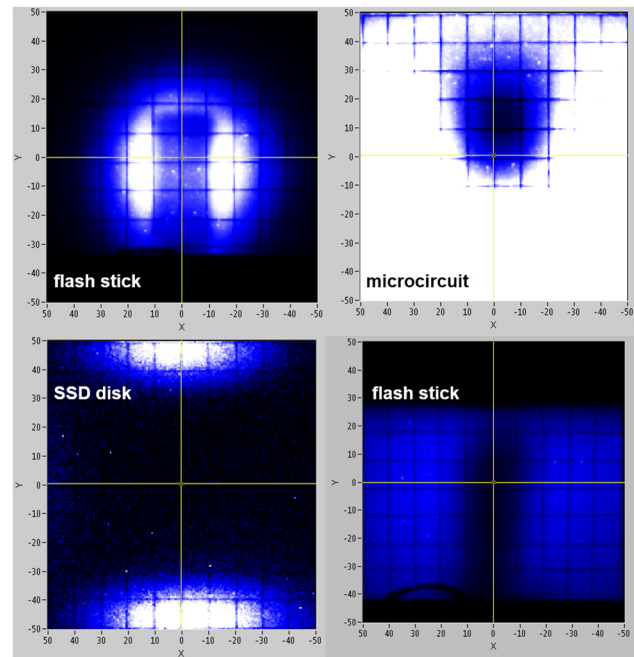


Figure 10: Images of "shadows" from beam irradiated objects at the phosphor screen.

After calibration a pulse particle count is also available by a software summation of image pixels intensities. The light yield remains linear in a full range of PS operation. However, a threshold sensitivity of PS is  $10^7\text{ p/cm}^2$ , while MGC can provide both current and profile measurements with beam densities down to  $10^5\text{ p/cm}^2$  due to a special differential signal read-out with a reference interference channel (Fig. 2). One extra stripe operates like an antenna for interferences from different linac equipment near PIF. This signal is subtracted then from the profile signals of the regular stripes, so one can obtain a spatial sensitivity better by two orders of magnitude.

## CONCLUSION

A new proton irradiation facility was constructed at INR RAS linac. To provide the beam diagnostics in a full range of operation parameters three devices were used:

- beam current transformer –  $10^{10}\div10^{12}$  p/pulse,
- phosphor screen –  $10^8\div10^{11}$  p/pulse ( $10^7\div10^{10}\text{ p/cm}^2$ ),
- gas counter –  $10^7\div10^{11}$  p/pulse ( $10^5\div10^{10}\text{ p/cm}^2$ ).

The limits of use are connected with the saturation and aging effects for high-density and with interferences and signal-to-noise ratio for low-density beams. The energy limit  $\sim21\text{ MeV}$  relates to the finite thickness of MGC.

The results of test operation and real measurements show the necessity of a further PIF diagnostics upgrade: a new luminescent screen with better surface uniformity and light yield, a gas-filled hermetical design of the gas counter, as well as an improvement of a radiation shield for CCD-camera and other back-end electronics.

## REFERENCES

- [1] P. Forck *et al.*, "Scintillation screen investigations for high energy heavy ion beams at GSI", in *Proc. DIPAC2011*, Hamburg, Germany, 2011, pp. 170-172.

# OVERVIEW OF BEAM INSTRUMENTATION AND COMMISSIONING RESULTS FROM THE COHERENT ELECTRON COOLING EXPERIMENT AT BNL\*

T. A. Miller<sup>†</sup>, J. C. Brutus, W. Dawson, D. M. Gassner, R. Hulsart, P. Inacker, J. Jamilkowski, D. Kayran, V. N. Litvinenko<sup>1</sup>, C. Liu, R. Michnoff, M. Minty, P. Oddo, M. Paniccia, I. Pinayev, Z. Sorrel, J. Tuozzolo, C-AD, BNL, 11973 Upton, NY, USA

<sup>1</sup> also at Department of Physics and Astronomy, SBU, 11794, Stony Brook, NY, USA

## Abstract

The Coherent Electron Cooling (CeC) Proof-of-Principle experiment [1], installed in the RHIC tunnel at BNL, has completed its third run. In this experiment, an FEL is used to amplify patterns imprinted on the cooling electron beam by the RHIC ion bunches and then the imprinted pattern is fed back to the ions to achieve cooling of the ion beam. Diagnostics for the CeC experiment have been fully commissioned during this year's run. An overview of the beam instrumentation is presented. This includes devices for measurements of beam current, position, profile, bunch charge, emittance, as well as gun photocathode imaging and FEL infra-red-light emission diagnostics. Design details are discussed and beam measurement results are presented.

## INTRODUCTION

During CeC's operation this year [2], its complete array of instrumentation proved useful in measuring the parameters of the 1.5 MeV electron beam, with bunch charges of 50 pC – 5 nC, 10 – 500 ps long, produced by the CeSb 112 MHz SRF Photoinjector and transported through the 704 MHz SRF 5-cell Linac [3]. The 15 MeV accelerated beam passes into the RHIC common section through the modulation drift section, undulator (or wiggler) amplification section, and kicker drift section before being diverted down the extraction line into the high-power aluminium beam dump, as shown in the layout in Fig. 1. Pulsed beam operation ran at a 1 Hz rate with trains of pulses spaced at 78 kHz (the RHIC revolution frequency).

The transport is equipped with differential current transformers and beam position monitors with positions alarms that provide the two primary machine protection measures. Plunging YAG:Ce profile monitors measure beam profile with a multi-slit mask in the injection section to measure

emittance. The high power and low power beam dumps are isolated to measure beam charge. The gun is equipped with cathode imaging optics in conjunction with the laser delivery system. Infrared (IR) emission from the undulators is characterized by an IR optics instrument array [4] beneath a diamond viewport in the RHIC beamline downstream of the CeC experiment.

## BEAM CURRENT AND CHARGE

In order to display and log the charge in the electron bunch, beam current can be collected in one of two beam dumps and is measured in two integrating current transformers (ICT).

### Faraday Cups

The two beam dumps in the beamline are electrically isolated to function as Faraday Cups (FC) to collect and measure the beam charge. These are the high-power beam dump at the end of the injection straight section and the low power dump at the end of the injection straight section. They are connected by ¼" Helix cable to integrating charge amplifiers located outside the tunnel to measure the collected charge and display in pC with an update rate of 1Hz. The FC's are terminated in the tunnel each with a 10 MΩ resistor and a 1nF capacitor. The signals are brought to a multiplexer for monitoring the signal on an oscilloscope or to be digitized. The majority of operations were made with the signals going to the oscilloscope.

**Temperature** The thermal mass of the high-power beam dump is fitted with two rad-hard thermocouples. The low power beam dump is fitted with an RTD-type probe. These probes are monitored by analog type 4-20 mA thermocouple transmitters mounted near the beam dumps. The thermocouple, made by Okazaki [5], is an AEROPAK

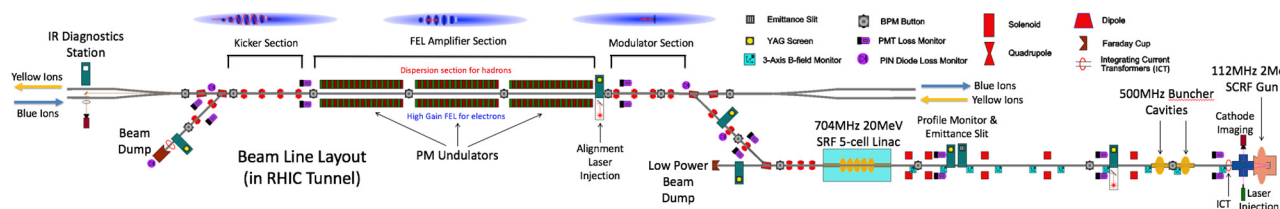


Figure 1: CeC beam line layout as installed at the 2 O'clock interaction point in the RHIC tunnel.

\*Work supported by U.S. DOE under contract No DE-AC02-98CH10886 with the U.S. DOE

<sup>†</sup>tmiller@bnl.gov

model, composed of a Type-K ungrounded hot junction, surrounded by MgO insulation packed in a thin Inconel tube, with a mini-plug termination. This plugs into a nearby chassis containing FlatPak series 250T analog 4-20 mA transmitters, by Acromag [6]. This model was chosen for its all analog design for increased radiation hardness.

### *Integrating Current Transformers*

Beam charge is non-destructively measured by two ICT type in-flange integrating current transformers from Bergoz. These are mounted, one just after the gun and one just before the beam dump. Both ICTs have a 1.25 Vs/C sensitivity

The two ICTs provide independent signals for instrumentation and provide differential signals for machine protection. The beam pulse charge is reported for every pulse and a charge difference between ICTs is provided as an input the Machine Protection System (MPS). Charge calculation occurs on every pulse and the array represents all the charge values captured in 1 second. Average current is reported as the quotient of average charge and average pulse rate.

In lieu of using the typical Integrate-Hold-Reset electronics from Bergoz, the ICT signals are digitized directly. To increase the sensitivity and signal to noise ratio of the ICTs, two amplifiers are installed for each ICT. The output is buffered to both a digitizer and an oscilloscope.

### *Digitization*

The ICT pulses are digitized with continuous acquisition and analysis without the need of an external trigger. The digitizer, referred to as the “Zynq” module, is based on the Xilinx Zynq proto-type module combined with a 4DSP FMC112 analog front end. ICT pulses are sampled at a max rate of 125 MHz with a 14-bit ADC. For every pulse, the Zynq integrates and calculates charge and performs a difference calculation. It uses the pulse charge information to determine the beam current and uses the differential measurements for beam efficiency calculations for the MPS.

**Zynq Processing Description** The charge is determined by integrating the raw signals from the ICTs. The integration is performed in two steps, first an integration window is specified followed by a baseline window, with indexes specified by the user. Integration calculations are performed on the upstream and downstream ICTs and the maximum instantaneous value is saved. Integral values are scaled and truncated to 16 bits and stored in DPRAM at a decimated rate (up to 32K samples) for display. When operating with a high number of pulses, the decimation rate must be increased in order to capture all the pulses. The integral values are also sent to a running average block, where a new variable length average is computed and displayed for each entry. The latency is approximately 8 nsec per the number of samples in average.

A one-second sum is computed, with a similar latency, for the integral data with a period based on the number of clocks in the average. The periodic timed sums are compared continuously to high maximum and low maximum alarm thresholds with single error thresholds and reported

to the MPS. The total losses are calculated as the difference of the scaled integrals for the upstream and downstream ICTs and saved in a data array. A periodic timed sum is computed from the difference of the two scaled integrals. This sum is continuously compared to a maximum alarm threshold with a single error threshold and reported to the MPS.

The faraday cup signals are terminated locally with 1M $\Omega$  and transported out of the RHIC tunnel to amplifiers in the instrumentation racks. These signals are then passed to the Zynq and are integrated using the same algorithm described for the ICTs.

### *Charge Build-up*

During the second year of operation, cumulative drifting of the electron beam was observed with fast returns to the original orbit along with a current spike in the ICT having a regular periodicity of about 17 minutes during pulsed beam operation at 1 Hz with pulse trains of 57 pulses of 200pC/pulse @ 78 kHz, (11.4 nA average current). This behavior is indicative of charge buildup on the ceramic and diverting the beam. A new ICT was ordered with an arbitrary aperture option, reducing the aperture to 60mm to hide the ceramic behind a 1-mm gap. This was installed for the second year of operation and this behavior was no longer observed.

### *Recent ICT Failure*

During the 2017 run, the ICT installed in the extraction line failed to produce a signal on June 21, just before the end of the run. The ICT was removed during the following shutdown and replaced with the ICT from the CeC gun, that was replaced by the new shielded version.

It was known that in preparation of the 2017 run, this ICT was over baked to 188C, 38C over the 150C temperature limit. As the Zynq was used for direct digitization, the calibration coefficient was changed to match the gun and dump ICT responses. This ICT functioned properly from April – the beginning of the run – until it failed on June 21. Upon inspection of the ICT by Bergoz, the only failure that was found was a decrease in core permeability, typically caused by over temperature. It was not discovered why the ICT continued to function after the over temperature incident, nor why it suddenly failed to operate. Radiation monitors were later installed nearby to monitor dose rates near the dump for increased protection of the hardware.

## **BEAM POSITION**

There are 12 button-style BPM pick-ups installed in the beam transport. These are attached with 1/4” Helix phase stabilized cable to 4-channel Libera [7] Single Pass E electronic modules installed in three 4-module chassis. Two additional four-button stations are mounted upstream and downstream of the CeC transport common to the RHIC ion beams for ion beam position measurement. These are connected to a fourth chassis with two Libera Single Pass H electronic modules installed. The electron beam position must be measured independently of the ion beam. This is possible while operating in background mode where the



electron bunch is injected into the RHIC abort gap without overlapping with the ion bunch. During this mode, the electron bunch is injected in the middle of the RHIC abort gap. Thus, the electron BPM's are triggered with the electron bunch, about 400 ns after the last ion bunch, and the ion BPM's are triggered with the ions, about 400 ns after the electron bunch for independent position measurements.

Position data logged during operations that shows a 200µm peak to peak variation is in line with a 30 – 40 µm rms standard deviation of position.

## BEAM PROFILE

A total of six beam profile monitors are installed in the transport. All consist of scintillating screens made of 30 mm diameter monolithic YAG:Ce crystals mounted normal to the beam, with a polished copper mirror behind for viewing by the camera optics. This arrangement provides an optical viewing area of 25 mm in diameter. To bleed off charge, the upstream face of the YAG crystal is coated with 100nm of aluminum. The YAG & mirror assemblies are inserted into the beam path by pneumatic actuators mounted on the top port of a six-way cross. The pneumatic actuators can be replaced without breaking vacuum.

Commissioning experience from the first year's run led to the design and installation of impedance limiting shields that slide up and down in the vertical bore to block off the transverse horizontal bore, including conical transitions in the bore for the optical viewport.

## Optics

Cameras with Gigabit Ethernet (GigE) interface were chosen for the simplest infrastructure. All cameras connect to a private network switch shared only by the video server. The video server has a second network interface card (NIC) to interface with the department network for serving images published by the software manager running on the server. The Prosilica GT1600 model camera, from Allied Vision Technologies (AVT) was chosen for its integrated lens p-iris control; which is a new type of stepper motor driven iris control that can be set and maintained through power cycles. The camera has a 1/1.8-type 2MP sensor with a wide gain of 0 – 26 dB. Its external trigger is synchronized to the electron beam and its exposure times range from 10µs to 68.7 sec. It is paired with a 50mm lens, Edmund Optics (EO) model 89-938, having a stepper motor driven iris with apertures of f/2.1 to f/95 in 42 increments. During bench tests the optical resolution was determined to be < 50 µm by the measured contrast, or modulation transfer function (MTF) > 27 % from a 10 line-pairs/mm resolution target.

A white LED ring on the face of the optical viewport illuminates the in-vacuum view to check the health of the screen. As a focusing aid, a 450nm blue laser is used to excite the YAG crystal. It is injected into the optical axis using a dichroic beam splitter (EO 69-899), 1mm thick with a 500nm cut-on, placed in front of the lens. This also blocks the laser light from the camera while allowing most of the YAG emission to pass through to the camera. For increased structure in the laser induced pattern, on which

to focus, on the crystal, a diffractive optical element, model D-ER-340 from Holoeye Photonic [8], diffracts the laser spot into a chopped cross pattern that is centered on the YAG screen.

## EMITTANCE

A multi-slit mask is installed in the injection section upstream of a profile monitor. It is inserted with a three-position pneumatic actuator with two insertable positions for horizontal and vertical slits and can be fully retracted from the beam aperture. The slit mask, as shown on the right in Fig. 2, with dimensions tailored for the expected beam divergence, was made of 1mm-thick tungsten having 10 slits that were wire-EDM cut to be 200 µm wide, spaced 2 mm apart, for both the horizontal and vertical positions.

The incoming beam is sampled by the multi-slit mask, as shown on the left in Fig. 2, where the effect of space charge is removed and the new beamlets propagate to the downstream profile monitor. The image of the beamlets is analyzed by an algorithm [9] developed at BNL to fit a multi-gaussian shape to the beamlets' profiles. The average divergence of each beamlet is calculated based on slit positions and gaussian peak positions. The rms divergence of beamlets are calculated from the rms of gaussian peaks. The emittance is then calculated from the position angle correlation and the rms divergence of the beamlets.

Special features are built into the image capture software so that a region of interest can be selected through the beamlets' projection and a resulting profile is generated, calibrated in mm instead of pixels. The user specifies the parameters of slit width, slit spacing, drift length, scaling factor, and angle of rotation. A multi-gaussian fit is performed and displayed with measurements of amplitude, sigma, and peak locations that are processed by an add-on algorithm to calculate the beam emittance.

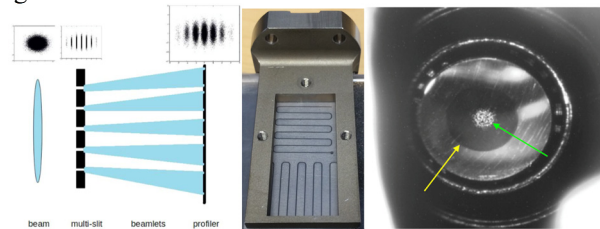


Figure 2: Left: Schematic of multi-slit emittance measurement, Middle: photo of tungsten mask in SS holder, Right: Image of polished molybdenum cathode puck surface. The dark circle (yellow arrow) is the 12 mm diameter activated cathode area. The bright spot in the center (green arrow) is the laser spot.

## GUN PHOTOCATHODE IMAGING

The surface of the polished molybdenum puck, with the activated cathode area, in the superconducting RF photoinjector is imaged, as shown in Fig. 2, for use during cathode insertion and alignment as well as for imaging the

laser spot on the cathode surface and checking the health of the cathode surface. The camera with illumination assembly is mounted in the laser exit table enclosure, 1.30 m downstream of the cathode, and uses the laser exit mirror

to view the cathode. A 2 MP GigE camera, AVT model Manta G201B, is fitted with a Navitar 6x ZoomXtender [10] lens assembly (working distance of 0.3 – 16 m) to overcome the long distance and limited aperture. Illumination of the cathode is made by a high power collimated single-die white LED with 800mW of output. This lamp illuminates on-axis with the optical path of the camera through a 50:50 UV Fused Silica broadband plate beam splitter. Nuisance reflections off of in-vacuum aperture limiting surfaces caused glare that bloomed into the image. This was mitigated by a spotlight arrangement with the LED mounted to dual condenser lenses around an iris, adjusted to focus the smallest spot through the limiting aperture to reduce the glare.

### FEL INFRA-RED-LIGHT EMISSION DIAGNOSTICS

Light emitted from the undulators in the “amplifier section” is detected and analyzed as a feedback of both the position of the electron beam in the wiggler as well as the degree of overlap of the electron and ion beams. An increase in emission power is expected to indicate the onset of coherent amplification in the undulators. The profile of the emission pattern will be a function of the angular trajectory through the undulators. In order to provide data on these parameters, an array of optical instruments is installed downstream of a RHIC DX magnet under an optical viewport where a copper mirror plunges in to extract the undulator light between the separated RHIC ion beams. All optics were designed to have a 50 mm aperture.

Although the experiment was designed for 21.8 MeV, giving an IR emission at 14  $\mu\text{m}$ , the 704 MHz SRF 5-cell Linac was operated at reduced energy during this year’s run. The resulting final beam energy of 15 MeV resulted in a shift of the expected undulator emission to 30  $\mu\text{m}$ . The ZnSe viewport was replaced with a CVD diamond viewport to transmit the longer wavelength as well as a green alignment laser, injected upstream of the undulators. The IR detectors were changed to Terahertz band detectors.

#### Power

In order to cover an optical power range wide enough to detect down to 10 nW from spontaneous emission and measure up to 3W during coherent amplification, three different detectors were used, as summarized in Table 1.

Three remote controlled flip mirrors are used to divert the light between detectors, as shown in the optics layout in Fig. 3. The 3A Thermoelectric detector has a slow 2.5 s response to CW light; whereas, the THZ51 Pyroelectric detector and Golay Cell require a chopped signal, provided by the chopper wheel. A thermal source is included with its own flipper mirror for an on-board test.

Table 1. Summary of IR Detectors

Detector (mfrg)	Range	Chop
3A-P-THz (Ophir)	15 $\mu$ – 3 W	DC
Golay Cell (Tydex)	10 n – 10 $\mu$ W	15 Hz
THZ51 (Gentech)	10 n – 128 $\mu$ W	5 – 25 Hz

#### Profile

A scanning pinhole, moved by two X-Y stepper motor drivers orthogonal to the light path, is scanned in a raster pattern over a user selectable area while the Golay Cell response is digitized to build an array of data that is assembled into an image with interpolation between points. With the iris set to 4 mm, a full scan of the 50mm beam is made with 20 horizontal lines (2.5 mm apart for a 50 x 50 mm scan) takes about 3 minutes to complete. The image building routine is embedded in our versatile profile monitor image viewing software.

#### Spectrum

The wavelength of the undulator emission is proportional to the absolute energy of the electron beam; which much be matched closely to the ion beam it will cool. A monochromator, model SP2150I from Princeton Instruments [11], is used to measure the emission wavelength. It has a mirror and a 30  $\mu\text{m}$  grating installed on s grating selection turret. The mirror is selected to pass all light during optical alignment. The wavelength of the undulator light was effectively measured at 31.2  $\mu\text{m}$ .

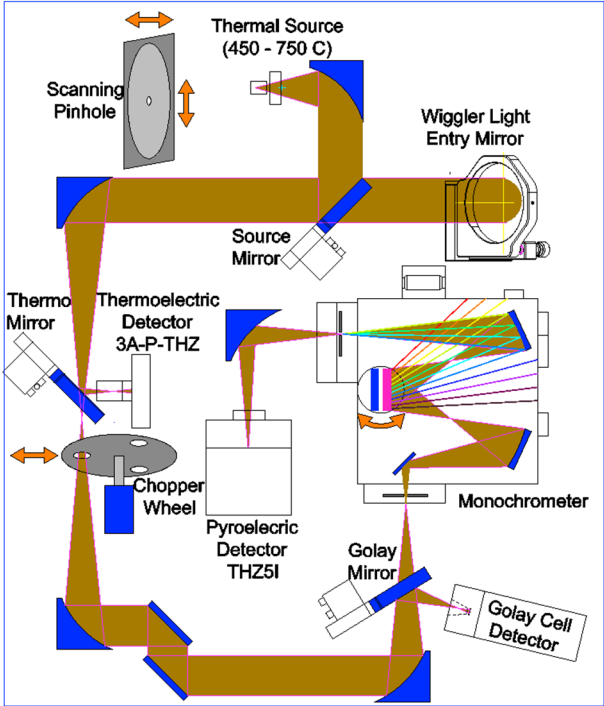


Figure 3: IR Optics layout.

### BEAM LOSS

A system to monitor beam losses during commissioning and tuning is installed but not connected to the MPS. There are seven beam loss monitor stations with loss monitors mounted on beam left and beam right (14 channels total). The detectors are photomultiplier tubes (PMT) mounted in light-tight housings with a test LED inside, fashioned after those used for the 12 GeV upgrade to CEBAF [12] at JLAB. The signals from the PMTs will be processed by VME based 8-channel FPGA electronics cards [13] purchased from JLAB. With a 1- $\mu\text{s}$  fast shutdown output to

the MPS, this PMT BLM card also has a parallel log amplifier signal path to provide 5 decades of dynamic response to aid in tuning of the machine with low power beam to reduce losses.

## STRAY MAGNETIC FIELDS

The energy of the electron beam was low enough for stray fields from the nearby RHIC magnets to deflect the beam. It was found during the first year of commissioning that these fields were difficult to compensate for with correctors. Thus, a series of 3-axis fluxgate magnetometers were installed, namely Watson Industries model FGM-301 [14]. A total of 10 units, with a range of  $\pm 700$  mGauss, were installed in the low energy section between the gun and the Linac

## ACKNOWLEDGEMENTS

The authors would like to thank J. Tuozzolo, Cliff Brutus, G. Mahler and other members of the engineering & design team, and M. Mapes, and other members of the Vacuum Group, and M. Harvey and other members of the Controls Group, and T. Curcio and D. Lehn and other members of the Accelerator Components & Instrumentation Group.

## REFERENCES

- [1] V. Litvinenko, et al “Proof-of-Principle Experiment for FEL-Based Coherent Electron Cooler”, in *Proc. FEL2011*, Shanghai, China, 2011, paper WEOA3
- [2] V. Litvinenko, et al “Status of Proof of Principle Experiment of Coherent Electron Cooling at BNL”, in *Proc. COOL'17*, Bonn, Germany, 2017, paper WEM22
- [3] I. Pinayev, et al, “Coherent Electron Cooling Diagnostics: Design Principles and Demonstrated Performance”, presented at the 7th Int. Beam Instrumentation Conf. (IBIC'18), Shanghai, China, Sept 2018, paper TUOB01, this conference
- [4] T. Miller, et al “Infrared Diagnostics Instrumentation Design for the Coherent Electron Cooling Proof of Principle Experiment”, in *Proc. FEL'14*, Basel, Switzerland, Aug 2014, paper THP074
- [5] Okazaki Manufacturing Company, <https://www.okazaki-mfg.com/en/BasicProducts/Aeropak.html>
- [6] Acromag, <https://www.acromag.com>
- [7] Instrumentation Technologies, <https://www.i-tech.si/>
- [8] Holoeys Photonics, <https://holoeys.com/diffractive-optics/>
- [9] C. Liu, et al., “Multi-slit based emittance measurement study for BNL ERL” in *Proc. IPAC'13*, Shanghai, China, May 12-17, 2013, paper MOPWA083
- [10] Navitar, <https://navitar.com/products/imaging-optics/high-magnification-imaging/zoom-6000/>
- [11] Princeton Instruments, <https://www.princetoninstruments.com>
- [12] J. Perry, et al., “The CEBAF Beam Loss Sensors”, in *Proc. PAC'93*, Washington DC, May 1993, pp 2184 - 2186
- [13] J. Yan and K. Mahoney, “New Beam Loss Monitor for 12 GeV Upgrade”, in *Proc. ICALEPCS'09*, Kobe, Japan, Oct. 2009, paper WEP092
- [14] Watson Industries, <http://watson-gyro.com/product/magnetometers/fluxgate-magnetometer-fgm-301/>



# THE DESIGN AND USE OF FARADAY CAGE IN LINAC TEMPORARY LINE OF CSNS

Ming Meng<sup>†</sup>, Taoguang Xu, Jilei Sun, Anxin Wang, Fang Li, Peng Li, Institute of High Energy Physics, Chinese Academy of Sciences (CAS), Beijing 100049, China and Dongguan Neutron Science Center, Dongguan 523803, China

## Abstract

In the end of linac temporary line in CSNS, we need a faraday cage to absorb the beam. in the experiment it will be mounted and used twice. according to the beam energy and current of CSNS, we choose water-cooled pipe structure with tilted panel after simulation with Ansys. the main principle of the faraday cage is to simplify the structure and reduce the radiation activation of it, to do this, we also do the simulation of radiation. to make sure the faraday cage is safe in beam experiment, we also plug in a pt100 Platinum resistance to monitor the temperature. after faraday cage is built and mounted on the line, it works well and sustain the beam bombardment.

## INTRODUCTION

China spallation neutron source (CSNS) is the first spallation neutron source in developing countries. In linac, there are a 50 keV H- iron source, a 3 MeV Radio Frequency Quadrupole(RFQ), and a 80 MeV Drift Tube Linac(DTL). In the first stage of beam experiment, when the H- come to the end of Medium Energy Beam Transport(MEBT) with 3 MeV energy and the end of DTL1 with energy 26.7 MeV, we need a temporary line with some beam measuring equipment like BPM, wire scanner to check the parameter of beam is right. And at the end of temporary line, we need to design a faraday cage to absorb the beam safely.

## MACHINE DESIGN OF FARADAY CAGE

### Plan Selection

In the 973 foundation project, we use “V” type beam stop as in Fig. 1, it is built with Oxygen free copper covered with aluminium using water cooling, and contain vacuum structure, the angle between the center line and surface is 8°. This beam stop is designed for 3.5 MeV proton, 20 mA beam current and 15% duty cycle, inside it , we use quadrate tunnel structure to improve cooling efficiency.

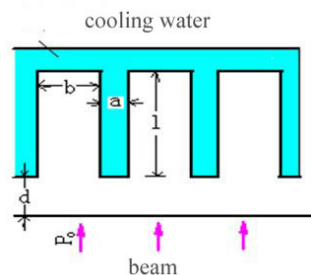


Figure 1: External shape and quadrate tunnel.

In the CSNS temporary line, because the “V” type cooling system is too complex that the welds leaks sometime, to simplify the design and machining, we decide to use just one tilted board and set the welds of water cooling pipe out of the vacuum structure. The faraday cage should be able to absorb beam as in Table 1.

Table 1: Parameter of Beam in Temporary Line

Energy	26.7 MeV	3 MeV
Peak current	15 mA	15 mA
Beam frequency	5 Hz	5 Hz
width	500 $\mu$ s	500 $\mu$ s

### Physical Design

To start the simulation, first we should get the peak heat flux from Eq. (1), in it we set up the beam sigma size to 2.5 mm temporarily,

$$A \cdot \int_0^{0.025} \int_0^{0.025} e^{-\frac{x^2+y^2}{2 \times 0.0025^2}} dx \cdot dy = 400 \text{ kW} \quad (1)$$

then we should get the heat exchange coefficient h as in Eq. (2), which is the thermal conductivity of cooling water, d is the equivalent diameter of cooling pipe, 4 times of cross-sectional area divide by perimeter, Nu is the Nusselt number as in Eq. (3),

$$h = \frac{\lambda \cdot Nu}{d} \quad (2)$$

for forced convection heat transfer of turbulent flow in the tube, the Dietus-Belt formula is widely used to get Nusselt number, for cooling water n=0.3, Pr is Prandtl number, and Re Critical Reynolds number.

$$Nu = 0.023 Re^{0.8} Pr^n \quad (3)$$

After all this is done, we build model and set the cooling water pipe to different size, while the interval between pipe is fixed to 4mm as in Fig. 2, and in the calculation before we find that if the faraday cage is vertical to beam we can't get temperature under melting point, so we set up a slope between faraday cage and central axis to 10°, and the beam size  $\sigma$  to 2.5 mm, with the slope of faraday board, the actual area of beam will become bigger to make the heat flux less.

<sup>†</sup> mengming@ihep.ac.cn

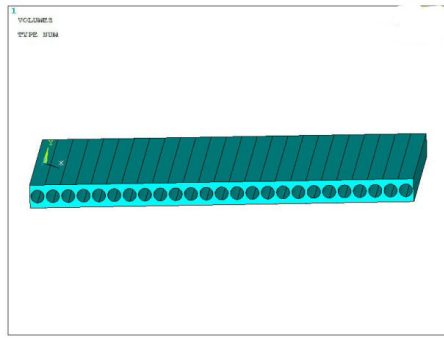


Figure 2: Model of beam stop with cooling pipe.

Then after simulation we get peak temperature distributed as follow in Fig. 3, from this we can check that 8 mm size of cooling pipe is most suitable.

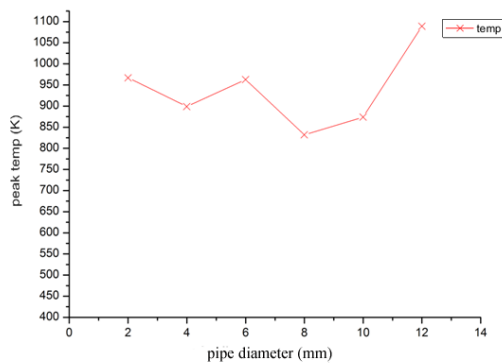


Figure 3: Temperature in different diameter of pipe.

To determine the distance between pipe, we use pipe diameter 8 mm as we got from last step, and change the distance until we get Fig. 4 below, we can find that 12 mm of pipe distance should be used to minimize temperature and suitable for machining.

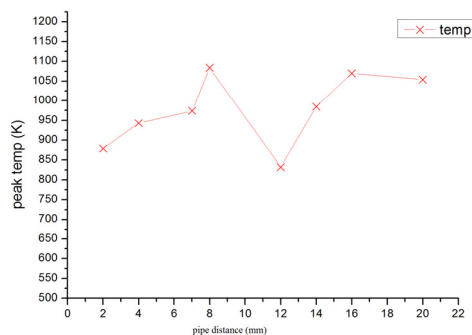


Figure 4: Temperature in different distance of pipe.

At last we should find out the minimum beam  $\sigma$  can be used for faraday cage. We build model with 8 mm pipe diameter and 12 mm distance, slope angle to 10°, change beam size and get Fig. 5, so if we want to make sure faraday cage is safe, the  $\sigma$  size at 3 MeV should be bigger than 0.7 mm, while at 26.7 MeV the minimum size is 2 mm.

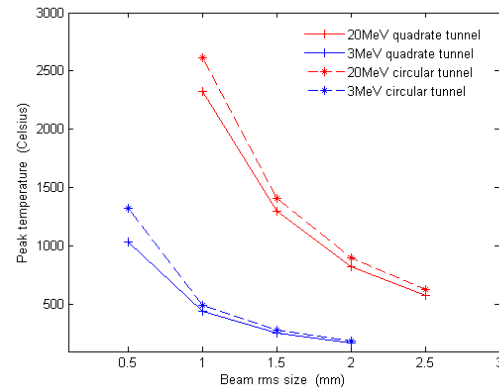


Figure 5: Temperature in different beam size.

The activation energy of Cu in proton particle is about 2.7 MeV, while the activation energy of C is 32 MeV, to reduce the activation probability of Cu, we plate one layer of graphite on the copper board. According to 26.7 MeV proton, the continuous-slowing-down approximation range [1] in graphite should be about 2 mm [2], so we set the thickness of graphite to 2.5mm. Because graphite has different thermal conductivity [3], we compare graphite with conductivity of 129 W/m.K and 1500 W/m.K, and find from Fig. 6 that higher conductivity is better and decide to use it.

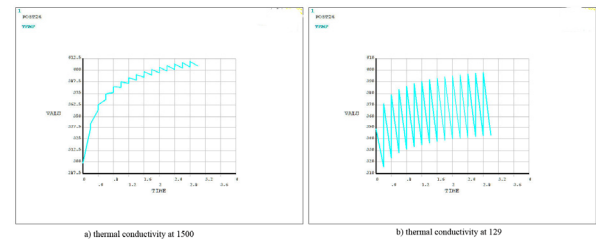


Figure 6: Peak temperature in different conductivity.

So far we can give the model of faraday cage according to the angel, pipe diameter, pipe distance, parameter of graphite board, as in Fig. 7.

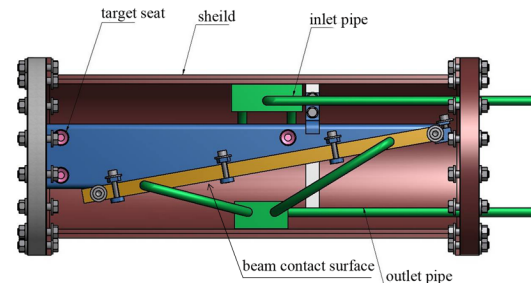


Figure 7: Model of faraday cage.

## Radioprotection

Considering that faraday cage will work long time under 26.7 MeV proton at 15 mA current, it is necessary to consider the radioprotection around it. In calculation we set beam width to 500 us, frequency 25 Hz, run continuously 100 day, and after stop 4 hours, the radiation dose near the surface of faraday cage can be 60 mSv/h, as in Fig. 8.

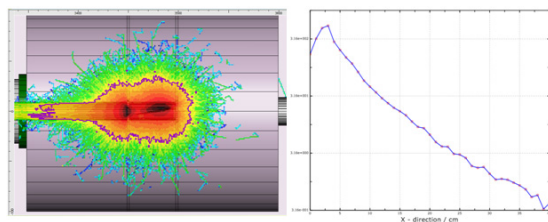


Figure 8: Residual radiation dose in horizontal mSv/h.

So it is necessary to add additional shielding facility, we use 5 cm thick lead plate to build box to cover faraday cage, and make residual radiation as equal as beam loss at 1 W/m. because the leap is very soft, we use concrete to support lead plate. After beam experiment is over, faraday cage will be totally activated and should be dealt as highly radioactive waste. About the cooling water of faraday cage, only low concentration and low life N-16 can be found, we need not to consider about it because its half life is only 7.13 s.

To make sure faraday cage is safe, we also add one PT100 thermal resistance on the faraday cage next to the water pipe, pt100 signals transformed by transmitter can be transported to work area to monitor the temperature during beam experiment.

## MACHINING INSTALLATION AND EXPERIMENT

After machining and necessary test like vacuum and water pressure is done, the installation is finished at the end of Medium Energy Beam Transport (MEBT) of CSNS, as in Fig. 9, here the energy is only 3 MeV and current is 5 mA, so the radiation and temperature is very low.

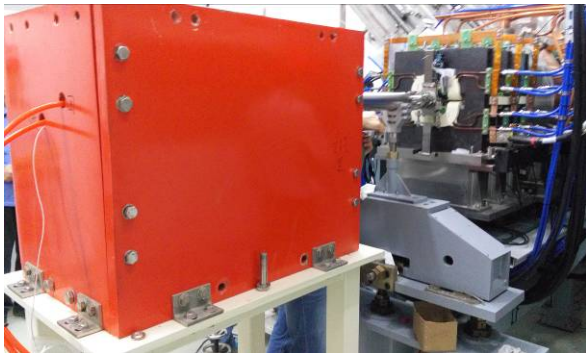


Figure 9: Installation at the end of MEBT.

Then it is moved to the end of the first quarter of Drift Tube Linac (DTL), in this place the final beam energy is 21.67 MeV, beam current 10 mA, pulse width is 400 us, repetition frequency is 5 Hz, the beam parameter is smaller than design to make sure safety of faraday cage. and in experiment the highest temperature from PT100 is under 30° .

## CONCLUSION

The faraday cage is designed to absorb beam of MEBT and first quarter of DTL in linac temporary line of CSNS, it should not be damaged at the energy of 26.7 MeV and current 15 mA, also the radioprotection should be considered. After all the beam experiment is done successfully, the faraday cage works well and residual radiation around it is safe, so we can conclude that this single sloping plate structure with cooling pipe meets the demands as expected.

## REFERENCES

- [1] Evans, *The Atomic Nucl eus*, McGraw-Hill, p. 624-625, 1965.
- [2] SRIM, 2003, <http://srim.org>
- [3] R. Valdiviez, *et al.*, "The Final Mechanic al Design, Fabrication, and Commissioning of a Wire Scanner and Scraper Assembly for halo-Formation Measurements in a Proton Beam," in *Proceedings of PAC'01*, Chicago, May 2001, p. 1324, paper TPAH045.



# FAST LUMINOSITY MONITORING FOR THE SuperKEKB COLLIDER (LumiBelle2 PROJECT)

C. G. Pang\*, P. Bambade, S. Di Carlo, D. Jehanno, V. Kubytskyi, Y. Peinaud, C. Rimbault  
LAL, Univ. Paris-Sud, CNRS/IN2P3, Université Paris-Saclay, 91400 Orsay, France  
Y. Funakoshi, S. Uehara, KEK, 305-0801 Tsukuba, Japan

## Abstract

*LumiBelle2* is a fast luminosity monitoring system prepared for SuperKEKB. It uses sCVD diamond detectors placed in both the electron and positron rings to measure the Bhabha scattering process at vanishing photon scattering angle. Two types of online luminosity signals are provided, Train-Integrated-Luminosity signals at 1 kHz as input to the dithering feedback system used to maintain optimum overlap between the colliding beams in horizontal plane, and Bunch-Integrated-Luminosity signals at about 1 Hz to check for variations along the bunch trains. Vertical beam sizes and offsets can also be determined from collision scanning. This paper will describe the design of *LumiBelle2* and report on its performance during the Phase-2 commissioning of SuperKEKB.

## INTRODUCTION

SuperKEKB uses the so-called *nano-beam scheme* to reach a very high instantaneous luminosity of  $8 \times 10^{35} \text{ cm}^{-2} \text{ s}^{-1}$  [1]. It consists of using a large crossing angle at the interaction point (IP) to enable colliding 2500 ultra-low emittance bunches with very small beam sizes (design value  $\sigma_y \sim 50 \text{ nm}$ ). The luminosity is very sensitive to beam-beam offsets, e.g., caused by vibration of mechanical supports induced by ground motion. In order to maintain the optimum beam collision condition, orbit feedback systems are essential at the IP [2]. At SuperKEKB, the beam-beam deflection method is used for orbit feedback for the vertical plane, while for the horizontal plane, a dithering orbit feedback system using the luminosity as input, similar to that operated in the past at PEP-II, has been adopted [3, 4].

For this purpose, a fast luminosity monitor based on sCVD diamond detectors, named *LumiBelle2*, was developed and tested during the Phase-2 commissioning of SuperKEKB. By measuring the rate of Bhabha events on each side of the IP at vanishing photon scattering angle, *LumiBelle2* can provide both Train-Integrated-Luminosity (TIL) signals and Bunch-Integrated-luminosity (BIL) signals simultaneously, over a large range of luminosities. TIL signals are needed by the dithering orbit feedback system at 1 kHz, with relative precisions better than 1 % [5]. BIL signals are important to probe potential luminosity differences between the numerous bunches along the trains. Another luminosity monitoring system named Zero Degree Luminosity Monitor (ZDLM) is also installed in the immediate vicinity. It uses Cherenkov

and scintillator detectors [6], providing important complementary measurements. In addition, the Electromagnetic Calorimeter Luminosity On-line Measurement (ECL-LOM) is operated in the backward and forward end-caps of the Belle II detector, measuring the coincidence rates of back-to-back Bhabha events in the opposite sectors, with the ability to provide absolute values of the luminosity after proper internal calibration [7].

In this paper, we describe the design of *LumiBelle2*, including results of detector tests with a Sr-90 electron isotope source, the experimental set-up and the DAQ based on an FPGA, and the report on obtained luminosity monitoring performances, based on simulation and measurements pursued during the Phase-2 commissioning period, both with colliding beams, and with single beams, for background evaluations.

## DESIGN AND LAYOUT

The placement of the *LumiBelle2* detectors was carefully studied with respect to signal rates and background contamination, resulting in choosing locations 10 and 29 m downstream of the IP in the Low Energy Ring (LER) and High Energy Ring (HER), to measure, respectively, Bhabha scattered positrons and photons [8]. To increase the rate of extracted positrons, a custom made beam pipe section with a depression of 15 mm and 45° inclined windows is used in the LER, see Figure 1. A Tungsten radiator with an effective thickness of 4 Radiation Lengths (1RL=3.5 mm) was added to enhance the electromagnetic showers and boost the detection efficiency [9].

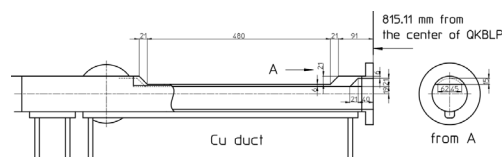


Figure 1: Designed window shape beam pipe.

The RF of SuperKEKB is about 500 MHz, with bunches stored nominally almost every other bucket (so called quasi 2-bucket fill pattern), which implies collisions every 4 ns. For BIL monitoring at high counting rate, signals from neighbouring bunches must be separated. A new diamond detector with a thickness of 140  $\mu\text{m}$ , coupled with a broadband 2 GHz 40 dB current amplifier from CIVIDEC [10] at the front-end, are used for this purpose. Low attenuation half-inch HELIAX coaxial cables are used to avoid signal broadening

\* pang@lal.in2p3.fr

during the transfer to the data acquisition system in the Belle II Electronic Hut located about 100 m away.

### Diamond Detector Test

Signal amplitudes and charges in the diamond detector were compared using data acquired with an oscilloscope, integrating the signal peaks to determine the charge, see Figure 2. The good observed linearity makes it possible to sum signal amplitudes turn by turn to evaluate integrated relative Bhabha scattering rates for each bunch crossing.

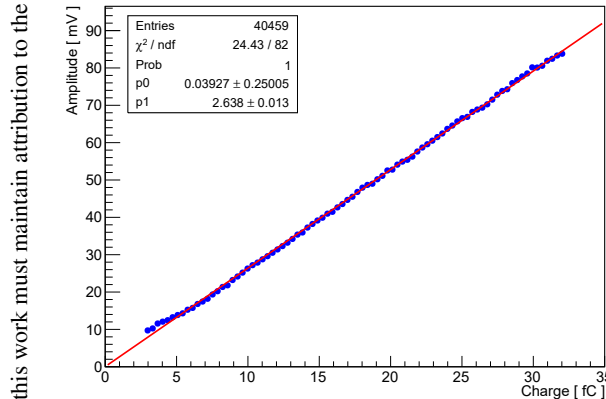


Figure 2: Relationship between signal amplitude and charge generated in diamond detector.

The Constant Fraction Discrimination (CFD) method was used to study the timing performance of the diamond detector, using a fraction of 5 %. As can be seen in Figure 3, the signal rise time peaks at 0.88 ns, and most signals (more than 98 %) are within 4 ns. The small impact from these partially overlapping pulses is at present neglected, but could in principle be taken into account as a correction.

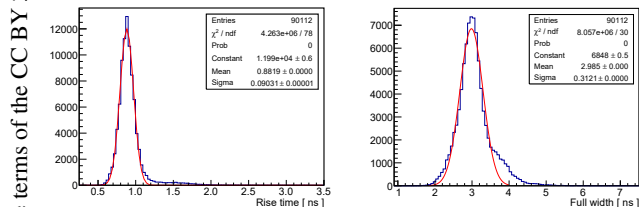


Figure 3: Distribution of rise time (l.h.s) and full width (r.h.s) of the signal in the diamond detector.

### Mechanical Set-up

The experimental layout for luminosity monitoring during the Phase 2 commissioning is shown in Figure 4. It consists of pillars supporting three *LumiBelle2* diamond detectors and the ZDLM counters in both rings [6]. One of the *LumiBelle2* diamond sensor in each ring has a remotely controlled motor to enable scans in the horizontal plane over a range of 25 mm.

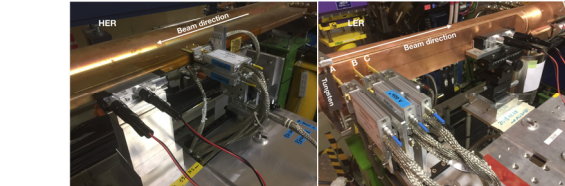


Figure 4: Experimental layout of *LumiBelle2* and ZDLM sensors in both ring (left: HER, right: LER).

### Data Acquisition System

The DAQ developed for *LumiBelle2* is located in the Belle II Electronics Hut. A functional diagram is shown in Figure 5. Four among the six provided signals are selected by connecting the corresponding cables to a GSPS 10-bit AC-coupled ADC board (FMC126, 4 DSP), requiring a clock at 1 GHz (twice the RF frequency). The four ADC digital outputs are then fed to a VIRTEX-7 FPGA board (VC707, Xilinx), which calculates the Train Integrated Luminosity (TIL), Bunch Integrated Luminosity (BIL), COUNT (event rate) and RAW SUM (direct summing all of samples) in real time, at a rate of up to 1 kHz, simultaneously for the four incoming inputs. The DAQ includes also a 16-bit DAC, providing eight analog outputs with 1 kHz bandwidth, that can be configured independently to convert to any TIL, BIL, COUNT or RAW SUM values, from any of the four input channels.

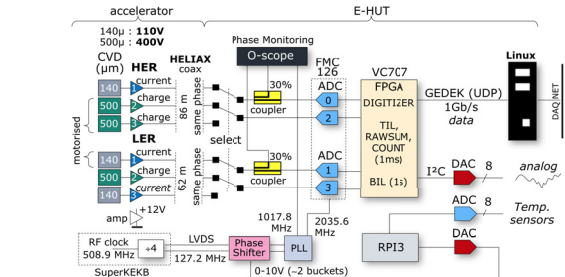


Figure 5: *LumiBelle2* DAQ function diagram.

The DAQ was initially designed to handle a maximum rate of one bunch every 2 ns, corresponding to train patterns with all or almost all buckets filled. It makes use of two principles: (1) the luminosity is proportional to the amplitudes and rates of signal peaks, and (2) the pulses and RF clock are synchronous, to enable sampling all peaks simultaneously. As the ADC is AC-coupled, the mean value of the pulse train is always centered at 0 V, requiring therefore to sample also the pedestals between subsequent pulses. For bunches separated by 2 ns, this implies sampling at twice the RF frequency. As illustrated in Figure 6, the current amplifiers used for the Phase 2 commissioning are fast enough only for the 4 ns bunch spacing used nominally at SuperKEKB. One sample (1) is then positioned on the peak (using the Phase Shifter shown on Figure 5 to find the optimum timing) and the pedestal is obtained from the third sample (+3). The luminosity process integrates over 1 ms the sum

of all differences  $\text{Diff}(n)$  between these samples above a defined threshold to provide the TIL value. The same process provides 5120 sums each 1 second corresponding to the BIL value for each bucket. The COUNT value gives the total number of pulses during 1 ms, and therefore the ratio  $\text{TIL}/\text{COUNT}$  gives the mean pulse amplitude. The RAW SUM value calculates the sum of all samples above a defined threshold and is intended for some channels which use Charge Amplifiers with a 10 ns FWHM, and that cannot be handled easily in terms of TIL and BIL. All the real time data are uploaded to a Linux machine through the GEDEK protocol (ALISE) over a UDP link at 1 GB/s, then converted into  $n$ -Tuple files and saved together with a number of related relevant machine parameters available through the EPICS protocol and important for the offline analysis. A subset of the *LumiBelle2* data were also uploaded to EPICS at a rate of about 1 Hz, for continuous display in the accelerator and Belle II control rooms. Moreover, for the purpose of the IP dithering orbit feedback, analog information from the DAC based on the 1 kHz TIL data was directly fed to the lockin amplifier used by that system.

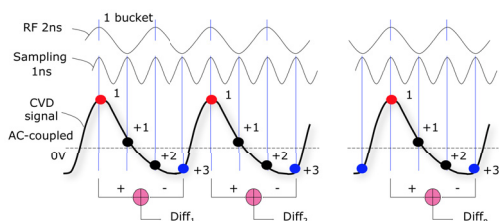


Figure 6: Illustration of DAQ signals processing for 4 ns bunch spacing.

## RESULTS IN PHASE-2

The Phase 2 commissioning of SuperKEKB started with single beam testing and tuning in March 2018. Beam collisions were first achieved on April 25, 2018, followed by luminosity and background tuning and studies until July 17, 2018.

### Background

During single beam operation, *LumiBelle2* measured single beam loss rates, mainly resulting from Bremsstrahlung accompanying scattering of beam particles on the nuclei of the residual gas in the straight section upstream of the sensors, and from Touschek scattering [11]. Figure 7 gives an example of background rates measured by *LumiBelle2* together with the beam currents and pressures during successive fills in both rings.

Good correlation was found between the measured background rates and key machine parameters in each ring. A detailed simulation of single beam loss rates was developed based on generating the basic processes and tracking final state particles with SAD, followed by modeling the signal collection in the detectors using GEANT4. Rather realistic estimates of the vacuum profile along the relevant parts of

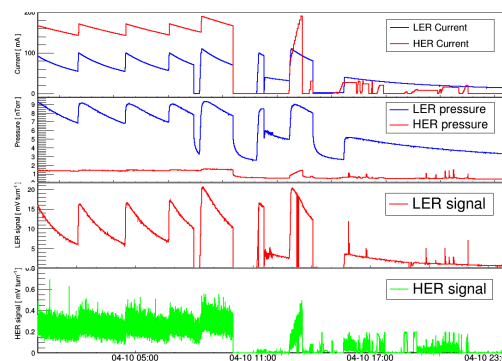


Figure 7: Example of background rates in *LumiBelle2* during single beam testing in 2018.

the interaction region, obtained by reweighting the measured vacuum levels using a detailed vacuum simulation [12], were obtained and used for the Bremsstrahlung process. Comparisons between simulation and *LumiBelle2* measurements as function of the product of current and pressure in each ring are shown in Figure 8. The simulation overestimates the loss rates in both rings by about 10 % to 20 %. This bias can be explained by the imperfect knowledge of the exact vacuum pressure in the narrow 1 cm radius beam pipe used at the IP, where most of the Bremsstrahlung scatters which can reach *LumiBelle2* sensors are produced. Also, the thresholds for signal detection used for the real and simulated data were not yet fully calibrated. The linear dependence in Fig-

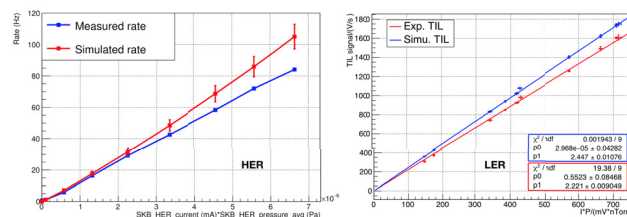


Figure 8: Comparison between the simulation and measurement in LER (l.h.s.) and HER (r.h.s.).

ure 8 indicates that the Bremsstrahlung process dominates the background loss rates in *LumiBelle2* in both rings. A dedicated 'Touschek study' was pursued at the end of the Phase 2 commissioning period, consisting of taking single beam loss data as a function of the vertical emittance (with  $\beta_x^* = 200/100$  mm for LER/HER and  $\beta_y^* = 3$  mm) to enable convenient extraction of the Touschek component from the background signals [11]. The Touschek and Bremsstrahlung processes represented 87 % and 13 % fractions of the measured *LumiBelle2* single beam loss rates in this experiment, respectively, consistent with the prediction from the simulation.

### Train Integrated Luminosity Monitoring

*LumiBelle2* and ZDLM luminosity monitors observed Bhabha scattering signals in both LER and HER when beams were collided for the first time on April 26, 2018 [6]. The



luminosity monitors were then used for machine tuning and luminosity optimization during the entire commissioning.

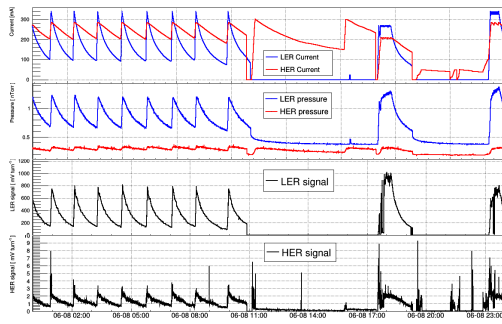


Figure 9: Example of measured *LumiBelle2* luminosity signals together with beam currents and pressures in both rings.

While the Train-Integrated-Luminosity signal integrates the signals' amplitude at 1 kHz to meet the requirements of the dithering feedback system, integrating and recording this luminosity signal at 1 Hz provides relative luminosity information which is quite useful for collision tuning and studies in the accelerator control room. Figure 9 gives an example of the *LumiBelle2* luminosity signals, together with the beam currents and pressures in both rings. In general, the luminosity signals follow the changes in the product of beam currents in both rings.

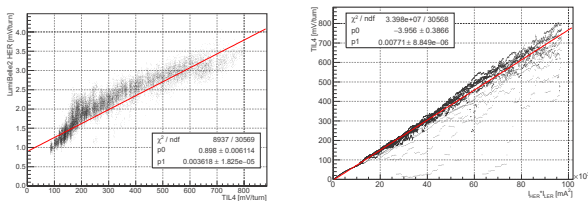


Figure 10: Luminosity signals in HER vs that in LER (l.h.s.) and LER luminosity signal as function of product of beam currents in both rings.

Thanks to the custom made beam pipe section with a depression of 15 mm and 45° inclined windows installed on the LER side, the corresponding Bhabha scattering positron signal collection was much more efficient than for the photons in the HER, see Figure 10 (l.h.s.), while still reasonably proportional to each other. The LER signals were typically proportional to the product of the beam currents, as illustrated in Figure 10 (r.h.s.), although vertical beam offsets at the IP can have a major impact large, e.g. due to ground motion or other effects.

Luminosity signals from ZDLM and ECL-LOM were compared with *LumiBelle2* in the LER, see Figure 11, showing good overall consistency. The ECL-LOM measurement has poor statistics because of much lower Bhabha rates at finite scattering angle. Studying the short term fluctuations in the 1 kHz TIL data, the statistical precision for the luminosity measurement in the LER was found to be 2.27 % for a luminosity of  $1.85 \times 10^{33} \text{ cm}^{-2} \text{ s}^{-1}$ . A relative precision of 1 % can thus be expected when luminosities reach

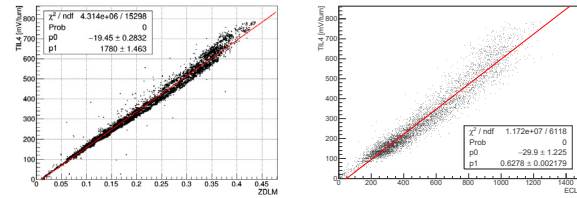


Figure 11: Comparison between luminosity signals from different monitors: *LumiBelle2* vs ZDLM (l.h.s.) and *LumiBelle2* vs ECL (r.h.s.).

$1 \times 10^{34} \text{ cm}^{-2} \text{ s}^{-1}$ . The 1 kHz relative luminosity signal were also used to test the performance of the dithering orbit feedback system, by deliberately introducing a horizontal beam-beam offset. The results show that the feedback system can correct the beam orbit at the IP. Details can be found in [13].

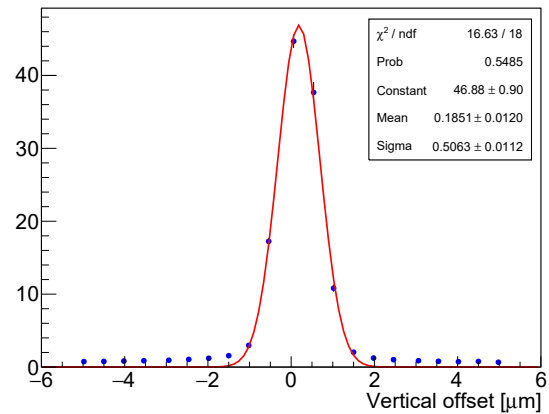


Figure 12: Relative luminosity signals against the vertical offset of  $e^-$  beam.

Based on the variation of TIL signal when scanning the vertical position of one beam across the other, averaged vertical beam size information and optimum collision position can be estimated. Figure 12 gives an example of *LumiBelle2* luminosity signal when scanning the vertical position of the electron beam. Fitting a Gaussian function, the optimum vertical offset was  $0.19 \mu\text{m}$  while the second moment of the distribution was  $\Sigma_y = 0.51 \mu\text{m}$ . Assuming both beams have Gaussian charge distributions and equal vertical beam sizes, and that beam blow-up from the beam-beam interaction can be neglected, then the vertical beam size could be evaluated as  $\sigma_y = \Sigma_y / \sqrt{2}$ . This latter assumption is only valid for very low beam intensities, and beam blow-up from the beam-beam interaction should in general be taken into account. The vertical beam offset scans enable also the SNR to be estimated by comparing the signal at peak position with that when the two beams are completely separated. During the above scan, the maximum luminosity provided by ECL-LOM was  $1.3 \times 10^{32} \text{ cm}^{-2} \text{ s}^{-1}$  and the observed SNR was 65. From simulation, the SNR was estimated as 42 under the same conditions. Some overestimation of the simulated

background may explain this difference, while it still needs to be studied in detail.

### Bunch Integrated Luminosity Monitoring

The number of bunches circulating in each ring is nominally 2500. Variations in the bunch transverse positions and sizes are in principle possible, through a variety of effects, and should be monitored, just like the bunch currents. The *LumiBelle2* BIL signal prepared for this purpose is illustrated in Figure 13 for the beam conditions at the end of the Phase 2 commissioning, when the instantaneous luminosity was about  $1.6 \times 10^{33} \text{ cm}^{-2} \text{ s}^{-1}$ , with 395 bunches circulating in each ring, separated by 32 ns (corresponding to sixteen RF buckets). The observed spread in bunch integrated luminosity signals was about 9.3 %, dominated by the measured spread in the product of bunch currents, which was found to be about 8.7 % using the bunch-by-bunch current monitor [14]. In comparison, the relative precision in the corresponding 1 kHz TIL data was 2.35 %, from which the average relative precision of BIL signals at 1 Hz could be estimated at the level of 1.5 % (by simple scaling in the assumption of uniform bunch current and alignment of the bunches along the trains in both rings).

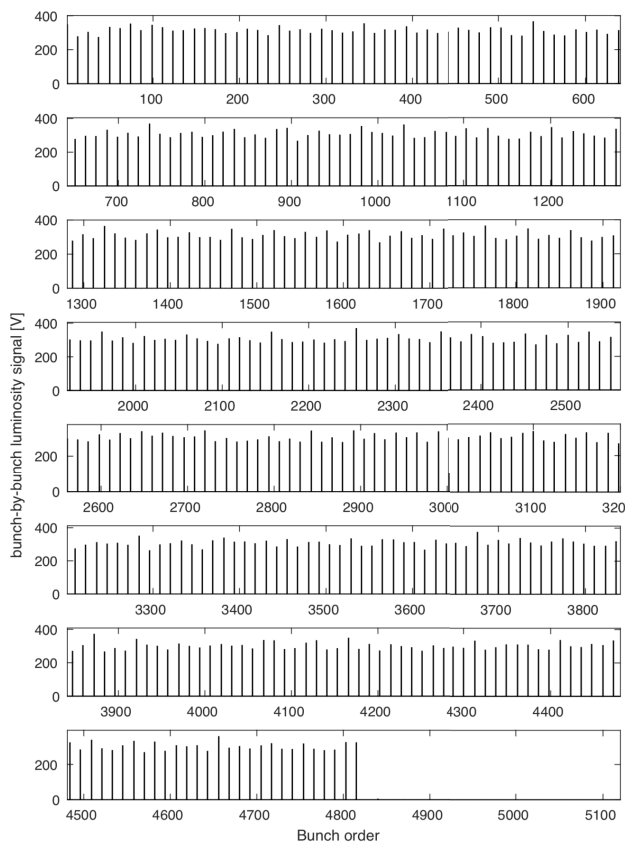


Figure 13: Bunch-by-bunch relative luminosity signals from *LumiBelle2* for 395 bunches circulating in each ring and colliding.

### CONCLUSION AND NEXT PLANS

Fast luminosity monitoring based on diamond sensors was developed and employed during the Phase 2 commissioning of SuperKEKB. With several months' operational experience in both single and colliding beam modes, good general performance and reliability were found. With the increase in luminosity and evolution of the machine in future years, some additional studies are needed, such as optimising the arrangement of sensors and amplifiers, both their combination and positions, to cover a large luminosity dynamic range while ensuring sufficient relative precision and minimizing accumulated radiation doses, shielding to mitigate activation of the beam pipe and radiator, upgrading the DAQ, etc. The dithering orbit feedback system was tested successfully and more tests are needed to ensure continuous operation in the future when beam sizes become much smaller. Potential variations in luminosity along the bunch trains from collective effects or other mechanisms can be studied using the provided bunch-by-bunch luminosity signals together with existing bunch current data in both rings.

### ACKNOWLEDGEMENTS

This work is supported by E-Jade, China Scholarship Council (CSC), and Toshiko Yuasa France Japan Particle laboratories (TYL-FJPPL). The authors would like to express their warm thanks to BEAST and KEK colleagues for their kindly help and fruitful discussion.

### REFERENCES

- [1] Y. Ohnishi *et al.*, "Accelerator design at SuperKEKB", *Prog. Theor. Exp. Phys.*, vol. 2013, pp. 03A011, 2013. doi:10.1093/ptep/pts083
- [2] Y. Funakoshi *et al.*, "Orbit feedback system for maintaining an optimum beam collision", *Phys. Rev. ST Accel. Beams*, vol. 10, pp. 101001, 2007. doi:10.1103/PhysRevSTAB.10.101001
- [3] A. S. Fisher *et al.*, "Commissioning the fast luminosity dither for PEP-II", Stanford Linear Accelerator Center, Stanford, CA 94309, USA, Rep. SLAC-PUB-12608, July 2007, <http://www.slac.stanford.edu/cgi-wrap/getdoc/slac-pub-12608.pdf>
- [4] Y. Funakoshi *et al.*, "Interaction point orbit feedback system at SuperKEKB", in *Proc. 6th Int. Particle Accelerator Conf. (IPAC'15)*, Richmond, VA, USA, May 2015, pp. 921–923. doi:10.18429/JACoW-IPAC2015-MOPHA054
- [5] C.G. Pang *et al.*, "Simulation study on luminosity feedback horizontal beam stabilization at SuperKEKB", in *Proc. 9th Int. Particle Accelerator Conf. (IPAC'18)*, Vancouver, Canada, May 2018, pp. 2250–2253. doi:10.18429/JACoW-IPAC2018-WEPAL037
- [6] C.G. Pang *et al.*, "First tests of SuperKEKB fast luminosity monitors during 2018 Phase-2 commissioning", in *Proc. 9th Int. Particle Accelerator Conf. (IPAC'18)*, Vancouver, Canada, May 2018, pp. 2254–2257. doi:10.18429/JACoW-IPAC2018-WEPAL038

- Content from this work may be used under the terms of the CC BY 3.0 licence (© 2018). Any distribution of this work must maintain attribution to the author(s), title of the work, publisher, and DOI.
- [7] Belle-ECL *et al.*, “Electromagnetic calorimeter for Belle II”, *J. Phys.: Conf. Ser.*, vol. 587, pp. 012045, 2015. doi:10.1088/1742-6596/587/1/012045
- [8] D. El Khechen *et al.*, “First Tests of SuperKEKB Luminosity Monitor During 2016 Since Beam Commissioning”, in *Proc. 7th Int. Particle Accelerator Conf. (IPAC’16)*, Busan, Korea, May 2015, pp. 81–83. doi:10.18429/JACoW-IPAC2016-MOPMB006
- [9] C. G. Pang *et al.*, “Preparation of CVD diamond detector for fast luminosity monitoring of SuperKEKB”, in *Proc. 8th Int. Particle Accelerator Conf. (IPAC’17)*, Copenhagen, Denmark, May 2017, pp. 135–138. doi:10.18429/JACoW-IPAC2017-MOPAB027
- [10] CIVIDEC, <https://cividec.at>
- [11] D. El Khechen, “Fast Luminosity Monitoring Using Diamond Sensors for SuperKEKB”, PhD thesis, Université Paris-Sud, Orsay, France, 2016.
- [12] M. Ady, “Monte-Carlo simulation of ultra high vacuum and synchrotron radiation for particle accelerators”, PhD thesis, école polytechnique fédérale de Lausanne (EPFL), Lausanne, Switzerland, July 2016.
- [13] M. Masuzawa *et al.*, “Early Commissioning of the Luminosity Dither Feedback for SuperKEKB”, presented at IBIC’18, Shanghai, China, Sep. 2018, paper TUPC13, this conference.
- [14] M. Tobiyama *et al.*, “Beam commissioning of SuperKEKB rings at phase 1”, in *Proc. Int. Beam Instrumentation Conf. (IBIC’16)*, Barcelona, Spain, 2016, pp. 6–10. doi:10.18429/JACoW-IBIC2016-MOAL03



# ELECTRON SPECTROMETER FOR A LOW CHARGE INTERMEDIATE ENERGY LWFA ELECTRON BEAM MEASUREMENT

K.V. Gubin, ILP SB RAS, Novosibirsk, Russia,  
A.V. Ottmar, Yu.I. Maltseva, T.V. Rybitskaya, BINP SB RAS, Novosibirsk, Russia

## ABSTRACT

The Laser-driven Compton light source is under development in ILP SB RAS in collaboration with BINP SB RAS. Electron spectrometer with energy range 10-150 MeV for using in this project is presented. Spectrometer based on permanent magnet and phosphor screen with CCD registrar and this geometry was optimized for best measurements resolution in compromise with size limitations. Preliminary collimation of electron beam allows achieving energy resolution up to 5-10 % of top limit. System has been tested at the VEPP-5 linear electron accelerator and obtained results corresponds to design objectives. Sensitivity of beam transverse charge density was experimentally fixed at 0.03 pC/mm<sup>2</sup>, that is practically sufficient for our LWFA experiments.

## INTRODUCTION

At the present time, the impressive progress in laser wakefield acceleration (LWFA) of charged particles gives grounds to consider LWFA as a perspective method of electron beam production in the GeV energy range.

The project of laser-driven Compton light source started in ILP SB RAS in collaboration with BINP SB RAS [1]. The first stage of the project is creation and studying laser based accelerated electron beam from the supersonic gas jet. At the next stage, it is planned to obtain a high-energy gamma-ray beam by means of Compton backscattering of a probe light beam on LWFA-accelerated electrons.

General parameters of the first stage LWFA stand are:

- laser system: repetition rate is 10 Hz, pulse energy is 100÷300 mJ, pulse duration is ~20 fs, central wavelength is 810 nm;
- acceleration area: diameter is ~ 10÷15  $\mu$ m, length is ~ 0.5 mm;
- supersonic He jet: diameter is ~1.2 mm, gas density is 10<sup>18</sup>÷10<sup>19</sup> cm<sup>-3</sup>, Mach number is 3.5÷4, gas backpressure is 5÷10 atm;
- expected parameters of the electron beam are: up to 100-150 MeV of energy, 1-10 pC of charge, 1-10 mrad of angular divergence,  $\leq$  0.1 ps of beam duration.

## SPECTROMETER PURPOSE AND REQUIREMENTS

Beam energy measurement is a necessary constituent of any accelerator facility. We choose the wide-used in LWFA experiments layout of spectrometer with magnetic dipole, phosphor screen and CCD camera as a signal register.

The spectrometer development is constrained by the following general demands:

- Compact size (full dimensions 20-25 cm) because of device must be placed inside limited volume of experimental vacuum chamber (Fig. 1) with diameter 70 cm and height 50 cm. It determines length and value of analyzing magnetic field: 0.7-1.2 T and 30-50 mm. It follows the use of permanent magnets.
- Materials must be nonactivated and vacuum usable. It determines the use permanent magnets for dipole.
- The use of special electron beam collimator to improve energy resolution (see below).
- Taking into account a very small beam charge (several pC per pulse), registration system (phosphor screen + CCD camera) must have high quantum efficiency and sensitivity. Also we should take into account that CCD camera will be placed maximally near to screen but, from other hand, outside the vacuum volume. It means the distance between camera and screen will consist 35-40 cm, and the objective should be an appropriate angle of view to project the screen (about 10cm) on the CCD (11 mm).

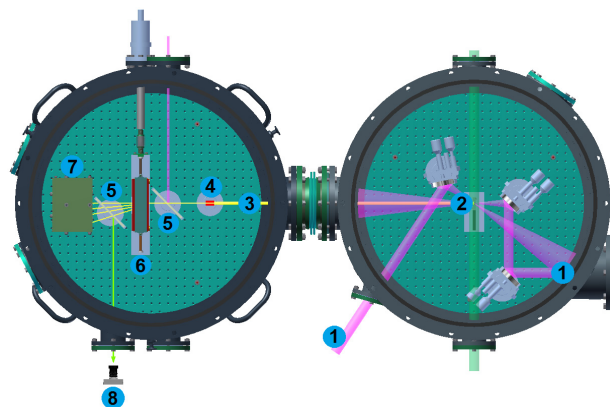


Figure 1: Experimental vacuum chamber. (1) Laser beams, (2) supersonic gas jet, (3) electronic beam, (4) collimator, (5) screens, (6) magnet dipole, (7) faraday cap, (8) CCD.

## MAGNETIC DIPOLE AND COLLIMATOR

The dipole has been designed on two permanent NdFeB magnets (Fig. 2) with magnetization 1 T. It allows to reach magnetic field inside a magnet bore close to 1 T. This field configuration provides sufficient beam deflection to place luminescent screen at 10-12 cm from the dipole. A movable mounting of the dipole allows to insert and remove it into a beam. Figures 3a and 3b show respectively the calculated and measured distribution of the magnetic field.

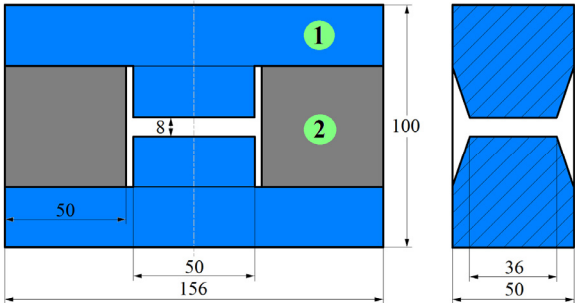


Figure 2: Magnetic dipole schematic. (1) Fe. (2) NdFeB.

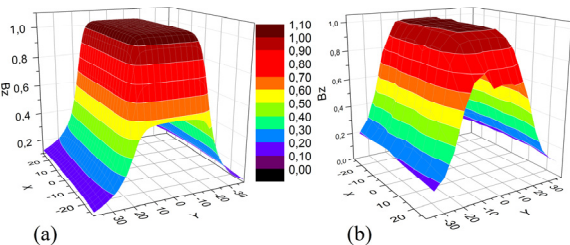


Figure 3: (a) Calculated and (b) measured magnetic field.

Laser accelerated electron beam usually has angle divergence up to 5-10 mrad and will reach a size of 5-7 mm in the experimental chamber, which will give an unsatisfactory energy resolution of 50-70% for the energy of 100 MeV and more (Fig. 4). To improve the resolution it was decided to use a special collimator that cuts the beam in the plane of rotation. Simple estimations show that reducing the size to 1 mm allows achieving a resolution of ~ 10%, to 0.5 mm - respectively ~ 5% (Fig. 4). Simulation of collimator for beam energy up to 150 MeV with use of GEANT4 program complex was performed. Results of simulations for simple slit tungsten collimator with a length of 6 cm, height of 1 cm and 1 mm width of slit are presented on Fig. 5. It is shown that this collimator geometry is sufficient for complete collimation of our electron beam. Electron beam at collimator output has width following a slit size and angle divergence close to 0.2°. Other electrons are completely stopped by collimator material.

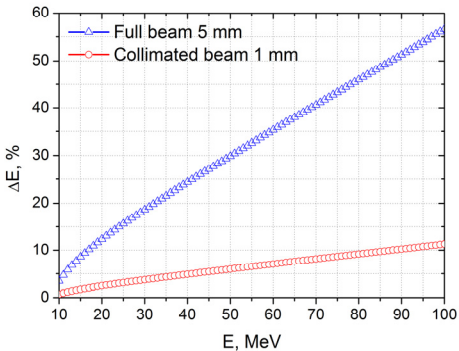


Figure 4: Energy resolution of beam energy.

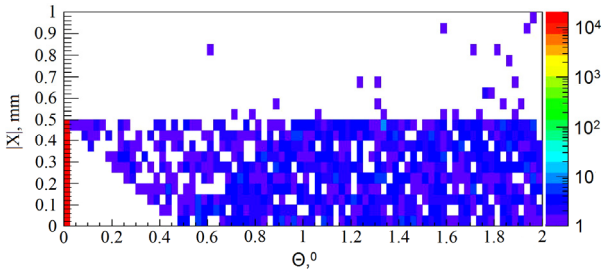


Figure 5: Collimated beam distribution.

## PHOSPHOR SCREEN AND CCD CAMERA

The phosphor screen produced by Renex [2] (Novosibirsk, Russia) and the CCD camera based on SONY ICX285 are used.

The screen has Gd<sub>2</sub>O<sub>2</sub>S-Tb phosphor and is an analogue of wide used of Kodak-Carestream Lanex screens. This type of screen has high charge linearity and weak energy dependency [3].

CCD camera developed in INP SB RAS. The choice was determined by its availability and satisfying characteristics. To achieve high sensitivity a Jupiter-3 (focal length 50mm and aperture 1.5) objective is used. Camera has the following key parameters: 100Mbit Ethernet interface, 1.4 MPix resolution, external trigger source, 4 fps speed, 63 dB dynamic range, 42 dB signal to noise ratio.

## SPECTROMETER BEAM TESTING

The general aims of test were to check up the real operation of basic elements of spectrometer: magnetic dipole, collimator and register system under real electron beam.

The spectrometer was mounted and tested at electron linac of Injection Complex VEPP-5, BINP [4,5]. Sketch of experiment is presented in Fig. 6. Beam energy at the experiment was 120 MeV, bunch duration was ~ 1 ns, tunable bunch charge was in the range between 4.8 nC (3·10<sup>10</sup> e<sup>-</sup>, nominal operational condition of VEPP-5 Injection Complex) and practically down to zero, repetition rate was 2 Hz. Beam charge was measured by high sensitive Faraday cup (FC) specially developed for LWFA experiment [6,7].

All spectrometer elements were located at geometry closed to estimate for LWFA experiment.

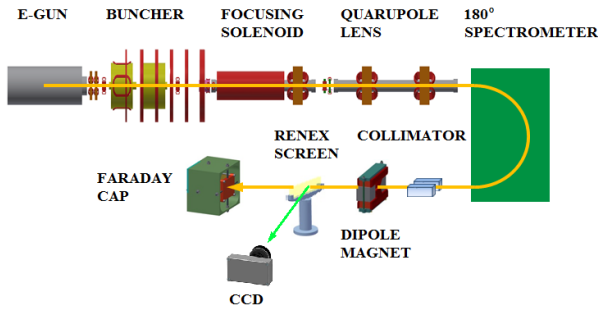


Figure 6: Test stand.

The first part of the experiment aimed to determine of real beam charge operation range of this equipment. The signals from CCD and FC were registered for some levels of beam charge. Analyzing the obtained data, we found the lower and upper limits of the operating range. Beam profile for low and middle charge values shown on Fig. 7a and Fig. 7b consequently.

Calculating the ratio of the maximum CCD signal (the center of the beam) to the FC signal for several points in the operating range gives the dependence of the signal from the CCD of the beam charge (Fig. 8).

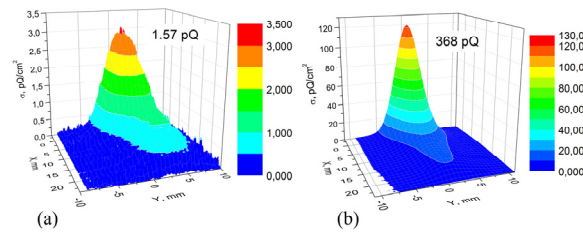


Figure 7: CCD signal for beam charge 1.57 pC (a) and 368 pC (b).

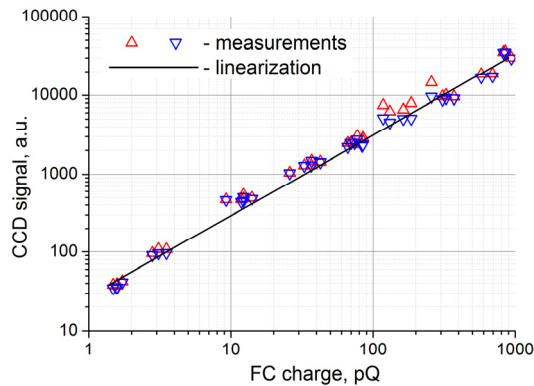


Figure 8: Dependence of CCD signal from the electron beam charge.

The final stage consisted in checking the work of the collimator and the magnetic dipole. The beams angular spread at the exit of the collimator by calculations (Fig. 5) is less than 0.025 degrees and the beam size at a distance

of 40 cm should be less than 1.3mm. Test measurements were carried out at normal pressure, not in vacuum chamber, it is also necessary to take into account the spreading of the beam in the atmosphere. Measured beam size (Fig. 9a) agrees well with the computed blur (Fig. 9b).

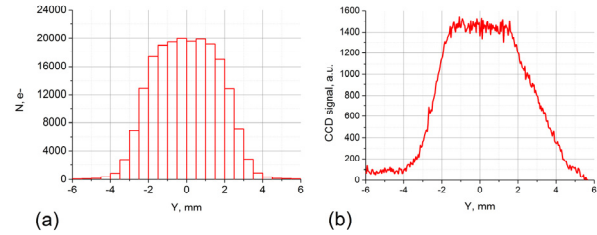


Figure 9: (a) Calculated and (b) measured beam size.

The measured beam deflection after magnetic dipole is equal 7.5cm (Fig. 10) and it agrees for calculations to 120MeV.

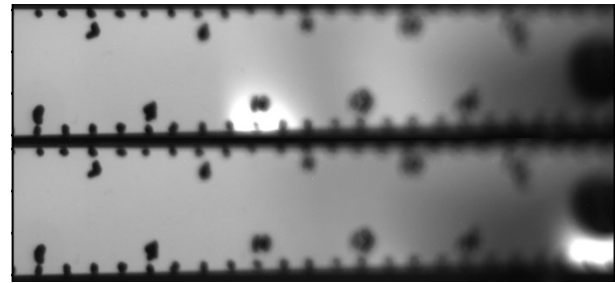


Figure 10: Beam position without dipole (above) and with dipole (below). Distance to the screen 40 cm, strokes on the screen every 5mm.

## CONCLUSIONS

Magnetic spectrometer for measurement of LWFA electrons energy was developed, fabricated and successfully tested under 120 MeV beam of VEPP-5 accelerator complex at Budker INP, Novosibirsk. Spectrometer allows measuring the energy of ultrashort ( $\tau \leq 0.1$  ps) low charge ( $\sim$  several pC) electron bunch with energy resolution better than 10 % in the range 10-150 MeV. Linearity of properties of spectrometer registration system allows using of it for beam density distribution measurement also.

This work was partially supported by RAS Program “Extreme laser radiation: physics and fundamental applications” (project N0. 115113010008) of ILP and by The Federal Agency for Scientific Organizations “New method of charged beam accelerating” N305-2014-0016 of BINP.

## REFERENCES

- [1] V.I. Trunov *et al.*, “Laser-driven plasma wakefield electron acceleration and coherent femtosecond pulse generation in X-ray and gamma ranges”, *IOP Conf. Series: Journal of Physics: Conf. Series*, Vol. 793, 2017, 012028 doi:10.1088/1742-6596/793/1/012028



- [2] A. A. Komarskiy *et al.*, “Reducing Radiation Dose by Using Pulse X-Ray Apparatus”, *Journal of Biosciences and Medicines*, vol. 2, pp 17-21, Apr. 2014.
- [3] Nakamura K. *et al.*, “Electron beam charge diagnostics for laser plasma accelerators”, *Physical Review Special Topics-Accelerators and Beams*, vol. 14, p 062801, Jun. 2011.
- [4] A.V. Alexandrov *et al.*, in *Proc. of LINAC'96*, Geneva, Switzerland, August 26- 30, 1996, pp. 821-823 (CERN-1996-007).
- [5] M.S. Avilov *et al.* *Atomic Energy*, Vol. 94, No.1, Jan 2003, pp. 50-55.
- [6] V. Gubin *et al.*, “A Faraday Cup for a Low Charge LWFA Electron Beam Measurement”, in *Proc. RuPAC'16*, St. Petersburg, Russia, Nov. 2016, paper THPSC047, pp. 635-637.
- [7] V.V. Gambaryan *et al.*, “Design and Test of a Faraday Cup for Low-charge Measurement of Electron Beams From Laser Wakefield Acceleration”, *Rev. Sci. Inst.*, vol. 89, no. 6 2018, p. 063303.

# DESIGN OF A COMPACT PERMANENT MAGNET SPECTROMETER FOR CILEX/APOLLON

M. Khojoyan, A. Cauchois, J. Prudent, A. Specka

LLR (Laboratoire Leprince-Ringuet), CNRS and Ecole Polytechnique, Palaiseau UMR7638, France

## Abstract

Laser Wakefield acceleration experiments make extensive use of small permanent magnets or magnet assemblies for analyzing and focusing electron beams produced in plasma accelerators. This choice is motivated by the ease of operation inside vacuum chambers, absence of power-supplies and feedthroughs, and potentially lower cost. Indeed, in these experiments space is at premium, and compactness is frequently required. At the same time, these magnets require a large angular acceptance for the divergent laser and electron beams which imposes constraint of the gap size. We will present the optimized design and characterization of a 100 mm long, 2.1 Tesla permanent magnet dipole. Furthermore, we will present the implementation of this magnet in a spectrometer that will measure the energy spectrum of electrons of  $\sim [60-2000]$  MeV with a few percent resolution in the CILEX/APOLLON 10PW laser facility in France.

## INTRODUCTION

CILEX (Centre Interdisciplinaire de la Lumière Extrême / Interdisciplinary Center for Extreme Light) is a research center which aims at using the Apollon-10P laser for exploring laser-matter interaction at extremely high laser intensities ( $\sim 10^{22} \text{ W/cm}^2$ ). The long focal length area of CILEX will be used to investigate plasma acceleration and radiation generation. It will be equipped with two interaction chambers able to accommodate laser focal lengths ranging from 3 m to 30 m. The spectrometer magnet presented here is designed to be compatible with the mentioned laser parameters.

A sketch of the laser-plasma interaction chamber is shown in Fig. 1. The total volume of interaction chamber is about  $3 \text{ m}^3$  and it is practical to use permanent magnets for characterization of electron beam. Permanent magnets as compared to electromagnets, do not need power supplies (and consequently cooling system) and can be more compact due to smaller apertures. In our case, the apertures of the magnets will be limited by the laser envelope size, which according to our requirements, should pass through the magnets unobstructed. The paper is organized as follows. First, the design considerations of a permanent magnetic dipole are introduced together with analytical and computational field estimations. Next, construction of a permanent dipole magnet and magnetic field measurements are presented. Finally, beam dynamics simulation results are obtained by applying the magnet as a spectrometer inside the interaction chamber of the CILEX facility.

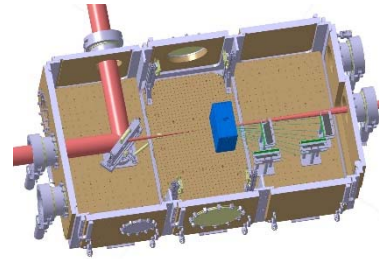


Figure 1: Schematic of interaction chamber at CILEX with laser envelope shown in red and magnetic dipole shown in blue. Measurement screens and reference electron trajectories are shown as well.

Let us consider a simple C shaped dipole (Fig. 2). The field in the gap of height  $h_g$  is driven by a permanent magnet of the same height  $h_{pm} = h_g$  and of width  $w_{pm}$ .

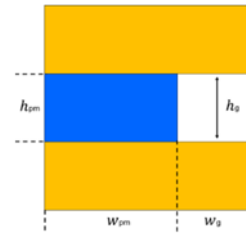


Figure 2: 2D view of a C shaped dipole with a permanent magnet shown in blue and steel/iron in yellow colors.

Assuming constant field in the gap (no horizontal field component) it is straightforward to calculate the magnetic flux density using Ampere's and flux conservation laws:

$$B_g = - \frac{B_r w_{pm}}{w_g + \frac{\mu_r h_g w_{pm}}{h_{pm}}} \quad (1)$$

with  $B_r$  and  $\mu_r$  being the remnant field and relative permeability of the permanent magnet. From Eq. 1 it follows that the maximum achievable field in the gap cannot exceed the remnant induction field of the magnet independent of how small the gap width ( $w_g$ ) and how large the magnet width ( $w_{pm}$ ) are. It becomes clear that for a permanent magnet (PM) dipole, to reach fields higher than remnant field of an individual magnet, a special arrangement of magnetic sub-materials is necessary. Common structures are Halbach [1] and Stelter [2] configurations. In [3] a cylindrical structure was originally proposed by Halbach and

has later on been improved [4] by using iron poles inside the structure. A spherical structure was introduced in [5] and was later improved by using FeCo material as a pole piece [6]. Nowadays, permanent magnet dipoles are widely used in magnetic resonance imaging applications [7], in facilities such as third [8-10] and next [11, 12] generation light sources. Neodymium iron Boron (Nd-Fe-B) magnets are the preferred candidates for generating strong magnetic fields due to their high remnant induction and the highest up to date BH energy product [13, 14]. Moreover, almost linear behaviour of the demagnetization curve [3] and relative permeability close to unity makes the analytical design of such systems relatively straight forward.

## DESIGN OF A PM DIPOLE: ANALYTIC ESTIMATION OF MAGNETIC FIELD

For design considerations of a magnetic dipole we assume that the magnet is H shaped with a 2D schematic view (upper half) shown in Fig. 3. The parts shown in yellow color represent iron material: pole tip as well as the yokes for the flux circulation. The pole tip is surrounded by neodymium iron boron magnets with arrows indicating magnetization direction of each magnet. In the same scheme  $h_g$  is half the gap height and  $w/h$  signify the width / height of each surrounding magnet. The main idea of using such geometry is the collection of the flux from the surrounding permanent magnets and concentration into the magnet gap. The strength of the magnet built in this way can therefore exceed the residual field ( $B_r$ ) of the permanent magnet materials and, in principle, reach the saturation field of pole material which can be more than 2 Tesla. Next, applying flux conservation and Ampere's laws [15] for the above magnetic circuit (and neglecting fringe field effects), one can obtain the following expression for magnetic flux density in the gap:

$$B_g = -\frac{1}{h_g} \frac{(w_1 + w_2 + w_3) B_r}{\left( \frac{w_g}{h_g} + \frac{\mu_r w_1}{h_1} + \frac{\mu_r w_2}{h_2} + \frac{\mu_r w_3}{h_3} \right)} \quad (2)$$

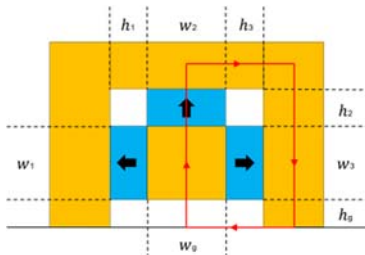


Figure 3. Schematic (2D) view of top half of H shaped magnet with a red flux line following Ampere's law. Iron is shown in yellow with the pole tip surrounded by Neodymium N40 grade magnets expressed in light blue.

It is possible to further optimize the latter expression assuming a square shape magnet poles and surrounding magnets of similar sizes. Since the gain in magnetic field over magnet weight is an important measure on designing a

magnet, Fig. 4 illustrates the total weight of the surrounding magnets and the peak magnetic field as function of pole size for a gap height of 10 mm. Note that the weight does not increase linearly with the pole size. In practice, the pole dimensions are chosen according to the needs of transverse good field region required from beam dynamics. In our case the pole size of 51 mm was rather chosen according to the sizes of Nd-Fe-B 40 grade magnets commercially available in the market.

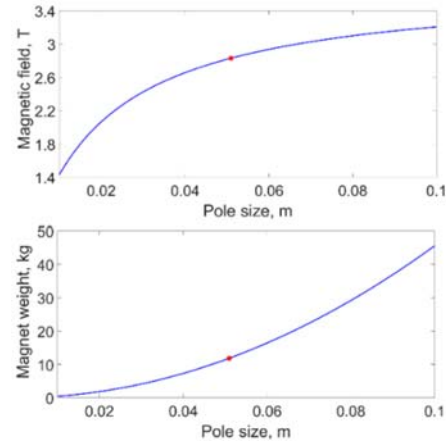


Figure 4: Total weight of magnets and peak magnetic field as function of pole size. Red asterisks represent the corresponding expected values for 51 mm magnet pole size. 10 mm gap size/height is assumed in the plot.

## DESIGN OF A PM DIPOLE: COMPUTATION OF MAGNETIC FIELD

The magnet geometry of Fig. 3 has been studied using three-dimensional TOSCA software [16]. Following dimensions have been used in the calculations:  $h_1 = h_3 = 5.08 \text{ cm}$ ,  $w_1 = w_3 = 7.08 \text{ cm}$ ,  $h_2 = w_2 = 5.08 \text{ cm}$ .

For the case of neodymium magnet, by taking advantage of linear BH behaviour in the second quadrant of BH curve, the slope  $\mu_r$  is calculated depending on the grade of the magnet. Non-linear iron properties have been used in TOSCA for induction versus field data. The aim was to reach magnetic field at the gap as close as possible to the saturation field of the pole material. A fixed ratio of 20 for magnet gap height over length was imposed. Figure 5 illustrates the expected peak magnetic flux density at the magnet gap for different gap heights obtained from TOSCA simulations (red circles) assuming 2.26 T saturation field for the iron. In the same plot analytical estimation of the field is shown applying an empirical scale factor  $2.26/2.96$ , where 2.96 T corresponds to the analytical peak field value for 10 mm gap allowing infinitely high saturation field for the iron. It can be seen from the plot that for the case of 10 mm gap, the value of peak magnetic field in the gap is close to the saturation field of the iron and, in the same time, for larger gap sizes the considered geometry is not optimum anymore.



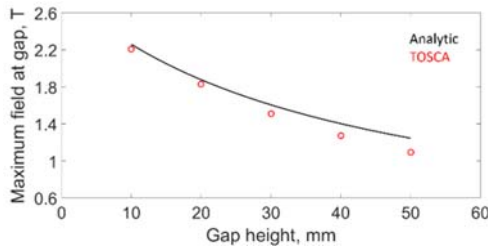


Figure 5: Magnetic induction in the gap for various gap sizes. Red dots: TOSCA calculations. Black curve: analytical estimation applying a factor 0.7635.

## DESIGN OF A PM DIPOLE: CONSTRUCTION AND MEASUREMENTS

The PM dipole has been constructed at LLR (Laboratoire Leprince-Ringuet) using Nd-Fe-B 40 grade magnets as surrounding magnet material and allied pure iron (2.18 T saturation field) as pole and yoke material. A dedicated mechanical tooling and careful adjustment were the key points during the magnet assembly due to strong force existent between the magnets and corrosion risks that are not negligible for neodymium magnets. Furthermore, special arrangement of 56 magnets was needed during the assembly to balance the field imperfections of individual magnets (Fig. 6). In this plot the dimensions (w x h x l) of the magnets are shown in legends. However, it is believed, that geometry with iron poles will smoothen the effects of field imperfections and defects in the magnet once the iron is saturated. The assembled dipole and corresponding TOSCA model of the magnet are presented in Fig. 7. Magnets shown in blue have been added to strengthen the flux on both sides of iron poles. The magnetic length of the dipole was 100 mm. Finally, the assembled magnet was measured at the measurement bench of LLR laboratory.

The position of the Hall probe was aligned to the magnet using an optical system with high magnification camera (50  $\mu$ m pixel resolution) in the field of view of 5 cm diameter centered on the pole gap at the magnet exit face (Fig. 8). The Hall probe was mounted on linear translation stages which, according to the manufacturer, have 0.07 microradians angular slope and 2 micrometers bidirectional repeatability [17]. Measured and simulated field profiles are summarized in Fig. 9. The result is remarkable yielding to less than 1 % disagreement between predicted and measured field values. No field weakening has been observed as a result of demagnetization effects [18] due to a very strong field at the specific corners of individual magnets (see TOSCA simulation of the magnet on the right side of the Fig. 7).

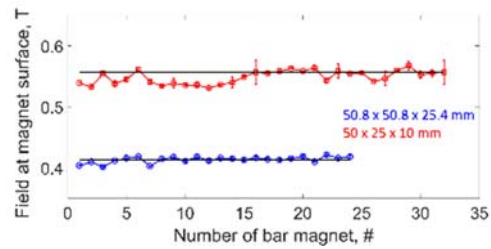


Figure 6: Measured magnetic induction at the surface of two types of neodymium magnets. For each case, black lines represent analytically estimated field value assuming 0.5 mm offset of Hall probe sensor from the magnet surface.

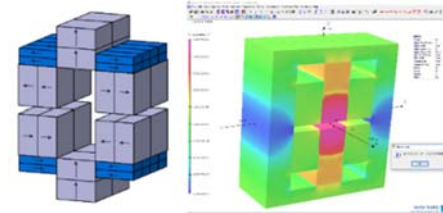


Figure 7: Left: overview of different block magnets used to assembly the dipole. Arrows on the blocks illustrate the magnetization directions. Right: TOSCA model of magnet yielding 2.092 T peak field value in the gap. The main component of induction field is shown in color map from blue (lowest value) to red (highest value).

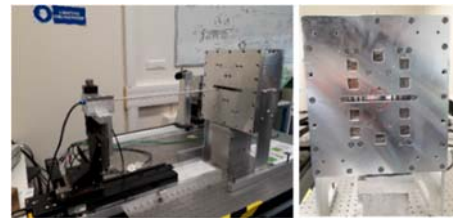


Figure 8: Left: LLR measurement bench with a Hall probe mounted on linear transition stages. Right: defined area of interest for hall probe alignment using optical system.

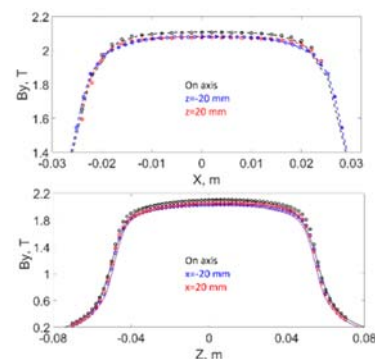


Figure 9: On and off-axis main component field profiles along horizontal (upper plot) and longitudinal (lower plot) directions. For each case dots correspond to the measured and curves to the simulated field values. A scaling factor ( $\sim 1$  %) is applied to match the measured and simulated field values.

## IMPLEMENTATIN OF PM DIPOLE AS A SPECTROMETER

ASTRA [19] simulation software has been applied to study the dynamics of different energy electrons through the designed magnet. The considered electron energy range of 56-2350 MeV has been defined as the lowest energy exiting the magnet from the side of the mechanical gap and the highest energy which is measurable out of 50 mrad divergent laser cone. An idealized electron bunch having Gaussian distribution in all sub spaces was assumed in simulations. Electron beam parameters are summarized in Table 1. 3D magnetic field map has been implemented into ASTRA for the correct treatment of fringe field effects. Electron reference trajectories of different energies and corresponding screens (marked as S#) are illustrated in Fig. 10. In the same figure, the mid plane magnetic field profile is shown in color map.

Table 1: Electron Beam Parameters used in ASTRA.

LPA beam parameter	Value
Charge, pC	10
Energy, MeV	56-2350
Transverse rms size, $\mu\text{m}$	2.5
Transverse rms divergence, mrad	2

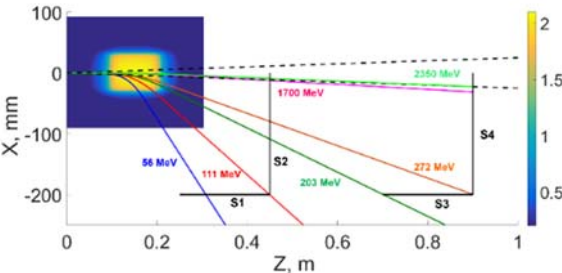


Figure 10: Range of electron trajectories and corresponding screen positions/orientations for energy measurement inside the interaction chamber of CILEX.

Horizontal displacement obtained from the simulated trajectories concedes very well with a simple geometrical estimation (assuming hard edge magnetic field profile) once the electrons exit on the side of the magnet (see Fig. 11). Figure 12 plots the beam envelopes at the positions of S1 and S2. In the plot the black line indicates the separation of the screens. Electrons of energies below 200 MeV are strongly affected by the fringe field focusing effects. In addition, the fringe field effects may be further enhanced / diminished by adjusting the magnet laterally. The rms energy resolution at various screens and at different energies is plotted in Fig. 13 which yields less than 8 % rms value within the whole energy range for 2 milliradians divergence of electron beam.

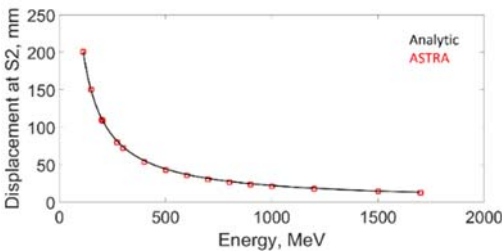


Figure 11: Horizontal displacement at the position of S2. Black curve: analytical estimation, red circles: ASTRA.

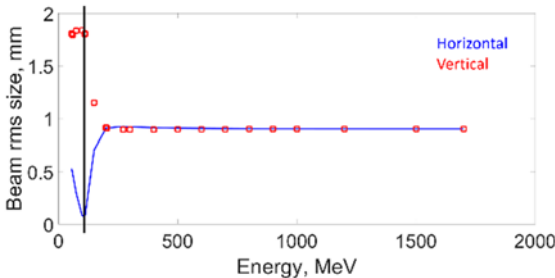


Figure 12: Beam rms transverse sizes at screen positions of S1 and S2. Blue line: horizontal, red rectangles: vertical.

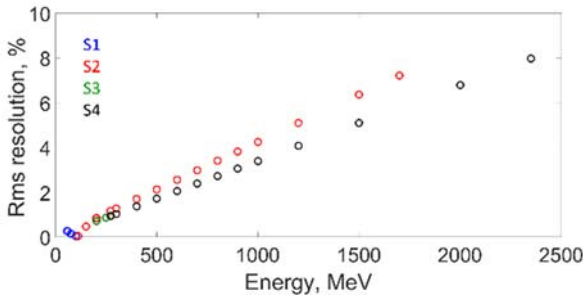


Figure 13: rms energy resolution estimated at different screens for 2 milliradians electron beam divergence. Different colors symbolize the outcome at different screen positions.

## SUMMARY

A 2.1 Tesla permanent magnet dipole has been designed, constructed, measured and characterized as a spectrometer for CILEX. Very good agreement ( $\sim 1\%$ ) between predicted and measured magnetic field values has been obtained. A precise electron beam tracking has been done afterwards by applying the 3D field map of the magnet into ASTRA simulation program. According to tracking results the magnet will enable to measure electrons from 56 MeV to 2.35 GeV with rms resolution of below 10 percent at full energy range. Besides, for smaller laser divergence the magnet can be shifted downstream and the energy resolution may be improved by adding a focusing element into the configuration.

## ACKNOWLEDGEMENTS

The work is partially supported by the European Union's Horizon 2020 Research and innovation programme under grant agreement No 730871.

## REFERENCES

- [1] K. Halbach, "Application of permanent magnets in accelerators and electron storage rings", *Journal of Applied Physics* vol. 57, p. 3605, 1985.
- [2] R. E. Stelter, "Dipole permanent magnet structure", United States patent, 1997.
- [3] K. Halbach, "Design of permanent multipole magnets with oriented rare earth cobalt material", *Nuclear Instruments and Methods*, vol. 169, pp. 1-10, 1980.
- [4] M. Kumada *et al.*, "Development of 4 Tesla permanent magnet", in *Proc. PAC'01*, Chicago, IL, USA, Jun. 2001, pp. 3221-3223.
- [5] H.A. Leupold and E. Potenziani, "Novel high-field permanent-magnet flux sources", *IEEE Transactions on Magnetics*, vol. 23, no. 5, pp. 3628-3629, 1987.
- [6] F. Bloch, O. Cugat, G. Meunier, and J. C. Toussaint, "Innovating approaches to the generation of intense magnetic fields: Design and optimization of a 4 Tesla permanent magnet flux source", *IEEE Transactions on Magnetics*, vol. 34, no. 5, pp. 2465-2468, 1998.
- [7] C. Li and M. Devine, "Efficiency of permanent magnet assemblies for MRI devices", *IEEE Transactions on Magnetics*, vol. 41, no. 10, pp. 3835-3837, 2005.
- [8] J.M. Ortega *et al.*, "Optimization of a permanent magnet undulator for free electron laser studies on the ACO storage ring", *Journal of Applied Physics*, vol. 54, p. 4776, 1983.
- [9] G. Tosin, R. Basilio, S. Casas, and R. J. F. Marcondes "Bending magnets made with permanent magnets for LNLS-2 electron storage ring", in *Proc. PAC'09*, Vancouver, BC, Canada, May 2009, paper MO6PFP001, pp. 127-129.
- [10] E. Nakamura, K. Egawa, K. Takayama, and K. Ogata, "Permanent magnets for the 500 MeV accumulator ring of the intensity doubler project in KEK-PS", in *Proc. 18th Int. Conf. on High-Energy Accelerators (HEACC 2001)*, Tsukuba, Japan, Mar. 2001, paper P20th11.
- [11] T. Watanabe *et al.*, "Permanent magnet based dipole magnets for next generation light sources", *Physical Review Accelerators and Beams*, vol. 20, p. 072401, 2017.
- [12] S.C. Gottschalk *et al.*, "Permanent magnet systems for free-electron lasers", *Nuclear Instruments and Methods in Physics Research A*, vol. 507, pp. 181-185, 2003.
- [13] J.F. Herbst *et al.*, "Structural and magnetic properties of Nd<sub>2</sub>Fe<sub>14</sub>B", *J. Appl. Phys.*, vol. 57, p. 4086, 1985.
- [14] D. Brown *et al.*, "Developments in the processing and properties of NdFeB-type magnets", *Journal of Magnetism and Magnetic Materials*, vol. 248, pp. 432-440, 2002.
- [15] B. C. Brown, "Design formulas for the strength, compensation and trimming of hybrid permanent magnets", Fermilab, Batavia, IL, USA, Rep. FERMILAB-Conf-96/273, 1996.
- [16] TOSCA, Opera-3d, Cobham Technical Services, <http://operafea.com/>, Software for electromagnetic design, Oxford, UK.
- [17] Thorlabs: Linear Translation Stages, see for example in: [https://www.thorlabs.com/newgrouppage9.cfm?objectgroup\\_id=7652](https://www.thorlabs.com/newgrouppage9.cfm?objectgroup_id=7652)
- [18] M. Katter, "Angular dependence of the demagnetization stability of sintered Nd-Fe-B magnets", *IEEE Transactions on Magnetics*, vol. 41, no. 10, pp. 2853-3855, 2005.
- [19] K. Floettmann, ASTRA, <http://www.desy.de/mpyf10>



# MOMENTUM COMPACTION MEASUREMENT USING SYNCHROTRON RADIATION

L. Torino\*, N. Carmignani, A. Franchi, ESRF, 38000 Grenoble, France

## Abstract

The momentum compaction factor of a storage ring can be obtained by measuring how the beam energy changes with the RF frequency. Direct measurement of the beam energy can be difficult, long or even not possible with acceptable accuracy and precision in some machines such as ESRF. Since the energy spectrum of the Synchrotron Radiation (SR) depends on the beam energy, it is indeed possible to relate the variation of the beam energy with a variation of the produced SR flux. In this proceeding, we will present how we obtain a measurement of the momentum compaction using this dependence.

## INTRODUCTION

The variation of path length ( $L$ ) with momentum ( $p$ ) is determined by the momentum compaction factor ( $\alpha_c$ ) defined by:

$$\frac{\Delta L}{L} = \alpha_c \frac{\Delta p}{p}, \quad (1)$$

with  $\frac{\Delta p}{p} \ll 1$  [1].

Assuming that particles are ultra-relativistic ( $v \simeq c$ , where  $c$  is the speed of light),  $\Delta L$  is directly related with RF frequency variation,  $\Delta f_{RF}$ :

$$\frac{\Delta L}{L} = -\frac{\Delta f_{RF}}{f_{RF}}, \quad (2)$$

while the measurement of the momentum variation leads to some difficulties.

Using the same assumption, the momentum  $p$  can be approximated to the beam energy  $E$  and:

$$\frac{\Delta p}{p} \simeq \frac{\Delta E}{E}. \quad (3)$$

Substituting Eq. (2) and Eq. (3) in Eq. (1) one obtains:

$$\frac{\Delta E}{E} = -\alpha_c \frac{\Delta f_{RF}}{f_{RF}}. \quad (4)$$

In high-energy accelerators, and in particular in synchrotron light sources, the most accurate way to measure the energy is via the “spin depolarization” [2–4]. Unfortunately this technique cannot be used in all the machines depending on the complexity of the lattice [5]. Moreover the whole measuring process is time consuming.

On the other hand the momentum compaction factor measurement can be obtained by measuring the relative energy variation  $\frac{\Delta E}{E}$ . A method to obtain this quantity has been proposed based on the observation of the shift of the spectral

peaks produced by an undulator [6, 7]. The observation is also quite complex and time consuming since it involves the access to a full beamline to measure the full SR spectrum.

The new technique to obtain  $\alpha_c$ , proposed in this proceeding, is based on the measure of  $\frac{\Delta E}{E}$  by using the relation between the produced SR flux and the beam energy.

## MOMENTUM COMPACTION AND SYNCHROTRON RADIATION

The total SR power emitted by a charged particle with unit charge in a bending magnet is given by:

$$P_0 = \frac{8}{3} \pi \varepsilon_0 r_0^2 c^3 \frac{E^2 B^2}{(mc^2)^2}, \quad (5)$$

where  $\varepsilon_0$  is the vacuum permittivity,  $r_0$  is the classical electron radius,  $m$  is the rest mass of the particle, and  $B$  is the magnetic field [8]. From Eq. (5), it is clear that  $P_0$  depends on the beam energy  $E$ , however a direct measurement of the total SR power is not possible.

A good observable is instead the intensity of the hard portion of the SR, which depends on  $P_0$ . The flux produced by an electron beam with an energy of 6.04 GeV, and one produced by increasing the beam energy of 5% are presented in Fig. 1: the fluxes start to be consistently different for photon energies larger than 100 keV.

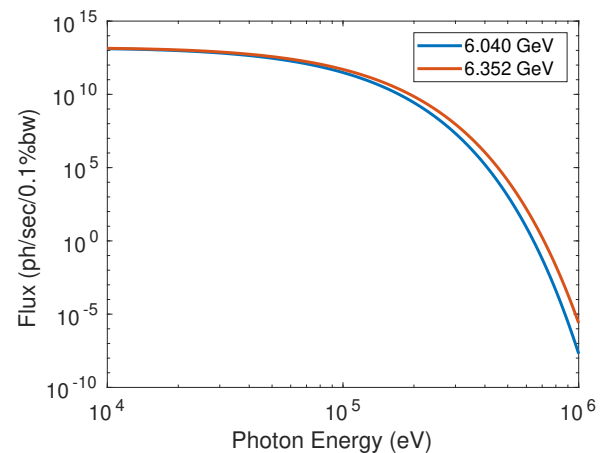


Figure 1: Photon flux produced by a beam of 6.04 GeV (blue) and the one produced by increasing the beam energy of 5% (orange).

High-energy photons can be selected by filtering the SR using an absorber, and detected by using, for example, a scintillator and a CCD camera.

The total intensity of the signal hence depends on the beam energy and although it is not possible to relate it with

\* laura.torino@esrf.fr

the absolute value, any relative energy variation can be detected and quantified from the relative change of the intensity detected by the CCD camera [9]. Figure 2 shows an example of intensity variation when performing a RF step of 100 Hz.

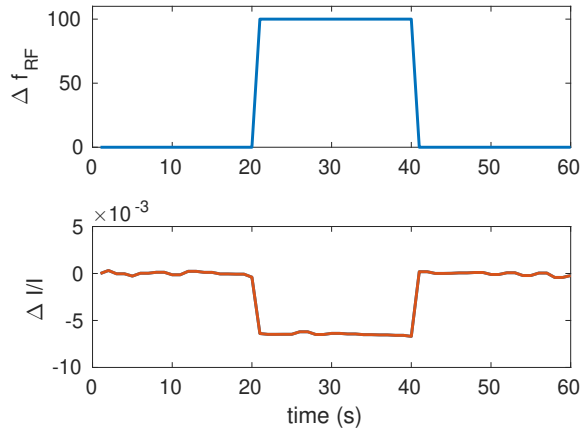


Figure 2: Example of RF step (top) inducing a SR intensity variation (bottom).

The relation between the electron beam energy and the SR intensity depends on the x-rays spectrum and on the radiation optical path.

In order to measure the momentum compaction factor, the idea is to record the SR intensity variation for different RF frequency steps. The relative change of SR intensity is then converted into electron beam energy variation using a coefficient given by the simulation of the SR passing through the optical path. Fitting the data with Eq. (4), the momentum compaction factor is obtained.

## CALCULATION OF THE CONVERSION COEFFICIENT

The software used to simulate the SR and the optical path is the X-ray Oriented Programs (XOP) [10].

XOP produces the emitted SR spectrum for a given beam. The parameters required are the machine radius, or equivalently the magnetic field, and the beam energy. Other parameters, such as the beam current, are not relevant for the scope of these simulations, since they are cancelled out when evaluating the relative variation of the SR intensity.

The same software also produces the transmittance and absorption curve of different material for a defined thickness, as a function of the photon energy spectrum. These curves are used to simulate the x-rays optical path.

A Python script has been written to propagate the x-ray spectrum through the different materials using the transmission curve, and to estimate the number of photons absorbed in the scintillator at the end of the optical path.

The photon absorbed are converted into visible light by the scintillator. The signal produced by the material is linear with the x-ray photon energy absorbed and the linear coefficient is provided by the scintillator manufacturer.

The whole process can be translated in formula as:

$$I(E) = \int_0^\infty f(E_p) \times T_{OP}(E_p) \times A_S(E_p) \times C_s \times E_p dE_p; \quad (6)$$

where  $I(E)$  is the intensity observed on the CCD and depends on the beam energy  $E$ , and  $E_p$  is the energy spectrum of the SR produced,  $f(E_p)$  is the initial flux at a given beam energy,  $T_{OP}(E_p)$  is the transmission of the optical path,  $A_S(E_p)$  is the absorption of the scintillator, and  $C_s$  is the scintillator linear coefficient.

The simulation has to be repeated for several energies in the range of the expected energy excursion. The final output is the dependence of the observed relative change of the SR intensity ( $\frac{\Delta I}{I}$ ) from the generated beam energy variation ( $\frac{\Delta E}{E}$ ).

## EXPERIMENTAL SETUP AND PREPARATION

Experiments were performed at the storage ring of the European Synchrotron Radiation Facility (ESRF). The machine parameters are presented in Table 1.

Table 1: ESRF Machine Parameters

Parameter	Unit	Value
Energy	GeV	6.04
RF frequency	MHz	352
Horizontal Emittance	nm	4
Vertical Emittance	pm	4
Magnetic Field	T	0.86

SR coming from the first bending magnet in cell 7 is extracted through an absorber made out of 28 mm of copper, and through a 2 mm aluminum extraction window. The absorber is a simple, solid, copper parallelepiped designed for non-destructive halo monitoring [11].

X-rays are converted into visible light by 6 mm of Cadmium-Tungstate scintillator ( $\text{CdWO}_4$ ,  $C_s \approx 13 \text{ ph/keV}$  [12]), and imaged through an objective to a CCD camera.

A sketch of the experimental setup is presented in Fig. 3, and Fig. 4 shows an example of the image obtained at the CCD.

### Coefficient Calculation

The coefficient  $K$  relating the relative SR intensity variation with the relative electron beam energy change,

$$\frac{\Delta I}{I} = K \frac{\Delta E}{E}, \quad (7)$$

has been found using XOP, as explained in the previous section.

The simulated SR spectrum (flux) before and after the optical path is presented in Fig. 5.

To calculate the conversion coefficient, the SR spectrum has been generated for beam energies corresponding to an

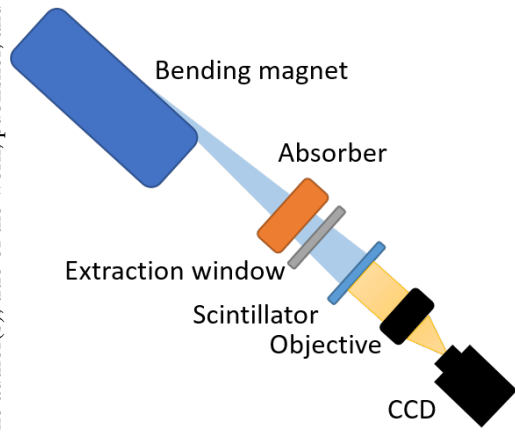


Figure 3: Momentum compaction experimental setup: SR produced by a bending magnets is filtered by a copper absorber and extracted through an extraction window. The radiation is then converted into visible light by a scintillator and imaged onto a CCD camera by an objective.

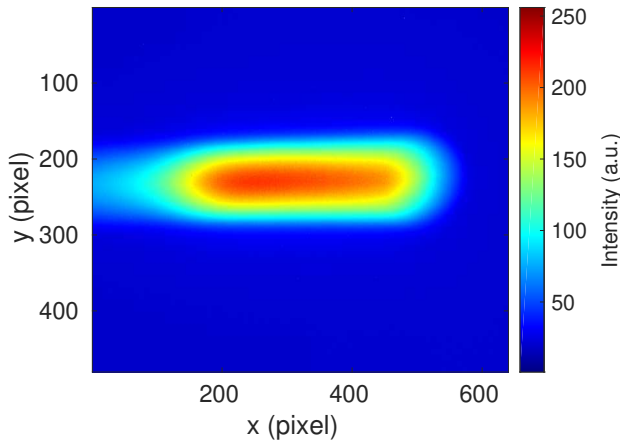


Figure 4: Image obtained at the CCD location.

RF excursion of  $\pm 40$  Hz ( $\approx \pm 10$  MeV). The spectra are propagated through the optical path, and the expected intensity has been calculated according to Eq. (6). The variation of intensity is given by:

$$\frac{\Delta I}{I} = \frac{I(E) - I(E_0)}{I(E_0)};$$

where  $I(E_0)$  is the intensity obtained at  $E_0 = 6.04$  GeV and  $I(E)$  is the intensity for a given beam energy,  $E$ .

The plot of the correspondence between electron beam energy and SR intensity is presented in Fig. 6. From the linear fit of this curve, the conversion coefficient  $K$  is inferred. The result is:

$$\frac{\Delta I}{I} = 17.16 \times \frac{\Delta E}{E}. \quad (8)$$

### Calibration Varying the Magnetic Field

In order to verify the accuracy of the optical path model, an independent, experimental, beam-based calibration has

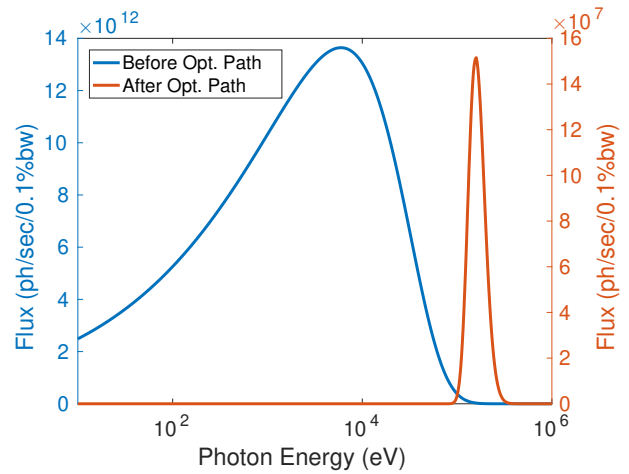


Figure 5: Energy spectrum of the produced SR at 6.04 GeV before the optical path (blue) and at the end of it (orange). Note the different scales on the right and left vertical axis.

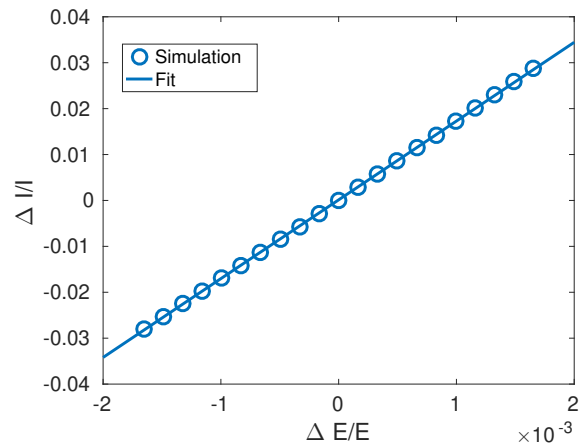


Figure 6: Relation between the electron beam energy and the SR intensity variation. Dots are obtained by XOP simulations, whereas the line is computed by a linear fit.

been performed by varying the magnetic field of all the bending magnets in the storage ring, and consequently the beam energy, maintaining the orbit length constant:

$$\rho \propto \frac{E}{B}, \quad (9)$$

being  $\rho$  is the machine bending radius.

For different values of  $B$  (and hence of  $E$ , since  $\frac{\Delta B}{B} = \frac{\Delta E}{E}$ ), the produced SR intensity has been recorded. The same experiment has been simulated using XOP.

The measured and the simulated intensity variations have been found to be in good agreement: results are shown in Fig. 7.

## RESULTS

Momentum compaction factor measurements have been performed three different times, in 2017. In general, the RF has been varied within a  $\pm 40$  Hz range, which corresponds



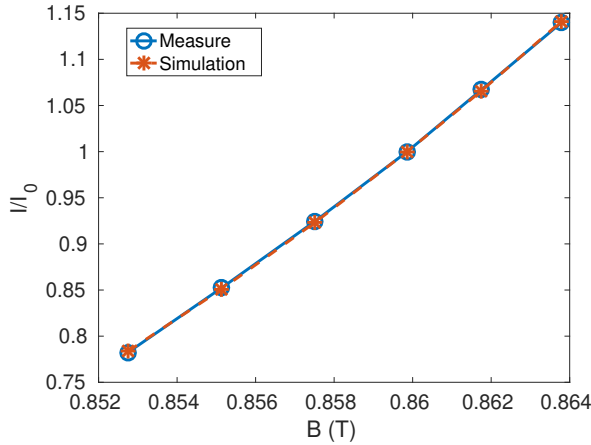


Figure 7: SR normalized intensity Vs dipole field  $B$  at a fixed orbit. Measured data in blue, simulation in orange.

to a relative change of beam energy of about  $6.4 \times 10^{-4}$ . Ten images per frequency has been saved, the intensity of each image was normalized to the beam current to account for possible beam losses during the frequency scan.

In order to avoid effects related with the CCD camera noise drift, the RF has been varied in an “alternate way”, as depicted in Fig. 8.

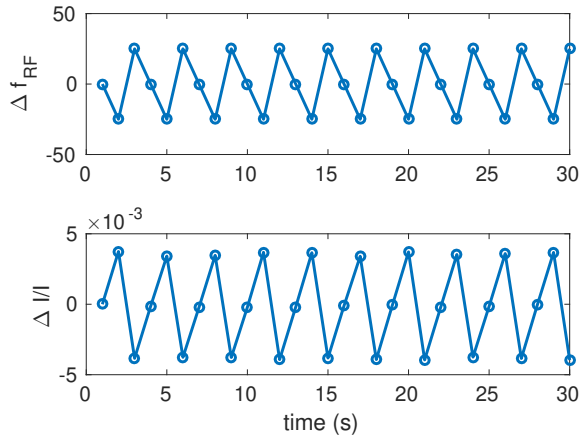


Figure 8: Set RF frequency shifts (top) and measured SR intensity variation (bottom). The “alternate RF variation” consists on the repeated sequence:  $f_{RF}$ ,  $f_{RF} - \Delta f_{RF}$ ,  $f_{RF} + \Delta f_{RF}$ .

To minimize the effect of the background noise, images are averaged and an image taken with no beam and same CCD settings is subtracted.

A suitable Region Of Interest (ROI) has been selected and the integral of the ROI has been used to calculate  $\frac{\Delta I}{I}$ . The energy variation  $\frac{\Delta E}{E}$  is calculated by inverting Eq. (8).

Results are then plotted as a function of the relative variation of the RF frequency  $\frac{\Delta f_{RF}}{f_{RF}}$  and fitted using Eq. (4): the coefficient of the fit provides the machine momentum compaction factor. An example is presented in Fig. 9. The ob-

tained result is:

$$\alpha_c = (1.814 \pm 0.004) \times 10^{-4}, \quad (10)$$

which is compatible with the one computed from the electron beam optics model obtained from the analysis of the Orbit Response Matrix (ORM)  $\alpha_{c,M} = 1.8172 \times 10^{-4}$ .

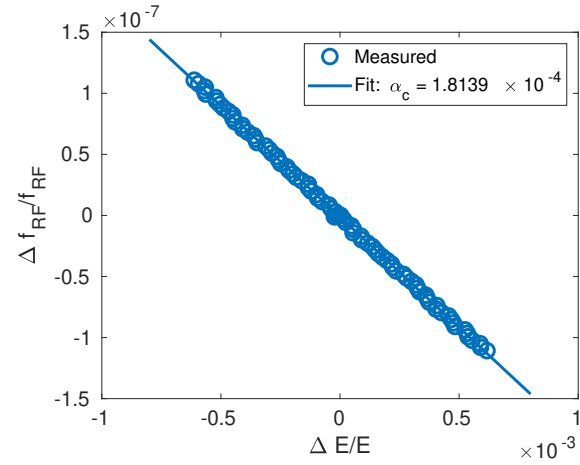


Figure 9: Example of momentum compaction factor measurement:  $\frac{\Delta E}{E}$  dots are calculated from the SR intensity measurements, whereas the solid line represents the fit from whose slope the momentum compaction is inferred.

Table 2 presents all the measurements of the momentum compaction factor obtained using this techniques over several months and the results inferred from the ORM.

Table 2: Results of momentum compaction factor measurements and from the ORM.

$\alpha_c \times 10^{-4}$	$\alpha_{c,M} \times 10^{-4}$
$1.814 \pm 0.004$	1.8172
$1.816 \pm 0.002$	1.833
$1.806 \pm 0.003$	1.8273

## CONCLUSION

In this proceeding a new technique to measure the momentum compaction factor based on SR intensity measurements has been proposed. Experimental tests performed at ESRF and their results have been presented proving the precision (better than  $10^{-6}$ ) and the reliability of the technique. The relative error on the measurement is in the order of 0.1%.

## ACKNOWLEDGMENTS

The authors would like to thank K. B. Scheidt for the main idea, F. Ewald for the help with the technical issues with the CCD cameras, and the ESRF accelerator and source division for the grate job in operating and maintaining the machine.

## REFERENCES

- [1] H. Wiedemann, *Particle Accelerator Physics I*, Berlin Heidelberg, Springer, 1998. doi:10.1007/978-3-662-03827-7
- [2] L. Arnaudon, *et al.*, “Accurate determination of the LEP beam energy by resonant depolarization”, *Zeitschrift für Physik C Particles and Fields*, vol. 66, no. 1, pp. 45–62, Mar. 1995. doi:10.1007/BF01496579
- [3] J. Zhang *et al.*, “Precise beam energy measurement using resonant spin depolarization in the SOLEIL storage ring”, *Nuclear Instruments and Methods in Physics Research Section A: Accelerators, Spectrometers, Detectors and Associated Equipment*, vol. 697, pp. 1–6, 2013. doi:10.1016/j.nima.2012.09.003
- [4] A.-S. Müller *et al.*, “Momentum compaction factor and nonlinear dispersion at the ANKA storage ring”, in *Proc. EPAC’04*, Lucerne, Switzerland, Jul. 2004, paper WEPLT068, pp. 2005–2007.
- [5] N. Carmignani *et al.*, “Modeling and measurement of spin depolarization”, in *Proc. IPAC’15*, Geneva, Switzerland, Jun. 2015, pp. 109–112. doi:10.18429/JACoW-IPAC2015-MOPWA013
- [6] E. Tarazona and P. Elleaume, “Measurement of the absolute energy and energy spread of the ESRF electron beam using undulator radiation”, *Rev. Sci. Instr.*, vol. 67, no. 9, p. 3368, 1996. doi:10.1063/1.1147371
- [7] B. Yang *et al.*, “High accuracy momentum compaction measurement for the APS storage ring with undulator radiation”, *AIP Conference Proceedings*, vol. 546, no. 1, pp. 234–241, 2000. doi:10.1063/1.1342591
- [8] A. Hofmann, “Characteristic of Synchrotron Radiation”, in *Proc. CERN Accelerator School, Synchrotron Radiation and Free Electron Lasers*, Chester, UK, Apr. 1989, pp. 115–141, published 1990, and CERN rep. CERN-90-03.
- [9] K. B. Scheidt, “Recent developments of novel beam diagnostics at the ESRF”, in *Proc. IPAC’13*, Shanghai, China, May 2013, paper TUOCB201, pp. 1143–1145.
- [10] X-ray Oriented Programs, <http://www.esrf.eu/Instrumentation/software/data-analysis/xop2.4>
- [11] K. B. Scheidt, “Non destructive vertical halo monitor on the ESRF’s 6 GeV electron beam”, in *Proc. IBIC’14*, Monterey, CA, USA, Sep. 2014, paper MOCYB1, pp. 2–6.
- [12] Saint Gobain, [www.crystals.saint-gobain.com](http://www.crystals.saint-gobain.com)

# ARIES-ADA: AN R&D NETWORK FOR ADVANCED DIAGNOSTICS AT ACCELERATORS\*

P. Forck<sup>†</sup>, M. Sapinski, GSI Helmholtzzentrum für Schwerionenforschung, Darmstadt, Germany

U. Iriso, F. Perez, ALBA Synchrotron, Cerdanyola del Vallès, Barcelona, Spain

R. Jones, CERN, Geneva, Switzerland

Ch. Gerth, K. Wittenburg, Deutsches Elektronen-Synchrotron, Hamburg, Germany

R. Ischebeck, Paul Scherrer Institut, Villigen, Switzerland

## Abstract

Accelerator Research and Innovation for European Science and Society, ARIES, is an initiative funded by the European Union. The activity comprises three major categories: Joint Research Activities; Transnational Access; Network Activities. One of 17 activities is a network related to Advanced Diagnostics at Accelerators, ADA with the task of strengthening collaborations between international laboratories and for coordinated R&D in beam diagnostics. This is performed by organizing Topical Workshops on actual developments and supporting interchange of experts between different labs. Since the start of the project in May 2017 four Topical Workshops were organized, each with 30-45 participants. Future workshops will address actual topics.

## THE INITIATIVE ARIES

*Accelerator Research and Innovation for European Science and Society*, ARIES [1], is an Integrating Activity which aims to develop European particle accelerator infrastructures, co-funded under the European Commission's Horizon 2020 Research and Innovation programme.

Within a four year funding period, the key aim of the initiative ARIES is related to the development of novel concepts and further improve existing accelerator technology. This is realized by improving the performance, availability, and sustainability of particle accelerators, transferring the benefits and applications of accelerator technology to both science and society, and enlarging and integrating the European accelerator community. Moreover, it aims to support innovative technologies with market potential by advancing concepts and designs for medical, industrial and environmental applications of accelerators for the benefits of European society as a whole. The consortium consists of 41 institutions from academia, accelerator laboratories and industry of 18 European countries. The initiative is organized in 17 scientific work-packages of three different categories:

- Within the 5 so called ‘*Joint Research Activities*’ several intuitions are working together on key technologies for accelerators like for super-conducting rf-cavities or very high gradient accelerators.
- As a second branch 5 so called ‘*Transnational Access*’ provides infrastructure for equipment testing like fully

equipped test benches for rf-cavities, access to electron and hadron accelerators with a wide range of beam parameters.

- The third branch comprises of 7 ‘*Network Activities*’ which aims for strengthening the collaborations concerning the worldwide accelerator research and development. These activities are related to e.g. the design of novel accelerators, efficient energy management, design of ultra-low emittance light sources, industrial applications, beam diagnostics and novel methods for student education.

## THE NETWORK ARIES-ADA

One of the Network Activities is related to ‘*Advanced Diagnostics at Accelerators*’, ADA [2]. To meet the demands of new accelerator facilities, novel beam instrumentation and diagnostics methods are required. Knowledge exchange between experts from worldwide research institutes is an efficient way of developing such systems efficiently. Topical Workshops with about 20 to 40 international participants ranging from novices to world-leading experts is an excellent way of summarizing state of the art developments in the field and transferring this knowledge to the young generation. A workshop duration of typically two days seems to be adequate to summarize the current status of a dedicated subject, provide the possibility to discuss novel ideas and trigger the collaboration between the participants. The collection of contributions acts as a comprehensive summary of the current R&D status. The subject of the workshops is oriented on actual topics; four of such dedicated workshops were organized in the first 14 month of the funding period (i.e. between May 2017 and June 2018).

The funding from the European Union for ARIES-ADA is administrated by the four beneficiary institutions ALBA, CERN, DESY and GSI. The budget covers mainly the general workshop costs as well as possible additional costs to enable the participations of the worldwide experts. The workshops are announced to the general audience from the ARIES website [1, 2]; key-speakers are invited directly by the workshop organizers.

In addition to the workshops, the exchange of experts for a typical duration of 2 weeks for common discussions and to carry out experiments were organised in the frame of ARIES-ADA to further strengthen the collaboration between the accelerator institutions. Within the first year of ARIES-ADA four of such visits were financed.

\* This project has received funding from the European Union's Horizon 2020 programme under Grant Agreement No 730871

<sup>†</sup> email address: p.forck@gsi.de.



In the following the Topical Workshops executed within the frame of ARIES-ADA are summarized and an outlook for further events is given; the entire contributions can be found on the cited INDICO pages.

### WORKSHOP ON IPM OPERATION AND SIMULATION

In May 2017 a Topical Workshop took place at GSI (Darmstadt, Germany) concerning ‘*Simulation, Design & Operation of Ionization Profile Monitors*’ [3] with 33 international participants. An Ionization Profile Monitor (IPM) is based on spatially resolving the ions or electrons generated from residual gas ionisation through beam impact. These monitors deliver the beam profile in a non-destructive manner with a spatial resolution of typically 50  $\mu\text{m}$  and time gating down to the 10 ns level. They are installed at both hadron synchrotrons and LINACs. Due to the increase in the beam power of future LINACs (e.g. at CERN, ESS, FAIR, ISIS) these IPMs will substitute the traditional invasive wire-based diagnostics. Even though the principle is well known, there are many technical challenges for the reliable operation of IPMs.

The experience and technical solutions from installations all over the world were presented by the experts in the field, with the results extensively discussed and the related contributions serving as a comprehensive catalogue of such systems.



Figure 1: Participants of the Topical Workshop executed in May 2017 at GSI.

One purpose of the workshop was to introduce the community to a recently completed simulation code called IPMSim [4, 5], which is freely accessible. This code was produced with the input of several experts to simulate the related physical processes (cross section for electron and ion production) under various conditions (beam distribution, space charge, external field configurations) from non-relativistic beams at LINACs to highly energetic beams at synchrotrons. The code features a modern programming style, a user-friendly GUI and can easily be expanded to include new physical models and applications. The code is freely available and its benchmarking was successfully demonstrated. Further extensions of the code (e.g. for Beam Induced Fluorescence Monitors) are currently included [6]. As different codes are produced by various laboratories, a common set of beam parameters were agreed on to perform such benchmarking between those codes. Possible experimental

verifications of such simulations were put forward at this workshop and many have now been performed.

This workshop acted as a follow-up of a previous workshop held at CERN in February 2016 [7]. Due the large interest in this field, a third workshop will be executed at J-PARC (Tokai, Japan) in September 2018 [8].

### WORKSHOP ON EMITTANCE MEASUREMENT AT LIGHT SOURCES

The Topical Workshop ‘*Emittance Measurements for Light Sources and FELs*’ [9] was organized at ALBA (Barcelona, Spain) in January 2018 with 37 participants. The Workshop addressed the challenges that this community is facing with such measurements for the next generation of ultra-low emittance machines. One day was devoted to emittance measurements at synchrotron light sources, and the second day to measurements at Free Electron Lasers. Experts working on emittance measurements for other types of machines such as hadron synchrotrons and Laser Plasma Accelerators were also invited to discuss possible synergies between the different communities. Due to the importance of the topic, a detailed summary of this workshop is given as an invited talk at this conference [10].



Figure 2: Participants of the Topical Workshop executed in January 2018 at ALBA.

For synchrotron light sources, the review of present techniques using synchrotron radiation showed that beam sizes down to the 2-3 $\mu\text{m}$  level can be measured through the careful design and choice of the instrumentation. These techniques include direct imaging techniques (X-ray pinhole cameras, Compound Refractive Lenses, or in-air X-ray detectors) and techniques based on the analysis of light coherence (visible light interferometers). Since this is at the limit for the beam sizes foreseen for the next generation of low emittance rings, the benefits of more complex techniques such as X-ray diffraction/interferometry and Heterodyne Speckle Fields (HNFS) were also deeply discussed during the workshop. A further conclusion of the workshop had been that these techniques need specific beamlines foreseen for their operation.

For Free Electron Lasers, beam sizes are typically measured using invasive methods through the interaction of the beam with movable obstacles, such as Optical Transition Radiation screens or wire scanners. It was demonstrated that wires as thin as 1  $\mu\text{m}$  can now be manufactured by lithographic techniques, which allow the

measurement of beam sizes down to 500 nm. In addition to discussing the current status of techniques such as laser wire measurements or Optical Diffraction Radiation Interferometry, the workshop also addressed new, innovative techniques such as Cherenkov Diffraction Radiation.

## WORKSHOP ON DIAGNOSTICS USING ELECTRO-MAGNETIC DETECTORS

A Topical Workshop with 32 participants on ‘*Extracting Information from electro-magnetic monitors in Hadron Accelerators*’ [11] took place in May 2018 at CERN (Geneva, Switzerland) with 32 participants. The goal was to strengthen the collaboration between the beam dynamics and beam instrumentation community as both communities have to contribute to a correct interpretation of advanced beam measurements. Additionally, people working at 3<sup>rd</sup> generation light sources participated as the topic is equally important for the electron- and hadron synchrotrons.



Figure 3: Participants of the Topical Workshop executed in May 2018 at CERN.

The workshop focused on various measurement methods of lattice parameters at synchrotrons, such as the machine tune and chromaticity. Recent results concerning betatron-function measurement and beta-beating determination were discussed. The different methods used for optics measurements were summarized in an overview talk. It was shown that part of the progress is related to improvements of the achievable accuracy of the BPM readout. The applicability of methods leading to significant noise reduction of the BPM data was demonstrated in several contributions. Moreover, the determination of advanced parameters such as intensity dependent tune shift and tune spread determined via quadrupolar oscillations are currently a ‘hot topic’ and were intensively discussed between instrumentation and beam dynamics experts. A comparison between simulations and measurements at CERN PS show a good correspondence as had been clearly depicted in one of the contributions.

Further on, Schottky signal analysis was discussed in several contributions. This method enables an observation of many parameters without any influence on the beam. The applicability for coasting and bunched beam for daily operation and detailed machine studies was discussed. Recently, the advanced Schottky system at LHC was realized and enable now online measurements e.g. of tune and chromaticity. Using Schottky analysis it is possible to perform BPM-based position measurements for a coasting

beam. Those contributions serve as a comprehensive collection of the standard and advanced applications.

## WORKSHOP ON LONGITUDINAL MEASUREMENTS AT FELS

In June 2018 the Topical Workshop ‘*Longitudinal Diagnostics for Free-Electron Lasers*’ [12] took place at DESY (Hamburg, Germany) with 45 participants. The workshop aimed at both fostering joint developments of longitudinal diagnostics for femtosecond electron bunches and bringing together experts working on beam instrumentation and detector development. Several participants working in the field of Laser Plasma Accelerators contributed to the workshop as these novel short-bunch accelerators are facing even higher demands on time resolution. The topic of transverse deflecting structures (TDS) was intentionally excluded as there exists a strong collaboration between CERN, PSI and DESY on the development of an X-Band TDS [13] with regular meetings.



Figure 4: Participants of the Topical Workshop executed in June 2018 at DESY.

The workshop was organised in 5 working groups with the goal of exchanging ideas, planning joint collaborations or measurement campaigns. The first day of the workshop was devoted to discussions within these working groups. On the 2<sup>nd</sup> and 3<sup>rd</sup> day the working group coordinators reported the discussion results and the participants presented their contributions in poster sessions.

*Compression Monitors and THz Detectors:* The intense coherent THz and IR part of diffraction or edge radiation emitted by the electron bunches is commonly used as a compression monitor for a feedback on the accelerator phase. The THz/IR beam transport, attenuation and detection need to be optimized depending on the bunch charge, profile and repetition rate. Further improvements of a multi-array Schottky diode detector developed by TU Dresden as a THz spectrometer were identified.

*Electro-Optical Diagnostics:* Electro-optical techniques are limited in time resolution but are fully non-invasive. Different read-out schemes were discussed to achieve single-bunch resolution at MHz repetition rates. Joint experiments are planned.

*THz Streak of the primary electron beam:* The goal of this working group was to discuss possibilities to streak the electron beam in a micro-structure operating at terahertz frequencies. The aim is to improve the resolution of radio frequency deflectors by increasing both frequency and deflecting fields. The application to low-energy beams has now been presented [14], and further studies at higher-energy facilities are planned.

**KALYPSO and fast digitization:** The KALYPSO (Kalruhe Linear detector for MHz-rePetition rate Spectroscopy) linear detector system has been developed as a flexible digitizer board to be compatible with different front-end electronic standards for many applications. Requirements for the next improved version were defined by the various applications of the linear detector board.

**Laser Heater operation and diagnostics:** The aim was to share experience of laser heater operation and optimization for the suppression of micro-bunching instabilities gained at different facilities. The cathode material of the photo-injector, e.g. Cu or Ce<sub>2</sub>Te, seems to have an influence on the micro-bunching instabilities and, therewith, on the operation of the laser heater. Further joint studies are planned.

## FUTURE WORKSHOPS

The next workshop with the title ‘*New Generation of Beam Position Acquisition and Feedback Systems*’ [15] will take place at ALBA in November 2018. This three days event is a ‘double workshop’ as it will bring the experts from hadron and electron community together in a common session to discuss closed orbit feedback achievements and the challenges at hadron and ultra-low emittance electron synchrotrons. The second and third day is separated into ‘Hadron BPM Analog and Digital Electronics’ and ‘Fast Feedback Systems for Electron Synchrotrons’ discussing the special requirements of both communities.

A workshop on ‘*Optical Profile Measurements by Scintillation Screens*’ will take place in Krakow in April 2019. It can be regarded as an update event of workshop organized in 2011 at GSI [16].

Further subjects of interest are related to the commissioning of hadron LINACs and longitudinal and transverse emittance measurements. For these LINACs methods for automatic beam steering will be discussed. For hadron synchrotrons the control of beam stability and advanced machine parameter determination including halo diagnostics is of major concern. For the electron synchrotron the requirements and related control for beam stability and impedance contributions is an important topic. For the LINAC-based light sources feedback system on an inter-pulse reaction will be discussed as well as methods for reliability determination. These workshops will be planned with about lead-time of about half a year prior to the execution to include actual developments accounting for the beam instrumentation needs. Proposals from the community for further subjects are welcome.

## CONCLUSION

Due to the funding by the European Union, Topical Workshops can be organized on actual beam instrumentation developments and usage of such diagnostics. The relevance of such workshops is obvious as typically 20 to 40 worldwide experts are interested to discuss about one dedicated subject in a more detailed manner as can be realized at a regular conference. The familiar atmosphere

with senior and young scientist forces discussions about layout details, which are normally not presented at large conferences and contribute to the successful design and operation of beam diagnostics. Moreover, the workshops served as a platform for young scientists to present their work and to mingle with experienced experts. The resulting collection of high quality contributions serves as a comprehensive reference summarising the actual status and the proposals for further developments. The workshops are generally open to the accelerator physics community; the workshop topics are oriented on actual developments and open questions within the community.

The exchange of personnel is not only of direct benefit to the person concerned, but helps to strengthen the collaboration and increases the efficiency for beam diagnostics R&D.

## ACKNOWLEDGEMENTS

The steady efforts by M. Vretenar (CERN) acting as the ARIES project leader are highly acknowledged; he and his team led ARIES to a successful program. The competent contributions by all participants and the lively discussions leading to successful workshops are warmly acknowledged. This project has received funding from the European Union’s Horizon 2020 Research and Innovation programme under Grant Agreement No 730871.

## REFERENCES

- [1] <https://aries.web.cern.ch/>.
- [2] <https://aries.web.cern.ch/content/wp8>
- [3] <http://indico.gsi.de/event/5366/>.
- [4] <https://twiki.cern.ch/twiki/bin/view/IPMSim/>.
- [5] M. Sapinski *et al.*, “Ionization profile monitor simulations status and future plans”, in *Proc. IBIC’16*, Barcelona, Spain, Sep. 2016, pp. 521-524. doi:10.18429/JACoW-IBIC16-TUPG71
- [6] D. Vilsmeier, P. Forck, and M. Sapinski, “A modular Application for IPM simulations”, in *Proc. IBIC’17*, Grand Rapids, MI, USA, Sep. 2017, pp. 335-338. doi:10.18429/JACoW-IBIC17-WEPC07
- [7] <https://indico.cern.ch/event/491615/>.
- [8] <https://conference-indico.kek.jp/indico/event/55/>.
- [9] <https://indico.cells.es/indico/event/128/>.
- [10] U. Irso *et al.*, ‘Summary of emittance measurements workshop for SLS and FELs’, presented at IBIC’18, paper WEOC01, this conference.
- [11] <https://indico.cern.ch/event/705430/>.
- [12] <https://indico.cern.ch/event/702602/>.
- [13] P. Craievich *et al.*, “Status of the PolariX-TDS project”, in *Proc. IPAC’18*, Vancouver, BC, Canada, May 2018, pp. 3808-3811. doi:10.18429/JACoW-IPAC18-THPAL068
- [14] D. Zhang *et al.*, “Segmented Terahertz Electron Accelerator and Manipulator (STEAM)”, *Nature Photonics*, vol. 12, pp. 336-342, 2018. doi:10.1038/s41566-018-0138-z
- [15] <https://indico.cern.ch/event/743699/>.
- [16] <https://www-bd.gsi.de/ssab>.



# HIGH-ENERGY SCRAPER SYSTEM FOR THE S-DALINAC EXTRACTION BEAM LINE – COMMISSIONING RUN\*

L. Jürgensen<sup>#</sup>, M. Arnold, T. Bahlo, R. Grewe, J. Pforr, N. Pietralla, A. Rost, S. Weih, J. Wissmann,  
Technische Universität Darmstadt, Germany  
F. Hug, Johannes Gutenberg-Universität Mainz, Germany  
C. Burandt, T. Kürzeder, Helmholtz-Institut Mainz, Germany

## Abstract

The S-DALINAC is a thrice recirculating, superconducting linear electron accelerator at TU Darmstadt. It delivers electron beams in cw-mode with energies up to 130 MeV. The high-energy scraper system has been installed in its extraction beam line to reduce the energy spread and improve the energy stability of the beam for the experiments operated downstream. It comprises three scraper slits within a dispersion-conserving chicane consisting of four dipole magnets and eight quadrupole magnets. The primary scraper, located in a dispersive section, allows to improve and stabilize the energy spread. In addition energy fluctuations can be detected. Scraping of x- and y-halo is implemented in two positions enclosing the position of the primary scraper. We will present technical details and results of the first commissioning run of the recently installed system at the S-DALINAC. Besides improving on the energy spread, it proved to be a valuable device to observe energy spread and energy fluctuations as well as to reduce background count rates next to the experimental areas.

## INTRODUCTION

Since 1987 the S-DALINAC serves nuclear- and astrophysical experiments at the Technical University of Darmstadt [1]. It is fed by either a thermionic or a photoemission gun which delivers a spin-polarized beam [2]. After pre-acceleration by the injector module the electron beam can either be used for experiments at the NRF-setup [3] or it is guided through a 180°-arc to enter the main linac. By passing the linac up to four times the maximum energy of about 130 MeV can be reached. The beam current can be adjusted from several pA up to 20  $\mu$ A. The layout of the S-DALINAC is given in Fig. 1.

The high-energy beam of the S-DALINAC is used for nuclear physics experiments with a need for high energy resolution and low noise next to the experimental area. The recently installed scraper system [4] is placed between the accelerator hall and the experimental hall and provides beam-cleaning and –monitoring features. The energy spread can be reduced by sending the dispersive beam through a narrow slit which determines the energy and the energy range that continues towards the

experimental areas. Blocked parts of that beam deposit their charge onto the high- and the low-energy side of that slit which allows for an online monitoring of energy fluctuations during long beam times.

If not optimized,  $\gamma$ -ray background from bremsstrahlung processes can prevent sensitive detection of photons from searched-for nuclear reactions. The background is produced by beam losses resulting from collisions of beam halo with beam line components. In order to remove beam halo the installed scraper system also contains halo scrapers that work in horizontal as well as in vertical direction.

## CONSTRUCTION

The presented high energy scraper system resembles a chicane which consists of four dipole magnets, eight quadrupole magnets, four vertical steerers and the three scraper chambers themselves. The system is depicted in Fig. 2. Beam scraping will be done in three different positions. This is necessary because beam dynamics have to be adjusted individually for halo scraping and for the energy defining scraper (see section *Beam Dynamics*). The system consists of three spherical vacuum chambers, each measuring 9" in diameter. The two chambers for halo scraping contain guided, water cooled copper blocks which are positioned using a stepping motor outside the vacuum. In this set-up a positioning accuracy better than 0.01 mm is possible. Downstream of the halo scrapers, BeO-screens can be inserted to check for beam position and shape. The amount of beam current, which is stopped during halo-scraping, is in the order of 1% of the total beam intensity. The energy defining scraper is however outlaid to deal with the full beam power. Additionally to the extensive cooling water system, both scraper brackets are mounted electrically isolated from the beam pipe. By measuring the current, one gains information about the amount of beam current which is stopped on each bracket. This helps to find the optimal position of the slit and in addition identify energy fluctuations of the beam. Monitoring this quantity will also help to detect and cure irregularities of the rf-system to further decrease the potential of failure.

\*Funded by Deutsche Forschungsgemeinschaft under grant No. GRK 2128  
<sup>#</sup>ljurgensen@ikp.tu-darmstadt.de

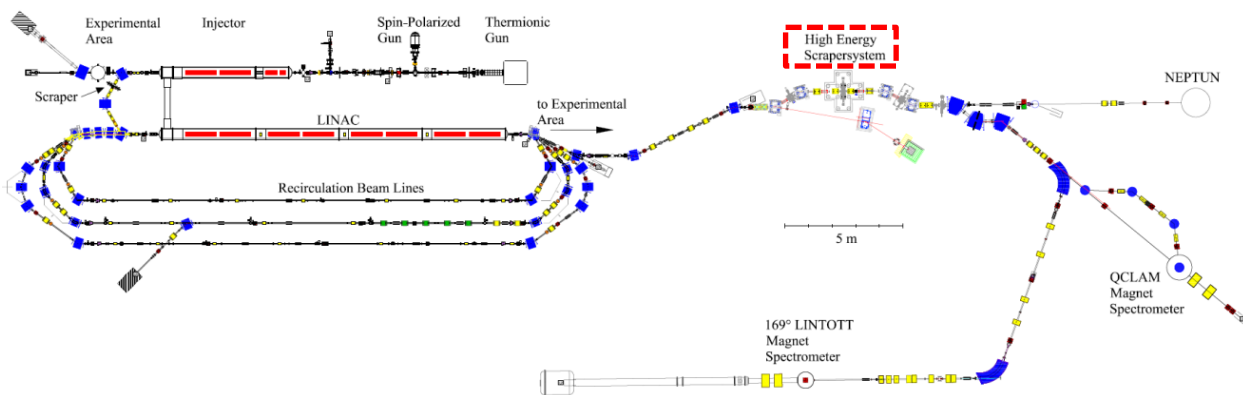


Figure 1: The S-DALINAC floor plan including accelerator hall, extraction beam lines and experimental areas. The scraper system is highlighted in red.

### BEAM DYNAMICS

The new system replaces a straight part of the former extraction beam line and therefore has to conserve dispersion and allow beam tuning independently for the rest of the beam line. The chicane had to be built within a space of 8 m x 2 m which set the limits for beam line design. The final results of the beam dynamics calculations using the *XBEAM* [5] code are shown in Fig. 3. Dipole positions and dipole chamfer angles, quadrupole positions and their gradients were outlaid to build a fully symmetric system with high transverse dispersion and small horizontal beam size at the position of the energy defining scraper. The width of the slit together with the dispersion at this position, determine the energy spread which can pass the scraper. A horizontal beam focus in this point allows using a narrow slit without losing too much beam current. The halo scrapers are positioned where dispersion and beam width are small.

### INSTALLATION

The high energy scraper system was built up in the extraction beam line of the S-DALINAC within the installation period for the third recirculation path [6]. Due to radiation shielding for the neighbouring experimental areas, the former extraction beam line has been placed inside a tunnel of concrete blocks which had to be opened and slightly changed to gain space for the chicane. After the removal of the old beam line, the chicane including dipole and quadrupole magnets were positioned. For the optimal performance of the system it is of great importance to meet the calculated drift lengths and magnet positions. In a first step the positions of the stands were marked using a laser tracker system. The beam axis has been marked in close collaboration with our partners from the geodetic groups of the Frankfurt University of Applied Sciences and Technische Universität Darmstadt [7].

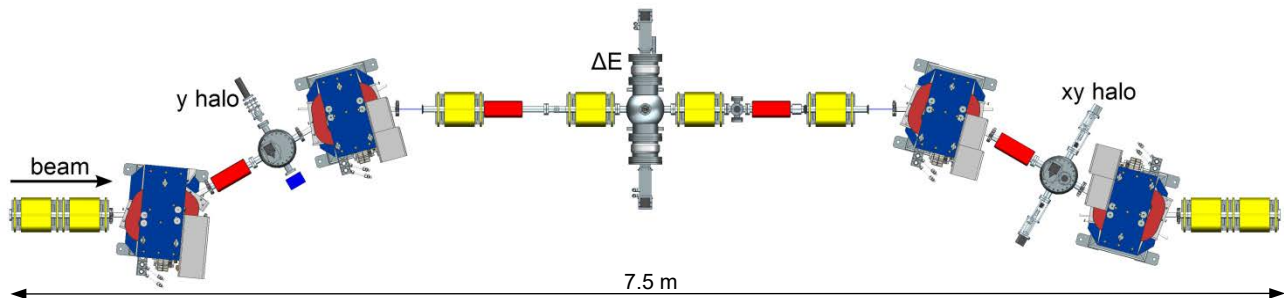


Figure 2: The high energy scraper system: from left to right the chambers for y halo-, energy defining- and xy halo-scraper can be seen, dipole magnets in blue, quadrupole magnets in yellow, steerers in red.

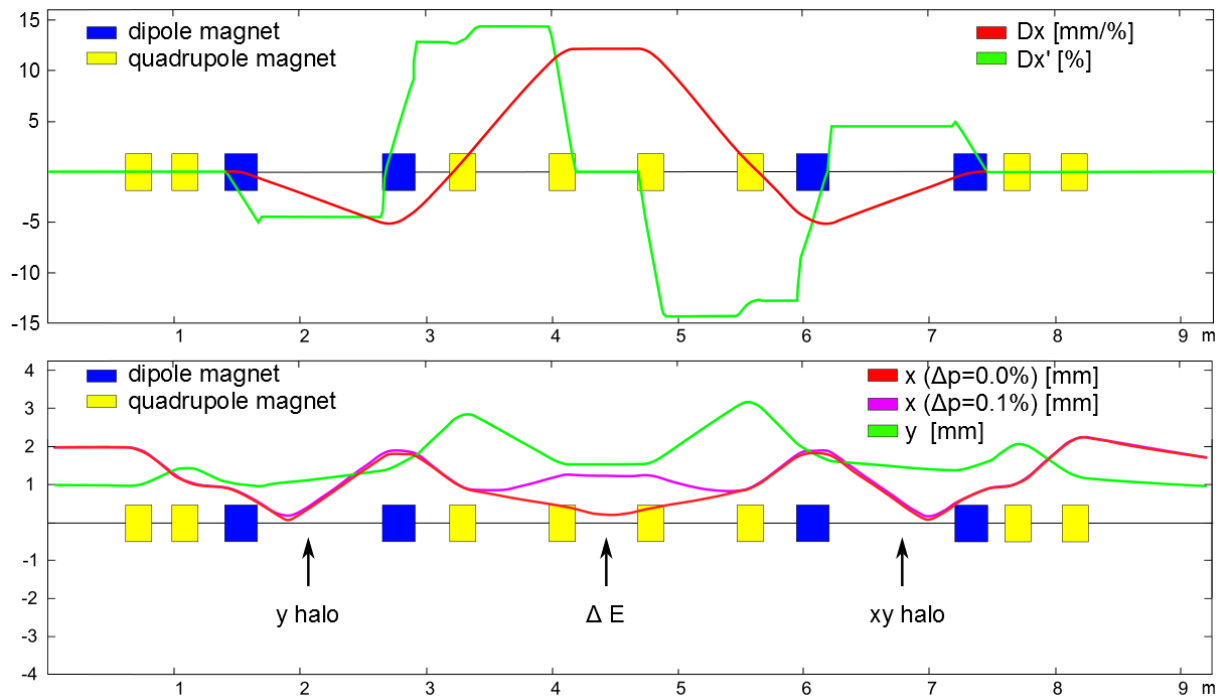


Figure 3: Beam dynamics calculation: The upper graphic shows the dispersion and its derivative along the new beam line. The beam envelope ( $1\sigma$  radius) for  $\Delta p = 0\%$  and  $\Delta p = 0.1\%$  is plotted below. The locations of the energy defining scraper ( $\Delta E$ ) and the halo scrapers are indicated by small arrows.

## COMMISSIONING RUN

During the experimental beam time in October and November 2017 the scraper system went into operation. Its impact on the energy spread was measured at beam energies of 42.5 MeV and 22.5 MeV while the latter will be presented here. Figure 4 shows the measured energy spread after the scraper system for a variation of the energy scraper's gap width. It can be seen that the energy spread could be reduced starting from 25 keV down to 5 keV. By measuring the deposited beam current on each of the energy scraper brackets we gained information on energy fluctuations. Decreasing error bars indicate an efficient reduction of energy fluctuations for small gap width. Further tests at a beam energy of 42.5 MeV showed a reduction of the energy spread to 8 keV.

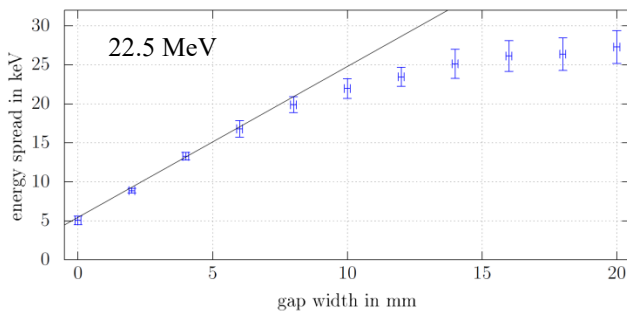


Figure 4: Measured energy spread for several gap widths of the energy scraper at a beam energy of 22.5 MeV.

Additionally several photon-sensitive detectors had been placed next to our experimental setup that showed an efficient reduction of the  $\gamma$ -ray background by closing the energy scraper slit (the count rate dropped below 10% of its initial value). Further reduction could be reached by using the halo scrapers. Their commissioning is scheduled within the next months.

## CONCLUSION

The new high-energy scraper system at the S-DALINAC and its first commissioning run have been presented in this contribution. The system will help to improve beam quality by halo and energy scraping of the beam after acceleration. The energy defining scraper performed well and therefore has already been used for experimental beam times. Using this new feature, future experiments with high resolution and low noise can be approached.

## REFERENCES

- [1] N. Pietralla, Nucl. Phys. News, Vol. 28, No. 2, S. 4-11, 2018.
- [2] J. Enders, AIP Conf. Proc. 1563, 223 (2013).
- [3] K. Sonnabend *et al.*, Nucl. Instr. & Meth. A 640, (2011), 6-12.
- [4] L. Jürgensen *et al.*, IPAC'16, Busan (2016) 101.
- [5] T. Winkler, In-house developed code (1993).
- [6] M. Arnold *et al.*, IPAC'16, Busan (2016), 1717.
- [7] M. Lösler *et al.* ZfV, Vol. 140(6), S. 346-356, 2015.



# PROGRESS IN THE STRIPLINE KICKER FOR ELBE

C. Schneider<sup>†</sup>, A. Arnold, J. Hauser, P. Michel, HZDR, Dresden, Germany

## Abstract

The linac based cw electron accelerator ELBE operates different secondary beamlines one at a time. For the future different end stations should be served simultaneously, hence specific bunch patterns have to be kicked into different beam-lines. The variability of the bunch pattern and the frequency resp. switching time are one of the main arguments for a stripline-kicker. A design with two tapered active electrodes and two ground fenders was optimized in time and frequency domain with the software package CST. From that a design has been transferred into a construction and was manufactured. The presentation summarises the recent results and the status of the project.

## INTRODUCTION

The electron beam with max. 40 MeV is mainly used for conversion into secondary radiation at different end stations; infrared, terahertz, gamma, positron, neutron und electron laser interaction (Figure 1). For every beam line dedicated energies and optimized settings have to be adjusted, but not every experiment demands the full 13 MHz cw capability of ELBE.

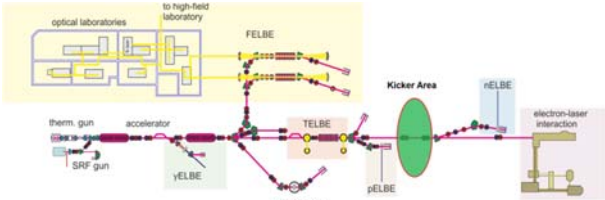


Figure 1: Overview of the ELBE layout with the position of the kicker station.

As an example the end stations from neutron an electron laser interaction are using high bunch charge but 200 kHz and 10 Hz respectively and are separated by just one beam line branch. Therefore a kicking device in front of the neutron and laser interaction beam line can serve both beam lines at a time.

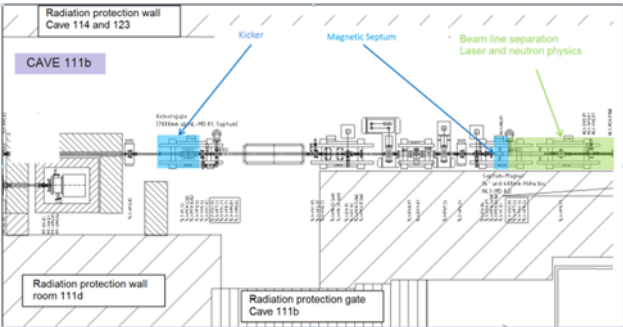


Figure 2: Detailed sketch of the ELBE kicker area.

A magnetic septum is installed to align the beam either to the neutron or laser interaction beamline (see Figure 2). The separation for the magnetic septum is about 10 mm beam displacement. The distance between kicker and septum will be around 7 m. Hence a kick angle of around 1.5 mrad must be realized. In the simulation with the CST software package a voltage of 427 V per strip-line and an electrode distance of 30 mm was used. This results in a mean kicking angle of the phase space distribution of 1.5 mrad.

## DESIGN AND OPTIMISATION

The ELBE strip-line kicker design uses the common approach [1, 2, 3] with two tapered active electrodes and two ground fenders. The slightly difference is the placing of the two ground fenders in the outer area of the electrodes.

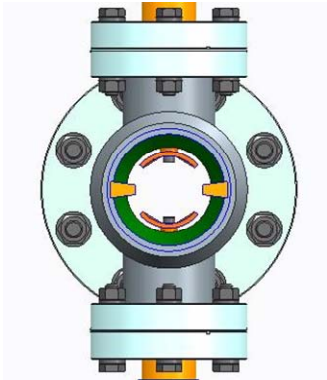


Figure 3: Sectional drawing of the ELBE kicker in the area of the connection ports.

The distance between the electrodes was chosen to 30 mm having a balance of lower HV supply and still feeding the electron beam in a homogenous field area through the kicker (Figure 3). The design was optimized with the CST package to fit best to 50 Ω impedances, for optimal S-parameters in the frequency domain as well as having best field flatness (Figure 4) in the significant area between the electrodes.

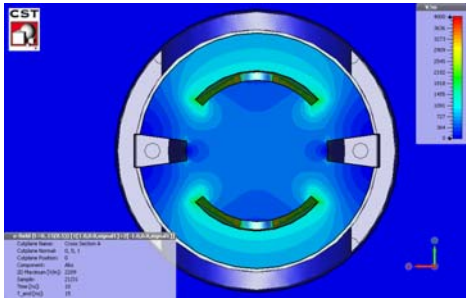


Figure 4: Sectional plot of the electric field in the medium section of the kicker structure.

## KICKER SETUP AT ELBE

The kicker will be installed in the radiation shielded cave 111b (see Figure 5). The HV-device to power the kicker

\* Work supported by BMBF  
<sup>†</sup> Christof.Schneider@hzdr.de

must be installed outside due to radiation protection reasons. Therefore two 25 m long RG213 cables are installed by special feed through into the cave. The HV-device will be connected to the ELBE synchronization system.

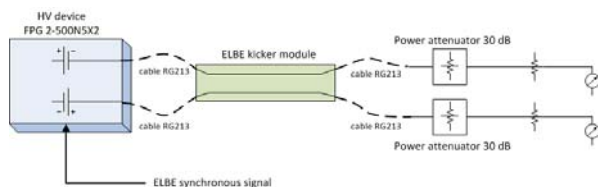


Figure 5: Basic kicker setup at ELBE.

The diagnostics for cooling water, temperature and voltage stability will be integrated into the ELBE control system

## HV-DEVICE CHARACTERISATION

The primarily favoured high voltage switches from the company Belke could not be brought into operation by the company. Therefore the high voltage pulse generator FPG 2-500N5X2 from the company FID had been chosen as the pulser source for the kicker. The parameters of the device are max.  $\pm 2$  kV in a 50 Ohm load and a repetition rate of max. 500 kHz. The pulse plateau length is around 5 ns.

An important feature of the device is the voltage and time stability in the 1% range. With the setup in Figure 5 but without the kicker the stabilisation measurement had been performed with an RTO1044 from Rohde&Schwarz. The plots in Figure 6 and Figure 7 showing the measured distribution of voltage and time jitter for 1 kV and the maximum repetition rate of 500 kHz parameters of the device. The standard deviation of the voltage distribution is around 1 V and the time jitter distribution around 60 ps.

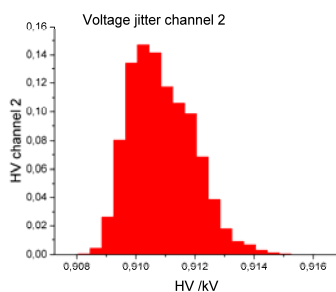


Figure 6: Voltage jitter distribution HV-pulser (SD ~ 1V).

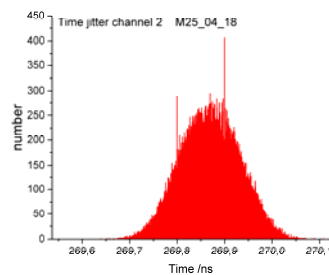


Figure 7: Time jitter distribution HV-pulser (SD ~ 61 ps).

While the voltage jitter is in the desired range the time jitter can lead to a larger voltage deviation due to the not flat pulse plateau.

## NWA MEASUREMENTS

A very important step in the evaluation of the kicker design is the comparison of the measured S-parameters with that from the CST simulation. In Figure 8 and Figure 9 NWA (network analyser) measured S-Parameter in reflection and transmission are shown.

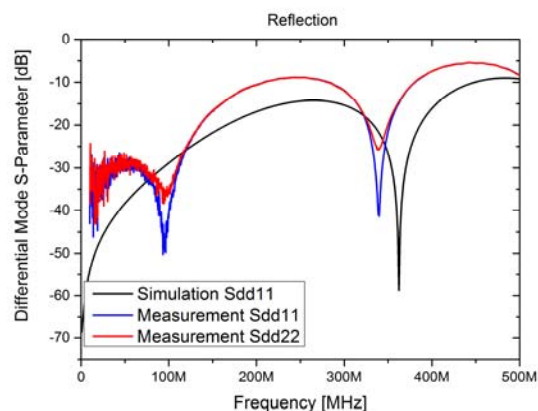


Figure 8: Comparison of measured S11 and S22 parameters in diff. mode excitation with the CST simulation.

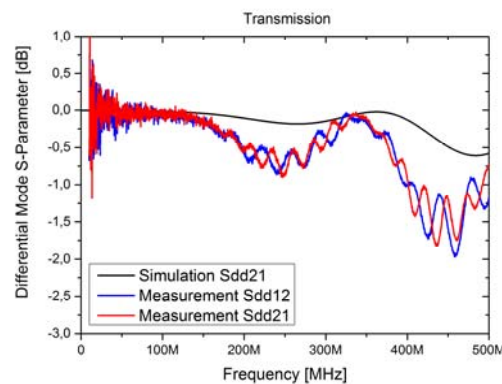


Figure 9: Comparison of measured S12 and S21 parameters in diff. mode excitation with the CST simulation.

The shape and notches in the attenuation of the reflective wave, see Figure 8 are well represented by the measurement, while the amplitude is about 8 dB higher. Perhaps, the reason is a not expected behaviour of the couplers, to be clarified in a further measurement. Also the transmission, see Figure 9, represents the overall shape of the CST simulation. The main deviation starts from the area above 200 MHz. When analysing the frequency content of the signal from the HV pulser, see Figure 10, it is obvious that mainly the frequency range lower than 200 MHz matters.

Figure 10 shows the system function extracted from the NWA measurement and the frequency spectrum from the incident generator pulse. Using the argument about the relevant frequency range the system function is  $\sim 1$ . Calculating the output signal from the kicker by the system function from the 4 pole measurement and the frequency content of the incident pulse and doing the back transformation into the time domain leads to the expected output signal past the kicker. The signal is shown together with the incident pulse from the generator in Figure 11. The nearly reproducible pulse leads to the conclusion that adaption in the relevant frequency domain is like expected from the CST simulation.

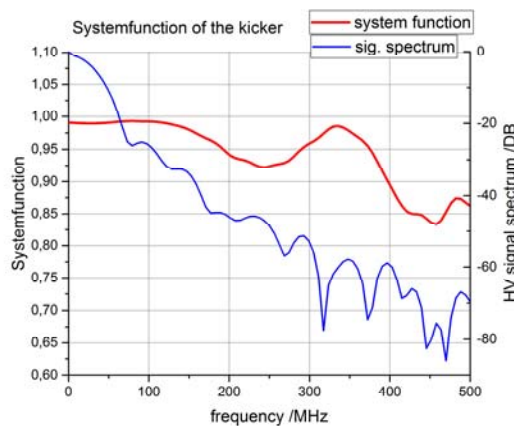


Figure 10: System function of the kicker and frequency spectrum of the incident HV pulse.

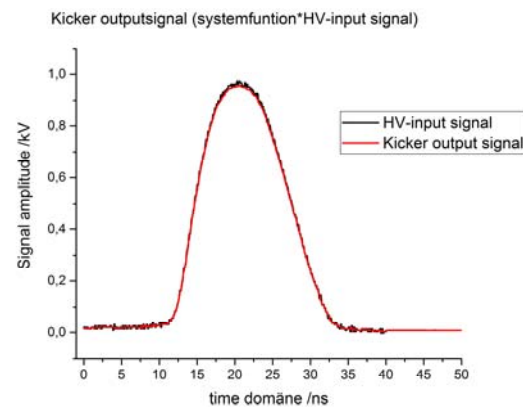


Figure 11: Incident HV pulse from the generator and estimated kicker output signal calculated with the system function from the NWA measurement.

## SUMMARY

The first NWA measurement of the kicker leads to the conclusion that - despite the attenuation level of the reflected wave - the kicker performs like from the design and CST optimization expected. Finalizing the lab measurement the kicker will be installed in the ELBE beam line in the end of the year. There the final tests and characterization of the device will be performed.

## REFERENCES

- [1] D. A. Goldberg and G.R. Lambertson, "Dynamic devices a primer on pickups and kickers", Lawrence Berkeley Laboratory, Berkley, California 94720, Internal Report
- [2] A.W. Chao. and M. Tigner, Handbook of Accelerator Physics and Engineering. Second Edition 2013, pp. 602
- [3] G. Staats et al," Kicker development at the ELBE facility", in *Proc. IPAC'14*, Dresden, Germany, June 2014, paper MOPME067



## DAΦNE LUMINOSITY MONITOR

A. De Santis\*, C. Bisegni, O. R. Blanco-García, O. Coiro, A. Michelotti, C. Milardi, A. Stecchi  
INFN - Laboratori Nazionali di Frascati, Frascati 00044 (Roma), Italy.

### Abstract

The DAΦNE collider instantaneous luminosity has been measured identifying Bhabha scattering events at low polar angle ( $\sim 10^\circ$ ) around the beam axis by using two small crystal calorimeters shared with the KLOE-2 experiment. Independent DAQ setup based on !CHAOS, a novel Control System architecture, has been designed and realized in order to implement a fast luminosity monitor, also in view of the DAΦNE future physics runs. The realized setup allows for measurement of Bunch-by-Bunch (BBB) luminosity that allows to investigate the beam-beam interaction for the Crab-Waist collisions at DAΦNE and luminosity dependence on the bunch train structure.

### INTRODUCTION

The luminosity of DAΦNE during KLOE-2 Physics run [1] has been measured by the experiment selecting on-line a special class of Bhabha scattering events directly at the trigger level while taking data [2, 3]. KLOE-2 dedicated DAQ process was used to provide a instantaneous luminosity measurement every 15 seconds with 3-5% relative uncertainty typically.

Furthermore two independent gamma monitors were installed to measure single bremsstrahlung [4] from both electron and positron beams. This diagnostic is well suited for collisions fast fine tuning because of the high rates of the observed process. The usage of gamma monitors for absolute luminosity measurement however is not possible because the acceptance of the detectors has a strong dependence on the machine setup and a large background hitting the diagnostic is observed.

The realization of a further luminometer based on the observation of the Bhabha scattering events emitted at low angle aims at combining accuracy and high repetition rate in the same diagnostic

### EXPERIMENTAL SETUP

The experimental apparatus is based on the small angle Crystal CALorimeters with Time measurement (CCALT) [5] of the KLOE-2 detector that measures the Bhabha scattering events, the dominant process in that angular region.

#### Detector Layout

The CCALT is constituted by two identical crystal calorimeters installed in front of the permanent defocusing quadrupole QD0 of the DAΦNE low- $\beta$  doublet providing the proper focusing of the beams at the Interaction Point (IP).

\* antonio.desantis@lnf.infn.it

The detector covers the polar angle between  $8^\circ$  and  $18^\circ$ . Each calorimeter is segmented in 48 small LYSO<sup>1</sup> crystal. Each segment is readout with Silicon Photo-Multiplier (SiPM). Signals from group of four crystal are analogically summed in CCALT sectors, acquired independently with respect the KLOE-2 data, to measure the luminosity. Each sectors covers an azimuthal angle of  $30^\circ$ . The detector assembly and final installation are shown in Fig. 1.

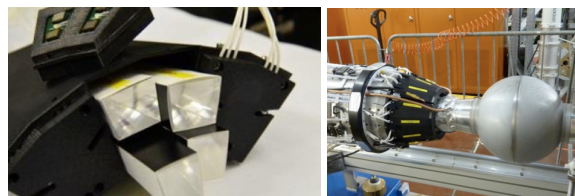


Figure 1: Left: CCALT detector macro-sector before the SiPM installation. The four crystal per sector are clearly visible. Each side of the detector is made of four macro-sectors. This segmentation is needed in order to leave space for the Beam position Monitor feed-trough.

Right: Detector fully assembled and installed in front of the QD0 magnets. The spherical beam pipe around the IP is also shown. Only one side of the detector is visible.

### DAQ and Control System

The DAQ scheme is sketched in Fig. 2. CCALT sectors signals are split and compared with a constant fraction discriminator<sup>2</sup> in order to measure arrival time and integrated charge.

Discriminated signals are used to feed the trigger logic: same side pulses are logically merged to reduce multiplicity, then time coincidence between the two side of the detector are used to form trigger pulses when single side signals overlap for at least 4 ns. When trigger pulse is received by the TDC<sup>3</sup> signals arrival time are determined.

The luminometer dedicated DAQ is completed with a programmable FPGA<sup>4</sup> that allows monitoring of DAQ rates and the acquisition dead-time. The most relevant source of dead-time is the injection trigger veto that must be used in order to reduce the trigger rate observed during the first 50 ms after the injection pulse. The veto length caused at least a detector efficiency loss of 10% (50 ms veto every 500 ms corresponding to the single shot of the injection cycle) that has to be taken into account for online measurement of the luminosity.

<sup>1</sup> Cerium-doped Lutetium Yttrium Orthosilicate.

<sup>2</sup> CAEN N843

<sup>3</sup> CAEN V775N.

<sup>4</sup> CAEN V1495

The DAQ acquisition chain and the data-flow is fully handled within the *!CHAOS* control system framework [6]. *!CHAOS* provides also tools for online monitoring of the DAQ status and luminosity measurement.

The *!CHAOS* environment provides also a synchronized acquisition of several other data sources: KLOE-2 luminosity, beam parameters as current, beam spot size, bunch number and bunch current structure from DAΦNE diagnostics.

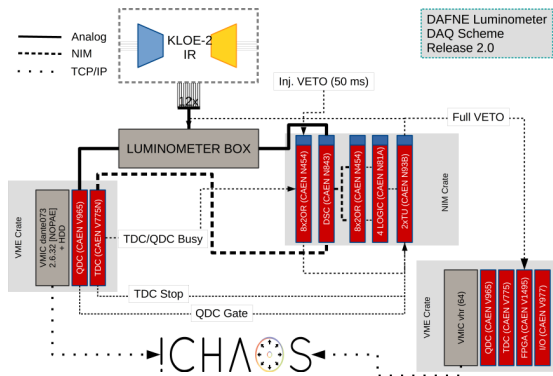


Figure 2: Schematic view of the DAQ acquisition. The signals coming from a corresponding sectors on the two sides are compared with a fixed threshold and used to measure arrival time and integrated charge when the trigger logic condition is fulfilled.

## DATA ANALYSIS

The data collected by the luminometer have been analyzed in order to extract the rate of Bhabha scattering events to be normalized with the KLOE-2 reference luminosity. The trigger logic already provides events acquisition when opposite detector sides are fired. The signal selection requires the expected geometrical correlation because candidate signal events fires opposite sectors of the luminometer, while accidental coincidence almost uniformly fires the whole detector.

Background events with wrong geometrical signature are discarded and their rate is measured in order to monitor the expected behavior of accidentals as a function of the beam currents.

Events with the expected signal signatures are retained and their rate is evaluated. Accidental coincidence are still expected in the selected sample, because of unavoidable statistical contamination. To evaluate the residual background in the signal selection the events with wrong geometrical signature are used by normalizing the background counting rate with the ratio between geometrical acceptance of the two category.

The observed signal rate has to be corrected taking into account the measured dead-time. The main source of the DAQ dead-time is the “injection-veto”, described previously,

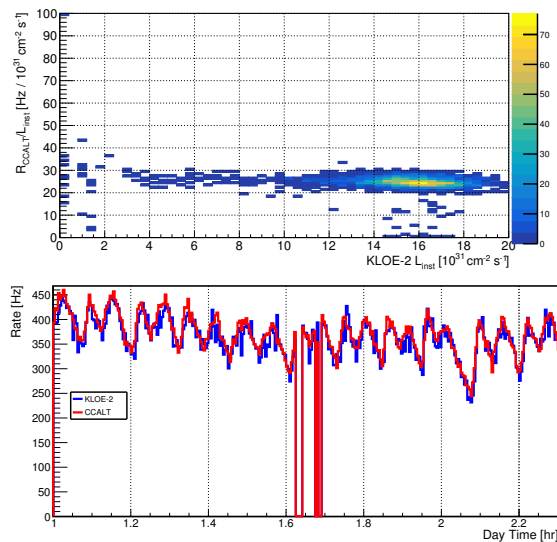


Figure 3: Top: Ratio between CCAL-T signal rate and luminosity reference measurement performed with KLOE-2 detector as a function of the luminosity. The linearity of the CCAL-T signal rate w.r.t. the luminosity is clearly seen. The increased spread in the ratio distribution at low luminosity is purely due to unavoidable statistical fluctuation. Bottom: Comparison between the Luminometer signal rate (red) and the reference luminosity measured by KLOE-2 (blue). The reference histogram has been rescaled with a scale factor obtained from the upper plot by fitting the data with a constant function. A good agreement can be appreciated. The scale factor is  $26.4 \pm 2.1$  Hz with an overall relative uncertainty of 10%.

that accounts for 10% relative contribution during the beam injection phase. The remaining 1-2% is related to the DAQ conversion and acquisition time. This contribution could increase depending on the total trigger rate and CHAOS infrastructure load. The CHAOS infrastructure allows for a time synchronization between the different DAQ sources at the level of the ms. This aspect is fundamental when we have to assign the dead-time measured by DAQ Monitor with a repetition rate of 0.5 Hz to each event with a trigger rate of  $\sim 400$  Hz.

In Fig. 3 the result of the measurement is shown. The calibration coefficient between luminometer signal rate and instantaneous luminosity is extracted by fitting the ratio of this two as a function of the reference luminosity. A good linearity is observed along the whole operating scale. This allows to use the luminometer signal rate as absolute luminosity measurement.

A complete Monte-Carlo (MC) simulation of the detector has been developed in order to fully understand the luminosity measurement process and to completely qualify the detector behavior. The Bhabha event generator used is BABAYAGA [7] and a GEANT4 [8] description has been implemented for the detector response. The simulation has

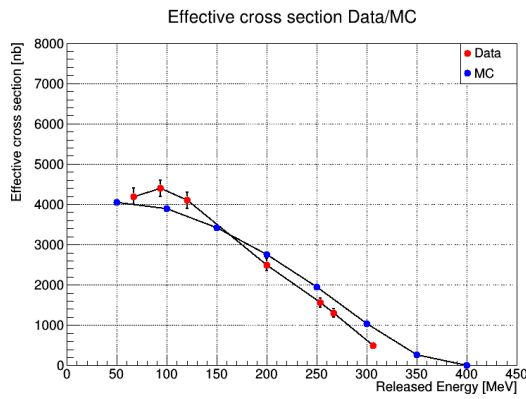


Figure 4: Preliminary comparison between real and simulated data. In the plot a comparison between the Bhabha scattering visible cross section is shown. The energy scale for the real data has been obtained rescaling the signal amplitudes used for the discrimination.

been performed only for the signal events (Bhabha scattering) while a full simulation with background insertion is still ongoing.

The MC simulation includes DAQ and Trigger behavior allowing to describe the different DAQ setup used during the data acquisition. The variation of the observed rate as a function of the discriminator threshold has been chosen for the preliminary validation of the MC simulation. In Fig. 4 the comparison between Bhabha scattering visible cross section measurement and simulation is shown. The cross section measurement has been obtained by varying the discriminator threshold in the range 25-115 mV and calculating the corresponding ratio between observed rate and KLOE-2 luminosity measurement as shown in Fig. 3 for each different threshold. The energy calibration has been obtained by comparing the simulation with the real data. The simulated cross section has been derived by applying the same analysis chain to the MC events. The agreement obtained is promising.

The validation of the MC simulation is fundamental for the usage of the same luminometer during the forthcoming SIDDHARTA-2 Physics run at DAΦNE [9].

## “BUNCH-BY-BUNCH” LUMINOSITY MEASUREMENT

The BBB luminosity measurement is one of the most intriguing features of this luminometer that allows to verify any dependence of the luminosity on collective effects (*e.g.* electron cloud) that can cause a non-negligible variation of bunch parameters, such as transverse bunch sizes and betatron tunes, along the batch.

The BBB measurement is performed measuring the arrival time of the revolution clock (fiducial) with respect to the single event trigger. In order to maintain a high efficiency, while operating in TDC common-stop mode, it is required to phase-lock the fiducial signal w.r.t. the trigger. The arrival

time of the first fiducial pulse after the trigger formation is measured. In the Fig. 5 the time distribution of the signal event is shown. The peak structure of the counting of fiducial signal as a function of the distance w.r.t. the trigger time reveals the underlying bunch structure of the beams.

To perform synchronization and calibration of the DAQ boards several special runs were performed. The Fig. 5 shows an example of a DAQ run acquired with a special batch fill pattern: one over five filled for a total of 10 buckets for both beams. The flat distribution between peaks is due to residual accidental coincidences. The different height of the peaks is related to the bunch current dishomogeneity.

The TDC setup imply for the scale a minimum time-to-count of  $T_{LSB} = 8.9 \text{ ns}/75 \approx 119 \text{ ps}$ . The intrinsic jitter in time induced by FEE on each single channel is of the order of 200-300 ps. The observed resolution for the fiducial time measurement, being due to a coincidence between two different channel is at the expected level.

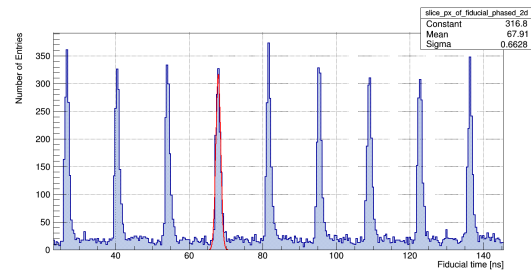


Figure 5: Distribution of the fiducial time w.r.t. the trigger for a special run acquired during KLOE-2 physics run (March 2018). The beam batch was filled with ten bunches only with a spacing between them of four buckets for both beams. The structure is clearly visible and the events due to a single bunch are well identified. The forth peak is fitted with a Gaussian showing a time resolution of 0.66 ns w.r.t. bunch spacing of 2.7 ns.

The BBB luminosity measurement requires, together with the determination of the instantaneous luminosity and the bunch association, also the knowledge of the bunch charge in order to correct for spurious effects on bunch luminosity purely induced by different intensities during the normal evolution of the beam current. The Fig. 6-bottom, shows the bunch current product between electron and positron beam when in DAΦNE there was 108 bunches circulating for a corresponding maximal current of 1.5 and 0.95 A for electron and positron, respectively.

The bunch luminosity is expected to be proportional to the bunches current product. To observe the luminosity along the batch a long time exposure is needed, then all the concurring effect (dead-time, bunches current variation, background contribution), have to be measured synchronously and corrected for along the time of the measurement in order to observe a genuine effect.

The BBB luminosity measurement capabilities are under investigation and the data analysis is still ongoing. In order

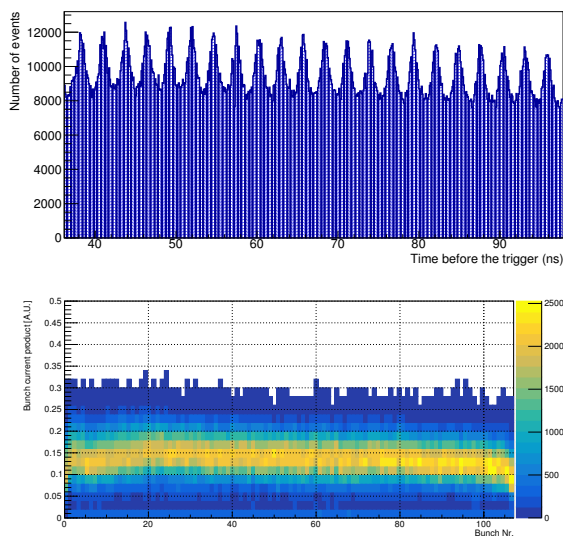


Figure 6: Top: distribution of the event w.r.t. the revolution period. The peak structure follows from the bunch structure of the beam. The time separation of 2.7 ns between highlights the luminometer effectiveness in resolving bunch structure. The time resolution forces to define a “No Man Land” between two peaks in order to minimize the misidentification of the corresponding bunch event by event. Bottom: beam charge product as a function of the bunch number. This information is needed to properly normalize the BBB signal event rate in order to compare the different bunches on the same beam current scale. Here the cumulative distribution in time is shown. The correction for the luminosity have to use the instantaneous value of the bunch current product to deconvolute variation along the time induced by bunch current dishomogeneity.

to verify the sensitivity a genuine bunch dependence has been induced in a special test run, shown in Fig. 7, where the positron beam fill was kept unbalanced with two different levels between the first fifty bunches and the following sixty.

### CONCLUSION

The CCALT based luminometer developed for DAΦNE has proven to be a suitable diagnostics in order to implement high rate absolute luminosity measurement. The work on the CCALT based luminometer for DAΦNE showed the possibility to perform accurate measurements of the absolute luminosity with this kind of device. The excellent time resolution of the detector allowed to resolve the single bunch structure. BBB study of the luminosity will improve the understanding of the collisions at DAΦNE. The experience gained and the data collected during the KLOE-2 run will be extremely useful for the forthcoming DAΦNE run for the SIDDHARTA-2 experiment [9].

### REFERENCES

[1] C. Milardi et al. A Review of the DAΦNE Performances During the KLOE-2 Run . page TUYGBD2, IPAC2018.

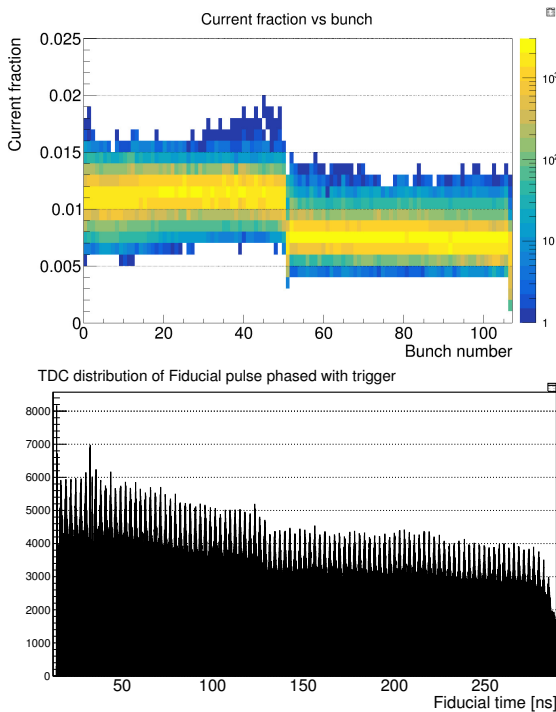


Figure 7: Top: positron beam fill. The vertical axis is the bunch current and the horizontal is the bunch position along the batch. The unbalance between the first fifty and the last sixty is clearly visible. Bottom: BBB luminosity for the corresponding test run. The difference between the two sections is clearly visible.

[2] A. Aloisio et al. The KLOE trigger system. (Addendum to the KLOE technical report). *LNF Preprints*, 96/043, 1996.

[3] Denig, A., Ngyen, F. The KLOE Luminosity Measurement. *KLOE NOTE*, 202, 2005.

[4] G. Mazzitelli et al. Single bremsstrahlung luminosity measurements at DAPHNE. *Nucl. Instrum. Meth.*, A486(2002)568.

[5] F. Happacher et al. Tile and crystal calorimeter for KLOE-2 experiment. *Nucl. Phys. Proc. Suppl.*, 197(2009)215.

[6] L. Catani et al. Introducing a new paradigm for accelerators and large experimental apparatus control systems. *Phys. Rev. ST Accel. Beams*, 15(2012)112804.

[7] G. Balossini, C. M. Carloni Calame, G. Montagna, O. Nicosini and F. Piccinini, Matching perturbative and parton shower corrections to Bhabha process at flavour factories. *Nucl. Phys. B* **758** (2006) 227

[8] S. Agostinelli et al. [GEANT4 Collaboration], GEANT4: A Simulation toolkit. *Nucl. Instrum. Meth. A* **506** (2003) 250.

[9] C. Milardi et al. Preparation Activity for the Siddharta-2 Run at DAΦNE. MOPMF088, IPAC 2018.



# BEAM PARAMETER MEASUREMENTS FOR THE J-PARC HIGH-INTENSITY NEUTRINO EXTRACTION BEAMLINE

M. Friend\*, High Energy Accelerator Research Organization (KEK), Tsukuba, Japan  
for the J-PARC Neutrino Beam Group

## Abstract

Proton beam monitoring is absolutely essential for the J-PARC neutrino extraction beamline, where neutrinos are produced by the collision of 30 GeV protons from the J-PARC MR accelerator with a long carbon target. Continuous beam monitoring is crucial for the stable and safe operation of the extraction line high intensity proton beam, since even a single misfired beam spill can cause serious damage to beamline equipment at  $2.5 \times 10^{14}$  and higher protons-per-pulse. A precise understanding of the proton beam intensity and profile on the neutrino production target is also necessary for predicting the neutrino beam flux with high precision. Details of the suite of monitors used to continuously and precisely monitor the J-PARC neutrino extraction line proton beam are shown, including recent running experiences, challenges, and future upgrade plans.

## OVERVIEW OF J-PARC AND THE NEUTRINO PRIMARY BEAMLINE

The J-PARC proton beam is accelerated to 30 GeV by a 400 MeV Linac, a 3 GeV Rapid Cycling Synchrotron, and a 30 GeV Main Ring (MR) synchrotron. Protons are then extracted using a fast-extraction scheme into the neutrino primary beamline, which consists of three sections containing a series of normal- and super-conducting magnets used to bend the proton beam towards a neutrino production target. Generated neutrinos travel 295 km towards the Super-Kamiokande detector for the Tokai-to-Kamioka Long-Baseline Neutrino Oscillation Experiment (T2K) [1], which started operation in 2009.

Table 1: J-PARC Proton Beam Specifications

	Protons/Bunch	Spill Rate
Current (2018)	$3.13 \times 10^{13}$	2.48 s
Upgraded (2021~)	$2.75 \rightarrow 4.00 \times 10^{13}$	$1.32 \rightarrow 1.16$ s

The J-PARC 30 GeV proton beam has an 8-bunch beam structure with 80 ns ( $3\sigma$ ) bunch width and 581 ns bucket length. J-PARC currently runs at 485 kW with the plan to upgrade to 750+ kW in 2020 and 1.3+ MW by 2026. This will be achieved by increasing the beam spill repetition rate from the current one spill per 2.48 s, to 1.32 s and finally 1.16 s, along with increasing the number of protons per bunch from  $\sim 3 \times 10^{13}$  to  $4 \times 10^{13}$ , as shown in Table 1.

The 30 GeV proton beam is extracted into the neutrino beamline preparation section. In the preparation section, the

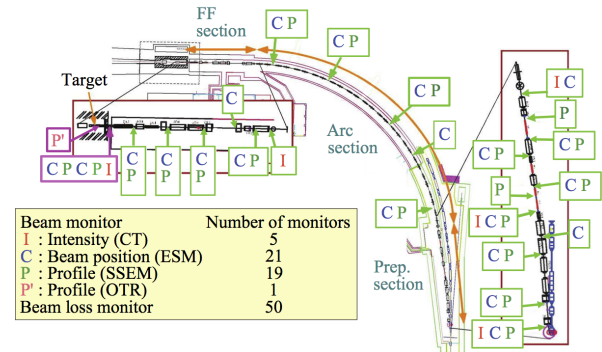


Figure 1: Beam monitor positions along the neutrino primary beamline.

position and width of the extracted beam are tuned by normal-conducting magnets in order to match the beam optics in the following arc section, where the beam is bent by  $80.7^\circ$  using super-conducting combined function magnets. Finally, in the final focusing section, normal-conducting magnets are used to direct the beam downward by  $3.647^\circ$  and tune the beam position and size to focus the beam onto the center of the neutrino production target.

Beam monitoring is essential for protecting beamline equipment from possible mis-steered beam as part of a machine interlock system, where even a single mis-steered beam shot can do serious damage at high intensities. Information from proton beam monitors is also used and as an input into the T2K physics analysis, and imprecisions on proton beam measurements can have a direct effect on the precision of the final T2K physics results.

## MONITORS IN THE J-PARC NEUTRINO PRIMARY BEAMLINE

The proton beam conditions are continuously monitored by a suite of proton beam monitors along the neutrino primary beamline, as shown in Fig. 1.

Five Current Transformers (CTs) are used to continuously monitor the proton beam intensity. Fifty Beam Loss Monitors (BLMs) continuously measure the spill-by-spill beam loss and are used to fire an abort interlock signal in the case of a high-loss beam spill. Twenty-one Electro-Static Monitors (ESMs) are used as Beam Position Monitors to continuously monitor the beam position and angle.

The proton beam profile (beam position and width) is monitored bunch-by-bunch during beam tuning by a suite of 19 Segmented Secondary Emission Monitors (SSEMs) distributed along the primary beamline, where only the most downstream SSEM (SSEM19) is used continuously. An

\* mfriend@post.kek.jp

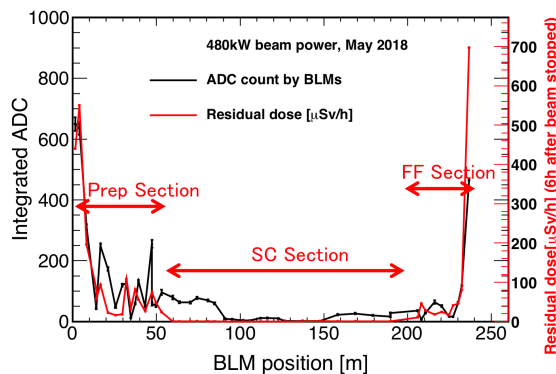


Figure 2: Beam loss and residual radioactivity along the beamline.

Optical Transition Radiation Monitor (OTR) [2], placed directly upstream of the production target, also continuously monitors the beam profile spill-by-spill.

Other beam parameters, such as the beam angle, twiss parameters, and emittance at the production target are extrapolated by a fit to several downstream SSEMs and the OTR during beam tuning. The beam position and angle at the target is continuously monitored spill-by-spill by a fit to several ESMs, SSEM19 and the OTR during standard running, while the other proton beam parameters are extrapolated by scaling the data from beam tuning runs (where all SSEMs are in the beam) with spill-by-spill SSEM19 and OTR information when SSEMs 1–18 are not in the beam.

## CONTINUOUS BEAM LOSS, INTENSITY, AND POSITION MONITORING

### Beam Loss Monitors

The spill-by-spill beam loss along the beamline is measured by Toshiba Electron Tubes&Devices E6876-400 BLMs, which are wire proportional counters filled with an Ar-CO<sub>2</sub> mixture. The signal from each BLM is integrated during each beam spill and if the signal from any BLM exceeds a set threshold, a beam abort interlock signal is fired. The beam loss and measured residual radioactivity along the J-PARC neutrino primary beamline are shown in Fig. 2.

### Current Transformers

The bunch-by-bunch beam intensity is measured by CTs, which are fabricated in-house and consist of a ferromagnetic core made of FINEMET® (nanocrystalline Fe-based soft magnetic material) from Hitachi Metals with a 50-turn toroidal coil inside a stainless steel and iron outer casing.

Periodic calibration of the CT readout electronics is necessary. Precise absolute calibration is also essential – the current systematic error on the number of protons is 2.7%, but a calibration campaign to reduce errors to <2% is ongoing.

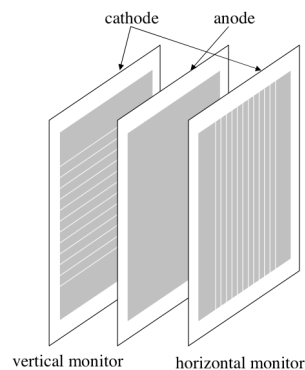


Figure 3: T2K Segmented Secondary Emission Monitor design.

### Electrostatic Monitors

The bunch-by-bunch beam position is measured by ESMs, which have four segmented cylindrical electrodes surrounding the proton beam orbit (80° coverage per electrode). The ESM beam position measurement precision is better than 450 μm, including 20–40 μm measurement fluctuations, 100–400 μm alignment precision, and 200 μm other systematic uncertainties. Possible methods to improve the ESM measurement precision are currently under consideration.

## BEAM PROFILE MONITORING

### Segmented Secondary Emission Monitors

The proton beam profile along the primary beamline is measured by a suite of 19 SSEMs.

Each SSEM consists of two 5 μm-thick titanium foils stripped horizontally and vertically, with a 5 μm-thick anode HV foil between them, as shown in Fig. 3. The strip width ranges from 2 to 5 mm, optimized according to the expected beam size at each monitor. When the proton beam passes through the SSEM, secondary electrons are emitted from each strip in proportion to the number of protons hitting the strip; the beam profile can be reconstructed by doing a Gaussian fit to the positive polarity signal from the strips.

Due to the  $\sim 3 \times 10^{-5}$  interaction lengths of material, one SSEM causes 0.005% beam loss. Therefore, only the most downstream SSEM (SSEM19), which sits in a high-radiation environment near the production target, can be used continuously; others are remotely moved into the beam during beam tuning.

The SSEM position measurement precision and stability are 0.07 mm and  $\sim \pm 0.15$  mm, respectively. The SSEM width measurement precision and stability are 0.2 mm and  $\sim \pm 0.07$  mm, respectively.

### Optical Transition Radiation Monitor

An OTR, shown in Fig. 4, continuously monitors the beam profile directly upstream of the production target.

The OTR active area is a 50 μm-thick titanium-alloy foil, which is placed at 45° to the incident proton beam. As

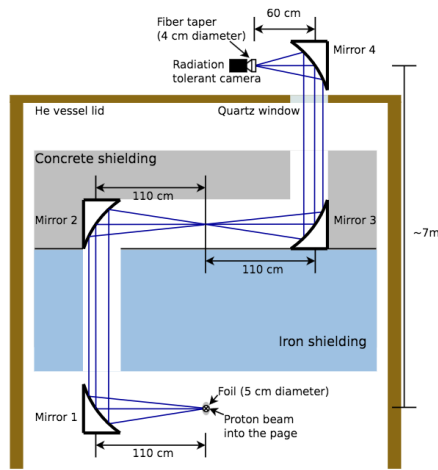


Figure 4: Schematic of the T2K Optical Transition Radiation monitor.

the beam enters and exits the foil, visible light (transition radiation) is produced in a narrow cone around the beam. The light produced at the entrance transition is reflected at  $90^\circ$  to the beam and directed away from the high-radiation environment near the neutrino production target by four aluminum  $90^\circ$  off-axis parabolic mirrors to an area with lower radiation levels. OTR light is then collected by a leaded glass fiber taper coupled to a charge injection device (CID) camera, which records an image of the proton beam profile spill-by-spill.

The OTR target foils sit in a rotatable disk with 8 foil positions, allowing for various OTR target types. A Ti 15-3-3-3 (15% V, 3% Cr, 3% Sn, 3% Al) foil without holes was originally designed for standard continuous data-taking, although recently a foil with 12 small holes in a cross pattern has been used without any issue.

### Measured Proton Beam Envelope

The horizontal proton beam envelope along the J-PARC primary beamline, as measured by the 19 SSEMs and the OTR during beam tuning, is shown in Fig. 5. The model calculation can reproduce the SSEM-measured optics very well, although the OTR measured width is consistently higher than the expectation. This discrepancy may be caused by using the OTR in a He environment, rather than in vacuum; background studies, with the aim of understanding this effect, are ongoing.

### PROFILE MONITOR DEGRADATION

A photograph of the upstream side of the SSEM19 foil after  $\sim 2.3 \times 10^{21}$  incident protons is shown in Fig. 6. Although no significant decrease in the secondary emission yield has been observed,<sup>1</sup> the foil has darkened significantly.

The same SSEM19 monitor head has been used since the beginning of T2K. A procedure for exchanging SSEM19, which is in a relatively inaccessible location behind a shield

<sup>1</sup> An initial burn-in period before  $\sim 5 \times 10^{19}$  incident protons was seen.

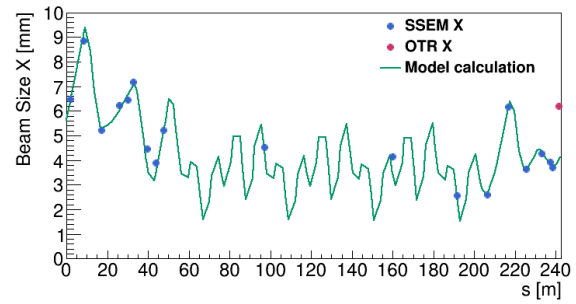


Figure 5: Horizontal beam envelope in the J-PARC neutrino beamline measured by the SSEMs and OTR.

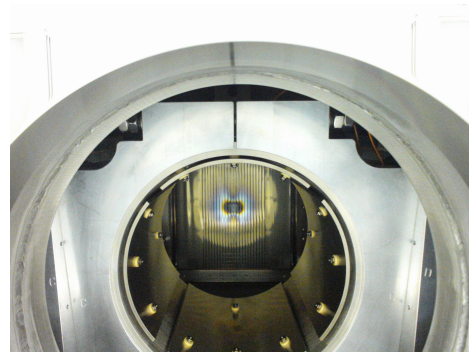


Figure 6: SSEM19 after  $\sim 2.3 \times 10^{21}$  incident protons.

wall separating the primary beamline and the production target, is currently being developed.

A photograph of the OTR foils and a plot of the OTR light yield as a function of integrated protons is shown in Fig. 7. The OTR foils have darkened where the beam hits. Some degradation of the OTR light yield is observed; currently this is thought to be due to both foil darkening and the radiation-induced darkening of the fiber taper used to shrink the OTR light image onto the CID camera sensitive area.

Radiation damage studies of used OTR foils are currently ongoing by the RaDIATE collaboration [3].

### PROFILE MONITOR UPGRADES

At higher beam powers, the total integrated beam loss due to profile monitors, as well as the rate of profile monitor foil

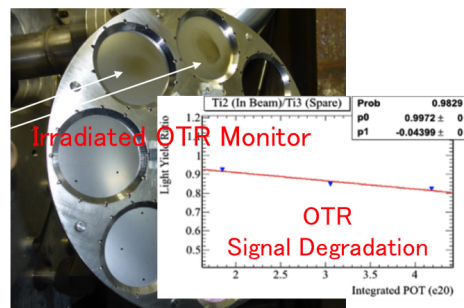


Figure 7: OTR foil darkening and yield decrease after  $\sim 4.2 \times 10^{20}$  incident protons.





# EVALUATION OF THE TRANSVERSE IMPEDANCE OF PF IN-VACUUM UNDULATOR USING LOCAL ORBIT BUMP METHOD

O. A. Tanaka<sup>†</sup>, N. Nakamura, T. Obina, K. Harada, Y. Tanimoto, N. Yamamoto, K. Tsuchiya, R. Takai, R. Kato, M. Adachi,  
High Energy Accelerator Research organization (KEK), 305-0801 Tsukuba, Japan

## Abstract

When a beam passes through insertion devices (IDs) with narrow gap or beam ducts with small aperture, it receives a transverse kick from the impedances of those devices. This transverse kick depends on the beam transverse position and beam parameters such as the bunch length and the total bunch charge. In the orbit bump method, the transverse kick factor of an ID is estimated through the closed orbit distortion (COD) measurement at many BPMs for various beam currents [1]. In the present study, we created an orbit bump of 1 mm using four steering magnets, and then measured the COD for two cases: when the gap is opened (the gap size is 42 mm) and when the gap is closed (the gap size is 3.83 mm). The ID's kick factors obtain by these measurements are compared with those obtain by simulations and analytical evaluations.

## INTRODUCTION

At KEK Photon Factory (PF) light source, we have four newly installed in-vacuum undulators (IVUs). They are located in short straight sections as shown in Fig. 1. The vacuum chambers of those IVUs have complex geometry: narrow gaps inside the undulators (the minimum gap is 3.83 mm) and tapers at the ends of undulators. Those gaps are much smaller than the typical aperture of the PF normal vacuum ducts.

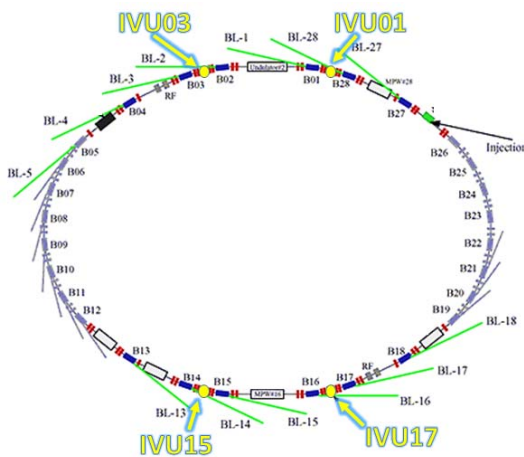


Figure 1: Locations of the IVUs in the PF ring.

First, the kick factors of the four IVUs were estimated analytically and by CST Studio simulations [2]. The total vertical kick factor due to 1 IVU including dipolar and

quadrupolar kicks of the taper and resistive-wall kick of the undulator copper plates is summarized in Fig. 2.

To confirm the accuracy of the calculated transverse kick factors, we have measured the transverse tune shift with a single bunch based on the RF-KO (RF Knock Out) method [3]. The additional tune shift corresponds to a difference of the vertical tune shifts for ID open (the gap size is 42 mm) and ID closed (the gap size is 3.83 mm) cases. The result of the tune shift measurement is shown at Fig. 3. All the three evaluations demonstrated very good agreements. Thus, theory gives the tune shift value per unit of bunch current of  $\Delta\nu/I_b = -10.60 \times 10^{-6} \text{ mA}^{-1}$ . The CST Studio simulation gives those of  $\Delta\nu/I_b = -10.06 \times 10^{-6} \text{ mA}^{-1}$ . And the tune shift measurement yields the value of  $\Delta\nu/I_b = -10.96 \times 10^{-6} \pm 1.86 \times 10^{-6} \text{ mA}^{-1}$  including the fitting error.

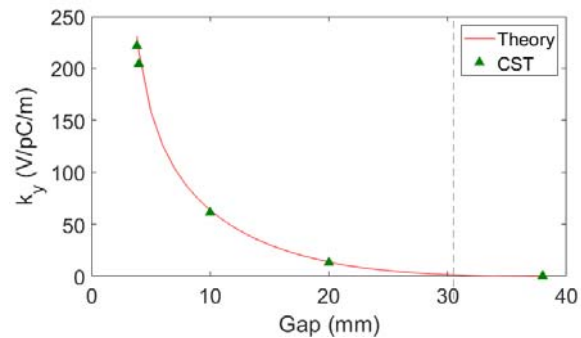


Figure 2: Total vertical kick factor due to 1 IVU (gap dependence, width fixed to 100 mm) by theory (red line), and by simulations (green triangle).

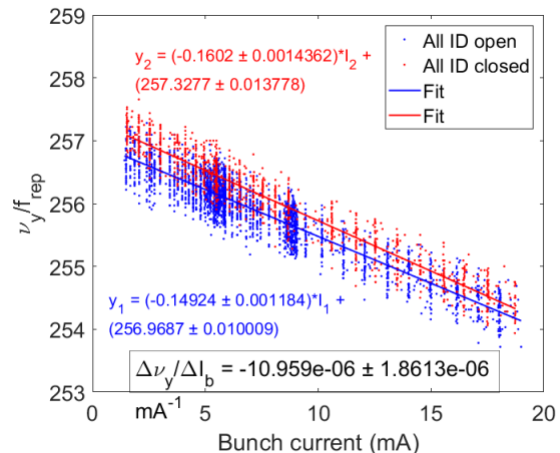


Figure 3: One of the measurement results of the additional tune shift due to the four IVU at PF.

<sup>†</sup> olga@post.kek.jp

The purpose of the present study is further check of the transverse kick evaluation accuracy. To do so, we adopted the orbit bump method. We created local orbit bump at the IVU15 location and measured CODs at various BPMs for different beam currents. From these measurements, we calculated the distribution of transverse kick factors along the undulator. In the following, we show more details of these measurements.

## ORBIT BUMP METHOD

The orbit bump method uses a local bump to create transverse kicks from components inside the bump. This technique was invented at Budker Institute, Novosibirsk [1]. It was successfully applied to the evaluation of the transverse impedance distribution along rings at Diamond light source [4], ESRF [5], APS [6], and many others.

The orbit bump method is found to be useful for beam ducts with considerable inhomogeneities such as flanges, ceramic breaks, bellows etc. The orbit bump generates orbit deviations at various places of the ring. Their differences for two different bunch currents are expressed by the following formula [4]:

$$\Delta y(s) = \frac{\Delta q}{E/e} k_y y_0 \frac{\sqrt{\beta(s)\beta(s_0)}}{2\sin(\pi\nu)} \cos[|\mu(s) - \mu(s_0)| - \pi\nu], \quad (1)$$

where  $\Delta q$  is the difference of the two bunch charges,  $k_y$  is the transverse kick factor of the ID,  $y_0$  is the bump size,  $\beta(s)$  is the betatron function at the  $s$  location. Note, that  $s_0$  corresponds to the location of the transverse kick. The parameter  $\mu(s)$  is the betatron phase advance,  $\nu$  is the betatron tune, and  $E$  is the total beam energy.

We have followed the procedure outlined by V. Smaluk [4]. The first procedure is to estimate orbit deviations at all BPM locations (there are 65 BPMs at PF ring) created by the local bump of 1 mm at IVU15 location (see Fig. 1) using the analytical evaluations and CST Studio simulations of impedance of the IDs. Here, major impedance sources are the resistive-wall impedance of the 500 mm long undulator and the geometrical impedance of the 108.5 mm long tapers [2–3].

In Smaluk's paper, the kick factors are lumped at the center of the undulator to estimate their effects approximately. This method does not work for our case, since the beta function at the ID is very small and thus the phase advance and the beta function are changing rapidly there. Thus, we have distributed the kick factors along the ID, as shown in Fig. 4, instead of lumping the total transverse kick factor to the center of ID. This trick allows us to obtain more accurate estimate of orbit deviations at the BPMs. The kick factor due to the resistive-wall impedance,  $k_{y,RW} = 88.6$  V/pC/m, was uniformly distributed among 5 segments of the undulator. The kick factors of the two taper's geometrical impedance,  $k_{y,taper} = 66.5$  V/pC/m, were placed at the center of each taper (see Fig. 4). The betatron

functions and the betatron phase advances at the corresponding locations were used. For an undulator of considerable length, this procedure is essential, because the phase advance will change significantly along the ID. Apparently from Eq. (1), the lumping approximation may not provide accurate estimate of orbit deviations. The values of the betatron and the betatron phase advance functions for ID15 are listed in Table 1.

The other parameters for the PF ring are: the bunch charge difference  $\Delta q = 6.25$  nC, the betatron tune  $\nu = 5.28$ , and the total beam energy  $E = 2.5$  GeV. With these parameters, we expected the maximum COD at BPM locations is  $\Delta y = 1.5$   $\mu$ m.

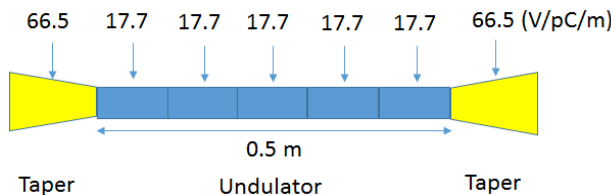


Figure 4: Transverse kick distribution along the ID.

Table 1: Betatron Functions and Betatron Phase Advances at the ID15 Locations

Position, m	Phase advance	Betatron fn, m
91.28374	14.58973	0.640564
91.41274	14.7194	0.520919
91.51274	14.89362	0.476824
91.61274	15.10334	0.47522
91.71274	15.2971	0.516108
91.81274	15.43696	0.599488
91.94174	15.53072	0.76981

## MEASUREMENT

For the ID15 measurement we used the following workflow:

- Change the operation to the single bunch mode.
- Open gaps of all IDs of the ring.
- Turn the feedback off.
- Adjust the beam orbit.
- First without bump. Measure the COD at all BPM locations several times for the ID gap open/closed cases and for the beam currents of from 4 mA to 24 mA with step of 4 mA.
- Create 1 mm bump and repeat the previous step.

The parallel bump (Fig. 5) with trapezoidal shape was created using the four steering magnets: two in upstream and two in downstream of the IVU15. An example of raw measurement results is shown in Fig. 4. Here the time evolution of the 65 BPM signals is shown. The upper graph gives the x-position difference, while the middle one gives those for the y-position. The bottom graph shows the changes in the ID gap. The red zones correspond to the ID gap open case, and the blue zones correspond to those where the ID gap is closed. The intermediate zones, where the gap size was changing are excluded from the following analysis.

There were slow drifts of measured beam positions. One of the possible reasons of the drift could be a time variation of the ring temperature after a user operation at 430 mA in the hybrid mode. Another concern is the position measurement resolution of the BPM, which is of the order of 1  $\mu\text{m}$ . To minimize these effects on measurement results, we have picked up for the analysis several short periods close to each other, and then averaged out about a thousands of BPM data at the both red and blue zones.

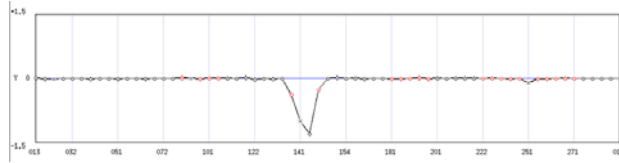


Figure 5: Orbit bump created at the ID15 location.

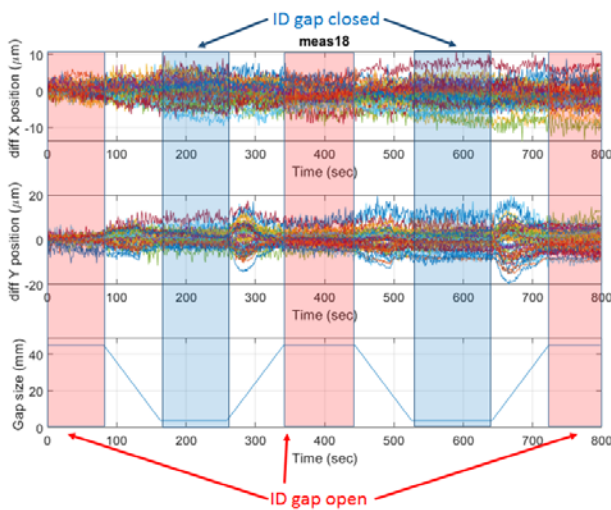


Figure 6: Example of the raw data.

## DATA ANALYSIS

Taking all these considerations into account, we have analyzed the measured data. The reference [4] suggests the

four-measurement combination to eliminate systematic errors by the bump itself. In this method, the difference of orbit deviation in Eq. (1) is expressed by:

$$\Delta y = (y_2 - y_1) - (y_{02} - y_{01}), \quad (2)$$

where  $y_{01}$  and  $y_{02}$  are measured without the bump at the low and high values of the beam current. Then, after the bump is generated,  $y_1$  and  $y_2$  are measured once again at the same values of the beam current.

In the process of the analysis, we have found that this technique is not good enough for us, since the contributions to the measurements from other devices inside the same bump orbit but outside of the IDs may be significant, and we could not distinguish them from the true signals. So, we decided to take differences for the ID open and close cases:

$$\Delta y = \left\{ (y_2 - y_1) - (y_{02} - y_{01}) \right\}_{ID\_gap\_closed} - \left\{ (y_2 - y_1) - (y_{02} - y_{01}) \right\}_{ID\_gap\_open}. \quad (3)$$

By extracting the ID open signals, we can eliminate the contributions from the extra components inside the same bump. Finally, Fig. 7 shows the measured data (based on Eq. (3) method) in red dots, while the analytical prediction based on Eq. (1) is shown in blue line. The high bunch current orbits  $y_2$  and  $y_{02}$  corresponds to the current value of  $I_b = 24$  mA, and the low current ones  $y_1$  and  $y_{01}$  corresponds to the current of  $I_b = 4$  mA. We have also evaluated the kick factors from the measurements by using the least square method. The result is shown by the green line in Fig. 7. The summary of the transverse kick factors for the ID closed case (the gap size is 3.83 mm) by the CST simulations, the analytical formulas and the measurements is presented in Table 2.

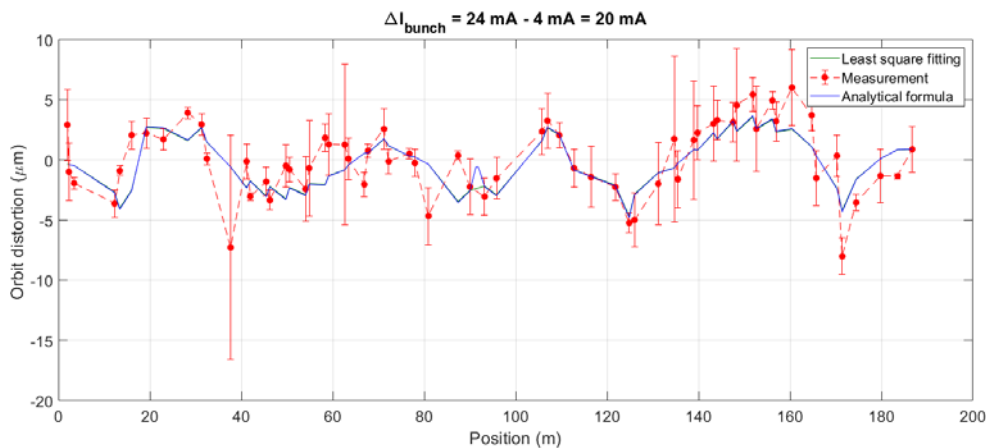


Figure 7: CODs at all the BPM locations by the measurement (red dots), by the analytical estimation (blue line), and by the least square fitting (green line).

the individual properties of each of four IDs affecting the transverse kick, together with its possible reasons.

	$k_{y \text{ R.W.}}, \text{V/pC/m}$	$k_{y \text{ taper}}, \text{V/pC/m}$
CST simulation	88.6	133.0
Analytical formula	86.1	145.4
Orbit bump measurement	91.2	135.3

## ACKNOWLEDGMENT

We would like to thank the members of PF storage ring, especially the monitor group and operational staff for their overall help.

- [1] V. Kiselev and V. Smaluk, *Nucl. Instrum. Methods A*, vol. 525, p. 433, 2004.
- [2] O. Tanaka, N. Nakamura, T. Obina, and K. Tsuchiya, in *Proc. of 60th ICFE Advanced Beam Dynamics Workshop on Future Light Sources (FLS'18)*, Shanghai, China, Mar. 4–9, 2018, pp. 160–165. doi:10.18429/JACoW-FLS2018-THP1WB02
- [3] O. A. Tanaka, N. Nakamura, T. Obina, K. Tsuchiya, R. Takai, S. Sakanaka, N. Yamamoto, R. Kato and M. Adachi, in *Journal of Physics Conference Series*, to be published.
- [4] V. Smaluk *et al.*, *Phys. Rev. ST Accel. Beams*, vol. 17, p. 074402, 2014.
- [5] E. Karantzoulis, V. Smaluk, and L. Tosi, *Phys. Rev. ST Accel. Beams*, vol. 6, p. 030703, 2003.
- [6] L. Emery, G. Decker, and J. Galayda, in *Proc., 19th Particle Accelerator Conference (PAC'01)*, Chicago, IL, USA, Aug. 2001, paper TPPH070, pp. 1823–1825.

We have evaluated the transverse kick factors of the PF in-vacuum undulator. The study suggests that we should distribute kick factors along the ID instead of lumping them to the center of ID for more accurate estimate of orbit deviations. Especially in the case of a long undulator this may be essential. We have also pointed out, that we should subtract contributions of other components inside the same bump orbit but outside of the undulator from analysis for more accurate estimate of kick factors. An evaluation of the impact of these “outside” components will be a natural extension of the present study. In conclusion we have compared the ID’s kick factors obtained by the measurements with those obtained by the simulations and the analytical evaluations. The upcoming study will include a research on



# COMPARISON AMONG DIFFERENT TUNE MEASUREMENT SCHEMES AT HLS-II STORAGE RING\*

L. T. Huang\*, T. Y. Zhou\*, Y. L. Yang, J. G. Wang, P. Lu, X. Y. Liu, J. H. Wei, M. X. Qian,  
F. F. Wu<sup>†</sup>, B. G. Sun<sup>‡</sup>

National Synchrotron Radiation Laboratory,  
University of Science and Technology of China, 230029 HeFei, China

## Abstract

Tune measurement is one of the most significant beam diagnostics at HLS-II storage ring. When measuring tune, higher tune spectral component and lower other components are expected, so that the tune measurement will be more accurate. To this end, a set of BBQ (Base Band Tune) front-end based on 3D (Direct Diode Detection) technique has previously developed to improve the effective signal content and suppress other components. Employing the BBQ front-end, four different tune measurement schemes are designed and related experiments performed on the HLS-II storage ring. Experimental results and analysis will be presented later.

## INTRODUCTION

The electron storage ring is the major part of HLS-II, and some of its main parameters are shown in Table 1 [1].

Table 1: Main HLS-II Storage Ring Main Parameters

Parameter	Value
Energy	800MeV
Beam current	300mA
RF frequency	204MHz
Revolution frequency	4.534MHz
Emittance	40nm*rad
Tune(fractional part)	0.45/0.35

The fractional part of the tune for a storage ring can be measured by observing the betatron sidebands on either side of the revolution harmonics [2]. The past tune measuring method is usually to put the signals from the beam position pick-up directly into the spectrum analyzer after some addition, subtraction, filtering and amplification processing, and then analyze the spectral data to obtain the fractional part of the tune. In general, beam pulse signals from the position pick-up is very narrow in the time domain, resulting in energy dispersion in a wide spectrum. This way only uses one betatron sideband, which causes most of the betatron energy to be wasted. This means that substantial beam excitation is necessary

in this method, which can lead to significant emittance degradation, so the system cannot be used during normal operation [3]. To solve this problem, 3D technique was initially developed at CERN for LHC to meet the requirements for measuring the tune of beam betatron oscillations with amplitudes below a micrometre [4]. The core of 3D technique is simple peak diode detector that can time-stretch the narrow beam pulses from the pick-up into slowly changing signals, meaning it's capable of moving most of the betatron energy to the baseband and improving the used betatron sideband intensity [5]. Using the BBQ front-end based on 3D technique, four different tune measurement schemes are designed for comparative experiments.

## 3D AND BBQ FRONT-END

3D technique uses two simple envelope detectors (also known as peak diode detector) connected to opposing electrodes of a pick-up. Followed by two DC blocking capacitors and a high impedance differential amplifier, a simplified BBQ front-end is completed, as shown in Fig. 1.

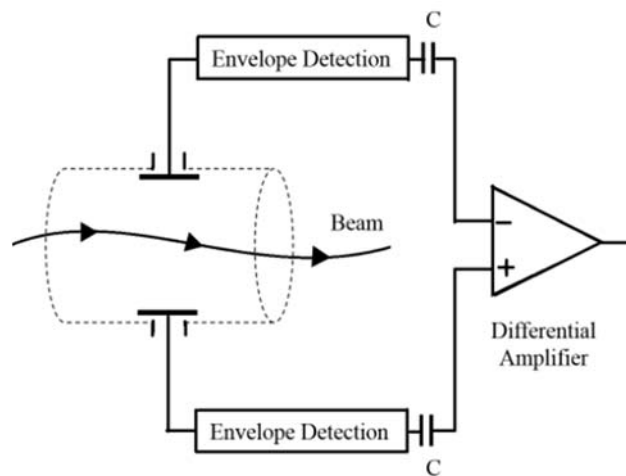


Figure 1: A simplified BBQ front-end schematic block diagram.

Based on the schematic block diagram above, a BBQ front-end was developed previously for HLS-II storage ring (see Fig. 2). The left two green parts are two peak diode detectors. The right box contains the rest: two capacitors and one differential amplifier.

\*Supported by the National Science Foundation of China (Grant No. 11705203, 11575181), Anhui Provincial Natural Science Foundation (Grant No. 1808085QA24), Chinese Universities Scientific Fund (Grant No. WK2310000057)

<sup>†</sup> Corresponding author (email: wufangfa@ustc.edu.cn)

<sup>‡</sup> Corresponding author (email: bgsun@ustc.edu.cn)



Figure 2: BBQ front-end physical picture.

## FOUR TUNE MEASUREMENT SCHEMES

### Scheme 1

Scheme 1 is the simplest one of four different tune measurement schemes (see Fig. 3). Sweep-frequency excitation (SFE) is used to excite the beam to generate proper betatron oscillations through stripline kicker. Without BBQ front-end, the signals from four electrodes of the stripline BPM are directly putted into the spectrum analyzer after some addition and subtraction processing.

### Scheme 2

Considering the large noise in the low frequency, a 204MHz down mixer is added, which can move the whole spectrum down by 204 MHz, as shown in Fig. 4. It means smaller effective betatron signals and meanwhile lower noise. So a low noise amplifier is employed to strengthen the signals.

### Scheme 3

Scheme 3 is one scheme using BBQ front-end (see Fig. 5). The signals, after addition processing, are firstly inputted into BBQ front-end.

### Scheme 4

One common feature of the above three schemes is the addition processing, which means the final signal contains both horizontal and vertical tune information. Scheme 4 gives up the addition processing and uses two BBQ front-ends: one for horizontal tune information and another for vertical tune information.

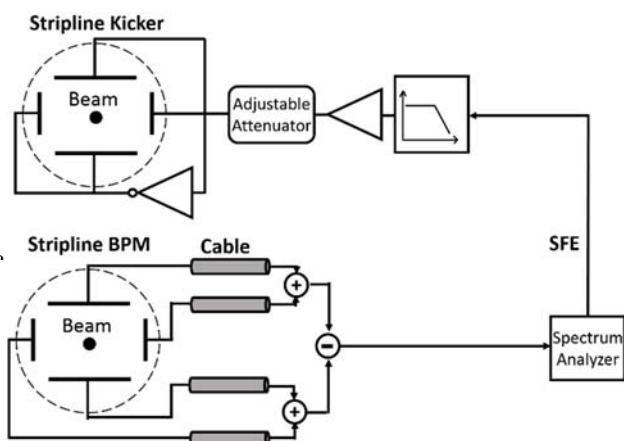


Figure 3: Scheme 1 schematic block diagram.

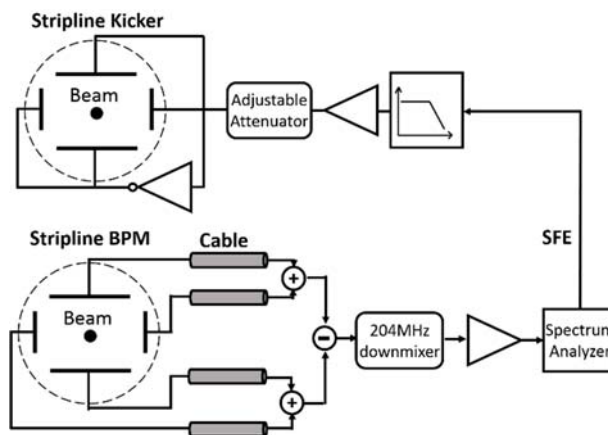


Figure 4: Scheme 2 schematic block diagram.

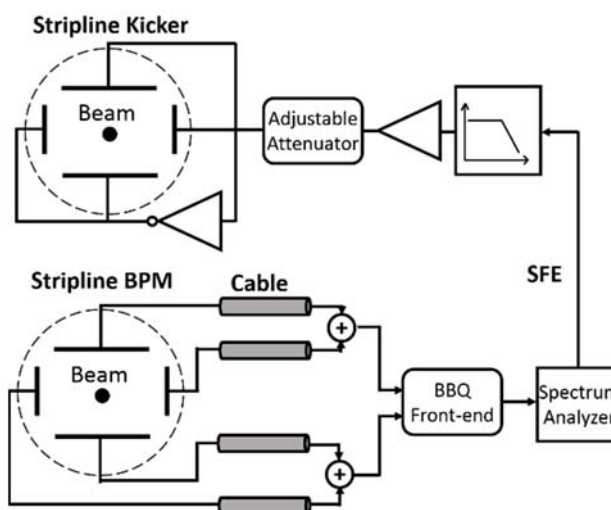


Figure 5: Scheme 3 schematic block diagram.

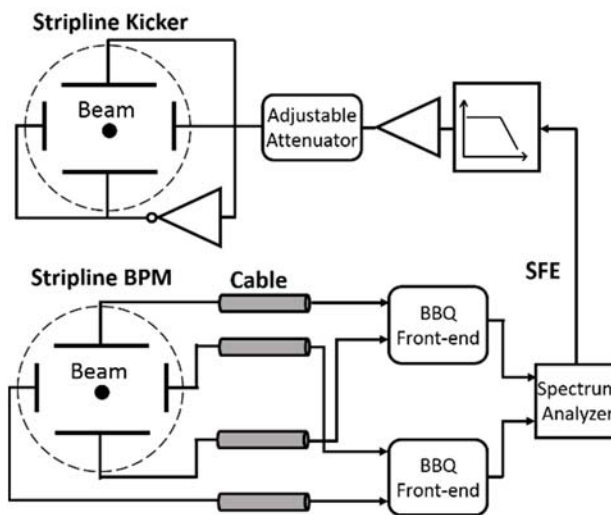


Figure 6: Scheme 4 schematic block diagram.

## RELATED RESULTS AND ANALYSIS

The result of scheme 1 with 0dBm SFE is shown in Fig. 7. It can be seen that the effective betatron sideband is quite weak and submerging in the noise (with SNR less than 10 dB).

In order to reduce the influence of noise, scheme 2 uses a down mixer to filter the low frequency noise. The result is shown in Fig. 8. It is clear that scheme 2 has higher SNR (more than 10 dB) when using lower excitation (-13 dBm SFE).

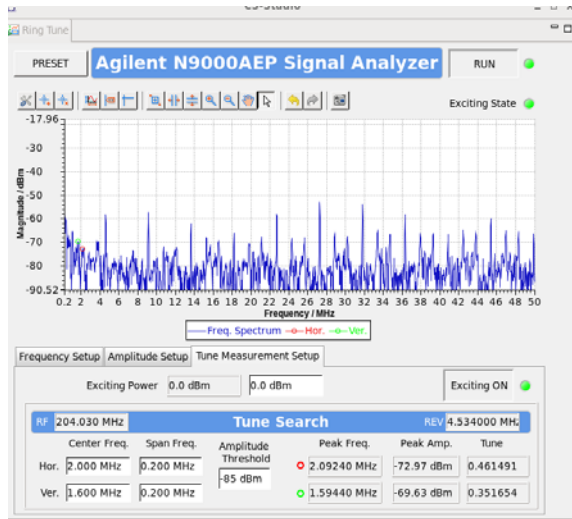


Figure 7: Result of scheme 1 (0 dBm SFE).

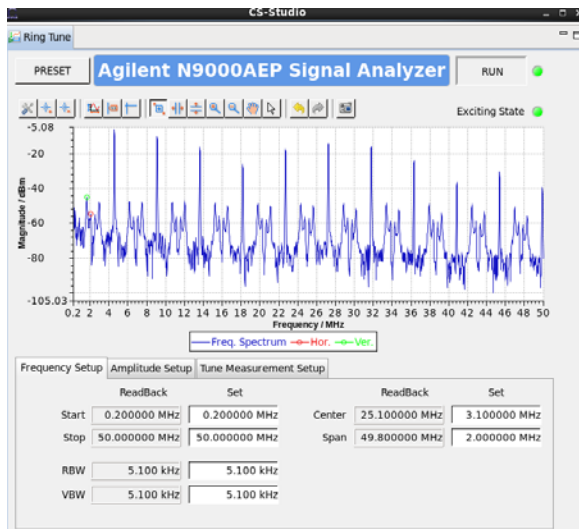


Figure 8: Result of scheme 2 (-13 dBm SFE).

In order to improve the effective betatron sideband intensity near the baseband, scheme 3 uses a BBQ front-end to convert the energy of betatron oscillation into the baseband, and the result under -13dBm SFE is shown in Fig. 9. It can be obviously seen that BBQ front-end indeed moves the betatron energy to the baseband, compared to the result of scheme 2. It makes the intensity of the effective sideband much higher than scheme 2 and the SNR is about 20dB as a result, although the energy of the noise is also converted to the baseband at the same time.

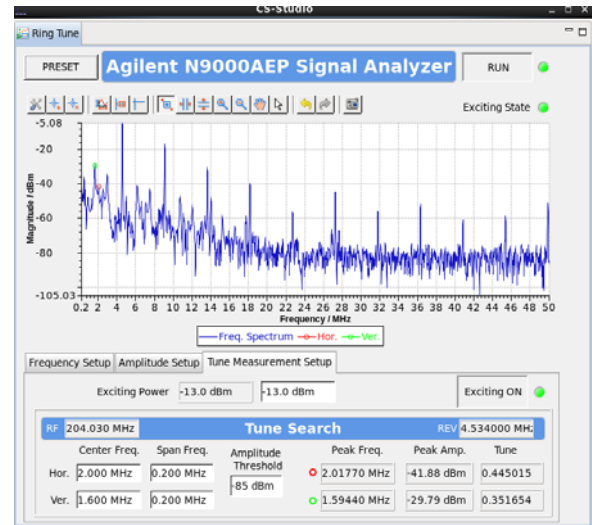


Figure 9: Result of scheme 3 (-13 dBm SFE).

Scheme 4 measures horizontal and vertical tune respectively, as shown in Fig. 10. Although it needs two BBQ front-ends, it obtains higher SNR than scheme 3. The key is the lower noise in the baseband.

Comparing the results under different SFE powers between scheme 2 and 3, it is found that scheme 3 can observe the tune precisely using lower SFE power (-40dBm) than scheme 2 (-34dBm), which proves the SNR improvement of BBQ front-end (see Fig. 11). 3D technique indeed makes the tune measurement more sensitive than before.

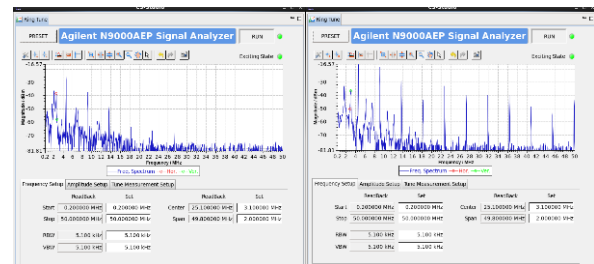


Figure 10: Result of scheme 4 (-13 dBm SFE). (left) horizontal tune; (right) vertical tune.

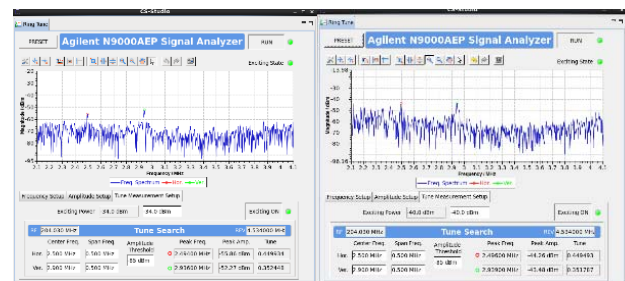


Figure 11: Comparison between scheme 2 and 3. (left) scheme 2 (-34 dBm SFE); (right) scheme 3 (-40 dBm SFE).

## CONCLUSION

This paper proposes four different tune measurement schemes based on BBQ front-end. Experimental results prove BBQ front-end indeed increases the betatron frequency content in the baseband, leading to higher sensitivity of tune measurement than before. Scheme 4 has the best performance in four schemes, but cost nearly twice that of scheme 3. Compromising performance and cost, scheme 3 is relatively the best choice with enough sensitivity (observe the obvious betatron sideband under -40dBm SFE) and low cost.

## REFERENCES

- [1] J. J. Zheng *et al.*, “Applications of the Tune Measurement System of the HLS-II Storage Ring”, in *Proc. IPAC'16*, Busan, Korea, May 2016, pp. 2892-2894.
- [2] M. Gasior and R. Jones, “High Sensitivity Tune Measurement by Direct Diode Detection”, in *Proc. DIPAC'05*, Lyon, France. Pp. 312-314.
- [3] L. T. Huang *et al.*, “Test of the Tune Measurement System based on BBQ at HLS-II Storage Ring”, in *Proc. IPAC'18*, Vancouver, BC, Canada, pp. 4926-4928. doi:10.18429/JACoW-IPAC2018-THPML111
- [4] M. Gasior, “Faraday Cup Award: High Sensitivity Tune Measurement using Direct Diode Detection”, CERN, Geneva, Switzerland, Rep. CERN-ATS-2012-246, Apr. 2012.
- [5] M. Gasior and R. Jones, “The Principle and First Results of Betatron Tune Measurement by Direct Diode Detection”, CERN, Geneva, Switzerland, LHC-Project-Report 853.



# A STUDY ON THE INFLUENCE OF BUNCH LONGITUDINAL DISTRIBUTION ON THE CAVITY BUNCH LENGTH MEASUREMENT\*

Q. Wang, Q. Luo<sup>†</sup>, B. G. Sun<sup>‡</sup>, F. F. Wu

NSRL, University of Science and Technology of China, 230029 Hefei, China

## Abstract

Cavity bunch length measurement is used to obtain the bunch length depending on the eigenmodes exciting inside the cavity. For today's FELs, the longitudinal distribution of particles in electron bunch (bunch shape) may be non-Gaussian, sometimes very novel. In this paper, the influence of bunch shape on the cavity bunch length measurement is analyzed, and some examples are given to verify the theoretical results. The analysis shows that the longitudinal distribution of particles in electron bunch has little influence on the cavity bunch length measurement when the bunch length is less than 1 ps and the eigenmodes used in measurement are below 10GHz.

## INTRODUCTION

Bunch length is one of the important characteristics of charged particle beam in accelerators. Compared with the traditional methods, bunch length monitor based on resonant cavities has great potential especially for high quality beam sources, for it has superiority, such as simple structure, wide application range, and high signal to noise ratio [1]. What's more, the eigenmodes of cavities are used in combined measurement of bunch length, beam intensity, position and quadrupole moment. For example, the monopole modes can be used to measure the bunch length and the beam intensity [2]. At the same time, the dipole modes are always utilized to obtain the beam position offset [3]. What's more, we could decide the quadrupole moment by analyzing the TM220 modes of the square resonators [4]. Therefore, the measurement device shows the characteristic of terseness and compaction.

The present FELs show characteristic of very short bunch. For example, the bunch length of Shanghai soft X-ray free Electron laser (SXFEL) is several hundred femtoseconds. At the same time, the longitudinal distribution of particles in electron bunch (bunch shape) may be non-Gaussian, sometimes very novel. While analyzing the beam-cavity interaction, we assume the longitudinal distribution of particles in electron bunch is Gaussian in a general way. Then what is the impact of the non-Gaussian bunch on the cavity bunch length monitor? In this paper, the influences of the different bunch shapes on the cavity bunch length measurement are analyzed under different circumstances, and the results provide theoretical support

for the future FEL bunch length measurements using resonant cavities.

## MESUREMENT OF GAUSSIAN BUNCH

While passing through a cavity, an electron whose charge is  $q$  can excite a series of eigenmodes. The voltage amplitude of an eigenmode can be expressed as

$$V_q = 2k_n q \quad (1)$$

Where  $k_n$  is the loss factor which is related to R/Q of the eigenmode [5]. It can be seen that the voltage is related to the charge  $q$ . As for a bunch whose total charge is  $Q_b$ , the voltage amplitude of an eigenmode excited inside the cavity is the superposition of the electrons in the bunch which arrive at the cavity at different times. The moments when the electrons arrive at the cavity depend on the longitudinal distribution of particles in electron bunch. Assume an electron bunch whose longitudinal normalized distribution function of electrons is  $f(t)$ . The moment when the center of the bunch arrives at the center of the cavity is defined as zero time. So the voltage amplitude of an eigenmode when the charge arriving at the cavity at time  $t$  can be expressed as

$$dV = 2k_n dq \quad (2)$$

Considering the voltage phases excited by electrons in different places is disparate, the voltage amplitude of an eigenmode can be written as

$$\begin{aligned} V_b &= \int_{-t_m}^{t_m} e^{i\omega_n t} dV \\ &= 2k_n \int_{-t_m}^{t_m} e^{i\omega_n t} dq \\ &= 2k_n \int_{-t_m}^{t_m} I(t) \times e^{i\omega_n t} dt \\ &= 2k_n Q_b \int_{-t_m}^{t_m} f(t) \times e^{i\omega_n t} dt \end{aligned} \quad (3)$$

Where  $\omega_n$  is the frequency of the eigenmode,  $t_m$  is the range of the bunch longitudinal distribution, and  $I(t)$  represents beam current. In a general way, the longitudinal distribution of the bunch is regarded as Gaussian distribution, so

$$f(t) = \frac{1}{\sqrt{2\pi}\sigma} \exp\left(-\frac{t^2}{2\sigma^2}\right) \quad (4)$$

\* Supported by National Key R&D Program of China (Grant No. 2016YFA0401900, 2016YFA0401903), the National Science Foundation of China (Grant No. 11375178, 11575181) and the Fundamental Research Funds for the Central Universities (WK2310000046).

<sup>†</sup> Corresponding author (email: luoqing@ustc.edu.cn)

<sup>‡</sup> Corresponding author (email: bgsun@ustc.edu.cn)

Where  $\sigma$  represents the bunch length. The voltage amplitude of an eigenmode excited by the bunch whose charge is  $Q_b$  can be described as

$$V_b = 2k_n Q_b \int_{-t_m}^{t_m} \frac{1}{\sqrt{2\pi}\sigma} e^{-\frac{t^2}{2\sigma^2}} e^{i\omega_n t} dt \quad (5)$$

$$= 2k_n Q_b e^{-\frac{\omega_n^2 \sigma^2}{2}}$$

Both  $Q_b$  and  $\sigma$  are unknown quantity, so we need two eigenmodes at least and the bunch length can be calculated by solving these equations.

$$\begin{cases} V_{b1} = 2k_{n1} Q_b e^{-\frac{\omega_{n1}^2 \sigma^2}{2}} \\ V_{b2} = 2k_{n2} Q_b e^{-\frac{\omega_{n2}^2 \sigma^2}{2}} \end{cases} \quad (6)$$

That is the conventional method used to obtain the bunch length.

## THE INFLUENCE OF BUNCH SHAPE

In this section, the influence of the longitudinal distribution of particles in electron bunch on the bunch length measurement mentioned above will be analyzed.

The root-mean-square value of the bunch longitudinal distribution is defined as bunch length  $\sigma$ . When the centre of the bunch is the origin of the normalized distribution function, the root-mean-square value is the same size as the standard deviation of the longitudinal distribution,

$$\sigma = \sqrt{\int_{-\infty}^{+\infty} f(t) \times t^2 dt} \quad (7)$$

It means a centralized region of most particles, not the entire range of the bunch longitudinal distribution. Define the integral in Eq. (3) is the bunch shape factor  $V_{shape}$ ,

$$V_{shape} = \int_{-t_m}^{t_m} f(t) \times e^{i\omega_n t} dt \quad (8)$$

Comparing Eq. (8) and Eq. (3), it can be seen that the voltage amplitude of an eigenmode excited by a particle and by a bunch are similar. The bunch shape factor  $V_{shape}$  is considered in Eq. (8). The following is the analysis of  $V_{shape}$ . The n-order Maclaurin series with Lagrange remainder term can be expanded as

$$e^{i\omega_n t} = 1 + i\omega_n t - \frac{\omega_n^2 t^2}{2!} - i\frac{\omega_n^3 t^3}{3!} + \frac{\omega_n^4 t^4}{4!} + \dots + \frac{(\omega_n t)^n}{n!} + \frac{e^{i\theta\omega_n t} (\omega_n t)^{n+1}}{(n+1)!} \quad (9)$$

Where  $0 < \theta < 1$ . We extract the real part of Eq. (9) and take the sum of first two terms,

$$\begin{aligned} V_{shape} &= \int_{-t_m}^{t_m} f(t) \times \left[ 1 - \frac{\omega_n^2 t^2}{2} + \frac{e^{i\theta\omega_n t}}{4!} (\omega_n t)^4 \right] dt \\ &= \int_{-t_m}^{t_m} f(t) dt - \int_{-t_m}^{t_m} f(t) \times \frac{\omega_n^2 t^2}{2} dt \\ &\quad + \int_{-t_m}^{t_m} f(t) \times \frac{e^{i\theta\omega_n t}}{4!} (\omega_n t)^4 dt \end{aligned} \quad (10)$$

Considering that  $f(t)$  is the normalized distribution function, according to the definition of bunch length, Equation (10) can be described as

$$V_{shape} \approx 1 - \frac{\omega_n^2 \sigma^2}{2} \quad (11)$$

The approximation error can be expressed by the Lagrange remainder term,

$$\Delta = \int_{-t_m}^{t_m} [f(t) \times \frac{\exp(i\theta\omega_n t)}{4!} (\omega_n t)^4] dt \quad (12)$$

Given  $f(t) > 0$ , divide Eq. (12) by  $V_{shape}$ ,

$$\begin{aligned} \frac{\Delta}{V_{shape}} &= \frac{\int_{t_{min}}^{t_{max}} [f(t) \times \frac{\exp(i\theta\omega_n t)}{4!} (\omega_n t)^4] dt}{\int_{t_{min}}^{t_{max}} f(t) \times \exp(i\omega_n t) dt} \\ &< \frac{\int_{-t_m}^{t_m} f(t) \times \frac{(\omega_n t)^4}{4!} dt}{\int_{-t_m}^{t_m} f(t) \times \exp(i\omega_n t_m) dt} \\ &< \frac{\int_{-t_m}^{t_m} [f(t) \times \frac{(\omega_n t_m)^4}{4!}] dt}{\exp(i\omega_n t_m) \times \int_{-t_m}^{t_m} f(t) dt} \\ &= \frac{(\omega_n t_m)^4}{24} \cos(\omega_n t_m) \end{aligned} \quad (13)$$

The maximum of the approximation relative error can be obtained by this equation. The relationship between  $\omega_n t_m$  and the maximum of the approximation relative error is shown in Fig. 1.

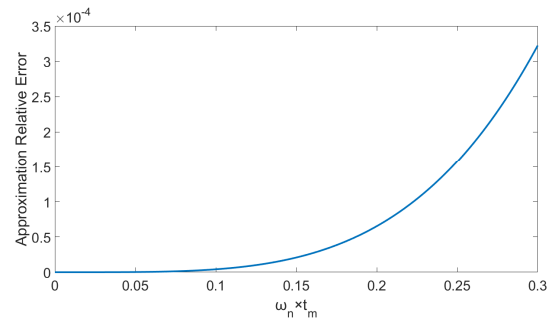


Figure 1:  $\omega_n t_m$  versus the maximum of the approximation relative error.

It can be seen that we preferred smaller  $\omega_n t_m$  which means the approximate value in Eq. (11) approaches to

the value of  $V_{shape}$ . The bunch length of today's FELs is about hundreds of femtoseconds, and the entire range of the bunch longitudinal distribution is approximately from -2 ps to 2 ps. The frequency of the eigenmode used for measurement can reach to about 10GHz. In this case,

$$\frac{\Delta}{V_{shape}} < 1.03 \times 10^{-5} \quad (14)$$

It can be seen from the results that we can take the approximation like Eq. (11) in spite of bunch shape and the approximation relative error is less than  $1.03 \times 10^{-5}$ . The voltage amplitude of an eigenmode excited by a bunch can be written as

$$V = 2k_n Q_b V_{shape} = 2k_n Q_b \left(1 - \frac{\omega_n^2 \sigma^2}{2}\right) \quad (15)$$

The voltage is irrelevant to the longitudinal distribution of particles in electron bunch. Therefore, the bunch is able to be regarded as Gaussian bunch in this case.

## VERIFICATION

Many different kinds of bunch longitudinal distributions are shown in Fig. 2 to Fig. 8. There are the normalized probability density function analytic expressions of uniformly distributed bunch, flat-topped bunch, parabolic bunch, Gaussian bunch, triangular bunch and two kinds of double-humped bunches, respectively.

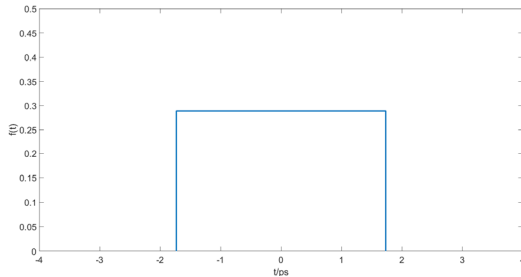


Figure 2: The normalized probability density function of uniformly distributed bunch.

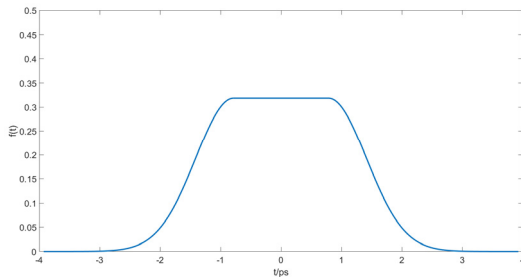


Figure 3: The normalized probability density function of flat-topped bunch.

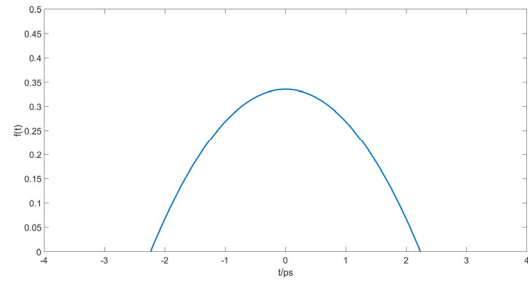


Figure 4: The normalized probability density function of parabolic bunch.

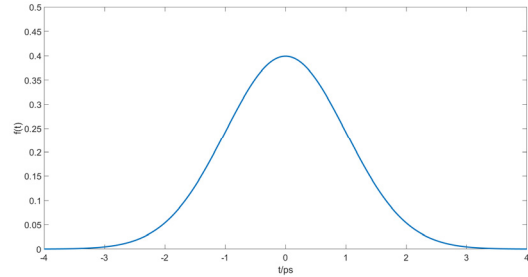


Figure 5: The normalized probability density function of Gaussian bunch.

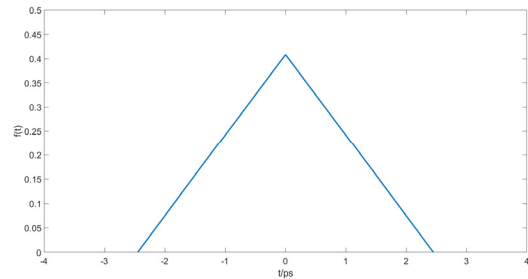


Figure 6: The normalized probability density function of triangular bunch.

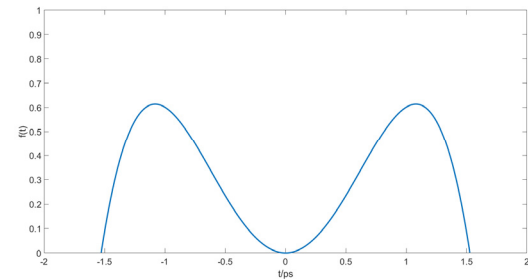


Figure 7: The normalized probability density function of double-humped bunch 1.

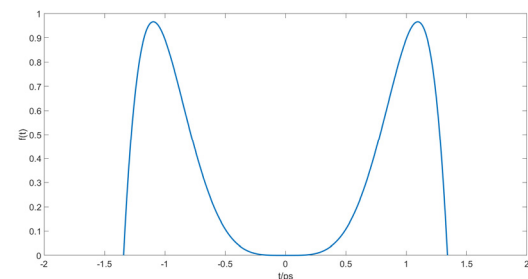


Figure 8: The normalized probability density function of double-humped bunch 2.

$$f(t) = \frac{\sqrt{3}}{6}, [-\sqrt{3}, \sqrt{3}] \quad (16)$$

$$f(t) = \begin{cases} \frac{1}{2} N(-\sqrt{\frac{3\pi}{9+2\pi}}, \frac{6}{9+2\pi}), (-\infty, -\sqrt{\frac{3\pi}{9+2\pi}}) \\ \frac{1}{2} \times \sqrt{\frac{12\pi}{9+2\pi}}, [-\sqrt{\frac{3\pi}{9+2\pi}}, \sqrt{\frac{3\pi}{9+2\pi}}] \\ \frac{1}{2} N(\sqrt{\frac{3\pi}{9+2\pi}}, \frac{6}{9+2\pi}), (\sqrt{\frac{3\pi}{9+2\pi}}, +\infty) \end{cases} \quad (17)$$

$$f(t) = -0.03 \times \sqrt{5} \times t^2 + 0.15 \times \sqrt{5}, [-\sqrt{5}, \sqrt{5}] \quad (18)$$

$$f(t) = N(0,1), (-\infty, +\infty) \quad (19)$$

$$f(t) = \begin{cases} \frac{t}{6} + \frac{\sqrt{6}}{6}, [-\sqrt{6}, 0) \\ -\frac{t}{6} + \frac{\sqrt{6}}{6}, [0, \sqrt{6}] \end{cases} \quad (20)$$

$$f(t) = -\frac{135}{196} \times \sqrt{\frac{3}{7}} \times t^4 + \frac{45}{28} \times \sqrt{\frac{3}{7}} t^2, [-\sqrt{\frac{7}{3}}, \sqrt{\frac{7}{3}}] \quad (21)$$

$$f(t) = -\frac{4375}{8748} \times \sqrt{5} t^6 + \frac{875}{972} \times \sqrt{5} t^4, [-\sqrt{\frac{9}{5}}, \sqrt{\frac{9}{5}}] \quad (22)$$

Their charges are all 1 nC and their bunch lengths (root-mean-square value of the distribution) are all 1 ps. The relationship between their corresponding shape factors  $V_{\text{shape}}$  and the eigenmode working frequencies  $\omega_n$  is shown in Fig. 9 and Fig. 10. Figure 10 is the larger version of Fig. 9 at the low frequency part.

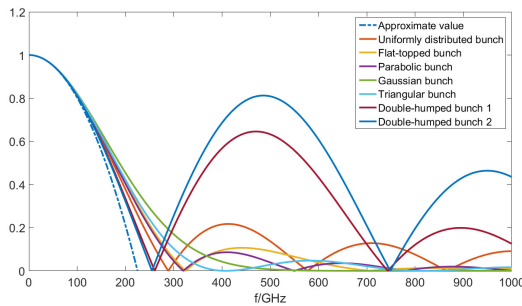


Figure 9: The relationship between  $V_{\text{shape}}$  and the eigenmode working frequencies  $\omega_n$ .

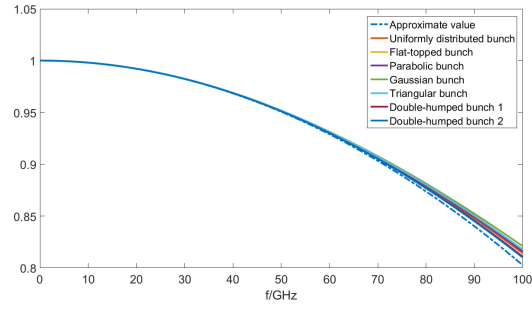


Figure 10: the larger version of Fig. 9 at the low frequency part.

The imaginary lines in the above pictures represent the approximate expression Eq. (11). It can be seen that an eigenmode voltage excited by a bunch in cavity is irrelevant to the longitudinal distribution of particles in electron bunch when the frequencies of the eigenmodes used for measurement are below 50GHz. In that case, the results of the Gaussian bunch measurements are able to take the place of the results of the bunches with other shapes measurements. Even if the frequency of the eigenmode used for measurement is equal to 50GHz, the maximum relative error is merely  $5.25 \times 10^{-3}$ .

## CONCLUSION

In this paper, the impact of bunch shape on cavity bunch length measurement is analyzed in theory. The shorter the bunch, the less the influence from the longitudinal distribution of particles in electron bunch is. For present and future FEL whose bunch length is less than 1ps, the longitudinal distribution of particles in electron bunch do not have to be taken into account when we use the cavity to obtain the bunch length. The bunch is able to be regarded as Gaussian bunch in that case. This conclusion provides theoretical support for the future FEL bunch length measurements using resonant cavities.

## REFERENCES

- [1] Q. Wang *et al.*, "Design and simulation of high order mode cavity bunch length monitor for infrared free electron laser", in *Proc. 8th Int. Particle Accelerator Conf. (IPAC'17)*, Copenhagen, Denmark, May 2017, pp. 309-311, doi:10.18429/JACoW-IPAC2017-MOPAB082
- [2] Z. C. Chen, W. M. Zhou, Y. B. Leng, L. Y. Yu and R. X. Yuan, "Subpicosecond Beam Length Measurement Study Based on The TM010 Mode", *Phys. Rev. ST Accel. Beams*, vol. 16, no. 7, p. 072801, Jul. 2013.
- [3] J. H. Su *et al.*, "Design and cold test of a rectangular cavity beam position monitor", *Chinese Physics C*, vol. 37, no. 1, p. 017002, Jan. 2013.
- [4] J. S. Kim, R. Miller, and C. D. Nantista, "Design of a standing-wave multicell radio frequency cavity beam monitor for simultaneous position and emittance measurement", *Review of Scientific Instruments*, vol. 76, no. 7, p. 073302, Jul. 2005.
- [5] H. Padamsee, J. Knobloch, and T. Hays, *RF Superconductivity for Accelerators 2nd Edition*. Weinheim, Germany: Wiley-VCH, 2008.



# ACTIVE MAGNETIC FIELD COMPENSATION SYSTEM FOR SRF CAVITIES

L. Ding, Laboratory GREYC, Caen, France

Jian Liang, Hanxiang Liu, Zaipeng Xie<sup>†</sup>, Hohai University, Nanjing, China

## Abstract

Superconducting Radio Frequency (SRF) cavities are becoming popular in modern particle accelerators. When the SRF cavity is transitioning from the non-conducting to the Superconducting state at the critical temperature ( $T_c$ ), the ambient magnetic field can be trapped. This trapped flux may lead to an increase in the surface resistance of the cavity wall, which can reduce the Q-factor and efficiency of the cavity. In order to increase the Q-factor, it is important to lower the surface resistance by reducing the amount of magnetic flux trapped in the cavity wall to sub 10-G range during the  $T_c$  transition.

In this paper, we present a 3-axis automatic active magnetic field compensation system that is capable of reducing the earth magnetic field and any local disturbance field. Design techniques are described to enhance the system stability while utilizing the flexibility of embedded electronics. This paper describes the system implementation and concludes with initial results of tests. Experimental results demonstrate that the proposed magnetic field compensation system can reduce the earth magnetic field to sub 1 mG even without shielding.

## Introduction

An important limiting factor in the performance of superconducting radio frequency (SRF) cavities in medium and high field gradients is the intrinsic quality factor and, thus, the surface resistance of the cavity [1]. The exact dependence of the surface resistance on the magnitude of the RF field is not well understood [2]. Lower Q factors may come from several sources, one of which is the presence of a trapped magnetic field inside the cavity walls at cool down [3], known as remanent magnetization,

Remanent magnetisation is often a function of the grain boundaries of the niobium material [4] used to construct the cavities. It is affected by the ambient field during the cooling cycle that necessary to superconductivity, and below 3 Gauss, 100% of the field is trapped [5]. A number of studies have been carried out on cool-down speed, and one report concludes that fast cool-down will be more uniform and can be expected to result in less trapped magnetic flux because perturbations to the phase boundary will be larger on average during slow cool-down [6] while others advocate a fast cool-down [7].

Therefore, if the magnetic field can be reduced during the cooling cycle this will reduce the remanent magnetisation in the SRF cavity.

Current state of the art is to place the SRF cavity in a tubular magnetic shield [8]. This tube and the SRF cavity

must then be located in an east-west orientation [8] [9]. In addition coils are then placed around the tube to provide further compensation. There is effectively no safety margin with this arrangement [8]. During the cool down phase fluxgate magnetometers monitor the magnetic field.

The typical remanent magnetic field requirement is less than 3-4 mG [10]. The earth's magnetic field is circa 500 mG so approximately 45dB attenuation of the earth field is required.

This paper proposes that the SRF cavity is placed inside a three axis Helmholtz coil system (Figure 1). Fluxgate magnetometers positioned as close to the cavity as possible, are used as feedback sensors for the cancellation system. With this active compensation in place, it is possible to achieve < 1 mG of trapped field in the cavity, thereby improving its RF performance.

Prior to the cooling cycle the compensation system is energized so the field in the SRF cavity is minimized. The monitoring and field adjustment continues during the cooling cycle.

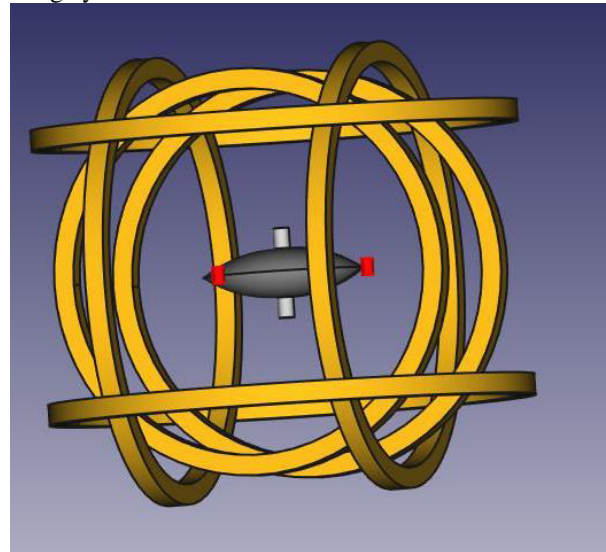


Figure 1: Coil setup with magnetometers in red.

## SYSTEM DESIGN

The system consists of a three axis Helmholtz coil around the SRF cavity, 3 axis fluxgate sensor mounted to the cavity, optional additional single axis sensors around the circumference of the cavity, and the control electronics. The sensors monitor the field seen by the SRF cavity to the control electronics. This signal is in analog form, so is digitized to provide a real-time update. The control electronics compares the signals from the sensors and immediately adjusts the current in the Helmholtz coils, thereby maintaining a very low level of magnetic field

<sup>†</sup> email address: zaipengxie@impcas.ac.cn

The control electronics consists of analog to digital converters optionally feeding data to a PC. This data is updated at each sample (currently 32000 Sample/s). The control electronics software filters the data, processes it through an algorithm to compare axes, and send adjusted data in real-time to the digital to analog converters that control the current in the coils (Figure 2 shows the block diagram of the system). This current, flowing through the Helmholtz coils creates a magnetic field to instantly cancel that of the Earth and any local disturbance. The algorithm limits the rate of change in this field to prevent the system oscillating.

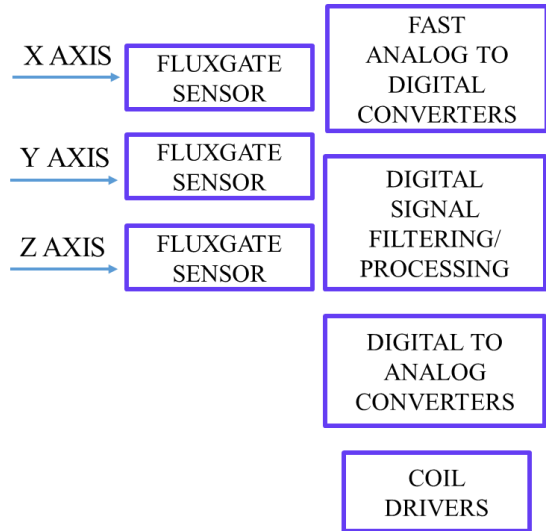


Figure 2: System block diagram.

### INITIAL EXPERIMENT AND RESULTS

Initial setup was carried out with 2 Helmholtz coil sets; each coil system having 3 axes, a 0.6 m nominal system inside a larger 1.3 m nominal diameter coil set (Figure 3 – note 2 axes of the larger coil have been removed for a little more clarity in this picture). Each coil set is 3 axes. The larger coil set is used to create a changing disturbance and the smaller coil set compensated for that field change. A reference magnetometer, as well as the feedback magnetometer was placed inside the smaller coil set. Both magnetometers were 3 axis fluxgate sensors.

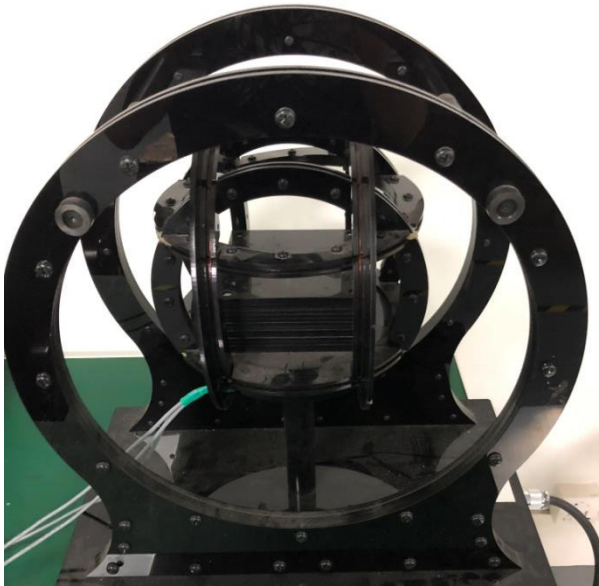


Figure 3: Test coil setup.

The smaller coil system was electronically adjusted to align the feedback magnetometer to the coils to ease mechanical alignment. The larger coil system was set to apply a field cancelling that of the Earth’s field. A defined field (to simulate different Earth field) was applied to the larger coil system, measured using the reference magnetometer, before the cancelling smaller coil system was activated.



Figure 4: Digitiser and 3 axis magnetometer.

The field was also measured by the feedback magnetometer and its output was feed into the control electronics (Figure 4). The control electronics then was activated to produce the required current to generate the cancelling field. The remaining field was then measured. The simulated field was increased in steps, each time the cancella-

tion system was turned off, so the simulation field could be measured, as in Figure 5.

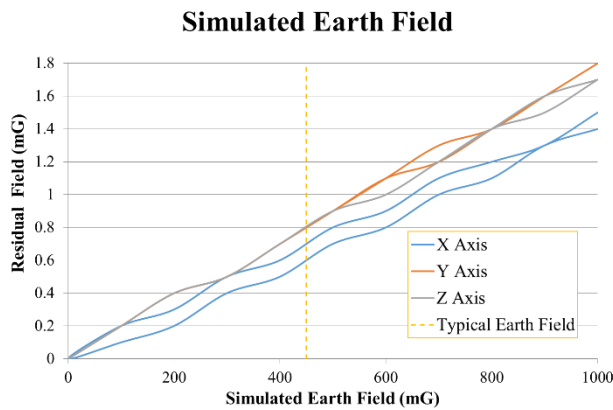


Figure 5: Simulated earth field cancelling.

An AC field was also applied of 35 mG rms. The frequency was stepped between 1 Hz and 60 Hz. The attenuation to this AC field was determined – Figure 6. Further work to the algorithm is to be undertaken to improve the attenuation.

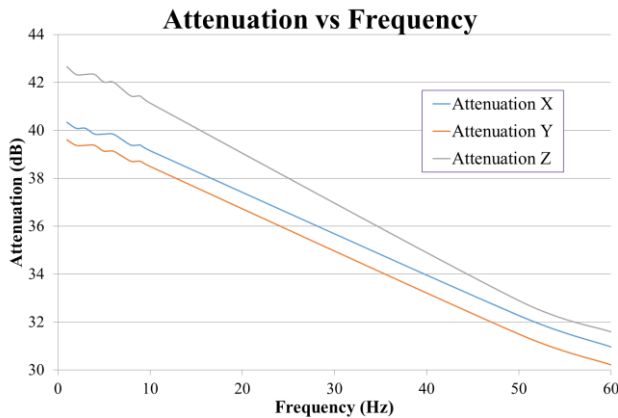


Figure 6: AC field attenuation.

## PROPOSED SYSTEM REQUIREMENT

### Magnetometer:

- Range 2 G
- Resolution better than 10  $\mu$ G
- Operating Temperature range < 4 K to > 300 K
- 3 Axes or Single axis, alignment is electronic better than 0.1°
- Linearity better than 0.01%
- Offset error less than 1 mG

### Coil Compensation system

- 3 Axes Range 1 G
- Size 1.3 m nominal diameter
- Range 2 G
- Resolution less than 1 mG
- Adjustment rate limited to prevent self oscillation
- DC field cancellation better than 46dB at typical Earth's field
- AC rejection better than 30dB at 60 Hz
- Multiple systems can be linked together

## CONCLUSION

The work to date has shown that the Earth field can be reduced to significantly less than 2-3 mG required for state of the art SRF cavity operation during the cool down phase, as well as providing compensation for AC fields. Further work is intended to improve the algorithm to enable further attenuation without compromising system stability, as well as work utilising a real SRF cavity.

## ACKNOWLEDGMENTS

I would like to thank Mr. Adrian Swinton for the technical assistance provided during the experimental work and review of this paper.

Also to Coliy Technology GmbH for partly funding this research, and the loan of equipment used in the study.

## REFERENCES

- [1] H. Padamsee, J. Knobloch, and T. Hays, *RF Superconductivity for Accelerators*, Wiley-VCH, 2nd edition, ISBN 978-3-527-40842-9, 2008.
- [2] P. N. Koufalas, *et. al.* "Understanding the field dependence of surface resistance in nitrogen-doped cavities", in *Proc. 17th Int. Conf. on RF Superconductivity (SRF2015)*, September 2015, Whistler, BC, Canada, paper MOPB004.
- [3] S. Belomestnykh,  
<http://uspas.fnal.gov/materials/09UNM/SRF>
- [4] S Aull, J. Knobloch "Depinning of Trapped Magnetic Flux in Bulk Niobium SRF cavities",  
<https://arxiv.org/abs/1507.04105>
- [5] C. Vallet *et. al.* "Flux trapping in superconducting cavities" EPAC 1992. in *Proc. Third European Particle Accelerator Conference (EPAC92)*, Berlin, Germany, March 1992, pp. 1295-1297.
- [6] J. Robbins and R. Eichhorn, "HOW UNIFORM ARE COOL-DOWNS?", in *Proc. 17th Int. Conf. on RF Superconductivity (SRF'15)*, September 2015, Whistler, BC, Canada, paper MOPB011.
- [7] D. Gonnella *et al.*, "Nitrogen-doped 9-cell cavity performance in a test cryomodule for LCLS-II", *Journal of Applied Physics.*, vol. 117, p.023908, November 2014.  
doi: 10.1063/1.4905681
- [8] Anthony C. Crawford "A Study of Magnetic Shielding Performance of a Fermilab International Linear Collider Superconducting RF Cavity Cryomodule"  
<https://arxiv.org/abs/1409.0828>
- [9] D. A. Edwards (editor) "TESLA Test Facility Linac Design Report", Chapter 4, version 1.0 1 March 1995.  
[http://tesla.desy.de/new\\_pages/TTFcdrTab.html](http://tesla.desy.de/new_pages/TTFcdrTab.html)
- [10] Genfa Wu, "Overview on Magnetic Field Management and Shielding in High Q Modules", in *Proc. 17th Int. Conf. on RF Superconductivity (SRF'15)*, September 2015, Whistler, BC, Canada, paper THBA06.



# SSRF BEAM OPERATION STABILITY EVALUATION USING BUNCH BY BUNCH BEAM POSITION METHOD \*

Ning Zhang <sup>†</sup>, Yimei Zhou, Yongbin Leng\*, Shanghai Institute of Applied Physics, CAS, Shanghai 201808, China

## Abstract

In order to improve the efficiency and quality of light in Top-up mode at SSRF, disturbance caused by leakage fields mismatch during injection should be minimized and stable. This could be evaluated by analysis of bunch by bunch residual betatron oscillation data, using this method, instability of tune distribution and damping repeatability could also be calculated. So we could evaluate the beam operation stability by the data analysis and discuss in the paper.

## INTRODUCTION

In Shanghai Synchrotron Radiation Facility (SSRF), the accelerator injection mode has been upgraded from Decay mode to Top-up mode since late 2012<sup>[1]</sup>, aiming to achieve uniform filling. This method results in more frequent beam injections (about 2 minutes per one injection period). Since the injection process involves a variety of equipment, Parameter imperfections can lead to a closed orbit distortion, which will leave a residual betatron oscillation during injection. For beam light users, this disturbance should be as little as possible.

Usually, parameter mismatches during injection mainly refers to:

- (1) Kicker excitation current mismatch (current waveform amplitude and timing).
- (2) Energy or phase mismatch, between the injected bunch from the booster and the stored bunches in the storage ring.
- (3). Mechanical error in the kickers.

Injection performance evaluation and analysis have been done by SSRF BI group <sup>[2][3]</sup>. In the experiment, bunch by bunch position measurement system was employed. A complete residual oscillation distribution was obtained by combining several groups of injection, which could be used for evaluate issue(1), and by harmonic analysis, The spectrum of the injected bunch position signal can be obtained for issue(2). Turn by turn SA data from Libera was used to observe the effect of issue (3).

For SSRF beam operation, the closed orbit distortion caused by kicker leakage field mismatch as well as tune and damping time should be as stable as possible, which would be good for further optimization. So operation stability should be evaluated by long-term measurement and evaluating the variation of parameters from different period.

Work supported by National Natural Foundation of China (11375255 and11375254)

<sup>†</sup> Email: zhangning@sinap.ac.cn \*Email: lengyongbin@sinap.ac.cn

## MESUREMENT SYSTEM

Raw position signals of beam in storage ring are excited by BUTTON BPMs installed in vacuum pipe. For building a bunch-by-bunch position measuring system to obtain the disturbance details of each bunch, the bandwidth of the system should be larger than 250 MHz, the data rates should be equal to or greater than 499.654 MHz (storage ring RF frequency), and the data buffer should be greater than 10 Mb.(determined by the loop damping time 5-6 ms).

The latest bunch by bunch position measurement method in SSRF is synchronous peak sampling at RF frequency<sup>[4]</sup>. The sampled pulse peak data with same phase from 4 input channels were calculated to obtain position and sum value for each bunch. For this purpose, ADQ14 data acquisition board developed by SP-devices Company was employed as Data Processing Board, used for raw BPM signals sampling and bunch position calculation in real-time. The board and chassis component were shown in Figure 1.



Figure 1: Data acquisition board and PXIe chassis forBTB position on-line measurement.

PC-based controller (Data I/O Unit) as well as Data Processing Board, was inserted into NI chassis, which controlled Data Processing Board using PXIe interface. We have designed an EPICS IOC running in Linux OS of the controller to implement DAQ control and data output.

Data Processing Board and Data I/O Unit consists the basic framework of bunch by bunch data acquisition system. By applying different front-end and IOC algorithm, the system could achieve transverse and longitudinal parameters<sup>[5]</sup> measurement. For bunch by bunch position, the front-end was designed for Phrase adjustment, Delay adjustment, Signal attenuation and Generating RF frequency doubling phrase-lock signal for external clock. The system structure is shown in Figure 2.



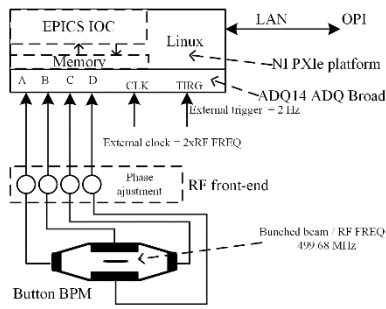


Figure 2: Bunch by bunch position DAQ system diagram in SSRF.

## EXPERIMENT AND DATA ANALYSIS

In SSRF normal Top-up operation, there are 720 buckets in the storage ring. 500 bunches was grouped as 4 bunch-trains in bunched beam, which spaced about 50 empty buckets, beam current was kept around 250mA, the filling pattern is shown as Figure 3. The injected bucket jumps 6 bunches for each injection.

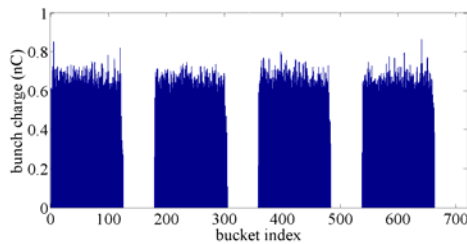


Figure 3: Measured Filling pattern of a snapshot during Top-up operation.

### Bunches Oscillation Processing

Bunch by bunch position data could be recorded and saved during each injection process by the measurement system. Using PYTHON or MATLAB script, individual bunch time-domain waveform could be easily curved, which was shown in Figure 4. The damping time could be calculated by counting the interval of damping.

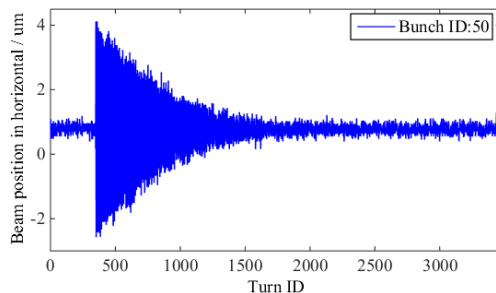


Figure 4: Individual bunch betatron oscillation during injection in horizontal plane.

And normalized frequency spectrum of each bunch was obtained by FFT to position array shown in Figure 5. The oscillation amplitude and tune could be calculated using this method.

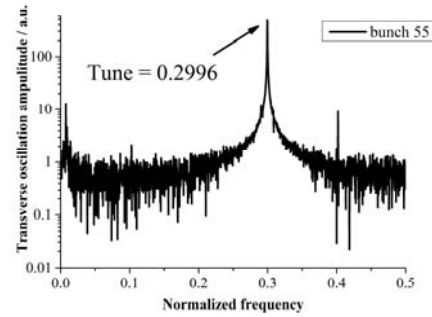
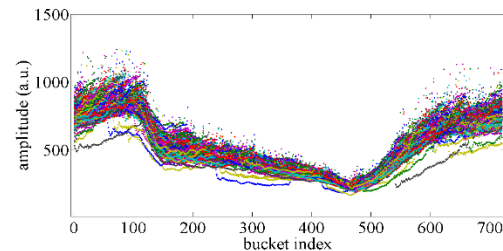


Figure 5: Individual bunch transverse oscillation normalized frequency.

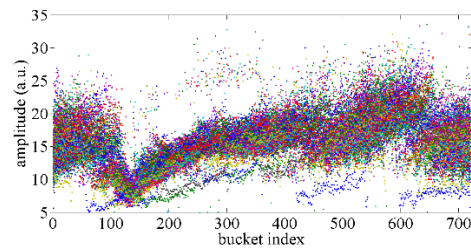
### Beam Parameter Drift Observation and Analysis

For observing the time drift of oscillation amplitude, damping time and tune, and evaluating the injection effect to operation stability, residual oscillation data during 18 hours was recorded and off-line processed. Using the time-domain and harmonic analysis discussed above, bunch by bunch parameters could be extracted and expressed in different way.

Since the effect of kicker leak fields mismatch to the injected bunch is strictly synchronous, residual oscillation distribution for all buckets could be obtained by combining several groups of injection data, stability of leak fields mismatch could be characterized by the time drift of the distribution. Figure 6 showed the long-term amplitude difference of the oscillation in vertical and horizontal plane. And Figure 7 showed the oscillation amplitude distribution variation during time.



(a): Horizontal plane



(b): Vertical plane

Figure 6: Residual oscillation distribution amplitude difference during 18 hours.

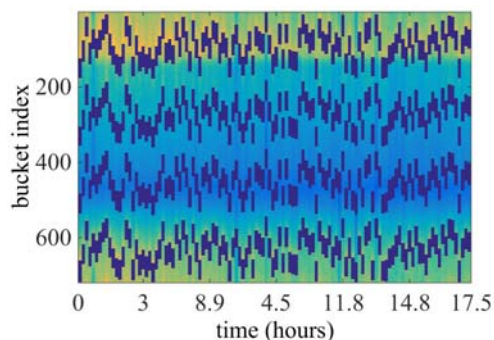


Figure 7: Buckets oscillation amplitude variation during time.

Regarding the bunch train as a whole, the average residual oscillation amplitude is the charge weighted average of each bunch oscillation amplitude. The time drift of the average oscillation amplitude is shown in Figure 8.

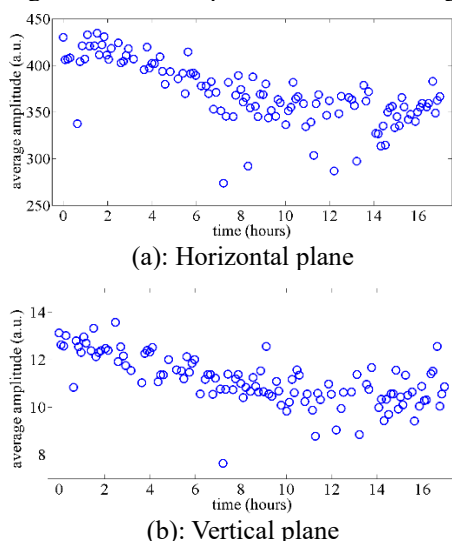


Figure 8: Time drift of average residual oscillation amplitude.

The whole beam damping time in horizontal plane could also be obtained by charge weighted average of the bunches damping, and the long term variation was shown in Figure 9.

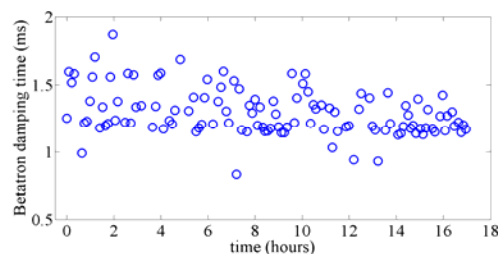


Figure 9: Beam damping time variation in 18 hours.

Tune drift indicate the Lattice structure instability of accelerator system, tune value of individual bunch could be acquired, and the tune distribution variation could also be expressed as Figure 10.

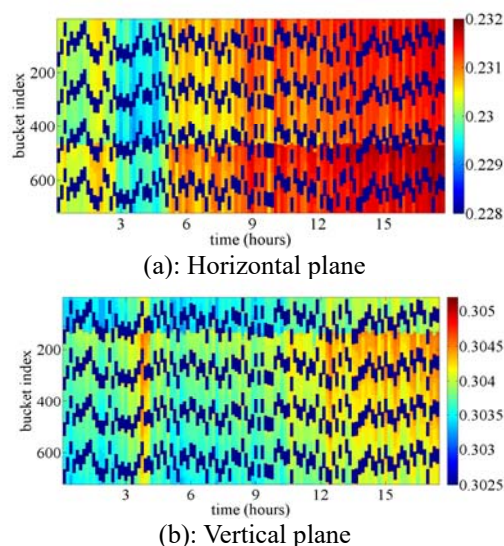


Figure 10: Time drift of tune distribution during budget ID.

## CONCLUSION

The bunch-by-bunch position measurement system is very effective in the evaluation and analysis of SSRF operation instability. It could obtain transient information for the injection and is more conducive to optimizing the injection system.

The analysis of multiple sets of data indicates that the distribution shape of the kicker leakage field is stable, but the long-term observation also showed the time drift of the distribution shape and damping time is serious, which is not constructive to feed-forward compensation in the future. The tune drift means that there is still optimization space for the whole accelerator system. Also, month-level observation is planned to enrich the long-term injection characteristic.

## ACKNOWLEDGEMENT

The authors would like to thank members in physics group and operation group of SSRF who contributed to this work through discussions and suggestions.

## REFERENCES

- [1] Z.T. Zhao, L.X. Yin, Y.B. Leng, "Performance Optimization and Upgrade of the SSRF Storage Ring", in *Proc. IPAC'13*, Shanghai, China, May. 2013, pp. 178-180.
- [2] Y. Yang et al., "Injection performance evaluation for SSRF storage ring", *Chinese Physics C.*, vol. 39, pp. 097003 1-5, 2015.
- [3] Y.B. Yan et al., "Beam Instrumentation System Optimization for Top-up Operation in SSRF", in *Proc. IPAC'13*, Shanghai, China, May. 2013, pp. 589-591.
- [4] N. Zhang, L.W. Lai, and Y.B. Leng, "Transverse Beam Instability Observation and Investigation using Bunch by Bunch On-line DAQ System", *Proceedings of IPAC2017*, Copenhagen, Denmark, May. 2017, pp. 335-337.
- [5] Y.M. Zhou, Y.B. Leng, N. Zhang and H.J. Chen, "Bunch Phase Measurement for Storage Ring", in *Proc. IPAC'17*, Copenhagen, Denmark, May. 2017, pp. 341-344.

# CONTINUOUS BEAM ENERGY MEASUREMENTS IN DIAMOND LIGHT SOURCE

N. Vitoratou\*, P. Karataev

John Adams Institute at Royal Holloway, University of London, Egham, UK

G. Rehm, Diamond Light Source, Oxfordshire, UK

## Abstract

Resonant Spin Depolarization (RSD) is a high precision technique that has been employed by Diamond Light Source (DLS) for beam energy measurements. In this project, we study a new approach to make RSD compatible with user beam operation and provide a continuously updated online measurement. An array of four custom-made scintillation detectors has been installed around the beam pipe, downstream of collimators to capture the highest fraction of lost particles and maximize the count rate. The excitation is gated to half of the stored bunches and the acquisition system counts losses in both halves independently. Using the count in the un-excited part for normalisation suppresses external factors that modify the loss rate. Different parameters of the measurement, like excitation kick strength and duration have been explored to optimise depolarisation and to increase the reliability of the measurement.

## INTRODUCTION AND MOTIVATION

The technique of RSD takes advantage of the natural spin polarisation due to synchrotron radiation emission and provides a high precision energy measurement with a relative uncertainty of typically  $10^{-6}$  [1]. A continuous beam energy measurement employing this technique could reveal any correlations with the photon energy fluctuations and give information about the stability of the bending magnets power supply. Thus, in Diamond Light Source, a method is being developed to make these measurements compatible with the user operation, where the main challenges are not to disturb the stored beam and counteract external factors that could influence the measurement.

## BEAM POLARISATION

The spin of the electron beam will develop a polarisation, due to the emission of the spin-flip radiation, according to Sokolov-Ternov effect, which is antiparallel with the magnetic field of the main bending magnets. In an ideal ring, in the absence of depolarizing effects, the maximum expected beam polarization is 92 % [2]. The amount of polarisation will be a combination of the polarising and depolarising effects that is given by [3] :

$$P(t) = P_{ST} \frac{\tau_d}{\tau_d + \tau_{ST}} \left[ 1 - \exp \left( -\frac{t}{\tau_{ST}} \left( \frac{\tau_d + \tau_{ST}}{\tau_d} \right) \right) \right] \quad (1)$$

where  $P_{ST}$  and  $\tau_{ST}$  are the Sokolov-Ternov values for the equilibrium polarisation level and time constant respectively,

\* Niki.Vitoratou.2016@live.rhul.ac.uk

and  $\tau_d$  the depolarisation time constant. Depolarising effects can occur by horizontal magnetic fields due to closed orbit distortions or quadrupoles misalignments. However, excellent alignment, orbit correction schemes and small vertical emittance in DLS weakens these effects and allow the beam to have an equilibrium polarisation level of 82 %.

Another limit in the polarisation level is introduced by wigglers. The wigglers increase the energy spread which is related with the asymptotic polarisation level given by Sokolov-Ternov effect [4]. This effect will reduce the polarisation level to 60 % for the case of DLS, as it is shown in Fig. 1.

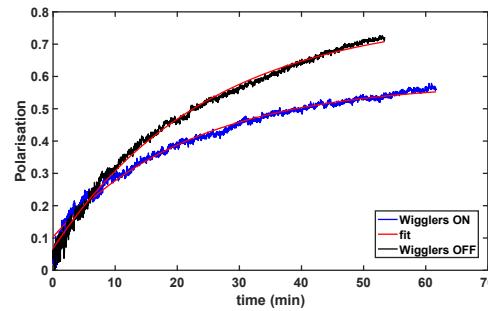


Figure 1: Polarisation build-up of stored beam with wigglers on and off, one hour after injection. The polarisation level is expressed as the relative increase of the lifetime. The lifetime is calculated by the inverse of the recorded beam losses normalised by the beam current [5]. The applied fit is based on Eq. (1).

## BEAM DEPOLARISATION

The spin precession frequency of an ultra-relativistic electron in a magnetic field follows the Thomas-BMT equation which for a light source storage ring where there are no significant solenoid magnetic fields, nor transverse electric fields, can be simplified to the below form [6]:

$$\Omega_z = \omega_0(1 + \alpha\gamma) \quad (2)$$

where  $\omega_0$  is the revolution frequency,  $\alpha$  the gyromagnetic anomaly and  $\gamma$  the relativistic factor. The product  $\alpha\gamma$  is the number of revolutions the spin vector makes about the vertical axis in one revolution of the storage ring defined as the spin tune. The equation above shows the relation between the energy of the beam and the spin precession frequency and by determining the unknown frequency, the energy can be calculated.

For the determination of the spin tune, the stored polarised beam is excited by a horizontal magnetic field produced by a pair of vertical striplines. The magnetic field is set to oscillate in different frequencies that match the fractional part of the spin tune:

$$f_{dep} = (\alpha\gamma - k) \cdot f_{rev} \quad (3)$$

where  $k$  is the integer part of the spin tune. When the excitation frequency corresponds to the spin tune, the spin vector starts to tilt away from the vertical axis by a small amount in consecutive revolutions as a result of the resonance. This will lead to the depolarisation of the beam which indicates the energy of the beam.

### Touschek Particles

The relation between the polarisation of the beam and the Touschek particles is used in this study to determine the level of the beam polarisation. Touschek particles are lost particles that result from a Möller scattering collision between two electrons. The electrons transfer high momentum from transverse to longitudinal motion and exceed the longitudinal acceptance limit. The scattering cross section is spin dependent hence the particle loss rate depends on the polarisation [7]:

$$-\frac{1}{N} \frac{dN}{dt} = \alpha [C(\varepsilon) + F(\varepsilon)P^2]N \quad (4)$$

where,

$$C(\varepsilon) = \varepsilon \int_{\varepsilon}^{\infty} \frac{1}{u^2} \left\{ \left( \frac{u}{\varepsilon} \right) - \frac{1}{2} \ln \left( \frac{u}{\varepsilon} \right) - 1 \right\} e^{-u} du \quad (5)$$

$$F(\varepsilon) = -\frac{\varepsilon}{2} \int_{\varepsilon}^{\infty} \frac{1}{u^2} \ln \frac{u}{\varepsilon} e^{-u} du \quad (6)$$

and

$$\varepsilon = \left( \frac{\delta_{acc}}{\gamma\sigma_{x'}} \right)^2 \quad (7)$$

where  $\delta_{acc}$  is the momentum acceptance,  $\gamma$  is the Lorentz relativistic factor and  $\sigma_{x'}$  is the standard deviation of the beam distribution in horizontal angle. For a measurement, these numerical integrals, can be treated as constants. Since the  $F(\varepsilon)$  integral is a negative number, a partial depolarisation will cause a rise of the loss rate.

### Froissart-Stora Equation

The initially vertical polarised beam which is perturbed by a horizontal magnetic field can be depolarised when the perturbation induces a spin resonance. The Froissart-Stora formula describes the spin transport through a single resonance where the final polarisation is given by [8]:

$$P_y(\infty) = \left( 2e^{\frac{\pi|\epsilon|^2}{2\alpha}} - 1 \right) P_y(-\infty) \quad (8)$$

where  $\epsilon$  is the resonance strength,  $\alpha$  the rate of resonance crossing which is given as function of the frequency step  $\Delta f$ ,

the excitation time  $\Delta t$  and the revolution frequency  $f_0$  by the equation  $\alpha = \frac{\Delta f_{rf}}{2\pi f_0^2 \Delta t}$ .  $P_y(\infty)$  and  $P_y(-\infty)$  refer to the initial and final polarisation, respectively. This formula shows that a large polarization loss can occur when the crossing speed is comparable to the square of the resonance strength.

## BEAM ENERGY MEASUREMENT SETUP

The setup for the energy measurements by means of beam depolarisation consists of a device that generates the depolarisation field and the beam loss monitors that record the beam losses and witness the beam depolarisation.

The horizontal oscillating magnetic field is generated by the vertical striplines to depolarise the vertical oriented electron spin. Two 30 cm long kicker striplines, part of the transverse multibunch feedback system (TMBF), can produce magnetic fields up to  $8 \mu\text{Tm}$ . Two additional characteristics that are integrated into TMBF system assist to perform the energy measurements during user operation. Firstly, there is the possibility of using different amplifications in the strength of the kickers in order not to disturb the small vertical size of the stored beam during the excitation. Another characteristic is a numerically control oscillator that can be modulated with an internally synchronized rectangular waveform. This waveform is used to gate the sinusoidal signal and consequently the magnetic field generated in the striplines. By this way, the excitation is acting only on a part of the beam as it is illustrated in Fig. 2.

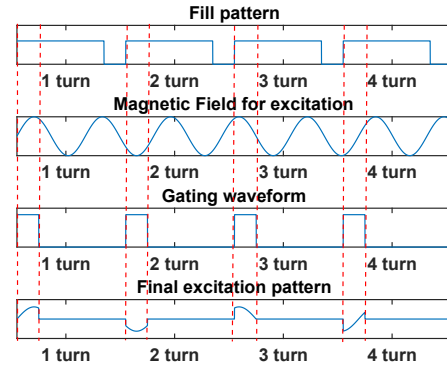


Figure 2: The sinusoidal signal is gated according to a rectangular waveform. By this way, only one selected part of the fill pattern is excited, and the rest is unaffected.

The beam loss monitor setup consists of a set of four detectors connected with a commercial acquisition instrument (Instrumentation Technologies Libera BLM [9]). Four blocks, 15 cm long, made by scintillator EJ204 [10], as it is shown in Fig. 3, were manufactured in order to fit around the octagonal shape of the beam pipe, and were installed downstream the collimators, where there is a limited physical aperture. Based on results from a radiochromic film that was installed in the same area, the highest fraction of the beam losses is captured with this custom-made blocks and the count rate is maximised [11].



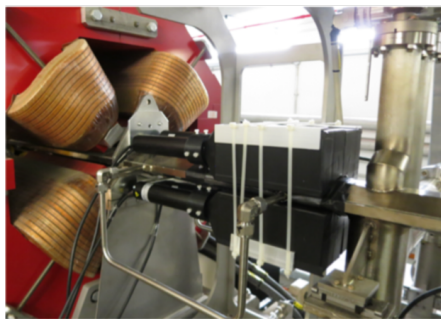


Figure 3: The four blocks of scintillator are installed downstream around the beam pipe to capture the highest fraction of the beam losses after the collimators, where the physical aperture is limited.

The four detectors are attached with a photomultiplier with a bi-alkali photocathode that matches with the wavelength of the scintillator light. Thin silicon pads were placed between the photocathode and the ending of the scintillator block in order to avoid any reflections when the light passes through the two different materials. The monitors are protected by a thin sheet of lead 1.3 mm thick from background ionizing radiation. The photomultipliers are connected with the acquisition instrument using two hardware interfaces. Four coaxial connectors are used for signal input and four RJ-25 connectors for power supplying and voltage gain control. The instrument is set with low impedance input of 50  $\Omega$  for short individual pulses. The input signals are sampled using an ADC with a clock which is locked to a quarter of bunch frequency, a little below 125 MHz.

The ADC data is continuously monitored and counted based on the difference between the two neighbouring samples. A dead time after a detected loss and a difference threshold are set and the counter increments the counts based on an algorithm that can detect individual pulses. The differential counting is an additional feature of the acquisition system to avoid pile-up events that were observed in pulses produced by the scintillator. The thresholds were chosen in order to avoid false triggers from electronic noise. Another characteristic of the acquisition system is the gating of the ADC samples. Two processing windows are generated synchronised to the revolution clock at 533 kHz. The processing window length is set to the number of ADC samples, which means that the beam loss events are accounted for over every four bunches. The processing delay is set to receive two independent sets of ADC samples to align with the excited/not excited parts of the fill pattern.

## ENERGY MEASUREMENTS

The new approach of this project is to make the energy measurements compatible with the user operation. Diamond Light Source operates with a small vertical emittance in the range of 8 pm rad and the main challenge is not to affect this quantity when the beam is excited for depolarisation. For this reason, a low current is applied in the striplines that is

enough to depolarise the beam but not to affect the size of the beam.

Another factor that disturbs these measurements is the beam losses that are created by different causes than depolarisation. To overcome these problems the idea of gating the excitation pattern and the beam losses was introduced. One part of the beam is excited and one mask of the acquisition system counts the resulting beam losses, while the second mask counts the beam losses from another, equivalent in charge, part of the beam. Thus, external factors that modify losses, like the changing of insertion device gaps, will be recorded by the two masks, but the losses that are created due to depolarisation will be seen only by one mask. Dividing the counts from the two masks, the ratio will be equal to one and only when the depolarisation occurs, this ratio will change and will indicate the spin precession frequency, as it is shown in Fig. 4.

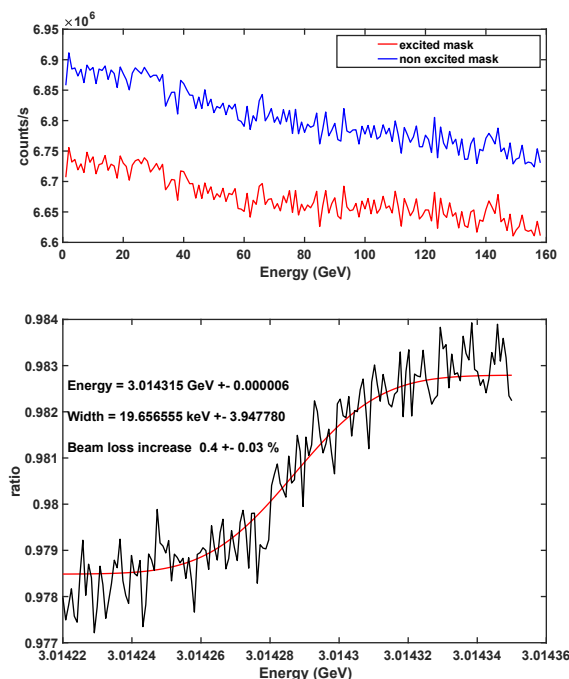


Figure 4: The red plot (mask 1) corresponds to the beam losses from the excited part of the beam while the blue plot (mask 2) to the beam losses of the unexcited part. The ratio between these two masks shows the depolarisation of the excited part and counteracts the common decreasing trend of the beam losses due to the current drop.

During the energy measurements, the beam is excited in different frequencies for a certain amount of time depending on the strength of the excitation. As it was referred, the excitation strength was chosen to be low, and this implies that for a decent amount of depolarisation the beam should be excited for a long time according to Froissart-Stora formula. Typically, scans last more than ten minutes which is the time interval for top-up at DLS. The top-up system selects to fill the bunches with the lowest charge and creates inequalities between the losses of the two masks, as the losses depend

on the total charge in each mask. Hence, the ratio between the counts of the two masks is recorded before and after the injection, without beam excitation, and the difference is calculated and included in the analysis. Using this method, we can have long scans keeping the count ratio of the two masks unrelated with the top-up injections.

In the end, the solution to another problem that has arisen due to the high sensitivity of the beam loss detectors is explored. The geometry of the detectors is optimised to capture the highest fraction of the beam losses and maximise the counting rate. As the data follow Poisson statistics a high number of counts means high precision in the measurements and can reveal any change that happens during the excitation, as for example, some weak higher order betatron resonances that are excited and create losses that interfere with the beam loss data due to depolarisation. For this purpose, after every excitation in each frequency, the scan is suspended for one second, the beam losses due to betatron resonances fade and only the losses due to depolarisation remain. With these techniques, energy measurements were accomplished in parallel with the user operation, giving continuous readings of the energy of the stored electron beam (Fig. 5).

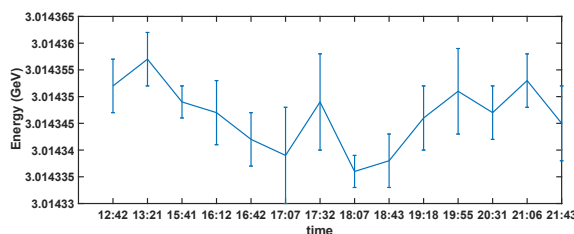


Figure 5: Continuous measurements of the energy during one day of user operation.

## DISCUSSION

The optimisation of the continuous energy measurements needs a better understanding of the beam loss rise due to depolarisation, which from our recent results cannot be higher than 0.4 % with the nominal settings that are used in the control room. A higher increase in the losses would make this measurement more precise, with a smaller fit error. Using stronger magnetic fields in the striplines, the maximum rise that has been achieved is 1 %. However, this is not in agreement with the 5 % decrease that has been observed during the beam polarisation. Different steps in the frequency, as well as in the duration of the excitation did not improve the beam loss rise. More studies are carried out in this direction with the goal of increasing the beam losses step when the depolarisation occurs.

## SUMMARY

The level of polarisation that can be achieved during the user operation, which includes wigglers on, has been evaluated. The characteristics of the measurements setup and the details of the technique that are used for the energy measurements have been described. A continuous reading of the energy every thirty minutes, that is the duration of each scan has been achieved and more details regarding the optimisation of the measurement are subject of the ongoing studies.

## REFERENCES

- [1] K. P. Wootton *et al.*, “Storage ring lattice calibration using resonant spin depolarization,” *Physical Review Special Topics - Accelerators and Beams*, vol. 16, no. 7, pp. 1–13, 2013.
- [2] J. R. Johnson, R. Prepost, D. E. Wiser, J. J. Murray, R. F. Schwitters, and C. K. Sinclair, “Beam polarization measurements at the SPEAR storage ring,” *Nuclear Instruments and Methods In Physics Research*, vol. 204, no. 2-3, pp. 261–268, 1983.
- [3] I. Martin, M. Apollonio, R. Fielder, G. Rehm, and R. Bartolini, “Energy measurements with resonant spin depolarisation at Diamond,” in *Proc. of IPAC’11*, San Sebastian, Spain, Sep. 2011, pp. 1404–1406, paper TUPC159.
- [4] A. Blondel and J. M. Jowett, “Dedicated wigglers for polarization,” CERN, Geneva, Tech. Rep. CERN-LEP-Note-606., 1988. <https://cds.cern.ch/record/442913>
- [5] T. Y. Lee, J. Choi, and H. S. Kang, “Simple determination of Touschek and beam-gas scattering lifetimes from a measured beam lifetime,” *Nuclear Instruments and Methods in Physics Research, Section A: Accelerators, Spectrometers, Detectors and Associated Equipment*, vol. 554, no. 1-3, pp. 85–91, 2005.
- [6] S. R. Mane, Y. M. Shatunov, and K. Yokoya, “Spin-polarized charged particle beams in high-energy accelerators,” *Reports on Progress in Physics*, vol. 68, no. 9, pp. 1997–2265, 2005.
- [7] N. Carmignani, “Touschek Lifetime Studies and Optimization of the European Synchrotron Radiation Facility,” pp. 9–19, 2016. doi:10.1007/978-3-319-25798-3
- [8] M. G. Minty and F. Zimmermann, *Measurement and control of charged particle beams*, ser. Particle acceleration and detection. Springer: Berlin, 2003.
- [9] *Beam Loss Monitor readout electronics*, Instrumentation Technologies, <http://www.i-tech.si>
- [10] Eljen Technology. <http://www.eljentechnology.com>
- [11] N. Vitoratou, P. Karataev, and G. Rehm, “Beam loss monitors for energy measurements in Diamond Light Source,” in *Proc. of IBIC’17*, Grand Rapids, MI, USA, Aug. 2017, pp. 482–486. doi:10.18429/JACoW-IBIC2017-TH1AB3

# USING A TE011 CAVITY AS A MAGNETIC MOMENTUM MONITOR\*

J. Guo#, J. Henry, M. Poelker, R. A. Rimmer, R. Suleiman, H. Wang,  
JLAB, Newport News, VA 23606, USA

## Abstract

The Jefferson Lab Electron-Ion Collider (JLEIC) design relies on cooling of the ion beam with bunched electron beam. The bunched beam cooler complex consists of a high current magnetized electron source, an energy recovery linac, a circulating ring, and a pair of long solenoids where the cooling takes place. A non-invasive real time monitoring system is highly desired to quantify electron beam magnetization. The authors propose to use a passive copper RF cavity in TE011 mode as such a monitor. If such a cavity is powered actively, it is also possible to be used as a beam magnetizer.

## INTRODUCTION

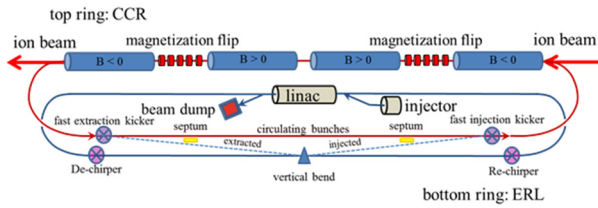


Figure 1: JLEIC Circulating Cooler Ring (CCR).

The proposed JLEIC is a high luminosity electron ion collider. The key to achieve JLEIC's luminosity goal is to maintain low ion emittance through bunched beam electron cooling in solenoid channels during the collision, as shown in Fig. 1. To avoid rotation of the electron beam in the cooling channel, the JLEIC cooling electron beam needs to be magnetized before entering the cooling channel [1]. Magnetized DC electron cooling is also necessary during the JLEIC ion beam formation.

Non-invasive measurement of the magnetic moment of a charged particle beam has long been on the wish-list of beam physicists. The previous efforts were mainly focused on measuring the beam polarization [2, 3, 4], which is in the order of  $\hbar/2$  per electron or proton. Even after enhanced by the Stern-Gerlach polarimetry, the RF signal in the cavity generated by the beam is still extremely hard to measure.

The magnetic moment per particle of the magnetized beam is typically a few orders of magnitude higher. As a demonstration of the source for the JLEIC e-cooler, the magnetized beam generated at JLab GTS [5] can have a magnetic moment  $M=200$  neV-s or  $3.0 \times 10^8 \hbar$ . The JLab GTS beam also has a typical energy of 300 keV and a low

$\gamma$ . These parameters make the magnetic moment more likely to be detected with an RF cavity.

One potential concern of the resonance type magnetic moment monitor is the signal excited by the non-magnetized current, usually due to the longitudinal component of electric field along the beam path. TE011 mode in a cylindrical symmetric cavity will only have azimuthal E-field, making it an ideal candidate for magnetic moment measurement.

## INTERACTION BETWEEN PILLBOX TE011 MODE AND MAGNETIZED BEAM

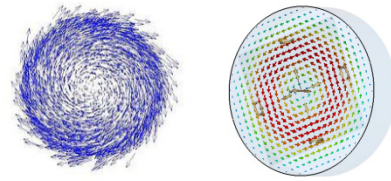


Figure 2: Left: Transverse motion of a longitudinally magnetized beam; Right: Transverse electric field in TE011 mode of a pillbox cavity.

The angular momentum and magnetic momentum of a charged particle is determined by its motion in azimuthal direction, as shown in Fig. 2, left.

$$\begin{aligned} L &= \gamma m \rho^2 \dot{\phi} \\ M &= L \frac{e}{2mc} \end{aligned} \quad (1)$$

For a cylindrical symmetric RF cavity, the electric field of TE011 mode has only azimuthal component, and will be zero in other directions (radial or longitudinal), as shown in Fig. 2, right. In the vicinity of the cavity axle, the TE011 mode azimuthal E-field's amplitude can be approximated as

$$E_{\phi}(z, t, \rho) = E_{\phi}(z, t) \rho \quad (2)$$

Assuming that the beam-cavity interaction has negligible perturbation on beam trajectory,  $\rho^2 \dot{\phi}$  is almost constant during the beam's path through the cavity. By integrating E-field tangential to the particle trajectory, the acceleration voltage when a particle travels through the cavity can be calculated as

$$\begin{aligned} V_{\perp} &= \int E_{\phi}(z, t, \rho) \rho d\phi \\ &= \frac{\rho^2 \dot{\phi}}{\beta c} \int E_{\phi}(z, t = \frac{z-z_0}{\beta c}) dz \end{aligned} \quad (3)$$

\* Authored by Jefferson Science Associates, LLC under U.S. DOE Contract No. DE-AC05-06OR23177 and supported by Laboratory Directed Research and Development funding. The U.S. Government retains a non-exclusive, paid-up, irrevocable, world-wide license to publish or reproduce this manuscript for U.S. Government purposes #jguo@jlab.org

The cavity transverse R/Q is

$$\frac{R_{\perp}}{Q} = \frac{V_{\perp}^2}{\omega U} \propto (\phi \rho^2)^2 \quad (4)$$

The power of the extracted RF signal is

$$P_{emitted} = I^2 \frac{R_{\perp}}{Q} \frac{Q_{loaded}^2}{Q_{ext}} \propto I^2 \langle (M/\gamma)^2 \rangle \quad (5)$$

which is proportional to the square of average magnetic moment of the beam and will be maximized if the cavity has critical coupling.

The cavity is basically detecting the rotation of the beam along the cavity's electric center axle. As a result, it cannot differentiate the rotation of beam center trajectory relative to the cavity's electric center axle. The beam needs to be well aligned to the cavity center to avoid this background. The wire stretching technique [6] can be used to find the cavity's electric center.

## CAVITY RF DESIGN AND SCALING

When the cavity scales with constant aspect ratio, the emitted RF power scales as

$$P_{emitted} \propto \omega^{1.5} \rho^4 \phi^2 \quad (6)$$

If the cavity beampipe size is not the limiting factor of the beam's maximum angular moment,  $P_{emitted} \propto \omega^{1.5}$ , so a smaller cavity with higher frequency will be more sensitive to the beam magnetization. With scaled fabrication error, small cavities also have lower longitudinal impedance. However, if the cavity beampipe size limits the beam's size and maximum angular momentum, a larger cavity can produce more RF signal with the same beam current.

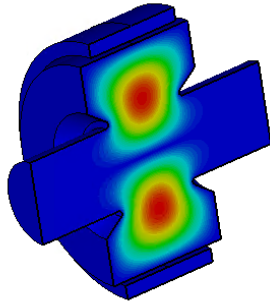


Figure 3: Electric field in the 2994MHz TE011 cavity.

Our final design chose a frequency of 2994 MHz instead of 1497 MHz, as any subharmonic beam can drive the cavity. The smaller cavity has better mechanical strength and is much easier to fabricate. The cavity is basically a pillbox with 2.375" beampipes. Nosecones are added to enhance the transit time factor (TTF) and impedance. The larger relative size of the beampipes resulted in stronger fringe field, cancelled the impedance gained from the reduced cavity size. For  $M=200$  neV-s  $\beta=0.78$  beam, the 2994 MHz cavity  $R_{\perp}/Q$  improves to

15.6  $\mu\Omega$ ; with critical coupling, the transverse impedance  $R_{\perp}=286$  m $\Omega$ , with  $\sim 3.6\mu W$  power expected to be extracted from 5 mA beam. The magnitude of the electric field in the cavity is shown in Fig. 3, and Fig. 4 shows the E-field tangential to the beam trajectory seen by a particle with  $\beta=0.78$  rotating along the 2994 MHz cavity's longitudinal axle.

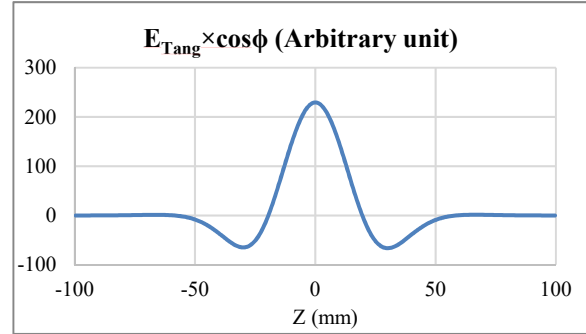


Figure 4: Tangential E-field seen by a  $\beta=0.78$  beam with  $x'=50$  mrad,  $y_0=0.01$  m, equivalent to  $M=2127$  neV-s.

To reduce the background signal excited by the beam current, the longitudinal R/Q in the TE011 mode needs to be controlled significantly below the transverse impedance, likely in  $\sim 100n\Omega$  level, with careful coupler design and fabrication precision.

## Cavity Coupler Design

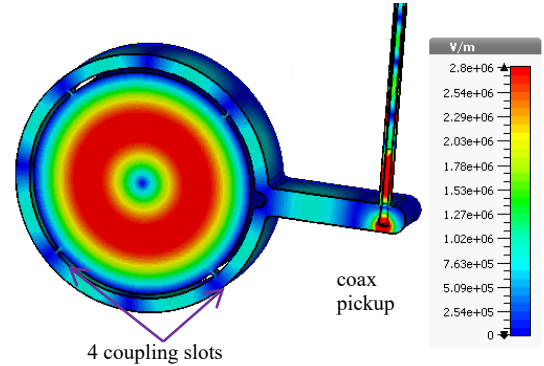


Figure 5: E-field in the coupler.

The coupler design strategy for this cavity to achieve low longitudinal impedance is to preserve the longitudinal mirror symmetry and the cylindrical symmetry as much as possible. We chose a design similar to the SLAC X-band wrap-around rectangular waveguide TE10 to circular TE01 mode launcher [7, 8]. As shown in Fig. 5, the cavity has four equally 90° spaced longitudinal slots coupling to the wrap-around waveguide, and a matched lip combining the two branches of the waveguide. The waveguide width is adjusted so the slot spacing equals  $\lambda_g$ . To make the waveguide width slightly smaller than the optimized cavity length, the number of slots has to be chosen at four. A matched coax pickup will couple to the instruments. The slot size is designed to achieve slight overcoupling based on ideal copper conductivity, budgeting for conductivity loss and mismatch in the coax pickup.



The four slots coupler design will be sensitive to TE(4N)xx modes, and rejects the other modes. This helps to filter out most of the noise from the unwanted modes. The frequencies of TE411 and TE811 modes can be tuned away from possible bunch excited frequencies. For the prototype, the only damping mechanism for the other HOMs and LOMs is the cavity wall loss, which could be sufficient for the purpose of proof-of-principal. For a device to be installed in an operating accelerator, beampipe dampers can be added.

## CAVITY FABRICATION

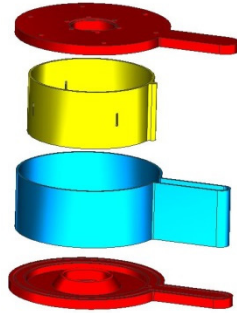


Figure 6: Exploded view of the cavity's copper parts.

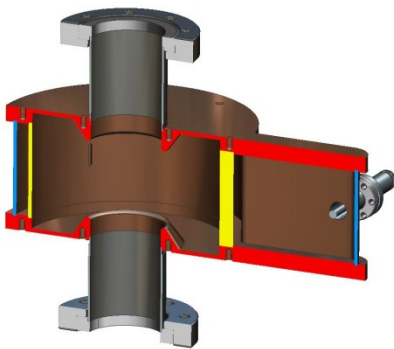


Figure 7: Cut view of the assembled cavity.

The mechanic design and choice of fabrication process for this cavity focus on minimizing the deformation and preserving the symmetry. The main cavity body consists of four parts machined from three blocks of OFHC copper, including two end-plates, the inner cavity wall, and the outer wrap-around waveguide wall, as shown in Fig. 6. The copper material was stress relieved before machining. The parts are machined with high precision wire EDM (electrical discharge machining). The four copper parts and two stainless steel beampipes will be brazed together, as shown in Fig. 7. RF bench measurement can be done by clamping the parts together before the final braze. Currently the cavity parts are being machined by our collaborator Electrodynamics in Albuquerque, NM. Figure 8 shows the test piece inner/outer wall machined with one piece of aluminium.

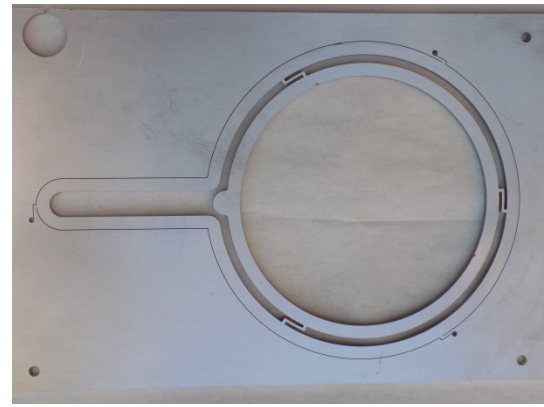


Figure 8: Cavity inner/outer wall wire EDM with a thin test piece of aluminium.

## SUMMARY

We proposed and designed a Beam Magnetic Momentum Monitor using an RF cavity in TE011 mode. The RF signal power excited by the beam is theoretically proportional to the square of the beam's magnetic momentum. For low energy beam (not fully relativistic), the cavity could provide sufficient signal strength and low noise. The prototype cavity is under fabrication. Such a cavity also has the potential to be adopted for Stern-Gerlach polarimetry, with possible improved sensitivity and noise level compared to previous attempts.

## REFERENCES

- [1] S. Abeyratne *et al.*, "MEIC Design Summary", 2015, arXiv:1504.07961
- [2] Ya. S. Derbenev, "RF-resonance Beam Polarimeter: Part 1. Fundamental Concepts", *Nucl. Instr. Meth. A*, vol. 336, pp. 12-15, 1993.
- [3] M. Conte *et al.*, "The Stern-Gerlach Interaction between a travelling particle and a time varying magnetic field", arXiv:physics/0003069v1
- [4] P. Cameron *et al.*, "Proposal for a Cavity Polarimeter at MIT-Bates", in *Proc. PAC'01*, Chicago, May 2001, paper WPAH136.
- [5] M. Mamun *et al.*, "Production of Magnetized Electron Beam from a DC High Voltage Photogun", in *Proc. IPAC'18*, Vancouver, BC, Canada, May 2018. doi:10.18429/JACoW-IPAC2018-THPMK108
- [6] G. Park *et al.*, "Improvement of Wire-Stretching Technique to the RF Measurements of E-Center and Multipole Field for the Dipole Cavities", in *Proc. IPAC'18*, Vancouver, BC, Canada. doi:10.18429/JACoW-IPAC2018-THPML095
- [7] S. Tantawi *et al.*, "The Generation of 400-MW RF Pulses at X-Band Using Resonant Delay Lines", *IEEE Trans. on MTT*, vol. 47, no. 12, Dec. 1999
- [8] C. Nantista, "Overmoded Waveguide Components for High-Power RF", in *Proc. 6th Workshop on High Energy Density and High Power RF*, Berkeley Springs, West Virginia, Jun. 2003, *AIP Conference Proceedings*, vol. 691, p. 263, 2003, <https://doi.org/10.1063/1.1635127>

# IDENTIFICATION OF FAULTY BEAM POSITION MONITOR BASED CLUSTERING BY FAST SEARCH AND FIND OF DENSITY PEAKS \*

R. T. Jiang<sup>†</sup>, Y. B. Leng<sup>‡</sup>, F. Z. Chen, Z. C. Chen

Shanghai Institute of Applied Physics, Chinese Academy of Sciences, 201800 Shanghai, China

## Abstract

The accuracy and stability of beam position monitors (BPMs) are important for all kinds of measurement systems and feedback systems in particle accelerator field. A proper method detecting faulty beam position monitor or monitoring their stability could optimize accelerator operating conditions. With development in machine learning methods, a series of powerful analysis approaches make it possible for detecting beam position monitor's stability. Here, this paper proposed a clustering analysis approach to detect the defective BPMs. The method is based on the idea that cluster centres are characterized by a higher density than their neighbours and by a relatively large distance from points with higher densities. The results showed that clustering by fast search and find of density peaks could classify beam data into different clusters on the basis of their similarity. And that, aberrant data points could be detected by decision graph. So the algorithm is appropriate for BPM detecting and it could be a significant supplement for data analysis in accelerator physics.

## INTRODUCTION

The storage ring in SSRF is equipped with 140 BPMs located at 20 cells of the storage ring to monitor the beam dynamics [1]. The BPMs at the beam lines after the insertion devices (ID) or the bending magnets are of great importance, because they also serve as the orbit feedback system to ensure stability of the electron Beams [2]. Meanwhile, the BPM confidence levels included in the feedback system can be used to estimate stability of the beam dynamics. Some BPMs can be also used to do measurements other than the beam position, such as the (relative) beam current or life time. Therefore, an abnormal BPM should be found and treated and a beam position monitor (BPM) system is an essential diagnostic tool in storage ring of a light source.

A typical BPM system consists of the probe (button-type or stripline-type), electronics (Libra Electronics/ Brilliance in SSRF) and transferring component (cables and such). Ever since the SSRF commissioning in 2009, the BPM have occurred all kinds of malfunction. They were permanently damage of individual probe or corresponding cable, misaligned (position/angle) probes, high-frequency vibrations, electronics noise, and others. These faults mean totally useless of the signals from the BPM, which should be ignored until its replacement or repair. Hence, it is essential

to find an effective method to detect the faulty BPM for operation of the storage ring.

With development in machine learning methods, a series of powerful analysis approaches make it possible for detecting beam position monitor's stability. Cluster analysis is one of machine learning methods. It is aimed at classifying elements into categories on the basis of their similarity [3]. Its applications range from astronomy to bioinformatics, bibliometric, and pattern recognition. Clustering by fast search and find of density peaks is an approach based on the idea that cluster centres are characterized by a higher density than their neighbours and by a relatively large distance from points with higher densities [4]. This idea forms the basis of a clustering procedure in which the number of clusters arises intuitively, outliers are automatically spotted and excluded from the analysis, and clusters are recognized regardless of their shape and of the dimensionality of the space in which they are embedded. In addition to, it is able to detect nonspherical clusters and to automatically find the correct number of clusters.

Based on the advantage of clustering by fast search and find of density peaks, this study researches the stability of beam position monitors to locate the BPM malfunctions at SSRF.

## EXPERIMENTAL DATA AND ANALYSIS METHOD

In this study, the experimental data were collected from the transverse oscillation of X direction. In general, the fluctuation of transverse oscillation of X direction means the stability of beam position monitors and the malfunctions could be judged by the abnormal fluctuations. It also has an important problem that is to detect the performance differences of different BPMs. Therefore, this study research the accuracy and stability of beam position monitors based on the data of transverse oscillation of X direction. Theoretically, the BPM could be considered as malfunction when its fluctuation ranges beyond the range of horizontal  $\beta$ -function which is reference value. On the other hand, the performance differences of different BPMs were be expect to distinguish by different cluster centres based on cluster analysis.

The clustering by fast search and find of density peaks has its basis in the assumptions that cluster centres are surrounded by neighbours with lower local density and that they are at a relatively large distance from any points with a higher local density. For each data point  $i$ , we compute two quantities: its local density  $\rho_i$  and its distance  $\delta_i$  from points of higher density. Both these quantities depend only

\* Work supported by National Nature Science Foundation of China (No.11375255)

<sup>†</sup> jiangruitao@sinap.ac.cn

<sup>‡</sup> lengyongbin@sinap.ac.cn

on the distances  $d_{ij}$  between data points, which are assumed to satisfy the triangular inequality. The local density  $\rho_i$  of data point  $i$  is defined as

$$\rho_i = \sum_j \chi(d_{ij} - d_c) \quad (1)$$

where  $\chi(x) = 1$  if  $x < 0$  and  $\chi(x) = 0$  otherwise, and  $d_c$  is a cutoff distance. Basically,  $\rho_i$  is equal to the number of points that are closer than  $d_c$  to point  $i$ . The algorithm is sensitive only to the relative magnitude of  $\rho_i$  in different points, implying that, for large data sets, the results of the analysis are robust with respect to the choice of  $d_c$ . In this paper, the  $d_c$  is 0.02. On the other hand,  $\delta_i$  is measured by computing the minimum distance between the point  $i$  and any other point with higher density:

$$\delta_i = \min_{j: \rho_j > \rho_i} (d_{ij}) \quad (2)$$

For the point with highest density, we conventionally take  $\delta_i = \max_j (d_{ij})$ . Note that  $\delta_i$  is much larger than the typical nearest neighbour distance only for points that are local or global maxima in the density. Thus, cluster centres are recognized as points for which the value of  $\delta_i$  is anomalously large. Generally, the value of  $\delta_i$  and  $\rho_i$  represent whether the point is cluster centre, the typical characteristic of cluster centre is the value of  $\delta_i$  and  $\rho_i$  are larger. Decision graph could depict the value of  $\delta_i$  and  $\rho_i$  and show which points are cluster centre.

## RESULTS AND DISCUSSION

Generally, the BPM malfunctions could be detected by the compare of actual transverse oscillation and the theoretical  $\beta$ -function. In the data processing, the BPM signals are 140 ID\* 2048 turns [5]. If the maximum amplitude of each BPM signal in 2048 turns exceeds the range of  $\beta$ -function, the BPM must be fault. Figure 1 showed that the maximum amplitude (normalized) of each BPM signal is normal, thus it is ineffective method to detect BPM. But the spectrum information can reflect the malfunction of BPMs.

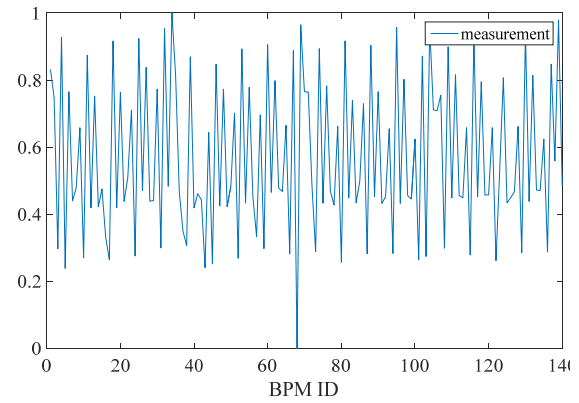
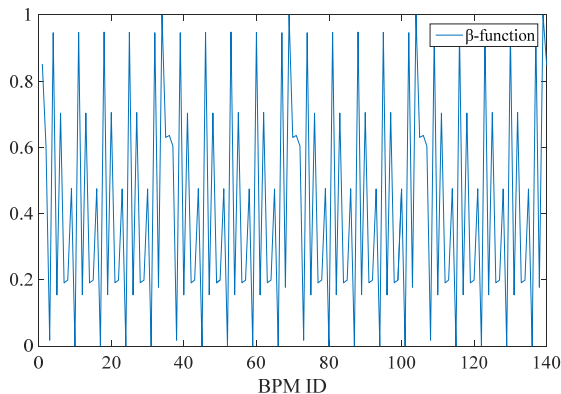
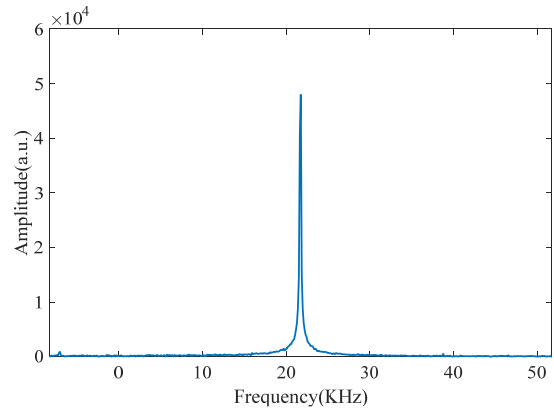
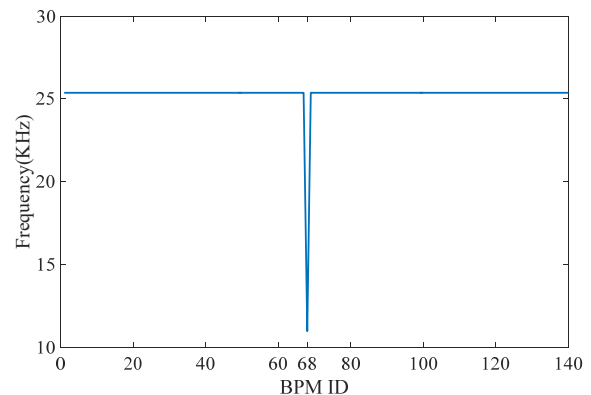


Figure 1: Transverse oscillation of x direction.

The spectrum information with respect to the 1# BPM is shown in Fig. 2(a) and the spectrum information of all BPM is showed in the Fig. 2(b). From the spectrum information of Fig. 2(b), it could be concluded that the 68# BPM is malfunction. Because its centre frequency is abnormal compared to other BPMs.



(a) Fourier Spectrum of 1#BPM



(b) Frequency of all BPMs

Figure 2: Spectrum of BPMs.

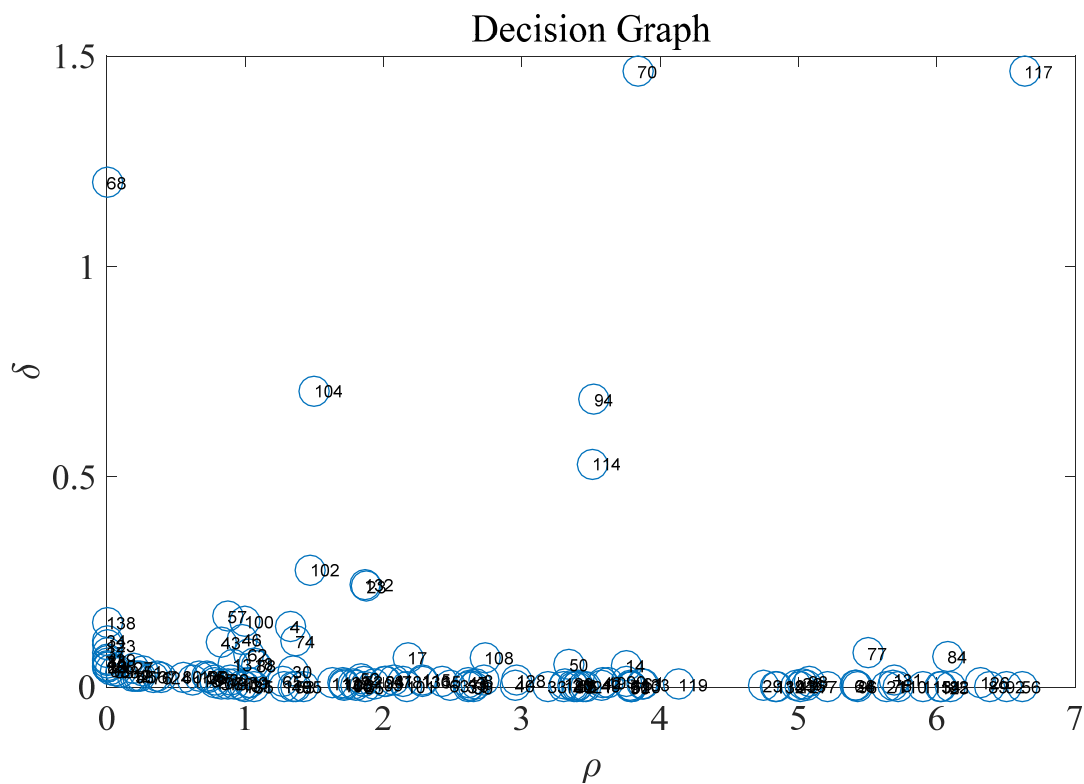


Figure 3: Decision graph for the data.

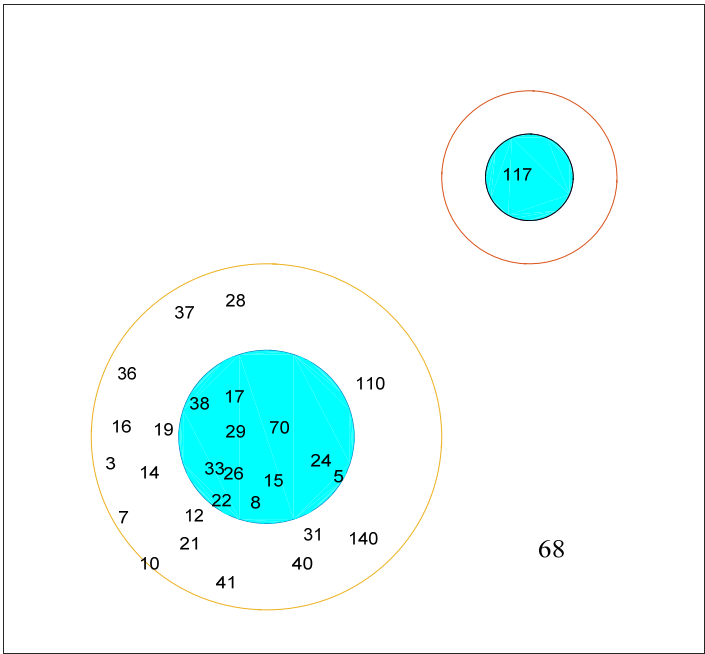


Figure 4: Clustering distribution.



Another key problem is to detect the performance differences of different BPMs. The research used the amplitude value of centre frequency of each BPM to performance cluster analysis. The idea comes from the basic assumption: if the data belongs to the same cluster, the feature of data should be same.

Based on the clustering by fast search and find of density peaks, the decision graph is showed in Fig. 3. As anticipated, the only points of high  $\delta$  and relatively high  $\rho$  are the cluster centres. 70 and 117 are two cluster cores in Fig. 3. Points 68 has a relatively high  $\delta$  and relatively low  $\rho$  because it is isolated, it can be considered as cluster composed of a single point, namely, meaning a faulty BPM.

After the cluster centres have been found, each remaining point is assigned to the same cluster as its nearest neighbour of higher density. The all BPMs' cluster is shown in Fig. 4. The BPMs which are marked number belong to the first core, the other BPMs belong to another core. The performance differences of different BPMs stability of beam position monitors could be judged by clustering distribution. Therefore, the result demonstrates the power of the algorithm on detecting the accuracy and stability of beam position monitors.

## CONCLUSION

As the key beam diagnostics tool, BPM systems are widely equipped in all kinds of accelerators and are being used in daily operation and machine study. To better ensure the operation of the light source, a proper method detecting faulty beam position monitor or monitoring their stability is essential. This study proposed a cluster analysis method based on clustering by fast search and find of density peaks to search faulty BPMs.

The experimental results demonstrate that the proposed cluster analysis method could capture the accuracy and stability of beam position monitors. Especially, the decision graph could be find more key information about BPMs. Considering future accelerator projects that will require more challenging optics control and more powerful analysis methods will be needed, the proposed method would be meaningful in the field of beam diagnosis.

## REFERENCES

- [1] Y.B. Leng *et al.*, Beam position monitor system for SSRF storage ring, *Nucl Sci Tech*, vol.33, no.6, pp. 401–404, 2012.
- [2] Z. C. Cheng *et al.*, “Performance evaluation of BPM system in SSRF using PCA method”. *CPC*, vol. 38, no. 6, pp. 112-116, 2014.
- [3] P. O. Brown *et al.*, “Cluster analysis”, *Qual. Quant.* vol. 14, no.1, pp. 75-100, 1980.
- [4] Rodriguez *et al.*, “Clustering by fast search and find of density peaks”, *Science*, vol. 344, no. 6191, p. 1492, 2014.
- [5] G. B. Zhao *et al.*, “Development of button-type pickup for SSRF ring”, *Nucl Sci Tech*, vol.25, no.6, pp.12–17, 2014.

# PRECISE MEASUREMENT OF SMALL CURRENTS AT THE MLS

Y. Petenev<sup>†</sup>, J. Feikes, J. Li, A. N. Matveenkov, Y. Tamashevich, HZB, 12489 Berlin, Germany  
R. Klein, J. Lubeck, R. Thornagel, PTB, 10587 Berlin, Germany

## Abstract

The Physikalisch-Technische Bundesanstalt (PTB), the National Metrology Institute of Germany, utilizes an electron storage ring – the Metrology Light Source (MLS), located in Berlin, as a radiation source standard in the VIS, UV and VUV spectral range. In order to be able to calculate the absolute intensity of the radiation, the electron beam current has to be measured with low uncertainty. In this paper we focus on the measurement of the beam current in a range of several nA to 1 pA (one electron) by means of Si photodiodes, detecting synchrotron radiation from the beam. Electrons are gradually scraped out of the ring and the diode signal is analyzed afterwards. The exact number of stored electrons then can be derived from the signal. The measurement is carried out automatically with an in-house developed software.

## INTRODUCTION

The Metrology Light Source (the MLS) is the electron storage ring owned by the Physikalisch-Technische Bundesanstalt located in Berlin and dedicated to metrology and technological developments in the spectral ranges from far IR to extreme UV [1]. The main parameters of the MLS are presented in Tab. 1.

Table 1: Main Parameters of the MLS

Parameter	Value
Circumference	48 m
Injection energy	105 MeV
Operation Energy	50 to 629 MeV
Revolution frequency	6.25 MHz
Beam Current	1 pA (1 electron) to 200 mA

The MLS is utilized as a primary source standard and, therefore, PTB has installed and is operating all the equipment required for the measurement of the storage ring parameters required for calculation of the spectral photon flux with high accuracy [2]. The spectral intensity of the synchrotron radiation can be calculated by means of the Schwinger equation [3]. One of the contributors into the spectral power accuracy is the value of the electron beam current, therefore it has to be measured and controlled with a lowest possible uncertainty.

At the MLS the beam current can be varied in the range from 200 mA to 1 pA (a current of a single electron). The current is controlled over the whole range with a good accuracy (typical relative uncertainty  $< 10^{-2}$  to  $10^{-4}$ ). In this paper the main point of interest is the lower range of the electron beam current (a few nA and less). In this range the accuracy of the current measurement can be

significantly improved by counting the exact number of the electrons circulating in the storage ring. Since the revolution frequency of the ring can be measured with high precision (better than  $10^{-8}$ ), the electron beam current is also known to this accuracy.

## MEASUREMENT OF THE ELECTRON BEAM CURRENT

In the upper range (from 1 mA and more), the current is measured by two commercially available DC parametric current transformers (PCTs, made by Bergoz Instrumentation, France) [4]. The PCTs have a relative uncertainty of about  $10^{-4}$  in this current range.

In the lower ranges the beam current is measured by 4 sets of Si photodiodes (AXUV100 and SXUV100 diodes with 10 mm x 10 mm area, made by Opto Diode Corp.). In each set there are 3 diodes (see Fig. 1) with a different attenuation of synchrotron radiation. The attenuation is made using two different Aluminum filters (3 diodes (D1) with a thick filter (8  $\mu$ m) cover the range of 20 mA and less, and 3 diodes (D2) with a thin filter (0.8  $\mu$ m) are used for the range below 0.01 mA. The third type is the unfiltered diode (D3 and D4) which covers the range of low currents (10 nA and less).

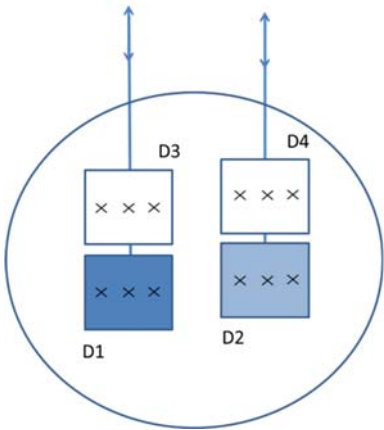


Figure 1: Photodiodes set-up at the MLS.

When the synchrotron light is hitting the diode, it produces a photocurrent which can be amplified, transferred into a voltage and then measured via a volt meter. All filtered diodes and two unfiltered diodes (1 on each set D3 and D4) are connected to Keithley 617 electrometers [5]. The rest of the diodes – 4 unfiltered diodes – are connected to the FEMTO current-voltage converters (I/U) [6] (FEMTO diode) followed by Agilent 34401A [7] a digital voltmeter (DVM), which have better signal to noise ratio than the Keithleys. The diodes connection scheme is presented in Fig. 2.

<sup>†</sup> yuriy.petenev@helmholtz-berlin.de

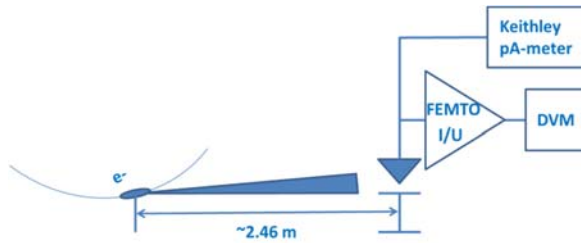


Figure 2: Diode connection scheme at the MLS.

## EXPERIMENTS AT THE MLS

At the MLS different experiments on the different current ranges are performed. Often it is required to reduce the beam current to a certain value. This is usually done by using a mechanical scraper, which is a tungsten plate, which can be moved close to the beam and the beam particles can be lost on it by hitting it. The scraper is manipulated by servomotor which can be moved with an accuracy of a few micrometers. The beam current is controlled over the whole range down to the required value. First by the PCTs, and when the thick filtered diode is inserted, the current value from the diode is matched with a value of PCT. If the required current is in the range of a thin filtered diode, the value of the thin filtered diode will be matched with the value of the thick filtered.

In some of the experiments at the low electron beam currents (1-2 nA and less) it is required to find out the exact value of the beam current. In this case the beam current is scraped down until the required value and then it is measured all the time during experiment by means of unfiltered diodes. After the experiment the exact number of electrons during experiment can be found. This can be done by gradual scraping of the electrons from the ring. So one can move the scraper closer to the beam until it loses a few electrons (the loss should not be too big, because it can introduce a counting error) then move it out to register the signal. Repeating this procedure until the beam will have 0 electrons and analyzing the signal afterwards, it is possible to define the exact number of electrons in the ring before the scraping and the number of remaining electrons during the scraping. Software written in Python has been developed for scraping and electron counting.

### Change of the Vertical Beam Size

At the beginning of this work it was supposed that bigger beam sizes are leading to easier scraping, therefore, it was assumed that the beam size should be increased during the scraping. Usually the vertical scraper is used. At the MLS it is possible to increase the vertical beam size by driving a stripline kicker with a “white noise” generator (WN). Dependence of the vertical beam size at 10  $\mu$ A beam current on the WN voltage is presented in Fig. 3. The beam size is measured by the source point imaging system [2]. Around 0.25 V and more the beam size is becoming WN defined. All data in this chapter were taken at the beam energy of 629 MeV.

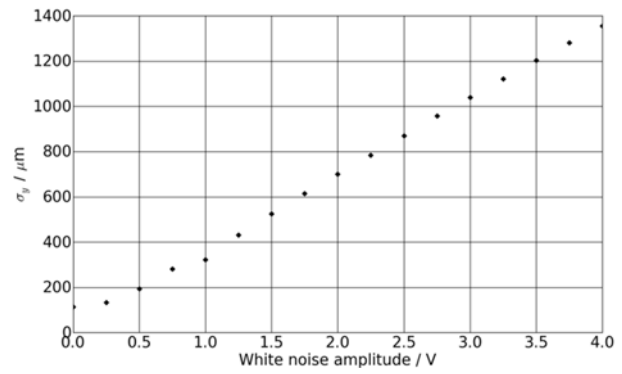


Figure 3: Dependence of the vertical beam size on the WN voltage (at 10  $\mu$ A electron beam current).

The diode signal depends on the white noise amplitude (or the beam size), see Fig.4. This can be explained by the fact that not all of the emitted photons are hitting the diode in the vertical direction.

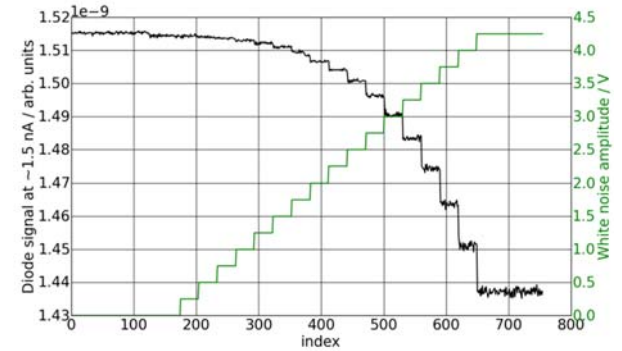


Figure 4: Dependence of the diode signal connected to FEMTO on the WN voltage (at  $\sim 1.5$  nA electron beam current).

In Fig. 4 one can see the loss of one electron at the index (each index point corresponds to 1 s) of about 125. Using this step one can roughly estimate the equivalent number of electrons from which the emitted light is not hitting the diode (see Fig. 5). So all in all at 4.25 V of WN the diode signal weakens for about 70 steps of a single electron.

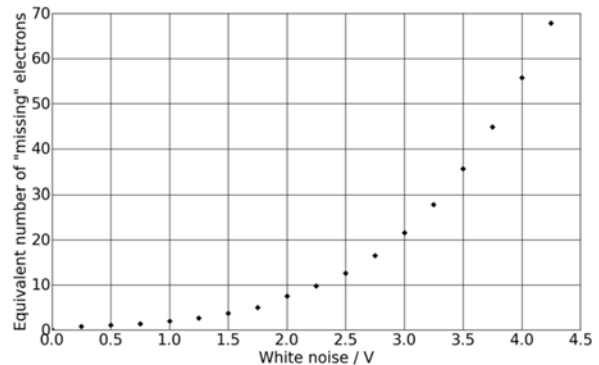


Figure 5: Number of “missing electrons” (equivalent of electrons from which the emitted light is not hitting the diode) depending on the WN voltage (at  $\sim 1.5$  nA electron beam current).

The synchrotron light of a single electron is radiated in the forward direction and most of the radiation is emitted within an angle of  $\pm 1/\gamma \approx 0.81$  mrad, where  $\gamma$  is Lorentz factor  $\sim 1231$  for the MLS at 629 MeV. Additional angular spread of the radiation is caused by the angular spread of the electrons in the beam, which is defined by the vertical beam emittance and Twiss parameter gamma. This angle can be written as  $\sigma_{y'} = \sqrt{\varepsilon_y \gamma_{twiss}}$ . Using the data from Fig. 3 and Twiss beta function = 11.5 m at the position of the size measurement system, the emittance change vs WN voltage can be found. Using this dependence and taking  $\gamma_{twiss} = 0.77$  1/m, the dependence  $\sigma_{y'}$  vs WN voltage can be found (see Fig. 6). The source point measurement system is located in the same beamline as the diodes.

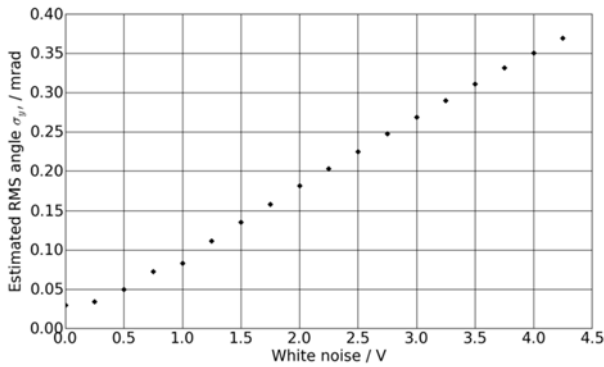


Figure 6: Estimated RMS angle depending on the WN voltage (at  $\sim 1.5$  nA electron beam current).

From Fig. 6 one can see that  $1/\gamma$  term is dominating for the MLS. This means that even without applying the WN voltage the diode is not detecting about 1% of radiated photons. This can be estimated assuming Gaussian beam as:

$$\left(1 - \operatorname{erf}\left(\frac{0.5d}{L\frac{1}{\gamma\sqrt{2}}}\right)\right) \cdot N \sim 18,$$

where  $d = 5 \cdot 10^{-3}$  m half of the diode size,  $L = 2.458$  m is the distance from the source point to the diode,  $N \sim 1487$  is the number of electrons in the ring and the error function:

$$\operatorname{erf}(x) = \frac{1}{\sqrt{\pi}} \int_{-x}^x e^{-t^2} dt.$$

For more precise estimation of this effect one could use the Schwinger equation and find the exact amount of radiation, which is not hitting the diode, but this is ongoing work and not covered in this paper yet.

The signal itself also becomes noisier when the WN is applied. The dependence of the noise of a FEMTO diode signal on the WN voltage at two different beam currents (rough estimations: 4.7 nA and 1.5 nA) is presented in Fig. 7. It was calculated in the following way. First, a part of the signal with constant white noise amplitude and without electron loss was normalized to its mean value, then the standard deviation of this signal was found. This

procedure was applied to each amplitude value of the white noise. For comparison, the standard deviations of the signal at 1.5 nA were additionally rescaled on the factor of 4.7/1.5. A rough estimation of a change of the signal, which corresponds to a loss of one electron, is presented in Fig. 7. This step is called further a single electron step. For the electron counting to be possible, the noise level should be less than half of the single step. The counting is much easier when the noise level is less than a quarter of the single step. So one can see that counting of 1.5 nA is possible but it becomes impossible at 4.7 nA using a signal from only one diode. It is not recommended to apply the WN voltage of more than 2 V, because after 2 V the noise level increases.

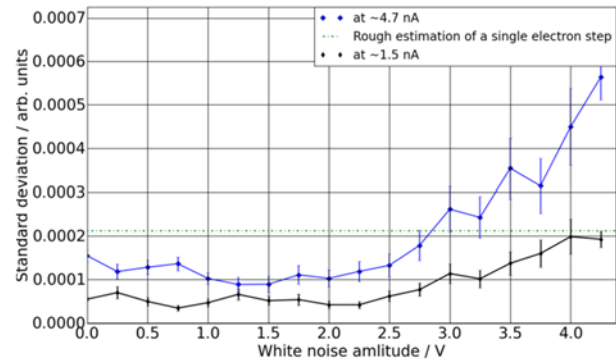


Figure 7: Dependence of the noise of the photodiode signal on the WN voltage (at  $\sim 4.7$  nA (blue) and  $\sim 1.5$  nA (black) electron beam current).

### Sum of Signals from Different Diodes

There are 6 unfiltered diodes installed at the MLS. Two of them are connected to Keithley pA meters and using them it is possible to count up to 1 nA. Then the noise level becomes too high. But one can use the 4 other diodes connected to the I/U converters (FEMTO) and their sum to decrease the noise level. One can assume that all diode signals are uncorrelated because they are all connected independently of each other. Nevertheless it was found that they become correlated after a certain value of applied WN voltage. The Pearson's correlation coefficients [8] of 3 FEMTO signals vs applied WN voltage are presented in Fig. 8.

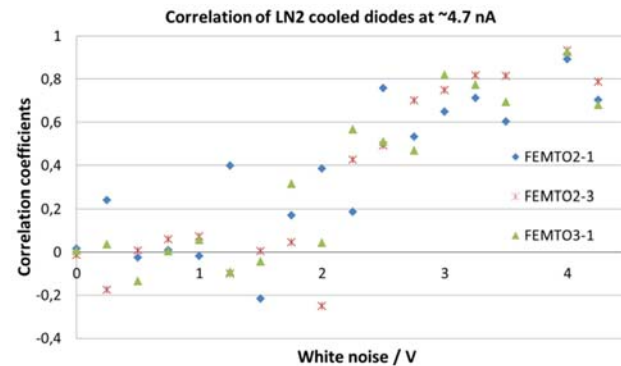


Figure 8: Correlation of 3 FEMTO diodes depending on the WN voltage (at  $\sim 4.7$  nA electron beam current).



The signals become correlated for the WN voltage of more than 2 Volt. This can be explained by the fact that photons emitted by a part of the electron beam with large angular deviation do not reach diodes and this happens for all diodes simultaneously.

In the standard user optic at the MLS the WN voltage is 0.75 V at low currents. At this voltage the diode signals are not correlated and therefore they can be summed in order to reduce the noise. In order to compare the noises of different signals depending on the beam current, the beam was scraped with big steps (1 nA to 0.25 nA) from about 5.8 nA down to 0. On each step the scraper was moved out and then long (more than 100 points) signals without electron loss were recorded, let's call such parts of the signals as plateau. One FEMTO diode at the day of measurement was out of order, so only 5 signals were measured.

The sum of the signals can be calculated as the weighted arithmetic mean in the following way:

- First all signals should be shifted to 0 at 0 electrons in the ring;
- At higher currents  $> 2$  nA the plateaus are linearly drifting with time due to the thermal effects. Therefore the signal should be fitted with a linear function and then one should remove the fitted slope from each plateau;
- Then each plateau of each signal should be normalized to the mean value of the plateau calculated for the highest value of the beam current (5.8 nA in this case) of the corresponding signal;
- Then one can find the standard deviation of the plateau signal, this is the noise level of the plateau. Doing this for each plateau and each signal one can find the noise levels depending on the beam current  $\sigma_{k,j}$ , where  $k$  is the number of diode signal and  $j$  is the number of plateau. That is what is plotted in Fig. 9.
- With the last step one should find the weighted mean of every signal, the weights are calculated as:  $w_{k,j} = \sigma_{k,j}/\sigma_{i,j}$ , where  $i$  is one fixed diode number, so the weight for  $k = i$  is equal 1. The sum of  $n$  signals can be found as:  $S_{\Sigma,j}(t) = \frac{\sum_{k=1}^n S_{k,j}(t) \cdot w_{k,j}}{\sum_{k=1}^n w_{k,j}}$  for each plateau  $j$  and each measured point  $t$ . Now one can find the noise level of the sum signal.

The horizontal line plotted in Fig. 9 marks estimated half of the single electron step. As it was already noticed above, the electron counting is reliable, when the noise level is around a quarter of a single step. This means less than 1500 electrons. Then with higher noise levels it is also possible to count but one needs more time to record longer plateaus in order to decrease the statistical error, and analyse the sum of the signals. So the possible number of counted electrons at the MLS is less than 3000, which corresponds to 3 nA of a beam current.

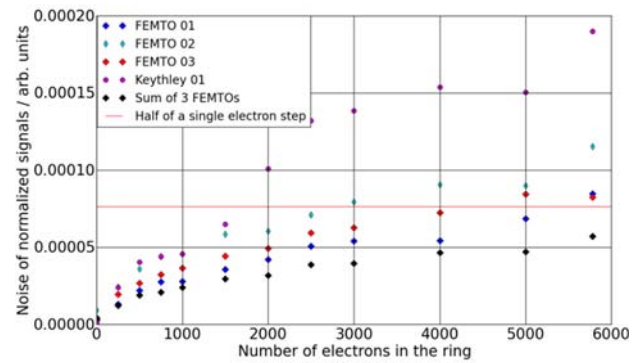


Figure 9: Noises of signals from different diodes depending on the number of electrons in the ring in standard user optic at the MLS.

## CONCLUSION

PTB uses the MLS as a radiation source standard, which is dedicated to metrology and technological developments in the spectral ranges from far IR to extreme UV. For the experiments at the MLS with the lower current (less than 3 nA) the exact amount of circulating electrons needs to be found after and during the experiment. This can be done with an in-house developed software. The number of electrons corresponding to currents up to 1.5 nA can be counted using only one signal. At the range of 1.5 nA to 3 nA counting is also possible but is not absolutely confident. Long scraping time and the use of the sum of the signals from different diodes is necessary.

It is not recommended to use the white noise voltage of more than 2 V, because the signals from different diodes become correlated and noisier. The sum of them will not improve the statistical error or the noise level of the signal. The signals should be summated as the weighted arithmetic mean.

## REFERENCES

- [1] R. Klein *et al.*, "Operation of the Metrology Light Source as a primary radiation source standard", *PRST-AB*, vol. 11, p. 110701, 2008.
- [2] R. Klein *et al.*, "Accurate measurement of the MLS electron storage ring parameters", in *Proc. IBIC'16*, Barcelona, Spain, Sep. 2016, pp. 600-603. doi:10.18429/JACoW-IBIC2016-WECL02
- [3] J. Schwinger, *Phys. Rev.*, vol. 75, p. 1912, 1949.
- [4] K. Unser, "The parametric current transformer, a beam current monitor developed for LEP", CERN, Geneva, Switzerland, Rep. CERN SL/91-42, 1991.
- [5] Keithley electrometer 617, Cleveland, Ohio, USA.
- [6] DPCA-300, I/U converter, Femto, Berlin, Germany.
- [7] Agilent 34401A 6½ Digit Multimeter, User's Guide, 2007.
- [8] Pearson correlation coefficient, <https://wikipedia.org>

# BEAM CHARGE MEASUREMENT AND SYSTEM CALIBRATION IN CSNS \*

W. L. Huang†, F. Li, L.Ma, S. Wang, T. G. Xu

Institute of High Energy Physics, Chinese Academy of Sciences, Beijing 100049, China Dongguan  
Neutron Source Center, Dongguan 523803, China

## Abstract

In China Spallation Neutron Source (CSNS), the beam charge monitors along the ring to the target beam transport line(RTBT) and the ring to the dump beam transport line(RDBT), are consisted of an ICT and three FCTs manufactured by Bergoz. The electronics includes a set of NI PXIe-5160 oscilloscope digitizer, and a Beam Charge Monitor (BCM) from Bergoz as supplementary. The beam charge monitors provide the following information: a) the quantity of protons bombarding the tungsten target; b) the efficiency of particle transportation; c) a T0 signal to the detectors and spectrometers of the white neutron source. With the calibration with an octopus 50Ω terminator in lab and an onboard 16-turn calibrating coils at the local control room, corrections for the introducing the 16-turn calibrating coils and the long cable were made. An accuracy of ±2% for the beam charge measurement during the machine operation has been achieved with the ICT/FCTs and a PXIe-5160 oscilloscope digitizer.

## INTRODUCTION

The accelerator and target layout of CSNS and beam instrumentations distributed on the linac , the RCS ring and beam transport lines are presented in Figure 1. After

the 50keV H- source, the 4-tank 324MHz drift tube linac (DTL) is designed to accelerate the H- beam from 3MeV to 81MeV, and the H- ions are injected into the RCS ring. During the injection, H- stripping by a carbon primary stripper foil (100μg/cm<sup>2</sup>) and a secondary stripper foil (200μg/cm<sup>2</sup>) is adopted for this high intensity proton synchrotron [1], then protons are accelerated to 1.6GeV in 20ms by 8 ferrite-loaded RF cavities before extraction [2]. There is an ICT sensor installed at the beginning of RTBT and RDBT beam line, one FCT sensor just in front of the R-dump, one FCT sensor in the mid of bending magnets RTB1 and RTB2 and the third FCT sensor in front of the tungsten target.

Before the installation, two sets of charge measurement methods were utilized for the sensor calibration. During the machine commissioning, the beam charge measurement was calibrated with the extracted particle numbers derived by the beam current measured by DCCT on the RCS ring and the RF frequency (round about 2.44MHz). Then we made a statistics analysis of the beam charge measurement during machine operation. It is showed that a sensitivity of  $1.0 \times 10^{10}$  protons/pulse and an accuracy of less than ±2% could be achieved in the beam charge measurement.

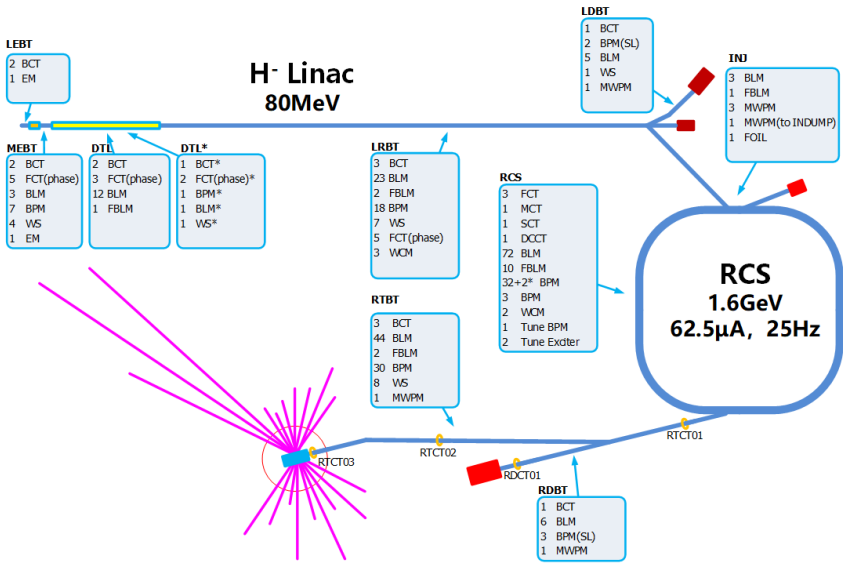


Figure 1: Accelerator and target layout and beam instrumentations of CSNS.

\*Work supported by Special fund for public welfare research and capacity building in Guangdong province, 2016A010102001  
† huangwei@ihep.ac.cn

## TIME STRUCTURE AND SPECTRUM OF EXTRACTED PROTON BEAM

The repetition rate of the extraction proton beam is 25Hz in operation, which can be configured as one-shot mode during machine commissioning. The RCS harmonic number is 2, thus there are two bunches accelerated in the ring and extracted simultaneously in a fast extracting time of 600ns. The maximum charge of each bunch is 1.248  $\mu\text{C}$ , corresponding to the beam power of 100kW bombarding the target. The interval of them is 409ns, a reciprocal of  $f_{\text{rf\_high}}$  (2.44MHz). According to the simulation of longitudinal beam dynamics [3], the extracted two bunches are in a kind of dual quasi Gaussian distribution, shown in Figure 2. An FFT analysis to the beam spectrum is performed using LabVIEW, and the result is showed in Figure 3. Above 15MHz, the amplitude of the beam manifests 15dB less than its maximum, and above 30MHz, it has a round about 30dB weaker amplitude.

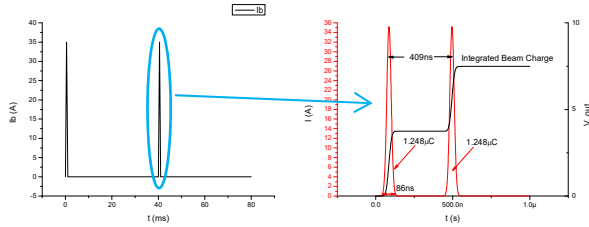


Figure 2: Time structure of the extracted proton beam.

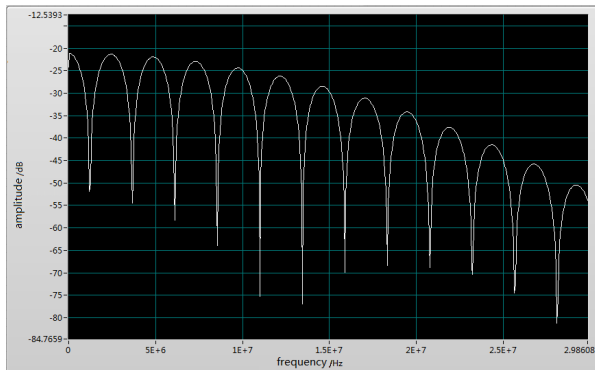


Figure 3: Spectrum of the extracted proton bunches.

Table 1 gives the main parameters of the FCTs installed on the RTBT/RDBT beam line. Thus, all the FCTs have a rise time of less than 500ps, and will response promptly to the extracted beam.

Table 1: Main Parameters of RTCTs/RDCT Sensors [4]

Position	RTCT02	RTCT03	RDCT01
Model	FCT-178-0.5	FCT-302-0.5-H	FCT-302-0.5
$f_{\text{low}}(-3\text{dB})/\text{Hz}$	134.5	122.3	149.5
$f_{\text{high}}(-3\text{dB})/\text{MHz}$	810	708.8	708.5
Droop/(%/us)	0.08	0.08	0.09
Risetime/ps	432	494ps	494
Pulse Response/ps	413→754	405→551	413→610
Step Response/ps	427→808	410→959	405→824
Differentiation	21.2%/300 $\mu\text{s}$	21.2%/300 $\mu\text{s}$	23.4%/300 $\mu\text{s}$

According to the frequency response measurement of Bergoz FCT, as shown in Figure 4, it's not as flat as that in middle frequency range (1 kHz ~ 1MHz), especially in frequency range of less than 200Hz and higher than 5MHz. Therefore, if we use an oscilloscope digitizer as the electronics of FCT to sample the current waveforms and integrate the pulse area to deduce the beam charge in a time window, the nominal sensitivity of 0.5V/A need specific corrections. Also, considering the long cable connecting the sensor and the electronics in local control room (60m~120m long separately), the signal attenuation and distortion due to the cable should be measured and corrected.

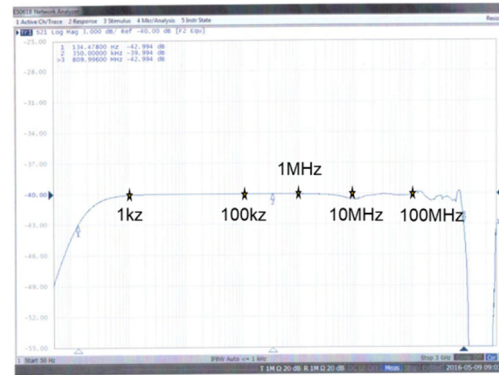


Figure 4: Frequency response of a Bergoz FCT (RTCT02).

## CALIBRATION IN THE LAB

The number of the protons hitting the target will be  $1.56 \times 10^{13}$ /pulse in design, and one tenth of that in the acceptance test. We designed a 16-turn 8-direction coil with a 50 $\Omega$  PCB board to realize the on-line calibration, showed in Figure 5.



Figure 5: FCTs and ICT tied up to a 16-turn 8-direction coil with a 50 $\Omega$  PCB board.

In order to evaluate the influence of the 16-turn coils and a 100m-long cable to the original FCT output, we also designed an octopus 50 $\Omega$  terminator [5], as showed in Figure 6. It was like a single turn calibration coil which was used in a single pulse beam charge monitor [6], but an isotropous calibration current was fed into the coil. A pulse with a width of 80ns and a leading/trailing time of 30ns is generated by a function generator Tektro-

nix AFG3102 and the signal was fed into an octopus 50Ω terminator. The output of the FCT/ICT was sampled by a Keysight MSO X3034T oscilloscope (2GSa/s, 8bit ADC). Then the pulse area was integrated and noise eliminated by a self-designed LabVIEW code.

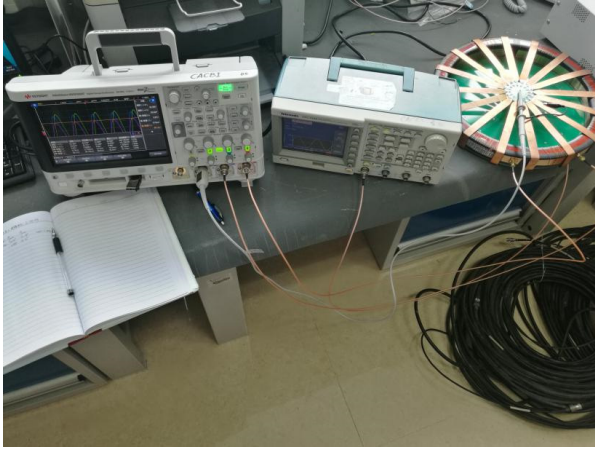


Figure 6: FCTs or ICT calibrated with a 50Ω octopus terminator.

We assume that if there is no calibration coils, but only the octopus as the primary winding ( $N=1$ ) of the FCT sensor ( $N_s=50$  turns and  $R_s=50\ \Omega$ ), the current in the secondary coil should be

$$i_s = \frac{s\tau_s}{1 + s\tau_s} \left( \frac{i_b}{N_s} \right) \quad (1)$$

$$\text{where } \tau_s = \frac{L_s}{R_s/2} = \frac{N_s^2 L_0}{R_s/2}$$

Here,  $s$  is the Laplace operator, and  $L_0$  is the inductance of the core with only one turn winding. Then we have an equivalent circuit of the FCT with both the secondary winding and the calibration winding (here  $N_c=16$  turns), where  $R_c=R_s=50\Omega$ , but it's in serial to the calibrating inductor (Figure 7). Then, the current in the secondary coil changes to be

$$i_s' = \frac{s\tau_s}{1 + s\tau_s + s\tau_c} \left( \frac{i_b}{N_s} \right) \quad (2)$$

$$\text{where } \tau_c = \frac{L_c}{2R_c} = \frac{N_c^2 L_0}{2R_c}$$

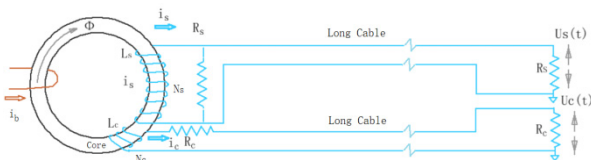


Figure 7: Equivalent circuit of an FCT with calibration coils.

We substituted the actual value into the variants of the above formula (1) and (2), and got the result of  $i_s'/i_s=100/102.56$ , for the correction of introducing the calibration coils to the FCT sensor.

Then we did the comparison of the pulse area of the FCT output with/without the calibration coils, and get a correction factor of 100/102.5, which agrees with the equivalent circuit analysis very well.

When the FCTs/ICT were installed in the ring tunnel, we did the calibration with long cables, and got the relation of the integrated pulse area (unit: nVs) with the particle number for each sensor. For example, Figure 8 shows the linearity and the error of the calibration for RTCT03, which is installed in front of the target and involved in the calculation of neutron production efficiency.

Table 2: Calibration Result of RTCTs/RDCT

Sensor ID	Particle Number (1E+10)	Error(%)
RTCT01	1.3083 * Area + 0.020	$\pm 2$
RTCT02	1.4013 * Area + 0.606	$\pm 2$
RTCT03	1.3755 * Area + 0.850	$\pm 1$
RDCT01	1.3329 * Area + 0.191	$\pm 2$

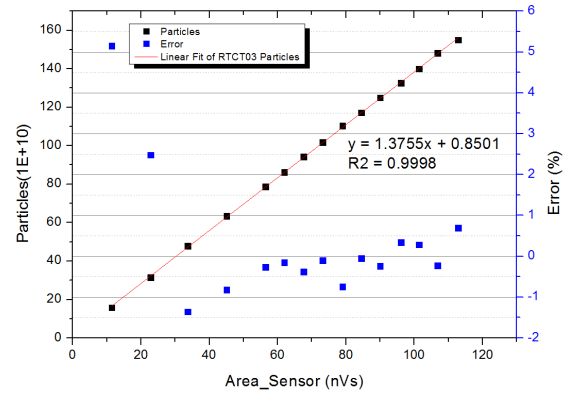


Figure 8: Calibration result of the RTCT03.

## BEAM CHARGE MEASUREMENT IN MACHINE OPERATION

Along with the commissioning of RTBT beam line, we did the calibration of RTCT01, RTCT02 and RTCT03 with the DCCT on the ring, when there is no obvious beam loss along the extraction and RTBT beam transport line. Figure 9 shows the two extracted proton bunches detected by the 3 CT sensors. At the end of RTCT02 cable, we used a power splitter for T0 signal of Back-n beam line, and an -6dB attenuator at the end of RTCT03 cable to avoid the CT output amplitude overload as the beam power increasing. The corrections of the power splitter and the attenuator were measured and taken into account of the pulse area integration. The proton number per pulse (two bunches) is  $1.56 \times 10^{12}$ , corresponding to the beam power of 10kW bombarding the target.



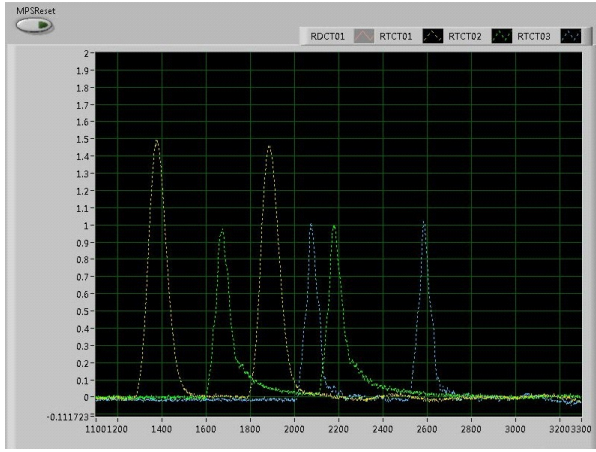


Figure 9: Two extracted proton bunches detected by the 3 RTCT sensors.

For the DCCT on the RCS ring, it measures the average current of the circulating beam, the relation of the beam charge  $Q$  and the revolution frequency  $f_{rev}$  or the RF frequency  $f_{rf}$  (harmonics number  $h=2$ ) is

$$Q = \frac{I_{beam}}{f_{rev}} = h \frac{I_{beam}}{f_{rf}} \quad (3)$$

At the extraction time,  $Q_{ext}$  can be derived by the beam current measured by DCCT and the RF frequency measured by WCM (or just the RF frequency configured by the LLRF code).

Figure 10 shows a statistic result of the RTCTs, which gives a standard deviation of  $\pm 2\%$ . During the past 6 months' running, the beam charge measurement system worked very well, and were programmed (EPICS) into the MPS system to inform the operator immediately when there was big beam losses happened along the RTBT beam line.

## CONCLUSION

It became complicate when we introduced the 16-turn calibration coils into the beam charge measurement. Cor-

rections including the calibration coils and the long cables were done in the lab and at the local control room. Finally, we obtained an accuracy of  $\pm 2\%$  with the 3 Bergoz FCTs, one ICT and an NI PXIe-5160 oscilloscope digitizer as the electronics. Up to last machine running in July, 2018, the maximum hitting-target proton number per pulse has achieved to  $3.6 \times 10^{12}$ , which means the beam power went up to 23kW, almost a quarter of the designed value 100kW.

## ACKNOWLEDGEMENT

We would like to acknowledge the help and advices from Mr. Bergoz (bergoz@bergoz.com) for the beam charge measurement and calibration with the octopus 50Ω terminator, and also the support from the conventional facility division and the corresponding technicians of domestic factories.

## REFERENCES

- [1] L. Kang *et al.* "Introduction about Key Techniques of Critical Equipment in CSNS", in *Proc. IPAC'17*, Copenhagen, Denmark, May 2017, paper THPVA049, pp.4548-4550.
- [2] H. Sun *et al.* "RF System of the CSNS Synchrotron", in *Proc. IPAC'13*, Shanghai, China, May 2013, paper WEPFI028, pp. 2765-2767.
- [3] N. Wang *et al.* "The Design Study on the Longitudinal Beam Dynamics for CSNS/RCS", in *Proc. HB2012*, Beijing, China, Sep. 2012, paper MOP216, pp. 89-92.
- [4] Bergoz Instruments "Certificate of Calibration FCT#3350, #3351, #3477", unpublished, 2016 and 2017.
- [5] J. Bergoz and H. Bayle, private communication, May 2016
- [6] B. Vojnovic, "A Sensitive Single-pulse Beam Charge Monitor for Use with Charged Particle Accelerators", *Radiat. Phys. Chem.* vol. 24, pp. 517-522, 1985.

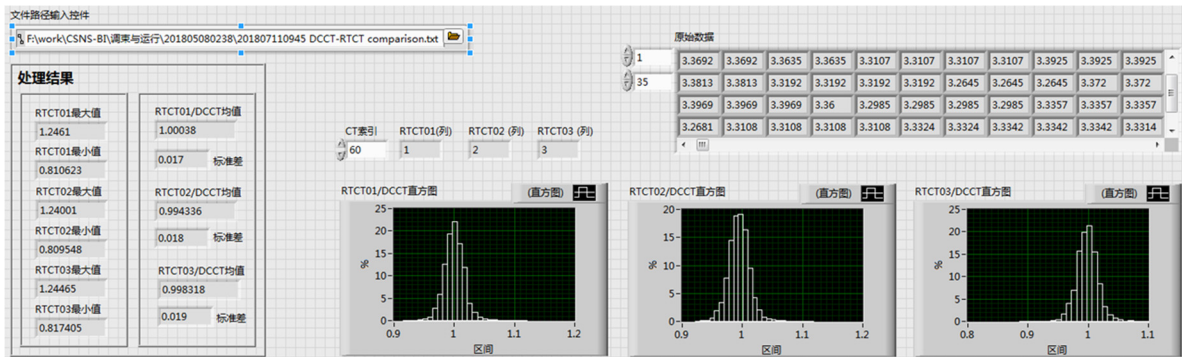


Figure 10: Statistics result of the comparison of RTCT and DCCT (No obvious beam loss along the extraction and RTBT beam line).

# COMPARATIVE MEASUREMENT AND CHARACTERISATION OF THREE CRYOGENIC CURRENT COMPARATORS BASED ON LOW-TEMPERATURE SUPERCONDUCTORS\*

V. Tympel<sup>†</sup>, Th. Stoehlker<sup>1,2</sup>, Helmholtz Institute Jena, 07743 Jena, Germany  
M. Fernandes<sup>3,4</sup>, J. Tan, CERN, 1211, Geneva 23, Switzerland  
C.P. Welsch<sup>3,4</sup>

<sup>3</sup>also at Cockcroft Institute, Sci-Tech Daresbury, WA4 4AD, Daresbury, Warrington, UK

<sup>4</sup>Department of Physics, The University of Liverpool, Liverpool, L69 7ZE, UK  
H. De Gersem, N. Marsic, W. Müller, Department of Electrical Engineering and  
Information Technology, TU Darmstadt, 64283 Darmstadt, Germany

D. Haider, F. Kurian, M. Schwickert, T. Sieber,

<sup>1</sup>at GSI Helmholtzzentrum für Schwerionenforschung, 64291 Darmstadt, Germany

J. Golm, R. Neubert<sup>5</sup>, F. Schmidl, P. Seidel, Institute of Solid State Physics, 07743 Jena, Germany  
M. Schmelz, R. Stolz, Leibniz Institute of Photonic Technology, 07745 Jena, Germany

V. Zakosarenko, Supracon AG, 07751 Jena, Germany

<sup>2</sup>also at Institute for Optics and Quantum Electronics, 07743 Jena, Germany

<sup>5</sup>also at Thuringia Observatory Tautenburg, 07778 Tautenburg, Germany

## Abstract

A Cryogenic Current Comparator (CCC) is a non-destructive, metrological-traceable charged particle beam intensity measurement system for the nano-ampere range. Using superconducting shielding and coils, low temperature Superconducting Quantum Interference Devices (SQUIDS) and highly permeable flux-concentrators, the CCC can operate in the frequency range from DC to several kHz or hundreds of kHz depending on the requirement of the application. Also, the white noise level can be optimized down to 2 pA/sqrt(Hz) at 2.16 K.

This work compares three different Pb- and Nb-based CCC-sensors developed at the Institute of Solid State Physics and Leibniz Institute of Photonic Technology at Jena, Germany: CERN-Nb-CCC, optimized for application at CERN Antiproton Decelerator (AD) in 2015 with a free inner diameter of 185 mm; GSI-Pb-CCC, designed for GSI-Darmstadt with a free inner diameter of 145 mm, 1996 completed, 2014 upgraded; GSI-Nb-CCC-XD, designed for the GSI/FAIR-project with a free inner diameter of 250 mm, 2017 completed. The results of noise, small-signal, slew-rate, and drift measurements done 2015 and 2018 in the Cryo-Detector Lab at the University of Jena are presented here.

## THE SYSTEM

After 25 years of development the Cryogenic Current Comparator (CCC) has been established as a useful tool for non-destructive and metrological-traceable beam intensity measurement in the nano-ampere range [1]. The principle behind the CCC is to pick up the azimuthal magnetic field of the moving charged particles. Figure 1

shows a superconducting meander structure which shields the non-azimuthal magnetic field components. The following pickup coil, enclosing a highly permeable flux-concentrating core, and the particle beam build up a current-transformer. The very low pickup coil current can be measured, via matching electronics, by a Low-Temperature Superconducting Quantum Interference Device (SQUID). The measured raw voltage of the SQUID electronics can be linked to a corresponding CCC input current using a calibration factor defined with a metrological-traceable calibration current.

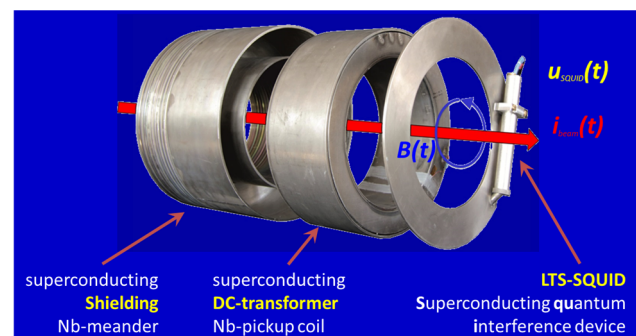


Figure 1: Components and operating principle of the CCC-sensor shown on a niobium-based system before it is assembled.

## Measurement Setups

Three CCC sensors (see Table 1) with different dimensions, varying meanders, and core materials were characterized by a setup consisting of a Dynamic Signal Analyzer HP35670A, a Vector Signal Analyzer HP89410A, an Agilent Function / Arbitrary Waveform Generator 33210A and a DAkKS (Deutsche Akkreditierungsstelle)-certified Keithley 2002 Multimeter. The lab measurements are done in a shielded chamber (see Fig. 2, left).

\* Work supported by BMBF, project numbers 05P15SJRBA and 05P18SJRBI.

<sup>†</sup> volker.tympel@uni-jena.de





Figure 2: Wide-neck bath cryostat in an acoustically and magnetically shielded chamber for the electrical CCC-testing at the Cryo-Detector Laboratory at the University of Jena (left), beamline cryostat of the GSI-Pb-CCC at GSI Darmstadt (middle), beamline cryostat and He-reliquefier of the CERN-Nb-CCC at CERN-Antiproton Decelerator (AD) (right).

Two sensors have a dedicated beamline cryostat (see Fig. 2 middle and right). The beamline cryostat for the GSI-Nb-CCC-XD is currently in production. For the 2-K-temperature range two dry scroll pumps SC15D were used.

Table 1: CCC Specifications

CCC-Sensor	GSI-Pb	CERN-Nb	GSI-Nb-XD
Completed	1996	2015	2017
Diameter (mm)			
inner	147	185	250
outer	260	280	350
Length (mm)	95	193	207
Meander	Pb	Nb	Nb
Pickup coil	Nb	Nb	Nb
Core	Vitrovac	Nanoperm	Nanoperm
	6025	M764	GSI328+
Inductance ( $\mu$ H)			
@1 kHz, 4.2 K	25	100	80

## MEASUREMENTS

The measurements were done in 2015 (CERN-Nb-CCC) [2] and 2018 (GSI-Pb-CCC, GSI-Nb-CCC-XD) at the Cryo Detector Laboratory at the University of Jena.

### Noise

The graph in Fig. 3 can be divided in three frequency regions. The  $1/f$ -region below roughly 2 kHz indicates the differences between the amorphous Vitrovac (GSI-Pb-CCC) and the nano-crystalline Nanoperm (GSI-Nb-CCC-XD) core material. Vitrovac shows up to four times higher noise values, but has a lower acoustic sensibility between 5 Hz and 50 Hz and less spontaneous current jumps (noise below 100 mHz). The next region up to 100 kHz or 500 kHz is characterized by an almost constant level of white noise below 5 pA/ $\sqrt$ Hz. The last region starts with small resonance peaks and a falling low-pass edge. The smaller bandwidth of the GSI-Nb-CCC-XD is a result of the balanced SQUID coupling described in [3].

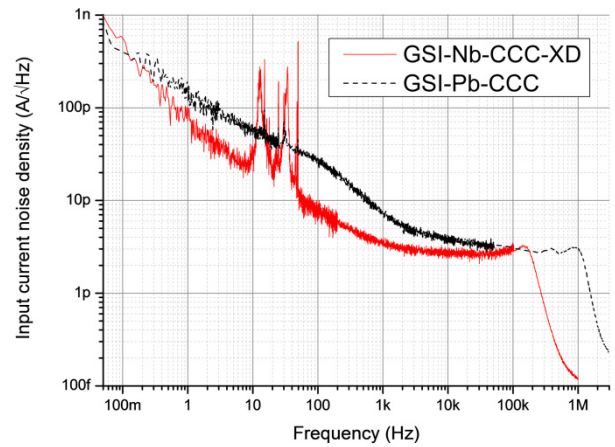


Figure 3: Current noise of the GSI-CCCs @ 4.2 K.

The original CERN-Nb-CCC also shows also typical nano-crystalline core behaviour (see Fig. 4, blue line). For the application in the CERN AD ring a 1 kHz RC-low-pass was added in front of the SQUID to realise an integration (see Fig. 4, green dots). Unfortunately the noise is therefore dominated by a thermal resistor noise.

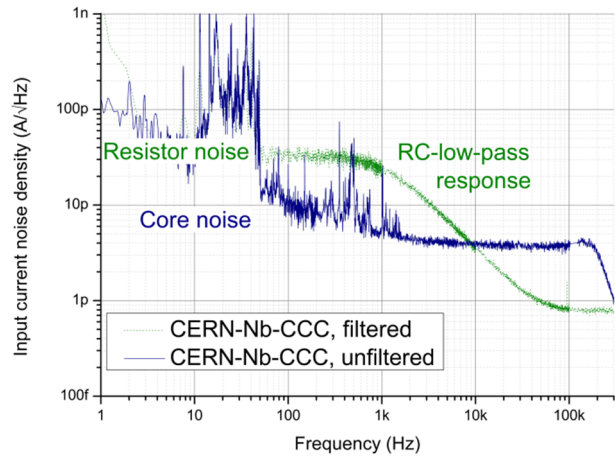


Figure 4: Current noise of the CERN-CCC before (blue line) and after optimization with a RC-low-pass (green dots) of the SQUID coupling.

## Superfluidity

To improve the measurement of thermal drifts and to isolate the influence of He bubbles the GSI-Nb-CCC-XD was cooled down below the  $\lambda$ -point at 2.1768 K @ 50.36 hPa. A transition to superfluid helium II without any gas bubbles takes place at the  $\lambda$ -point. Figure 5 shows that, with bubbles, the noise baseline and the building vibration peak @ 11.5 Hz are up to five times higher than without bubbles. That corresponds to the behaviour that on the way down to the  $\lambda$ -point it was impossible to make any reasonable measurements with the SQUID but below the  $\lambda$ -point and also on the way up to 4.2 K a normal SQUID flux locked loop (FLL)-mode is problem-free.

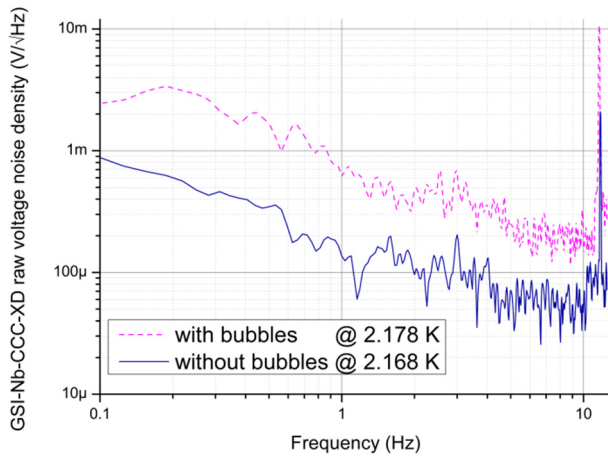


Figure 5: Change of the noise near the  $\lambda$ -point (SQUID amplifier-mode), above the  $\lambda$ -point with gas bubbles (magenta dashes) and below without bubbles (blue line).

Below the  $\lambda$ -point a decrease of white noise down to a value of 2 pA/√Hz is detectable (see Fig. 6). In general it is possible to improve the performance of the system with superfluid helium but the effort can be high and we have to avoid additional acoustic disturbances.

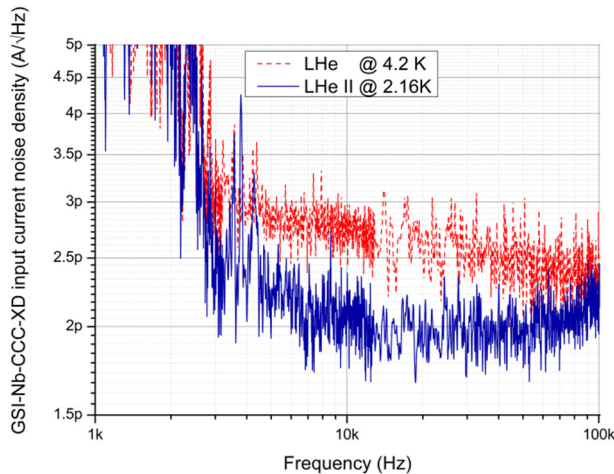


Figure 6: White noise current density of the GSI-Nb-CCC-XD between 3 kHz and 100 kHz (SQUID FLL-mode) at 4.2 K (red dashes) and below the  $\lambda$ -point at 2.16 K (blue line).

## Small Sine Signals and Slew-Rates

More important than the noise level by itself is the signal-to-noise ratio. At first we have compared the small-signal behaviour using sinusoidal current waves. A current in an electrical wire through the centre of the CCC sensor is used to simulate the charged particle beam. The SQUID signal was analysed with a HP89410A in average mode for the noise measurement and peak-hold mode for noise and swept sine current inputs. As shown in Fig. 7 (GSI-Nb-CCC-XD) and in Fig. 8 (GSI-Pb-CCC) the small-signal response follows the noise densities. Using additional signal processing it should be possible to achieve a bandwidth of up to 1 MHz (GSI-Nb-CCC-XD) or up to 3 MHz (GSI-Pb-CCC) for small signals.

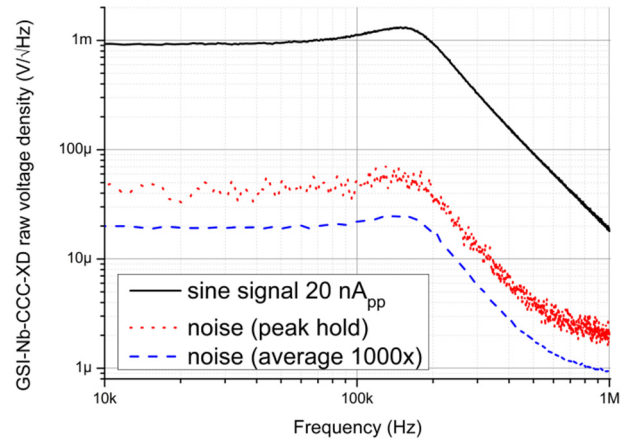


Figure 7: Correlation between noise and signal of the GSI-Nb-CCC-XD.

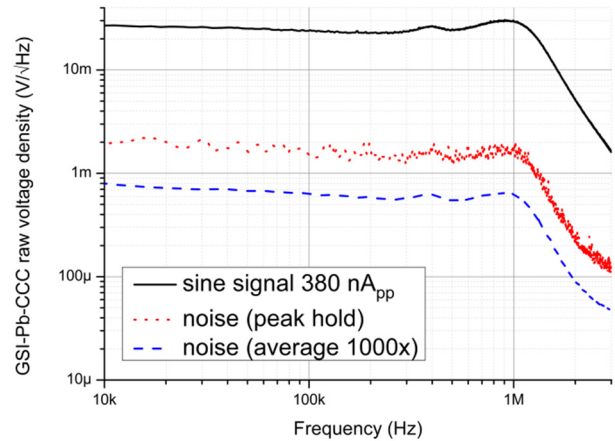


Figure 8: Correlation between noise and signal of the GSI-Pb-CCC.

For the application in a beamline the large-signal response is very important. Using a sine current a slew-rate (SR) can be defined as the product of a given circular frequency and maximum current amplitude for a stable CCC operation. At a frequency of 200 kHz the balanced GSI-Nb-CCC-XD reached SR = 0.16 A/s (direct version: 0.33 A/s) and the GSI-Pb-CCC reached SR = 0.30 A/s. The CERN-AD beam injection with 8.6 kA/s requires a 1 kHz low-pass in the CERN-Nb-CCC [1].



## Thermal Drift

Naturally, the SQUID by itself has a temperature-dependence in its electrical parameters. In a classical beamline CCC with a large, highly permeable core the thermal drift of the SQUID output voltage is dominated by the properties of the core [4]. Via pressure and temperature changes close to 4.2 K and measurements during the warm-up from the  $\lambda$ -point to 4.2 K at atmospheric pressure conditions for the GSI-Nb-CCC-XD a drift of 15 nA/mK and for the GSI-Pb-CCC a drift of 30 nA/mK was measured.

In a second experiment, the temperature of the helium bath was kept constant with the help of the large specific thermal capacity of liquid helium at the  $\lambda$ -point and the pressure was changed rapidly from 50 hPa to 1000 hPa. Despite the dramatic change in pressure a drift below 1 nA/mK could be found. Therefore, the drifts close to 4.2 K are generated by the temperature changes and not by the pressure changes.

## ACKNOWLEDGEMENT

We thank our former staff member René Geithner for the raw measurement data and exploded view image of the CERN-Nb-CCC from 2015.

## CONCLUSION

It was possible to extend the dimensions of the CCC-sensor for the use in beamlines with a large diameter without losing any system performance. With a core that is optimized for low-temperature applications is it possible to achieve a white noise of 3 pA/ $\sqrt{\text{Hz}}$ . Unfortunately, the influence of acoustic disturbances is increasing too. Cooling with bubble-free superfluid helium leads to a better performance. Using additional data processing, small-signal bandwidths in the MHz-range are possible by core-based CCCs. The best achieved slew-rate at the moment is below 0.4 A/s. With a low-pass in front of the SQUID the application in storage rings with slew-rates of kA/s can be realized. The lowest thermal current drift that was measured is 15 nA/mK. Therefore, a constant baseline current can only be achieved by a strong temperature stabilisation or with a core-less CCC design [5].

## REFERENCES

- [1] M. Fernandes, "SQUID-Based Cryogenic Current Comparator for Measuring Low-Intensity Antiproton Beams", Ph.D. thesis, University of Liverpool, UK, 2017.
- [2] R. Geithner, "Optimierung eines kryogenen Stromkomparators für den Einsatz als Strahlmonitor", Ph.D. thesis, Dept. Phys., F. Schiller University Jena, Jena, Germany, 2013.
- [3] P. Seidel *et al.*, "Cryogenic Current Comparators for Larger Beamlines", in *IEEE Trans. Appl. Supercond.*, vol. 28, no. 4, pp. 1-5, Art no. 1601205, June 2015, doi: 10.1109/TASC.2018.2815647
- [4] F. Kurian, "Cryogenic Current Comparators for precise Ion Beam Current Measurements", Ph.D. thesis, Dept. Phys., University of Frankfurt, Frankfurt, Germany, 2015.
- [5] V. Zakosarenko *et al.*, "Coreless SQUID-based Cryogenic Current Comparator (CCC) for non-destructive Intensity Diagnostics of charged Particle Beams", *Supercond. Sci. Technol.*, to be published.

# BEAM INTENSITY MONITORING WITH NANOAMPERE RESOLUTION – THE CRYOGENIC CURRENT COMPARATOR (CCC)\*

D. M. Haider<sup>†</sup>, P. Forck, F. Kurian, M. Schwickert, T. Sieber

GSI Helmholtzzentrum für Schwerionenforschung, 64291 Darmstadt, Germany

M. Fernandes, J. Tan, CERN, 1211 Gevena 23, Switzerland

J. Golm<sup>1</sup>, F. Schmidl, P. Seidel, FSU Jena, 07743 Jena, Germany

T. Stoeckler<sup>2,3</sup>, V. Tynpel, Helmholtz Institute Jena, 07743 Jena, Germany

M. Schmelz, R. Stolz, V. Zakosarenko<sup>4</sup>, IPHT, 07751 Jena, Germany

H. De Gersem, N. Marsic, TEMF, TU Darmstadt, 64289 Darmstadt, Germany

<sup>1</sup>also at Helmholtz Institute Jena, 07743 Jena, Germany

<sup>2</sup>also at GSI Helmholtz Centre for Heavy Ion Research, 64291 Darmstadt, Germany

<sup>3</sup>also at Institute for Optics and Quantum Electronics, 07743 Jena, Germany

<sup>4</sup>also at Supracon AG, 07751 Jena, Germany

## Abstract

The storage of low current beams as well as the long extraction times from the synchrotrons at FAIR require non-destructive beam intensity monitoring with a current resolution of nanoampere. To fulfill this requirement, the concept of the Cryogenic Current Comparator (CCC) based on the low temperature SQUID is used to obtain an extremely sensitive beam current transformer. During the last years CCCs have been installed to do measurements of the spill structure in the extraction line of GSI SIS18 and for current monitoring in the CERN Antiproton Decelerator ring. From these experiences lessons can be learned to facilitate further development. The goal of the ongoing research is to improve the robustness of the CCC towards external influences, such as vibrations, stray fields and He-pressure variations, as well as to develop a cost-efficient concept for the superconducting shield and the cryostat.

## INTRODUCTION

In modern accelerator facilities there are many applications, from rare isotopes and antiprotons in storage rings to slow extracted beams for nuclear physics experiments, which require absolute and non-destructive monitoring of ion beams with intensities down to nanoamperes. This need cannot be addressed by standard current diagnostics. Typical AC and DC current transformers are limited to intensities above microamperes. More sensitive devices like Faraday cups or secondary electron monitors (SEM) are at least partially destructive, which limits their application in storage rings, and – in case of the SEM – require elaborate calibration to compensate for aging effects. Although Schottky monitors can provide some current information, they are often not able to reach the desired accuracy at low currents and special care must be taken to

calibrate them correctly, especially for their use across large frequency ranges [1].

With the high magnetic sensitivity of a SQUID sensor (Superconducting Quantum Interference Device) the cryogenic current comparator (CCC) expands the detection threshold of the traditional current transformers and can provide absolute, non-destructive current measurements independent of particle species. In the most recent installation at the Antiproton Decelerator (AD) at CERN the CCC has shown a current resolution of 5.8 nA [1] and is actively used as part of the accelerator control system during the commissioning and routine operation. In a clean lab environment, currents down to 1.3 nA with a current noise lower than  $3 - 30 \text{ pA}/\sqrt{\text{Hz}}$  (7 Hz – 100 kHz) can be measured [2]. Furthermore, bandwidths of up to 200 kHz with a slew rate of  $0.16 \text{ }\mu\text{A}/\mu\text{s}$  are possible [2].

With our work, we aim to further increase the current resolution by improving the stability against electromagnetic and mechanical perturbations. A custom beamline cryostat is designed to minimize interferences as well as to expand the usability by adding a self-sufficient liquid helium cooling cycle. Ultimately, we plan to install a CCC in the storage rings (CRYRING and Collector Ring) and transfer lines of FAIR in order to supply low intensity current data to both the machine experts and users, and thus have a tool to better understand the processes during slow extraction from synchrotrons as well as the physics of low intensity experiments.

In this contribution, we look at the history of the CCC to show possible applications and the problems that we encountered, followed by the latest research to address these challenges. This includes studies toward alternative (coreless) shielding geometries and superconducting materials, as well as the analysis of mechanical resonances of the housing cryostat.

## HISTORIC DEVELOPMENTS

The CCC was developed in national standards laboratories to compare extremely small electric currents. One of the first who used the emerging SQUID sensors for current measurements was I.K. Harvey in 1972 [3]: see

\* Work supported by the European Union's Horizon 2020 research and innovation programme under the Marie Skłodowska-Curie grant agreement No 721559 as well as by the BMBF with the project numbers 05P15SJRBA and 05P18SJRBI.

<sup>†</sup> d.haider@gsi.de

Table 1: Historic development of the Cryogenic Current Comparator

Institute	Date	Reference	Comment
NSL/NMI, Australia	1972	I. K. Harvey [3]	One of the first CCCs for current measurements.
PTB, Germany	1977	K. Grohmann <i>et al.</i> [4,5]	Shield design and first tests with an $e^-$ beam.
Fermilab, USA	1985	M. Kuchnir <i>et al.</i> [6]	Proposal to install a CCC in the Antiproton Accumulator at Fermilab.
GSI & HIJ, Germany (GSI-Pb-CCC)	1996	A. Peters, H. Reeg, W. Vodel <i>et al.</i> [7]	Installation in the extraction line of the heavy ion synchrotron SIS18 at GSI.
INS, Japan	1998	T. Tanabe <i>et al.</i> [8]	Installation in the storage ring TARN II at KEK.
NPL, UK	2001	L. Hao <i>et al.</i> [9]	Test of HTC SQUID and shielding (in liquid $N_2$ ).
RIKEN, Japan	2004	T. Watanabe <i>et al.</i> [10]	Test of HTC SQUID and shielding (w. pulse tube).
DESY/HOBICAT, Germany	2010	R. Geithner, R. Neubert, W. Vodel <i>et al.</i> [11]	Dark current measurements of SC cavities for the TESLA linear accelerator and the EU-XFEL.
GSI & HIJ, Germany	2014	R. Geithner, F. Kurian <i>et al.</i> [12, 13]	Study of materials for flux concentrator (HIJ) and measurement of SIS18 slow extraction (GSI).
CERN, Switzerland (CERN-Nb-CCC)	2016	M. Fernandes, J. Tan <i>et al.</i> [1, 14]	Current monitor for the Antiproton Decelerator with a closed refrigeration system.
FAIR, Germany (GSI-Nb-CCC-XD, others in development)	exp. 2019	CCC collaboration [2, 15, 16, 17, 18]	Tests of the FAIR prototype, verification of shielding geometry with numeric simulations and efforts toward alternative (coreless) designs.

Table 1 for an overview of the developments. Soon after, in 1977, the German national standards laboratory (PTB) saw the potential of this method to measure the electron beam current of 100 nA generated by their Van de Graaff accelerator at an energy of 2.5 MeV [4]. For practical applications, the shielding of external magnetic fields became an important aspect, which was studied at the theoretical level by K. Grohmann *et al.* [5]. This work lead to the ring topology, which is still used for diagnostics of charged particle beams. In modern systems with this design typical attenuations of 135 dB are achievable [18].

M. Kuchnir *et al.* were one of the first to propose the installation of a CCC in an accelerator facility for the purpose of monitoring the beam intensity in the Antiproton Accumulator at Fermilab [6]. They manufactured several prototypes and adapted the design of K. Grohmann *et al.* using sheets of lead to construct the superconducting shield. The first application of a CCC to measure a hadron beam, however, was implemented at the extraction line of SIS18 at GSI by A. Peters *et al.* in 1996 [7]. They measured the spill structure of a beam of  $^{20}\text{Ne}^{10+}$  with an energy of 300 MeV/u and with an average current of 12 nA and achieved a resolution of  $0.1 - 0.3 \text{ nA}/\sqrt{\text{Hz}}$ , depending on the selected frequency range. Soon afterwards, in 1998, T. Tanabe *et al.* achieved a similar current resolution of 1 nA with a bandwidth of 10 Hz at the storage ring TARN II [8], which improved the accuracy of atomic cross sections measurements.

It is important to note, that these groups had to deal with a strong baseline drift of the SQUID signal following the cool down. After several days at liquid helium temperature, the drift gradually decreases and in modern installations it is confined to variations below  $0.3 \text{ nA/s}$  ( $25 \text{ nA}$  per cycle of 85 s) and is linear over many seconds

[1]. However, it has been shown that it is possible to compensate for these drifts to achieve absolute measurements throughout several minutes [1]. Our assumption is that the magnetic domains in the flux-concentrating core needs some time, which is longer at low temperatures, to reach an equilibrium state and the change of its magnetic permeability during this time is the reason for this baseline drift.

Once high-temperature superconductors (HTC) became accessible, in the early 2000s, L. Hao *et al.* at the National Physical Laboratory in the UK [9] and T. Watanabe *et al.* at RIKEN, Japan [10] used HTC-SQUIDS to implement CCCs that were cooled with either liquid nitrogen or a pulse-tube cooler, respectively. In general, they were less sensitive than their low-temperature counterparts and were operated with beam currents down to several microamperes.

## MODERN INSTALLATIONS

In 2010, R. Geithner *et al.* adapted the CCC to perform dark current measurements on a superconducting cavity for the TESLA linear collider [11]. The dark current of 5 nA could be measured successfully with a noise limited current resolution of  $0.2 - 50 \text{ nA}/\sqrt{\text{Hz}}$  (determined between 5 and 500 Hz). Especially in this setup, it became apparent that the mechanical and acoustic vibrations raise the current noise significantly so that their suppression became an important factor in the development.

In 2011, a detailed investigation to decrease the noise contribution of the flux-concentrating core was performed by R. Geithner *et al.* [12] and modern SQUID electronics was installed. In combination with a higher shielding factor against magnetic perturbations, this resulted, in 2014, in a current resolution of  $3.5 - 35 \text{ pA}/\sqrt{\text{Hz}}$  under ideal conditions, depending on the selected frequencies

(7 Hz – 10 kHz) [13]. This CCC system was later adapted to cope with the beam at the Antiproton Decelerator (AD) at CERN, where it is installed now [1]. In addition, the CCC prototype at GSI has been updated with new electronics in 2013 and the spill structure of the slow extraction from the SIS18 synchrotron at GSI could be measured. Ultimately, these measurements lead to an improvement of the spill quality. However, with increasing sensitivity, the thermal variations caused by pressure fluctuations of the liquid helium start to become significant and compromise the current signal. In the latest setup this drift was 15 nA/mK [15].

Since it was known that mechanical perturbations can pose a problem, the CCC cryostat at the AD at CERN was designed (leading up to 2016) with an emphasis to keep the mechanical eigenmodes off critical frequency values (e.g. 50 Hz) [14]. In addition, while previous CCCs had to be filled with liquid helium manually before each measurement campaign, a closed refrigeration system was implemented. Moreover, the CERN-Nb-CCC is fully incorporated into the accelerator control system. When the beam is injected into the AD the beam of antiprotons is bunched and the slew rate of the magnetic flux can reach 93.5 G $\phi$ /s. This is significantly higher than what the SQUID can track. As a result, at injection instead of following the current, the zero offset of the SQUID changes sharply. Nevertheless, this flux jump can be corrected with adequate calibration after each cycle. In the working configuration, a stable current resolution of 5.8 nA is achieved [1].

## NEW CCC GENERATION FOR FAIR

By learning from past applications, we aim to design a cryostat that incorporates a closed refrigeration system and that is robust against mechanical perturbations. However, the cryostat should still offer the flexibility to easily mount and exchange different components of the CCC. With this CCC test bench, which is planned to be installed at the storage ring CRYRING, we will be able to test new shielding geometries and materials in an accelerator environment. Currently, the detailed mechanical design of the cryostat is done iteratively with an analysis of the resonant frequencies, with the objective of reducing the effect of mechanical perturbations.

Furthermore, simulations have shown that there is a possibility to adapt the CCC shielding geometry in a way which significantly reduces the production effort [17, 18]. The application of superconductive coatings might further reduce the material cost. Other ideas, like using two SQUID sensors in a gradiometer setup to filter out global mechanic oscillations and the use of an active damping system are explored.

Moreover, advances in SQUID technology give us the opportunity to remove the flux-concentrating core. The magnetic fluctuations of the core are the dominating intrinsic noise source and many external perturbations are amplified by the core itself, therefore, efforts to eliminate this noise are very promising [18]. A new challenge that has to be addressed before an installation at FAIR, is the

radiation environment and the accumulation of a non-negligible radiation dose during an operation through many years. Therefore, the deployed Magnicon<sup>®</sup> and Supracon<sup>®</sup> SQUID sensors will be tested up to a total dose of 700 Gray at the CHARM irradiation facility at CERN.

## SUMMARY AND OUTLOOK

Cryogenic current comparators have been used actively in accelerator facilities around the world to measure nanoampere currents of ion beams and expand the detection threshold of standard diagnostics. The performance of the ring-shaped magnetic shielding is well documented [5, 16, 17]. The flux-concentrating core is a major source of noise and there are promising efforts to remove it relying on modern SQUID technology [18]. It has been shown at the AD that the effect of magnet ramps, pulse tube coolers and pressure variations (periodic or well defined perturbations) can be filtered during data processing to obtain meaningful current readings for many seconds [1]. Mechanical vibrations are a source of noise and a careful design and an analysis of the mechanical eigenmodes of the cryostat are needed to avoid interference with the measurements [14]. New concepts for the CCC at FAIR will be tested in CRYRING in 2019.

## REFERENCES

- [1] M. Fernandes, “SQUID based cryogenic current comparator for measuring low-intensity antiproton beams”, Ph.D. thesis, University of Liverpool, UK, Jun. 2017
- [2] P. Seidel, V. Tympel *et al.*, “Cryogenic current comparators for larger beamlines”, *IEEE Trans. Appl. Supercond.*, vol. 28, no. 4, p. 1601205, Jun. 2018, doi: 10.1109/TASC.2018.2815647
- [3] I. K. Harvey, “A precise low temperature dc ration transformer”, *Rev. Sci. Instrum.*, vol. 43, no. 11, pp. 1626-1629, Nov. 1972, doi: 10.1063/1.1685508
- [4] K. Grohmann *et al.*, “A cryodevice for induction monitoring of dc electron or ion beams with nano-ampere resolution”, *Superconducting quantum interference devices and their applications*, Walter de Gruyter & Co., p. 311, 1977
- [5] K. Grohmann *et al.*, “Field attenuation as the underlying principle of cryo-current comparators, 2. Ring cavity elements”, *Cryogenics*, vol. 16, no. 10, pp. 601-605, Oct. 1976, doi: 10.1016/0011-2275(76)90192-2
- [6] M. Kuchnir, J. D. McCarthy, and P. A. Rapidis, “SQUID based beam current meter”, *IEEE Trans. Magn.*, vol. 21, no. 2, pp. 997-999, Mar. 1985, doi: 10.1109/TMAG.1985.1063601
- [7] A. Peters *et al.*, “Review of the experimental results with a cryogenic current comparator”, in *Proc. 5<sup>th</sup> European Particle Accelerator Conf. (EPAC'96)*, Barcelona, Spain, Jun. 1996, p. 1627
- [8] T. Tanabe *et al.*, “A cryogenic current-measuring device with nano-ampere resolution at the storage ring TARN II”, *Nucl. Instrum. Methods Phys. Res. A*, vol. 427, pp. 455-464, 1999, doi: 10.1016/S0168-9002(99)00058-3
- [9] L. Hao *et al.*, “Design and performance of an HTS current comparator for charged-particle-beam measurements”



- IEEE Trans. Appl. Supercond.*, vol. 11, no. 1, Mar. 2001, doi: 10.1109/77.919424
- [10] T. Watanabe *et al.*, “A prototype of a highly sensitive cryogenic current comparator with a HTS SQUID and HTS magnetic shield”, *Supercond. Sci. Technol.*, vol. 17, pp. S450-S455, 2004, doi: 10.1088/0953-2048/17/5/073
- [11] R. Geithner *et al.*, “Dark current measurements on a superconducting cavity using a cryogenic current comparator”, *Rev. Sci. Instrum.*, vol. 82, p. 013302, 2011, doi: 10.1063/1.3527063
- [12] R. Geithner *et al.*, “A non-destructive beam monitoring system based on an LTS-SQUID”, *IEEE Trans. Appl. Supercond.*, vol. 21, no. 3, pp. 444-447, Jun. 2011, doi: 10.1109/TASC.2010.2089956
- [13] R. Geithner *et al.*, “A squid-based beam current monitor for FAIR/CRYRING”, *Phys. Scr.*, vol. 2015, no. T166, p. 014057, 2015, doi: 10.1088/0031-8949/2015/T166/014057
- [14] A. Lees *et al.*, “Design and optimisation of low heat load liquid helium cryostat to house cryogenic current comparator in antiproton decelerator at CERN”, *J. Phys. Conf. Ser.: Mater. Sci. Eng.*, vol. 171, p. 012033, 2017, doi: 10.1088/1757-899X/171/1/012033
- [15] V. Tympel *et al.*, “Comparative measurement and characterisation of cryogenic current comparators based on low-temperature superconductors”, presented at the 7th Int. Beam Instrum. Conf. (IBIC’18), Shanghai, China, Sep. 2018
- [16] H. De Gersem *et al.*, “Finite-element simulation of the performance of a superconducting meander structure shielding for a cryogenic current comparator”, *Nucl. Instrum. Methods Phys. Res. A*, vol. 840, pp. 77-86, 2016, doi:10.1016/j.nima.2016.10.003
- [17] N. Marsic *et al.*, “Numerical analysis of a folded superconducting coaxial shield for cryogenic current comparators”, *Nucl. Instrum. Methods Phys. Res. A*, under review
- [18] V. Zakosarenko *et al.*, “Coreless SQUID-based cryogenic current comparator (CCC) for non-destructive intensity diagnostics of charged particle beams”, *Supercond. Sci. Technol.*, submitted for publication

# UPGRADE AND IMPROVEMENT OF CT BASED ON TMR

Ying Zhao, Yaoyao Du, Ling Wang, Institute of High Engy Physics. CAS, Beijing, China

## Abstract

The CT based on TMR sensor has been developed in the lab. For Improving the accuracy and linearity, reducing the influence of sensor position, a series simulation and calculation have been done which conduct an upgrade both in the mechanical structure and electronics design. Lab test shows good results and test on beam will be carried on soon.

## INTRODUCTION

The CT based on TMR sensor's principle is like hall ammeter. Beam pass through a magnetic ring with a gap, a TMR sensor is put in a gap of the ring. The output of the sensor changes with the beam current [1]. The a principle diagram and the whole profile are shown in Figure 1. First test indicate that the resolution and linearity error could not meet the demand, improvement of the magnetic core and electronics design has been done, most details are present in this paper.

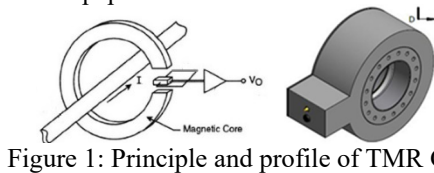


Figure 1: Principle and profile of TMR CT.

## STUDY AND IMPROVEMENT OF CORE DESIGN

One of the key parameter that involves the resolution are the core with a cutoff section. The soft alloy which has been processed is used as the magnetic core. The initial permeability is changed, so does other characteristic.

The cutoff section is an air gap, for a toroid core with air gap and ignore the edge flux, a equivalent permeability  $\mu_e$  can be calculate as below.

$$I_{beam} = \frac{B_{core}}{\mu_0 \mu_r} l_{core} + \frac{B_{gap}}{\mu_0} l_{gap} = \frac{B_{core} l_{core}}{\mu_0 \mu_r} \left(1 + \frac{\mu_r l_{gap}}{l_{core}}\right)$$

$$\mu_e = \frac{1}{\frac{1}{\mu_r} + \frac{l_{gap}}{l_{core}}}$$

$l_{core}$  is average core circumference  $2\pi r_{core}$  ( $r_{core} = (r_{out} + r_{in})/2$ ,  $r_{out}$  and  $r_{in}$  are outer and inner radius of the core),  $l_{gap}$  is length of the air gap. When  $\mu_r$  is large enough, the  $\mu_e$  is related to the  $l_{gap}$  and  $l_{core}$ . It means the core magnetic permeability is decreased and linearized.

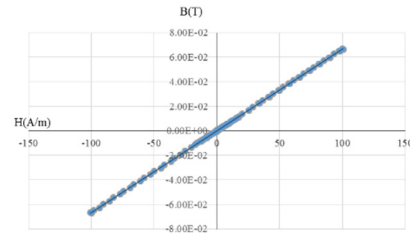


Figure 2: Magnetization curve test result of the core with air gap.

The magnetization curve of the core with air gap is test in the lab as shown in Figure 2. The magnetization curve with air gap can be seen as the synthesis of magnetization characteristic of the core and air gap. The air gap reduces the remanence and the core saturation. It also means most of the loss is gathered in the gap instead of the core.

High frequency signal brings hysteresis loss. If the magnetic core cross section area is  $A_{core}$ , the exciting signal are  $u(t)$  and  $i(t)$ . As indicate in Figure 3, the area  $A_1$  of  $-B_r \rightarrow S \rightarrow B_m \rightarrow -B_r$ , means the exciting signal varies from zero to the maximum, in the half period  $T/2$ , the total energy can be calculate below:

$$\int_{\alpha}^{\alpha+\frac{T}{2}} u(t)i(t)dt = \int_{-B_r}^{B_r} A_{core} \frac{dB}{dt} H l_{core} dt$$

The area  $A_2$  from  $S$  to  $B_m$  is the part of recoverable energy. The energy of the core loss is proportional to the area around the hysteresis loop, is related to the area of  $A_1-A_2$ . With air gap the  $A_1-A_2$  is small enough to be ignored.[2]

$$A_{core} l_c \left( \int_{-B_r}^{B_s} H dB - \int_{B_s}^{B_r} H dB \right) = A_{core} l_c (A_1 - A_2)$$

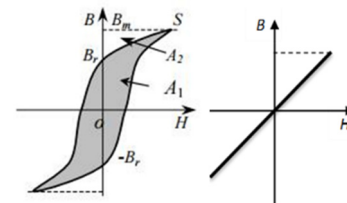


Figure 3: Magnetization curve without (left) and with (right) air gap.

Primary design and test result shows that output resolution is influenced by sensor's position and angle in the gap. Focusing on how to uniform the magnetic field distribution doesn't show effective improvement. As the sensing area is 2mm much smaller than the gap section area 20mm x 20mm, gathering the magnetic field is a feasible option. A perpendicular cutoff is made to reduce the cross section as shown in the Figure 4. The gap section area is 10mm x 20mm after this improvement.



Figure 4: Sketch of the perpendicular cutoff.

One of the side-effect of perpendicular cutoff is the increasing of edge flux. Basic knowledge, magnetic fields are not insulated, the space around the air gap can be also seen as part of the magnetic circuit, so does the side section. The edge flux and gap flux are in parallel, it equivalent to enlarge the air gap section area, and leading the increase of the inductance  $L$  of the core. A simulation result also shows that the field in the air is concentrated and the edge flux is more obvious in Figure 5[2]. Another aspect concerned is the edge flux that may impact the electronics nearby which so far do not observed in the test.

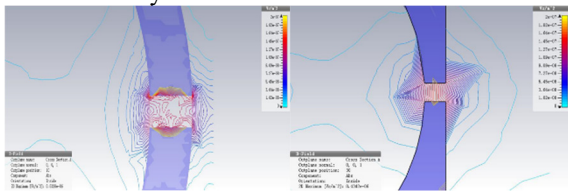


Figure 5: Simulation results of before (left) and (after) perpendicular cutoff.

## ELECTRONICS DESIGN

The electronics has two simple main function: power supply for the TMR sensor and processing the output signal. The TMR rated operational voltage determines the output sensitivity  $S$  mV/V/Gauss. Choosing of operational voltage focuses on the high enough sensitivity and flat stable work area. Temperature drift at different working voltage as shown in the figure. From 1 to 6 volt to driving, [3] A 14 hours continuous electronics temperature drift test from 18-27°C has been recorded, results show less dependence, for large scale of temperature test should be done in the future.

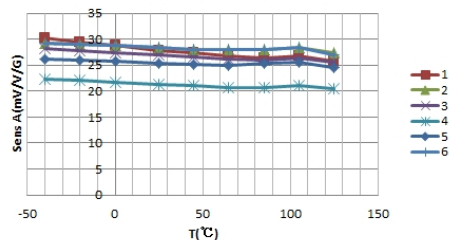


Figure 6: Sensitivity drift with temperature at different working voltage.

One of the aspects that involved the sensing area is the stress between the TMR board and the main electronics board. The vibration conducted to the TMR board leads to sensitivity change. The flat cable is chosen to connect the two boards, showing much improvement. A FFC (Flexible Flat Cable) is also a proper one. Range control protects the TMR sensor's saturation, it is integrated on the

board which may change to remote control in the future. Figure 7 shows the component of the electronics.

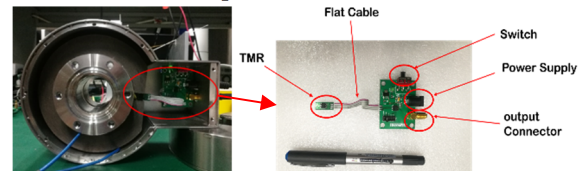


Figure 7: CT structure and the electronics.

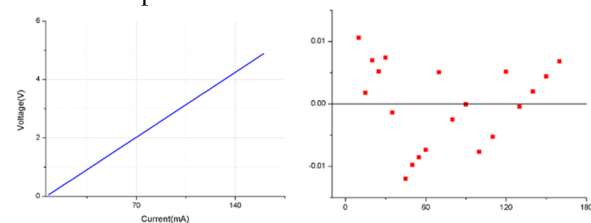
## MECHANICAL DESIGN

Mechanical structure design aims to be easy installed and stable. Two layers of low permeability steel and copper are used for shielding and conducting the wall current. In the first design, a vacuum chamber with ceramic gap and flange is made integral with the core and electronics. Further plan is making two semicircle core and clip on the beamline for do not need to break the vacuum. The structure is shown in Figure 7.

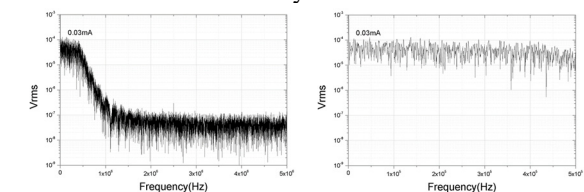
## TEST RESULTS

In the Lab, the CT's performance has been tested using 30 meters long transmission cable, including: 1. DC linearity and resolution test, using transimle 3041 calibration and Keithley 34401A DC current meters. NI PCI 4070 (DC) with external trigger [2]. Square signal response and bandwidth test, using LeCroy oscilloscope 6GHz 40GS/s, Agilent 33250A waveform generator.

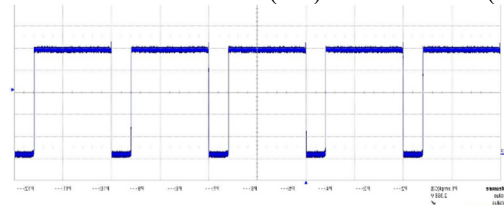
The 200mA range test results are shown in Figure 8. The linearity error of full scale is less than 0.2%. For TMR's bandwidth is DC-5MHz [3], the step at 1MHz of resolution result is because of the electron component's bandwidth limit which can be increased in the next version. The CT's bandwidth is low enough as the square signal response shows no droop.



Linearity error result



Resolution result of 0-5MHz (left) and 0-500KHz (right)



Square signal response

Figure 8: Test results of 200mA range.

## CONCLUSION

The improvement and upgrade study shows good results in the performance, especially amend of core structure. An extra calibration winding and electronics are plan to complete the function. For further online test, vacuum need to be promote, shielding from disturb and noise are the key issue should be concerned.

## REFERENCES

- [1] Ying Zhao et al, A new current sensor based on TMR, International Beam Instrumentation Conference, Grand Rapids, USA, Aug. 2017, WEPCF11
- [2] X.K.Zhao, Theory and design of magnetic elements for switching power supply, Beijing university of aeronautics and astronautics press, 2014
- [3] CST Manual, <http://www.CST.com>
- [4] Specification of Dowaytech sensor, <http://www.dowaytech.com>



# DATA ACQUISITION SYSTEM FOR BEAM INSTRUMENTATION OF SXFEL AND DCLS\*

Y.B. Yan<sup>†</sup>, Y.B. Leng, L.W. Lai, L.Y. Yu, W.M. Zhou, J. Chen, H. Zhao, C.L. Yu

Shanghai Synchrotron Radiation Facility (SSRF)

Shanghai soft X-ray Free-Electron Laser facility (SXFEL)

Shanghai Institute of Applied Physics, Chinese Academy of Sciences

Shanghai 201204, P.R. China

## Abstract

The high-gain free electron lasers have given scientists hopes for new scientific discoveries in many frontier research areas. The Shanghai X-Ray Free-Electron Laser (SXFEL) test facility is commissioning at the SSRF campus. The Dalian Coherent Light Source (DCLS) has successfully commissioned in the northeast of China, which is the brightest vacuum ultraviolet free electron laser facility. The data acquisition system for beam instrumentation is based on the EPICS platform. The field programmable gate array (FPGA) and embedded controller are adopted for the signal processing and device control. The high-level applications are developed using Python. The details of the data acquisition system will be reported in this paper.

## OVERVIEW

The Shanghai soft X-ray Free-Electron Laser facility (SXFEL) is being developed in two steps, the SXFEL test facility (SXFEL-TF) and the SXFEL user facility (SXFEL-UF). The SXFEL-TF is a critical development step towards the construction a soft X-ray FEL user facility in China, and is under commissioning at the Shanghai Synchrotron Radiation Facility (SSRF) campus. The test facility is going to generate 8.8 nm FEL radiation using an 840 MeV electron Linac passing through the two-stage cascaded HGHG-HGHG or EEHG-HGHG (echo-enabled harmonic generation, high-gain harmonic generation) scheme, as shown in Figure 1. The construction of the SXFEL-TF started at the end of 2014. Its accelerator tunnel and klystron gallery were ready for equipment installation in April 2016. The installation of the SXFEL-TF Linac and radiator undulators were completed by the end of 2016. In the meantime, the SXFEL-UF, with a designated wavelength in the water window region, began construction in November 2016. It was based on upgrading the Linac energy to 1.5 GeV, and the building of a second undulator line and five experimental end-stations. It is scheduled to be open to users in 2019[1].

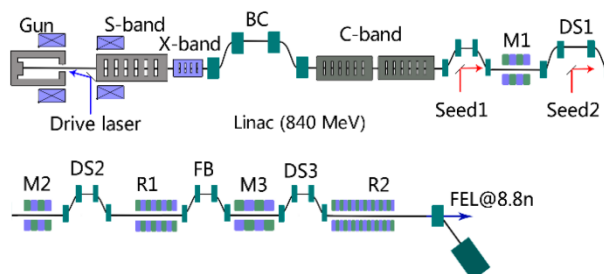


Figure 1: Schematic layout of the SXFEL-TF.

The Dalian coherent Light Source (DCLS) is a FEL user facility, which can deliver world's brightest FEL light in the energy range from 8 to 24 eV, making it unique of the same kind that only operates in the Vacuum Ultra Violet (VUV) region. It use a 300MeV Linac to produce fully coherent photon pulses in the wavelength range between 50-150nm by HGHG scheme. This project was launched at the beginning of 2012, and has successfully commissioned by the end of 2016. It was a close collaboration between the scientists and engineers from Dalian Institute of Chemical Physics and Shanghai Institute of Applied Physics, two institutes of Chinese Academy of Sciences.

The data acquisition system for beam instrumentation is a part of the SXFEL and DCLS control system, which is based on the EPICS (Experimental Physics and Industrial Control System) platform. The system architecture is shown in Figure 2. The FPGA (Field Programmable Gate Array) and embedded controller (such as Raspberry Pi, BeagleBone Black) are adopted for the signal processing and device control. The high-level applications are developed using Python.

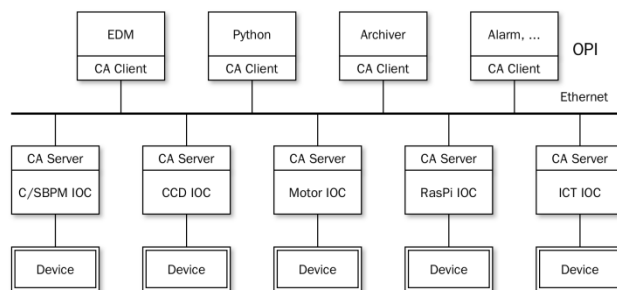


Figure 2: Data acquisition system architecture for beam instrumentation.

\* Work supported by the National Development and Reform Commission (NDRC) and the National Natural Science Foundation of China (NSFC)

<sup>†</sup> yanyingbing@sinap.ac.cn

BPM IOC

The digital BPM signal processor was developed in SINAP, which meets the requirements of SXFEL and DCLS. They are used on the signal processing of both stripline BPM and cavity BPM[2-3]. The processor is a standalone system and provides 4 channels 120MSa/s, 16 bits ADC and Virtex-5 FPGA, as shown in Figure 3.



Figure 3: Digital BPM signal processor.

In the processor, an IMX6Q is adopt as the system controller. It is set to boot from a micro SD card, which is convenient for the batch production. The IMX6Q runs embedded Linux operating system and processes the raw data read from FPGA.

The IOC is based on the asynDriver, which is a general purpose facility for interfacing device specific code to low level communication drivers. Both the Fast Fourier Transformation (FFT) and Hilbert transform algorithms are implemented to calculate the amplitude and phase for each channel. The IOC architecture of digital BPM signal processor is shown in Figure 4.

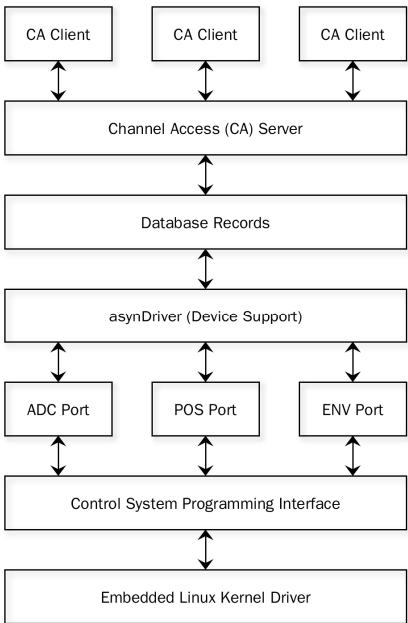


Figure 4: The IOC architecture of digital BPM signal processor.

In the SXFEL and DCLS control system, the EDM (Extensible Display Manager) is used as the default user interface. A unified integrated framework is designed and implemented. The BPM panels are also based on the framework, as shown in Figure 5.

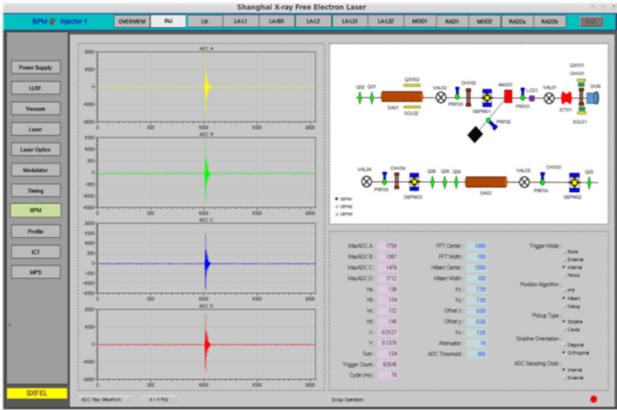


Figure 5: The stripline BPM panel of SXFEL.

The archiver is based on the PostgreSQL, which is a powerful, open source object-relational database system. The RDB Channel Archiver of CSS (Control System Studio) is adopted. Users can access the historic beam position data using the CSS Data Browser.

The high-level applications are important tools for system performance evaluation, physical parameters measurement, machine optimization, etc. They were written using Python. The CA (Channel Access) interface select PyEpics [4] and Cothread [5].

CCD IOC

The industrial cameras support multiple buses, such as FireWire, USB, GigE Vision, Camera Link, CoaXPress and so on. The GigE Vision is a globally accepted camera interface standard developed using the Gigabit Ethernet communication protocol. It offers the greatest technical flexibility in terms of bandwidth, cable length and multi-camera functionality. In the SXFEL and DCLS, the GigE Vision cameras (JAI and Basler) are adopted, which can simplify the system architecture. A dedicated network is employed to transmit the images to the servers.

The CCD IOCs are mainly responsible for the image acquisition of the beam profile measurement and laser diagnostics system. They acquire the image data from cameras via network switch and process on the servers (IBM System x3550 series). The software is based on the areaDetector. The image processing contains image rotations, flips, ROI (Region of Interest), profiles, etc. The EDM panels are shown in Figures 6 and 7.

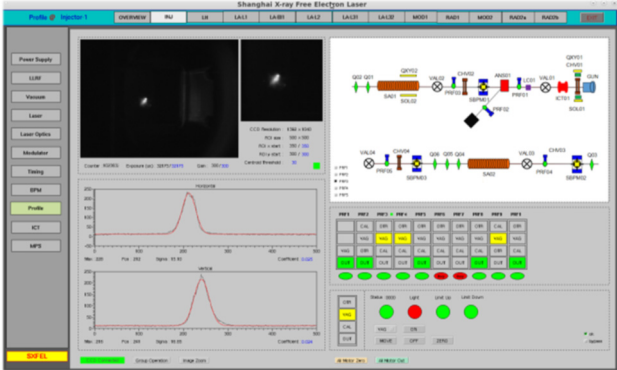


Figure 6: Beam profile measurement panel of SXFEL.

Content from this work may be used under the terms of the CC BY 3.0 licence (© 2018). Any distribution of this work must maintain attribution to the author(s), title of the work, publisher, and DOI.

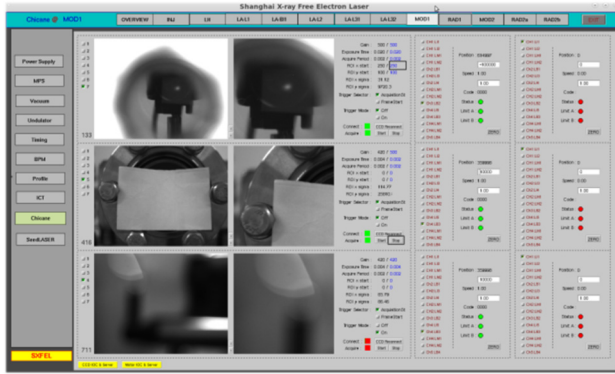


Figure 7: Laser diagnostics panel of SXFEL.

## MOTOR IOC

In the beam instrumentation, microwave and laser diagnostics system of SXFEL and DCLS, the network-based step-servo motors (MOONS SSM24Q-3RG) are adopted. The motors integrate with controller, driver, encoder and digital I/O interface. The digital I/O can be used as limit protection, illumination control, etc.

The motors can be accessed via TCP/IP protocol. The IOCs are based on the streamDevice, which also runs on the IBM servers. The motors control panels are shown in the right part of Figures 6 and 7.

## ICT IOC

The Keysight digital oscilloscopes are used for the data acquisition of integrated current transformers, which are LXI (LAN eXtensions for Instrumentation) devices. The LXI consortium defines standard ways for Ethernet-based instruments to communicate, operate and function. The data is transmitted to the servers through the dedicated network. The IOC software is based on the asynDriver and VISA (Virtual Instrument Software Architecture). The data rate can reach 20Hz for 4 Channels 50K waveform, as shown in Figure 8.

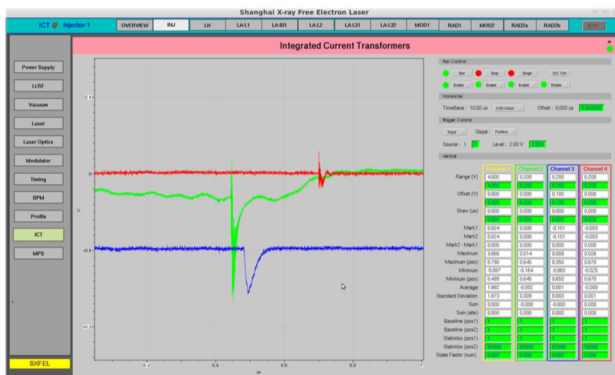


Figure 8: Beam charge measurement panel of SXFEL.

## RASPI IOC

The embedded Linux boards, such as Raspberry Pi and BeagleBone Black are credit-card-sized single-board computers. They are low-cost and equipped with a huge array of GPIO (General Purpose Input Output), which can

be used to take readings from sensors and control external devices. The active development community and open-source nature also make them ideal choices for many applications. They can be integrated with the accelerator control system [6].

In the SXFEL and DCLS, they were embedded in the customized chassis. The dedicated circuits were designed to control the power supply via electric relays. They run as the IOCs and control the power supplies of CCD cameras and step-servo motors remotely.

## CONCLUSION

The data acquisition system for beam instrumentation of the SXFEL-TF and DCLS have been designed and developed. Up to now, the systems have operated steadily for one year, and play important roles during the daily operation and beam commissioning. With the new equipment installation of SXFEL-UF, more functionality will be added. Further optimization will be also carried out.

## ACKNOWLEDGEMENT

We would like to thank everyone who contributed to this work through discussions and suggestions.

## REFERENCES

- [1] Z.T. Zhao *et al.*, “Status of the SXFEL Facility”, *Applied Sciences*, 7(6), 607, June 2017.
- [2] L.W. Lai, F.Z. Chen *et al.*, “Batch Applications of Digital BPM Processors from the SINAP”, in *Proc. 5th International Beam Instrumentation Conference (IBIC'16)*, Barcelona, Spain, September 2016, paper WEPG17.
- [3] L.W. Lai, Y.B. Leng, Y.B. Yan *et al.*, “Design and Performance of Digital BPM Processor for DCLS and SXFEL”, in *Proc. 8th International Particle Accelerator Conference (IPAC'17)*, Copenhagen, Denmark, May 2017, MOPAB092.
- [4] PyEpics3, [http:// cars9.uchicago.edu/software/python/pyepics3](http://cars9.uchicago.edu/software/python/pyepics3)
- [5] Cothread, [http:// cothread.readthedocs.io](http://cothread.readthedocs.io)
- [6] Y.B. Yan, Y.B. Leng *et al.*, “Application of Embedded Linux Boards in SSRF and SXFEL Control System”, in *Proc. 7th International Particle Accelerator Conference (IPAC'16)*, Busan, Korea, May 2016, THPOY007.

# THE RADIAL DETECTOR IN THE CYCLOTRON OF HIMM

Min Li<sup>1</sup>, Shenpeng Li<sup>2</sup>, Xincai Kang<sup>1,3</sup>, Weilong Li<sup>1,4</sup>, Ruishi Mao<sup>1</sup>, Haihong Song<sup>1</sup>, Tiecheng Zhao<sup>1</sup>, Yucong Chen<sup>1</sup>, Yonggan Nie<sup>1</sup>, Yongchun Feng<sup>1,3</sup>, Yan Yin<sup>1</sup>, Yanmou Wang<sup>1</sup>, Weinian Ma<sup>1</sup>.

<sup>1</sup>Institute of Modern Physics, Chinese Academy of Science, Lanzhou 730000, China;

<sup>2</sup>Lanzhou Kejintaiji Corporation, LTD, Lanzhou 730000, China

<sup>3</sup>Lanzhou University of Technology, Lanzhou 730050, China

<sup>4</sup>University of Chinese Academy of Sciences, Beijing 100049, China

## Abstract

The cyclotron is designed as the injector of the Heavy Ion Medical Machine (HIMM) in Wuwei city, China. It provides 10 uA carbon beams to fulfill the requirement of the accumulation in the following synchrotron. The Radial detector is used to measure the beam current and beam turn motion in this Cyclotron. The beam current signal gathered by radial detector is acquired by four picoammeters, meanwhile the beam time structure is measured with FPGA and real time operating system. This paper introduces the design of radial detector, the motion control and data acquisition system for it of the cyclotron. Finally, the beam current and turn pattern measurement results at HIMM are presented in this paper.

## INTRODUCTION

The first Heavy Ion Medical Machine (HIMM) has passed the registration tests and now enters the clinical trials phase which was constructed at the Institute of Modern Physics, China [1]. A compact cyclotron is designed as the injector of a synchrotron which forms the HIMM, and it accelerates the <sup>12</sup>C<sup>5+</sup> from ion source to 7.0MeV/u, meanwhile the extracted beam current is more than 10uA [2].

As its compact structure of the cyclotron, there are 2 radial probes installed on the hill and in the valley respectively of Cyclotron. The one installed in the valley is used to monitor the beam current during the injection period, and the other one installed between the extraction deflector and extraction dipole is used to monitor the extraction beam current. Furthermore, the beam centre measurement can be done with the two targets during the acceleration period. The radial probe installed on the hill is shown in Fig.1. And for each radial probe, it is driven with a servo motor. The moving distance of the radial probe is 795 mm.

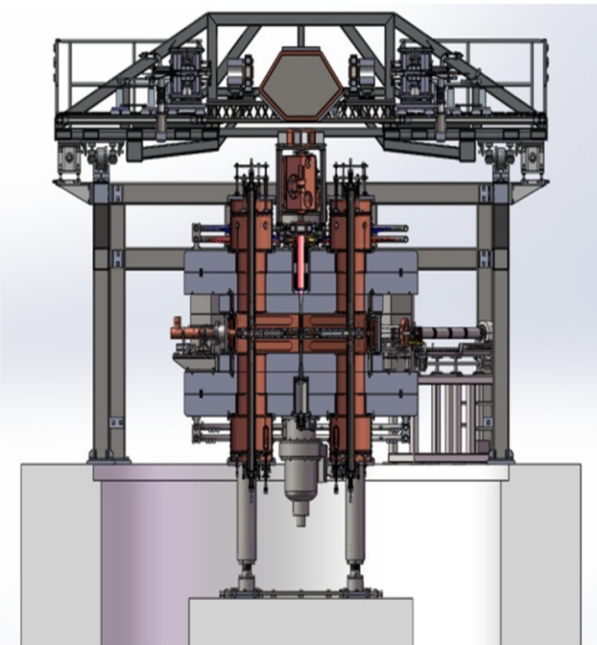


Figure 1: Radial probe installed on the Cyclotron.

## DESIGN OF RADIAL PROBE

### Mechanical Design

The radial probe target tip, making up by one integral block and 3 differential fingers which are distributed concurrently in the horizontal direction, measure the beam distribution on axial and radial directions by blocking the beam [3]. The 3 differential fingers are distributed uniformly in the vertical direction with the gap of 5mm. The sizes of the integral and differential target tips are listed in table 1. The radial probe target tips are made by copper. The top view of the radial probe is displayed in Fig.2 and the target probe structure is shown in Fig.3.

Table 1: The Size of Four Fingers

Finger Name	Size(mm)
Integral Finger	40
Differential Top	10
Differential Middle	10
Differential Bottom	10



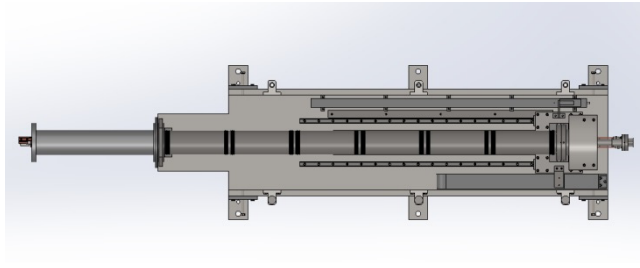


Figure 2: Structure of the radial probe from the top view.

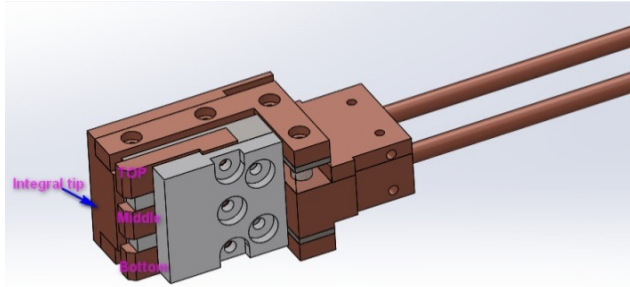


Figure 3: Structure of the radial probe the target tips.

### Thermal Structural Analysis

The extraction beam energy of Cyclotron is 7MeV/u, and the beam current is 10uA. The beam profile hit on the radial probe is set to 10 mm. The structure of the radial probe without and with water-cooled is analysed with the above parameters in this paper. As shown in Fig. 4, it can be seen that the temperature of the radial probe target tips is more than 2500°C which exceeds the melting point of the copper, which can directly cause damage to the target. As a result, it is essential that a water-cooled structure is a necessary design.

For the water-cooled structure of the probe, by setting the flow rate is 4m/s, the water pressure is 5kg, and then the flow analysis result is introduced into the thermal analysis. According to the results of thermal analysis, as shown in Fig.5, it can be seen that the maximum surface temperature is about 500°C, which is much lower than the melting point of tantalum of 2996°C, also much lower than the melting point of copper of 1083°C. Therefore, the water-cooled radial probe structure with these designed parameters is in the range of the thermal tolerance. What's more, between the integral and the differential tips is a layer of heat conducting ceramic made of aluminium nitride that can enhance the effect of water cooling[3].

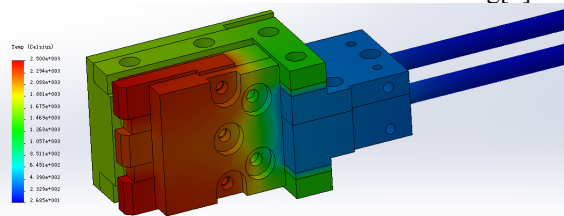


Figure 4: Thermal structural analysis of the radial probe without water-cooled design.

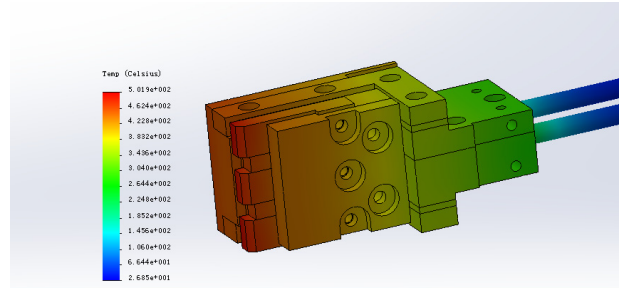


Figure 5: Thermal structural analysis of the radial probe with water-cooled design.

### CONTROL AND THE DATA ACQUISITION SYSTEM OF THE RADIAL PROBE

The control hardware of the radial probe is based on FPGA and real-time (RT) operating system. The application of FPGA can realize the precise timing, trigger, control, synchronization and user-defined high speed communication protocol requirements. The real-time operating system can ensure the realization of the deterministic control, data processing and data logging. Furthermore, the whole control system is based on the National Instruments CompactRIO hardware. The control and the data acquisition system are shown in Fig.6.

The NI CompactRIO 9075[4] is in charging of acquiring the beam current from the picoameters where the beam current is convert to voltage linearly. Meanwhile, the position of the radial probe detector is read by the resolver and sampled simultaneously with the beam current signal at the FPGA and then transferred to RT by FIFO. Accordingly, the beam current and the related position are finally parsed at the GUI. The position information is acquired from the Kollmorgen servo motor with a resolver encoder whose resolution is 24 bits [5]. And the mechanical position precision is less than 1mm almost to 0.5 mm which means the whole control system can reach the 0.5 mm position precision compared with the encoder position resolution.

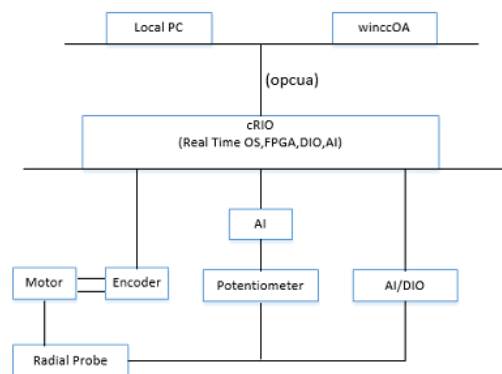


Figure 6: The hardware framework of the radial probe control system.



# THE DESIGN OF DOSE PARAMETER ACQUISITION AND CONTROL SYSTEM FOR A PENCIL BEAM SCANNING SYSTEM IN HUST-PTF\*

Y.Y. Hu, P. Tan<sup>†</sup>, Y.J. Lin, X.Y. Li, Y.C. Yu, H. Lei, H.D. Guo

State Key Laboratory of Advanced Electromagnetic Engineering and Technology,  
School of Electrical and Electronic Engineering, Huazhong University of Science and Technology,  
Wuhan 430074, China

## Abstract

Pencil beam scanning (PBS) technology is a flexible and accurate dose delivery technology in proton therapy, which can deliver beams adapting to irregularly shaped tumors, while it requires precise diagnostic and real-time control of the beam dose and position. In this paper, a dose parameter acquisition and control system for the pencil beam scanning system based on the EPICS and LabVIEW is designed for HUST-PTF. The EPICS environment is built to realize the data exchange function between the front-end devices and control system. A channel access server (CAS) is designed to convert treatment parameters into the process variables (PVs) and expose them to the network for data sharing. Under current experimental conditions, the simulated beam current is generated according to the dose parameters in the treatment plan file. The current are processed by a digital electrometer and transmitted to the EPICS database in real time. Then the control system user interface based on LabVIEW is realized for displaying and parameter analysis.

## INTRODUCTION

The pencil beam scanning nozzle is located at the end of the proton therapy machine in Huazhong University of Science and Technology Proton Therapy Facility (HUST-PTF). It is composed of scanning magnets, ionization chambers and other beam diagnostic equipment as well as related electronic devices and controllers. It is the last guarantee to accurately deliver the proton beam to the designated location of the tumor with accurate dose. This paper mainly focuses on the technology of controlling dose safety, and the dose parameter acquisition and control system has been designed by using software and hardware redundancy analysis.

Firstly, the dose monitoring system of the nozzle needs to obtain the treatment plan accurately from the Treatment Control System (TCS), extract the scan dose parameter, convert it into the actual machine parameters correctly, and confirm and display these data. Then, the control software needs to transmit data with the front-end devices efficiently. It sends the corresponding instrument parameters to the hardware devices in the nozzle accurately and gets feedback data, so as to control and monitor the beam dose accurately in real time. At the same time, fast interlocking protection can be carried out under exceptional conditions.

As the main equipment for dose monitoring, two separate working ionization chambers are designed as redundant measures to ensure that the ionization chamber operates normally all the time. And the alarm threshold of the second ionization chamber is set to be 5% larger than that of the first device to ensure that when the first ionization chamber fails, the other device can still work normally, and the fault signal can be transmitted to the superior system.

In order to make the operation of the control system more intuitive and convenient, the graphical user interface (GUI) of the system is built with the LabVIEW development platform. The interface displays treatment plan parameters, actual treatment data, treatment progress, the working status of front-end devices and so on.

Finally, the treatment results are uploaded to the TCS when the treatment is finished. Also, if treatment is interrupted, the dose already applied must be uploaded in order to allow correct continuation after interruption. The corresponding framework of the control system is shown in Fig.1.

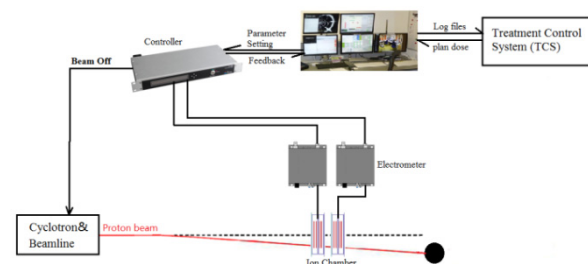


Figure 1: Control system framework.

## LOGICAL DESIGN OF THE SYSTEM

Before the start of treatment, the first step is to accurately analyse the treatment plan file and obtain the ideal dose parameters. In order to ensure the safety of the transmission and correct interpretation of the treatment plan file, the DICOM standard data format is uniformly used for data interaction throughout the whole treatment process. The essence of the DICOM file is the binary file. Each data element contains four parts: Tag (Data element Identification), VR (Value Representation), VL (Value Length), VF (Value Field)<sup>[1]</sup>. By identifying the Tag of the dose parameter, the data element of planned dose parameter can be extracted out. Dose parameters are stored in VF part in hexadecimal from. Then we convert them to

\* Work supported National Key R&D Program of China (No.2016YFC0105308).

<sup>†</sup> Corresponding author, tanping@mail.hust.edu.cn

floating point numbers and display the results on the control software user interface.

Second, the conversion calculation from the treatment parameters to the instrument parameters should be designed. According to the working principle of the plate ionization chamber shown in Fig.2, when the proton beam passes through the ionization chamber, the gas molecules filled in the ionization chamber will be ionized, the positive charges and electrons will move toward the two plates under the traction of the high voltage of the plates. The amount of induced charge on the two plates will change with the beam current and time. The time-varying current signal will be obtained and amplified by an electrometer. Therefore, the dose parameter will be converted to a corresponding current value for quick comparison with the measured value from the electrometer.

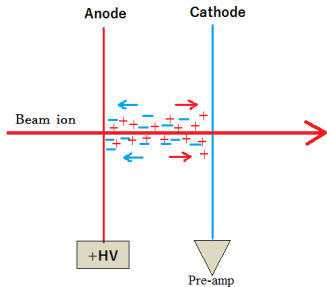


Figure 2: The principle of the ionization chamber.

The gain, which represents the number of electrons generated by a proton particle passing through the ionization chamber, can be obtained by Monte Carlo simulation. The relationship between the gain and the energy of the proton beam has been given in references [2]. When the time is known, the relationship between electrons and current can be obtained, in which case the dose can be associated with the current value.

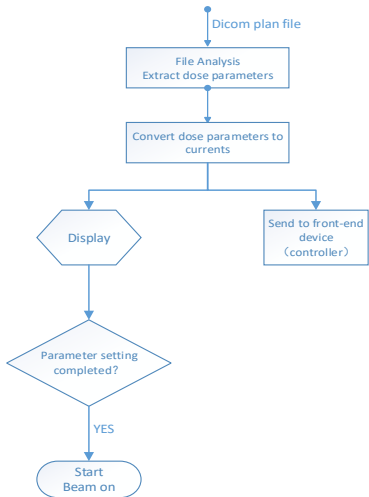


Figure 3: The workflow during the preparation.

After obtaining the correct instrument parameters, the parameters of each layer are sent to the front-end monitoring device for parameter setting, which needs to be implemented in the EPICS environment. After the setting is completed, the front-end device sends the confirmation

signal to the control software indicating that it is ready to turn on the beam for treatment. The corresponding logic block diagram is shown in Fig. 3.

During the treatment, the ionization chamber is always in operation, monitor the dose in real time and feedback the data to the controller. In the EPICS environment, the controller sends monitoring data to the control software for caching. The current waveform diagram and the running status of the front-end device are displayed by the user interface, and compared with the ideal plan parameters. Once a parameter is found to exceed the allowable safety tolerance scope, the controller outputs the beam off instruction immediately to turn off the beam and issues a warning in the user interface.

When the last point of the layer is illuminated, it is also necessary to immediately output the beam off instruction, turn off the beam, and display all monitoring data and treatment results by the control software, and save the record in txt format. The corresponding logic block diagram is shown in Fig. 4.

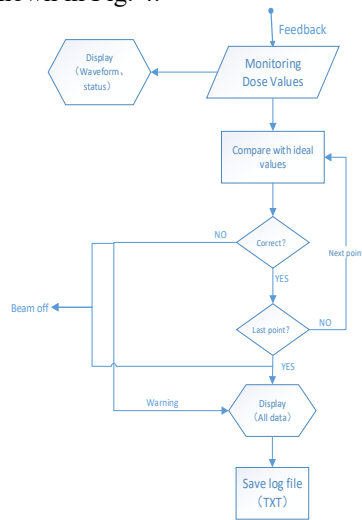


Figure 4: The workflow during the treatment.

## SAFETY ANALYSIS

The normal operation of the system requires three important elements: monitoring equipment, logic blocks, and terminal response components. Fault analysis can be done from these three aspects. The possible causes of overdose error could be: (1) the failure of the dose monitoring device (ionization chamber). It fails to detect that the dose value has exceeded the safe range, or fails to feed back the detected dose value to the upper controller; (2) the logic block of the controller is not working properly. It fails to generate the beam-off signal in time, or sends an unplanned beam-on signal; (3) the terminal physical component is broken, and unable to respond immediately after receiving the correct signal, which causes the beam to fail to shut down in time, or to start the beam when no instructions are received from the superior controller.



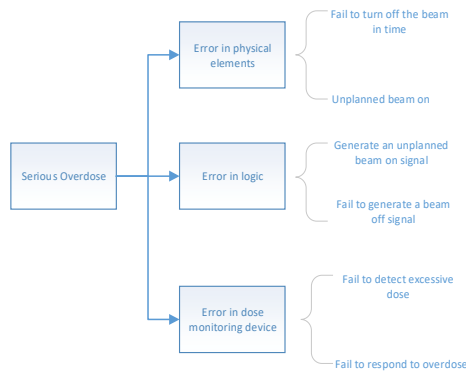


Figure 5: Fault tree.

According to the safety requirements of medical devices, the dose error should not exceed 5% of the planned value. For the fault analysis in Fig.5, we can take certain safety redundancy measures. First of all, to ensure the normal operation of the dose monitoring equipment, two sets of ionization chamber equipment are used for dose monitoring at the same time. The two sets of devices work independently by respective power supply, and the alarm threshold of second ionization chamber is set 5 % larger than the first set. The measurement results from two sets of devices are both fed back to the controller to ensure that when the first device fails, the other device can still work normally. When the difference between the dose values monitored by the two independent ionization chambers reaches  $\pm 5\%$ , the controller perform to turn off the beam and issue an alarm immediately.

During beam transmission, it is necessary to prevent the beam from being delayed due to the failure of the terminal physical elements, so multiple redundant devices are set up to control beam transfer. When the controller generates erroneous operating signals, such as overdose signals, the kicker magnet responds first and deflects beam out of axis rapidly. If it fails, there is an electrostatic deflector in cyclotron to control the beam. If it still doesn't work, then there is a High Frequency Generator in cyclotron, which can reduce the power to at least 20%. The "Proton Source Electronics Unit (PSEU)" can be the last measure to controls the ion source. When all terminal elements fail, it can turn off the proton source should be directly.

## DATA TRANSMISSION

After obtaining the correct instrument parameters, an EPICS environment is built in the PC to achieve the data exchange function between the control software and the front-end equipment. An EPICS Channel Access Server (CAS) is configured as Input/Output Controller (IOC) in LabVIEW-based control software. Its function is to convert the treatment data into EPICS PV values, expose them to the network [3]. Then any clients in the network can access the data by inputting the PV name.

The electrometer used in this experiment is IC101 ion chamber controller produced by Pyramid, it is intended for the measurement of small charges or currents (from pA to  $\mu$ A) generated by ionization chambers. Also, Pyramid

supplies an executable called IG2. In the database of IG2, the "channel" and the "wire" can be configured. Users can define any number of channels according to the function and interface of the device. These channels map one-to-one to EPICS PVs, and correspond to the "wire" (real physical channel of the device). The client can directly access any channels in the system according to the custom channel name, and all the channel names defined in the IG2 database will be recognized as PV by EPICS client program. So IG2 is used as an optional Channel Access Server in the system.

```

<channels>
  <channel name="r_IC101_3_current" wire="analog_in_current"/>
  <channel name="r_IC101_3_charge" wire="analog_in_accumulated_charge"/>
  <channel name="c_IC101_3_range" wire="analog_out_range"/>
  <channel name="c_IC101_3_init" wire="digital_out_initiate"/>
  <channel name="c_IC101_3_accum" wire="digital_out_accumulate_charge"/>
  <channel name="c_IC101_3_period" wire="analog_out_integration_period"/>
  <channel name="c_IC101_3_resol" wire="int_out_resolution"/>
  <channel name="c_IC101_3_capacitor" wire="int_out_capacitor"/>
  <channel name="c_IC101_3_calibrate" wire="digital_out_calibrate"/>
  <channel name="c_IC101_3_bias" wire="int_out_external_bias"/>
  <channel name="c_IC101_3_biasmax" wire="int_out_external_bias_max"/>
</channels>
</board>
</hardware>
  
```

Figure 6: The example of IC101 channel configuration.

In this paper, the channels of IC101 are defined by IG2. Figure 6 shows the example of IC101 channel configuration, the channel "r\_IC101\_3\_current" is connected to wire "analog\_in\_current". The wire correspond to the physical IC101 signal input channel which is used to collect measured current data. The channel named "c\_IC101\_3\_initiate" is used to activate device motion. The client accesses the channel to convert the initiating instruction into the corresponding PV value, then the real physical channel outputs a pulse signal to activate the device. And there is an analog signal output channel to limit the measured current values. The channel is used to set the normal operating current range for IC101. When the measuring current exceeds the range, it stops working immediately to avoid damaging the equipment. According to the working principle of IC101, if we measure the charge accumulated on the capacitor in a defined period, we can know the average current during that time interval. It shows that both the capacitor size and the integration time have an impact on the measurement results. Therefore, IC101 measurement capacitance and integration time are set in IG2 database to make the measurement of current more accurate.

The function of IC101 is only to collect and feedback the monitoring data continuously. The device can not process the data. This function needs the upper controller to complete. In this experiment, the A560 Real-time controller produced by Pyramid is selected. It is intended to provide high-performance real-time processing of the data. The measured data fed back by the electrometer are compared with the ideal plan parameters in the controller. When the measured current or accumulated charge is different from the ideal plan parameters and the deviation exceeds the safety tolerable range, the beam should be shut down in time. In the simple connecting in Fig. 7, the IC101 connected to the A560 controller via fiber optics, and the A560 controller communicates with a GUI computer system via a Ethernet interface. The PVs of IC101 are

exposed to the network by the IG2 (CAS) . Other client GUI computers can then access the values.

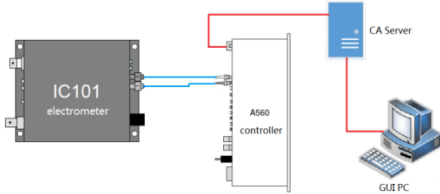


Figure 7: Example connecting for control system.

### CONTROL SOFTWARE

A GUI software is designed, which can interact with EPICS to transmit and receive values of records. It is easy to realize with an extension tool named “CALab” which allow CA support in LABVIEW. Since the device and the PC are connected through the network cable, instead of serial communication the queue operation function group is used to implement the data caching in LabVIEW. The role of the queue function is data transfer, call up the treatment data in the CALab tool database and enqueue them for caching, then dequeue the cached elements into the spreadsheet when the treatment is stopped. The Obtain Queue function sets the maximum size of the queue. The default value is infinite, which avoids data overflow during the treatment process and causes some data loss.

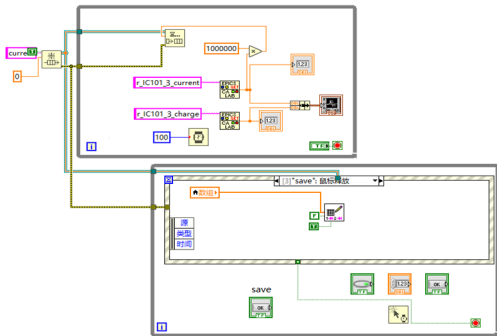


Figure 8: The example block diagram of control system.

Since the actual proton beam could not be obtained in the experimental stage, this experiment used a programmable digital source meter to generate a varying current to simulate the current signal which should be generated by the ionization chamber after receiving the proton beam to verify the function of the control software. Figure 9 shows the partial analog current waveform generated by the source meter according to the actual treatment plan parameters. The unit is A. The IC101 electrometer is connected to the current source meter through a coaxial-cable.

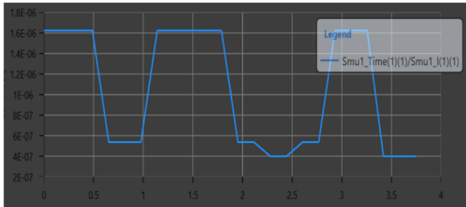


Figure 9: Analog current waveform.

In Fig.10, it shows that the control software user interface display the actual current waveform and the working status of the monitor devices. Compare the actual data saved in the log file with ideal values, due to external environmental interference and other reasons, there is a little error within the tolerable range. The actual current waveform is basically the same with the ideal current.

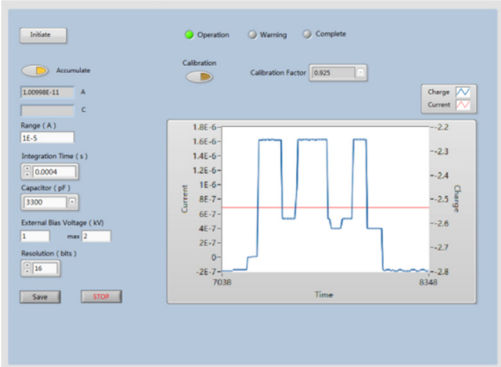


Figure 10: The design of the user interface.

### CONCLUSION

In this paper, a preliminary design of the dose parameter acquisition and control system was carried out. Firstly, by interpreting the DICOM file of treatment plan, the planned dose parameters required for proton therapy are obtained, and then the acquisition and conversion of the planned treatment parameters are carried out through the design of the algorithm program. Next, the transmission of data between the control software and the end device is realized by setting up an EPICS environment in the PC. Finally, according to the dose safety requirements, corresponding redundancy measures are proposed. The working statuses of front-end devices are real-time displayed in the GUI. And the control software is designed in LabVIEW to display and save the actual treatment data, realize real-time monitoring and fast response of the signal to ensure safe and efficient operation of the treatment nozzle dose control system.

### REFERENCE

[1] A. Le, J. Documet,,A. Sullivan,*et al.*, “A prototype of image-guided outcome analysis for prostate proton therapy patients based on DICOM-RT ePR”. SPIE, 2009, doi: 10.1117/12.813909

[2] Guo Huidong, “Design and simulation of the nozzle dose monitoring system in proton therapy”, Master Thesis. Huazhong University of Science and Technology, China, 2018.

[3] W. Oakes, J. Spencer, “EPICS: engineering projects in community service” [J]. 2004, 21(1):1455-1455

# THE DEVELOPMENT AND APPLICATIONS OF DIGITAL BPM SIGNAL PROCESSOR ON SSRF \*

L.W. Lai, Y.B. Leng<sup>†</sup>, Y.B. Yan, W.M. Zhou, F.Z. Chen, N. Zhang  
SSRF, SINAP, Shanghai, China

## Abstract

The development of Digital BPM Signal Processors (DBPM) for SSRF started from 2008. The first prototype for SSRF storage ring was completed in 2012, with turn-by-turn resolution better than 1 $\mu$ m. From 2016 to 2017, SSRF successively constructed two FEL facilities in China, DCLS and SXFEL test facilities. The second version DBPM was developed and used in large scale during this period to meet the requirements of signal processing for stripline BPMs and cavity BPMs. After that, we turned to the development of DBPM for SSRF storage ring based on the second version hardware, including FPGA firmware, EPICS IOC, EDM control panel. The development was completed and tests were carried out in early 2018. Test results showed that the position data is accurate and can monitor beam movement correctly, and online turn-by-turn position data resolution reaches 0.46 $\mu$ m. This paper will introduce the design of DBPM for the SSRF storage ring and the tests carried out to verify the data accuracy and evaluate the system performance.

## INTRODUCTION

SSRF is the first 3<sup>rd</sup>-generation synchrotron light source built in China, which came into service in 2009. The circumference of the storage ring is 432 meters, and the ring contains 20 cells that can serve up to 40 beamlines. The 499.654 MHz RF system produces 720 buckets of which typically 500 contain charge distributed in 4 bunch trains to minimize ion accumulation. There are 7 BPM electronics in each cell totaling more than 140 sets Libera BPM electronics around the ring measuring the beam orbit for beam control and feedback.

SSRF started the development of Digital BPM Processor (DBPM) in 2008. A first version prototype was developed in 2012 for the SSRF storage ring<sup>[1]</sup>. Later a second version DBPM hardware was developed in 2016<sup>[2,3]</sup>, which was more compact and more versatile. The new DBPM was first used on two FEL facilities, DCLS and SXFEL, in large scale. The development of new SSRF DBPM based on the new version hardware was taken from that design.

Table 1 lists the DBPM requirements based on considering accelerator performance and current technical level. After years of on and off development and improvement, a second version DBPM was developed and tested on SSRF this year.

\*Supported by The National Science Foundation of China (Grant No.11375255, 11575282); The National Key Research and Development Program of China (Grant No. 2016YFA0401990, 2016YFA0401903).

<sup>†</sup> lengyongbin@sinap.ac.cn

Table 1: DBPM Requirements

Requirements	Value
ADC	4 channels, 16bits
Central Frequency	499.654MHz
Sampling clock	External/internal
Sampling rate	117.2799MHz
Turn-by-turn rate	693.964kHz
Trigger	External/internal/period
Signal processing	FPGA
Data	ADC/TBT/FA/SA
Resolution	~1 $\mu$ m@TBT
OS	ArmLinux
Control	EPICS

## FIRMWARE AND SOFTWARE DESIGN

The DBPM was designed to provide position data at five different rates, including raw ADC data, turn-by-turn data, 50kHz fast acquisition (FA) data, 10kHz FA data, 10Hz slow acquisition (SA) data. Figure 1 shows the DBPM signal processing diagram, with the processing including four steps, and data rate reduced after each step. Position data is read out in small scale streaming mode or large scale capture mode.

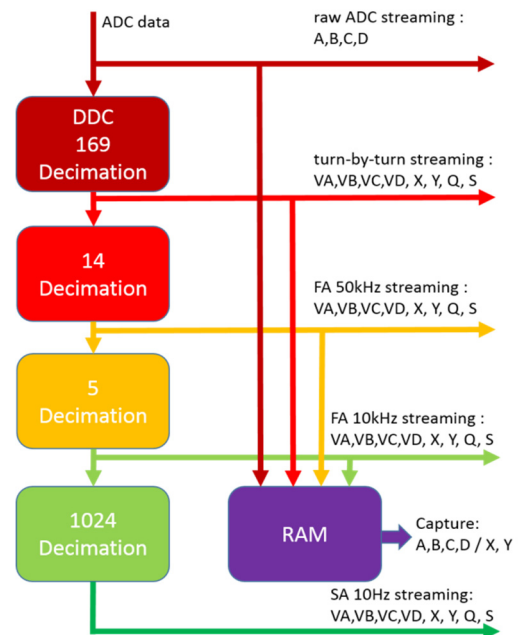


Figure 1: DBPM signal processing diagram.



Figure 2 shows the EDM control panel for the DBPM system. The left panel shows the streaming readout data waveforms. The upper right section displays some signal information (including max ADC value, trigger count value) and parameter settings (including  $K_{x/y}$ , offset, attenuator, inner trigger threshold value). The lower right section shows the configuration of the trigger mode (including none, external, internal, period), clock source (internal, external) along with data and display selection.

Figure 3 is the screenshot of turn-by-turn data during injection (left) and SA data output (right).

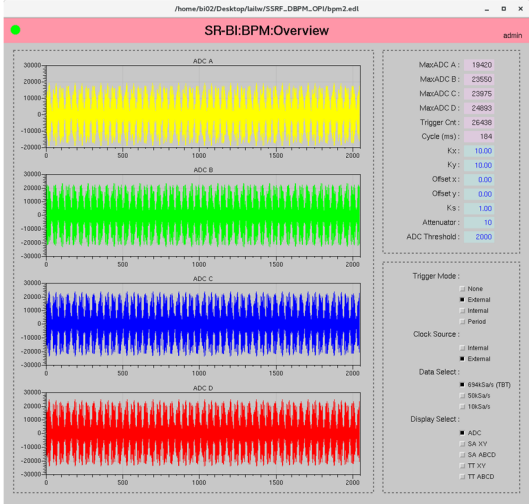


Figure 2: DBPM control panel.

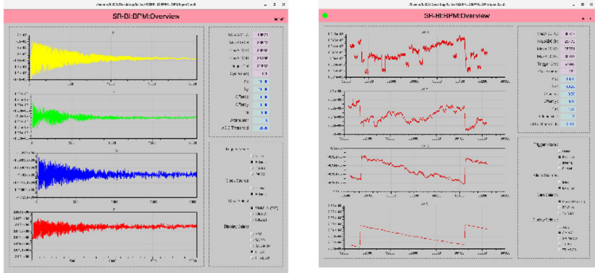


Figure 3: Turn-by-turn data during injection (left) and SA data (right).

### VERIFICATION TESTS

The BPM electronics at SSRF include Libera Electron and Brilliance. Brilliance is widely used for its excellent performance where turn-by-turn data resolution reaches  $1\mu\text{m}$ . SSRF online tests have been carried out to verify the accuracy of DBPM processor by comparing the position value between Brilliance and DBPM. The signal of a spare BPM on Cell 11 was divided into two and fed into the Libera Brilliance and DBPM modules. Figure 4 shows the test diagram and field installation picture.

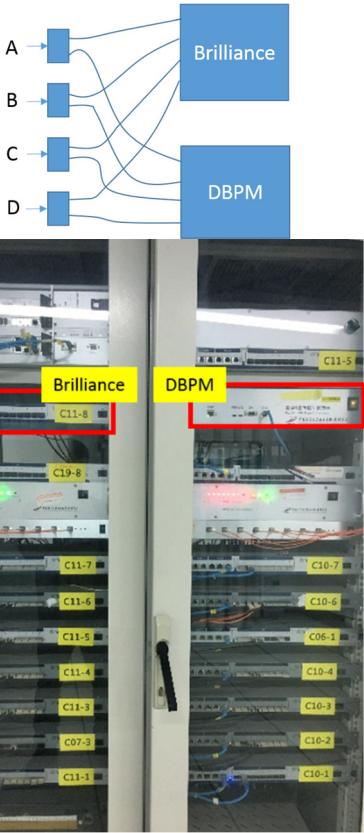
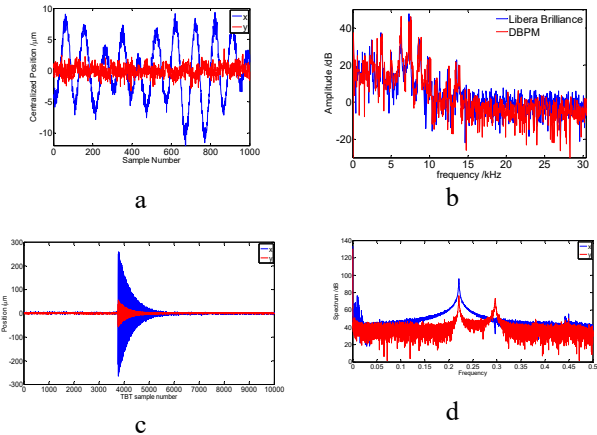


Figure 4: Verification tests and installation.

Test results are shown in Figure 5. Figure 5(a) shows the DBPM turn-by-turn position data waveform. X (horizontal) data shows oscillations compared to Y (vertical) because of energy oscillations in horizontal plane. Figure 5(b) shows the turn-by-turn position data spectrum of Brilliance and DBPM, and they fit quite well. Figure 5(c) is the DBPM turn-by-turn data during injection, the induced oscillation can be seen clearly, and the tune value can be calculated during this time (d). As for the 10Hz SA data, five hours data shows that they fit well (e), and the RMS of the five hour difference is  $0.83\mu\text{m}$  (f).





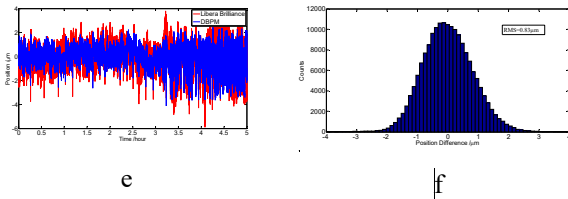


Figure 5: Verification results.

## PERFORMANCE TESTS

The DBPM performance evaluation test was carried out as depicted in the block diagram in Figure 6. Input signals include BPM four pickup sum signal and 499.654 MHz RF signal from a signal generator.

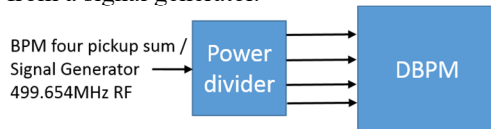


Figure 6: Evaluation test diagram.

Figure 7 shows the performance evaluation results. Figure 7(a) is the turn-by-turn resolution result on SSRF, 0.46  $\mu\text{m}$  rms calculated with 524288 turns. The resolution of FA 50kHz data and FA 10kHz data is 0.19  $\mu\text{m}$  7(b) and 0.10  $\mu\text{m}$  7(c), respectively. The benchtop signal generator test result shows that the SA 10Hz data resolution only 43 nm using 600 points.

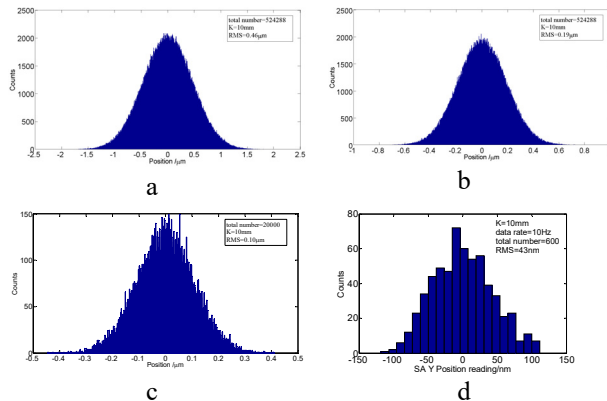


Figure 7: Evaluation results.

## CONCLUSION

The development of a new DBPM processor for SSRF is based on new hardware that started at the end of 2017, including FPGA firmware development, EPICS IOC development and EDM control panel design. The second version of the SSRF DBPM is a fully functioning processor which provides ADC data, turn-by-turn data, FA data, SA data, and can be accessed through EPICS.

Online tests were carried out in early 2018 on SSRF. Test results show that DBPM processor can measure the beam orbit accurately when comparing the results with Libera Brilliance. The turn-by-turn data resolution can reach 0.46  $\mu\text{m}$  rms, much better than the first version.

We can draw the conclusion from above results that the new version DBPM meets the requirement of beam orbit

measurements on the storage ring, and can be used for beam position control. However, more time and resources are still needed to make the DBPM more stable before final deployment.

At the same time, more applications are being planned and developed based on the same hardware<sup>[4,5]</sup>, including booster DBPM, LINAC DBPM, a smart tune measurement processor, bunch-by-bunch tune measurement and bunch-by-bunch charge measurements with an interleaving technique. Some of these projects have been completed, and some are still in progress. The results will be introduced in the near future.

## ACKNOWLEDGEMENTS

Gratefully acknowledge the paper guidance from Jeff Corbett at SLAC.

## REFERENCES

- [1] L.W. Lai, Y.B. Leng, Y.B. Yan *et al.*, "Batch Applications of Digital BPM Processors from the SINAP", in *Proc. of IBIC'16*, Barcelona, Spain, 2016, p.658-660.
- [2] L.W. Lai, Y.B. Leng, Y.B. Yan *et al.*, "Design and Performance of Digital BPM Processor for DCLS and SXFEL", in *Proc. of IPAC'17*, Copenhagen, Denmark, 2017, paper MOPAB092, p.338-340.
- [3] L.W. Lai, Y.B. Leng, Y.B. Yan *et al.*, "Upgrade of Digital BPM Processor at DCLS and SXFEL", in *Proc. of IPAC'18*, Vancouver, British Columbia, Canada, paper THPML071.
- [4] Lai L W, Leng Y B, Yan Y B *et al.*, "An intelligent trigger abnormal beam operation monitoring processor at the SSRF", in *Proc. of IPAC'15*, Richmond, VA, USA, 2015, p.978-980.
- [5] F. Z. Chen , L. W. Lai , Y. B. Yan, Y.B. Leng, "Design of a new type of beam charge monitor based bunch by bunch DAQ system", in *Proc. of IBIC'17*, Grand Rapids, MI, USA, 2017, p.284-286.

# ON-LINE CROSSTALK MEASUREMENT AND COMPENSATION ALGORITHM STUDY OF SXFEL DIGITAL BPM SYSTEM\*

F. Z. Chen<sup>†1</sup>, Y. B. Leng<sup>‡</sup>, J. Chen<sup>1</sup>, L. Y. Yu, L. W. Lai, R. X. Yuan, T. Wu<sup>1</sup>  
 Shanghai Institute of Applied Physics, Chinese Academy of Sciences, 201800 Shanghai, China  
<sup>1</sup>also at University of Chinese Academy of Sciences, 100049 Beijing, China

## Abstract

Shanghai soft X-ray Free Electron Laser (SXFEL) has acquired the custom designed Digital BPM processor used for signal processing of cavity BPMs and stripline BPMs. In order to realize monitor the beam position accurately, it has high demand for DBPM system performance. Considering the crosstalk may introduce distortion and influence beam position resolution, it is important to analyze and compensate the crosstalk to improve the resolution. We choose the CBPM signal to study the crosstalk for its narrowband and sensitive for phase position. The main experiment concept is successive accessing four channels to form a signal transfer matrix, which including amplitude frequency response and phase response information. And the compensation algorithm is acquire four channel readouts, then using the signal transfer matrix to reverse the true signal to ensure the accurate beam position measurement. This concept has already been tested at SXFEL and hopeful to compensate the crosstalk sufficiently.

## BACKGROUND

### SXFEL

SXFEL is one of the high-gain FELs constructed in China. Key technologies have been tested through prototype developments. Based on the research and development prototype of hard X-ray FEL. The construction of the user facility in soft XFEL has already finished. The SXFEL facility consists of an electron injector with a thermionic cathode, main accelerate section including C-band high-gradient accelerators along with S-band accelerators, and in-vacuum undulators. Figure 1 is SXFEL undulator layout [1, 2].

SXFEL is designed to generate a coherent x-ray beam using a self-amplified spontaneous emission (SASE) process.

\* Work supported by National Science Foundation of China (No.11375255)  
<sup>†</sup> chenfangzhou@sinap.ac.cn  
<sup>‡</sup> lengyongbin@sinap.ac.cn

In order to meet the harsh demands, the beam diagnostic system achieving high precision resolution is one of the most important technical issues. Cavity BPM meets the hash demands for the precise measurement of the resolution of the SXFEL undulators system. Figure 2 is the picture of one Cavity BPM installed in the tunnel.

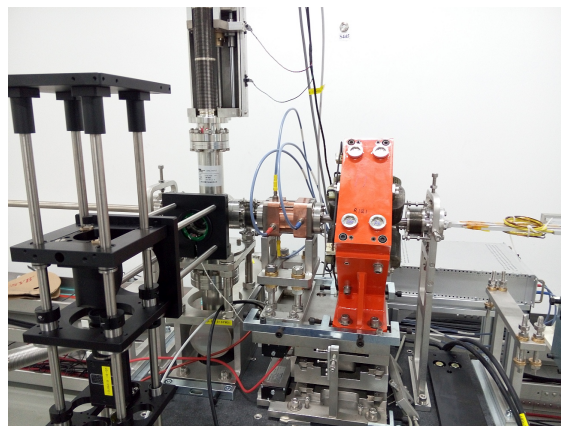


Figure 2: Cavity BPM installation spot picture.

**Cavity BPM** CBPM is a key beam instrumentation component for SXFEL beam diagnostics. As the requirement of undulator should reach sub-micron level position resolution. The high Q cavity BPM. As the key beam diagnostics tool, BPM systems are widely equipped in all kinds of accelerators. Cavity Beam Position Monitors are main beam diagnostic instruments in SXFEL. There are more than 20 CBPM conducted in SXFEL used for the measurement and adjustment of beam orbit. Moreover, the sum of four SBPM electrodes signal can also apply in relative beam charge measurement. RF cable extract beam signal from CBPM pickup, RF front-end module modulated signal to proper amplitude, then led the signal to digital BPM processor.

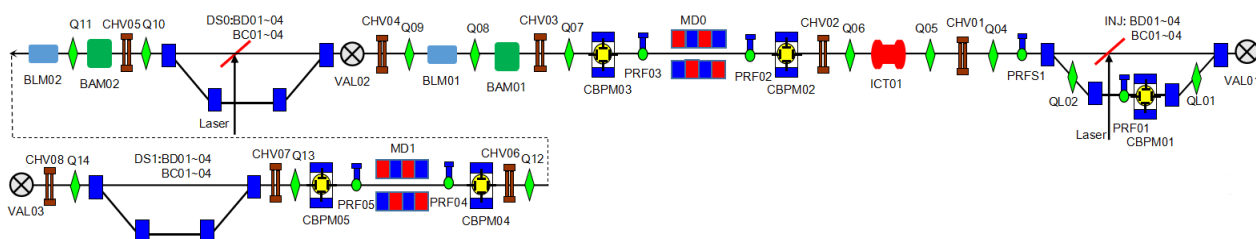


Figure 1: Partial layout of SXFEL undulator.

**Digital BPM Processor** The Digital BPM processors are custom designed to measure the beam positions, every cavity beam position monitor is connected to a digital BPM processor. The centre frequency of the DBPM processor is 500 MHz, and the bandwidth is 20 MHz. The processor consists of the RF pre-processing module and the analog to digital conversion module. The ADC conversion module carried a 16 bit high-resolution ratio ADC and advanced FPGA chip. The analog board of the DBPM has many analog devices and circuits, which may form considerable crosstalk. Figures 3 and 4 show the simplified architecture of the processor.

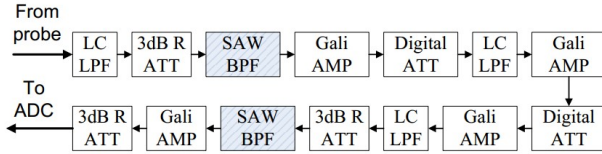


Figure 3: Analog devices module of DBPM processor.

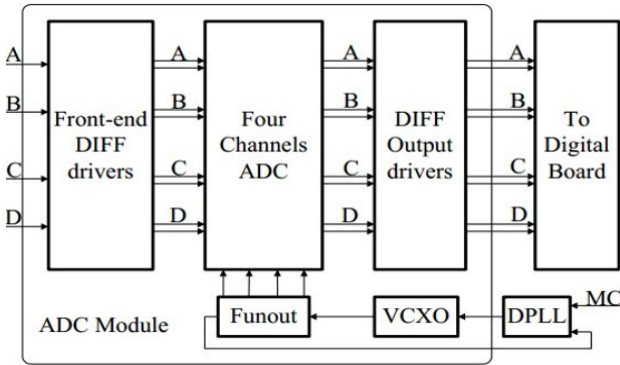


Figure 4: ADC module of DBPM processor.

## BEAM EXPERIMENT

### Target of Beam Experiment

One of the most important technical issues of the DBPM processor is to acquire high-fidelity signal. The beam position resolution in SXFEL BPM system should be better than sub-micron. Considering the crosstalk may introduce distortion and influence beam position resolution, it is important to analyze and compensate the crosstalk to improve the resolution.

### Experiment Details

At normal SXFEL machine running status, we select one Cavity BPM reference cavity readout signal for the amplitude of signal is bigger and position independent. The architecture of experiment is shown below Fig. 5.

It consists of cavity BPM, DBPM processor and upper computer. The first experiment is measuring channel crosstalk in sequence. Signal from Cavity BPM successive guide into four channels of DBPM processor while other

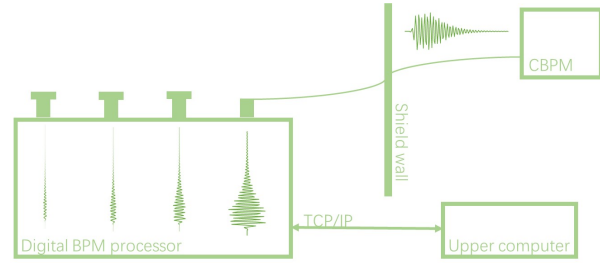


Figure 5: The architecture of the crosstalk calibration platform.

channels have impedance matching, host computer access four channels readouts at the same time. The upper computer carry Linux operating system, using python script to acquire the beam position data from the DBPM processors. The second experiment is using two channels of DBPM processor to access cavity BPM position.

## EXPERIMENT ANALYSIS

Figure 6 is the experimental result of fours channels at successive signal input. According to the experimental data, the crosstalk at adjacent channels is obviously. The crosstalk of both sides are smaller than middle due to the placement and routing of the analog board. The most significant crosstalk is between channel B and channel C. After deep analysis, the variance of noise background is 38.05, while the variance of crosstalk section is up to 740.77. Figure 7 is the spectrogram of the channel B and channel C.

### Principle Component Analysis

Although there is crosstalk between channels, however the amplitude of the crosstalk and the noise background are on the same scale. It's difficult to measure crosstalk using simple algorithm. The principal component analysis (PCA) method is introduced to analysis the experimental data. PCA is a powerful data analysis tool, capable of extracting useful information hidden in noise and doing pattern separation. Accumulation of 1024 experiment data samples of four channels, readouts of each channel contains characteristics of signal and crosstalk. The characteristics have complicated correlation relationships with each other, which makes it possible for dimensionality reduction with PCA. For convenience of description, let the  $4 \times 512 \times 2048$  matrix X denote the signal containing the crosstalks. The key point of PCA is how to derive the crosstalk from noise background. Figure 8 is the mode index of matrix X. Figure 9 is the pattern separation.

### Principle of Measurement

The voltage signal coupled to the mid-end impedance Z is expressed as Eq. (1):

$$V_{out} = \frac{\omega q}{2} \sqrt{\frac{Z}{Q_{next}}} \left( \frac{R}{Q} \right)_0 \exp \left( -\frac{\omega^2 \sigma_z^2}{c^2} \right) \frac{x}{x_0}, \quad (1)$$



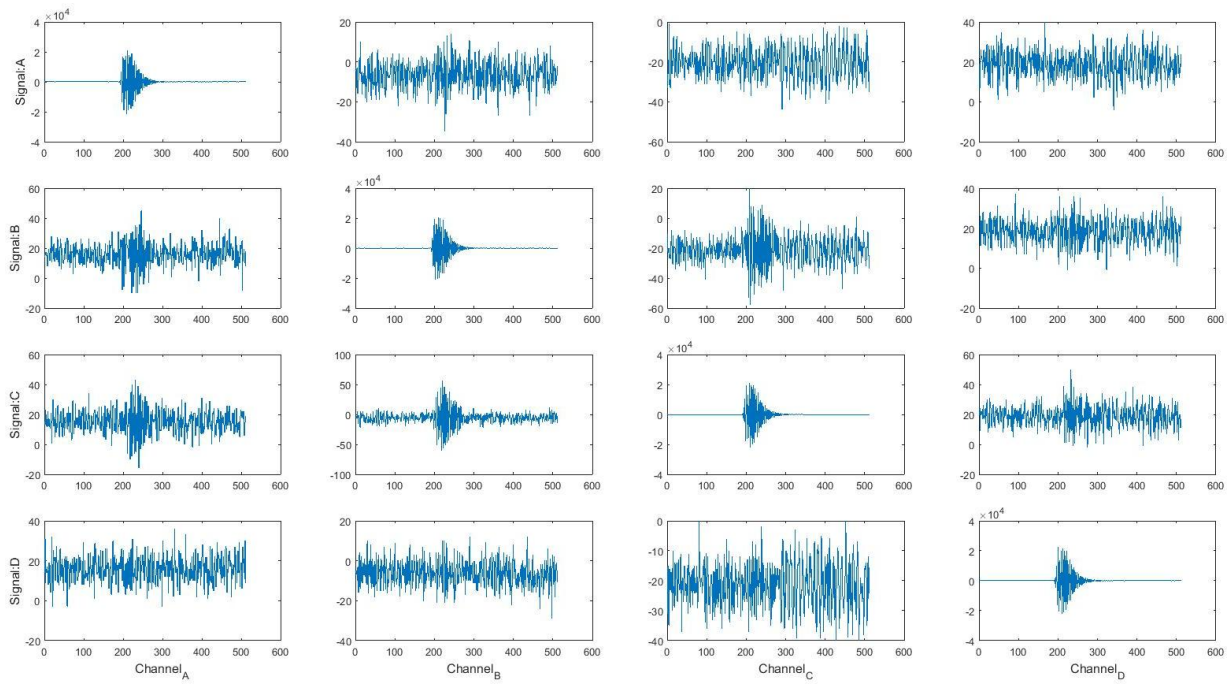


Figure 6: Crosstalk result of four channels at successive signal input.

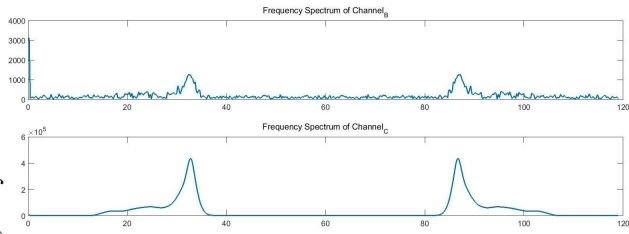


Figure 7: The spectrogram of the channel B and channel C.

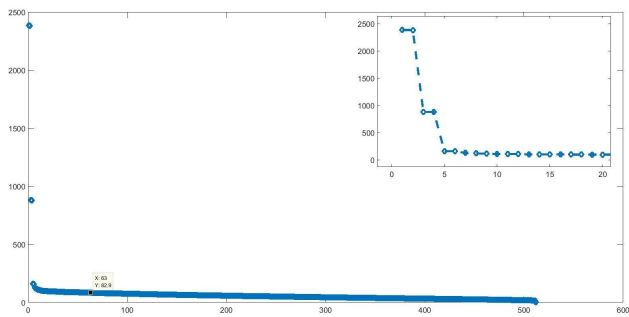


Figure 8: Eigenvalue distribution.

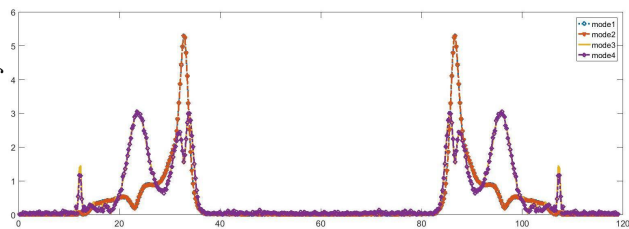


Figure 9: Pattern separation.

where  $R$  is the radius of the cavity,  $c$  is the electric field density,  $\omega$  is the angular frequency of the resonance,  $\sigma_{beam}$  is the RMS width of the source spot,  $\sigma_z$  is the length and  $q$  is the charge of the Gaussian distribution bunch,  $\frac{R}{Q}$  is the shunt impedance when the beam current is deviated from the electrical center of the cavity. The expression of the signal in the time domain is as Eq. (2):

$$V(t) = V_{out} e^{-\frac{t}{\tau}} \sin(\omega), \quad (2)$$

where  $\tau$  is the attenuation constant of the signal [3].

Considering the system is linear time invariant, we acquire a simplify system. Assuming the expression of signal is  $f(t)$ , then the crosstalk is  $k f(t')$ . According to PCA, statistical procedure to elucidate the underlying covariance structure in the multidimensional data. Eigenvector of the largest four eigenvalue presents the I,Q component of the signal and the crosstalk. The crosstalk component is extracted from the background noise, the specific value of amplitude is 0.0022. The sampling frequency is 119 MHz, phase difference convert to time delay is 67.2 ns. Figure 10 is the rough crosstalk compensation result.

## CONCLUSION

In this article, we introduce the SXFEL digital BPM system. In order to evaluate the crosstalk performance of the SXFEL digital BPM system, we designed two experiments and introduced PCA to measure the crosstalk. The crosstalk of SXFEL digital BPM system is better than 57.76 dB, the distortion and influence introduced by the crosstalk is within the allowable error range.



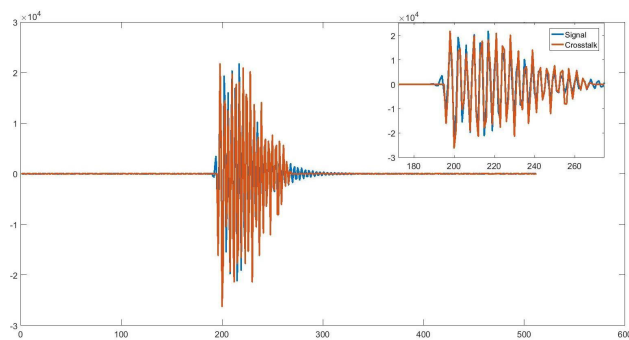


Figure 10: Crosstalk compensation.

## REFERENCES

- [1] L. W. Lai *et al.*, “Design and Performance of Digital BPM Processor for DCLS and SXFEL”, in *Proc. IPAC’17*, Copenhagen, Denmark, May 2017.  
doi:10.18429/JACoW-IPAC2017-MOPAB092
- [2] F. Z. Chen *et al.*, “SXFEL Linac BPM System Development and Performance Evaluation”, in *Proc. IPAC’18*, Vancouver, Canada, May 2018.  
doi:10.18429/JACoW-IPAC2018-THPML067
- [3] *Study of Cavity BPM Signal Processing Technology*, Doctoral thesis, UCAS, China, May 2013, pp. 21–25.

kW in 2018. The MR plans to upgrade the beam power up to 1.3MW.

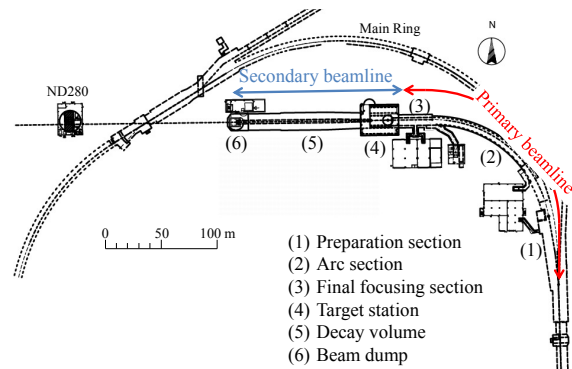


Figure 1: Layout of the T2K experimental facility.

## MOTIVATION

We handle a high intensity proton beam at the neutrino facility. In the beamline, one mistaken shot can potentially do serious damage to the beamline equipment. To avoid such a consequence, a lot of beamline equipment interlocks, called MPS (Machine Protection System) to stop the beam operation are implemented. We have more than 800 interlock sources. Multiple sources can cause an interlock at the same time. For example, many BLM (Beam Loss Monitors) sometimes issue an interlock simultaneously. In that case, it is difficult for the beamline operators to understand quickly what happened in the beamline and these can lead to a time loss of the beamline operation.

When an essential beamline equipment fails, it may take a long time to restore the beam operation. For example, a helium compressor in the helium circulation system at the target station was broken in January 2017. We lost about two weeks of the beam time due to this trouble.

To improve these situations, we plan to introduce a beamline expert system to the neutrino facility.

## BEAMLINE EXPERT SYSTEM

Figure 2 shows a schematic diagram of the beamline expert system. The beamline expert system consists of three components such as a data collection component, inference engines and a result presenting component. The data collection component continuously collects beamline information and the inference engines infer the beamline status from

\* kazuo.nakayoshi@kek.jp

beamline monitor data. Finally the result presenting component presents the inferred results.

The **inference engine** is a key component of the expert system. Although a typical expert system inference engine is rule-based [2], we adapt machine-learning(ML) based inference engine in our expert system. We studied two types of inference engines:

- a supervised trained engine for classification of MPS events
- an unsupervised trained engine for detection of equipment anomalies

The beamline expert system runs during the beam operation of the neutrino facility. If MPS is activated at the neutrino facility, the expert system infers the MPS reason and presents a recovery procedure. For detection of equipment anomalies, the expert system continuously collects the status of the beamline equipment and informs the abnormality to a beamline operator if it detects a sign of a equipment anomaly.

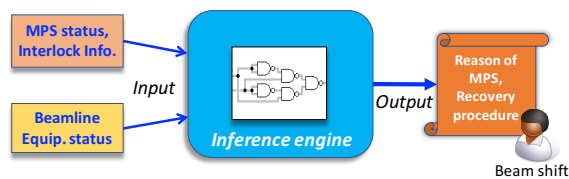


Figure 2: Schematic diagram of the beamline expert system.

## MPS CLASSIFICATION BY SUPERVISED TRAINING

### Actual Examples of MPS Events

Here we introduce some actual examples of MPS events. A failure of the fast extraction magnets of the MR, such as the septum magnets (FX septum) and/or kicker magnets (FX kicker), cause simultaneous BLM interlocks at the primary beamline. And it has some possibility of doing serious damage to the beamline. It is also difficult to quickly understand the source of the MPS just looking at these BLM interlock patterns. We carried out the initial evaluation of the ML-based inference engine considering the following cases:

- A case where the simultaneous BLM interlocks occur at the primary beamline. This is caused by either a failure of the FX septum or FX kicker magnets.
- A case where there is an MPS from a source other than a BLM, such as the normal-conducting magnets, etc.

Our initial evaluation is to classify the MPS events into three labels, which are (0) FX septum, (1) FX kicker or (2) others, using the ML-based inference engine.

## Model and Supervised Training

We evaluated the following procedure:

1. We built a model using **TensorFlow™** [3], which is a famous open-source library for ML developed by Google.
2. Training was performed using training data which simulates the real MPS events. The model parameters were optimized by a supervised training.
3. Finally we used the trained model as an expert system inference engine, as well as to evaluate it using actual MPS events.

We used a 2-layer neural network model for the evaluation [4]. Figure 3 shows a schematic diagram of the 2-layer model. The MPS bit stream is put into the input layer. The output layer is 3 nodes and it is taken to represent the classification of FX septum, FX kicker or other.

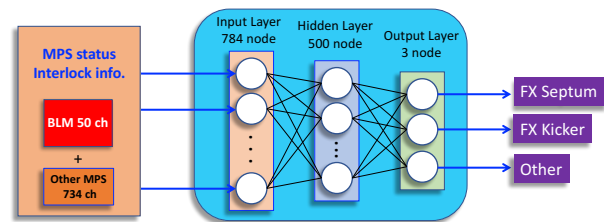


Figure 3: 2-layer neural network model.

### Performance Evaluation by Actual MPS Events

We evaluated the performance of MPS classification of the inference engine by actual MPS events during about six months beam operation. Table 1 shows the results of MPS classification. The inference engine predicted two FX kicker events although there were no FX kicker misfire MPS events during this period. The accuracy was 98.3%. We investigated two mis-predicted MPS events in Table 1. One of them was an event where a beam instability in the MR occurred and a lot of BLM in the primary beamline were activated. On the other hand, it was found that another event was similar to the FX kicker misfire event by analyzing the beam monitor data. The horizontal position of the extracted beam in the primary beamline was shifted by about +0.2mm and the extracted horizontal angle was quite large. Figure 4 shows the horizontal orbit for that spill shown in red line, as well as two normal spills shown in blue and black. This result suggests that even if a prediction fails, the expert system can suggest to investigate the beam condition carefully to the beam operator in order to reduce the risk of potential for unknown failure condition.

Table 1: Results of the Actual MPS Classification (Oct. 2017 - Dec. 2017, Mar. 2018 - May 2018)

	True	Prediction
FX septum	0	0
FX kicker	0	2
Other	120	118

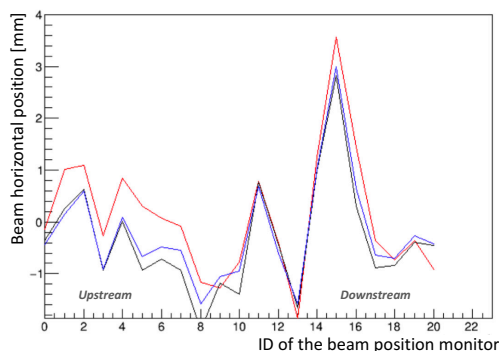


Figure 4: The graph shows horizontal beam orbit which extracted in the primary beamline. The red line shows the horizontal beam orbit corresponding to the mis-prediction MPS event. The blue and black lines show normal events.

## ANOMALY DETECTION BY UNSUPERVISED LEARNING

We also investigated a method of anomaly detection for the beamline equipment using ML. Figure 5 shows a schematic diagram of the anomaly detection scheme in the beamline expert system. An inference engine, which is different from the MPS classification one, infers anomaly of the beamline equipment.

### Autoencoder and PCA

We found that Autoencoder (AE), a model of NN, can predict the anomaly. The essential part of the AE is a dimension reduction [5]. The anomaly can be detected by comparing the input data with the predicted data which is calculated from a restoration from the dimension reduced data. We also studied PCA (Principal Component Analysis). The PCA can be used as a tool of the dimension reduction. The PCA is also mathematically equivalent to AE with some restrictions. For our initial study, we used the PCA in our inference engine.

First, a matrix for the dimension reduction ( $F$ ) is calculated by PCA. PCA can calculate the matrix by an eigenvalue decomposition of the covariance matrix of the input data during the normal condition of the beamline equipment. A matrix for the restoration ( $G$ ) is also calculated as the transposed matrix of  $F$ . Second, the predicted data  $\hat{y}$  is calculated from the input data  $y$  and those matrices,  $\hat{y} = GFy$ . Finally, a  $Loss$  defined by  $\|y - \hat{y}\|^2$  is calculated

as a metric for the anomaly detection since it could be large value if the predicted data is not consistent with the input data.

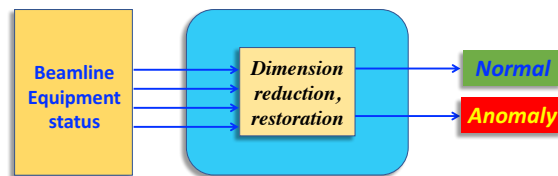


Figure 5: Anomaly detection by beamline expert system.

### Initial Evaluation Using Three-Dimensional Normal Distribution

We performed an evaluation of the inference engine using PCA for the anomaly detection. One hundred sets of a three-dimensional normal distribution data  $\{x_1, x_2, \dots, x_{100}\}$  (dataset-A) and another ten set of three-dimensional normal distribution data  $\{y_1, y_2, \dots, y_{10}\}$  (dataset-B) are generated as shown in Fig. 6. Dataset-A and dataset-B emulates the data in normal and anomaly condition, respectively. We calculated the  $Loss$  for those data. Figure 7 shows the distribution of the  $Loss$ . The  $Loss$  of the dataset-B is larger than one of the dataset-A and therefore it is possible to detect the anomaly condition from the  $Loss$  values.

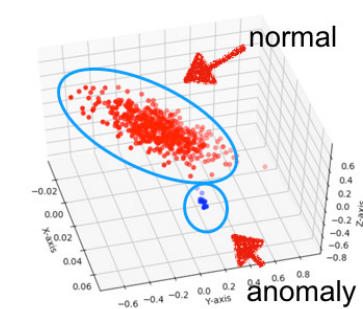


Figure 6: Three-dimensional normal distribution emulating a normal condition and emulating an anomaly data.

### Actual Monitor Data of the Beamline Equipment

We also studied to use the PCA based inference engine to the actual beamline data. Our challenge is to detect a sign of the failure of the helium compressor happened in January 2017. Figure 8 shows a schematic view of the helium circulation system for the helium vessel. We utilized seventeen relevant monitor data, such as the supply pressure and temperature of helium gas. Figure 9 shows the distribution of each monitor data during a certain one hour when the helium compressor system was normally running. It looks that the distribution of those data are almost similar to the normal distribution. On the other hand, some of the variances was changing over the time, as shown in Fig. 10. Therefore, it is necessary to predict the present covariance



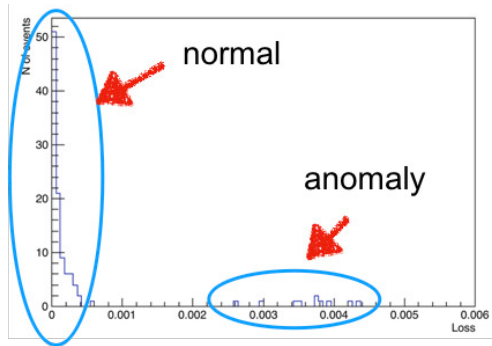


Figure 7: The distribution of the reconstruction error (*Loss*). By calculating the value of *Loss*, we know if the anomaly occurs in the equipment.

matrix from the past data in order to utilize the PCA based inference engine because the PCA assumes that the input data follow a normal distribution which is constant over the time.

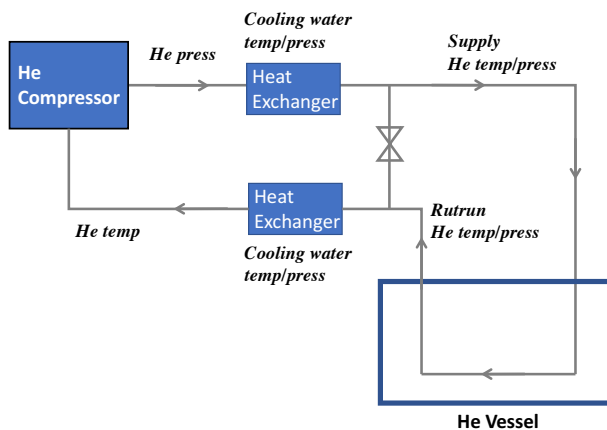


Figure 8: Schematic diagram of the helium circulation system for the helium vessel.

## SUMMARY AND FUTURE PROSPECT

We are developing ML-based beamline expert system for efficient beamline operation. We developed a prototype inference engine for the classification of MPS events and performed initial evaluation using actual MPS events during six months beam operation. The accuracy of the inference engine was 98.3%. There were two mis-prediction during the evaluation period. We investigated two mis-prediction MPS events and found that one of MPS events was similar to FX kicker misfire event by analyzing the beam monitor data. The results indicate that the inference engine in the supervised training is promising. We also studied anomaly detection of the beamline equipment using the unsupervised training. We confirmed the performance for anomaly detection by PCA using three-dimensional normal distribution data. However, the variance of helium compressor data varied with time. As a solution to this, we will develop another engine which infers the present variance of data using the past variance. We show possibility of efficient beamline operation using ML-based expert system in this study.

## REFERENCES

- [1] K. Abe, *et al.*, "The T2K experiment", Nucl. Instr. and Meth. **A659**, Issue 1, 11 Dec. 2011, pp106-135.
- [2] A. Kazarov, *et al.*, A rule based verification and control framework in ATLAS Trigger-DAQ, IEEE Trans. Nucl. Sci. **54** 604-608, 2007.
- [3] TensorFlow™, <https://www.tensorflow.org>.
- [4] K. Nakayoshi, Y. Fujii, T. Nakadaira and K. Sakashita, "Development of an Expert System for the High Intensity Neutrino Beam Facility at J-PARC," doi:10.18429/JACoW-ICALEPCS2017-THCPA07.

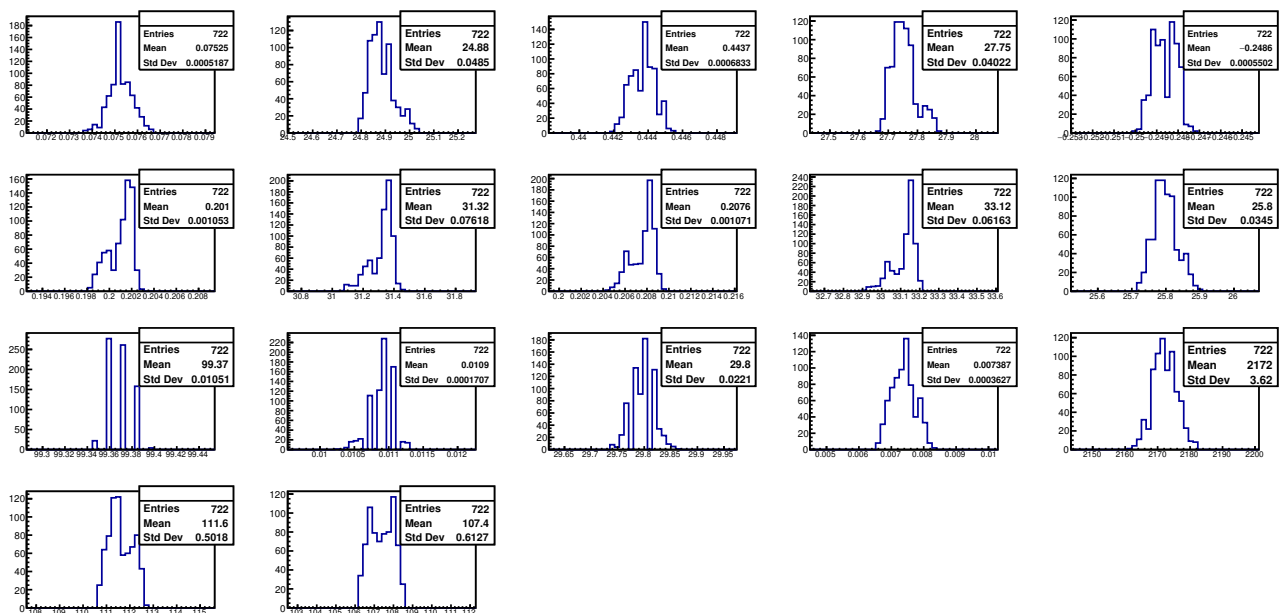


Figure 9: The distribution of the data for 1 hours. The horizontal axis shows the hour.



# VIRTUAL SIGNAL SPECTRUM ANALYZER DEVELOPMENT BASED ON REDPITAYA AND EPICS FOR TUNE MEASUREMENT IN BEPC-II

Y.H Lu<sup>†</sup>, J. He, BEPCII, IHEP, 100049 Beijing, P. R. China

## Abstract

An independent tune measurement system was developed in BEPCII using Direct Diode Detect (3D) technique. The system includes two diagonal electrode signals of a set of BPMs, a self-designed board based on Direct Diode Detect (3D) technique, and a commercial spectrum analyzer. For replacement of the commercial spectrum analyzer and integrated to the central EPICS system, an EPICS device driver is developed based on the EPICS base and ASYN module support, using an open source digital electronics Red Pitaya and its software “Spectrum”. According to the application requirements of tune measurement in BEPCII, the device driver finds the frequency point and power value corresponding to the X&Y tune between 631 to 874 kHz. The spectral resolution is 119 Hz. An EPICS IOC is built and run on Red Pitaya for accessing the device driver. A CSS-based user interface shows the signal’s power spectra and the tune frequency directly.

## INTRODUCTION

The betatron tune is one of the most important parameters of the storage ring, especially for colliders. It plays a crucial role in brightness optimization. At present, the tune measurement system in BEPCII [1] can only be monitored when the beam betatron oscillation amplitude is large enough due to its sensitivity problem. In order to solve the defect, a high-sensitivity tune measurement system based on a diode peak hold circuit is under development and being tested, which is referred to as Direct Diode Detection (3D) tune measurement system. An original 3D tune measurement system was developed by Marek Gasior originally in CERN according to the work of predecessors [2, 3].

The 3D tune measurement system requires a spectrum analyzer to perform spectrum observation. And its results are expected to be integrated to the central control system EPICS and database system of BEPCII. The commercial spectrum analyzers are usually expensive, and the integration with the central control system cannot be achieved easily for non-open-source.

This paper presents development of a virtual spectrum analyzer for the 3D tune measurement system in BEPCII. It is based on a digital electronics platform named Red Pitaya [4] with an embedded linux operating system on it. An API for BEPCII 3D tune measurement is developed firstly based on the open source code “Spectrum” of Red Pitaya, allowing users to survey frequencies corresponding to the X&Y tunes of the collider. Then, an EPICS driver support for spectrum analyzer is written, based on

ASYN [5], redpitaya-epics [6] and the API source code. An EPICS IOC for 3D tune measurement system is built and tested with a CSS-BOY interface.

## HARDWARE ARCHITECTURE

The hardware architecture of 3D tune measurement system is demonstrated in Fig. 1. Signals from the two BPM diagonal pickups, with main frequency range  $499.8 \pm 1.262$  MHz, are processed by the 3D tune measurement electronics, and then transferred to an EPICS virtual spectrum analyzer running on the Red Pitaya board. The graphical user interface was developed using CSS (Control System Studio) which executes on a remote PC, which located in the same LAN (Local Area Network) with the Red Pitaya board.

Red Pitaya is built around a Xilinx Zynq-7010 SoC processor combined with an FPGA. The board has two 14 bits ADCs with sampling rates up to 125MHz and a SD-Card slot for holding a Linux operating system. Spectrum Analyzer turns Red Pitaya into a 2-channel DFT Analyzer, with frequency span from DC up to 62.5MHz.



Figure 1: The hardware architecture of the 3D tune measurement system for BEPCII.

## SPECTRUM ANALYZE API FOR BEPCII 3D TUNE MEASUREMENT

All Red Pitaya applications are web-based and do not require any software configurations on the remote PC. Users can access APIs via a web browser (such as Firefox). Red Pitaya is known for its open source, but the spectrum analyzer API that is currently in use is spectrumPro. The original open source code of spectrum analyzer API we use is outdated and written in the C language and is independent of the present header files like rp.h which are responsible for data interaction with the DDR3 memory.

To solve “Application Not Loaded” problem when access the spectrum Analyzer API, lots of debug statements are added to the C source code. Then according to error or warning messages in the debug.log file, the API can be accessed remotely via a web browser after many “nignx [7]: worker process: symbol lookup error” errors are excluded.

Data sampled and initially processed by Red Pitaya is located in the internal storage area of Zynq, and its storage depth is limited to  $16 \times 1024 \times 14$  bits. However, considering the problems of network traffic and data refresh rates on the web browser, the spectrum analyzer extracts

<sup>†</sup> luyh@ihep.ac.cn, BI Group, Accelerator Centre, IHEP

data at a ratio of 4:1 after the DFT algorithm, which increases the spectral resolution by 4 times.

In the tune measurement system, the amplitude of the signal input to Red Pitaya is less than 1V, and the signal frequency is less than 1.262 MHz. Since the tune of the collider is semi-integer symmetrical, the most effective frequency is distributed between DC and 631kHz or between 631 and 1262kHz. Due to lots of noise signals locate in the frequency range 0~631kHz, the spectrum components between 631 and 1262kHz are more interesting. Therefore, the sampling frequency 1.97 MHz is selected to detect the effective spectral component of the tune measurement system. Then the effective spectrum range is 0~976kHz with a corresponding spectral resolution 477Hz.

In the BEPCII 3D tune measurement system, it is required to have at least multiple power points in the range of 1.262kHz to detect the peak power frequency accurately. To improve the spectral resolution 477Hz, an offset is brought into the frequency output calculation system instead of data extraction without changing the output point number  $2 \times 1024$ . Then the spectrum API ranges from 631kHz to 874kHz with a spectral resolution 119Hz. Since the tune frequencies of BEPCII is very close to half-integer which equals to the frequency 631kHz, 874kHz is larger enough to show all the interesting frequency components.



Figure 2: Tests for spectrum API: The upper one is tests in Laboratory with signal at 667kHz & 220mV; The bottom one is tests in the BEPCII IP Station, in which the peak frequency 624 & 638kHz both correspond to the X tune in BEPCII.

The focus of the tune measurement system is to detect the X&Y tune frequency points automatically. In view of the fact that there is no overlap between the X and Y tune frequency band in BEPCII, the 631 to 874kHz frequency

band is divided into two sections respectively corresponding to the frequency range of the X&Y tunes. Methods for finding the tunes are:

1. Calculates the power of the data after the DFT algorithm is executed;
2. Finds the peak power points separately in the two sections, and record their power and frequency value;
3. Calculates the X&Y tune values with their frequency divided by 1.262MHz respectively.

After the modification and compilation of the API is completed, tests are carried out in laboratory and the BEPCII IP (Instrumentation Position) station. The results are shown in Fig. 2. Tests in the laboratory demonstrates that the smaller the input amplitude, the better the signal-to-noise ratio on the spectrum charts; Tests in the IP station shows that the virtual spectrum analyzer API is fully capable of meeting the needs of BEPCII 3D tune measurement system.

## SPECTRUM ANALYZER BASED ON EPICS

EPICS is a set of Open Source software tools, libraries and applications developed collaboratively and used worldwide to create distributed soft real-time control systems for scientific instruments such as a particle accelerators, telescopes and other large scientific experiments [8]. Asyn is a general purpose facility for interfacing device specific code to low level communication drivers, and its primary target is for EPICS IOC device support [5]. Andraz Pozar from Australian Synchrotron developed an EPICS device driver support for Red Pitaya based on asyn, named redpitaya-epics, which supports for fast data acquisition and analogue and digital in/outs [9]. This paper aims to contribute a virtual spectrum analyzer based on EPICS for the BEPCII 3D tune measurement. Works for spectrum analyzer development is based on both the spectrum API and the redpitaya-epics source code. There are some problems to be solved for Spectrum Analyzer realization:

1. Redpitaya-epics calls for the header file `rp.h` to access the memory areas. While the file `fpga.h` in the spectrum API accesses the memory data independently, which conflicts with functions in the file `rp.h`.
2. Redpitaya-epics is based on C++ while the spectrum API is based C language. This makes many functions in the Spectrum API not recognized by redpitaya-epics.
3. The default equalization filter parameters and the default sampling frequency setting in Red Pitaya library file `librp.a` or `librp.so`, are very different from parameters in Sepctrum API source code.

The EPICS driver support is developed for ai and wave-form record support. And an EPICS IOC is created based on the driver support and runs on the Red Pitaya Linux operating system. The CSS GUI on a remote PC access the EPICS PVs and presents users the results of



power spectral and the auto-detected peak power points, which is shown in Fig. 3. This EPICS virtual spectrum analyzer has been tested in laboratory and its noise is main-tained in the range of -110~-120dBm.

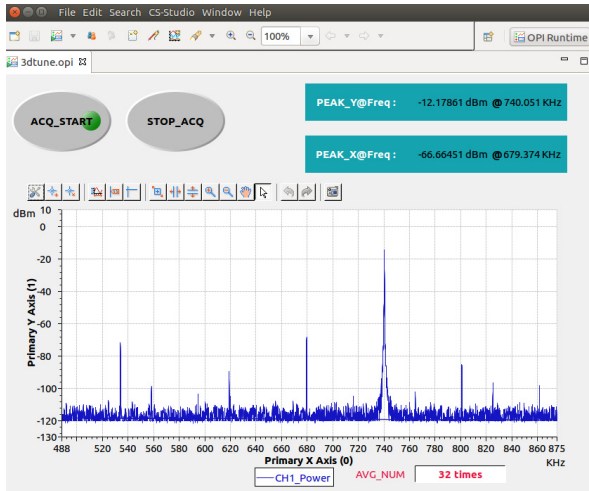


Figure 3: Tests for the EPICS IOC as a Spectrum Analyzer.

## CONCLUSION

A virtual spectrum analyzer is integrated into EPICS and meeting the requirements of BEPCII 3D tune measurement system. An EPICS IOC based on spectrum analyzer driver support is created and tested in laboratory. Tests will go on in the IP Station in future when BEPCII runs in Collision mode. More importantly, the development of the Red-Pitaya-based EPICS IOC provides a choice for device selections in future data acquisition systems.

## ACKNOWLEDGEMENTS

Authors would like to thank Professor Andraz Pozar (Australian Synchrotron) for the original EPICS driver support for RedPitaya based on asynPortDriver.

## REFERENCES

- [1] BEPCII, <http://english.ihep.cas.cn/doc/1840.html>
- [2] M. Gasior, "Faraday cup award: High sensitivity tune measurement using direct diode detection", in *Proc. 15th Beam Instrumentation Workshop (BIW'12)*, Newport News, VA, USA, Apr. 2012, pp. 1-8.
- [3] M. Gasior and R. Jones, "The principle and first results of betatron tune measurement by direct diode detection", CERN. Geneva, Switzerland, LHC-Project-Report 853
- [4] RedPitaya, <https://redpitaya.com/>
- [5] ASYN, <https://epics.anl.gov/modules/soft/asyn/>
- [6] RedPitaya-epics, <https://github.com/AustralianSynchrotron/redpitaya-epics>
- [7] NGINX, <https://en.wikipedia.org/wiki/Nginx>
- [8] EPICS, <https://epics.anl.gov/index.php>
- [9] Redpitaya-epics Release, <https://github.com/AustralianSynchrotron/redpitaya-epics/releases/tag/v1.0>

# THE DIAGNOSTIC SYSTEM AT THE EUROPEAN XFEL: COMMISSIONING AND FIRST USER OPERATION\*

D. Nölle†, DESY, 22603 Hamburg, Germany  
on behalf the European XFEL Diagnostic Team

## Abstract

The European XFEL is now commissioned and user operation has started. Long bunch trains up to 500 bunches are established. The role of and experience with the electron beam diagnostic will be reported. Highlights, problems and their solutions will be discussed

## INTRODUCTION

The European XFEL (Fig. 1) is an X-ray free-electron-laser based light source with soft and hard X-ray beamlines that will finally provide intense radiation from about 0.25 to 25 keV at TW level with pulse durations of a few 10 fs [1].

The length of the facility is about 3.5 km and the accelerator tunnel is crossing below inhabited areas in the city of Hamburg. It offers 5 photon tunnels ending in a big experimental hall. In the current configuration two hard X-ray FELs and one soft X-Ray FEL are in operation. The FELs are driven by a superconducting accelerator based on TESLA technology [2] with up to 17.5 GeV electron beam energy. The long RF pulse of 650  $\mu$ s allows to accelerate up to 2700 bunches per RF pulse. With a repetition rate of 10 Hz this corresponds to up to 27000 X-ray pulses per second that can be distributed between the different undulator lines to allow for simultaneous operation of experiments.

Only 9 months after the cool down of the superconducting accelerator and initial beam commissioning first user experiments started. The total operation time in 2017 was about 7000 h. Currently the facility is mainly operated at 14 GeV with 1 – 60 bunches per RF pulse and photon energies around 9.3 keV, based on the users demands.

Up to now two photon beamlines served by the hard X-ray FEL device SASE1 are in operation and have started their user program. The soft X-ray FEL SASE3 driven by

the spend electron beam of SASE1 is lasing routinely at photon energies around 900 eV and the commissioning of the photon beamline is in an advanced state. The user program of this beamline will start in fall 2018. The second hard X-ray FEL SASE2 is also lasing. Even lasing with all 3 devices in parallel was already demonstrated.

During special tests a photon energy range of 7.2 to 19.3 keV was easily achieved by tuning the gaps of the variable gap undulators. In test runs an average power of the X-ray beam of up to 6 W, running a bunch train of 500 bunches per RF pulse, as well as the design energy of 17.5 GeV have already been demonstrated.

## LAYOUT OF THE FACILITY

The accelerator has an injector located in a separate vault. It consists of the normal conducting gun, one accelerating module of the TESLA type and a 3.9 GHz module [3] for phase space linearization, a laser heater system [4], followed by a diagnostic section. This installation was completed and commissioned one year before the main LINAC, so that most essential parts of almost all systems could be commissioned during this time [5, 6].

From the injector the beam is fed to the main accelerator tunnel. The accelerator is laid out with a 3 stage bunch compression and bunch compressors B0 at 130 MeV, B1 at 700 MeV and the final stage B2 at 2.4 GeV. The stages are separated by the LINAC systems L1 and L2, consisting of 4 and 12 accelerator modules, respectively. At 700 MeV and 2.4 GeV the compressors include diagnostic sections; the high energy one is equipped with a transverse deflecting system (TDS) for longitudinal phase space diagnostics [7]. After bunch compression to a few 10 fs, the beam is accelerated in the main LINAC build out of 80 accelerator modules. The RF system is designed such, that one RF station serves four modules.

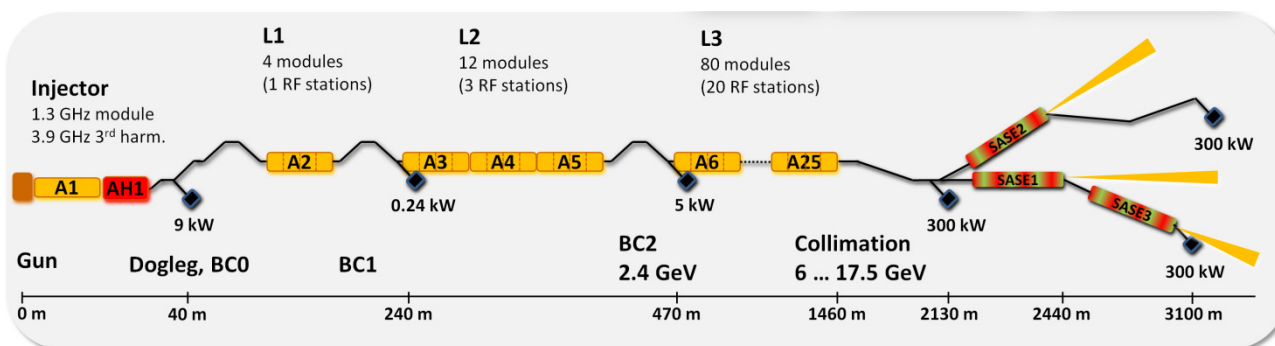


Figure 1: Block Diagram of the EXFEL.

\* Work supported by the respective funding agencies of the contributing institutes; for details please see <http://www.xfel.eu>

† dirk.noelle@desy.de

The main LINAC is followed by a collimation section providing both collimation of transverse phase space to about  $60\sigma$  and energy down to 2% relative energy deviation. Between collimation and beam distribution the Intra-Bunch-Train-Feedback System (IBFB) [8] for fast trajectory feedback within the bunch train is located.

The beam distribution system [9] is built from two switchyards, based on a kicker system in combination with a Lambertson septum. The first system allows to kick single bunches out of the train into the first 300 kW main dump line (TLD) at the end of the accelerator tunnel. The bandwidth of the kicker system allows to remove single bunches out of the train, even at 4.5 MHz bunch repetition rate. The second system uses a high precision kicker, having a rise time on the order of 20  $\mu$ s and a precise flat top. With this system the bunch train is split into two parts, one going straight to the SASE1/3 branch, and the other being kicked into the SASE2 branch. Both beam lines are terminated by another 300 kW electron beam dump each. In the SASE1/3 branch, the electron beam first passing the hard X-ray FEL SASE1, is also send to the soft X-ray FEL SASE3. The initial planning was to use the spent beam from SASE1 in SASE3, but it turned to be more efficient to suppress lasing in one of the FELs by means of a kicker [10]. This scheme called “soft-kick” or “fresh bunch technique” provides a decoupling of the two FELs by sending parts of the bunch train to different orbits in the same beamline. The other branch currently contains the hard X-ray FEL SASE2 only, but the tunnel system has space for up to 2 more FELs. Corresponding to the 5 possible photon sources five tunnels for photon beamlines are available (3 beamlines are already installed.). Each beamline can serve up to 3 experiments. The beam distribution system allows providing beam to all FELs simultaneously, thus serving experiments for real simultaneous operation.

## COMMISSIONING HISTORY AND OPERATIONAL HIGHLIGHTS

The commissioning of the EXEL started with the operation of the injector in December 2016. Within a half year run all relevant beam parameters of the injector have been demonstrated [5]. Furthermore the injector run provided the possibility to commission devices from almost all diagnostic systems [6].

Commissioning of the main LINAC started in January 2017, immediately after the 3 weeks cool down of the superconducting accelerator [11]. Beam commissioning was started in parallel to the commissioning of the RF systems. This was possible due to the flexibility of the timing system [12] that allows shifting single RF stations away from the arrival time of the electron beam. After recommissioning of the injector, first beam was achieved in B1 on January 15<sup>th</sup> and first accelerated beam on January 19<sup>th</sup>. Beam up to B2 was possible on February 2<sup>nd</sup>. On February 22<sup>nd</sup> for the first time an accelerated beam of 2.5 GeV was produced up to B2. With this energy the beamline through the main linac up to the TLD beamline was

set up, and first beam at the end of the main linac tunnel was demonstrated on February 24<sup>th</sup>. While final assembly and technical commissioning work in the SASE1/3 tunnels were continuing, the RF stations in L3 were commissioned in parallel to beam operation, so that the beam energy could be increased in steps up to 12 GeV. On April 27<sup>th</sup> the operation permission for the SASE1/3 branch was granted, and in the evening a 10.5 GeV beam was transported up to the dump in the SASE1/3 beamline. Shortly after establishing first beam, the SASE1 undulator was closed and first SASE operation was demonstrated in the night from May 2<sup>nd</sup> to 3<sup>rd</sup> with a 6.4 GeV beam at 9 Å [13]. After this successful but rather empirical first lasing attempt, a systematic program for photon beamline and diagnostics started. Beam based alignment (BBA) of SASE1 was resulting in position corrections of the movable quadrupoles of the undulator intersections. With these new settings and some basic photon diagnostics available, lasing at 2 Å or 6.2 keV with a 10.4 GeV beam was demonstrated on May 24<sup>th</sup>. Due to optimization of machine and undulator settings the SASE power could be increased to the mJ level within the next days. With ongoing commissioning work the beam energy was further increased up to 14 GeV and a first standard working point at 9.3 keV was established with SASE levels of more than 500  $\mu$ J and up to 30 bunches/train. This working point was used for the commissioning of the photon beamlines, the initial commissioning of the two experimental stations of SASE1 and during the first user period, just 10 month after start of beam commissioning. The number of bunches per RF pulse is steadily increasing. For the first user period up to 30 bunches were provided. Currently pulse numbers between 1 and 120 pulses per RF pulse with up to 1.5 mJ/pulse and a photon energy range from 7.5 to 14 keV can be provided. The pulse number is limited by safety aspects of the experiments. With the shutters of the experiments closed, the machine was running 500 bunches per RF pulse (5000 pulses/s) at a repetition rate of 4.5 MHz with an average SASE pulse energy of 1.3 mJ/pulse, thus more than 6 W of average power.

Parallel to the ongoing user program of SASE1, commissioning work of the soft X-Ray FEL and beamline as well as the completion of the second branch with the SASE2 hard X-ray FEL have been done. As soon as the initial photon commissioning of the SASE3 beamline was ready, first lasing of SASE3 at 13 Å or 900 keV was possible on February 8<sup>th</sup> 2018. Instead of just using the spent beam of SASE1 for lasing in SASE3, a scheme using fast kickers to send individual bunches on different lasing orbits in SASE1 and SASE 3 was established. This scheme called “soft kick” or “fresh bunch technique” allows decoupled hard X-ray operation in SASE1, while “SASE3 bunches” produce up to 7 mJ pulse energy in the soft X-ray regime.

On March 13<sup>th</sup> the beam was send to the SASE2 branch for the first time. 100 % transmission and stable beam conditions in the about 1 km beamline could be established within a single shift. Due to user program and shutdown work, the first lasing attempt for SASE2 had to





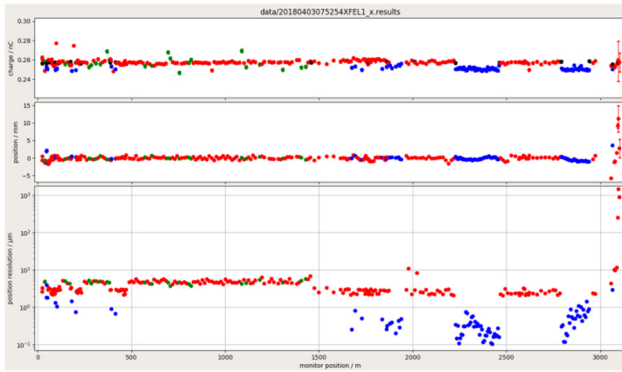


Figure 2: Plot of the horizontal BPM resolution versus longitudinal position in the accelerator. The upper two sub-plots show charge and position along the beamline. The lower sub-plot gives the position resolution of the BPMs in the horizontal plane. The colour code is red for button, green for re-entrant and blue for cavity BPMs. The first 6 cavity BPMs show higher resolutions due to an attenuation of the signals with 10 dB for safety. The 10  $\mu\text{m}$  resolution for 2 button BPMs at about 2000 m position is due to a larger pipe diameter of 100 mm.

During the normal operation BPMs are a reliable backbone of operations. They provide a resolution superior to specification and work reliable even below 10 pC charge. As shown in Figure 3, BPM resolution is well below 10  $\mu\text{m}$  even in the rather large 78 mm beam pipe of the cold LINAC, and about 5  $\mu\text{m}$  for the 40.5 mm standard type. Cold button (red) and re-entrant cavity (green) BPM perform comparable. Cavity BPMs (blue) have a resolution below 1  $\mu\text{m}$ . The 10 mm type in the undulator sections turns out to be the best, as expected.

### Charge Monitoring

European XFEL uses 3 kinds of monitors to measure the charge: In the gun region a destructive method with simple Faraday cups is used. The main working horse is the so called toroid, a type of current transformer commonly used at many DESY accelerators [20]. In addition the machine uses single cell stainless steel 1.3 GHz cavities, the so called dark current monitors [21]. Due to pile up in the resonator even the very small charge of dark current with 1.3 GHz repetition rate from the gun or field emission of the module produces a reasonable signal, allowing measurements down to the noise level at about 50 nA. In addition the charge signals from the beam can be measured. Depending on the settings of the electronics fC charge levels can be measured. This turned out to be useful, finding the first beam signals in the photo-injector, while phase and laser position on the cathode were still unknown. Such monitors are installed after the gun and around all 4 cold LINAC sections.

The toroid charge monitors have sensitivity of less than a pC and a resolution of about 100 fC at the usual operation charge of 250 pC. The high sensitivity together with the self-triggering mode has proven to be essential for the reliable beam detection during initial commissioning. The 37 monitors of this type are connected in a kind of chain

by a fibre network. The electronics is based on a commercial ADC board with a FPGA. Fast digital data processing allows sending charge information of one monitor to the next upstream toroid via the fibre connections. Also branching of the beamlines is taken into account. Using this information a fast transmission interlock signal is implemented. The signals are used by the machine protection system (MPS) to stop the beam within a bunch train. Additional features are interlocks stopping the beam due to persisting poor transmission, or to stop beam production at certain integrated charge limits. A further useful feature is an alarm, if bunches are in the expected bucket. In addition an error margin of the timing error is provided, that can be used for corrective actions, e.g. to align the injector laser to the correct RF timing.

The digital backend of the toroids with a powerful Virtex 6 FPGA provides potential and flexibility for implementing new requirements to control transmission or global beam loss on various time scales and under different aspects. With their well-defined interface to the MPS system the toroids are very valuable and customizable sensors to protect the machine.

### Beam Size Measurements

In total 67 screens and 12 wire scanners are distributed along the facility. Besides of screens for the rather big beam pipes before dumps and septa that are foreseen mainly for observation, European XFEL uses 2 types of precision screens for measurements.

The systems use scintillator crystals instead of OTR targets, which are oriented perpendicular to the beam axis. This geometry allows for spatial suppression of potential COTR effects on the crystal surface. Observation is under  $45^\circ$  and the optics features a depth of field extension using the Scheimpflug principle, either with 1:1 or 1:4 reproduction scales [22]. Initially LYSO was chosen as the screen material, but it turned out, that intrinsic quenching at high charge densities results in an overestimation of the beam size [23]. Therefore, other materials are under investigation. The currently most promising materials are YAG (Fig. 4) and YAP, which is now installed in the injector. Most of the screens are installed in groups of 4 at prominent locations in order to provide matching points for the optics with the 4 screen method, like in the injector and in the diagnostic sections after the bunch compressors. For the low energy sections the screen stations provide so called off axis screens, being smaller crystals leaving the beam axis uncovered. With dedicated kicker systems arbitrary single bunches are kicked out of the long bunch train and are hitting the screens [24].

In the high energy regime after the main LINAC, most of the screens have longer version of the vacuum chamber that allows integrating wire scanners, thus having two independent beam size measurements optically at one place. 4 matching sections after the main LINAC and before each SASE undulator are equipped with wire scanners [25].

The wire scanner type developed for European XFEL provides slow and fast scans. With the fast mode the wire is passing through the beam with a speed of 1 m/s, so that a profile can be taken within a single bunch train. Since long bunch trains are up to now not standard operation the scanners are used in slow mode. For the evaluation of new screen materials, the wire scanners are used as a reference measurement for the beam size [23]. Furthermore they turned out to be sensitive tools to study beam halo and its suppression in the collimation system [26].

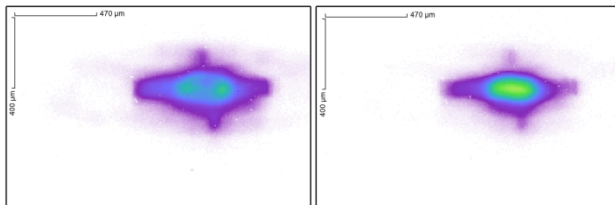


Figure 3: Comparison of LYSO (left) and YAG scintillators (right). The two scintillators are installed in the same screen station at 1650 m. The pictures are taken under the same conditions with a 14 GeV 250 pC beam. One can see for the LYSO a drop of intensity in the middle, so that the area of highest intensity looks like a “smoke ring” [23]. The YAG screen does not show such an artefact in the middle.

### Beam Loss and Radiation Dose

In order to control beam loss in the machine a beam loss monitor (BLM) system with 470 monitors is installed [27]. The BLMs are based mainly on plastic scintillators read out by photomultipliers. At positions, where either high particle loss is expected, or hard X-ray synchrotron radiation would also trigger the BLM, the scintillators are replaced with quartz rods of the same dimensions. The use of Cherenkov radiation makes the BLMs sensitive to particle loss only. The BLM system can interrupt the operation via the MPS, acting on different time scales; there are single bunch alarms and multi-bunch alarms with different thresholds, as well as an integral alarm, sensitive to losses from dark current or field emission, emitted by the gun or the accelerating modules. In parallel to the digital data processing using an ADC and FPGA board, there is a simple analogue comparator circuit, able to generate alarms independent of timing or firmware issues.

Like for the toroids also the beam loss monitors firmware includes a kind of memory, if too many (configurable) events happen in a row, the bunch train is not only cut, but beam production is stopped via the MPS, and continues only after acknowledgment from the operator.

A difficult issue for BLMs is always how to calibrate the system. Even if BLMs would be calibrated to a given dose or loss rate, the location within the machine makes it difficult to judge the readings due to different loss and shielding situations of each BLM. European XFEL does not use individually calibrated BLMs, but makes use of the activation profile of the accelerator. The activation of the machine is measured on a regular level. If at certain

positions the activation is judged to be too high, the alarm thresholds of the BLMs are tightened at these positions. On the other hand thresholds can be relaxed, as long as activation is reasonably low. Following this strategy, measurements even shortly after runs with up to 5000 bunches per seconds show a very moderate activation profile of the machine. Even at the collimators and in the dump regions the activation is currently well below 100 μSv/h. Of course it is expected that with increasing average power, BLM thresholds will get tighter and nevertheless activation at critical places of the machine will increase.

Beam halo monitors (BHM), a special kind of loss monitor, are located in the main dump lines (and in the injector) [28]. They are using 4 diamond and 4 sapphire detectors each and are working like solid state ionisation chambers. Due to their location around to the beam pipe after the last focussing element, they act like a virtual aperture. All trajectories passing the inside of this aperture will pass the dump window without losses. Due to the possible high average power of the beam the robustness of solid state detectors was necessary. The BHMs are connected to the MPS system and provide fast interlock signals to cut the bunch train within the RF pulse.

In addition to the fast acting loss monitors the European XFEL diagnostic suite also includes a dosimetry system [29]. It is based on about 630 RadFet sensors and delivers data on the integrated (gamma) dose at certain points inside the accelerator installation. The electronics of the RadFet sensors developed as an FMC board that can be installed and read out by any FMC interface. In addition to internal sensors the FMC board provides an interface to a custom made field bus providing access to external sensors.

The internal and external sensors are adapted for different purpose. Using a bias voltage and high sensitivity the internal ones are used for a dose survey in the electronics racks. Corresponding FMC boards are installed on the MPS electronics as well as in the BPM crates, creating a widespread measurement network in the tunnel infrastructure. Without bias voltage the sensors are less sensitive, but can measure higher dose levels. In this mode they are used as external sensors mainly in the undulator section, with two sensors installed on the undulator yoke close to the beam entrance. During commissioning it turned out, that the RadFet sensors, like the standard BLMs with plastic scintillator, are also sensitive to high energy X-rays. Therefore the dose readings in the last part of the undulators are dominated by spontaneous radiation. As a countermeasure 4 mm lead shields for the RadFet sensors are in preparation.

### Longitudinal Diagnostics

Two S-band transverse deflecting structures (TDS) provide bunch length measurements with a resolution better than 200 fs in the injector and about 15 fs after the second bunch compressor. In order to use these systems with long bunch trains, the kicker systems and off axis screens are used [30].

In order to measure and later to feedback the arrival time of the beam, 7 beam arrival time monitors (BAM) are installed; the first in the injector, a pair around the chicane in B1 and B2 and a last station in front of the switchyard [31]. The arrival time jitter after the bunch compression is typically of the order of 30 fs. It is expected that this value improves, as soon as the intra-train arrival time feedbacks get operational.

The main working horse of the longitudinal diagnostics is the bunch compression monitor (BCM) [32]. Based on coherent diffraction radiation by a 5 or 7 mm aperture, the intensity of the coherent radiation in the far IR or terahertz regime is measured. Assuming a decent working point for the compression the general shape of the beam is assumed to be rather constant. Therefore changes of the coherent intensity should reflect slight changes of the bunch length without significant changes of the beams form factor. This qualitative signal with bunch to bunch resolution is suited to feedback the RF systems to keep the compression constant. During SASE operation feedbacks using these signals on injector, L1 and L2 chirp or phase are used routinely.

## MACHINE PROTECTION SYSTEM

With the large number of bunches, typical for the superconducting machines, strict and fast machine protection is mandatory [33]. The European XFEL uses a scalable distributed system. It is implemented as FPGA firmware on a  $\mu$ TCA board, that collects interlock data from many different sources and that acts on different actuators and combinations of them like the photo injector laser, the dump kicker as well as on RF systems. Inputs are provided by fast systems like BLMs and toroids as well as slow inputs like magnets or vacuum interlocks. Depending on the machine settings the system determines allowed beam destinations as well as allowed number of bunches, individual for the two SASE lines. If there is a magnet failure or BLM alarm in one branch, operation is only stopped for this branch. In case a screen is inserted the beam is only limited in this branch to single bunch.

The fast signals from BLMs and toroids are able to stop beam production within the long bunch train. The latency is dominated by signal travel and varies from less than 4  $\mu$ s close to the injector to about 35  $\mu$ s at the end of the SASE lines. With the highest repetition rate of 4.5 MHz this would correspond to more than 120 bunches, that would still be accelerated. Therefore the fast kickers of the distribution switchyard are also used to stop the beam in the SASE lines in order to reduce the latency to about 15  $\mu$ s.

## FAST INTRA BUNCH TRAIN FEEDBACK

Besides of slow orbit feedbacks to stabilize the electron beam orbit at essential points of the machine, there is a fast system to stabilize the orbit also within the bunch train. The IBFB, installed between the collimation section and the switchyard, is an in kind contribution from Switzerland [8]. Using 4 cavity BPMs with sub-micron preci-

sion, a set of two stripline kickers and fast FPGA logics the system, the system is able to stabilize the electron orbit along the train and to correct for pulse to pulse jitter of the incoming train. Adaptive feedforward algorithms and feedback reduce the bunch by bunch orbit deviations along the bunch train, as well as the pulse to pulse position deviation to the level of a few  $\mu$ m. The time constant for the initial stabilization is on the order of a 10  $\mu$ s, the latency for bunch to bunch stabilization is on the order of 1-2  $\mu$ s.

The initial part of the bunch train, needed for fast feedbacks to start regulation, can be kicked into the dump system before the SASE lines.

## CONCLUSIONS

Commissioning and the onset of standard operation of the European XFEL have been very successful. The superconducting accelerator is operating according to specs. Within one year first lasing of all three FELs from soft to hard X-rays could be achieved. First user operation started on schedule 9 months after the first beam. This effective turnover from construction to operation was strongly supported by the diagnostic systems; almost all have been available from  $t_0$ . Therefore, the goal to commission the beam with diagnostics and not the diagnostics with beam was fully reached. In the current phase of “early operation” the diagnostics provide reliable and precise systems for further optimisation and improvement of the facility.

## ACKNOWLEDGEMENTS

Construction and commissioning of the diagnostics for European XFEL was the effort of a bigger team. Therefore, the author would like to thank all colleagues, who have participated in the work to set up the diagnostic system for the European XFEL. These thanks especially include the BPM collaboration, together with PSI and CEA, and also the colleagues from IHEP, Protvino, who have participated in the construction of the BLMs.

## REFERENCES

- [1] M. Altarelli *et al.* Ed., “The European X-Ray Free-Electron-Laser – Technical Design Report”, DESY, Hamburg, Germany, Rep. DESY 2006-097, July 2017.
- [2] R. Brinkmann *et al.* Ed., “TESLA Technical Design Report – Part II: The Accelerator”, DESY, Hamburg, Germany, Rep. DESY 2001-011, March 2001.
- [3] C. Maiano *et al.*, “Commissioning and Operation Experience of the 3.9 GHz System in the EXFEL Linac”, in *Proc. IPAC'17*, Copenhagen, Denmark, MOPVA059, pp. 999-1002.
- [4] M. Hamberg *et al.*, “Electron Beam Heating with the European XFEL Laser Heater”, in *Proc. FEL'17*, Santa Fe, USA, WEP018, pp 450-451.
- [5] F. Brinker, “Commissioning of the European XFEL Injector”, in *Proc. IPAC'15*, Busan, Korea, TUOCA03, pp. 1044-1047.
- [6] D. Lipka *et al.*, “First Experience with the Standard Diagnostics at the European XFEL Injector”, in *Proc. IBIC'16*, Barcelona, Spain, MOBL02, pp. 14-19.



- 7<sup>th</sup> Int. Beam Instrumentation Conf.  
ISBN: 978-3-95450-201-1
- IBIC2018, Shanghai, China  
doi:10.18429/JACoW-IBIC2018-TUOA01
- JACoW Publishing
- Content from this work may be used under the terms of the CC BY 3.0 licence (© 2018). Any distribution of this work must maintain attribution to the author(s), title of the work, publisher, and DOI.
- [7] M. Hüning, “Bunch Length Measurements using transverse Deflecting Systems”, to be presented at LINAC’18, Beijing, China, Sep. 2018.
  - [8] B. Keil *et al.*, “Status of the European XFEL Transverse Intra Bunch Train Feedback System”, in *Proc. IBIC’15*, Melbourne, Australia, TUPN064, pp. 492-496.
  - [9] W. Decking and F. Obier, “Layout of the Beam Switchyard at the European XFEL”, in *Proc. EPAC’08*, Genoa, Italy, WEPC073, pp. 2163-2165.
  - [10] E. A. Schneidmiller and M.V.Yurkov, “Baseline Parameters of the European XFEL”, in *Proc. FEL’17*, Santa Fe, USA, MOP033, pp. 109-112.
  - [11] T. Schnautz *et al.*, „First operation of the XFEL linac with the 2K cryogenic system”, presented at CEC-ICMC 2017, Madison, USA.
  - [12] A. Aghababayan *et al.*, “XFEL Timing System Specifications”, Conceptual Design Report - Version 2.2, Hamburg, Germany, May 2013, <http://ttfinfo2.desy.de/doocs/Timing/CDRV2.2short.pdf>.
  - [13] W. Decking and H. Weise, “Commissioning of the European XFEL Accelerator”, in *Proc. IPAC’17*, Copenhagen, Denmark, MOXAA1, pp. 1-6.
  - [14] B. Keil *et al.*, “The European XFEL Beam Position Monitoring System”, in *Proc. IPAC’10*, Kyoto, Japan, MOPE064, pp. 1125-1127.
  - [15] C. Simon *et al.*, “Design and Beam Test Results of the Reentrant Cavity BPM of the European XFEL”, in *Proc. IBIC’16*, Barcelona, Spain, TUPG17, pp. 356-359.
  - [16] D. Lipka *et al.*, “Development of Cavity BPM for the European XFEL”, in *Proc. LINAC’10*, Tsukuba, Japan, TUP094, pp. 629-631.
  - [17] D. Lipka *et al.*, “Button BPM Development for the European XFEL”, in *Proc. DIPAC’11*, Hamburg, Germany, MOPD19, pp. 83-85.
  - [18] B. Keil *et al.*, “Production Tests, Calibration and Commissioning of Button BPMs for the European XFEL”, in *Proc. IBIC’17*, Grand Rapids, USA TUPCF19, pp. 259-262.
  - [19] B. Keil *et al.*, “Beam-based Calibration and Performance Optimization of Cavity BPMs for SwissFEL, E-XFEL and FLASH2”, in *Proc. IBIC’14*, Monterey, USA WEPD11, pp. 665-669.
  - [20] M. Werner *et al.*, “A Toroid Based Bunch Charge Monitor System with Machine Protection Features for FLASH and XFEL”, in *Proc. IBIC’14*, Monterey, USA WEPF02, pp. 521-524.
  - [21] D. Lipka *et al.*, “Dark Current Monitor for the European XFEL”, in *Proc. DIPAC’11*, Hamburg, Germany, WEOC03, pp. 572-574.
  - [22] C. Wiebers *et al.*, “Scintillating Screen Monitors for Transverse Electron Beam Profile Diagnostics at the European XFEL”, in *Proc. IBIC’13*, Oxford, UK, WEPF03, pp. 807-810.
  - [23] G. Kube *et al.*, “A Simple Model to Describe Smoke Ring Shaped Beam Profile Measurements with Scintillating Screens at the European XFEL”, presented at IBIC’18, Shanghai, China, this conference.
  - [24] M. Scholz and B. Beutner, “Electron Beam Phase Space Tomography at the European XFEL Injector”, in *Proc. IPAC’17*, Copenhagen, Denmark, May 2017, paper MOPAP047, pp 196-198.
  - [25] T. Lensch and S. Liu, “Status and Commissioning of the Wire Scanner System for the European XFEL”, in *Proc. IPAC’18*, Vancouver, Canada, WEPAF047, pp. 1919-1922.
  - [26] S. Liu *et al.*, “First Beam Halo Studies using Wire Scanners at the Wire Scanner System for the European XFEL”, in *Proc. FEL’17*, Santa Fe, USA, TUP003, pp. 255-258.
  - [27] T. Wamsat, “The European XFEL Beam Loss Monitor System”, presented at IBIC’18, Shanghai, China, WEOB03, this conference.
  - [28] A. Ignatenko *et al.*, “Beam Halo Monitor for FLASH and the European XFEL”, in *Proc. IPAC’12*, New Orleans, USA, MOPPR018, pp. 816-818.
  - [29] F. Schmidt-Föhre *et al.*, “Commissioning of the new Online-Radiation-Monitoring System at the European XFEL Injector with first Tests of the High-Sensitivity-Mode for Intra-Tunnel Rack Surveillance”, in *Proc. IBIC’15*, Melbourne, Australia, WECLA02, pp. 585-588.
  - [30] C. Gerth *et al.*, “Online Longitudinal Bunch Profile and Slice Emittance Diagnostics at the European XFEL”, in *Proc. IBIC’17*, Grand Rapids, USA TUPCC03, pp. 259-262.
  - [31] M. Viti *et al.*, “The Bunch Arrival Time Monitor at FLAS and European XFEL”, in *Proc. ICALEPCS’17*, Barcelona, Spain, TUPHA125, pp. 701-705.
  - [32] P. Peier *et al.*, “Coherent Radiation Diagnostics for Longitudinal Bunch characterization at European XFEL”, in *Proc. FEL’14*, Basel, Switzerland, THP083, pp. 925-928.
  - [33] S. Karstensen, *et al.*, “XFEL Machine Protection System (MPS) Based On UTCA”, in *Proc. Real Time Conference (RT) 2014 19th IEEE-NPSS*, Nara, Japan, May 2014, pp. 1-4.



# APPLICATION OF MACHINE LEARNING TO BEAM DIAGNOSTICS

E.Fol<sup>†</sup>, J. Coello de Portugal, R. Tomas, CERN, CH-1211, Geneva, Switzerland

<sup>†</sup>also at Johann Wolfgang Goethe-University Frankfurt, 60323 Frankfurt am Main, Germany

## Abstract

Machine learning (ML) techniques are widely used in science and industry as a powerful tool for data analysis and automation. Currently, in accelerator physics ML is represented as a young research field, demonstrating mixed results in the latest attempts. The presented work is devoted to exploration of appropriate ML methods for beam diagnostics. The target is to provide an overview of ML techniques which can be applied to improve beam diagnostics and general accelerator performance. Besides the results of ML tools currently used in modern accelerators and evaluation of these tools, we also demonstrate possible concepts with the potential for further investigation and give recommendations on efficient use of ML techniques in accelerators.

## HISTORICAL MOTIVATION

### Traditional Optimization Techniques

Various optimization problems arise in modeling and operation of accelerators. Multi-parameter optimization can be performed using well established methods such as simplex, as it was shown at KEKB [1] applied on minimization of vertical emittance in injector linac. Another examples for the application of simplex as optimization technique for accelerators can be found in [2], where the method was applied on tuning of beam delivery system in CLIC simulations.

Linear optics corrections using optimization algorithms to find a minimum beam size with multi-parameter knobs as input were performed already in 1993 [3]. Luminosity maximization and beam lifetime are typical multivariate optimization tasks also in circular colliders [4, 5].

For light sources, such methods as random-walk optimization are being used to reduce the vertical beam size [6]. Also online optimization using various measures of accelerator performance as objective functions is being successfully applied in operation [7]. An illustrating example towards applying ML is the development of machine based optimization using genetic algorithms, which have been used as well in accelerator design [8–10].

### Limitations of Traditional Methods

The described examples demonstrate successful performance of traditional optimization tools in applications on linear optics corrections and problems with limited amount of optimization targets. Bigger challenges emerge when diagnostics of complex non-linear behavior is required and several variables have to be taken into account as final objective. The amount of time and computational power required by traditional methods might become unacceptable for future accelerators such HE-LHC and FCC. The main limitation of

traditional optimization methods is that the objective function or specific rules and thresholds have to be known. In opposite, Machine learning (ML) methods can learn from given examples without requiring explicit rules.

## RELEVANT MACHINE LEARNING CONCEPTS

ML techniques aim to build computer programs and algorithms that automatically improve with experience by learning from examples with respect to some class of task and performance measure, without being explicitly programmed [11].

Depending on problem and existence of learning examples, different approaches are preferred. If pairs of input and desired output are available, an algorithm can generalize the problem from the given examples and produce prediction for unknown input. ML algorithms that learn from input/output pairs are called *supervised learning* algorithms. Opposite to supervised learning, *unsupervised learning* algorithms solve the tasks where only input data is known. Unsupervised learning is suitable for the problems such anomaly detection, signal denoising, pattern recognition, dimensionality reduction and feature extraction. In the following a brief overview on significant machine learning concepts that can be used as supervised as well as unsupervised approaches is presented.

### Artificial Neural Network

Artificial Neural Networks (ANNs) are well suited for learning tasks, where data is represented by noisy, complex sensor signals and the target output function may consist of several parameters. A basic ANN consists of a single processing unit (*neuron*), that takes the *weighted* inputs and an additional activation function to introduce the nonlinearity in the output. For more complex practical problems, ANNs are composed of several interconnected *hidden layers* with multiple neurons stacked.

ANNs can be used for both regression and classification problems. In case of classification the output can be either a class label or a probability of an item belonging to a class. The learning of ANN is performed using *backpropagation* algorithm [12] on a set of examples. For each example the training algorithm computes the derivatives of the output function of the network. The obtained gradients with respect to all weights are then used to adjust the weights in order to achieve a better fit to the target output. In backpropagation *stochastic gradient descent* or one of its improved extensions Adam [13] and AdaGrad [14] is applied as optimization method in order to minimize the loss between the network output values and the target values for these outputs by updating the connection weights.

One interesting property of the backpropagation based learning is its ability to discover useful intermediate representation inside the network. Features that are not explicitly given can be extracted using layers between input and output layers (*hidden layers*). Thus, properties of the input that are most important for the learning can be discovered. This ability is a great advantage of this method in contrast to ML techniques that use only predefined features. ANNs with many hidden layers called *deep neural networks* are able to use fewer neurons per layer and have a better generalization ability [15], however the optimization of these networks is not trivial. There are no strict rules for building ANN architecture (number of neurons, layers, initial weights) as it usually heavily depends on a particular problem. However, techniques to adjust the architecture parameters exist. A detailed overview on various ANN architectures and training methods and their suitability for different applications can be found in [16–18]. A broad presentation of concepts and applications of ANN to particle accelerators is given in [19].

### Decision Trees and Ensemble Methods

Decision tree learning is a method for approximating discrete-valued target functions, which are represented by decision trees. Considering the case of classification, decision trees sort down the input instances from the root to leaf nodes. Usually, the splitting is based on one of the input parameters or a specified set of rules [20, 21]. Each leaf corresponds to one class representing the most appropriate class label. For the regression the leaf nodes correspond to target values.

Using a single tree, a model might not be able to generalize and perform poorly on unexplored sample. One possible solution to overcome this problem is to build ensembles of trees [22]. By training several slightly different models and taking the average prediction, the variance of the model can be reduced.

Compared to ANNs, decision trees are simpler to interpret and to understand its way of obtaining the final results and the underlying process, e.g. through the feature importance analysis. Feature importance analysis helps to understand the contribution of each input parameter to the correct decision during the training process. The ability of decision trees to evaluate the importance of input parameter is a significant advantage of these algorithms. Knowing the importance of the features we can reduce the model complexity and simplify the data preprocessing steps without significant accuracy loss.

### Clustering

Cluster analysis includes methods of grouping or separating data objects into clusters, such that dissimilarity between the objects within each cluster is smaller than between the objects assigned to different clusters [23, 24]. Cluster analysis is used in a wide range of applications. Data clusters can be considered as a summarized representation of the data, such that group labels can describe patterns or similarities and differences in the data. Moreover, clustering can be

used for prediction, such that classification of unseen data is performed based on knowledge about the properties of present data and by evaluating their similarity to the incoming data sample. The significant benefit of cluster analysis is the *unsupervised learning* approach, which means that no labeled data is needed to find a solution.

The simplest and the most commonly used clustering algorithm is k-means [25], which is based on centroid search. Another kind of clustering algorithms are the density-based algorithms such as DBSCAN [26], that views clusters as areas of high density separated by areas of low density, instead of looking for the centroids. Decision tree based methods also can be applied for cluster analysis using the data splits based on different features. Most of cluster analysis techniques allow to build clusters in a multidimensional space.

Apart from classification and pattern recognition, cluster analysis can be used as denoising method looking for abnormalities in the signal. Moreover, building clusters combining a large set of different observables can simplify the data visualization and manual analysis, such elimination of outliers in the measurements and detection of anomalies.

## OVERVIEW ON CURRENT APPLICATIONS

Meeting the demand of experimenters induce various challenges for accelerator design in general and in particular for beam control and diagnostics. Considering impressive results of ANNs applied in various scientific fields [27–31], among others in HEP [32] and the increase in available computational power, ML can cast the light on novel solutions for these challenges. In the following we demonstrate some ML applications currently being used in accelerator technology and ongoing research on potential ML based approaches.

### Optimization and Prediction

A complex system such as an accelerator, which beam dynamics exhibits nonlinear response to machine settings can be considered as a typical ML task. ML methods are especially suited for non-linear and time-varying systems with large parameter spaces. Due to the constant increase of machine design complexity and development of new interacting systems, traditional techniques might become insufficient.

ANN based application has been successfully applied at the Linac Coherent Light Source (LCLS) to predict x-ray pulse properties using electron beam and x-ray parameters as input [33]. The method is general and can be applied at any XFEL facility to obtain fast x-ray diagnostics. ANN is able to decode complex hidden correlations between parameters obtained from slow diagnostics such as photon energy and properties measured by fast diagnostics. For the training, small samples obtained at low repetition rate are used to predict complex diagnostics at a high repetition rate.

Similar approach has been applied at TEU-FEL by training an ANN with controllable machine settings such RF power and solenoid strengths as inputs in order to produce

prediction of electron beam parameters such beta functions and emittance [34].

A special kind of ANN, *convolutional neural networks* (CNN) [35] have been applied at FAST on image based diagnostic during beam operation [36]. A combination of a CNN and a feed-forward NN yields promising results for the prediction of beam parameters on simulated datasets. The model uses simulated cathode images, solenoid strengths and the gun phase as inputs and produces a prediction for various downstream beam parameters.

Extremum Seeking (ES) technique [37,38] in combination with ML is being applied to accelerator tuning and optimization providing promising results. In this application ANN is used for fast tuning in order to obtain a close approximation for the target settings. ES is used for beam-based adaptive feedback to track the actual time-varying optimal parameter settings. The advantages of this method are the model-independent approach, the ability to perform the tuning on many coupled parameters and handle time-varying noisy data.

Another example concerning the prediction of beam parameters is the application of various ML algorithms to the problem of inferring the actual beam profile width from measured profiles that are distorted by space-charge effects [39]. The promising results obtained on simulations data show the potential of the method to be further investigated on real measurements in order to reduce cost of Ionization Profile Monitors.

### Automation of Operation

Often there is a need to introduce various experiment-driven settings. In this case a large amount of free parameters has to be taken into account in order to meet the requirements and find optimal machine settings under given limitations. Only few parameters can be processed by a human at once and it is not feasible to produce forecasts taking into account all possible factors and correlations. Moreover, humans can perform differently on the tasks where the decisions can be subjective, which might lead to significantly different results. Also the automation of routine tasks could bring significant improvements into daily operation, such that the focus of operation can be transferred to complex tasks and rare events that require an expertise.

Apart from ANN, it is also possible to apply other kinds of regressors or classifiers in accelerator control such Gradient Boosting classifier [40] as it was shown in beam loss pattern classification for LHC [41]. The beam loss maps performed in controlled conditions are used in order to train a model to classify the type of losses during the LHC machine cycle.

Another example of ML based automation is the automatic alignment of collimators in SPS and LHC [42]. The method computes optimum angular settings for the collimators without human intervention. Fully automated alignment was achieved after the introduction of the ML based detection of alignment spikes in the losses which are used in order to determine if a collimator needs to be moved.

Table 1: Performance of Trained Models

Injection optics		
Model	MAE [ $1 \times 10^{-5} \text{ m}^{-2}$ ]	Explained $\sigma^2$
Random Forest	0.005	0.99
OMP	0.04	0.97
Neural Network	0.35	0.38

$\beta^* = 40 \text{ cm}$		
Model	MAE [ $1 \times 10^{-5} \text{ m}^{-2}$ ]	Explained $\sigma^2$
Random Forest	0.005	0.99
OMP	0.21	0.76
Neural network	0.33	0.47

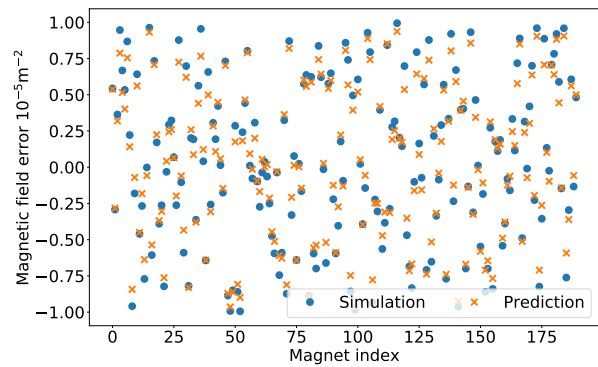


Figure 1: Random Forest prediction result on a random sample from the test set giving mean absolute error  $0.02 \times 10^{-5} \text{ m}^{-2}$ .

### Lattice Imperfections Correction

Attempts to build beam diagnostics and beam control systems using ML have been made already in the past decades [43–45]. The application described in [45] was built to detect dipole errors aiming to develop rapid commissioning. In this application, the dipole errors are obtained from the deviation of the measured beam position from the computed one. The simulations and tests have been performed on a relatively small machine (8 FODO cells, 8 BPMs), however the accuracy of the trained models decreased significantly after introduction of more than 2 dipole field defects. Anyway, given the early stage of ANN technology in that time, the obtained results have shown the potential of ML solution to be applied in beam control systems.

Recently, we applied ML on optics correction at LHC to predict the correction knobs settings required to cancel the quadrupole field errors [46,58]. In this case, optics correction is defined as a regression problem that can be solved by training a model using past measurements or simulations and its corresponding corrections (supervised learning).

In order to create a training set, random errors are introduced into the MADX-variables that represent physical circuits. In real measurements the optics errors are caused



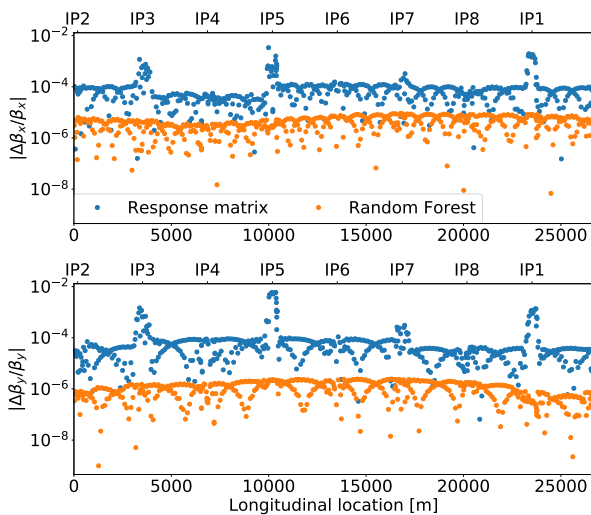


Figure 2: Expected beta-beating after applying corrections computed with linear response matrix and Random Forest regressor on simulated measurement.

by individual magnets instead of the circuits, in the following study we neglect this since the corrections can be done only using the circuit variables. The differences between the nominal model phase and the phase produced by perturbed simulations are provided as input and the corresponding errors as output of the model. Simulations data set of 10000 samples was divided into train and test set (60% and 40% respectively), each sample pair consist of 1046 inputs (number of BPMs in both planes) and 190 outputs (correction variables).

Comparison between logistic regression, ANN, Orthogonal Matching Pursuit [47] and Random Forest [48] models trained on two different optics setting are shown in Table 1. Random Forest algorithm achieves the most accurate prediction on test data set, the behavior on arbitrary sample from the test set is shown in Fig. 1.

The comparison to the traditional response matrix method as implemented in LHC [49,50] is performed on an independently simulated measurement perturbed by random errors with the absence of BPMs noise and triplet errors. The differences in obtained global optics corrections are shown in Fig. 2. Random Forest achieves an overall better correction on the given simulation and demonstrates that further enhancement in traditional method are required in order to treat the errors around interaction points (IP). The problem of the traditional method can be also related to the linear behavior of the response matrix, concerning possible nonlinearities in these regions.

Further improvements in ML based optics correction can be achieved using more realistic simulations that include other sources of optics error. The quality of the model can be significantly improved by combining different optics models in one training set in order to achieve better generalization. Potentially efficient approach for the training is *Transfer Learning*, a method where a trained model can use the learned representation to solve similar tasks after be-

ing re-trained on a very small data set [51,52]. Thus, small amount of real optics measurements and performed corrections can be used to tune the model trained on simulations to significantly increase the model quality.

## Anomaly Detection

Anomaly detection techniques are suitable for the detection of unusual events that do not conform to expected patterns. They also can be used to identify outliers and remove noise. Anomaly detection can be performed using classification on labeled data (supervised learning), cluster analysis (unsupervised learning) or applying semi-supervised learning methods such as autoencoder, a special ANN representing the model trained on normal data set and then detect the anomalies based on the value of the loss function generated by the representative model on the given test sample [53].

An early example on anomaly detection in beam diagnostics in storage ring (Pohang Light Source) is the application of ANN to predict the orbit at particular BPM based on measurements at other BPMs [54]. A large deviation between measured and predicted orbit should mark malfunctioning BPM.

An example for anomaly detection using cluster analysis is the detection of faulty BPMs at LHC based on harmonic analysis on turn-by-turn data [55]. The main issue regarding the problem of faulty BPMs is the appearance of unphysical data in the reconstructed optics functions. Most of the noise can be removed using traditional methods based on SVD and FFT [56] and manual cleaning, however, faulty data samples still can be observed in the optics functions. Since no labeled data is available and the data analysis has to be performed on multidimensional parameter space, clustering appears as an effective solution. The analysis as shown in Fig. 3 is performed on a three dimensional parameter space containing the betatron tune, the amplitude of the measured oscillations and the noise to amplitude ratio. The data is normalized to the range [0, 1] and separated into IR and Arcs BPMs due to the different data points distribution in these regions.

Since the appearance of outliers in the data affects the computation of the mean of parameters, the algorithms based on centroids search such as K-means are not appropriate for our problem. Instead of centroid-based algorithms, DBSCAN and Isolation Forest (IF) [57] have been applied on the turn-by-turn data after harmonic analysis. Compared to the application of DBSCAN [58] better results could be achieved using IF algorithm. IF uses an ensemble of randomized decision trees averaging the path lengths, which represent the number of splits required to isolate a data point. Shorter paths are produced for anomalies. Due to the randomization and combination of several decision trees, the method performs better than single-model methods. Another advantage of IF is that the algorithm requires only the number of trees and the proportion of outliers in the data set (threshold for the decision function) as input parameter.

This method is fully integrated into optics measurements at LHC and has been successfully used during commission-



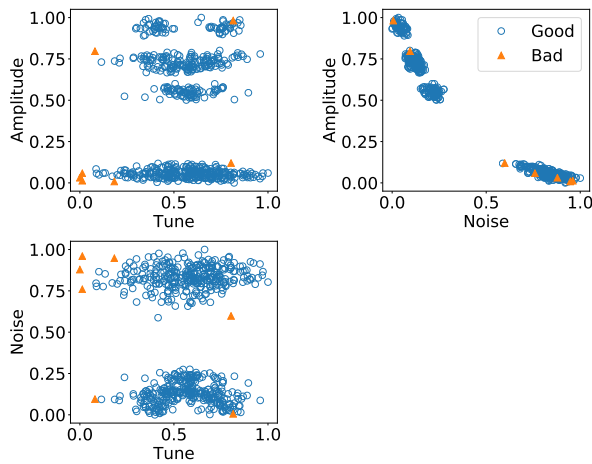


Figure 3: 2D-projection of 3D analysis with IF on arcs measurements of tune, amplitude and signal noise in horizontal plane. The data is scaled to the range [0, 1]. The triangular points correspond to BPMs marked as anomaly.

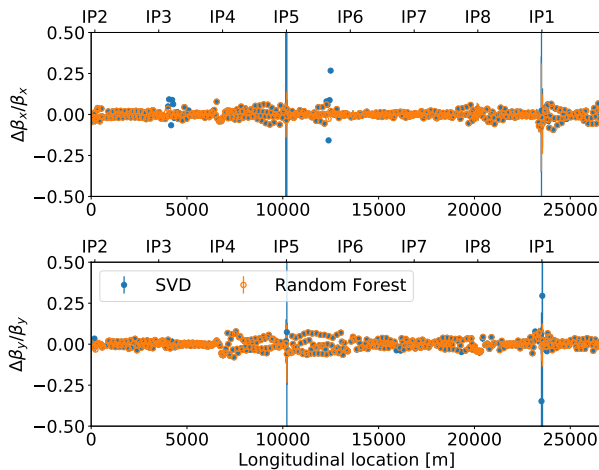


Figure 4: Beta-beating from the measurement cleaned with SVD before and after applying IF. IF decreased the number of unphysical outliers in the computed optics and significantly reduced the errorbars.

ing and machine developments under different optics settings in 2018. An illustration of results obtained during commissioning is presented in Fig. 4. The method can be further improved by introducing an adaptive decision function threshold based on corresponding normality score, that can be obtained for each sample during training process. The decision function can be then adapted depending on the numbers of BPMs lying under the threshold.

## CONCLUSION

The understanding of the concepts in the field of ML and AI provides new opportunities for incorporating this discipline into accelerator technology, however the benefits in comparison to traditional tools and the efficiency of introduced ML and AI based methods need careful evaluation.

ML is well known for surpassing human performance in some specific tasks such fraud detection, forecasting of market trends and risks, online recommendations, recognition of voice and images and in general in discovering correlations in large scale datasets. Most of the named tasks can find analogies in beam control and diagnostics. For example, anomaly detection methods applied for fraud detection can be used to detect defects in the instrumentation and forecasting techniques can be transferred to predict beam behavior during operation.

Typical characteristic of supervised ML tasks is the ability to deal with large amount of structured data. This leads to the conclusion that the implementation of supervised ML solutions requires large existing training datasets or development of appropriate data acquisition tools in order to provide the data in "machine-understandable" format, which is not necessarily available out-of-the-box since the traditional control systems usually imply human intervention. The effort that has to be put on automation such as building data acquisition infrastructure and training of complex models might be more costly and resources expensive than traditional methods. On the other hand, automation of some particular systems using ML as it was done for collimators alignment at LHC [42] is very effective and can save operational resources. Diagnostics of beam losses and beam optics corrections can also benefit from ML as it was shown in [41] and [58], since these methods rely on already existing data from dedicated measurements.

The ability of unsupervised learning to discover unknown patterns in the data is useful especially for anomaly detection tasks such as detection of instrumentation defects, e.g. using clustering for faulty BPMs signal. Such methods can be performed directly without training in arbitrary accelerator systems.

## Further Applications

Besides presented applications, another field where we can potentially benefit from ML are highly complex simulation tasks which demand large computational power or even are not solvable using the available resources. The predictive power of ANNs could offer an alternative solution for problems such as dynamic aperture computation avoiding costly turn-by-turn simulations. Moreover, different ML methods can be potentially used for maintenance of accelerators, such that system defects can be predicted based on deviations from expected performance and required intervention can be performed prior to actual failures [59]. Beam lifetime optimization is another task where ML techniques can be potentially applied [60]. Such methods as decision trees and autoencoders appear suitable for analysis of beam parameters correlations and their importance for beam lifetime prediction and maximization.

## REFERENCES

- [1] J. W. Flanagan *et al.*, “A simple real-time beam tuning program for the KEKB injector Linac”, in *Proceedings of the 1998 International Computational Accelerator Physics Conference*, Monterey, CA, USA, KEK Report No. 98-208, 1999.
- [2] B. Dalena *et al.*, “Beam delivery system tuning and luminosity monitoring in the Compact Linear Collider”, *Phys. Rev. ST Accel. Beams*, vol. 15, p. 051006, 2012. doi:10.1103/PhysRevSTAB.15.051006
- [3] N. J. Walker, J. Irwin, and M. Woodley, “Global tuning knobs for the SLC final focus”, SLAC, CA, USA, Rep. SLAC-PUB-6207, 1993.
- [4] Y. Funakoshi *et al.*, “Performance of KEKB with crab cavities”, in *Proceedings of the 11th European Particle Accelerator Conference*, Genoa, Italy, 2008, paper WEXG01, pp. 1893–1897.
- [5] W. Fischer, J. Beebe-Wang, Y. Luo, S. Nemesure, and L. K. Rajulapati, “RHIC proton beam lifetime increase with 10- and 12-pole correctors”, in *Proceedings of IPAC’10*, Kyoto, Japan, May 2010, paper THPE099, pp. 4752–4754.
- [6] M. Aiba, M. Boege, N. Milas, and A. Streun, “Ultra low vertical emittance at SLS through systematic and random optimization”, *Nucl. Instrum. Methods Phys. Res., Sect. A*, vol. 694, pp. 133–139, 2012. doi:10.1016/j.nima.2012.08.012
- [7] X. Huang, J. Corbett, J. Safranek, and J. Wu, “An algorithm for online optimization of accelerators”, *Nucl. Instrum. Methods Phys. Res., Sect. A*, vol. 726, pp. 77–83, 2013. doi:10.1016/j.nima.2013.05.046
- [8] K. Tian, J. Safranek, and Y. Yan, “Machine based optimization using genetic algorithms in a storage ring”, *Phys. Rev. ST Accel. Beams*, vol. 17, p. 020703, 2014. doi:10.1103/PhysRevSTAB.17.020703
- [9] L. Yang, D. Robin, F. Sannibale, C. Steier, and W. Wan, “Global optimization of an accelerator lattice using multi-objective genetic algorithms”, *Nucl. Instrum. Methods Phys. Res., Sect. A*, vol. 609, no. 1, pp. 50–57, 2009. doi:10.1016/j.nima.2009.08.027
- [10] Y. Li, W. Cheng, L. H. Yu, and R. Rainer, “Genetic algorithm enhanced by machine learning in dynamic aperture optimization”, *Phys. Rev. ST Accel. Beams*, vol. 21, p. 054601, 2018. doi:10.1103/PhysRevAccelBeams.21.054601
- [11] T. Mitchell, *Machine Learning*, 1st ed., New York, USA: McGraw-Hill, Inc., 1997.
- [12] D. Rumelhart, G. Hinton, and R. Williams, “Learning representations by back-propagating errors”, *Nature*, vol. 323, pp. 533–536, 1986. doi:10.1038/323533a0
- [13] D. Kingma and J. Ba, “Adam: a method for stochastic optimization”, *arXiv:1412.6980*, 2014.
- [14] J. Duchi, E. Hazan, and Y. Singer, “Adaptive subgradient methods for online learning and stochastic optimization”, *Journal of Machine Learning Research*, vol. 12, pp. 2121–2159, 2010.
- [15] Y. Bengio, Y. LeCun, and G. Hinton, “Deep Learning”, *Nature*, vol. 521, pp. 436–444, 2015. doi:10.1038/nature14539
- [16] S. Haykin, *Neural Networks: A Comprehensive Foundation*, 2nd ed., NJ, USA: Prentice Hall PTR Upper Saddle River, 1998.
- [17] J. Schmidhuber, “Deep learning in neural networks: An overview”, *Neural Networks*, vol. 61, pp. 85–117, 2015. doi:10.1016/j.neunet.2014.09.003
- [18] K. G. Vamvoudakis, F. L. Lewis, and Shuzhi Sam Ge, “Neural Networks in Feedback Control Systems”, in *Mechanical Engineer’s Handbook*, New York, USA: John Wiley, 2015. doi:10.1002/9781118985960.meh223
- [19] A. L. Edelen, S. G. Biedron, B. E. Chase, D. Edstrom, S. V. Milton, and P. Stabile, “Neural Networks for Modeling and Control of Particle Accelerators”, *IEEE Transaction of Nuclear Science*, vol. 63, no. 2, pp. 878–897, 2016. doi:10.1109/TNS.2016.2543203
- [20] O. Maimon and L. Rokach, *Data Mining and Knowledge Discovery Handbook*, Secaucus, NJ, USA: Springer-Verlag New York, Inc., 2005.
- [21] L. Breiman, J. H. Friedman, R. A. Olshen, and C. J. Stone, “Classification and Regression Trees”, in *Statistics/Probability Series*, Belmont, USA: Wadsworth Publishing Company, 1984.
- [22] T.G. Dietterich, “Ensemble Methods in Machine Learning”, in *Proceedings of the First International Workshop on Multiple Classifier Systems*, Cagliari, Italy, 2000, pp. 1–15. doi:10.1007/3-540-45014-9
- [23] T. Hastie, R. Tibshirani, and J. Friedman, “The Elements of Statistical Learning”, in *Springer Series in Statistics*, New York, USA: Springer New York Inc. 2001. doi:10.1007/978-0-387-21606-5
- [24] A. K. Jain, M. N. Murty, and P. J. Flynn, “Data clustering: a review”, *ACM computing surveys (CSUR)*, vol. 31, no. 3, pp. 264–323, 1999. doi:10.1145/331499.331504
- [25] S. P. Lloyd, “Least squares quantization in PCM”, *IEEE Transactions on Information Theory*, vol. 28, no. 2, pp. 129–137, 1982. doi:10.1109/TIT.1982.1056489
- [26] M. Ester, H. Kriegel, J. Sander, and X. Xu, “A density-based algorithm for discovering clusters in large spatial databases with noise”, in *Proceedings of the Second International Conference on Knowledge Discovery and Data Mining, KDD’96*, Portland, Oregon, USA, Aug. 1996, pp. 226–231.
- [27] S. Chatterjee, A. Iyer, S. Avva, A. Kollara, and M. Sankarababu, “Convolutional Neural Networks In Classifying Cancer Through DNA Methylation”, *arXiv:1807.09617*, 2018.
- [28] M. Vidyasagar, “Machine learning methods in the computational biology of cancer”, in *Proceedings of the Royal Society A*, vol. 470, no. 2167, 2014. doi:10.1098/rspa.2014.0081
- [29] O. Hegazy, O. S. Soliman, and M. A. Salam, “A Machine Learning Model for Stock Market Prediction”, *International Journal of Computer Science and Telecommunications*, vol. 4, no. 12, pp. 17–23, 2013.
- [30] S. Hara, T. Ono, R. Okamoto, T. Washio, and S. Takeuchi, “Anomaly detection in reconstructed quantum states using a machine-learning technique”, *Physical Review A*, vol. 89, no. 2, p. 022104, 2014. doi:10.1103/PhysRevA.89.022104

- [31] P. Graff *et al.*, “SkyNet: an efficient and robust neural network training tool for machine learning in astronomy”, *Monthly Notices of the Royal Astronomical Society*, vol. 441, no. 2, pp. 1741–1759, 2014. doi:10.1093/mnras/stu642
- [32] A. Aurisano *et al.*, “A convolutional neural network neutrino event classifier”, *Journal of Instrumentation*, vol. 11, no. 9, p. P09001, 2016. doi:10.1088/1748-0221/11/09/P09001
- [33] A. Sanchez-Gonzalez *et al.*, “Machine learning applied to single-shot x-ray diagnostics in an XFEL”, *Nature Communications* vol. 8, p. 15461, 2017. doi:10.1038/ncomms15461
- [34] A.L. Edelen, S. Biedron, S.V. Milton, and P.J.M. van der Slot, “Using Neural Network Control Policies for rapid switching between beam parameters in an FEL”, in *Proceedings of the 38th International Free Electron Laser Conference*, Santa Fe, NM, USA, Feb. 2017, pp. 488–491. doi:10.18429/JACoW-FEL2017-WEP031
- [35] Y. LeCun, K. Kavukcuoglu, and C. Farabet, “Convolutional networks and applications in vision”, in *Proc. International Symposium on Circuits and Systems (ISCAS’10)*, Paris, France, Jun. 2010, pp. 253–256. doi:10.1109/ISCAS.2010.5537907
- [36] A.L. Edelen *et al.*, “First steps toward incorporating image based diagnostics into particle accelerator control systems using convolutional neural networks”, in *Proc. NAPAC2016*, Chicago, IL, USA, 2016, pp. 390–393. doi:10.18429/JACoW-NAPAC2016-TUP0A51
- [37] A. Scheinker, “Model independent beam tuning”, in *Proceedings IPAC’13*, Shanghai, China, May 2013, paper TUPWA068, pp. 1862–1864.
- [38] A. Scheinker *et al.*, “Bounded extremum seeking with discontinuous dithers”, *Automatica*, vol. 69, pp. 250–257, 2016. doi:10.1016/j.automatica.2016.02.023
- [39] D. Vilsmeier, M. Sapinski, R. Singh, and J. W. Storey, “Reconstructing space-charge distorted IPM profiles with Machine Learning algorithms”, in *Proceedings IPAC’18*, Vancouver, Canada, Jul. 2018, pp. 2099–2102. doi:10.18429/JACoW-IPAC2018-WEPAK008
- [40] J.H. Friedman, “Greedy function approximation: a gradient boosting machine”, *Ann. Statist.*, vol. 29, no. 5, pp. 1189–1232, 2001. doi:10.1214/aos/1013203451
- [41] G. Valentino and B. Salvachua, “Machine learning applied at the LHC for beam loss pattern classification”, in *Proceedings IPAC’18*, Vancouver, Canada, Jun. 2018, pp. 2020–2023. doi:10.18429/JACoW-IPAC2018-WEPAF078
- [42] G. Azzopardi *et al.*, “Automatic angular alignment of the LHC collimators”, in *Proceedings of ICALEPCS’17*, Barcelona, Spain, Jan. 2017, pp. 928–933. doi:10.18429/JACoW-ICALEPCS2017-TUPHA204
- [43] E. Bozoki and A. Friedman, “Neural network technique for orbit correction in accelerators/storage rings”, *AIP Conference Proceedings*, vol. 315, pp. 103–110, 1994. doi:10.1063/1.46759
- [44] E. Meier, Y.R.E. Tan, and G. S. LeBlanc, “Orbit correction studies using neural networks”, in *Proceedings of IPAC’12*, New Orleans, Louisiana, USA, May 2012, paper WEP0057, pp. 2837–2839.
- [45] Y. Kijima, M. Mizota, K. Yoshida, and K. Suzuki, “A beam diagnostic system for accelerator using neural networks”, in *Proceedings of 3rd European Particle Accelerator Conference*, Berlin, Germany, Mar. 1992, pp. 1155–1157.
- [46] E. Fol, “Evaluation of machine learning methods for LHC optics measurements and corrections software”, Master thesis, CERN, Geneva, Switzerland, Rep. CERN-THESIS-2017-336, 2017.
- [47] R. Rubinstein, M. Zibulevsky, and M. Elad, “Efficient implementation of the K-SVD algorithm using batch orthogonal matching pursuit”, Technion, Computer Science Department, Rep. CS-2008-08-2008, 2008.
- [48] L. Breiman, “Random forests”, *Machine Learning*, vol. 45, no. 1, pp. 5–32, 2001. doi:10.1023/A:1010933404324
- [49] T. Persson, F. Carlier, J. Coello de Portugal, A. Garcia-Tabares Valdivieso, A. Langner, E.H. Maclean, L. Malina, P. Skowronski, B. Salvant, R. Tomas, and A.C. Garcia Bonilla, “LHC optics commissioning: a journey towards 1% optics control”, *Phys. Rev. Accel. Beams*, vol. 20, p. 061002, 2017. doi:10.1103/PhysRevAccelBeams.20.061002
- [50] R. Tomás, M. Aiba, A. Franchi, and U. Iriso, “Review of linear optics measurement and correction for charged particle accelerators”, *Phys. Rev. Accel. Beams*, vol. 20, p. 054801, 2017. doi:10.1103/PhysRevAccelBeams.20.054801
- [51] J. J. Lim, R. Salakhutdinov, and A. Torralba, “Transfer learning by borrowing examples for multiclass object detection”, in *Proceedings of the 24th International Conference on Neural Information Processing Systems*, Granada, Spain, Dec. 2011, pp. 118–126.
- [52] S. J. Pang and Q. Yang, “A survey on transfer learning”, *IEEE Transactions on Knowledge and Data Engineering*, vol. 22, no. 10, pp. 1345–1359, 2010. doi:10.1109/TKDE.2009.191
- [53] G.E. Hinton and R.R. Salakhutdinov, “Reducing the dimensionality of data with neural networks”, *Science*, vol. 313, no. 5786, pp. 504–507, 2006. doi:10.1126/science.1127647
- [54] J. W. Leea, S. Chob, and M. Yoon, “A neural-network method for diagnosing beam-position monitors in storage ring”, *Nucl. Instrum. Methods Phys. Res., Sect. A*, vol. 402, no. 1, pp. 14–20, 1998. doi:10.1016/S0168-9002(97)01063-2
- [55] E. Fol, “Detection of faulty beam position monitors”, presented at *ICFA Beam Dynamics Mini-Workshop: Machine Learning Applications for Particle Accelerators*, Menlo Park, CA, USA, 2018, unpublished.
- [56] R. Calaga and R. Tomás, “Statistical analysis of RHIC beam position monitors performance”, *Phys. Rev. ST Accel. Beams*, vol. 7, p. 042801, 2004. doi:10.1103/PhysRevSTAB.7.042801
- [57] F. Liu, K.M. Ting, and Z. Zhou, “Isolation forest”, *Proceedings of the 2008 Eighth IEEE International Conference on Data Mining*, Pisa, Italy, 2008, pp. 413–422. doi:10.1109/ICDM.2008.17
- [58] E. Fol, F. Carlier, J. Coello de Portugal, A. Garcia-Tabares Valdivieso, and R. Tomás, “Machine learning methods for optics measurements and corrections at LHC”, in *Proceedings IPAC’18*, Vancouver, Canada, May 2018, pp. 1967–1970. doi:10.18429/JACoW-IPAC2018-WEPAF062

- [59] M. Hebbel, private communication, Jul. 2018.
- [60] L. Coyle, “Machine learning techniques applied to life-time optimization in LHC-2016 data set analysis”, <https://indico.cern.ch/event/738306/>.



# OPTICS MEASUREMENTS IN STORAGE RINGS: SIMULTANEOUS 3-DIMENSIONAL BEAM EXCITATION AND NOVEL HARMONIC ANALYSIS

L. Malina<sup>1</sup>, J. Coello de Portugal, J. Dilly, P. K. Skowroński and R. Tomás,  
CERN, Geneva 23, Switzerland

<sup>1</sup> also at University of Oslo, 0316 Oslo, Norway

## Abstract

Optics measurements in storage rings employ turn-by-turn data of transversely excited beams. Chromatic parameters need measurements to be repeated at different beam energies, which is time-consuming. We present an optics measurement method based on adiabatic simultaneous 3-dimensional beam excitation, where no repetition at different energies is needed. In the LHC, the method has been successfully demonstrated utilising AC-dipoles combined with RF frequency modulation. It allows measuring the linear optics parameters and chromatic properties at the same time without resolution deterioration. We also present a new accurate harmonic analysis algorithm that exploits the noise cleaning based on singular value decomposition to compress the input data. In the LHC, this sped up harmonic analysis by a factor up to 300. These methods are becoming a "push the button" operational tool to measure the optics.

## INTRODUCTION

One of the ways to perform optics measurements in a storage ring is to excite the beam and acquire turn-by-turn (TbT) beam position monitor (BPM) data showing the coherent betatron motion [1]. The beam is excited using either kickers or AC-dipoles [2]. AC-dipoles can ramp up and down the oscillation adiabatically [3], i.e. without any measurable emittance growth. Typical optics measurements consist of several excitations at different beam energies, in order to measure the linear optics as well as the chromatic properties.

Based on the experience with optics measurements in the LHC, there are two main time-consuming tasks during the measurements. First, the human intervention to change beam energy by adjusting the RF-frequency and check other beam parameters, which usually takes up to 15 minutes. Second, the AC-dipole needs about 70 seconds to cool down after every single excitation. Addition of longitudinal excitation [4] can be used to speed up the measurement when performed adiabatically.

In the analysis process, TbT BPM data is first cleaned of noise using methods [5–7] based on Singular Value Decomposition (SVD). The SVD of a matrix  $\mathbf{A}$  is given by:  $\mathbf{A} = \mathbf{U}\mathbf{S}\mathbf{V}^T$ . Cleaning keeps only the modes corresponding to the largest singular values, in this way it improves precision and accuracy. It also reduces the amount of information without changing the size of the data, typically about a factor 40 larger than the reduced  $\mathbf{U}$ ,  $\mathbf{S}$  and  $\mathbf{V}^T$  matrices.

Later the harmonic analysis is performed on cleaned TbT data BPM by BPM (further referred to as "bpm" method). The Discrete Fourier Transform (DFT) is obtained performing Fast Fourier Transform (FFT). The refined frequency of the strongest signal obtained from FFT is found using Jacobsen frequency interpolation with bias correction [8] based on 3 DFT peaks. The refined complex amplitude of the signal is obtained as an inner product of a unit signal corresponding to the refined frequency with the TbT data. This signal is subtracted from the TbT data and the whole procedure starting with FFT is repeated [9], typically 300 times in the LHC. As a result the TbT data is approximated by the sum of the 300 strongest harmonics.

The framework presented here implements new methods to also increase the speed of harmonic analysis by its combination with precedent data cleaning.

## ADIABATIC BEAM EXCITATION

In the LHC, the beam is excited using AC-dipoles in both transverse directions simultaneously. This gives the BPM reading as shown in Figure 1, for one of the planes. Once the beam energy is changed the measurement is repeated. This time-consuming process can be avoided by fast modulation of RF-frequency. RF-frequency change is normally used to adjust the beam energy, or it is modulated in order to measure the chromaticity. However, the frequency of the modulation for the chromaticity measurement is typically about 0.1 Hz, such that the Base-Band Tune (BBQ) system [10] can measure the tune.

We employ the RF-modulation at its maximal frequency of 5 Hz, which is still far from the natural synchrotron frequency of about 20 Hz. The RF-frequency modulation is ramped up before the actual AC-dipole excitation starts. Three periods of adiabatic energy variation (forced synchrotron oscillation) fit within acquired 6600 turns (with LHC's revolution frequency of 11.3 kHz). A sample of TbT reading at a dispersive BPM is shown in Figure 2.

The adiabaticity of this mode of excitation has been experimentally demonstrated in the LHC, as it can be seen from the beam size measurement from Beam Synchrotron Radiation Telescope (BSRT) during the 3-dimensional (3D) excitations shown in Figure 3.

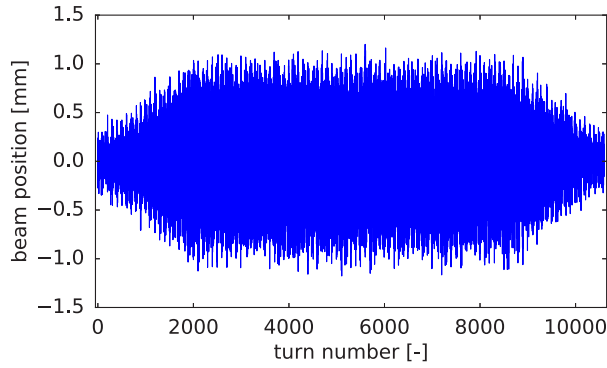


Figure 1: Sample BPM TbT data excited by an AC-dipole performing driven coherent betatron oscillation. Note the ramp-up and ramp-down of the oscillation amplitude, which is important to avoid emittance growth [3] (in hadron machines).

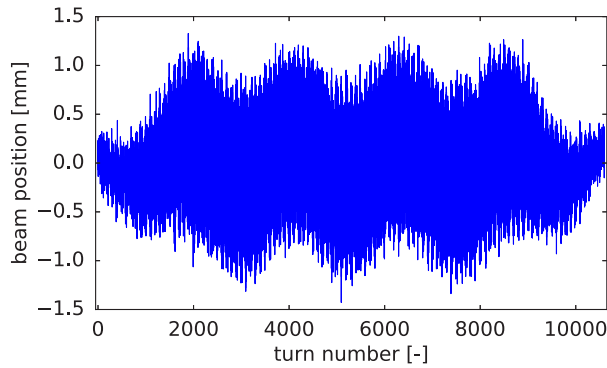


Figure 2: Sample BPM TbT data at a dispersive BPM excited by an AC-dipole when the frequency of the RF system has been simultaneously modulated. The beam performs driven coherent betatron oscillations and the beam energy is adiabatically varied.

## HARMONIC ANALYSIS OF DECOMPOSED DATA

As SVD and refined harmonic analysis are both linear operations, they can be combined. The cleaned TbT data can be reconstructed from SVD matrices elements:

$$x_{jn} = \sum_{l=0}^{N_{modes}-1} u_{jl} s_{ll} v_{nl}, \quad (1)$$

where  $j$  and  $n$  are the BPM index ( $j < N_{BPM}$ ) and the turn number ( $n < N$ ).  $N_{modes}$  stands for number of SVD modes used. The complex coefficients  $X_{ja}$  corresponding to an arbitrary frequency  $a/N$  are given by:

$$X_{ja} = \sum_{n=0}^{N-1} \sum_{l=0}^{N_{modes}-1} u_{jl} s_{ll} v_{nl} e^{i2\pi na/N} = \quad (2)$$

$$= \sum_{l=0}^{N_{modes}-1} u_{jl} \sum_{n=0}^{N-1} s_{ll} v_{nl} e^{i2\pi na/N} = \sum_{l=0}^{N_{modes}-1} u_{jl} X_{la}, \quad (3)$$

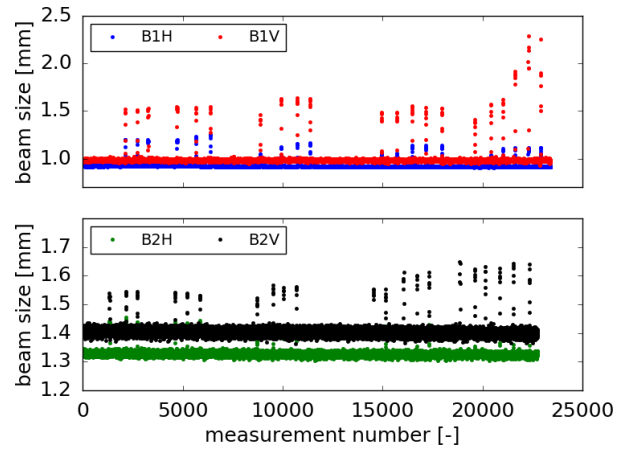


Figure 3: The beam size measurement using BSRT during the 3D excitations, the spikes refer to AC-dipole excitations. No beam size growth is observed after more than 20 3D excitations.

the second summation of Eq. (3) represents the complex coefficient corresponding to frequency  $a/N$  in the  $l^{th}$  row of  $\mathbf{SV}^T$ . Putting all this together, we obtain complex coefficients corresponding to frequency  $a/N$  in cleaned TbT data from all BPMs as a linear combination of complex coefficients corresponding to the same frequency in the rows of  $\mathbf{SV}^T$  with the multiplication factor being the rows of  $\mathbf{U}$ . Two algorithms were developed, in order to identify the frequencies corresponding to the largest harmonics. The aforementioned harmonic analysis is performed on:

- the sum  $\sum_{l=0}^{N_{modes}-1} s_{ll} v_{nl}$  of the rows of reduced  $\mathbf{SV}^T$  giving a single set of frequencies, hereafter referred to as "fast" method
- each of the rows of reduced  $\mathbf{SV}^T$ , giving a union of frequencies, found for every row, hereafter referred to as "svd" method

The complex coefficients, corresponding to resulting frequencies, are calculated for each of the rows of reduced  $\mathbf{SV}^T$  matrix by the inner product in the time domain (last sum in Equation (3)). At this point, the vectors in the frequency domain are no longer orthogonal. The perturbation of the orthogonality of the two arbitrary vectors (in the frequency domain) is influenced by two factors:

- the difference (in the time domain) between the vector under study and the vector the harmonic analysis was performed on
- the spectral response of a windowing function, that can be used to filter the signal in the time domain

A rectangular window, which does not change the signal and has the best frequency resolution, is used in the following. On the other hand, in a case of the rectangular window spectral leakage is more pronounced compared to other windowing functions [11], which should be kept in mind.

The harmonic analysis performed on decomposed TbT BPM data is faster than the "bpm" method by up to a factor of  $N_{BPM}/N_{modes}$  using the "svd" method and up to a factor of  $N_{BPM}$  in the "fast" method. Computational speed is essential for efficient beam operation, for example, in automatic coupling correction [12], where these methods are used. Harmonic analysis by "fast" method of one set of LHC data set takes about 2 seconds in a single thread compared to about 18 seconds in 32 threads in the "bpm" method.

## ACCURACY OF HARMONIC ANALYSIS

The accuracy of the harmonic analysis performed on decomposed TbT data is studied in this section. TbT data of the LHC injection optics was simulated. A realistic noise of about 8 % amplitude compared to coherent betatron motion at focusing quadrupoles was added. Results of the aforementioned analysis corresponding to a given spectral line consist of its frequency  $\in (0, 1)$ , initial phase in units of  $2\pi$  and its amplitude. The accuracy is estimated by the root mean square of the difference to the value defined in a simulation in a set of all BPMs. The two methods ("svd" and "fast") are compared to the original harmonic analysis the "bpm" method. The betatron tune is found in the spectra from all three methods.

Both "svd" and "fast" methods have accuracies in frequency and phase comparable or slightly better compared to the "bpm" method. An exception is the "svd" analysis performed on a low number of turns, where it shows less accurate results. The differences in relative amplitude accuracy are negligible. Generally, "svd" and "fast" methods seem to be better suited for a larger number of turns and larger noise levels. For a small number of turns or small noise levels, the situation is the opposite. Additionally, a weaker spectral line with about 14 % amplitude at focusing BPMs and 0.01 away in frequency from the betatron tune was investigated. Here, the methods perform all similar in terms of frequency accuracy. In terms of its phase accuracy, the "bpm" method is better than the other two. The amplitude accuracy shows similar behaviour as the phase accuracy. For more details, see [13].

## CHROMATIC PROPERTIES ANALYSIS

The largest advantage of simultaneous 3D excitation is that the chromatic properties, such as normalised dispersion  $D_x/\sqrt{\beta}$  [14] or the W-function [15] can be a ratio of certain spectral lines amplitudes. The following notation of the driven spectral lines has been adopted, for example  $H(2,0,1)$  being at frequency  $2 \cdot Q_x^F + 0 \cdot Q_y^F + 1 \cdot Q_s^F$  in the horizontal plane ( $Q_{x,y,s}^F$  denotes fractional forced tunes).

### Relative Beam Momentum Change

Under the assumption of linear dispersion and of beam oscillation around stable orbit (closed orbit), the amplitude of relative beam momentum variation  $\Delta p_{amp}$  is measured. The closed orbit change in the arc BPMs (with larger dispersion) in the horizontal plane is used at the extremes of beam

momentum variation. The extremes are identified from frequency and phase of synchrotron spectral line  $H(0,0,1)$ , i.e. where  $|\cos(Q_s n_{turns} + \phi_s)| > 0.9$ . A model dispersion is assumed in the calculation of relative beam momentum variation. For measurements in the LHC a variation of  $10^{-4}$  is utilized.

### Normalised Dispersion

Using the above-mentioned spectral line notation the normalised dispersion [14] is proportional to the ratio of spectral line amplitudes corresponding to dispersion and  $\sqrt{\beta}$ :

$$|D/\sqrt{\beta}| = C \frac{H(0,0,1)}{H(1,0,0)}, \quad (4)$$

where  $C$  is a global multiplication factor (related to excitation amplitudes) obtained as a ratio of average measured and average model normalised dispersions in the arc BPMs:

$$C = \frac{\sum_{arcBPMs} \frac{H(0,0,1)}{H(1,0,0)}}{\sum_{arcBPMs} \left| \left( \frac{D}{\sqrt{\beta}} \right)_{model} \right|}, \quad (5)$$

As the spectral line amplitude is always positive, we need to compare the phase of  $H(0,0,1)$  at the given BPM with the average phase in the arc BPMs, i.e. if the phases are opposite the dispersion is negative.

## OPTICS MEASUREMENT PRECISION

In this section, we compare the precision of the normalised dispersion and the linear optics measurements [16] using 3D and 2D driven beam excitations. The analysis of linear optics quantities is the same as in the 2D case, i.e. N-BPM method [17, 18] is applied. In terms of driven motion, the TbT BPM data differs only in presence of spectral lines related to adiabatic energy variation. The normalised dispersion measurements in high  $\beta$  optics at injection energy (with fractional natural tunes of 0.305 and 0.315 in the horizontal and the vertical plane) were performed by the two methods, one right after the other. Their comparison is shown in Figure 4. In the 3D driven excitation based measurement, TbT data from 6 acquisitions are combined, while 11 acquisitions are combined in 2D case. The measurement error distributions are shown in Figure 5 including the mean errors. The residuals scaled by the errors of measurements combined in quadrature are shown in Figure 6. The mean value of such distribution close to zero demonstrates no systematic bias. The standard deviation shows the agreement within the measurement errors (i.e. smaller than 1). The two methods are in excellent agreement.

The agreement of linear optics quantities, measured the same way (except for normalised dispersion) using both types of beam excitation is summarized in Table 1. As a drift of betatron tunes and coupling was observed during the measurement, the linear coupling is not included. However, the impact of tune drift on measured phase advances and  $\beta$ -functions is assumed to be negligible compared to measurement errors. No statistically significant bias, nor

Table 1: Comparison of Linear Optics Quantities Measured Using the 2D AC-Dipole Excitation With or Without RF-frequency Modulation at the Same Time

Quantity	Mean norm. residuals	Std norm. residuals	avg. error 3D / avg. error 2D
Horizontal phase advance	0.003	0.52	1.22
Vertical phase advance	-0.003	0.51	1.11
Horizontal $\beta$ -beating from phase	0.003	0.87	1.12
Vertical $\beta$ -beating from phase	0.019	0.76	1.04
Horizontal $\beta$ -beating from amplitude	0.049	0.95	0.98
Vertical $\beta$ -beating from amplitude	0.020	0.84	0.90
$\Delta D_x / \sqrt{\beta_x}$	0.006	0.42	0.75

precision loss were observed in any of the quantities (phase advances,  $\beta$ -functions from phase and from amplitude, and already mentioned normalised dispersion). However, slight differences in precision between the horizontal (dispersive) and the vertical planes are visible.

In ESRF [19] the transverse 2D kicks were performed, however, a residual synchrotron oscillation corresponding to a relative beam energy variation of  $5 \cdot 10^{-5}$  was visible in the data. The normalised dispersion can also be measured by the 3D method from the residual synchrotron motion of bunch centroids using transverse kicks only. The obtained normalised dispersion is only 4 times less precise, even though the amplitude of residual synchrotron motion is about 30 times smaller than relative beam energy changes of 0.16% applied for the standard measurement.

The RF-modulation seems to disturb neither the precision nor the accuracy of phase advances and  $\beta$ -functions.

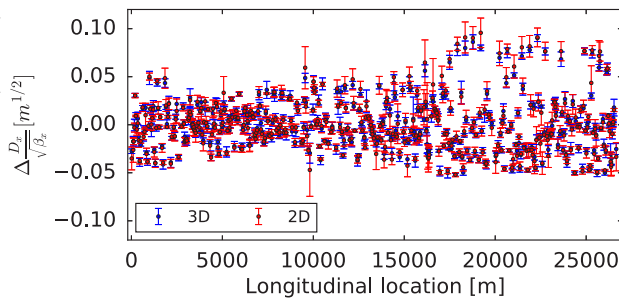


Figure 4: Comparison of LHC normalized dispersion difference to the LHC lattice model measured from TbT data using simultaneous 3D driven excitation (in blue) and 2D driven beam excitation at multiple beam energies (in red).

## CONCLUSIONS AND OUTLOOK

The optics measurement method based on simultaneous 3D beam excitation allows measuring linear beam optics quantities simultaneously with chromatic properties. The employed beam excitation does not deteriorate the beam quality. The precision of measured quantities is not deteriorated comparing to standard optics measurements based on 2D excitation. A new normalised dispersion measurement technique has been developed, demonstrating faster measurement (fewer beam excitations) with the same or better

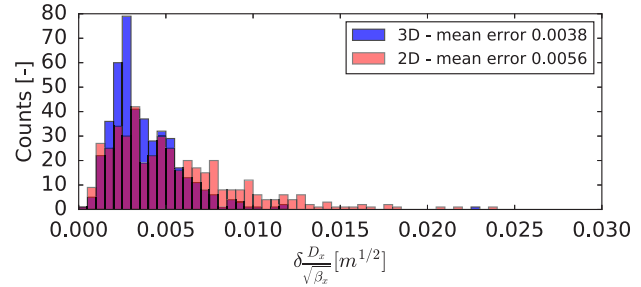


Figure 5: Distributions of the normalised dispersion measurement errors from (Figure 4) for both methods: 3D excitation (in blue) and 2D excitation (in red).

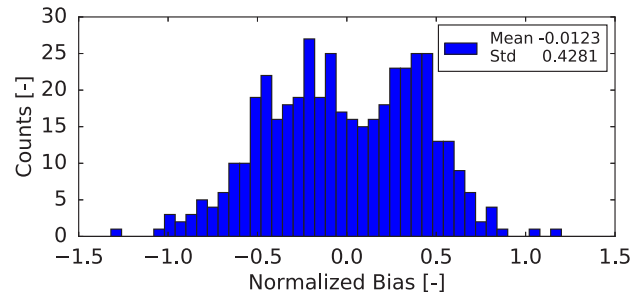


Figure 6: Distribution of differences between the two normalised dispersion measurements from (Figure 4), normalised by their errors combined in quadrature.

precision. This represents an important step towards fast online optics measurements and corrections. In cases where beam excitation is not a limiting factor, e.g. when a single beam excitation is used the analysis may become a bottleneck, in terms of speed. Tests with a transverse damper as an exciter are foreseen, since its repetition is not limited.

New techniques performing harmonic analysis directly on decomposed data instead of the recomposed data have been developed. When used in LHC, they are up to 300 times faster and are better suited for noisy data, compared to the standard method. The choice of a windowing function and the orthogonality perturbation is being studied to further improve the accuracy. Synchro-betatron lines observed in the beam frequency spectra after 3D excitation are also being studied with the aim to measure W-function or potentially chromatic coupling.



## REFERENCES

- [1] R. Tomás, M. Aiba, A. Franchi, and U. Iriso, “Review of linear optics measurement and correction for charged particle accelerators”, *Phys. Rev. Accel. Beams*, vol. 20, p. 054801, 2017.
- [2] M. Bai *et al.*, “Experimental test of coherent betatron resonance excitations”, *Phys. Rev. E* vol. 56, p. 6002, 1997.
- [3] R. Tomás, “Adiabaticity of the ramping process of an ac dipole”, *Phys. Rev. ST Accel. Beams*, vol. 8, p. 024401, 2005.
- [4] G. Rumolo and R. Tomás, “Decoherence of a longitudinally kicked beam with chromaticity”, *Nucl. Instr. Meth. A*, vol. 528, p. 670-676, 2004.
- [5] J. Irwin *et al.*, “Model-Independent Beam Dynamics Analysis”, *Phys. Rev. Letters* Vol. 82, p. 1684, 1999.
- [6] R. Calaga and R. Tomás, “Statistical Analysis of RHIC beam position monitors performance”, *Phys. Rev. ST Accel. Beams*, vol. 7, p. 042801, 2004.
- [7] X. Huang, S. Y. Lee, E. Prebys, and R. Tomlin, “Application of independent component analysis to Fermilab Booster”, *Phys. Rev. ST Accel. Beams*, vol. 8, p. 064001, 2005.
- [8] Ç. Candan, “A method For Fine Resolution Frequency Estimation From Three DFT Samples”, *IEEE Signal Process. Lett.*, vol. 18, p. 351-354, 2011.
- [9] J. Laskar, “Frequency analysis for multi-dimensional systems. Global dynamics and diffusion”, *Physica D* vol. 67, p. 257-281, 1993.
- [10] A. Boccardi, M. Gasior, R. Jones, P. Karlsson, and R. J. Steinhagen “First results from the LHC BBQ tune and chromaticity systems”, Rep. CERN-LHC-Performance-Note-007, 2009.
- [11] G. Heinzl, A. Rüdiger, and R. Schilling, “Spectrum and spectral density estimation by the Discrete Fourier transform (DFT), including a comprehensive list of window functions and some new flat-top windows”, <http://edoc.mpg.de/395068>, 2002.
- [12] T. Persson *et al.*, “Transverse coupling measurements with high intensity beams using driven oscillations”, in *Proc. IPAC’18*, Vancouver, Canada, May 2018, paper MOPMF047.
- [13] L. Malina *et al.*, “Performance optimization of turn-by-turn beam position monitor data harmonic analysis”, in *Proc. IPAC’18*, Vancouver, Canada, May 2018, paper THPAF045.
- [14] R. Calaga, R. Tomás, and F. Zimmermann, “BPM calibration independent LHC optics correction”, in *Proc. PAC’07*, Albuquerque, New Mexico, USA, Jun. 2007, paper THPAS091, pp. 3693-3695.
- [15] B. W. Montague. “Linear Optics for Improved Chromaticity Correction”, CERN, Geneva, Switzerland, Rep. CERN-LEP-NOTE-165, 1979.
- [16] T. Persson *et al.*, “LHC optics commissioning: A journey towards 1% optics control”, *Phys. Rev. Accel. Beams*, vol. 20, p. 061002, 2017.
- [17] A. Langner and R. Tomás, “Optics measurement algorithms and error analysis for the proton energy frontier”, *Phys. Rev. ST Accel. Beams*, vol. 18, p. 031002, 2015.
- [18] A. Wegscheider, A. Langner, R. Tomás, and A. Franchi, “Analytical N-beam position monitor method”, *Phys. Rev. ST Accel. Beams*, vol. 20, p. 111002, 2017.
- [19] L. Malina *et al.*, “Improving the precision of linear optics measurements based on turn-by-turn beam position monitor data after a pulsed excitation in lepton storage rings”, *Phys. Rev. Accel. Beams*, vol. 20, p. 082802, 2017.

# DEMONSTRATION OF A NEWLY DEVELOPED PULSE-BY-PULSE X-RAY BEAM POSITION MONITOR IN SPring-8\*

Hideki Aoyagi<sup>†</sup>, Yukito Furukawa, Sunao Takahashi, Atsuo Watanabe  
 Japan Synchrotron Radiation Research Institute (JASRI), Hyogo, Japan

## Abstract

A newly designed pulse-by-pulse X-ray beam position monitor (XBPM), which is photoemission type, has been demonstrated successfully in the SPring-8 synchrotron radiation beamline. Conventional XBPMs work in the direct current (DC) mode, because it is difficult to measure a beam position in the pulse mode under the severe heat load condition. The key point of the design is aiming at improving heat-resistance property without degradation of high frequency property. This monitor is equipped with microstripline structure for signal transmission line to achieve pulse-by-pulse beam position signal. A photocathode is titanium electrode that is sputtered on a diamond heat sink to achieve high heat resistance. We have manufactured the prototype, and demonstrated feasibility at the SPring-8 bending magnet beamline. As a result, we observed a unipolar single pulse with the pulse length of less than 1 ns FWHM and confirmed that it has pulse-by-pulses position sensitivity. Furthermore, this monitor can be also used in the DC mode with good stability and good resolution. The operational experience will be also presented.

## INTRODUCTION

Development of a pulse-by-pulse X-ray beam position monitor (XBPM) aiming at measuring every isolated pulses for insertion devise (ID) beamline of the synchrotron radiation facility SPring-8 is being advanced. Conventional XBPMs used widely are photoemission type, and blade-shaped tungsten is usually employed as a detector head to raise heat-resistance [1]. However, it is impossible to measure the beam position of every isolated pulses with the conventional XBPMs, because of long time constant of the current signal and ringing due to stray capacitance and impedance mismatch. Therefore, we tried to settle this problem by adopting polycrystalline diamond as a heat sink to improve the heat resistance, and downsized detector heads to reduce the stray capacitance [2]. In addition, the microstripline structure [3-6] is adopted in the vacuum chamber of the monitor to prevent attenuation and reflection of the unipolar single pulse.

## DESIGN AND MANUFACTURE

The pulse-by-pulse XBPM that we have been developing is photoemission type in the same way as the conventional XBPMs, and having four blade-shaped diamond heat sinks with titanium plated electrodes (detector heads)

in top/bottom and right/left near the beam axes to measure the beam position in horizontal and vertical directions. The detector heads are inclined by 1/20 against the beam axis to be irradiated mainly on the unilateral side of the blade. As a result, photoemission can be controlled efficiently with the applied voltage of the charge collecting electrodes (collectors).

Figure 1 (a) shows a photograph of diamond heatsinks mounted on the water-cooling base. According to the thermal finite element analysis [7, 8], the thermal contact conductance between the heat sink and the cooling holder needs to be  $>10^4 \text{ W}/(\text{m}^2 \cdot \text{K})$ . Therefore, indium foils of the 50 $\mu\text{m}$  thickness are inserted between them to improve the thermal contact conductance. Figure 1 (b) shows a photograph of a signal transmission line with microstripline structure, which is mounted on an ICF70 flange. According to the high frequency properties test, the time domain reflectometry using the pilot model of the detector head has been performed in advance. It was confirmed that the unipolar single pulse of sub-nanosecond can be obtained [7, 8].

Figure 2 shows a 3D image of the combination of the detector head (Fig. 1 (a)) and the microstripline structure (Fig. 1 (b)). The structure of the pulse-by-pulse XBPM is shown in Fig. 3. The shading mask is mounted directly on the upstream side of the 6-way cross-chamber to prevent the cooling base from irradiation. By arranging a pair of collectors on both sides of left and right of the detector heads, photoelectron emitted from the detector heads can be attracted or retarded according to the polarity of the collector. In the direct current (DC) mode operation, in the same way as the conventional XBPM, current signal can be stabilized by applying the voltage, which is usually +100 V. In the pulse-mode operation, the negative voltage is applied to retard the emission of low energy photoelectron that distort the pulse waveform.

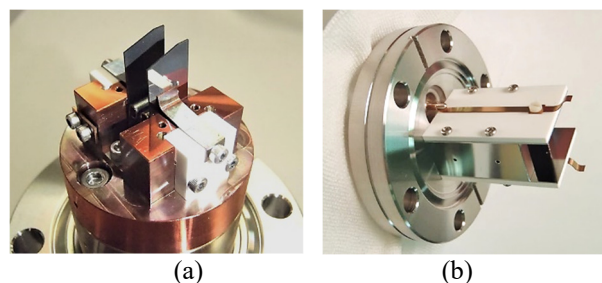


Figure 1: (a) Photograph of diamond heatsinks (20 mm  $\times$  8 mm  $\times$  0.3 mm). (b) Photograph of signal transmission lines with microstripline structure.

\* This work was partly supported by Japan Society for the Promotion of Science through a Grant-in-Aid for Scientific Research (c), No. 20416374 and No. 18K11943.

<sup>†</sup> aoyagi@spring8.or.jp

This monitor was installed in the Spring-8 bending magnet beamline BL02B1 frontend and performance tests have been carried out [9]. Among four signal cables, HUBER+SUHNER, SucoFeed 1/2", which has small attenuation, is used for one of the cables (UL, upper-left) to observe a pulse waveform. As for the three remaining cables, HUBER+SUHNER, S-04272B is used because the DC mode measurement is mainly performed.

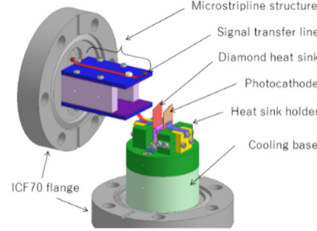


Figure 2: Combination of detector heads and microstripline structure.

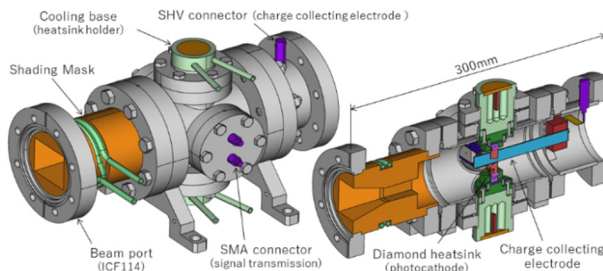


Figure 3: Structure of a monitor chamber.

## PERFORMANCE IN PULSE-MODE

### Observation of the Pulse Waveform

Figure 4 shows the typical pulse waveform of the current signal of this monitor. The filling pattern of the storage ring was "1/7 filling + 5 bunches" mode, and the isolated unipolar single pulse is observed. Oscilloscope is used for pulse waveform observation under the conditions of 4 GHz B. W., 20 GS/s, 100-time average. The pulse length with a full width at half maximum (FWHM) of 0.8 ns was obtained. As shown in Fig. 5, the various pulse waveforms were observed by changing the voltage of the collectors. The pulse waveform (height, length) greatly depends on polarity and height of the voltage. It can be seen that lowering the applied voltage decreases the pulse height and width. However, as the negative voltage is increased, the double peak at the top of the pulse waveform becomes obvious. The reason for this phenomenon cannot be explained by the resonance of the high frequency component in the vacuum vessel, because it would decays over time if it is a resonance. For the same reason it is not a reflection between the blade tip and the end of the microstripline structure. We can understand the cause of the double peak in the following way. The first peak is caused by photoelectrons reaching the collector with high energy enough not to be affected by the voltage of the collector. In addition, the second peak occurs because low-energy photoelectrons reach the collector with a little delay while being decelerated by the negative voltage of the collector.

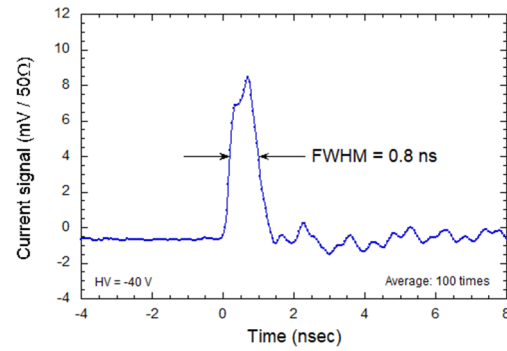


Figure 4: Pulse waveform of current signal.

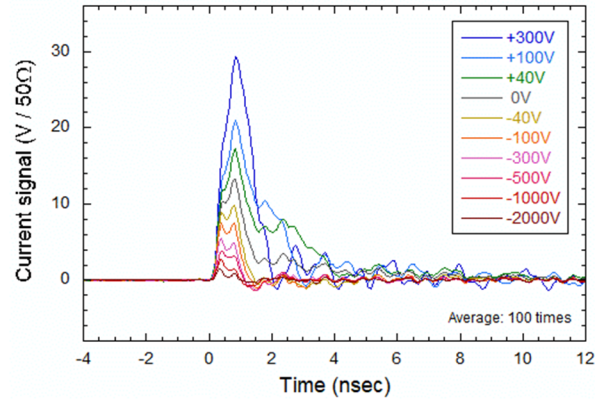


Figure 5: Various waveforms due to difference in applied voltage.

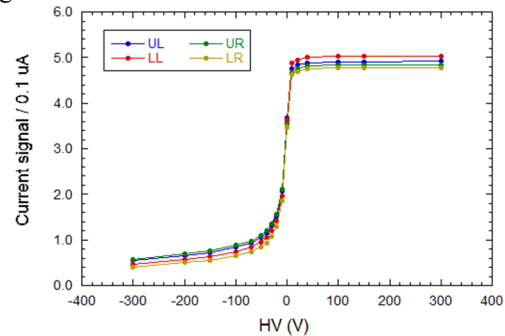
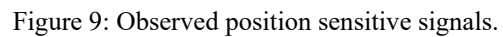
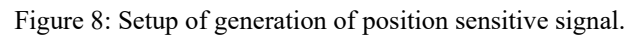


Figure 6: Applied voltage dependence of current signal.

Figure 6 shows the current signal with respect to the applied voltage of the collector using this monitor in the DC mode same as the conventional monitor. The current signal of each blade is greatly changed, especially around 0 V of the collector, and the retarding effect is obvious on the negative side. The reason for this is that the blades of this monitor have a slight inclination from parallel to the beam axis and only one side of the outside of the blades are irradiated so that the effective electric field is high. As a result, it is possible to suppress emission of slow electrons of several tens of volts, and to suppress increase in pulse length. When the voltage of the collector is +40 V or more, the current signal keeps a constant value. This is consistent with the phenomenon, as shown in Fig. 5, that the integrated current value becomes constant (the tail gets shorter while the pulse height gets higher), when the applied voltage is +40 V or more.

**TUOB03**  
**184**

the pulse height of the "difference" signal responds sensitively to the beam position.



### Position Sensitivity and Resolution

Figure 1 is a graph showing the current signal of four photodiodes (UL, UR, LL, LR) as a function of vertical position (mm). The left y-axis represents the current signal in microamperes ( $\mu A$ ), ranging from 0 to 10. The right y-axis represents the difference/sum of the signals, ranging from -1.0 to 1.0. The x-axis represents the vertical position in millimeters, ranging from -1.0 to 1.0. Four data series are plotted: UL (blue solid line with circles), UR (green solid line with circles), LL (orange solid line with circles), and LR (yellow solid line with circles). A red dashed line represents the sum of the signals (X (diff/sum)), and a blue dashed line represents the difference of the signals (y (diff/sum)). A black dashed line indicates the linear region, with a slope of  $Ax$  (1/slope) = 1.25.

Figure 10: Scan measurement in 0.2 mm step.



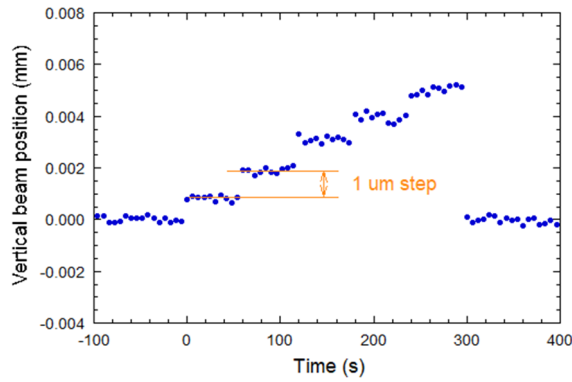


Figure 11: Scan measurement in 1  $\mu\text{m}$  step.

### Proportionarity of Current Signal

As shown in Fig. 12 (a), the sum signal of the four blades is proportional to the ring current of the storage ring. The result of calculation of "difference/sum" of the four blades is shown in Fig. 12 (b). For the vertical direction (y), as the ring current increases, the displacement of about 4  $\mu\text{m}$  is observed significantly. On the other hand, no movement in the horizontal direction (x) has been observed because the radiation from the bending magnet beamline spreads in the horizontal direction. This indicates that this monitor operates normally even in the DC mode when the ring current is 10 mA or more.

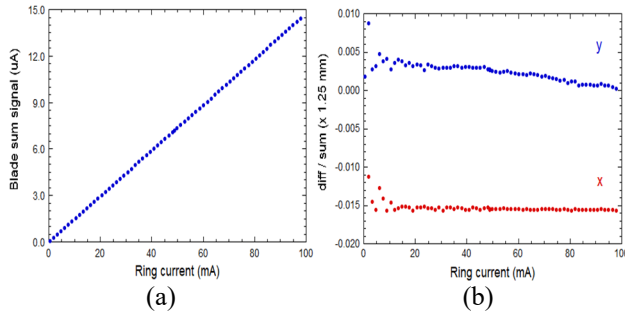


Figure 12: Proportionality in DC mode. (a) Blade sum signal vs ring current. (b) Difference/Sum vs ring current.

### Long-term Stability

This monitor can be regarded as having a pair of left and right XBPMs for vertical measurement of the same type equipped with two upper and lower blades. In principle, the calculated vertical positions should have the same behaviour in both the left and right XBPMs. Figure 13 shows a trend graph over two months of the vertical position from the left and right XBPMs and the difference of them. Each data was acquired with samplings every 6 seconds using an ADC with a time constant of about 1 s. The value of the difference drifted by about 0.2  $\mu\text{m}$  after short shut down of several days. In addition, the difference over the whole period of 0.14  $\mu\text{m}$  RMS was observed, which corresponds to the resolution of the XBPM. The stability is demonstrated to be very good for two months.

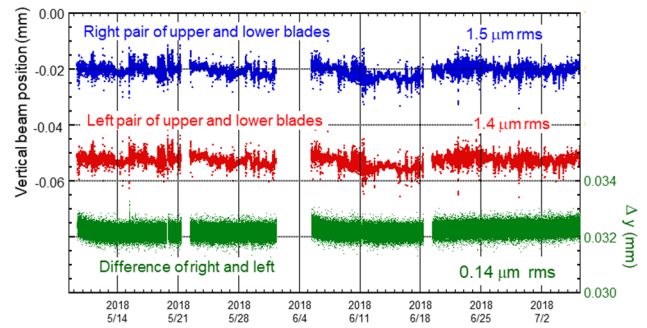


Figure 13: Stability in three months.

## CONCLUSION

The pulse-by-pulse XBPM has been newly designed and manufactured, and performance tests were carried out at the SPring-8 bending magnet beamline BL02B1 front end. A unipolar single pulse of 0.8 ns FWHM was obtained. We qualitatively understood the cause of the double peak of the pulse. The pulse height is proportional to the bunch current of the storage ring and the pulse waveform can be controlled by adjusting the voltage of the collector. We demonstrated that the position sensitive signal can be generated directly by combining reflected pulses at the open end and the short end of the stub cables. In the DC mode operation, the correction coefficient  $A_y$  of 1.25 was calculated from the vertical scan measurements and the resolution of 0.12  $\mu\text{m}$  RMS was obtained. In addition, good long-term stability was confirmed.

## ACKNOWLEDGEMENTS

The authors would like to thank T. Nakamura, K. Kobayashi, S. Kimura and H. Osawa of Japan Synchrotron Radiation Research Institute (JASRI) for the useful advice regarding high frequency analysis. The design and fabrication of the pulse-by-pulse XBPM has been achieved by getting cooperation of Vacuum and Optical Instruments (Shinku-Kogaku, Inc., Tokyo, Japan).

## REFERENCES

- [1] H. Aoyagi *et al.*, *Nucl. Instr. and Meth. A*, Vol. 467-468, pp. 252-255, 2001.
- [2] H. Aoyagi *et al.*, in *Proc. of the 12th Annual Meeting of PASJ*, 2015, pp.1224-1226.
- [3] H. Aoyagi *et al.*, in *Proc. of the 3rd Annual Meeting of PASJ*, 2016, pp.159-162.
- [4] H. Aoyagi *et al.*, in *AIP Conf. Proc.* 879, 2017, p1018.
- [5] H. Aoyagi *et al.*, in *Proc. of DIPAC'11*, 2011, paper MOPD91, pp. 260-262.
- [6] H. Aoyagi *et al.*, *Phys. Rev. ST Accel. Beams*, Vol. 16, p.032802, 2013.
- [7] H. Aoyagi *et al.*, in *Proc. of the 13th Annual Meeting of PASJ*, pp. 1118-1121, 2016.
- [8] H. Aoyagi *et al.*, in *Proc. of MEDSI'16*, paper WEPE10, pp.333-335.
- [9] H. Aoyagi *et al.*, in *Proc. of the 14th Annual Meeting of PASJ*, 2017, pp.192-196.

# A VERTICAL PHASE SPACE BEAM POSITION AND EMITTANCE MONITOR FOR SYNCHROTRON RADIATION

N. Samadi\*, University of Saskatchewan, S7N 5E5 Saskatoon, Canada  
 L. Dallin, Canadian Light Source, S7N 2V3 Saskatoon, Canada  
 D. Chapman<sup>1</sup>, Canadian Light Source, S7N 2V3 Saskatoon, Canada  
<sup>1</sup>also at University of Saskatchewan, S7N 5E5 Saskatoon, Canada

## Abstract

We report on a system (ps-BPM) that can measure the electron source position and angular motion at a single location in a synchrotron bend magnet beamline using a combination of a monochromator and an absorber with a K-edge to which the monochromator was tuned in energy. The vertical distribution of the beam was visualized with an imaging detector where horizontally one part of the beam was with the absorber and the other part with no absorber. The small range of angles from the source onto the monochromator crystals creates an energy range that allows part of the beam to be below the K-edge and the other part above. Measurement of the beam vertical location without the absorber and edge vertical location with the absorber gives the source position and angle.

Measurements were made to investigate the possibility of using the ps-BPM to correct experimental imaging data. We have introduced periodic electron beam motion using a correction coil in the storage ring lattice. The measured and predicted motions compared well for two different frequencies.

We then show that measurement of the beam width and edge width gives information about the vertical electron source size and angular distribution.

## INTRODUCTION

The stability of the photon beam which is dependent on the stability of the electron source in a synchrotron is critical and essential to the performance of the machine and the beamlines. It is becoming a more important issue as fourth generation storage rings are planned and coming alive and as many other facilities are upgrading their existing rings. The fourth-generation light sources are pushing to very low emittance, so the stability of the electron beam becomes increasingly important as it has a direct effect on the emittance of the machine.

The vertical position of the photon beam at some distance from the source is determined by the vertical position and angle of the electron beam.

We have developed a method to measure the vertical position and angle of the synchrotron electron beam at a single location in a bend magnet beamline at the Canadian Light Source (CLS). The discovery of this system came during an imaging experiment at the Biomedical Imaging and Therapy (BMIT) beamline [3-5] at CLS [1]. Normally to measure the beam angle, two measurements of

the beam position at two separated distances from the source are required. This is a difficult task in a beamline due to both lack of space and presence of many beamline optics and components that will interfere with the location and operation of beam position monitors.

The system we have developed relies on measurements of the photon beam profile with and without an absorption edge filter and at the same location in the beamline. In the initial experiments a Bragg type (reflection geometry) Double Crystal Monochromator (DCM)[2] was used to prepare the photon beam at an energy of the filter's absorption edge.

In this paper we present the implementation and results of a system using (1) a single Laue monochromator setup which is compact and is less susceptible to beam power loading and thus energy drift. We have used this system to assess the ability to (2) measure periodic beam motion with the future intent of (3) using these measurements both to show some of the temporal features of the system and to use the beam position and angle measurements to correct experimental imaging data.

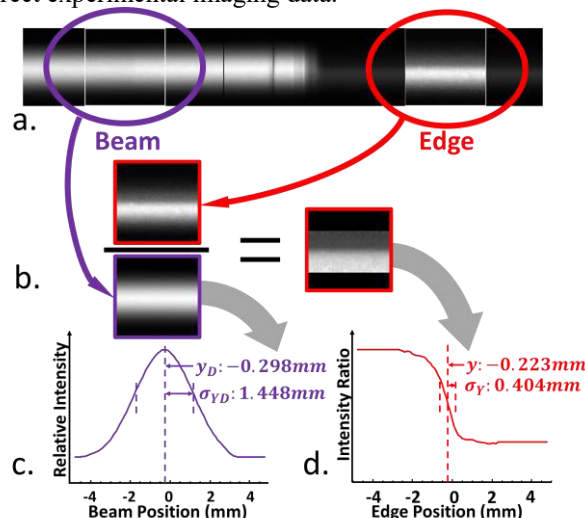


Figure 1:: Beam and edge data (a) plus schematic representation of the data analysis steps (b,c,d).

## Synchrotron

The vertical photon distribution of a bend magnet or wiggler synchrotron beam can be well fitted with a Gaussian function for photon energies what are well above the critical energy of the device (see Fig. 1c where the Gaussian center and width are shown). In our case, the critical energy of the CLS bend is 7.57keV and the absorption edge of the iodine filter is 33.17keV. Figure

\* email address Nazanin.Samadi@usask.ca

1a shows the vertical spatial distribution of an imaging beam prepared by a Si (220) DCM at 25m from the source on the left side while the right side shows the effect of an iodine filter. The part in the red circle has been enhanced to show the edge. The edge is found by normalizing the filter side by the beam side. The result is shown in Fig. 1d where the location and Gaussian width is found.

### Diffraction, Dispersion and Absorption Edge

The vertical angular distribution of a synchrotron source will present a range of angles onto a crystal monochromator if there are not intervening optics between the source and monochromator as in our case. The small range of angles will prepare a quasi-monochromatic beam that has a range of energies as determined by Bragg's law. Thus, the beam prepared by the monochromator will have a continuous range of energies across the vertical range of angles (energy dispersion) from the source. At some distance, again 25m in our case, this range of angles corresponds to a spatial distribution. Thus, the distance scale in Fig. 1 can also be interpreted as an energy scale. As an example, the energy range contained in our beams (reflection or transmission) is of the order of 50+eV at 33.17keV. This energy range is sufficient to easily cover the energy range of the absorption edge of the iodine filter which was used in these experiments.

## THE SYSTEM

The experiments were done at the bend magnet beamline at the BMIT facility at the CLS[3-5]. The beamline was used in "White Beam" mode.

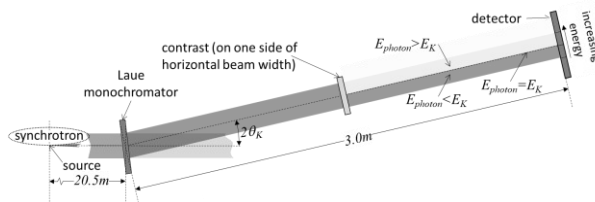


Figure 2: Schematic layout of the ps-BPM system for a single crystal Laue monochromator.

The Laue system is shown schematically in Fig. 2. The crystal was located in the bend magnet imaging hutch approximately 20.5m from the source. The distance from the crystal to the detector is 3m and 23.5 m from the source. A (3, 1, 1) type reflection from a commercially available silicon (5, 1, 1) wafer was used for the Laue monochromator which was tuned to 33.169keV at the absorption K-edge of iodine. The Bragg angle for the lattice planes was 6.55 degrees.

A combination monochromator was prepared for this experiment, one side of this monochromator was the bent Laue for Spectral KES and the other side a flat Laue for beam motion measurements. The Spectral KES is an imaging method using for imaging contrast elements such as iodine in biomedical systems [6, 7]. The simultaneous measurement of imaging data and beam motion data is for using beam motion information to correct the resulting

images. The data correction part will be discussed elsewhere. All the beams were intercepted by the same detector (bent Laue for Spectral and flat Laue with and without a contrast filter for beam motion). The advantage of this approach was that the imaging and the correction data were acquired simultaneously. The detector was a Hamamatsu flat-panel with 100 micron pixel size and 30 frames per second acquisition speed.

Each measurement contained data in the form of tiff images in sets of 400. For each measurement a set of 10 flats (images of the beam with no object in the way) and 10 darks (images of detector response with no beam) were also collected to normalize data.

A combination of 0.05 mm copper and 2.5 mm aluminum were used to filter the white beam and prevent thermal loading on the monochromator.

The incident photon beam at the monochromator was around 6 mm high and 178 mm wide.

Two types of data were collected, one during normal operations of the machine and the other one in special request shifts were a known frequency beam motion was introduced in the ring.

While the data was being collected with the ps-BPM system at the beamline, different currents with different frequencies were used in an orbit corrector at location CY1 in Figure 3 to introduce a perturbation in the electron ring. This corrector is the first vertical orbit corrector in cell 3.

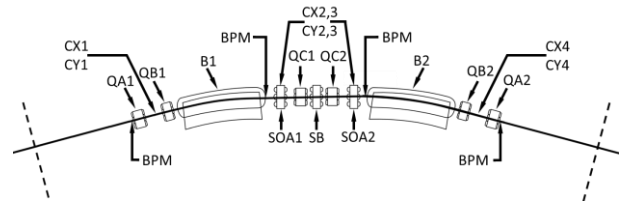


Figure 3: Schematic layout of a cell (one of 12) in the CLS storage ring. CX and CY are orbit correctors, QA, QB, QC are quadrupole magnets, BPMs are electron beam position monitors, SOA, SB are sextupole magnets and Bs are dipole magnets. The dashed lines show the extent of a cell.

The measurements were made using the first bend magnet in cell 5 (B1). The center of the bend magnet beam is 5 degrees into the 15 degree bend provided by the magnet.

These perturbations had frequencies of 5Hz and 10Hz each with currents of 0, 0.12, 0.24 and 0.6A in the orbit corrector.

Both the orbit correction and the transverse feedback system were on during all the measurements and the ring was operating at 250mA current in decay mode.

## RESULTS AND DISCUSSION

Measurements were made while the beam was sinusoidally modulated using an orbit corrector while the motion was monitored with the ps-BPM system at the BMIT beamline.

From the design specification the vertical kick for a corrector is given by

$$kick[\mu rad] \approx 7.637 \times I[A] \tag{1}$$

where  $I[A]$  is the current driving the corrector. So, for a 0.12A excitation the kick is 0.916 microradians. The effect of a vertical kick was simulated with DIMAD [8] at the nominal tunes of the CLS lattice. The closed orbit was calculated with a kick of 1.018 microradians at the position of the orbit corrector 1 in cell 3. With this kick the closed orbit at the position of the BMIT bend magnet (B1 in cell 5) beamline is:  $y = -6.83$  micron and  $y' = -1.089$  microradians for the peak values. For larger kicks the position and angle are assumed to scale with the input current.

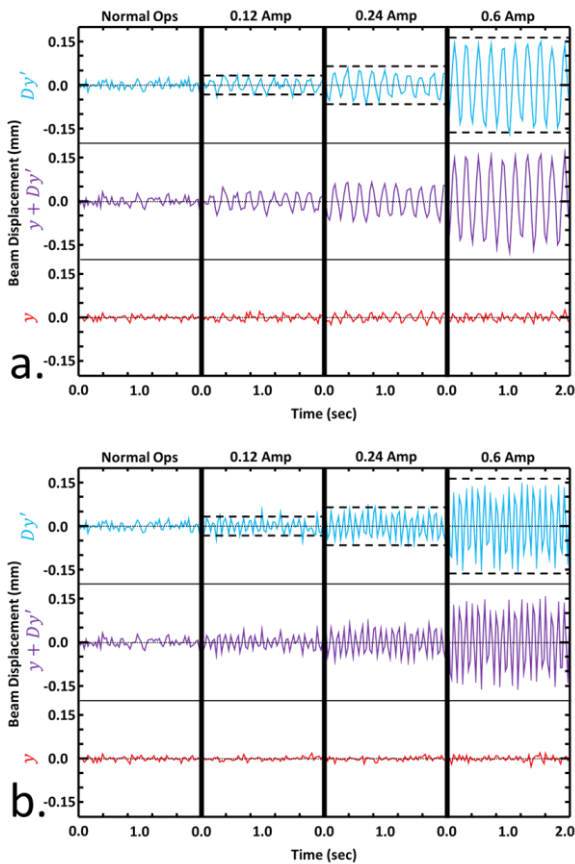


Figure 4: ps-BPM measurements as the orbit corrector current is increased (0, 0.12, 0.24, 0.6A) for 5Hz (Figure a) and 10Hz (Figure b). The dashed black lines indicate the expected peak to peak amplitude of the electron beam motion.

The temporal measured and predicted beam motions are shown in Fig. 4. The measured values are  $y$  (red) and  $y + Dy'$  (violet). The derived angular motion  $Dy'$  is shown in blue. Modulation currents of 0, 0.12, 0.24 and 0.6A where used as shown for frequencies of 5Hz (Fig. 4a) and 10Hz (Fig. 4b). The expected amplitude of  $Dy'$  appears as black dashed lines. The expected values of  $y$  were too small to mark on the plots.

The measured and expected peak to peak values for the beam motions in Fig. 4 are given in table 1.

There is a good agreement between the predicted and measured values for all currents and frequencies.

Table 1: Measured and Predicted Values (in parentheses) of beam motion for corrector currents and frequencies given in the text and Fig. 4

f (Hz)	I (A)	y(μm)	Dy'(μm)	y'(μrad)	y + Dy'(μm)
0	0.0	7.7 ± 2	13.6 ± 2	0.5 ± 0.1	16.2 ± 3
5	0.12	15.6 ± 2 (13.7)	42.5 ± 3 (51.7)	1.6 ± 0.1 (2.2)	57.9 ± 3
10	0.12	9.9 ± 4 (13.7)	51.1 ± 3 (51.7)	2.0 ± 0.1 (2.2)	51.4 ± 3
5	0.24	27.3 ± 2 (27.4)	92.7 ± 3 (103.4)	3.6 ± 0.1 (4.4)	119.9 ± 4
10	0.24	21.3 ± 3 (27.4)	82.9 ± 3 (103.4)	3.2 ± 0.1 (4.4)	104.0 ± 4
5	0.60	43.7 ± 8 (68.3)	255.8 ± 9 (256.2)	9.8 ± 0.3 (10.9)	299.5 ± 5
10	0.60	28.3 ± 6 (68.3)	227.2 ± 7 (256.2)	8.7 ± 0.3 (10.9)	255.1 ± 10

With the similar setup described at the original paper [1] measurements were done while the electron beam size and angular distribution were adjusted using skew quads. The vertical source size and angular size were measured by the system and compared against measurements of the source size made by a pinhole camera at the X-ray Synchrotron Radiation (XSR) diagnostic beamline [9]. The ps-BPM measurements correlate well with beam size measurements at the XSR beamline. Figure 5 shows the measured direct beam width (Fig. 5b) and the edge width (Fig. 5a) from which we can estimate the vertical emittance of the source. The parabolic-type behavior of the measurements indicate that other terms contribute in quadrature to the widths. The results correlate with each other but require further interpretation.

## CONCLUSION

A newly developed phase space beam position monitor has been used to measure induced beam motions in a synchrotron source. There is good agreement between the expected motion and those measured by this monitor. The results presented here are the first aspect of using this monitor to correct experimental data for an imaging method, Spectral KES, which is susceptible to the vertical position and angle motion. The fact that these measurements accurately show this motion, gives a good indication that we will be successful in correcting this data.

Also measurements have been made of the widths of the beam and K-edge as skew quads were used to increase the vertical size and angular size of the electron beam. Both size and angular size were shown to increase indica-



tion that the vertical emittance can be measured. At this point the sensitivity of these measurements is being assessed as well as other contributors to the measured widths.

Both the data correction and measurements of emittance will be the topics of future papers.

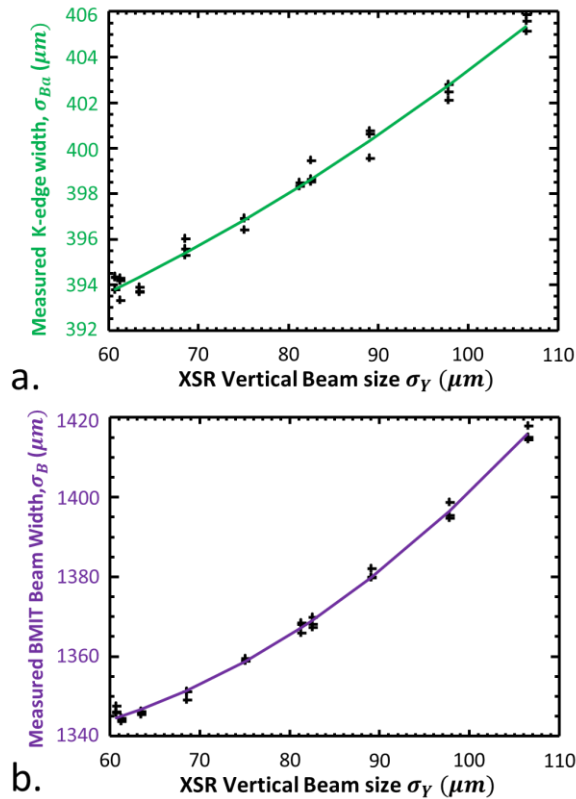


Figure 5: Measured widths of the beam (Figure b) and the K-edge (Figure a) as skew quads are used to increase the vertical beam size. The horizontal axis is the vertical size as measured by XSR beamline.

## ACKNOWLEDGMENTS

The authors acknowledge the financial support of Canadian Institutes of Health Research (CIHR) Training Grant –Training in Health Research Using Synchrotron Techniques, Saskatchewan Health Research Foundation Team Grant, Natural Sciences and Engineering Research Council of Canada (NSERC) Discovery Grant, the University of Saskatchewan, and Canada Research Chair Program. Research described in this paper was performed at the Canadian Light Source, which is funded by the Canada Foundation for Innovation, NSERC, the National Research Council Canada, CIHR, the Government of Saskatchewan, Western Economic Diversification Canada, and the University of Saskatchewan.

## REFERENCES

- [1] N. Samadi, B. Bassey, M. Martinson, G. Belev, L. Dallin, M. de Jong, *et al.*, "A phase-space beam position monitor for synchrotron radiation," *J Synchrotron Radiat*, vol. 22, pp. 946-55, Jul 2015.
- [2] J. A. Golovchenko, R. A. Levesque, and P. L. Cowan, "X-ray monochromator system for use with synchrotron radiation sources," *Review of Scientific Instruments*, vol. 52, pp. 509-16, 04/ 1981.
- [3] T. W. Wysokinski, D. Chapman, G. Adams, M. Renier, P. Suortti, and W. Thomlinson, "Beamlines of the biomedical imaging and therapy facility at the Canadian light source - Part I," *Nuclear Instruments & Methods in Physics Research Section a-Accelerators Spectrometers Detectors and Associated Equipment*, vol. 582, pp. 73-76, Nov 11 2007.
- [4] T. W. Wysokinski, D. Chapman, G. Adams, M. Renier, P. Suortti, and W. Thomlinson, "Beamlines of the Biomedical Imaging and Therapy Facility at the Canadian Light Source - Part 2,," *11th International Conference on Synchrotron Radiation Instrumentation (Sri 2012)*, vol. 425, 2013.
- [5] T. W. Wysokinski, D. Chapman, G. Adams, M. Renier, P. Suortti, and W. Thomlinson, "Beamlines of the biomedical imaging and therapy facility at the Canadian light source - part 3," *Nuclear Instruments & Methods in Physics Research Section a-Accelerators Spectrometers Detectors and Associated Equipment*, vol. 775, pp. 1-4, Mar 1 2015.
- [6] Y. Zhu, N. Samadi, M. Martinson, B. Bassey, Z. Wei, G. Belev, *et al.*, "Spectral K-edge subtraction imaging," *Physics in Medicine and Biology*, vol. 59, pp. 2485-2503, 2014.
- [7] N. Samadi, M. Martinson, B. Bassey, A. Gomez, G. Belev, and D. Chapman, "An energy dispersive bent Laue monochromator for K-edge subtraction imaging," *AIP Conference Proceedings*, vol. 1741, p. 040004, 2016.
- [8] R. V. Servranckx, K. L. Brown, L. Schachinger and D. Douglas, "Users Guide to the Program DIMAD," Stanford Linear Accelerator Laboratory, Stanford Linear Accelerator Laboratory, 1990.
- [9] J. C. Bergstrom and J. M. Vogt, "The optical diagnostic beamline at the Canadian Light Source," *Nuclear Instruments and Methods in Physics Research Section A: Accelerators, Spectrometers, Detectors and Associated Equipment*, vol. 562, pp. 495-512, 6/15/ 2006.

# INTEGRATION OF A PILOT-TONE BASED BPM SYSTEM WITHIN THE GLOBAL ORBIT FEEDBACK ENVIRONMENT OF ELETTRA

G. Brajnik\*, S. Bassanese, G. Cautero,  
 S. Cleva, R. De Monte, Elettra-Sincrotrone Trieste, Trieste, Italy

## Abstract

In this contribution, we describe the advantages of the pilot tone compensation technique that we implemented in a new BPM prototype for Elettra 2.0. Injecting a fixed reference tone upstream of cables allows for a continuous calibration of the system, compensating the different behaviour of every channel due to thermal drifts, variations of cable properties, mismatches and tolerances of components. The system ran successfully as a drop-in substitute for a Libera Electron not only during various machine shifts, but also during a user dedicated beamtime shift for more than 10 hours, behaving in a transparent way for all the control systems and users. The equivalent RMS noise (at 10 kHz data rate) for the pilot tone position was less than 200 nm on a 19 mm vacuum chamber radius, with a long-term stability better than 1  $\mu$ m in a 12-hour window. Two main steps led to this important result: firstly, the development of a novel RF front end that adds the pilot tone to the signals originated by the beam, secondly, the realisation of an FPGA-based double digital receiver that demodulates both beam and pilot amplitudes, calculating the compensated X and Y positions.

## INTRODUCTION

Like many other lightsources, also Elettra (the Italian synchrotron) is planning its upgrade to Elettra 2.0, a low emittance machine. To obtain the promised figures of merit (high stability, reduced emittance, etc. [1, 2]), these new generation machines need several beam diagnostics improvements. In particular, for what concerns electron beam position monitors (eBPMs), the following features are mandatory: nanometer-scale accuracy, long-term stability, reduced current dependence, compensation of different channel behaviours.

Previous experiences in developing analog front end have shown that eBPMs based on pilot tone compensation can fulfil most of these requirements [3, 4]. So, we decided to go one step further to demonstrate its usefulness in a real environment, firstly with the realisation of an FPGA-based double digital receiver that demodulates both beam and pilot amplitudes and calculates the compensated beam positions, secondly with the integration of this system in the Elettra Global Orbit Feedback (GOF), replacing a Libera Electron during the normal machine operation.

## ELECTRON BPM PROTOTYPE

In order to have maximum flexibility and to compensate the different channel behaviours, including the cables, a

modular approach that allows to place the front end in service area is essential. The modules are essentially two, the RF analog front end and the FPGA-based Digital Receiver.

## Improved Analog Front End

The front end is similar to the one presented at IBIC 2016 [4], but enhanced and re-engineered in a more compact solution. In the present version the low-noise PLL has been integrated in the box (Fig. 1), together with diagnostic functionalities (voltage and temperature sensors) and complete Ethernet control. Figure 2 illustrates the block diagram of the front end, with the following elements:

1. low-pass filter;
2. high reverse-isolation combiner for the pilot tone;
3. band-pass filter;
4. variable attenuator;
5. low-noise amplifier;
6. splitter;
7. low-noise PLL for the pilot tone generation.

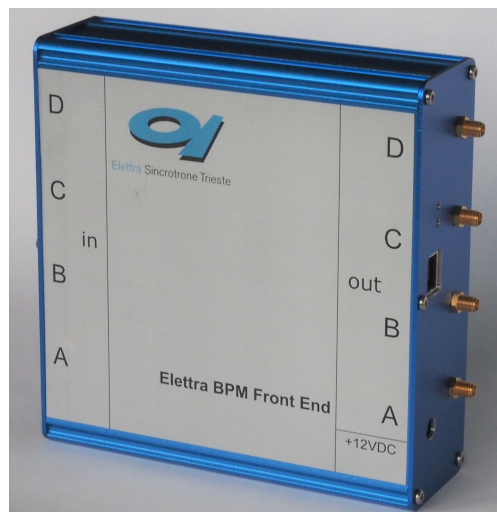


Figure 1: Elettra eBPM analog front end.

## FPGA-based Digital Receiver

In the previous publications [4, 5] we described an in-house assembled digitiser (based on Linear Technology LTC2209 ADCs and Altera Stratix III FPGA) developed for first tests of the system, catching only the raw ADC data and transmitted via an Ethernet link thanks to an FPGA. The major limitation of that approach was the off-line processing with the FFT technique. To overcome this issue, the FPGA code has been completely rewritten, implementing a parallel double digital receiver.

\* gabriele.brajnik@elettra.eu

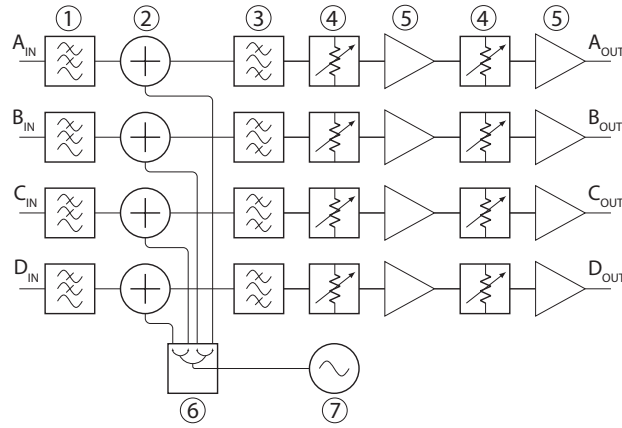


Figure 2: Analog front end block diagram.

The ADC data (running at 150 MHz) are multiplied by sine and cosine generated from a NCO (numerically controlled oscillator) at the undersampled beam RF frequency. The down-converted signals are then decimated using CIC (cascaded integrator-comb) and FIR (finite impulse response) filters at revolution frequency (turn-by-turn, 1.156 MHz). Finally, the amplitudes are demodulated using I and Q data and subsequently decimated again to 10 kHz rate. After this, X and Y position are calculated with the traditional difference-over-sum (DoS) algorithm.

A second NCO, tuned at the pilot frequency, feeds a replicated parallel processing chain that retrieves the pilot positions (Fig. 3). The compensation takes place at 10 kHz

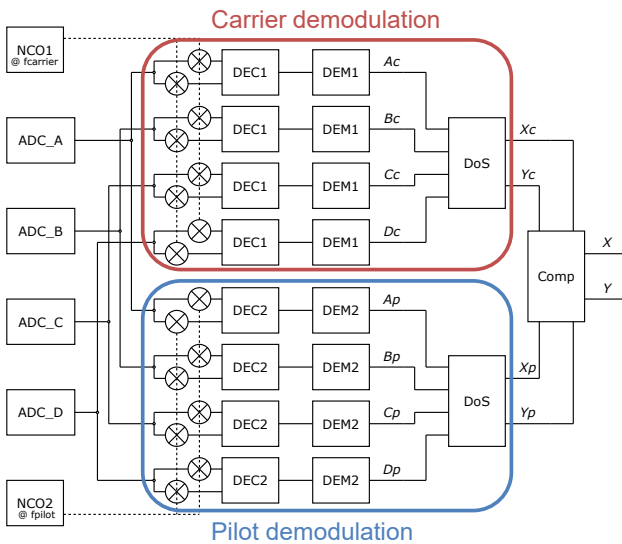


Figure 3: Digital receiver block diagram.

rate, subtracting the pilot coordinates from the beam ones. This is a “non-linear” compensation easier to implement in FPGA (it requires only adders), different from the one used in a previous work [3], that was implemented since it was measured that, in spite of its higher simplicity, returns the same values for small variations, up to 10 mm from the centre.

Three Gigabit Ethernet interfaces on SFP modules are used to control the system and to transmit data to Elettra global orbit feedback. Figure 4 shows the digitiser in Elettra Service Area.

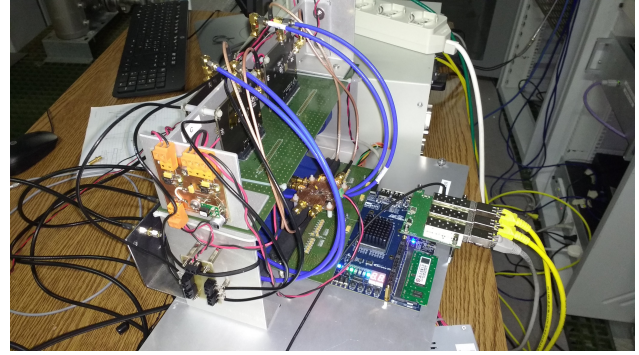


Figure 4: Digitiser in Elettra service area.

## CHARACTERIZATION

In order to verify the correct functionality of the system, we decided to emulate a fixed beam at first using a Rohde&Schwarz RF signal generator plus a 4-way splitter, then summing the signals from the beam and dividing them with two back-to-back splitters. Both the approaches gave the same results. The carrier frequency is 499.654 MHz, while the pilot frequency is 501.281 MHz.

### Performances

Feeding directly the ADCs inputs without the front end and driving them approximately at 80% of full scale gives an rms noise of about 80 nm on 10 kHz data rate, considering a scale factor of 20 mm. Adding the analog front end, the noise increases up to 180 nm rms, in line with the noise figure of about 6 dB of the front end.

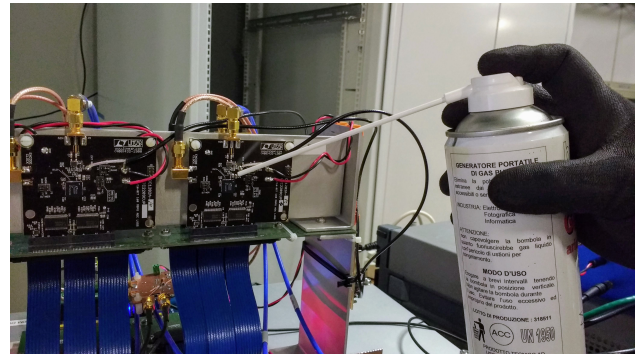


Figure 5: Changing temperature of ADC D.

### Temperature Changes and Cables Wobbling

Several test were performed to confirm once again the effectiveness of the compensation. As shown in Fig. 5, the ADC D temperature was lowered by blowing compressed air on the chip. While the resulting drifts for the carrier (beam) and the pilot positions were similar and about 25  $\mu$ m for both the coordinates (Figures 6 and 7), the compensated ones (Fig. 8) exhibited residual drifts less than 1  $\mu$ m.



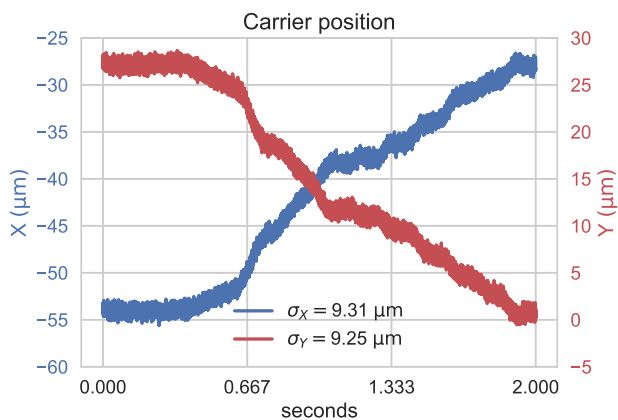


Figure 6: Carrier position during ADC temperature change.

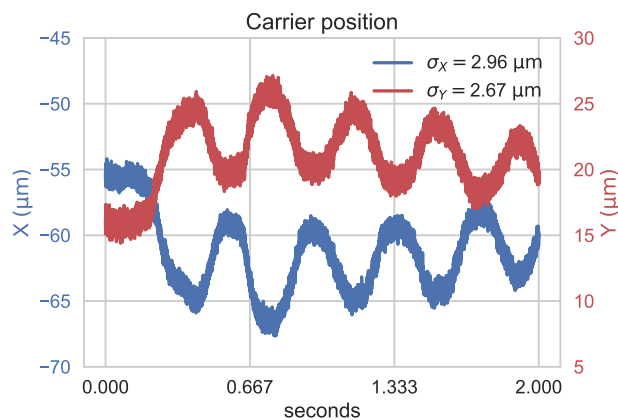


Figure 9: Carrier position during cable wobbling.

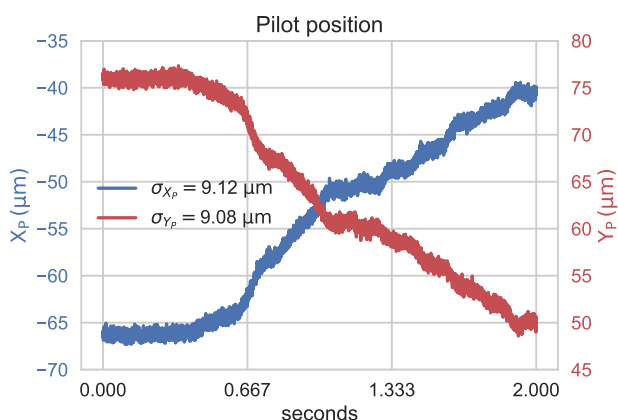


Figure 7: Pilot position during ADC temperature change.

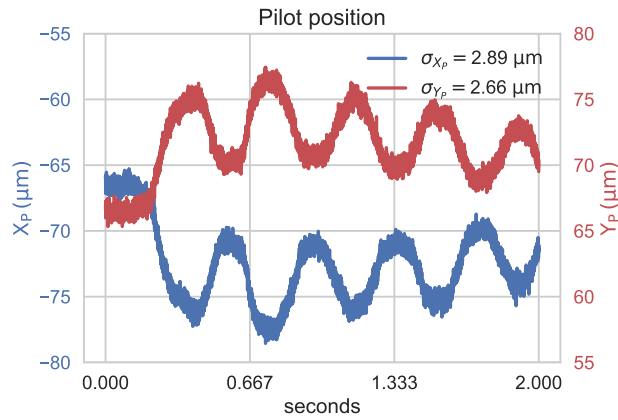


Figure 10: Pilot position during cable wobbling.

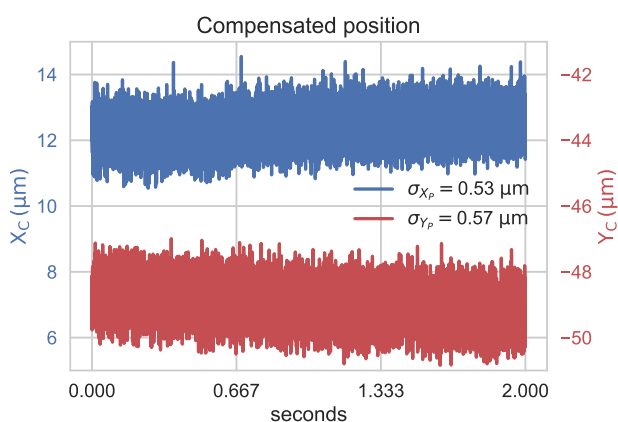


Figure 8: Compensated position during ADC temperature change.

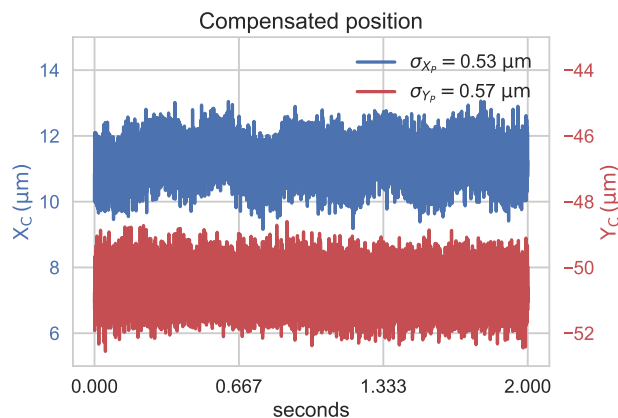


Figure 11: Compensated position during cable wobbling.

The next step was to bend and wobble a coaxial cable located between the front end and the digitiser. During this operation, the positions oscillated in an interval of about 10 μm, as stated in Fig. 9 for the carrier and in Fig. 10 for the pilot. Also in this case the compensation dramatically reduces the effect, showing residual oscillations less than the peak-to-peak noise (Fig. 11).

### Spectral Coherence

Intuitively, the compensation is a powerful tool for correcting “slow” mismatches: thermal drifts, cable variations, gain differences. To optimize the system, a good practice should be to limit the bandwidth of the pilot positions. This would allow to reduce the high frequency content that does not have meaningful information, reducing further unwanted noise on the compensated positions.



A way to estimate the frequency range where the effectiveness is maximum is using the spectral coherence  $C_{xy}(f)$ : it measures the relation between the signals  $x$  and  $y$ . We recall its definition in the following equation:

$$C_{xy}(f) = \frac{|G_{xy}(f)|^2}{G_{xx}(f)G_{yy}(f)} \quad (1)$$

where  $G_{xy}(f)$  is the cross-spectral density between the two signals, and  $G_{xx}(f)$  and  $G_{yy}(f)$  the power spectral density of  $x$  and  $y$  respectively. Figure 12 shows the calculated coherence between  $X$  of the carrier and  $X$  of the pilot ( $C_{X_C X_P}(f)$ ) on the 10 kHz data, taking 100 000 samples (equivalent time of 10 s) and zooming up to 200 Hz. The result indicates that the compensation can be useful up to roughly 100 Hz, with a coherence index of about 0.8. The coherence of  $Y$  coordinate ( $C_{Y_C Y_P}$ ) is not shown on the figure for space reasons, but behaves nearly in the same way.

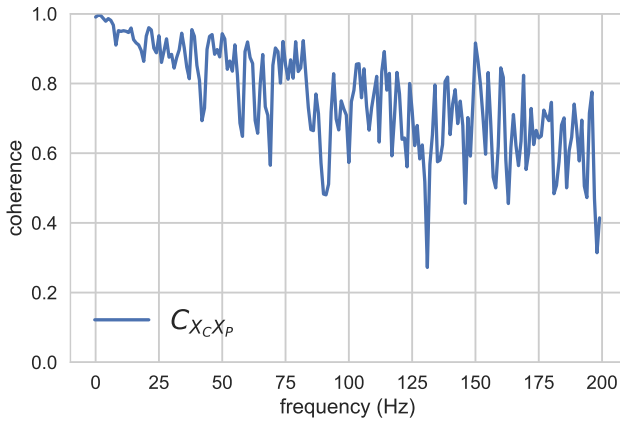


Figure 12: Coherence between  $X$  of the carrier and  $X$  of the pilot.

## RESULTS WITH BEAM

The best way to validate the prototype is to test it in real conditions. So, we replaced an existing Libera Electron BPM in section 7 of Elettra storage ring. The goal was to show that the new system not only provides better performances, but can also replace through and through a commercial eBPM in a transparent way for all the control systems. Figure 13 shows the block diagram of the complete system, and Fig. 14 the setup in Elettra Service Area.

The right operation of the Global Orbit Feedback relies not only on the goodness of the data acquired by the BPMs, but also on their correct synchronisation with respect to the revolution clock (or machine clock, MC). Elettra GOF acquires the whole set of BPM data at about 10 kHz (MC divided by 116) and the maximum time mismatch allowed between two packets in the same collecting point must be less than 20  $\mu$ s. Each BPM emits an UDP packet on an Ethernet link that contains the  $X$  and  $Y$  positions together with some extra useful information, such as the demodulated amplitudes of the four electrodes ( $V_a$ ,  $V_b$ ,  $V_c$ ,  $V_d$ ), the sum of them ( $S$ ) and the quality factor ( $Q$ ).

So, the following constraints must be satisfied in order to replace the commercial Libera Electron with the in-house developed BPM:

1. time synchronisation: the UDP packet must be emitted in the same time window of the other BPMs belonging to the same collecting point;
2. the existing packet data format has to be maintained;
3. legacy housekeeping control interface (i.e. Tango server).

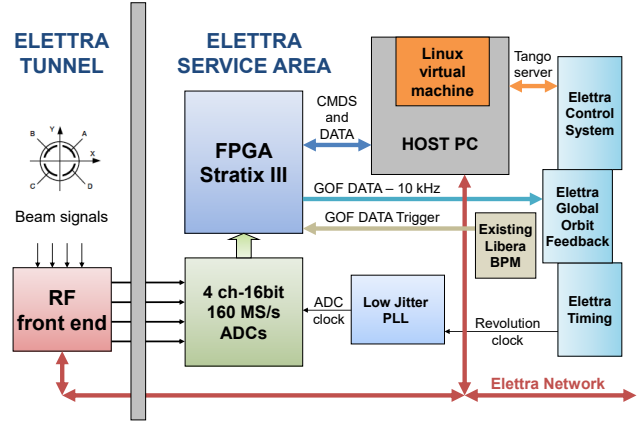


Figure 13: Block diagram of the complete system.

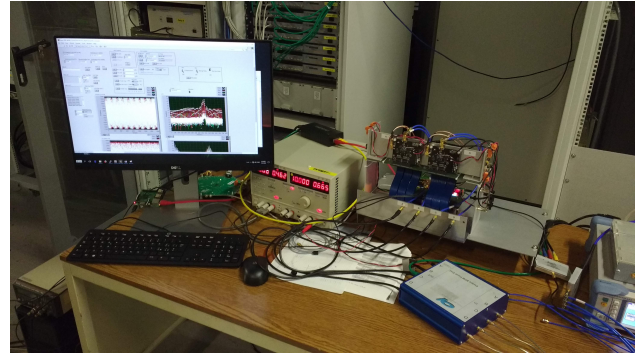


Figure 14: System setup in Elettra Service Area.

## Differences with Current Libera System

Our system is phase-locked with the 1.156 MHz machine clock: the generated ADC clock is 150.358 MHz (130 times the MC). All the internal FPGA processing is synchronous and in-phase with the ADC clock and thus with the revolution clock. The processing chain done inside the Libera is different: its clocking system has a FLL (frequency-locked-loop) locked to the MC and the regenerated ADC clock is slightly detuned with respect to the exact MC multiple. This leads to a difference of a 0.02 Hz between the 10 kHz data from the Libera and from our eBPM, resulting in a periodical drop of packets every 50 s, due to the time scrolling of the GOF acceptance window.

This issue was solved by using the replaced Libera: due to the unavailability of trigger outputs on the Libera, we acquire the sent UDP packet via a SFP link with our electronics and use it as a trigger.

### Tango and GOF Integration

The prototype has a basic connectivity on the three Gigabit Ethernet interfaces:

- the first port is reserved to GOF connection: the UDP packets are structured in the same way as the Libera ones, containing the compensated positions;
- the second is dedicated for trigger purposes explained in the previous section;
- the third is used for configuration and on-demand data (NCO tuning, raw ADC buffers, calculated positions of pilot and carrier).

The latter communicates with a Linux virtual machine installed on a host computer. Its task is to analyse the data at 10 kHz and therefore perform additional operations (Fig. 15):

- configure in a proper way the gain of the analog front end (automatic gain control, AGC) and the amplitude of the pilot tone;
- log all the relevant data for diagnostic purposes;
- instance correctly a Tango BPM server for all the control systems outside the GOF, calculating slow data at 10 Hz and less.

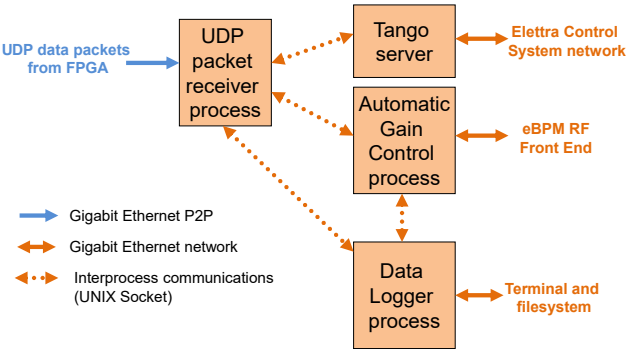


Figure 15: Internal processes of the Linux VM.

### Data Obtained During Dedicated and User Shifts

The machine ran successfully with our electronics for more than 24 hours during a dedicated shift. The obtained resolution was about 180 nm, while the long term stability was better than 800 nm in 24 hours, operating at 2.0 GeV and 310 mA, always considering a scale factor of 20 mm and a data rate of 10 kHz. Figure 16 clearly shows the different behaviour on the position caused by real beam movements or attenuation changes/thermal drifts.

The trial was extended in order to include also 10 hours of user shift: during these tests no packet losses, no software or firmware hangs or structural issues have been detected.

### Using Pilot as System Diagnostic

The pilot approach has also some not obvious advantage as system diagnostic tool: during the preliminary test an unusual drift on pilot positions was recorded. Looking to the demodulated amplitudes of the four channels, a drop was noticed in channel C. A detailed inspection of the hardware revealed a broken link of the common reference voltage towards ADC C (Fig. 17).

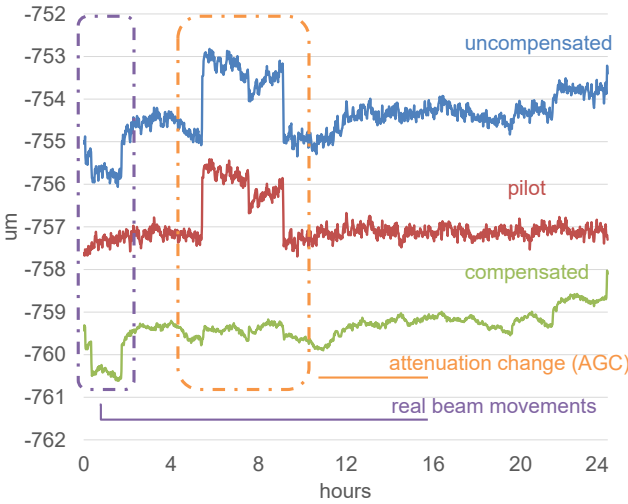


Figure 16: Beam Y-position in a 24-hours time window.

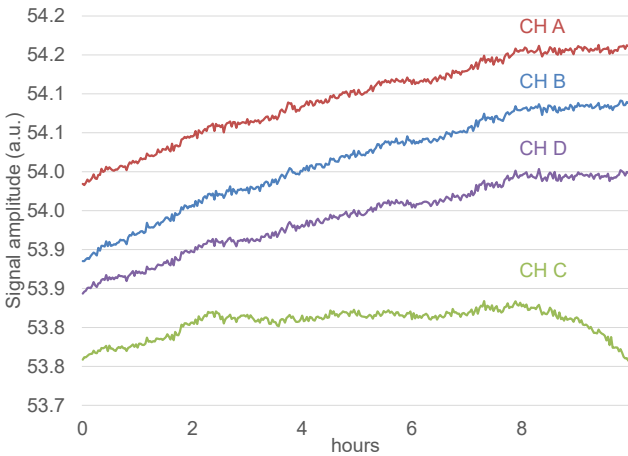


Figure 17: Issue on ADC reference voltage.

Without the pilot information (that should be stable), this kind of malfunction could be detectable only developing an offline dedicated setup, while thanks to the presence of the pilot it is immediately available online.

## CONCLUSION

In this paper we presented the successful integration in the Elettra global orbit feedback environment of a modular eBPM prototype based on pilot-tone compensation, consisting in an analog front end and a FPGA-based digitiser capable of parallel demodulation of beam and pilot signals, with resolution and long-term stability both at sub-micron level. The effectiveness of the compensation has been proven during dedicated and user machine shifts: not only as a corrector of thermal drifts, cable variations and gain changes but also as an on-line diagnostic of the system.

When time-domain processing is needed, the system allows to catch the not compensated raw ADC values (e.g. first turn measurements) just turning off the pilot tone, remaining useful for calibration purposes to be done just before the measurement or between bunches. In fact it has to be reminded that all BPM systems based on decimation process

treat data in frequency domain, which means that a stable machine with a stored beam, or, at least, capable to accumulate a sufficient number of turns to have significant data at 10 kHz is required.

Finally, research on further upgrade of the system is still ongoing about many crucial points: hardware changes will be evaluated, considering various bandpass filters, newer ADCs and so on, and taking in account different scenarios, like first turn, turn-by-turn and tune measurements.

## ACKNOWLEDGEMENTS

The authors would like to thank Giulio Gaio for the global orbit feedback support and Guenther Rehm for the very useful discussions about BPM behaviours and spectral coherence.

## REFERENCES

- [1] E. Karantzoulis, “The Diffraction Limited Light Source Elettra 2.0”, in *Proc. IPAC2017*, pp. 2660–2662, 2017. doi:10.

18429/JACoW-IPAC2017-WEPAB036

- [2] E. Karantzoulis, A. Carniel, R. De Monte, S. Krecic and C. Pasotti, “Status of Elettra and Future Upgrades”, in *Proc. IPAC2018*, pp. 4054–4056, 2018. doi:10.18429/JACoW-IPAC2018-THPMF010
- [3] G. Brajnik, S. Carrato, S. Bassanese, G. Cautero and R. De Monte, “Pilot Tone As a Key to Improving the Spatial Resolution of eBPMs”, *AIP Conference Proceedings*, vol. 1741, p. 020013, 2016. doi:10.1063/1.4952792
- [4] G. Brajnik, S. Bassanese, S. Carrato, G. Cautero, and R. De Monte, “A Novel Electron-BPM Front End With Sub-Micron Resolution Based on Pilot-Tone Compensation: Test Results With Beam”, in *Proc. IBIC2016*, pp. 308–311, 2017. doi:10.18429/JACoW-IBIC2016-TUPG02
- [5] G. Brajnik, S. Bassanese, G. Cautero, R. De Monte, M. Feriannis, and G. Rehm, “Reducing Current Dependence in Position Measurements of BPM Systems by Using Pilot Tone: Quasi-Constant Power Approach”, in *Proc. IBIC2017*, pp. 301–303, (2018). doi:10.18429/JACoW-IBIC2017-TUPWC09

# COMMISSIONING OF THE OPEN SOURCE SIRIUS BPM ELECTRONICS

D. O. Tavares\*, G. B. M. Bruno, S. R. Marques, L. M. Russo, H. A. Silva, LNLS, Campinas, Brazil

## Abstract

Sirius is a 3 GeV 4<sup>th</sup> generation circular light source designed to achieve an emittance of 0.25 nm-rad [1]. During the early stages of the machine design, the BPM electronics was selected as one of the projects to be developed by the LNLS team. This paper will report on the manufacturing and deployment processes of the referred electronics as well as the achieved reliability and performance.

## INTRODUCTION

All units of the Sirius BPM Electronics have been manufactured and are currently being prepared for deployment in the machine. In total, 21 BPM racks will be deployed along the accelerator, of which 20 racks are dedicated to booster's and storage ring's electron BPMs, white photon beam BPMs and fast orbit feedback, and 1 rack is dedicated to transfer lines BPMs. A 22<sup>nd</sup> BPM rack will be kept in the Beam Diagnostics laboratory as a homologation rack for repairs and new developments. Not included in this list are the Linac BPM electronics, which were supplied by SINAP as part of a turnkey Linac contract. They will not be covered in this paper.

## SIRIUS BPM ELECTRONICS

As shown in Fig. 1 the assembly of a BPM rack is composed of the following parts: (i) one 12-slot MicroTCA.4 crate; (ii) several RF Front-End (RFFE) modules, one per BPM; (iii) one 24-port Ethernet switch; (iv) one isolated AC/DC linear power supply serving the RFFE modules; (v) RF coaxial cables between RFFE modules and digitizer boards; (vi) Ethernet cables for RFFEs and crate.

The MicroTCA.4 crate is populated with modular FPGA carrier boards following PICMG AMC [2] and VITA FMC [3] standards, each of them playing the role of either a timing receiver, a 4-channel RF signals digitizer or a 4-channel digital picoammeter, depending on the I/O mezzanine modules attached to it. In the future, an additional crate slot will be used as fast orbit feedback (FOFB) processor and fast orbit correctors' power supply, for which multi-gigabit optical I/O mezzanines and an open hardware 10 kHz bandwidth linear power supply rear-transition module (RTM) will be employed.

The RFFE is an Ethernet-controlled analog front-end module providing the following core functions to the BPM system: (i) low-pass filtering of high accelerator RF frequency harmonics; (ii) 2x2 switching of diagonally opposed BPM antenna signals, with optional RF switches temperature stabilization; (iii) narrow band-pass filtering to avoid aliasing of revolution harmonics to the baseband; (iv) RF signals amplification with digitally controlled gain.

\* daniel.tavares@lnls.br

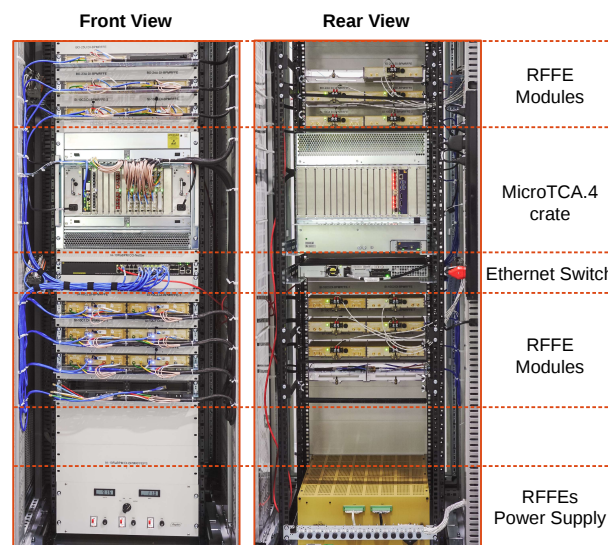


Figure 1: BPM rack layout.

Following ESRF's and Soleil's approach [4], the signals from the BPM pick-ups will be brought to the electronics by delay-matched cable assembly with (160 ps peak-to-peak error), composed of four LMR195 coaxial cables extruded within a common encapsulation, aiming at minimizing the position drifts caused by unequal thermal variations of cables' characteristics. This is a critical part of the system, since such drifts could not be calibrated by the RFFEs switching scheme. Cables lengths vary from 25 m to 70 m.

Another bundle of cables connect the 4 RFFE RF outputs and switching clock signal input to the digitizer's 4 ADC RF inputs and trigger output of one BPM, respectively. The 4 RF cables are also delay-matched with peak-to-peak error below 20 ps. They are double-shielded 2 m long RG316 coaxial cables providing more than 100 dB isolation.

The digitizer sampling clock is generated in each FMC ADC module and is synchronized with the accelerator's master oscillator by means of a timing receiver in the crate [5]. A reference clock is delivered by the timing receiver and sent to all BPM digitizers through one of the MicroTCA.4 backplane's low jitter clock line.

Each RFFE is controlled via Ethernet (TCP/IP) by the crate CPU. They are physically connected to the rack's Ethernet switch but logically isolated from the accelerator's control network by means of Virtual LANs. Only the crate CPU has access to the RFFE IP addresses of the corresponding rack. The AMC FPGA boards are in turn accessed via PCI Express. The BPM EPICS IOC of each BPM run in the crate CPU and publish the BPM PVs to the control network.

The BPM project followed an open source design philosophy aiming at facilitating collaboration with other institutes [6]. The RFFEs, RF digitizers, FPGA carrier and



timing modules are all open hardware projects licensed under CERN Open Hardware License [7]. Software and gateware designs are published at GitHub under open source licenses [8].

## MANUFACTURING

The next sections describe the processes of manufacturing, testing and integrating the Sirius BPM electronics. It also summarizes the failures and difficulties found along the way.

### Procurement

Two strategies were evaluated for manufacturing ready-to-commissioning boards: (i) assembling the boards through contract manufacturers (CM) and doing all testing, system setup and installation at LNLS; (ii) contracting a turnkey provider who could arrange board manufacturing, board testing and occasional repairs.

From 2016 through 2017, several companies were evaluated, local and foreign ones, for both strategies. On the turnkey side, two Brazilian companies developed test benches for the boards as part of the *Desafio Sirius* (Sirius Challenge) project, a government subvention program that financed third-party technology development in several areas of the Sirius project. Electronics suppliers which traditionally serve the accelerators community were also contacted.

A decision for a mixed approach, where LNLS contracted the board manufacturing directly from a CM while also contracting a third-party for tests, integration and system assembly was made in 2017. An important reason for this decision was the late development of some boards, for instance the 4-channel 250 MS/s ADC FMC module (FMC ADC), which had improvements being made to the project until 2017. These late developments, while not a departure from the overall architecture of any boards, meant less time for a full project transfer that would be necessary for a turnkey arrangement.

Both parts of the RF BPMs digitizer, the AMC FMC Carrier (AFC) FPGA board and the FMC ADC modules, and the SFP rear transition module (RTM-SFP) used in the timing receiver, were manufactured by the Polish CM Creotech [9], who was selected due to prior experience as developer and manufacturer of these boards. The RFFE boards were in turn manufactured by the Brazilian CM CADService [10], who supplied most of the electronic components, hired the PCB manufacturer, assembled the boards and performed standard electrical testpoint checks and visual inspection.

### System Integration

All of the manufactured BPM electronics boards were individually tested by ATMOS Sistemas [11], one of the successful companies in *Desafio Sirius*. They developed test benches for automated testing and report generation (Fig. 2), and also worked as a system integrator, by assembling the electronics boards, cables and mechanical parts into the BPM racks. In summary, the contract which was established between LNLS and ATMOS had as deliverable a set of

22 fully functional BPM racks accompanied with detailed reports of each board.

Most digital signals and components, including high-speed transceivers, were tested in a pass/fail basis by the integrator. To allow for future analysis, low-frequency analog signals, clock waveforms, raw ADC data captures and RF signals test results had their measurements stored and attached to the test reports. Besides standard acceptance procedure, these reports were also meant to facilitate detailed life cycle and maintenance analysis.

After individual boards testing, the system proceeded to integration: the FMC modules were mounted to their corresponding AFCs and installed in the MicroTCA crates. A set of automated scripts programmed the FPGAs gateware, loaded the crates' CPU operating system and application software images and configured the MicroTCA crate controllers (MicroTCA Carrier Hub - MCH) with application-specific settings. The crates were then run in the bench without RF signals for evaluating basic functions such as communication between CPU, MCH and all installed boards. These tests allowed to detect any problems in the digital part of the assembled crate: CPU and MCH setup, EPICS and other software installations, PCIe links between AMCs and CPU, timing system clock acquisition, locking and distribution, and proper control of FMC modules. After this test, the populated crates were mounted in the already-built BPM rack and all internal cables were connected.

Once the BPM racks were fully assembled they underwent a burn-in procedure intended to stress the system enough to catch *infant mortality* failures and possible occurrences of performance degradation. The burn-in procedure was specified at 100 hours. If any failures were detected, the corresponding BPM electronics were replaced by another unit which had previously been "burned" and the defective parts sent for diagnostics and repair.

After the burn-in procedure, a final inspection was performed at the integrator site and the racks were packaged for delivery. After arriving and being unpacked at the LNLS site, the racks underwent the final performance tests before being sent to the deployment at Sirius's instrumentation rooms.

### Failures

The extensive automated tests enabled the detection of manufacturing issues in an early production stage, especially in the RFFE modules, which were not passed though functional tests at the manufacturer. Table 1 presents a summary of the manufacturing failures segmented by boards/modules models.

The RFFE internal analog boards had the majority of the defects found during these tests, with about 20 RF channels not passing the test, from a total of 1040 channels. In contrast, the RFFE power supply and controller baseboard, which are much less sensitive than the analog boards, had a lower fail rate. The main source of failure was the presence of solder flux residues on the Ethernet jack preventing the boards from establishing Ethernet communication. These

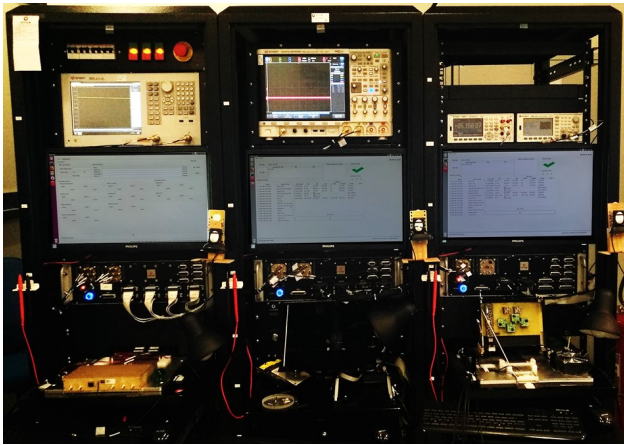


Figure 2: Manufacturing test benches at ATMOS Sistemas. Each cabinet is dedicated for individual tests of one board model, either AFC, FMC ADC or RFFE.

boards were sent back to the CM for rework and then resent to the system integrator.

Most problems found in the AFC board were related to the button switch and LEDs in the power panel, and may have been caused during FMC mounting or other board manipulation. Improvements to board design were suggested to avoid this issue in future versions. The new tests also revealed a previously unknown problem with the clock signal path coming from the AFC to the FMCs, which are harmless to the BPM electronics but could affect other applications. Moreover, one specific transceiver of four boards, which had previously passed Creotech's tests did not pass the new tests at ATMOS. Their causes are still unclear and are still under investigation.

The FMC ADC tests showed an unexpected issue in the clock circuitry, in which a small percentage of the boards (about 7%) showed an unexpected noise in the clock output when the oscillator is turned off. These boards do not exhibit any abnormal behaviour during operation, and were not removed from the production pool. The most prominent functional issues were related to the trigger output/input circuit, accounting for 1.5% of the total number of boards tested.

A recurring failure of SMA cables' connectors occurred in 12 units from a total of 236 cable assemblies. In these cases, the male SMA connector nut lost the grip after a small torque was applied. This does not always happen in the first connection, and often are detected during the burn-in procedure or after delivery, requiring the replacement of the whole cable assembly. An investigation together with the cable supplier showed that the C-spring holding the SMA coupling nut to the connector body did not have enough elasticity, applying less force than necessary to hold the nut at the specified torque. New connector assembly and cable test procedures were developed with the cable supplier to avoid further issues.

Commercial off-the-shelf equipment was not immune from failures. All MicroTCA CPUs (NAT NAT-MCH-RTM-

ComEx model) had an incorrectly soldered resistor, resulting in the operating system not being able to access or identify part of the installed SDRAM memory. The repair consisted in desoldering that resistor from all the CPU modules. The rework was performed by the integrator under the manufacturer guidance and presented no further issues. Besides that failure, two MicroTCA fan trays failed out-of-the-box and will be returned to the manufacturer.

Table 1: Failure Rate for Different BPM Equipment

Equipment	Total	Rejected	Failure %
RFFE (RF boards)	520	20	3.8%
RFFE (Control board)	260	1	0.4%
AFC	175	7	4.0%
FMC ADC	257	11	4.3%
Intra-rack Cables	1180	14	1.2%

## ISSUES FOUND

The next sections describe all important issues affecting performance, reliability and maintainability found between the last prototype phase and deployment.

### *RFFE Microcontroller Ethernet PHY*

When preparing for final production, a few spur sidelines with slowly varying frequency were spotted on the RF signals' spectra of the pilot batch RFFEs. It had the same frequency for all 4 channels but different frequencies among other RFFE units. Those spurs unequivocally explained occasional position measurement drifts of a few hundreds nanometers, since the spurs' frequency could get arbitrarily close to the RF carrier frequency and even pass through it as it wandered.

By investigating the issue it could be nailed down to the clock recovery circuitry inside the RFFE microcontroller board's Ethernet PHY, which generated sharp edges in the 125 MHz clock, thus producing harmonics close the BPM frequency, roughly 500 MHz. The hardware in use was a general purpose commercial microcontroller, mbed [12], which did not have precautions to avoid interferences in its carrier board. The spurs was generated at two frequencies, one related to the locally-generated TX clock, and one related the RX board, and dependent on the frequency of the Ethernet switch clock.

In order to isolate and filter out those spurious lines, a new microcontroller module was designed to serve as replacement to mbed, namely the RFFE-uC [13]. Among the measures which were taken to circumvent the issues were a better decoupling of PHY and microcontroller power supplies, EMI shielding around the PHY circuit to avoid any possible radiated noise, trace layout to reduce coupling between PHY signals and other circuits, and a better common-mode choking of the Ethernet traces. The noise from the RX clock was below the RFFE noise floor after the PHY IC was properly decoupled. The noise from the TX

clock was more resilient, and even though it was reduced by more than 30 dB with the aforementioned measures, only by adding a spread-spectrum clock generator the interference could be reduced to below the RFFE noise floor.

Figure 3 shows the RFFE channel spectra comparison between mbed and the RFFE-uC.

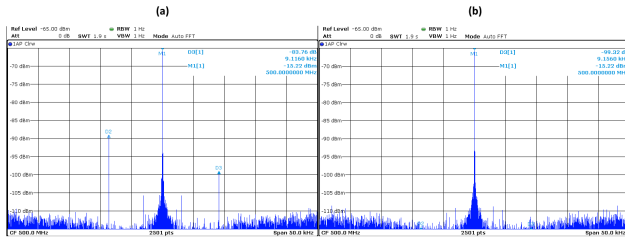


Figure 3: Comparison of RFFE output spectra when employing the mbed microcontroller board and the RFFE-uC board designed at LNLS. (a) mbed; (b) RFFE-uC.

### RFFE Attenuator

During burn-in tests several RF channels showed abrupt gain variations in the order of 0.05%, in intervals of hundreds of milliseconds or a few seconds. By taking a closer look to the problem it was found that those gain changes occurred in the Mini-Circuits DAT-31R5A-SP+ digital step attenuator. Since this behavior was not detected in prototyping phases, one of the raised hypothesis to explain such failure was that the attenuator IC batch was defective and needed replacement. However, by contacting the manufacturer it was found the DAT-31R5A-SP+ needed to be supplied with -3.6 V in one of its pins to operate in a spurious-free mode. By testing a supposedly defective DAT-31R5A-SP+ unit with -3.6 V supply on a Mini-circuits attenuator evaluation kit, it was verified that the unexpected gain variations completely vanished.

The DAT-31R5A-SP+ part number soldered to the final production boards was in fact a replacement of the DAT-31R5-SP+ part number, an older IC which became obsolete in the course of the project. By digging into the problem it was found the DAT-31R5-SP+'s datasheet required grounding one of the pins for which the DAT-31R5A-SP+'s required supplying with -3.6 V to operate in spurious-free mode, although this change in interface was not reported in the DAT-31R5-SP+'s replacement guide nor was mentioned in the datasheet. Although the investigation of the root causes by the manufacturer started very satisfactorily, with responsive replies and exchange of information, the final solution has not been reached since the manufacturer suddenly stopped replying to any of LNLS's contacts.

Fortunately a footprint-compatible replacement provided by another manufacturer was found, namely the IDT F1953. It can operate spurious-free without the need of a negative supply. Figure 4 shows the comparison of Mini-Circuits and IDT chips.

Although the replacement of the Mini-circuits DAT-31R5A-SP+ by the IDT F1953 seems to solve the reported

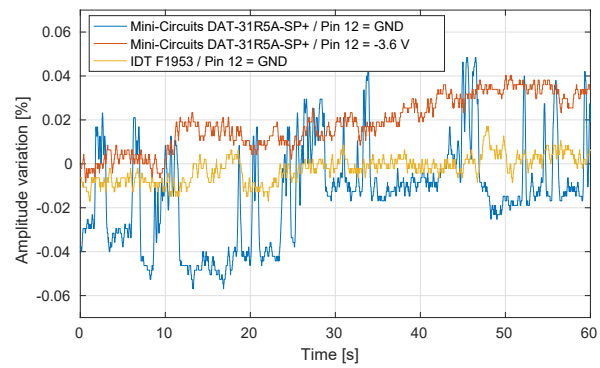


Figure 4: Attenuator gain behavior measured with R&S FSV spectrum analyzer at zero span and 5 Hz bandwidth. Mini-Circuits B14-TB-342 and IDT F1953EVB1 evaluation kits were used.

issue, its actual suitability to the design still needs to be demonstrated with a fully assembled RFFE and long term tests. At present, LNLS has not yet made a decision on whether or not to proceed with a gradual rework of all the manufactured RFFEs for making this replacement.

### Interference of Reference Clock into the RF Path

Along the project's prototyping phases, the chosen frequency of the reference clock sent through the crate backplane was  $f_{RF}/8 = 62.5$  MHz. However, during the validation tests it was noticed the 8<sup>th</sup> harmonic of such reference clock interfered with the RF signals being digitized by the ADCs, causing a dependence of the position measurements with signal's phase. This is explained by the fact that the sum of two sinusoidal waves, one with fixed amplitude and phase (the reference clock interference) and the other with varying relative phase (the RF signal), translates into a varying amplitude of the resultant signal and ultimately in the position measurements.

The solution was to choose a different reference clock for which no harmonics would interfere with the RF signal. The chosen reference was  $f_{RF} \cdot 5/36 = 69.44$  MHz, which is a revolution frequency harmonics of both booster ( $h = 828$ ) and storage ring ( $h = 864$ ) machines and is close to the previously validated reference frequency, 62.5 MHz. Figure 4 shows a comparison of position measurement sensitivity to phase variation, where a phase modulation of  $2\pi$  rad peak-to-peak of 0.2 Hz was applied to the RF generator and the power level was adjusted to provide -4 dBm at the ADC board inputs. Although the improvement is relatively small, in the order of 60 nm, it has roughly the same order of magnitude of the targeted long-term stability, 100 nm.

### System Reliability

Besides the extensive tests performed along the manufacturing process, system integration and burn-in phases, the performance tests carried out by the LNLS team proved to be an essential step for final validation. With the increase of units to be tested and within a more realistic installation



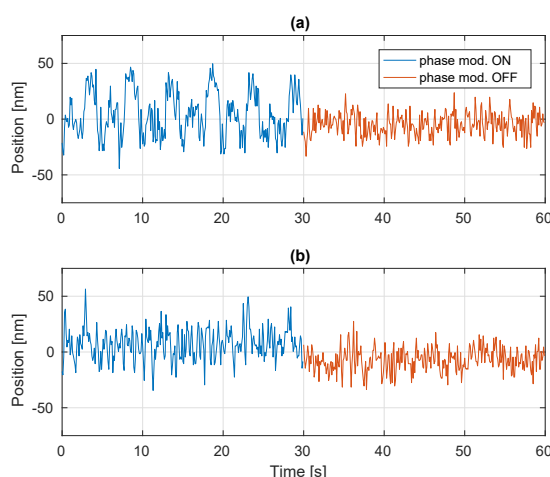


Figure 5: Position measurement variation caused by 5 Hz phase modulation in RF signal caused by reference clock interference: (a)  $f_{refclk} = f_{RF} / 8$ ; (b)  $f_{refclk} = f_{RF} \cdot 5/36$ .

scenario, issues which were not detected during prototyping phase started to emerge.

Occasional and unexpected failures such as FPGA boards' erratic resets and bad recovery from power outage helped the LNLS team to tune specific parts of the system. Other issues such as the replanning of VLAN and network routes inside the crate CPU and discovery of identification accessories affecting the tightening of SMA connectors along the RF signal path helped anticipating problems prior to the accelerators' commissioning.

At the time of writing, the true concern in terms of system reliability comes from the sporadic and unrecoverable loss of communication with RFFE modules, for which no cause has been identified yet. The first effort to overcome this issue was the implementation of a watchdog mechanism in the RFFE microcontroller to allow resetting the RFFE firmware when it is not able to receive heartbeat requests from its sole client, i.e., the MicroTCA crate CPU. This operation will happen transparently to the RF channels operation, since absolutely no effects will be caused in the digital attenuator settings, RF switching or power supplies of the RF channels.

### FPGA Gateway Update

One of the strengths of MicroTCA.4 is its hardware management capabilities. For instance it gives remote access to the JTAG bus of each AMC card in a crate for debugging, FPGA gateway programming, etc. However, besides the advertised MicroTCA capabilities, the available solution for remotely programming the FPGAs' FLASH memory via JTAG yields 40 min update time per FPGA board in the chosen MicroTCA crate model. Since this process must be done sequentially, it results in a total of 7 h and 20 min when updating a fully populated BPM crate (11 AMC boards). This unexpectedly high programming time is explained by two factors: (i) low JTAG maximum frequency, currently at

4.1 MHz; (ii) a constant exchange of messages between the Xilinx Virtual Cable (XVC) server and its clients.

The MCH vendor, N.A.T., is developing two features to overcome the aforementioned issues: a clocked JTAG Switch Module (JSM) gateway which will increase the JTAG frequency up to 20 MHz and a scriptable way of uploading SVF files to the MCH. With this two new features in place the total update time of a full crate should decrease to roughly 1 h.

Further improvement is still possible if the update is managed by the application gateway itself, and the new firmware bitstream is sent to the FPGAs via PCIe. With this mechanism implemented, the full set of 22 racks with fully populated crates could be updated at less than 5 min. There would still be the risk of corruption if the update is interrupted. In this case the previous method using the JSM could be used as fallback solution. This mechanism will be implemented by LNLS in future gateway/software releases.

## ACHIEVED PERFORMANCE

As the BPM racks were being delivered by the integrator, the LNLS team started executing the last performance tests prior to installation. A 25 m<sup>2</sup> area in the LNLS's Metrology building was made available for receiving up to 9 BPMs racks simultaneously. The building's temperature is controlled within 1 °C peak-to-peak, thus close to the planned temperature stability inside Sirius's instrumentation rooms, 20 ±0.25 °C. The setup is capable of testing 1 complete BPM rack per day. It takes 3 h for measuring beam current dependence (BCD) and resolution, 8 h for long term drift data taken, 1 hour of cables disassembling and assembling and half an hour for final checks and preparation for running the automated scripts. At the time of writing, 90 BPM electronics (8 BPM racks) have been tested, out of a total of 250 units.

All tests presented in the next sections were performed using a R&S SMA100A signal generator as RF source and timing master clock reference. The RF frequency was set to 500 MHz and the timing reference clock, provided by R&S SMA100A's auxiliary clock output, was set to 625 MHz in order to avoid artificial interferences with the RF signal. A SINAP Event Generator (EVG) was used as timing master and provided a fiber connection to the Event Receiver placed inside the BPM's MicroTCA crate. The RF signal was split by 16 (Mini-Circuits ZB16PD-72+) and further by 4 (Mini-Circuits ZFSC-4-1+) right before entering each of the BPM electronics inputs. 1 dB and 2 dB attenuators (Mini-Circuits VAT-1+ and VAT-2+) were connected to 6 units of the 1:4 splitters in order to simulate 0.5 mm off-centered beams in both planes. All unused splitter outputs were matched with 50 Ω loads.

Since the Sirius BPM Electronics employs a 2x2 RF channels switching scheme, a modified version of the *difference-over-sum* method was employed, as shown in Eqs. (1, 2). It allows better suppression of common gain drifts in the



pair of channels being swapped without meaningful loss of accuracy when compared to the standard method.

$$x = \frac{K_x}{2} \left( \frac{TO - BI}{TO + BI} - \frac{TI - BO}{TI + BO} \right) \quad (1)$$

$$y = \frac{K_y}{2} \left( \frac{TO - BI}{TO + BI} + \frac{TI - BO}{TI + BO} \right) \quad (2)$$

where  $TO$ ,  $BO$ ,  $TI$  and  $BI$  denote the amplitudes of top-outside, bottom-outside, top-inside and bottom-inside antennas in a 45°-rotated BPM.  $K_x$  and  $K_y$  are standard *difference-over-sum* BPM geometric factors, which were set to 10 mm during the performance tests for easy comparison with other reported data. Sirius's storage ring and booster button BPM geometric factors are  $K_x = K_y = 12 \text{ mm}/\sqrt{2} = 8.49 \text{ mm}$  and  $K_x = K_y = 18.1 \text{ mm}/\sqrt{2} = 12.76 \text{ mm}$ , respectively.

When varying the generator power level for testing beam current dependence (BCD) and RMS resolution, the RFFE attenuators were set accordingly to provide -5.6 dBm signal power level in the RFFE outputs, which corresponds to roughly 8% of ADCs' full-scale.

### Resolution and Beam Current Dependence

Figure 6 shows the average resolution and beam current dependence for all tested electronics at different input power levels. The horizontal axis also displays the expected signal level which will be delivered by Sirius's storage ring BPM pickups after cables. The resolution is given in two different bandwidths, from 0.1 Hz to 1 Hz and from 1 Hz to 1 kHz.

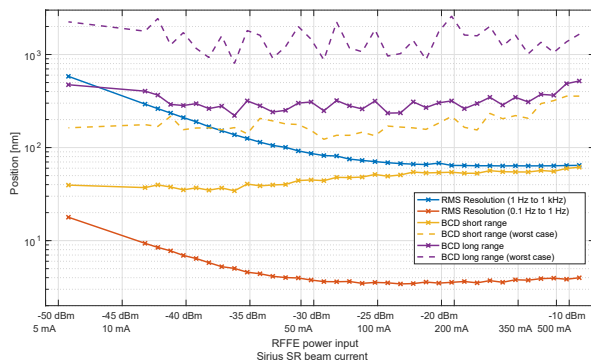


Figure 6: BCD and resolution performance.

The most stringent Sirius one sigma resolution specification is 80 nm in a 0.1 Hz to 1 kHz frequency band. These numbers are set to allow reaching position stability of 5% beam size at 1 kHz bandwidth when operating with FOFB on. Taking into account the BPM geometric factor re-scaling for storage ring button BPMs, the results show that the specified resolution can be met for beam currents from 500 mA down to 50 mA at Sirius storage ring.

BCD specifications were defined for two scenarios: (i) long range, where amplitudes are varied 30% peak-to-peak and simulates electron beam in decay mode; (ii) short range, where amplitudes are varied 2% peak-to-peak simulating

top-up operation. The targeted BCD performances are 1  $\mu\text{m}$  in long range and 100 nm in short range. The results show these performances can be met on average but are exceeded in a few BPM units.

### Long-term Drift

The Sirius BPM Electronics must reach a peak-to-peak drift performance of less than 100 nm in an 1 hour span and 5  $\mu\text{m}$  in an one week span. Figure 7 shows the 8-hour drift performance for all tested electronics, plotted as the histogram of the peak-to-peak value of position waveforms collected at 10 Hz and decimated to a 1 min sampling period. A threshold of 200 nm was set to segment the data set in BPMs with acceptable and unacceptable performances.

During the tests, a -20 dBm signal level was used at the RFFE input, roughly equivalent to a 200 mA beam current in Sirius storage ring.

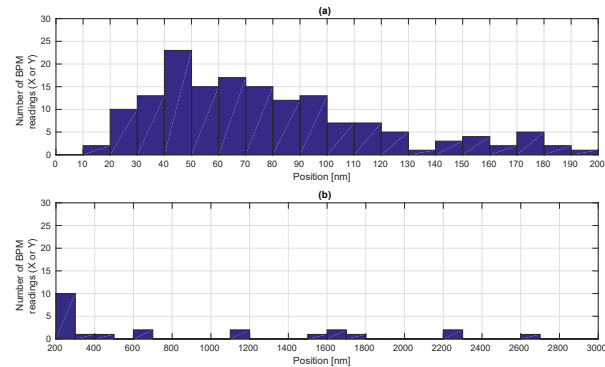


Figure 7: Peak-to-peak 8-hour drift performance histograms. (a) Position readings below 200 nm; (b) Position readings between 200 nm and 3  $\mu\text{m}$ .

The causes of the drifts above 200 nm had not yet been completely identified at the time of writing. In two BPMs (i. e. four X and Y position readings) the out-of-specification performance has been traced down to defective RFFE RF channels. For other BPMs, it has been noticed the performance is improved in the long run when the BPMs of a rack are left drifting for many days (3 or more), then slowly approaching the drift specification. It suggests the accommodation of the test setup's cables may explain some of the unwanted behavior. The issue will be further investigated.

Figure 8 shows the 8-hour drift waveforms for 20 selected BPMs where drift performance stayed below 200 nm. The traces were ordered from the highest to lowest performance BPMs.

## FUTURE PLANS

All tests herein presented were performed with CW signals. The manufactured BPM electronics should start receiving real beam signals before the end of 2018, when booster commissioning is planned to occur. Several aspects which were not covered by the described tests will have to be validated, for instance the quality of BPM cables assembly,

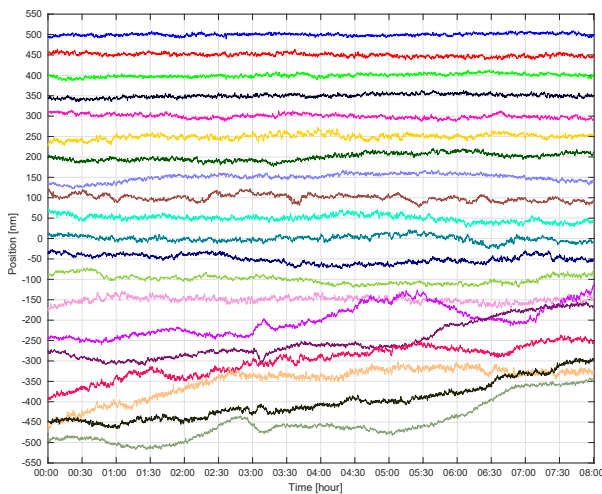


Figure 8: 8-hour drift of selected BPM readings, in ascending order of performance.

shielding and grounding, the effect of tunnel thermal stability on the long term position measurements, overall control and data acquisition software reliability and user experience.

The Sirius BPM Electronics project is rather a live project at this point in time. Bug reports and feature enhancements are posted on GitHub repositories' issue tracker and are tackled according to the priority and resources.

A few hardware projects should come on line in the first half of 2019: (i) an EPICS-controlled rack manager which will be able to provide rack's temperature monitoring and power distribution units control; (ii) fast orbit corrector Power Supply in MicroTCA RTM module [14], which will be attached to an AFC FPGA board used as FOFB controller and provide small signal analog bandwidth of 10 kHz on magnets with up to 3.5 mH inductance and 1 A maximum current.

## CONCLUSION

The Sirius BPM Electronics project is in its final stage of deployment. The reported production failure rates and achieved performance so far points to a smooth commissioning with real beam signals. Many critical issues were found along the way and solved, whereas the digital step attenuator spurious gain behavior still remains open for the already manufactured boards. Nonetheless, it seems it has not spoiled short- and long-term performances in a significant way. The issue may be very likely solved by replacing the attenuator part number on new production batches.

By adopting the strategy of developing the electronics in house, LNLS had also experienced the role of developing manufacturing processes and establishing partnerships with local and foreign companies for the task. That was a long and laborious process until reaching the required final quality. In total, 6 years have elapsed since the first conceptual ideas and the final production.

Differently from other approaches, the Sirius BPM Electronics architecture was thought as a modular system. Many parts of the system are reused in several subsystems, for instance the same FPGA AMC (AFC) design is currently shared among RF and X-Ray BPM electronics, timing system and FOFB, with the same MicroTCA crate hosting all these systems. The AFC and FMC ADC comply with the AMC and FMC industry standards and can be used in other contexts, or even be leveraged by commercially available modules, such as the CAENels FMC-Pico-1M4 picoammeter [15] used for X-Ray BPMs or Faster Technology FM-S14 FMC SFP module [16] to be used in the FOFB solution. Moreover, the RFFE module is a standalone electronics, Ethernet-controlled, which can be used in conjunction with non-MicroTCA digitizers.

The same modularity concept is present in the gateway and software solutions, where well established infrastructure was adopted as the basis for the application-specific code, for instance the Wishbone bus for interconnecting HDL cores inside the FPGA and the ZeroMQ messaging library [17].

By releasing modular, standard-compliant and open source hardware, gateway and software designs, the barriers for reusing the Sirius BPM Electronics – as a whole or by picking some of its specific modules – are significantly reduced.

## ACKNOWLEDGEMENTS

The authors would like to thank LNLS's SIL and GAE groups for the infrastructure they made available for the performance tests in the Metrology Building. We also express our gratitude to CAENels, who authorized publishing their FMC-Pico-1M4 ADC data acquisition Verilog code at our public repositories.

## REFERENCES

- [1] A. Rodrigues *et al.*, "Sirius Light Source Status Report," in *Proc. 9th Int. Particle Accelerator Conf. (IPAC'18)*, Vancouver, BC, Canada, April 29-May 4, 2018, Jun. 2018, pp. 2886–2889. doi: 10.18429/JACoW-IPAC2018-THXGBD4.
- [2] PICMG AMC Standard website. <https://www.picmg.org/openstandards/advanced-mezzanine-card/>
- [3] VITA FMC Standard website. <https://www.vita.com/fmc>
- [4] K. Scheidt and N. Hubert, Private communication, 2016.
- [5] J. Brito, S. Marques, D. Tavares, L. Russo, and G. Bruno, "A MicroTCA.4 Timing Receiver for the Sirius Timing System," presented at IBIC2018, Shanghai, China, paper WEPA01, this conference, Sep. 2018.
- [6] G. B. M. Bruno *et al.*, "Open Hardware Experience on LNLS' Beam Diagnostics," in *Proc. 16th Int. Work. on Personal Computers and Particle Accelerator Controls (PCaPAC'16)*, Campinas, Brazil, Oct. 2016, pp. 75–79. doi: 10.18429/JACoW-PCaPAC2016-THHWPLC004.
- [7] CERN Open Hardware Licence. <https://www.ohwr.org/projects/cernohl/wiki>
- [8] lns-dig: a collection of LNLS Beam Diagnostics Group open source hardware, firmware, gateway and software repositories. <https://github.com/lnls-dig>

- [9] Creotech website. <http://creotech.pl/en/>
- [10] CADService website. <http://www.cadservice.com.br/en/>
- [11] ATMOS Sistemas website. <http://atmossistemas.com.br/en/>
- [12] Mbed microcontroller board. <https://www.mbed.com>
- [13] lnls-dig/rffe-uc-hw: RFFE microcontroller module. <https://github.com/lnls-dig/rffe-uc-hw>
- [14] lnls-dig/rtm-damp-dvb: RTM Digital Amplifier design validation board. <https://github.com/lnls-dig/rtm-damp-dvb>
- [15] CAENels FMC-Pico-1M4 Floating Ammeter. <https://www.caenels.com/products/fmc-pico-1m4/>
- [16] Faster Technology FM-S14 FMC SFP. <http://www.fastertechnology.com/products/fmc/fm-s14.html>
- [17] L. M. Russo, "Software and Gateware Development for Sirius BPM Electronics Using a Service-Oriented Architecture," in *Proc. 16th Int. Conf. on Accelerator and Large Experimental Physics Control Systems (ICALEPCS'17)*, Barcelona, Spain, Oct. 2017, pp. 1736–1741. doi: 10.18429/JACoW-ICALEPCS2017-THPHA149.

# DEVELOPMENT OF BEAM POSITION MONITOR FOR THE SPring-8 UPGRADE

H. Maesaka<sup>†</sup>, RIKEN SPring-8 Center, 679-5148 Sayo, Hyogo, Japan

H. Dewa, T. Fujita, M. Masaki, S. Takano<sup>1</sup>, Japan Synchrotron Radiation Research Institute,  
679-5198 Sayo, Hyogo, Japan

<sup>1</sup>also at RIKEN SPring-8 Center, 679-5148 Sayo, Hyogo, Japan

## Abstract

A precise and stable beam position monitor (BPM) system has been developed for the low-emittance upgrade of SPring-8. The requirements for the BPM system are: (1) a single-pass resolution of 100  $\mu\text{m}$  rms for a 100 pC single-bunch and an electric center accuracy of 100  $\mu\text{m}$  rms for the initial beam commissioning to achieve the first turn, (2) a closed-orbit distortion (COD) resolution better than 0.1  $\mu\text{m}$  rms for a 100 mA stored beam and a position stability of less than 5  $\mu\text{m}$  to maintain a photon beam axis. We designed a button electrode and a BPM block and produced some prototypes for performance evaluation. The development of readout electronics based on the MicroTCA.4 standard and the evaluation of a commercial electronics have also been conducted. The prototype BPM system was installed to the present SPring-8 storage ring to confirm the performance with an actual electron beam. We obtained sufficient signal intensity, electric center accuracy, position resolution, position stability, etc. by the beam test. Thus, the new BPM system is almost ready for the SPring-8 upgrade.

## INTRODUCTION

SPring-8 has a low-emittance upgrade plan of the storage ring, SPring-8-II, to provide much more brilliant X-rays to users [1]. The beam energy is lowered to 6 GeV from the current 8 GeV and the lattice is changed to 5-bend achromat (5BA). As a result, the emittance is  $\sim 140$  pm rad without radiation damping of insertion devices (IDs) and further reduced to  $\sim 100$  pm rad by radiation damping of IDs, while the emittance of the present storage ring is 2.4 nm rad. The X-ray brilliance below 60 keV is expected to be more than 20 times higher than the present SPring-8 ring. In order to utilize brilliant X-rays, it is quite important to maintain the optical axis well within its intrinsic divergence by stabilizing the electron beam orbit. In addition, the beam orbit must be aligned to the magnetic center of each quadrupole or sextupole magnet at the commissioning stage to achieve the first beam storage, since the dynamic aperture of the new ring is narrower than the amplitude of closed orbit distortion caused by alignment error of magnets. Therefore, the resolution and the accuracy of the single-pass BPM measurement is crucial.

For the stability of the optical axis, the tolerances of the source point and the direction of X-rays are approximately 1  $\mu\text{m}$  and 1  $\mu\text{rad}$ , respectively, since the electron beam size is 28 (H)  $\times$  6 (V)  $\mu\text{m}^2$  std. and since the divergence of

X-rays is 5 (H)  $\times$  17 (V)  $\mu\text{rad}^2$  std. for 10 keV photon energy. Thus, we set the closed-orbit distortion (COD) mode BPM stability to 5  $\mu\text{m}$  peak-to-peak for 1 month. In this case, the angular stability of 1  $\mu\text{rad}$  can be expected, because the distance between the two BPMs at the both ends of a straight section for an insertion device is 5 m.

For beam commissioning, the beam must be steered within a narrow dynamic aperture of approximately 10 (H)  $\times$  2 (V) mm<sup>2</sup>. The required single-pass (SP) position resolution is 100  $\mu\text{m}$  std. for a 100 pC single-bunch. Furthermore, the electric center of each BPM must be aligned within 100  $\mu\text{m}$  std. ( $\pm 200$   $\mu\text{m}$  max.) with respect to the magnetic center of an adjacent quadrupole magnet.

In order to satisfy these requirements, we designed a button BPM electrode, BPM block and readout electronics. Some prototypes of BPM components were produced and some of them have been tested with an actual electron beam at the present SPring-8 storage ring. In this article, we describe design of the BPM system, evaluation of prototypes, result of beam test, etc.

## DESIGN AND BASIC PERFORMANCE OF THE BPM SYSTEM

### BPM Electrode and Block

We took the following things into account for the design of a BPM electrode and block.

- Sufficient signal intensity for the SP-mode.
- Small heat generation by trapped modes etc.
- Nonmagnetic materials not to distort the field of adjacent magnets.
- Same cross-section as the vacuum chamber to be connected.

As a result, we designed a BPM electrode and block, as illustrated in Fig. 1.

Button electrodes are arranged on 20 mm-wide flat surfaces on the top and bottom of the vacuum chamber with a vertical aperture of 16 mm. The button diameter was set to 7 mm and the horizontal span of the electrodes was to 12 mm in order to obtain a signal as large as possible and to fit the electrodes to the flat top. Each electrode is inserted into the hole with 8 mm diameter, and hence the gap between the hole and the electrode is 0.5 mm. A cooling water channel is equipped with the block so as to suppress the temperature rise due to an electron beam.

We selected molybdenum for the material of the electrode. Since molybdenum has a good electric and thermal conductivity, the heat generation due to trapped modes can be reduced and the temperature rise can be sup-

<sup>†</sup> maesaka@spring8.or.jp



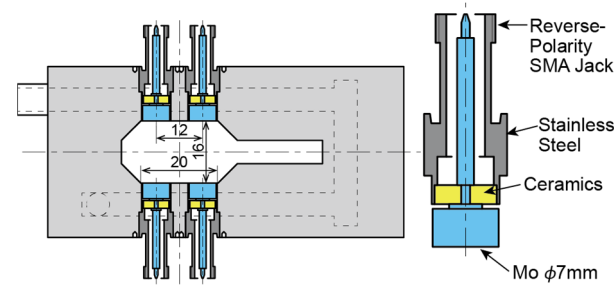


Figure 1: Schematic drawings of the BPM block (left) and the BPM electrode (right).

pressed. Since the thermal expansion coefficient of molybdenum is close to that of the insulator ceramics, it is easy to bond them together by brazing.

The material of the BPM block is stainless steel, which is the same as the other parts of the vacuum chambers. Since stainless steel has lower electrical conductivity than molybdenum, the stainless-steel part dissipates larger heat due to trapped modes than the molybdenum part. Each electrode is bonded to a block by electron-beam welding (EBW). This is because the heat input of EBW can be well controlled compared to TIG welding. Therefore, the shrinkage at the welded part is expected to be kept almost constant and the error on the electric center due to the button position difference can be suppressed.

The position sensitivity, the signal strength, trapped modes, etc. of the BPM were analyzed by using three-dimensional electromagnetic simulation code, CST Studio [2]. The position sensitivity coefficients,  $k_x$  and  $k_y$ , were computed to be 6.8 mm and 7.7 mm, respectively, when the beam position is calculated by,

$$\begin{pmatrix} X \\ Y \end{pmatrix} = \begin{pmatrix} \frac{k_x}{2} \left( \frac{V_1 - V_2}{V_1 + V_2} + \frac{V_4 - V_3}{V_4 + V_3} \right) \\ \frac{k_y}{2} \left( \frac{V_1 - V_4}{V_1 + V_4} + \frac{V_2 - V_3}{V_2 + V_3} \right) \end{pmatrix}.$$

Here,  $V_1, \dots, V_4$  are the signal intensities from the electrodes. The signal intensity from a 100 pC single-bunch was estimated to be -53 dBm at the acceleration frequency of 508.76 MHz with the bandwidth of 10 MHz. In this case, the SP-mode position resolution was expected to be 70  $\mu$ m std., which is sufficient for the requirement. The signal intensity from a stored beam of 100 mA was estimated to be -12.5 dBm at 508.76 MHz, which was sufficient for the COD-mode position resolution of 0.1  $\mu$ m std. at 1 kHz bandwidth.

The dimensions of the electrode were optimized so that the heat generation due to trapped modes was minimized. The detailed optimization process can be found in Ref. [3]. The heat dissipation in the optimized BPM electrode and block was calculated and plotted in Fig. 2. Although the natural bunch length after the upgrade is 7 ps rms, it will be longer than 10 ps for a 0.5 mA bunch current and longer than 14 ps for a 1 mA bunch current. Therefore, the heat generation in the BPM block was estimated to be 5 W maximum. The temperature of each part of the BPM block was analyzed by using ANSYS [4].

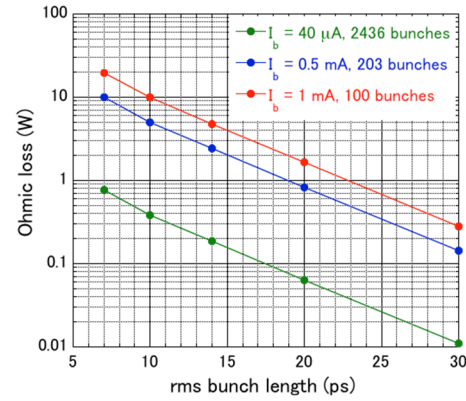


Figure 2: Calculated heat dissipation in the BPM block for the beam current of 100 mA with bunch currents of 0.04 mA (green), 0.5 mA (blue) and 1 mA (red) as functions of the bunch length.

When the BPM block is cooled by 30 °C cooling water, the maximum temperature of the electrode was estimated to be 35 °C. Thermal deformation is expected to be sufficiently small for this temperature rise.

### Prototype of BPM Electrode and Block

We ordered prototype BPM electrodes to two companies. The mechanical structure of the products from both companies are almost identical except for the slight difference in the shape of the ceramics part. The prototype electrodes were appropriately manufactured without any troubles, such as a vacuum leak. The machining error of both products was 10  $\mu$ m level, which was small enough to fulfill the requirement for the electric center error. The mechanical strength and thermal cycle reliability were also confirmed to be sufficient. We measured Time-Domain Reflectometry (TDR) waveforms to check the RF characteristics. The data from both prototypes were almost identical and consistent with the simulation.

Some prototypes of BPM blocks were also produced. The machining accuracy was sufficient to satisfy the requirement for the electric center displacement (100  $\mu$ m std., 2 $\sigma$  max.). The condition of the EBW process to attach electrodes to a block was investigated and optimized by using dummy electrodes and blocks. As a result, the shrinkage of the welded part was controlled within 50  $\mu$ m and the corresponding electric center error was estimated to be less than 80  $\mu$ m.

### Signal Cable

The BPM system uses three types of signal cables serially connected, a short cable from the BPM block (A-cable), a long cable from the accelerator tunnel to the maintenance gallery (B-cable), and a short cable to the readout electronics (C-cable). The variation of the characteristics of these cables may cause a drift of the beam position. Therefore, the cables are necessary to be stable against irradiation, temperature change, etc.

From the operation experience of the SPring-8 BPM system, the stability of the A-cable is crucial for the BPM stability. In fact, some humidity-dependent drifts were

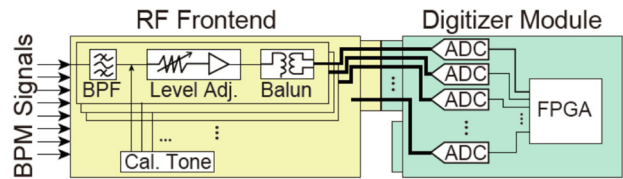


Figure 3: Schematic diagram of the MicroTCA.4-based BPM electronics.

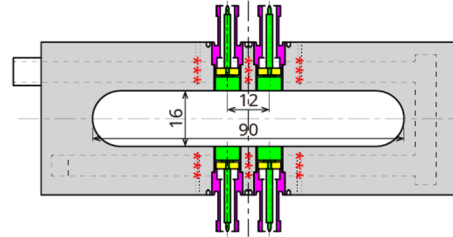


Figure 4: Schematic drawing of the BPM block for a beam test.

20 mm along the beam orbit, consisting of sixteen electrodes in total. A cooling water channel is embedded to maintain the temperature of the block. Some thermometers are inserted to holes around the electrodes (red \*\*\* part in the figure). The readout electronics is the current version of Libera Brilliance+.

### Waveform and Intensity of Raw Signals

A signal waveform from a single bunch beam is shown in Fig. 5. A Bipolar impulse signal was appropriately obtained. Although some ringing can be seen, it disappears after 2 ns where the next bunch arrives. The signal intensity for a 100 mA stored current was  $-12.5$  dBm at 508.76 MHz, which was consistent with the design value.

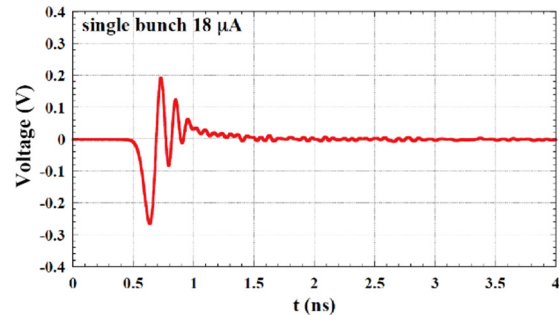


Figure 5: BPM signal waveform from a single-bunch electron beam.

## BEAM TEST

### Setup

The prototype BPM system was installed to the present SPring-8 storage ring to confirm the performance with an actual electron beam. A schematic drawing of the BPM block for the beam test is shown in Fig. 4. The vertical aperture of the vacuum chamber is the same as that of upgraded ring, but the horizontal opening is fitted to the aperture of the present ring. The position of each BPM electrode is the same as the design for SPring-8-II. The BPM block is equipped with four BPMs separated by

### Position Resolution

The position resolution was evaluated by comparing the data of the inside two BPMs with the line connecting the data from the outside two BPMs. The deviation of position data of one of the inside BPM to the reference value defined by the outside two BPMs is plotted in Fig. 6. The SP-mode data was taken with a 100 pC single-bunch and the position resolution was approximately  $70 \mu\text{m rms}$ . The COD-mode data was taken with a 100 mA stored beam and the position resolution was about  $0.01 \mu\text{m rms}$ . The position resolution is sufficient for our requirement of each detection mode.

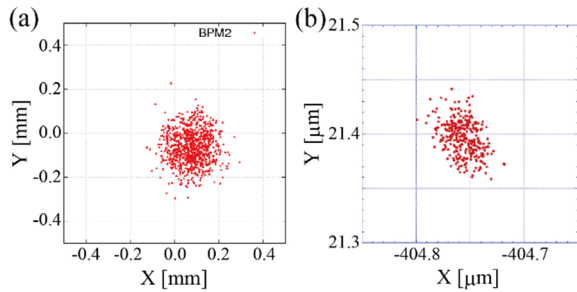


Figure 6: Beam position difference between a middle BPM data and the prediction from two BPMs at both ends. (a) is SP-mode data and (b) is COD-mode data.

### Electric Center

The electric center precision was estimated by comparing the data from the four BPMs, as shown in Fig. 7. The beam position data from all the four BPMs are well within a circle of 0.1 mm radius. This result indicates that the electric center error is within 0.1 mm for the entire BPM system. Although the statistics is not enough, we expect that the electric center can satisfy 100  $\mu\text{m}$  std. ( $2\sigma$  max.).

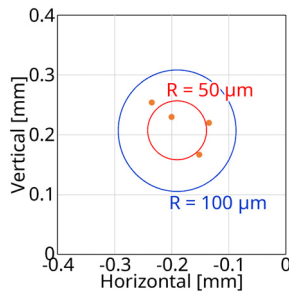


Figure 7: Beam positions from 4 BPM sets.

### Long-term Stability

We use beam position values calculated from three electrodes to evaluate the long-term stability. There are four combinations to select three electrodes and the position value from each combination is ideally identical. We define balance error as the maximum difference among the four values [5]. If the balance error shows drifts, we suspect some drifts of the BPM system.

A trend graph of the balance error is plotted in Fig. 8. Since the filling pattern was changed every 2 weeks or so, the balance error showed small jump at that time. For a constant beam condition, the fluctuation of the balance error was within 5  $\mu\text{m}$ . Thus, the long-term stability satisfies the requirement of 5  $\mu\text{m}$  peak-to-peak.

### Temperature Rise

The temperature around the BPM electrode was recorded during the beam test. The temperature difference with and without a beam was 0.1–0.5  $^{\circ}\text{C}$ , depending on the thermometer position and filling pattern. This result was consistent with the thermal analysis result by using ANSYS within 0.15  $^{\circ}\text{C}$ . Therefore, the heat input estimation and the thermal analysis are considered to be performed with sufficient accuracy. According to the thermal simula-

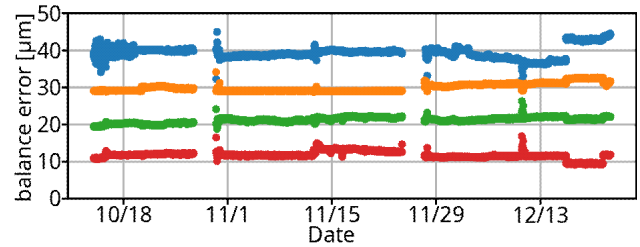


Figure 8: Trend graph of balance errors of 4 BPMs for 2.5 months.

tion, the hottest part is the molybdenum button electrode and its temperature is 35  $^{\circ}\text{C}$ . Since the temperature rise of the BPM block is appropriately estimated, the temperature of the electrode is considered to be correct enough. The deformation due to thermal expansion is negligible in case of the maximum temperature of 35  $^{\circ}\text{C}$ .

### SUMMARY

We have developed a high-resolution and highly stable BPM system for low-emittance upgrade of SPring-8. The BPM electrode and block was designed so that both enough signal intensity and enough electric center accuracy were obtained and that heat generation due to trapped modes was minimized. Some radiation-resistant coaxial cables were selected to prevent any drifts due to radiation damage of signal cables. For a readout electronics, we are developing original electronics based on the MicroTCA.4 standard and evaluating Libera Brilliance+. A beam test was performed by using a prototype BPM in the present SPring-8. The position resolution of 0.01  $\mu\text{m}$  rms was obtained for the COD-mode and 70  $\mu\text{m}$  rms for the SP-mode with a 100 pC single-bunch. The long-term stability was evaluated to be within 5  $\mu\text{m}$  for a month. The temperature rise of the BPM block was also consistent with the results of the electromagnetic simulation and the thermal simulation. Thus, the developed BPM system satisfied the requirements for the SPring-8 upgrade.

### REFERENCES

- [1] SPring-8-II Conceptual Design Report, Nov. 2014, <http://rsc.riken.jp/pdf/SPring-8-II.pdf>
- [2] CST Studio Suite, <https://www.cst.com/>
- [3] M. Masaki *et al.*, “Design Optimization of Button-type BPM Electrode for the SPring-8 Upgrade”, in *Proc. IBIC'16*, Barcelona, Spain, Sep. 2016, pp. 360–363, doi:10.18429/JACoW-IBIC2016-TUPG18
- [4] ANSYS, <https://www.ansys.com/>
- [5] T. Fujita *et al.*, “Long-term Stability of the Beam Position Monitors at SPring-8”, in *Proc. IBIC'15*, Melbourne, Australia, Sep. 2015, pp. 359–363, doi:10.18429/JACoW-IBIC2015-TUPB020
- [6] PICMG MicroTCA open standard, <https://www.picmg.org/openstandards/microtca/>
- [7] Instrumentation Technologies, <https://www.i-tech.si/>
- [8] T. Ohshima *et al.*, “Development of a New LLRF System Based on MicroTCA.4 for the SPring-8 Storage Ring”, in *Proc. IPAC'17*, Copenhagen, Denmark, May 2017, pp. 3996–3999, doi:10.18429/JACoW-IPAC2017-THPAB117



# PIN DIODE IN A MEDICAL ACCELERATOR – A PROOF OF PRINCIPLE AND PRELIMINARY MEASUREMENTS

A. Pozenel<sup>1</sup>, M. Eichinger, S. Enke, M. Furtinger, C. Kurfurst, M. Repovz  
 EBG MedAustron, 2700 Wr. Neustadt, Austria

## Abstract

The MedAustron Ion Therapy Center located south of Vienna, Austria, is a cancer treatment facility utilizing a particle therapy accelerator optimized for protons and carbon ions. The beam is injected into the synchrotron, accelerated to the desired speed and extracted to be guided into one of four irradiation rooms. During extraction a certain amount of particles is lost which is measured with a PIN diode. In this paper the measurement method of this system is presented, as well as some measurement attempts documented.

## INTRODUCTION

MedAustron is a therapy center capable of both offering cancer treatment with proton and carbon beams up to 250 MeV and 400 MeV/n, respectively. In addition to that higher energy beams up to 800 MeV will be available soon for non-clinical research purposes.

The particle beam is circulated in a synchrotron until it has reached a given energy and is then extracted to reach one of three irradiation rooms. Naturally one wants to extract in an efficient way and avoid particle losses on physical components of the accelerator. As such, thorough commissioning of the extraction process and components is needed, which heavily relies on beam diagnostic devices. One of these devices at MedAustron is the PIN system described in this paper [1].

A description of the measurement principle will be given, followed by the theoretical implementation at MedAustron and concluded by the development process, challenges and lessons learned. Finally, an outlook on further plans at MedAustron regarding the PIN system and extraction efficiency investigation will be given.

## PRINCIPLE OF OPERATION

A PIN diode is a diode with a wide intrinsic region, compared to a standard diode which has a much narrower P and N junction. The idea is to operate the diode in reverse bias mode so it does not conduct in normal conditions, except for a small dark current. When a charged particle impacts on the intrinsic region it creates electron-hole pairs. The carriers are immediately swept out of the region by the reverse bias field which creates a measureable current. The depletion region extends almost over the complete intrinsic region of the diode, and naturally the bigger the intrinsic region is, the more area there is where impacting particles can be detected.

By adjusting the reverse bias voltage across the diode anode and cathode the size of the depletion region can be influenced. Naturally, a higher voltage results in a wider region. However, a higher voltage also results in a higher dark current, which can be a problem for small signals.

## IMPLEMENTATION AT MEDAUSTRON

In MedAustron's case (see Figure 1) the diode is made from hydrogenated<sup>2</sup> amorphous silicon (a-Si:H) with chromium-gold metallization on both surfaces. The active detector area is 15 mm by 40 mm and has a thickness of 0.3-0.5 mm.

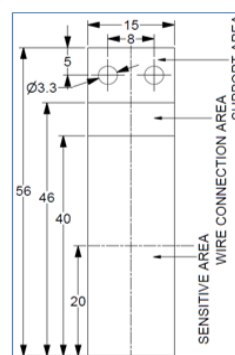


Figure 1: Mechanical structure of PIN.

The PIN diode used at MedAustron is suited for voltages from -10 V to +1 V. However, these reverse bias levels only apply for vacuum and should be applied gradually (e.g. over 30 s). Depending on the voltage level it can take up to one hour until a stable dark current is reached [2].

Connections to the electrodes are established using two clamps made from copper beryllium that can be adjusted with screws, with cables leading to two SMA connectors.

The PIN is mounted on a flange that is fixed to the beam-line and located in the extraction magnetic septum in a way that the active detector area covers most of the wall area (see Figure 2). This way, close to all particles that are lost on this surface during extraction should be detected.

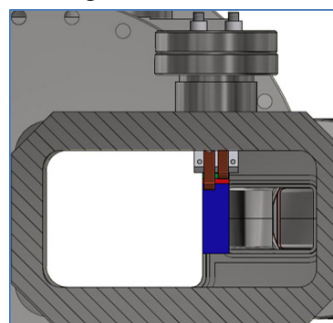


Figure 2: PIN as seen by beam.

<sup>1</sup> alexander.pozenel@medaustron.at

<sup>2</sup> Hydrogenation is necessary to improve photoconductivity in amorphous silicon



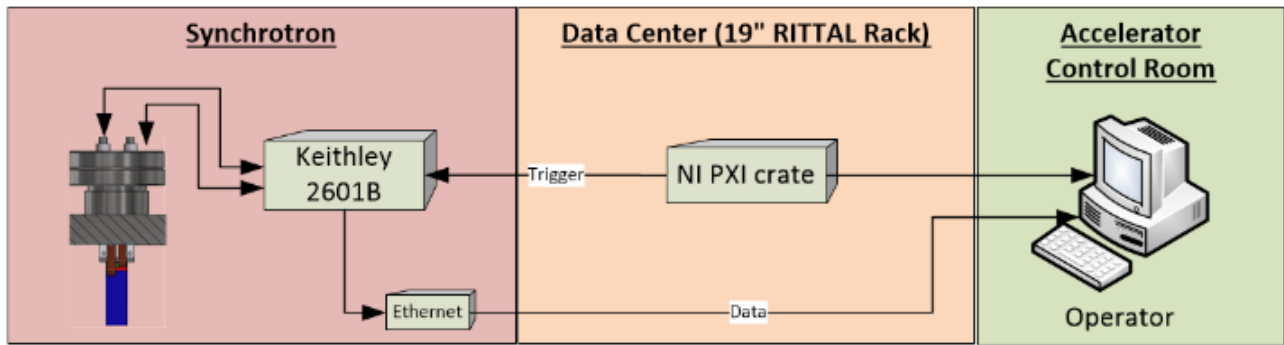


Figure 3: PIN system block diagram.

For supplying power to the diode and reading signals back a Keithley 2601B sourcemeter unit (SMU) is used. Two CB50 cables with SMU connectors, about 15 meters in length each, are used to establish a connection between the diode and the SMU. A connection to the control system is established using the Ethernet port of the SMU and the TSP-Link which is extensively explained in the manufacturer documentation [2].

Triggers for starting a measurement are provided to the device from a National Instruments PXI crate [3] via optical signals that are converted to TTL logic using a simple circuit that was developed in-house, connected to the Digital IO DSUB25.

For a complete system block diagram please refer to Figure 3. It is split into the three regions where PIN hardware or software is located.

## MEASUREMENTS SO FAR

As mentioned before, it was known from previous research and basic electrical principles that the diode has some kind of charge-up time until the depletion region is fully formed and the dark current does not change significantly any more.

The first measurements with a PIN at MedAustron were performed using the aforementioned sourcemeter connected directly to a laptop running the software KickStart available from the manufacturer. A remote desktop connection to the laptop was established from the Accelerator Control Room (ACR) and the accelerator settings were changed so a lot of beam would impact on the PIN. As can be seen in Figure 4 the current generated by the beam particles hitting the PIN is visibly measurable.

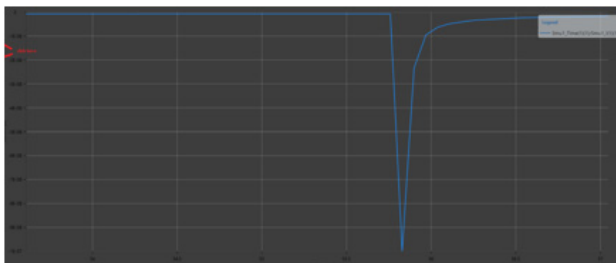


Figure 4: First PIN measurement.

With this proof of principle a complete system design was done to fit to the MedAustron Beam Diagnostic architecture. As the next step was developing a setup that would allow us to control and read out the sourcemeter remotely via MedAustron's Accelerator Control System (ACS) [4] a communication protocol needed to be chosen. It was decided to use an Ethernet connection to the sourcemeter and control it via TSP-Link.

The Controls team developed a GUI that was integrated into the accelerator control system that allows the user to change parameters like the voltage applied to the diode, the measurement time and a deadtime before values are added to the measurement. It also shows a plot of the acquired values over time, collected charge and the time elapsed since the device was turned on. This last parameter is of great importance as the manufacturer of the sourcemeter recommends a waiting time of 60 minutes before performing any measurements to guarantee a certain accuracy.

The first voltage applied was -1 V, which did beautifully show the charge-up time of the diode (see Figure 5). The oscillations can most likely be traced back to measurement noise. As one always has to send a cycle to the PIN to start a measurement of, in this case, 30 seconds interruptions between the individual measurements can be seen in the plot. From the graph one can estimate that it takes about six minutes until the dark current is somewhat stable<sup>3</sup>, i.e. does not have a significant slope any more.

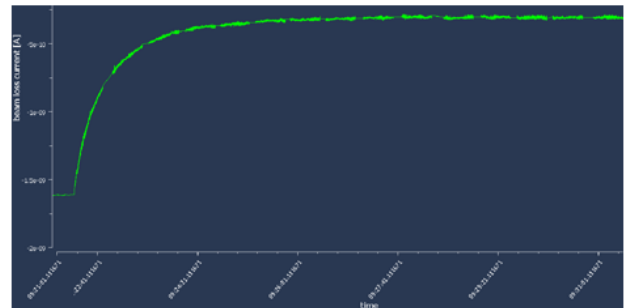


Figure 5: PIN charge-up at -1V.

The next voltage applied was +1 V, mainly to see what would happen. As expected, the results were not very good (see Figure 6) and the diode did not settle on a stable dark current. This proves that the measurement calls for the diode being used in reverse biased mode.

<sup>3</sup> Eleven 30-second increments plus some time in between to start the measurements

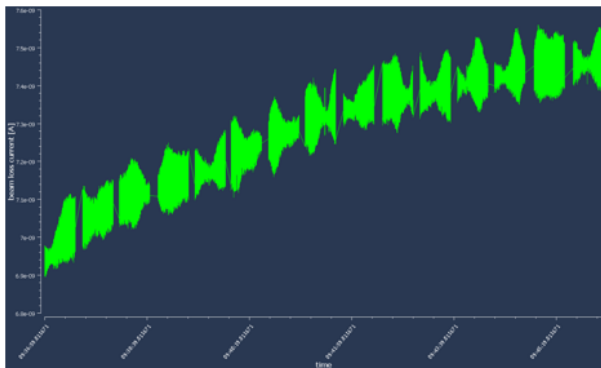


Figure 6: PIN charge-up at +1V.

Naturally, it was decided to go back to reverse bias mode with an increased voltage of -3 V. Again, the charge-up can nicely be seen in Figure 7 plus it is worth noting that it happened much faster at this voltage.

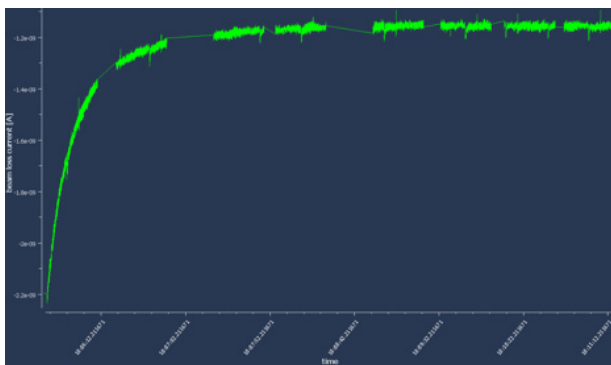


Figure 7: PIN charge-up at -3V.

It is not yet clear what the spikes visible in the plot are, as their pattern cannot be related to anything specific at the moment. More measurements are needed to investigate these occurrences, unfortunately this will not be possible in time to be included in this paper.

## SUMMARY AND CONCLUSIONS

The measurements taken seem to prove that the PIN works in principle, however there is still a great need for further investigation and fine-tuning. Further extensive studies of the PIN system's behaviour, finding of optimum parameters or acquisition of sufficient data for the investigation of impacts that machine settings have on the measurement are important topics for the future.

Further measurements are planned and will hopefully allow the relation of beam behaviour and PIN measurement. The measurements taken certainly look promising.

For the future it is planned to compare the measurement results of the PIN system to the profile intensity monitor at the immediate start of the Extraction line, the QIM.

It is furthermore planned to use the PIN to compare the efficiency of two extraction principles: RF-Knockout and Betatron extraction, the latter being the currently used one at MedAustron.

## REFERENCES

- [1] F. Osmic, M. Feurstein, A. Gyorgy, A. Kerschbaum, M. Repovz, S. Schwarz, "Overview of the Beam Diagnostic in the MedAustron Accelerator: Design Choices and Test Beam Commissioning"  
<http://accelconf.web.cern.ch/accelconf/ipac2012/papers/moppr002.pdf>
- [2] Tektronix Keithley Current SourceMeter SMU Manuals  
<https://www.tek.com/keithley-source-measure-units/smu-2600b-series-sourcemeter>
- [3] M. Caldara, H. Caracciolo, Univ. Milano Bicocca, Italy, "Diamond Detector Specifications in CNAO machine"
- [4] J. Dedič, Z. Kroflič, R. Štefanič, R. Tavčar, J. Gutleber, "Timing System for MedAustron Based on Off-The-Shelf MRF Transport Layer", Proceedings of IPAC2011, held from 4 - 9 September 2011 in San Sebastián, Spain, <https://accelconf.web.cern.ch/accelconf/IPAC2011/papers/mopc147.pdf>
- [5] J. Gutleber, A. Brett, R. Moser, M. Marchhart, C. Torcato de Matos, J. Dedič. "The MedAustron Accelerator Control System", Proceedings of ICALEPCS2011, held from 10-14th October 2011 in Grenoble, France, <http://accelconf.web.cern.ch/AccelConf/icallep2011/papers/mobaust03.pdf>

# A MICROMEGAS BASED NEUTRON DETECTOR FOR THE ESS BEAM LOSS MONITORING

L. Segui\*, H. Alves, S. Aune, T. Bey, J. Beltramelli, Q. Bertrand, M. Combet, D. Desforge, F. Gougnaud, T. Joannem, M. Keibiri, C. Lahonde-Hamdoun, P. Le Boulout, P. Legou, O. Maillard, Y. Mariette, J. Marroncle, V. Nadot, T. Papaevangelou, G. Tsiledakis, IRFU-CEA, Université Paris-Saclay, F-91191 Gif-sur-Yvette, France  
I. Dolenc Kittelmann, T. J. Shea, European Spallation Source ERIC, Lund, Sweden

## Abstract

Beam loss monitors are of high importance in high-intensity hadron facilities where any energy loss can produce damage or/and activation of materials. A new type of neutron BLM has been developed aiming to cover the low energy part. In this region typical BLMs based on charged particle detection are not appropriate because the expected particle fields will be dominated by neutrons and photons. Moreover, the photon background due to the RF cavities can produce false beam loss signals. The BLM proposed is based on gaseous Micromegas detectors, designed to be sensitive to fast neutrons and insensitive to photons (X-rays and gamma). In addition, the detectors will be insensitive to thermal neutrons, since part of them will not be directly correlated to beam loss location. The appropriate configuration of the Micromegas operating conditions will allow excellent timing, intrinsic photon background suppression and individual neutron counting, extending thus the dynamic range to very low particle fluxes. The concept of the detectors and the first results from tests in several facilities will be presented. Moreover, their use in the ESS nBLM system will be also discussed.

## INTRODUCTION

In the new high-intensity hadron linear accelerators, a small loss of the beam is capable of damaging or activating materials in the machine. Thus Beam Loss Monitors (BLM) detectors with a sensitivity to very small fraction of beam losses are required. This limit approaches the 0.01 W/m loss value, which, in the case of the ESS, means a 0.001 % of the total 5 MW power lost over 600 m.

Moreover, an important background of photon fluxes is induced by the RF cavities due to the acceleration of electrons emitted from the cavity surfaces. The electrons will generate bremsstrahlung photons when interacting with some material of the accelerator. The spectrum of the produced photons ranges from X-rays to gammas of few MeV. If the BLM is photon-sensitive this implies an irreducible background that can mislead to a false beam loss or hide a real one [1]. This is of particular relevance in the low energy part of the accelerators where only photons and neutrons are produced in a beam loss situation. For this reason, a detector insensitive to photons is proposed.

Another requirement of a BLM is to obtain information about the loss location. In the low energy part, only neu-

trons and photons are emitted, as indicated above. With thermal neutrons their location information is lost, while fast neutrons can still provide such information.

In this paper the concept and first experimental results of a new neutron Beam Loss Monitor sensitive to fast neutrons and insensitive to X-rays and gammas are presented. It is based on the Micromegas detector technology. This new neutron BLM (nBLM) was already discussed in IBIC2016 [2] presenting results from MonteCarlo simulations that had proof the concept. In this paper experimental results will be discussed. The use of these detectors is planned for the ESS nBLM system.

## NEUTRON BEAM LOSS MONITOR CONCEPT

Micromegas detectors (MICRO-MESh Gaseous Structures) [3] are a type of Multi-Pattern Gaseous Detectors (MPGD). As other MPGD detectors, Micromegas have a high gain, fast signals, and a very good spatial and energy resolution. They are largely in use in nuclear and particle physics experiments since their invention in 1996. In addition, among the Micromegas family, the bulk Micromegas technology [4] appears as a very robust detector, with a simplified manufacturing process that reduces its cost and allows its industrialization.

Micromegas detector is a two-stage avalanche chamber with three electrodes: the cathode or drift, a micromesh and an anode. The micromesh separates the two regions. First region between the cathode and the micromesh is the conversion region. The second region is defined by the micromesh and the anode and is a very narrow amplification region of the order of  $\sim 128 \mu\text{m}$ . When a charged particle enters in the conversion region it ionizes the gas producing primary electrons that are drifted towards the amplification gap by a constant electric field. In the amplification region an avalanche of electrons takes place due to the higher electric field applied in this region ( $\sim 10^5 \text{ V/cm}$ ). The Micromegas detector itself consists of the anode and the micromesh, usually constructed as a unity. The planarity between both is obtained by insulator pillars established by lithographic process. To detect neutrons (neutral particles) a neutron-to-charge converter is placed at the entrance of the drift.

The neutron BLM is conceived to be tunable to specific experimental conditions. It can be adapted to a wide range of neutron measurements with appropriate neutron-to-charge converters and neutron absorber and moderators [5]. More-

\* laura.segui@cea.fr

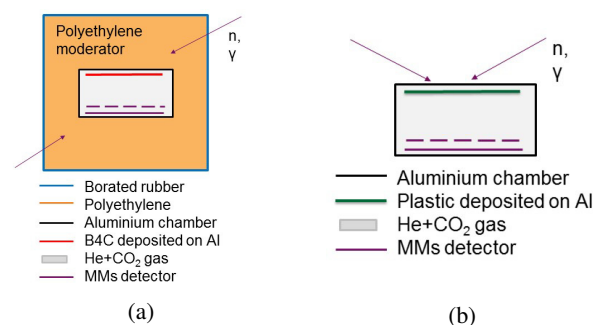


Figure 1: Neutron detection principle of the slow module (a) and of the fast one (b). More details can be found in the text.

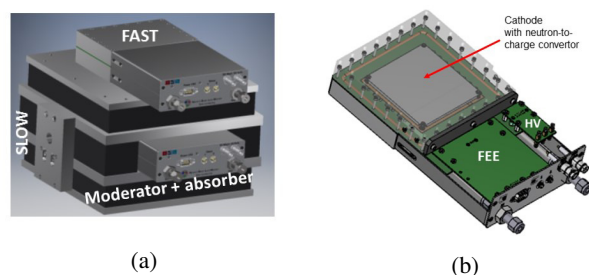


Figure 2: (a) Assembly of the fast and slow modules. They can be used as a single unity. (b) Schematic view of the Micromegas nBLM chamber. Same gas chamber and detector have been designed for both modules. Fast FEE will be mounted on-board.

## DETECTOR PERFORMANCE

The neutron BLM based on Micromegas detectors is a new application of such a detector in the field of BLM. Thus, the response of the detectors should be studied both experimentally and with MonteCarlo simulations. Initial results with Geant4 simulations to optimize the geometry were discussed in [2]. Several data campaigns have been carried out in different irradiation facilities to validate the simulations, finalize the design and proof of concept. In this section, some of the main results are discussed. A detailed paper with all the results and the comparison with Geant4 simulations is in preparation.

Measurements were done at the AMANDE (Accelerator for metrology and neutron applications for external dosimetry) installation, of the IRSN Cadarache, France. It produces mono-energetic neutron reference fields for metrology and calibration of neutron devices. Data was measured with both the fast and slow module at different neutron energies from 565 keV to 14.8 MeV. We performed measurements with different polyethylene thicknesses and different converters. For a polyethylene thickness of 5 cm, a  $^{10}\text{B}_4\text{C}$  thickness of  $1.5 \mu\text{m}$  and an active surface of  $8 \times 8 \text{ cm}^2$ , we obtain an overall efficiency of  $\sim 0.4\%$  almost constant all over the energy range. This implies we are sensitive to few counts/s for an initial neutron fluence of  $1 \text{ s}^{-1}\text{cm}^{-2}$ . Depending on the neutron



energy, a factor of 1-2 orders of magnitude lower efficiency has been observed with the fast module in agreement with the simulations.

### Gamma Rejection

During the measurements at AMANDE with the 565 keV neutrons, a LiF target was used to produce such neutronic field, including a gamma field of 6-7 MeV coming from the  $^{19}\text{F}(p,\alpha\gamma)^{16}\text{O}$  reaction. The target can be replaced by a  $\text{AlF}_3$  one what assures the production of only gammas. Data was collected in both cases with both detectors. The energy spectrum measured is shown in Figures 3 and 4 for the slow and fast detector respectively. In both cases we can see a clear rejection for gammas (red) compared to neutron+gamma (black). Applying an amplitude cut (7 keV for the slow corresponding to 0.3 V in Figure 3 and 14 keV for the fast corresponding to 2 V in Figure 4) we obtain a sensitivity of  $1.8 \times 10^{-4}$  for the slow and of  $3.6 \times 10^{-3}$  for the fast. We should mention that the drift distance in both detectors was not the same, being of 0.4 mm for the slow and 1.9 mm for the fast, what increases the rejection potential in the case of the slow due to the short interaction space for the gammas.

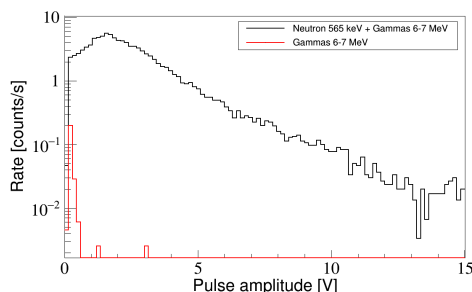


Figure 3: Response of the slow detector to the mixed field of 565 keV neutrons and 6-7 MeV gammas (black) and in the case of only gammas (red).

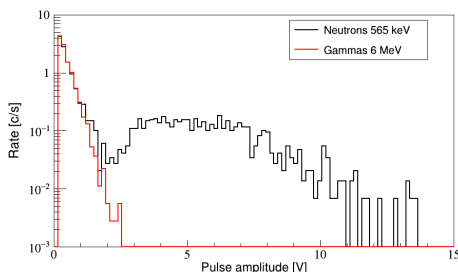


Figure 4: Response of the fast detector to the mixed field of 565 keV neutrons and 6-7 MeV gammas (black) and in the case of only gammas (red).

### Time Response

Tests were also performed at the IPHI (High-Intensity Proton Injector) proton beam installation at CEA Saclay. It accelerates protons up to 3 MeV in a pulsed beam of 90  $\mu\text{s}$

at a repetition frequency of 1 Hz. During the tests a Beryllium target was used to produce a neutron field. Data was recorded with both detectors to study their time response in a pulsed beam. Results are shown in Figures 5 and 6 for the fast and slow detectors respectively. The fast detector shows an immediate response, in agreement with the simulations. Moreover, we can see how the count rate is in direct correlation with the intensity of the beam current measured in the target (red). In the case of the slow detector, the moderator layer will delay most of the events which are recorded with a delay of few hundreds of  $\mu\text{s}$ . The measured distribution shown in Figure 6 is a convolution of the moderation time within the time duration of the beam. In the same plot we show the cumulative distribution obtained from the Monte-Carlo simulations (red) showing the delay produced by the moderator process with an instantaneous beam.

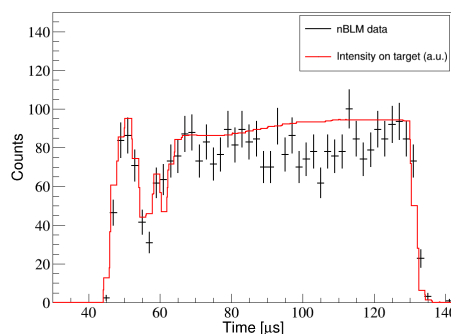


Figure 5: Time response of the fast module as measured at IPHI following the 90  $\mu\text{s}$  proton beam pulse (black). It is compared with the measured current on the neutron target (red).

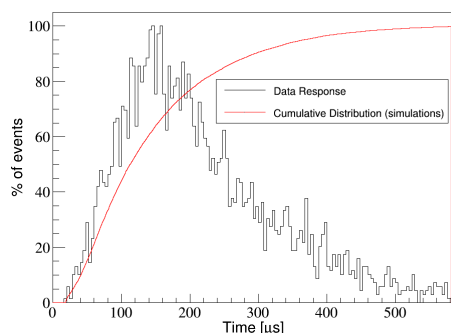


Figure 6: Time response for the slow detector as measured at IPHI following the 90  $\mu\text{s}$  proton beam pulse (black). The response is delayed with respect to the one obtained with the fast module due to the moderation process of the neutrons in the polyethylene. In red the cumulative distribution obtained from MonteCarlo simulations is also shown for a instantaneous pulse.

Other results have been obtained, like the measured rate to different beam intensities which show a linear dependency.

Moreover, the detector is planned to be installed at LINAC4 to study their response in a similar environment to the one at ESS. Specially relevant will be to study its behaviour in a RF field. This will also be studied during the commissioning of the ESS RF cavities at Uppsala or at CEA/Saclay. In addition, the electronics will be exposed to high gammas field and neutron equivalent fields to study their radiation resistance.

## ESS NBLM SYSTEM

The ESS nBLM system is one the BLM subsystems at the ESS proton linac, dedicated manly to the low energy parts of the machine. 84 detectors will be installed along the accelerator, being 42 fast and 42 slow. Most of them will be placed in the DTL tanks (41) and another 26 in the Spokes region. Even if their main region of interest is the low energy part, some of them will also be tested in the high energy region, including Spokes section, for development purposes.

The ESS nBLM system includes, besides the Micromegas detectors, the back-end electronics (BEE) and data acquisition system (DAQ), the high and low voltage power supplies, the gas system and the EPICS based control and monitoring system. The BEE is based on the MicroTCA.4 platform and the acquisition of the analogue signal of each detector is performed by an IOxOS IFC\_1410 AMC equipped with one IOxOS ADC\_3111 FMC board with 8 channels at 250 MS/s. The real time processing of the signals is done with an FPGA located on the IFC14010 card.

In the Micromegas detector each neutron will produce an individual pulse that can be identified and counted. We used ESS loss scenarios [7] as input to the Geant4 MonteCarlo simulation to study the expected response of the detectors. Results show few counts expected within 1  $\mu$ s for a beam loss of 0.01 W/m, while at high loss levels the system can experience pile-up. In this later case the number of neutrons can be recovered integrating the charge per detector. The FPGA based data processing passes from counting mode to current mode automatically and the obtained number of counts per  $\mu$ s can be correlated to the beam loss for machine protection and monitoring purposes.

## CONCLUSION

A new type of neutron Beam Loss Monitor has been presented based on the detection of fast neutrons using Micromegas detectors with a correct combination of neutron-to-charge converters and moderators. The detectors are tunable in terms of efficiency and sensitivity for different neutron flux. The nBLM aims, mainly, to enlarge the sensitivity to losses to the low energy region of an hadronic accelerator, where a neutron and photon field are dominant, although they can also be foreseen for the high energy region. To avoid the possible signals from gammas produced by the RF cavities they have been designed to have a strong gamma

to neutron suppression. Two type of detectors have been designed for the ESS nBLM system tuned to operate in the low energy parts of the ESS linac, with complementary objectives: fast reaction time when high particle fluxes are produced and monitoring of slow losses for long term activation. The response of the detectors have been proven experimentally at different irradiation facilities as discussed along the paper, with emphasis in showing their time response and their gamma rejection. More tests are foreseen in the coming months to study their response in RF field environments as LINAC4.

## ACKNOWLEDGEMENTS

The authors would like to thank V. Gressier and the IRSN team at AMANDE facility and J. Schwindling and the IPHI staff. The authors will also like to thank R. Hall-Wilton, C. Höglund and L. Robinson from the ESS Detector Coatings Workshop in Linköping, Sweden for the fabrication and production of the boron converter. L. Segui would like to acknowledge the financial support of Enhanced Eurotalents program (an FP7 Marie Skłodowska-Curie COFUND program). The project was supported by the French in-kind contribution to ESS and the H2020 project AIDA-2020, GA no.654168.

## REFERENCES

- [1] A. Zhukov, "Experience with the SNS loss monitoring and machine protection" in *Proc. North-American Particle Accelerator Conference (PAC'13)*, Pasadena, USA, Sep. 2013, paper WEYA2, pp. 174.
- [2] J. Marroncle *et al.*, "A New Beam Loss Monitor Concept Based on Fast Neutron Detection and Very Low Photon Sensitivity" in *Proc. 5th Int. Beam Instrumentation Conf. (IBIC'16)*, Barcelona, Spain, Sep. 2016, paper TUAL02, pp. 278–282.
- [3] I. Giomataris, P. Rebougeard, J.P. Robert, G. Charpak, "MICROMEGAS: a high-granularity position-sensitive gaseous detector for high particle-flux environments", *Nucl. Instr. Meth. A*, vol. 376, p. 29, 1996.
- [4] I. Giomataris *et al.*, "Micromegas in a bulk", *Nucl. Instr. Meth. A*, vol. 560, pp. 405–408, 2006.
- [5] F. Belloni, F. Gunsing, and T. Papageorgiou, "Micromegas for neutron detection and images", *Mod. Phys. Lett. A*, vol. 28, p. 1340023, 2013.
- [6] P. Legou *et al.*, "Beam Spectrometers using Micromegas in Time Projection Chamber mode" in *Proc. HB'06*, Tsukuba, Japan, 2006, paper WEBZ03, p. 256.
- [7] I. Dolenc Kittelmann and T. Shea, "Simulations and detector technologies for the beam loss monitoring system at the ESS linac", in *Proc. 57th ICFA Advanced Beam Dynamics Workshop on High-Intensity and High-Brightness Hadron Beams (HB'16)*, Malmo, Sweden, July 2016, paper THAM6Y01, pp. 553–558, 2016.

# TEST OF NEW BEAM LOSS MONITORS FOR SOLEIL

N. Hubert<sup>†</sup>, M. El Ajjouri, D. Pédeau, Synchrotron SOLEIL, 91192 Saint-Aubin, France

## Abstract

SOLEIL is currently testing new beam loss monitors to replace its pin-diode based system. The new detectors are made of plastic scintillators associated with photomultiplier and connected to Libera BLM dedicated electronics. This new detector should provide both fast (turn by turn) and slow loss measurement, post mortem capabilities and should be less sensitive to the beam directivity compared to the pin-diodes. Different methods for a relative calibration of the modules are under investigation, either using a photodiode or a cesium radioactive source. Calibration results and first measurements in SOLEIL storage ring are presented.

## INTRODUCTION

In the storage ring, the electron beam is subjected to Touschek effects and to interactions with the residual gas, causing particle losses and impacting the lifetime. These losses may be regular or irregular, fast or slow, localized or distributed.

In order to monitor these losses, 36 loss monitors have been installed along the storage ring since the commissioning of SOLEIL in 2006. These monitors consist of two PIN diodes in coincidence [1] used in counting mode (Fig 1). This system has been in operation during 12 years but with some limitations. Only slow losses are detected and the high directivity of the sensor makes the comparison between two detectors quite difficult. The count rate is indeed very sensitive to the orientation of the detector with respect to the loss source.

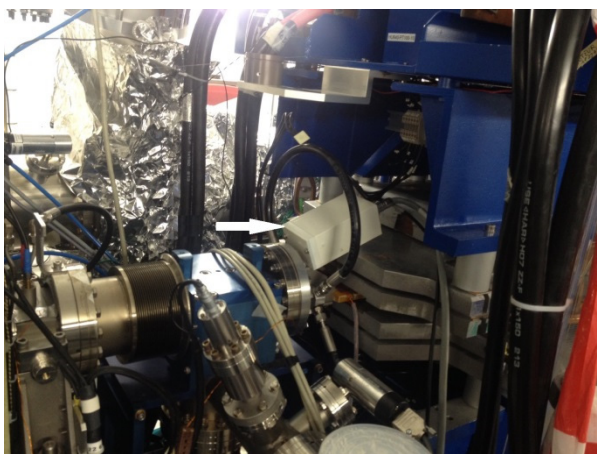


Figure 1: PIN diode loss monitor in its lead housing installed upstream of the HU640 undulator in the SOLEIL storage ring.

In order to prepare the upgrade of the system, we have decided to test new Beam Loss Monitors (BLMs) based on a scintillator and a photomultiplier.

## SYSTEM DESCRIPTION

The new BLM system has to fit the following requirements:

- Allow a relative calibration in between the detectors to enable a comparison of the losses amplitudes around the machine.
- Provide slow and fast losses measurement.

Based on the work conducted by ESRF [2], we have tested BLM modules made of a scintillator (or a quartz Cerenkov radiator) and a photomultiplier. The plastic scintillator is a rod EJ-200 [3] wrapped into high reflectivity aluminum foil to improve photon flux on photosensor input. The photomultiplier is a photosensor module from Hamamatsu (series H10721, models 110, 113 and 210 [4]).

Those two elements are embedded in a compact aluminium housing (Fig.2).

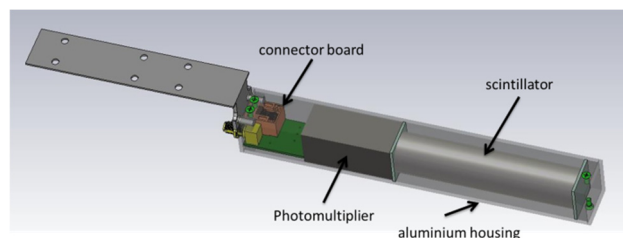


Figure 2: New BLM components and their Al housing.

The acquisition is performed by the Libera BLM electronic module which provides four 14 bits-125 MS/s ADCs together with a power supply and again control for the photosensor modules [5].

## SYSTEM CALIBRATION

Having a relative calibration between the modules in order to be able to compare the losses amplitude measured by different detectors was one of the motivations for the upgrade of the system. We ideally targeted a relative calibration between all detectors better than 10%. Two different calibration methods have been investigated: using a LED or using a cesium source.

### Diode

A dedicated housing has been realized to install a diode emitting at 455 nm, i.e. close to the maximum of the photosensor spectral response (250nm to 650 nm). The flux of the diode can be adjusted with a dedicated power-supply, whereas the photosensor is connected to the Libera BLM for acquisition and gain control (Fig. 3).

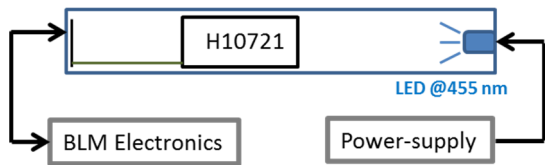


Figure 3: Setup for the calibration with a diode.

While increasing the control voltage, we have measured the gain of the different photosensors. All photosensors have a very similar gain response with respect to the control voltage, see Fig. 4.

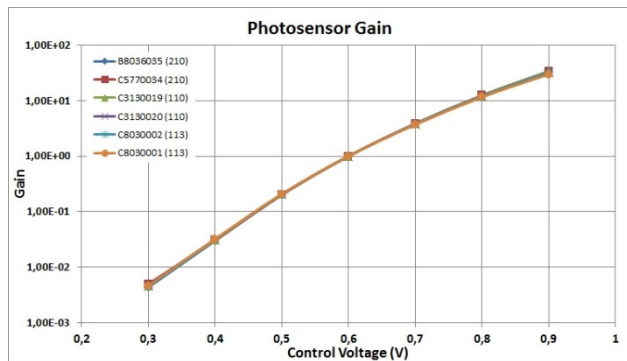


Figure 4: Gain of photomultipliers versus control voltage. Measurements have been normalized by the response value at 0.6V for each photosensor. The dispersion over the average is less than 6%

Relative sensitivity between photosensors has also been measure (for a fixed gain) and is found to be in a good agreement with the data provided by the manufacturer (Fig. 5).

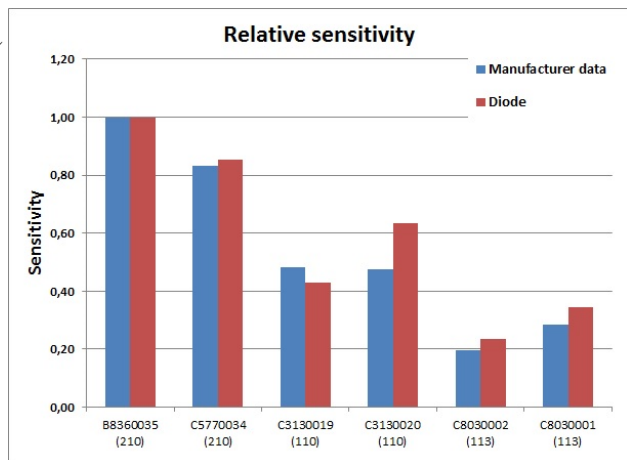


Figure 5: Relative photosensor sensitivity measured with the diode and compared with the manufacturer data (also measured with a diode).

### Source

The calibration measurement with the diode qualifies only the photosensor whereas the use of a gamma source would characterize the scintillator together with the photosensor. A cesium source has been used and placed directly on the side of the BLM housing (Fig. 6).

To determine the best position of the source in order to maximize the incident flux in the scintillator, the source position with respect to the BLM has been scanned.

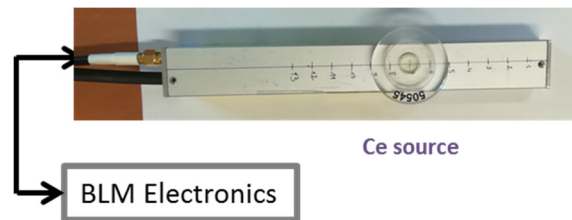


Figure 6: Source based calibration setup.

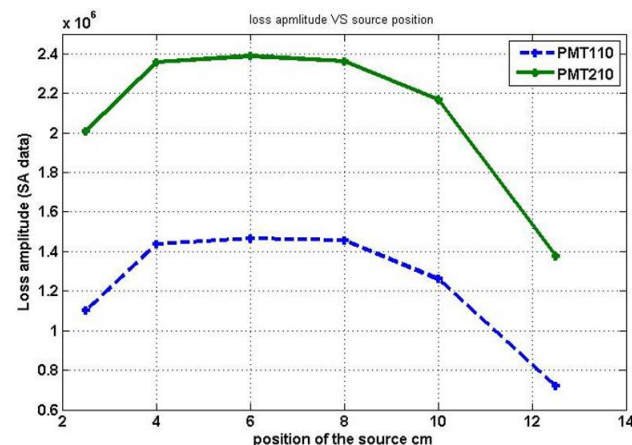


Figure 7: Loss amplitude in function of the cesium source position for a control voltage of 0.8V with PMT 110 (blue) and PMT210 (green).

As presented in Fig. 7, the maximum flux was measured for the source placed between 4 and 8 cm from the top of the housing, corresponding to the middle part of the scintillator.

Keeping the source at the same position and using the same photosensor (control voltage at 0.7V), the relative yield of the scintillators was measured. The dispersion between scintillators is small, below 5 % (Fig. 8).

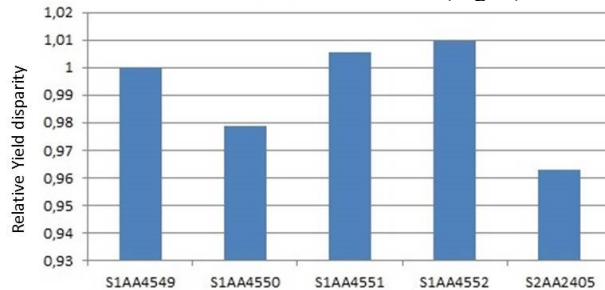


Figure 8: EJ-200 scintillator relative yield disparity.

Then, still with the source at a fixed position and using always the same scintillator, the relative sensitivity of the photosensor has been measured again with this calibration method (Fig. 9).



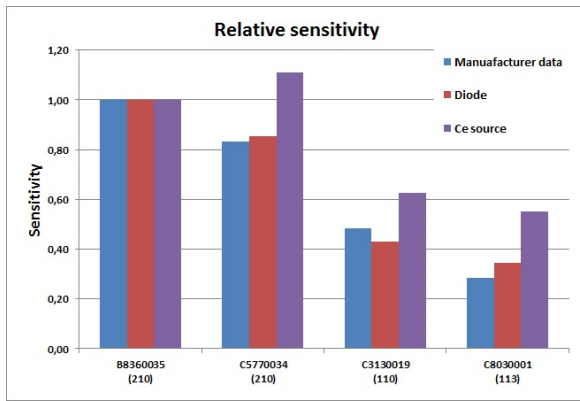


Figure 9: Comparison of the relative sensitivity for the two calibration methods.

The calibration with the cesium source gives different results compared to the calibration with the diode. This may be due to the fact that with the source, the scintillator is emitting in a broader spectrum (400 to 500 nm) compared to the diode (with dispersion in the response of the photosensors on this range).

## FIRST TESTS WITH BEAM

Four BLMs have been installed in the injection section of the SOLEIL storage ring, just behind the vertical scraper in order to be able to modulate the amount of losses and number of particles showered on the monitors (Fig 10).



Figure 10: four BLMs installed behind the vertical scraper in the injection section of SOLEIL storage ring.

The four BLMs have different configurations in terms of detector (plastic scintillator or Cerenkov radiator), in terms of photosensor type but also in terms of lead thickness around the scintillator. The aim was to compare different BLM setups. The Cerenkov radiators have the advantage of being insensitive to X-rays, which is not the case of plastic scintillators, but they produce smaller photon flux. Plastic scintillators need a thick lead shielding to be blinded from synchrotron radiation.

### Losses Versus Scraper Gap

Among the four BLMs, the closest one with respect to the storage ring vacuum chamber is used as a reference and its configuration remained unchanged during all acquisitions (PMT type 210, 2 mm lead shielding and gain voltage = 0.6V). For the other detectors, we measure the amplitude of the signal detected for different gain voltages and thicknesses (0, 1, 2 or 3mm) of the lead shielding (Fig.11).

es and thicknesses (0, 1, 2 or 3mm) of the lead shielding (Fig.11).

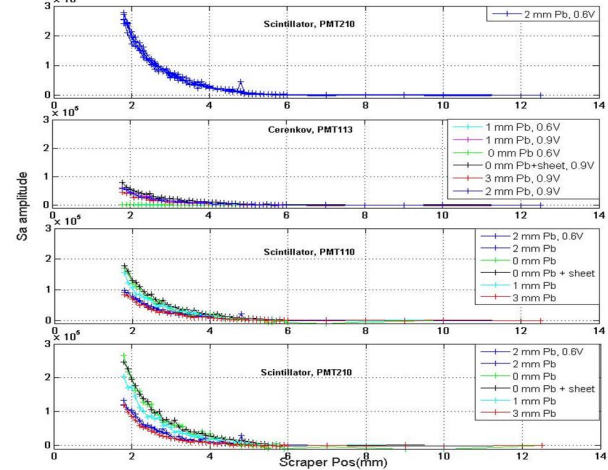


Figure 11: Loss amplitude vs scraper position for different shield thicknesses.

The signals from the two external BLMs, when operated in the same configuration, show that the distribution of lost particles is not the same on all BLMs. (the closest to the vacuum chamber measured twice the amplitude of the farthest).

It also clearly appears that, as expected, the Cerenkov radiator is far less sensitive than the plastic scintillator (by a factor ~60), and will not be retained for next tests. As expected, the sensitivity of PMT 110 is lower to PMT 210, but it is enough for our needs.

### Lifetime and Losses Correlation

The physical vertical acceptance of the storage ring is regularly checked by measuring the variation of the beam lifetime versus the vertical scraper position. This acceptance is defined as the vertical aperture of the scraper for which a change of slope in the lifetime is observed.

This measurement usually takes one hour since the lifetime measurement requires integration time. Using the BLMs installed at the scraper location, the same measurement could be performed with a better resolution and within a few minutes only. (Fig. 12).

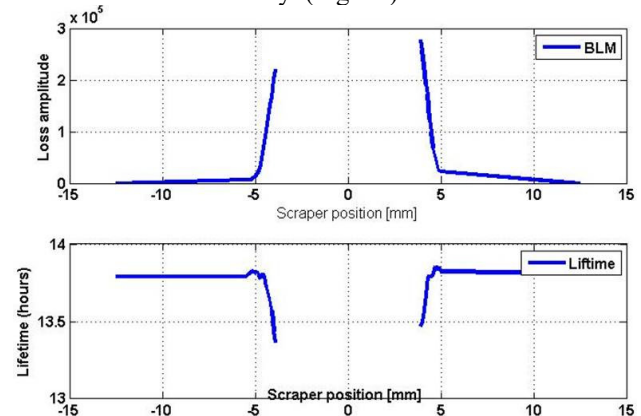


Figure 12: Physical vertical acceptance measurement of the storage ring using BLMs (top) or lifetime (bottom).

BLMs data give better resolution and measurement is performed much faster.

### Fast Losses Observation

Without beam in the storage ring, the vertical scraper is inserted. The aim is to lose all the particles injected in the storage ring on the scraper. The BLM electronics is configured in fast detection mode with an input impedance of 50 ohms. In this mode, the temporal resolution of the BLM system (8 ns) shows that the particles are not all lost on the first turn but some of them perform a second or even a third turn (Fig. 13). The temporal structure of the losses is also nicely correlated with the filling pattern of the injected beam (104 bunches or 1 bunch).

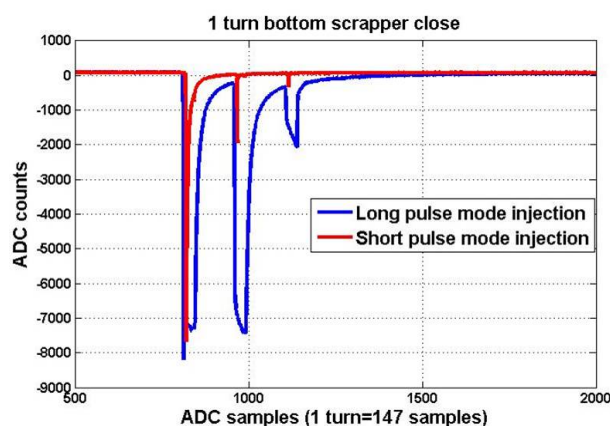


Figure 13: Fast losses versus time using BLMs in two modes of injection: long pulse mode (blue) for trains of 104 bunches and short pulse mode (red) for single bunch when the vertical scraper is inserted in the storage ring.

### Post Mortem

The BLM electronics provides a postmortem functionality which freezes the data that were recorded just before (2, 5 ms) a beam loss (Fig. 14). This functionality enables a better understanding of the origin of the loss and the postmortem data can be correlated with the data from other postmortem systems (Beam Position Monitors, bunch by bunch transverse feedback, RF system, etc.).

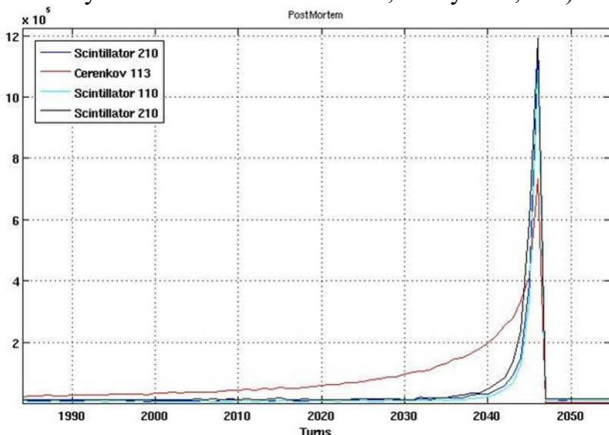


Figure 14: PostMortem data of four BLMs installed behind the scraper in the storage ring (scintillators have a

0.6V gain voltage whereas the Cerenkov has a 1V gain voltage).

## CONCLUSION

A new BLM system is currently tested at SOLEIL. The first results are very promising. Two different (laboratory) calibration methods have been tried, using a LED or a cesium source, and measurements with beam are ongoing.

Compared to plastic scintillators, quartz Cerenkov radiators did not give sufficient flux and therefore plastic scintillators with additional lead shielding has been retained for our next tests.

Compared to the current loss monitoring system in operation at SOLEIL, this new BLM system shows better sensitivity, lower directivity (by design) and enables to measure slow as well as fast losses (with a temporal resolution better than one turn). The next step will be the deployment of a large number of BLMs in two sections of the storage ring during the next winter shut down.

## ACKNOWLEDGEMENTS

The authors would like to warmly thank the ESRF Diagnostics team that designed this BLM detector and in particular Kees Scheidt and Laura Torino.

## REFERENCES

- [1] Bergoz, <http://www.bergoz.com/en/blm>
- [2] K Scheidt et al, "Prototype results with a complete beam loss monitor system optimized for synchrotron light sources", in *Proc. IPAC'15*, Richmond, VA, USA, May 2015. doi.org/10.18429/JACoW-IPAC2015-MOPTY041
- [3] Eljen Technology: <https://eljentechnology.com/products/plastic-scintillators/ej-200-ej-204-ej-208-ej-212>
- [4] Hamamatsu: <https://www.hamamatsu.com/eu/en/product/type/H10721-110/index.html>
- [5] Instrumentation Technologies: [https://www.i-tech.si/accelerators-instrumentation/libera-blm/benefits\\_15](https://www.i-tech.si/accelerators-instrumentation/libera-blm/benefits_15)

# ANALYSIS OF INTERLOCKED EVENTS BASED ON BEAM INSTRUMENTATION DATA AT J-PARC LINAC AND RCS

N. Hayashi\*, S. Hatakeyama, A. Miura, M. Yoshimoto, JAEA/J-PARC, Tokai, Ibaraki, Japan  
K. Futatsukawa, T. Miyao, KEK/J-PARC, Tokai, Ibaraki, Japan

## Abstract

J-PARC is a multi-purpose facility. Accelerator stability is the one of important issues for users of this facility. To realize stable operation, we must collect data on interlocked events and analyze these data to determine the reasons for the occurrence of such events. In J-PARC Linac, data of interlocked events have been recorded using several some beam loss monitors and current monitors, and these data have been analyzed and classified. In J-PARC RCS, new instrumentation is being introduced to obtain beam position. We discuss the present status and future plans related to this subject.

## INTRODUCTION

The Japan Proton Accelerator Research Complex (J-PARC) is a complex research facility consisting of three accelerators [1] and three experimental facilities. The first accelerator, Linac, was upgraded in 2014 by adding the Annular-ring Coupled Structure (ACS) after the separated drift-tube-linac (SDTL) and by replacing front-end system, a RF-driven ion source and a 50-mA Radio-frequency Quadrupole (RFQ). The injection system of the second accelerator, a 3-GeV Rapid-Cycling Synchrotron (RCS), was upgraded as well to accept 400 MeV  $H^-$  beams. Nominal RCS beam power of the Materials and Life Science Experimental Facility (MLF) was recovered to 500 kW in 2018. Because of the two neutron target failures in 2015, the beam power recovery program was executed with a very conservative schedule.

The design beam power for 1-MW operation was demonstrated for 1 h recently. Some fraction of the RCS beam is delivered to either the Neutrino Experimental Facility (NU) or the Hadron Experimental Facility (HD) through the Main Ring (MR) at intervals of 2.48 or 5.2 s, respectively. The beam power supplied to these two facilities was increased gradually to about 490 kW and 50 kW, respectively [2].

Availability of the facilities is as important as high beam power. To this end, the numbers of un-scheduled beam stoppage events, also called interlocked events, should be reduced. At least, it is necessary to understand the causes underlying accelerator interruption. Hence, we record and analyze interlocked events in detail. One of the J-PARC interlock subsystems is called Machine Protection System (MPS). There are several sources of MPS, for instance, mal-function of an apparatus, vacuum problem, or beam loss signal from the proportional-type Beam Loss Monitor (BLMP). Individual BLM MPS events lead to short down-times, but the number of Linac BLMP MPS events is large and comparable

to the number of RFQ MPS events. The total down-time of such events is non-negligible [2]. BLMP MPS events are classified into three categories: events associated with other machine MPS, multiple BLMP MPS events without other MPS and finally single BLMP MPS events [3].

Especially, for the Linac, most of events are single BLMP triggered MPS. Neighboring BLMPs show no specific sign of being affected. In such an event, it may not be necessary to stop operation because the beam loss signal of single BLMP event continues only for one intermediate pulse length, which is less than 1  $\mu$ s. However, in the case of RF-interlock-associated BLMP signal, the beam loss signal extends over multiple intermediate pulses. We believe that the single BLMP MPS does not represent significant beam loss. Hence, we are of the opinion that such events can be eliminated.

## INSTRUMENTATION

### Beam Loss Monitor

Most BLMs are proportional chambers [4]. The BLM detectors used in the Linac and the RCS are the same, but their operational conditions are different. In the Linac, the high voltage of the BLM detector is -2 kV, and its pre-amp input impedance is 50  $\Omega$  for better time response. Raw output signals from the signal amplifier are used for MPS in the Linac. By contrast, integral signals from BLMP are used to trigger MPS in the RCS. Different HV is applied to each BLMP because of individual optimization. High pre-amp input impedance is selected.

The present setting is excessively sensitive for the Linac, as discussed later. Therefore, we investigate a new parameter setting to reduce the number of single BLMP events. To this end, we decrease HV from -2 kV to -1.5 kV and select high impedance (10 k $\Omega$ ). Pre-amp gain is maintained at  $\times 100$ . The new settings are applied gradually because the pre-amp or the other filter module sets off an alarm if HV is lower than a certain value. Some pre-amps have a pre-set value is higher than -1.5 kV. Recent MPS statistics are presented in later.

BLMP detectors are located all over the accelerator bodies (93 in Linac and 90 in RCS). Particularly, one of the most important detectors is at the beam transport line from Linac to the 3-GeV RCS (L3BT). It is called L3BT:BLMP21, and it is located just before the first bending magnet BM01 of the 90-degree arc section. SCT12, a Slow Current Transformer for detecting beam current, is located between the last accelerating cavity ACS21 and BM01.

\* naoki.hayashi@j-parc.jp



## Data Archive System for Linac

A waveform archive system consists of many oscilloscopes (Yokogawa DL1640). Its memory can be used in a segmented memory, and the last 20 triggered waveforms are stored in memory. If an MPS event is triggered, those waveforms are archived into the permanent storage disk. The sampling rate is 100 Msamples/s, and the record length is 100 ksamples, which translates into a recording duration of 1 ms [3]. The triggering condition is optimized for instantaneous trigger stop by abandoning the monitoring function. The system has almost no dead time. All BLMP integral signals are digitized using VME ADC boards. These boards can digitize all 25-Hz pulses encountered over the last 30 min. In addition, they record the maximum values within the last two seconds and store these data in long-term data archiver.

## Data Archive System for RCS

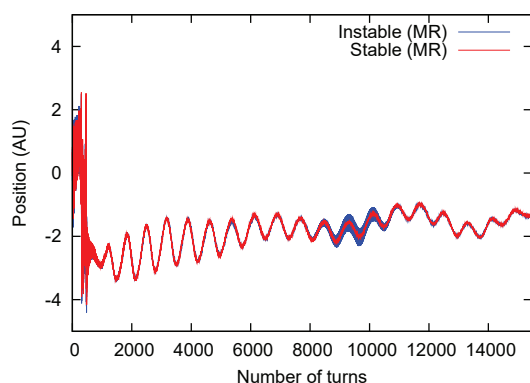


Figure 1: Bunch-by-bunch horizontal beam position data. Under the unstable condition (blue), the position data indicates slightly larger oscillation around 9000 turns.

The RCS archive system has been described in the literature [5,6]. Although its time resolution is limited, the system records all 25-Hz pulses, beam intensity, and BLMP integral signals. The RCS is required to provide a very different beam to the MLF and the MR. Hence, there is insufficient margin to satisfy the requirements of both MLF and MR at the same time. Occasionally, RCS may approach the beam instability condition. It is straight-forward to see turn-by-turn BPM (beam position monitor) data and useful to judge immediately whether instabilities occur. Libera Hadron [7] can provide bunch-by-bunch beam position online. Moreover, it can store event data whenever an interlocked event occurs. The stable beam and the slightly unstable beam are plotted in Fig. 1. The unstable part is shown in the middle of acceleration period. A BPM detector was used for tune measurement because its electrodes are configured as parallel four electrodes.

TUPA04

220

## INTERLOCKED EVENTS

### Linac Multiple BLMP Events

Such type of events are usually rare. However, last fall, the number of this type of events increased abruptly. Later, this increase was found to have been caused by a problem with the timing system. The timing system distributes three types of signals, namely, 12-MHz clock signal, 25-Hz trigger signal, and so-called “Type signal.” The “type signal” specifies the delay parameter of each instrument for the next trigger in advance. It was noticed that some “type signal” were inconsistent. Each sub-system works properly without MPS because it only follows the sequences defined by its “type signal”. Because the beam conditions are different between the MR and the MLF beams, the power supplies or other apparatuses must know the mode in which to operate for the next pulse. If a wrong “type signal” is received, the apparatuses work, but they are not synchronized properly.

It took some time to identify and solve the above-described problem because the problem is intermittent and does not reoccur for a few days at a stretch. These messy events occurred all over the Linac area, as opposed to a specific cavity or station. Hence, we suspected that the events originated in the uppermost part of the signal distributor. Probably, one of electric-optic converters degraded and the optic output signal weakened. Some receiver modules did not work properly owing to the weak signal. After replacing the electric-optic converter module, the problem disappeared, and multiple BLMP events were not detected.

### Linac Vacuum MPS Event

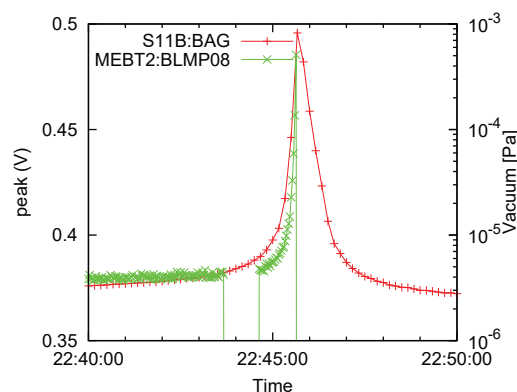


Figure 2: Occurrence of vacuum MPS events close to SDTL11 cavity. One BLMP shows increased signal owing to bad vacuum.

Occasionally, the vacuum pressure worsens and a BA gauge triggers MPS. The BA gauge threshold is  $1 \times 10^{-4}$  Pa. Particularly, worsen vacuum event often happens at SDTL section. One BLMP at MEBT2 (medium-energy beam-transport line between SDTL and ACS section) shows a very clear correlation, as in Fig. 2, although the signal is not sufficiently large to hit the MPS threshold. The BA gauge data are archived at intervals of 10 s. Hence, the pressure



data are not very precise, but the vacuum worsened and recovered by itself within a few minutes. During that period, the amplitude of the integrated BLMP signal of MEBT2 BLMP08 increased by about 20% within a short period.

### Linac BLMP Integral Signal

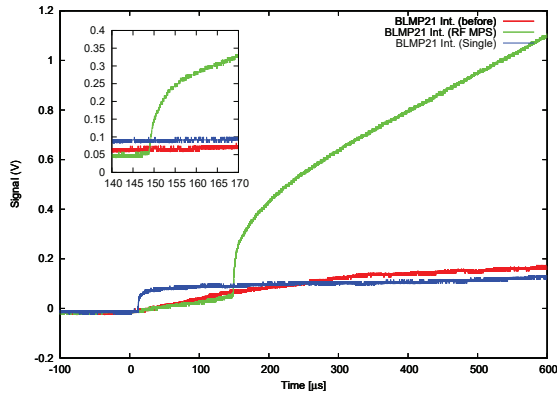


Figure 3: L3BT:BLMP21 integral signal comparison for various categories. Normal (red), RF MPS (green), and single BLMP events (blue).

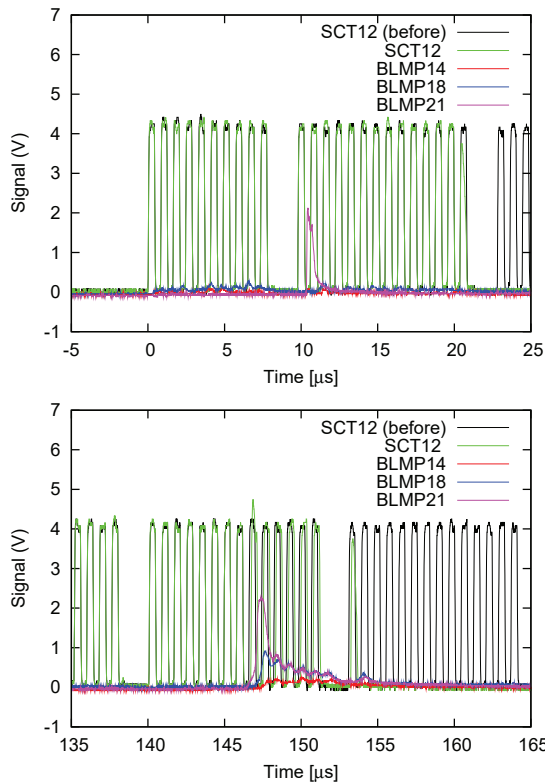


Figure 4: L3BT:BLMP raw signals and SCT for single BLMP (upper) and RF failure associated events (lower).

The BLMP signal unit provides two outputs: one is a raw waveform signal and the other is a signal integrated over 2 ms. As mentioned above, RCS uses integrated BLMP signals for MPS because they are more stable, whereas the

raw signal is used in Linac. As examples, the integrated BLMP signals of two different types of events are shown in Fig. 3. For these events, the length of the beam pulse was 320  $\mu$ s. The red part in Fig. 3 indicates a normal event. The blue part is a single BLMP (this L3BT:BLMP21 only) MPS, and it corresponds to Fig. 4 (upper). There is a small jump at the beginning, but the integral signal is lower than the normal signal after 250  $\mu$ s. The RF MPS associated BLMP event (green in Fig. 3), the signal is considerably larger at the end. However, its rise time is not adequately fast to distinguish it within 10  $\mu$ s, if MPS threshold is set to 0.3 V or higher.

### New BLMP Setting for Linac

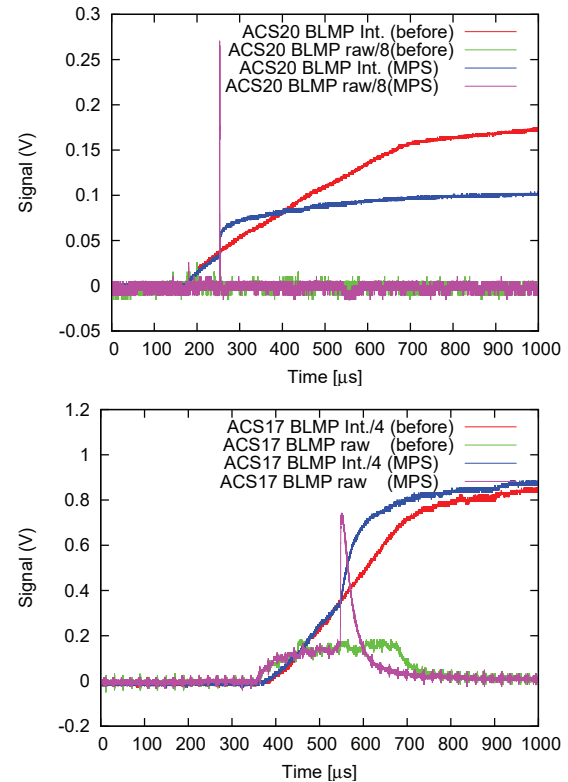


Figure 5: BLMP signals of old (upper) and new (lower) settings for various events.

A similar study was performed for the ACS section BLMP, and the new BLMP setting was applied to it. Signals of ACS20 and ACS17 BLMP are shown in Fig. 5. These BLMPs did not show any MPS event related to RF MPS. There are only single BLMP MPS events. Raw BLM signals of MPS events contain very sharp peaks, but the integrated signals of MPS event are smaller than those of normal events.

Application of the new parameters was started in user runs over the last month. As a result, the number of single BLMP events decrease significantly. Although these statistics are inadequate, the number of events seems to have decreased by one order of magnitude. Various L3BT BLMP signals are shown in Fig. 6. New (BLMP23, 27, 30) and old (BLMP21) setting data are plotted together. The expanded time window

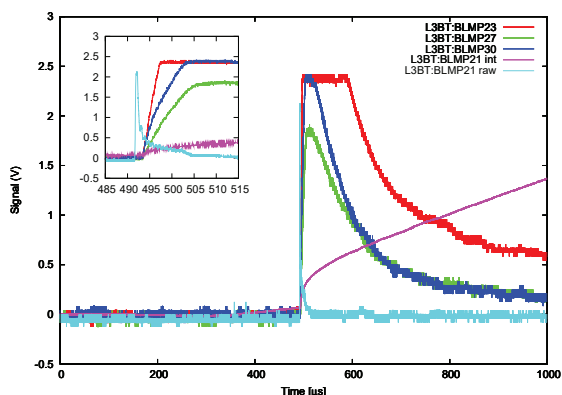


Figure 6: BLMP integral signal comparison with RF MPS events. Signals are saturated over 2 V.

is shown for visualizing the rising edges of these signals. The raw signals are fast enough to be compared with the integral of the old setting. MPS response may depend on its threshold, but even with 1 V, the response time would be within 5  $\mu$ s, which is acceptable.

### RCS BLM MPS Data

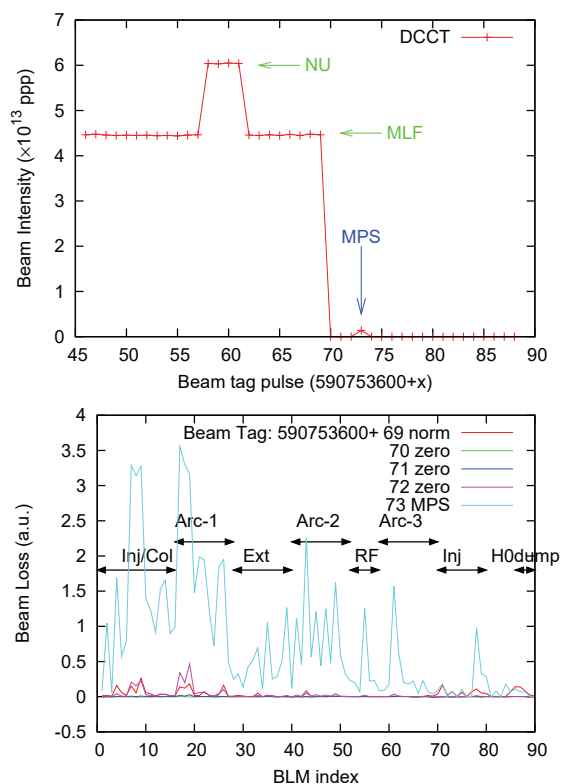


Figure 7: RCS beam intensity (up) and BLM pattern data (low) of the MPS and just before events. The intensity is almost zero for just a few pulses before. The MPS event causes massive beam loss, but its intensity is considerably lower than that of normal pulses.

The number of RCS BLM MPS events is considerably smaller than the number of Linac events. However, once an event occurs, it tends to be followed by the other events. The reason for this tendency is not known at present. The total number of RCS MPS events was about 150 over three months of user operation, whereas the number of Linac BLMP MPS events is around one thousand. Similar to Linac, these events classified into a few categories. The most major category is BLMP-only events. They can be divided into two types: only single or a few BLMP events, and multiple BLMP events. In the single BLMP case, usually, a few specific BLMPs, are located in the dispersion peak area. Most likely, the injected beam momentum is shifted slightly from the target value. This was proved by the beam position variation in the L3BT dispersion section. There were some evidences that the Linac momentum fluctuated within 0.1%. In the multiple BLMP event case, the amplitude of the BLMP signal increased, and large losses were encountered all around the ring. One example is shown in Fig. 7. It was suspected to have occurred owing to beam instability. However, it was a very low intensity event because RCS setting are very sensitive, and it is difficult to accelerate a low-intensity beam under the stable condition.

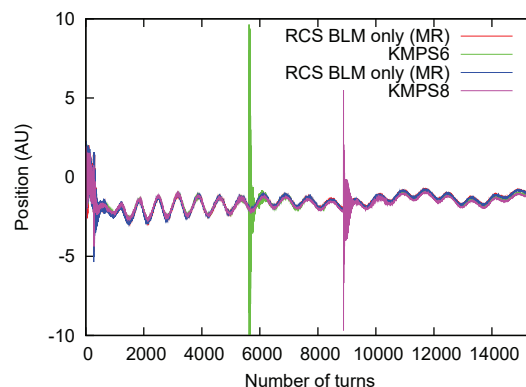


Figure 8: Same as Fig. 1, but they are kicker magnet mis-fire events (green and magenta) and large beam loss events (red and blue).

But it is not all the case. Another example is shown in Fig. 8 (red and blue), although there is no clear evidence of instability. Other than BLMP MPS, a few kicker magnet mis-fire events are shown (Fig. 8, green and cyan). The figure can be used to determine when one of the kicker magnets mis0fire and show how the beam is forced to oscillate by an accidental kicker mis-fire.

## SUMMARY

Data on MPS events caused by subsystem failure can be used to determine what should be improved. However, events caused by BLMP alone must be analyzed to determine the underlying essential reasons. The Linac BLMP encounters excessive single BLMP events, which seems to be not related to substantial beam loss. A new BLMP operational condition is investigated and applied. The number of

single BLMP events has decreased since the application of this condition. In addition, RCS MPS events were analyzed partly. However, we should continue to analyze more events and improve accelerator stability.

## REFERENCES

- [1] Y. Yamazaki eds., KEK-Report 2002-13; JAERI-Tech 2003-044.
- [2] K. Hasegawa *et al.*, in *Proc. IPAC'18*, Vancouver, BC, Canada, April 29 - May 4, 2018, pp. 1038-1040.
- [3] N. Hayashi *et al.*, in *Proc. IBIC'16*, Barcelona, Spain, Sep. 2016, pp. 368-371.
- [4] S. Lee *et al.*, in *Proc. EPAC'04*, Lucerne, Switzerland, May 2014, pp. 2667-2669.
- [5] N. Hayashi *et al.*, in *Proc. IPAC'14*, Dresden, Germany, June 12-17, 2014, pp. 3800-3802.
- [6] N. Hayashi *et al.*, in *Proc. IBIC'15*, Melbourne, Australia, September 13-17, 2015, pp. 381-385.
- [7] Libera Hadron, user manual, Instrumentation Technologies.

# COLLIMATOR FOR BEAM POSITION MEASUREMENT AND BEAM COLLIMATION FOR CYCLOTRON

Lexing Hu<sup>1</sup>, Yuntao Song<sup>†</sup>, Kaizhong Ding, Junjun Li, Qingxi Yang,  
 Institute of Plasma Physics, Chinese Academy of Sciences, Hefei, Anhui, China  
 Kai Yao, Yucheng Wu, Yonghua Chen,  
 Hefei CAS Ion Medical and Technical Devices Co., Ltd, Hefei, Anhui, China  
<sup>1</sup>also at University of Science and Technology of China, Hefei, Anhui, China

## Abstract

In order to restrict the beam dispersion and diffusion at the extraction area of the cyclotron and to detect abnormal beam loss, a beam collimator system has been designed to collimate the beam and to measure its transverse positions. The collimator system is composed of a vacuum cavity, two pairs of beam targets, a set of driving and supporting mechanism, and a measurement and control unit. The beam target with the size determined by the diameter of the beam pipe, the particle energy and beam intensity, will generate current signal during particle deposition. Each pair of beam targets has bilateral blocks which forms a slit in either horizontal or vertical direction. Servo motor and screw rod are used so that the target can reciprocate with the repeatability of less than 0.1mm. The measurement and control system based on LabVIEW can realize the motion control and current measurement of the targets and then calculate the beam transverse positions.

## INTRODUCTION

The project of superconducting cyclotron for proton therapy SC200 is under development at ASIPP (Hefei, China) and JINR, which will be able to accelerate protons to the energy 200 MeV with the maximum beam current of 400 nA [1-3].

The collimator has been developed to reduce beam diffusion at the extraction area of the cyclotron and to detect abnormal beam loss, and then to measure the beam positions in horizontal and vertical directions.

The beam collimation system works in high-radiation areas and requires high heat dissipation, radiation resistance, positioning accuracy, stability and high vacuum performance, while considering the remote operation and maintenance functions of the collimator [4].

## STRUCTURAL DESIGN

### Mechanical Design

The collimator system is composed of a support gantry, servo drive unit, a vacuum chamber, bellows, and tungsten targets.

The vacuum chamber of the collimator is connected to the beam line through the flange before and after, and the

overall leak rate is less than  $1.0 \times 10^{-11}$  Pa·m<sup>2</sup>/s. Four tungsten targets are installed respectively in the upper, lower, left and right directions of the vacuum chamber to collimate the beam and to measure its transverse positions.

The tungsten target is connected to the slide table of the lead screw through a transmission rod. A bellows is used to ensure the vacuum of the vacuum chamber. The lead screw is driven by a servo motor.

The entire collimator is mounted on the support structure, and four bolts are used to achieve height adjustment and level adjustment of the collimator.

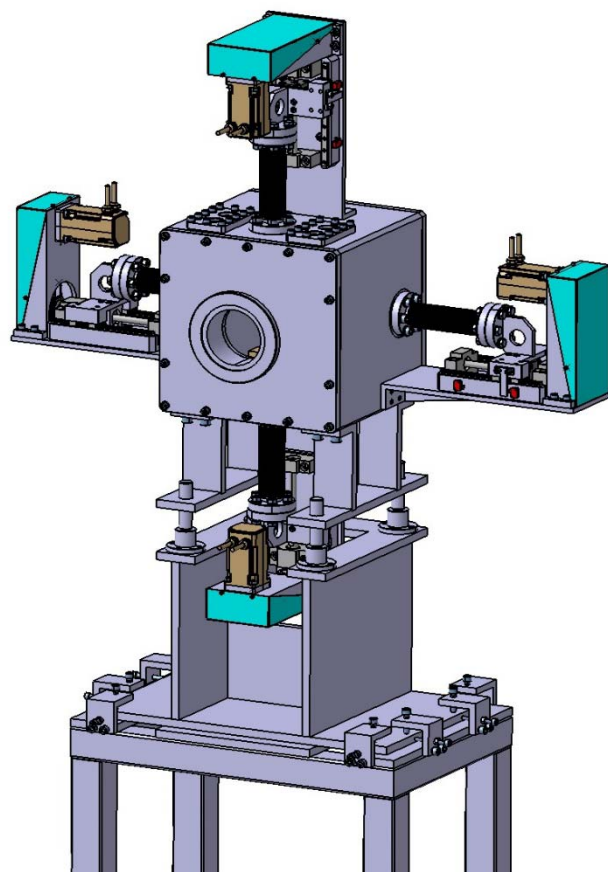


Figure 1: Layout of the collimator.

\* Work supported in part by grants 1604b0602005 and 1503062029.

<sup>†</sup> email address: hulx@ipp.ac.cn



## Installation Position

The collimator is installed at the Beam extraction area of the cyclotron, and the distance between the collimator and the centre of the cyclotron is 1.8m. The assembly picture of the collimator is shown in Fig. 2.

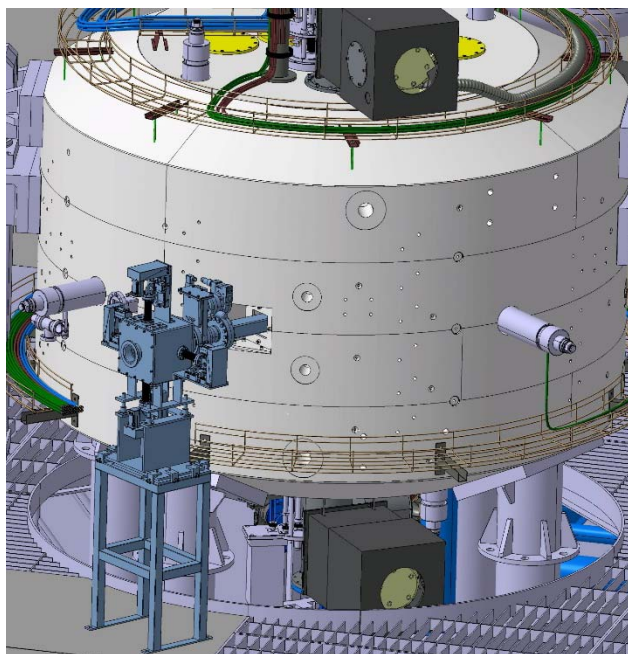


Figure 2: The assembly picture of the collimator.

## THERMAL STRUCTURAL COUPLING ANALYSIS

Thermal structural coupling analysis has been performed to provide guidance for the structural design and material selection of the collimator system.

Energy deposition occurs when beam is bombarded onto a tungsten target, so thermal analysis of the tungsten target is required. The calculation results indicates that when the insulating block material is made of peek engineering plastic, the temperature of peek is much greater than its melting point. Because of the higher thermal conductivity and higher melting point of the alumina ceramics, the material of the insulating block is replaced with alumina ceramic from peek. The calculation result which shown in Fig. 3 indicates that the maximum temperature of the target is 392.47 °C, which meets the design requirements.

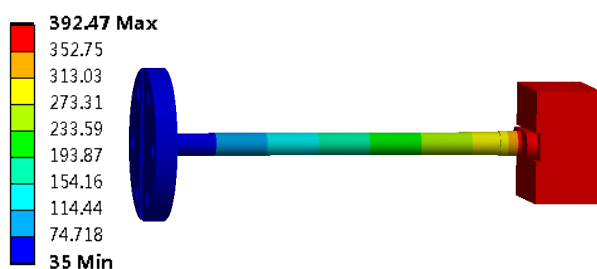


Figure 3: The distribution of the temperature field/°C.

The size of each tungsten target is 40mm×40mm×25mm. According to the design requirements, the deformation of the tungsten target and the transmission rod due to its own weight must be less than 0.5mm.

According to the thermal structure coupling calculation which shown in figure 4, the maximum deformation is 0.288mm, and it can be eliminated by applying pre-stress.

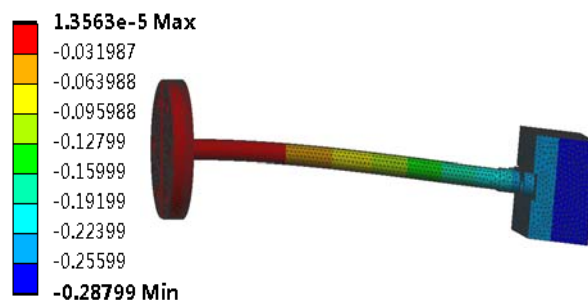


Figure 4: The distribution of the displacement.

## CONTROL SYSTEM

### Design Requirements

The control system can achieve precise control of the displacement of the collimator target and achieve high precision measurement of beam current. According to the physical design requirements, the repeat positioning accuracy is required to be higher than  $\pm 0.1\text{mm}$ , and the beam current intensity measurement accuracy is higher than  $\pm(1+5\%\text{rdg})\text{nA}$ .

### Hardware Design

The control system consists of a motion control unit and a beam current measurement unit, whose hardware architecture diagram is shown in Fig. 5.



Figure 5: Hardware architecture.

The collimator control system is built on a distributed architecture, and the NI CompactRIO real-time controller is used as the server computer to realize the integrated control of the underlying device. Four Keithley 6485 picoammeters have been adopted to realize accurate measurement of the beam current from four tungsten targets. A serial server is equipped to convert serial ports of picoammeters to one Ethernet port for integrated control and communication.

Content from this work may be used under the terms of the CC BY 3.0 licence (© 2018). Any distribution of this work must maintain attribution to the author(s), title of the work, publisher, and DOI.

Keithley 6485 picoammeters has the function of converting input current into analog voltage signal proportionately [5]. Moreover, an analog input module has been equipped for the rapid measurement of the analog voltage output by picoammeters.

In order to achieve high-precision beam collimation and adjust the beam shape and beam quality, a high precision multi-axis motion control system is designed. The motion control system uses servo motors as actuators to reduce motion errors caused by knocking. Considering that the centre position of the bunch may be offset from the centre of the axis of the collimator, the extreme position of the tungsten target crosses the centre axis, which results in the possibility of collision between the two opposing tungsten targets during the movement. In order to ensure the safety of the movement, the software limit is designed at the same time while the hardware limit switch is set to prevent the collision of the two tungsten targets.

Four servo motors are all controlled by the CompactRIO real-time controller, and the communication protocol is EtherCAT which has the advantages of good synchronization, strong real-time performance, and suitable for any topology [6].

### Software Design

As the client of the distributed system, the accelerator control system (ACS) works as the GUI client, and realizes the display, processing and storage of data. The OPC UA communication protocol is used for communication between the collimator control system and the accelerator control system.

The local control system of collimator requires functions such as data acquisition, picoammeter control, motion control, heartbeat monitoring, error handling, and master control communication, and requires synchronization of data acquisition and motion control. The components of the local control program need to communicate constantly with each other, between the components, and between the local control and the ACS. The communication logic is very complicated and difficult to implement with general control logic.

The AMC (Asynchronous Message Communication) reference library is a general-purpose LabVIEW API that can be used to transfer messages within one process, between processes, and between different LabVIEW terminals. The QMH (Queued Message Handler) design template is a general-purpose VI program architecture. The QMH design template based on the AMC API can realize the transmission and reception of messages within the process, between different processes and between different terminals [7, 8]. So the QMH design template based on AMC reference library has been adopted to achieve the programming of the software of the collimator local control system.

### TESTING AND CALIBRATION

According to the design experience, the insulation between different tungsten targets and the insulation to the ground must be greater than 100MΩ to ensure that the

leakage current is small enough, and then to increase measurement accuracy. The insulation resistances have been measured by using a megger. It is known from the measurement results that the insulation resistance between the targets of the collimator is greater than 2000 MΩ, and the insulation resistance to ground is greater than 1000 MΩ, which all meet the design requirements.

The measurement accuracy of the collimator control system may be affected by the environmental background noise, so the background noise has also been measured. The background noise measurement results are shown in Fig. 6, which indicates that the background noise is small enough.

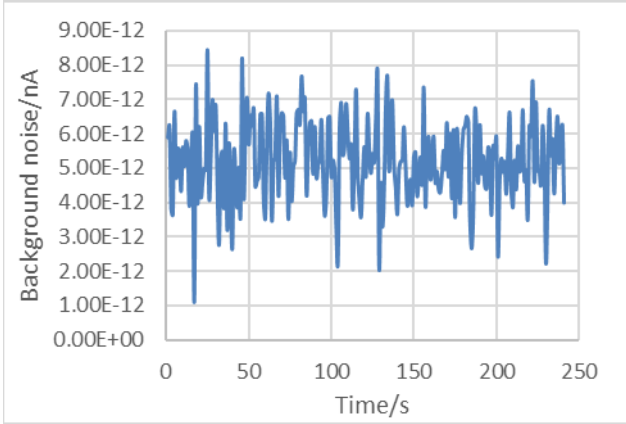


Figure 6: The background noise.

In order to ensure that the measurement accuracy of the collimator control system meets the design requirements, a high-precision current source is used as a reference signal to simulate the true beam current. The current input values are set to 15%, 25%, 50%, 75%, and 100% of the range for the 2nA, 20nA, 200nA, and 2μA ranges of the Picoammeter, respectively. Taking the ratio of the current set value to the picoammeter range as the abscissa, the relative error between the measured average value and the set value is plotted on the ordinate. The relative error of the measurement of different current input values under different ranges can be obtained, as shown in Fig. 7.

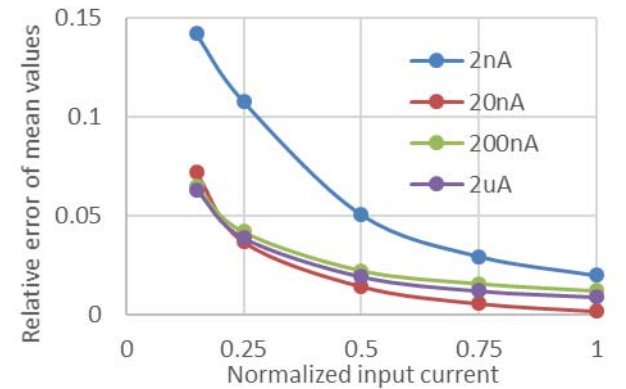


Figure 7: The relationship curves between relative measurement errors and normalized input current at different measurement ranges of the picoammeter.

As can be seen from Fig. 7, the measurement accuracy meets the design requirements.

The repetitive positioning accuracy of the transmission unit has also been measured by a micrometer to make sure that the motion accuracy meets the design requirements. And the measurement results which are shown in Fig. 8 indicate that the repetitive positioning accuracy is about  $\pm 0.006\text{mm}$ , which is much smaller than  $\pm 0.1\text{mm}$ .

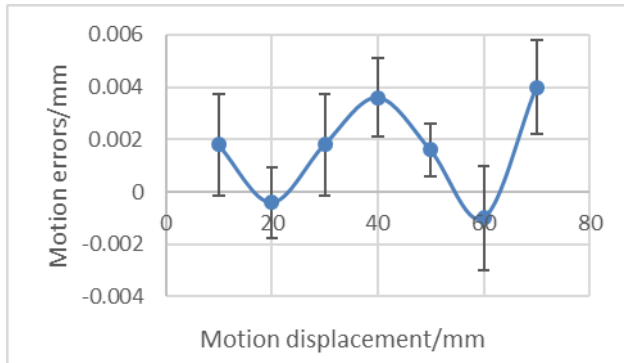


Figure 8: The repetitive positioning accuracy of the transmission unit.

## CONCLUSION

The beam collimation system has been machined and assembled, and its key parameters have also been tested, and all test items have been proven to meet design requirements.

## ACKNOWLEDGEMENTS

This work is supported in part by grants 1604b0602005 and 1503062029.

## REFERENCES

- [1] K. Ding *et al.*, “Study of the Beam Extraction from Superconducting Cyclotron SC200”, in *Proc. 21st Int. Conf. on Cyclotrons and Their Applications (Cyclotrons’16)*, Zurich, Switzerland, Sep. 2016, pp. 87-89.
- [2] G. Karamysheva *et al.*, “Compact Superconducting Cyclotron SC200 for proton therapy”, in *Proc. 21st Int. Conf. on Cyclotrons and Their Applications (Cyclotrons’16)*, Zurich, Switzerland, Sep. 2016, pp. 371-373.
- [3] G. Karamysheva *et al.*, “Research and Development of a Compact Superconducting Cyclotron SC200 for Proton Therapy”, in *Proc. 7th Int. Particle Accelerator Conf. (IPAC’16)*, Busan, Korea, May 2016, pp. 1262-1264. doi:10.18429/JACoW-IPAC2016-TUPMR016
- [4] P. Li *et al.*, “The Conceptual Design of the Collimation System in the CSRm”, in *Proc. 13th Symposium on Accelerator Physics (SAP’17)*, Jishou, China, Aug. 2017, pp. 44-47. doi:10.18429/JACoW-SAP2017-WEPH09
- [5] Tektronix Keithley 6485, Release Date 17 Sep. 2015, <https://www.tek.com/low-level-sensitive-and-specialty-instruments/series-6400-picoammeters-manual/model-6485-instruction>
- [6] EtherCAT Technical Manual, <http://www.EtherCAT.org/default.htm>
- [7] Asynchronous Message Communication (AMC) Library, <https://www.ni.com/example/31091/en>
- [8] Queued Message Handler Template Documentation, <http://www.ni.com/tutorial/53391/en>

# ARC DISCHARGE DETECTORS FOR THE CiADS SUPERCONDUCTING RF CAVITIES\*

Zaipeng Xie<sup>†</sup>, Jian Liang, Yukai Ding, Hanxiang Liu  
Hohai University, Nanjing, China

Yuan He, Yongming Li, Institute of Modern Physics,  
Chinese Academy of Sciences, Lanzhou, China

## Abstract

Arc discharge due to the electron emission is one of the key issues in the CW superconducting RF(SRF) for the CiADS particle accelerator. Arc discharges can deteriorate the SRF cavities and damage the facility. Monitoring arc discharges is important for the purpose of machine protection. In this paper, an arc discharge detector has been designed to provide fast response upon events of arc discharge using open-source hardware and LabVIEW software. Electronic design techniques are described to enhance the system stability while utilizing the flexibility of embedded electronics. The proposed detector system gives about 700 ns of response time and it employs a LabVIEW based graphic user interface. The system has the capability of detecting the instantaneous arc discharge events in real time. Timestamps of the event will be recorded to assist beam diagnostics. This paper describes the hardware/software implementation and concludes with initial results of tests at CiADS.

## INTRODUCTION

The superconducting proton LINAC has been built for the China initiative accelerator driven subcritical(CiADS) facility. In the LINAC [1], a 1.5 GeV, 10 mA proton beam is produced using the CW superconducting RF(SRF) cavities that requires a high availability for the beam diagnostics. In the CiADS SRF cavity, field emission can start at the emitters located on the cavity surface and result in electron emission. Secondary electrons can be produced from multipacting by ions, radicals, or photons. Electron emissions from cavity surfaces by thermionic and field emissions can occur in a small area of the surface and lead to a voltage breakdown that yields a gas discharge such as an arc or a glow discharge [2]. The onset of the discharge is usually accompanied by local temperature rises that can melt a small region of the emitter and produce starburst craters on the cavity surface. This process can deteriorate the cavity performance by eroding the electrode and lead to catastrophic failure in the insulator, which can eventually damage the SRF facility. Methods [3], such as the high-pressure water rinsing (HPR) and the high pulse power processing (HPP) technique, have been explored to mitigate the electron emission and arc discharge at CiADS. However, since the sources of electron emitters are caused by random material defects and contaminants introduced

during assembling, arc discharge can still occur occasionally. Arcs can be suppressed by shutting the RF power down and it requires a minimal response time on detecting an SRF arc event. Hence, fast response detectors are desired that can detect the arc discharge and abort the machine to prevent further damages.

There are only a few commercial products available for the application and they require an increased expense. Recent advances in the Internet of Things (IoT) technology has made low cost and open access scientific tools accessible to researchers in vast industrial applications. For example, Hughes et al. [4] developed a hyperion particle- $\gamma$  detector array that employs an Arduino based open source hardware to control its cryogenic fill system. Tavares et al. [5] implemented an open-source hardware platform for the BPM and orbit feedback system at the Brazilian Synchrotron Light Laboratory. Open source hardware for instrumentation and measurement [6] has been adopted in several scientific applications [7] at CERN.

This paper explores an open-source hardware solution for the arc discharge detector that can provide modularity and economic viability. One of the main consideration of this paper is to provide a fast development and deployment open-source solution with a reasonable system reliability. This paper present the basic building elements for delivering an open-hardware based infrastructure of the arc discharge detector that brings flexibility and manageability.

## SYSTEM OVERVIEW

The arc discharge detector for the CiADS superconducting RF cavities is designed as a machine protection instrument that requires a maximum 10  $\mu$ s response time on detecting an arc event. The system is triggered by the incident light near its installation site. A optical sensor is employed in the system that is connected with a fast circuit for the signal processing. Since the arc has to be in the line-of-sight, the detector is installed to the monitoring of specific elements such as the T-junction and the vacuum feed-through. The detector system requires a high level of reliability and dust deposition or irradiation of the optical fibers are also major issues that require attention. The system efficiency is determined by the maximum false alarm rate of the detector. Maintenance and testing operations are also factors that need to be taken into consideration.

Figure 1 shows a diagram of the system. The arc discharge detector is composed of a hardware and a software platform. The hardware employs an optical sensor, a cus-

\* Work supported by the National Natural Science Foundation of China (Grant No.11505255, No.91026001) and the Fundamental Research Funds for the Chinese Central Universities(2015B29714)

<sup>†</sup> zaipengxie@impcas.ac.cn



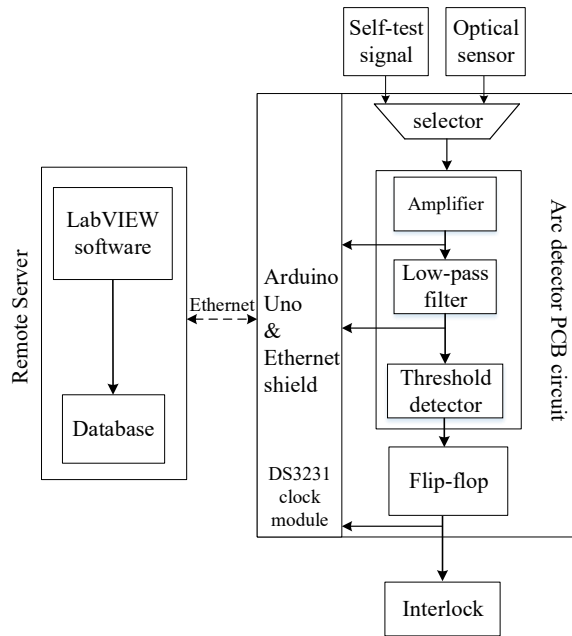


Figure 1: System diagram of the Arc Detector System for CiADS.

tomized printed circuit board (PCB) for signal processing, a PCB for supplying power, and an Arduino Uno [8] with Ethernet Shield that monitors the signal from the circuits. The output of the detector is in the form of TTL signal and is sent to an interlock system to shut down the RF power on arc events. The LabVIEW software is running on the remote server for monitoring the system in real-time.

## HARDWARE DESIGN

The hardware is implemented using a customized signal processing PCB, a PCB for supplying power, a DS3231 clock module, and an Arduino Uno and Ethernet shield board. The PCBs are connected via support pillars as shown in Fig. 2. The upper board implements the signal processing that includes amplifier, low-pass filter, voltage threshold detector,

and a flip-flop. The lower board acts as the power supply for the overall system.

The signal from the optical sensor is sent to a high-precision, high-speed operational amplifier(model OPA656 [9]). After the amplifier, the signal is passed through a low-pass filter and then sent to a voltage comparator (model TLV3502AIDR [10]) that serves as a threshold detector. The output of the comparator is captured by a D-type flip-flop (model CD74HC74M [11]) and eventually sent to the accelerator interlock system. The interlock signal is a TTL signal and it will remain HIGH at normal state and switch to LOW on detecting an arc event until the accelerator interlock system resets the arc detector.

The Arduino Uno with Ethernet shield is generally used as a digitizer to monitor the status of the PCB board via pins soldered on the board. The Arduino Uno board also plays the role of transmitting signals to a remote server via Ethernet. The signal that are passed to the Arduino Uno board includes the interlock signal, the output of the operational Amp, and the output of the comparator.

The DS3231 clock module is configured as a time manager that provides timestamps for arc and reset events. Each timestamp is sent along with the signals to the remote server so that events can be recorded in order.

## LABVIEW SOFTWARE

A LabVIEW Software is developed for monitoring the status of the hardware and its internal signals. Figure 3 shows a flow chart for algorithm of the LabVIEW program. The software is implemented as a producer-consumer model where the signal acquisition process running on the Arduino Uno board synchronizes with the process running on the remote server. The software can be configured in two mode: configuration mode and working mode. In the configuration mode, the user may reset the system from the software front panel. The system time is maintained by the DS3231 clock module and can be configured directly from the front panel. In the working mode, the software is running continuously to monitor reset and arc events. The events are stored in a MySQL database and indexed by timestamps. The current

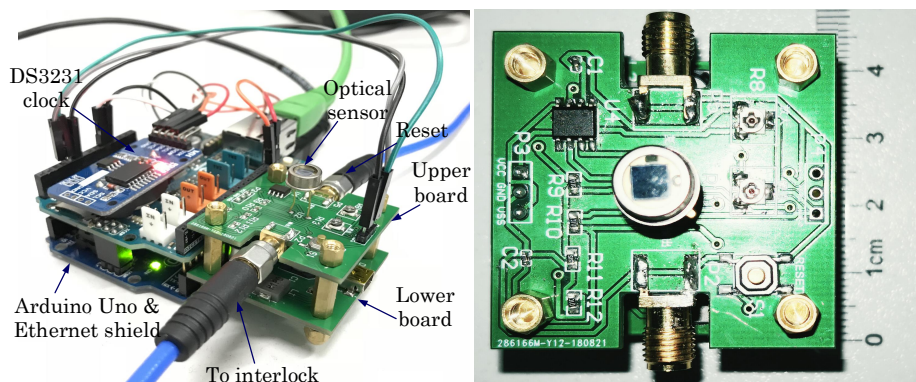


Figure 2: Annotated photograph of the assembled arc detector.

readings of the interlock signal, operational Amp signal, and the comparator signal are displayed on the front panel as waveforms.

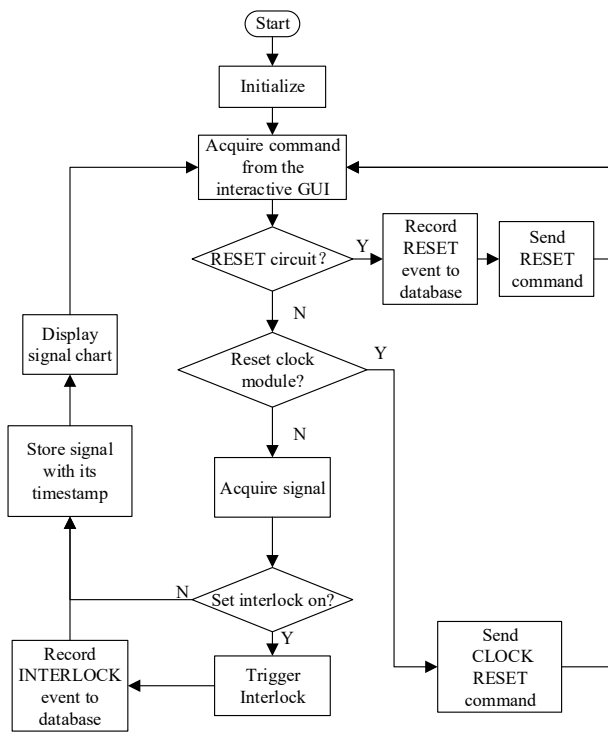


Figure 3: Flowchart for the LabVIEW software.

## EXPERIMENTAL RESULTS

In order to evaluate the arc detector system, a test bench was set up as shown in Fig. 4 where an excitation light source was utilized to simulate arc events in free space.

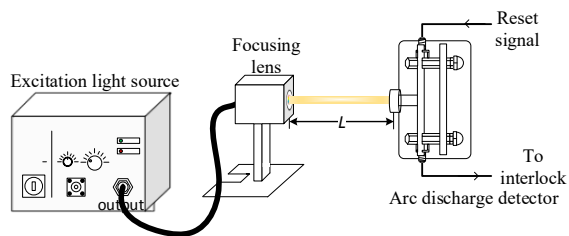


Figure 4: Setup of the testbench for the CiADS arc Detector.

The optical sensor used in our design is a Si PIN photodiode of the Hamamatsu S1223 series [12], which has a wide working range from 320 nm to 1100 nm in wavelength and a high sensitivity of about 0.45 A/W at 600 nm wavelength. In the experiments, tests were performed using a light pulse with two different wavelengths, i.e. 510 nm and 655 nm. The time width of the light pulses was set to 2000  $\mu$ s at 1 Hz rate and the rising/falling edge of the pulse was about 2.5 ns. The system latency  $\Delta T$ , defined as the time between the falling edge of input stimulus and the interlock signal, was measured as shown in Fig. 5.

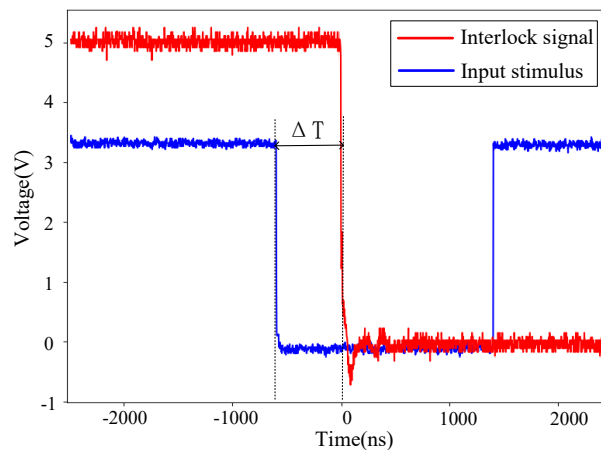


Figure 5: Measurement result of the system response time.

The time requirement of machine protection system is usually determined [13] by the beam energy, beam current and the current density. For applications in RF cavities at CiADS, the requirement for machine protection is about 10  $\mu$ s in response time. Experimental results demonstrate that the response time of the proposed arc detector is about 700 ns. The total component cost and manufacturing expense add up to \$85 USD. The response time of the electronic system is related to its bandwidth, and it can be improved by adopting electronic components with higher bandwidths, which may increase the cost.

The power consumption performance is another important factor of arc detectors. During the experiments, we measured that the average input current for the overall system is approximately 57mA and the input voltage is about 5V. Hence, the power consumption of the overall system is approximately 285mW.

## CONCLUSION

Arc discharge in SRF cavities is detrimental to the cavity performance. Fast response detectors are desired to detect arc discharge and abort the machine to prevent catastrophic failure in the SRF facility. In this paper, an arc discharge detector is designed to provide fast response upon events of arc discharge. Our implementation utilizes both open-source hardware and LabVIEW software to enhance the system stability while utilizing the flexibility of embedded electronics. The designed detector system gives about 700 ns of system latency and it can detect both the instantaneous arc event in real time. Timestamps of events can be recorded in database to assist beam diagnostics. A discussion of the hardware/software implementation and the initial results of tests at CiADS are presented.

## ACKNOWLEDGMENT

The authors would like to sincerely thank the CiADS Beam Instrumentation and SRF group at the Institute of Modern Physics, Chinese Academy of Sciences for their support and technical expertise.

## REFERENCES

- [1] S.-H. Liu *et al.*, “Physics design of the CIADS 25MeV demo facility,” *Nuclear Instruments and Methods in Physics Research Section A: Accelerators, Spectrometers, Detectors and Associated Equipment*, vol. 843, pp. 11–17, 2017.
- [2] H. Padamsee, “The science and technology of superconducting cavities for accelerators,” *Superconductor science and technology*, vol. 14, no. 4, p. R28, 2001.
- [3] T.-M. Huang *et al.*, “High Power Input Couplers for C-ADS,” in *Proceedings of SRF2015*, Whistler, BC, Canada, 2015.
- [4] R. Hughes *et al.*, “The hyperion particle- $\gamma$  detector array,” *Nuclear Instruments and Methods in Physics Research Section A: Accelerators, Spectrometers, Detectors and Associated Equipment*, vol. 856, pp. 47–52, 2017.
- [5] D. O. Tavares *et al.*, “Development of an open-source hardware platform for SIRIUS BPM and Orbit feedback,” in *Proc. of ICALEPCS 2013*, San Francisco, CA, USA, 2013.
- [6] C. Harnett, “Open source hardware for instrumentation and measurement,” *IEEE Instrumentation & Measurement Magazine*, vol. 14, no. 3, 2011.
- [7] CERN Open Hardware Repository, <https://www.ohwr.org/projects/cernohl/wiki>
- [8] M. Banzi and M. Shiloh, *Getting started with Arduino: the open source electronics prototyping platform*. Maker Media, Inc., 2014.
- [9] Texas Instruments. OPA656U Manual, <http://www.ti.com/lit/ds/sbos196h/sbos196h.pdf>, 2017-12-25.
- [10] Texas Instruments. TLV3502AIDR, <http://www.ti.com/lit/ds/sbos321e/sbos321e.pdf>, 2018-1-10.
- [11] Texas Instruments. CD74HC74M, <http://www.ti.com/cn/cn/lit/ds/symlink/cd74hc74.pdf>, 2018-2-3.
- [12] Hamamatsu S1223 Photosensor, [https://www.hamamatsu.com/resources/pdf/ssd/s1223\\_series\\_kpin1050e.pdf](https://www.hamamatsu.com/resources/pdf/ssd/s1223_series_kpin1050e.pdf), 2018-8-25.
- [13] C. Sibley, “Machine protection strategies for high power accelerators,” in *Proc. of PAC’2003*, Portland, OR, USA, vol. 1, pp. 607–611, 2003.

# THE MONTE CARLO SIMULATION FOR THE RADIATION PROTECTION IN A NOZZLE of HUST-PTF\*

Y.C. Yu, P. Tan†, H.D. Guo, L.G. Zhang, Y.J. Lin, X.Y. Li, Y.Y.Hu

State Key Laboratory of Advanced Electromagnetic Engineering and Technology,  
School of Electrical and Electronic Engineering, Huazhong University of Science and Technology,  
Wuhan 430074, China

## Abstract

Nozzle is the core component in proton therapy machine, which is closest to the patient and is necessary to consider the radiation impacts on patients and machine. The ionization chamber and the range shifter in active scanning nozzle are the main devices in the beam path that affect the proton beam and produce secondary particles during the collision, causing damage to the patients and machine. In this paper, the spatial distribution of energy deposited in all regions, the distribution of the secondary particles of 70-250MeV proton beam in the nozzle in Huazhong University of Science and Technology Proton Therapy Facility(HUST-PTF) are studied with Monte Carlo software FLUKA in order to provide reference for radiation shielding design. Six types of materials commonly used today as range shifters are analyzed in terms of the influence on radiation,so that the most suitable material will be selected.

## INTRODUCTION

In order to ensure the safety of the patients, as well as the machine, the effect of radiation should be considered when designing the nozzle. Due to the application of the active scanning nozzle in HUST-PTF, the collimator and scatter are not required on the beam path, so the scattering and secondary particle radiation will be significantly reduced[1].However, it is still necessary to analyze the radiation distribution in the nozzle and develop a corresponding radiation shielding scheme. At the end of nozzle, a range shifter is placed very close to the patient in order to decrease the proton beam energy so that the shallow tumors can be treated. Selecting a suitable material for the range shifter will significantly reduce its radiation impacts on patients.

The scanning nozzle is mainly composed of a vacuum window, a pixel ionization chamber, a helium pipe, an ion chamber, and a series of mechanical support structures in Huazhong University of Science and Technology Proton Therapy Facility(HUST-PTF). The vacuum window, made of 30μm kapton, is installed at the end of the beamline as a boundary between the beamline transmission system and the nozzle system. The pixel ionization chamber is used to monitor the initial beam states which is located 100mm away from the vacuum window. The helium pipe, passing through two scanning magnets, is placed behind the pixel

ionization chamber to reduce energy loss and transverse scattering. The plate ion chamber is placed 800 mm from the isocenter plane and is used to monitor the position and the dose of the proton beam, so that the accuracy of the dose and position can be ensured. The structure of pixel ionization chamber and plate ion chamber in HUST-PTF is shown in Fig.1. In order to simulate the human body composition, a water phantom is placed after the isocenter plane. The structure of nozzle in HUST-PTF is shown in Fig. 2.

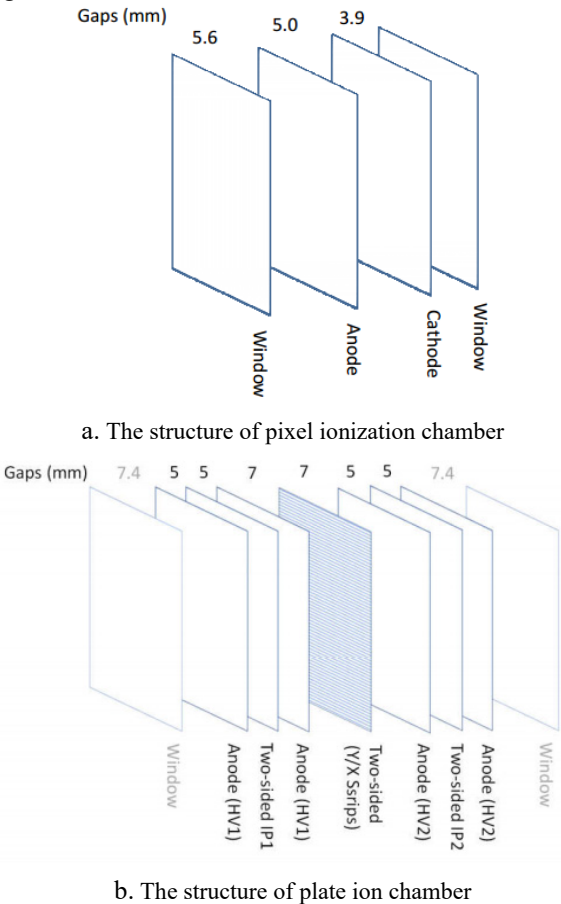


Figure 1: The structure of pixel ionization chamber and plate ion chamber.

In this paper, the model of the nozzle in HUST-PTF is constructed in three dimensions by using the Monte Carlo software FLUKA[2]. The energy loss when the proton beam passes through the nozzle, the secondary particle yield, the spatial distribution of neutrons and photons are calculated by using FLUKA. At the same time, the

\* Work supported by National Key R&D Program of China (No.2016YFC0105308)  
† Corresponding author, tanping@mail.hust.edu.cn



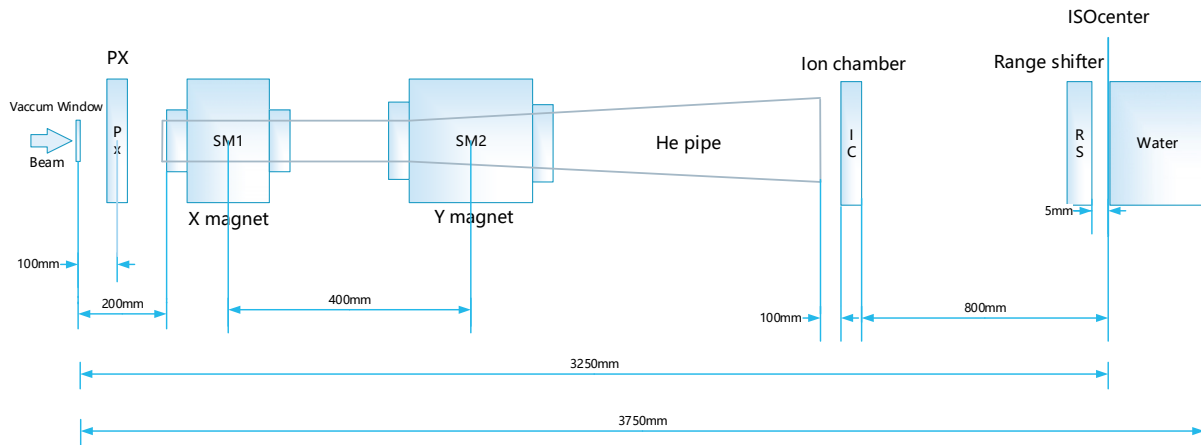


Figure 2: The structure of the nozzle in HUST-PTF.

influence of range shifters made of different materials are also calculated.

### SPATIAL DISTRIBUTION OF ENERGY DEPOSITED IN NOZZLE

Due to the Coulomb's scattering in the air and the collision with the materials, the energy loss and transverse scattering of proton beam in the nozzle will be brought. The energy loss of proton beam will affect the beam quality and should be calculated in all regions. The three-dimensional structure of the nozzle in HUST-PTF is constructed in FLUKA (as shown in Figure 2), and the energy loss of the 70-250 MeV proton beam in the nozzle has been calculated. The number of protons is  $5 \times 10^6$ . The results are listed in Table 1.

Table 1: The Energy Loss of Beam in Each Region of the Nozzle

Region	Proton energy/MeV			
	70		250	
	Energy Loss /MeV	Percentage of Initial Energy (%)	Energy Loss /MeV	Percentage of Initial Energy (%)
Pixel IC	0.021	0.03	0.002	0.0008
He Pipe	0.087	0.124	0.034	0.0136
Plate IC	0.074	0.106	0.008	0.0032
Air gap	1.098	1.569	0.476	0.1904
Total	1.28	1.829	0.52	0.208

The larger the proton beam energy is, the smaller the energy loss is brought throughout the nozzle. Also, the energy loss mainly emerges in the air gap, and the losses in the pixel ionization chamber, the helium pipe, and the ion chamber are small. Since the energy loss generated in each of the main components is small, the thermal effect is not significant and the treatment requirements can be met. As is shown in Fig.3, the main energy losses are concentrated in the water phantom.

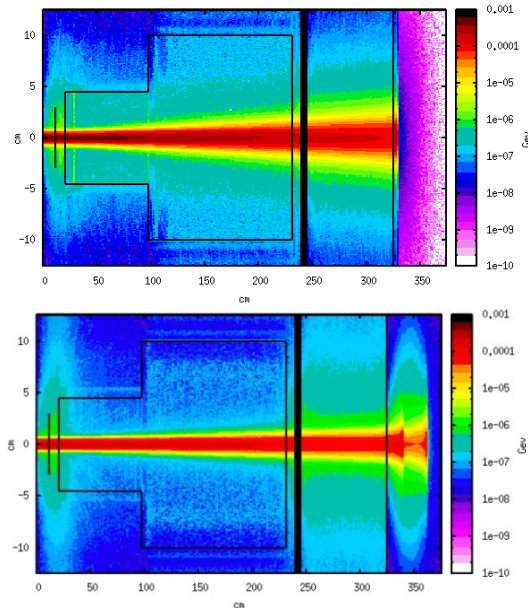


Figure 3: 2D distribution of energy deposition of 70MeV (upper) /250MeV(lower) in the nozzle in HUST-PTF.

### THE DISTRIBUTION OF THE SECONDARY PARTICLES OF 70-250MEV PROTON BEAM IN THE NOZZLE

During the transmission in the nozzle, elastic and non-elastic collision with the nuclei of different materials will happen, producing a large number of secondary particles that will adversely affect the patient and reduce the machine's expected service life. So it is necessary to calculate the distributions of secondary particles. Number of secondaries generated in inelastic interactions per beam particle when proton beam pass through the nozzle is shown in Table 2.

Table 2: Number of Secondaries Generated in Inelastic Interactions per Beam Particle

Particle category	Prompt radiation		
	70MeV	150MeV	250MeV
4-HELIUM	29.4%	23.4%	20.3%
3-HELIUM	0.7%	1.1%	1.2%
TRITON	0.3%	0.6%	0.7%
DEUTERON	1.6%	2.1%	2.3%
PROTON	42.9%	42.6%	43.3%
PHOTON	15.4%	12.1%	10.5%
NEUTRON	9.8%	18.0%	21.6%

It can be seen that the  $\alpha$  particles, neutrons and photons are the main secondary particles generated in the collision during the beam transmission in the nozzle. As the proton beam energy increases, the number of neutrons produced will increase significantly and the number of photons will decrease. In the radiation shielding design, the main consideration is the shielding of the neutrons, so it is necessary to calculate the distribution as well as the fluence, so that a corresponding shielding scheme should be established. The two-dimensional distribution of neutrons and photons is shown in Fig.4 and Fig.5 :

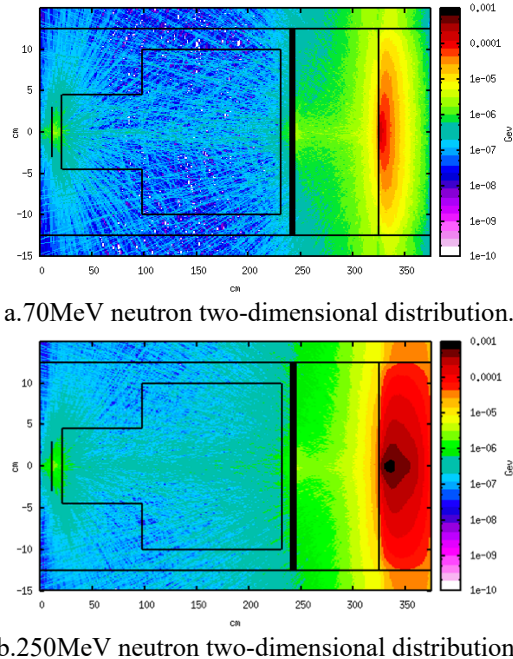


Figure 4:Neutron two-dimensional distribution.

From the diagram of the neutron two-dimensional distribution, it can be seen that during the transport of the proton beam in the nozzle, there will be neutrons gathered around the pixel ionization chamber, after the plate ionization chamber, and in front of the water phantom. Corresponding shielding devices should be placed in these areas and the electronic equipment should not be in the vicinity.

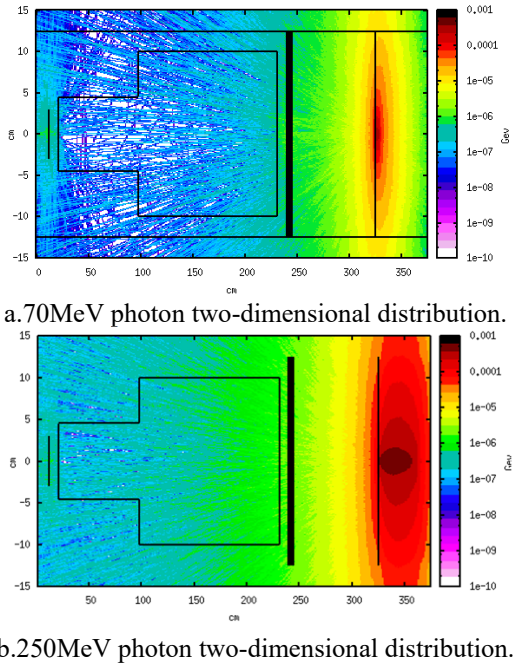


Figure 5: Photon two-dimensional distribution.

Currently used neutron shielding materials are concrete, aluminum, stainless steel and some new materials. One of the materials is made of boron carbide as a functional filler and epoxy resin as a matrix material. It has good neutron shielding properties and strong absorption, and is suitable as a material for local neutron shielding. Therefore, a suitable neutron shielding facility should be installed at the end of the ionization chamber, in front of the water phantom and around the pixel ionization chamber. Also, the placement of electronic equipments at these locations should be reduced, thereby reducing the impact of neutrons on patients and machines.

### INFLUENCE OF RANGE SHIFTER ON RADIATION

The range shifter, one of the important components for the nozzle system, plays a role in decreasing the energy of the proton beam at the end of the nozzle. By properly selecting the range shifter material, it is possible to significantly control the transverse scattering and decrease the damage to healthy tissue, as well as the radiation impacts caused by neutrons.

In this paper, the Monte Carlo method is utilized for analysis. Similar to the selection of materials in the reference paper[3], six materials are selected for analysis, and water is included as a reference material. Each material has the same water equivalent thickness(WET).

By comparing the fluence of neutrons produced after the proton beam passed through the range shifters, the material with the minimum radiation effect can be selected. The following model is constructed: the human body is simulated in a water phantom with a length, width and height of 40 cm, and the range shifter is placed 50 cm from the entrance of the proton beam, which is a vacuum section. The model is shown in Fig.6.

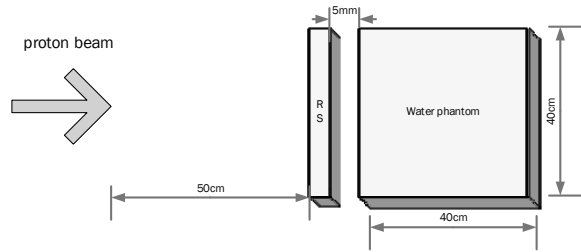


Figure 6: The model of the simulation for influence of range shifter on radiation.

In this simulation, the beam parameters before the range shifter is designed as the same, and the proton beam energy was set to 150 MeV. The neutron flux at the surface of the water phantom after the proton beam passed through a range shifter composed of different materials was calculated by using FLUKA. According to the proton energy, the neutron energy spectrum shown in Fig.7 is obtained.

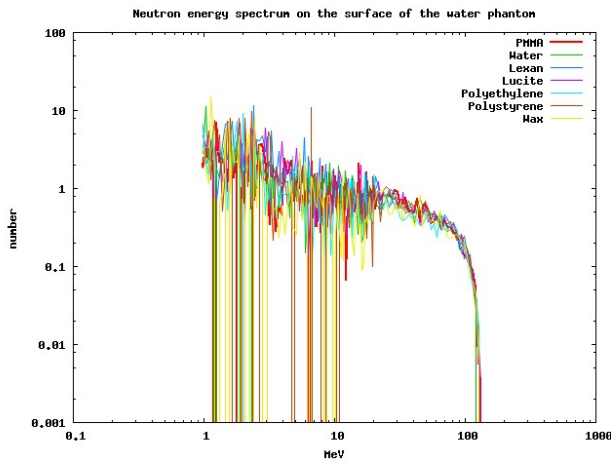


Figure 7: Neutron energy spectrum on the surface of the water phantom.

Neutrons can be divided into fast neutrons, medium energy neutrons, slow neutrons, and thermal neutrons according to the based on energy of the neutrons. The faster the neutron is, the harder it is to be absorbed. Since the position of the range shifter is already very close to the human body, no matter what kind of energy neutron, it will definitely enter the human body and be absorbed by the human body. Therefore, when considering the choice of range shifter materials, more attention should be paid to the comparison of the total flux of neutrons. Table 3 shows the comparison of the neutron fluence with different materials.

Table 3 Comparison of the Neutron Fluence

Material	Thickness (cm)	Neutron fluence		Total
		Neutron Energy/MeV		
		0~20	20~150	
Water	7	130.92	17.72	148.64
PMMA	5.44	144.30	13.34	157.64
Lexan	6.08	206.38	19.06	225.44
Lucite	5.99	179.92	17.72	197.64
Polyethylene	6.91	142.72	14.66	157.38
Polystyrene	6.64	184.45	17.97	202.42
Wax	7.00	120.21	16.14	136.35

It can be seen from the above analysis that when wax, PMMA and Polyethylene are used as the material of the range shifter, the number of neutrons generated is relatively small; while Lexan, Polystyrene will generate a large number of neutrons. From the perspective of the similarity with the characteristics of water, Wax, PMMA and Polyethylene will be better choices.

In practice, the selection of the material of range shifter should also consider the ability to decrease the transverse scattering, the processing costs as well as the strength and stability. From the perspective of radiation protection, Wax, PMMA and Polyethylene are more suitable as the range shifter materials.

## CONCLUSION

During the transmission of the proton beam in the nozzle in HUST-PTF, the energy loss is mainly concentrated in the air gap, while the energy loss caused by the pixel ionization chamber, the helium pipe, and the plate ion chamber is small. Neutrons, photons, and  $\alpha$  particles are the main secondary particles in the process. Among them, neutrons mainly appear around the pixel ionization chamber and water phantom. And as the energy increases, the neutron yield increases further. Photons also appear more in the air at the end of the nozzle. Neutron shielding facilities should be installed at the end of the ionization chamber, in front of the water phantom and around the pixel ionization chamber. Also, the placement of electronic equipment at these locations should be reduced. Wax, PMMA and Polyethylene are better choices as the range shifter materials when considering the radiation protection.

## REFERENCE

- [1] M. Krengli, F. Bourhaleb, L. Cozzi, *et al.*, "Treatment planning comparison of photon IMRT, active and passive proton therapy, and carbon ion therapy for treatment of head and neck tumors", *International Journal of Radiation OncologyBiologyPhysics*, Jan 2006, Vol 66, pp. 669-S669.
- [2] A. Ferrari, P. R. Sala, A. Fasso, *et al.*, "FLUKA: A Multi-Particle Transport Code", *Lancet*, 2005, Vol. 7740, pp. 44-45.
- [3] J. Shen, W. Liu, A. Anand, *et al.*, "Impact of range shifter material on proton pencil beam spot characteristics.", *Medical Physics*, 2015, Vol. 42, No. 3, pp. 1335-1340.



# BEAM LOSS MONITORING IN THE ISIS SYNCHROTRON MAIN DIPOLE MAGNETS

D. M. Harryman\*, S. A. Fisher†, W. A. Frank, B. Jones, A. Pertica, D. W. Posthuma de Boer,  
C. C. Wilcox, STFC, Rutherford Appleton Laboratory, Oxfordshire, UK

## Abstract

Beam loss monitoring at the ISIS Neutron and Muon Source is primarily carried out with gas ionisation chambers filled with argon. Thirty-nine ionisation chambers are distributed evenly around the inner radius of the synchrotron, with additional devices for the linac and beam transport lines. To improve loss control, a programme has been implemented to install six scintillator Beam Loss Monitors (BLMs), each 300 mm long, inside each of the ten main dipole magnets of the synchrotron. Using these scintillator BLMs the accelerator can be fine-tuned to reduce areas of beam loss that were previously unseen or hard to characterise. Installation of the system is now complete and this paper reviews: the installation of the scintillator BLMs, the electronic hardware and software used to control them, and the initial measurements that have been taken using them.

## INTRODUCTION

### ISIS Beam Loss Monitoring

ISIS has two systems for beam loss detection: a main “global” system using thirty-nine argon filled ionisation chambers [1]; and a finer system, using BC-408 plastic scintillators, that provides additional monitoring in selected areas [2]. The gas ionisation chambers in the synchrotron are 3 m long and distributed evenly around the inner radius, about 2 m from the beam axis. As beam losses inside the synchrotron’s main dipole magnets are shielded by the magnet yokes, they can be undetectable using the existing ionisation chambers. Therefore, to supplement these monitors, scintillator BLMs were initially installed inside the main dipole magnet downstream of the collimation straight, Dipole 2, as this had occasionally suffered beam related damage. This initial set of scintillators detected beam losses which were not measured on the ionisation chambers, and as such the decision was taken to install scintillators inside all ten of the main dipole magnets around the synchrotron. Each of the main dipole magnets is 4.4 m long, and for the initial set-up of Dipole 2, twelve BC-408 detectors were installed between the vacuum vessel and magnet yoke. Based on experience from Dipole 2, a configuration of six detectors has been installed in each of the main ring dipoles, which provided an optimal balance of cost, complexity and resolution. A key benefit of the scintillator detector design, with their entirely non-metallic construction, is that they avoid potentially serious problems with Eddy currents in the fast cycling ISIS magnets.

## System Overview

Figure 1 shows an outline of a scintillator system for one dipole, including main hardware, subsystems, locations, and connections.

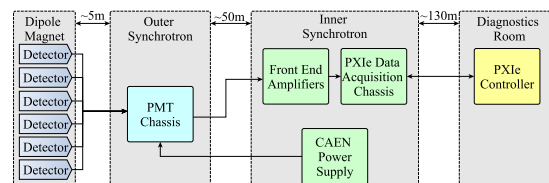


Figure 1: Overview of system hardware used for a single dipole.

As with the initial installation in Dipole 2, all detectors are installed within the main dipole magnets, between the magnet yoke and the vacuum vessel. All of the detector assemblies are installed on the inside radius of each dipole. Approximately 5 m from each dipole is a Photo Multiplier Tube (PMT) chassis holding six PMTs, one for each detector. The PMTs convert the light generated by the detectors into electrical “beam loss” signals. Each PMT is connected to a high voltage power supply and front end amplifiers, which are both located in the inner synchrotron area. This area is shielded by several metres of concrete, meaning radiation levels there are relatively low during accelerator operations. The CAEN power supply provides high bias voltages for each PMT. The front end amplifiers buffer the PMT outputs into a voltage which can be read by the PXIe data acquisition system.

Although the inner synchrotron area is shielded, some sensitive equipment, like the PXIe controller, can suffer from radiation-induced failure. Therefore, while the data acquisition cards for the system are located in the inner synchrotron area, the controller is located 100 m away, where radiation levels are negligible and access is unrestricted. The long distance connections between the two PXIe sub-systems is achieved with a custom optical fibre link, as detailed below.

## DETECTORS

### Detector Design

The detectors are based on the same design as those described in [2], based on BC-408 plastic scintillators. When high-energy particles interact with BC-408, light is generated [3]. The detector is covered in a light proof cover to eliminate background light, and connected to a PMT via optical fibres (see Fig. 2). As each detector has slightly different characteristics and responses, each detector and PMT pair is calibrated with a known radiation source in the

\* daniel.harryman@stfc.ac.uk

† sarah.fisher@stfc.ac.uk



lab prior to installation. The calibration voltages are then scaled to optimise the gain of each PMT.



Figure 2: BC408 scintillating detector and optical fibres with light proof covering, connected to a Photo Multiplier Tube (PMT).

### Mounting and Installation

The detectors are screwed onto 300 mm fibreglass panels with polyaryletheretherketone (PEEK) screws and fibreglass mounts (see Fig. 3).

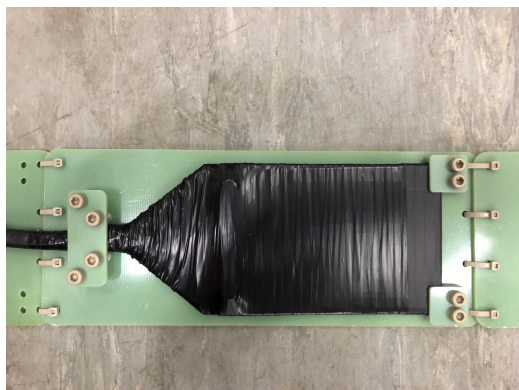


Figure 3: Detector mounted to fibreglass panel.

The scintillators are assembled in two sets of three, and each set is installed from opposite ends of the dipole on the inner circumference, between the magnet yoke and the vacuum vessel. To ensure that the detectors are equally spaced throughout the dipole, each 1.8 m assembly is made up of five panels, each 300 mm in length. Two of these serve as spacers between the detectors, and two additional, shorter 150 mm panels are attached to each end (see Fig. 4). All of the panels are connected using PEEK cable ties, to allow for

some flexing during installation. PEEK was chosen as the material for the fastenings as it is non-metallic and resistant to ionising radiation [4]. Figure 4 shows the arrangement of the detectors inside the dipole. The half panels on the outside ends of the dipole make it easier to install and remove the detector assembly. Each dipole has a 19-inch chassis installed locally, which houses the PMTs for that dipole (see Fig. 5). Optical fibres trail out of each side of the dipole from the detectors to these PMTs. A patch panel is also housed inside this chassis, used for connecting the PMTs to the front end amplifiers and high voltage power supply.



Figure 5: Chassis to house PMTs for a single dipole.

## FRONT END ELECTRONICS

### High Voltage Power Supply

The PMTs are supplied with a variable bias voltage of ~1 kV, which controls the tube gain. Previous experience shows that these scintillators will discolour and their outputs will degrade with exposure to radiation. This degradation can be somewhat compensated for by increasing the gain on each PMT [2]. Ten of the twelve initial detectors installed in Dipole 2 provided useful data for ten years. Ultimately, their lifetimes were limited by fibre breakage rather than discolouration of the scintillating material. As each PMT and scintillator pair may need different gain levels, each of the sixty PMTs are supplied with independently adjustable voltage channels.

PMT bias voltages are provided by a CAEN power supply housed in the inner synchrotron. From here, bias cables are laid to each PMT chassis in the synchrotron hall. Even though the inner synchrotron area is shielded, previous CAEN power supplies suffered failures every one or two

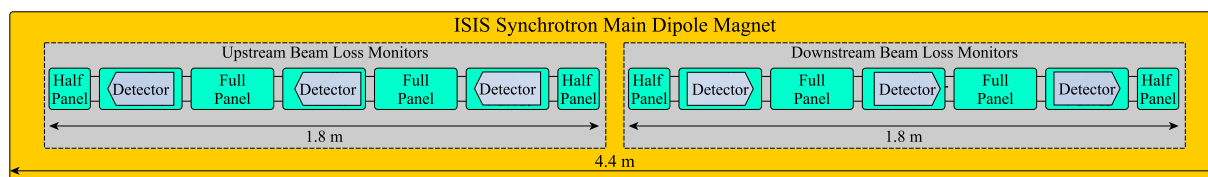


Figure 4: Arrangement of Beam Loss Monitors inside the dipole magnets (side view).

weeks during accelerator operation, which required a power cycle of the unit, or replacement of the damaged modules. To overcome this, ‘rugged’ power modules supplied by the manufacturer are now used instead of the off-the-shelf models. Since these new modules have been installed, there has been a significant reduction in the rates of failures, with the ‘rugged’ power supply requiring only a single power cycle in three months of operation.

### Front End Amplifiers

Amplifiers with two stages are used to convert the current from each PMT into suitable voltages for the data acquisition system. The first stage, a transimpedance amplifier, is used to convert and amplify the signal. The second stage is a single order low pass filter, with a cut off frequency of 100 kHz, used to improve the signal to noise ratio of the output signal. The amplifiers are housed in a number of Eurocard PCBs. Each amplifier PCB has eight channels, routed through a backplane PCB to a connector card, which interfaces with the data acquisition system. Each amplifier channel is connected to a relay which can be enabled by a Digital Input/Output (DIO) line on the data acquisition system, allowing a calibration pulse to be fed into the amplifiers.

## DATA ACQUISITION SYSTEM

### Remote Controller for Radiation Tolerance

The ISIS Beam Diagnostics section has standardised on the National Instruments PXI platform for data acquisition [5]. A PXI chassis contains a controller and a number of data acquisition cards. The controller houses typical PC components such as a CPU and hard drive, whereas the data acquisition cards house the ADCs, DACs, and DIO. When these PXI systems were first installed in the inner synchrotron area, radiation levels regularly caused the controller’s hard drives to fail. To avoid this, a MXI link was installed, to allow for the controller and data acquisition cards to be placed in separate chassis, connected together with an optical fibre cable of up to 200 m in length. The data acquisition cards remained in the inner synchrotron, and the controller was moved to the diagnostics room outside ionising radiation areas.

As this project requires data transfer rates beyond those supported by PXI systems, the newer PXIe platform was used. NI PCIe/PXIe-8735 MXIe cards and cables were used to connect a PXIe chassis to a rackmount controller RMC-8354. Instead of passive LC connectors, active CX4 to CX4 cables are required [6]. The maximum CX4 cable length officially supported by National Instruments is 100 m [6]. However, custom cables of 130 m length were built and tested. Back bone cables with Multi-fibre Termination Push-on (MTP) connectors were used at each end to connect to a patch panel at each location. MTP to CX4 cables are used from each patch panel to connect the two systems together. At the time of writing, this system has been in use for six months without issue.

### Data Acquisition Cards

The PXIe chassis inside the inner synchrotron features a MXIe card to interface with the remote controller, and four National Instruments PXIe 6358 cards. Each 6358 card has sixteen analogue input channels and a number of DIO lines. Figure 6 shows the PXIe chassis and the 6358 cards connected to the front end amplifiers used for signal conditioning.

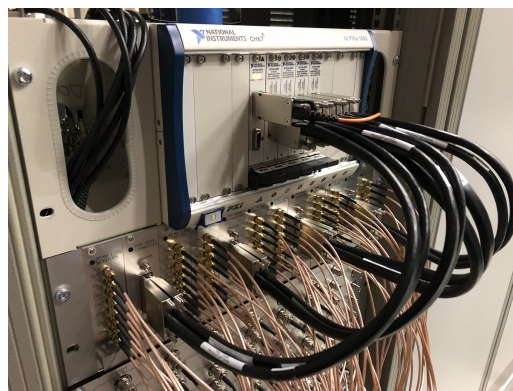


Figure 6: National Instruments PXIe system connected to front end Amplifiers.

The cards can sample up to a maximum rate of 1.25 MS/s. Data acquisition is triggered with every 50 Hz accelerator ramp, allowing for detailed beam loss data to be captured over the entire 10 ms cycle from injection to extraction.

## APPLICATION SOFTWARE

### Software Design

Data acquisition and display software has been developed in LabVIEW, and the DAQ software is deployed to the real-time RMC-8354 controller. The software acquires data from the acquisition cards and makes it available to the front end graphical user interface (GUI) via the TCP/IP protocol. It is also responsible for handling communication to the CAEN power supply server and the trigger timers on the ISIS control system: VISTA VSystem [7].

### Graphical User Interface

Figure 7 shows the front panel of the LabVIEW user interface VI, developed to display live data from the scintillators. This VI has been built into an executable application stored on a network drive, which can be run from any Windows machine on the ISIS network. The VI receives data from the RMC-8354 and displays it as a histogram of the integrated loss on each monitor over each 10 ms acceleration cycle, and a sum of the loss from all monitors. More detailed graphs of the loss within each dipole, or on each individual detector channel, can also be viewed, and reference levels can be saved for each channel.

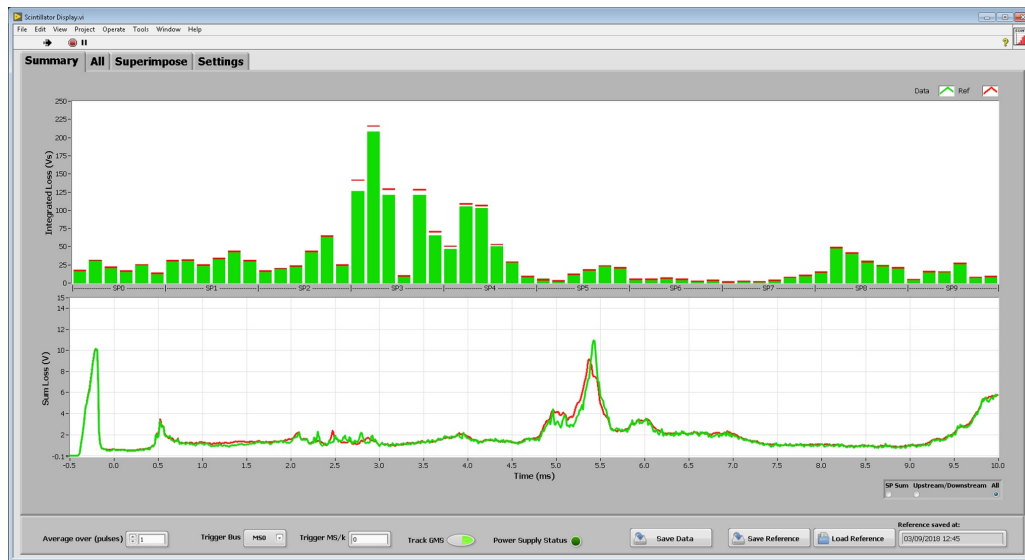


Figure 7: Scintillator Beam Loss Monitor GUI, showing loss in all ISIS dipoles.

## CONCLUSION

### *Initial Performance and Future work*

The program of installing new monitors into all of the main dipoles is now complete, and ISIS now has a beam loss monitoring system that will enable detailed machine tuning that was previously unavailable.

During the phased installation of the scintillators over multiple user cycles, radiation surveys showed reduced activation of those dipoles containing scintillators. As a result, synchrotron parameters will now be adjusted to minimise losses within all the main dipoles. With dipole losses accurately measured and minimised, the optimisation of the collimation system can now be reviewed and it may be possible to increase the machine acceptance and, potentially, increase operating beam intensity.

While all of the detectors and PMTs have been calibrated before installation, the detectors will degrade with prolonged radiation exposure. While this degradation can be somewhat compensated for by increasing the gain of the PMTs, accurate knowledge of the condition of each scintillator is unavailable. As the detector assembly itself may become activated, removal and recalibration of the detectors is not a practical solution. Instead, the dose received by each scintillator will be monitored with local total ionisation dosimeters and compared with separate characterisation measurements of detector degradation, performed by exposing a spare detector to a well-controlled dose [8].

## REFERENCES

- [1] M A Clarke-Gayther *et al.*, "Global Beam Loss Monitoring Using Long Ionisation Chambers at ISIS", in *Proc. EPAC'94*, London, England, Jun.-Jul. 1994, pp. 1634–1636.
- [2] S. J. Payne and S. A. Whitehead, "Fine Spatial Beam Loss Monitoring for the ISIS Proton Synchrotron", in *Proc. EPAC'06*, Edinburgh, Scotland, Jun. 2006, pp. 1079–1081.
- [3] Saint-Gobain Crystals, "BC-400, BC-404, BC-408, BC-412, BC-416 Premium Plastic Scintillators", BC-408 datasheet, Feb. 2018.
- [4] A. S. Vaughan and S. J. Sutton, "On radiation effects in oriented poly(ether ether ketone)", *Polymer*, vol. 36(8), pp. 1549–1554.
- [5] S. J. Payne *et al.*, "Beam Diagnostics at ISIS", in *Proc. HB'08*, Nashville, TN, USA, Aug. 2008, pp. 466–471.
- [6] National Instruments, "Fiber-Optic MXI-Express x4 for PXI Express Series User Manual", NI PCIe-8735, NI PXIe-8735 user manual, Nov. 2009.
- [7] B. Mannix and T. Gray, "Vista Controls Vsystem at the ISIS pulsed neutron facility", presented at ICALEPCS'07, Knoxville, TN, USA, Oct. 2007, unpublished.
- [8] D. M. Harryman and A. Pertica, "Online Total Ionisation Dosimeter (TID) Monitoring Using Semiconductor Based Radiation Sensors in the ISIS Proton Synchrotron", in *Proc. IBIC'16*, Barcelona, Spain, Sep 2016. doi:10.18429/JACoW-IBIC2016-TUPG24



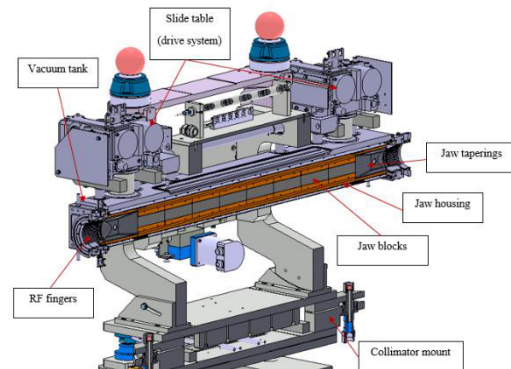


Figure 1: Section view of a typical horizontal secondary collimator.

The main component of the jaw assembly is the active absorption area. In primary and secondary collimators, this is made up of several blocks of low-Z material, such as a graphite composite or carbon reinforced carbon, to ensure low electrical induced impedance whilst maintaining mechanical robustness. These blocks are then clamped to a dispersion strengthened copper (Glidcop®) housing. The blocks are clamped to the housing rather than being rigidly fixed as this is not easily achieved. This is also to ensure a certain amount of slippage as the thermal expansion of Glidcop® is far greater than the thermal expansion of the low-Z blocks. Within the Glidcop® housing is also the jaw cooling system. The cooling system is designed to be able to evacuate the high heat loads generated by loss absorption (up to 47kW for HL-LHC cases) in an effort to minimise thermal deformations, which may be induced [4]. The cooling pipes are sandwiched between the block-housing stiffener on the front and an intermediate stiffener on the back then vacuum brazed together to ensure a good thermal conductivity, as shown in figure 2.

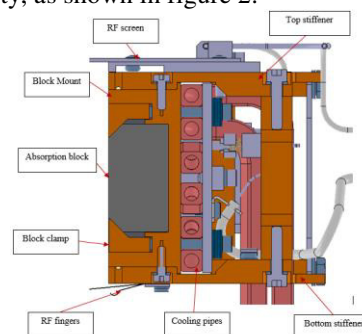


Figure 2: Cross section of current HL-LHC jaw assembly.



The jaws are then housed inside an electron beam welded vacuum tank. To ensure compliance with the vacuum requirements for the LHC the collimator tank must be leak tight to ultra-high-vacuum (UHV) standards with static pressures in the range of  $10^{-9}$  Pa to ensure beam stability and suitable beam lifetime [5]. In addition, the tank has several Conflat® knife design flanges to allow electrical feedthroughs currently servicing the beam position monitors and temperature sensors.

Finally, mounted outside the vacuum tank and connected to the jaws through a series of flexible UHV bellows is the actuation system. The actuation system allows the jaws to be moved precisely both laterally and angularly in relation to the beam. The system can laterally position the jaw within  $10\mu\text{m}$  and angularly within  $15\mu\text{rads}$  [6].

However, whilst the actuation system can position the jaws precisely with respect to the beam axis, the geometric form of the jaws must be kept to a very high precision. Key to the jaws cleaning efficiency is the straightness of the collimator jaw with which the beam interacts. Transverse deformations in the jaw can significantly change the jaws interaction with the beam in terms of cleaning efficiency and deposited thermal loads. The transverse deformation can vary over the length of the jaw due to the flatness of the jaw blocks, angular misalignment, mechanical error or thermal deformation. For secondary collimators, like the design the ACS is based upon, the maximum admissible straightness deviation is  $100\mu\text{m}$  [7].

Whilst angular misalignment can to some degree be corrected by the actuation system, and flatness and mechanical errors can be reduced during assembly, thermal deformations are difficult to monitor and are inherent due to the nature of the beam dynamics.

## LOSS EFFECTS ON COLLIMATOR JAWS

The robustness of collimators is fundamental to their operation within the LHC. They must be able to deal with a multitude of beam loss scenarios all of which can have a detrimental effect on jaw straightness, whether it is steady state losses from varying beam dynamics and differing variations in the LHC, or from accidental cases caused by machine failure. For this investigation, the loss scenarios that have been reviewed and used as the basis for this design study are as follows [8] [9]:

- Slow losses-
  - Steady state – 1h beam lifetime (BLT),  $1.68 \times 10^{11}$  p/s at 7TeV leading to a 9.38kW energy deposition on the most loaded jaw.
  - Accidental state – 0.2h BLT,  $8.34 \times 10^{11}$  p/s at 7TeV leading to 46.9kW on the most loaded jaw.
- Dynamic Losses
  - SPS injection error – 288 bunches at 450GeV
  - Asynchronous beam dump – 8 nominal LHC bunches at 7TeV.

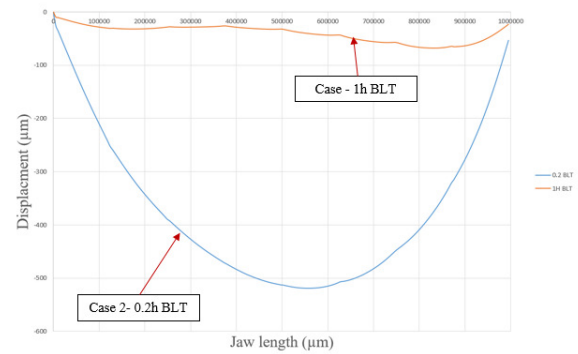


Figure 3: Jaw thermal deformation due to energy disposition from slow losses.

In terms of straightness error and deformation, cases one and two produce slow retarding elastic deformations that will return to their nominal position over time. Shown in figure 3 is jaw deflection due to quasi-static losses outlined in cases one and two. For the 1h BLT case the maximum deflection is about  $65\mu\text{m}$ . However this value is only indicative of the thermal load on the jaw combined with its own self weight. If a mechanical tolerance of  $40\mu\text{m}$  is also taken into account then from Equation 1, the quadratic average of the deflections the overall deflection increases to  $76.3\mu\text{m}$ .

$$S_{total} = \sqrt{S_{thermal}^2 + S_{mechanical}^2} \quad \text{Eq 1}$$

Whilst this is below the acceptable deviation limit for this style of collimator, it is potentially very close.

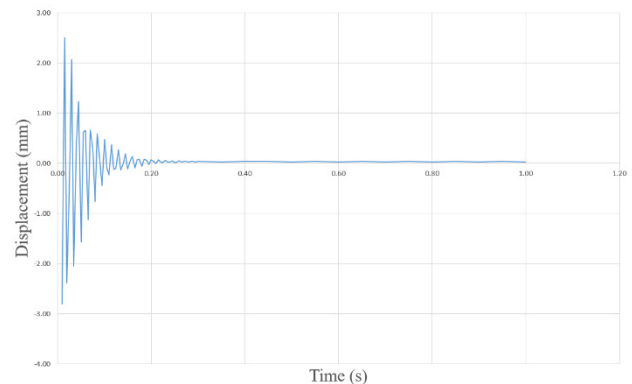


Figure 4: vibrational response of jaw after simulated SPS injection error.

In case two, the 0.2h BLT the maximum deformation is about  $500\mu\text{m}$ , clearly exceeding the  $100\mu\text{m}$  tolerance limit.

Whilst these losses cause slow elastic deformations, direct beam impacts will have an intensely more violent effect. Simulating an injection error with 288 bunches ( $6.4 \times 10^{13}$  total protons) at 440GeV, has the energy to plastically deform the Glidcop® housing [10] and will induce an underdamped dynamic flexural response, seen in figure 4. This response can have a period in excess of 120Hz in

accordance with the first natural modal frequency [11], combined with a large amplitude potentially over 2mm. Note: the above cases are based upon the TCSPM secondary collimator design utilising molybdenum-graphite blocks [12].

ADAPTIVE COLLIMATION SYSTEM

In an effort to correct the thermal deformations induced on collimators, an adaptive collimation system is proposed. The ACS is a closed loop approach to monitoring and correcting the straightness errors in collimator jaws, consisting of real-time measurement and integrated actuation. The base design is that of the current secondary TCSPM collimator, under deployment at CERN[13]. The TCSPM has been re-designed to allow to the integration of the measurement and actuation systems into the jaws and the necessary services that they require. Figure 5 shows the new TCSPM ACS jaw layout.

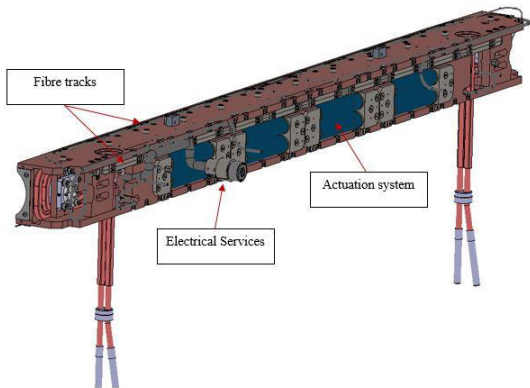


Figure 5: ACS Jaw design.

Measurement

The measurement system is a fibre based dispersed reference interferometry (DRI) measurement system, shown in figure 6. The DRI system [14] utilises several fibre-based probes mounted in the jaw to monitor the deflection. A fibre-based system was chosen due to space constraints

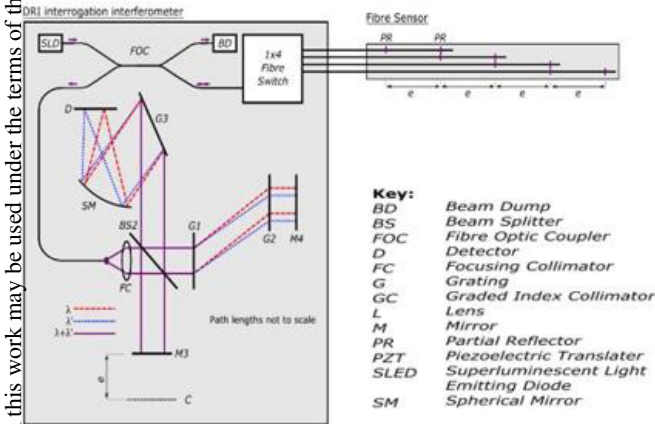


Figure 6: DRI system layout.

inside the vacuum tank, and because optical fibres are more resilient to radiation than electrical based sensors, even when considering susceptibility to fibre darkening. Whilst fibre darkening is an issue when using optical fibres in high radiation environments, the DRI system can operate on as little as four percent returned light.

The system consists of twelve probes split into two groups, with six mounted on the front of the jaw and six mounted on the rear side. Mechanically clamped to the jaw the probes will elongate as the jaw deforms, providing a deduced value of strain. The differentiation between the strain values at the front against the values at the back, in corresponding probes will allow the deduction of displacement direction and magnitude.

Of the six probes in each track, only five will be used for strain measurement. The sixth will be unclamped allowing it to elongate freely. By doing this the expansion of optical fibres due to temperature in the jaw can be observed and extrapolated against the actual values of expansion due to jaw displacement.

As glues and other adhesives are generally not permitted in LHC components due to issues with out-gassing, the optical fibre probes will be clamped in purpose built mounts (figure 7) that will be fixed to jaw housing that will run the full length of the jaw.

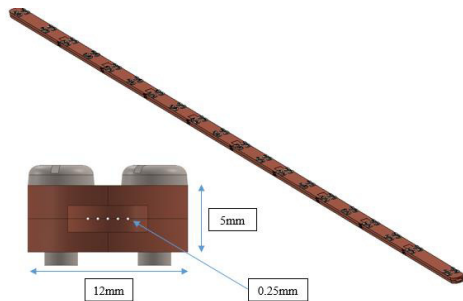


Figure 7: Fibre mount and cross section.

Table 1 shows the summary of the DRI measurement system.

Table 1: DRI Summary	
No of measurement arms	2
Measurement cavities intervals	200mm
No. of cavities	6 per arm (12 per jaw)
Optical Resolution	850nm at 50nm bandwidth
Strain resolution	±0.417 µε
Rate of acquisition	4KHz
Temperature range	10-300°

## Actuation

The actuation system for the ACS jaw comprises a series of high-powered piezo-ceramic (PZT) stack actuators (figure 8). The current design of the TCSPM jaw makes it inherently stiff, requiring large amounts of force to manipulate it. One of the reasons PZT actuators were chosen is for their high force generation. Each actuator in the ACS has a blocking force of 14000N and a maximum displacement at 0N of 120 $\mu$ m at 1000V. The number of actuators required

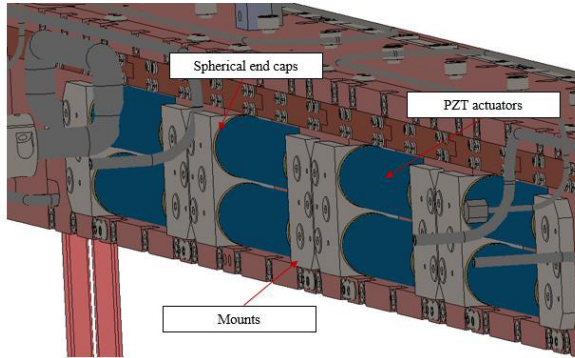


Figure 8: Piezo mount.

to manipulate the jaw was determined by their proximity to the jaws neutral plane. Due to space constraints inside the vacuum tank, the actuators have to be placed unavoidably close to the jaws neutral plane. This decreases the moment and therefore requires a higher force to deform the jaw to the desired amount, thus leading to the use of eight actuators currently in the design. Fewer could have been used, reducing the cost and complexity, if it had been possible to locate them further from the neutral plane. Because of this, the actuators are embedded in what would traditionally be the back stiffener of the collimator. They are mounted on universal semi-spherical mounts to avoid the undesirable exertion of external lateral forces and torques on the actuators.

It is envisaged that the actuation system will be operated in two distinct modes. One, the actuators will expand at constant rate to reverse the effects of the slow elastic thermal deformation in order to keep the jaw's straightness value below the specified limit. This scenario has been run in an FEA simulation, which shows the current design configuration can achieve the correction of a 500 $\mu$ m displacement, the same as that caused in a 0.2h BLT. The results of this are shown in figure 9.

The second mode of operation will be a vibrational response capable of acting as an active damping system designed to respond to the events caused during a direct beam impact. By pulsing the actuators out of phase with the frequency caused by a beam impact the two frequencies should interfere with each other destructively thus reducing the amplitude. This still has to be proved analytically, but

in theory the actuators expansion speed can easily match the resultant frequency caused by a beam impact.

The theoretical speed at which the actuators can expand is governed by the actuators resonant frequency  $f_o$  and given by:

$$T_{min} = \frac{1}{3 \cdot f_o} \quad \text{Eq 2}$$

If the electrical supply were not taken into account this would give a rise time of 33ns. However, the rise time is governed by the current supply, which due to the UHV electrical feedthroughs is capped at 3A. This gives a rise time even of 0.86 $\mu$ s, given by:

$$I = C \cdot \frac{dV}{dt} \quad \text{Eq 3}$$

where C is the capacitance of the actuator. This would give a frequency response in the KHz range, easily capable of matching the jaws first order natural frequency.

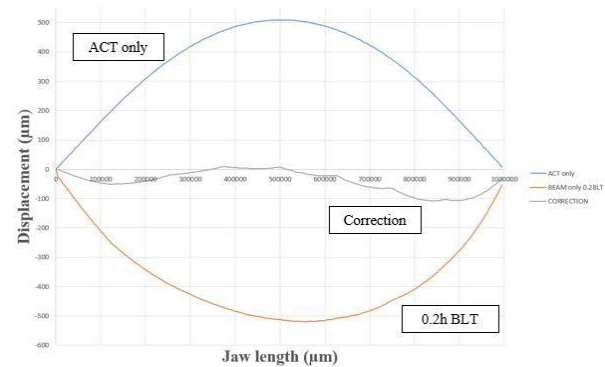


Figure 9: 0.2h BLT displacement and actuated correction.

## CONCLUSION

The design of the ACS and its integration into a current collimator design poses serious challenges. A large amount of additional hardware must be added into a compact space that cannot be altered. The fundamental parts of the collimator design, cooling system, active area etc. cannot be radically redesigned in fear of altering the collimators primary function. This leads to further difficulties in regards to integrating the ACS. Whilst the fundamental parts that make up the ACS have been used separately and with high degrees of success, combining them and making them fit for purpose for operation in the LHC is still uncertain. However, initial FEA simulations show promising results concerning the current hardware specification. In addition to FEA, several test rigs have been planned to facilitate the final design. Chief among these was a dedicated line in HiRadMat 36 [15] [16] at CERN. The results for the ACS line in the "Multimat" experiment will be published in due course. In addition to this a 1/3 scale jaw has been developed to review the design intents of the ACS as well as the relationship between the measurement and actuation systems, and the controls that links the two. The ACS will continue to develop over the next fifteen months with a full-scale working collimator ready for the end of 2019.

## REFERENCES

- [1] O. S. Bruning *et al.*, “LHC design report”, CERN, Geneva, Switzerland, Rep. CERN-2004-003-V1, Jul. 2004.
- [2] G. Arduini *et al.*, “High Luminosity LHC: Challenges and Plans”, in *Proc. 14<sup>th</sup> Topical Seminar on Innovative Particle and Radiation Detectors (IPRD'16)*, Siena, Italy, Dec 2016, doi: 10.1088/1748-0221/11/12/C12081
- [3] E. Holzer *et al.*, “Beam Loss Monitoring for LHC Machine Protection”, *Physics Procedia*, vol. 37, pp. 2055-2062, 2012, doi: 10.1016/j.phpro.2012.04.110
- [4] A. Bertarelli *et al.*, “The Mechanical Design for the LHC Collimators”, in *Proc. 9<sup>th</sup> European Particle Accelerator Conf. (EPAC'04)*, Lucerne, Switzerland, Jul 2004, paper MOPLT008, pp. 545-547.
- [5] J. M. Jimenez, “Vacuum Requirements for the LHC Collimators”, CERN, Geneva, Switzerland, Rep. LHC-LVW-ES-0004 rev 0.1, Dec 2003.
- [6] A. Bertarelli *et al.*, “Analysis and Design of the Actuation System for the LHC Collimators (Phase 1)”, CERN, Geneva, Switzerland, Rep. CERN-EN-Note-2009-001, Aug 2009.
- [7] R. Assmann *et al.*, “Requirements for the LHC Collimation System” in *Proc. 8<sup>th</sup> European Particle Accelerator Conference (EPAC'02)*, Paris, France, Jun 2002, paper TU-AGB001, pp 197-199.
- [8] F. Carra, “Thermomechanical Response of Advanced Materials under Quasi-Instantaneous Heating, Ph.D thesis, Politecnico di Torino, Italy, 2017.
- [9] A. Mereghetti *et al.*, “BLM Thresholds and Damage Limits for Collimators”, in *Proc. 6<sup>th</sup> Evian Workshop on LHC Beam Operations*, Evian les Bains, France, Dec 2015, pp 197-202.
- [10] M. Cauhi *et al.*, “Thermomechanical Assessment of the Effects of a Jaw-Beam Angle during Beam Impact on Large Hadron Collider Collimators”, *Phys. Rev. ST Accel. Beams*, vol. 18, no.2, p. 021001, Feb 2015, doi:10.1103/PhysRevSTAB.18.021001
- [11] M. Cauhi *et al.*, “Thermomechanical response of Large Hadron Collider Collimators to Ion and Proton Beam Impacts”, *Phys. Rev. ST Accel. Beams*, vol. 18, no. 4, p. 041002, Apr 2015, doi:10.1103/PhysRevSTAB.18.041002
- [12] J. Guardia-Velenzuela *et al.*, “Development and Properties of High Thermal Conductivity Molybdenum Carbide – Graphite Composites”, *Carbon*, vol. 135, pp. 72-84, 2018, doi:10.1016/j.carbon.2018.04.010
- [13] F. Carra *et al.*, “Mechanical Engineering and Design of Novel Collimators for HL-LHC”, in *Proc. 5<sup>th</sup> International Particle Accelerator Conference (IPAC'14)*, Dresden, Germany, Jun 2014, pp. 369-372, doi:10.18429/JACoW-IPAC2014-MOPR0116
- [14] J. Williamson *et al.*, “High Resolution Position Measurement from Dispersed Reference Interferometry using Template Matching”, *Optics Express*, vol. 24, pp. 10103-10114, 2016, doi:10.1364/OE.24.010103
- [15] F. Carra *et al.*, “The "Multimat" experiment at CERN HiRadMat Facility: Advanced Testing of Novel materials and Instrumentation for HL-LHC Collimators”, *J. Phys.: Conf. Ser.*, vol. 874, no.1, p. 012001, doi:10.1088/1742-6596/874/1/012001
- [16] A. Bertarelli *et al.*, “Dynamic testing and characterization of advanced materials in a new experiment at CERN HiRadMat facility”, in *Proc. 9<sup>th</sup> International Particle Accelerator Conference (IPAC'18)*, Vancouver, Canada, May 2018, pp. 2534-2537, doi:10.18429/JACoW-IPAC2018-WEPMF071



# SIGNAL PROCESSING FOR BEAM LOSS MONITOR SYSTEM AT JEFFERSON LAB

J. Yan, T. Allison, S. Bruhwel, W. Lu, Jefferson Lab, Newport News, VA 23606, U.S.A.

## Abstract

Ion Chambers and Photomultiplier Tubes (PMT) are both used for beam loss monitoring in the Machine Protection System (MPS) at Jefferson Lab. These detectors require different signal processing, so two VME-based signal processing boards, Beam Loss Monitor (BLM) board and Ion-Chamber board, were developed. The BLM board has fast response ( $< 1 \mu s$ ) and 5 decades of dynamic range from 10 nA to 1 mA, while the Ion-Chamber board has a slower response but 8 decades of dynamic range from 100 pA to 10 mA. Both boards feature machine protection and beam diagnostics, in addition to a fast shutdown (FSD) interface, beam sync interface, built-in-self-test, remotely controlled bias signals, and on-board memory buffer.

## INTRODUCTION

The Beam Loss Monitor (BLM) system is an important part of the Jefferson Lab Machine Protection Systems (MPS) [1]. It detects bremsstrahlung radiation from low level beam loss during tune-up and beam operations and provides a machine protection trip well before the beam can damage accelerator components. Two types of radiation detectors, 931B PMT [2] and CERN Ion Chamber [3], are installed for the beam loss monitor system of the CEBAF at Jefferson Lab. An 8-channel VME based BLM board, which has replaced the original 4-channel CAMAC based board, are developed as the current acquisition electronics for PMT detectors, with negative current between -5 nA to -1 mA and a fast response time. Meanwhile, a newly designed 5-channel Ion Chamber (IC) VME board provides the current

acquisition for CERN Ion Chamber, which has a slow time response and a large dynamic range.

## NEW BLM BOARD DESIGN

The new 8-channel BLM signal processing board has a functional block diagram that consists of analog signal processing and digital processing. The analog processing includes linear signal tuning, operational amplifier (op-amp) integrating signal processing, Howland voltage-to-current converter circuits, and logarithmic current signal processing. The digital processing includes FSD signal logic, analog-to-digital (ADC) data acquisition, and FPGA digital control. The linear tuning is an op-amp circuit with a gain of 5490. It converts negative current from PMT to voltage, referred to as the pre-amplified voltage. The pre-amplifier voltage signal then serves as the input for both integrating and log circuits. Figure 1 shows the diagram of the analog signal processing for each channel. The integrating processing circuit is op-amp based and performs the mathematical operation of integration to cause the output voltage to respond to changes of the input voltage over time. The integrated output voltage is connected both to the ADC for data sampling and to a fast voltage comparator for FSD detection. The equation of the ideal voltage of the op-amp integrator is

$$V_{\text{int}} = -\int_0^t \frac{V_{\text{in}}}{R_{\text{in}} \cdot C} dt.$$

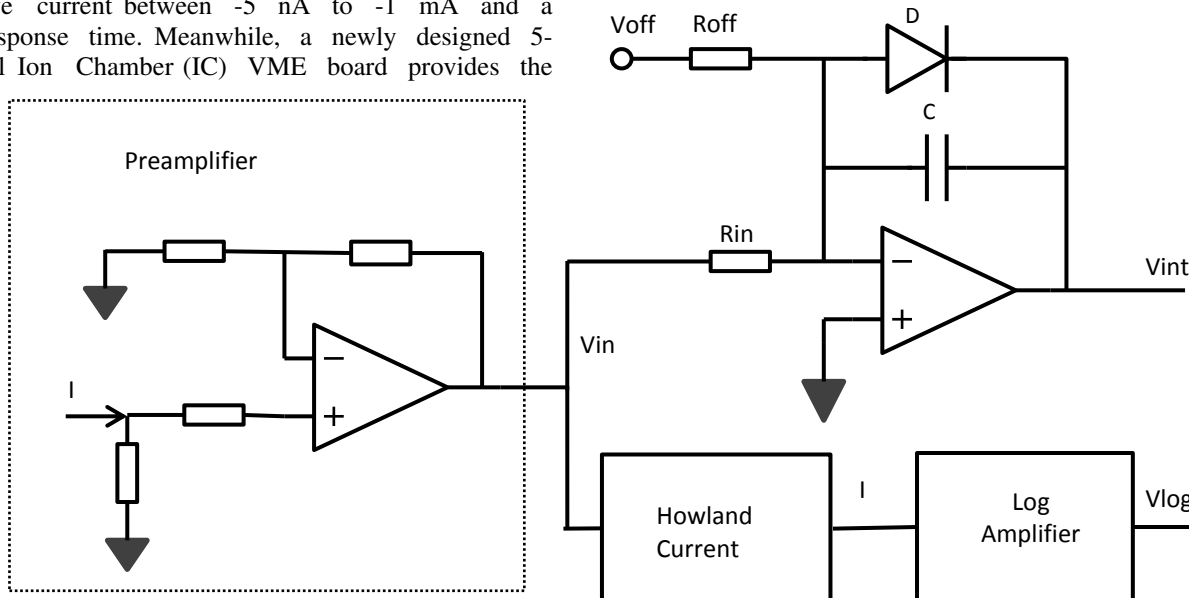


Figure 1: Diagram of the analog signal processing.

The RC time constant  $= R_{in} \cdot C$  is designed as 0.1  $\mu$ s, and the cutoff frequency  $f_c = 1/2\pi\tau$  is 1.6 MHz. A variable bias voltage  $V_{off}$  is added to the integrating circuit, which defines the threshold input voltage that initiates the integration. If  $V_{off}R_{off} + V_{in}R_{in} > V_F$ , the current passes through the diode and no integrating occurs; if  $V_{off}R_{off} + V_{in}R_{in} < V_F$ , the diode blocks the current and the circuit operates as an op-amp integrator. Here  $V_F$  is the Forward Voltage Drop of the diode D. The bias voltage  $V_{off}$  is driven by a DAC with a range of 0 to 5V. The DAC is programmed by the FPGA, so that the bias value can be controlled to avoid a ramp-up of the integrator on background noise.

The logarithmic signal processing consists of a Howland current source and a log converter circuit based on the log amplifier MAX4206. The MAX4206 is a precision trans-impedance logarithmic amplifier with 5 decades of input current across a 10 nA to 1 mA dynamic range. It computes the log ratio of the input current relative to an externally or internally generated reference current and provides a corresponding voltage output with a default 0.25V/decade scale factor. By adjusting the output scale factor and output offset voltage, the output voltage is designed to be from 0V to 5V corresponding to a 10 nA to 1 mA input current, namely 1V/decade. Since the input of the log amplifier requires a positive current source, a converter circuit has to be applied to convert the preamplifier voltage to a positive current.

The Howland current source is an op-amp circuit topology that effectively forms a linear differential voltage-to-current converter. Figure 2 shows the schematic diagram of the basic Howland Current Pump circuit, where input resistors  $R_1=R_3$  and feedback resistors  $R_2=R_4$ . When the ratios of  $R_1/R_2$  and  $R_3/R_4$  are the same, the feedback from the output to both the + and - inputs of the op-amp is at equal strength [3,4]. The load current  $I_L$ , which takes the form below, mathematically analyses the circuit.

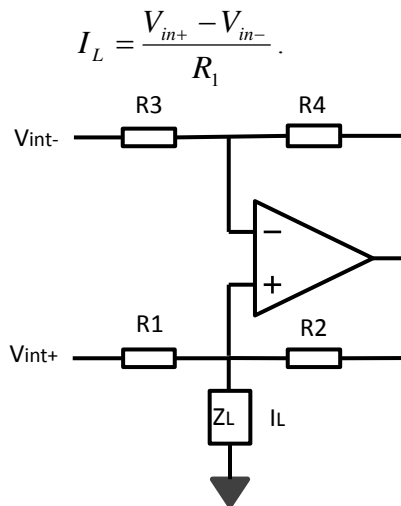


Figure 2: Schematic diagram of the Howland current source [5].

This equation shows that the output current per change of the input voltage is equal to  $1/R_1$ . If the input resistors and feedback resistors are matched, the output impedance of the source is high, so that the gain is identical for all output voltages and impedances, and for all inputs. However, all 4 resistors have tolerances and the resistor network will not be perfectly matched. For this application, a full precision conversion is required, so 0.1% tolerance resistors are used. The value of the resistor  $R_1$  is selected to convert the output current precisely as the input from the PMT. The gain 5490 of the preamplifier and the gain  $-1/5490$  of the V/I converter are chosen for the design. The current  $I_L$  is directly fed to the log amplifier and then converted to a voltage, which will be sampled by the ADC AD7656.

The AD7656 contains six 16-bit, fast, low-power, independent ADCs. Three AD7656 ADCs are applied to sample the integrated and log signals from 8-channels simultaneously. The FPGA communicates with these ADCs through a serial interface with a sample rate of 100 ksp/s for each independent channel. All the data are stored in a 16 Mb, 16 bit SDRAM in a ring buffer configuration and the data will provide beam loss transition play-back whenever required.

## BLM TESTING AND MEASUREMENTS

The critical functions of the new BLM board are tested before the final production. They include machine protection and diagnostics, fast response for FSD, self-test, pulse measurement and continuous monitoring, and data acquisition.

A Keithley 6221 Current Source provides an input current to the BLM board and a multimeter is used to measure the integrated and log signals. The input current demonstrates 5 decades of dynamic range from -10 nA to -1 mA. Figure 3 shows how the integrated voltage ( $V_{int}$ ) and log voltage ( $V_{log}$ ) change with the input current  $I$ . Here  $|I|$  is the absolute value of the input current. The log voltage has a logarithmic relation to the input current, and variation of 1V per decade of current. This curve shows that a change of current (or beam loss) is precisely monitored and it can be applied to beam loss diagnostics. The integrated voltage changes slightly, when current is low, but at a certain point (10  $\mu$ A in this case) it jumps to 5.8V, which is the saturation voltage of the integrator. When the input current is less than 10  $\mu$ A, the sum of the bias voltage  $V_{off}$  and the preamplified voltage  $V_{in}$  is higher than the Forward Voltage Drop  $V_F$  of the diode, and no integration occurs. When the input current exceeds 10  $\mu$ A, the summation of  $V_{off}$  and  $V_{in}$  is less than  $V_F$ , so integration kicks in and the voltage reaches saturation, which will trigger the voltage comparator to generate a FSD signal. The value of the current that triggers the integrator is dependent on the bias voltage as mentioned before.

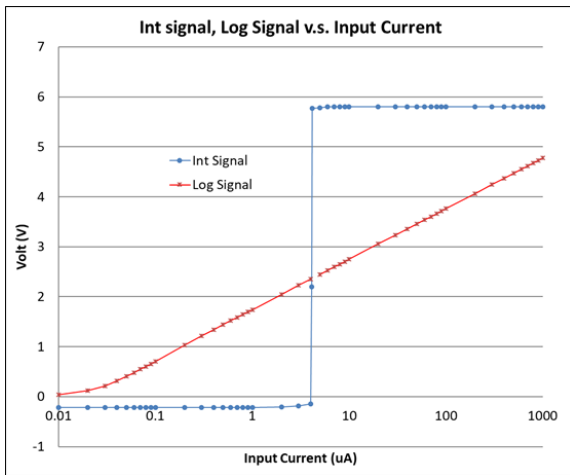


Figure 3: Integrated voltage and Log voltage dependence on the input current  $|I|$  ( $\mu$ A).

Each channel of the BLM board has a self-test function that feeds into a constant-on or single programmable-length current pulse, where the current can be generated by a PMT unit or an on-board signal injection. The PMT unit is connected to the BLM board via a D-9 connector and driven by a high voltage power supply. The FPGA controls the test LED inside the PMT unit. If the LED is on, the PMT will generate a negative current and output it to the analog channel of the BLM board. The test signal can be programmed as constant-on or an adjustable single pulse. The BLM board also can be tested with on-board signal injection, whereby the current is generated by a circuit on the BLM board instead of using the PMT. By using on-board testing, we measured the FSD response time of the BLM board, and studied how the integrated voltage and log voltage changed with time in pulse mode. Figure 4 shows the integrated signal, log signal, and FSD signal correspond respectively to a pulse input signal.

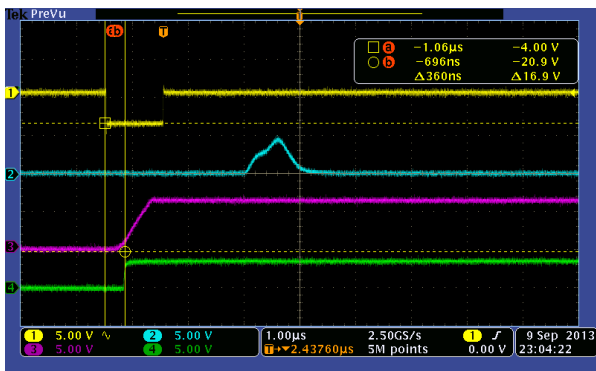


Figure 4: Oscilloscope measurement of pulse signal, integrated signal, log signal, and FSD signal.

In Figure 4, curve 1 (yellow) is a  $1 \mu$ s pulse test signal controlled by the FPGA. Curve 2 (blue) is the log signal. Curve 3 (purple) is the integrated signal, and curve 4 (green) is the FSD signal. When the preamplifier circuit is subjected to the pulse input, the integrated signal starts to increase with time. After 360 ns, the integrated signal

reaches a voltage higher than the FSD voltage comparator, and immediately triggers the FSD signal to surge. After 840 ns, the integrated signal reaches the saturation voltage. After  $2.5 \mu$ s the log amplifier starts to convert the input current to a log voltage. From Figure 4 we obtain the most important timing of the BLM board, the FSD response. It is measured as  $0.360 \mu$ s, less than the required  $1 \mu$ s. This figure clearly shows how the integrated signal, log signal, and FSD signal correspond to a pulse input. The PMT self-test is also performed, and the measurement results are similar to those from the on-board testing.

## IC BOARD DESIGN AND TEST

Compared with BLM board, the analog design of Ion Chamber board is much simpler. It doesn't require preamplifier, integrating, or Holland current circuit. The conditioned positive current from Ion Chamber inputs into a log amplifier ADL5303, which is a monolithic logarithmic detector optimized for the measurement of signal with a large dynamic range of 160 dB ranging from 100 pA to 10 mA. By adjusting the output scale factor and output offset voltage, the corresponding voltage output has 0.5V/decade scale factor. The output voltage ( $V_{\log}$ ) is sampled with a 16-bit ADC ADS8860 at 500K sample rate. Since the IC has slow time response, about 89  $\mu$ s, the signal integration for machine protection can be executed within FPGA firmware. When the  $V_{\log}$  is higher than bias set ( $V_{\text{Bias}}$ ), FPGA starts to integrate the number of  $V_{\log} - V_{\text{Bias}}$  at 2  $\mu$ s interval and obtain an integrated signal ( $V_{\text{Int}}$ ). If  $V_{\text{Int}}$  exceeds the Threshold setpoint ( $V_{\text{Thrd}}$ ), an integrated Ion Chamber FSD fault will be tripped. Figure 5 shows how integration and FSD trip work. The x axis is the time with unit of  $\mu$ s and Y axis is the signal with ADC counts. When  $V_{\log}$  is less than  $V_{\text{Bias}}$ , there is no integration and  $V_{\text{Int}}$  equals zero. After 268  $\mu$ s,  $V_{\log}$  exceeds  $V_{\text{Bias}}$ , and  $V_{\text{Int}}$  starts integration till it is more than  $V_{\text{Thrd}}$  at time 340  $\mu$ s. Figure 5 shows that the time to trip a FSD fault is about 72  $\mu$ s, which meets the requirement of our Ion Chamber machine protection.

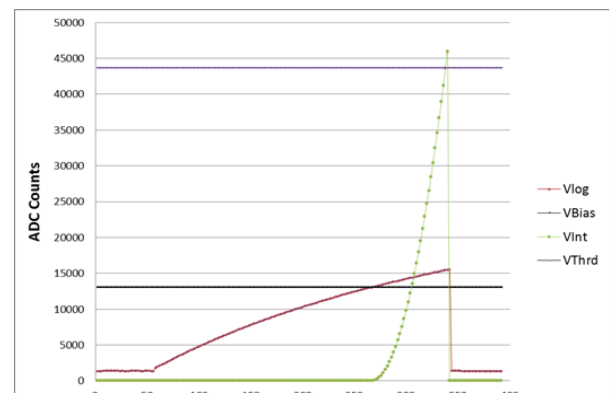


Figure 5: ADC Counts of  $V_{\log}$ , and  $V_{\text{Bias}}$ ,  $V_{\text{Int}}$ , and  $V_{\text{Thrd}}$  signals and FSD trip.

## CONCLUSIONS

The new VME based BLM and IC signal processing and data acquisition boards have been developed for the CEBAF machine protection system. The BLM board provides eight-channel analog and digital signal processing, while the IC board provides five channels, and both boards have diagnostic and machine protection functions. On the BLM board, an integrating circuit is applied to trigger the FSD fault with a response time less than 1  $\mu$ s, and a Howland current source circuit is added to convert the input current for log amplifier. The integrated signal and log signal are processed simultaneously by the FPGA controlled ADCs and buffered on an on-board SDRAM memory. On the IC board, the current from Ion Chambers is directly sampled by the ADC, and all the signal integration and FSD triggering are executed within the FPGA. By monitoring the integrated and FSD signals at pulse mode, BLM board has the FSD response time of 0.36  $\mu$ s, and IC board has 72  $\mu$ s of FSD triggering time. Both BLM and IC boards are installed for the CEBAF operation and meet the 12GeV Upgrade requirements.

## ACKNOWLEDGEMENT

Thanks to Fab Group for laying out the BCP and front panel, to Keith Cole coordinating the fabrication, and to Fab Shop for assembling the boards.

Notice: Authored by Jefferson Science Associates, LLC under U.S. DOE Contract No. DE-AC05-06OR23177. The U.S. Government retains a non-exclusive, paid-up, irrevocable, world-wide license to publish or reproduce this manuscript for U.S. Government purposes.

## REFERENCES

- [1] K. Mahoney, J. Coleman, "Overview of the Jefferson Lab Machine Protection Beam Loss Monitors", [http://www.jlab.org/accel/ssg/papers\\_Pres/sspres/beamloss/index.html](http://www.jlab.org/accel/ssg/papers_Pres/sspres/beamloss/index.html).
- [2] J. Yan, K. Mahoney, "New Beam Loss Monitor for 12 GeV Upgrade", *Proceedings of ICALEPCS2009*, Kobe, Japan, page 582- 584.
- [3] S. S. Gilardoni, et al., CERN-ATS-2011-131.
- [4] P. Pouliquen, J. Vogelstein, R. Etienne-Cummings, "Practical Considerations for the use of a Howland Current Source for Neuro-Stimulation", *BioCAS 2008*, IEEE, page 33-36.
- [5] Robert A. Pease, "A Comprehensive Study of the Howland Current Pump", *National Semiconductor Application Note 1515*, Jan. 29, 2008.



## STATUS OF THE BNL LEReC MACHINE PROTECTION SYSTEM\*

S. Seletskiy<sup>†</sup>, Z. Altinbas, D. Bruno, M. Costanzo, A. Drees, A. Fedotov, D. M. Gassner, X. Gu, L. Hammons, J. Hock, R. Hulsart, P. Inacker, J. Jamilkowski, D. Kayran, J. Kewisch, C. Liu, K. Mernick, T. Miller, M. Minty, M. Paniccia, W. Pekrul, I. Pinayev, V. Ptitsyn, V. Schoefer, L. Smart, K. Smith, R. Than, P. Thieberger, J. Tuozzolo, W. Xu, Z. Zhao  
BNL, Upton, USA

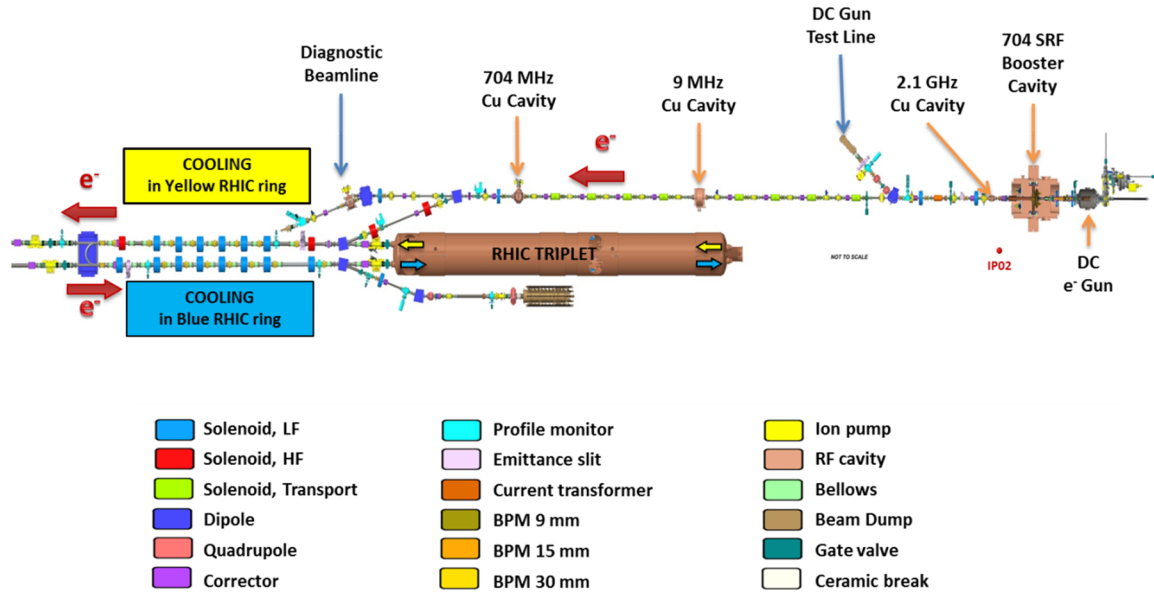


Figure 1: LEReC layout.

### Abstract

The low energy RHIC Electron Cooler (LEReC) will be operating with 1.6-2.6 MeV electron beams having up to 140 kW power. It was determined that under the worst case scenario the missteered electron beam can damage the vacuum chamber and in-vacuum components within 40 us. Hence, the LEReC requires a dedicated fast machine protection system (MPS). The LEReC MPS has been designed and built and currently is under commissioning. In this paper we describe the most recent developments with the LEReC MPS.

### LEREC LAYOUT AND PARAMETERS

The LEReC accelerator [1] consists of the 400 kV DC photo-gun followed by the 1.2-2.2 MV SRF Booster, the transport line and the merger that brings the beam to the two cooling sections (CS1 and CS2) followed by the 140 kW dump. The LEReC also includes two dedicated diagnostic beamlines: the low-power beamline capable of accepting 15 kW beam (DC Gun Test Line) and the RF diagnostic beamline.

The LEReC layout is schematically shown in Fig. 1.

The LEReC beam train consists of 9 MHz macro-bunches. Each macro-bunch (MB) consists of  $N_b=30$  bunches repeated with 704 MHz frequency. The length of

each bunch at the cathode is 40 ps. The charge per bunch ( $Q_b$ ) can be as high as 200 pC.

The LEReC can work with macro-bunch trains of various length ( $\Delta t$ ), various number of macro-bunches per train ( $N_{mb}$ ), and various time delay ( $T$ ) between the trains.

The nominal LEReC beam parameters pertinent to the MPS design are summarized in Table 1.

Table 1: LEReC Beam Parameters.

Kinetic Energy, MeV	1.6	2	2.6
Electron bunch (704 MHz) charge, pC	130	170	200
Bunches per macro-bunch (9 MHz)	30	30	24-30
Charge per macro-bunch, nC	4	5	5-6
Average current, mA	35	46	44-55
Average power, kW	56	93	114-142

In addition to the baseline operational modes listed in Table 1 the LEReC might also be operated with CW 704 MHz beam of 85 mA (at 1.6 MeV) and 68 mA (at 2 MeV).

There are also several additional beam modes required for accelerator commissioning, study and transition to operational conditions. All these modes of operation comprise the MPS beam modes.

The relation between the MPS beam mode and allowed destinations of the beam will be discussed in the following sections.

The LEReC MPS beam modes and their use are summarized in Table 2.

\* Work supported by Brookhaven Science Associates, LLC under Contract No. DE-AC02-98CH10886 with the U.S. Dept. of Energy.

<sup>†</sup> seletskiy@bnl.gov

Table 2: LEReC MPS Beam Modes

Beam modes	Goals
Low Current Mode (LCM) $N_b = 30$ ; $N_{mb} = 1$ ; $T = 1$ s $Q_b = 30 - 200$ pC	Optics commissioning; Rough RF settings; Emittance measurement
RF Studies Mode (RFSM) $N_b = 10, 15, 20, 25, 30$ ; $\Delta t \leq 250$ us; $T = 1$ s – 5 s; $Q_b \leq 200$ pC	RF fine-tuning. Study beam longitudinal phase space.
Transition Mode (TM) $N_b = 30$ ; $\Delta t = T$ ; $Q_b \leq 200$ pC	Transition from LCM to HCM with gradual adjustment of $Q_b$ .
High current Mode (HCM) $N_b = 30$ ; $\Delta t = T$ ; $Q_b = 130 - 200$ pC	Getting nominal e-beam parameters in the cooling sections.
CW Mode (CWM) 704 MHz CW; $Q_b = 95 - 120$ pC	Alternative to HCM.

## MPS OVERVIEW

### MPS Parameters

The LEReC MPS [2, 3] is designed to protect the machine from damage caused by the loss of electron beam.

We determined the MPS parameters from the studies of tolerable beam losses under various failure scenarios. The main MPS parameters are shown in Table 3.

Table 3: Main MPS Parameters

Parameter	Symbol	Value
Reaction time	$t_{\text{react}}$	40 us
Tolerable routine losses	$I_{\text{loss}}$	1 uA
Current threshold for ultimate safe operation mode (USOM)	$I_{\text{USOM}}$	40 nA

The MPS reaction time was derived under assumption that beam optics studies are performed in LCM only and that in HCM the beam trajectory is kept in some reasonable range and that some magnet power supply currents are kept at operational values.

We assume that the eventual setting for tolerable loss threshold will be found experimentally while  $I_{\text{loss}}=1$  uA is an initial setting. The beam current used in such studies must not exceed 600 uA.

In the USOM any operations with the electron beam are allowed. For beam studies the LCM is the same as the USOM.

### MPS Related Diagnostics

The MPS relies on the numerous LEReC beam diagnostic systems [4].

The MPS utilizes the fast current transformer (FCT) located at the gun exit to measure the beam current and to determine what beam and equipment manipulations are allowed at the moment. Two other devices supplementing the FCT are a dedicated fast photodiode (PD) measuring the laser intensity and the readback on the position of the half-wave plate (HWP) in a laser trailer. The switching between

the pulsed and CW modes is produced by introducing the HWP in the path of the laser and if HWP is in CW mode position then the MPS assumes the HCM.

To monitor the beam trajectory the MPS relies on a few beam position monitors (BPMs) located along the beam-line. The BPMs are equipped with fast electronics providing a few microseconds response.

A number of photomultipliers, fitted with a few feet long optical fibre, are used as beam loss monitors (BLMs) that determine the routine beam losses.

The ion gauges (IG) measuring the vacuum are also an integral part of the MPS. The gun IG plays a special role in machine protection – the MPS is required to trip the gun high voltage power supply (HVPS) when the gun IG readings exceed the predefined limit.

The MPS monitors the on/off status and the phase/amplitude settings of the LEReC RF cavities and the cryogenic system temperature.

Finally, the MPS monitors several magnet power supplies (PS) as well as the gun HVPS.

In the case of a trip condition, the MPS interlocks the laser by removing the voltage from the Pockels Cell (PC) and by closing the mechanical shutter.

### MPS Logic

The schematic of the MPS logic is presented in Fig. 2.

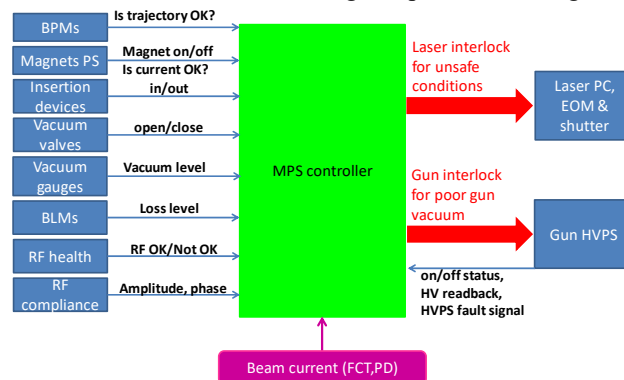


Figure 2: Schematic of LEReC MPS.

The MPS assesses the surface that the beam is hitting from the settings of the dipoles and from what insertion devices are inserted into the beamline. These inputs to the MPS are called “qualifiers” and the surface hit by the beam defines the “machine mode” (MM). Operations with beam in each particular MM is only allowed below a certain current level.

The actual beam current is independently determined from both the FCT and the PD measurements. The MPS compares the measured beam current to the allowed current level and if the measured current exceeds the limit set for the present MM, then the MPS interlocks the laser.

Other causes for the MPS to trip the machine above a certain current level are the BPM readings, RF phase and amplitude readings or magnet PS readings being outside of the allowed range.

Finally, above a certain current level, the MPS trips the beam if the loss measured by the BLMs is above the  $I_{\text{loss}}$ .

## RECENT MPS EXPERIENCE

### MPS Commissioning

The prototype MPS was successfully commissioned and operated during the LEReC gun test performed from April – August of 2017 [5]. The gun test included studying a 400 keV beam produced by the gun and transporting it to the DC Gun Test Line. Based on the results of the LEReC gun test, the full MPS was devised and implemented for the 2018 LEReC commissioning run.

The commissioning procedure of the full LEReC MPS consisted of 3 main steps:

The integrated system test consisted of checking the interaction between the MPS controller, the MPS diagnostic subsystems, the laser, and the gun HVPS.

The second step was the MPS test without the beam. In that step we verified the logic of the MPS controller by emulating various fault conditions and observing the laser interlocks.

In the final step we commissioned the entire integrated LEReC MPS with electron beam. Working in the LCM we successively adjusted the current levels of interest below the current measured by the FCT, created all possible beam faults and observed the expected machine trips.

### MPS Reaction Time

To measure the MPS reaction time: the BPM signal, the fault signal from BPM controller to the MPS, the MPS trip signal to the laser and the MPS PD signal were monitored on the scope. The fault condition was created at the monitored BPM and the reaction time was measured by observing the delay between the fault registered by the BPM and the disappearance of the signal on the fast photodiode.

The example of such a measurement is shown in Fig. 3.

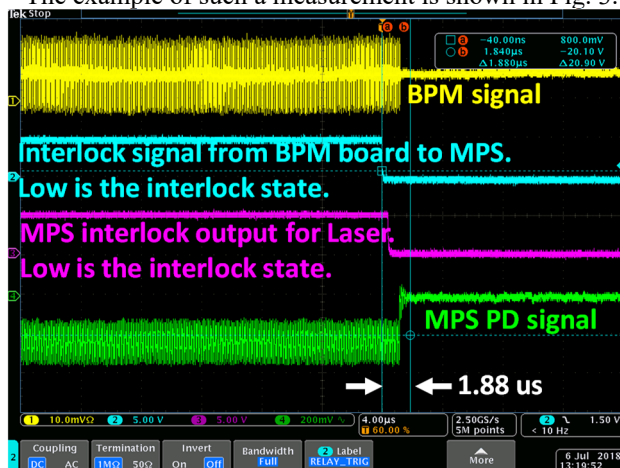


Figure 3: Measurement of the MPS reaction time.

As it can be seen from the presented plot the MPS controller response time is 500 ns (blue trace to purple trace). The overall MPS reaction time, or the time from an interlock to ‘no-beam’ condition, is within 2  $\mu$ s. A generous 3  $\mu$ s of processing and cable delay time can be added to this result. Hence, the overall MPS reaction time is 5  $\mu$ s, which is an order of magnitude less than the required 40  $\mu$ s.

### Adjusting MPS Diagnostic Configuration

The majority of the MPS related diagnostic devices were commissioned and integrated into the prototype MPS during the LEReC gun test. Nonetheless, during this year’s run we discovered that some configuration changes were required for proper MPS operation.

The FCT, which is customized by Bergoz to optimize its sensitivity at 704 MHz was affected by the RF noise produced by the nearby SRF Booster. While it was not a problem for CW operation, in the pulsed mode the noise was interpreted as real beam current and caused multiple erroneous trips. Better shielding of RF connections helped somewhat with the noise problem but eventually, to completely eliminate this issue, we had to bypass the FCT amplifier, increase the FCT noise threshold and recalibrate the FCT.

Another example, before enabling the BLMs in the MPS we had to reduce the BLM gains. Although their new settings allowed the BLMs to be utilized for monitoring the losses in CW mode, the reduced sensitivity made them much less useful for fine-tuning of the beam transfer efficiency. Presently we are considering having two configurations for the BLMs. One for monitoring the losses during CW operations and another for optimising beam transfer in preparation to run CW.

### LEReC Commissioning

Successful implementation and utilization of the MPS allowed us to operate the LEReC with the desired beam parameters required for 2018 accelerator commissioning.

Figure 4 shows the example of the recent CW run of the LEReC.

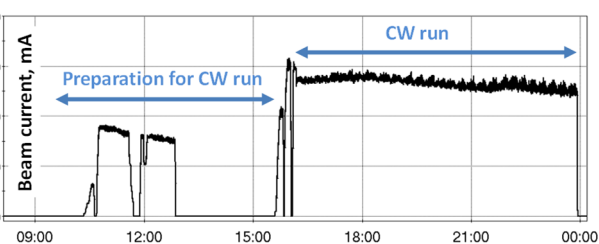


Figure 4: Eight-hour long LEReC CW run.

## CONCLUSION

We described the current status of the Machine Protection System for the Low Energy RHIC Electron Cooling accelerator. The MPS was successfully commissioned and utilized in the 2018 LEReC commissioning run. Presently we are preparing our accelerator for commissioning of the first-ever bunched electron cooling during 2019 RHIC run.

## REFERENCES

- [1] A.V. Fedotov *et al.*, “Accelerator Physics Design Requirements and Challenges of RF Based Electron Cooler LEReC”, in *Proc NAPAC’16*, Chicago, IL, USA, Oct. 2016, paper WEA4CO05, pp. 867-869.
- [2] S. Seletskiy *et al.*, “Conceptual Design of LEReC Fast Machine Protection System”, in *Proc. IBIC’16*, Barcelona, Spain, Sep. 2016, paper WEPG19, pp. 666-669.

- [3] S. Seletskiy et al., BNL-113798-2017-IR, 2017.
- [4] T.A. Miller et al., “LEReC Instrumentation Design & Construction”, in *Proc. IBIC'16*, Barcelona, Spain, Sep. 2016, paper TUPG35, pp. 418-422.
- [5] S. Seletskiy *et al.*, “Status of the LEReC Machine Protection System”, in *Proc. IBIC'17*, Grand Rapids, MI, USA, Aug. 2017, paper TH1AB4, pp. 487-490.



# THE INSTALLATION AND COMMISSIONING OF THE AWAKE STRIPLINE BPM\*

Shengli Liu<sup>†</sup>, Victor Alexandrovich Verzilov, Paul Eric Dirksen, TRIUMF, Vancouver, BC, Canada  
Franck Guillot-Vignot, Lars Soby, David Medina Godoy, Spencer Jake Gessner, CERN, Geneva, Switzerland

## ABSTRACT

AWAKE (The Advanced Proton Driven Plasma Wakefield Acceleration Experiment at CERN) stripline BPMs are required to measure the position of the single electron bunch to a position resolution of less than 10  $\mu\text{m}$  rms for electron charge of 100 pC to 1 nC. This paper describes the design, installation and commissioning of a such BPM system developed by TRIUMF (Canada). Total 12 BPMs and electronics had been installed on AWAKE beam lines and started commissioning since Fall of 2017. The calibration and measurement performance are also reviewed.

## SYSTEM OVERVIEW

AWAKE facility is a proof-of-principle R&D experiment at CERN and the world's first proton driven plasma Wakefield acceleration experiment [1]. Its construction has been completed and the commissioning has been started since Fall of 2017, which includes the stripline BPMs for tuning the electron beam. Refer to Fig. 1 for the layout of the AWAKE electron beamline and the common beamline, the electron BPMs locations and other diagnostic devices.

A total 12 BPMs have been installed on the AWAKE, with 6 on the electron beamline, and 6 on the common beamline. Those on the electron beamline are 40 mm aperture, while those on the common beamline are 60 mm aperture. They both have coverage angle of 38 degree, and with longitudinal length of 120 mm and 124 mm. Because of these parameters, their sensitivities are supposed to be slightly different. The processing electronics, i.e. BPM DSP (Digital Signal Processor), is in the hall way which has about 30 ~ 60 meters to the BPMs. The radiation dose rate level there is low enough that the electronics is not designed to be radiation hard. Refer to Fig. 2 for the system diagram, which describes the electronics, network and data acquisition computer. All the BPM DSPs are powered through the power bars that support Ethernet interface, which allows the DSP boxes to be power cycled in the situation that the communication becomes dead. Such situation happened several times during the commissioning, this remote reset scheme prevented human access to the site which is difficult or impossible during SPS operation. Besides the FEC (Front End Computer) which runs the DAQ software FESA server (FESA: What also is shown in the diagram is the triggers which signal the presence of the electron or proton beam bunches.

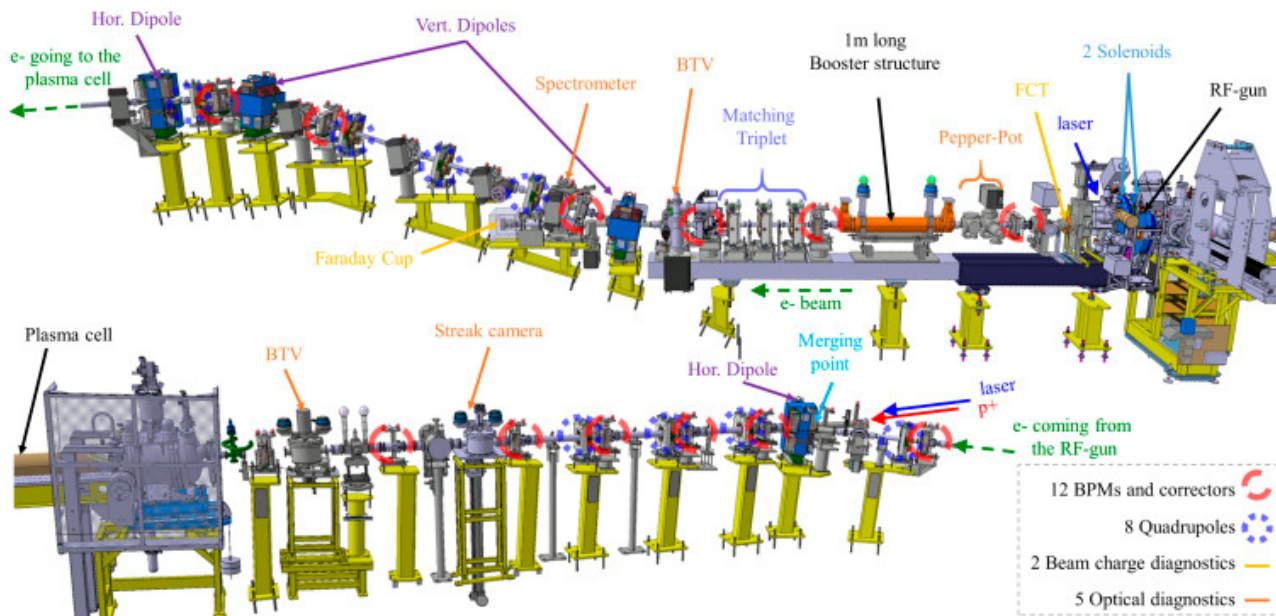


Figure 1: AWAKE beam lines and BPM locations.

\* TRIUMF contribution was supported by NSERC and CNRC

<sup>†</sup> sliu@triumf.ca

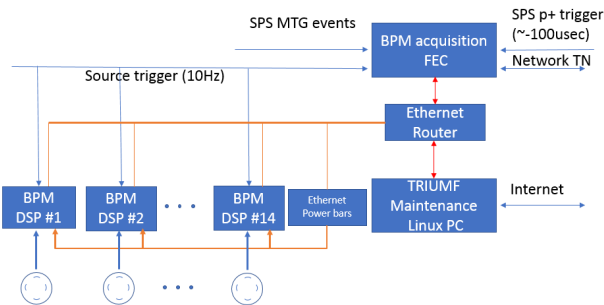


Figure 2: AWAKE stripline BPMs: electronics, triggers, DAQ, and Maintenance computers.

The system so far has been working with self-trigger mode, which continuously detect the beam pulse and trigger itself for event processing. The Fig. 3 shows an installed 40 mm BPM installed on the electron beamline, with the four antenna cables not yet connected.

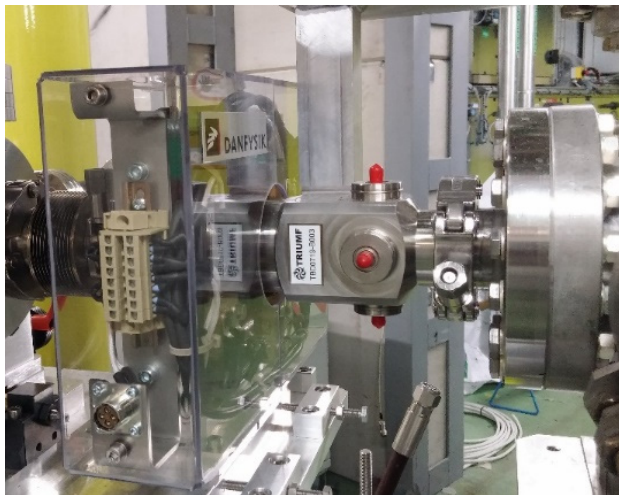


Figure 3: 40 mm AWAKE stripline BPM on the electron beam line.

The Fig. 4 is the BPM DSP rack, total 14 DSP boxes and one LO source, one calibration source are installed in the rack. Low loss BPM signal RF cables are routed to the back of the DSP rack, and then extended with thinner semi-rigid RF cables to reach to the input SMA connectors located on the front panels of the 1U DSP boxes. For the BPMs mounted on the common beam line, there is a customize designed Mini-Circuit high power band pass filter for each BPM signal to prevent the sensitive front end electronics to be damaged by the much stronger proton bunch signals.

### BPM ELECTRONICS

The single electron pulse's horizontal/vertical position and intensity could be calculated from the signals induced on the four BPM antennas by that electron pulse. To the first order approximation, the position X or Y could be calculated as  $X = S \cdot \text{Diff/Sum}$ , with Diff/Sum is the ratio of the signal difference over signal summing from the two opposite electrodes, and S as the sensitivity constant [2]. On the AFE board (Analog Front End), the four signals are band pass filtered, frequency down converted and

amplified, and then digitized by a 16-bit flash ADC at 100MSPS on the digitizer board. On the FPGA board, A Xilinx SPARTAN6 processes the waveforms to get the position and intensity information, and pack them into an event data. The FESA server running on the FEC readout the event packets from each DSP module at a frequency of about 10 Hz, and publish the data to client software when requested on the local technology network. Refer to Fig. 5 for the hardware electronics, three boards: AFE, Digitizer and FPGA board are integrated into a 1U crate, named BPM DSP 1030, are stacked on the standard 19 inches rack. Each DSP module receives four antenna signals from one BPM, and a trigger signal. The TTL trigger signal multi-dropped at each DSP and terminated with 50 ohm at the last DSP module. Also there is one LO (Local oscillator source) input to receive the 434MHz LO signal for the frequency mixer, and calibration input to receive an ultra-fast pulse for drift calibration purpose. At self-trigger mode, the DSP module runs at the full speed clock, and consumes more than 20 watts, thus four +12V DC fans are equipped on the back panel to keep the inside temperature low. The detailed design of the AFE, Digitizer and FPGA firmware has been described in a previous paper [3].



Figure 4: BPM DSP rack and TRIUMF Linux PC.

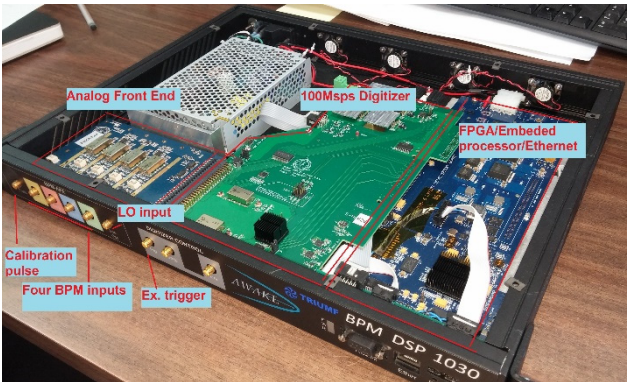


Figure 5: BPM DSP 1030 module inside: AFE, digitizer, FPGA board.



## CALIBRATION

The calibration of the BPM system involved two types of offset errors, one is related to the electronics channel inside DSP module, and another one is the offset introduced by the BPM mechanical tolerance, unbalanced cable/connectors.

The first one was performed with an ultra-fast pulse generator (AVTECH AVM-2, amplitude 15.6V, FWHM 250 ps), connected to a 1:4 wide band RF power splitter and then fed to the four inputs of the DSP module. The channel gain parameters were adjusted to zero any position offset. Since the first attenuator (Digital Attenuator) in the AFE is a single channel type and its gain value varies from chip to chip slightly, the above calibration procedure needs to be performed on each of the three attenuator gain settings: 0, -10 -20 dB. For the same reason, the other gain setting on the digital attenuator should not be used since they are not calibrated. The second attenuator in the VGA (Variable Gain Amplifier) on the AFE has two channels on the same die and does not suffer this issue.

The second one is defined as Skew parameter in the FPGA firmware and stay unchanged with the associated BPM and its cables. In Table 1, the 40 mm BPM calibration data are listed. The first part is the offset due to the BPM mechanical tolerance and was measured in house at TRIUMF before shipped to CERN. The second part is the offset due to the cable/connectors and measured on site after the installation. The two offset parts are multiplied to get the Skew factors, which are to be applied to each measured. The procedure was to use the same AVTECH pulse generator as above, to drive one of the four BPM antennas, and measure the position offset from the opposite plane.

Table 1: 40 mm BPM Static SKEW Calibration Data

Electronics module #	4	0	1	7	6	5	2
Monitor #	2	3	4	5	6	7	10
Offset, a-c plane, mm	-0.069	0.067	0.07	-0.22	0.028	0.059	0.086
Offset, b-d plane, mm	0.019	-0.035	-0.025	0.047	-0.042	-0.053	0.018
ratio value a/c	0.9866	1.0132	1.0138	0.9579	1.0055	1.0116	1.0170
ratio value b/d	1.0037	0.9932	0.9951	1.0092	0.9918	0.9897	1.0035
cable offset a-c plane, um	40	25	35	-90	-40	26	0
cable offset b-d plane, um	80	180	-10	-160	150	400	-43
ratio value a/c	1.0053	1.0033	1.0047	0.9881	0.9920	1.0035	1.0000
ratio value b/d	1.0107	1.0243	0.9987	0.9789	1.0305	1.0548	0.9943
accumulated ratio a-c	0.991864	1.016581	1.018535	0.946435	0.997483	1.015126	1.016972
accumulated ratio b-d	1.014489	1.0173	0.993794	0.987937	1.022022	1.043911	0.997792
SKEW a-c	1.0082	0.9837	0.9818	1.0566	1.0025	0.9851	0.9833
SKEW b-d	0.9857	0.9830	1.0062	1.0122	0.9785	0.9579	1.0022

There is another calibration situation for the dynamic offset error (drift) due to temperature fluctuation, this is to be compensated with a calibration pulse input on the front panel of the DSP. This pulse could be turned on when there is no beam operation, and X, Y position offset could be checked along the long period running. Compensation could be applied to channel gain parameters if it becomes necessary to zero any position measurement offset.

## COMMISSIONING

The stripline BPM system for the electron beam measurement was put into commissioning in Fall of 2017. Since then, there was once firmware updating in March of 2018 and one DSP module was replaced due to the damaged AFE board.

One design feature was approved to be valuable especially at the beginning of the commissioning: the capability of the remote reset of the DSP modules which allowed quick recovery from the dead DAQ communication. Such situation disappeared after the firmware updating.

The BPMs installed on the common beam line had to see the much stronger proton beam which could damage the sensitive AFE that is designed for electron pulse. A customized designed high power BPF from Mini-Circuit had been installed in front of the DSP module for these BPMs.

One critical specification of the BPM system is the position measurement resolution which is specified as 10  $\mu$ m rms. Due to the much larger beam centroid jitter at this stage of the AWAKE operation, the BPM's resolution performance is not obvious from the measurement data of each BPM. The Singular Value Decomposition (SVD) algorithm was applied to a recent run data from all 12 BPMs. Figure 6 shows the beam jitter for the vertical direction before and after the SVD, with the five most significant eigenmodes removed. In Fig. 6, the beam direction is indicated, and the horizontal axis is the event number, the vertical axis is the position in unit of mm. There is nearly no change for the beam jitter at the BPM430010, this could be explained by the fact that the acceleration cavity isolated this BPM from all other ones. Shown in both Fig. 6, and Fig. 7 that a strong correlated motion only exists at BPM430028 and 430039. At the BPM412345, a higher frequency beam jitter (or electronics noise) exists, which does not relate to any other BPM locations, this might be indicating a real electronics problem. Figure 8 shows the beam position S.T.D. values before and after the correlated beam centroid jitter is removed. These data indicated the best rms resolution reached to 6.2  $\mu$ m at BPM#11.

## CONCLUSION

For the first time in the world, on May 26 2018 AWAKE successfully accelerated electrons to 2 GeV from 19 MeV using a wakefield generated by protons through a 10 meter long plasma cell [4].

The performance of the stripline BPM system has been approved to be satisfied to assist the operation of the electron beamline and the precise alignment of the electron beam with the proton beam. Its input dynamic range extends beyond of the specified 100 pC to 1nC electron charge. One observed position rms resolution has reached to 6.2  $\mu$ m from the recent run data, which is also within the specified rms resolution 10  $\mu$ m.

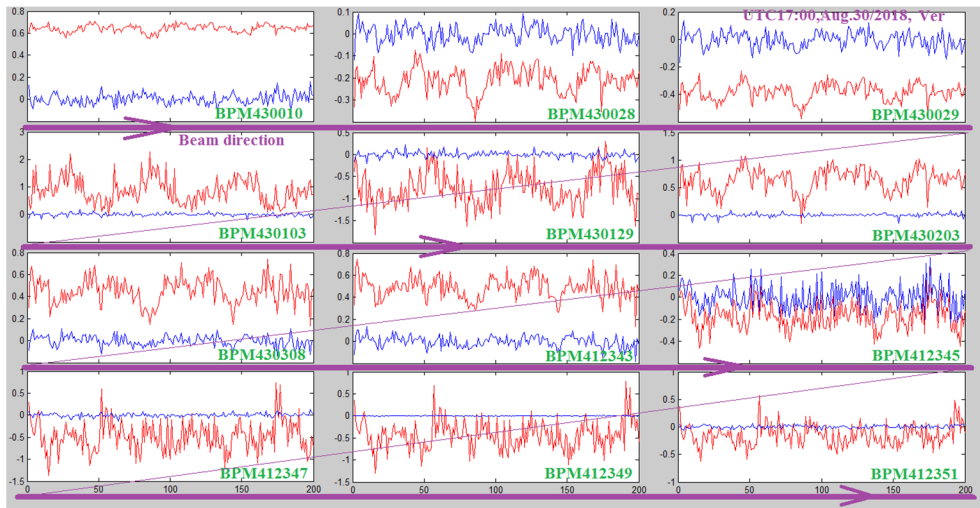


Figure 6: Correlated beam jitter vs. beam jitter removed through SVD algorithm.

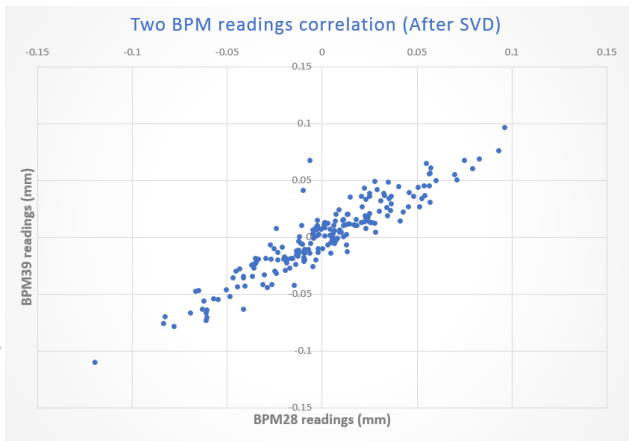


Figure 7: Correlated beam jitter at BPM430028,430039 after SVD.

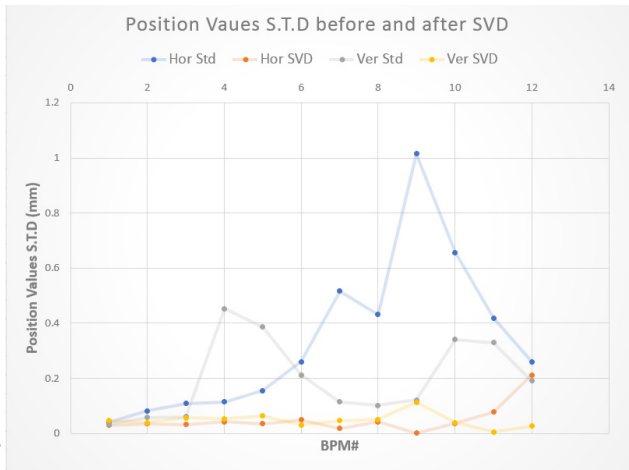


Figure 8: Beam position STD before and after SVD.

ACKNOWLEDGMENTS

Authors would like to thank the AWAKE operation team for the assistance during the beam time.

REFERENCES

[1] E. Gschwendtner *et al.*, “AWAKE, The Advanced Proton Driven Plasma Wakefield Acceleration Experiment at CERN”, *Nucl. Instr. Method. Physics Research Section A: Accelerator, Spectrometers, Detectors and Associated Equipment*, vol. 829, 1 Sep. 2016, pp. 76-82.

[2] R. Shafer, “Beam Position Monitoring”, *AIP Conf. Proc. on Accelerator Instrumentation*, Upton, NY, 1989.

[3] S. Liu *et al.*, “Development of AWAKE Stripline BPM Electronics”, in *Proc. Int. Conf. on Technology and Instrumentation in Particle Physics 2017*, pp. 237-242, [https://link.springer.com/chapter/10.1007/978-981-13-1313-4\\_46](https://link.springer.com/chapter/10.1007/978-981-13-1313-4_46)

[4] E. Adli *et al.*, “Acceleration of electrons in the plasma wakefield of a proton bunch”, *Nature*, Aug. 29, 2018. <https://www.nature.com/articles/s41586-018-0485-4>



# COMPLETE TEST RESULTS OF NEW BPM ELECTRONICS FOR THE ESRF NEW LE-RING

B.K. Scheidt, ESRF, Grenoble, France

## Abstract

Among the 320 BPMs in the ESRF new low-emittance ring, a set of 128 units will be equipped with new electronics, while the other set (192) will be served by the existing Libera-Brilliance electronics. These new electronics are an upgraded version of the low-cost Spark electronics originally developed 3 years ago for the ESRF's injector complex. All these 128 units have been installed in the first half of 2018 on existing BPM signals (through duplication with RF-splitters) and subsequently been tested thoroughly for performance characteristics like stability, resolution and reliability. It shows that while these Sparks have a very straightforward and simple concept, i.e. completely omitting calibration schemes like RF-cross-bar switching, pilot-tone introduction or active temperature control, they are fully compatible with all the beam position measurement requirements of this new ring.

## OVERVIEW OF THE BPM SYSTEM

The BPM system in this new storage ring will be a hybrid type with both two types of BPM-block geometries, and two types of BPM electronics. The lattice parameters of the new ring are given in Fig. 1 that represents one complete cell out of the total of 32, with the 10 BPMs indicated in triangles.

The Fig. 2 shows some numeric details of that lattice, the distribution in a cell of the large and the small geometry, and the distribution of the 2 types of electronics.

For the latter we will use a) 192 Liberas that were bought nearly 10 years ago and b) 128 newly developed and procured Sparks. [1]

The old storage ring with 224 BPMs is served with an equal number of Libera-Brilliance units with satisfactory performance and reliability over these 10 years and therefore the logical choice would have been to procure more of them to make-up for the new total number of 320 BPMs. [2]

However, these units had become obsolete. In looking for a satisfactory alternative, we have turned towards a different device that was developed, 3 years earlier, for new Booster BPMs. These relatively simple, straight-forward and of moderate cost Spark electronics offered enough scope for upgrading in order to make them comply with our overall BPM needs and requirements of this new storage ring. [3, 4]

By re-using 192 Libera units out of the 224 presently active units we have increased our cover for spares.

These two different electronics provide data-streams, and buffers with identically synchronised sampling-rates. However, the Fast-Orbit-Correction will only use the 10 kHz stream provided by the 192 Liberas. [5]

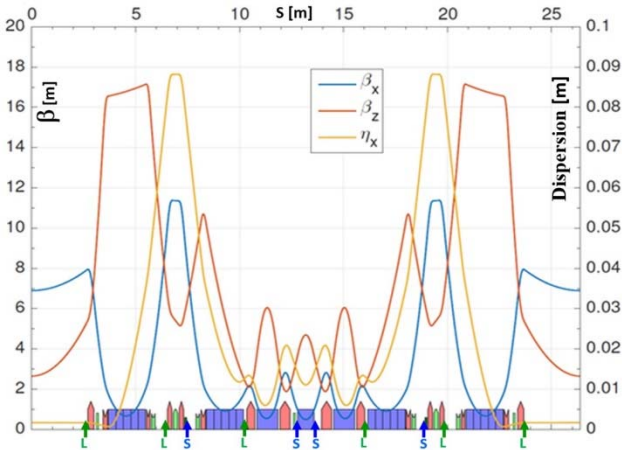


Figure 1: The lattice of one complete cell with the 10 BPM positions indicated by blue/green triangles

BPM	Geom.	Libera/Spark	S [m]	$\beta$ Hor [m]	$\beta$ Vert [m]	Disp.[cm]
1	Large	Libera	2.65	7.92	5.30	0.2
2	Large	Libera	6.48	9.50	7.17	8.0
3	Large	Spark	7.52	7.82	6.54	7.3
4	Small	Libera	10.29	1.93	2.33	1.3
5	Small	Spark	12.73	1.13	3.39	1.5
6	Small	Spark	13.64	1.13	3.39	1.5
7	Small	Libera	16.08	1.93	2.33	1.3
8	Large	Spark	18.86	7.82	6.54	7.3
9	Large	Libera	19.90	9.50	7.17	8.0
10	Large	Libera	23.72	7.92	5.30	0.2

Figure 2: The BPM geometry and the type of electronics.

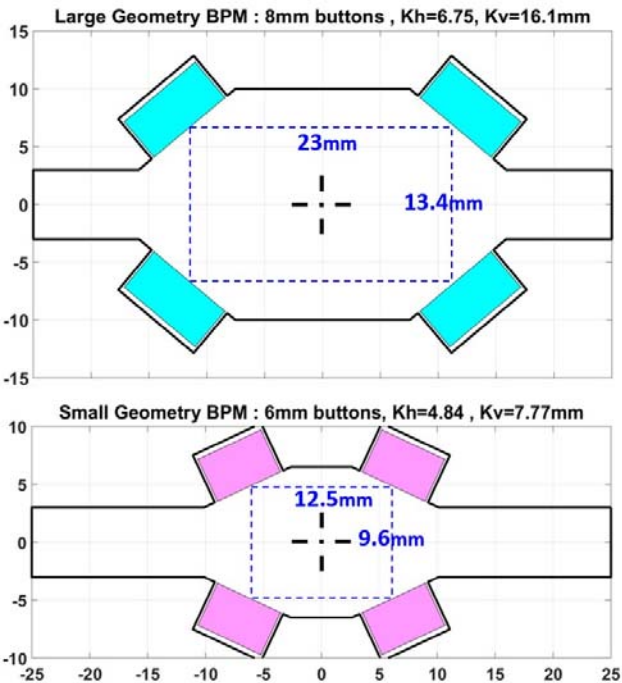


Figure 3: The distinct geometries of the two BPM blocks.



## Drift, Stability and Reproducibility Tests of The Sparks over Short and (Very) Long Periods

It is recalled here that the Spark device is basically a 4 channel digitizer for RF-signals, without any active calibration or compensation scheme. In other BPM electronics such a scheme aims at keeping the 4 sensitivities of each channel equal, typically  $< 1\text{E-}4$  rms (relative variation) which would correspond to  $0.5\text{ }\mu\text{m}$  rms positional stability in a BPM system (for  $K=10\text{ mm}$ ). Instead, the Spark relies on an intrinsic stability of its 4 channels, obtained by a careful and compact design, with the absence of internal ventilators. Verifications of this important stability requirement on a few prototypes had been successful. However, the remaining challenge was to now satisfy this requirement: a) in numerous units ( $>100$ ), and b) over much longer time-scales then obtained with a typical laboratory set-up.

The performance in terms of resolution, for short lengths of measurements (i.e 1 ms to 1 sec) had already been verified on the prototypes, and were found to be excellent and better than those from the Libera-Brilliance units. [7]

The noise value of 10 nm rms on the SA-stream (see Fig. 4) applies for a 1 sec measurement time. The described test configuration of (up to)  $32 \times 4$  Sparks allowed us to now measure this same value (now better qualified as drift) for measurement times from minutes up to months.

The general method was to detect any deviation (in H & V position data, with  $K=10\text{ mm}$ ) between each of the 4 units, being themselves in strict parallel & identical conditions. The RF-splitters themselves are supposed without any drift, and so any deviation (drift) detected is attributed to the Spark devices. The initial position offsets (at  $T_0$ ) of each on the 4 units were removed, with rms drift recorded from then on.

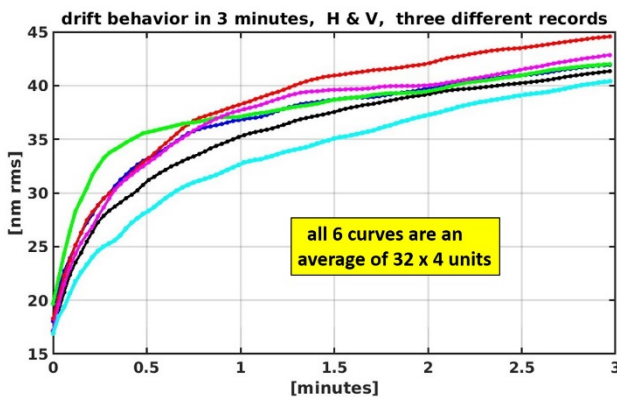


Figure 6: Drift evolution in a 3 minutes period.

Figures 6 and 7 show this drift behaviour over periods of respect. 3 minutes and 6 hours. A total of 6 curves are shown, to simply illustrate that such behaviour is not strictly identical or very reproducible. However, to be noted are the small values: after 3 minutes the rms drift is below 45 nm and after 6 hours below 200 nm.

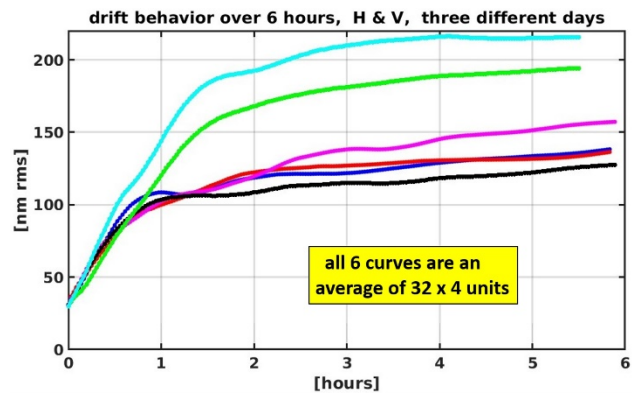


Figure 7: Drift evolution over 6 hours.

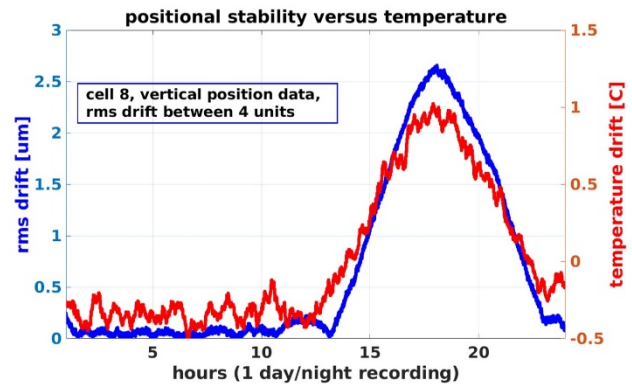


Figure 8: Temperature dependence during 24 hrs period.

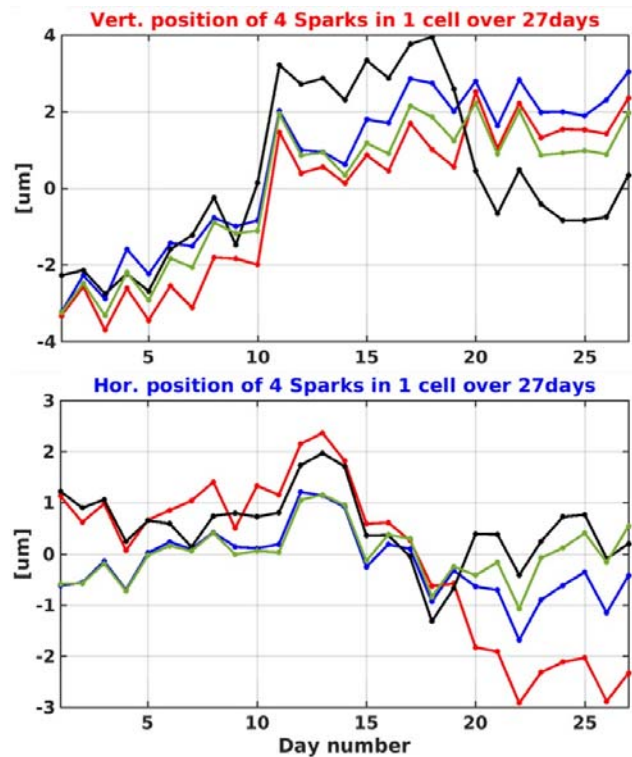


Figure 9: Stability of 4 Sparks over 27 days, top-graph: vertical position, lower-graph: horizontal position.



Assessing this drift over a (continuous) period of much longer than 6 hours was not possible since the temperature stability in our present cubicles is rather poor. The Sparks are affected by it as can be seen in Fig. 8: The temperature rises in afternoon by about 1.3 °C and the rms drift between the 4 units rises correspondingly to about 2.6  $\mu\text{m}$ . This is compatible with the device specifications of  $<3 \mu\text{m}/^\circ\text{C}$ . We will improve the cubicle's global temperature control in the future, and notably suppress this strong 24 hrs fluctuation.

To effectively assess that drift now over longer periods, e.g. one month, we took the H & V position data at each day on an average of data within 1 hr of stable temperature (typically taken in the night). The Fig. 9 shows the stability over 27 days of 4 such Sparks in one cubicle. The curves show a) some common variation (attributed to motion of the beam in that common BPM) and b) the non-common part that can be attributed to drifts of the Sparks.

The rms value of the 4 position values, both hor. and vert. is calculated, but now on 24 such cells (i.e. 96 Sparks) and shown in Fig. 10. The conclusion is that the average stability over a 24 days period is below 1  $\mu\text{m}$ .

Drift versus beam current was also assessed and found to be below 1  $\mu\text{m}$  for  $>50\%$  variation of beam current.

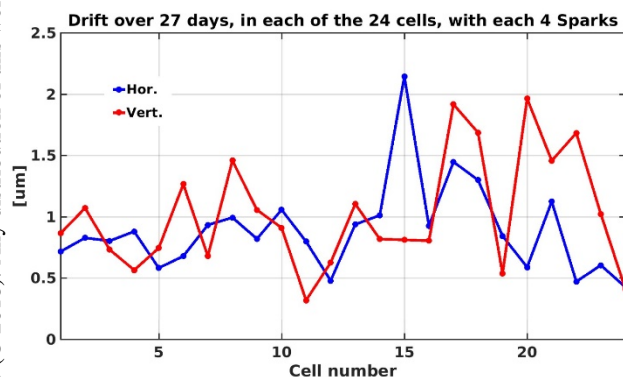


Figure 10: Drift rms over 24 days on 24 x 4 BPM stations.

## SOFTWARE AND OTHER TOPICS

The devices include a Tango interface provided by the company, with the source code available to our ESRF software engineers, allowing modifications and the implementation of position calculations based on polynomial approximations. The latter are more accurate than the ordinary delta-over-sum (dos) algorithm.

We did the assessment of such polynomial-based calculation on the embedded dual core ARM processor of the unit. It offers very good performances for double precision floating point arithmetic, with up to 700K positions calculations per second using a seventh order, 2 dimensional polynomial. This speed is sufficient for the 40 Hz real time stream and to yield triggered buffers without problems or any noticeable extra delay.

The simulations done with boundary-element methods have shown that the dos formula is strongly un-precise, for both BPM geometries, even for moderate displacements from the BPM centre. The same tool (Bpmlab) used for these simulations also allows the calculation of a suitable set of polynomials. [8]

These polynomials and their coefficients, with different sets for the two BPM geometries, are conveniently uploaded into the above software. When selected, under Tango control, they provide the beam coordinates with much higher accuracy even for a strongly off-centred ( $>10\text{mm}$ ) beam position as can be expected during the beam trajectory studies at the initial commissioning period of this new ring.

However, for the fast orbit control, the 10 kHz FA-data-stream (provided by the 192 Libera-brilliance units only), will only use the dos algorithm as before.

## CONCLUSION

We tested a large number of Spark BPM electronics simultaneously and for many months under situations and conditions comparable to normal use for beam orbit control, i.e. with real BPM input signals, corresponding timing & clock signals, and with full integration into the computer network. The results are very satisfactory in terms of resolution, stability and reproducibility, also concerning the overall reliability of this device. We thereby demonstrated that this Spark, characterised by a careful design that omits complexity, can fully satisfy the orbit measurement requirements of the ESRF's new low emittance ring from 2020 onwards.

## ACKNOWLEDGEMENTS

The author would like to thank the colleagues in the ACU-unit, and notably J-L.Pons, for the smooth integration of these devices in the ESRF control & computer system. Colleagues in the Diagnostics group have also been very helpful, and notably F.Taoutaou, for the physical installation, connectorization and configuration of the devices and all the RF cables & components in the cubicles.

## REFERENCES

- [1] Instrumentation Technologies, <https://www.i-tech.si/>.
- [2] K.Scheidt, "Installation and commissioning of a complete upgrade of the BPM system for the ESRF Storage Ring", in *Proc. DIPAC'09*, paper MOPD05.
- [3] K.Scheidt, "First results with the prototypes of new BPM electronics for the Booster of the ESRF", in *Proc. IBIC'14*, paper TUPF15.
- [4] M.Cargnelutti, "Commissioning results of the new BPM electronics of the ESRF Booster", in *Proc. IPAC'15*, paper MOAB3.
- [5] E.Plouviez, "The orbit correction scheme of the new EBS of the ESRF", in *Proc. IBIC'16*, paper MOPG09.
- [6] K.Scheidt, "Newly developed Buttons for the BPMs in the ESRF Low-Emittance Ring", in *Proc. IBIC'14*, paper TUPF14.
- [7] K.Scheidt, presentations at Libera and DEELS workshops in 2015, 2016.
- [8] A. A. Nosych, U. Iriso, J. Olle, "Electrostatic finite-element code to study geometrical nonlinear effects of BPMs in 2D", in *Proc. IBIC'15*, paper TUPB047.



# RESULTS OF SPIRAL2 BEAM POSITION MONITORS ON THE TEST BENCH OF THE RFQ

M.B. Abdillah †, P. Ausset, Institut de Physique Nucléaire, IPN, Orsay, France  
R.Ferdinand, Grand Accélérateur National d'Ions Lourds, GANIL, Caen, France

## Abstract

SPIRAL2 project is based on a multi-beam superconducting LINAC designed to accelerate 5 mA deuteron beams up to 40 MeV, proton beams up to 33 MeV and 1 mA light and heavy ions ( $Q/A = 1/3$ ) up to 14.5 MeV/A. The accurate tuning of the LINAC is essential for the operation of SPIRAL2 and requires measurement of the beam transverse position, the phase of the beam with respect to the radiofrequency voltage, the ellipticity of the beam and the beam energy with the help of Beam Position Monitor (BPM) system. The commissioning of the RFQ gave us the opportunity to install two BPM sensors, associated with their electronics, mounted on a test bench. The test bench is a D-plate fully equipped with a complete set of beam diagnostic equipment in order to characterize as completely as possible the beam delivered by the RFQ and to gain experience with the behaviour of these diagnostics under beam operation. This paper addresses the measurements carried with the two BPMs on the Dplate: energy, transverse position and ellipticity under 750 keV proton beam operation.

## GENERAL DESCRIPTION OF SPIRAL2

SPIRAL2 facility is being installed in Caen, France. It includes a multi-beam driver accelerator (5mA/40MeV deuterons, 5mA/14.5MeV/A heavy ions). The injector is constituted by an ECR ion source ( $Q/A = 1/3$ ), an ECR deuteron/proton source, a low energy beam line (LEBT) followed by a room temperature RFQ which accelerates beam up to an energy of 0.75MeV/u. A medium energy line (MEBT) transfers the beam to the superconducting Linac.

The Linac is composed of 19 cryomodules: 12 contain one  $\beta = 0.07$  cavity and 7 contain two  $\beta = 0.12$  cavities. The cavities operate at  $F_{acc} = 88.0525\text{MHz}$ .

Main beams accelerated by the superconducting Linac are mentioned in table 1.

Table 1: SPIRAL2 Main Beams Parameters

Particle	Current(mA)	Energy(MeV/u)
Proton	0.15-5	2 -33
Deuteron	0.15-5	2 -20
$Q/A = 1/3$	0.15-1	2 -14.5
$Q/A = 1/6$	0.15-1	2 -8

SPIRAL2 nominal mode of operation is planned to be C.W. mode. The considerations on commissioning and tuning periods of the LINAC lead to a pulsed mode operation in order to minimize the mean power of the beam. The

shortest duration of a macro-pulse will be 100  $\mu\text{s}$ . The repetition period varies from 1ms to 1s. The intermediate configurations have to be taken in account in order to reach the C.W. operation. The step to increase or decrease either the macro pulse duration or the repetition rate will be 1  $\mu\text{s}$ .

## SPIRAL2 BEAM POSITION MONITORS

A doublet of magnetic quadrupoles is placed between the cryomodules for the horizontal and vertical transverse focusing of the beam. Beam Position Monitors (BPMs), of the electrostatic type, is inserted in the vacuum pipe located inside the quadrupoles of the LINAC.

20 BPMs are installed along the SPIRAL2 linac. They enable the measurement of Beam transverse position, phase and transverse beam ellipticity as defined in [1]. The combination of the measured phases of two adjacent BPMs enables the measurement of Beam energy.

SPIRAL2 BPM [1] is composed of 4 capacitive sensors. Each BPM was characterized on a dedicated test bench based on a coaxial transmission line. The characterization delivers BPM electrical centre coordinates, position and ellipticity sensitivities and offsets at  $\beta \approx 1$  [2].

Each BPM sensor feeds an electronic module through 23 meters long coaxial cables. The 20 BPM electronics modules are located in four VME 64x crates. Each module contains an analog and a digital board. The design of the analog module of the card is based on the scheme of auto-gain equalization using offset tone having frequency slightly offset from the RF reference [3]. The electronic module works either at  $F = 88.0525\text{MHz}$  or at  $2 \cdot F = 176.1050\text{MHz}$  to deliver the required information.

Two prototypes of the BPM readout electronics module were qualified in IPN leading to several upgrades in order to meet specifications. Series of 22 electronic modules is presently under qualification at IPN.

## THE SPIRAL2 INTERMEDIATE TEST BENCH (SP2-ITB)

An "Intermediate Tests Bench" (ITB) has been assembled as part of the injector commissioning plan [4]. The ITB is positioned after the focusing quadrupole following the first re-buncher of the M.E.B.T. Two other focusing quadrupoles are placed between the re-buncher, and the RFQ. A beam stopper able to withstand nearly the full power of the beam terminates the ITB which includes 18 beam diagnostics identical to the SPIRAL2 driver ones. The aim of the ITB is to fully characterize the properties of the beam accelerated by the RFQ and also to study the behaviour of these diagnostics. Figure 1 shows the ITB.

† abdillah@ipno.in2p3.fr

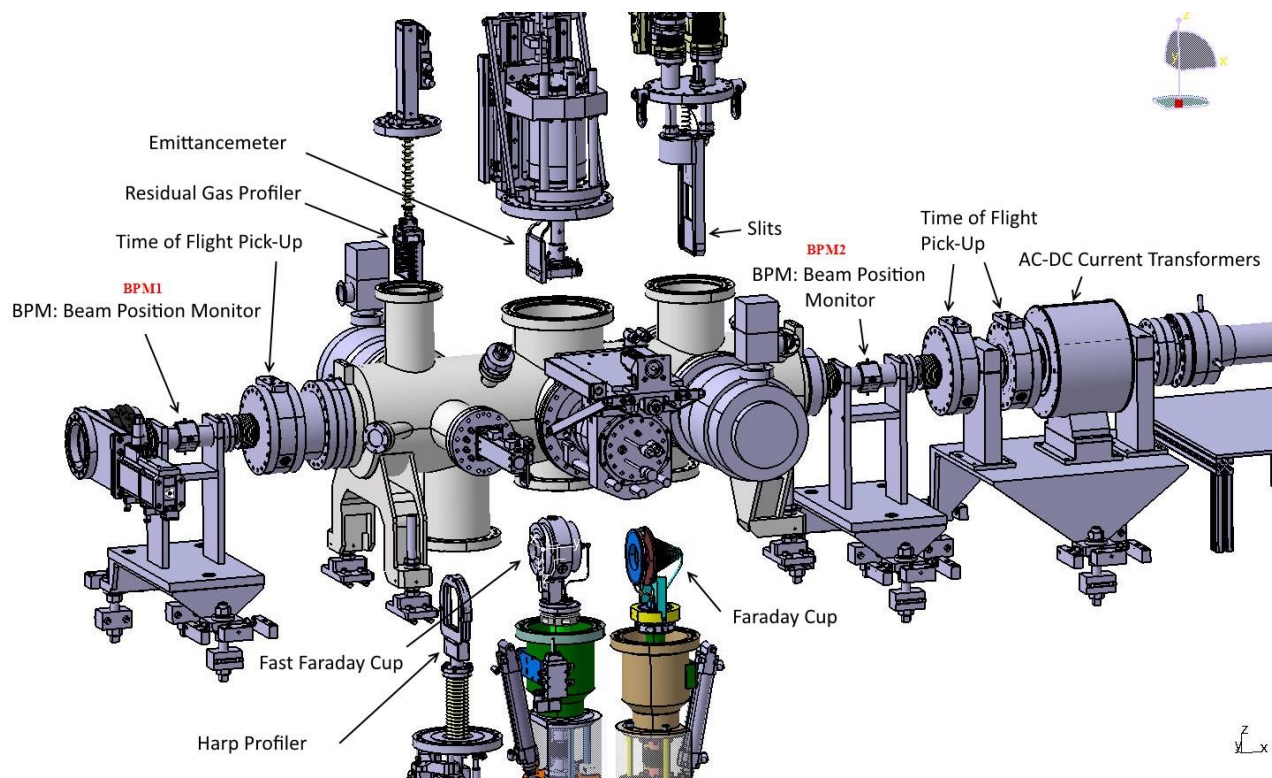


Figure 1: View of the SPIRAL2 Intermediate Test Bunch (SP2-ITB) equipped with a full set of beam diagnostics

All kinds of measurements may be carried: beam intensity, transverse beam position, profiles and emittance, phase and longitudinal emittance with a beam energy equal to 750keV/A.

Control command operation gathers the measurements performed by all these diagnostics almost on real time (every 200ms).

### BPM MEASUREMENTS ON SP2-ITB

BPM1, at the left in Fig. 1, was mounted in 2015, BPM2 was mounted in 2017. Operations with the BPM1 took place in 2016; their results were reported in [1]. Operations with both BPMs took place in fall 2017 and April 2018. The following information should be mentioned:

- Nominal relative beam velocity  $\beta_{\text{nom}}=0.03949$ .
- Distance between the 2 BPM:  $D=1,692\text{m}$ .
- Proton beam used.
- A movable slit system is located ahead BPM2 at the right of Fig. 1. It includes four slits: two in the X axis and two in the Y axis. Each slit can move in a  $\pm 5\text{mm}$  range.
  - The movable slit system induces a rectangular shape of the XY cut of the beam seen by BPM2. The centre coordinates and the lengths are controlled: for example, if the two slits on the X axis are respectively positioned at  $-4\text{mm}$  and  $2\text{mm}$  and if the two slits positioned on the Y axis are respectively positioned at  $0\text{mm}$  and  $4\text{mm}$ , then the XY cut of the beam out of the movable slits system is a rectangle centred at  $(-1\text{mm}; 2\text{mm})$  with lengths equal to  $6\text{mm}$  and  $4\text{mm}$  respectively on the X and Y axes.

- Mean Current measured by the Faraday Cup is  $1.2\text{mA}$ .
- Current measured at the beam dump at the end of the SP2-ITB varies from  $40\mu\text{A}$  corresponding to a beam aperture of  $2\text{mm}$  by  $2\text{mm}$  and to  $1\text{mA}$  corresponding to a beam aperture of  $10\text{mm} \times 10\text{mm}$ .

### BPM Current Dynamic Range

BPM1 measurements on SP2-ITB were run at early 2016, only BPM1 at the left of the image in Fig. 1 was installed and used. Measurements of BPM current dynamic range were run on January 2016 and repeated on June 2016. The following dynamic range were obtained [1]:

- $75\mu\text{A} - 5.5\text{mA}$  at F.
- $60\mu\text{A} - 5.5\text{mA}$  at  $2^*F$ .

### BPM Phase Measurements

The phase relative to the accelerating RF signal has been measured simultaneously by the two BPMs and by the three electrostatic P.U. electrodes of the time of flight (TOF) energy measurement system mounted on the SP2-ITB. The BPMs are measuring the phase at F and  $2^*F$  whereas the TOF is only measuring it at F. The RFQ phase was swept over  $360^\circ$  with a  $10^\circ$  step over different beam currents. The results show a proper behaviour of the BPM measurement system, either at F or  $2^*F$ , and a good agreement with the electrode of the TOF system over the measured beam current dynamic range: Measurements run in February 2016 showed a fluctuation within  $1^\circ$  for medium and high current where as it is less precise for the TOF at low beam currents [1].

Further measurements run in December 2017 showed less fluctuation for TOF measurements (within 1° as well).

### BPM Energy Measurements

Therefore, at a given moment, an estimated  $n=12$  bunches of protons are located between the two BPMs.

Measurement of beam energy at F is performed using the following equation:

$$E_{mes} = E_p * ((1 - \beta_{mes})^{-0.5} - 1). \quad (1)$$

where

$$\beta_{mes} = D * F_{acc} / c / (n + \Delta\phi / 360). \quad (2)$$

where  $c$  is the light velocity in vacuum,  $E_p$  is the proton energy  $E_p=938,27208\text{MeV}/c^2$ , and  $\Delta\phi$  is the difference between the phases measured by the 2 BPM.

At  $2^*F$ , equation (3) is used instead of equation (2)

$$\beta_{mes} = D * F_{acc} / c / (n + \Delta\phi / 720). \quad (3)$$

Either at F or  $2^*F$ , measured phases at BPM1 and BPM2 mostly vary only by  $0.4^\circ$ , this leads to a very precise measurement of beam energy as shown in Fig. 2.

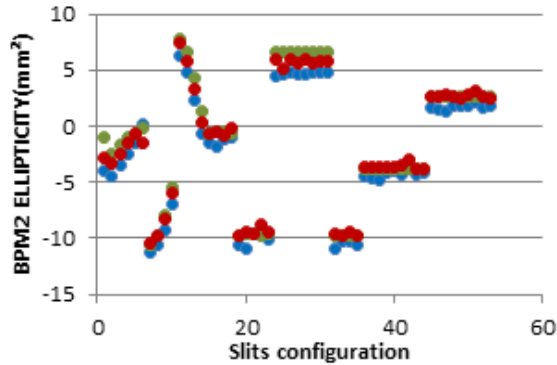


Figure 2: Beam energy measured at  $2^*F$ .

The energy measured at F is 727.6keV whether it is measured at 727.1keV with dispersion less than 200eV for both frequencies. These figures are within the precision requested for beam energy measurements ( $\Delta E/E < 10^{-3}$ ).

### BPM Position Measurements

Measurements in 2016 were run only with BPM1; the position sensitivity was preset to 25.7mm, the BPM position delivered by the readout electronics were corrected based on R.Shafer study [5]. Results showed a good agreement between profiler measurements and BPM1 measurements at F or  $2^*F$  [1].

In April 2018, the same corrections were applied for BPM1 and BPM2 position measurements. Over 50 slits configurations were used, the beam position X and Y coordinates changed in the range  $[-3\text{mm}; 2\text{mm}]$ . The beam dump current varied between  $40\mu\text{A}$  and  $1\text{mA}$ .

As Profiler was not included in operation, comparison between results of the BPM2 at both frequencies (F and

$2^*F$ ) is carried: the red dots refer to the corrected measurements at F whether the blue dots refer to the corrected measurements at  $2^*F$ .

Figures 3 and 4 show a good agreement between position measurements at both frequencies (F and  $2^*F$ ), which the good behavior of the readout electronics. Differences were under  $50\mu\text{m}$  for most slits configurations, only configuration leading to a beamdump current of  $40\mu\text{A}$  gives about 1mm difference between the measurements; though, one should notice that at the current, BPM2 sensor output amplitude is about -70dBm at both frequencies.

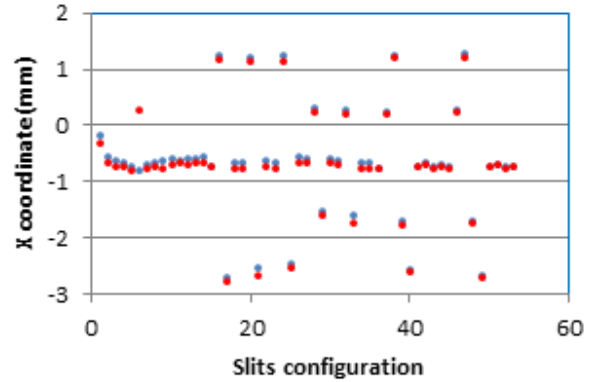


Figure 3: Beam position X coordinate measured by BPM2 vs slits configuration

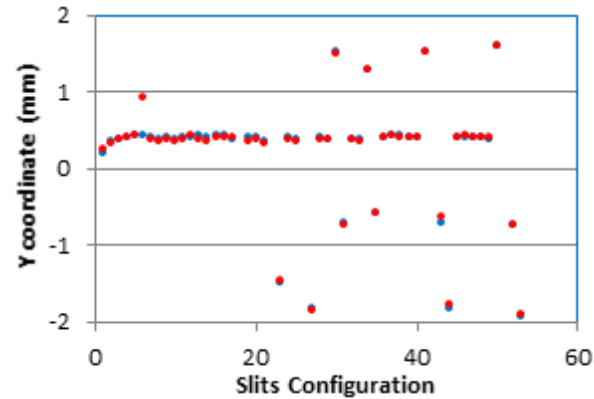


Figure 4: Beam position Y coordinate measured by BPM2 vs slits configuration).

### BPM Ellipticity Measurements

BPM ellipticity is defined as  $\sigma_x^2 - \sigma_y^2$  where  $\sigma_x$  and  $\sigma_y$  are the standard deviations of the transverse size of the beam [1]. In 2016, the beam transverse shape was modified by changing the current in the quadrupole Q13 located before BPM1. The results showed that BPM1 measurements behave in a similar way to profiler measurements and TraceWin simulations [1]. Precisions asked by specifications were not met due to different reasons, especially the lack of deep investigation of beam ellipticity sensitivity.

In 2016, the ellipticity sensitivity was set to  $354\text{mm}^2$  which is the ellipticity sensitivity measured during BPM characterization in IPNO [2], it was measured at the BPM electrical centre at  $\beta \approx 1$ . A deep study of the behaviour of



ellipticity sensitivity regarding processing harmonic change and low  $\beta$  beam was carried:

- on one side, R. Shafer [5] detailed a method to compute the BPM sensor output level at any processing harmonic for low  $\beta$  beam using modified Bessel functions. Shafer concluded with an approximate polynomial function to calculate beam position sensitivity for low  $\beta$  beam at any processing harmonic.
- On the other side, R.H. Miller [6] detailed for ultra-relativistic beams ( $\beta=1$ ) an equation to measure beam ellipticity using BPM sensors output signals.

The method detailed in [5] combined with the equation in [6] were combined to compute BPM ellipticity sensitivity for low  $\beta$  beams at any processing harmonic.

In April 2018, the position sensitivity was again set to 25.7mm and the ellipticity sensitivity was set to 374mm<sup>2</sup>, the beam position and ellipticity given by BPM readout electronics were corrected using the results of the study detailed above. The beam ellipticity was also simulated with TraceWin (TW) at BPM2 location.

The results of the over 50 slits configurations are gathered in Figure 5, the red dots refer to the corrected measurements at F, the blue dots refer to the corrected measured at 2\*F and the green dots refer to TW simulation results. The results show a good agreement between BPM measurements at both harmonics and TW simulations. The error is below the 20% threshold recommended in BPM electronics specifications.

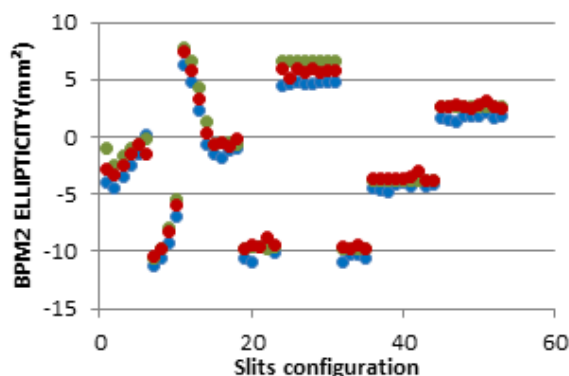


Figure 5 Ellipticity measurements by BPM2 vs Slits configuration

Ellipticity at BPM11 is kept unchanged (55mm<sup>2</sup>  $\pm$  2mm<sup>2</sup>) no matter the data used (BPM measurements at F and 2\*F, TW simulations).

## CONCLUSION

Two BPM sensors with their associated electronics for the Linac of SPIRAL 2 have been put on operation on the SP2-ITB on 2018.

Measurements of beam energy are successful and within accelerator specifications ( $\Delta E/E < 10^{-3}$ ).

The beam transverse position is measured with 50 $\mu$ m to 100 $\mu$ m precision which is within specifications (less than 150 $\mu$ m).

The phase of the beam with respect to the RF signal is measured with 0.4deg precision which is within specifications (less than 1deg).

Deep investigations were made concerning the ellipticity measurement. The results show a good agreement between TraceWin simulations and BPMs corrected measurement at low  $\beta$  beams and both harmonics. The 20% precision asked by specifications is fulfilled.

## ACKNOWLEDGMENTS

It is a pleasure to acknowledge the constant support of the SPIRAL 2 team during these experiments. We would like to acknowledge as well the constant support of BARC team to improve the BPMs readout electronics.

## REFERENCES

- [1] P. Ausset and M. Ben Abdillah, "Operation of the beam position monitor for the SPIRAL2 linac on the test bench of the RFQ", in *Proc. 2nd Int. Beam Instrumentation Conf. (IBIC'16)*, Barcelona, Spain, September 2016, paper WEPG11, pp. 642-645.
- [2] M. Ben Abdillah and P. Ausset, "Development of beam position monitors for the SPIRAL2 LINAC", in *Proc. 1st Int. Beam Instrumentation Conf. (IBIC'12)*, Tsukuba, Japan, October 2012, paper TUPA18, pp. 374-377.
- [3] G. Joshi et al., "An offset tone based gain stabilization technique for mixed-signal RF measurement systems", *Nucl. Instr. Meth.*, vol. A 795, 2015, pp. 399-408.
- [4] P. Ausset et al., "SPIRAL2 injector diagnostics", in *Proc. DIPAC 09*, Basel, Switzerland, pp. 110-112.
- [5] R.E. Shafer, "Beam Position Monitor Sensitivity for Low- $\beta$  Beams", in *Proc. 17th Linac Conf. (LINAC'94)*, Tsukuba, Japan, August 1994, paper THPA84, pp. 905-907.
- [6] R.H. Miller et al "Non intercepting emittance monitor"; SLAC- PUB - 3186. August 1983.



# DEVELOPMENT OF A NEW BUTTON BEAM-POSITION MONITOR FOR BESSY VSR\*

J.-G. Hwang<sup>†</sup>, G. Schiwietz, A. Schällicke, M. Ries, V. Dürr, D. Wolk

Helmholtz-Zentrum Berlin für Materialien und Energie GmbH (HZB), Berlin, Germany

## Abstract

An extreme operation mode such as the BESSY-VSR conditions stimulates the development of a high accuracy bunch-by-bunch beam-position monitor (BPM) system which is compatible with the bunch-selective operation for the orbit feedback system. Such a system will also greatly benefit to accelerator R&D such as transverse resonance island buckets (TRIBs). Compensation of the long-range ringing signal produced by the combined effect of impedance mismatching inside the button and trapped TE-modes in the aluminum-oxide insulator ( $\text{Al}_2\text{O}_3$ ) material is required essentially to improve the resolution. This is important since the ringing causes a misreading of the beam position and current of following bunches. We show the design study of a new button-type BPM to mitigate the influence of the ringing signal as well as to reduce wake losses by improving the impedance matching in the button and by replacing the insulator material.

## INTRODUCTION

Since 2017, the Helmholtz-Zentrum Berlin launches the BESSY variable-pulse-length storage ring (BESSY VSR) project which is an upgrade project of the existing storage ring of BESSY II to fulfill the future increasing demands to study sub-picosecond, picosecond and longer dynamics in complex systems. This is feasible by installing additional superconducting cavities with harmonic frequencies of 1.5 GHz and 1.75 GHz [1]. The cavities will be installed in a straight section of BESSY II to create long and short photon pulses simultaneously for all beam lines. This also provides a high degree of flexibility in a bunch filling pattern. Potentially, it will lead to more complex filling patterns, such as shown in Fig. 1 [2].

The filling pattern, however, has the disparity in the beam current of long and short bunches since the long bunch buckets have relatively high bunch charge to preserve the present average brilliance of BESSY II. The short bunches are added to relax beam lifetime and to supply THz power as well as high repetition rate short X-ray pulses.

## PRESENT BESSY II BUTTON BPM

From the measurement of the present button-type beam position monitor (BPM) signal with 1 mA single bunch with 1.25 MHz revolution frequency in the BESSY storage ring, we observed long-range and strong trapped modes inside the BPM. The trapped modes are also not fully damped

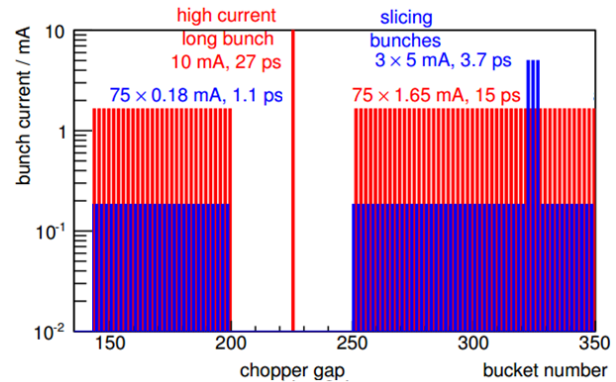


Figure 1: Section of a possible filling pattern with short bunches (blue) and long bunches (red). Trains of short bunches are added to supply THz power as well as high repetition rate short x-ray pulses.

within 2 ns, which corresponds to the bunch spacing in the ring, and it causes a signal superposition for neighboring bunches. Especially, the future filling pattern which has a large disparity in the beam charge between the short and long bunches such as BESSY VSR can cause a misreading of the beam position of the short (low-intensity) bunches. The measured BPM signal during single-bunch operation is shown in Fig. 2.

In the spectrum of the measured BPM signal, two strong trapped modes are present at the frequencies of 5.2 GHz and 5.5 GHz. Since the desirable transverse electromagnetic (TEM) mode is allowed to propagate at all frequencies, but at frequencies above the cutoff frequency ( $f_{\text{cut}}$ ), the first higher-order mode ( $\text{TE}_{11}$ ) is also allowed to propagate. The low-frequency cutoff for the undesired  $\text{TE}_{m1}$ -mode in a coaxial waveguide can be defined as [3]

$$f_{\text{cut}}^{\text{TE}_{m1}} = \frac{1}{\sqrt{\epsilon_r}} \frac{c}{\pi} \frac{m}{r_i + r_o}, \quad (1)$$

where  $r_i$  and  $r_o$  are the radii of the inner and outer conductors, respectively,  $m = 1, 2, 3, \dots$ , which indicates the field variation in azimuthal direction, and  $\epsilon_r$  is dielectric constant. Since the  $f_{\text{cut}}$  in a coaxial waveguide is inversely proportional to the square root of a dielectric constant of the insulator, the button has minimum  $f_{\text{cut}}$  value at the insulator.

In the BESSY II, the present button BPM has a diameter of 10.8 mm and gap of 0.3 mm. The thickness of button electrode is 2.6 mm and an aluminium oxide ( $\text{Al}_2\text{O}_3$ ) insulator with the diameter of 11.4 mm and thickness of 3 mm was used for a vacuum seal. Therefore, the cutoff frequency at the insulator is 5 GHz. The source of the trapped mode is

\* Work supported by German Bundesministerium für Bildung und Forschung, Land Berlin, and grants of Helmholtz Association.

<sup>†</sup> ji-gwang.hwang@helmholtz-berlin.de

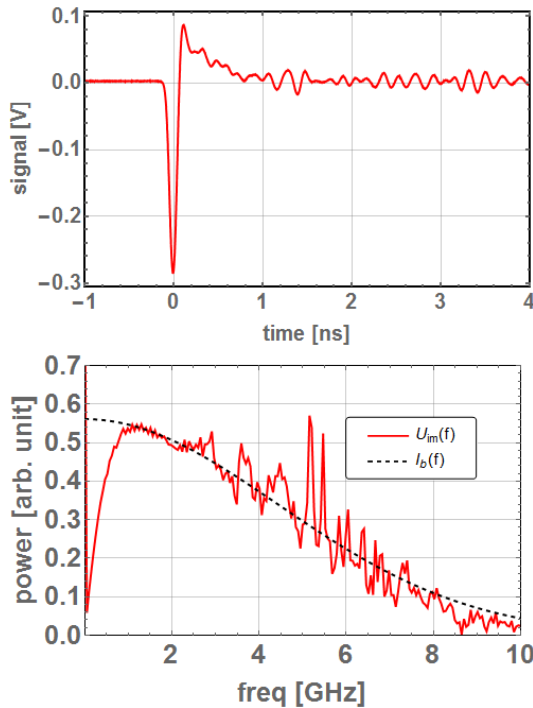


Figure 2: Measured single-bunch signal with the beam current of 1 mA (top) and the frequency spectrum of the signal (bottom) from the BESSY II button BPM. The curve named  $U_m$  is the Fourier transform of the measured signal and  $I_b$  is the spectrum of a Gaussian beam.

confirmed by a numerical simulation using CST-MWS [4]. The electric field distribution of the trapped mode is shown in Fig. 3.

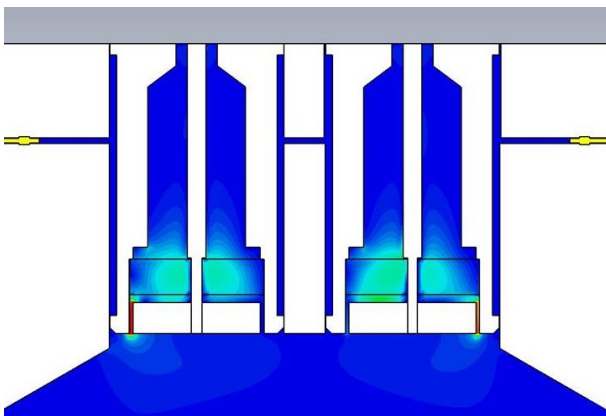


Figure 3: Computed electric field distributions of the trapped mode in aluminum oxide insulator of original button BPM at BESSY II.

## NEW BUTTON BPM DESIGN

The vacuum chamber of one straight section including fourteen button BPMs will be completely refurbished for the installation of a cryomodule for BESSY VSR. Main considerations for a new button BPM design are the smaller vacuum

chamber dimensions and the mitigation of the trapped mode. The dimension of the vacuum chamber is reduced to 24 mm × 55 mm to improve a vacuum condition and to secure the free space of 10 mm between the vacuum chamber and the magnet bore for heating jackets. The clearance gap between the button housing and vacuum chamber is also minimized to avoid the generation of high order modes. The new BPM buttons are planned to be directly welded on the vacuum chamber without flanges. In order to mitigate the coupling between the ports, the diameter of the button is reduced to 8.4 mm. The thickness of button is also reduced to 2 mm to enhance the signal intensity by reducing the capacitance of the button. The BPM chamber has an asymmetric shape to avoid the power deposited by synchrotron radiation. The cross-section diagram of the new button BPM is shown in Fig. 4.

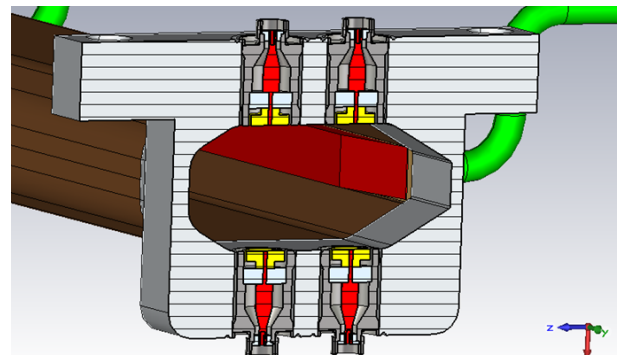


Figure 4: Cross-sectional diagram of new button BPM with diameter of 8.4 mm, thickness of 2 mm, and gap of 0.3 mm.

The insulator materials are evaluated carefully to satisfy a fabrication process and to push the cutoff frequency of the trapped mode higher such that it is damped fully within 0.5 ns. A fused silica ( $\text{SiO}_2$ ), which has the dielectric constant of 3.74, is preferred. The internal button structure is also optimized to match with the impedance of 50  $\Omega$  for reducing TEM-modes reflected back to the chamber. The optimization of the relative edge position between the inner and outer conductor is performed because the direction of TEM wave at the edge is varied at the taper. The comparison plots of calculated impedance and signal behavior between old and new buttons is shown in Figs. 5 and 6.

Since the trapped resonance modes excited in the insulator and the gap between the electrode and button housing lead to heating and beam coupling instability [5], the longitudinal beam impedance as a function of the frequency is computed. Calculations have been performed for several combinations of gap, button size, and insulator material because the amplitude of the trapped resonance modes is relevant to the geometric dimension and the material of button, housing, and insulator. This is shown in Fig. 7.

The narrow gap can reduce the stored energy, thus, it requires tighter machining tolerance to avoid electric short between the button and the housing hole. The gap of 0.3 mm and the insulator material of  $\text{SiO}_2$  are selected because it

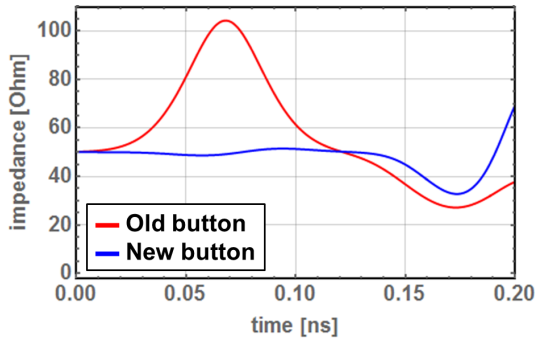


Figure 5: Comparison of calculated characteristic impedance between old and new buttons. The characteristic impedance of new button is almost constant at 50  $\Omega$  up to the end of button.

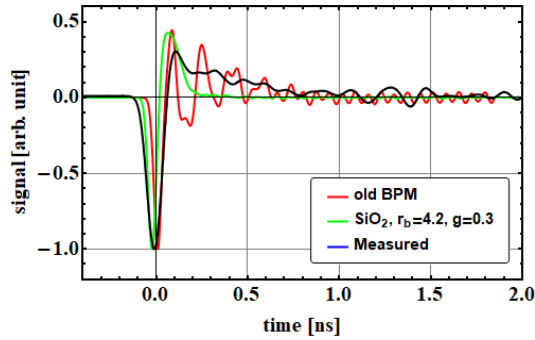


Figure 6: Comparison of signal behavior of old BPM (from CST), new BPM ( $\text{SiO}_2$ ,  $r_b=4.2$ ,  $g=0.3$  / from CST) and measured signal from present BESSY II BPM.

has almost the same amplitude but has at a higher frequency. The gap of 0.3 mm is equivalent to the present BESSY II BPM button since we have experienced no troubles with the BPM. The material of the button is determined to be molybdenum, which has an electrical conductivity  $\sigma_{MO}=17 \times 10^6 \text{ S/m}$ , because the power of the trapped mode will be predominantly dissipated in the BPM chamber rather than in well-conducted button [6].

The acceptable limit of the narrow-band impedance for avoiding coupled-bunch instabilities is a function of the frequency of the resonant mode and is given by [7]

$$Z_{lim}[\text{k}\Omega] = \frac{3 \times 10^9}{f} e^{(2\pi f \sigma_z / c)^2}, \quad (2)$$

where  $f$  is the resonant frequency,  $\sigma_z$  is the bunch length, and  $c$  is the speed of light. In order to evaluate the effect of the longitudinal impedance, the acceptable limit of the narrow-band impedance as a function of the frequency is calculated with the bunch length of  $\sigma_z = 18 \text{ ps}$  which corresponds to the nominal bunch length of BESSY II and long bunches of BESSY VSR. This is shown in Fig. 8.

The acceptable limit of the narrow-band impedance is relaxed when the resonance frequency of the trapped mode is increased. Since the new button has relatively high res-

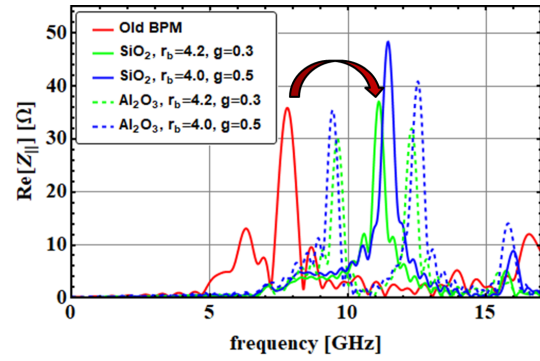


Figure 7: Longitudinal impedance as function of frequency for BPM buttons with various dimensions of button size and gap, and insulator materials.

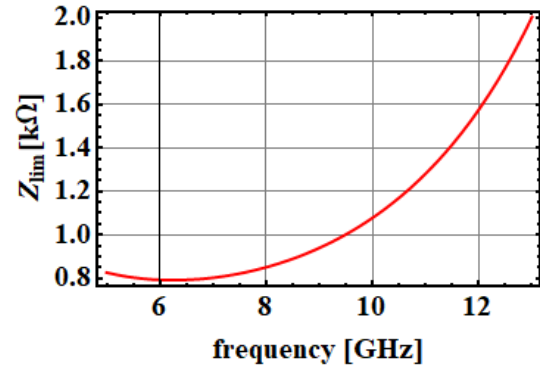


Figure 8: Acceptable limit of narrow-band impedance as function of frequency with bunch length of 18 ps.

onance frequency, the effect of the narrow-band coupled-bunch instabilities are not foreseen.

## SUMMARY

We investigated the trapped mode in the present button BPM of the BESSY II storage ring which can cause a misreading of the beam position of neighboring bunches on extreme operation modes such as BESSY VSR [8] and transverse resonance island buckets (TRIBs) [9]. The trapped mode is produced by the aluminium oxide insulator in the button and the mode has a long decay time and the resonance frequency of 5.2–5.5 GHz. In addition to the investigation, the design study of a new button-type BPM is performed to mitigate the influence of the ringing signal as well as to reduce wake losses by improving the impedance matching in the button and by replacing the insulator material. The calculation result of the new button BPM shows great promise. It could be integrated with a recently improved treatment of RF-signals for bunch resolved position determinations at a few  $\mu\text{m}$  uncertainties [10].

## REFERENCES

- [1] A. Jankowiak *et al.*, “The BESSY VSR Project for Short X-ray Pulse Production”, in *Proc. IPAC'16*, Bu-

- san, Korea, May 2016, pp. 2833–2836. doi:10.18429/JACoW-IPAC2016-WEP0W009
- [2] A. Jankowiak, J. Knobloch, *et al.*, “Technical Design Study BESSY VSR”, Helmholtz-Zentrum Berlin, 2015, doi:10.5442/R0001.
- [3] A. Blednykh *et al.*, “NSLS-II storage ring BPM button development”, in *Proc. IPAC’15*, Richmond, USA, 2015, pp. 748–750. doi:10.18429/JACoW-IPAC2015-MOPMN021
- [4] CST-MWS, <https://www.cst.com/>.
- [5] M. Masaki *et al.*, “Design optimization of button-type BPM electrode for the SPring-8 upgrade”, in *Proc. IBIC’16*, Barcelona, Spain, 2016, pp. 361–364. doi:10.18429/JACoW-IBIC2016-TUPG18
- [6] I. Pinayev and A. Blednykh, “Evaluation of heat dissipation in the BPM buttons”, in *Proc. PAC’09*, Vancouver, Canada, 2009, paper TH5RFP014, pp. 3471–3472.
- [7] C.-K. Ng *et al.*, “Simulation of PEP-II Beam Position Monitors”, SLAC, CA, USA, Rep. SLAC-PUB-95-6899, May 1995.
- [8] P. Schnizer *et al.*, “Status of the BESSY VSR project”, in *Proc. IPAC’18*, Vancouver, Canada, 2018, pp. 4138–4141. doi:10.18429/JACoW-IPAC2018-THPMF038
- [9] P. Goslawski *et al.*, “Transverse resonance island buckets as bunch separation scheme”, in *Proc. IPAC’17*, Copenhagen, Denmark, 2017, pp. 3059–3062. doi:10.18429/JACoW-IPAC2017-WEPIK057
- [10] F. Falkenstern *et al.*, “Accurate bunch resolved BPM system”, in *Proc. IBIC’16*, Barcelona, Spain, 2016, pp. 312–315. doi:10.18429/JACoW-IBIC2016-TUPG03



# DESIGN OF A CAVITY BEAM POSITION MONITOR FOR THE ARES ACCELERATOR AT DESY

D. Lipka\*, M. Dohlus, M. Marx, S. Vilcins, M. Werner, DESY, Hamburg, Germany

## Abstract

The SINBAD facility (Short and INnovative Bunches and Accelerators at DESY) is foreseen to host various experiments in the field of production of ultra-short electron bunches and novel high gradient acceleration techniques. The SINBAD linac, also called ARES (Accelerator Research Experiment at SINBAD), will be a conventional S-band linear RF accelerator allowing the production of low charge (within a range between 0.5 pC and 1000 pC) electron bunches. To detect the position of low charge bunches, a cavity beam position monitor is being designed based on the experience from the European XFEL. It will consist of a stainless steel body with a quality factor of 70, a resonance frequency of 3.3 GHz and a relative wide gap of 15 mm to reach a high position sensitivity of 4.25 V/(nC mm) of the dipole resonator. The design considerations and simulation results of the dipole and reference resonator will be presented.

## INTRODUCTION

SINBAD is a dedicated accelerator R&D facility currently under construction at DESY, Hamburg, and will host the ARES linac (Accelerator Research Experiment at SINBAD). It will consist of a normal conducting photo-injector and a 100 MeV S-band linear accelerator with beam repetition rates between 10 and 50 Hz for the production of low charge beams (0.5–30 pC) with (sub-) fs duration and excellent arrival time stability [1–3]. For dedicated user experiments bunch charges up to 1000 pC are foreseen. To observe the beam transverse position with highest precision the requirements include a resolution of 5  $\mu$ m for a beam charge between 5 and 100 pC. To achieve this requirement a cavity beam position monitor (CBPM) is developed.

## DESIGN

For the general design the resonance frequency and quality factor have to be chosen for the dipole and reference resonator of the CBPM. Both parameters should be similar for the dipole and reference resonator to simplify the signal processing. Since the inner tube diameter is 34 mm with a cut-off frequency of 6.75 GHz the resonance frequency should be smaller. To receive a reliable resonance field with this tube diameter a resonance frequency of  $f = 3.3$  GHz is defined. The relative low beam repetition rate would allow to use a long *ringing* signal to analyze the waveform. Therefore a relative high quality factor with a long decay time could be applied. But the voltage amplitude and following the sensitivity would be small therefore a low loaded quality

factor of  $Q_L = 70$  is chosen which results in a bandwidth of 47 MHz. This allows a monitor production in stainless steel. The basic design is depicted from the SACLA facility [4] which was modified for the European XFEL [5]. The quality factor and resonance frequency of the new design are similar to the European XFEL CBPMs for synergy but with other tube diameter and resonator thickness of the dipole resonator.

## Dipole Resonator

The  $TM_{11}$  mode of the dipole resonator provides a signal proportional to beam offset and charge. The amplitude sensitivity  $S = \pi f \sqrt{\frac{Z}{Q_{ext}}} \left(\frac{R}{Q}\right)^1$  [6], with the line impedance  $Z = 50 \Omega$  and the normalized shunt impedance  $\left(\frac{R}{Q}\right)$ , is increased by a relative small external quality factor  $Q_{ext}$ . The antenna position defines the value of the external quality factor; a low value dominates the loaded quality factor because  $\frac{1}{Q_L} = \frac{1}{Q_{ext}} + \frac{1}{Q_0}$  with  $Q_0$  the internal quality factor (which is still relative large compared to  $Q_{ext}$  for stainless steel). To obtain a larger sensitivity the normalized shunt impedance can be increased by using a large resonator thickness  $l$  because  $\left(\frac{R}{Q}\right) \propto l$  [7], in this design  $l = 15$  mm is applied. The Eigenmode solver of the simulation tool CST [8] is used to design and investigate the resonator properties. The resulting geometry is shown in Figs. 1 and 2.

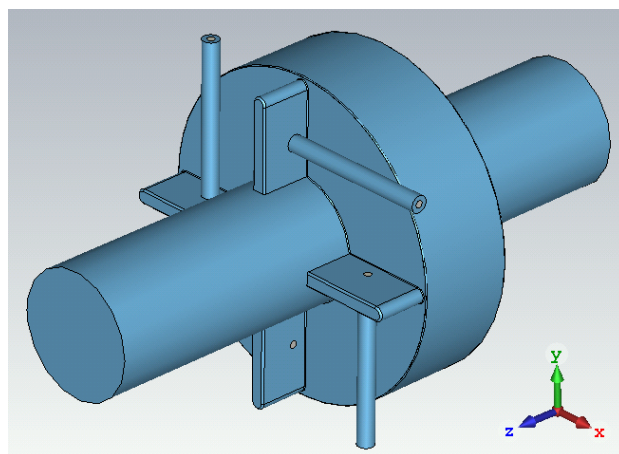


Figure 1: 3-dimensional simulation view of the vacuum part of the dipole resonator.

The resonator has a kink to decrease the resonator diameter which bends the dipole field. This is an advantage for a smaller overall monitor transverse size. The dipole field is propagating into the four slots where the dominating

\* dirk.lipka@desy.de

<sup>1</sup> The development of this equation is described in the appendix.

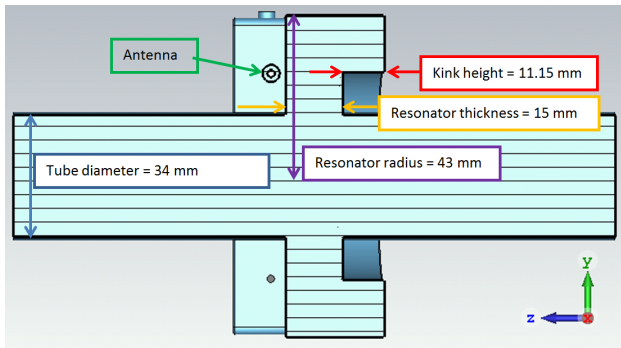


Figure 2: Cut view of the simulated dipole resonator with main design parameters.

monopole field  $TM_{01}$  is attenuated and therefore in comparison with the dipole signal negligible at the antenna positions [9].

An additional signal is generated when the beam is not parallel to the CBPM axis with a phase difference of  $90^\circ$  compared to the offset signal, this signal will increase with the resonator thickness [10]. To simulate the beam angle signal, the “particle in cell” (PIC) solver of CST [8] is used. The resulting relative angle compared to the offset amplitude results to be 8.7 mm/rad, this means that a beam angle of 1 rad results in the same signal amplitude as a beam offset of 8.7 mm. This value is even smaller compared to the European XFEL design with 40.5 mm tube diameter of 15.7 mm/rad, although a resonator thickness of 3 mm is used<sup>2</sup>.

Dedicated simulations are done to investigate the angle influence based on different resonator thicknesses with the same tube diameter. Here the angle signal is increased by 10 % between  $l = 3$  mm and 10 mm resonator thicknesses. This shows that the resonator thickness is not the main contribution to the angle influence; the tube diameter influence is larger.

In Table 1 the property results are summarized. The resonance frequency and loaded quality factor are investigated with mechanical tolerances. When all geometric tolerances are taken into account and will add linearly to a difference of the design value, a maximum deviation is obtained; the results are shown in Table 1 too. The values show that the deviation of the resonance frequency is expected to be small compared to the bandwidth and therefore no tuners are necessary for the production of the resonator.

### Reference Resonator

The reference resonator is used to measure a charge dependent signal to normalize the dipole signal and define the direction of the offset by RF phase comparison between both resonators. Here a smaller resonator thickness can be used because the sensitivity of the  $TM_{01}$  mode is much higher compared to the dipole signal. To compare the phase of

<sup>2</sup> A dipole resonator with 10 mm tube diameter and 3 mm resonator thickness with the same resonance frequency and quality factor results in 0.9 mm/rad.

Table 1: Dipole Resonator Property Results

property	value
$f$	$(3300.0 \pm 5.8)$ MHz
$Q_L$	$69.9 \pm 2.3$
$Q_0$	1264 (Stainless steel)
$Q_{ext}$	74.1
$S$	4.25 V/(nC mm)

the dipole and reference resonator signals the resonance frequency and loaded quality factors should be similar. Therefore the goal values of the resonator are equal to the dipole resonator. The design of the reference resonator is shown in Figs. 3 and 4.

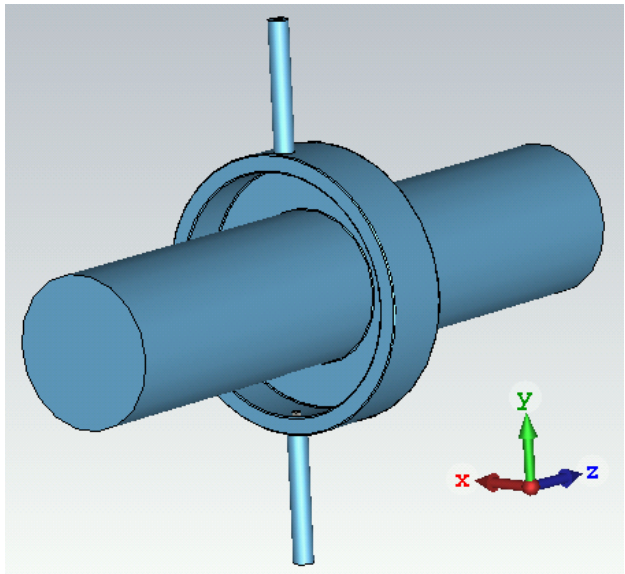


Figure 3: 3-dimensional simulation view of the vacuum part of the reference resonator.

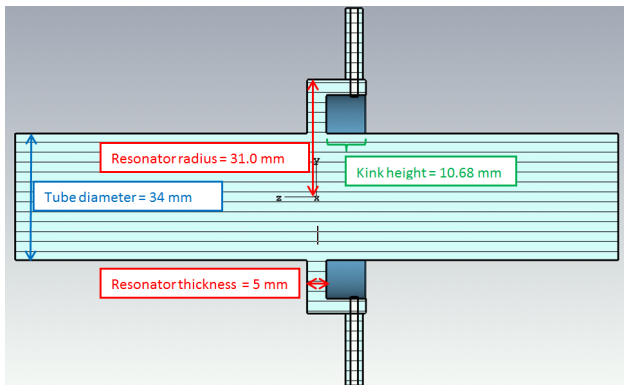


Figure 4: Cut view of the simulated reference resonator with main design parameters.

Two antennas are foreseen to add a symmetry to the design and be able to get a second charge output. A kink is used for the reference resonator too; this bends the monopole

mode into it and the antenna can transfer the signal to a perpendicular port (compared to the beam direction). This is useful for a compact longitudinal mechanical size of the CBPM. The kink high is smaller compared to the resonator thickness to decrease the external quality factor to the desired value.

In Table 2 the resulting reference resonator properties are summarized. The resonance frequency is the same as for the dipole resonator, the loaded quality factor is slightly smaller, but still within an acceptable limit. Tolerance studies with the expected mechanical deviations result in maximum possible deviations of the resonance frequency and quality factor. Here the deviation of the frequency is larger due to a higher impact of the kink thickness and length. But the maximum deviation of dipole and reference signal is still smaller than the bandwidth. Therefore this design can be produced without tuners for the reference resonator as well.

Table 2: Reference Resonator Property Results

property	value
$f$	$(3300.0 \pm 13.3)$ MHz
$Q_L$	$68.9 \pm 2.6$
$Q_0$	514 (Stainless steel)
$Q_{\text{ext}}$	79.6
$S$	44.5 V/nC

### Compound of Both Resonators

Joining both resonators results in the complete CBPM. But the strong monopole field of the reference resonator at the same resonance frequency can influence the dipole field. To minimize this influence the distance between both resonators has to be specified. We assume that the dipole field is negligible when the resulting offset is below  $0.1 \mu\text{m}$ ; this corresponds to a sensitivity of  $S_{\text{dipole}}(0.1 \mu\text{m}) = 0.424 \text{ mV/nC}$ , see Table 1. The ratio  $20 \log_{10}(S_{\text{dipole}}(0.1 \mu\text{m})/S_{\text{reference}}) = -100.4 \text{ dB}$  defines the maximum transmission for any combination between the ports of both resonators. Since the dipole antennas are not arranged in a symmetry plane, the transmission to the reference resonator are not the same for all antennas. Here one needs to identify the plane with the highest influence. In the present design the  $-100 \text{ dB}$  requirement is fulfilled with a distance of  $120 \text{ mm}$  between both resonators, compare with Fig. 5. The antennas with the highest influence in the dipole resonator have the same orientation as the antennas in the reference resonator.

## SUMMARY

The CBPM is designed for the ARES accelerator to fulfill the requirements. For the dipole resonator, a wide gap was selected for high sensitivity, resulting in a still tolerable beam angle influence. Tolerance studies are performed and show that the required resonance frequencies and loaded quality factors can be achieved without tuners. The distance between

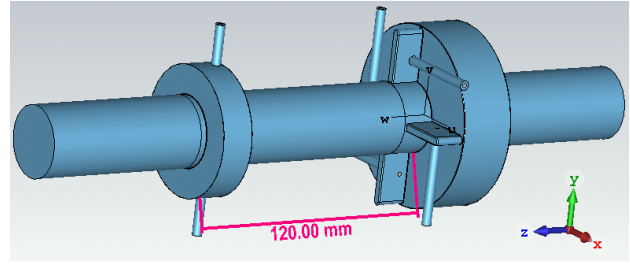


Figure 5: 3-dimensional simulation view of the vacuum part of both resonators with distance.

both resonators are defined to get a negligible influence of the reference to the dipole resonator.

## APPENDIX

The development of the sensitivity equation is following. The voltage on an integration path in a cavity is defined to be  $U(x, y) = \left| \int E_z(x, y, z) e^{\frac{i\omega z}{c}} dz \right|$  with  $E_z$  the field inside the cavity and the loss factor  $k(x, y) = \frac{|U(x, y)|^2}{4W_{\text{tot}}}$ . The total energy loss in one resonance mode can be expressed in terms of the loss factor of a beam of charge  $q$  to be

$$W_{\text{mode}}(x, y) = q^2 k(x, y) \quad (1)$$

and is distributed to the external and internal losses

$$W_{\text{mode}}(x, y) = \left( \sum_i^{\text{\#Ports}} \frac{Q_L}{Q_{\text{ext,Port } i}} + \frac{Q_L}{Q_0} \right) W_{\text{mode}}(x, y). \quad (2)$$

Here one needs to consider that each port has its own external quality factor. For a dipole mode two  $Q_{\text{ext,Port}}$  are connected to the same mode; these external quality factors have usually the same value

$$\sum_i^{\text{\#Ports}} \frac{1}{Q_{\text{ext,dipole } i}} = \frac{1}{Q_{\text{ext,Port1}}} + \frac{1}{Q_{\text{ext,Port2}}} \quad (3)$$

and therefore the common external dipole quality factor is

$$\frac{1}{Q_{\text{ext,dipole}}} = \frac{2}{Q_{\text{ext,Port}}}. \quad (4)$$

The output power on one port results to be

$$P_{\text{Port}}(x, y, t) = \frac{Q_L}{Q_{\text{ext,Port}}} W_{\text{mode}}(x, y) \frac{2}{\tau} e^{-\frac{2t}{\tau}} \quad (5)$$

with the decay time  $\tau = \frac{Q_L}{\pi f}$ . With equation (1) it can be rewritten to

$$P_{\text{Port}}(x, y, t) = \frac{2q^2 \pi f k(x, y)}{Q_{\text{ext,Port}}} e^{-\frac{2t}{\tau}}. \quad (6)$$

The voltage on a port can be expressed with  $U^2(x, y, t) = P_{\text{Port}}(x, y, t) Z$  with  $Z$  the impedance of the port, usually  $50 \Omega$ , and is for this case

$$U(x, y, t) = q e^{-\frac{t}{\tau}} \sqrt{\frac{2\pi f Z}{Q_{\text{ext,Port}}} k(x, y)}. \quad (7)$$

The loss factor can be expressed to be

$$k(x, y) = \frac{\omega}{2} \left( \frac{R}{Q} \right) (x, y) \quad (8)$$

with the geometric dependent normalized shunt impedance of the mode [7]. The resulting sensitivity is the charge normalized voltage at  $t = 0$

$$S = \frac{U(x, y, t = 0)}{q} = \pi f \sqrt{\frac{2Z}{Q_{\text{ext,Port}}}} \left( \frac{R}{Q} \right) (x, y). \quad (9)$$

For the dipole mode the term  $\frac{2}{Q_{\text{ext,Port}}}$  can be replaced by  $\frac{1}{Q_{\text{ext,dipole}}}$  (compare with equation (4)) which is the case in [6]. In the presented design two antennas are used in the reference resonator therefore equation (9) can be applied in the similar way like the dipole resonator. Usually the reference resonator has only one antenna therefore equation (3) reduces to one term such that the common external quality factor is the same as the single port external quality factor.

## REFERENCES

- [1] U. Dorda *et al.*, “Status and objectives of the dedicated accelerator R&D facility (SINBAD) at DESY”, in *Proc. 3rd European Advanced Accelerator Concepts Workshop (EAAC'17)*, Elba, Italy, Sept. 2017, <https://arxiv.org/pdf/1801.02825.pdf>.
- [2] U. Dorda *et al.*, “The dedicated accelerator R&D facility SINBAD at DESY”, in *Proc. 8th Int. Particle Accelerator Conf. (IPAC'17)*, Copenhagen, Denmark, May 2017, pp. 869–872. doi:10.18429/JACoW-IPAC2017-M0PVA012
- [3] B. Marchetti *et al.*, “Status update of the Sinbad-Ares linac under construction at DESY”, in *Proc. 8th Int. Particle Accelerator Conf. (IPAC'17)*, Copenhagen, Denmark, May 2017, pp. 1412–1414. doi:10.18429/JACoW-IPAC2017-TUPAB040
- [4] H. Maesaka *et al.*, “Sub-micron resolution rf cavity beam position monitor system at the SACLA XFEL facility”, *Nucl. Instrum. Meth.*, vol. 696, pp. 66–74, Dec. 2012. doi:10.1016/j.nima.2012.08.088
- [5] D. Lipka, D. Nölle, M. Siemens, S. Vilcins, “Development of cavity BPM for the European XFEL”, in *Proc. 25th Linear Accelerator Conf. (LINAC'10)*, Tsukuba, Japan, pp. 629–631, Sep. 2010, <http://accelconf.web.cern.ch/accelconf/linac2010/papers/tup094.pdf>.
- [6] S. Walston *et al.*, “Performance of a high resolution cavity beam position monitor system”, *Nucl. Instrum. Meth.*, vol. 578, issue 1, pp. 1–22, 2007. doi:10.1016/j.nima.2007.04.162
- [7] R. Lorenz, “Cavity beam position monitors”, in *Proc. 8th Beam Instrumentation Conf. (BIW'98)*, Stanford, USA, AIP Conference Proceedings, vol. 451, no. 1, pp. 53–73, 1998. doi:10.1063/1.57039
- [8] Computer Simulation Technology, <http://www.cst.com>
- [9] V. Balakin *et al.*, “Experimental results from a microwave cavity beam position monitor”, in *Proc. 18th Particle Accelerator Conf. (PAC'99)*, New York, USA, March 1999, pp. 461–464. doi:10.1109/PAC.1999.795732
- [10] T. Shintake, “Development of nanometer resolution RF-BPMs”, in *Proc. 17th Internat. Conf. on High Energy Accelerators (HEACC'98)*, Dubna, Russia, Sep. 1998, [http://inspirehep.net/record/920873/files/HEACC98\\_340-344.pdf](http://inspirehep.net/record/920873/files/HEACC98_340-344.pdf).



# STABILITY STUDY OF BEAM POSITION MEASUREMENT BASED ON HIGHER ORDER MODE SIGNALS AT FLASH

J. H. Wei<sup>†</sup>, NSRL, University of Science and Technology of China, 230026 Hefei, P. R. China  
and Deutsches Elektronen-Synchrotron, 22607 Hamburg, Germany

L. Shi, Paul Scherrer Institut, 5232 Villigen PSI, Switzerland

N. Baboi, Deutsches Elektronen-Synchrotron, 22607 Hamburg, Germany

## Abstract

FLASH is a free-electron laser driven by a superconducting linac at DESY in Hamburg. It generates high-brilliance XUV and soft X-ray pulses by SASE (Self Amplified Spontaneous Emission). Many accelerating cavities are equipped with HOMBPMs (Higher Order Mode based Beam Position Monitors) to align the beam and monitor the transverse beam position. However, these lose their position prediction ability over time. In this paper, we applied an efficient measurement and signal analysis with various data process methods including PLS (Partial Least Square) and SVD (Singular Value Decomposition) to determine the transverse beam position. By fitting the HOM signals with a genetic algorithm, we implemented a new HOMBPM calibration procedure and obtained reliable beam prediction positions over a long time. A stable RMS error of about 0.2 mm by using the spectra of signals and 0.15 mm by using the new method over two months has been observed.

## INTRODUCTION

FLASH [1] was originally a test facility for various physics studies of the superconducting technologies. It serves nowadays as a Free Electron Laser (FEL) user facility as well as a test facility for advanced Linac facilities such as the European XFEL and ILC. Figure 1 shows the schematic layout of FLASH with three beam lines. FLASH1, FLASH2 are used for generation of high brilliance ultra-short ultraviolet (XUV) and soft X-ray pulses. They are able to provide a beam for two experiments simultaneously. The third beamline accommodates FLASH-Forward, a beam-driven plasma-wakefield experiment. There are seven accelerating cryo-modules along the linac. Each module contains eight TESLA superconducting cavities with 1.3 GHz working frequency. There is also one module with four 3.9 GHz cavities to linearize the energy chirp induced by the first accelerating module in the longitudinal phase space.

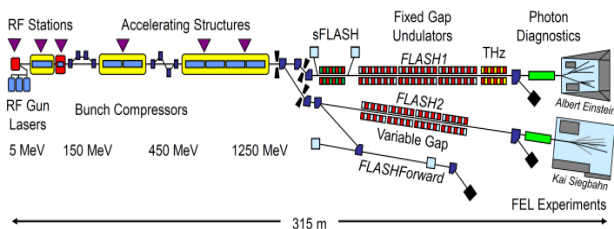


Figure 1: Schematic layout of FLASH [1].

<sup>†</sup> junhao.wei@desy.de.

When an electron beam passes through the cavities, it excites wakefields, which can deteriorate the beam quality and may result in a beam-break-up instability in the worst case [2]. Therefore two couplers installed at both sides of the TESLA cavity are specially designed to extract them (see Fig. 2). The wakefields can be expanded as a multipole series of so-called modes. The modes with higher frequency than the accelerating mode are named Higher Order Modes (HOMs). Among these, dipole modes can be utilised to determine the beam position since their amplitude has linear dependence on the beam offset. Based on this, a HOMBPM system was built. A 4  $\mu\text{m}$  resolution rms was observed in one cavity [3]. However, the beam position readout calibration is unstable over time [4]. In order to solve this problem, we use a method based on genetic algorithm (GA) to fit the beam excited signals. After that, several methods are applied to predict the beam position.

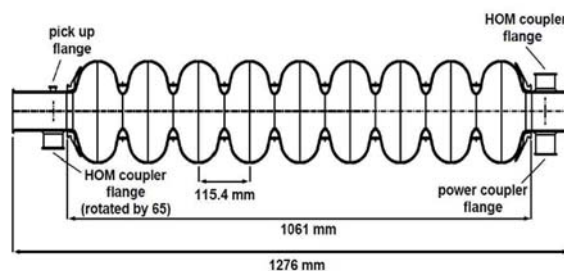


Figure 2: Drawing of the TESLA cavity with nine cells, one power input coupler, one probe antenna and two HOM couplers.

Next section introduces the measurement principle of the dipole mode signal and the GA fitting procedure. The following section presents the results of the HOMBPMs in several cavities with different calibration methods. The paper ends with conclusions.

## DIPOLE MODE SIGNAL

The dipole mode signal from the HOM ports excited by a traversing bunch can be affected by four beam parameters: the bunch charge, the trajectory offset, the trajectory tilt and the bunch tilt [5]. For short bunches, as is the case at FLASH, the bunch tilt signals are vanishingly small compared with beam offset signals. A 5 mrad trajectory tilt will excite the signal with the same amplitude as 1 mm bunch offset for 1.3 GHz cavities [6]. In our measurement, the

trajectory tilt is less than 1 mrad and therefore the contribution from the trajectory tilt to the HOM signals is very small.

### Signal Measurement

Measurements have been made at the 5<sup>th</sup> cryo-module at FLASH. Figure 3 shows a sketch of the experiment [3]. The beam position was varied using two pairs of steerer magnets. The HOM signals generated when a bunch passes through the module, are measured by the electronics. The charge was read out synchronously from a nearby toroid, and the beam position from two BPMs located upstream and downstream of the module for the same bunch.

The dipole mode TE111-6 at around 1.7 GHz was selected for the HOMBPM based on the simulation results in the 1.3 GHz TESLA cavity [7]. It has strong coupling to the beam, reflected in the high R/Q parameter, and therefore it can provide higher sensitivity to the beam position. The signal is processed by a narrow band electronics. It filters the HOM signal at 1.7 GHz with a 20 MHz narrow bandpass and down mixes to 20 MHz IF (intermediate frequency), which is then sampled at about 108 MHz by an ADC. An example of a signal waveform from cavity 4 in the FLASH module 5 and its FFT spectrum are shown in Fig. 4. The dipole mode contains two close peaks, which correspond to the two polarization directions of the mode. The amplitudes of the peaks are linearly related to the beam position in the cavity.

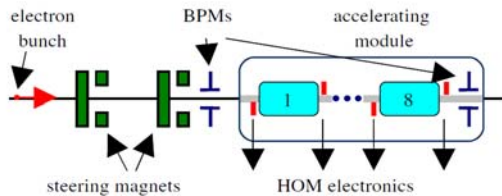


Figure 3: Setup for HOM beam position measurement.

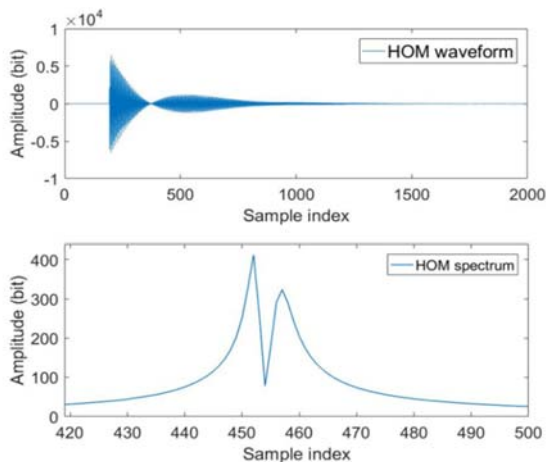


Figure 4: An example of the HOM dipole mode waveform from the HOMBPM electronics and its spectrum.

### Signal Curve Fitting

As we mentioned in the first section, the HOMBPM calibration loses its reliability over days. This is mainly because of phase drifts. It proved to be difficult to reliably calculate and correct the phase drift from the waveform directly, in part because of the uncertainty in the mode frequency. Therefore we determine the phase drifts by fitting the dipole mode signal. This consists mainly of two components corresponding to the two signal peaks. Therefore the general expression of the HOM signal can be written as:

$$A = a_0 + a_1 \sin(\omega_1 t + \phi_1) e^{-\frac{t}{\tau_1}} + a_2 \sin(\omega_2 t + \phi_2) e^{-\frac{t}{\tau_2}}, \quad (1)$$

where  $a_0$  is the signal offset,  $a_{1,2}$  are the peak amplitudes,  $\omega_{1,2}$  the angular frequencies,  $\phi_{1,2}$  the phases and  $\tau_{1,2}$  the decay times of the two peaks. This function can be used to fit the signal waveform. In order to determine the parameters ( $a_{1,2}$ ,  $\phi_{1,2}$ ,  $\omega_{1,2}$  and  $\tau_{1,2}$ ), we used the genetic algorithm (GA) to minimize the STD (Standard Deviation) of the difference between the measurement signal and the fitting signal.

We cut off the parts from the signal with small Signal-Noise Ratio (SNR) as well as the transient signal since these parts hardly carry any information on the beam offset. Figure 5 shows the evolution process of the STD value during the fit procedure. When the genetic iteration number is over 150, the calculation result tends to converge.

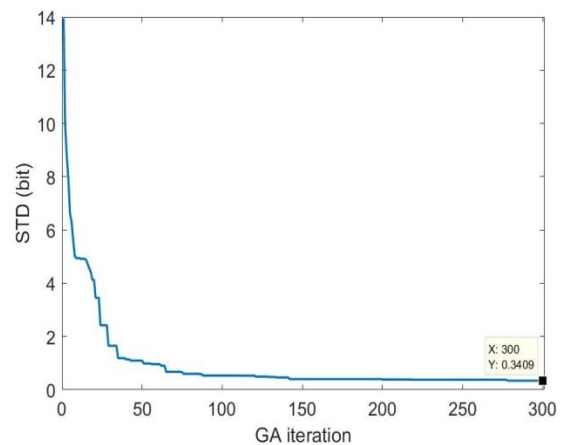


Figure 5: Iterative process of the GA.

The final STD is 0.34 bits, which is equivalent to the system noise level. The fitting curve compared with the original waveform is shown in Fig. 6. The fitting signal is basically coincident with the measured signal. The goodness of fit can be determined by the coefficient of determination ( $r^2$ ), which is over 0.9990. Therefore, this method has a quite good fitting effect.

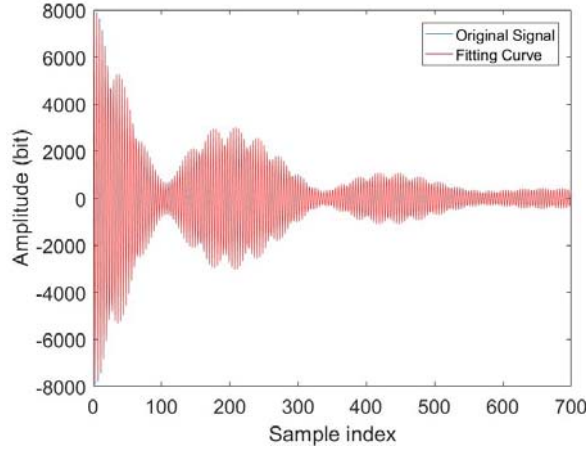


Figure 6: The original signal waveform (blue) and the fitting signal curve (red).

## HOM BEAM POSITION MEASUREMENT

### Data Preparation

Measurements have been implemented in the 5<sup>th</sup> cryo-module at FLASH. Data was taken on February 5<sup>th</sup> and on April 4<sup>th</sup>. In order to extract the beam position information concealed in the dipole modes signals, we construct the measurement signals in matrix form:

$$A = \begin{pmatrix} data_1 \\ data_2 \\ \vdots \\ data_m \end{pmatrix} = (a_1, a_2, \dots, a_n, 1) \in R^{m \times n}. \quad (2)$$

Matrix A represents the data for  $m$  measurements. It contains one additional column of ones to represent the intercept term. Both the time domain waveform and the frequency domain spectrum can be used to construct the data matrix A.

The beam position data is also put in matrix form:

$$P = \begin{pmatrix} x_1 & y_1 \\ x_2 & y_2 \\ \vdots & \vdots \\ x_m & y_m \end{pmatrix} \in R^{m \times 2}. \quad (3)$$

Matrix P represents the beam position coordinates in a given cavity interpolated from the BPM readings for all measurements.

Next we calculate the correlation between matrices A and P, to obtain the calibration matrix M:

$$A \cdot M = P. \quad (4)$$

Here the equal is used in the least square sense. For a new measurement, the beam position can be predicted by multiplying the HOM signal by the calibration matrix.

### Calibration Based on PLS and SVD

Direct Linear Regression (DLR) is a straight forward method for modelling relations between sets of observed data. However, the least squares regression model is vulnerable to noise from measurement. Therefore, we apply Particle Least Square (PLS) and Singular Value Decomposition (SVD) to solve the linear system (4) to calculate the calibration matrix.

The underlying assumption of PLS is that the observed data is generated by a system driven by a small number of latent variables [8]. The PLS method can find the latent components that have high correlation with the beam position in the HOM data.

Singular Value Decomposition (SVD) is also a useful method to reduce the dimension of the system and easily find a small number of prominent components from matrix A [4]. Matrix A is decomposed into three matrices ( $A = U \cdot S \cdot V^T$ ). The amplitudes for each signal can be constructed by:

$$A^{SVD} = A \cdot V = (A_1^{SVD}, A_2^{SVD}, \dots, A_n^{SVD}). \quad (6)$$

$A_n^{SVD}$  is a vector that contains the amplitudes for all measurements in the  $n^{th}$  SVD mode. Normally, we select 6 ~ 10 SVD modes to construct the amplitude matrix, depending on the cavity. Figure 7 shows the calibration results of PLS and SVD using the waveforms in cavity 4 in matrix A, compared to the beam positions in the same cavity interpolated from the BPMs. Table 1 gives the corresponding RMS errors. SVD has a smaller RMS error. Therefore, we choose SVD as the conventional signal processing method.

Table 1: RMS Error of Calibration using PLS and SVD

RMS error	X	Y
PLS	0.124 mm	0.150 mm
SVD	0.118 mm	0.132 mm

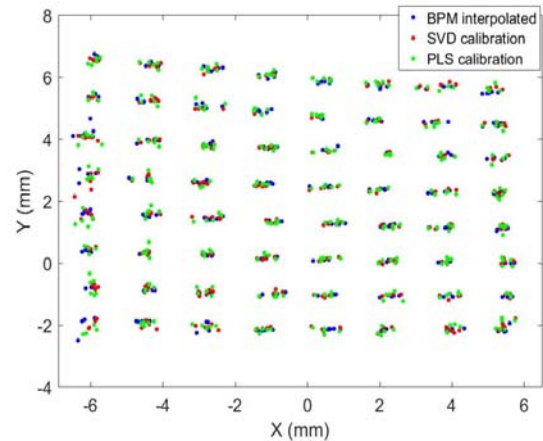


Figure 7: Calibration samples of PLS (red) and SVD (green) compared with interpolated beam positions (blue) by using the HOM waveforms.



Long Term HOMBPM Validation

Apart from the data used for calibration, further data was measured on April 4<sup>th</sup> to validate the reliability of the HOMBPM on a short time. Also, in order to validate the long-term stability of the HOMBPM system, we applied the same calibration matrix, based on the SVD method to data taken on February 5<sup>th</sup>. For the data measured on the same date (April 4<sup>th</sup>), it is quite easily to do calibration and prediction by using the signal waveform directly. We calculated the resolution of the predicted beam position in all cavities in module 5 based on the 3-BPM method, for a small position range. The best resolution was obtained for cavity 5, 8  $\mu\text{m}$  in X and 5  $\mu\text{m}$  Y rms. However, there is a phase drift in the HOM time domain waveform over a long time. This leads to a mismatch of the sample amplitudes between the calibration data and the validation data. Therefore, the calibration matrix bases on waveform gives much higher RMS error. In order to solve this problem, we use the HOM spectra with SVD method.

The predicted beam positions with HOM spectra in cavity 4 are shown in Fig. 8. The RMS error is 0.22 mm in x and 0.17 mm in y in a roughly 10 mm  $\times$  10 mm scan range. The calibration and the prediction errors are basically kept on the same level over 2 months.

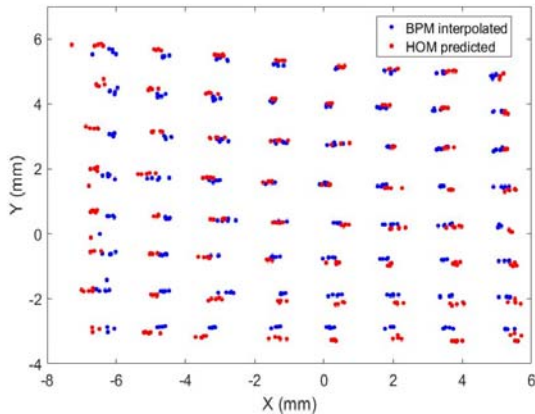


Figure 8: Predicted beam positions (red) on Feb. 5<sup>th</sup> based on HOM spectra by using SVD method compared with the BPM interpolated positions (blue).

Apart from the SVD-based methods described above, based on waveforms and on spectra, a new method of determining the beam position based on dipole signals has been developed. Based on Eq. (1), the waveform signals are reconstructed by a fitting script. The amplitudes of the two dipole mode peaks thus are obtained, which have linear dependence on the beam position. We use these amplitudes to build matrix A, and then get the calibration matrix in cavity 4 by DLR. PLS and SVD do not help here since the data is already “cleaned” by the fitting process. Afterwards, the calibration matrix is applied to the data on Feb. 5<sup>th</sup>. The results are shown in Fig. 9. This new method gives better results than the SVD/spectra method as shown in Table 2. The RMS errors remain small and comparable for the calibration and prediction samples. We plan to apply

the signal fitting process to all cavities of the 5<sup>th</sup> cryo-module.

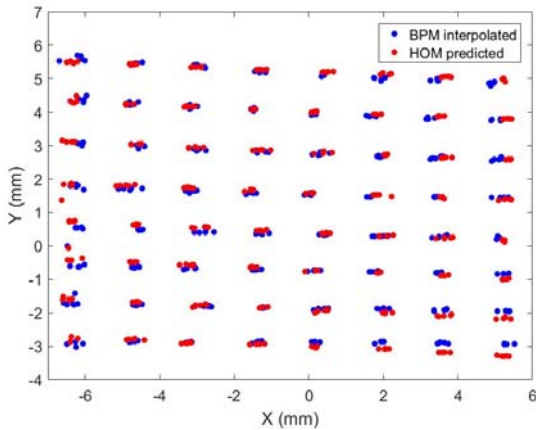


Figure 9: Predicted beam positions (red) on Feb. 5<sup>th</sup> by using the fitting method and the BPM interpolated positions (blue) as reference in cavity 4.

Table 2: RMS Error of Calibration and Prediction using Signal Fitting Method in Cavity 4

RMS error	X	Y
Calibration	0.141 mm	0.152 mm
Prediction	0.153 mm	0.137 mm

CONCLUSION

In this paper we report on a new method to stably determine the beam position over time based on HOM signals in superconducting cavities at FLASH.

When using dipole spectra, we achieved a RMS error of the beam position of about 0.2 mm over two months in the 4<sup>th</sup> cavity of 5<sup>th</sup> module. The new method gives a RMS error around 0.15 mm. The beam range was about 10 mm  $\times$  10 mm. Note that the RMS error depends on the measurement range. We remark here that this is not the resolution of the system, which is determined for a small position range. A resolution around 10  $\mu\text{m}$  has been achieved in most cavities. In the future, we plan to improve the HOMBPM signal analysis method and make it work as a regular diagnostic tool at FLASH. Besides, electronics are under design for the European XFEL [9].

REFERENCES

[1] M. Vogt *et al.*, “Status of the Soft X-ray Free Electron Laser FLASH”, in *Proc. IPAC’17*, Copenhagen Denmark, May 2017, pp. 2628-2630. doi:10.18429/JACoW-IPAC2017-WEPAB025

[2] K. Yokoya, “Cumulative Beam Breakup in Large Scale Linacs”, DESY, Hamburg, Germany, Rep. DESY 86-084, 1986.

[3] S. Molloy *et al.*, “High Precision SC Cavity Alignment Measurements with Higher Order Modes”, *Meas. Sci. Technol.*, vol. 18, pp. 2314-2319, Jul. 2007.

[4] L. Shi *et al.*, “Stability and Resolution Studies of HOMBPMs for the 1.3 GHz Superconducting Accelerating Cavities at FLASH”, *Phys. Proc.*, vol. 77, pp. 42-49, 2017.



- [5] S. Molloy *et al.*, “High Precision Superconducting Cavity Diagnostics with Higher Order Mode Measurements”, *Phys. Rev. ST Accel. Beams*, vol. 9, p. 112802, Nov. 2006. doi:10.1103/PhysRevAccelBeams.9.112802
- [6] T. Hellert *et al.*, “Higher-Order Mode-Based Cavity Misalignment Measurements at the Free-Electron Laser FLASH”, *Phys. Rev. ST Accel. Beams*, vol. 20, p. 123501, Dec. 2017. doi:10.1103/PhysRevAccelBeams.20.123501
- [7] W. Ackermann, Private Communication, Germany, 2015. [http://www.desy.de/xfel-beam/data/talks/files/2015.09.22\\_10\\_55\\_55\\_00\\_1\\_Tesla13-ModeAtlas\\_2015.pdf](http://www.desy.de/xfel-beam/data/talks/files/2015.09.22_10_55_55_00_1_Tesla13-ModeAtlas_2015.pdf)
- [8] R. Rosipal *et al.*, “Overview and Recent Advances in Partial Least Squares”, in *Subspace, Latent Structure and Feature Selection Techniques*, Berlin, Germany, Springer; 2006, pp. 34-51.
- [9] S. Jabłoński, N. Baboi, U. Mavrič, and H. Schlarb, “RF Electronics for the Measurement of Beam Induced Higher Order Modes (HOM) Implemented in the MicroTCA.4 Form Factor”, in *Proc. IPAC'18*, Vancouver, BC, Canada, May 2016, pp. 1916-1918. doi:10.18429/JACoW-IPAC2018-WEPAF046

# THE EVALUATION OF BEAM INCLINATION ANGLE ON THE CAVITY BPM POSITION MEASUREMENT\*

J. Chen<sup>1</sup>, Y. B. Leng<sup>†</sup>, L. Y. Yu, L. W. Lai, R. X. Yuan

Shanghai Institute of Applied Physics, Chinese Academy of Science, 201204 Shanghai, China

<sup>1</sup>also at University of the Chinese Academy of Science, 100049 Beijing, China

## Abstract

Cavity beam position monitor (CBPM) is widely used to measure the transverse position in free-electron laser (FEL) and international linear collider (ILC) facilities due to the characteristic of high sensitive. In order to study the limiting factors of the position resolution of cavity BPM, the influence of beam inclination angle on the measurement of CBPM position and the direction of beam deflection was analyzed. The simulation results show that the beam inclination angle is an important factor limiting the superiority of CBPM with extremely high position resolution. The relative beam experiments to change the relative inclination angle between the cavity and the electron beam based on the kicker were performed in Shanghai Soft X-ray FEL (SXFEL) facility, the experiment results will also be mentioned as well.

## INTRODUCTION

The free electron laser (FEL) is a fourth-generation light source based on the interaction between electromagnetic fields and ultra-relativistic electron bunches which travel along the axis of a vacuum beam-pipe. In order to achieve high efficiency operation of FEL, the electron beam and the generated photo beam need to be overlapped strictly and that both can pass through the entire undulator section. Therefore, requirements on the BPM system for the FEL are very stringent, especially on position stability.

Cavity BPM systems [1] adopt a resonant cavity structure and through the use of anti-symmetric characteristic mode, coupled from the cavity, to measure the beam position which can meet that requirements, so it is widely used in FEL facilities. In order to maximize the advantages of cavity BPM with extremely high-resolution, a detailed analysis of the limiting factors affecting CBPM performances is needed, especially the effect of beam inclination angle on CBPM performance. Based on this purpose, the influence of beam trajectory angle on the amplitude of position signal and the direction judgement of beam position was simulated in this paper.

Shanghai soft X-ray FEL facility is a user experiment facility with an expected capacity to generate 9-nm X-ray laser by adopting an FEL frequency doubling of ultraviolet band seeded laser of 265 nm. A total of 20 CBPM systems are installed in the undulator section for the beam position measurement. Therefore, SXFEL is also an excellent test platform for experiment verification of beam trajectory angle simulation which mentioned above. De-

tailed calculation principles, simulation results and online beam verification results will be given in the following sections.

## CALCULATION PRINCIPLE

In order to calculate the signal intensity generated when the beam trajectory has an angle through the cavity, a method of dividing a large cavity into a plurality of small cavities is adopted. As shown in Fig. 1. The position of the bunch in each small cavity can be considered to be parallel to the Z axis. Then, all the small cavities can be integrated to obtain the signal intensity when the beam has an angle and pass through the entire cavity.

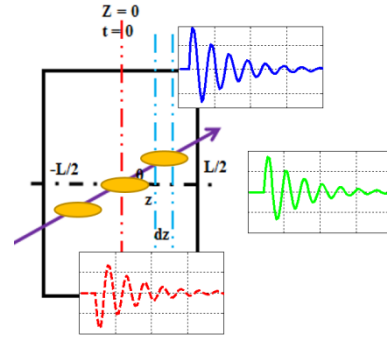


Figure 1: Model of cavity segmentation.

When the beam is parallel to the Z axis and the distance from the electrical center is x, the cavity excitation signal can be expressed by Eq.(1):

$$V_p = \frac{\omega q}{2} \sqrt{\frac{Z}{Q_{ext}}} \left[ \frac{R}{Q} \right]_0 * e^{-\frac{\omega^2 \sigma_z^2}{c^2}} * \frac{x}{x_0} * e^{-\frac{t}{2\tau}} * \sin(\omega t) \quad (1)$$

Assume that the length of the bunch is constant during this process, the cavity parameters are also fixed, and the constant term can be separated, it can expressed by Eq. (2) briefly:

$$V_p = Ax * e^{-\frac{t}{2\tau}} * \sin(\omega t) \quad (2)$$

When the beam passes through the center of the cavity but with an inclination angle  $\theta$ , the excitation voltage of the small cavity whose cavity length is dz can be written by Eq. (3):

$$dv = A * z * \tan(\theta) * e^{-\frac{t}{2\tau}} * \sin(\omega t) * \frac{dz}{L} \quad (3)$$

So the signal intensity when the beam has an angle  $\theta$  and pass through the entire cavity can be calculated by

\*Work supported by The National Key Research and Development Program of China (Grant No. 2016YFA0401903, 2016YFA0401900)

<sup>†</sup>lengyongbin@sinap.ac.cn

integrating Eq. (3) over the entire length  $L$  of the cavity, which can be expressed by Eq. (4):

$$v_\theta \approx \frac{A \tan(\theta)}{L} * e^{-\frac{t}{2\tau}} * \int_{-\frac{L}{2}}^{\frac{L}{2}} z * \left[ \cos(\omega t) * \sin\left(\frac{\omega z}{c \cos(\theta)}\right) \right] dz \quad (4)$$

$$= \frac{A \tan(\theta)}{L} * e^{-\frac{t}{2\tau}} * \cos(\omega t) \left[ \frac{2c^2 \cos^2 \theta}{\omega^2} \sin \frac{\omega L}{2c \cos \theta} - \frac{Lc \cos \theta}{\omega} \cos \frac{\omega L}{2c \cos \theta} \right]$$

From the Eq. (4), when the beam pass through the cavity center with an angle  $\theta$ , the phase of the excitation signal is  $90^\circ$  out of phase with the positional offset signal. Therefore, the signal excited by the angle cannot be eliminated by the movement of the beam.

## SIMULATION RESULTS

Based on the Eq. (4) and the cavity parameters designed by SINAP [2-3], the simulation results on the relationship between the beam angle  $\theta$  and the equivalent beam offset is shown in Fig. 2.

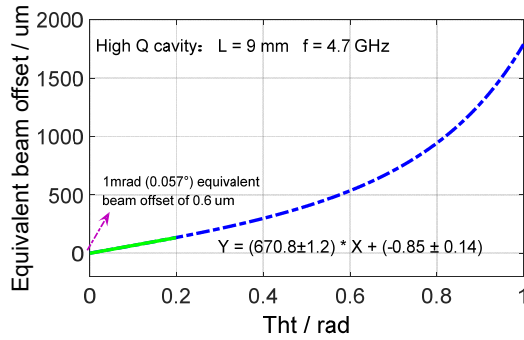


Figure 2: Relationship between the beam angle and the equivalent beam offset.

The results show if the beam trajectory has an angle about 1 mrad, the excited signal equivalent to the beam offset about 0.6  $\mu\text{m}$  and this excited signal cannot be eliminated by the movement of the beam. It means that CBPM cannot be resolved if the beam offset is less than 0.6  $\mu\text{m}$ .

When the beam trajectory has an angle, the effect of cavity length  $L$  on the equivalent beam offset is also evaluated. The results can be seen in Fig. 3.

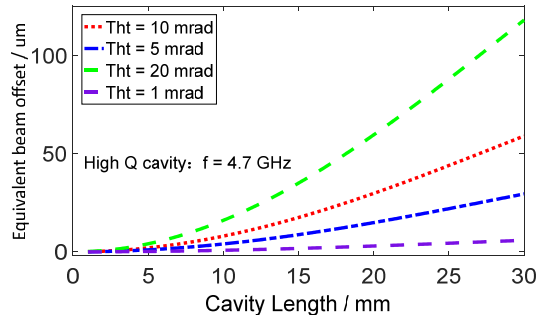


Figure 3: The effects of cavity length  $L$  on the equivalent beam offset.

The simulation results show that when the angle of beam trajectory is fixed, the equivalent beam offset increases with the increase of the cavity length, which is consistent with the physical theory.

For another case, when the beam trajectory with an angle of  $\theta$  but not pass through the electrical center of the cavity, as shown in Fig. 4.

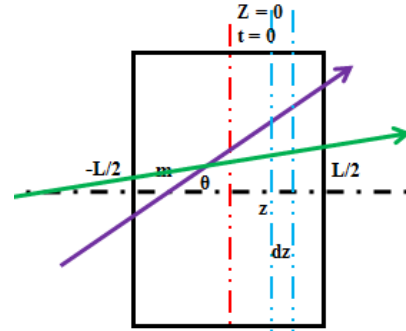


Figure 4: Diagram when the beam with an angle but not pass through the electrical center.

Assume the beam trajectory with an angle of  $\theta$  and the cross point with the  $Z$  axis is the  $m$ , then the excited signal about the can be expressed by Eq. (5):

$$v_\theta = A \int_{-\frac{L}{2}}^{\frac{L}{2}} (z - m) * \tan(\theta) * e^{-\frac{t - \frac{z}{c \cos \theta}}{2\tau}} * \sin \left[ \omega \left( t + \frac{z}{c \cos(\theta)} \right) \right] * \frac{dz}{L} \quad (5)$$

$$= \frac{A \tan(\theta)}{L} * e^{-\frac{t}{2\tau}} * \cos(\omega t) \left[ \frac{2c^2 \cos^2 \theta}{\omega^2} \sin \frac{\omega L}{2c \cos \theta} - \frac{Lc \cos \theta}{\omega} \cos \frac{\omega L}{2c \cos \theta} \right]$$

$$- \frac{A m \tan(\theta)}{L} * \frac{2c \cos(\theta)}{\omega} * \sin \left( \frac{\omega L}{2c \cos(\theta)} \right) * e^{-\frac{t}{2\tau}} * \sin(\omega t)$$

It can be divided into two parts to explain, the first part is the same with the Eq. (4) which can be equivalent to the case where the bunch has an angle but passes through the center of the cavity. The second part which can be equivalent to the case that the beam parallel to the  $Z$  axis with a beam offset. So the relationship between beam offset and equivalent beam offset with different beam trajectory angle can be illustrated in Fig. 5.

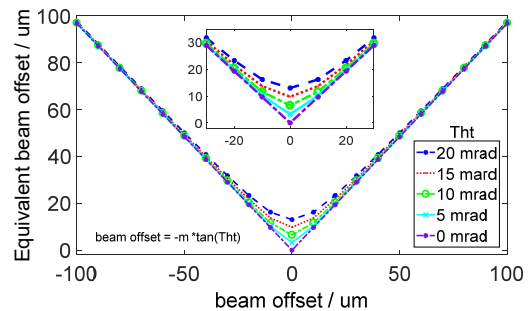


Figure 5: Relationship between beam offset and equivalent beam offset with different beam trajectory angle.

Due to the existence of beam trajectory angle, the effects on resolution is greater when working near the electricity center, while the effects is relatively small when the beam is off center ( $>50\mu\text{m}$ ).

What is discussed above is the case when the beam trajectory has an angle, so it is also necessary to discuss the effects when the bunch itself has an angle. Assuming that the bunch distributed in a Gaussian, the length of the

bunch is  $\sigma$ , the charge of the bunch is  $q$ , and the inclination of the bunch is  $\alpha$ . The model can be seen in Fig. 6.

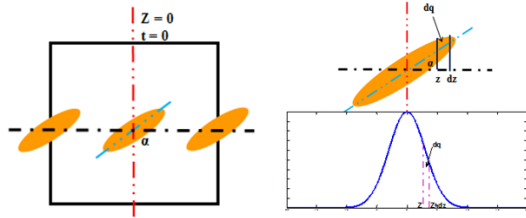


Figure 6: Diagram when the bunch itself has an angle.

When the bunch passes through the cavity along the Z axis, the equivalent result is considered to divide the bunch into a group of electrons with a charge  $dq$  distributed along the z-axis, can be written as Eq. (6):

$$dq = \frac{q}{\sqrt{2\pi}\sigma_z} * e^{-\frac{z^2}{2\sigma_z^2}} dz. \quad (6)$$

Integrating the entire space, the excited signal can be expressed by Eq. (7):

$$\begin{aligned} v_\alpha &= A * \frac{\tan(\alpha)}{\sqrt{2\pi}\sigma_z} \int_{-\infty}^{+\infty} z * e^{-\frac{z^2}{2\sigma_z^2}} * e^{-\frac{(t-\frac{z}{c})^2}{2\tau^2}} * \sin\left[\omega(t-\frac{z}{c})\right] dz \\ &= A \frac{\tan(\alpha)}{\sqrt{2\pi}\sigma_z} * e^{-\frac{t^2}{2\tau^2}} \int_{-\sigma_z}^{+\sigma_z} z * e^{-\frac{z^2}{2\sigma_z^2}} * e^{\frac{z}{2c\tau}} * \sin\left[\omega(t-\frac{z}{c})\right] dz \\ &\approx A \frac{\omega\sigma_z^2 \tan(\alpha)}{c} * e^{-\frac{t^2}{2\tau^2}} * \cos(\omega t) \end{aligned} \quad (7)$$

Therefore, when the bunch itself has an angle, the phase of the excitation signal and the position offset signal are also  $90^\circ$  out of phase. The simulation results on bunch angle and equivalent beam offset is shown in Fig. 7.

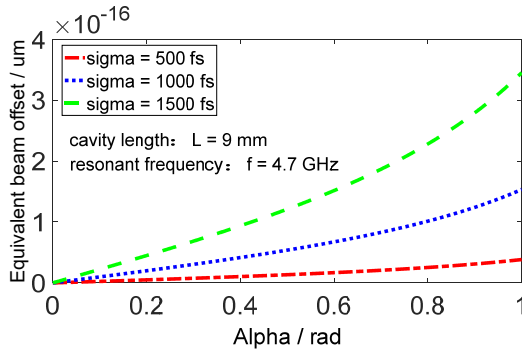


Figure 7: Simulation results on bunch angle and equivalent beam offset.

Compared with the beam trajectory angle, at the same angle of inclination, beam itself angle differs by about 18 orders of magnitude in the equivalent beam offset. Therefore, it can be considered that in the cosine term introduced by this case, the influence of the angle of the bunch itself on the beam position measurement is negligible.

## BEAM EXPERIMENTS

Some experiments based on the cavity BPM and corrective magnet which can change the angle of the beam

trajectory to verify the simulation qualitatively. Schematic of the experiment is shown in Fig. 8.

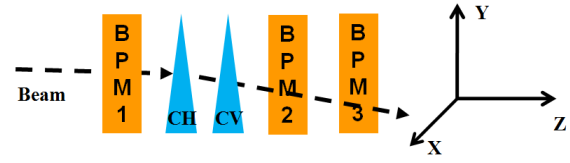


Figure 8: Experiment schematic to verify the simulation results.

Through the corrective magnet located in front of the CBPM to change the angle  $\theta$  and cross point with the Z axis and calculate current position.

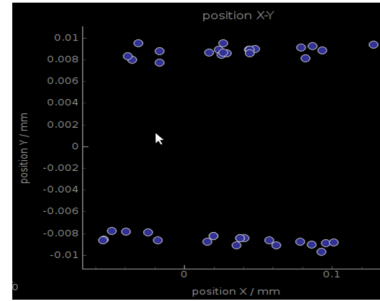


Figure 9: Experiment results when bunch with an angle.

As shown in Fig. 9, we adjusted the beam with an angle and closed to the cavity center, but we cannot find the position of electrical center. From the Fig. 9, we can find there has an indistinguishable area about 8 um. Verified the simulation qualitatively but a more accurate verification test still needs to be built on the four-dimensional mobile platform for testing.

## CONCLUSION

In this paper, the influence of the beam trajectory angle and beam's angle on the CBPM for beam position measurement was considered, related calculation and simulation has been done. Simulation results shown that the beam trajectory angle will have effects for the resolution of CBPM when electron beam closed to the electric center. Preliminary validation experiment was performed in SXFEL, but more quantitative experiments need to build a 4D mobile platform in SXFEL. And we are looking forward to getting better results in the future.

## REFERENCES

- [1] Y. Inoue *et al.*, "Development of a high-resolution cavity-beam position monitor", *Phys. Rev. Lett.*, vol. 11, pp. 062801(1-13), Jun. 2008.  
doi:10.1103/PhysRevSTAB.11.062801
- [2] J. Chen *et al.*, "Beam test results of high Q CBPM prototype for SXFEL", *Nuclear Science and Techniques.*, vol. 28, pp. 51(1-8), Aug. 2017. doi:10.1007/s41365-017-0195-x
- [3] J. Chen *et al.*, "Cavity BPM for DCLS", in *Proc. IBIC'16*, Barcelona, Spain, Sep. 2016, pp. 661-664.  
doi:10.18429/JACoW-IBIC2016-WEPG18



# DESIGN AND SIMULATION OF STRIPLINE BPM FOR HUST PROTON THERAPY FACILITY

J.Q. Li, K.J. Fan<sup>†</sup>, Q.S. Chen, K. Tang, P. Tian

State Key Laboratory of Advanced Electromagnetic Engineering and Technology  
Huazhong University of Science and Technology,  
Wuhan 430074, China

## Abstract

Proton beams used in Huazhong University of Science and Technology Proton Therapy Facility (HUST-PTF) have extreme low currents of the order of nanoampere, which is a great challenge to beam diagnostics due to low signal level. Conventional destructive beam diagnostic devices will affect the quality of the beam and cannot work online during the patient treatment, so a non-destructive stripline beam position monitor (BPM) is designed. This study will introduce some analysis and simulation results of the stripline BPM, such as the coupling between the electrodes, impedance matching, signal response, etc. We also discussed how to increase the output signal by geometry optimization.

## INTRODUCTION

Huazhong University of Science and Technology Proton Therapy Facility (HUST-PTF) is a dedicated proton therapy facility [1]. As shown in Fig. 1, it is made up of a 250 MeV superconducting cyclotron, an energy selection system, two rotating gantries, the beam line and a fixed treatment room. The beam current becomes ultra low after the proton beam passes through a degrader, which is a great challenge to measure the beam position. The beam main parameters after the degrader are described in Tab.1. Conventional measurements, such as using an ionization chamber, will introduce some degradation of the beam energy dispersion. From experience of iThemba LABS [2], we plan to design a stripline BPM for HUST-PTF.

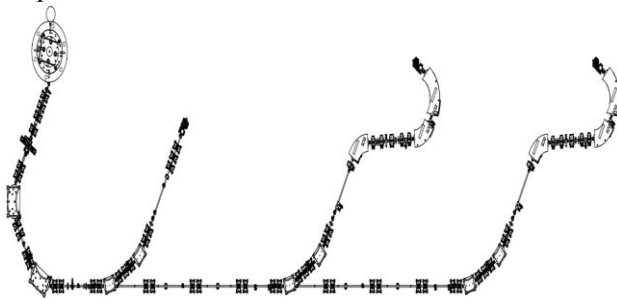


Figure 1: Layout of HUST-PTF.

Table 1: Beam Parameters After a Degraded

Parameters	value
Bunch length	~200mm
Bunch frequency	73MHz
Bunch radius	2-10mm
Beam energy	70-230MeV
Average current	0.4-4nA

The stripline BPMs can be regarded as transmission-line circuits in microwave engineering. The schematic of stripline BPM is shown in Fig. 2. It is suited for short bunch measurement because the signal propagation is considered. When a Gaussian bunch passes through the BPM, the voltage signal of the upstream port is:

$$V_U(t) = \frac{\phi Z}{4\pi} \left( \exp\left(-\frac{(t+l/c)^2}{2\sigma^2}\right) - \exp\left(-\frac{(t-l/c)^2}{2\sigma^2}\right) \right) I_b(t) \quad (1)$$

Where  $\sigma$  represents bunch length.  $l$  represents electrode length.  $\phi$  represents electrode radius. The frequency domain expression of the output signal can be written as:

$$V_U(\omega) = \frac{\phi Z}{\sqrt{2\pi}} I_b(\omega) \sin\left(\frac{\omega l}{c}\right) \quad (2)$$

$V_U(\omega)$  is made up of a series of maximum for  $f = (2n-1)c/4l$ . For a given electronic device the first voltage maxima is located at  $l = c/4f$ . Because of Libera Single Pass [3] we plan to work at  $500 \text{ MHz} \pm 5 \text{ MHz}$  in frequency domain, the electrode length is 150 mm to get the voltage maxima at 500 MHz.

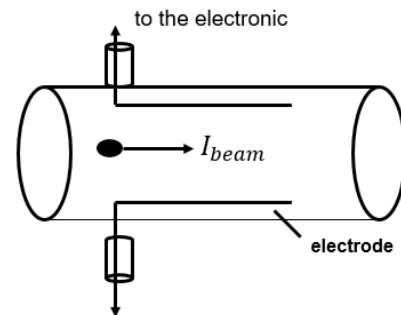


Figure 2: Schematic of stripline electrodes.

## IMPEDANCE MATCHING

From Fig. 3 it is clear that the stripline BPM has four electrodes, which support four independent TEM modes, namely a sum mode, two dipole modes (horizontal dipole and vertical dipole), and a quadrupole mode. As shown in Figs. 4 and 5, the electrodes and vacuum pipe can be

\* Work supported by national key R&D program, 2016YFC0105303.

<sup>†</sup> email address: kjfan@hust.edu.cn

regarded as transmission-line circuits, which can be handle by even-odd mode analysis method.

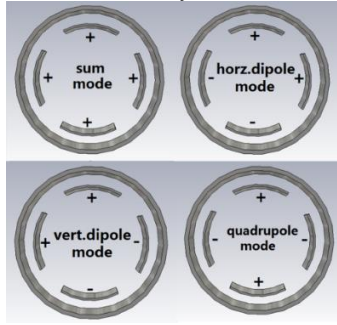


Figure 3: A typical 4 conductors BPM electrode.

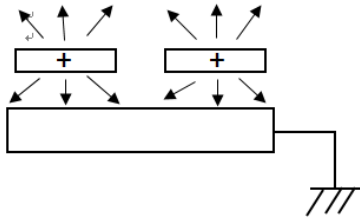


Figure 4: Even mode of coupling transmission line.

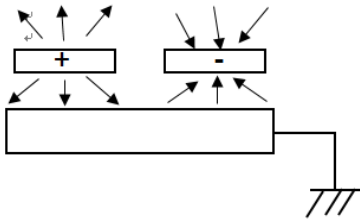


Figure 5: Odd mode of coupling transmission line.

The characteristic impedances of two dipole modes are identical because of the symmetric structure. Calculations shows that the pick-ups are optimally matched to the cable when the following conditions are satisfied [4]:

$$\sqrt{Z_{\text{sum}} Z_{\text{quad}}} = Z_{\text{dipole}} = R_0 \quad (3)$$

$R_0 = 50 \Omega$  is the transmission line impedance.

CST EM Studio can calculate the capacitance/length and field energy [5]. A simple electrode model is built in Fig. 6. Then the solution for the impedance follows directly by the relationship  $Z = \frac{1}{cC}$ . The calculated impedances of every mode are:

$$\begin{aligned} Z_{\text{sum}} &= 66.26 \Omega \\ Z_{\text{quad}} &= 43.59 \Omega \\ Z_{\text{dipole}} &= 49.81 \Omega \end{aligned} \quad (4)$$

Then the solution follows:

$$\sqrt{Z_{\text{sum}} Z_{\text{quad}}} \approx \sqrt{Z_{\text{horz}} Z_{\text{vert}}} \approx 50 \Omega \quad (5)$$

From the calculation, the impedances matching is ideal.

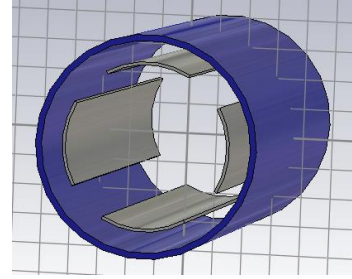


Figure 6: The electrode model in CST EM Studio.

## ELECTRODE COUPLING ANALYSIS

Excessive coupling will affect the BPM sensitivity, so it is necessary to calculate the coupling between electrodes. The electric field is concentrated in the transverse direction when the beam passes through the BPM, so the coupling analysis can be done by analyzing electrostatic field [6]. The coupling coefficient can be written as:

$$\begin{aligned} K_{12} &= C_{12} / C_{10} \\ K_{13} &= C_{13} / C_{10} \end{aligned} \quad (6)$$

CST MWS can be used to analyze the coupling between the electrodes. As shown in Fig. 7, a current source is placed on the port 1 and then other port's currents are observed.

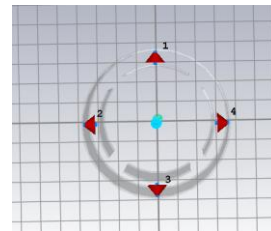


Figure 7: A BPM model in CST MWS.

Figures 8 and 9 show that current signal at port 1 and other ports respectively. The coupling coefficients between adjacent electrodes are  $K_{12} = K_{14} = 3.70\%$ . The coupling coefficient between opposite electrode is  $K_{13} = 1.45\%$ . The adjacent electrode coupling coefficients are larger than the opposite electrode coupling coefficient because of the shielding effect of the adjacent electrodes.

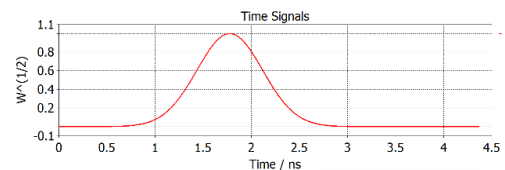


Figure 8: The current at port 1.

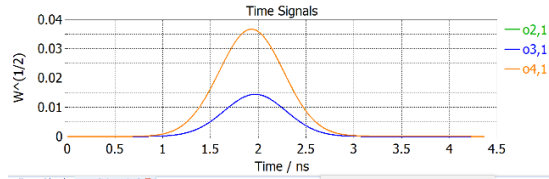


Figure 9: The currents at other ports.

Increasing the distance between adjacent electrodes can decrease the coupling, so can the sensitivity be improved. But large distance between adjacent electrodes also means that electrode radius is small, which will decrease output signal amplitude. A compromise should be made between the coupling coefficients and the output signal amplitude.

## BPM MODELING

CST Particle Studio is used to design the stripline BPM. The length of the electrode 150 mm is determined by the electronics of the BPM. The BPM geometry is determined by transmission line impedance, coupling between the electrodes and output signal amplitude. There is a positive correlation between electrode angle and output signal amplitude. However, excessive electrode angle will enlarge the electrode coupling, which will reduce BPM sensitivity. Together with the aforementioned considerations, the parameters of stripline BPM are chosen:  $\varphi=60^\circ$  ( $\varphi$  represents the electrode angle),  $\phi=27.5\text{mm}$ ,  $R=37\text{mm}$  ( $R$  represents the pipe radius). The BPM model is shown in Figure.10.

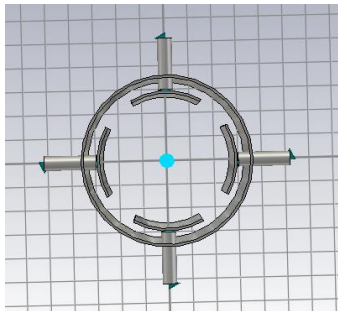


Figure 10: A BPM model in CST MWS.

Table 2: Geometry Parameters of the BPM

Parameters		value
Electrode radius		27.5mm
Electrode angle		60°
Pipe radius		37mm
Pipe thickness		1mm

A proton beam of 70\_MeV/0.4\_nA and 230\_MeV/4\_nA are used in our simulations, the output voltage signal are 19nV and 0.35uV, respectively (see Fig.11 and Fig.12). According to the experience of iThemba LABS, the voltage of the order of nanovolt can be used to detect beam position by a specified electronic equipment [7].

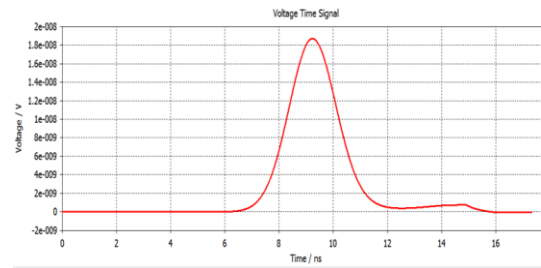


Figure 11: Time-domain output signal at 70Mev/0.4nA.

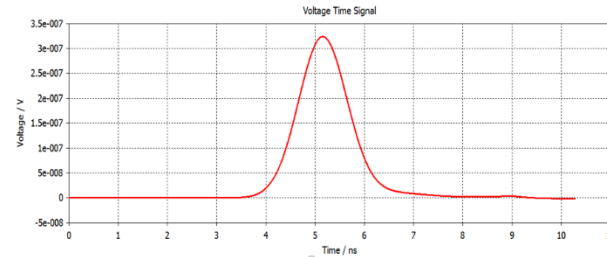


Figure 12: Time-domain output signal at 230Mev/4nA.

## CONCLUSIONS

A stripline BPM is designed for HUST-PTF. The even-odd mode analysis method is used to calculate the BPM impedance and make it match optimally to the cable. Then electrode coupling is calculated by CST MWS. Finally, a proton beam of 70\_MeV/0.4\_nA and 230\_MeV/4\_nA are simulated by CST Particle Studio, the output signal are 19\_nV and 0.35\_uV respectively, which can be used to detect beam position by the specific electronic system.

## REFERENCES

- [1] B. Qin *et al.*, "Progress of the beamline and energy selection system for HUST proton therapy facility", in *Proc. IPAC'17*, Copenhagen, Denmark, May 2017, paper THPVA112, pp. 4719-4721.
- [2] D.T. Fourie *et al.*, "Non-destructive beam position measurement in a proton therapy beam line", in *Proc. DIPAC'09*, Basel, Switzerland.
- [3] Matjaz Znidaric, Libera\_brilliance\_Single Pass\_User\_Manual\_v\_2.00[R], Instrumentation Technologies Company, 2009.
- [4] C. Deibele, "Synthesis and Considerations for Optical Matching to a Beam Position Monitor Circuit Impedance" SNS-NOTE DIAG31,2002.
- [5] CST - Computer Simulation Technology, <http://www.cst.com..>
- [6] Suwada T, Kamikubota N, Fukuma H, *et al.*, Stripline-type beam-position-monitor system for single-bunch electron/position beam[J]. Nuclear Instruments and Methods in Physics Research, 2000, A440:307-319.
- [7] J.L. Conradie *et al.*, "Beam Phase Measurement in a 200 MeV Cyclotron", in *Proc. EPAC'06*, Edinburgh, June 2006, TUPCH077, p. 1187 (2006); <http://www.JACoW.org>.

# MACHINE STUDIES WITH LIBERA INSTRUMENTS AT THE SLAC SPEAR3 ACCELERATORS\*

S. Condamoor, D. Martin, S. Wallters, J. Corbett<sup>†</sup>, SLAC, Menlo Park, CA 94025, USA

Q. Lin, Donghua University, Shanghai, China

L. Lai, Shanghai Synchrotron Radiation Facility, Shanghai, China

P. Leban, M. Cargnelutti, Instrumentation Technologies, Solkan, Slovenia

## Abstract

Turn-by-turn BPM readout electronics were tested on the SPEAR3 booster synchrotron and storage ring to identify possible improvements in data acquisition. For this purpose, Libera Spark [1] and Libera Brilliance+ [2] instruments were customized for the booster (358.4 MHz) and SPEAR3 storage ring (476.3 MHz) radio-frequencies, and tested during machine studies. Even at low single-bunch booster beam current, the dynamic range of the Libera Spark provided excellent transverse position resolution during the linac-to-booster beam capture process, the energy ramp phase and during beam extraction. Booster injection efficiency was analyzed as a function of linac S-band bunch train arrival time. In SPEAR3, turn-by-turn Libera Brilliance+ measurement capability was evaluated for single and multi-bunch fill patterns as a function of beam current. The single-turn measurement resolution was found to be better than 15 microns for a single 1.5 mA bunch. The horizontal single-bunch damping time was then observed with the 238 MHz bunch-by-bunch feedback system ON and OFF, and the multibunch fill pattern stability evaluated as a function of total beam current.

## INTRODUCTION

SPEAR3 is a 3<sup>rd</sup> generation, 3 GeV synchrotron light source with 234 m circumference. The storage ring nominally operates with 500 mA circulating beam current and approximately 1.8 mA/bunch (1.4nC). Topup occurs every 5 minutes using about 50 pulses of single-bunch charge at a 10 Hz rate. The booster synchrotron features a 10 Hz resonant-driven White circuit with a 100 MeV to 3 GeV energy ramp in ~37 ms. Of significance, injection into the booster consists of about 7 S-band bunches selected from a 1  $\mu$ s S-band bunch train produced in a thermionic RF electron gun. The S-band bunches are not phase-locked to the booster and the arrival time can vary due to thermal and electronic drift over time.

Libera BPM processor electronics were installed in the booster ring and in the SPEAR3 storage ring to study measurement performance under different beam conditions. The Libera Spark was configured for highest sensitivity and was able to accurately measure single bunch position during the 37 ms booster ramp phase. Analog signals from four booster BPM striplines were connected to the Libera Spark front end processor equipped with 352

MHz bandpass filters. The filters stretch the response which is then sampled by PLL-controlled ADCs clocked at 109.8 MHz. The baseband signals were sampled 49 times each revolution (1 turn=466 ns).

For SPEAR3 a Libera Brilliance+ module was installed to monitor beam position from a set of four button-style BPM electrodes. In this case the sampling clock was 112.7 MHz and the baseband signal was sampled 88 times during the 781 ns revolution period. At this sampling rate the Brilliance+ module can resolve two diametrically opposite bunches separated by 390 ns in SPEAR3.

## BOOSTER BPM MEASUREMENTS

The SPEAR3 charge transfer sequence starts in a 100 MeV linac followed by a 3 GeV booster and finally injected into SPEAR3 at a 10 Hz repetition rate every 5-minute topup cycle. At each 10 Hz injection event, the single-bunch booster beam is accelerated and extracted in about 37 ms.

The original 1990's-era booster BPM system consists of a commercial multiplexor that switches individual BPM button signals through an electronic peak detector followed by a sample-and-hold-digitization circuit chain. As a result, the measurement resolution for the electron beam position is sub-optimal and can only read the beam orbit every 1.5 ms during the energy ramp.

By introducing the Libera Spark module, it is now possible to measure the single bunch beam position turn-by-turn and with much higher resolution throughout the ramp. Figure 1 for example shows raw turn-by-turn data over three turns from one booster ring BPM pickup.

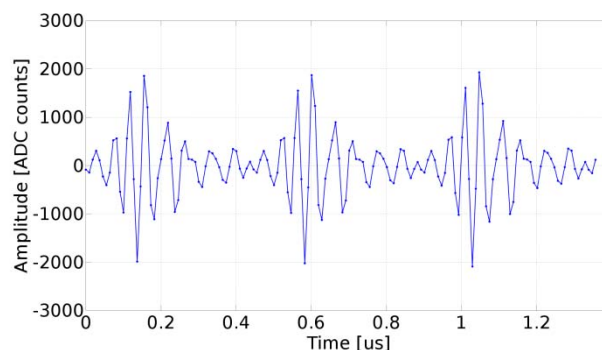


Figure 1: Three-turn single bunch measurement in the SPEAR3 booster ring.

Figure 2 shows the beam position and charge (SUM) throughout the full booster acceleration cycle. The turn-by-turn data was clocked using the injection timing trigger and processed in the time domain.

\* Work sponsored by US Department of Energy Contract DE-AC03-76SF00515 and Office of Basic Energy Sciences, the China Scholarship Council and Instrumentation Technologies.

<sup>†</sup>corbett@slac.stanford.edu



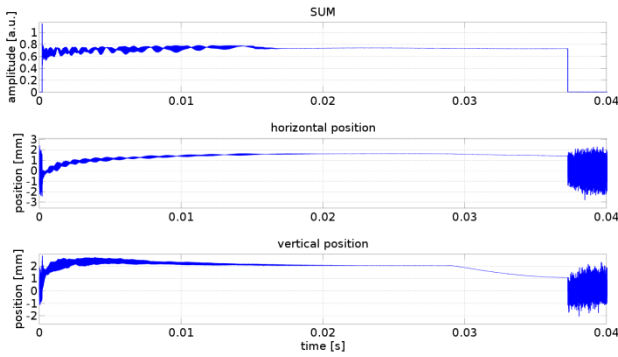


Figure 2: Single acceleration cycle in the SPEAR3 booster ring as measured with Libera Spark.

Of interest, modulations are evident in both the position and amplitude data out to about 17 ms. The modulations are believed originate in the beam capture process. At each injection cycle about 7 S-band bunches are injected from the linac into a single booster RF bucket. The S-band bunches are separated by 250 ps and radiation-damp into a single booster bunch during the energy ramp. By 17 ms the radiation damping process is complete. The modulations seen in Figure 2 are due to complex longitudinal phase oscillations during the ramp.

In practice, the overall charge capture efficiency depends on the S-band bunch train arrival time. To test this dependence we manually varied the arrival time and monitored the injection dynamics with the Libera Spark. The nominal arrival time setpoint was 2.5 V where each 0.1 V corresponds to a delay of 40 ps. Figure 3 shows the SUM (charge) for series of different S-band bunch train arrival times. The injection efficiency went down by over 50% for a setpoint of 2.8 V (-120 ps delay) with a smaller decrease when the timing was advanced. Amplitude SUM values in plot were normalized to the tail of the 2.7 V setting for comparison. Based on the scan results the optimum injection efficiency was found near the original setting of 2.5 V as indicated by the upper magenta line.

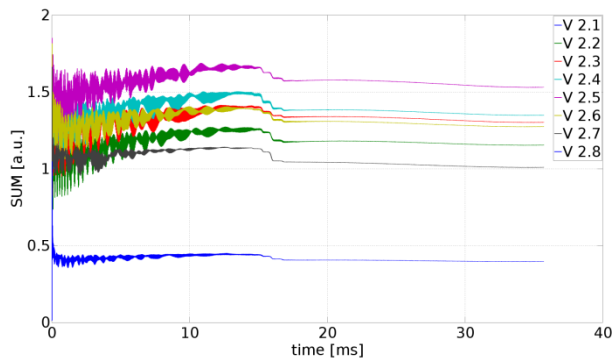


Figure 3: Booster injection efficiency scanning.

Another significant effect detected by the Libera Spark processor occurs at the at the top of the energy ramp. Referring to Figure 4, we see a -1 mm vertical orbit shift when the extraction septum magnet is activated. The 'half-sinewave' character of the field profile in time is evident just prior to beam extraction and the beam steering into the transfer line must be adjusted to compensated for this effect.

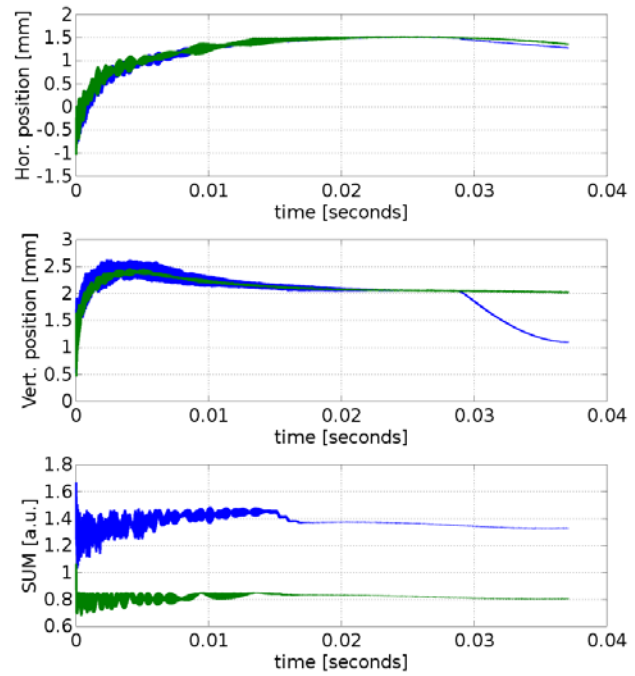


Figure 4: Injection cycle with septum magnet ON (blue line) and OFF (green line).

## SPEAR3 BPM MEASUREMENTS

The SPEAR3 storage ring contains 18 magnet girders with 3 operational BPM's per girder. The original BPM processors are Bergoz type with custom built-in electronics to provide both x/y and individual button signals a-b-c-d which are digitized at a 4 kHz rate for the beam interlock and fast orbit feedback systems, respectively. In addition, the storage ring is equipped with several Echotek BPM processor modules to provide turn-by-turn orbit information. To evaluate the potential for a hardware upgrade, turn-by-turn beam measurements were made with a Libera Brilliance+ processor demonstrating accurate, single-bunch, single-pass measurements down to a bunch current of about 250  $\mu$ A (200 pC charge).

For these measurements the Brilliance+ was not optimized for gain or phase compensation rather simply provided turn-by-turn data at each current level. As seen in Figure 5, above low-charge single bunch values of 30-50 nA, the beam position measurements stabilized to approximately 10  $\mu$ m pk-pk between 0.2 to 3.7 mA. After 2 mA, the automatic gain control in Brilliance+ increased channel attenuation two times. Since the gain compensation circuit was not activated, a position deviation is observed in the vertical direction between 2 and 3 mA.

Turn-by-turn noise performance was then evaluated for single bunch currents ranging from 0.5 to 5 mA. For these measurements, the  $K_x$  and  $K_y$  scaling coefficients were set to 15 mm (default 10 mm). The results listed in Table 1 indicate the RMS noise figures are satisfactory providing reliable readout of the electron beam orbit position in single bunch mode. Since the BPM buttons are located in a region of non-zero dispersion, significant contributions from  $\sim 11$  kHz synchrotron oscillations were found above

1.5 mA bunch current and add between 3-5  $\mu\text{m}$  systematic RMS noise. The vertical turn-by-turn noise figures are also listed in Table 1.

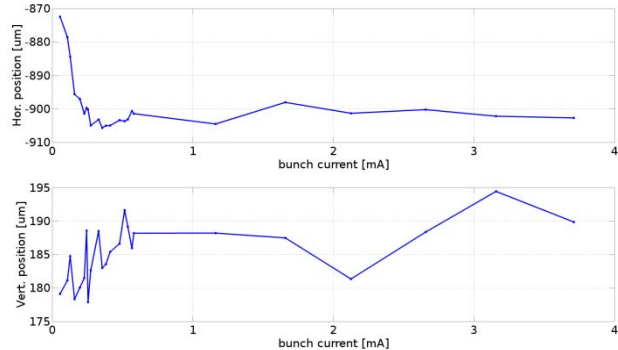


Figure 5: Single bunch, single turn measurement capability as a function of electron beam current.

Table 1: Single Bunch, Turn-by-turn Noise Performance in a Bandwidth of 0 – 0.6 MHz

Beam current	Horizontal plane (RMS)	Vertical plane (RMS)
0.5 mA	39 $\mu\text{m}$	38 $\mu\text{m}$
1 mA	20 $\mu\text{m}$	19 $\mu\text{m}$
1.5 mA	15 $\mu\text{m}$	14 $\mu\text{m}$
2 mA	14 $\mu\text{m}$	12 $\mu\text{m}$
2.5 mA	12 $\mu\text{m}$	9 $\mu\text{m}$
3 mA	10 $\mu\text{m}$	8 $\mu\text{m}$
3.5 mA	11 $\mu\text{m}$	9 $\mu\text{m}$
4 mA	10 $\mu\text{m}$	8 $\mu\text{m}$
4.5 mA	10 $\mu\text{m}$	8 $\mu\text{m}$
5 mA	9 $\mu\text{m}$	7 $\mu\text{m}$

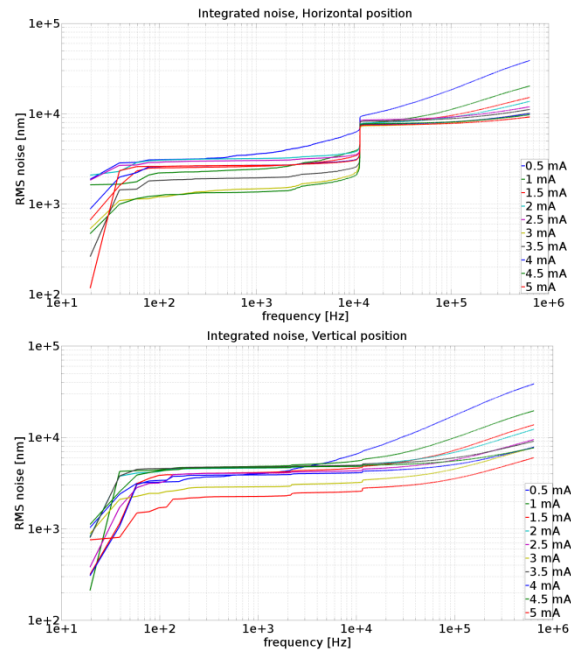


Figure 6: Integrated FFT plot for horizontal and vertical planes.

Using the same single-bunch data from Table 1, the FFT algorithm was applied to the raw turn-by-turn data. The resulting frequency content is plotted in Figure 6 over a  $\sim 650$  kHz measurement bandwidth. Other than a noticeable 'jump' in horizontal RMS noise content at 11 kHz, the noise figure grows monotonically with frequency and as expected improves with higher bunch charge for both planes.

Figure 7 shows the same horizontal data where we 'zoom-in' on the low frequency band near the 11 kHz synchrotron oscillation frequency. Above the low 500  $\mu\text{A}$  current level, the step seen at the synchrotron frequency is approximately equal for all bunch charges.

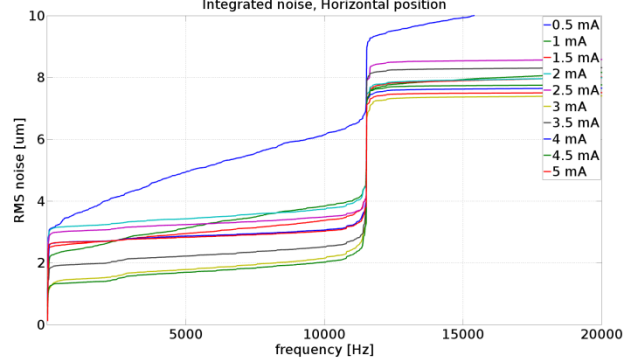


Figure 7: Noise contribution from synchrotron oscillations detected at a position of nonzero dispersion.

The power spectra calculated from the turn-by-turn data are plotted as a function of single bunch current in Figure 8.

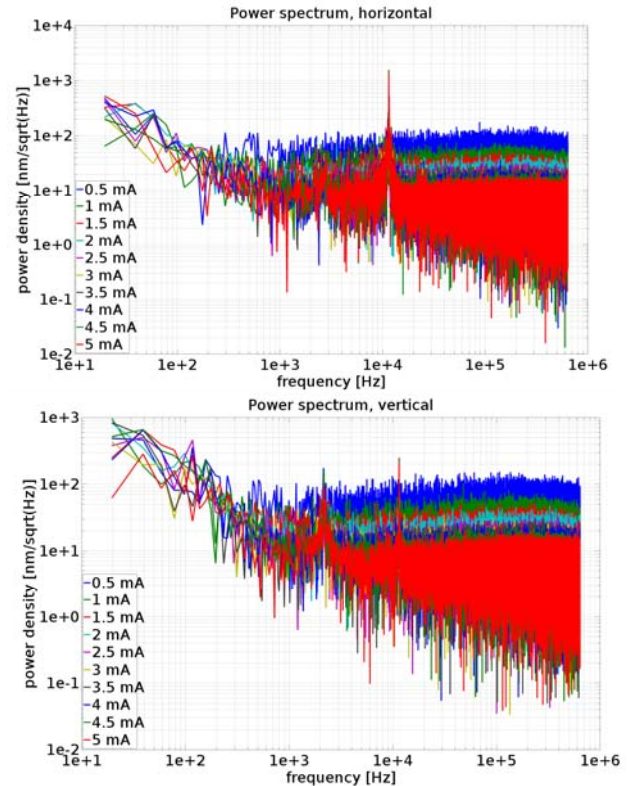


Figure 8: Power spectrum for horizontal and vertical planes.

To test the Brilliance+ module in a 'dynamic' beam motion environment, we pulsed a single horizontal injection kicker to instantaneously ping the beam in the horizontal plane. Tests were performed with the 235 MHz bunch-by-bunch (BxB) feedback system OFF and ON and the Brilliance+ module triggered synchronously with the 10 Hz injection kicker. With feedback OFF, the horizontal betatron oscillations damp with the characteristic few msec exponential damping time for the SPEAR3 magnet lattice (Figure 9, blue). The 'scallop' pattern seen on the beam envelop is again due to synchrotron oscillations. When the BxB feedback is switched ON, the betatron oscillations decay in about 1 ms (1,300 turns). In this case the characteristic linear amplitude reduction is due to the BxB feedback system driving the BxB kicker as hard as possible each turn. The lower plot shows coupling into the vertical plane is relatively small.

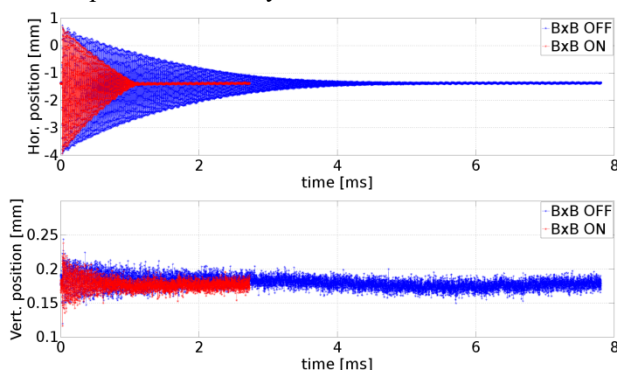


Figure 9: Damping time with BxB feedback ON / OFF.

We can further characterize the effect of BxB feedback by zooming in on the betatron oscillation motion embedded in the turn-by-turn BPM data. Figure 10 shows horizontal oscillation data across two different time intervals. The top plot shows data for the first 75 turns where the effect of feedback is still relatively small. The bottom plot starts at 800  $\mu$ sec and shows 100 turns after the initial injection kicker event. In this case we see both the damping action of the BxB feedback system and a phase shift due to an effective change the reactive impedance seen by the beam with the feedback loop closed.

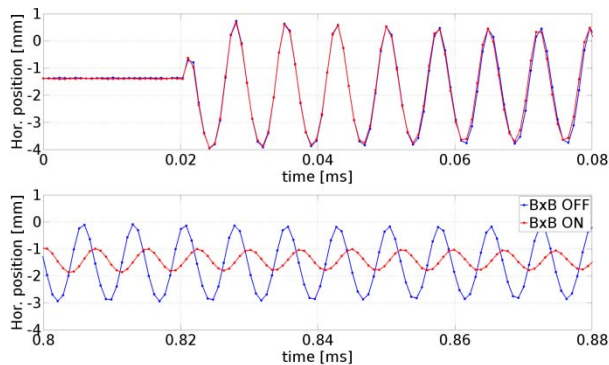


Figure 10: Horizontal oscillation data with BxB switched OFF and ON.

To test the Brilliance+ performance in multi-bunch mode, beam was injected into the standard bunch fill pattern with the total beam current increasing from 0.1 mA to 500 mA. The resulting beam position measurements are shown in Figure 11. Based on the data, we suspect the observed drift in beam position is due to current-dependence of the SPEAR3 fast orbit feedback system. The Brilliance+ was operating in the fully-automatic mode with the cross-bar switch enabled [3]. In this state the anticipated dependence on beam current is typically under 1  $\mu$ m across the full dynamic range.

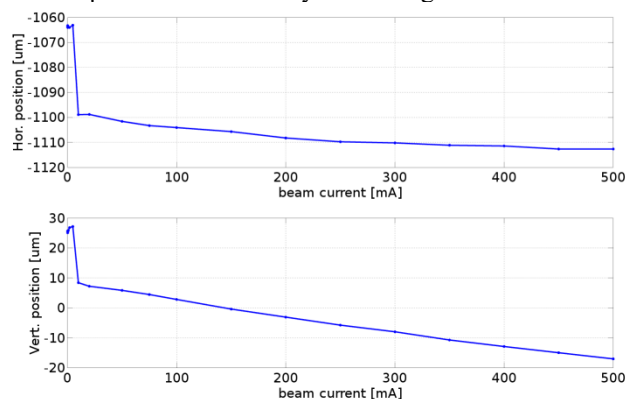


Figure 11: Beam position recorded over full current range.

## SUMMARY

In this paper we report preliminary tests of Libera Spark and Libera Brilliance+ BPM processors operating on the SPEAR3 booster and main ring, respectively. At the booster, the Spark processor provides more accurate transverse beam position data with much better time resolution than previously available. An important effect involving vertical beam orbit shift induced by the pulsed extraction septum at the top of the energy ramp was discovered.

The Libera Brilliance+ processor also provided accurate turn-by-turn beam position measurements over a wide range of single-bunch and multi-bunch operating conditions in SPEAR3. Since the physical BPM buttons were located at a region of horizontal dispersion, an FFT of the data clearly indicated the presence of synchrotron oscillations. Of interest the Brilliance+ turn-by-turn data provides an accurate beam diagnostic tool for dynamic BxB feedback events including the ability to resolve phase shift in the oscillation data. In the near future SSRL will install a Libera Spark processor on the Booster and is in the process of testing a Spark processor on the SPEAR3 ring to upgrade turn-by-turn diagnostic capabilities.

## ACKNOWLEDGEMENTS

The authors would like to thank C. Haggart, P. J. Boussina, L. Campos, C. Ramirez and the SPEAR3 operations staff for technical assistance.

## REFERENCES

- [1] P. Leban, “Libera Spark User Manual”, Instrumentation Technologies d.d., 2017, Slovenia
- [2] P. Leban, “Libera Brilliance+ Specifications 2.0”, Instrumentation Technologies d.d., 2016, Slovenia
- [3] U. Mavric “Innovative RF Design Unites Benefits of Multiplexed and Multi-channel System”, in *Proc. 11<sup>th</sup> Beam Instrumentation Workshop (BIW’04)*, May 2004, Knoxville, TN, USA; *AIP Conference Proceedings*, vol. 732, p. 373, 2004.  
<https://doi.org/10.1063/1.1831171>



# STABILITY TESTS WITH PILOT-TONE BASED ELETTRA BPM RF FRONT END AND LIBERA ELECTRONICS

M. Cargnelutti\*, P. Leban, M. Žnidarčič, Instrumentation Technologies, Solkan, Slovenia  
S. Bassanese, G. Brajnik, S. Cleva, R. De Monte, Elettra-Sincrotrone Trieste, Trieste, Italy

## Abstract

Long-term stability is one of the most important properties of the BPM readout system. Recent developments on pilot tone capable front end have been tested with an established BPM readout electronics. The goal was to demonstrate the effectiveness of the pilot tone compensation to varying external conditions. Simulated cable attenuation change and temperature variation of the readout electronics were confirmed to have no major effect to position data readout. The output signals from Elettra front end (carrier frequency and pilot tone frequency) were processed by a Libera Spark with the integrated standard front end which contains several filtering, attenuation and amplification stages. Tests were repeated with a modified instrument (optimized for pilot tone) to compare the long-term stability results. Findings show the pilot tone front end enables great features like self-diagnostics and cable-fault compensation as well as small improvement in the long-term stability. Measurement resolution is in range of 10 nanometers RMS in 5 Hz bandwidth.

## INTRODUCTION

The recent developments about eBPMs analog front ends capable of pilot tone compensation [1,2] have shown a growing interest towards this topic. In order to verify the usefulness of this approach and its benefits with an existing BPM readout electronics, the eBPM analog front end developed at Elettra has been coupled with an Instrumentation Technologies' Libera Spark.

## ELETTRA EBPM RF FRONT END

The front end is similar to the one presented at IBIC 2016 [2], but enhanced and re-engineered in a more compact solution. In the present version the low-noise PLL has been integrated in the box, together with diagnostic functionalities (voltage and temperature sensors) and complete Ethernet control. Figure 1 shows the block diagram of the system: a low-phase-noise PLL (7) generates the pilot tone (whose frequency and amplitude are programmable), which is split into four paths by a high-reverse-isolation splitter (6) that guarantees more than 52 dB of separation between the outputs. A coupler (2) sums the tone with the signal from the pick-ups, adding further 25 dB of isolation to prevent inter-channel crosstalk from the path of the pilot tone. At this point, all the signals pass through a bandpass filter (3), centered at 500 MHz with a bandwidth of 15 MHz, and two variable-gain stages, composed of low-noise, high-linearity amplifiers (5) ( $G=22$  dB,  $F=0.5$  dB,  $OIP3=+37$  dBm,  $P1dB=+22$  dBm) and

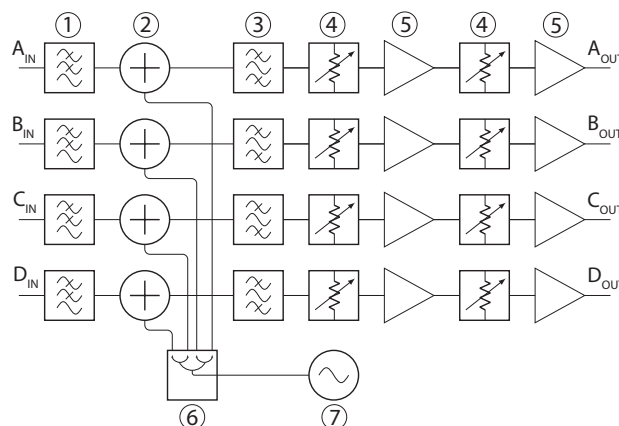


Figure 1: Analog front end block diagram.



Figure 2: Frequency response of the front end at full gain.

digitally controlled attenuators (4) (7 bits, up to 31.75 dB of attenuation, steps of 0.25 dB).

In order to achieve the expected results, the splitter must be temperature-insensitive, as well as the four couplers. Indeed, this architecture allows us to compensate the part of the system after the couplers, i. e. filters, attenuators, amplifiers. It has to be noted that being the front end a separate unit, it can be placed as near as possible to the pick-ups (tunnel area), with two main advantages: better signal-to-noise ratio and the possibility to compensate the cables (which are usually long). The frequency response of the front end is shown in Fig. 2.

## LIBERA ELECTRONICS

Libera Spark was used to process the A, B, C and D signals from the Elettra eBPM analog front end. Libera Spark is

\* manuel.cargnelutti@i-tech.si

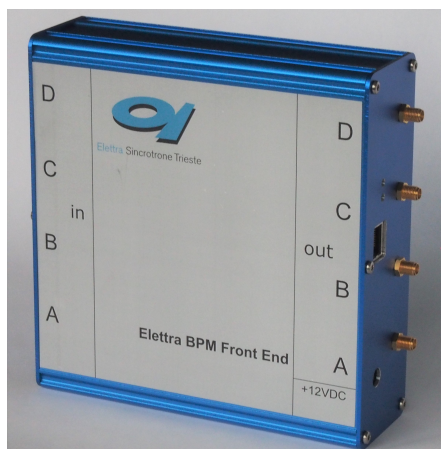


Figure 3: Elettra eBPM analog front end.

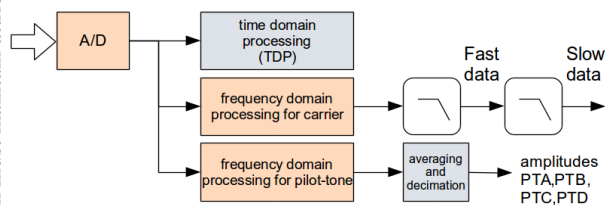


Figure 4: Double DDC processing.

a standard beam position processor used in several synchrotron lightsources and provides data from turn-by-turn down to slow data streams [3,4]. Initial measurements were done with a standard unit. Raw ADC data was taken periodically over several hours and post analysed. Position was calculated in frequency domain by measuring the frequency components of the carrier frequency (RF, 499.654 MHz) and of the pilot tone's frequency (PT, 501.282 MHz). The sampling frequency was set to 116.8 MHz and was not locked to any external reference clock (normally it should be). First results of combined tests (Elettra eBPM analog front end and Libera Spark) were encouraging and show several benefits. To ease further analyses, a new digital-down-conversion processing branch was implemented in the programmable logic (FPGA) of the Libera Spark which was then able to process the RF and PT in frequency domain (independently) and A/D data in time-domain which ensures clean turn-by-turn measurement. As a proof-of-principle, the implementation was simplified and the PT DDC processing branch only outputs highly averaged A, B, C and D amplitudes at ~8.8 Hz update rate (Fig. 4).

The DDC processing chain for the carrier frequency is tuned to the 32.38 MHz component which is then filtered and decimated in 2 stages to provide the user with fast (10-30 kHz) data streams and slow (10-40 Hz) data streams with narrower bandwidth. The -3 dB bandwidth of the turn-by-turn data is approximately 350-400 kHz. The additional DDC processing chain is tuned to the 34.01 MHz component which comes from the pilot tone's frequency. For this test set, amplitudes (PTA, PTB, PTC, PTD) were only highly averaged and provided to user space with slow update rate. The

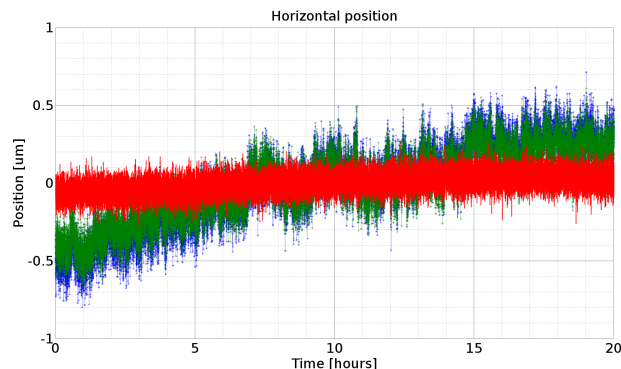


Figure 5: Horizontal position drift at 25 °C stable temperature.

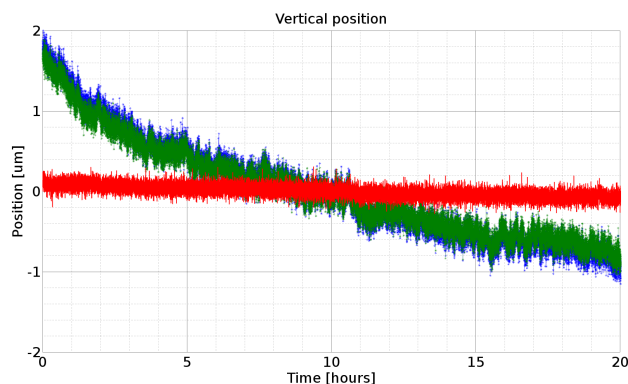


Figure 6: Vertical position drift at 25 °C stable temperature.

PTA, PTB, PTC and PTD were used for on-line compensation in the upper software layer (EPICS) so compensated data could be observed in quasi real-time. There was a little drawback in such simplified implementation (asynchronous amplitude update/calculation) but this will be easily fixed with complete FPGA implementation.

## TEMPERATURE COMPENSATION

A very important property of beam position processor is how calculated position drifts when environmental temperature changes. For evaluation and better understanding, we put the whole system inside the temperature chamber. First measurements were done at 25 °C stable temperature over 20 hours. For this test, all equipment, including the RF generator, were placed inside the chamber. Position data was taken every 1 second. Horizontal position data from the carrier (blue) and from the pilot tone (green) drifted for approximately 0.8  $\mu\text{m}$  (mean value) whereas the compensated position (red) showed an almost negligible drift of approximately 100 nanometers (Fig. 5). In vertical direction, the compensated position drifted for the same amount (~100 nanometers) but the carrier's and pilot tone's position drifted for about 3  $\mu\text{m}$ .

A more interesting measurement was done with a temperature profile. Temperature was changed in the range from 20 °C to 30 °C in 1 °C steps. Complete temperature profile is

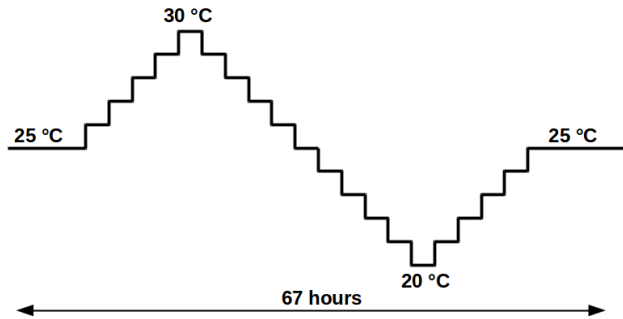


Figure 7: Long-term temperature profile.

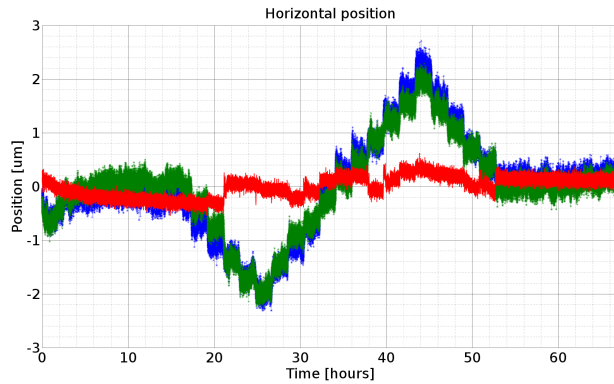


Figure 8: Horizontal position drift at temperature profile.

shown in Fig. 7. For this test, the RF generator and a 4-way splitter were put out of the temperature chamber and left at room temperature.

Carrier's and pilot tone's position drifted for 2  $\mu\text{m}$  and 4  $\mu\text{m}$  in horizontal and vertical directions, respectively (0.2  $\mu\text{m}/^\circ\text{C}$  and 0.4  $\mu\text{m}/^\circ\text{C}$ ) while the compensated position drifted approximately 0.8  $\mu\text{m}$  and 1.5  $\mu\text{m}$ . in total over 10  $^\circ\text{C}$  (horizontal and vertical, respectively). Obtained results show an improvement factor of 2 of original vs compensated position (as shown in Table 1). Taking into account typical environmental conditions, expected drift can be easily neglected.

Table 1: Position Drifts (Peak-to-Peak)

Position drift	Non-compensated	Compensated
Horizontal	4 $\mu\text{m}$	0.8 $\mu\text{m}$
Vertical	2.5 $\mu\text{m}$	1.5 $\mu\text{m}$

## CABLES WOBBLING

To demonstrate the validity of cable compensation, a coaxial cable connected between the front end and the Libera Spark was bent and wobbled. Figure 9 shows the position variation of the carrier and the pilot during this operation, with a peak-to-peak deviation of about 6  $\mu\text{m}$ . Residual oscillations in the compensated positions have a deviation 10 times smaller (about 500 nm peak-to-peak), excluding the

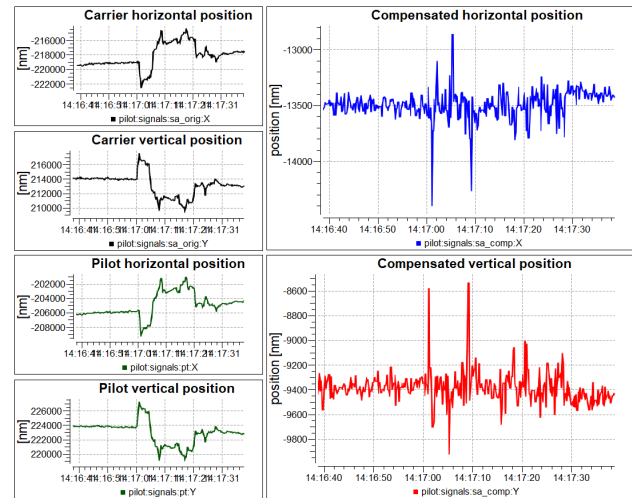


Figure 9: Cable wobbling.

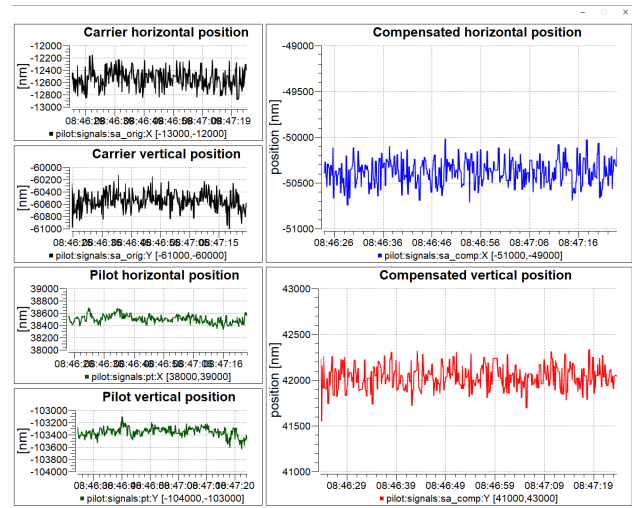


Figure 10: Noise on carrier and beam positions at different amplitudes.

spikes due to the asynchronous calculations as stated in previous sections.

## QUALITY OF THE MEASURE

Another interesting feature is in using pilot tone as an indication of the quality of the measure. In a traditional BPMs, is difficult to have a complete on-line indication of the correct behaviour of the system: if beam position has much noise than expected or weird deviations are noticed, doubts about a possible malfunction of the electronics will remain until a complete test on the unit will be done.

In Fig. 11, carrier amplitude has been deliberately reduced by more than 10 times, increasing the noise on it (about 600 nm peak-to-peak, Fig. 10). Since the noise on the pilot is in the expected range, it gives the indication that the system is functioning in a correct way, thus the carrier position behaviour is real.





# NEW BEAM POSITION MONITORS FOR THE CERN LINAC3 TO LEIR ION BEAM TRANSFER LINE

G. Baud, M. Bozzolan, R. Scrivens, L. Søby  
CERN, 1211, Geneva, Switzerland

## Abstract

The ion injection line into the CERN Low Energy Ion Ring (LEIR) has recently been equipped with nine, new, electrostatic Beam Position Monitors (BPMs) in order to measure and optimize the trajectory of the low intensity ion beams coming from Linac3. In this paper, we describe the design of the BPM, the low noise charge amplifier mounted directly on the BPM, and the digital acquisition system. There is special emphasis on the first commissioning results where the measured beam positions were perturbed by EMI and charging of the BPM electrodes by secondary particles. The effect of mitigation measures, including repelling voltages on the electrodes and external magnetic fields, are also discussed.

## INTRODUCTION

The CERN Linac3 provides heavy ions, mainly  $\text{Pb}^{54+}$  at an energy of 4.2 MeV/u, to the Low Energy Ion Ring (LEIR). Here the ions (pulses of up to 30  $\mu\text{A}$ , 200  $\mu\text{s}$ ) are accelerated to 72 MeV/u, extracted to the PS and further to the SPS where the fully stripped ions are either extracted for fixed target physics, or transferred to the LHC for ion collisions. In order to optimize the injection efficiency into LEIR, the transfer line between Linac3 and LEIR has recently been equipped with nine highly sensitive electrostatic BPMs (Figure 1).

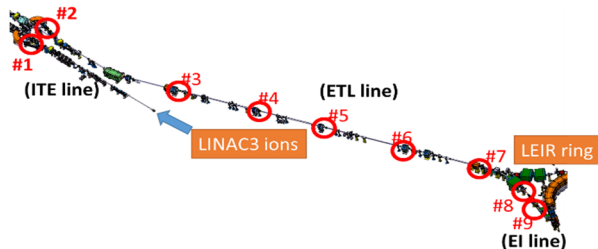


Figure 1: Linac3 to LEIR transfer line BPM layout.

## BPM DESIGN

Table 1 summarises the BPM system specifications.

Table 1: BPM Specifications

Parameter	Value	Comment
Accuracy	0.5mm	-
Resolution	0.2mm	For 4uA current
Time resolution	1us	Along 200us pulse
Max. Beam displ.	$\pm 15$ mm	-
Max beam current	50uA	-
Nb. of injections	1-13	Every 100-200ms

The BPMs are of a dual plane electrostatic type with an aperture of 196mm and a length of 200mm. The azimuthal width of the electrodes is 75° and the distance to ground is 21.5mm. The  $\sim 20\text{pF}$  electrodes are connected to high impedance charge amplifiers mounted directly onto the BPM body, via 75 $\Omega$  cables, see Figure 2. The transfer impedance is about 30 $\Omega$  yielding an electrode signal of  $\sim 0.1\text{mV}$  for a centred beam. All parts are of 316 LN stainless steel. The two BPMs nearest the LEIR ring have a non-evaporable getter (NEG) coating on the chamber walls to lower the overall vacuum level in this region.

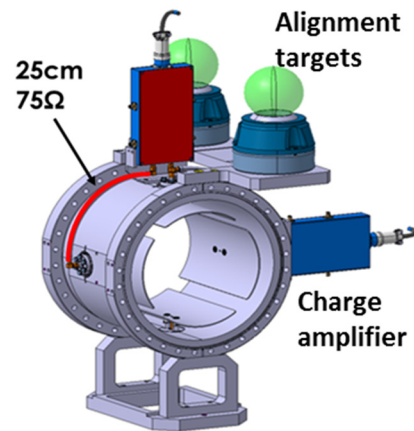


Figure 2: 3D model of the BPM.

## ACQUISITION SYSTEM

### Electronics

The input stage of the front-end electronics mounted directly on the BPMs is a charge amplifier. Gain calibration is performed by injecting a known charge into each input through a low capacitance calibration capacitor (1pF). After charge amplification, further amplifier stages generate the sum ( $3 \times 10^{12}$  V/C gain) and difference ( $6 \times 10^{12}$  V/C gain) signals. The -3dB bandwidth is 60Hz to 2MHz. A more detailed description of the head amplifier can be found in [1]. Coaxial cables transmit the signals to the control room where commercial, 8 channel, 12 bit Analogue to Digital Converters (ADCs) sample the signals.

### Front-End Software: FESA

The Front-End Software Architecture (FESA) is a C++ framework used at CERN to design, develop, test and deploy real-time control software. It is used to provide software control and monitoring of the acquisition triggers, data read-out, processing and calibration. It also allows the data to be easily integrated with standard tools such as the beam steering Graphical User Interface (GUI) or long-term logging database.

For each LEIR cycle of 2.4 or 3.6 seconds, depending on the configuration, the FESA class prepares the ADCs, and starts the acquisition 200 $\mu$ s before each LEIR injection. 4096 samples at a sampling rate of 6.125 MHz are captured, corresponding to a 650 $\mu$ s time period centred on the 200 $\mu$ s Linac pulse. These are then read-out 10ms after each injection trigger.

As the acquisition system is linear, positions are computed using a simple scaling of the difference/sum ratio of electrode signals. Various algorithms are available to provide instantaneous or average positions. Providing the position at the end of the pulse proved to be particularly useful to counter the baseline drifts discussed in the following sections.

## BEAM MEASUREMENTS

The two first BPMs were installed in the ITE line at the beginning of 2017, and tested during the 2017 run with Ar<sup>11+</sup> beams. The remaining seven BPMs were installed at the beginning of 2018 with all nine BPMs now used to measure nominal Pb<sup>54+</sup> beams. The signals from the first beam tests showed perturbations due to both EMI and low energy secondary particles hitting the electrodes.

### EMI from Quadrupoles

Figure 3 shows the perturbation of the baseline observed close to the start of the Linac pulse. This perturbation was found to be due to a nearby, pulsed quadrupole creating ground currents that ran along the screen of the coaxial input cables to the front-end amplifiers. By adding high mu toroidal cores around these cables, this interference was completely suppressed.

### Secondary Particles

Even though the aperture of the first BPM is nearly twice that of the neighbouring vacuum chambers the electrode signals were found to be completely saturated. While the signals from the second BPM did not enter saturation, they clearly showed a baseline drift along the beam pulse. An example is given in Figure 3, which also shows the baseline distortion due to EMI before the beam passage.

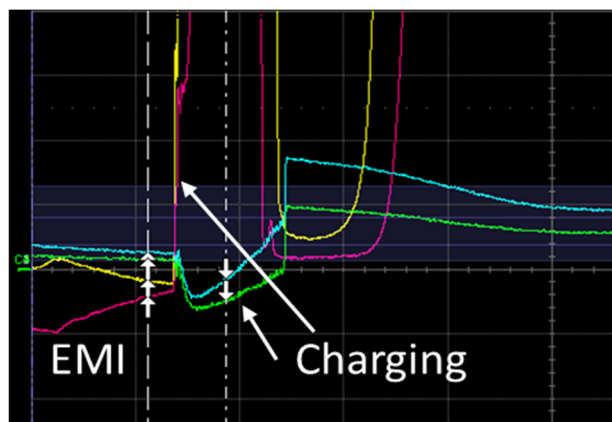


Figure 3: Horizontal and vertical sum signals from the first two BPMs in the ITE line. Yellow /Blue: BPM1/BPM2 horizontal sum. Purple/Green: BPM1/BPM2 vertical sum.

Simulating a continuous negative charging of the electrodes during the beam passage, as shown Figure 4, one obtains a result similar to what is observed in Figure 3, indicating that secondary electrons are directly impacting on the electrodes.

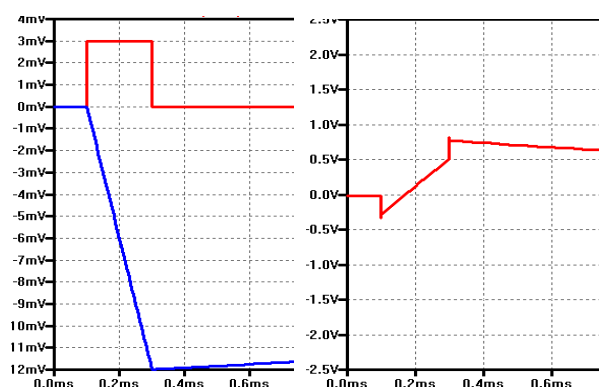


Figure 4: Left: Square 200us beam pulse (red) and continuous charging by electrons (blue). Right: Result of summation of the two signals and amplification.

### Repelling Potential on Electrodes

Suspecting secondary electrons either from ionisation of the rest gas or desorption from the vacuum chamber, the front-end electronics was modified to enable a repelling voltage to be added on each electrode. This significantly improved the quality of the observed signals (see Figure 5). When scanning the repelling voltages, it is usually possible to find a setting where the primary beam pulse signal is unaffected by charging (in this case close to -4V). Further increasing the voltage results in positive charging of the electrodes (amplifier response is inverted), which we believe is due to the attraction of ions from the rest gas ionisation. Unfortunately, this ideal repelling potential is different for each electrode and was seen to depend on both beam and Linac parameters. This was therefore not a final mitigation for this issue.

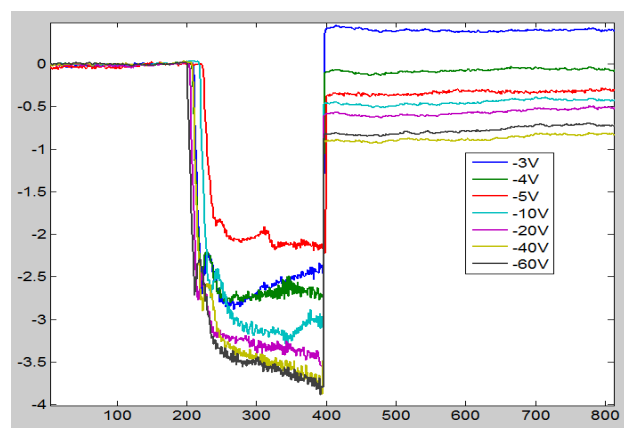


Figure 5: Electrode charging as function of repelling voltage.

## Solenoids and Dipoles

A series of iterations with simulations (see later) and installations of low field solenoids and dipoles around or close to the BPMs confirmed the presence of secondary electrons ( $<100\text{eV}$ ) generated close to the BPM. At present, all but one of the BPMs have been equipped with solenoids as shown in Figure 6. Combining this solenoid field with the clearing voltage on the electrodes allowed saturation to be avoided on all BPMs and enabled a measurement of the beam position to be performed at one single point at the end of the pulse (see Fig. 7). This is adequate for steering the beam along the transfer line. However, measurements along the pulse, important to tune the source and RF parameters, are still not possible as the form of the charging profile is unknown.

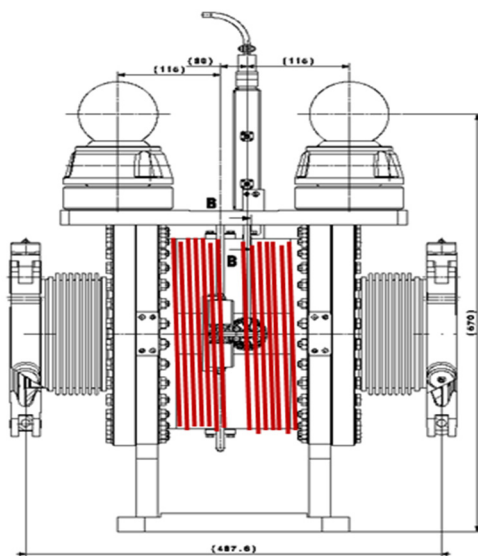


Figure 6: BPM with solenoid

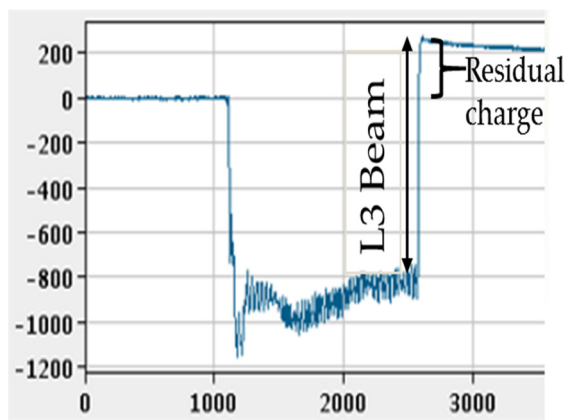


Figure 7: Sum signal from one BPM equipped with both solenoid and electrode bias. The residual charge caused by electrode charging is visible as a baseline shift at the end of the pulse.

## SIMULATIONS

In order to understand the source of the secondary particles and how the suppression schemes work, simulations were performed using the IBSIMU code [2]. A simplified

geometry was constructed, including the vacuum chamber and the four separated electrodes of the BPM, which can be electrically biased. Magnetic fields generated by solenoids or dipoles are then imported into the simulation.

Secondary particles are generated as either:

- secondary electrons from the walls, with an energy distribution based on [3] for the creation of low energy electrons ( $<100\text{eV}$ )
- protons and electrons from the center of the vacuum chamber in order to represent residual gas ionization.

The pressure in the line is below  $10^{-8}$  mbar. The beam density is low enough that space charge fields can be neglected. For simplicity, secondary particles from the beam pipe are emitted normally to the vacuum chamber, and at  $\pm 45^\circ$  to the wall normal.

Images of the tracked secondary particles are shown in Figure 8 for a solenoid field of  $0.6\text{mT}$  and an electrode bias voltage of  $-5\text{V}$ . In such a configuration we see that only a small number of wall-emitted electrons can strike the electrodes, whereas a higher fraction of ions from the gas can reach the electrodes. Electrons from rest gas ionization are not shown and do not reach the BPM electrodes.

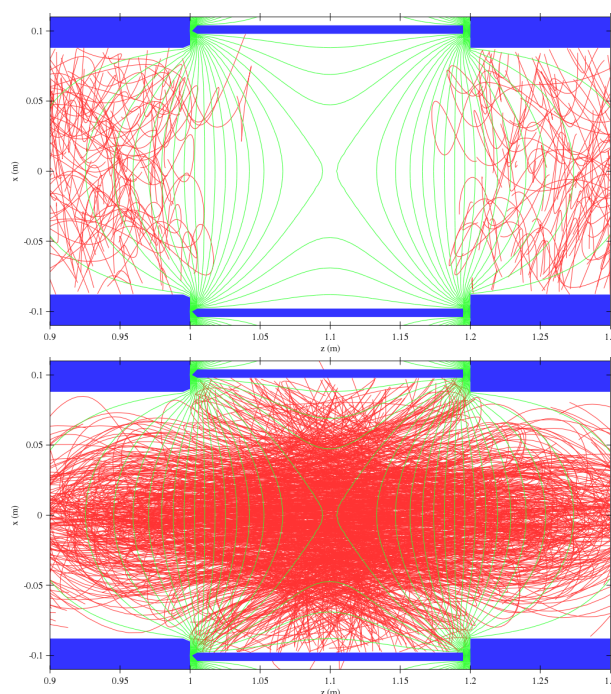


Figure 8: Secondary particle tracks in the simulation, with an applied magnetic field from a solenoid along the beam axis. Top: Electrons emitted from the vacuum chamber walls. Bottom: Ions Generated from the gas ionization. Blue: Vacuum chamber and electrodes. Red: Secondary particle tracks. Green: Equipotentials of the electrode bias voltage.

Expected production rates for secondary particles from the walls depends on local losses of a small fraction of the beam (the loss rate along the line is on average  $10^{-3}$  per meter), and the production of gas ions depends on the local pressure (which can vary along the transfer line). The production of secondaries from the two processes can there-



fore be scaled to fit the measurements at each BPM location. Figure 9 shows a comparison of simulation and measurements as a function of the applied solenoid field, which is seen to be in agreement. In this case the second BPM (right plot) is subject to three times as many secondary particles as the first (left plot). These simulations, however, predict a fully symmetric collection of secondary particles by all four electrodes, whereas measurements typically show a strong asymmetry, which might be due to factors such as asymmetric loss pattern or the influence of nearby magnetic components. The result is that it has not been possible to find magnetic and electric field distributions that can suppress the secondaries on all electrodes simultaneously. A fully reliable beam position measurement as a function of time in the beam pulse has therefore not been achieved.

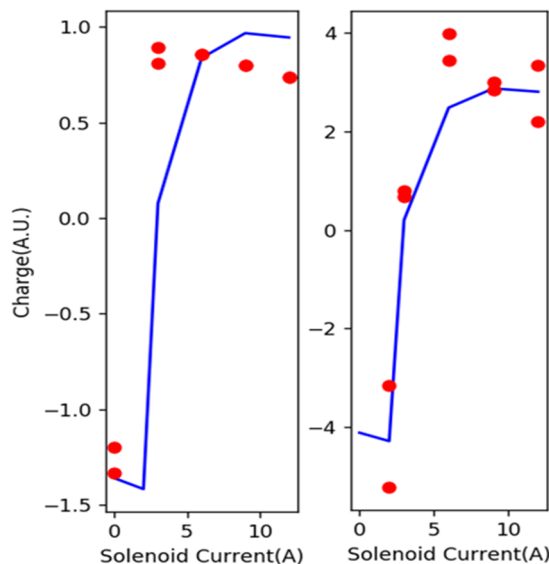


Figure 9: Collected charge on BPM electrodes as a function of the applied solenoid current (0.2mT/Ampere) and electrode repelling voltage of -5V. Red dots show measurements of collected charge summed on all four electrodes. The blue line is the simulated collected charge. Left and right plots correspond to two different BPMs, based on the same simulation.

## HIGH FREQUENCY ACQUISITION

The bunching frequency of the Linac is 101.3MHz, with a complete de-bunching expected at the end of the transfer line due to the energy spread. A BPM acquisition system at this frequency was therefore not initially pursued, leading to the development of the baseband system described above. However, after having modified one of the front-end amplifiers to transmit this higher frequency part of the beam spectrum, it was seen that sufficient bunching is still present at the last BPM before injection into LEIR for position measurements. The signals in Figure 10 were obtained using an 8-bit oscilloscope running at 500MS/s and a Matlab script performing a 2MHz bandpass filter and AM demodulation. Computing the position from this last BPM in the transfer line yields a position resolution along the

pulse of better than 0.5mm when averaged over 5 $\mu$ s. Such a measurement is completely insensitive to the slow charging of the electrodes by secondary particles. The signal to noise ratio is dominated by the 8-bit oscilloscope and a dedicated acquisition system is therefore expected to perform significantly better. Such a system is currently being constructed to overcome the issues observed with the baseband acquisition.

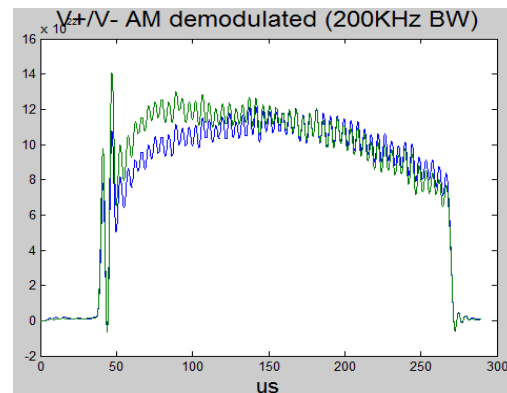


Figure 10: Electrode signals after filtering and AM demodulation.

## CONCLUSION

Nine electrostatic BPMs have been installed in the Linac3 to LEIR transfer line with the aim of being able to measure the beam position along the 200 $\mu$ s beam pulse. The signals from all the BPMs but one showed significant charging of the electrodes by secondary particles, which subsequent simulations showed were mainly electrons emitted from the chamber walls, but also ions from rest gas ionisation. Different configurations of electrode bias voltages and external magnetic fields significantly improves the signal quality but cannot guarantee a correct position measurement along the beam pulse, with only a single point measurement at the end of the pulse reliably used during operation.

A new system, using the 101MHz bunching component of the Linac, which has been shown to be present even at the last BPM, is insensitive to the slow charging of the electrodes and will now be implemented to provide beam position measurements along the pulse.

## ACKNOWLEDGEMENTS

We would like to thank F. Guillot-Vignot and B. Moser for their help during the installation phases of the BPMs and the installation of magnets.

## REFERENCES

- [1] L. Søby *et al*, ELENA orbit and Schottky measurement systems, in *Proc. of IPAC'15*, Richmond, VA, USA, May 2015, paper MOPTY056.
- [2] T. Kalvas, *et al*, "IBSIMU: A three-dimensional simulation software for charged particle optics", *Rev. Sci. Instrum.*, Vol. 81, 02B703, 2010.
- [3] M. S. Chung, T. E. Everhart, *J App Phys*, vol. 45, 1974, pp. 707-709, <http://dx.doi.org/10.1063/1.1663306>



# AUSTRALIAN SYNCHROTRON BPM ELECTRONICS UPGRADE

Y.-R. E. Tan\*, R. Hogan, Australian Synchrotron - ANSTO, Clayton, Australia

## Abstract

The storage ring at the Australian Synchrotron (AS) had been originally equipped with 98 Libera Electrons. In late 2017 the all 98 of the BPM electronics has been upgraded to Libera Brilliance+. This report will outline plans that were put in place for the transition and the results from commissioning the new system.

## INTRODUCTION

The Australian Synchrotron (AS) is a 3rd generation light source that was commissioned in 2006. The storage ring is a Chassman-Green lattice with 14 sectors each equipped with 7 Beam Position Monitors (BPMs) connected to Instrumentation Technology's Libera Electrons (98 Electrons) [1–3]. The booster ring is a FODO lattice with 4 sectors each equipped with 8 BPMs connected to Bergoz MX processors that is then digitized by NI DAQ cards [4]. Since an upgrade to the booster BPM system in 2010 increasing hardware problems has resulted in a continuous decline in the number of usable BPMs. Simultaneously, between 2013 and 2016 the Libera Electrons in the storage ring began to display an increasing number of hardware problems. In 2016 the decision was made to replace the storage ring Libera Electrons with Brilliance+ electronics [5] and to re-purpose the Libera Electrons in the booster ring.

Additional improvements to the system has also been the integration of the Brilliance+ directly into the Micro-Research Timing Event system with the EVR module and the option to increase the fast acquisition (FA) data rate from 10 kHz to 30 kHz. The increase in the FA data rate was added to push the performance of our Fast Orbit Feedback System (FOFB) [6] by reducing the group delay of the FA data.

## PERFORMANCE MEASUREMENTS

To get the Libera Brilliance+ units ready for installation and to confirm that the performance met the requirements a initial configuration script and acceptance testing script were used. The configuration script configured the Linux subsystem to use some of the standards at the AS. The acceptance test script confirmed that the basic functionality was working such as locking to the machine clock and the unit was correctly reading the event data stream. The script would sweep the input power to each of the BPM cards in the Brilliance+ unit from -2 dB to -63 dB (Instrumentation Technology RF clock generator and power splitter) and log the position data at Turn-by-Turn (TbT; 1.389 MHz) and FA data rates (10 kHz) at different power levels. The average and spread of  $\sigma_{x,y}$  across 110 cards is shown in Fig. 1.

\* eugene.tan@ansto.gov.au

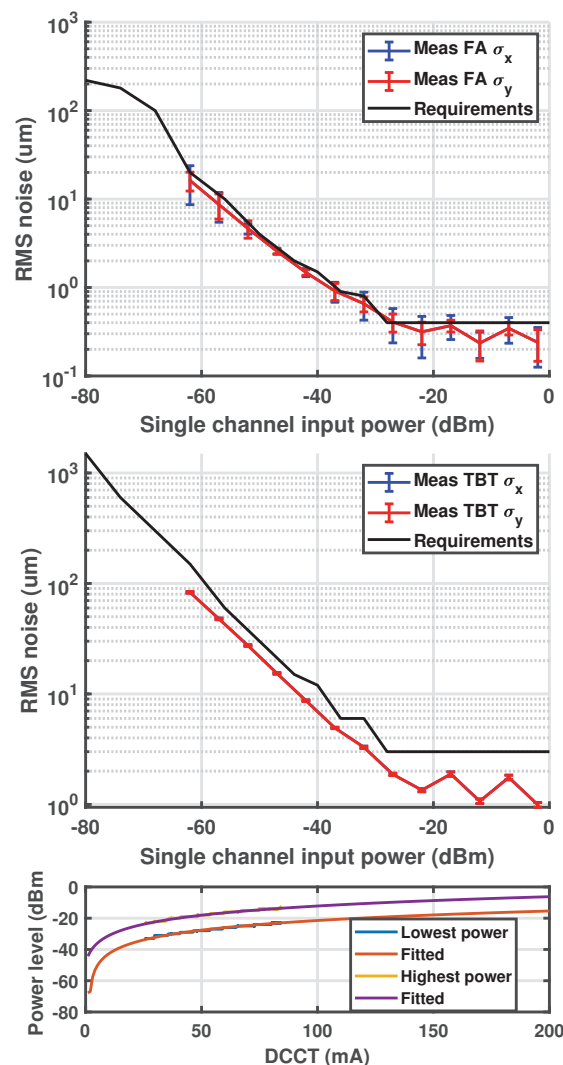


Figure 1: The average and spread of  $\sigma_{x,y}$  across 110 BPM modules measured at TbT (1.389 MHz) and FA (10 kHz) data rates. The spread of the FA data rate is higher than expected where there was not enough time allowed for the digital signal conditioning learning cycle to complete before taking measurements. The corresponding input power graphs shows that below 30 mA the position resolution starts to increase.

The beam current/input power dependence was measured at the FA data rate and shown to be less than 1  $\mu\text{m}$  from -60 dBm to -5 dBm which covers the range from 5 mA up to 200 mA in the storage ring.

The temperature dependence was measured by restricting the air flow to the crate, causing a 10 degree change in temperature. Using the internal airflow temperature sensors the temperature dependence was found to be an average of 0.8  $\mu\text{m}/^\circ\text{C}$  (switching enabled) and 0.4  $\mu\text{m}/^\circ\text{C}$  (switching

disabled) on one of the crates tested. This was higher than the stated performance but was still within our requirements.

## MACHINE MEASUREMENTS

### Transverse Coupling and RF Cable Attenuation

One of the known issues with the Libera Electrons was a insufficient isolation between the four RF channels that resulted in an effective transverse coupling of  $\sim 2\%$  [3]. The new Brilliance+ has a significantly improved channel to channel isolation and the transverse coupling has been practically removed as shown in Fig. 2. The remaining variation in the coupling has been confirmed to come from the small differences in the attenuation ( $\sim 0.5$  dB) of the RF cables [3].

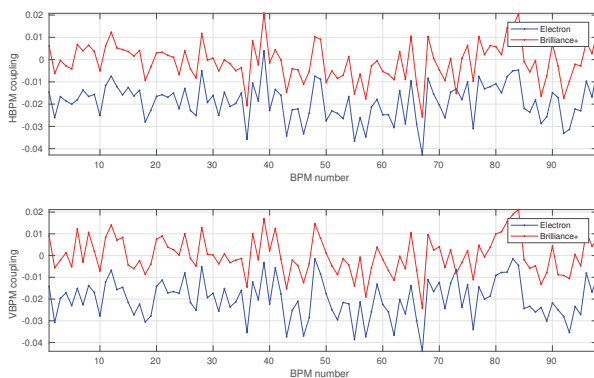


Figure 2: Improvement in the systematic transverse coupling on all BPMs. With the Electron the measured transverse coupling was 2% between planes and this has been reduced to  $< 0.2\%$  in the Brilliance+. The variation across BPMs is a result of differences in the attenuation of the four RF cables ( $\sim 0.5$  dB). BPM coupling calculated with Linear Optics from Closed Orbit method (LOCO).

In the transition a patch panel was installed and all connections were re-measured, see Fig. 3. A few years ago the cables were re-terminated to phase match the 4 BPM cable to less than 10 degrees at 500 MHz in an attempt to improve the beam current dependence, however the results have been inconclusive. A consequence of the phase matching has been an increase in the attenuation between the four RF cables. is The largest impact may be the effective coupling created due to the differences in the cable attenuation. One proposed method to minimise this effect is to include a calibration factor for each of the four RF inputs.

### FA Data Noise Floor

Figure 4 compares the beam motion spectrum measured just before and after the installation of the Brilliance+. The figure shows an improvement in the noise floor of the FA data from 9 (H) and 13 (V)  $\text{nm}/\sqrt{\text{Hz}}$  to 6 (H) and 7 (V)  $\text{nm}/\sqrt{\text{Hz}}$  at 1 kHz.

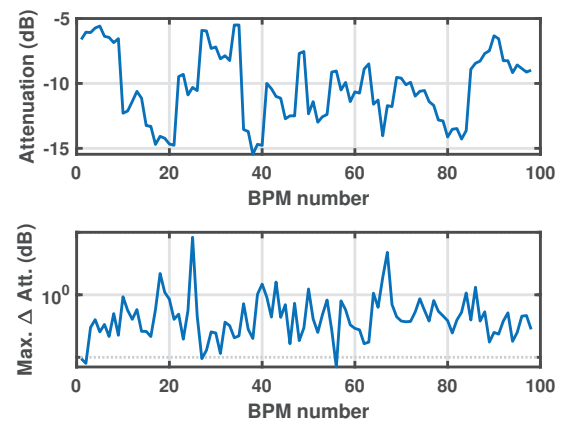


Figure 3: RF cable attenuation and input power for the BPM modules. Attenuation differences greater than 2 dB were the result of faulty connectors that have since been fixed.

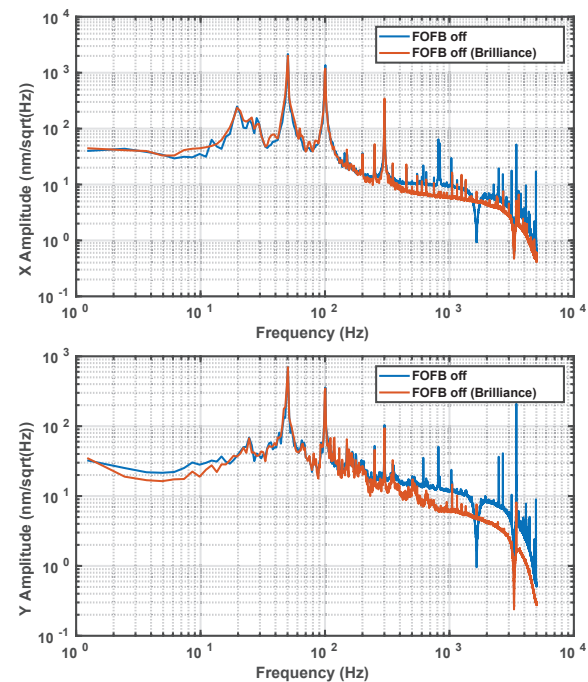


Figure 4: Comparison of the beam spectrum of the electron beam before and after the installation of the Brilliance+. The improvement in the noise floor is notable in the FA data ( $K_x = K_y = 15 \times 10^6$ ).

### 30 kHz FA Data

One of the improvements that was commissioned was an attempt to improve the performance of the FOFB system by reducing the latency of the FA data. Aside from the limitations of the vacuum chamber, the BPM processing latency was the second largest contributor to the overall latency of the feedback system. The FA data stream comprised of a CIC (decimation factor of 3) + Polyphase FIR filter to reduce the data rate from 1.388 MHz to 10 kHz. Instrumentation Technology was able to reduce the group delay to  $< 150 \mu\text{s}$  by removing the initial CIC decimation

filter. The simulated step response of the initial design of  $\tau_s^{10\text{kHz}} = 227 \mu\text{s}$  and a bandwidth of 2 kHz was reduced to  $\tau_s^{30\text{kHz}} = 55 \mu\text{s}$  and a bandwidth of 5 kHz. The initial test of the increased data rate FA data measured a decrease of the step response from  $\tau_{\text{meas}}^{10\text{kHz}} = 200 \mu\text{s}$  and a bandwidth of 2.0 kHz, to  $\tau_{\text{meas}}^{30\text{kHz}} = 40 \mu\text{s}$  and a bandwidth of 5.8 kHz. The measurement results are shown in Figs. 5 and 6.

The increased FA data rate is not currently used as the effects of switching noise and the optimisation of the notch filter has yet to be evaluated.

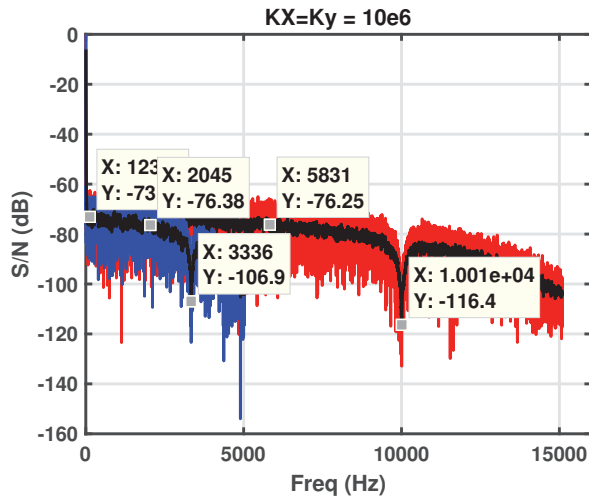


Figure 5: The integrated FA data noise increases from  $\sigma_x^{10\text{kHz}} = 203 \text{ nm}$  to  $\sigma_x^{30\text{kHz}} = 346 \text{ nm}$  from the wider bandwidth of 5.8 kHz.

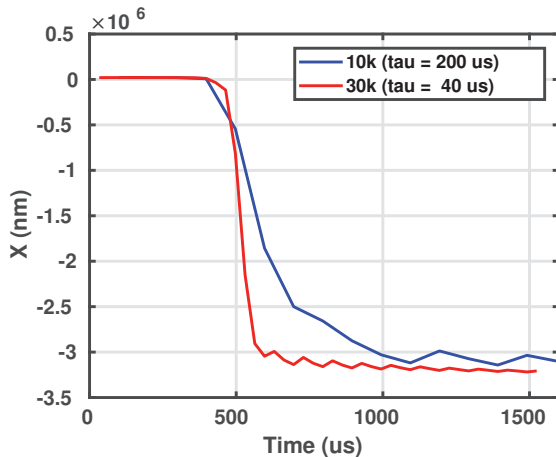


Figure 6: The improvement in the response time however can improve the performance of the FOFB system and has been shown to have reduced from  $\tau = 200 \mu\text{s}$  at 10 kHz to  $\tau = 40 \mu\text{s}$  at 30 kHz. Simulations predicted a reduction from  $\tau = 230 \mu\text{s}$  to  $\tau = 55 \mu\text{s}$ .

## CONCLUSION

Aside from some firmware bugs the installation and commissioning of the Brilliance+ system was smooth. The new system has removed the systematic coupling of 2% of the Electron and reduced the beam current dependence from  $\sim 10 \mu\text{m}$  to  $1 \mu\text{m}$ . Initial measurements of the 30 kHz FA data has confirmed the predicted improvement in the response time. Further work is still needed to quantify the effect of the wider bandwidth before it is used in the FOFB system.

## ACKNOWLEDGEMENTS

The authors would like to thank Adam Michalczyk for leading the project, Peter Leban from Instrumentation Technology, Noel Basten, and the amazing group of operators and the electrical team at the Australian Synchrotron that put in a significant amount of time into the project.

## REFERENCES

- [1] G.S. LeBlanc *et al.*, “The Australian synchrotron project storage ring and injection system overview”, in *Proc. EPAC’04*, Lucerne, Switzerland, 2004, paper THPKF005, pp. 2260–2262.
- [2] M.J. Spencer *et al.*, “Diagnostics and timing at the Australian synchrotron”, in *Proc. EPAC’06*, Edinburgh, Scotland, UK, 2006, paper TUPCH003, pp. 995–997.
- [3] Y.-R. E. Tan *et al.*, “Storage ring turn-by-turn BPMS at the Australian synchrotron”, in *Proc. PAC’07*, Albuquerque, New Mexico, USA, 2007, paper FRPMN004, pp. 3865–3867.
- [4] E. van Garderen *et al.*, “Upgrade of the booster beam position monitors at the Australian synchrotron”, in *Proc. IPAC’10*, Kyoto, Japan, 2010, paper MOPD080, pp. 882–884.
- [5] C.H. Kuo *et al.*, “Preliminary BPM electronic testing for the Taiwan photon source project”, in *Proc. IPAC’11*, San Sebastián, Spain, 2011, paper TUPC144, pp. 1362–1364.
- [6] Y.-R. E. Tan *et al.*, “Commissioning of the fast orbit feedback system at the Australian synchrotron”, in *Proc. IPAC’17*, Copenhagen, Denmark, 2017, pp. 1170–1173. doi: 10.18429/JACoW-IPAC2017-TUPIK040



# BEAM QUALITY MONITORING SYSTEM IN THE HADES EXPERIMENT AT GSI USING CVD DIAMOND MATERIAL\*

A. Rost<sup>1†</sup>, J. Adamczewski-Musch<sup>2</sup>, T. Galatyuk<sup>1,2</sup>, S. Linev<sup>2</sup>, J. Pietraszko<sup>2</sup>, M. Traxler<sup>2</sup>

<sup>1</sup>Institut für Kernphysik, TU Darmstadt, Darmstadt, Germany

<sup>2</sup>GSI Helmholtzzentrum für Schwerionenforschung GmbH, Darmstadt, Germany

## Abstract

In this contribution a beam monitoring system which consists of a chemical vapor deposition (CVD) diamond sensor, a fast readout electronics and a monitoring and visualization software used at GSI will be introduced. The sensor has been designed to measure the reaction time (T0) in the HADES Spectrometer, but also possesses beam quality monitoring capabilities which is of great importance to ensure high efficiency data recording. In the following, the diamond based sensor, its read-out chain and the online analysis and visualization software are described. Special emphasis will be put on an online visualization of important beam parameters namely the beam intensity, its position during extraction and the beam particle time structure.

## INTRODUCTION

For experiments with the HADES [1] detector at GSI in Darmstadt and for the future CBM [2] experiment at the FAIR facility, radiation hard and fast beam detectors are required. The detectors should feature high rate capability, low interaction probability and perform precise T0 measurements ( $\sigma_{T0} < 50$  ps). In addition, the sensors should offer beam monitoring capabilities. These tasks can be fulfilled by utilizing single-crystal Chemical Vapor Deposition (scCVD) diamond based detectors. This material is well known for its radiation hardness and high drift velocity of both electrons and holes, making it ideal not only as Time-of-Flight (ToF) detectors placed in the beam but also as luminosity monitors. With the help of striped read-out electrodes position information can be obtained for beam monitoring purposes. The main detector system used for this purpose in the HADES experiment consists of two diamond based sensors made of pcCVD and scCVD materials. Both sensors are equipped with a double-sided strip segmented metallization (300  $\mu$ m width) which allows a precise position determination of the beam position. Those sensors are able to deliver a time precision <100 ps RMS and can handle rate capabilities up to  $10^7$  particles/channel. Having the precise time measurement and precise position information of the incoming beam ions one can monitor important beam parameters namely the beam intensity, its position during extraction and the beam particle time structure. The read-out of the sensors is based on the NINO [3] chip in combination with the already well established TRB3 (Trigger Readout Board - Version 3) platform [4], developed by the TRB Collaboration [5]. On

this platform high precision multi-hit TDCs (up to 264 channels, time precision <10 ps RMS) are implemented inside FPGAs. The TRB3 system serves as a fast and flexible Data Acquisition System (DAQ) with integrated scaler capability. The analysis and online visualization is performed using the Data Acquisition Backbone Core (DABC) [6] framework.

## CVD DIAMOND BASED BEAM DETECTOR

The detector, which is used in HADES in order to construct the reaction time determination (T0) and beam quality monitoring, is made of single crystal chemical vapor deposition (scCVD) diamond material with an active area of 4.7 mm  $\times$  4.7 mm. The sample thickness of 70  $\mu$ m is chosen in order to reduce the nuclear interaction probability of the beam ions in the detector material. For example for an Au beam at 1.25 AGeV the interaction probability is about 0.36 %. The sensor is metalized with a 50 nm Cr layer, annealed at 500  $^{\circ}$ C for 10 min, deposited on the scCVD diamond and covered by a 150 nm Au layer. A similar detector [7] was used as T0 sensor in HADES for a  $^{197}\text{Au}^{69+}$  beam, with a kinetic energy of 1.25 AGeV and currents between  $10^6$ – $10^7$  ions/s delivered from the SIS 18 accelerator. The metallization is arranged in 16 strips (each 300  $\mu$ m wide) on each side which allows a beam profile measurements in  $x$  and  $y$  directions. A close-up picture of the multi-strip segmentation of the diamond based sensor is shown on in Fig. 1.

The diamond sensor is glued to a Printed Circuit Board (PCB), which serves as a holder and provides electrical con-

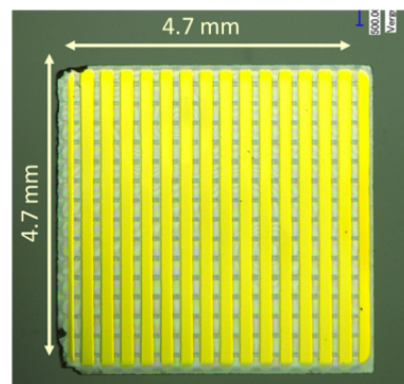


Figure 1: Close-up photography of the scCVD diamond based sensor. The metallization is arranged in 16 strips (each 300  $\mu$ m wide) on each side which allows beam profile measurements.

\* Work supported by the DFG through GRK 2128 and VH-NG-823.

† a.rost@gsi.de



nections to the read-out electronics. The read-out segments of the diamond sensors are bonded, using aluminum wires, to the conducting traces on the PCB. The scCVD diamond sensor mounted on a PCB is shown in Fig. 2.

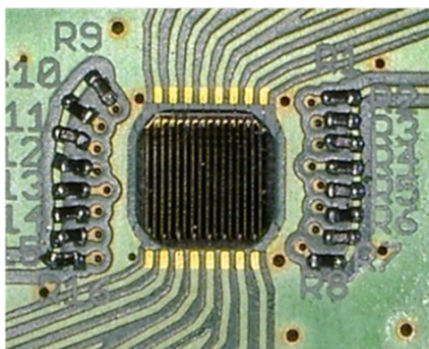


Figure 2: The diamond sensor is mounted on a PCB plates and the read-out electrodes are bonded to the PCB traces using aluminum wires.

As the T0 sensor has to be installed in vacuum very close to the HADES target, an additional mechanical holding structure is used for this purpose. The PCB with the sensor is installed on four PCB rods serving as a mechanical holder and ensures a electrical connection needed for the sensor read-out. The T0 sensor mounted on a holder structure is shown in Fig. 3. The T0 detector is located 2 cm in front of the reaction target. In addition the HADES experiment uses a diamond based veto-detector which is located 70 cm behind the target. Both detectors are aligned with the beam axis and the beam is focused on the target.

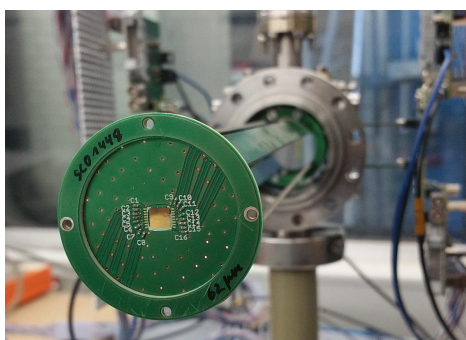


Figure 3: The diamond sensor as it is mounted into the HADES beam tube.

## READ-OUT CONCEPT AND ONLINE VISUALIZATION

The read-out electronics of the diamond sensor is based on the NINO chip. In Fig. 4 a NINO-based read-out board is shown. Each board offers eight input channels. A fan-out implementation delivers eight fast Low Voltage Differential signals (LVDS) for trigger purposes and eight fast LVDS signals for timing measurements. Timing measurements

are performed using the TRB3 platform. A large variety of front-end electronics is available for the TRB3 in order to extend its functionality i.e. discriminator boards [8].

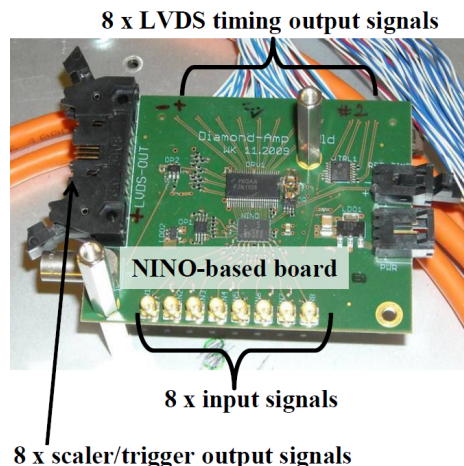


Figure 4: The NINO-based board used for T0 readout in HADES. This board offers LVDS timing outputs and scaler/trigger outputs.

The Data Acquisition Backbone Core (DABC) [6] is a DAQ framework with modular components for data-flow on multiple nodes. It provides a C++ runtime environment with all basic services, such as: threads and event handling, memory management, command execution, configuration, logging and error handling. User written DAQ applications can be executed within this environment by means of a plug-in mechanism. It offers advanced possibilities for on-line analysis of data samples via TCP/IP sockets, and monitoring of run variables via HTTP clients. A specialized web server [9], based on an embeddable Civetweb http server, has been implemented in DABC. This server can deliver data directly from running applications to a web browser where JavaScript-based code powers an interactive web graphics.

For this application DABC collects the data from the TRB3 boards, performs the needed online time calibrations, and carries out online data analysis. Results of the data processing in form of histograms are provided to the DABC web server for visualization. For online beam monitoring purposes trend plots showing the beam position in x- and y-direction, the time structure of the beam, and the beam intensity have been implemented. Those plots are rendered as a live display in any web browser to be used by the accelerator operators.

## System Performance

A prototype system consisting of one segmented diamond sensor connected to NINO based discriminator boards and read-out by one TRB3 board has been prepared and tested with very low intensity Ca beam, about 200 Ca ions/s, and with pulse generator signals. Further beam tests are planned and will be conducted soon. The readout system can transfer up to 100 MB/s data without data losses to the linux PC running the DABC analysis system. This amount of data can

be online analyzed, the preprogrammed histograms can be prepared and visualized on a dedicated web server. In Fig. 5 a trend plot of the spill structure of a calcium beam is shown as an example. The 100 MB/s of data corresponds to the hit rate of about 20 MHz hits in a single TDC channel. At higher hit rates some hits will get lost as the TRB3 can currently transfer only 100 MB/s lossless. In order to increase the data transfer bandwidth one can use several boards in parallel.

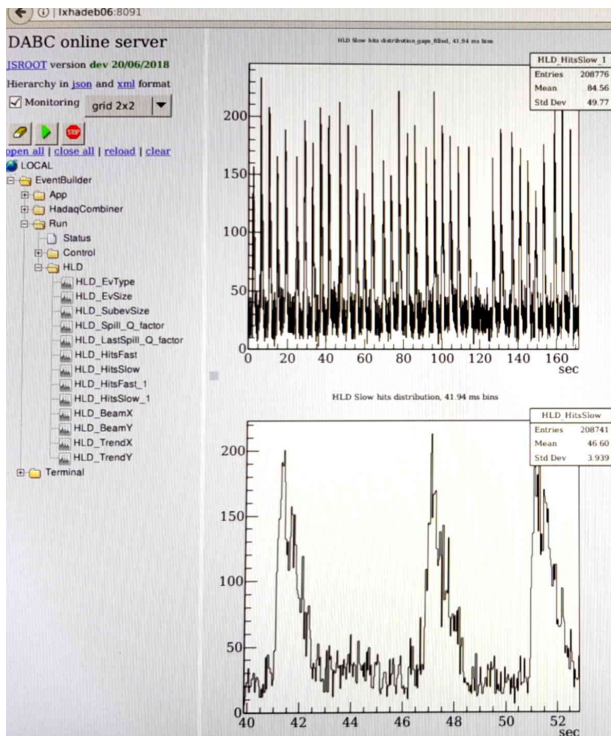


Figure 5: Spill structure of a calcium beam monitored by DABC in a web browser.

## SUMMARY AND OUTLOOK

A scCVD diamond based beam sensor was presented in detail. The sensor provides T0 determination for time-of-flight measurements in the HADES spectrometer. Besides that it is used for beam monitoring purposes. A segmented metallization allows a precise determination of the beam position. Utilizing state of the art read-out electronics based on the NINO ASIC and the TRB3 platform and the comprehensive DABC software framework, beam quality trends can be visualized in a web-browser in real-time.

Currently, the HADES collaboration prepares the spectrometer for a production beam time with a 1.65 AGeV silver beam. A four week physics beam time is planned for end of 2018. The introduced beam monitoring concept will be used. For further diamond detector developments a test set-up is currently installed at the Superconducting Darmstadt Electron Linear Accelerator (S-DALINAC) [10] of Technical University Darmstadt. The accelerator is designed for electron beams with an energy of 130 MeV and currents up to 10  $\mu$ A. It provides an excellent condition for diamond detector research and developments, especially for Minimum Ionizing Particles (MIPS).

## REFERENCES

- [1] G. Agakishiev *et al.* [HADES Collaboration], “The High-Acceptance Dielectron Spectrometer HADES,” *Eur. Phys. J. A* **41** (2009) 243.
- [2] Peter Senger *et al.* [CBM Collaboration], “Cosmic Matter in the Laboratory: The CBM Experiment at FAIR,” *Nuclear Physics News*, 28:2, 23-27 (2018).
- [3] F. Anghinolfi *et al.*, “NINO: An ultra-fast and low-power front-end amplifier/discriminator ASIC designed for the multigap resistive plate chamber,” *Nucl. Instrum. Meth. A* **533** (2004) 183.
- [4] A. Neiser *et al.*, “TRB3: a 264 channel high precision TDC platform and its applications,” *JINST* **8** (2013) C12043.
- [5] The TRB Collaboration, “<https://trb.gsi.de>”.
- [6] J. Adamczewski-Musch *et al.*, “Developments and applications of DAQ framework DABC v2,” *J. Phys. Conf. Ser.* **664** (2015) no.8, 082027.
- [7] J. Pietraszko *et al.* [HADES Collaboration], “Radiation damage in single crystal CVD diamond material investigated with a high current relativistic  $^{197}\text{Au}$  beam,” *Nucl. Instrum. Meth. A* **763** (2014) 1.
- [8] A. Rost *et al.* [TRB and HADES and CBM Collaborations], “A flexible FPGA based QDC and TDC for the HADES and the CBM calorimeters,” *JINST* **12** (2017) no.02, C02047.
- [9] J. Adamczewski-Musch *et al.*, “Web interface for online ROOT and DAQ applications,” 19th IEEE-NPSS Real Time Conference (2014).
- [10] Norbert Pietralla, “The Institute of Nuclear Physics at the TU Darmstadt,” *Nuclear Physics News*, 28:2, 4-11 (2018).

# BPM SYSTEM UPGRADE AT COSY

I. Bekman, C. Böhme, V. Kamerdzhev, B. Lorentz, S. Merzliakov,  
P. Niedermayer, K. Reimers, M. Simon, M. Thelen  
FZJ, Jülich, Germany

## Abstract

The beam position monitoring system of the Cooler Synchrotron (COSY) has been upgraded in 2017. The upgrade was driven by the requirement of the JEDI collaboration to significantly improve the orbit control and by the electronics approaching end-of-life. The entire signal processing chain has been replaced. The new low noise amplifiers, mounted directly on the BPM vacuum feedthroughs, were developed in-house and include adjustable gain in 80 dB range and in-situ test and calibration capabilities. The signals are digitized and processed by means of commercial BPM signal processing units featuring embedded EPICS IOC. The decision path, technical details of the upgrade and performance of the new system are presented.

## INTRODUCTION

The necessity of upgrading the COSY Beam Position Monitor (BPM) system arose from the requirement of the JEDI collaboration to significantly improve the beam orbit control and by the electronics approaching end-of-life. The upgrade affected all electronics sub-systems: amplifiers and their control, data collection and processing, networks, and the way measurement results are stored and presented. New sub-systems were added, for example, the calibration sub-system utilizing in-situ test signal generation and fine control of amplifier gain and as the main part - the Hadron Beam Position Processor Libera. Below the block-diagram (Fig. 1) and a brief description of the main components of BPM system are presented. 31 capacitive BPM are installed in

the COSY ring. This number includes two BPM of the 2 MeV electron cooler which are also capable of measuring proton orbit. These are not affected by the upgrade presented here. Each COSY BPM utilizes 4 electrically isolated electrodes that make beam position measurements in both X and Y planes possible. The electrodes are connected via N-type vacuum feedthroughs to the amplifiers. Close to the amplifiers high precision ( $4 \cdot 10^{-4}$ ) four-way splitters are placed to feed test signals from generators of the calibration sub-system into the amplifiers. The 116 amplified signals are transmitted from the tunnel via coaxial cables to eight Libera beam position processors [1] installed at 6 location in the accelerator hall (Fig. 2). The 19-inch racks house also the crates of the trigger system as well as additional crates accommodating the amplifier power supply and calibration sub-system. Newly developed graphical user interfaces based on Control System Studio allow for display of measured beam orbit and turn-by-turn data, amplifier gain control and calibration as well as provide additional software tools for display and control of Libera parameters, ADC data etc.

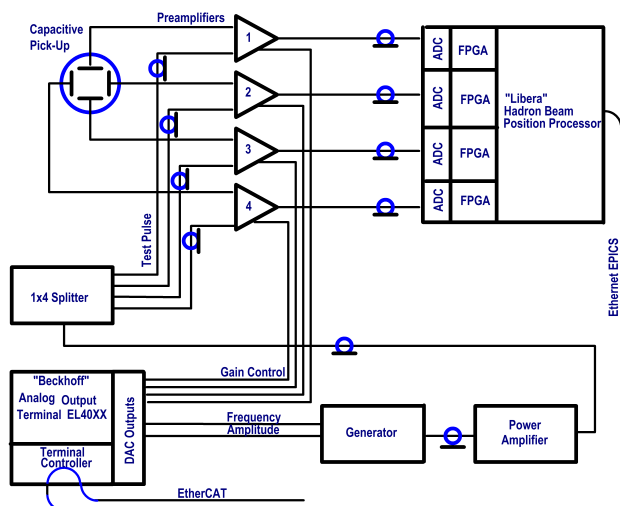


Figure 1: Block diagram of the new COSY BPM system. Only one pickup and corresponding electronics are shown.

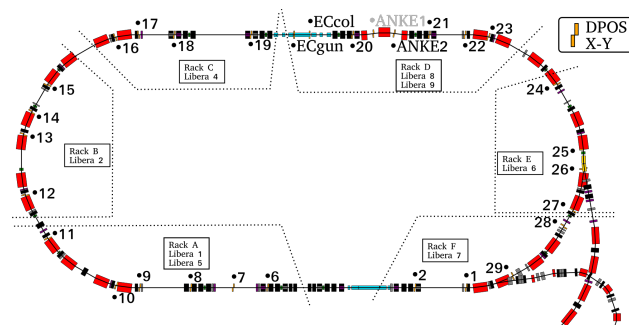


Figure 2: Operational BPM hardware around the COSY ring.

## BPM AMPLIFIERS

The BPM amplifiers are housed in a 100-50-25 mm die-cast aluminum case and are installed directly on the vacuum feedthroughs. They are connected to the Libera beam position processors and the calibration sub-system. For analog signals RG214 coaxial cables are used. CAT 6 Ethernet cables are used to power the amplifiers and for gain control. Figure 3 shows the block diagram of a BPM amplifier.

Each unit consists of two stages: input stage and amplification stage. Table 1 summarizes the properties and performance of the input stage. The amplification stage is based on the variable gain amplifier chip AD8330 and features variable gain up to 80 dB. Control of the amplifier gain is done by means of commercial EtherCAT DACs.



Figure 3: Block diagram of BPM amplifier. A1 - input stage (6 or 20 dB), A2 output stage (-6 dB), A3 - single to differential signal converter (0 dB), A4 and A5- 1st (0 - 50 dB, 0 - 1.5 V or 30 mV/dB) and 2nd stage (-30 - 20 dB, 0 - 4.8 V, nonlinear) of main amplifier, A6 - output buffer.

Parameter	Value
Input impedance	500 k $\Omega$
Output impedance	50 $\Omega$
Gain	6 dB or 20 dB
Output Range	$\pm 1$ V at 50 $\Omega$
Bandwidth	1 kHz - 80 MHz (-3 dB)
Temperature coefficient	0.05 % / $^{\circ}$ C
Input noise	1.4 nV / $\sqrt{Hz}$ at 10 MHz

Based on the  $\mu$ TCA 4.0 platform, the commercially available LIBERA electronics [1] from Instrumentation Technologies digitizes the analog signals and provides several calculated data streams. The main purpose is the recognition of the single beam bunches and providing the calculated position of those. However, other data is available, like the 10 Hz averaged position data stream, the ADC raw data or the FFT of the bunch data. In the case it is not possible to acquire bunch-by-bunch data (insufficient signal quality or unexpected bunch shape like in case of barrier-bucket operation), a so called narrow-band analysis can be used. In this case the signal is highly integrated before trying to calculate beam position.

The available data can be sent towards the control system in several ways, out of the box the possibility for the EPICS or TANGO data communication is provided. Because of the larger user base, and therefore more software being developed, the usage of EPICS was chosen to slowly replace the proprietary data communication protocol used at COSY.

The LIBERA electronics needs further input signal references: a trigger signal, a RF frequency reference and a 10 MHz reference (based on central COSY clock) for synchronization between single units. These signals are gener-

Figure 4: Control System Studio [2] graphical user interface views of raw ADC data (left) gain and generator control panel (right).

ated on a central platform and then distributed to the units via equally long cables.

The power and calibration modules for the 4 power sensors are packed in 19-inch crates. The sizes of all modules are 3 U, 8 TE, length 160 mm. Inside the crate Beckhoff EtherCAT DAC modules, which control the amplifier gains and the parameters of the calibration system are installed (see below). The calibration sub-system for one BPM consists of: 4-channel Beckhoff DAC, quartz synchronous generator, power amplifier and four-way splitter (the latter are installed in the tunnel). The generator is used for performance testing and calibration. It produces a series of Gaussian shaped pulses of different amplitudes (0–2 V) and frequencies (0.3–3 MHz). Frequency and amplitude control are done via EtherCAT remotely or using front panel controls locally. Precision of amplitude and frequency, as well as long term stability is better than 0.1 %. At the output of the generator a low pass filter of second order and a buffer amplifier based on OP LMH6639 is used. Power amplifier is based on the ADA 4870 operation amplifier. The device has a gain of 14 dB, and is capable to provide signals up to 10 V to four splitters with 50  $\Omega$  input impedance each. The main feature of the four-way splitter is the high accuracy of the power distribution between the 4 outputs. Input and output impedance of the device is 50  $\Omega$ , the attenuation from input to one output is 14.4 dB, flat. The maximum measured error of the attenuation for 30 splitters (120 channel) is  $4 \cdot 10^{-4}$  (calculation error  $2 \cdot 10^{-4}$ ). The second feature of the splitter is the possibility to work with 10 V input signal for a frequency range from DC to 300 MHz.

The gain of the amplifiers and calibration generators is controlled by Beckhoff DAC modules using the EtherCAT communication protocol [3]. Modules listed in Table 2 are used per crate, with a total of 8 crates. The DAC modules provide adjustable current (EL41xx) and voltage (EL40xx) levels, which are converted to control signals delivered to the amplifiers and the generator modules. For each BPM amplifier two control lines are provided - a coarse common



Table 2: Beckhoff Modules per Crate<sup>1</sup> of the BPM System

EK1101	EL4114	EL4114	EL4104	EL4114	EL4114	EL4104
EtherCAT Bus Coupler	4 Ch DAC Fine Gain (L)	4 Ch DAC Fine Gain (U)	4 Ch DAC Common Gain	4 Ch DAC Fine Gain (R)	4 Ch DAC Fine Gain (D)	4 Ch DAC Generator

<sup>1</sup>One crate being connected to fewer BPMs, there the last two DACs of type EL4114 are absent.

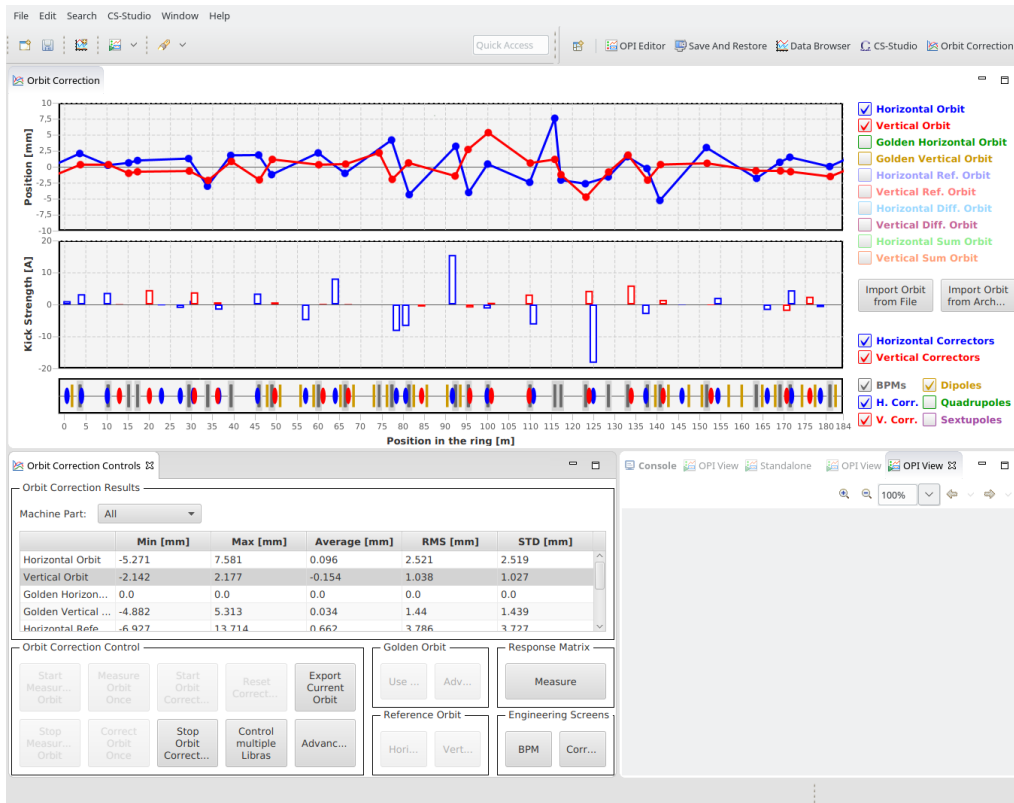


Figure 5: Screenshot of the orbit correction GUI. The measured beam orbit (10 Hz data stream) is displayed in the upper part.

gain for a group of up to 4 amplifiers and a fine gain to control individual devices.

The communication with the modules via the EtherCAT standard is realized by means of a specially prepared server with a separate compatible network card, modified Linux kernel, and device drivers based on EtherLab package running in a standard Debian distribution.

Libera, gain, and calibration generators are controlled and read out via EPICS [4] protocol and relevant values are being archived continuously. Several EPICS graphical user interfaces were implemented for ease of use by the operators and maintainers based on CSS software package.

## GAIN CALIBRATION PROCEDURE

Preliminary calibration of a single BPM was performed with a sine generator. Gain parameters were scanned and data was read out from the ADC of Liberas via EPICS. The results are shown in Figs. 6 and 7. The precision of a given gain setting was determined to be on the order of 0.04 dB, the stability over 60 h was determined to be better than 0.01 dB.

## SUMMARY AND OUTLOOK

The new hardware was successfully installed in July 2017. Since then the new system was routinely operated for orbit measurements and orbit correction. Minor issues were resolved and did not cause interruptions of beam operation. One-time calibration of the amplifier components is scheduled for the machine maintenance weeks in the Fall 2018. Currently the automatic gain calibration software is being commissioned. Once operational the feature should be used regularly and after every gain adjustment. It is expected that this would push the accuracy of measured beam position below 100  $\mu\text{m}$ .

## REFERENCES

- [1] Libera Hadron, *Hadron Beam Position Processor*, User Manual, Version 1.01, Instrumentation Technologies, Velika Pot 22, SI-5250 Solkan, Slovenia
- [2] Control System Studio Webpage, <http://controlsystemstudio.org/>

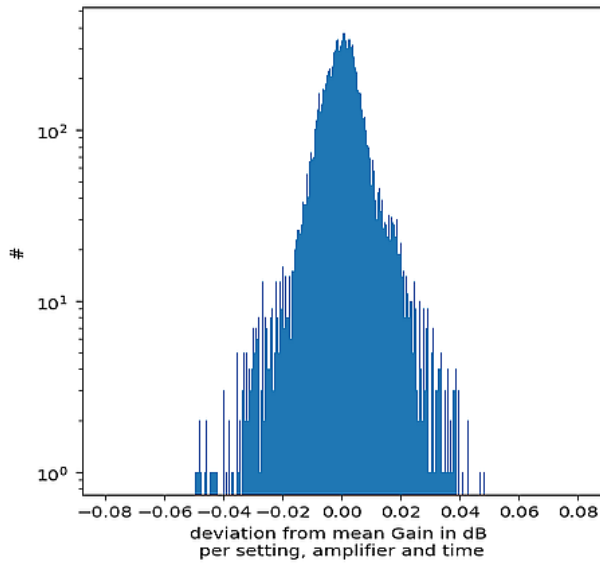


Figure 6: For gains below 57 dB for four different amplifiers both common and fine gain settings were scanned repeatedly in a calibration procedure. The plot shows statistical distribution of mean gain values per setting from which the precision over all settings can be estimated.

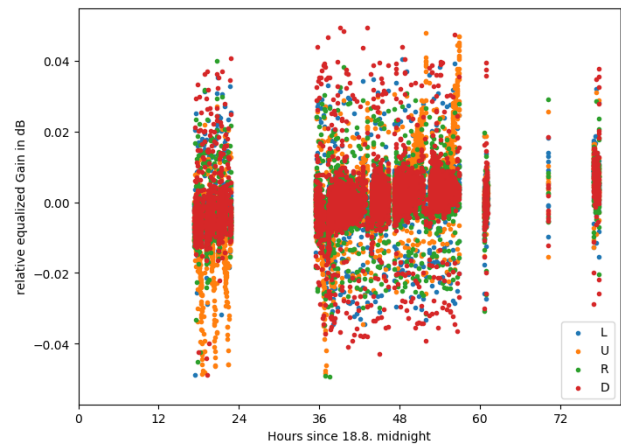


Figure 7: Repeated measurements for four amplifiers over several hours shows good stability.

- [3] EtherCAT standard,  
<http://www.beckhoff.com/EtherCAT-System/>
- [4] Experimental Physics and Industrial Control System (EPICS),  
<http://www.aps.anl.gov/epics>

# INFLUENCE OF SAMPLING RATE AND PASSBAND ON THE PERFORMANCE OF STRIPLINE BPM

T. Wu<sup>1</sup>, Y. B. Leng, L. W. Lai, S. S. Cao, J. Chen, F. Z. Chen, Y. M. Zhou,  
Shanghai Institute of Applied Physics, Chinese Academy of Science, Shanghai, China  
<sup>1</sup>also at University of the Chinese Academy of Science, 100049 Beijing, China

## Abstract

It is obviously that the property of strip-line BPM is influenced by data acquisition system, but how the procedure of data acquisition and processing takes effect is still room for enquiring into it. This paper will present some data simulation and experiment results to discuss the function between resolution and passband, sampling rate or other influence factor. We hope that this paper would give some advice for building up data acquisition system of SBPM.

## INTRODUCTION

Thanks to its compact design and high precision, SBPM is widely used for bunch position measurement just as what was in SXFEL [1]. As part of the modularization and generalization of the system, the digital BPM parameter settings used in SBPM measurements are the same as that in other part of beam diagnostics system. As a result, the analog signal measured by SBPM passes through a filter with a passband of 495 MHz-505 MHz, and then is undersampled by a sampling rate of 119 MHz and converted into a digital signal for subsequent processing.

The final measurement accuracy meets the need for beam position measurement of beam diagnostics system in SXFEL. However, With the improvement of machine performance requirements, the optimization of SBPM performance has gradually become more realistic and urgent. Under the premise that it is difficult to greatly optimize the performance of probes, it is a good choice to optimize the filter passband and sampling rate in electronics front-end design.

## NUMERICAL SIMULATION

The corresponding signal and spectrum of strip-line BPM are showed below in Figure 1. We assume that the photon in the beam bunch Gaussian distribution, so as the signal waveform [2].

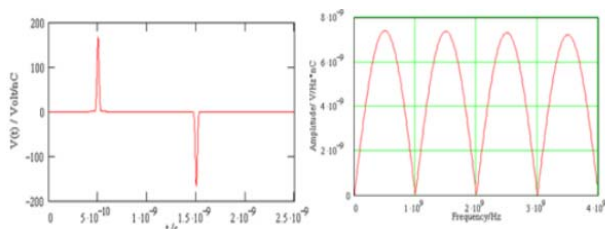


Figure 1: SBPM output signal(left) and the spectrum under the ideal conditions [3].

According to the spectrum, when center of the passband is nearing 500 MHz, the resolution would be optimal. That is the reason why passband is 490 MHz-510 MHz. But when put SBPM in a data measurement system, the conclusion may be different.

In SXFEL, the analog signal of SBPM will be transferred into digital signal before data processing [4]. Considering the influence of ADC, the spectrum of SBPM is shown in Figure 2.

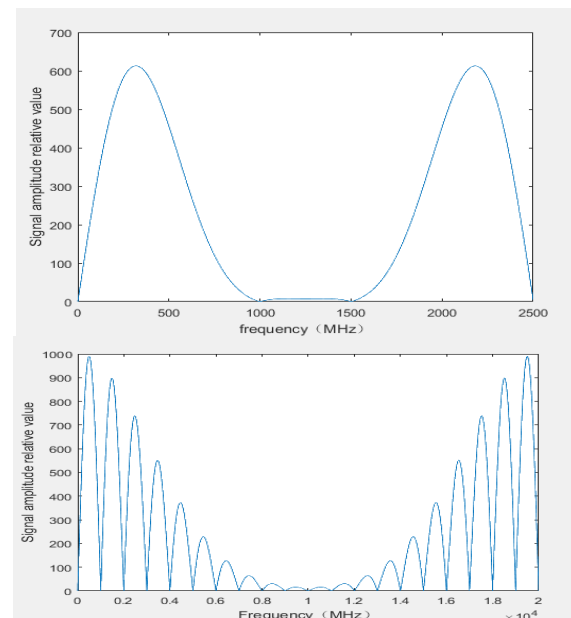


Figure 2: SBPM output spectrum influenced by ADC. Sampling rate are 2.5 GHz (top) or 10 GHz (bottom).

The result of numerical simulation reflects in one aspect how the sampling rate affects SBPM performance. 500 MHz is no longer the peak of the signal frequency after analog to digital conversion. Instead, a lower frequency takes its place. This phenomenon becomes more pronounced as the sampling rate of the ADC decreases. Considering undersampling, the spectral characteristics changes brought by ADC will be more complicated and need to be calculated according to the specific scheme [5].

The above is discussing the effect of the sampling rate on the peak of signal in frequency domain. On the other hand, the bandwidth of passband would also effect the resolution of SBPM. However, how it matters is more complicated. It depends on the noise composition. When the signal noise from SBPM probe is the main part of the

noise of the measurement system, it is obviously that a narrow band around the peak is optimal. However, if the noise is mainly derived from electronic noise, the electronic front-end design needs to be taken into consideration.

In this situation, if there is no more than filter and ADC in the electronics front-end, the power of the noise changes little. It means that the wider the bandwidth, the larger the signal to noise ratio. However, as the bandwidth changes, the signal waveform may be following form in the Figure 3.

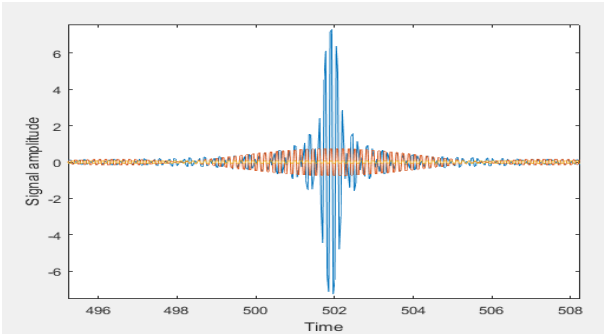


Figure 3: Simulation results of signal waveform while bandwidth changing.

It can be seen that as the bandwidth is gradually reduced, the peak value of the signal is continuously reduced, and the time of the signal is gradually lengthened. For an integrated DBPM system, this means that an amplifier may need to be introduced (Figure 4). On the other hand, too narrow a signal may also result in too little measurable data, resulting in reduced resolution. The impact of this factor needs to be analyzed in combination with specific situations [6].

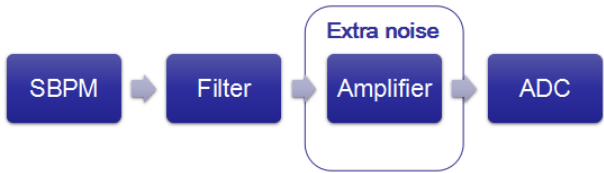


Figure 4: Simple block diagram.

## EXPERIMENTAL COMPARISON

### Signal Peak Shift

The signal used in the experiment came from the SBPM in SXFEL. According to the specific experimental parameter settings, the signal was filtered by filter and finally collected by a 2.5 GHz sampling rate oscilloscope. Figure 5 shows a set of signals that were directly measured without filter.

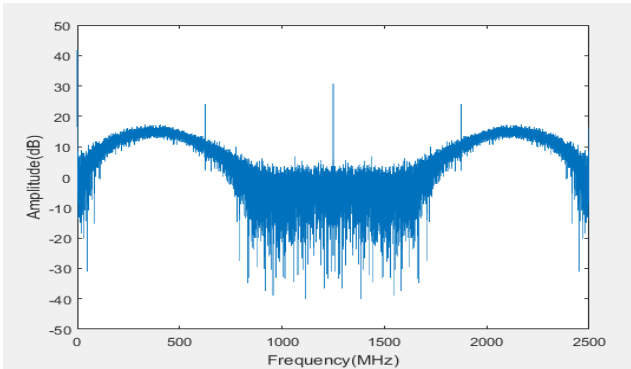


Figure 5: Spectrum when sampling rate is 2.5 GHz (Self-contained 2.5 GHz filter in the oscilloscope).

This situation is more closer to the simulations in the Figure 2 rather than that under ideal condition, which indicated that The ADC does cause the movement of the signal peak.

In order to more comprehensively compare simulation data with experimental data, multiple sets of filtering schemes are provided. Since the passive filters are selected as the experimental device, the passband of the filter is not selectable to some extent. So we can only experiment with existing conditions. The filters used in the experiments are shown in the table below.

Table 1: Filter Passband Schemes used in Experiments

Num.	Passband start frequency (MHz)	Passband end frequency (MHz)	Vpp (V)
1	0	94	0.7
2	0	400	2.0
3	0	560	3.2
4	0	700	3.1
5	450	550	1.2
6	250	560	1.6
7	250	650	1.8

Using the simulation data at the 2.5 GHz sampling rate in Figure 2, we were able to obtain the relative values of the signal power fanned by SBPM under different passbands. Comparing this with the actual experimental measured data, it is possible to define whether there is a change of the signal distribution in the frequency domain compared with that under ideal condition. The resulting contrast image is shown in Figure 6. The abscissa indicates the signal power level under the filtering scheme in the simulation, and the ordinate indicates the SINAD of signals measured.



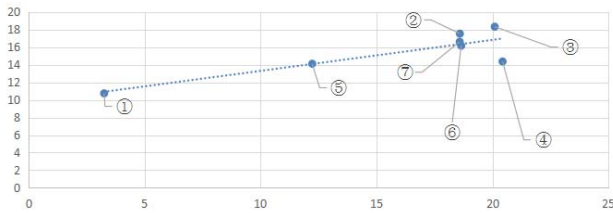


Figure 6: Comparison of simulation data and experimental results.

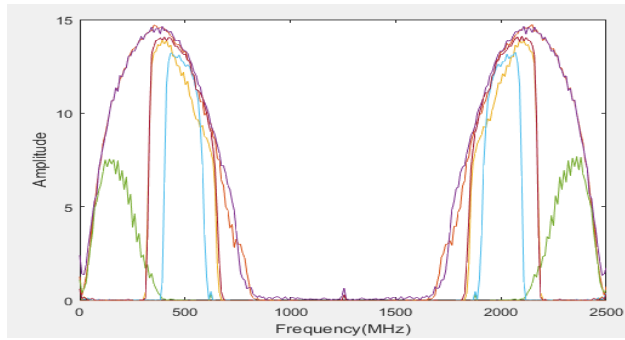


Figure 7: Spectrum of experimental data. In order to reduce the number of data points on the abscissa to simplify the graph, the data on the ordinate is transformed, which made it without unit.

Except for the fourth set of data, the other data matched the simulation results well. As can be seen from Figure 7, the noise on the stopbands of the fourth set is significantly larger than the other groups. And from the results, the experimental data is more different from the data under ideal conditions. So it can be qualitatively said that the preliminary experimental results support the simulation data.

### *Influence of Bandwidth*

As shown in Figure 5, the noise introduced by the SBPM is not the main part in the experiment. Therefore, in the actual selection, a wider passband may be a better choice until the resulting electronic noise affects the system measurement accuracy.

However, the range of the ADC is limited, which brings the amplifier into the DBPM, introducing a new influencing factors. Due to the limitations of experimental conditions, the amplifier was not used in the experiment. Instead, the effects of the amplifier were gotten by data simulation. In Table 1, the peak-to-peak values of the signals in different passbands were listed, and 2V was selected as a suitable range of ADC. Assuming the noise of the amplifier is 6.5nV/rtHz and the noise is all electronics noise, the simulation result could be gotten based on the experimental data, which is shown in Figure 8.

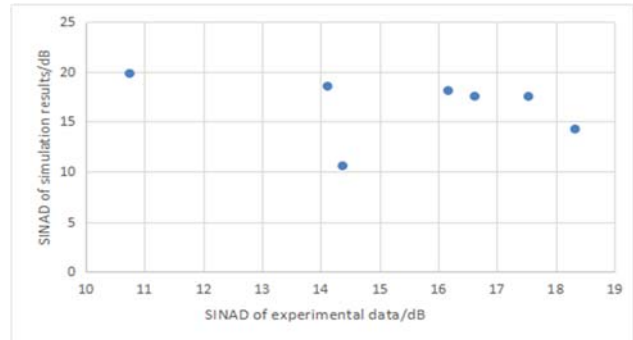


Figure 8: Comparison of experimental data and simulation results of SINAD.

Unlike previous conclusions, narrower bandwidth is better under the influence of electronic factors. This is because of the effects of the ADC. However, when the bandwidth is too small, the noise of the SBPM will be too large, as shown in Figure 9. Therefore, the optimal value of bandwidth needs to consider the influence of multiple factors.

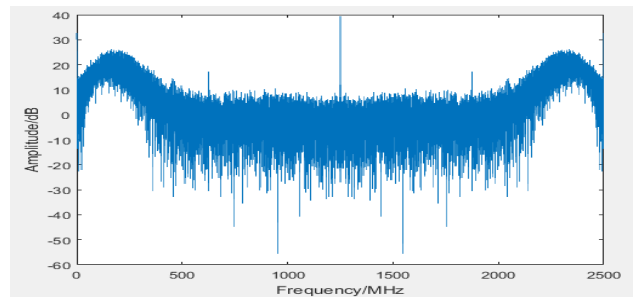


Figure 9: Spectrum of the first set of experiment.

## **FURTHER RESEARCH**

The further research will focus on the experimental part. We would build an integrated measurement platform with FPGA as the core, in order to maximize the experimental verification. Active filtering schemes will also be considered in order to measure the effects of passbands on the measured signals.

## **CONCLUSION**

In this paper, we have simulated and measured the accuracy of the SBPM measurement system around the influence of sampling rate and passband selection. The research mainly focuses on the movement of the signal peak and the influence of the bandwidth on the accuracy of the measurement system, and some experimental results are obtained.

The long-term goal of this research is to establish a simulation and evaluation system, so that designer could filter out the optimal parameter setting in different situations.

## REFERENCES

- [1] U. Bergmann *et al.*, “Science and Technology of Future Light Sources”, LBNL, Berkeley, CA, Rep. LBNL-1090E-2009, Jan. 2009. doi:10.2172/948040
- [2] Y.B. Leng *et al.*, “Precise beam current measurement for storage ring using beam position monitor”, *High Power Laser Particle Beam*, vol. 22, pp. 2973-2978, 2010 (in Chinese). doi:10.3788/HPLPB20102212.2973
- [3] L. W. Lai *et al.*, “The development and applications of the digital BPM signal processor at SINAP”, in *Proc. 60th ICFA Advanced Beam Dynamics Workshop on Future Light Sources (FLS'18)*, Shanghai, China, 5-9 March 2018, pp. 43-45. doi:10.18429/JACoW-FLS2018-TUP1WD03
- [4] Y. Yan, Y. B. Leng, L. W. Lai, L. Y. Yu, W. M. Zhou, J. Chen, H. Zhao, and C. L. Yu., “Data acquisition system for beam instrumentation of SXFEL and DCLS”, presented at IBIC'18, Shanghai, China., Sep. 2018, paper MOPC11, this conference.
- [5] V. Sargsyan, “Comparison of stripline and cavity beam position monitor”, TELS, Hamburg, Germany, Rep. TESLA Report 2004-03, Mar. 2004.
- [6] Y.B. Leng *et al.*, “SSRF beam instrumentations system”, in *Proc. ICALECPS'07*, Knoxville, TN, USA, Oct. 2007, pp. 205-207.

## FIRST RESULTS OF BUTTON BPMS AT FRIB\*

S. Cogan<sup>†</sup>, S. Lidia, J. Crisp, T. Ford, Facility for Rare Isotope Beams, East Lansing, MI, USA

### Abstract

Commissioning and tuning the linac driver for the Facility for Rare Isotope Beams (FRIB) requires a large network of warm and cryogenic beam position monitors (BPMS), with apertures of 40 - 150 mm, sensitivity to beam currents of 100 nA to 1 mA, and accurate for beams with velocities as low as 0.03c. We present initial results of the BPM system, analog and digital signal processing, and energy measurements for low energy beams.

### COMMISSIONING AND TUNING

The Facility for Rare Isotope Beams (FRIB) is a new scientific user facility for low energy nuclear science. Under construction on campus and operated by Michigan State University, FRIB will provide the highest intensity beams of rare isotopes available anywhere [1].

The accelerator is being commissioned and tuned in sections. The Front End, RFQ, and first three superconducting RF cavities have been commissioned with beam [2]. BPMS are the primary tool used to determine beam position and beam energy. Beam of  $^{40}\text{Ar}^{9+}$  was accelerated up to 2.3 MeV/u and BPM position and phase proved accurate down to currents as low as 100 nA. Figure 1 shows a portion of the linac and placement of 15 BPMS.

### BPM Characterization and Correction

At FRIB, we primarily utilize two types of 4-button BPMS, with aperture diameters of 41.3 and 47.6 mm. Buttons are circular with 20 mm diameter. With a 4-button BPM, the simple formula (1) for position utilizes the ratio of difference over sum for two of the buttons signals (R, L or T, B) along with a scale factor incorporating the BPM aperture (D)

$$H = \frac{D}{\pi} \left( \frac{R-L}{R+L} \right), \quad V = \frac{D}{\pi} \left( \frac{T-B}{T+B} \right) \quad (1)$$

Formula (1) approximates beam position well, but distortion increases further away from center. A polynomial correction (2) was determined for each BPM type to correct for non-linear distortions. Each BPM was characterized using a translation stage to raster scan wire positions within the BPM aperture. Fiducials on the BPM housing, shown

in Fig. 2, allow accurate position survey and correlation with pre-installation wire measurements to within 100  $\mu\text{m}$ . Consistent BPM manufacturing allows the use of the same correction for all BPM assemblies of the same type.

$$H_{\text{new}} = p_{00} + p_{10}H + p_{30}H^3 + p_{50}H^5 + p_{12}HV^2 + p_{14}HV^4 + p_{32}H^3V^2 \quad (2)$$

There is an additional position distortion present with very low-beta ( $v/c \ll 1$ ) beams, resulting from the non-relativistic electric fields and asymmetrical pickup of the higher order beam harmonics when the beam is off-center [3]. This effect is most significant when  $\beta < 0.10$ , and can be ignored when  $\beta > 0.15$ . Formula (3) corrects for low-beta distortion, where  $a$  and  $b$  are factors dependent on beta, frequency, and geometry [3].

$$H_{\text{new}} = aH + bH^5 \quad V_{\text{new}} = aV + bV^5 \quad (3)$$

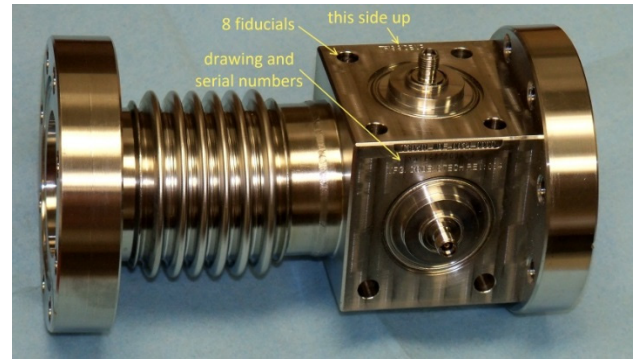


Figure 2: FRIB BPM assembly.

### DAQ ELECTRONICS AND SIGNAL PROCESSING

The BPM data acquisition electronics were designed to be MicroTCA [4] based, where up to 10 BPM electronics boards communicate (using PCIe) to a single CPU which serves data to the control system network. The electronics consist of a rear-transition module (RTM) which includes +35 dB amplification, analog filter (either lowpass or bandpass), and ADC digitization. This RTM digitizes two 4-button BPMS plus a reference (REF) clock. An FPGA digital processing board performs digital down-conversion

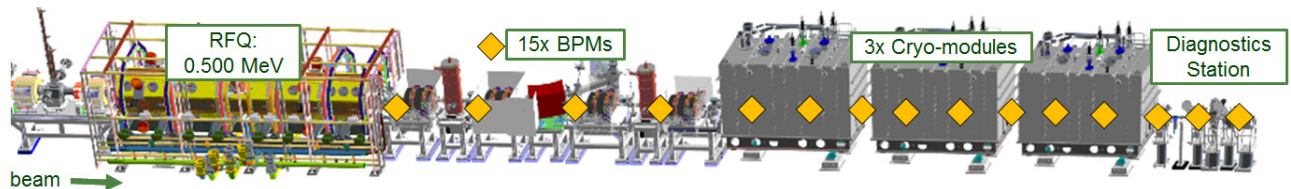


Figure 1: A portion of the FRIB linac, including medium energy beam transport (MEBT), first 3x cryo-modules with 12x accelerating SRF cavities, and diagnostics station as temporary beam stop. 15 BPMS locations were studied, 6 of which were “cold” BPMS inside cryo-modules.

\* This material is based upon work supported by the U.S. Department of Energy Office of Science under Cooperative Agreement DE-SC0000661, the State of Michigan and Michigan State University.

<sup>†</sup> cogan@frib.msu.edu





group of 4 long run cables for a BPM have been phase-matched and trimmed to within  $1^\circ$  phase at 80.5 MHz, but it was not practical to trim all BPM cables to the same length throughout the machine. Our BPMs report signal phase relative to an 80.5 MHz reference (REF) clock distributed throughout the machine and to each BPM DAQ board. This same REF clock system is used by the RF accelerators and bunchers. To measure the signal delay contribution from long run cables and DAQ electronics, a signal is generated near the BPM device which is phase-locked to the REF clock. This signal is split 1:4 and connected to the long run cables for a single BPM, and the phase is recorded. The same REF clock signal cable is used to measure all BPMs, one at a time. These BPM phases represent the offset due to cabling and electronics, and must be subtracted prior to beam energy estimation. Figure 7 shows an example where BPM #6 cables and electronics are being measured for calibration using REF clock.

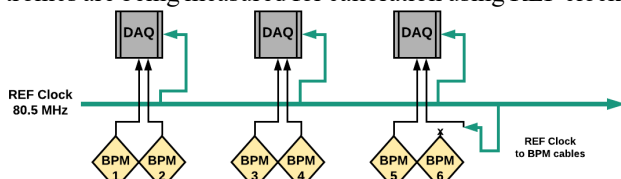


Figure 7: BPM system calibration diagram.

Short 1 meter patch cables exist on both ends of the long cables. The device side patch cables were not measured during the calibration procedure. If all patch cables were the same length, this would not be relevant, but in our case, two types of patch cables were used for warm and cold BPMs. The cold BPM patch cables add an additional  $36.5^\circ$  phase, which was also subtracted for cold BPMs only.

### Energy Calculation and Uncertainty

The approach described in [5] involves using 3 BPM pickups; one pair closely spaced, for coarse velocity estimation, and one pair spaced far apart, for better velocity accuracy. Our BPM installation does not allow for BPMs placed close together, so we need a more general approach. We use 3 BPMs to generate 3 pairs, each with different spacing. Each of these pairs has some energy uncertainty, due to unknown number of full periods, but we can determine the real energy by noticing where these possible energies overlap, giving the same answer in all three cases.

In any real system, there are error sources which prevent the energy estimates from giving an exact match. Sources of additional variance and uncertainty include position survey accuracy, accuracy of cable calibration, and signal phase noise. The last is largely a function of beam intensity and the signal/noise performance of the front-end electronics. Adding the variances from these sources is fairly straightforward, assuming they are uncorrelated and represented by normal distributions. In our case, typical stack-up of uncertainties resulted in an RMS phase uncertainty of about  $0.5^\circ$ .

We incorporate these uncertainties by modelling a normal distribution centered at each possible energy estimate, which generates a pseudo-probability distribution for each

BPM pair. The joint energy probability distribution is estimated by a point-by-point multiplication of the three individual distributions. We report the peak value of this combined probability distribution, which is itself properly weighted; BPM pairs with less uncertainty have more impact on the final answer. Figure 8 illustrates this approach using real data from 3 BPMs, showing beam energy of 2.011 MeV/u. For improved visibility of normal distributions, variances for the normal distributions in this figure were exaggerated to  $10^\circ$  (instead of the actual  $0.5^\circ$ ).

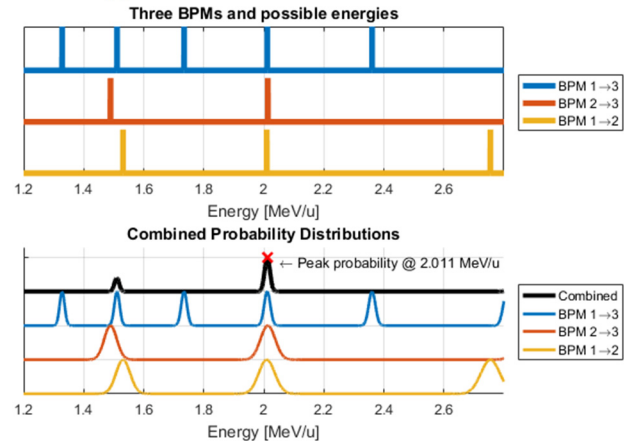


Figure 8: Beam energy calculation using 3 BPMs.

## CONCLUSION

The BPM system is supporting linac commissioning, with beam currents as low as 100 nA. Beam of  $^{40}\text{Ar}^{9+}$  was accelerated from 0.5 MeV/u at the exit of the RFQ to 2.3 MeV/u after 12 SRF accelerating cavities in 3 cryo-modules.

Polynomial corrections and low-beta corrections performed as expected to improve BPM accuracy when beam is not centered. Using calibrated BPM phase results, we calculated beam energy to 1% accuracy. Our BPM energy calculation algorithm is flexible enough to use any three BPMs in a combined manner for very high accuracy. The full linac, when complete, will have 150 BPMs distributed throughout the machine. Our approach will allow real-time, non-intercepting beam energy reporting at any point in the linac.

## REFERENCES

- [1] S. Lidia *et al.*, "Overview of beam diagnostic systems for FRIB," in *Proc. IBIC'15*, Melbourne, Australia, Sep. 2015, pp. 221-225, doi:10.18429/JACoW-IBIC2015-M0PB070
- [2] Q. Zhao *et al.*, "Commissioning Results from FRIB," presented at the 7th Int. Beam Instrumentation Conf. (IBIC'18), Shanghai, China, Sep. 2018, paper MOOC01, unpublished.
- [3] R.E. Shafer, "Beam Position Monitor Sensitivity for Low- $\beta$  beams", *AIP Conf. Proc.* vol. 319, pp. 303-308, 1994.
- [4] PICMG MicroTCA Overview, <https://www.picmg.org/openstandards/microtca/>
- [5] P. Strehl, "Measurements with Capacitive or Inductive Pickups", in *Beam Instrumentation and Diagnostics*: Springer, 2006, pp. 179-186.

# INITIAL RESULTS FROM THE LHC MULTI-BAND INSTABILITY MONITOR

T.E. Levens\*, T. Lefevre, D. Valuch, CERN, Geneva, Switzerland

## Abstract

Intra-bunch transverse instabilities are routinely measured in the LHC using a “Head-Tail Monitor” based on sampling a wide-band BPM with a high-speed digitiser. However, these measurements are limited by the dynamic range and short record length possible with typical commercial oscilloscopes. This paper will present the initial results from the LHC Multi-Band Instability Monitor, a new technique developed to provide information on the beam stability with a high dynamic range using frequency domain analysis of the transverse beam spectrum.

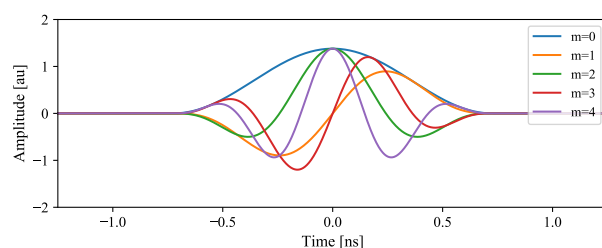
## INTRODUCTION

Transverse beam instabilities are regularly observed during routine operation of the Large Hadron Collider (LHC). As many of the sources of instabilities scale with the bunch intensity and emittance, their mitigation remains an important consideration for delivering the maximum luminosity to the LHC’s experiments. Regular studies into the causes of these instabilities are performed during dedicated “machine development” sessions [1] in order to find adequate mitigation techniques [2]. In addition to these studies, it is important to have instrumentation available that can diagnose any instabilities that may occur during regular operation.

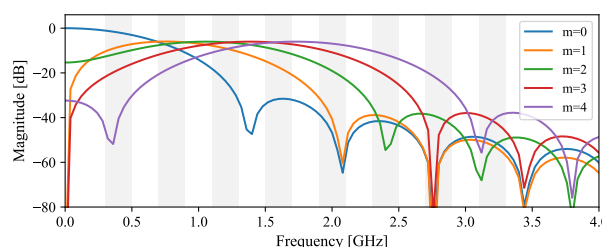
A fundamental tool for the measurement of transverse instabilities is the LHC “Head-Tail Monitor” [3] which can resolve the intra-bunch beam position by sampling a wide-band beam position monitor (BPM) with a fast oscilloscope. Similar techniques have been used since the first direct observation of transverse instabilities in CERN’s PS and Booster in the 1970s [4]. However, the short bunch length in the LHC ( $4\sigma \approx 1.1$  ns) requires sampling at a much higher rate than has been previously necessary, up to 10 GSPS in the case of the LHC.

While the Head-Tail Monitor provides a direct measurement of the intra-bunch motion, and is an important tool for instability studies, it poses a number of challenges for use during regular operation. The original oscilloscopes used in the LHC could provide a maximum of 11 turns of data every 15 seconds. Furthermore, due to the limited dynamic range of their 8-bit high-speed digitisers, only larger oscillation amplitudes were visible. These limitations lead to the development of an online trigger system to precisely trigger the acquisition during an instability [5]. For the 2018 LHC run, new 10-bit oscilloscopes have been installed which offer a higher dynamic range and longer acquisition lengths of up to 450 turns. While easing the demands for precise triggering, the increase in data size of up to 3 GB per acquisition makes data processing and storage challenging.

\* tom.levens@cern.ch



(a) time domain



(b) frequency domain

Figure 1: Simulated comparison of time domain (a) and frequency domain (b) analysis for a typical LHC bunch with head-tail instability modes 0 to 4.

As an alternative to “brute-force” time domain sampling, the Multi-Band Instability Monitor (MIM) uses a frequency domain approach to measure intra-bunch motion. Similar techniques are often used on very short electrons bunches where the spectrum extends to frequencies that cannot be easily measured directly by temporal detection schemes [6]. As shown in Fig. 1, it is expected that for an unstable bunch there will be a shift in the spectral power to higher frequencies as the instability mode increases. In order to measure this shift, the signal from a wideband BPM is split into a number of frequency bands using a bank of radio frequency (RF) band-pass filters. Each band can then be mixed down to base-band and digitised in parallel. As the signal from each band has limited bandwidth, it can be digitised at a much higher resolution than would be possible for the wideband BPM signal. While full time domain reconstruction would require amplitude and phase information from each band, with only the amplitude it is still possible to determine the mode from the relative power in the bands. This simplification permits the use of highly sensitive diode detectors, as are used in the LHC’s base-band tune (BBQ) system [7].

After the MIM concept was first demonstrated in the SPS and LHC [8], it has also been tested for short electron bunches using an “optical BPM” at the Australian Synchrotron, measuring synchrotron radiation in three frequency bands up to 12 GHz [9]. In this paper we present the first results from the fully implement MIM system in the LHC.

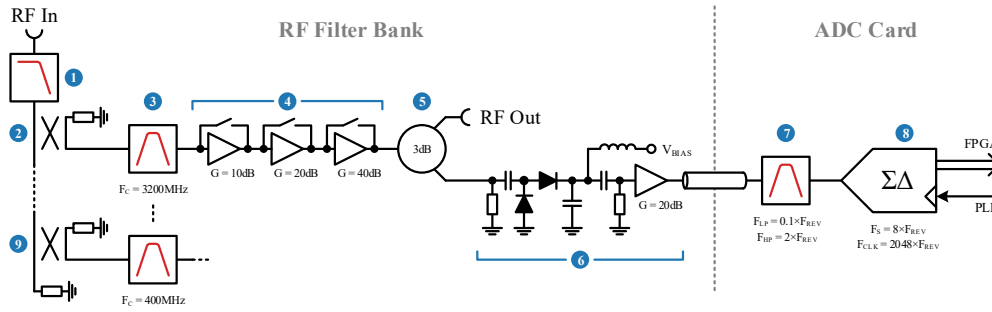


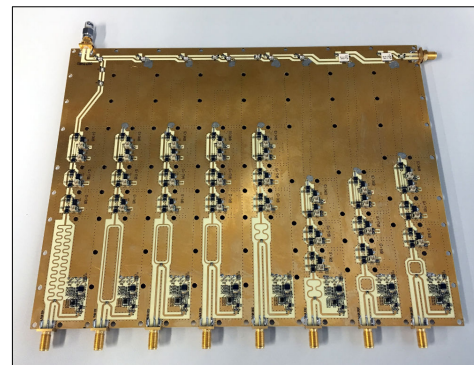
Figure 2: Layout showing a single band of the MIM front-end. Elements: ❶ image suppression low-pass filter; ❷ directional coupler for highest band; ❸ RF band-pass filter; ❹ RF programmable gain amplifier (PGA); ❺ 3 dB Wilkinson divider; ❻ diode detector; ❼ base-band filter; ❽ analogue to digital converter (ADC); ❾ directional coupler for lowest band.

## MIM HARDWARE DESIGN

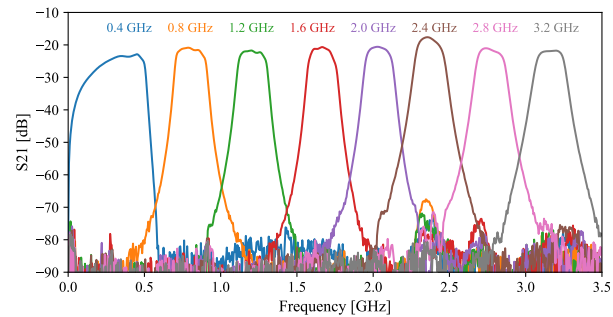
The LHC MIM RF front-end consists of a bank of band-pass filters to select different components of the beam spectrum. Figure 2 shows the layout of the front-end. For each band, a portion of the difference signal from a BPM is coupled from a “through-line” with a directional coupler. The filters are implemented as a strip-line structures on an internal layer of a PCB, shown in Fig. 3a, allowing precise control of the RF properties. As this topology of filter exhibits a periodic frequency response at odd multiples of the centre frequency, lumped low-pass filters in the through-line suppress the unwanted high-frequency signal from subsequent bands. The bandwidth of each filter is approximately 200 MHz and was optimised in order to limit the ringing of the filter output to 25 ns. Although the current implementation of the MIM is not capable of making bunch-by-bunch measurements, this consideration allows the potential in the future. A network analyser measurement of the filter bank is shown in Fig. 3b.

After filtering, a RF programmable gain amplifier (PGA) provides up to 70 dB amplification in 10 dB steps to compensate for the expected difference in signal level between the bands. The amplified signal is split using a 3 dB Wilkinson divider to provide both a RF output for monitoring, and to feed the input of a diode detector. The detector diodes are connected as a voltage doubler [10] and DC biased to provide maximum sensitivity. Finally, the base-band output of the detector is band-pass filtered and digitised using a high resolution 24-bit sigma-delta ADC sampling at a multiple of the revolution frequency ( $F_{REV}$ ).

Two RF filter banks are packaged into a 2U front-end chassis, shown in Fig. 4. Each of the sixteen ADC channels is implemented on an individual PCB that is mounted on a custom “backplane” for power and data distribution. A fractional phase locked loop (PLL) generates the required  $2048 \times F_{REV}$  ADC clock from the 40 MHz beam-synchronous clock ( $3564 \times F_{REV}$ ). A Xilinx Zynq 7030 FPGA is used to interface to the ADCs and includes a dual-core ARM processor running an embedded Linux distribution. The processor can run real-time signal processing algorithms directly and allows control and data acquisition over Ethernet.



(a) PCB



(b) measured frequency response

Figure 3: MIM RF filter bank PCB and frequency response measured with a vector network analyser.

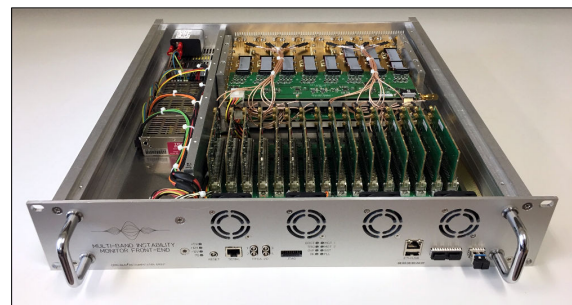


Figure 4: MIM front-end chassis.



## MIM MEASUREMENT RESULTS

### Tune Measurements

Since the BBQ is known to be sensitive to oscillations at a sub-micron level, making a betatron tune measurement with the MIM and comparing it to that obtained with the BBQ can reveal some indication of the sensitivity of the MIM. A comparison of the spectra obtained from the BBQ and the 400 MHz band of the MIM during a normal LHC physics fill with 2556 bunches at 6.5 TeV is shown in Fig. 5. While it is clear that the MIM has a higher noise floor than the BBQ, which would limit the sensitivity for single bunch measurements, with a large number of bunches the spectrum is remarkably similar between the two instruments.

It is notable that the prominent peaks, appearing at multiples of 50 Hz, that are commonly seen the BBQ are also present in the MIM spectrum with a very similar amplitude. The source of these lines, which are more extreme in the horizontal plane and only appear after injecting a large number of bunches, is not well understood and different perturbation sources are currently being studied. One question is whether these lines only appear close to DC or whether they are also present at a higher frequencies. It is not possible to determine this from the BBQ as it is limited to acquiring the spectrum between DC and  $0.5 \times F_{REV}$  due to the aggressive analogue band-pass and notch filtering in the front-end and the limited sampling rate of the high-resolution audio ADCs used for acquisition.

In contrast, the base-band band-pass filters in the MIM have a cut-off frequency of  $2 \times F_{REV}$  and have a slow roll-off allowing the spectrum well above the first revolution frequency line to be acquired. Figure 6 shows the spectrum recorded with the MIM up to the eighth revolution harmonic with a zoom of the spectrum up to the second revolution harmonic. While the 50 Hz lines are very evident around the base-band tune (Q) and lower revolution side-band ( $F_{REV} - Q$ ), they disappear completely above approximately 8 KHz. An interesting observation is that the upper revolution side-band ( $F_{REV} + Q$ ) is clean allowing much better measurements than the base-band. This side-band has been used for the MIM instability analysis. The possibility of modifying the BBQ front-end electronics and acquisition system to observe this side-band is currently being studied.

### Instability Measurements

Data from the MIM has been recorded during a number of dedicated machine development sessions where the machine parameters (chromaticity, octupole strength, etc) are varied in order to study the impact on instabilities [11]. Figure 7 shows an example of a measurement made with the MIM during a study on 3<sup>rd</sup> December 2017 that was aimed at comparing the instability threshold between trains that had different bunch structures. At flat-top energy, the main octupole strength was progressively lowered until the bunches started to become unstable. The plots cover approximately

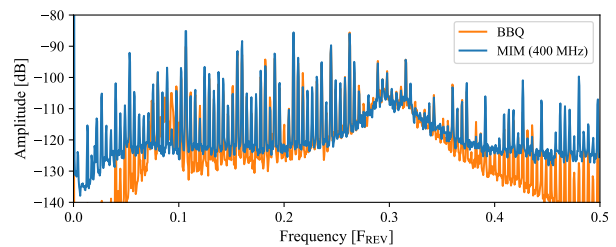


Figure 5: Comparison between tune spectrum measured with BBQ and 400 MHz band of the MIM during a normal LHC physics fill with 2556 bunches.

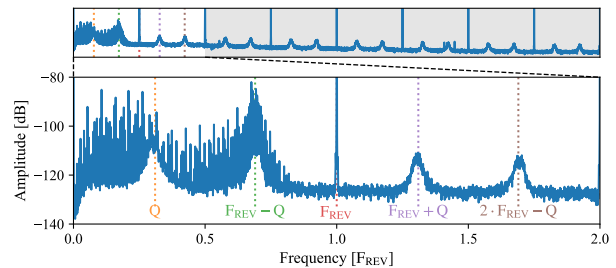


Figure 6: Spectrum from 400 MHz MIM band extended up to the eighth revolution harmonic with a zoom of the spectrum up to the second harmonic.

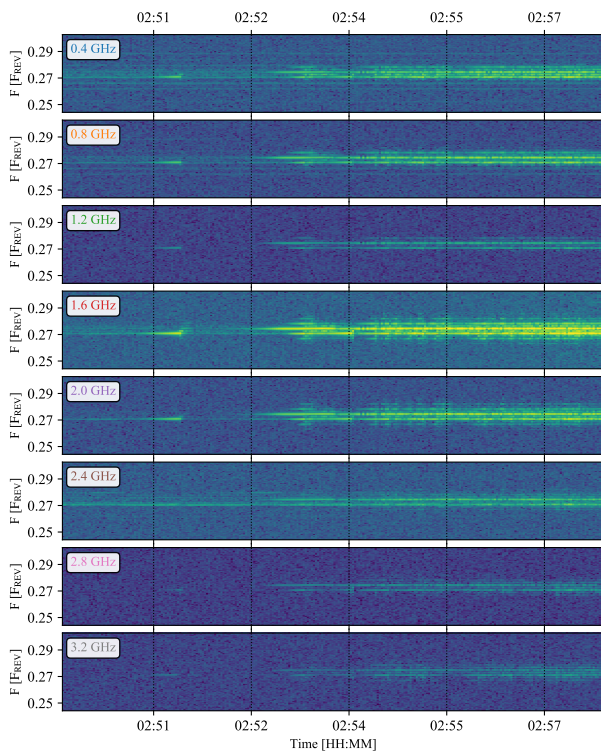
eight minutes starting at 02:50 during which time different bunches in a train became unstable sequentially.

Figure 7a shows spectrograms of the MIM bands, zoomed around the nominal horizontal betatron tune value of approx. 0.27 in order to show only the tune side-band. Plotting the peak value of the  $F_{REV}$  line and tune side-band, as done in Fig. 7b allows the growth of the instabilities to be more clearly visualised. Three measurements from the Head-Tail Monitor are shown in Fig. 7c with timestamps corresponding to the dashed lines in Fig. 7b.

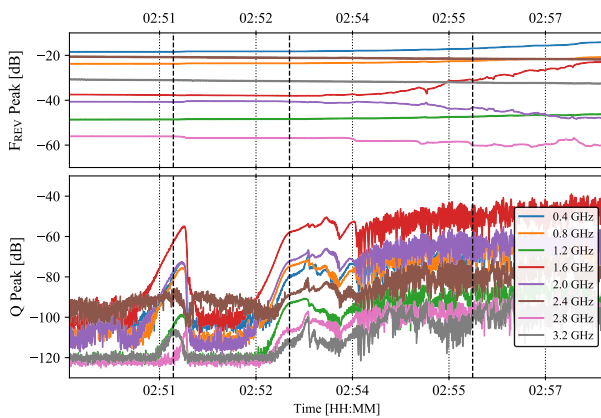
A first instability event is evident around 02:51, visible as an increase in amplitude around the betatron frequency. During this event, the Head-Tail monitor shows a single bunch becoming unstable with a mode  $m=2$  with an amplitude below 100  $\mu\text{m}$ . While this instability is barely visible on the Head-Tail Monitor, it shows a clear signature in the MIM bands. Figure 7d shows the reconstruction of the relative power in the bands at the moment of the Head-Tail measurement. The distribution matches the expectation for a mode  $m=2$  with a peak in region of 1.2 to 1.6 GHz band and notches in the 2.4 and 3.2 GHz bands.

A second event starts around 02:52 and continues until the end of the acquisition. A different bunch in the train first goes unstable with an amplitude of around 200  $\mu\text{m}$ , again resulting in a very clear rise in power from the MIM bands. From the spectrogram it is possible to see that the initial rise of this instability happens on a different synchrotron side-band of the tune indicating a different azimuthal instability mode number. As the event proceeds multiple bunches become unstable at the same time which result in multiple peaks in the tune spectrum at different synchrotron side-bands. Again

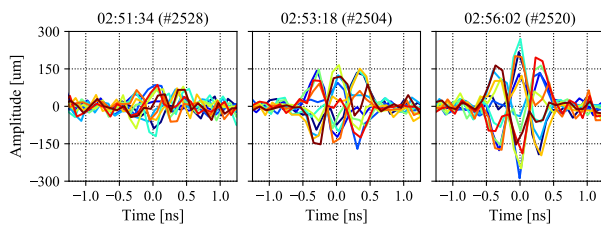




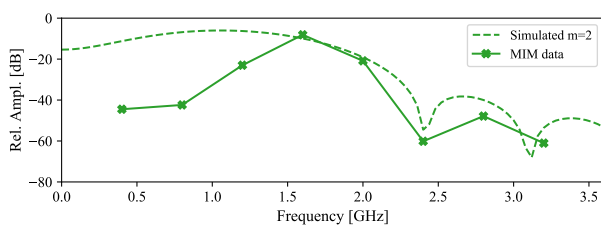
(a) MIM spectrogram



(b) MIM FREV and tune peak amplitudes



(c) Head-Tail delta signal



(d) MIM reconstruction

Figure 7: An instability recorded during a machine development session on 3<sup>rd</sup> Dec. 2017 from 02:50 to 02:58.

the Head-Tail reveals clear  $m=2$  oscillations with amplitudes around 300  $\mu\text{m}$ . Also notable during the second event is that there is a change in power of the  $F_{\text{REV}}$  peak in the higher bands as the instability progresses, which is indicative of a distortion of the longitudinal bunch shape.

## CONCLUSION

A new Multi-Band Instability Monitor has been developed for the LHC based on the analysis of independent frequency bands of the transverse beam spectrum. The RF filter bank provides eight bands from 400 MHz to 3.2 GHz, each of which is detected using a high-sensitivity diode detector and sampled with a high-resolution ADC. The initial results show that the sensitivity achieved for a full machine is similar to the BBQ and the increased sampling rate of the ADCs provides some insight into the nature of the 50 Hz lines which are a common feature of the LHC tune spectra. During known instabilities a clear increase in signal power is seen in all of the bands and the ratio is indicative of the mode of the instability. Future work will focus on developing a real time identification of the instability mode for instabilities occurring during normal operation.

## REFERENCES

- [1] L.R. Carver *et al.*, “Transverse beam instabilities in the presence of linear coupling in the large hadron collider”, *Physical Review Accelerator and Beams*, vol. 21, p. 044401, 2018. doi:10.1103/PhysRevAccelBeams.21.044401
- [2] M. Schenk *et al.*, “Experimental stabilization of transverse collective instabilities in the LHC with second order chromaticity”, *Physical Review Accelerator and Beams*, vol. 21, p. 084401, 2018. doi:10.1103/PhysRevAccelBeams.21.084401
- [3] R. Jones *et al.*, “Recent Advances in the Measurement of Chromaticity via Head-Tail Phase Shift Analysis”, in *Proceedings of DIPAC03*, Mainz, Germany, 2003, paper PM08, pp. 107–109.
- [4] J. Gareyte, “Head-tail type instabilities of the CERN PS and Booster, pt 1-2”, CERN, Geneva, Switzerland, Rep. CERN-MPS-BR-74-7, 1974.
- [5] T.E. Levens, K. Lasocha, and T. Lefevre, “Recent developments for instability monitoring at the LHC”, in *Proceedings of IBIC2016*, Barcelona, Spain, 2016, pp. 853–856. doi:10.18429/JACoW-IBIC2016-THAL02
- [6] A.E. Dabrowski *et al.*, “Measuring the bunch frequency multiplication at the 3rd CLIC test facility”, *Journal of Instrumentation*, vol. 7, p. P01005, 2012.
- [7] M. Gasior, “Faraday cup award: high sensitivity tune measurement using direct diode detection”, in *Proceedings of BIW2012*, Newport News, VA USA, 2012, paper MOAP02, pp. 1–8.
- [8] R.J. Steinhagen, M.J. Boland, and T.G. Lucas, “A Multiband-Instability-Monitor for High-Frequency Intra-Bunch Beam Diagnostics”, in *Proceedings of IBIC2013*, Oxford, UK, 2013, paper TUBL3, pp. 327–330.

- [9] T.G. Lucas *et al.*, “An optical intra-bunch instability monitor for short electron bunches”, in *Proceedings of IBIC2015*, Melbourne, Australia, 2015, pp. 161–164. doi:10.18429/JACoW-IBIC2015-MOPB049
- [10] Hewlett-Packard Co., “Schottky diode voltage doubler”, Application Note 956-4, 1995.
- [11] L.R. Carver *et al.*, “Current status of instability threshold measurements in the LHC at 6.5 TeV”, in *Proceedings of IPAC2016*, Busan, Korea, 2016, pp. 1434–1437. doi:10.18429/JACoW-IPAC2016-TUPMW011

# THE DESIGN OF SCANNING CONTROL SYSTEM FOR PROTON THERAPY AT CIAE\*

L. Cao<sup>†</sup>, T.Ge, F.P.Guan, S.G.Hou, L.P.Wen, X.T.Lu, Y.Wang, China Institute of Atomic Energy, Beijing, China

## Abstract

A novel proton therapy facility is designed and constructed at China Institute of Atomic Energy (CIAE) in Beijing, which includes a superconducting cyclotron CYCIAE-230 to provide 230 MeV proton beams for cancer therapy. As a part of therapy control system, the scanning control is designed to scan the beam for the access of required tumour volume field. Two set of dipole magnet is driven for changing the beam path. Meanwhile, interfaces between scanning system and other systems will be built for beam control and safe considering. In order to acquire high precise feedback control, the beam position and dose monitor ionization chambers will be constructed in the nozzle. Detailed description will be presented in this paper.

## INTRODUCTION

Proton therapy has proven to be an effective cancer treatment with minimal side effects. Due to the progress of superconducting devices, very compact cyclotrons, suitable for hospital installations, can be manufactured with lower cost. In order to promote the development of proton therapy in China, CIAE (China Institute of Atomic Energy) has designed a superconducting cyclotron, which would produce a 230 MeV, 300 nA proton beam [1].

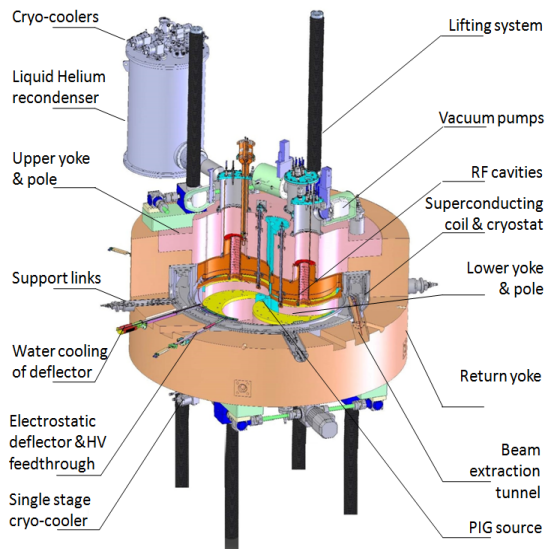


Figure 1: Layout of CYCIAE230 Cyclotron.

As the essential Part of Proton therapy, CYCIAE230 are in commissioning phase, including the cryogenic system and RF system as shown in Fig. 1. Meanwhile, the

beamline and gantry are in construction. The specification of cyclotron is shown in Table1. The treatment control system is needed for whole treatment. Scanning control system belongs to the treatment control system and is the core part to do the main process. So, a dedicated scanning control system is designed for the proton therapy facility. Detailed system design will be presented below.

Table 1: Cyclotron Specifications

Parameter	Value
Extraction energy	>230MeV
Extraction current	>500nA
Injection/Extraction field	2.35 T / 2.95 T
RF frequency	~71.3 MHz
RF voltage	70 kV/110 kV

## SCANNING CONTROL SYSTEM

In the whole control system of proton therapy, scanning control take a important role. Whatever any scanning mode was used. Also there are complex interfaces with other subsystems. Scanning control system require the the therapy data table to direct the scanning to target volume and the field feedback data to verify the scan process. Figure 2 shows the positon of scanning control system in the whole control system, which is essensial for proton therapy system. The device layer is mainly comprises of needed hardware for convetional process, which accept the control of relatively target front end. The lower layer is safe related function that protects the patient against over dose radiation. The central interlock system will act as a protector for treatment. The last layer is control layer. In this layer, scanning control system is the coordinator to arrange other subsystem to work together smoothly under the defined process. The interface to cyclotron is through the data exchange to cyclotron control system.

## Functionalities

Fast dynamic scanning functional specification is as follows:

Interface with accelerator control system to adjust the vertical deflector to stabilize the beam current. The repetition rate is about 1kHz, and the beam off time is lower than 50usec, intensity stability is lower than 5%.

Scanning mode: step & shoot, continue scanning ‘TV’ or contours scanning, the two sweeper magnets should control the beam position up to 2cm/Ms.

Scanning delivery function comes out that scanning control system dynamically operate the actuators according to the feedback data which involves the position and beam intensity.

\* Work supported by National Natural Science Foundation of China under Grant No.11375273 and 1146114103.

<sup>†</sup> clyoung@163.com

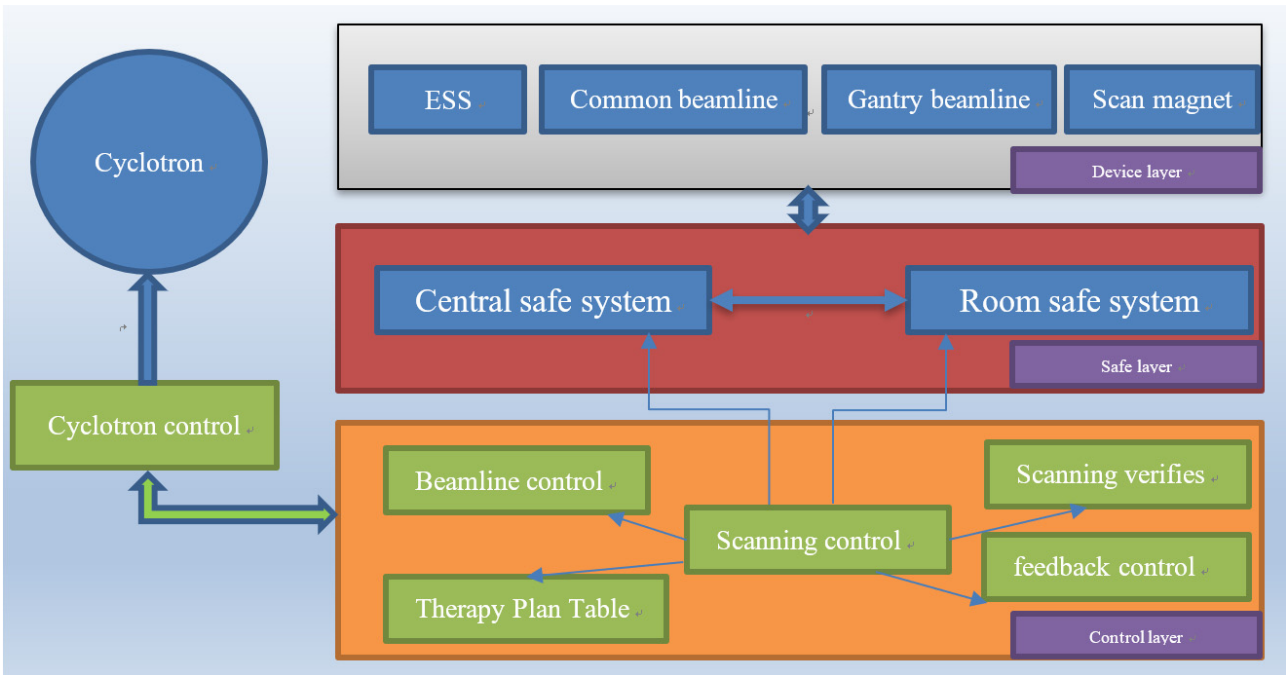


Figure 2: Scanning control system interfaces with other subsystems.

Scanning verifying function facilities a fast data acquiring board to pick up data periodically around 10us. The board is connected to field hall probe to verify the sweep magnet, and to ionization chambers to verify beam current.

Fast control function is based on FPGA technology to validate measured data or interrupt beam in case of coincidence.

### Hardware Design

The scanning system is composed of three different parts. The digital compute board is the master component. Another part is ADC/DAC part, which is in charge of signal convert rapidly to magnet controller or from field sensors. Through the therapy plan data achieved from treatment control system, master computer gives the final output signal instantly according the designed algorithm. The final part is the ionization chamber for beam position and dose value feedback. The final scanning control cabinet is shown in Fig. 3.

Connections between main compute board and ions chamber eletronics are via fibre optics to ensure stable and robust transmission against radiation damage and single event upset to electronics.



Figure 3: Layout design of scanning control cabinet.

The next stage of design is the ionization chamber to monitor the position of beam and verify the dose rate. The

sensitive area of ionization chamber is 41mm diameter and the readout pixel for position monitoring is 180. In order to protect beam quality, extra thin film window and electrodes is designed so as to negligible beam scattering. The energy range is from 30 MeV to 250 MeV for proton. The integral linearity is better than 30 um maximum deviation relative over sensitive area. Depend on signal to noise ratio, the best position resolution is about 10um.

### Software Design

The scanning control software is comprised of four modules, and the modules interfaced internally with fast bus. These main modules are as following corresponsing the hardware. Core compute module (CCM): This module is mainly responsible for actually current value output and directing the feedback flow. This is the master module which operates the whole scanning system and handles beam stable situations throughout the feedback loop. It communicates with other subsystems over a fast TCP/IP network connection. User Interface Module (UIM): It provides device screens to operators which display live scanning information [2,3]. Covert Management Module (CMM): This module is designed to produce the interpolation values result from the delivery table. Safe Interlock Module (SIM) : This is the import module because the beam safe operation is depent on the fast respond to cut off. With the safe policy, a proper action should be carried out as soon as possible. Above the four modules, critical alghrithm is developed to implement the system requirement best. For example, during the beam delivery session, any illegal action is not allowed. There are also some interface modules to related systems for data information.



## *Safety Interlock System*

The scanning control system is directly connected to safety interlock system that consists of a fast interlock system that cuts off RF sources switch to the RF amplifier. It is built on the cyclone series FPGA platform. It supports 32 fast digital inputs (100 ns response time), 32 slower (response within 10 $\mu$ s) and 16 analogue channels (100 kHz).

In addition, there is a slow interlock system based on a Siemens S7-400 PLC system. The current system support about 1000 i/o channels but enough memory space is ready for expansion if safety needed. The data is collected by a server which broadcast the readout over Ethernet to be easily picked up by the EPICS channel access client. The radiation protection area is protected by a door interlock. A unique procedure is required before closing the door. This is implemented in the slow interlock safety PLC.

## *Other Demand*

The scanning control system is sensitively to beam stable capability. So, there is strictly requirement for accelerator with stable beam position and continuous and stable beam. Also, requirement for ESS for fast adjustable beam intensity and fast adjustable beam energy. In emergency condition, the fastest beam cut-off is to shut down the RF source.

Due to the open loop control of magnet power supply, over-shot will occur, and the delay feedback of ionization chamber also have a side effect for high accuracy dose

delivery. A new method for fast dose feedback needs to be developed for high accuracy protection.

## CONCLUSION

CIAE has designed a scanning control system for proton therapy that integrates all the different subsystems necessary for treatment process. The fast feedback system is based on FPGA technology with state-of-art algorithm. The use of EPICS simplifies the extensible feature for coming requirement of other subsystems.

## ACKNOWLEDGEMENTS

The authors would like to thank Dr. Rok Harvin of Cosylab in Slovenia, and Dr. Marco Schippers in PSI for their great effort on proton therapy control system. This work is supported by the National Natural Science Foundation of China under Grant No.11375273 and 1146114103.

## REFERENCES

- [1] T. Zhang, C. Wang, et al. "Developments for 230 MeV superconducting cyclotrons for proton therapy and proton irradiation", Nuclear Instruments and Methods in Physics Research Section B, Volume 406, Part A, 1 September, 2017, Pages 244-249.
- [2] JACoW, <http://www.jacow.org>
- [3] EPICS, <http://www.aps.anl.org>

# DESIGN OF AN ULTRAFAST STRIPLINE KICKER FOR BUNCH-BY-BUNCH FEEDBACK

Jianxin Wang<sup>1,2#</sup>, Longgang Yan<sup>1,2</sup>, Peng Li, Dai Wu, Dexin Xiao

<sup>1</sup>Institute of Applied Electronics, China Academy of Engineering Physics,  
 Mianyang, 621900, P. R. China

<sup>2</sup>Graduate school of China Academy of Engineering Physics, Beijing, 100088, P. R. China

## Abstract

The CAEP THz Free Electron Laser (CTFEL) will have a fast transverse bunch-by-bunch feedback system on its test beamline, which is used to correct the beam position differences of individual bunches with interval of about 2 ns. In this paper, we are proposing an ultrafast wideband stripline kicker, which is able to provide a kick to the bunch in a 2 ns time window. The structure design and simulation results of this kicker are also discussed

## INTRODUCTION

China Academy of Engineering Physics (CAEP) has developed a terahertz free electron laser (CTFEL) facility with Peking University and Tsinghua University, which is the first high average power FEL user facility in China [1]. CTFEL is a kind of oscillator type FEL and mainly consists of a GaAs photocathode high-voltage DC gun, a 1.3 GHz 2x4-cell superconducting RF linac, a planar undulator and a quasi-concentric optical resonator. The first saturated lasing of CTFEL was obtained in 2017 [2]. Since then, CTFEL has realized stable operation and some user experiments have been done. The repetition rate of THz beams is 54.17 MHz and the THz frequency can be adjusted from 1.87 THz to 3.8 THz continuously. The average output power in macro pulse is more than 10 W and the peak power is beyond 0.5 MW [3]. Now,

fast machine protection system is under developed and CW operation will be realized soon. Moreover, CTFEL is expected to upgrade to cover the THz band from 1 THz to 10 THz and greatly promote the development of THz science as well as many other cutting-edge fields in the future.

The CTFEL will have a test beam line behind the 90 degree analysis magnet, a fast transverse intra-bunch train feedback system to stabilize the beam position will be developed. The time interval of the micro-pulse will set to be about 2ns. Several beam elements and diagnostics device will be installed in the test beam line. Figure 1 shows the location of the CTFEL diagnostics device. This paper gives an overview of the design and analysis of the strip-line kicker.

A stripline kicker consists of two parallel electrodes housed in a conducting vacuum pipe: each of the electrodes is driven by an equal but opposite polarity pulse. The most technology challenges are the following: first, good power transmission by achieving good impedance matching to the electrical circuit; second, the excellent field homogeneity was need in the center region of the vacuum pipe. The stripline design has been carried out by using CST MICROWAVE STUDIO and CST EM STUDIO[4].

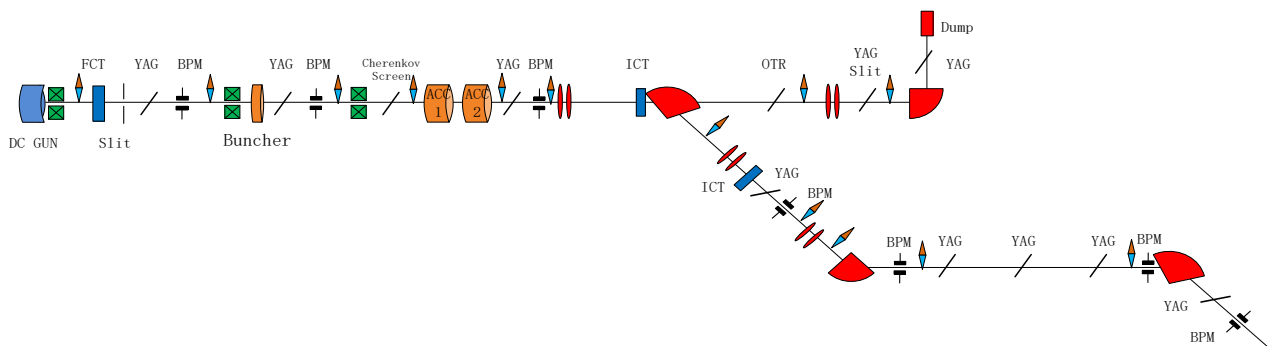


Figure 1: Location of CTFEL diagnostics device.

## DESIGN STUDY OF THE STRIPLINE KICKER CROSS SECTION

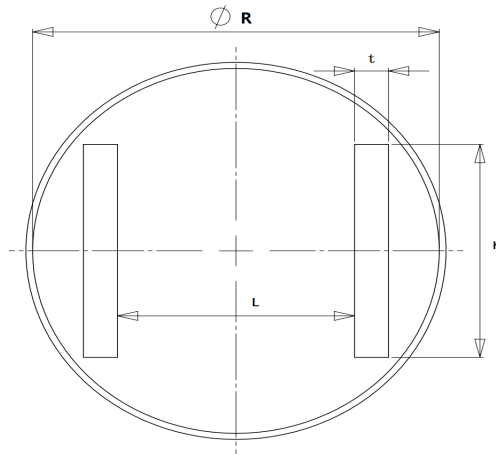


Figure 2: Geometry of the cross section.

The stripline kicker has 2 electrodes connected to electrical feedthrough at both ends. The cross section of the striplines defines the characteristic impedance and homogeneity of the electromagnetic field in the center region. The geometry of the cross section is showed in Fig 2. The model is parameterized for changing and optimizing the shape of the electrode. The distance between the electrodes was chosen to be 35mm for avoiding disturbing of the beam. The parameters of the model and the specification of the kicker is listed in table 1.

Table 1: Parameters of the Stripline Kicker

Parameter	Symbol	
diameter of the vacuum pipe	R	60 mm
distance between the electrodes	L	35 mm
thickness of the electrodes	t	5 mm
width of the electrode	h	35 mm

A feedthrough is needed to transfer the power to the strip-line electrode. The characteristic impedance of the connection form the feedthrough to the stripline electrode is not 50 ohm. This impedance mismatching will introduce reflection to the transmission of the pulse power. So a 3D model (see in Fig 3) with 4 feedthroughs is studied to analyse the influence of the geometries on the reflection.

Set the input side of feedthroughs as waveguide port1, port2, port3, port4. The plot of S11 parameter for strip-line kicker is showed in Fig. 4.

It presents the reflection coefficient vs the frequency. The S11 is small than -20 dB in 500 MHz, so the reflected power can be estimated less than 1%.

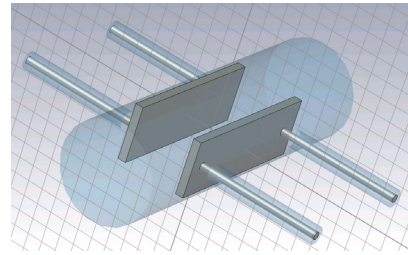


Figure 3: 3D model of the stripline with 4 feedthroughs.

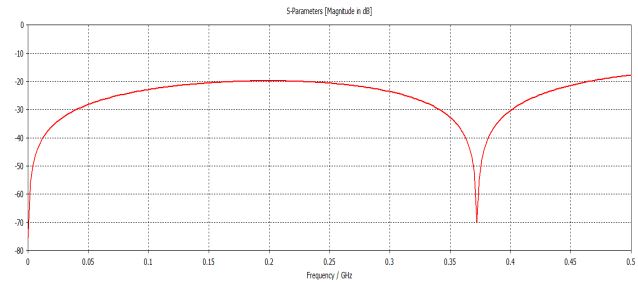


Figure 4: S11 plot for strip-line kicker.

The feedthrough position refer to the stripline and the inner radius of the feedthrough were studied to analyze the influence on the reflection parameter magnitude, but no significant differences were found through parameters sweep.

The field homogeneity was analysed using the CST EM STUDIO. The same magnitude but opposite polarity voltages were imposed on the two striplines as the excitation. The E-Field distribution of the working space was got using the E-Field solver which is showed in Fig.4.

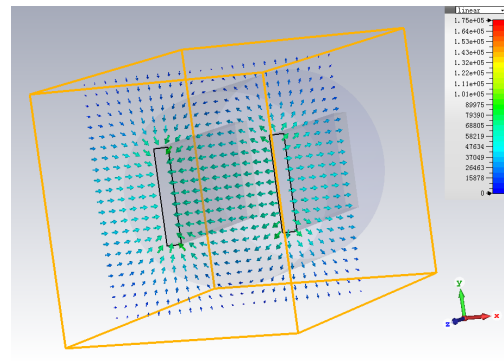


Figure 4: E-Field distribution of the kicker.

The E-Field strength vector of any point in the working space can be got through post-processing of the CST EM STUDIO data. The X direction field strength of the region 'z=0, x(-5,5), y(-5,5)' was used to analyze the field homogeneity. The field homogeneity is about 3% in this region with the step of the region is 1mm.

## SUMMARY

The preliminary geometry design of the stripline kicker for the CTFEL is presented. The cross section optimization of the stripline kicker is almost complete: the 50 ohm characteristics impedance and less than 1% reflection coefficient from the port. But the field inhomogeneity 3% is beyond the specification of the design. Ongoing simulation include: further studies of the geometry to optimize the field inhomogeneity, studies of the shunt impedance and beam coupling impedance of the kicker.

## REFERENCES

- [1] Xu Zhou, Yang Xing-fan, Li Ming *et al.*, “Design of a high average power terahertz-FEL facility”, *Journal of Terahertz Science and Electronic Information Technology*, 2013, Vol. 11, No. 1, p. 6.
- [2] Li Ming, Yang Xing-fan, Xu Zhou *et al.*, “First lasing of CAEP THz free electron laser”, *High Power Laser and Particle Beams*, 2017, Vol. 29, No. 10, pp. 1-2.
- [3] Li Ming, Yang Xing-fan, Xu Zhou *et al.*, “Experimental study on the stimulated saturation of terahertz free electron laser”, *Acta Phys. Sin.*, 2018, Vol. 67, No.8, 084102.
- [4] CST Studio, [www.cst.com](http://www.cst.com).
- [5] C. Belver-Aguilar *et al.*, “Beam Impedance Study of the Stripline Kicker for the CLIC Damping Ring”, in *Proc. of IPAC’12*, Louisiana, USA, May 2012, Paper TUPPR018.
- [6] C. Belver-Aguilar, M.J. Barnes, L. Ducimitière, “Review on the Effects of Characteristic Impedance Mismatching in a Stripline Kicker”, in *Proceedings of IPAC’16*, Paper THPMW034, doi:10.18429/JACoW-IPAC2016-THPMW034, 2016.



# BEAM TRANSVERSE QUADRUPOLE OSCILLATION MEASUREMENT IN THE INJECTION STAGE FOR THE HLS-II STORAGE RING\*

F.F. Wu, B.G. Sun<sup>†</sup>, T.Y. Zhou<sup>‡</sup>, F.L. Gao, J.G. Wang, P. Lu, L.T. Huang, X. Y. Liu, J. H. Wei  
National Synchrotron Radiation Laboratory  
University of Science and Technology of China, Hefei, 230029, China

## Abstract

Beam transverse quadrupole oscillation can be excited in the injection stage if injected beam parameters (twiss parameters or dispersion) are not matched with the parameters in the injection point of the storage ring. In order to measure the beam transverse quadrupole oscillation in the injection stage for the HLS-II storage ring, some axially symmetric stripline BPMs were designed. Transverse quadrupole component for these BPMs was simulated and off-line calibrated. Beam transverse quadrupole oscillation has been measured when beam was injected into the HLS-II electron storage ring. The spectrum of the transverse quadrupole component showed that beam transverse quadrupole oscillation is very obvious in the injection stage and this oscillation isn't the second harmonic of beam betatron oscillation. The relationship between transverse quadrupole oscillation and beam current was also analyzed and the result shows that the relationship is not linear.

## INTRODUCTION

When twiss parameters and dispersion of injected beam are not matched with injected point of storage ring, some oscillations can be excited [1, 2]. The most obvious oscillation is beam betatron (transverse dipole) oscillation, which can be used to measure betatron tune. In some machines, beam transverse quadrupole oscillation can also be excited in the injected stage. In the HLS-II electron storage ring, beam transverse quadrupole oscillation can be measured based stripline BPM in the injected stage.

## TRANSVERSE QUADRUPOLE OSCILLATION MEASUREMENT SYSTEM INTRODUCTION

Axially symmetric stripline BPM was used to measure beam transverse quadrupole oscillation in the HLS-II electron storage ring. The cross-section of this stripline BPM is shown in Fig. 1.

The stripline BPM should be offline calibrated before experiment. Simulation of beam position and transverse quadrupole component can be as shown in reference 3. Offline calibration of beam position and transverse quadrupole component can be as shown in reference 4. Beam transverse quadrupole component can be obtained and is shown as follows:

$$\sigma_x^2 - \sigma_y^2 = \frac{1}{0.0011} \left( \frac{Q_{\Delta\Sigma} + 0.7870 - 0.0011x_0^2}{+0.0011y_0^2 - 0.0006x_0 - 0.0004y_0} \right) \quad (1)$$

$Q_{\Delta\Sigma}$  is the beam transverse quadrupole signal acquired by the difference/sum method and can be expressed as:

$$Q_{\Delta\Sigma} = \frac{V_R + V_L - V_T - V_B}{V_R + V_L + V_T + V_B} \quad (2)$$

$V_R$ ,  $V_T$ ,  $V_L$ ,  $V_B$  are induced voltages on the right, top, left, bottom electrode.  $Q_{\Delta\Sigma}$  can be obtained by BPM processor (Libera Brillianceplus). Beam position (x, y) can be obtained based the equation (4) of the reference 4. So beam transverse quadrupole component ( $\sigma_x^2 - \sigma_y^2$ ) can be finally obtained.

The measurement system block diagram is shown in Fig. 2. In the injected stage, the stripline BPM electrode signals are processed by Libera Brillianceplus and the turn-by-turn data is obtained by Labview code (or Matlab code) of PC, then, the relationship between beam transverse quadrupole component ( $\sigma_x^2 - \sigma_y^2$ ) and injected turn number n can be obtained.

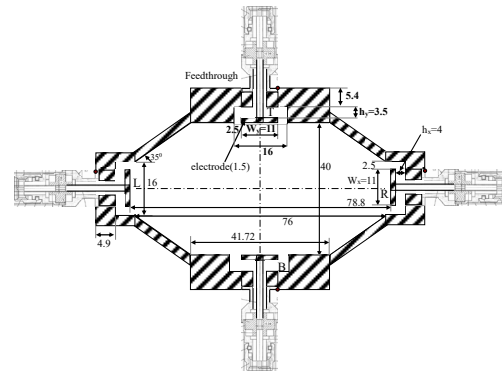


Figure 1: The cross-section of the stripline BPM.

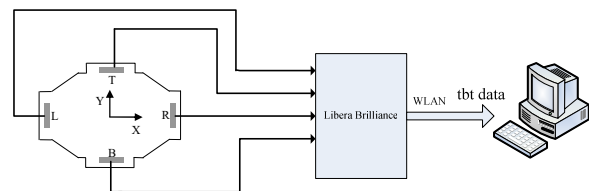


Figure 2: Measurement system block diagram for beam transverse quadrupole oscillation in the injected stage.

## EXPERIMENT AND DATA ANALYSIS

The turn-by-turn data of beam position (x, y) can be used to measure fractional part of machine tune ( $\Delta\nu_x$ ,  $\Delta\nu_y$ ). When

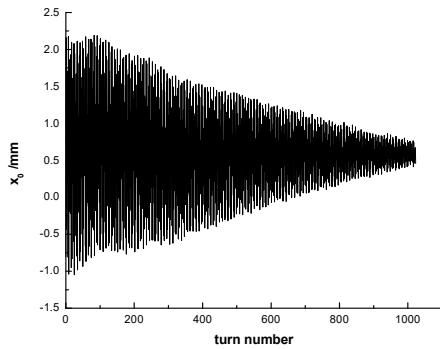
\* Work supported by the Anhui Provincial Natural Science Foundation (Grant No. 1808085QA24), National Science Foundation of China (Grant No. 11705203, 11575181, 11605202), Chinese Universities Scientific Fund (Grant No. WK2310000057)

<sup>†</sup>Corresponding author (email: bgsun@ustc.edu.cn)

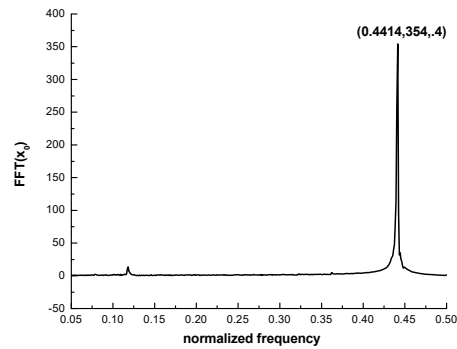
<sup>‡</sup>Corresponding author (email: tianxy86@ustc.edu.cn)

multi-bunches were injected into the HLS-II electron storage ring and beam current was 174.8 mA, horizontal position and corresponding spectrum normalized to revolution frequency(4.534 MHz) were acquired and is shown in Fig. 3. Vertical position and corresponding spectrum normalized to revolution frequency were acquired and is shown in

Fig. 4. Beam transverse(horizontal) quadrupole signal and corresponding spectrum normalized to revolution frequency were acquired and is shown in Fig. 5.

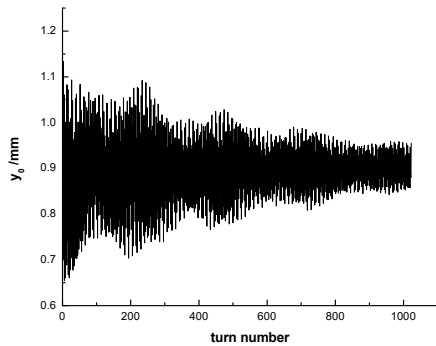


(a) Horizontal position  $x_0$

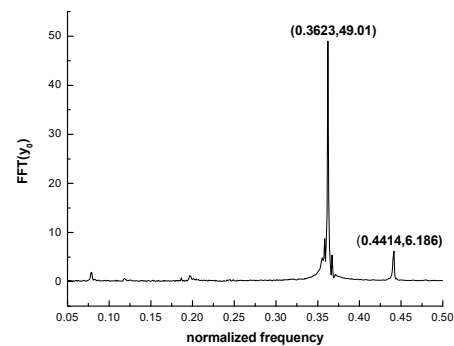


(b) The spectrum of  $x_0$

Figure 3: Horizontal position and corresponding spectrum in the injected stage.

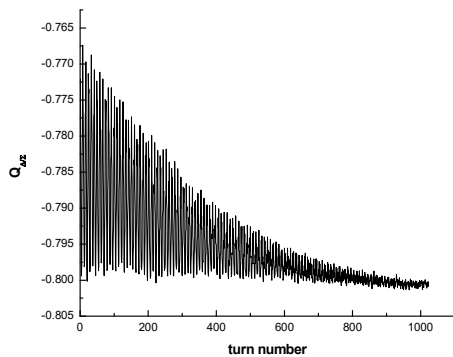


(a) Vertical position  $y_0$

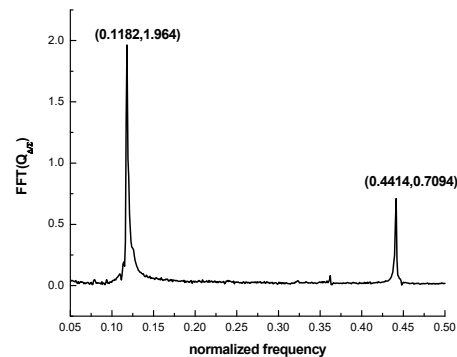


(b) The spectrum of  $y_0$

Figure 4: Vertical position and corresponding spectrum in the injected stage.

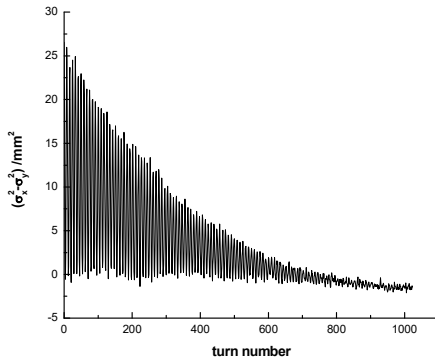


(a) Beam transverse quadrupole signal  $Q_{\Delta\Sigma}$

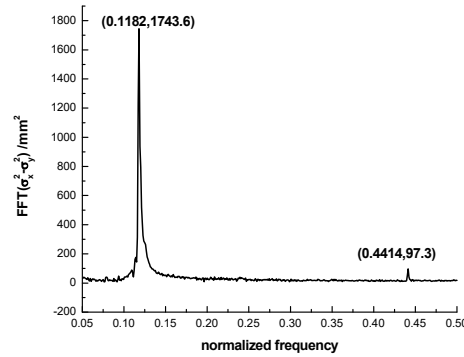


(b) The spectrum of  $Q_{\Delta\Sigma}$

Figure 5: Beam transverse quadrupole signal and corresponding spectrum in the injected stage.



(a) Beam transverse quadrupole component ( $\sigma_x^2 - \sigma_y^2$ )



(b) The spectrum of ( $\sigma_x^2 - \sigma_y^2$ )

Figure 6: Beam transverse quadrupole component and corresponding spectrum in the injected stage.

As is shown in Fig.3, Fig.4 and Fig.5, machine tune  $\Delta\nu_x=0.4414$ ,  $\Delta\nu_y=0.3623$ . The fraction part tune  $\Delta\nu_Q$  of beam transverse quadrupole oscillation can also be obtained and is equal to 0.1182.  $\Delta\nu_Q$  is equal to  $(1-2*\Delta\nu_x)$ . So beam transverse quadrupole oscillation can be measured based stripline BPM in the injected stage.

According to the equation(1), beam transverse quadrupole component ( $\sigma_x^2 - \sigma_y^2$ ) can be obtained. ( $\sigma_x^2 - \sigma_y^2$ ) and corresponding spectrum normalized to revolution frequency were acquired and is shown in Fig. 6. From the result of Fig.6, the spectrum peak of beam transverse quadrupole component is very obvious. Since contribution of beam position to ( $\sigma_x^2 - \sigma_y^2$ ) is eliminated, the effect of beam position for ( $\sigma_x^2 - \sigma_y^2$ ) is very small.

The relationship between beam transverse quadrupole component ( $\sigma_x^2 - \sigma_y^2$ ) and beam current in the injected stage was obtained and is shown in Fig.7. Since duration turn number of beam transverse quadrupole oscillation is not too long(about 1000 turns), interpolated FFT method was used to improve frequency domain measurement resolution. As is shown in the Fig.7, the relationship between beam transverse quadrupole oscillation and beam current is nonlinear.

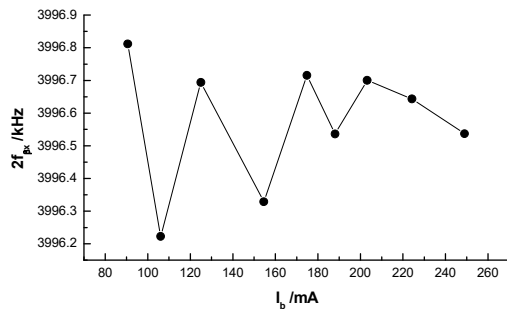


Figure 7: The relationship between beam transverse quadrupole component ( $\sigma_x^2 - \sigma_y^2$ ) and beam current in the injected stage.

## CONCLUSION

Based on the stripline BPM, beam transverse quadrupole oscillation can be measured. The relationship between beam transverse quadrupole component ( $\sigma_x^2 - \sigma_y^2$ ) and beam current was also obtained. In the future, beam transverse quadrupole oscillation for different bunches will be excited by stripline transverse quadrupole kicker.

## REFERENCES

- [1] J. Dietrich, I. Mohos, "Broadband FFT Method for Betatron Tune Measurement in the Acceleration Ramp at COSY-Jülich". *AIP Conference Proceedings* 451, BIW'98, Stanford, CA, May 1998, pp. P454-458.
- [2] A. Jansson, L. Søby. "A non-invasive single-bunch matching and emittance monitor for the CERN PS based on quadrupole pick-ups", in *Proceedings of PAC'01*, Chicago, 2001, pp. 528-530.
- [3] F. F. Wu, Z.R. Zhou, B.G. Sun, *et al.*, "Design and Calculation of the Stripline Beam Position Monitor for HLS II Storage Ring", *Proceedings of IPAC'13*, Shanghai, China, pp. 562-564.
- [4] Wu F. F., Zhou Z. R., Sun B. G., *et al.*, "Offline calibration of the stripline beam position monitor for HLS II. High Power Laser and Particle Beams", 2011, 23(12): pp. 2971-2975.

# EARLY COMMISSIONING OF THE LUMINOSITY DITHER SYSTEM FOR SuperKEKB\*

M. Masuzawa<sup>†</sup>, Y. Funakoshi, T. Kawamoto, S. Nakamura, T. Oki, M. Tobiyama, S. Uehara,  
R. Ueki, KEK. 305-0801 Tsukuba, Japan  
A. S. Fisher, M.K. Sullivan, D. Brown, SLAC, 94025 Menlo Park, CA, USA  
U. Wienands, ANL 60439 Argonne, IL, USA  
P. Bambade, S. Di Carlo, D. Jehanno, C. Pang, LAL, 91898, Orsay, France  
D.El Khechen, CERN, 1211 Geneva, Switzerland

## Abstract

SuperKEKB is an electron–positron double ring collider that aims to achieve a peak luminosity of  $8 \times 10^{35} \text{ cm}^{-2} \text{ s}^{-1}$  by using what is known as the “nano-beam” scheme. A luminosity dither system is employed for collision orbit feedback in the horizontal plane. This paper reports the dither hardware and algorithm tests during the SuperKEKB Phase II luminosity run.

## INTRODUCTION

The SuperKEKB collider [1] employs a luminosity dither system that is based on the collision feedback system previously used at SLAC for PEP-II [2, 3] for finding the horizontal offset at the interaction point (IP) that maximizes luminosity. The dithering feedback is different from that used for KEKB collision orbital feedback, where beam–beam deflection was used in both the vertical and horizontal planes. With the “nano-beam” scheme, the horizontal beam–beam parameters are much smaller than those at KEKB, and the detecting luminosity maximum orbit using beam–beam deflection is not as effective as KEKB. Therefore, a dithering method was introduced for SuperKEKB. A good collision condition is sought for by dithering the positron beam (LER), and once a good collision condition is found, it is maintained by an active orbital feedback, which moves the electron beam (HER) relative to the LER by creating a local bump at the IP. The dither system was tested with colliding beams for SuperKEKB Phase II commissioning.

## DITHERING SYSTEM

### Principle

When an LER beam is dithered sinusoidally in the horizontal plane, where the relative offset of the LER and HER are  $x_0$ , the variation in luminosity  $L$  is described as a function of the relative offset of the two beams  $x$ , as follows:

$$L(x) = L_0 \exp\left(-\frac{x^2}{2\Sigma_x^2}\right) \quad (1)$$

where

$$x = x_0 + \tilde{x} \cos \omega_x t \quad (2)$$

and

\*Work supported by U.S.-Japan Science and Technology Cooperation Program in High Energy Physics.

<sup>†</sup> mika.masuzawa@kek.jp

$$\Sigma_x^2 = \sigma_{x+}^{*eff2} + \sigma_{x-}^{*eff2} \quad (3)$$

The parameters  $\tilde{x}$ ,  $\omega_x$ ,  $\sigma_{x+}^{*eff}$ , and  $\sigma_{x-}^{*eff}$  represent the dithering amplitude, dithering frequency, effective horizontal LER, and HER beam size at the IP, respectively. The effective horizontal beam size is denoted as follows:

$$\sigma_{x\pm}^{*eff} = \sigma_z \sin \phi_c \quad (4)$$

where  $\phi_c$  and  $\sigma_z$  are the half crossing angles of the two beams at the IP and bunch length, respectively. Figure 1 shows a conceptual drawing of the colliding beams at SuperKEKB.

Expanding Eq. (1) for small offset  $x_0$  and dither amplitude  $\tilde{x}$ ,  $L$  can be rewritten as follows:

$$L(x) = L_0 \left( 1 - \frac{x_0 \tilde{x}}{\Sigma_x^2} \cos \omega_x t - \frac{\tilde{x}^2}{2\Sigma_x^2} \cos^2 \omega_x t \right) \exp\left(-\frac{x_0^2}{2\Sigma_x^2}\right) \quad (5)$$

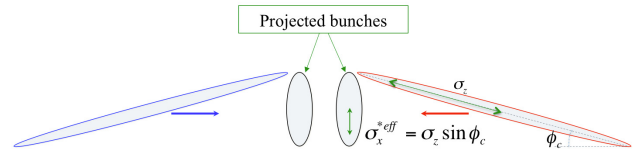


Figure 1: SuperKEKB colliding beams.

When the beam is dithered around the “center,” where luminosity peaks, luminosity drops on either side of the peak, giving a modulation at  $2\omega$ . When dithered off center, there is additional modulation at the fundamental, as indicated in Fig. 2.

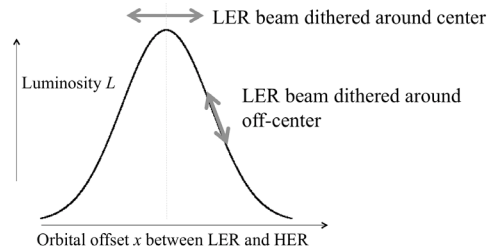


Figure 2: Luminosity dependence on the orbital offset between LER and HER at the IP.



In the dithering feedback loop, the offset between LER and HER at the IP is adjusted at each feedback cycle to minimize the amplitude of the fundamental harmonics in the luminosity signal. Twelve steering magnets in the HER, which are dedicated to orbital feedback, create a local bump at the IP to adjust the offset.

### Luminosity Monitors

Two types of fast luminosity monitors were used for studying dither in Phase II. They both detect photons, recoiled electrons, or positrons from radiative Bhabha scattering in the very forward (“zero degree”) direction. One monitoring system is called zero degree luminosity monitor (ZDLM) and is based on Cherenkov and scintillation counters [4]. The other system is developed by LAL, which uses diamond sensors and is called “LumiBelle2” [5]. The luminosity signals are input to the lock-in amplifier, which mixes them with the reference dither signal and then low-pass filtering to provide an output voltage proportional to  $L_0$  and  $x_0$  as follows:

$$V_x = CL_0 \frac{x_0 \tilde{x}}{\sqrt{2\Sigma_x^2}} \exp\left(-\frac{x_0^2}{2\Sigma_x^2}\right) \quad (6)$$

where  $C$  is the output conversion factor of the luminosity monitor.  $V_x$  is proportional to offset  $x_0$  and becomes zero when luminosity is maximized.

The feedback loop determines the amount and direction of offset correction. An algorithm based on Newton’s method with PI control was used for finding the zero of  $V_x$ .

### Dithering Hardware

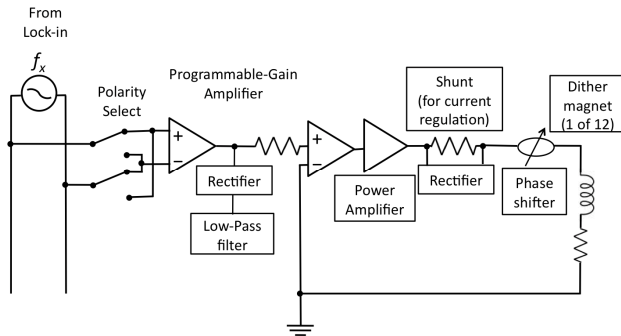


Figure 3: Dithering circuit.

A schematic diagram of the dithering system is shown in Fig. 3. A lock-in amplifier (AMETEK ADVANCED MEASUREMENT TECHNOLOGY model 7230) is used to generate a sine wave at a dither frequency. We chose 79 Hz as the dither frequency to avoid interference from the 50-Hz power line and injection frequencies of 1, 2, 5, 12.5, and 25 Hz. The sine wave is used as an input to the power supplies via a programmable-gain amplifier. There are 12 air-core Helmholtz coils installed in the LER to form a closed bump at the IP. The programmable-gain amplifier and coils were designed and fabricated by SLAC [6]. The

time delay was adjusted through the programmable amplifier by using the phase-shifter. The fudge factors of each coil were obtained by analyzing the actual beam orbit. They were used to improve the bump orbit during beam commissioning. The block diagram of the dither system is described elsewhere [7].

## COMMISSIONING

This section summarizes the results from the dithering study with colliding beams. The luminosity signals from ZDLM and LumiBelle2 were used as input to the lock-in amplifier. To maintain stable collision conditions, the collision feedback in the vertical direction (“iBump FB”) and continuous closed orbit correction (“CCC”), which keeps the global orbit in the entire ring to the reference orbit, were kept on. The HER and LER beam currents were kept as constant as possible by injecting the beam to both rings frequently. The current in the HER was varied from 235 mA to 250 mA, while it was varied from 285 mA to 300 mA in the LER. The LER beam was dithered at 79 Hz, with the dither amplitude being 20  $\mu\text{m}$  at the IP.

Four scanned data sets were taken using LumiBelle2 and ZDLM alternatively as input to the lock-in amplifier, with varying HER horizontal bump height at the IP, as shown in the example in Fig. 4. Table 1 summarises the scans.

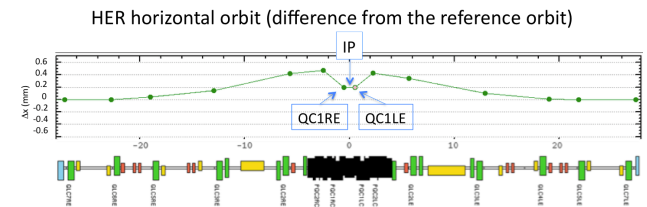


Figure 4: Local bump (0.2 mm as an example) at the IP in the HER is shown.

Table 1: Summary of Dither Study

	Input to lock-in amplifier	Scan range ( $\mu\text{m}$ )
Scan 1	LumiBelle2	-250 ~ +250
Scan 2	LumiBelle2	+250 ~ -250
Scan 3	ZDLM	-150 ~ +150
Scan 4	ZDLM	+150 ~ -150

### Luminosity Scan

Figure 5 shows the luminosity response when the bump height at the IP was changed during scan 3, as an example. The luminosity is normalized to its peak for each luminosity monitor. The normalized luminosity  $L_0$  is fitted by the following Gaussian functions:

$$L_0 = m_1 + \exp\left(-\frac{(x - m_2)^2}{2m_3^2}\right) \quad (7)$$

where  $x$  is the beam position monitored by the beam position monitor (BPM) at a magnet called “QC1LE”. The fitted parameters  $m_2$  and  $m_3$  represent the HER beam position where the luminosity peaks and exhibits standard deviation, respectively.

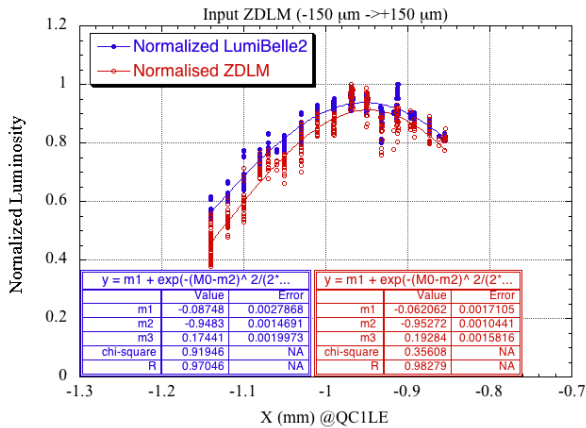


Figure 5: Luminosity is plotted against the beam position measured at the QC1LE BPM during scan 3.

Table 2 summarizes the fitted parameters. Luminosity peaks when the HER beam position measured at QC1LE is -0.95 mm for all scans, indicating that the effects of the bump magnet hysteresis and drift of the beam orbits are negligible.

Table 2: Summary of Gaussian-fitted Parameters

Detector	LumiBelle2		ZDLM	
Fit:	m <sub>2</sub>	m <sub>3</sub>	m <sub>2</sub>	m <sub>3</sub>
Scan 1	-0.94	0.27	-0.95	0.24
Scan 2	-0.94	0.21	-0.95	0.18
Scan 3	-0.95	0.17	-0.95	0.19
Scan 4	-0.94	0.20	-0.95	0.18

### Response of Lock-in Amplifier to Luminosity

The output voltage from the lock-in amplifier,  $V_x$  in Eq. (6) is plotted as a function of the horizontal beam position at QC1LE in Fig. 6 for scans 3 and 4, where the ZDLM signal was used as input to the lock-in amplifier. The output voltage becomes zero and the phase jump takes place at  $x = -0.95$  mm in both scans, which are consistent with the position of the luminosity peak.

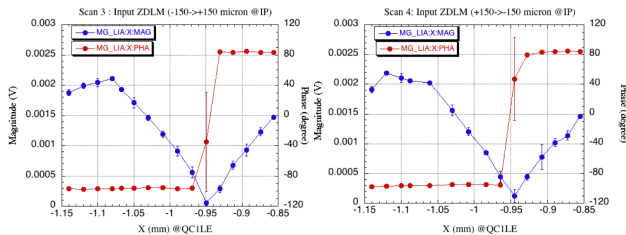


Figure 6:  $V_x$  (blue) and phase (red) are plotted against the HER beam position  $x$  for scans 3 (left) and 4 (right).

The plots of  $V_x$  and the phase for scans 1 and 2 are shown in Fig. 7, where LumiBelle2 was used as input to the lock-in amplifier. When  $V_x$  is zero, or close to zero, phase jump occurs. However, the beam position is not at  $x = -0.95$  mm but at  $x = -1.05$  mm. This does not match the beam position where luminosity peaks. The magnitude curve is not symmetric with respect to its minimum either, which is not the case with scans 3 and 4. The cause of this mismatch and asymmetric behavior will be investigated during Phase III that is scheduled to start in the spring of 2019.

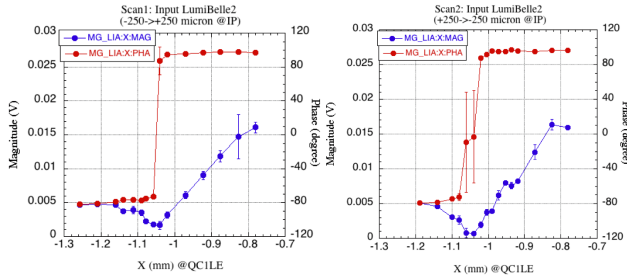


Figure 7:  $V_x$  (blue) and the phase (red) are plotted against the HER beam position  $x$  for scans 1 (left) and 2 (right).

### Dither Feedback

A feedback algorithm based on Newton’s method with PI control was first tested in May. The luminosity signal,  $V_x$ , and the bump height at the IP are plotted in Fig. 8.

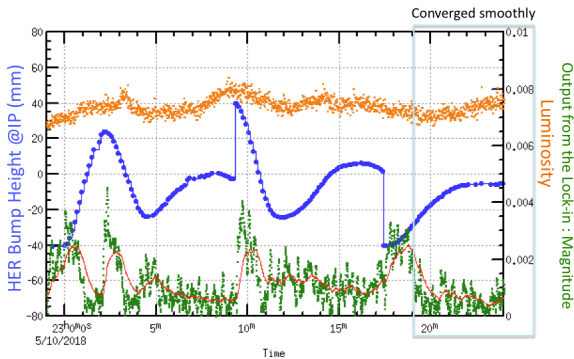


Figure 8:  $V_x$  (green) and bump height at the IP (blue) are plotted with luminosity (orange) during the dither feedback test.

The feedback algorithm loop runs in the main computer system. It determines a proper size and direction of the offset at the IP in the HER. These parameters are then sent to the magnet control system via EPICS to create a bump in the HER. The feedback loop set a bump in the correct direction and made the output from the lock-in amplifier smaller, though there were a couple of overshoots initially. After finding a good feedback parameter set, the feedback converged smoothly to an optimum value without any overshoot and  $V_x$  was brought to close to zero. The luminosity response was not clear this time, as the beam size was large and luminosity was low. Luminosity was not very sensitive to the horizontal beam offset in May.

The second feedback test was carried out in July when the beam size was smaller and luminosity was higher. We were expecting a clearer luminosity response to dither feedback but it turned out that it was not the case. This is probably because we used LumiBelle2 as input to the lock-in amplifier. LumiBelle2 seemed to have a problem when used as the input to the lock-in amplifier, as described earlier. Figure 9 shows  $V_x$  and the bump height that the dither feedback set. When the bump height was set to  $-40\text{ }\mu\text{m}$ , the magnets reached the strength limit. An additional bump was created using different sets of steering magnets. When the feedback restarted,  $V_x$  continued to become smaller, though it did not stay at the minimum. An optimization of the feedback parameters in the PI control was needed, as the machine parameters were different. Though we did not have time to optimize the parameters, it is validated that the feedback algorithm can find the minimum  $V_x$  and the algorithm works in principle.

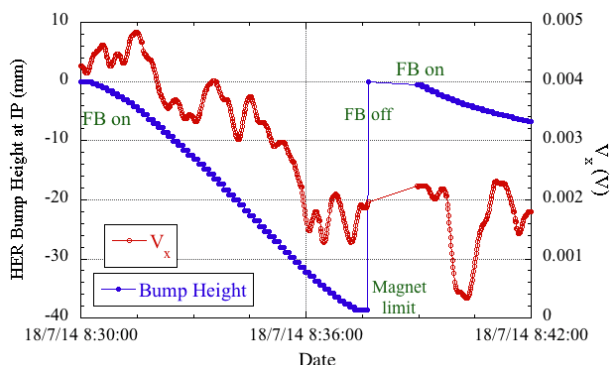


Figure 9:  $V_x$ , the bump height at the IP are plotted during the dither July feedback test.

### Response of Luminosity to Offset

Luminosity was fitted by Eq. (7) for the scans in the previous section. The bunch length was measured to be  $\sim 5.5\text{ mm}$  for both LER and HER when the bunch current is  $\sim 0.3\text{ mA}$  [8]. Using  $41.5\text{ mrad}$  for  $\phi_c$  and  $5.5\text{ mm}$  for  $\sigma_z$ , we obtain  $\sim 0.23\text{ mm}$  for  $\sigma_{x\pm}^{\text{eff}}$  from Eq. (4). This is  $\sim 15\%$  larger than  $m_3$  in Table 2, except for scan 1. Luminosity degraded more than expected with a horizontal offset. This can be explained by considering the hourglass effect. When there is a crossing angle at the IP as is in SuperKEKB, a horizontal offset shift introduces a collision point shift in the beam direction, as is indicated in the left side drawing in Fig. 10. The vertical beta-function  $\beta_y$  is plotted on the right side. A  $100\text{-}\mu\text{m}$  horizontal offset makes  $\beta_y$  larger, which degrades luminosity by approximately 10% if  $\beta_y$  at the IP is  $3\text{ mm}$ . If a horizontal offset causes beam blow-up at the IP, an additional degradation in luminosity will take place.

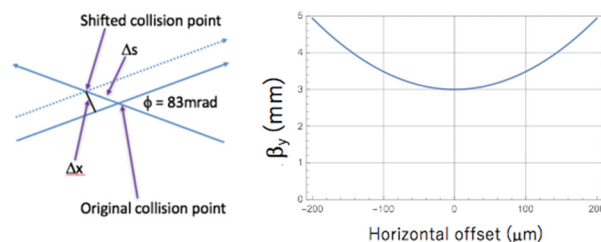


Figure 10: Hourglass effect when there is a horizontal offset at the IP.

## SUMMARY

The dither feedback system finds the optimum horizontal offset between the LER and HER to maximize luminosity by determining the minimum  $V_x$ . The optimum horizontal offset was found successfully when ZDLM was used as input to the lock-in amplifier. There was a shift of approximately  $100\text{ }\mu\text{m}$  between the luminosity maximum offset and  $V_x$  minimum offset when LumiBelle2 was used as input. This will be investigated during the Phase III run.

The dependence of luminosity on offset agrees with the prediction estimated from the crossing angle, bunch length, horizontal beam size at the IP, and hourglass effect.

## REFERENCES

- [1] Y. Ohnishi *et al.*, “Report on SuperKEKB phase 2 commissioning”, in *Proc. IPAC’18*, Vancouver, BC, Canada, Apr.-May 2018, pp. 1-5. doi:10.18429/JACoW-IPAC2018-MOXGB1
- [2] S. Gierman *et al.*, “New fast dither system for PEP-II”, in *Proc. EPAC’06*, Edinburgh, UK, Jun. 2006, pp. 652-654.
- [3] A.S. Fisher *et al.*, “Commissioning the fast luminosity dither for PEP-II”, in *Proc. PAC’07*, Albuquerque, NM, USA, Jun. 2007, pp. 4165-4167. doi:10.1109/PAC.2007.4440072
- [4] T.Hirai, S. Uehara and Y.Watanabe, “Real-time luminosity monitor for B-factory experiment”, *Nuclear Instruments and Methods in Physics Research, Section A*, vol. 11, , pp. 670-676, Feb. 2001.
- [5] S. Di Carlo *et al.*, “Early Phase 2 Results of LumiBelle2 for the SuperKEKB Electron Ring”, in *Proc. IPAC’18*, Vancouver, BC, Canada, Apr.-May 2018, pp. 2934-2935. doi:10.18429/JACoW-IPAC2018-THYGBE4
- [6] U. Wienands *et al.*, “Dither coils for the SuperKEKB fast collision feedback system”, in *Proc. IPAC’15*, Richmond, VA, USA, May 2015, pp. 3500-3502. doi:10.18429/JACoW-IPAC2015-WEPWI006
- [7] Y. Funakoshi *et al.*, “Recent progress of dithering system at SuperKEKB”, in *Proc. IPAC’17*, Copenhagen, Denmark, May 2017, pp. 1827-1829. doi:10.18429/JACoW-IPAC2017-TUPIK059
- [8] H. Ikeda, private communication, Aug. 2018.

# OPTICAL INVESTIGATION TO MINIMIZE THE ELECTRON BUNCH ARRIVAL-TIME JITTER BETWEEN FEMTOSECOND LASER PULSES AND ELECTRON BUNCHES FOR LASER-DRIVEN PLASMA WAKEFIELD ACCELERATORS\*

S. Mattiello<sup>†</sup>, Andreas Penirschke, Technische Hochschule Mittelhessen, Friedberg, Germany  
Holger Schlarb, DESY, Hamburg, Germany

## Abstract

In a laser driven plasma based particle accelerators a stable synchronization of the electron bunch and of the plasma wakefield in the range of less than 2 fs is necessary in order to optimize the acceleration. For this purpose we are developing a new shot to shot feedback system with a time resolution of less than 1 fs. As a first step, stable THz pulses are generated by optical rectification of a fraction of the plasma generating high energy laser pulses in a nonlinear lithium niobate crystal. It is planned that the generated THz pulses will energy modulate the electron bunches shot to shot before the plasma to achieve the time resolution of 1 fs. In this contribution we systematically investigate the influence of the optical properties as well as the theoretical description of the THz generation on the conversion efficiency of the generation of short THz pulses, in undepleted approximation. We compare different approximations for the modeling of the generation dynamics and of the dielectric function in order to investigate the importance of a detailed description of the optical properties. First results by considering intensity decreasing of the laser pump will be presented.

## INTRODUCTION

Particle accelerators are important tools for fundamental research as well for the industry and human life. In fact, they allow to achieve crucial new discoveries, e.g. the Higgs boson, to test and develop the standard model and to deeply understand the strong interaction and in particular the properties of the quark gluon plasma. On the other side, accelerators have several applications in material science, biology, medicine, industry and for security purposes and point-to-point communications. As examples we mention the systematic investigation of basic materials using ions beams in order to achieve new technologies, the repair of complex DNA lesions as well as cancer treatment, where the high-energy particle beams can be targeted to destroy tumors [1, 2].

The technology of standard accelerators is coming to its limit given by the physical-chemical properties of the material used for the construction as well as by the huge size of new accelerators and by the financial costs.

Because of their extremely large accelerating electric fields, plasma-based particle accelerators driven by either

lasers or particle beams allow to overcome these problems. In this method, known as plasma wakefield acceleration (PWA), the accelerating gradients in plasmas can be 3–4 orders of magnitude higher than in conventional accelerators [3].

The period of these fields is in the range of 10 fs to 100 fs so that for an optimization of the acceleration a stable synchronization of the electron bunch and of the plasma wakefield in the range of few femtoseconds is necessary. Consequently, the minimizing the electron bunch arrival-time jitter becomes a central point for the realization of these accelerators. We are planning a new shot to shot feedback system, which should be able to synchronize the electron bunch with the plasma exciting laser pulse with a time resolution of less than 1 fs.

In a first step, stable Terahertz (THz) pulses should be performed by optical rectification (OR) of high energy laser pulses in a nonlinear crystal. These pulses allow an energy modulation in the modulator placed in a chicane of the electron bunch in order to achieve the required resolution. This paper focuses on the first step of the feedback system, i.e. the generation of THz pulses.

For our purpose an efficient and stable generation of THz pulses is a challenging task. Consequently, the main focus is to maximize the conversion efficiency of the THz generation defined in term of the THz frequency component of the electric field as [4],

$$\eta = \frac{\pi \epsilon_0 c \int_0^\infty d\Omega n(\Omega) |E(\Omega, z)|^2}{F_p}, \quad (1)$$

where  $F_p$  and  $\epsilon_0$  indicate the pump fluence and the vacuum dielectric constant respectively.

For optical rectification the selection of the nonlinear material is fundamental aspect. Because of its high nonlinear optical coefficient, lithium niobate ( $\text{LiNbO}_3$ , LN) is a suitable material for THz generation.

The optical properties of the material and in particular the details of the adsorption of the THz radiation and material dispersion effects are important for the optimization of the efficiency. In this contribution we investigate the influence of the optical properties, where we focus on a periodically poled lithium niobate crystal (PPLN) [4].

The paper is organized as follows. First, we derive the general equations for the description of the THz generation and then we present the calculation of the optical properties of the material and the different approximations for the solution of the THz generation. Therefore we investigate in

\* The work of S. Mattiello is supported by the German Federal Ministry of Education and Research (BMBF) under contract no. 05K16ROA.

<sup>†</sup> stefano.mattiello@iem.thm.de



this framework the role of the optical properties of PPLN on the conversion efficiency of the generation of THz pulses. A treatment of the influence on  $\eta$  of the intensity decreasing of the laser pump is presented. The conclusions finalize this work.

## DERIVATION OF THE THZ GENERATION EQUATIONS

Starting from the Maxwell equations the one dimensional wave equation for the optical and THz waves can be derived as [5, 6],

$$\left( \frac{\partial^2}{\partial z^2} + \epsilon\mu \frac{\partial^2}{\partial t^2} - \mu\sigma \frac{\partial}{\partial t} \right) E_{\text{tot}}(t, z) = -\mu \frac{\partial P_{\text{NL}}(t, z)}{\partial t^2}, \quad (2)$$

$\epsilon$  denotes is the dielectric constant,  $\mu$  is the magnetic permeability of vacuum,  $\sigma$  denotes the electrical conductivity and  $P_{\text{NL}}$  is the nonlinear polarization.

The electric field  $E_{\text{tot}}(t, z)$  is the sum of the electric field of an optical frequency component (laser pulse),  $E_p(t, z)$  and a THz frequency component,  $E(t, z)$ . Consequently the equation of motion can be treated as a set of coupled wave equation for  $E_p$  and  $E$ .

Several works consider only the equation for the THz component, i.e. the depletion of the laser pump is neglected [7–9]. In this undepleted approximation the generation of the THz wave can be expressed in frequency domain as

$$\left( \frac{\partial^2}{\partial z^2} + \frac{\Omega^2}{c^2} \epsilon(\Omega) \right) E(z, \Omega) = -\mu_0 \omega^2 P_{\text{NL}}(\Omega, z), \quad (3)$$

where  $\epsilon(\Omega)$  is the generalized (complex) dielectric function, in which the contribution of the electric conductivity is encoded. The polarization reads

$$P_{\text{NL}}(\Omega, z) = \epsilon_0 \chi^{(2)} \int_0^\infty d\omega A_p(\omega + \Omega, z) A_p^*(\omega, z) e^{i(k(\Omega + \omega) - k(\omega))z} \quad (4)$$

where the parameter  $\chi_{\text{eff}}^{(2)}(z)$  is the effective second order nonlinear susceptibility which can be a function of the spatial coordinate  $z$ . Here we used that for arbitrary  $z$  holds

$$E_p(\omega, z) = A_p(\omega) e^{-ik(\omega)z}, \quad (5)$$

where  $k(\omega)$  denotes the module of the wave vector.

These equations show that the optical properties of the material in two different frequency ranges are the relevant physical inputs for the THz generation, i.e. for the dielectric function  $\epsilon(\Omega)$  in the THz region and for the module of the wave vector  $k(\omega)$ , which is connected to the dielectric function at the frequency  $\omega$ .

Consequently, before we discuss the solutions of Eq. (3), we present the description of the optical properties for the two different frequency ranges.

## MODELING THE MATERIAL PROPERTIES

In order to determine the optical properties, we have to calculate the complex dielectric function  $\epsilon(\omega)$  of the material. In general the relation between  $\epsilon(\omega)$  and the wave vector, the refractive index and the adsorption coefficient is given by

$$n(\omega) = \frac{k(\Omega)c}{\Omega} = \Re \sqrt{\epsilon(\omega)} \quad \text{and} \quad \alpha(\omega) = \frac{2\Omega}{c} \Im \sqrt{\epsilon(\omega)}. \quad (6)$$

Because in the polarization integral the optical properties enter in term of the expression  $k(\Omega + \omega) - k(\omega)$ , only the real part of the dielectric function is relevant in the frequency region around  $\omega_0$ .

In literature, several works [7–9] perform a linear approximation of this term, i.e.

$$k(\Omega + \omega) - k(\omega) \approx \frac{n_{\text{gr}}}{c} \Omega, \quad (7)$$

which is independent on the integration variable, so that for a Gaussian enveloped laser pulse  $P_{\text{NL}}$  can be expressed analytically.

Nevertheless, the dispersion plays an important role that cannot be neglected in our contribution. In order to systematically implement this effect, we describe the refractive index squared as function of the frequency using the Sellmeier equation given in Ref. [10]. For the THz frequency region we use a physical motivated description for the dielectric function based on an oscillator model, i.e.

$$\epsilon(\Omega) = \epsilon_\infty + \sum_j \frac{S_j \Omega_j^2}{\Omega_j^2 - \Omega^2 - i\Omega \Gamma_j}, \quad (8)$$

where the summation over the lattice oscillators with the strength  $S_j$ , angular resonance frequency  $\Omega_j$  and resonance width  $\Gamma_j$  is performed and the bound electron contribution to the dielectric function is denoted as  $\epsilon_\infty$  [11]. In this contribution we use the parameter set Schall(1999) from Ref. [11] as well as our parameter Mattiello(2017) [2], in order to investigate the influence of the dielectric function on  $\eta$ .

Additionally, free carries (FC) are generated by the pump adsorption in the material [8,9]. Then, the dielectric function has to be modified, so that it includes systematically the FC contribution. We use a dielectric function, in which the contribution of the free carries is implemented along the line of a Drude model

$$\epsilon_{\text{tot}}(\Omega) = \epsilon_{\text{osc}}(\Omega) - \frac{\omega_{\text{pl}}^2}{\Omega^2 + i\Omega/\tau_{\text{sc}}}. \quad (9)$$

Hereby  $\tau_{\text{sc}} = 200$  fs [9] is the electron scattering time and the plasma frequency  $\omega_{\text{pl}}^2$  is related to the density of free charge carries  $\rho_{\text{FC}}$  by

$$\rho_{\text{FC}} = \frac{\epsilon_0 \epsilon_\infty^{\text{FC}} m_{\text{eff}}}{e^2} \omega_{\text{pl}}^2, \quad (10)$$

where  $e$  and  $m_{\text{eff}} = 0.25m_e$  are the electron charge and effective mass respectively [9]. Herby  $m_e$  indicates the electron mass. Instead to systematically modify the dielectric function, in several works a simple sum approximation is used,

$$\alpha(\Omega) = \alpha_{\varepsilon}(\Omega) + \alpha_{\text{FC}}(\Omega) \quad (11)$$

where the two terms are calculated separately starting from a dielectric function without free carries and the dielectric function of a Drude model respectively [8, 9].

For PPLN, the physical relevant input  $\rho_{\text{FC}}$  can be described by the three-photon-adsorption process(3PA) of the pump beam in the medium [9]

$$\varrho_{3\text{PA}}(I_p) = \frac{\tau\lambda_0}{hc} \frac{1}{3} \gamma_3 I_p^3 \quad (12)$$

with  $\gamma_3 = 1.3 \times 10^{-4} \text{ cm}^3 \text{ GW}^{-2}$ . Here  $I_p$  is the time-averaged pump pulse intensity over pulse duration  $\tau$ ,  $\lambda_0$  is the pump central wavelength and  $\gamma_3$  denote the absorption coefficients for three-photon process. However, by further increasing pump fluence, saturation of absorption contribution of FC seems to occur, leading to an increase of THz conversion efficiency. This behavior was observed by LN crystals [9]. To investigate this effect we parametrize the saturation with the following phenomenological expression

$$\varrho(I_p) = \varrho_s - A e^{-a(I_p - I_0)}, \quad (13)$$

setting the saturation concentration of free carriers in LN crystal to  $\varrho_s \approx 4 \times 10^{14} \text{ cm}^{-3}$  at pump fluence  $F_s = 50 \text{ mJ cm}^{-2}$  [9]. Hereby  $I_0$  denotes the intensity of the laser, where this saturation formula set on.

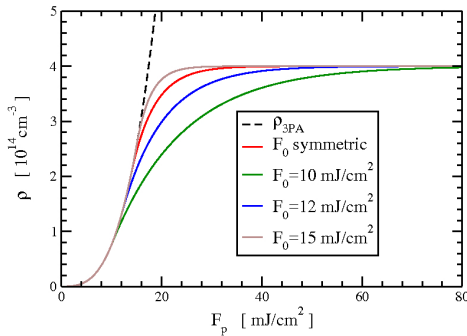


Figure 1: The density of free charge carriers as function of the fluence in strict 3PA (dashed black line) and for different values of  $F_0$  for a Gaussian pulse with duration  $\tau_{\text{FWHM}} = 25 \text{ fs}$  and  $\lambda_0 = 1030 \text{ nm}$  as indicated.

The Fig. 1 shows the density of free charge carriers as function of the fluence in strict 3PA (dashed line) and for different values of  $F_0$  for a Gaussian pulse with duration  $\tau_{\text{FWHM}} = 25 \text{ fs}$  and  $\lambda_0 = 1030 \text{ nm}$  as indicated. Herby we used that in the case of Gaussian pulses, fluence and intensity are proportional. With symmetric we indicate the parametrization, in which the transition occurs at the half of the saturation density, i.e.  $\varrho_{3\text{PA}}(F_0) = \varrho_s/2 = 2 \times 10^{14} \text{ cm}^{-3}$ . We expect

that the different parametrizations for the saturation lead to sizeable different behaviors of the efficiency as function of the fluence. We discuss this point in the section RESULTS.

## MODELING THE THZ GENERATION

Not only the different implementation of the optical properties and the approximations (full Sellmeier equation or linear approximation for the dispersion, systematic implementation of the free charge carries, different parametrization of the saturation behavior), but also the way to solve the equation of motion (3) lead to diverse results for the conversion efficiency.

### Slope Varying Approximation

Almost all investigations confine themselves to a slope varying approximation (SVA) [4, 7–9], in which neglecting the second spatial derivate of the amplitude leads to a linear differential equation of the first order,

$$\frac{\partial}{\partial z} A(\Omega, z) = -\frac{\alpha(\Omega)}{2} A(\Omega, z) - i \frac{\Omega}{2k(\Omega)c^2} \frac{P_{\text{NL}}(\Omega, z)}{\varepsilon_0} e^{ik(\Omega)z}. \quad (14)$$

In the linear approximation for the polarization integral, i.e. if Eq. (7) is used, the absolute value of the field squared can be expressed by

$$|A(\Omega, z)|^2 = \frac{\Omega^2 \tilde{P}_{\text{NL}}^2(\Omega, z)}{4c^2 n^2(\Omega) \varepsilon_0^2} \frac{1}{(\Delta k_0)^2 + a_1^2(\Omega)/4} \times \left( \left( 1 - e^{-\frac{\alpha(\Omega)z}{2}} \right)^2 + 4 e^{-\frac{\alpha(\Omega)z}{2}} \sin^2 \left( \frac{\Delta k_0 z}{2} \right) \right), \quad (15)$$

where the effective nonlinear polarization  $\tilde{P}_{\text{NL}}$  is given by

$$\tilde{P}_{\text{NL}}(\Omega, z) = \varepsilon_0 \chi_{\text{eff}}^{(2)}(z) \int_0^\infty d\omega A_p(\omega + \Omega, z) A_p^*(\omega, z). \quad (16)$$

Here the mismatching  $\Delta k$ , which for PPLN is in general defined by

$$\Delta k = k(\Omega + \omega) - k(\omega) - k(\Omega) + \frac{2\pi}{\Lambda}, \quad (17)$$

becomes, using Eq. (7),  $\Delta k \rightarrow \Delta k_0 = \frac{\Omega}{c}(n_{\text{opt}}^{\text{gr}} - n(\Omega)) + \frac{2\pi}{\Lambda}$ , where  $\Lambda = 237.74 \mu\text{m}$  is the quasi-phase-matching orientation-reversal period [4].

In general, beyond the linear approximation in the polarization integral, the amplitude can be written as

$$A(\Omega, z) = -i \frac{\Omega^2 \chi_{\text{eff}}^{(2)}}{2k(\Omega)c} \int_0^\infty d\omega \left[ \frac{A_p(\omega + \Omega) A_p^*(\omega)}{\alpha/2 - i\Delta k} \times \left( e^{-i\Delta k z} - e^{\alpha z/2} \right) \right], \quad (18)$$

where  $\Delta k$  is a function of the integration variable  $\omega$ . If the quantity

$$\tilde{J}_1(\omega, \Omega) = \frac{A_p(\omega + \Omega) A_p^*(\omega)}{\alpha^2/4 + (\Delta k)^2} \quad (19)$$

is real,  $A$  can be expressed as linear combinations of integrals involving  $\tilde{J}_1(\omega, \Omega)$  [2]. Consequently, a(semi)analytical calculation of the efficiency  $\eta$  without any approximation for the dispersion relation in the optical range can be performed.

## Solution for the Second Order Equation

Assuming a forward propagation of the THz wave a formal solution for Eq. (3) can be given as

$$E(\Omega, z) = \frac{\Omega^2 \chi_{\text{eff}}^{(2)}}{c^2} e^{-ik(\Omega)z} \int_0^\infty d\omega \left[ \left( e^{-i\Delta k z} - e^{\alpha z/2} \right) \times \frac{A_p(\omega + \Omega) A_p^*(\omega)}{(\Delta k_- + i\alpha/2)(\Delta k_+ - i\alpha/2)} \right], \quad (20)$$

where the generalized mismatch vectors are given for PPLN by

$$\Delta k_{\pm} = k(\Omega + \omega) - k(\omega) + \frac{2\pi}{\Lambda} \pm k(\Omega). \quad (21)$$

As in the case of the SVA, using the linear approximation for the polarization function an analytic expression for the absolute value of the field squared can be given by

$$|A(\Omega, z)|^2 = \frac{\Omega^4 \tilde{P}_{\text{NL}}^2(\Omega, z)}{c^4} \frac{1}{(\Delta k_-)^2 + \alpha^2/4} \frac{g_1^2 + g_2^2}{(\Delta k_+)^2 + \alpha^2/4} \times \left( \left( 1 - e^{-\frac{\alpha(\Omega)z}{2}} \right)^2 + 4 e^{-\frac{\alpha(\Omega)z}{2}} \sin^2 \left( \frac{\Delta k_0 z}{2} \right) \right), \quad (22)$$

where we define  $g_1 = (k(\Omega + \omega) - k(\omega))^2 - k^2(\Omega) + \alpha^2/4$  and  $g_2 = -\alpha k(\Omega)$ .

Similarly, if for the dispersion relation the Sellmeier equation is used, under the requirement that

$$\tilde{J}_2(\omega, \Omega) = \frac{A_p(\omega + \Omega) A_p^*(\omega)}{\alpha^2/4 + (\Delta k_-)^2} \frac{1}{\alpha^2/4 + (\Delta k_+)^2} \in \mathfrak{R}, \quad (23)$$

we calculate  $\eta$  semianalytically, because  $E$  can be expressed as linear combination of integrals involving  $\tilde{J}_2(\omega, \Omega)$  [2].

## RESULTS

In the following we consider a periodic polarized congruent lithium niobate crystal with  $\chi_{\text{eff}}^{(2)} = 336 \text{ pm V}^{-1}$  at room temperature with a Gaussian laser beam pulse with central wave length  $\lambda_0 = 1030 \text{ nm}$  and a pulse duration at full width of half-maximum  $\tau_{\text{FWHM}} = 25 \text{ fs}$  [4, 7, 9]. In this case  $\tilde{J}_1$  as well as  $\tilde{J}_2$  are real and the reduced nonlinear polarization reads

$$\tilde{P}_{\text{NL}}(\Omega, z) \equiv \tilde{P}_{\text{NL}}(\Omega) = \varepsilon_0 \chi_{\text{eff}}^{(2)} \frac{E_0^2 \tau}{2\sqrt{2}\pi} \exp \left( -\frac{\tau^2 \Omega^2}{8} \right). \quad (24)$$

where  $E_0$  is the peak value of the electric field,  $\tau$  is given by  $\tau = (2\sqrt{2})^{-1/2} \tau_{\text{FWHM}}$  and  $n_0 = n(\lambda_0)$  is calculated using the Sellmeier equation.

We firstly present our results obtained in SVA. In Fig. 2 we show the conversion efficiency  $\eta$  for a fixed pump fluence  $F_p = 5 \text{ mJ cm}^{-2}$  as function of the crystal length  $L$  using different approximation for the optical properties and the parameters set Schall(2009).

The solid and dashed lines refer to the calculation using the Sellmeier equation for the optical dispersion and the linear approximation in the polarization integral, see Eq. (7), respectively. The colors indicate the different modeling of the

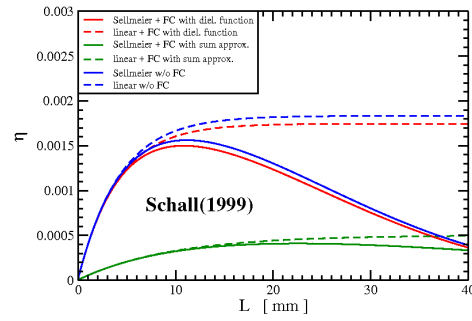


Figure 2: The conversion efficiency  $\eta$  for a fixed pump fluence  $F_p = 5 \text{ mJ cm}^{-2}$  as function of the crystal length  $L$  using different approximation for the optical properties and the parameters of Schall [11] within SVA.

dielectric function: red indicates the systematic implementation of the free charge carriers contribution using the dielectric function of Eq. (9), green denotes the approximation of the FC contribution as sum of the adsorption coefficient of the oscillator and of the Drude model, see Eq. (11), and the blue lines indicate the results by neglecting the free charge carriers, i.e. using for the dielectric function of Eq. (8).

The results with the linear approximation for the dispersion relation in the optical range show a saturation of  $\eta$  for large crystal lengths. The functional behavior of the efficiency changes by considering their full optical dispersion given by Sellmeier equation.

For  $L > 10 \text{ mm}$   $\eta$  is a decreasing function of the crystal length. For the calculation with the systematically modified dielectric function we note non monotonic behavior of  $\eta(z)$ , that is in line with the depleted results of Ref. [4]. This agreement can be understood, if we consider that the consistent implementation of the free charge carriers can be viewed as a coupling of the laser pulse with the optical properties via the plasma frequency, which directly depends on the FC density.

In general, we find sizeable modifications, if the contribution of the free carriers is implemented using the sum approximation. This strong suppression of the efficiency in this approximation can be an indication that such a modeling of the FC could lead to unphysical underestimation of the  $\eta$ . Additionally, the calculation of  $\eta$  for a fixed pump fluence  $F_p = 5 \text{ mJ cm}^{-2}$  as function of the crystal length  $L$  using the parameters set Mattiello(2017) show a quantitative approximate independence of the results for the efficiency from the oscillator models for small pump fluence.

For the investigation of the dependence of  $\eta$  from the parametrization of the density of the free charge carriers as well as from the choice of the dielectric function at higher pump fluence we consider the efficiency as function of the pulse fluence at fixed crystal length using both parameters sets. In Fig. 3 we show  $\eta$  for a crystal length of  $L = 5 \text{ mm}$  as function of  $F_p$  using the Sellmeier equation for the polarization integral and different parametrization of the FC density, labeled by  $F_0$  as indicated. For comparison, we plot as dashed line the results for the efficiency calculated with-

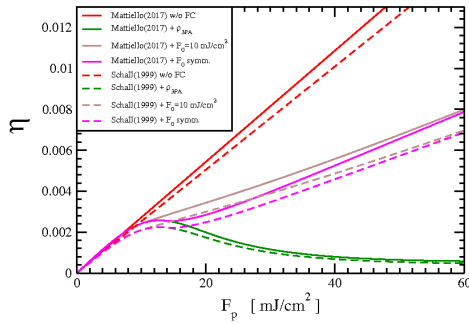


Figure 3: Comparison of the conversion efficiency  $\eta$  for a crystal length of 5 mm as function of  $F_p$  calculated with our parameters [2](solid line) and with these of Schall [11] (dashed line) in SVA using the Sellmeier equation. The different parametrizations of the FC density are labeled by  $F_0$  as indicated. As reference the efficiency by neglecting FC has been shown as solid and dashed red line respectively.

out FC contribution. The efficiencies calculated with our parameters [2] and these with the parameter of Schall [11] are shown as solid and dashed line respectively. If the FC contribution is neglected, the behavior of the efficiency as function of the fluence is linear. For unsaturated density of FC, the THz conversion efficiency increases for small values of  $F_p$ , show a local maximum and then decreases by increasing pump fluence.

A different behavior occurs for saturated  $\rho_{FC}$ . For  $F_0 > 10 \text{ mJ cm}^{-2}$  we observe a local maximum and a local minimum of the efficiency, so that three different monotonic regimes, i.e. increasing, decreasing and again increasing behavior as function of the fluence, can be founded. For smaller values of  $F_0$  the efficiency increases with increasing pump fluence. Nevertheless, the point, which for larger  $F_0$  corresponds to the local maximum of  $\eta$ , becomes the value, where the slope of the increasing behavior changes. These findings show the importance of a dynamical description of the generation and saturation of the free charge carriers in order to explain in such an effective calculation the behavior of the THz generation efficiency. Additionally, we note sizeable differences between the results achieved using the two models for the oscillator part of the dielectric function.

This indicates the existence regions of value of the physical parameters, i.e.  $L$  and  $F_p$ , where  $\eta$  strongly on the models of  $\epsilon_{osc}$ . Therefore, in particular for this range of crystal length and fluence, a better description of the optical properties is needed.

In order to investigate the deviation, which emerges by solving the equation of motion as differential equation of the second order, we consider the efficiency as function of the crystal length at fixed fluence. In Fig. 4 we compare the results for the conversion efficiency  $\eta$  for a fixed pump fluence  $F_p = 5 \text{ mJ cm}^{-2}$  as function of the crystal length  $L$  between the second order calculation (solid lines) and the SVA (dashed lines) using the parameters set Schall(1999) and our systematic implementation of FC using the dielectric function of Eq. (9). Using the linear approximation within

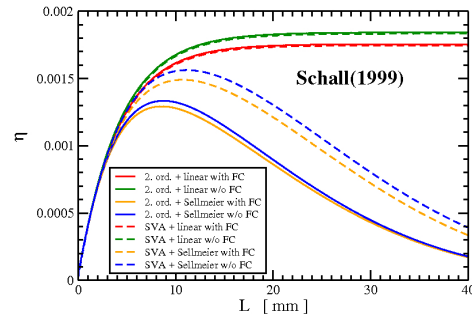


Figure 4: The conversion efficiency  $\eta$  for a fixed pump fluence  $F_p = 5 \text{ mJ cm}^{-2}$  as function of the crystal length  $L$  for the second order calculation (solid lines) and the SVA (dashed lines) using the parameters of Schall [11] labeled by different colors as indicated.

the polarization integral, only small deviations emerge. If the Sellmeier equation for the dispersion relation has been used, the quantitative deviations are sizeable. Therefore, at small fluences, the importance of the second order dynamic seems to be stronger than the effects of the free charge carriers. On the other side, further investigations show that for large fluence, sizeable but small deviation emerge between the second order and SVA calculations. Consequently, we can argue, that, at high fluences, the value of  $\eta$  is dominated by the details of the formation and saturation of FC and that the deviations coming from second order effects are small<sup>1</sup>.

## DECREASING OF THE PUMP INTENSITY

We present now our first calculations of the influence on  $\eta$  of the intensity decreasing of the laser pump induced by the three photon adsorption in SVA approximation with the linear approximation for the dispersion relation in the optical range. By neglecting the linear adsorption the intensity is

$$I_p(t, z) = I_0(t - t_0) \left( 1 + 2\gamma_3 I_0^2(t - t_0) \right)^{-1/2} \quad (25)$$

where  $I_0(t)$  denotes the intensity at  $z = 0$  and the time shift is given by  $t_0 = n_{opt}^{gr} z/c$ . After the Fourier Transformation of the Taylor expansion of the intensity we can write

$$I_p(\Omega, z) = e^{-iqz} \sum_{n=0}^{\infty} \tilde{I}_n z^n \quad (26)$$

$$\tilde{I}_n = \frac{u_n}{2\sigma_n \sqrt{\pi}} e^{-\frac{\Omega^2}{4\sigma_n^2}} \quad (27)$$

where we define  $u_n = \binom{-1/2}{n} I_0 (2\gamma_3 I_0^2)^n$ ,  $\sigma_n^2 = \frac{2}{\tau^2} (2n + 1)$  and  $q = \Omega n_{opt}^{gr}/c$ . Because the nonlinear polarization and the intensity are proportional, this expression can be inserted in Eq. (14), so that in the inhomogeneous term of the equation of motion the decreasing of the intensity is automatically encoded. For a Gaussian pulse the amplitude  $A$  can be

<sup>1</sup> For the limited number of this contribution we resign to present the corresponding figure.



written as

$$A(\Omega, z) = \sum_{n=0}^{\infty} a_n z^n, \quad (28)$$

$$a_n = \begin{cases} e^{-iqz} \sum_{m=1}^{\infty} \frac{p_{n+m}}{b} \frac{(n+m)!}{m!} & \text{if } n \geq 1; \\ e^{-\alpha z/2} \sum_{m=1}^{\infty} \frac{p_{n+m}}{b} \frac{(n+m)!}{m!} & \text{if } n = 0. \end{cases}, \quad (29)$$

with  $b = \alpha/2 - i\Delta k_0$  and  $p_m = -i \frac{\Omega \chi_{\text{eff}}^{(2)}}{2kc^3 n_0 \epsilon_0} \tilde{I}_n$ .

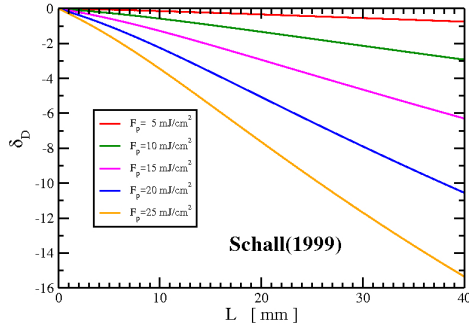


Figure 5: Percentual deviation  $\delta_D$  as function of the crystal length  $L$  using the parameters set Schall(1999) without FC contribution for different values of the pump fluence as indicated in SVA.

Using this expansion, we can calculate the efficiency  $\eta_D$  by including the laser intensity decreasing. We estimate the influence of this effects in SVA using the percentual deviation from the  $\eta$  without it  $\delta_D = (\eta_D - \eta) \eta^{-1} \times 100$ , that we show in Fig. 5 as function of the crystal length  $L$  using the parameters set Schall(1999), without considering the FC contribution, for different values of the pump fluence as indicated.

We note a significant reduction of the efficiency because of the decreasing of the laser pump intensity, in particular for large crystal length and high fluence. In this region, this effect cannot be neglected. Additionally, at fixed  $L$ , the deviation become stronger by increasing fluence. This suggests that the efficiency as function of the fluence is no linear anymore, but a saturation behavior is expected. The investigations of this dependence are in progress.

## CONCLUSION

The optical properties of the lithium niobate crystal play a crucial role for the generation of THz pulses and consequently for the planned shot to shot feedback system, which have to perform the synchronization between electron bunch and the ultrashort laser for laser driven plasma wakefield accelerators, with a time resolution of less than 1 fs.

We present systematic calculations of the optical properties of the lithium niobate crystal and of their influence on the efficiency of the generation of THz pulses. We compare different approximation for the modeling of the generation dynamic (SVA vs. second order calculation) as well as for the modeling of the dielectric function. In this way we can clearly show the importance of a consistent description of

the optical properties, not only in the THz range, but also at higher frequencies, the consideration of the complete, i.e. second order, equation of motion for the THz field as well as the inclusion of the effects of the decreasing intensity of the laser pump.

## ACKNOWLEDGEMENT

The work of S. Mattiello is supported by the German Federal Ministry of Education and Research (BMBF) under contract no. 05K16ROA.

## REFERENCES

- [1] A. G. Stepanov, S. Henin, Y. Petit, L. Bonacina, J. Kasparian, and J.-P. Wolf, “Mobile source of high-energy single-cycle terahertz pulses”, *Appl. Phys. B*, vol. 101, no. 1, pp. 11–14, 2010.
- [2] S. Mattiello, H. Schlarb, and A. Penirschke, “Optical rectification for a new shot to shot feedback system for laser-driven plasma wakefield accelerators”, in *Proc. SPIE 10684, Non-linear Optics and its Applications (SPIE:18)*, Strassbourg, France, May 2018, pp. 1068412, doi.org/10.1117/12.2306429
- [3] T. Tajima and J. M. A. Dawson, “Laser Electron Accelerator”, *Phys. Rev. Lett.*, vol. 43, no. 4, pp. 267–270, 1979.
- [4] K. Ravi, D. Schimpf, and F. Kärtner, “Pulse sequences for efficient multi-cycle terahertz generation in periodically poled lithium niobate”, *Optics Express*, vol. 24, no. 22, pp. 25582–25607, 2016.
- [5] T. Hattori and K. Takeuchi, “Simulation study on cascaded terahertz pulse generation in electro-optic crystals”, *Optics Express*, vol. 15, no. 13, pp. 8076–8093, 2007.
- [6] A. Schneider, M. Neis, M. Stillhart, B. Ruiz, R. Khan, and P. Günter, “Generation of terahertz pulses through optical rectification in organic DAST crystals: theory and experiment”, *J. Opt. Soc. Am. B*, vol. 23, no. 9, pp. 1822–1835, 2006.
- [7] K. Vodopyanov, “Optical generation of narrow-band terahertz packets in periodically-inverted electro-optic crystals: conversion efficiency and optimal laser pulse format”, *Optics Express*, vol. 14, no. 6, pp. 2263–2276, 2006.
- [8] J. A. Fülöp *et al.*, “Generation of sub-mJ terahertz pulses by optical rectification”, *Optics Letters*, vol. 37, no. 4, pp. 557–559, 2012.
- [9] S. Zhong *et al.*, “Optimization of terahertz generation from LiNbO3 under intense laser excitation with the effect of three-photon absorption”, *Optics Express*, vol. 23, no. 24, pp. 31313–31323, 2015.
- [10] L. H. Deng *et al.*, “Improvement to Sellmeier equation for periodically poled LiNbO3 crystal using mid-infrared difference-frequency generation”, *Optics Communications*, vol. 268, no. 1, pp. 110–114, 2006.
- [11] M. Schall, H. Helm, and S. R. Keiding, “Far Infrared Properties of Electro-Optic Crystals Measured by THz Time-Domain Spectroscopy”, *International Journal of Infrared and Millimeter Waves*, vol. 20, no. 4, pp. 595–604, 1999.

# FIRST ELECTRO-OPTICAL BUNCH LENGTH MEASUREMENTS AT THE EUROPEAN XFEL

B. Steffen\*, M.K. Czwalińska, Ch. Gerth, P. Peier†,  
Deutsches Elektronen-Synchrotron DESY, Hamburg, Germany

## Abstract

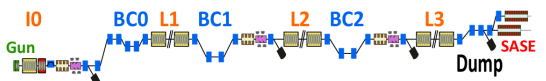
Three electro-optical bunch length detection systems based on spectral decoding have been installed and are being commissioned at the European XFEL. The systems are capable of recording individual longitudinal bunch profiles with sub-picosecond resolution at a bunch repetition rate 1.13 MHz. Bunch lengths and arrival times of entire bunch trains with single-bunch resolution have been measured as well as jitter and drifts for consecutive bunch trains. In this paper, we present first measurement results for the electro-optical detection system located after the second bunch compressor. A preliminary comparison with data from the bunch arrival-time monitor shows good agreement.

## INTRODUCTION

The accelerator for the European X-ray Free-Electron Laser (E-XFEL) delivers femtosecond electron bunches at an energy of up to 17 GeV at a repetition rate of up to 4.5 MHz in bursts of up to 2700 bunches every 100 ms. The electron bunches can be distributed between three undulator beam-lines, and the generated femtosecond X-ray laser pulses at wavelengths between 0.05 nm and 6 nm can serve up to three user experiments in parallel [1].

Short electron bunches with a high peak current are needed to drive the SASE process in the magnetic undulators. To reach these short bunches, the initially long electron bunches created at the photocathode gun are compressed in three magnetic bunch compressor chicanes BC0, BC1 and BC2 downstream of the respective accelerating sections I0, L1 and L2 (see Table 1).

Table 1: Design electron bunch lengths (rms) for different operation modes [2].



	130 MeV	700 MeV	2.4 GeV	17.5 GeV
20 pC	4.5 ps	1.5 ps	190 fs	5 fs
100 pC	4.8 ps	1.6 ps	200 fs	12 fs
250 pC	5.3 ps	1.7 ps	220 fs	25 fs
500 pC	6.0 ps	2.0 ps	260 fs	43 fs
1 nC	6.8 ps	2.2 ps	300 fs	84 fs

Various diagnostic devices have been installed along the accelerator to measure the longitudinal properties of the electron bunches. Transverse deflecting structures (TDS) have been installed in the injector [3] and downstream of

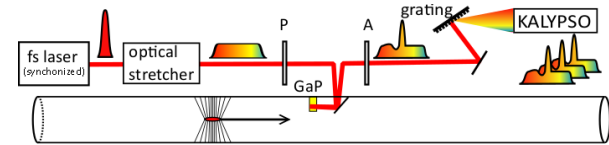


Figure 1: Schematic drawing of a spectrally encoded electro-optical detection setup. P: polarizer; A: analyzer (quarter-wave plate, half-wave plate, polarizer).

BC2 at final bunch compression for the measurement of slice emittance, longitudinal phase space and longitudinal bunch profile. These properties can be measured for single electron bunches with high accuracy, since the electron bunches are streaked and imaged onto a screen. However, as a consequence, the bunch properties are degraded and these bunches are not delivered to the undulators but deflected by fast kicker magnets out of the bunch train into a dump upstream of the undulators .

Electro-optical bunch length detection (EOD) [4] offers the possibility of measuring the longitudinal bunch profile and arrival time in a non-destructive manner with single bunch resolution for every bunch in the bunch train. Three EOD systems have been installed: One downstream of the injector linac I0 at 130 MeV, one downstream of BC0 (and L1) and one downstream of BC1 at a beam energy of 700 MeV. An EOD system was not foreseen downstream of BC2 due to the limited time resolution.

Bunch arrival time monitors (BAM) [5] have been installed downstream of the injector linac and after each of the bunch compressors BC0, BC1 and BC2. The BAMs measure the arrival time of individual electron bunches with femtosecond precision relative to an optical reference system and can be used for a feedback on the RF of the accelerating modules to stabilize the arrival time which is critical in pump-probe user experiments.

## ELECTRO-OPTICAL BUNCH LENGTH DETECTION

Electro-optically active crystals like gallium phosphide (GaP) become birefringent in the presence of an electric field. The electro-optical detection techniques use this effect to transfer the temporal profile of fast changing electric fields by sampling the change in birefringence with laser pulses. Afterwards, the modulated temporal profile of the laser pulse can be analyzed with classical laser techniques.

Several different electro-optical detection techniques have been established for single-shot bunch length measurements at different electron accelerators in the past decade, among them:

\* bernd.steffen@desy.de  
† now at METAS, Bern, Switzerland

**Spectrally resolved electro-optical detection (EOSD):** It uses a chirped laser pulse, where the frequency components of a broadband laser pulse are sorted in time and the temporal profile can be retrieved from its modulated spectrum using the known relationship between wavelength and longitudinal (temporal) position in laser pulse [6] (see Fig. 1).

**Spatially resolved electro-optical detection:** A short laser pulse passes through the EO crystal at an angle, mapping the temporal profile of the field pulse in the transverse profile of the laser pulse due to its different arrival times at different positions of the crystal surface [7].

**Temporally resolved electro-optical detection:** The temporal profile of the modulated laser pulse is measured in a single-shot cross-correlation with another short laser pulse [8].

The maximum rate of all systems is limited by both the repetition rates of the laser system and line detector. Temporally and spatially resolved detection offer a high time resolution as good as 60 fs, but they have higher demands on the imaging system for the laser and need higher laser pulse energies compared to EOSD.

With the EOSD it has been shown that sub-ps electron bunches of about 100 pC charge can be measured with about 200 fs resolution using the Coulomb field of the relativistic electron bunch [4, 9]. For a more comprehensive description of electro-optical detection techniques and theory see [9, 10].

Since the E-XFEL is build in a single-tunnel design, the laser and all electronics have to be placed in radiation shielded racks underneath the electron beam line. The EOSD scheme was chosen for the E-XFEL to design a compact, fully remote-controlled and reliable system, meeting the requirements for bunch length measurements up to the entrance of bunch compressor BC2.

## EOD SYSTEM AT THE E-XFEL

The EOD system consists of six sub-systems:

- Ytterbium fiber laser and amplifier,
- Optics set-up at the beam line vacuum chamber incl. the GaP crystal,
- Spectrometer with the KALYPSO MHz line detector,
- MicroTCA.4 crate with the analogue and digital boards for laser synchronization and data readout,
- Laser to RF synchronization unit with other supporting electronics,
- Driver unit for the motors in the laser and at the beam line.

All but the optics set-up are placed in the radiation shielded 19" rack underneath the electron beam line with a total of 25 height units.

The laser consists of an Ytterbium fiber oscillator (adapted from the design developed at the Paul-Scherrer-Institute [11]) with a repetition rate of 54.167 MHz which is synchronized to the radio-frequency (RF) master oscillator of the E-XFEL timing system [12]. Before the fiber amplifier the repetition rate is reduced by an acusto-optical modulator based pulse

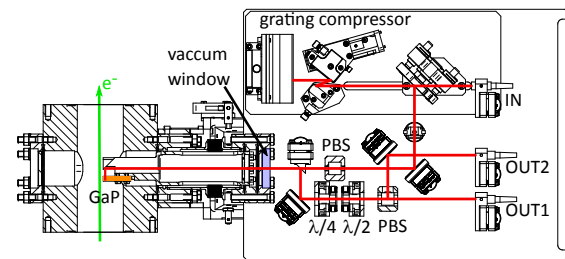


Figure 2: Assembly drawing of the optics set-up at the electron beam line including the vacuum chamber (left). PBS: polarizing beam splitter.

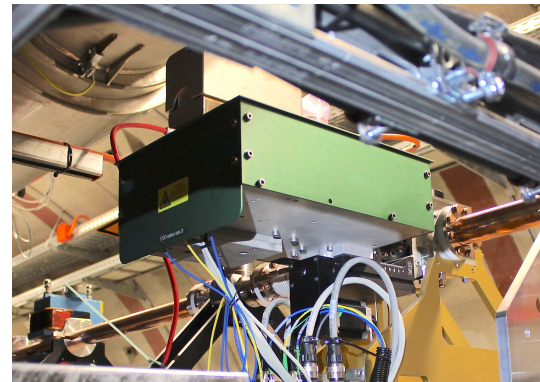


Figure 3: Picture of the optics set-up and vacuum chamber at the electron beam line.

picker to ms long bursts at 10 Hz with a pulse spacing of 886 ns (1.13 MHz E-XFEL operation frequency).

The resulting laser pulses with a bandwidth of about 100 nm, a central wavelength of 1050 nm and a pulse energy of 20 nJ-100 nJ are led by a 10 m long polarization maintaining optical fiber to the optics set-up at the vacuum chamber in the accelerator beam line.

This set-up is adapted from the design for the Swiss-FEL [13], but additionally equipped with a grating compressor to adjust the length and chirp of the incoming laser pulse from full compression to about 5 ps (FWHM). The GaP crystal and the downstream mirror are mounted on a holder which is mounted on a motorized vacuum feed-through (see Figs. 2 and 3). The set-up in the injector is equipped with a 5 mm-thick GaP crystal whereas both systems downstream of BC0 and BC1 are equipped with 2 mm-thick GaP crystals to match the bunch lengths to be measured. Outside the vacuum a small breadboard is fixed to the feed-through which holds the required optics including the fiber couplers. This way all optical elements from the fiber coming from the laser to the fiber going to the spectrometer, including the EO crystal are rigidly coupled, avoiding any misalignment or timing changes when the crystal is moved closer to the electron beam or withdrawn from the beam-pipe [13].

The output pulse is then send via an optical fiber to a simple grating spectrometer with approx. 1 nm resolution. It is equipped with an InGaAs-KALYPSO (Karlsruhe Linear array detector for MHz rePetition rate Spectroscopy) [14]



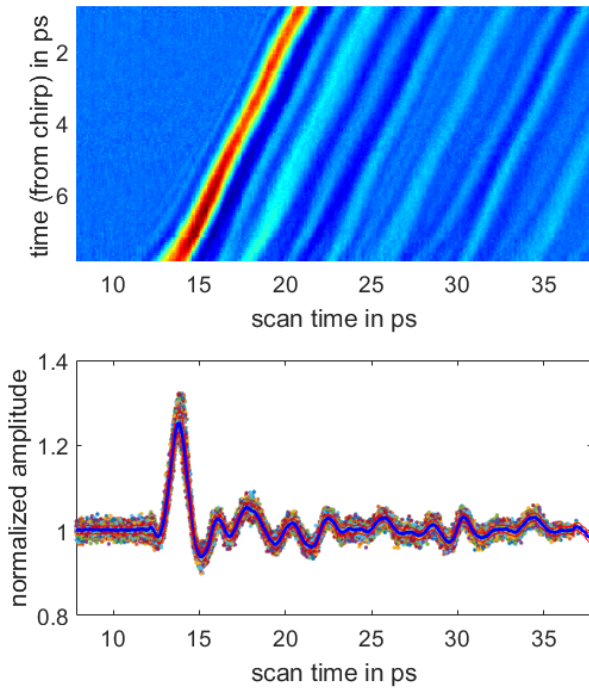


Figure 4: Top: 2D plot of single-shot EOD traces (vertical) taken at different laser timings (horizontal). Bottom: Stacked EOD traces from the scan above. The blue line shows the average, the red lines the standard deviation.

line detector, which can deliver single shot spectra with 256 pixels and a repetition rate of up to 2.26 MHz to the High-speed Optical Line Detector readout FPGA mezzanine card (HOLD) [15]. The data is transferred via a high-speed optical data link to the MicroTCA.4 [16, 17] crate, which also carries the analogue and digital boards for laser synchronization, timing and triggers and provides the link to the accelerator control system.

## MEASUREMENTS

All measurements presented in this paper have been performed during commissioning of the SASE1 undulator and photon beam lines. The data was taken at the EOD station downstream of BC1 at a electron beam energy of 700 MeV, a bunch charge of approx. 500 pC and SASE pulse energies of 500  $\mu$ J and 800  $\mu$ J for the first data-set (Figs. 4 and 5) and second data-set (Figs. 6 and 7), respectively.

For a given laser chirp, defined by the initial chirp of the pulses from the laser system and the setting of the grating compressor at the beam line, a time calibration can be done by scanning the laser pulse over the electron bunch at stable accelerator conditions. The laser synchronization allows sub-picosecond time steps with high accuracy and the resulting shift of the bunch signal in the laser spectrum allows a detector pixel to time calibration.

The result of a calibration is shown in Fig. 4 (top), where each vertical line represents an average of five single-shot EOD traces taken at the laser timing given at the horizontal

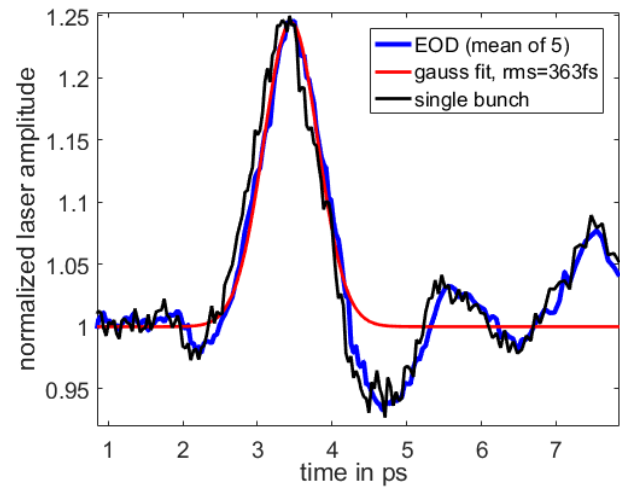


Figure 5: A single-shot EOD measurement together with an average of five consecutive bunches and a Gaussian fit to the average.

axis. Shifting each trace by the known laser time shift, the traces can be stacked to give an averaged signal over the full time window scanned (Fig. 4, bottom).

Figure 5 shows a single-shot EOD trace from the same data set. The signal from the electron bunch is almost Gaussian with a length of about 360 fs (rms), which is in good agreement with the simulated electron bunch shape for the given accelerator parameters, which are similar but not identical to the design values (Table 1). It is followed by signal components from transverse wake fields that decay over several ten picoseconds.

Measurements over full bunch trains are possible at a bunch repetition rate of 1.13 MHz or 2.26 MHz, whereas at operation of the accelerator at 4.5 MHz only every second bunch can be measured. The bunch lengths and arrival times of individual electron bunches in a 30 bunches long train is shown in Fig. 6 together with the standard deviation of

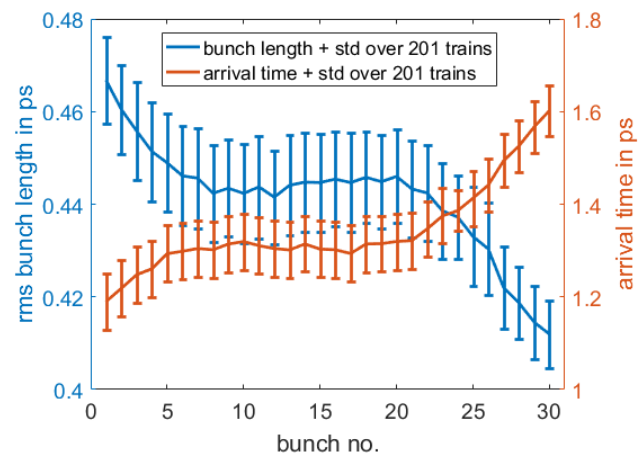


Figure 6: Bunch length and arrival time along the bunch train with a bunch repetition rate of 1.13 MHz.



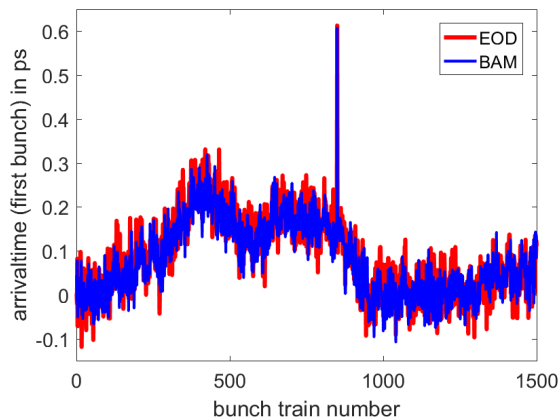


Figure 7: Arrival time of the first bunch in consecutive bunch trains measured with EOD and BAM

the values at each position. The bunch lengths change from 470 fs at the first bunch to 410 fs at the end together with a shift in arrival time by 500 fs caused by a slight shift in bunch energy over the train, leading to a different compression and beam path length in BC1.

The arrival time of the bunches is also measured by a BAM in the direct vicinity of the EOD, and the data is in good agreement. The standard deviation of the difference in the measurements of the arrival time by BAM and EOD is 39.2 fs over the 2.5 minutes shown in Fig. 7. This gives an upper limit for the synchronization jitter of the laser system.

## CONCLUSION

A compact EOD system has been developed for the measurement of longitudinal bunch profiles. Apart from the optics set-up, which comprises the GaP crystal holder and is mounted to the electron beam line, all other sub-systems fit into standard 19" crates with a total of 25 height units. The EOD systems are located inside the accelerator tunnel in the injector and downstream of the first two bunch compression chicanes and installed in radiation shielded racks below the electron beam line in the vicinity of the optics set-up. The spectrometer has been equipped with a MHz line detector [14] to be capable of recording single-shot measurements at 1.13 MHz over full bunch trains.

First measurement results of the EOD system downstream of the second bunch compressor chicane (BC1 in Table 1) have been presented. The measured single-shot bunch lengths are in good agreement with predictions from simulation codes and slightly larger than the predicted design values. The installation of a TDS at this location is delayed but will provide an independent measurement result after installation. The measurement of the distribution of the bunch lengths along the bunch train helps for the optimization of low-level RF regulation and will become especially valuable for setting up long bunch trains of up to 2700 bunches. The results of the measured arrival times are in good agreement with results obtained with a BAM at the same location.

## ACKNOWLEDGEMENTS

Special thanks to M. Caselle and L. Rota (KIT, Karlsruhe, Germany) and D. Makowski and A. Mielczarek (DMCS, Łódź University of Technology, Poland) for the great collaboration in developing the KALYPSO and its readout system.

## REFERENCES

- [1] D. Nölle, "Commissioning of the European XFEL," in *Proc. LINAC18*, Beijing, China, 2018.
- [2] G. Feng *et al.*, "Beam dynamics simulations for European XFEL," DESY, Tech. Rep., 2013, TELS-FEL 2013-04.
- [3] C. Gerth, B. Beutner, O. Hensler, F. Obier, M. Scholz, and M. Yan, "Online longitudinal bunch profile and slice emittance diagnostics at the European XFEL," in *Proc. IBIC 2017*, Grand Rapids, USA, 2017.
- [4] B. Steffen *et al.*, "Electro-optic time profile monitors for femtosecond electron bunches at the soft X-ray free-electron laser FLASH," *Phys. Rev. ST Accel. Beams*, vol. 12, no. 3, 2009.
- [5] M. Viti *et al.*, "The bunch arrival time monitor at FLASH and European XFEL," in *Proc. ICALEPCS 2017*, Barcelona, Spain, 2017.
- [6] I. Wilke, A. M. MacLeod, W. A. Gillespie, G. Berden, G. M. H. Knippels, and A. F. G. van der Meer, "Single-shot electron-beam bunch length measurements," *Phys. Rev. Lett.*, vol. 88, p. 124 801, 12 2002.
- [7] A. L. Cavalieri *et al.*, "Clocking femtosecond x rays," *Phys. Rev. Lett.*, vol. 94, no. 11, 114801, p. 114 801, 2005.
- [8] G. Berden, S. P. Jamison, A. M. McLeod, W. A. Gillespie, B. Redlich, and A. F. G. van der Meer, "Electro-optic technique with improved time resolution for real-time, nondestructive, single-shot measurements of femtosecond electron bunch profiles," *Phys. Rev. Lett.*, vol. 93, p. 114 802, 2004.
- [9] B. Steffen, "Electro-optic methods for bunch length diagnostics at FLASH," PhD thesis, University of Hamburg, 2007.
- [10] S. Casalbuoni, H. Schlarb, B. Schmidt, P. Schmüser, B. Steffen, and A. Winter, "Numerical studies on the electro-optic detection of femtosecond electron bunches," *Phys. Rev. ST Accel. Beams*, vol. 11, p. 072 802, 7 2008.
- [11] F. Müller, S. Hunziker, V. Schlott, B. Steffen, D. Treyer, and T. Feurer, "Ytterbium fiber laser for electro-optical pulse length measurements at the SwissFEL," in *Proc. DIPAC2009*, Basel, Switzerland, 2009.
- [12] M. Felber *et al.*, "Compact MTCA.4 based laser synchronization," in *Proc. IPAC2014*, Dresden, Germany, 2014.
- [13] B. Steffen, V. Schlott, and F. Müller, "A compact single shot electro-optical bunch length monitor for the SwissFEL," in *Proc. DIPAC09*, Basel, Switzerland, 2009.
- [14] L. Rota *et al.*, "KALYPSO: A Mfps linear array detector for visible to NIR radiation," in *Proc. IBIC 2016*, Barcelona, Spain, 2016.
- [15] A. Mielczarek *et al.*, "Real-time Data Acquisition and Processing System for MHz Repetition Rate Image Sensors," *IEEE Transactions on Nuclear Science*, vol. in print, 2018.
- [16] T. Wilksen *et al.*, "The control system for the linear accelerator at the European XFEL - status and first experiences," in *Proc. ICALEPCS2017*, Barcelona, Spain, 2017.
- [17] <https://www.picmg.org/openstandards/microtca/>

# THE APPLICATION OF BEAM ARRIVAL TIME MEASUREMENT AT SXFEL \*

S. S. Cao<sup>†1,2</sup>, R. X. Yuan<sup>1</sup>, J. Chen<sup>1,2</sup>, Y. B. Leng<sup>\*1</sup>

<sup>1</sup> Shanghai Institute of Applied Physics, CAS, Jiading campus, Shanghai 201808, China

<sup>2</sup> University of Chinese Academy of Sciences, Shijingshan District, Beijing 100049, China

## Abstract

The Shanghai soft X-ray free electron laser (SXFEL) is able to generate high brightness and ultra-short light pulses. The generation of the light sources relies on the synchronization between seed laser and electron bunch. Beam arrival time play an important role to keep the synchronization. For the SXFEL, a beam arrival time resolution under 100 fs is required. In this paper, the application of beam arrival time measurement scheme at SXFEL has been presented. Especially, a two-cavities mixing scheme to measure the beam flight time or pseudo beam arrival time has been proposed and compared with the typical RF phase detection scheme. The experiment results of the two scheme based on the dual-cavities BAM have also been discussed.

## INTRODUCTION

The Shanghai Soft X-ray Free-Electron laser facility (SXFEL) is under commissioning now<sup>[1]</sup>. Figure 1 shows the layout of the SXFEL-TF. The main parameters of SXFEL-TF is shown in Table 1.

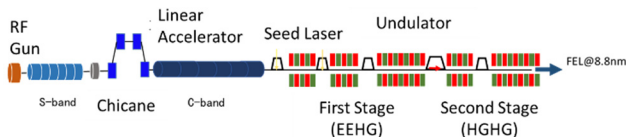


Figure 1: Electron beam characteristic.

Table 1: Main Parameters of SXFEL-TF

Parameter	Value	Unit
Beam energy	0.84	GeV
Beam charge	0.5	nC
Bunch length	~0.5	ps
Pulse repetition rate	10	Hz
Peak current	~0.5	A

For the FEL facility, its operation relies on the precise synchronization between the electron bunches and the seed laser pulses in three-dimensional space. Its longitudinal position can be measured by a beam arrival time monitor. The measured beam arrival time can be applied for feedback to adjust the timing of seed laser and also to reduce the timing jitter of accelerator. And the beam arrival time can be used

to correct for timing drifts from the accelerator to the experiments<sup>[2]</sup>. Currently, there are typically two schemes to measure the beam arrival time, electron-optical detection scheme and RF cavity detection scheme. Although the electron-optics detection scheme can acquire better performance, its biggest limitations is its great complexity and quite expensive. In contrast, the RF cavity based detection scheme is simple and inexpensive. In addition, its best resolution can be better than 13 fs.

This paper will focus on the discussion of the RF-phase detection scheme. In detail, the scheme selection, dual-cavities design, fabrication, installation, and beam arrival time experiment as well as beam flight time experiment have been presented.

## BEAM ARRIVAL TIME MEASUREMENT SCHEME

The typical RF cavity phase detection scheme is quite mature. Several FEL facility have conducted the research of beam arrival time with this scheme, such as LCLS<sup>[3]</sup>, SACLA<sup>[4]</sup>, PAL-XFEL<sup>[5]</sup>. Figure 2 gives the diagram of a typical RF cavity based phase detection scheme.

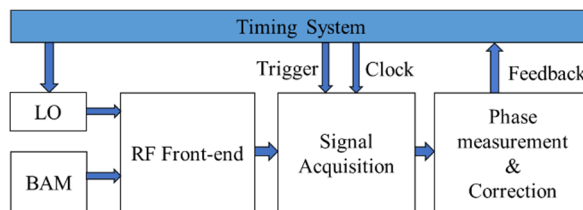


Figure 2: Diagram of a typical RF cavity based phase detection.

The typical BAM system consists of a narrow-band beam arrival time monitor, a reference signal, an RF front-end electronics, a signal acquisition system, and a phase processing/correction system. When an electron bunch passing through the BAM, a variety of electro-magnetic field modes will be excited. Typically, the strongest mode is TM010, a centro-symmetrical mode, whose signal strength is generally proportional to the bunch charge while independent of bunch offset within a paraxial approximation. However, single arrival time phase is meaningless, only when it is relative to a reference time. The two signals, a cavity signal and a reference signal, then be mixed to an intermediate frequency (IF). The beam arrival time can finally be evaluated via a signal acquisition system and phase processing system. However, its limitation is requiring a reference signal with high phase stability. Normally, the reference signal needs to be transmitted over a long dis-

\* Work Supported by The National Key Research and Development Program of China (Grant No. 2016YFA0401903, 2016YFA0401900)  
<sup>†</sup> lengyongbin@sinap.ac.cn

tance and the thermal expansion of the conventional material is about 30 fs/°C<sup>[2]</sup>. For SXFEL, a high performance reference signal is not available at present. Especially, the flight time of the electron beam is significant in some special cases, such as in the chicane section of a SASE self-seeding FEL. Therefore a two-cavities mixing detection scheme is proposed in this paper. Figure 3 shows the diagram of a two-cavities mixing based phase detection scheme. The diagram contains two scheme: using a BAM installed at the injection exit instead of a reference signal to measure the pseudo beam arrival time; using two BAM installed at the entrance and exit of the chicane separately to measure the beam flight time.

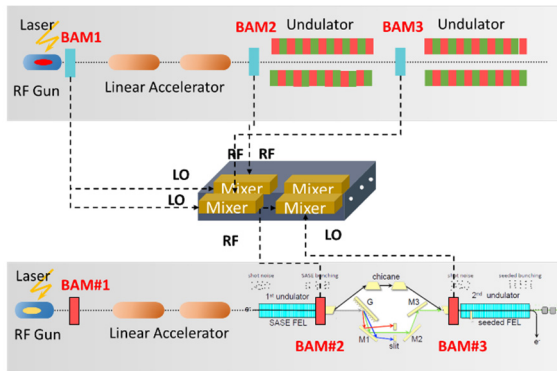


Figure 3: Diagram of a dual-cavities mixing based phase detection.

Considering the above two schemes, one BAM has to be equipped with two frequency so as to realize two-cavities mixing. Therefore, a dual-cavities BAM has been designed and fabricated. Moreover, four sets of BAM have been installed at the SXFEL facility. Two of them are installed near the injection, the other two installed at the modulator section. Figure 4 presents the BAM diagram. Table 2 gives the fundamental parameters of the BAM.

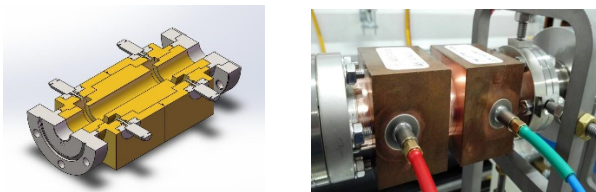


Figure 4: (Left) Schematic diagram of the BAM; (Right) The photo of the fabricated BAM;

Table 2: Fundamental Parameters of the BAM

Parameter	Cavity #1	Cavity #2
Frequency/GHz	4685	4720
Bandwidth/MHz	1.0	1.0
Decay time constant/ns	318	318
$Q_{load}$	4671	4716
$Q_0$	4796	4835
$Q_e$	1.8e5	1.9e5
R over Q /Ohm	107	108

## BEAM EXPERIMENT

### Beam Arrival Time Experiment

The beam arrival time experiment has been conducted with above BAMs. The diagram of the BAM experiment setup has been performed in Fig.5.

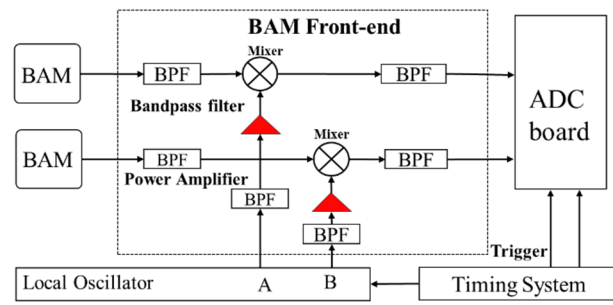


Figure 5: Diagram of the BAM experiment setup.

A 2856 MHz sinusoidal signal serves as the input signal of local oscillator (LO) and output three optional signals, a 119 MHz signal, a 4760MHz signal, as well as a 4640 MHz signal. In this experiment, the LO frequency is determined to be 4641MHz. The frequencies of two cavity signal are both about 4.69 GHz. The generated IF signal then was sampled by DBPM with a sampling rate of 119 Ms/s and 16 bits. In order to reduce the crosstalk between the channels, two IF signal are connected to the channel A and channel D, separately. Figure 6 shows the sampled IF signals and their frequency spectrum. The two IF are 51.9MHz and 52.5 MHz, separately. Thus the frequency difference is about 0.6 MHz.

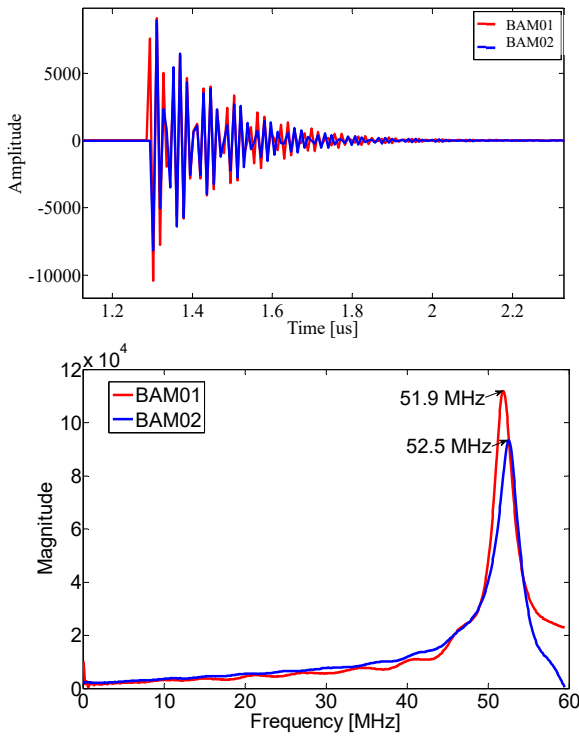


Figure 6: The raw IF signal and their frequency spectrum.

The extracted beam arrival times over 5600 samples (about 1 hour) are shown in Fig.7. And the measured resolution are 1.05 ps and 968 fs, respectively. The two value are larger than expected. However, the two beam arrival times have a strong linear correlation, as shown in Fig.8. The beam flight time resolution between the two BAMs can reach 60 fs via comparing the arrival time, see Fig. 9. Two possible causes are the trigger jitter and the reference signal drift. If the trigger signal stagger one sampling point, there will be a 0.3 radian phase error.

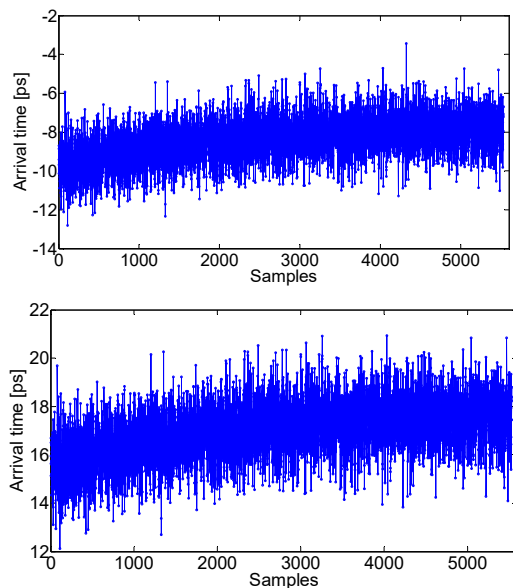


Figure 7: The two arrival time measured by two BAMs. (Above: BAM01 Below: BAM02)

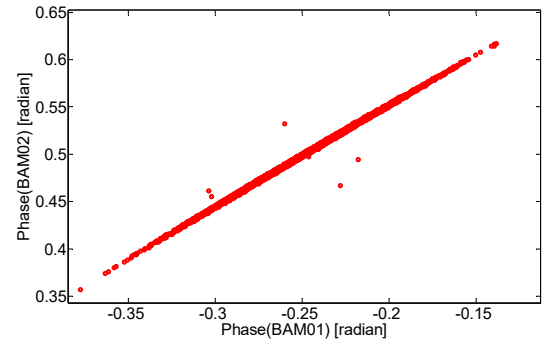


Figure 8: The correlation between the two BAMs

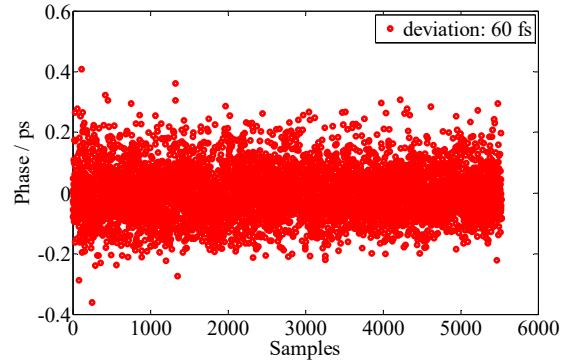


Figure 9: Beam flight time between the two BAMs.

### Beam Flight Time Experiment

Using two RF signal induced by two cavities of one BAM, we can evaluate the practicable of the proposed two-cavity mixing scheme. The diagram show in Fig.10. The digitized IF signals show in Fig.11. As discussed above, the IF signal frequency are 35 MHz. The measured beam flight time passing through the two cavities are 37 fs and 66 fs, respectively, as presented in Fig.12. This difference may be related to the BAM port's tiny difference. Moreover, the current RF front-end electronics are put outside the tunnel, thus the RF signals through a long-distance transmission will cause the transmission path inconsistency. Therefore, the RF front-end and signal acquisition system can be placed inside the tunnel in the subsequent optimization experiments to shorten the transmission length.

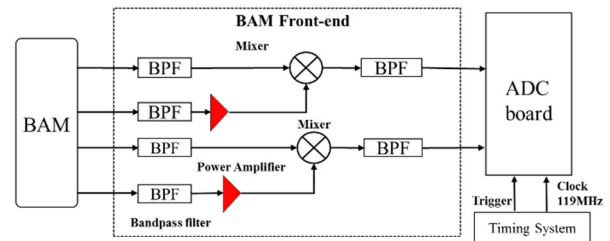


Figure 10: Diagram of the two-cavity mixing setup.



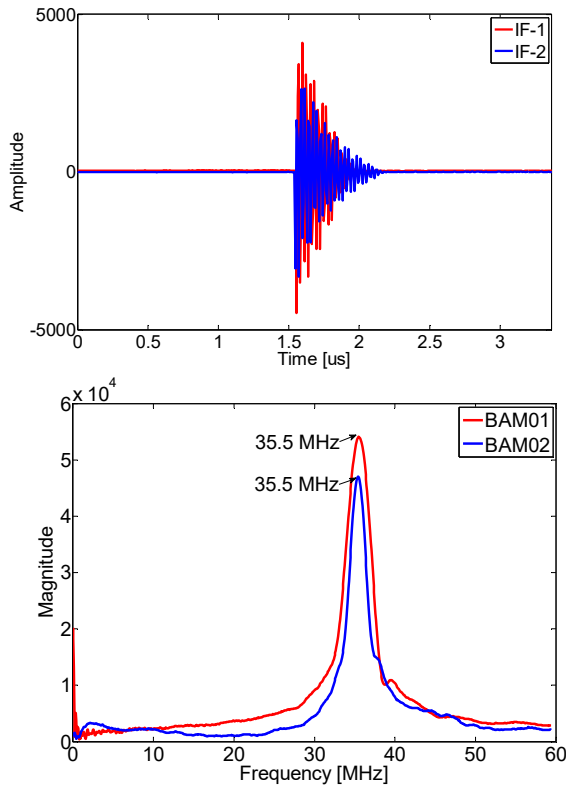


Figure 11: The raw IF signal and the frequency spectrum.

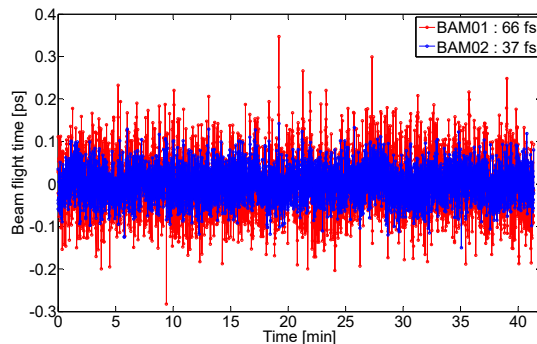


Figure 12: The beam flight time passing through BAM01.

## CONCLUSION

In this paper, we have proposed a two-cavity mixing scheme to measure the beam flight time and approximate beam arrival time. Moreover, we have compared the typical RF phase BAM detection scheme and the proposed scheme via conducting the experiment. The typical RF phase detection results shows the beam arrival time resolution of 1.05 ps and 968 fs, respectively, while the beam flight time resolution are 37 fs and 66 fs. Both two mentioned experiments are using the same RF front-end and signal acquisition system. Since the reference signal is the key difference of the whole setup, thus it is suspected to have a great jitter which mainly caused by the transiting process. In the near future, more detailed work will be done, such as optimize the RF cables and the environment

of IF signal and signal acquisition system and better results are expected to obtain

## REFERENCES

- [1] Zhao Z, Wang D, Gu Q, *et al.* "SXFEL: A Soft X-ray Free Electron Laser in China", *Journal of Synchrotron Radiation News*, vol. 30, no. 6, p. 29-33, 2017
- [2] Frisch J. "Beam Arrival Time Monitors", in *Proceedings of the 4th International Beam Instrumentation Conference (IBIC2015)*, Melbourne, Australia, 13-17 September 2015. JACOW, Geneva, Switzerland, 2016: 256-262.
- [3] Brachmann, Bostedt C., Bozek J., *et al.*, "Femtosecond operation of the LCLS for user experiments", in *Proceedings of 2010 Particle Accelerator Conference*, Kyoto, Japan, May 2010, paper MOP623, pp. 338.
- [4] Ohshima T, Maesaka H, Otake Y, *et al.*, "Variation of Beam Arrival Timing at SACLA", in *Proceedings of FEL 2012*, Nara, Japan, 26-31 August 2012, paper TUPD36, pp.317-320.
- [5] Han J. H., Hong J. H., Kim C., Yang H., "Bunch Arrival Time Monitor Test at PAL-XFEL ITF", in *Proceedings of 2016 Particle Accelerator Conference*, Busan, Korea, May 2016, MOPMB058, pp.223.

# NEW BEAM LOSS DETECTOR SYSTEM FOR EBS-ESRF

L. Torino\*, K.B. Scheidt, ESRF, 38000 Grenoble, France

## Abstract

In view of the construction and the commissioning of the new Extremely Brilliant Source (EBS) ring, a new Beam Loss Detector (BLDs) system has been developed, installed and tested in the present European Synchrotron Radiation Facility (ESRF) storage ring. The new BLD system is composed of 128 compact PMT-scintillator based BLDs, distributed evenly and symmetrically at 4 BLDs per cell, controlled and read out by 32 Libera Beam Loss Monitors (BLMs). The detectors fast response and the versatility of the read-out electronics allow to measure fast losses with an almost bunch-by-bunch resolution, as well as integrated losses useful during the machine operation. In this paper the different acquisition modes will be explained and results obtained during injection and normal operation will be presented.

## INTRODUCTION

Beam Loss Detectors (BLDs) are an important part of the accelerators diagnostics. They are used during normal operation to identify and locate partial beam losses that may be caused by the malfunctioning of various devices, vacuum leaks, unexpected obstacles, misalignment, and so on. BLDs may be even more relevant during machine commissioning where this kind of problems are recurrent [1].

The European Synchrotron Radiation Facility (ESRF) is a 6 GeV light source, operating in Grenoble for more than 20 years. The facility will undergo through a major update, leading to the new Extreme Brilliant Source (EBS), in which a lower emittance will guarantee a brighter and more coherent x-ray beam [2,3]. The ESRF dismantling phase will start at the very end of 2018, and the commissioning is expected to take place between the end of 2019 and mid 2020.

Since the ESRF storage ring will still be operational until December 2018, several sub-systems which will be later used in EBS, such as the BLD system, are already under test.

The opportunity of having and testing the BLD system on the current machine will not only be a great help for the EBS commissioning, but will also allow to compare levels and loss distributions of the two machine.

## NEEDS FOR THE NEW BLD SYSTEM

In order to fulfill the requirement for EBS, the new BLD system has to be able to detect both “slow” and “fast” losses [1]. This capability depends on the system dynamic range and bandwidth.

Slow losses are unavoidable and are the one that determine the beam lifetime. They are usually confined in some hot-spots and are due to the presence of collimators, scraper,

septa, or other aperture limits. They also depend on the beam size and the population of the buckets, which lead to a deterioration of the Touschek lifetime. The typical time scale for slow losses is in the order of the second.

Fast losses are instead related with accidental effect, or some traumatic events such as perturbation due to injection. These losses can be distributed all around the machine, and can be visible on the single bunch or the single turn time scale.

Another constrain for the new BLD system is the limited amount of space in the EBS machine. For this reason new detectors have to be compact.

These requirements lead to the choice of PMT-scintillator based detectors, read out by a commercial Libera Beam Loss Monitor (BLM) unit [4].

## BEAM LOSS DETECTOR SYSTEM

### Detector

A scintillator-PMT based detector has been chosen for the new BLD system [5].

The BLD has to detect losses generated by the 6 GeV electron beam. When a high-energy electron is lost, it crashes on the vacuum chamber and creates an electromagnetic shower composed by electrons, positrons, and  $\gamma$ -rays. In order to detect showers, a suitable plastic scintillator can be used to convert the energy deposited by particles into visible light, which can then be detected by a commercial PMT.

The scintillator chosen is a EJ-200 rod (100 mm length, 22 mm diameter), wrapped in reflective foil to minimize the light losses. The maximum emission wavelength is 425 nm [6].

The selected PMT is a Hamamatsu H10721-110, with a cathode sensitivity centered in the scintillator emission wavelength, and a 8 mm diameter active area. The PMT requires to be powered by 5 V, and has a 0-1 V control gain [7].

The PMT-scintillator system is enclosed in a metallic casing, and an electronic card has been designed to optimize PMT power supply, gain, and signal connections. The metallic casing is also sealed to provide a first ambient-light isolation. Figure 1 presents a model of the detector.

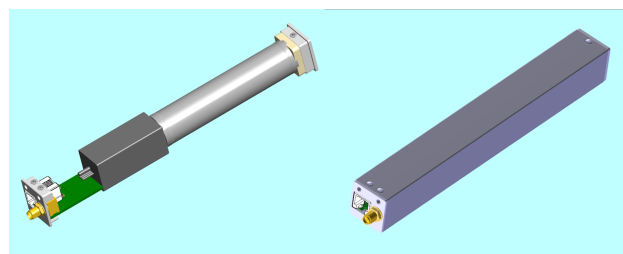


Figure 1: Model of the PMT-scintillator system without and with the metallic casing.

\* laura.torino@esrf.fr

In order to minimize the background signal due to the synchrotron radiation scattered x-rays, each BLD is finally covered by a 3mm lead shielding. To obtain a complete protection from ambient light, a “black hood” is added on top.

## Electronics

The electronics chosen to power and readout the detectors is the Libera BLM unit by Instrumentation Technology [4], which is shown in Fig. 2. Each of these units is able to control 4 different detectors.

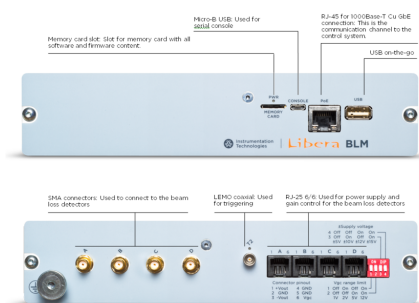


Figure 2: Libera BLM unit.

The Libera BLM is equipped with 4 independent power supplies, each of which provides the 5 V needed for the PMT operation. Four independent 0 to 1 V gain controls are also available. Power and gain are transported to the detector through RJ-25 cables.

The detector output signal can be read either on a 50 Ohm or a 1 MOhm impedance, allowing the detection of both slow (1 MOhm) and fast losses (50 Ohm). Also in this case the choice of the impedance can be done independently for each of the 4 channels.

The integrated ADC has a granularity of 14 bits. To improve the overall dynamic range, and to protect the electronics, the Libera BLMs also allow to select a different attenuation for each channel in the range 0 - 31 dB.

Each unit can be triggered by an external signal to allow the synchronization with the machine clock. The 125 MHz ADC provides a temporal resolution of 8 ns, and the data acquisition can go as fast as 10 MHz. These characteristics, together with the possibility of selecting a 50 Ohm impedance, allow the measurement of fast losses almost to the bunch-by-bunch scale. Some others features, such as the integration over one turn, or the average over several turns, are already embedded in the unit and available.

Slow losses are instead obtained integrating asynchronous data, acquired with an impedance of 1 MOhm over a long period that can also be chosen according to the machine characteristics.

Libera BLM unit can be integrated in the control system by connecting the device through another RJ-25 cable. Tango and Epics graphic control interface are available. The operative system of ESRF is Tango, and a the development of the

device server and of the user application has been followed and customized by Instrumentation Technology [5].

## PMTS CALIBRATION

A very useful feature of the Libera BLM is the possibility of inserting a calibration value dependent on the PMT sensitivity. This allows to obtain data which is independent on the PMTs characteristics and directly comparable.

The general data-sheet of PMTs provides an indicative value for the anode sensitivity, which may vary more then a factor 10 between different units of the same device. For this reason, each PMT comes with a specification paper indicating the real parameters for the given detector.

Moreover the sensitivity of a PMT is not constant over the long term, but may vary depending on the aging of the device.

Finally, the signal intensity also depends on the applied gain. This dependency has also to be taken into account for the data calibration.

To check both the sensitivity and the gain signal dependency of all the PMTs used for the BLD system, and to be able to repeat the calibration anytime, two techniques have been developed at ESRF: one involves the use of a blue LED, and the other a Ce137 radioactive source.

## Anode Sensitivity Measurements

Data from the individual PMT specification papers shows that the average sensitivity given by the manufacturer of the 128 PMTs is 130% larger with respect to the one indicated in the general data sheet, and that the values fluctuate with a standard deviation of about 70%.

The calibration using the blue LED is done in one of the ESRF diagnostics laboratories. A Libera BLM unit is used both to control the PMT, and the LED. A metallic casing has been adapted to host a blue LED on its top. The PMT was positioned in the casing, and the signal obtained with the LED on and a PMT gain of 0.6 V was registered.

A similar procedure has been applied using a radioactive source. This kind of calibration has been performed in-situ, without need of dismantling BLDs or move them from their position inside the tunnel.

The source used is a Ce137 and is brought around the machine and attached to the metallic casing at the high of the scintillator to calibrate the whole detector. 660 keV  $\gamma$ -rays coming from the Cesium decay are converted into visible light in the scintillator and detected by the PMT. The signal produced by the source is measured for an applied gain of 0.7 V.

The average of the results over several PMTs has been used as reference to compare the sensitivity measured in house with the two techniques (arbitrary units), and the one given by Hamamatsu (in A/lm). Both procedures have been performed for all PMTs: results from the comparison between the manufacture sensitivity and the one measured in house are presented in Fig. 3.

A comparison between the sensitivity given by the manufacturer ( $S_H$ ), the one measured with the blue LED ( $S_L$ ), and the Cesium source ( $S_{Ce}$ ) is presented in Fig. 3.

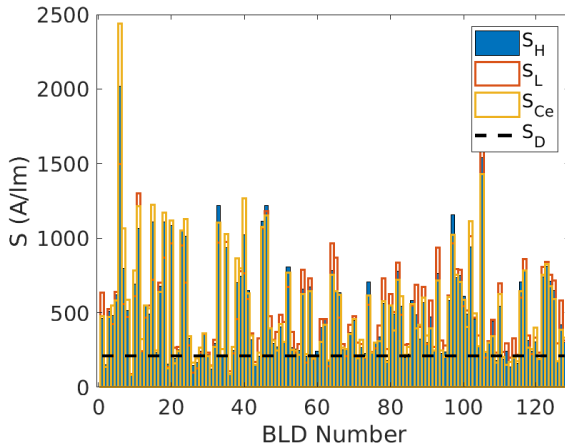


Figure 3: PMTs anode sensitivity provided by the manufacturer ( $S_H$ , blue), sensitivity measured in-house with the blue LED ( $S_L$ , orange), and with a Cesium source ( $S_{Ce}$ , yellow), for all the 128 detectors. The dashed black line is the sensitivity provided by the general data sheet ( $S_D$ ).

The sensitivities measured in house are compatibles with the one provided by the manufacturer: for the LED the average of the ratio  $S_H/S_L$  is 1.06, and the standard deviation is 20%, while for the Ce137 source the ratio  $S_H/S_{Ce}$  is 1.002 with a standard deviation of 12%, as shown in Fig. 4.

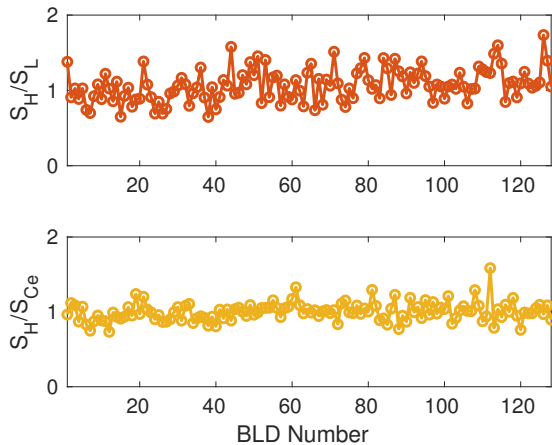


Figure 4: Ratio between the anode sensitivity by the manufacturer ( $S_H$ ), and the one measured with the LED ( $S_L$ , top), and the one between  $S_H$  and the one measured with the Cesium ( $S_{Ce}$ , bottom).

### Calibration application

The calibrated data  $SA_C$  are calculated according to the formula:

$$SA_C = SA \times G \times C \times A; \quad (1)$$

where  $SA$  is the raw data,  $G$  is a value which depends on the applied gain,  $C$  is the inverse of the anode sensitivity, and  $A$  is given by the applied attenuation.

In particular  $G$  ensures Independence of the calibrated signal on the applied gain. It is calculated by taking the ratio of the signal produced by a given light intensity at 0.6 V and the one produced at different gains between 0.3 V and 0.9 V. The result, presented in Fig. 5, is an average of the ratio obtained from all the 128 PMTs. In this case the LED technique has been preferred to the Ce137 source one since it covers the entire gain dynamic range.

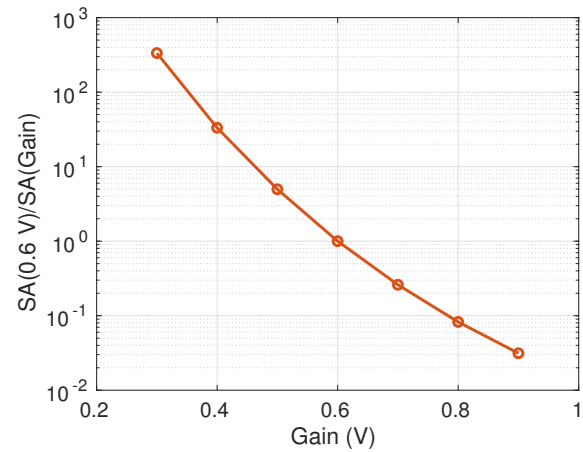


Figure 5: Ratio between the signal ( $SA$ ) produced at 0.6 V and the one at different gains (from 0.3 V to 0.9 V).

## LOCATION

In order to cover all the machine and obtain a consistent loss pattern, 4 detectors have been installed in each of the 32 ESRF cell, for a total of 128 BLDs. Since each Libera BLM can power and readout 4 BLDs, 32 devices have been also installed outside the tunnel.

The position of the BLDs in each cell in both ESRF and EBS is presented in Fig. 6. BLDs are located in such a way that the scintillator is at the same height of the vacuum chamber.

As a general rule, BLDs have to be located close to hot-spots of the machine, such as collimators, and with a regular distribution in the different cells.

In a circular machine, BLDs are usually located on the inner side part of bending magnets: since all sources of particle losses are driven by an energy loss, particles with lower energy entering in a bending magnet will be bent more, and will more likely crash on the vacuum chamber, creating an electromagnetic shower.

The 64 BLDs from the old ESRF system are positioned according to this rule [8], and two of the BLDs of the new system have been located close to the old detectors in order to allow a direct data comparison. Another BLD has been located before the second dipole of each cell, but will be moved on the inner side of a dipole in EBS.



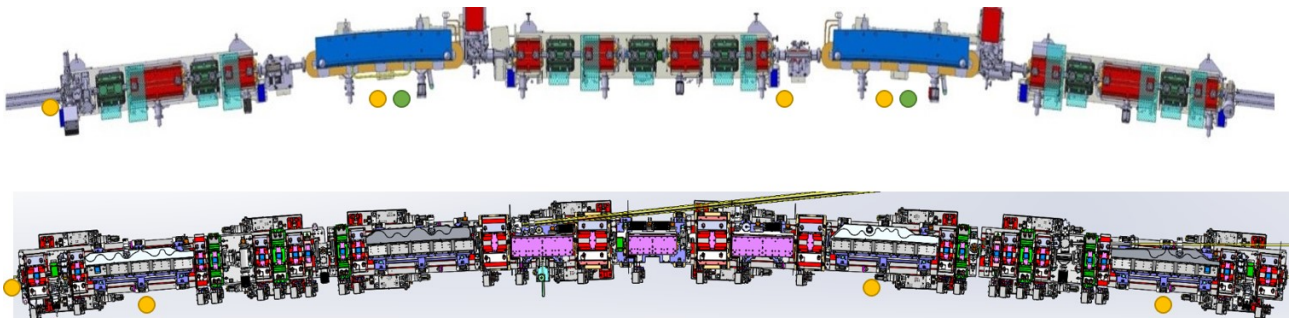


Figure 6: Distribution of BLDs in a cell for ESRF (top) and EBS (bottom). Yellow circles represent the new BLDs and green circles represents BLDs from the “old” system.

Another important part of the BLD system functionality is the monitor losses at the IDs location. The gap of an in-vacuum ID can be closed down to 5 mm, and for this reason the ID magnets are extremely sensitive to the beam losses happening upstream. IDs can in fact block and absorb these losses which may cause demagnetization.

Shielding effects due to IDs gap closure can be monitored using BLDs, and, for this reason, the first detector of each cell has been attached to the vacuum chamber of the straight section, which usually hosts IDs. Vacuum chambers of most straight sections will remain the same both for ESRF and EBS, so BLDs will almost sit in the same position in the two machines and provides comparable data.

## X-RAYS BACKGROUND

The main source of background for beam loss detection, using this particular BLD configuration, is represented by the scattered synchrotron radiation x-rays. The chosen scintillator is in fact sensitive both to charged particles and  $\gamma$ -rays. To avoid false losses reading due to x-rays, the detector has been protected with a light lead shielding.

Tests to find out the sufficient thickness of the shielding have been performed using the machine operating in “minimal losses” condition.

Minimal losses condition can be achieved at ESRF using a 2/3-fill or a uniform filling pattern, at relatively low current ( $\approx 20$  mA or lower) to obtain low-populated bunches, and high vertical emittance. In this situation the beam lifetime is very high ( $> 500$  hours) since Touschek effects are suppressed, and losses are reduced drastically.

In general, the flux of synchrotron radiation depends from the current in the storage ring. To quantify the influence of this background on the BLDs signal, the current has been scraped from 20 to 0 mA, and slow losses from the BLDs have been registered. In minimal losses condition one would expect to see no or very weak dependency of the beam losses from the current. If this is not the case, the signal is mainly due to the scattered x-rays background.

Tests has been performed using 2 or 3 mm Pb shielding to protect the detectors. An example of the result is presented in Fig. 7: a strong dependence of the registered losses from the beam current is observed when using 2 mm of lead. In

this case the effect of the losses provoked by the scraping of the beam to reduce the current is comparable with the one measured in decay mode due to x-rays. The lifetime when not scraping has always been larger than 500 hours, so this behavior of the losses cannot be related with other effect than x-rays scattering. This background is strongly attenuated when using one extra mm of lead. In this case losses due to the scraping are much stronger with respect to the background signal observed in decay mode.

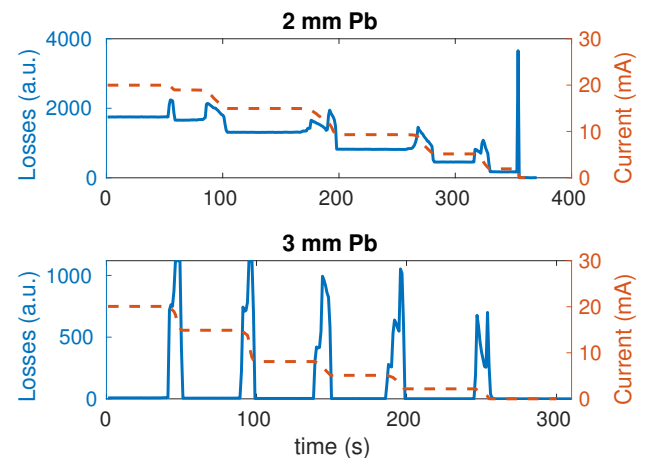


Figure 7: Beam losses (blue) measured when scraping the current (orange) from 20 to 0 mA. A strong dependency on the current is observed when using 2 mm (top), while the dependency is attenuated when using 3 mm (bottom).

These tests show that 3 mm lead shielding is enough to reduce the background due to synchrotron radiation scattered x-rays, and all the 128 BLDs have been equipped accordingly.

## COMPARISON BETWEEN NEW AND OLD SYSTEM

The advantage of having an overlap between the old and new BLDs system consists in the possibility of a direct comparison between data obtained by the two independent setups.

Data from a 20 to 0 mA scraping has been registered both with the new and the old BLD systems. A scaling factor

Content from this work may be used under the terms of the CC BY 3.0 licence (© 2018). Any distribution of this work must maintain attribution to the author(s), title of the work, publisher, and DOI.

has to be applied in order to have comparable results. An example of losses is presented in Fig. 8. Detectors are bot PMT-scintillator based, and are located at about 50 cm one from each other. Losses have the same temporal evolution, and the same amplitude, proving the correct behaviour of the new BLDs system.

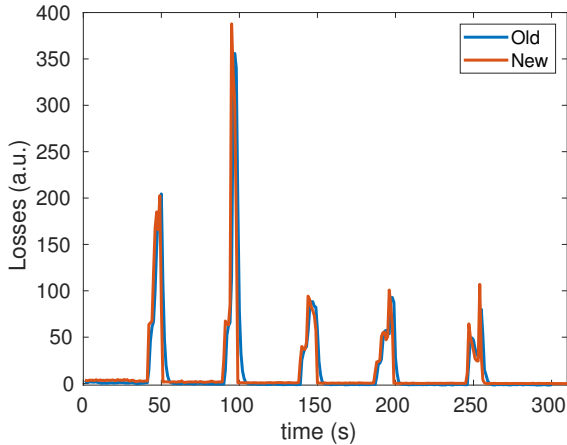


Figure 8: Comparison of losses registered during a scraping from 20 to 0 mA from an old (blue) and a new (orange) BLD.

### BLD SYSTEM OPERATION

After having the 128 BLDs mounted, calibrated, and tested, the system has been put in operation at ESRF. A software application has been developed to easily monitor the loss distribution and to control all detectors from the control room. A screen-shot of the Graphical User Interface (GUI) is presented in Fig. 9.

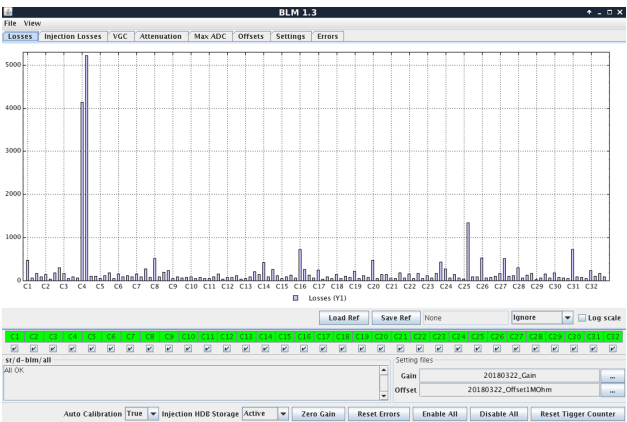


Figure 9: Application gui: slow losses are displayed during decay mode.

### Auto-Gain

The application also controls an “Auto-Gain” routine, which automatically reduces the PMT gain, or increase the Libera BLM attenuation, when the signal is close to saturation.

Since the data are calibrated, the saturation level is different for each BLD. For this reason look-up tables providing the saturation level for each gain, and each BLD have been created as reference.

### Operation Mode

Two different modes are available to measure loss during the user operation. The first measures the slow losses during the decay mode, and the other registers fast losses at the injection. Data are stored and are available for consultation and post-processing.

**Decay Modes** During the machine decay time, slow, asynchronous losses are registered at a 1 Hz rate. To do so the Libera BLM impedance is set on 1 MOhm, and the decimation level is set to 17 in order to integrate over  $\approx 130.000$  turns. Being the revolution period of ESRF storage ring roughly 3  $\mu$ s, the total integration time per acquisition is about 0.4 s.

The loss distribution is in general quite stable, specially when the machine is working correctly. Vacuum behaviour, emittance blow-ups, or the motion of some ID-gaps can induce changing in the loss distribution. Having all this data archived helps to correlate anomalous losses with one of these events.

An example of identification and localization of losses is presented in Fig. 10 and in Fig. 11. Figure 10 shows the slow losses registered by all the 128 BLDs (vertical), over 10 minutes (horizontal). The evolution looks regular, apart at about 240 s after the starting point, where some perturbations appear starting from the BLD 87 and continuing after. Figure 10 shows the detail of BLD 87, corresponding to the BLD located in Position 4 (second dipole) of Cell 22. An analysis of the vacuum in the downstream part of this Cell shows a vacuum burst exactly at the same time of the losses, which has then been recognized as the cause.

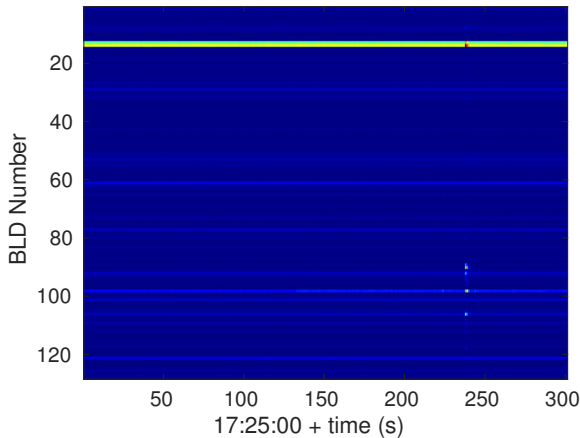


Figure 10: Temporal evolution of all the BLDs. Around BLD number 87 (Cell 22, Position 4), and time  $\approx 240$  s some strange behaviour appears.

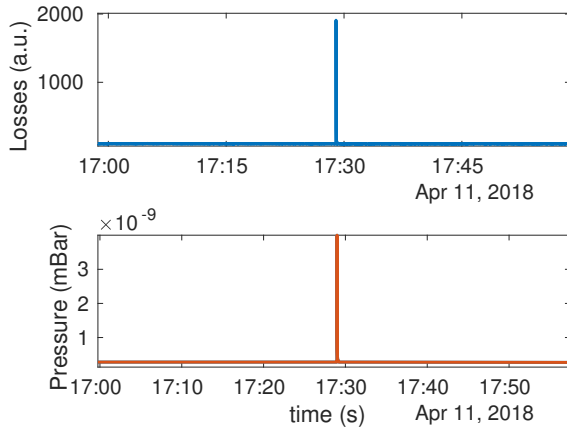


Figure 11: Correlation between unexpected losses seen by BLD 87 (Cell 22, Position 4), and the vacuum measurement in one of the penning gauge of Cell 22.

**Injection Mode** When linac and injection kicker are on, the BLD system switches automatically to injection mode. During this phase more losses are generated, and to avoid the saturation of the BLDs fast losses are registered. The Libera BLM impedance is set to 50 Ohm, and the so called “average mode” is enabled. This mode allows to register the average of a given number of turns. In particular at ESRF, the average decimation number is set to 2, in order to obtain the average of 4 turns. Finally the integration of a buffer of 10 samples is registered.

Data are synchronous with the injection in the storage ring, with a repetition rate of 4 Hz, and are also stored at the same rate.

Injection losses are useful to study the status of the injection system and the perturbation induced. Figure 12 presents an injection during the 7/8+1 operation mode (7/8 of the storage ring filled uniformly, and a single bunch in the gap). During this mode the injection sequence foresees first the injection of two bunches, then of 4 to fill the main train, and finally of 1 bunch to fill the single bunch. This can be seen both in the injection losses evolution and in the booster end current measurement. Data from one of the BLDs and from the booster current transformer are well correlated in time.

## APPLICATIONS

Apart from operational purpose, the new BLD system has several capabilities which will be useful for the EBS commissioning and other studies.

### Turn-by-Turn Losses

Turn-by-Turn (TbT) losses are obtained enabling the “Sum” mode of the Libera BLM. Considering that the BLM ADC sample is 8 ns and that the revolution period of ESRF is 2.816  $\mu$ s, the decimation sum has to be set to 352 to integrated over the losses produced in one turn. Being fast and synchronous losses, the impedance has to be set to 50 Ohm and the Libera BLM has to be triggered.

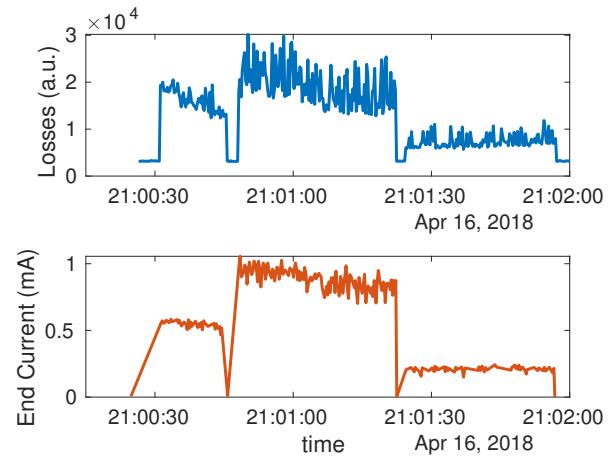


Figure 12: Correlation between losses at the injection registered from one of the BLDs (blue, top), and the one of the booster end current registered by the current transformer (orange, bottom).

TbT losses will be useful during the early part of EBS commissioning, when they will complement data from BPM.

As an example TbT data, taken during the injection in the storage ring with the RF off, is presented in Fig.13. Data show that the beam is lost after about 60 turns, and that the bigger amount of the losses is concentrated in the BLD number 100 (corresponding to the position 1 of Cell 26).

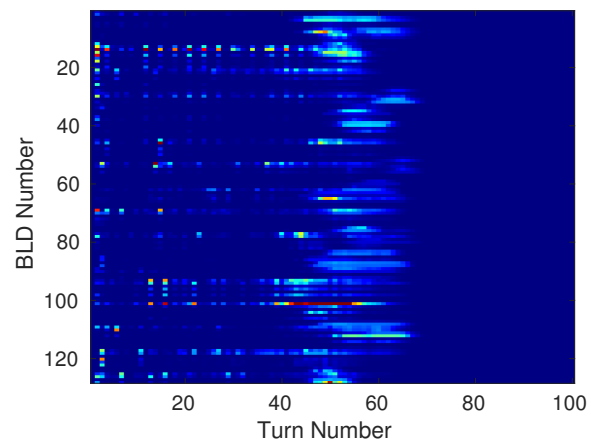


Figure 13: TbT losses with RF off. The beam preforms about 60 turns and is lost mainly close to BLD number 100 (Cell 26, position1).

### Almost Bunch-by-Bunch Losses

ADC Losses provides data with a resolution of 8 ns. These are useful to observe phenomena almost at the bunch scale.

Also in this case the impedance has to be set to 50 Ohm and the Libera BLM has to be triggered to obtain synchronous data.

A typical example of bunch-by-bunch losses is given by the losses registered during an injection in “short pulse”

mode, presented in Fig. 14 for one of the BLDs during 4 turns. In this specific example, five bunches are injected in the storage ring. Vertical grey lines in the plot represent a revolution period. After one revolution period from the trigger signal, bunches enter in the storage ring and loose some particles during the first turn, though most of the losses appear during the second turn. Not all the bunches have the same quantity of losses, this may depends on the population of the injected bunches, or on the shape of the extraction pulsed-magnet pulse.

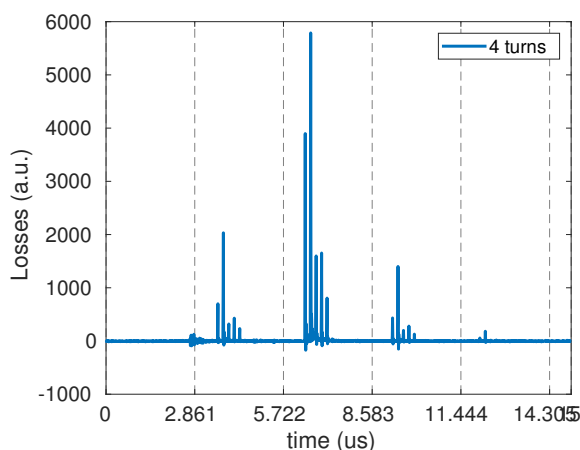


Figure 14: ADC losses during an injection of five bunches. Vertical grey lines indicate the turns. The injection happens during the second turn when some losses are registered, most of the losses appears in the second turn. Not all the bunches show the same losses.

## OUTLOOK

A new BLD system is now operational to measure the losses at the ESRF storage ring. The components of the system, their characterization and the final operation applications have been presented in this proceeding. The capability of the system to measure slow and fast losses and to monitor the behavior of the machine have been proven. The new BLD system and the application developed will be installed and intensively used during the commissioning and the normal operation of the future EBS machine.

## ACKNOWLEDGMENTS

Authors would like to thanks N. Benoist and F. Taoutaou for the support with the mechanical design of the BLDs casing and support, and with the installation of the devices. Many thanks also to J.L. Pons for the development of the ESRF software application, and to P. Colomp and the safety group for the calibration with the radioactive source. Strong inputs has been received from the IDs groups which also deserve a special mention. Many thanks to the operation group for the collaboration and the machine dedicated time. Finally thanks to P. Leban for the support from Instrumentation Technology

## REFERENCES

- [1] K. Wittenburg, “Beam loss monitors”, in *Proceedings of the CERN accelerator school*, pp. 249, 2009.
- [2] *ESRF Upgrade Programme Phase II (2015-2022) - Technical Design Study*, [http://www.esrf.fr/Apache\\_files/Upgrade/ESRF-orange-book.pdf](http://www.esrf.fr/Apache_files/Upgrade/ESRF-orange-book.pdf)
- [3] J.L. Revol *et al.*, “Status of the ESRF-extremely brilliant source project”, in *Proc. 9th International Particle Accelerator Conference (IPAC’18)*, Vancouver, BC, Canada, 2018, pp. 2882–2885. doi:10.18429/JACoW-IPAC2018-THXGBD3
- [4] *BLM: beam loss monitor readout electronics*, <https://www.i-tech.si/accelerators-instrumentation/libera-blm/functionalities>
- [5] K. B. Scheidt, F. Ewald, and P. Leban, “Optimized beam loss monitor system for ESRF”, in *Proc. of International Beam Instrumentation Conference (IBIC’16)*, Barcelona, Spain, Sep. 2016, pp. 86–89. doi:10.18429/JACoW-IBIC2016-MOPG20
- [6] *General purpose EJ-200, EJ-204, EJ-208, EJ-212*, <https://eljentechnology.com/products/plastic-scintillators/ej-200-ej-204-ej-208-ej-212>
- [7] *Hamamatsu photosensor modules H10720/H10721 series*, [https://www.hamamatsu.com/resources/pdf/etd/H10720\\_H10721\\_TPM01062E.pdf](https://www.hamamatsu.com/resources/pdf/etd/H10720_H10721_TPM01062E.pdf)
- [8] B. Joly *et al.*, “Beam loss monitors at the ESRF”, in *Proc. DIPAC 1999*, Chester, UK, paper IT03, pp. 3–6.



# RadFET DOSE MONITOR SYSTEM FOR SOLEIL

N. Hubert<sup>†</sup>, F. Dohou, D. Pédeau, Synchrotron SOLEIL, 91192 Saint-Aubin, France

## Abstract

SOLEIL is currently testing new dose measurement monitors based on RadFET transistors. This new monitor at SOLEIL will provide a measurement of the dose received by equipment that are damaged by the radiations in the storage ring, in order to anticipate their replacement. This monitor should be very compact to be placed in tiny areas, sensitive to all kind of radiation and low cost to install many of them around the ring. A readout electronic module is being developed in-house, and a first prototype has been built and installed on the machine. Description of the system and first results recorded on the machine are presented here.

## INTRODUCTION

After more than ten years of operation, SOLEIL pieces of equipment in the storage ring are damaged by radiations. The damage level is strongly dependent on the tunnel localization [1]. In order to have a better knowledge of the deposited dose, and to anticipate the replacement of the equipment, a dose monitor system has to be deployed around the storage ring.

This system must:

- Have a compact sensor that can be installed as close as possible to the equipment, and sometimes in tiny areas.
- Be sensitive to all kind of radiation, including X-rays since we know that in some particular locations X-rays are responsible of damages.
- Be low cost to be able to deploy a large number of sensors around the ring.

RadFET sensors, which have already been used with success by the accelerator community [2, 3], fit those specifications. SOLEIL has tested one kind of RadFET during the last months. A dedicated multiplexed electronics has been designed to periodically and automatically read the dose measurements.

## RADFET SENSORS

### Description

RadFET are Metal Oxide Semiconductor Field Effect Transistors (MOSFET), optimized for radiation sensitivity. When ionizing radiations go through the gate oxide layer, they generate pairs of electron-hole, leading to a permanent modification of the layer with trapped positive charges (Fig. 1). As a consequence, the threshold voltage of the transistor is modified. The voltage shift depends on the amount of radiation that hits the device. By measuring the threshold voltage shift (forcing a fixed DC current in the device), the dose received by the RadFET can then be deduced.

<sup>†</sup> nicolas.hubert@synchrotron-soleil.fr

RadFETs are sensitive to all kind of radiations (X-rays, gamma, electrons...). They give a measure of the total integrated dose received.

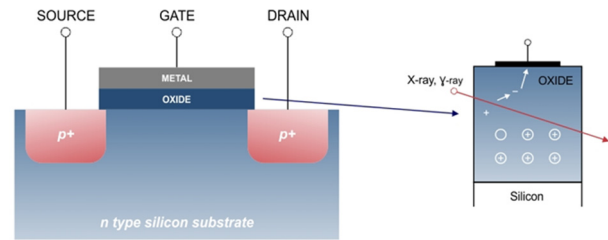


Figure 1: RadFET schematics (source Tyndall).

RadFETs used at SOLEIL are provided by Tyndall Works and manufactured by Tyndall National Institute in Ireland [4]. The TY1004 chip embeds two identical RadFETs with a gate oxide thickness of 400 nm. The active area (gate oxide surface) is very small: 300 μm by 50 μm.

### Calibration

RadFETs TY1004 are given for a measurement range from 1 rd to 100 krd (1 cGy to 1 kGy). Since their response is non-linear with the deposited dose, calibration curves are provided by the manufacturer to retrieve the dose value from the measured voltage shift  $\Delta V$  according to the following formula:

$$\Delta V = A * Dose^B$$

The A and B coefficients are obtained exposing one RADFET to discrete dose values using a Co60 source (see Fig. 2). It is then assumed that all RADFETs of a same batch follow the same calibration curve.

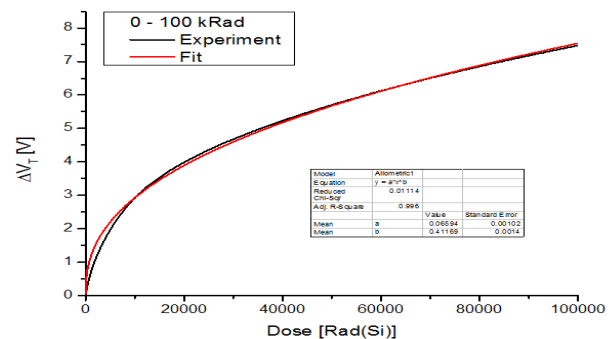


Figure 2: Calibration curve for dose range 0 – 100 krd / 1 kGy (Source: Tyndall).

A and B coefficients are not constant over the full measurement range. This is why a set of coefficients is given depending on the dose range (Table 1).

Table 1: Calibration Coefficients (Source: Tyndall)

Dose Range	A	B
0 – 1 kRad	0.0014	0.8900
0 – 5 kRad	0.0052	0.6976
0 – 10 kRad	0.0090	0.6306
0 – 50 kRad	0.0478	0.4438
0 – 100 kRad	0.0659	0.4117

### Sensitivity

The sensitivity of the RadFET to irradiation depends on:

- The gate oxide layer thickness: the sensitivity increases with the thickness of the gate oxide layer [5].
- The gate bias: by applying a constant DC voltage on the gate the electron-hole generation process is improved and following, the sensitivity of the device. Nevertheless, this improvement of the sensitivity is done to the detriment of the measurement range.

In our case the thickness is fixed at 400 nm (by design), and we do not want to reduce the maximum possible measured dose value. Gate biasing is therefore not used, and all pins are grounded during irradiation.

### Operating Modes

In order not to modify the sensitivity of the RadFET, the readout of a RadFET should be avoided during irradiation. As a consequence, RadFET sensors have two modes of operation:

- An exposure mode for which all pins are grounded.
- A readout mode for which a fixed current is forced between ground and source. This is preferably done without irradiation (no beam) or punctually during short time. We use the same current value (10  $\mu$ A) than the one used during calibration by the manufacturer. This is the current giving the minimum temperature dependence of the threshold voltage.

## READOUT ELECTRONICS

A dedicated electronics has been designed to perform the acquisition of the RadFET and to control the two modes of operation described previously. This electronics allows automatic and periodic measurements. For cost efficiency, a multiplexing system gives the possibility to connect up to seven RadFETs on a single reader.

### Acquisition

The acquisition (among other tasks) is performed by a Red Pitaya board [6]. One of the two 14 bits ADCs is used in the extended range configuration ( $\pm 23$  V) providing a resolution of 2.8 mV (2 rd). The input impedance being of the same order of magnitude than the one of the RadFET (at 10V threshold), a unity gain buffer amplifier has been added in front of the Red Pitaya input.

This board was easily integrated into our Tango control system by embedding the generic Tango device server on the ARM processor.

### Current Source

A DC stable current source is needed to provide the 10  $\mu$ A to the RadFET accordingly to the manufacturer calibration data. The terminal adjustable current source LM334 from TI has been selected for its good stability. It gives the possibility (if needed) to cancel the thermal effects, even if the stability records in the lab revealed that it wasn't necessary for our need: the 24 hours stability is indeed below 7 pA rms (Fig. 3). The amplitude of the current provided by the source can be easily adjusted by a potentiometer knob on the front panel. This value is continuously monitored by the second ADC of the Red Pitaya when the RadFETs are not being read.

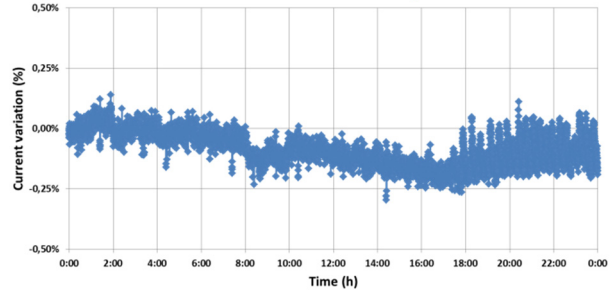


Figure 3: Stability (in % of variation) of the DC 10  $\mu$ A current source over 24 hours.

### Multiplexing

To be able to read several RadFETs with the same readout module (and minimize the costs), a multiplexing scheme has been set up. It is based on double poles power relays, and allows to switch the reading from one RadFET to the other on the same chip, or to switch from one chip to the other. The 16 digital I/Os from the Red Pitaya that is performing the acquisition are used to drive the relays through photocouplers for isolation and voltage adaptation (from 3.3V to 24V). One electronic module is thus able to read 7 chips, that is to say 14 RadFETs (Fig. 4).

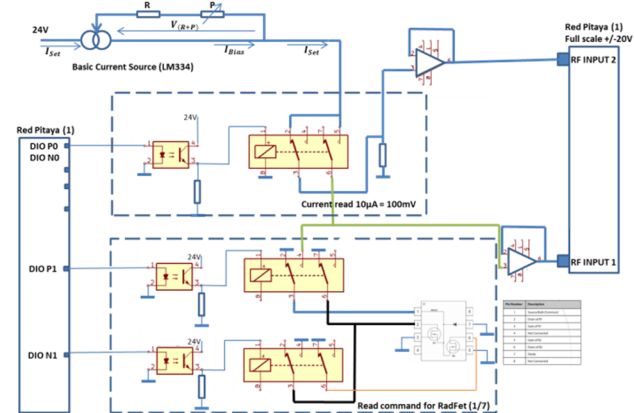


Figure 4: Simplified schematic of the RadFET readout electronics.

### Mechanical Integration

The different elements (power supply, Red Pitaya and PCB for multiplexing and current source) are integrated

into a 2U 19" crate, with a set of diodes on the front panel to know if and which RadFET is being read (Fig. 5)

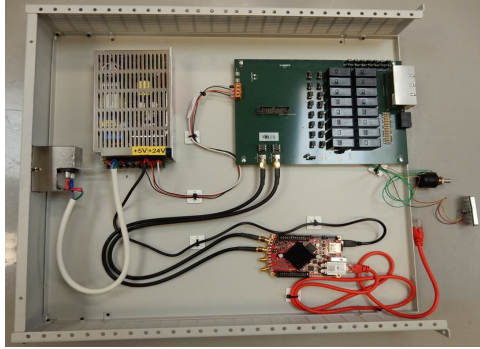


Figure 5: RadFET Electronic rack.

The chip is mounted on a small PCB equipped with a RJ45 connector (Fig. 6). The resulting size is 18x32x15 mm making the device very easy to install on the machine even in confined areas. If it is required, the chip and the cables can be soldered directly on the PCB to reduce further the thickness.

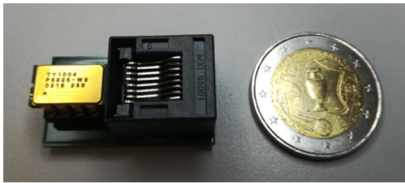


Figure 6: RadFET chip mounted on its PCB with RJ45 connector.

## FIRST MEASUREMENTS WITH BEAM

### CCD Survey

The first location where RadFETs have been installed is in the optical box of the two pinhole cameras (Fig 7). Indeed, despite appropriate shielding, the CCD camera installed in cell 02 shows a significantly faster degradation (to be replaced every year) compared to the one in C16 (although very close to the injection section).

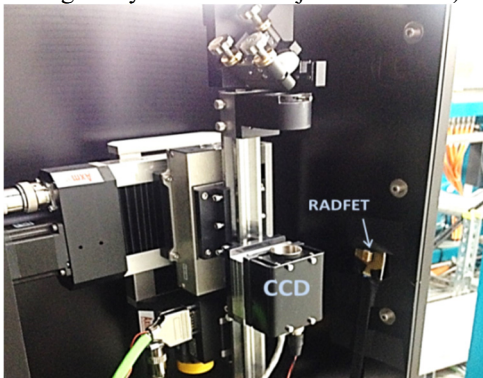


Figure 7: RADFET installed in the C02 pinhole camera optical box to monitor the dose received by the CCD camera.

The two RadFETs on a same chip give dose values that are in very good agreement. Measurements showed that the recorded dose in the optical boxes is linear with the integrated current in the machine and is not correlated to

beam losses. It also confirmed that the dose received in the C02 optical box is three times higher than in C16 (Fig. 8).

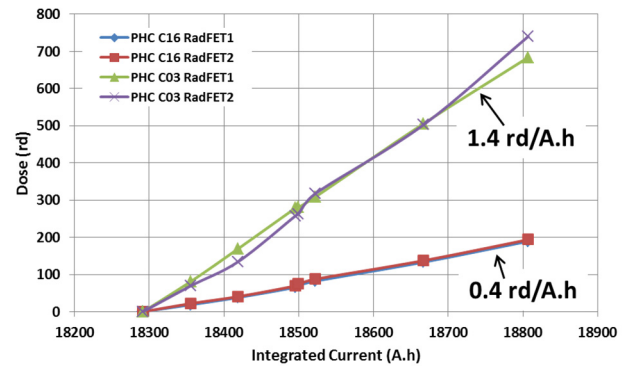


Figure 8: Dose measurement in the pinhole camera optical boxes confirming that the CCD in C02 is more exposed to radiation than the one in C16.

Recently, and for independent reasons, the pinhole crotch absorber has been modified (reduced horizontal aperture) and the optical box realigned. Since then, RadFET measurements show a drop in the dose rate inside the box (Fig. 9). Likewise, the new CCD camera installed at the same time in the box is not damaged as fast as the previous ones. We suppose that part of the X-rays where hitting an unexpected element in the box creating reflected or secondary emitted X-rays.

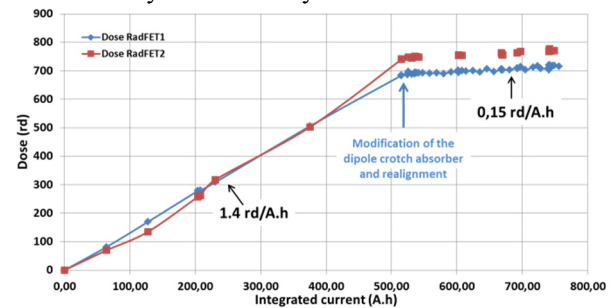


Figure 9: Dose measurement in the C02 pinhole camera optical box. The change in the slope is correlated with modification of the upstream crotch absorber (reduced aperture) and a realignment of the box.

### Insulator Survey

SOLEIL equipment located around aluminium vacuum chambers located downstream dipoles are suffering from radiation with faster damages compared to other locations. In particular, cable insulators that become brittle and backing film glue that is reduced to dust, have to be replaced periodically (Fig. 10). The radiation at those locations consists of X-rays that originate from the interception of synchrotron radiation from upstream dipole by the vacuum chamber. When the vacuum chamber is in aluminium, X-rays are not damped significantly (compared to other materials like stainless steel or copper).



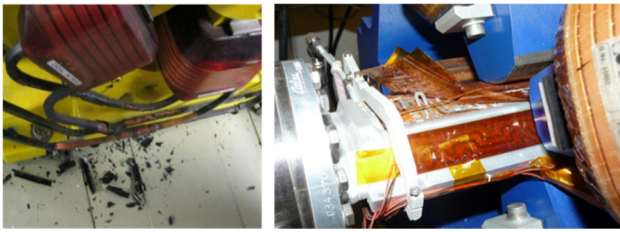


Figure 10: Damages caused by radiation around aluminium vacuum chamber located downstream bending magnets.

A set of 5 RadFETs have also been installed in cell 03: two on BPM cables (Fig. 11) (one upstream and one downstream a dipole), one close to damaged sextupole insulators, and two on the tunnel wall (on internal and external side of the machine).

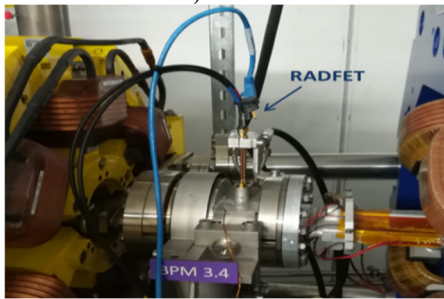


Figure 11: RadFET installed on BPM cables downstream bending magnet.

Here again, the measurements are in very good accordance with the damages observed on the machine, with a very high dose deposition (20 krd/A.h) nearby the aluminium vacuum chamber downstream bending magnets whereas doses recorded upstream the dipole (0.4 rd/A.h) or on the wall (24 rd/A.h) are more reasonable (Fig. 12).

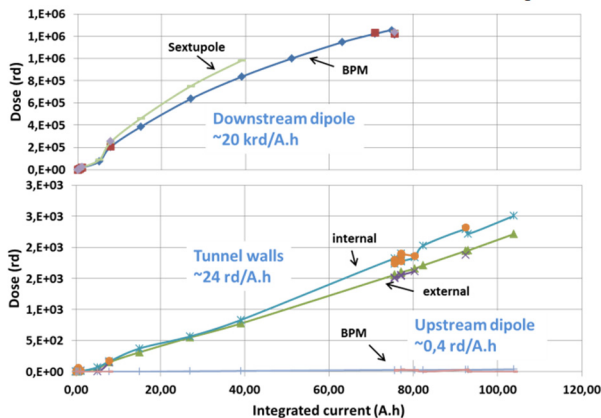


Figure 12: Doses recorded by RadFET sensors in C03.

Nevertheless absolute dose values recorded in this case with X-ray radiation are probably overestimated since the RadFET sensitivity is not the same for X-rays and gamma-rays, whereas the calibration has been done with a gamma source. Measurements made in 2013 [1] with Gafchromic films showed a dose rate a factor two lower (9.4 kRad/A.h). A dedicated calibration of the RadFETs for X-rays will be done in the future.

## Fading

Spontaneous electron-hole annealing in the RadFET degrades the threshold voltage when irradiation stops. This fading effect has been measured on two RadFETs exposed at ~11 krd below 3% during the 4.5 weeks after the stop of irradiation (Fig. 13). This decay is small enough to avoid any compensation of the fading.

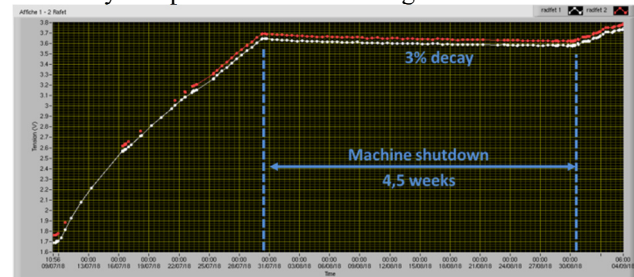


Figure 13: Fading measurement.

## CONCLUSION

RadFET sensors have been tested and used with success at SOLEIL to monitor the deposited dose around equipment damaged by radiations. The dependence of the calibration curves with respect to the type of irradiation (X or gamma) has to be measured.

A dedicated electronics has been designed and a prototype tested to read up to 7 RadFET chips. The low cost of this system will give us the possibility to install several monitors in every cell of the storage ring depending on our needs.

## ACKNOWLEDGEMENTS

The authors would like to warmly thank Aleksandar Jaksic from Tyndall and Lars Froehlich from DESY for useful discussions about RadFET. We are also grateful to Monique Taurigna from LAL for the development of the Red Pitaya Tango device server.

## REFERENCES

- [1] N. Hubert *et al.*, "Radiation Damages and Characterization in the SOLEIL Storage Ring", in *Proc. International Beam Instrumentation Conf. (IBIC'13)*, Oxford, UK, Sep. 2013, pp. 644-647.
- [2] F. Schmidt-Foehre *et al.*, "A New Embedded Radiation Monitor System for Dosimetry at The European XFEL", in *Proc. International Particle Accelerator Conf. (IPAC'11)*, San Sebastian, Spain, pp. 2364-2366.
- [3] L. Fröhlich *et al.*, "Instrumentation For Machine Protection at FERMI@ELETTRA", in *Proc. Diagnostics International Particle Accelerator Conf. (DIPAC'11)*, Hamburg, Germany, pp. 286-288.
- [4] Tyndall Works, <http://www.tyndallworks.com/>.
- [5] M. Pejovic, "P-Channel MOSFET as a Sensor and Dosimeter of Ionizing Radiation", *Electronics and Energetics*, vol. 29, no. 4, p. 509-541, Dec. 2016, doi:10.2298/FUEE1604509P
- [6] Red Pitaya, <http://www.redpitaya.com/>.



# THE EUROPEAN XFEL BEAM LOSS MONITOR SYSTEM

T. Wamsat\*, T. Lensch

Deutsches Elektronen-Synchrotron DESY, Hamburg, Germany

## Abstract

The European XFEL MTCA based Beam Loss Monitor System (BLM) is composed of about 470 monitors, which are part of the Machine Protection System (MPS). The BLMs detect losses of the electron beam, in order to protect accelerator components from damage and excessive activation, in particular the undulators, since they are made of permanent magnets. Also each cold accelerating module is equipped with a BLM to measure the sudden onset of field emission (dark current) in cavities. In addition some BLMs are used as detectors for wire-scanners. Experience from the already running BLM system in FLASH2 which is developed for XFEL and tested here, led to a fast implementation of the system in the XFEL. Further firmware and server developments related to alarm generation and handling are ongoing.

The BLM systems structure, the current status and the different possibilities to trigger alarms which stop the electron beam will be presented.

## INTRODUCTION

The Beam Loss Monitor (BLM) system at the European XFEL is the main system to detect losses of the electron beam, thus to protect the machine hardware from radiation damage in particular the permanent magnets of the undulators. As part of the Machine Protection System (MPS) [1] the BLM system delivers a signal which stops the electron beam as fast as possible in case the losses get too high.

In addition, there are Beam Halo Monitors (BHM) [2] in front of the beam dumps using the same digital backend as the BLM electronics.

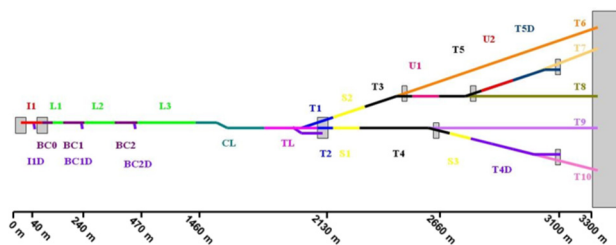


Figure 1: Section overview of the European XFEL accelerator [3].

About 470 BLMs are installed along the XFEL Linac which schematically is shown in Fig. 1. The BLMs are positioned at locations near the beamline, where losses can be expected or where sensitive components are installed, thus most of the BLMs are installed in the undulator area (see Table 1). Since even a big number of BLMs cannot

provide a complete survey of losses, there is also a toroid based Beam Current Monitor system [4] installed, which provides transmission interlock system to stop the beam if too much charge gets lost along the machine. Also each superconducting accelerating module is equipped with one BLM at the end to detect the field emission produced by cavities (Correlation work still ongoing, no paper available yet).

Table 1: BLM Distribution

Section	#
II, BC0	24
BC1	18
BC2	23
L1, L2, L3 (field emission)	98
CL, TL	71
S1, T4	80
S3	48
T4D	10
S2, T3	80
U1, T5, U2, T5D	20

Some selected BLMs are also used as additional detectors for wire scans [5].

## SYSTEM OVERVIEW

The hardware consists of the BLM devices, a dedicated Rear Transition Module (RTM) in combination with the DESY Advanced Mezzanine Card DAMC2. Furthermore a MPS card is required for alarm output collection.

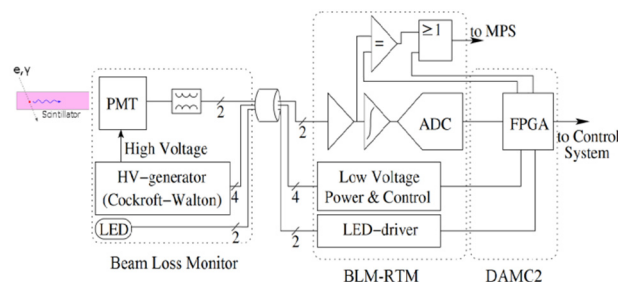


Figure 2: BLM system scheme.

The BLM includes either an EJ-200 plastic scintillator or a SQ1 quartz glass rod. The latter are used mainly in the undulator intersection. In contrast to scintillators, that are also sensitive to hard x-rays, the Quartz rods work with Cherenkov effect, that is sensitive to particle loss only.

The high voltage for the photomultiplier (PMT) is generated within the BLM, so no high voltage cables are needed (see Fig. 2), just a CAT 7 cable with RJ-45 connectors is used. A LED can be switched on within the

\* thomas.wamsat@desy.de

BLM to provide test pulses to check if the PMT is still working.

In addition to the digital processing chain implemented in the FPGA, there is a simple comparator circuit, which is operating completely independent from infrastructure signals like clocks, triggers and even timing.

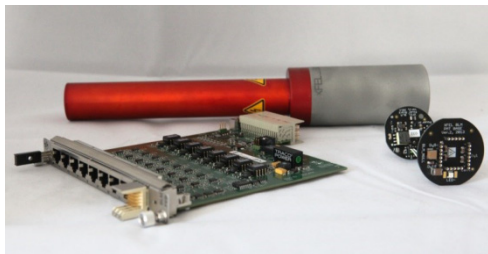


Figure 3: BLM, BLM-RTM and BLM circuit boards, PMT base and high voltage generator.

The BLM-RTM (see Fig. 3) provides 8 channels and includes the analog signal processing plus a 45 MHz 14 bit ADC and also the analog comparator circuit for backup alarm generation. Dedicated servers on each MTCA Crate CPU integrate the firmware into the DESY control system.



Figure 4: MTCA Crate RTM side with BLM-RTMs.

There are about 80 uTCA Crates for diagnostics distributed along the machine in the tunnel where 58 of them are equipped with BLM hardware like shown in Fig. 4.



Figure 5: BLMs in undulator section (S1).

The BLMs are mounted as close as possible to the beam pipe like shown in Fig. 5.

## SYSTEM FEATURES

Each BLM is configurable individually. The control voltage for the PMT, the starting point and length of the test LED signal can be set and switched on or off and a test signal for the MPS can be provided. Indicated readouts are the set control voltage for the high voltage generator in the BLM, the result and generated high voltage and its current consumption (see Fig. 6). The value for the PMT pedestal is calculated by the firmware before the bunch train starts and subtracted from the displayed ADC output to remove the analog signal offset at the indicated plot.

There are different configurable alarms which can be used to cut the bunch train. The so called single alarm, multi alarm, integral alarm, comparator alarm and additional a not cutting single2 alarm. Each kind of alarm increments a dedicated Slow Protection alarm counter. The alarms are explained in the following.

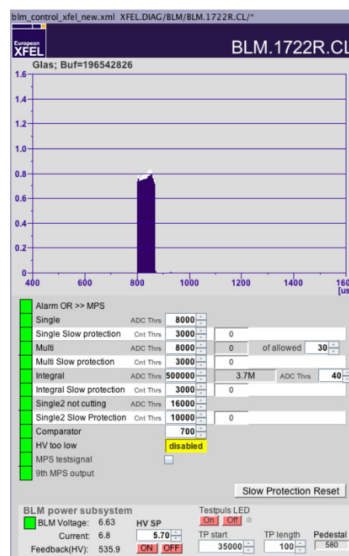


Figure 6: BLM panel in the XFEL control system, 300 bunches @ 4.5 MHz.

### Kind of Alarm Generation

#### Single

Triggers, as soon as the set limit is exceeded  
 Y-axis scaled to this value → amplitude of 1 → alarm threshold reached

#### Multi

Needs two terms to trigger:

1. Signal exceeds threshold
2. Number of allowed pulses over threshold reached

#### Integral alarm

Triggers if the number of integrated samples exceeds threshold

#### Single2 not cutting

If the Single2 threshold is passed, it does not send an alarm but the Slow Protection Counter increases

#### Comparator alarm

Analog backup, threshold is chosen thus it triggers a little bit above single threshold

## HV tracing alarm

When the high voltage gets to low so the PMT cannot work properly it causes a permanent alarm, can be disabled

## Slow Protection alarms

Counts recurrent alarms from macropulse to macropulse, if alarm is gone the counter decreases. When number of recurrent alarms is exceeded it causes a permanent alarm → no beam possible; reset by operator is needed, switches back to single bunch operation

Each alarm kind has its own individual Slow Protection counter threshold

## MPS test signal

Can be activated to test BLM alarm response easily

The 9<sup>th</sup> MPS output is triggered if a Slow Protection Alarm is generated. This is an additional alarm line which summaries all eight channels of one BLM-RTM.

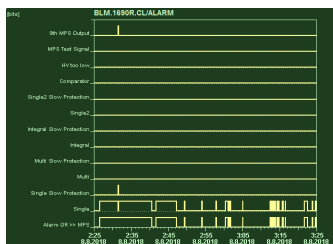


Figure 6: BLM alarm history plot.

The BLM software provides an alarm history of each BLM (see Fig. 7). It can be shown by clicking on the left alarm indicator column.

The maximum latency of the complete system BLM, MPS and Laser controller to switch off the electron beam is about 28  $\mu$ s, so up to 130 bunches at the highest possible bunch repetition rate of 4.5 MHz will be transported through the machine before the laser can stop beam production.

In case of intentional losses, for example using the Transverse Deflecting Structure [6] or of axis screens for emittance measurements [7], the BLM system can mask the alarm output for dedicated bunches.

## BLM Operating

There are different panels to observe beam losses in the machine. Two main panels are the “BLM & Toroid alarm overview” and the “BLM overview” panel.



Figure 7: BLM and Toroid alarm overview panel.

Figure 8 shows all BLMs and Toroids which can stop the electron beam. By clicking on one BLM the panel shown in Fig. 5 will open. Also the BLMs are included on this panel as for operating they act like a BLM since they even use the same RTM and firmware.

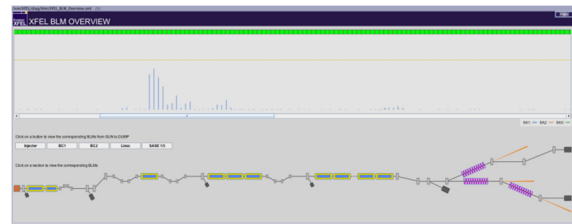


Figure 8: Actual maximum amplitudes of each BLM.

The panel shown in Fig. 9 displays the maximum amplitude of each BLM, this is used during setup to observe the result and loss change. The dotted line indicates the headroom before reaching the most sensitive alarm threshold.

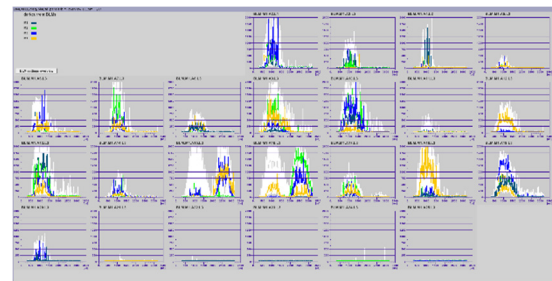


Figure 9: Signals of field emission produced by the RF in the superconducting modules as seen by the BLMs. Four BLM signals are shown in one plot. White areas indicate a kind of signal history: In this case one can see that the RF pulse was shifted off beam (delayed).

The goal of the field emission BLMs is to capture sudden onset of field emission associated dark current in the XFEL Linac. Adequate thresholds of these BLMs can be used to shut down the RF [8]. This work is still ongoing and not completed yet.

## OUTLOOK

Firmware improvements and adjustments are still ongoing. The maximum bunch number in the machine was so far 500 bunches, so settings for long bunch trains up to 2700 bunches per bunch train have to be found.

## CONCLUSION

The BLM system gives a fast feedback in case of too high losses and stops the beam if thresholds are reached. Overview panels show the loss situation along the machine. Settings of each BLM can be matched to its particular position. In summary the BLM system is operating reliable and provides a back bone for safe operation of the accelerator. The evaluation of the activation profile during 2017 and 2018 shows that losses and thus activation can be kept on a very low level.

## REFERENCES

- [1] S. Karstensen *et al.*, “XFEL Machine Protection System (MPS) based on uTCA”, in *Proc. ICALEPCS'15*, Melbourne, Australia, Oct. 2015, paper MOM308, pp. 82-85.
- [2] A. Ignatenko *et al.*, “Beam Halo Monitor for FLASH and the European XFEL”, in *Proc. IPAC'12*, New Orleans, USA, May 2012, paper MOPPRO18, pp. 816-818
- [3] D. Reschke *et al.*, “The Commissioning of the European XFEL Linac and its Performance”, in *Proc. SRF'17*, Lanzhou, China, Jul. 2017, pp. 1-5. doi:10.18429/JACoW-SRF2017-MOXA02
- [4] M. Werner *et al.*, “A Toroid based Bunch Charge Monitor System with Machine Protection Features for FLASH and XFEL”, in *Proc. IBIC'14*, Monterey, USA, Sep. 2014, paper WEPF02, pp. 521-524.
- [5] T. Lensch and S. Liu, “Status and Commissioning of the Wire Scanner System for the European XFEL”, in *Proc. IPAC'18*, Vancouver, Canada, May 2018, pp. 1919-1922. doi:10.18429/JACoW-IPAC2018-WEPAF047
- [6] A. A. Zavadtsev, “Three Transverse Deflecting Systems for Electron Beam Diagnostics in the European Free-Electron-Laser XFEL”, in *Proc. RUPAC'16*, St. Petersburg, Russia, November 2016, paper THXSH02, pp. 196-200.
- [7] S. Meykopff and B. Beutner, “Emittance Measurement and Optics Matching at the European XFEL”, in *Proc. ICALEPCS'17*, Barcelona, Spain, Oct. 2017, pp. 165-167. doi:10.18429/JACoW-ICALEPCS2017-THPHA116
- [8] J. Branlard *et al.*, “Superconducting Cavity Quench Detection and Prevention for the European XFEL”, in *Proc. ICALEPCS'13*, San Francisco, USA, Oct. 2013, paper THPP072, pp. 1239-1241.



# REVIEW OF RECENT STATUS OF CODED APERTURE X-RAY MONITORS FOR BEAM SIZE MEASUREMENT\*

J.W. Flanagan<sup>†1</sup>, High Energy Accelerator Research Org., KEK, 305-0801 Tsukuba, Japan  
<sup>1</sup>also at the Graduate University for Advanced Science, SOKENDAI, 305-0801 Tsukuba, Japan

## Abstract

X-ray beam profile monitors based on coded aperture imaging use an array of pinholes or slits to achieve large open apertures, which provide improved photon collection efficiency over single pinholes or slits. The resulting improvement in photon statistics makes possible single-bunch, single-turn measurements at lower bunch currents than are possible with a single pinhole or slit. In addition, the coded aperture pattern provides extra information for beam profile reconstruction, which makes possible somewhat improved resolution, as compared to a single slit. The reconstruction algorithm for coded aperture imaging is more complicated and computing-intensive than that for a single slit, though with certain classes of coded apertures a faster reconstruction method is possible. This paper will provide a survey of efforts to use coded aperture imaging for beam profile diagnostics at accelerators to date, covering principles and practical experiences with the technique, as well as prospects for the future at SuperKEKB, where it forms the primary means of measuring vertical beam sizes.

## INTRODUCTION

Coded aperture imaging is a form of wide-aperture imaging with roots in x-ray astronomy. This paper will start with reviews of wide-aperture imaging in x-ray astronomy, including coded aperture telescopes. This will be followed by a review of the principles of coded aperture imaging. Finally, there will be a discussion of experiences at Diamond Light Source, CsrTA, ATF2 and SuperKEKB, and a summary.

## WIDE-APERTURE IMAGING IN X-RAY ASTRONOMY

The existence of x-rays coming from outside the solar system was first discovered in 1962, using non-imaging detectors [1]. This gave birth to the field of x-ray astronomy, for which Riccardo Giacconi later received the Nobel Prize. Due to the attenuation of x-rays in the atmosphere, x-ray telescopes need to be placed on rockets, high-altitude balloons, or satellites. The first fully imaging x-ray satellite dedicated to extra-solar astronomy was the HEAO-B (Einstein) satellite, which operated from 1978 to 1982 [2]. Imaging was accomplished via grazing-incidence mirrors. To increase the light collection efficiency (open aperture), a set of 4 nested mirrors was used. This worked for x-rays up to 8 keV.

\* Work supported in part by Kakenhi and Japan-US Cooperation in High Energy Physics

<sup>†</sup> john.flanagan@kek.jp

This basic approach has evolved over the years, with ever-increasing numbers of nested mirrors employed. For example, the NuSTAR satellite [3] employs 133 nested mirrors. In addition, it employs multi-layers on the surface of the mirrors, made up of alternating layers of high- and low-index of refraction materials. The multi-layers enhance reflectivity through constructive interference at higher x-ray energies, giving the satellite a usable spectral range of 3-79 keV, limited by the optics.

Another approach used for x-ray and gamma-ray astronomy is coded aperture (CA) imaging, which will be discussed in the next section. An example of a CA-based x-ray telescope is the balloon-borne protoMIRAX experiment [4], which used a rectangular mask pattern of apertures to modulate the incoming x-rays. Advantages of CAs over reflective optics include wider angular and spectral acceptances (spectral acceptance being determined primarily by detector efficiency rather than optics), and a shorter required distance between optics and detector -- the NuSTAR satellite for example, requires 10 m separation between optics and detectors to focus at 79 keV (due to the required shallowness of the grazing incidence angle), while protoMIRAX reaches up to 200 keV in a much more compact package.

## PRINCIPLES OF CODED APERTURE IMAGING

CA imaging is a technique developed by x-ray astronomers, gamma-ray astronomers and others using a mask made up of multiple apertures to modulate incoming light. The resulting image must be deconvolved through the mask response to reconstruct the object. The primary advantage of a CA mask over a single pinhole is increased light-collection efficiency, with typical CA masks in use having open apertures of around 50%.

X-ray astronomer R.H. Dicke proposed to use multiple pinholes to increase photon-collection efficiency [5]. He proposed a randomly-spaced arrangement of pinholes. Such an arrangement produces a complicated detector image, that can be recovered by deconvolution by cross-correlation with the original mask image.

In principle, however, any set of multiple apertures can be considered a “coded aperture.” Prior to Dicke (and prior to the advent of x-ray astronomy), the use of Fresnel zone plates (FZPs) had been proposed [6]. If an FZP is detuned so as not to act like a lens, then it provides a uniformly spaced set of aperture widths and spacings, for uniform spatial resolution over a range of sizes.

A notable class of coded aperture is Uniformly Redundant Arrays (URAs) [7, 8]. URAs are made up of a pseudo-random arrangement of apertures, designed to have the

nice mathematical property that its auto-correlation is a delta function. This ensures that the reconstruction has no side-lobe artifacts, as tend to occur for truly random arrays (and FZPs).

### Coded Aperture Image Reconstruction

Following [7], for an object  $O$ , aperture  $A$  and noise function  $N$ , the recorded image  $P$  is given by

$$P = (O * A) + N,$$

where  $*$  is the correlation operator. Two methods for finding the reconstructed object  $O^R$  from  $P$  are the Fourier transform method and the correlation method. In the former,

$$O^R = RF^{-1} \left[ \frac{F(P)}{F(A)} \right] = O + RF^{-1} \left[ \frac{F(N)}{F(A)} \right],$$

where  $F$  is the Fourier transform,  $F^{-1}$  the inverse Fourier transform, and  $R$  the reflection operator. In the latter,

$$O^R = P * G = RO * (A * G) + N * G,$$

where  $G$  is the postprocessing array, which is chosen such that  $A * G$  approximates a delta function. In principle, both methods should give the same result, though the Fourier method may be more sensitive to noise, depending on the mask pattern. In this paper, the above methods will be termed “direct reconstruction methods.”

In practice, due to issues of dealing with background and detector noise, many practical applications of coded aperture imaging for x-ray astronomy have been based on iterative methods, rather than direct reconstruction. In such methods, one repeatedly modifies a proposed source distribution until it generates an image similar to the measured detector image, when propagated through a model of the system. In astronomy, one does not know what the source distribution should look like, and it is important not to create spurious sources through reconstruction artifacts.

For accelerator measurements, in addition to noise, we have additional issues due to not operating in the classical limit, which the direct reconstruction method assumes, and where x-ray and gamma-ray astronomy telescopes operate. In particular, diffraction effects need to be accounted for, as well as the variation of spectrum on- and off-axis in the synchrotron fan and how it affects transmission through the mask and folds into the spectral response of the detector as a function of angle off-axis. There is also the non-uniform intensity profile of the incident beam to take into account, unlike the uniform illumination that can be assumed for astronomical sources. These effects are not accounted for in the direct reconstruction methods.

In the case of a stable accelerator beam, unlike the case in astronomy, we generally do know what the source distribution should look like: usually a single Gaussian of unknown size and position, to be determined. A very successful technique that has used so far in such cases is template fitting: one creates a collection of simulated detector images representing different beam sizes and positions, then compares the measured image against the simulated images to find the closest match. This approach is very brute-force, but with multi-CPU recon-

struction machines, it is possible to keep up with measurement rates of one to a few Hz. It also permits more accurate beam size measurement in the case of stable beam than direct reconstruction does, since all the effects due to operating in a non-classical and non-uniform illumination regime can be accounted for.

The templates can be created in advance from a weighted sum of point-response functions (PRFs) that each represent the detector image from a point source, with the weighting chosen to represent the beam distribution. For each PRF, a set of source SR wavefront amplitudes is calculated [9], then propagated through a model of the system, with a Kirchhoff integral over the mask surface, and taking into account transmission and phase shift effects due to all materials in the system and detector response [10]. The source beam is considered to be a vertical distribution of point sources. This approach can also be applied to sources with non-zero angular dispersion and longitudinal extent, for more accurate simulation of emittance and source-depth effects. For the machines discussed below these effects are small, so for computational speed we restrict ourselves to 1-D vertical distributions.

### Why a URA or Other CA Mask?

The question could reasonably be asked, if one is not going to use direct reconstruction, what are the advantages of a URA (or other coded aperture) pattern?

For accelerators, as for astronomy, the primary advantage of any coded aperture over a single pinhole or slit is greater open aperture for single-shot measurements at low currents, when photon statistics can become the dominant source of measurement uncertainty. At SuperKEKB, for example, optics tuning is done at low currents to protect the physics detector from beam-loss backgrounds, before ramping back up to full currents for collision data-taking. The optics group needs beam sizes at low currents to evaluate tuning effectiveness. In general, single-shot (single-bunch, single-turn) measurements are preferred for emittance measurements, so as to eliminate any effect of bunch position motion on apparent beam size.

In addition, even though CAs are essentially collections of multiple pinholes, CAs give somewhat better resolution than single pinholes due to the presence of peak-valley ratios in the image, in addition to the peak width, which provides more information to be fit. CA images also make use of more detector pixels than do single-slit images, and so are less sensitive to the presence of individual dead or mis-calibrated pixels.

Having decided to use a CA, how does one choose what pattern to use? What about a simple equally-spaced array of pinholes/slits, for example? One advantage of a URA pattern is a flatter spatial frequency response than an equal-spaced array (or random array or FZ). This gives a flatter response over a range of beam sizes (and shapes, if one does direct or iterative reconstruction, for example). A URA or other non-repeating pattern also provides

unique position determination, if that is important for one's application.

On the other hand, an equally-spaced array can offer superior resolution over a narrower range of sizes, at the sacrifice of poorer resolution outside that range. Such an array may, for example, be suitable for a very stable machine, such as a light source. For instability studies (due to electron clouds, e.g.) or other machine studies, or for a luminosity machine which is always running at the limit of stability, a URA mask may be more suitable for use over a broader range of expected bunch sizes (and shapes, depending on reconstruction method). The choice of optimal pattern thus depends on the intended application.

## EXPERIENCES AT ACCELERATORS

In this section will be discussed experiences applying coded aperture imaging at 4 machines: CEsrTA, Diamond Light Source, the ATF2 and SuperKEKB. All four machines are low-emittance electron and/or positron rings, with minimum beam sizes at the x-ray source point of 10 microns or less, and beam energies ranging from 1.3 to 7 GeV.

### *Experience at Diamond Light Source*

Diamond Light Source is a third generation light source in Didcot, Oxfordshire, UK. It has a beam energy of 3 GeV. In 2013, a high-energy CA chip was installed in the x-ray beam diagnostic line. The pattern is a 10-micron minimum-feature-size URA, with 59 "pixels" (not apertures). The mask was made of 18.2 micron Au on a 625 micron Si substrate. The resulting image was detected on a 200 micron thick LuAG:Ce screen, viewed by a 1024(H)x768(V) pixel camera. This readout set-up only permits time-averaged measurements, not single-shot ones, but the high resolution of the images provided good verification that the template generation method provides good fits to observed images.

A study was then performed varying the beam size and comparing measurements made with the CA and with the pre-existing single-slit aperture [11]. Results showed good correlation between the CA and the single-slit measurements, though with a small systematic difference in measured sizes.

### *Experience at CEsrTA*

Single-shot measurements were carried out at CEsrTA, an ILC damping ring and low-emittance ring test machine, with a focus on low-emittance tuning and electron-cloud studies, located at Cornell University in Ithaca, NY, USA. The majority of experiments were carried out at 2 GeV [12,13], with some at 4 GeV [14]. The detector was a 32-pixel InGaAs detector with 50-micron pitch, and the optics chips used were generally made of 0.5 micron Au on 2.5 micron Si substrate. In addition there was a single-slit aperture made of tungsten.

The readout system was designed to take single-shot, turn-by-turn data, which allowed for the demonstration of measurements of electron-cloud blow-up along a bunch train [15]. Two types of CA were used. The first one

tried was a 31-"pixel" detector with 10 micron pitch, which turned out to be sub-optimal since it was not optimized for the detectable spectrum at CEsrTA, although it was successfully used. An alternate CA design was also tried, not based on a URA design but based on the idea of intentionally designing slit widths and spacing in order to enhance diffraction peaks over the detectable spectrum, creating sharper edges in the PRFs. (Note that no monochromator was used, just the natural bandwidth of the detectable spectrum.) Both CAs showed better single-shot resolutions than the single-slit at the smallest beam sizes, with the second CA design outperforming the first between 10 and 50 microns at 2 GeV [13].

### *Experience at ATF2*

The ATF is an ILC damping ring test machine, with an extraction line, the ATF2, designed for ILC final-focus optics and beam instrumentation testing. An x-ray extraction line was installed at the last strong bend before the straight section in the extraction line, and a 47-element URA mask installed close to the bend. Readout was done by scanning a single InGaAs pixel (of the same type as used at CEsrTA) across the detector plane in 50-micron steps to build up the image over successive bunch extractions.

A study was carried out while changing the beam size via dispersion [16]. Preliminary results indicate that the minimum measured beam size was around 10 microns.

### *Experience at SuperKEKB*

SuperKEKB is an e<sup>+</sup> e<sup>-</sup> two-ring energy-asymmetric collider for new physics searches. It is an extensive upgrade to the KEKB B Factory collider. X-ray beam lines have been installed at both the 4 GeV Low energy ring (LER) and the 7 GeV High Energy ring (HER) for the purpose of beam size measurement. Phase 1 of SuperKEKB commissioning occurred in spring of 2016, with Phase 2 in spring of 2018. Phase 3 is planned for Spring of 2019.

A fast readout system capable of bunch-by-bunch, turn-by-turn measurements is being developed at the University of Hawaii, and a 128-pixel deep Si detector with 50 micron pitch has been developed at SLAC, both in collaboration with KEK. It is hoped to start commissioning this fast readout system during Phase 3 of SuperKEKB commissioning. Meanwhile, time-averaged measurements have been carried out using YAG:Ce and LuAG:Ce scintillators, viewed by cameras.

Three sets of optics chips, made of 18 microns of Au on a 600 micron CVD diamond substrate, were designed for each ring [17]: A single slit mask, a multi-slit CA mask, and a URA CA mask. The minimum slit widths of the masks were chosen to minimize the point spread of a single slit PRF. The multi-slit mask was hand-optimized to provide the best single-shot resolution at the smallest beam sizes; it is expected to outperform the URA mask below about 15 microns, with the URA mask outperforming above that. Both CA masks outperform the single-slit mask at all beam sizes. Since the performance and noise



The resulting beam profiles were then fit with Gaussians, and the results compared with the results of template fitting. Good agreement was found with all three methods in the range between 40 and 80 microns, with the correlation methods agreeing somewhat better than the Fourier transform method. Outside that size range, systematic divergences were found between the direct reconstruction methods and the template fitting method. Further studies of the systematics involved are planned. This is believed to be the first application of direct beam image reconstruction using coded apertures.

For the next iteration of masks, it is planned to create a set of repeating URA mask patterns, such that the projection on the detector always contains the projection of one whole (cyclically shifted) URA pattern, even if the beam center shifts. The importance of this in preserving the delta-function nature of  $A^*G$ , and thus minimizing reconstruction artifacts when the beam position shifts, is pointed out in [7].

## SUMMARY

Coded aperture techniques have been tested for beam-size measurement at CEsrTA, Diamond Light Source, the ATF2 and SuperKEKB, using both URA and other mask patterns. Coded aperture imaging forms the primary beam size measurement system at SuperKEKB.

Template fitting methods for measuring the beam size have been well demonstrated. Direct deconvolution has been tested for faster reconstruction at SuperKEKB, with further studies and improvements planned.

## REFERENCES

- [1] R. Giacconi, H. Gursky, F.R. Paolini, and B.B. Rossi, "Evidence for x Rays from Sources Outside the Solar System," *Phys. Rev. Lett.* vol. 9, p. 439, Dec. 1962.
- [2] R. Giacconi *et al.*, *Astrophysical Journal*, vol 230, p 540, 1979.
- [3] F. A. Harrison *et al.*, "The Nuclear Spectroscopic Telescope Array (NuSTAR) high-energy x-ray mission," *The Astrophysical Journal*, 770:103 (19pp), 2013 June 20, 2013. doi:10.1088/0004-637X/770/2/103
- [4] J. Braga *et al.*, "The protoMIRAX hard X-ray imaging balloon experiment," *Astronomy and Astrophysics*, vol. 580, p. A108, Aug. 2015. doi:10.1051/0004-6361/201526343
- [5] R. H. Dicke, "Scatter-hole cameras for x-rays and gamma rays," *Astrophys. Journ.*, vol. 153, p. L101, Aug. 1968.
- [6] L. Mertz and N. Young, in *Proceedings of the International Conference on Optical Instruments and Techniques*, Chapman and Hall, London, p. 305, 1961.
- [7] E. E. Fenimore and T.M. Cannon, "Coded aperture imaging with uniformly redundant arrays," *Appl. Optics*, vol. 17, no. 3, p. 337, Feb. 1978.
- [8] E. E. Fenimore, "Coded aperture imaging: predicted performance of uniformly redundant arrays," *Appl. Optics*, vol 17, no 22, p 3562, November 1978.
- [9] K.J. Kim, *AIP Conf. Proc.* 184 (1989).



- [10] J.W. Flanagan *et al.*, “Performance of coded aperture x-ray optics with low emittance beam at CEsrTA,” in *Proc. PAC’09*, Vancouver, BC, Canada, p. 3561, May 2009.
- [11] C. Bloomer, G. Rehm, J.W. Flanagan, “Measurements of small vertical beam size using a coded aperture at diamond light source,” in *Proc. IBIC’14*, Monterey, CA, USA, Sep. 2014, p. 279.
- [12] J.P. Alexander *et al.*, “Vertical beam size measurement in the CESR-TA e<sup>+</sup> e<sup>-</sup> storage ring using x-rays from synchrotron radiation,” *Nuclear Instruments and Methods in Physics Research*, vol. A748, pp. 96–125, 2014. doi:10.1016/j.nima.2014.02.040
- [13] J.P. Alexander *et al.*, “Design and performance of coded aperture optical elements for the CESR-TA x-ray beam size monitor,” *Nuclear Instruments and Methods in Physics Research*, vol. A767, pp. 467–474, 2014. doi:10.1016/j.nima.2014.09.012
- [14] J.P. Alexander *et al.*, “Operation of the CESR-TA vertical beam size monitor at E<sub>b</sub> = 4 GeV,” *Nuclear Instruments and Methods in Physics Research*, vol. A798, pp 127–134, 2015. doi: 10.1016/j.nima.2015.07.028
- [15] M.A. Palmer *et al.*, “Electron cloud at low emittance in CEsrTA,” in *Proc. IPAC’10*, Kyoto, Japan, p 1251, 2010.
- [16] J.W. Flanagan *et al.*, “First measurements with coded aperture x-ray monitor at the ATF2 extraction line,” in *Proc. IBIC’12*, Tsukuba, Japan, p. 237, 2012.
- [17] E. Mulyani and J.W. Flanagan, “Design of coded aperture optical elements for SuperKEKB x-ray beam size monitors,” in *Proc. IBIC’15*, Melbourne, Australia, p 377, 2015.
- [18] E. Mulyani and J.W. Flanagan, “Calibration of x-ray monitor during Phase 1 of SuperKEKB commissioning,” in *Proc. IBIC’16*, Barcelona, Spain, p 524, 2016.
- [19] E. Mulyani, J. Flanagan, M. Tobiyama, H. Fukuma and H. Ikeda, “First measurements of the vertical beam size with an x-ray beam size monitor in SuperKEKB rings,” submitted for publication.
- [20] K. Ohmi *et al.*, “Electron cloud studies in SuperKEKB Phase I commissioning,” in *Proc. IPAC’17*, Copenhagen, Denmark, May 2017, p. 3104, 2017. doi:0.18429/JACoW-IPAC2017-WEPIK075
- [21] E. Mulyani *et al.*, “Image reconstruction technique based on coded aperture imaging for SuperKEKB x-ray beam size monitor,” in *Proc. IPAC’18*, Vancouver, BC, Canada, Apr.-May 2018. doi:10.18429/JACoW-IPAC2018-THPML074

# A SIMPLE MODEL TO DESCRIBE SMOKE RING SHAPED BEAM PROFILE MEASUREMENTS WITH SCINTILLATING SCREENS AT THE EUROPEAN XFEL

G. Kube, S. Liu, A. Novokshonov, M. Scholz, DESY, Hamburg, Germany

## Abstract

Standard beam profile measurements of high-brightness electron beams based on optical transition radiation (OTR) may be hampered by coherence effects induced by the microbunching instability which render a direct beam imaging impossible. For the European XFEL it was therefore decided to measure transverse beam profiles based on scintillating screen monitors using LYSO:Ce as scintillator material. While it is possible to resolve beam sizes down to a few micrometers with this kind of scintillator, the experience during the commissioning of the XFEL showed that the measured emittance values were significantly larger than the expected ones. In addition, beam profiles measured at bunch charges of a few hundreds of pico-Coulomb show a ‘smoke ring’ shaped structure. While coherent OTR emission and beam dynamical influence can be excluded to explain this observation, it is assumed that the beam profile distortions are caused by effects from the scintillator material. A simple model is presented which takes into account quenching effects of excitonic carriers inside a scintillator in a heuristic way. Based on this model, the observed beam profiles can be understood qualitatively. Together with the model description, first comparisons with experimental results are presented.

## INTRODUCTION

Transverse beam profile diagnostics in electron linacs is widely based on optical transition radiation (OTR) as standard technique which is observed in backward direction when a charged particle beam crosses the boundary between two media with different dielectric properties. Unfortunately, microbunching instabilities in high-brightness electron beams of modern linac-driven free-electron lasers (FELs) can lead to coherence effects in the emission of OTR, thus rendering it impossible to obtain a direct image of the particle beam and compromising the use of OTR monitors as reliable diagnostics for transverse beam profiles. The observation of coherent OTR (COTR) has been reported by several facilities (see e.g. Ref. [1]), and in the meantime the effect of the microbunching instability is well understood [2].

For the European XFEL it was therefore decided to use scintillation screen monitors because the light emission in a scintillator is a multistage stochastic process from many atoms which is completely insensitive to the longitudinal bunch structure. In a series of test measurements performed in the past few years, the applicability of inorganic scintillators for high resolution electron beam profile measurements was investigated [3, 4]. Most notably, the dependency of the resolution on the scintillator material and on the obser-

vation geometry was studied with respect to resolve beam profiles in the order of several tens of micrometers, and it was concluded that LYSO ( $\text{Lu}_{2(1-x)}\text{Y}_{2x}\text{SiO}_5\text{:Ce}$ ) is a suitable material because it gives the best spatial resolution. Based on these measurements, screen monitor stations were designed for the European XFEL using 200  $\mu\text{m}$  thick LYSO screens [5]. In a high resolution beam profile measurement using an XFEL-type screen it was demonstrated that it is possible to resolve a vertical beam size of  $\sigma_y = 1.44 \mu\text{m}$  [6].

However, the experience during the commissioning of the XFEL showed that the measured emittance values were significantly larger than the expected ones [7, 8]. In addition, beam profiles measured at bunch charges of a few hundreds of pico-Coulomb show a ‘smoke ring’ shaped structure, see e.g. Fig. 1. While the contribution of COTR emission

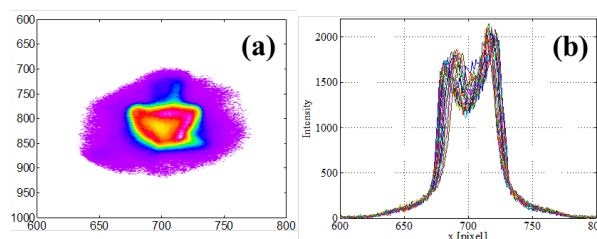


Figure 1: (a) Typical smoke ring shaped beam profile as measured with an XFEL screen monitor based on a 200  $\mu\text{m}$  thick LYSO screen. (b) Various horizontal cuts through the 2D-profile demonstrate the intensity drop in the central part of the beam spot.

from the scintillator surface, beam dynamical influence, and camera effects could be excluded to explain this observation, it is assumed that the beam profile distortions are caused by effects from the scintillator material.

In the following a simple model is described which takes into account quenching effects of excitonic carriers inside a scintillator in a heuristic way. Based on this model, the observed beam profiles can be understood qualitatively.

## BASIC CONSIDERATIONS

Degradation effects in scintillator based beam profile measurements are reported in a number of publications, see e.g. Refs. [9–13]. The scintillator influence is mainly interpreted as saturation of the measured profiles, caused e.g. by full excitation of the luminescent centers in some regions inside the scintillator. While inspecting Fig. 1 it is obvious that the XFEL observations cannot simply be described by a saturation effect which would result in a flattening of the measured beam profiles. It rather leads to the conclusion

that luminescent centers may even be quenched in the central part of the beam spot such that the scintillating light intensity is decreased in these regions.

Taking into account the experience of high energy physics, it is known that scintillator based electron calorimeters possess a non-linear energy resolution, and the degree of non-linearity depends on the scintillator material. Following the explanations e.g. in Ref. [14] this effect can be attributed to the ionization density inside the material: In the primary interaction of a particle with the calorimeter material an electromagnetic shower is generated, and the shower particles create excitonic states (electron/hole or e/h pairs, excitons ...) inside the scintillator material. As the shower particles slow down, the ionization density increases as described by the kinematical factor  $\propto \beta^{-2}$  (with  $\beta = v/c$ ) of the Bethe-Bloch equation such that the initial part of the particle track has lower ionization density than the final portion of the track. The light output in a scintillator depends on the ionization density, if the density is above a critical limit excitonic states can annihilate in an Auger-like process without creating a scintillating photon. As a result, the relative light yield in a scintillator typically decreases with decreasing electron energy, see e.g. Ref. [15] and the figures therein. As shown in Fig. 1 of this reference, the light yield of a LSO:Ce scintillator (which has very similar properties than a LYSO:Ce scintillator, the small yttrium contribution of  $x \sim 0.1$  simply serves to stabilize the crystal growth by the Czochralski method and to reduce the production costs [16]) exhibits a strong non-linear behavior which seems to be a general property of the class of "Silicates" as LSO, YSO, LPS where the oxygen is intimately bound to the silicon as a  $\text{SiO}_4^{4-}$  moiety [15].

To be more precise, the general scheme of relaxation of electronic excitations in crystalline scintillators can be subdivided in 5 stages [17], (1) the energy conversion and e/h generation via inelastic scattering, (2) the thermalization of the e/h pairs, (3) their localization, i.e. e/h capturing at traps, (4) the energy transfer to the luminescent centers, and (5) their radiative relaxation. Following Refs. [14, 17] it is stage (4) which causes the non-linearity in the scintillator light yield. Therefore, improving the linearity of a scintillator should in principle correlate with the minimization of the interaction time of excitonic states.

## SCINTILLATOR MODEL

In the following the principal considerations from the previous section are transferred to the field of beam profile diagnostics of ultra-relativistic electron beams. Main idea is that the ionization track density which is responsible for the non-linear scintillator behavior is determined by the primary beam particle density rather than by the secondary energy of shower particles. Because of the similarity between LSO and LYSO scintillators, in the subsequent estimations LSO is used due to the simpler chemical composition.

If an ultra-relativistic electron beam traverses a scintillator it generates ionization and radiative losses. However, the

Bremsstrahlung mean free path length in a LSO scintillator can be estimated to 1.24 mm which is much larger than the scintillator thickness of 200  $\mu\text{m}$  as it is the case for the LYSO screens at the XFEL. Therefore, electromagnetic shower generation is strongly suppressed and energy conversion and e/h generation in stage (1) are simply governed by the collisional stopping power. For ultra-relativistic electron energies, the stopping power is in the region of the Fermi-plateau and the energy loss of about  $\Delta E = 266 \text{ keV}$  in a 200  $\mu\text{m}$  LSO scintillator is negligible compared to GeV beam energies.

In a classical picture the onset of the Fermi-plateau is described as cancellation of the incoming particle field by the induced polarization field of the electrons in the medium, thus giving a measure for the transverse extension of the e/h formation region. According to Ref. [18] the particle field extension has a limiting value of  $R_\delta = c/\omega(1 - \epsilon)^{-1/2} \approx c/\omega_p$  using the simplified model of a free-electron gas with  $\omega_p$  the plasma frequency which amounts to  $R_\delta = 3.85 \text{ nm}$  in the case of a LSO scintillator. In the following  $R_\delta$  is used as estimate for the radius determining the ionization density. Furthermore, taking into account multiple scattering inside a 200  $\mu\text{m}$  thick LSO scintillator, with about 900 scattering events the mean path length between individual scattering is much larger than  $R_\delta$ . Moreover, considering characteristic interaction time scales, the particle flight time through the scintillator and the bunch length of an uncompressed bunch are  $\leq 10^{-12} \text{ sec}$  while dynamical processes in scintillator take place in the order of  $10^{-12}$ – $10^{-10} \text{ sec}$ . With respect to the particle beam dynamics, in the subsequent model the passage of a single electron through the scintillator is therefore described by the generation of a static ionization tube with radius  $R_\delta$  which is homogeneously filled with e/h pairs.

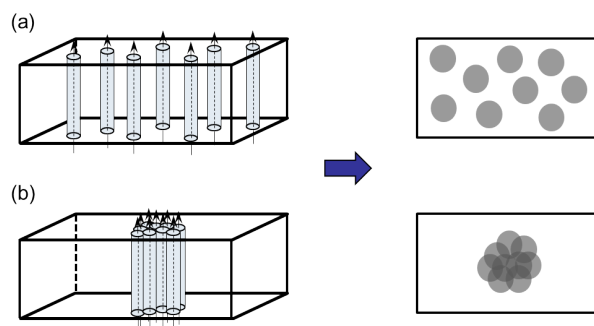


Figure 2: Passage of individual electrons through a scintillator in the case of (a) low and (b) high particle density. Each electron creates a homogeneous ionization tube. Due to the static behavior of the ionization tubes a two-dimensional representation is sufficient.

The situation is schematically depicted in Fig. 2 for the case of a beam with low and with high particle density. Due to the static behavior of the ionization tubes, for the description of the ionization track density a two-dimensional representation is sufficient as shown on the right side of this

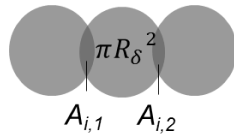


Figure 3: The ionization track density  $n_t$  is geometrically estimated by the ionization tube area and the sum of the track intersections:  $n_t \propto \pi R_\delta^2 + \sum_k A_{i,k}$

figure. In order to estimate the particle track density in the case of a beam with high particle density, a simple geometrical model is used which is based on the 2D-representation. As shown in Fig. 3 the cross section of each ionization tube is described by a circle with area  $\pi R_\delta^2$ . If the particle density is high, individual ionization tubes may overlap and the track density is simply estimated as the sum of tube area and track intersections.

The calculation of a distorted beam profile then consists of four consecutive steps. In the first step the transverse particle beam profile (which is assumed to be Gaussian in the following) is transformed into a 2D surface density profile describing the local particle density  $\sigma(x, y)$ . Assuming an adiabatic change in the local density concentration, in the second step the mean distance between the ionization tubes  $D(x, y)$  is calculated considering the nearest neighbor distribution according to  $D(x, y) = \frac{1}{2}\sigma^{-1/2}(x, y)$ , see the formalism described in Ref. [19]. In the next step, with knowledge of the mean distance between the ionization tubes a regular grid of neighboring tubes is constructed and the local ionization track density  $n_t(x, y)$  is geometrically estimated as described above. Finally, for each point of the beam profile a weighting factor  $w(x, y)$  is calculated

$$w(x, y) = \frac{1}{1 + \alpha \frac{dE}{dx}(x, y)}$$

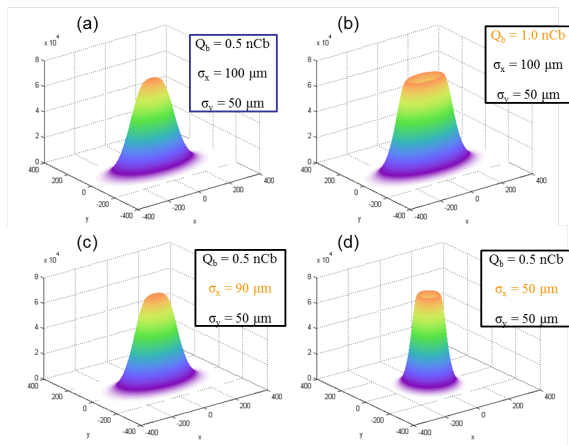


Figure 4: Calculated beam profiles according to the model described in this work. Starting with typical XFEL beam parameters (a) and assuming that  $\alpha = 6.4 \times 10^{-5}$ , beam profiles for increased bunch charge (b) or decreased horizontal beam size (c,d) are shown.

which is similar to the formula of Birks [20] describing the non-linearity in the scintillator light yield. Here it is assumed that  $\frac{dE}{dx} \propto n_t^3$  and  $\alpha$  is a freely adjustable parameter describing the quenching strength.

## MODEL CALCULATION

Figure 4 shows calculated beam profiles according to the model presented in this work. Starting with a Gaussian beam profile and typical XFEL beam parameters (a) it can be seen that both increasing the bunch charge (b) and reducing the beam size (c,d) may result in a pronounced beam profile degradation which is caused by an increase in the local ionization track density in the central part of the beam interaction region with the scintillator. Thereby it is possible to produce smoke ring shaped beam profiles as observed at the XFEL.

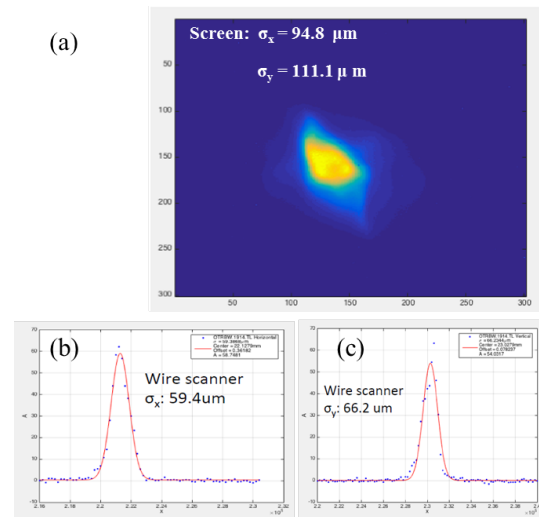


Figure 5: Beam profile measurements with the XFEL screen monitor (a) and wire scanner system (b,c), taken at the same location for the same beam parameters.

In the next step a profile measurement taken at the XFEL is directly compared to the presented scintillator model. Fig. 5(a) shows a profile measurement taken with a screen monitor together with the fit results for the projected horizontal and vertical intensity distributions, assuming Gaussian profiles. In addition, wire scanner profile scans are plotted below (b,c) which were taken at the same location and for the same beam parameters with the XFEL wire scanner system described in Ref. [21]. As can be seen, the screen monitor based analysis systematically overestimates the transverse beam sizes. However, using the wire scanner beam sizes as input for the scintillator model calculation, a 2D beam profile was calculated. A fit of the calculated horizontal and vertical intensity projections results in beam sizes of  $\sigma_x = 97 \mu\text{m}$  and  $\sigma_y = 108 \mu\text{m}$  which is close to the measured sizes from the screen monitor, c.f. Fig. 5(a). Thus the proposed scintillator model is able to produce smoke ring shaped beam profiles with beam sizes close to the measured ones. However, the calculated beam shape strongly depends



on the quenching parameter  $\alpha$  which is freely selectable up to now.

## SUMMARY AND OUTLOOK

Based on the observation of smoke ring shaped beam profiles using the screen monitor stations at the XFEL which utilize LYSO as scintillator material, a simple model is presented which takes into account quenching effects of excitonic carriers inside a scintillator in a heuristic way. Following the experience of calorimetry in high energy physics, the main idea is that the ionization track density which is responsible for non-linear scintillator behavior is determined by the primary beam particle density. The track density is estimated using simple geometrical considerations for the ionization tubes which are generated from beam particles crossing the scintillator. With the help of the proposed scintillator model it is possible to reproduce smoke ring shaped beam profiles as observed at the XFEL, the level of quenching in the central part of the beam generated spot in the scintillator depends on bunch charge and beam size, i.e. it is controlled by the particle density. Moreover, the discrepancy in extracted beam sizes between a screen and a wire scanner measurement can be explained based on this model. However, so far the quenching parameter  $\alpha$  is freely adjustable in the model. Presently studies are under way in order to get a better insight into the underlying physical processes.

In order to support the assumption that the quenching of excitation centers causes smoke ring shaped beam profiles, it is again referred to the experience of the scintillator community for high energy physics. In Ref. [15] scintillator electron response measurements from 29 screen materials are compiled and fitted based on a model combining different theories. One of the fit parameters,  $(dE/dx)_{\text{BIRKS}}$ , characterizes the effect of exciton-exciton quenching, materials with a low magnitude of this parameter experience greater annihilation. Comparing this parameter for LSO and for YAG which is widely used in particle beam diagnostics, with  $(dE/dx)_{\text{BIRKS}} = 133\text{--}185\text{ MeV/cm}$  for LSO:Ce (depending on the doping level) compared to  $526\text{ MeV/cm}$  for YAG:Ce the first material should exhibit much stronger non-linearity and should be prone to smoke-ring shaped beam spots. Figure 6 shows a comparison of beam spot measurements taken under the same experimental conditions at the XFEL. As can be seen, the LYSO screen measurement shows indeed a clear signature of a smoke ring while the YAG measurement is unaffected.

Finally the question for suitable scintillator materials for beam profile diagnostic applications remains open. In the case of hadron beams the question is especially difficult to tackle. Due to the higher rest masses the beam particles usually have a much higher energy loss according to the Bethe-Bloch equation such that even individual particle tracks may be prone to excitation quenching. In the case of ultra relativistic electron beams one can refer again to the compilation in Ref. [15] where LuAG doped either with Ce or Pr exhibits a very high  $(dE/dx)_{\text{BIRKS}}$  such that the

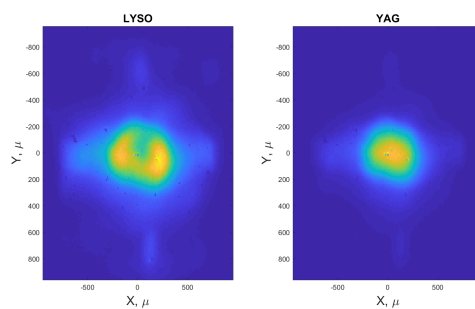


Figure 6: Beam spots measured with a screen monitor station using a LYSO (left) and a YAG scintillator (right) for the same beam parameters. Both screens are mounted in the same station.

exciton-exciton quenching should be small. However, the resolution study performed in Ref. [4] showed that the spatial resolution of a LuAG scintillator was worse compared to a LYSO screen. Therefore other materials could be more promising. As already mentioned before, improving the linearity of a scintillator should in principle correlate with the minimization of the interaction time of excitonic states. In this context scintillator materials where gadolinium is stoichiometrically incorporated in the crystal structure seem to be promising [15]. In these materials it is assumed that excitation carriers can rapidly transfer their energy to excited states of gadolinium, and a rapid migration of this energy among the Gd sub-lattice is expected until a Ce doping ion is reached. According to Ref. [22] YAP could also be an interesting material because it exhibits a high mobility of excitonic carriers which may reduce the quenching probability. A first study with YAP was already performed at the XFEL, the screen material shows indeed better linearity and resolution compared to LYSO, cf. Fig. 7. However, the light yield of YAP is rather low. Presently more detailed studies are in preparation and different scintillator materials like YAG, YAP, LuAG, and GGAG will be investigated in view of linearity and resolution.

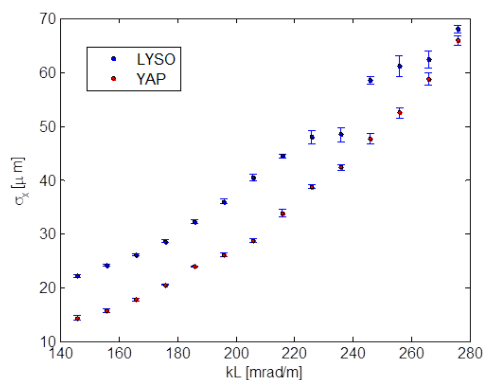


Figure 7: Comparative resolution study using a YAP:Ce and a LYSO:Ce scintillator at the XFEL. The measurements were taken under the same experimental conditions.

**WEOC03**

- 370

# SPACE CHARGE EFFECTS STUDIES FOR THE ESS COLD LINAC BEAM PROFILER

F. Belloni<sup>†</sup>, F. Benedetti, J. Marroncle, P. Abbon, G. Coulloux, F. Gougnaud, C. Lahonde-Hamdoun,  
P. Le Boulout, Y. Mariette, J. P. Mols, V. Nadot, L. Scola,  
CEA-Saclay, 91191 Gif-sur-Yvette, France  
C. Thomas, ESS, 221 00 Lund, Sweden

## Abstract

Five Ionisation Profile Monitors are being built by CEA in the framework of the in-kind contribution agreement signed with ESS. The IPMs will be installed in the Cold Linac where the proton energy range they need to cover extends from 90 MeV to 2 GeV. The ESS fields intensity of  $1.1 \times 10^9$  protons/bunch delivered at a frequency of 352 or 704 MHz, with a duty cycle of 4%, may strongly affect the trajectories of the ionised molecules and electrons created by the passage of the beam through the residual gas. In order to quantify and to develop a correction algorithm for these space charge effects, a code was initiated at ESS and completed at CEA Saclay with the possibility to include real case electric fields calculated with Comsol Multiphysics. A general overview of the code and its preliminary results are presented here.

## INTRODUCTION

The first proton beam at the European Spallation Source (ESS), in construction at Lund (Sweden) is expected by 2019. A perfect beam alignment and focusing are necessary to prevent beam losses and the resulting activation of the accelerator and pipes. Transversal beam profile monitors are therefore among the diagnostics needed by the accelerator.

ESS proton fields are too intense for interceptive monitors, causing material vaporization and radiation damage. Non invasive monitors are the only option for monitoring the ESS transversal beam profile. NPMs (Non-Interceptive Profile Monitors) can rely on ionisation (IPMs) or on fluorescence emission (FPMs). The two processes have different cross sections at different energies, the latter being less likely at high proton energies than the former.

The Cold Linac, where the pressure is expected to be below  $10^{-9}$  mbar, will be therefore equipped with 5 NPMs of IPM type: one in the Spoke section (protons in the 90 MeV - 216 MeV energy range), 3 in the Medium  $\beta$  section (216 MeV – 571 MeV) and one in the High  $\beta$  section (571 MeV – 2 GeV). Every NPM will be installed in a chamber in-between the cryomodules and is composed of two IPMs set at  $90^\circ$  with respect to each other, and each one measuring one transversal beam profile.

Physically, an ESS-IPM is a cube missing two opposite walls. Out of the four remaining walls, two opposite ones are metallized to be used as electrodes for imposing an electric field in the cage and the other two are in insulating

material but equipped with resistors to make the field as more uniform as possible. The proton beam enters the cage through one missing wall and exits from the other missing one.

## SPACE CHARGE EFFECTS

The effects of space charge are twofold: they affect the charged particle beam itself and any other charge in its proximity. Our focus is on this second aspect.

A charge generated at rest between two parallel plates kept at different voltages drifts towards the electrodes travelling parallel to the electric field lines. In an ideal case of perfectly uniform electric field, the point where the charge meets the plate will simply be the projection of its initial position on the electrode. In IPMs, charges are created via gas ionisation and the beam profile is reconstructed this way. But the presence of a charged particle beam, necessary to create ionisation charges, induces an electromagnetic field which modifies the trajectories of the electrons and of the ionised gas molecules and thus introduces a shift between the point where they should have ideally meet the electrode and the point where they really reach it. The measured beam profile therefore will differ from the real one by an amount which depends on the beam intensity, the beam size, the beam energy and the strength of the electric field applied between the electrodes.

## CODE TO QUANTIFY THE SPACE CHARGE EFFECTS

### ESS Core

The core of the code was written in MATLAB at ESS [1] and translated in C++ at CEA Saclay. Its mathematics is based on [2]. Briefly, let's consider the reference frames K and K', with cartesian axis respectively x,y,z and x',y' and z'. K is the laboratory system where a Gaussian bunch with total charge  $Q_b$  is moving with speed  $v_b$  along the z axis, while K' is the reference frame co-moving with the bunch. The charge density of the bunch in the co-moving frame is given in Eq. (1)

$$\rho(\bar{x}, \bar{y}, \bar{z}) = \frac{Q_b}{(2\pi)^{3/2} \sigma_{\bar{x}} \sigma_{\bar{y}} \sigma_{\bar{z}}} \exp\left(-\frac{\bar{x}^2}{2\sigma_{\bar{x}}^2}\right) \exp\left(-\frac{\bar{y}^2}{2\sigma_{\bar{y}}^2}\right) \exp\left(-\frac{\bar{z}^2}{2\sigma_{\bar{z}}^2}\right) \quad (1)$$

<sup>†</sup>francesca.belloni@cea.fr

The electric potential  $\Phi$  generated by such charge density can be calculated in the co-moving system from the Poisson equation:

$$\nabla^2 \Phi(\bar{x}, \bar{y}, \bar{z}) = -\frac{1}{\epsilon_0} \rho(\bar{x}, \bar{y}, \bar{z}) \quad (2)$$

The solution to Eq. (2) results:

$$\Phi(\bar{x}, \bar{y}, \bar{z}) = \frac{Q_b}{4\pi\epsilon_0\sqrt{\pi}} \int_0^\infty \exp\left(-\frac{\bar{x}^2}{\xi_{\bar{x}}^2} - \frac{\bar{y}^2}{\xi_{\bar{y}}^2} - \frac{\bar{z}^2}{\xi_{\bar{z}}^2}\right) \frac{1}{\sqrt{\xi_{\bar{x}}\xi_{\bar{y}}\xi_{\bar{z}}}} d\xi \quad (3)$$

with  $\xi_x = \xi + \sigma_x^2$ ,  $\xi_y = \xi + \sigma_y^2$ ,  $\xi_z = \xi + \sigma_z^2$ , and  $\xi$  being an integration variable. The electric field generated by the Gaussian bunch in the co-moving system K is then obtained as:

$$\begin{aligned} \bar{E}_{\bar{x}} &= -\frac{\partial}{\partial \bar{x}} \Phi(\bar{x}\bar{y}\bar{z}) \\ \bar{E}_{\bar{y}} &= -\frac{\partial}{\partial \bar{y}} \Phi(\bar{x}\bar{y}\bar{z}) \\ \bar{E}_{\bar{z}} &= -\frac{\partial}{\partial \bar{z}} \Phi(\bar{x}\bar{y}\bar{z}) \end{aligned} \quad (4)$$

The electric field in the co-moving rest frame can be transformed into electric and magnetic fields in the laboratory frame through Lorentz Transformations as shown in Eq. (5):

$$E = \frac{\gamma_b \bar{E}_{\bar{x}}}{\gamma_b \bar{E}_{\bar{y}}} B = \frac{-\gamma_b \beta_b \bar{E}_{\bar{y}}/c}{(-\gamma_b \beta_b \bar{E}_{\bar{x}}/c)} \quad (5)$$

The force felt by a test charge  $q$  because of the electric and magnetic fields is computed as:

$$F = q(E + v \times B) \quad (6)$$

with  $\mathbf{v} = (0, v_b, 0)$ . Once the force has been calculated, the equations of motion can be derived and the trajectory of the charge  $q$  under the influence of the electromagnetic fields generated by the Gaussian bunch can be simulated.

### CEA Implementation

Two main additions to the code have been implemented at CEA to account for electric field inhomogeneities and for the initial momenta of the ionisation products.

The electric field is fed to the code as a list of 3D points and their corresponding 3D field components ( $E_x$ ,  $E_y$  and  $E_z$ ) after being simulated using Comsol Multiphysics [3]. A header-only library for Nearest Neighbour (NN) search with KD-trees [4] is used to go through the file generated by Comsol and find the location of the points closest to the position of the test charge. The number N of points searched for is decided by the user. The found N 6D arrays

(3D points and 3D fields) are then used as a 3D-net and the value of the electric field at the position of the test charge is computed via Radial Basis Function interpolation.

The momenta of the electrons generated via ionisation are calculated using Garfield++ [5] and fed to the code in an external file. Garfield++ is a toolkit for detailed simulations of particle detectors that use gas and semi-conductors as sensitive medium. Its validity is limited to high energy incident particles (relativistic and quasi relativistic beams) and it can not give information about ionised gas molecules. To compute their momenta, a simplifying assumption is introduced: the incident beam has not been deviated and therefore, for momentum conservation, the electron and ionised molecule are emitted with opposite momenta:

$$v_e = \frac{m_{ion}}{m_e} v_{ion} \quad (7)$$

## RESULTS

ESS requires that the transverse beam profile shall be measured with a maximum total error in the RMS extension of the beam of less than  $\pm 10\%$ . In order to determine the conditions fulfilling this requirement, several simulations have been performed.

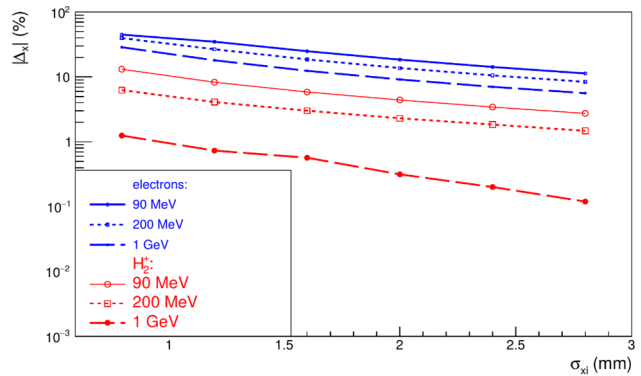


Figure 1: Space charge effects (given as deviation between the beam width input in the simulations and the one obtained by running the code) for different  $\sigma_{xi}$  (i.e. input  $\sigma_x$ ) and incident beam energies when  $\sigma_y=\sigma_z=2\text{mm}$  and  $\mathbf{E} = E_y = 300 \text{ kV/m}$ .

The residual gas in the accelerator tube at ESS is expected to be composed mainly by hydrogen (79 %) and for this reason the influence of the electromagnetic field generated by the ESS beam on the trajectories of the ionisation products has been performed both for electrons and  $\text{H}_2^+$ . The space charge effects have been initially computed for different beam energies (90 MeV, 200 MeV and 1 GeV), beam widths ( $\sigma_x = 1.2 \text{ mm}$ ,  $1.6 \text{ mm}$ ,  $2 \text{ mm}$ ,  $2.4 \text{ mm}$  and  $2.8 \text{ mm}$ ,  $\sigma_y = 1.2 \text{ mm}$ ,  $1.6 \text{ mm}$ ,  $2 \text{ mm}$ ,  $2.4 \text{ mm}$  and  $2.8 \text{ mm}$  and  $\sigma_z = 2 \text{ mm}$ ) and uniform electric fields (from 50 kV/m to 300 kV/m). Figure 1 reports the trend of the space charge effects with respect to different  $\sigma_x$ , beam



energies and test particles when  $\mathbf{E} = E_y = 300$  kV/m, and both the  $\sigma_y$  and  $\sigma_z$  input in the simulation measure 2 mm.

It is evident that the lower the beam energy and the higher is the deviation between the input beam width and the one obtained by running the code.

This is true for the particular simulations run, but it is not a general rule. As a matter of fact, for a different set of electric field strength and  $\sigma_x$ ,  $\sigma_y$  and  $\sigma_z$  values, the opposite behaviour can be obtained. This underlines the complexity of the phenomenon, which results from the interplay of various factors. Nevertheless, it is possible to draw some conclusions. First, the larger the initial beam width and the lower the space charge effects. Finally, the discrepancy between the  $\sigma_x$  input in the simulations and the one obtained as their results is larger for electrons than for ions, due to their high difference in mass.

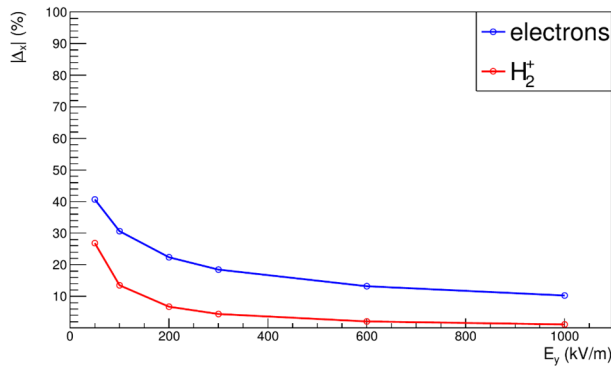


Figure 2: Comparison between the space charge effects for electrons and singly ionised hydrogen molecules  $H_2^+$ , for a 90 MeV proton beam with beam size  $\sigma_x = \sigma_y = \sigma_z = 2$  mm in an homogeneous electric field.

In Fig. 2 the trend of the space charge effects as a function of a homogeneous electric field  $\mathbf{E} = E_y$  is studied only for lowest possible energy of the cold Linac cryomodule (90 MeV), i.e., for the worst case scenario of the results of Fig. 1. The values of  $\sigma_x$ ,  $\sigma_y$  and  $\sigma_z$  were fixed to 2 mm, which corresponds to the average beam size in the Spoke section of the accelerator.

As expected, the lower the field, the lower the speed of the drifting test charges, the more time they spend in the electromagnetic field generated by the ESS beam and the larger the space charge effects.

From Fig. 2 it can be inferred that if electrons are used to measure the beam profile, an electric field higher than  $10^6$  kV/m is needed to meet the ESS uncertainty requirement of 10%. On the other hand, the same condition is fulfilled for much weaker electric fields if singly ionised hydrogen molecules are detected. A difference of potential of 15 kV between the two electrodes of the IPM cube of 10 cm side is already enough to measure the transverse profile with a maximum total error in the RMS extension of the beam of less than  $\pm 10\%$ . Since these simulations do not account for effects such as the space resolution of the detector and are themselves affected by an uncertainty estimated to less than 2%, it was decided that an electric field higher than 150 kV/m is preferable. As a matter of fact, to more efficiently counterbalance the space charge

effects, the electric field needs to be as high as possible.  $E_y = 300$  kV/m has been selected as maximum electric field realistically reachable in the experimental set-up.

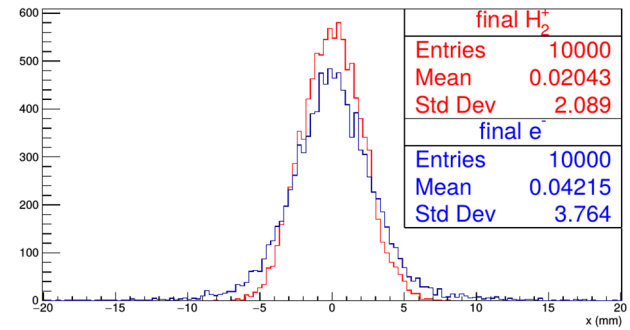


Figure 3: Comparison between the space charge effects felt by electrons and ions when initial momenta distributions are accounted for. Both test charges are created by a 90 MeV proton beam in the Spoke configuration and a perfectly homogeneous electric field  $\mathbf{E} = E_y = 300$  kV/m has been considered.

The results reported in Fig. 2 are obtained considering that electrons and ions are created at rest. This is not true and the impact of the initial momentum distributions of electrons and  $H_2^+$  on the beam profile measurements has therefore been simulated. The outcome was that this factor is negligible for massive particles, but not for electrons. Figure 3 shows the comparison between the results of the simulations run for the two test charges when the Spoke configuration (90 MeV proton beam with beam size  $\sigma_x = \sigma_y = \sigma_z = 2$  mm) and an homogeneous  $\mathbf{E} = E_y = 300$  kV/m are considered. For these conditions, if electrons are produced at rest,  $|\Delta x| < 25\%$ , while it increases to  $|3.764 - 2|/2 \sim 88\%$  when their initial momenta distributions are accounted for. For singly ionised hydrogen molecules instead  $|\Delta x|$  remains stable to  $\sim 4\%$  both when they are generated at rest and with an initial momentum distribution.

It is therefore evident that, to fulfill the ESS requirement, the IPMs cannot be polarized in such a way to detect electrons on the read-out.

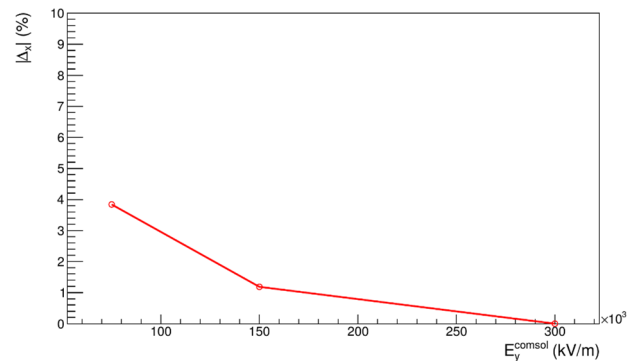


Figure 4: Space charge effects for singly ionised hydrogen molecules  $H_2^+$  created at rest at Spoke conditions for different real case electric fields.

Finally, real case electric field simulations of two IPMs, orthogonal to each other were performed at CEA-Saclay and fed to the code. This allowed to check the influence of the other field components ( $E_x$  and  $E_z$ ) on the transverse beam profile measurements. Having proved that we can use IPMs only in ion configuration and that, in such a case, the initial momenta distributions can be neglected, a study for  $H_2^+$  molecules created at rest was performed for Spoke conditions and three sets of resistors on the IPMs, giving rise to three different  $E_y^{COMSOL}$  field configurations aiming to be as close as possible to  $E_y \rightarrow 75$  kV/m,  $E_y \rightarrow 150$  kV/m and  $E_y \rightarrow 300$  kV/m. Since resistors do not come with every desirable value, a choice towards sets resulting in a slightly focusing electric field was performed at the expenses of sets creating slightly defocusing electric fields. This helps to counterbalance the impact of the space charge effects on the transverse beam profile measurements (see Figure 4).

## CONCLUSIONS

Five transversal beam profilers have to be built for the ESS Cold Linac. The nominal gas pressure will be  $10^{-9}$  mbar and it is expected to mainly consist of hydrogen. For this reason, detailed simulations of the space charge effects felt by electrons and  $H_2^+$  molecules have been performed with an in-house code in different steps. In the beginning the ionisation charges were considered to be produced at rest in an ideally homogeneous electric field to study the impact of the beam parameters and of the field itself on their trajectories.

In a second step, the contributions of a real case electric field and of initial momenta distributions of the ionisation products to the misreconstruction of the transversal beam profiler have been separately added to understand their weight.

The studies performed allowed to exclude the possibility of operating the IPMs in electron if the ESS requirement of a maximum total error in the RMS extension of the beam of less than  $\pm 10\%$  needs to be fulfilled.

Also, electric fields as high as possible are desirable, keeping always in mind that a top value of 300 kV/m needs to be considered as the highest realistically reachable value in our set-up.

## REFERENCES

- [1] C.A. Thomas, F. Belloni, and J. Marroncle, "Space charge studies for the ionization profile monitors for the ESS Cold Linac", in *Proc. 5th Int. Beam Instrumentation Conf. (IBIC'16)*, Barcelona, Spain, Sep. 2016, pp. 555-558. doi:10.18429/JACoW-IBIC16-TUPG81
- [2] R. Wanzenberg, "Nonlinear motion of a point charge in the 3D space charge field of a Gaussian bunch", DESY, Hamburg, Germany, Internal Rep., DESY M 10-01, May 2010.
- [3] COMSOL Multiphysics, <http://www.comsol.com>
- [4] nanoflann: a C++11 header-only library for Nearest Neighbor (NN) search with KD-trees, <https://github.com/jlblancoc/nanoflann>
- [5] K. Baraka, S. Biagi, A. Folkestad, J. Renner, H. Schindler, N. Shiell, I. Smirnov, R. Veenhof, and K. Zenker, "Garfield++ simulation of tracking detectors", <http://garfieldpp.web.cern.ch/garfieldpp>

# A MicroTCA.4 TIMING RECEIVER FOR THE SIRIUS TIMING SYSTEM

J. L. N. Brito\*, S. R. Marques, D. O. Tavares, L. M. Russo, G. B. M. Bruno, LNLS, Campinas, Brazil

## Abstract

The AMC FMC carrier (AFC) is a MicroTCA.4 AMC board which has a very flexible clock circuit that enables any clock source to be connected to any clock input, including telecom clock, FMC clocks, programmable VCXO oscillator and FPGA. This paper presents the use of the AFC board as an event receiver connected to the Sirius timing system to provide low jitter synchronized clocks and triggers for Sirius BPM electronics and other devices.

## INTRODUCTION

Sirius is a 4th generation synchrotron light source based on a 5BA magnetic lattice, currently under construction in Brazil by LNLS [1]. The machine, designed to achieve a beam emittance of 0.25 nm-rad and scheduled for commissioning at the end of 2018 [2], consists of a 150 MeV Linac, a 150 MeV to 3 GeV booster and a 3 GeV storage ring with 518 meters circumference and 20 straight sections. Both booster and storage ring RF frequency is 499.658 MHz and the Linac will inject in single or multi-bunch mode at 2 Hz.

Sirius timing system [3] is a star topology optical fiber network where an event generator (EVG) broadcasts event frames to the event receivers. An event frame decoded by an event receiver can generate clock and trigger signals synchronized to the Sirius RF frequency for the beam injection process and other subsystems such as electron BPMs. The system is composed of Ethernet-configured standalone modules developed by SINAP through a collaboration with LNLS and remotely controlled by an EPICS soft IOC designed by LNLS [4].

The Sirius BPM and orbit feedback systems were developed as an open-source hardware platform [5] based on MicroTCA.4 crates, AMC and FMC modules, 1 Gigabit Ethernet and PCI Express connectivity. The digital back-end of these systems is the AMC FMC carrier (AFC) [6], a MicroTCA.4 AMC board partially based on Simple PCIe FMC carrier (SPEC) [7] design.

Thanks to the flexible clock circuits, the trigger and clock distribution options and the digital interfaces available in the AFC board, the same hardware platform was used to develop a timing receiver board to provide triggers and synchronized clocks for Sirius BPM electronics and other devices, upgrading the MicroTCA clock distribution board developed 3 years ago [3]. From now on, the timing receiver board shall be referred to as AFC timing.

## HARDWARE

This section presents the AFC board focused on timing applications and the interface boards FMC 5 POF and MicroTCA RTM 8 SFP+.

\* joao.brito@lnls.br

## AFC

The AFC board was specified by LNLS and designed by WUT (Warsaw University of Technology) as a double-width AMC card with 2 fully populated high-pin count FMC mezzanine slots, 8 multigigabit links routed to the MicroTCA Rear Transition Module (uRTM) connector, 8 M-LVDS trigger and 2 clock lines available through the AMC backplane connector, connectivity to PCIe at Fat Pipe 1 (x4 link), redundant 1 Gb Ethernet ports, full hardware support for the White Rabbit [8] timing system and provision for standalone operation.

It has a Xilinx Artix-7 200T FFG1156 FPGA and the available clocking resources are: (I) a clock switch (Analog Devices ADN4604) allowing routing of MicroTCA.4 low-jitter clocks to any of the FMC slots or the AMC connector, (II) a 10-280 MHz I<sup>2</sup>C programmable VCXO oscillator (Silicon Labs Si571, 571BJC000121G), (III) a 25 MHz VCTCXO (Mercury VM53S3-25.000) connected to a frequency synthesizer (Texas Instruments CDCM61004) configured to 125 MHz, (IV) a 20 MHz VCXO (IQD VCXO026156) and (V) 3 DACs (Analog Devices AD5662) for oscillators control.

Once inside a MicroTCA crate, an AFC timing board outputs triggers and a low-jitter synchronized clock to the other AFC boards running in the same crate through the MicroTCA crate backplane. This clock will be used as a reference clock to the BPM electronics ADCs.

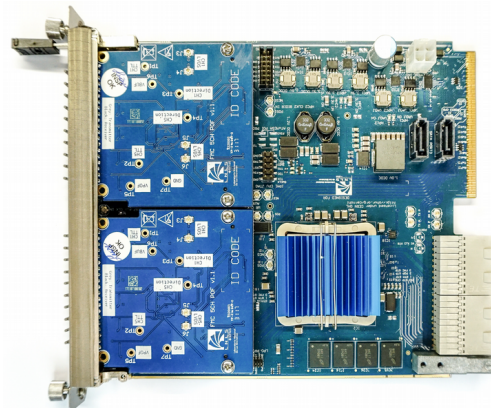


Figure 1: AFC board with two FMC 5 POF mounted.

## FMC 5 POF

The FMC 5 POF board [9] has 5 plastic optical fiber (POF) transceivers mapping the same number of trigger lines from the FPGA through a FMC connector on the AFC board. As the input and output transceivers are different components with the same footprint, the board can be manufactured with up to 5 POF inputs or outputs. In Sirius timing system, it will output synchronized triggers for varied devices

around the accelerator's facility, where most of them will be quadrupoles and sextupoles power supplies of booster and storage ring.

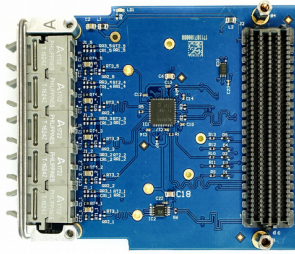


Figure 2: FMC 5 POF, a FMC board with 5 plastic optical fiber outputs.

### MicroTCA RTM 8 SFP+

The MicroTCA RTM 8 SFP+ [10] is a Rear Transition Module board MicroTCA.4 standard. Its main components are 8 SFP+ connectors, which will provide optical fiber interface with the timing system, and a general purpose 10–280 MHz I<sup>2</sup>C programmable XO oscillator (Silicon Labs Si570, 570BCC000121G) that outputs a reference clock to the FPGA GTP transceivers.

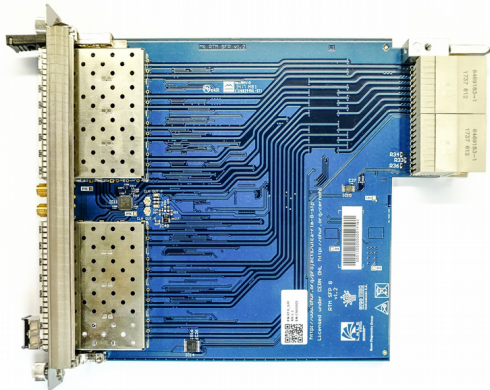


Figure 3: RTM with 8 SFP slots.

## FPGA GATEWARE

The present section describes the main aspects of the FPGA gateware to implement an event receiver and a frequency and phase locked loop that outputs a low-jitter synchronized reference clock to the BPM electronics ADCs.

### Event Receiver

An event frame sent from the EVG consists of an 8-bit event code and an 8-bit distributed data bus (DBUS). Each bit of the DBUS maps a synchronized clock generated by the EVG, that is continuously sending event frames at the event clock rate, which is  $\frac{1}{4}RF = 124.9145$  MHz. The AFC timing can monitor one bit of the DBUS, to output a clock, or one event, to output a trigger or a pulse train.

There are 18 independently configurable monitoring channels in the AFC timing, 10 POF outputs from 2 FMC 5 POF boards and 8 AMC configurable as input or output. When outputting, each one of these 18 channels can adjust the pulse width and the delay with a resolution of one event clock period ( $\sim 8$  ns), as well as the pulse polarity level (low to high or high to low) and the number of pulses generated from 1 to 65535. An AMC channel operating as input can receive a general purpose trigger from another AFC board and, for example, send a corresponding event to the EVG.

### Frequency and Phase Locked Loop

The AFC clocking resources were used to implement a frequency and phase locked loop (Fig. 4) to generate a low-jitter synchronized reference clock to the ADCs of the BPM electronics using the Si571 VCXO.

From the event clock recovered by the FPGA GTP transceiver, a Mixed-Mode Clock Manager (MMCM) generates the reference clock and also the DMTD clock, which is used by the frequency and phase feedback controller to measure the phase difference between the reference and the output clocks. Defining, respectively, the event, reference, DMTD and output clocks as  $f_{evt}$ ,  $f_{ref}$ ,  $f_{dmt}$  and  $f_{out}$ , we have

$$f_{evt} = \frac{1}{4}RF \approx 124.915 \text{ MHz}$$

$$f_{out} = f_{ref} = \frac{5}{36}RF \approx 69.397 \text{ MHz}$$

$$f_{dmt} = f_{ref} \frac{N}{N+1} \approx 68.918 \text{ MHz}; N = 144$$

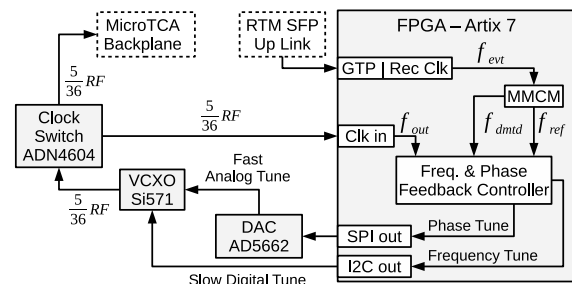


Figure 4: Synchronized reference clock block diagram.

The frequency and phase feedback controller (Fig. 5) is characterized by a frequency detector (FD) and a phase detector (PD) running in two independent feedback loops at the same time.

The FD counts the rising edges of the two input clocks during a fixed time window and calculates the difference between them to output a value proportional to  $f_{ref} - f_{out}$ . The length of the time window determines the sample rate, which is also the resolution of the FD, configured to be 18 Hz. A proportional and integral controller closes the loop and tunes the VCXO frequency via the I<sup>2</sup>C, an interface that allows adjusts up to  $\pm 3500$  ppm from the center frequency configuration.



The PD is a digital version of the Dual Mixer Time Difference (DMTD) [11], shown in Figure 6, a linear method to measure the phase difference between two clock signals at same or near frequencies. It consists of two D flip-flops connected to the same clock source  $f_{dmt}$ , which frequency is slightly lower than the one from the input clocks, under-sampling  $f_{ref}$  and  $f_{out}$ . The phase difference between the clocks on the flip-flop outputs is the same as the inputs, although the output frequencies are lower and equal or near to  $f_{beat} = f_{ref} - f_{dmt}$  and hence the time interval relative to the phase difference between the output clocks is an integer number of  $f_{dmt}$  periods. Therefore, a time counter running at  $f_{dmt}$  was used to measure the time interval and output a value  $n$  proportional to  $\phi_{ref} - \phi_{out}$ , which is the phase difference between  $f_{ref}$  and  $f_{out}$  given on the interval  $[0, 2\pi]$  radians. It is equivalent to measure the time interval between  $f_{ref}$  and  $f_{out}$  with a resolution of  $\Delta t_{min}$  given by

$$\Delta t_{min} = \frac{1}{f_{dmt}} \frac{f_{beat}}{f_{ref}} = \frac{1}{N f_{ref}} \approx 100 \text{ ps}$$

$$f_{beat} = f_{ref} - f_{dmt} = \frac{f_{dmt}}{N} \approx 478.6 \text{ kHz}$$

and hence, the resulting phase different is

$$\phi_{ref} - \phi_{out} = \frac{2\pi n}{N}; n \in [0, N]$$

A moving average filter followed by a proportional controller closes the phase feedback loop driving the control voltage input of the VCXO using the DAC AD5662 controlled by an SPI interface. This configuration allows a frequency adjust range of  $\pm 192$  ppm and an update rate of 478.6 kHz, as the update rate of the DAC's output is higher than the  $f_{beat}$ .

When both feedback loops are running, a large difference between  $f_{ref}$  and  $f_{out}$  turns the PD output negligible and the VCXO is driven by the frequency feedback loop, thereby moving  $f_{ref}$  toward  $f_{out}$ . Thus, the FD output decreases gradually until the frequency feedback loop becomes inactive. At the same time, the PD output becomes stable and the phase feedback loop output increases, turning the phase difference  $\phi_{ref} - \phi_{out}$  constant. The frequency feedback loop maximizes the capture range, the maximum value of  $|f_{ref} - f_{out}|$  for which the loop locks. The PI controller gains and the sample rate were adjusted to minimize the locking time.

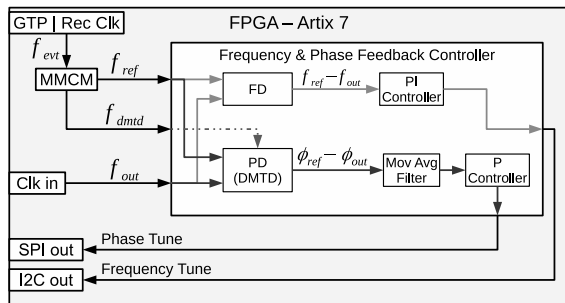


Figure 5: Frequency and phase feedback controller.

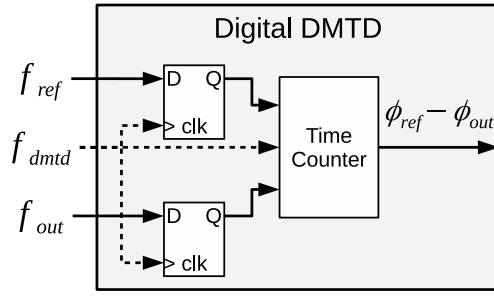


Figure 6: Digital Dual Mixer Time Difference.

## PHASE NOISE PERFORMANCE

The Figure 7 shows the phase noise of the reference clock (trace 3) and the VCXO, while free-running (trace 2) and controlled (trace 1), characterized using a Rohde & Schwarz FSUP signal source analyzer, as well as the respective integrated RMS jitter (1 Hz - 5 MHz). Taking the traces 2 and 3 is possible to see that the free-running VCXO is better than the reference clock at high frequencies and the traces are crossing at about 200 Hz. The integrated RMS jitter was about 78 ps and 25 ps, respectively. Hence, the cutoff frequency of the phase feedback loop should be around 200 Hz, which was nearly achieved adjusting the moving average filter parameters and the proportional gain, as shown by the trace 1, resulting in an integrated RMS jitter of about 4 ps.

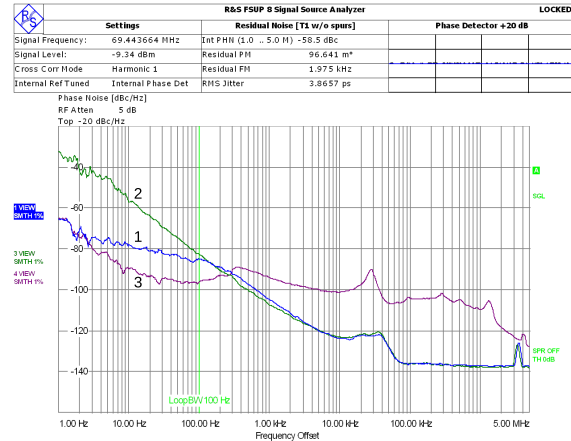


Figure 7: Phase noise characterization of VCXO controlled (1), VCXO free-running (2) and reference clock (3).

## SOFTWARE INTERFACE

The AFC timing will be interfaced with the control system by means of the HALCS framework [12, 13]. It provides a modular approach for abstracting gateway modules as software services that can be exported to a control node and controlled through an RPC API (Application Programming Interface based on Remote Procedure Call). Because of that approach, all of the already supported gateway modules can be leveraged without extra effort, as the framework will automatically identify known modules and export its functionality.

On top of that, an EPICS IOC with an asyn-based driver was developed to interface with HALCS, mapping the exported RPC API to EPICS PVs and providing access to all of the AFC timing receiver gateway functionalities.

## CONCLUSION

Thanks to an open hardware project, the AFC board was developed to be the hardware platform of the Sirius BPM and orbit feedback systems. Now, it is also integrating the Sirius timing system, where more than 20 AFC timing boards will generate synchronized clocks and triggers for the BPM system and hundreds of synchronized triggers for power supplies around the accelerator.

However, the project is not concluded yet. There are some desirable features to implement as, for example, a phase compensation method to automatically align the output triggers, avoiding manual calibrations during the Sirius commissioning and operation.

## REFERENCES

- [1] L. Liu, F. H. de Sá, and X. R. Resende, "A new optics for sirius," in *Proc. 7th Int. Particle Accelerator Conf. (IPAC'16)*, Busan, Korea, May 2016, pp. 3413–3416. doi: 10.18429/JACoW-IPAC2016-THPMR013.
- [2] A. Rodrigues *et al.*, "Sirius status report," in *Proc. 7th Int. Particle Accelerator Conf. (IPAC'16)*, Busan, Korea, May 2016. doi: 10.18429/JACoW-IPAC2016-WEPOW001.
- [3] J. L. N. Brito, S. R. Marques, D. O. Tavares, and L. A. Martins, "Status and Development of Sirius Timing System," in *Proc. 15th Int. Conf. on Accelerator and Large Experimental Physics Control Systems (ICALEPCS'15)*, Melbourne, Australia, Oct. 2015, pp. 1007–1010. doi: 10.18429/JACoW-ICALEPCS2015-WEPGF128.
- [4] sinap-timing-epics-ioc GitHub repository. <https://github.com/lnls-dig/sinap-timing-epics-ioc>
- [5] D. O. Tavares *et al.*, "Development of an Open-Source Hardware Platform for Sirius BPM and Orbit Feedback," in *Proc. 14th Int. Conf. on Accelerator and Large Experimental Physics Control Systems (ICALEPCS'13)*, San Francisco, USA, Oct. 2013, pp. 1036–1039.
- [6] AFC GitHub repository. <https://www.ohwr.org/projects/afc/wiki>
- [7] SPEC wiki page at the Open Hardware Repository. <https://www.ohwr.org/projects/spec/wiki>
- [8] P. Moreira, J. Serrano, T. Wlostowski, P. Loschmidt, and G. Gaderer, "White rabbit: Sub-nanosecond timing distribution over ethernet," in *2009 International Symposium on Precision Clock Synchronization for Measurement, Control and Communication*, Oct. 2009, pp. 1–5. doi: 10.1109/ISPCS.2009.5340196.
- [9] FMC-POF GitHub repository. <https://github.com/lnls-dig/fmc-5POF-hw>
- [10] RTM-SFP GitHub repository. <https://github.com/lnls-dig/utca-rtm-8-sfp-hw>
- [11] D. W. Allan and H. Daams, "Picosecond time difference measurement system," in *29th Annual Symposium on Frequency Control*, 1975, pp. 404–411.
- [12] L. M. Russo and J. V. F. Filho, "Gateway and Software Frameworks for Sirius BPM Electronics," in *Proc. 11th International Workshop on Personal Computers and Particle Accelerator Controls (PCaPAC'16)*, Campinas, Brazil, Oct. 2016. doi: 10.18429/JACoW-PCaPAC2016-THDAPLC003.
- [13] L. Russo, "Software and Gateway Development for Sirius BPM Electronics Using a Service-Oriented Architecture," in *Proc. of International Conference on Accelerator and Large Experimental Control Systems (ICALEPCS'17)*, Barcelona, Spain, Oct. 2017. doi: 10.18429/JACoW-ICALEPCS2017-THPHA149.

# RECENT PROGRESS OF BUNCH RESOLVED BEAM DIAGNOSTICS FOR BESSY VSR \*

J.-G. Hwang<sup>†</sup>, G. Schiwietz<sup>‡</sup>, M. Koopmans, T. Atkinson,  
A. Schällicke, P. Goslawski, T. Mertens, M. Ries, A. Jankowiak

Helmholtz-Zentrum Berlin für Materialien und Energie GmbH (HZB), Berlin, Germany

## Abstract

BESSY VSR is an upgrade project of the existing storage ring BESSY II to create long and short photon pulses simultaneously for all beam lines by installing additional superconducting cavities with harmonic frequencies of 1.5 GHz and 1.75 GHz. The storage-ring operation will be influenced by a transient beam-loading effect of all cavities and by the complex filling pattern due to the disparity in the current of long and short bunches. This, in turn, could introduce a variation of beam trajectory, transverse profile, and length for the different bunches. This stimulates the development of bunch-resolved monitors for bunch length, beam size, filling pattern and beam trajectory displacement. In this paper, we show new developments of crucial beam diagnostics including measurements of the bunch-resolved temporal profile with a resolution of less than 1 ps FWHM and bunch-resolved profile with a resolution of less than 10  $\mu\text{m}$  rms. The upgrade of the booster beam-diagnostics will be discussed as well.

## INTRODUCTION

The BESSY Variable-pulse-length Storage Ring (BESSY VSR) project was launched at the Helmholtz-Zentrum Berlin to provide the capability of user accessible picosecond pulses at a high repetition rate, up to 250 MHz [1, 2]. The installation of additional harmonic-frequency superconducting radio-frequency (SRF) cavities generates a beating of the voltages of two SRF systems, thereby creating alternating buckets for long and short bunches [3]. BESSY VSR preserves the present average brilliance of BESSY II by filling more beam current in the long bunch buckets since the short bunch buckets have relatively low bunch charge to avoid the longitudinal microwave instability that occurs above a certain threshold current. This results in the disparity in 6-D phase space particle distribution such as spatial distribution, angular spread, and energy spread. The implementation of the 1.5 GHz and 1.75 GHz SRF cavities for BESSY VSR enhances a relative phase shift along multi-bunch train due to combined effects of a transient beam-loading in the cavities and complex filling pattern. The relative phase shift can cause a variation of beam trajectory, transverse profile, and length for the different bunches. This stimulates the development of bunch-resolved monitors for transverse and longitudinal electron distribution, relative arrival phase, fill-

ing pattern and central beam trajectory. We are in the process of carefully evaluating and define all feasible monitors for BESSY VSR [4].

## BEAM DIAGNOSTICS PLATFORM REFURBISHMENT

Due to confined space of our present beam diagnostics platform and the installation of a new cryogenic system for BESSY VSR cryomodule near the platform in section 3 of BESSY II, we need to move diagnostics to a new platform in the section 12 of the ring. Several modifications are requested for the new platform, as shown in Fig. 1. The main modifications are the installation of the dedicated hutch for keeping a clean environment and constant temperature, and preparation of the second optical beam line for separating the ports of the profile monitor and bunch length monitor, respectively. The third beam line for THz-based diagnostics will be also prepared inside the accelerator bunker. During summer machine shutdown, the extension of the stage and preparation of new optical beam line such as drilling a hole into the accelerator bunker was conducted. The installation of the hutch is scheduled for next year for a smooth transition will allow time for commissioning of all devices at the new platform.

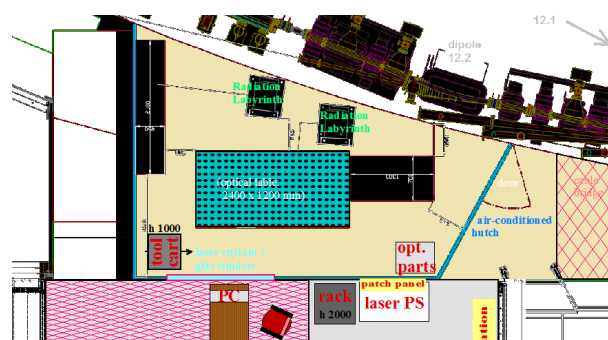


Figure 1: Schematic layout of new optical beam diagnostics platform for BESSY VSR with two beam lines and three separated optical tables.

In addition, we are putting in a great deal of effort into the evaluation and optimization of the optical transport system for timing experiments, which consists of a elliptical mirror with a hexapod 6-axis stage and toroidal mirror with a degree of freedom in angles. Based on a ray-tracing simulation and experimental results, we hope to improve the light output and the position sensitivity with less timing distortion. We are also preparing the isolation of optical tables from ambient vibration sources such as cryogenic compressors, vacuum

\* Work supported by German Bundesministerium für Bildung und Forschung, Land Berlin, and grants of Helmholtz Association.

<sup>†</sup> ji-gwang.hwang@helmholtz-berlin.de

<sup>‡</sup> schiwietz@helmholtz-berlin.de



Content from this work may be used under the terms of the CC BY 3.0 licence (© 2018). Any distribution of this work must maintain attribution to the author(s), title of the work, publisher, and DOI.

pumps, magnet-cooling water, and internal cooling fans of electronic devices since the strong vibrations are observed on the optical table during long-term investigations. The measured result is shown in Fig. 2.

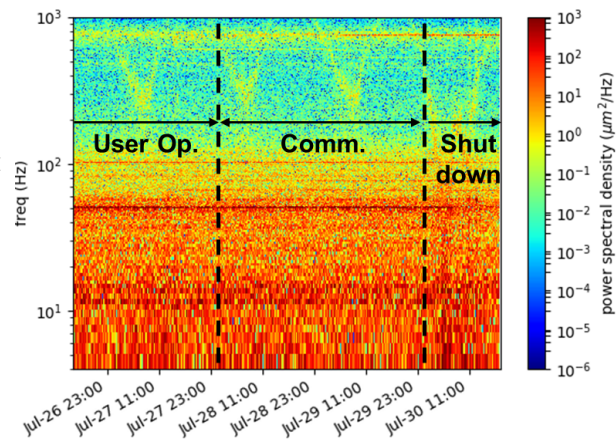


Figure 2: Power spectral density of vibration on optical table during 4 days.

The main peak at around 50 Hz and a long-term drift component are from the cryogenic compressor and internal cooling fan of a streak camera, respectively. This motivates the implementation of passive damped legs and separation of the devices onto different tables.

## STATUS OF OPTICAL DIAGNOSTICS

Research and development of several optical monitors are on going for the measurement of bunch-resolved transverse distribution, temporal structure, and filling pattern. The beam-size monitor based on an interferometric technique with double and quadrature slit was investigated at BESSY II and the performance is verified by a careful comparison with X-ray pinhole monitors in several operation modes [5, 6]. For the bunch-resolved beam-size measurement, it needs a special charge-coupled device (CCD) camera, which applies a fast gating technique with the gate time of shorter than the bunch spacing of 2 ns, to select the light from a single bunch. However, the gating technique reduces the photon flux and therefore an intensified CCD (ICCD) with an iterative gating technology is practically necessary to compensate for the photon flux reduction. Since an ICCD can obtain shot-noise-limited operation by increasing the gain that causes the shot noise to overwhelm the noise generated by the camera electronics, the evaluation of the noise contribution on interferometric beam size measurement in a low photon flux mode ( $9.1 \times 10^6$  photons/shot) is performed using the Monte-Carlo method. The result is shown in Fig. 3.

Based on the numerical simulation, the minimum number of photons per single shot for a reliable resolution is about  $10^5$  which corresponds to the bunch current of 7  $\mu$ A. By improving the optical transport system, we can enhance the operation range by a factor of 5 – 10 for the beam-size monitor.

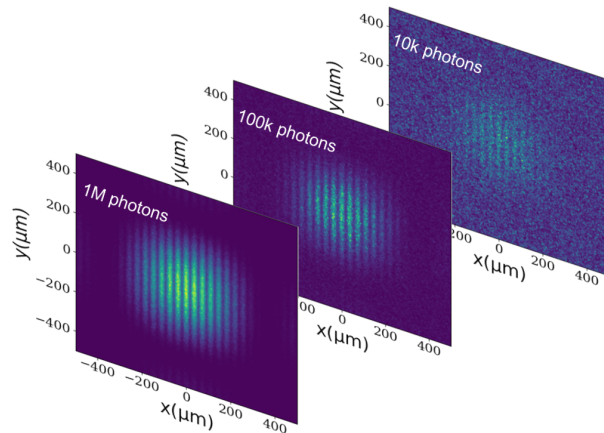


Figure 3: Monte-Carlo simulation-based approach to estimate minimum photon flux due to noise contribution on interferometric beam size measurement.

For bunch-resolved bunch length and phase measurements of BESSY VSR, a new streak camera (Hamamatsu C10910-05) with a synchro-scan repetition rate of up to 1 kHz was delivered and the evaluation of the temporal resolution is performed. We derive the resolution of  $0.88 \pm 0.18$  ps FWHM. In addition to the improvement of the horizontal scanning rate, the optimization of the new beam port enhances the photon flux by a factor of about 80. We also anticipate the minimum operating range of a few  $\mu$ A. We prepared a new high-accuracy translation stage with the position precision of a few  $\mu$ m and movable range of up to 80 cm, which corresponds to  $\Delta t_{\text{delay}} \sim 5.3$  ns. It allows the calibration of not only the vertical axis in specific time range but positive and negative slope in the streak camera with the accuracy of about 10 fs. The measurement result of relative synchronous phase evolution in BESSY II standard user mode is shown in Fig. 4.

Since the streak camera is not suitable device for continuous monitoring, a fast and reliable monitoring system using

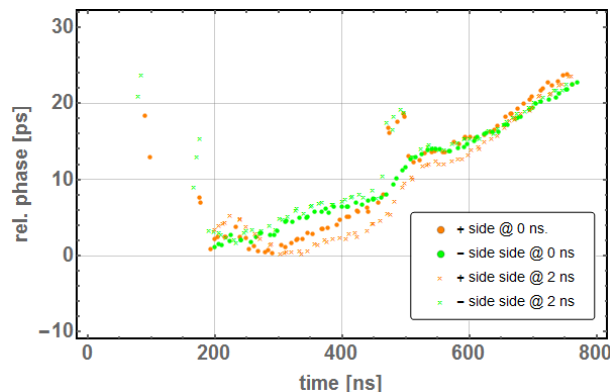


Figure 4: Measurement result of relative synchronous phase evolution in BESSY II standard user mode by using the streak camera calibrated by the high-accuracy translation stage.



a GaAs metal-semiconductor-metal (MSM) photo-detector (Hamamatsu G4176-03) having 30 ps response time for both rise and fall while keeping a low dark current of 100 pA at  $T_a = 25^\circ\text{C}$  is prepared. The diode is calibrated by short pulses produced by synchrotron radiation and a careful comparison with the streak camera. The result of bunch length measurement after the deconvolution is shown in Fig. 5.

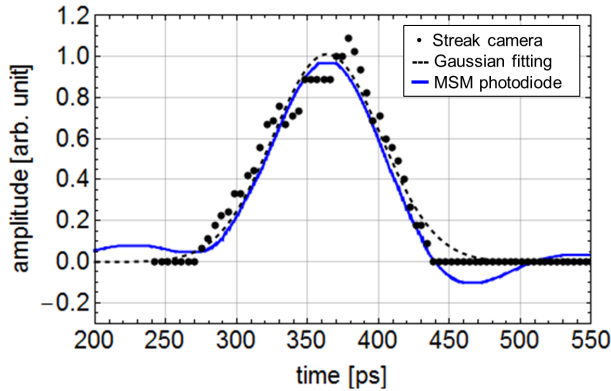


Figure 5: Temporal profile measurement using the streak camera and diode after applying the calibration in 15 mA high current single bunch operation. The measured bunch lengths using the streak camera and photodiode are 88 ps FWHM and 87.4 ps FWHM, respectively.

Apart from the development of major optical beam diagnostics stated above, the research of several feasible ideas is currently underway simultaneously.

## STATUS OF RF DIAGNOSTICS

A sophisticated operation mode, such as transverse resonance island buckets (TRIBs) for spatial separation of photon pulses has been proposed and tested at BESSY II and is being prepared for BESSY VSR [7–9]. Furthermore, fundamental power coupler of BESSY VSR cavities provide additional transverse kicks, perturbing a closed orbit and effecting transverse beam dynamics [10]. The calculation has been confirmed that beam trajectory distortions of about 100  $\mu\text{m}$  occur between the long and short bunches. This stimulates the development of a bunch-by-bunch beam position monitoring system and bunch-selective orbit feedback system. For a reliable and accurate bunch-by-bunch beam position monitor (BPM) system, the signal conditioning is required to improve position measurement quantitatively because the signal interference to the neighboring bunches by some pulse-reflections and long-range trapped mode inside the BPM electrode were observed.

Since typical LC low-pass filters produce long-range ringing due to logarithmic phase variation at the upper stopband, a linear-phase response low-pass filter is currently under investigation. In addition, a new methodology based on analog signal mixing with reflected pulses was tested and it is very promising for reducing long-time disturbances [4]. The preliminary test result of the signal conditioning with analog signal mixing with reflected pulses is shown in Fig. 6.

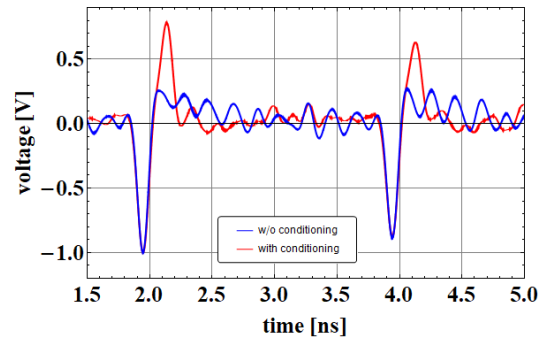


Figure 6: Preliminary test result of BPM signal conditioning with analog signal mixing with reflected pulses.

A new button-type BPM design is also under consideration to push the frequency of the trapped mode higher such that it is damped fully within 1 ns [11]. In parallel, the upgrade towards a digital BPM system for bunch-by-bunch position data acquisition is underway, particularly, involving tests with several wide-bandwidth digitizers with the analog bandwidth of more than 1 GHz and sampling speed of 1 GSa/s.

## BOOSTER DIAGNOSTICS

The bunch length on injection into the storage ring may determine the injection efficiency, particularly, the short bunch bucket in the BESSY VSR. In order to keep the high injection efficiencies, additional RF cavities will be installed to reduce the bunch length [12]. The beam commissioning of the new cavities needs essentially the monitoring of beam parameters such as the transverse beam size, bunch length, and position for actively controlling the beam in all dimensions. For the bunch length measurement, the MSM photo-diode will be installed inside the bunker. To avoid any signal distortion in time-domain by the bandwidth of digitizer, a pico-sampler developed by Karlsruhe Institute of Technology (KIT) is proposed. It is based on the state of art in wideband digitization technology using a track-and-hold amplifier [13]. The development of the pico-sampler was conducted within the ST-3 ARD Helmholtz collaboration. A frequency beating scheme which intentionally offsets the operating frequency of the digitizer will be used, thereby naturally scanning the signal with 3 ps sampling over time and scanning all signals. The preliminary test of the beating scheme is shown in Fig. 7.

## SUMMARY

Various research and development activities are currently underway in parallel to move towards BESSY VSR which is the upgrade project of the existing BESSY II ring. It is essential to improve the performance of the electron-beam diagnostics installed in the storage ring and booster. During the summer shutdown this year, the refurbishment of the floor of the new platform was successfully finished. From October this year, we plan to relocate and install existing optical diagnostics to the new platform with passive isolation

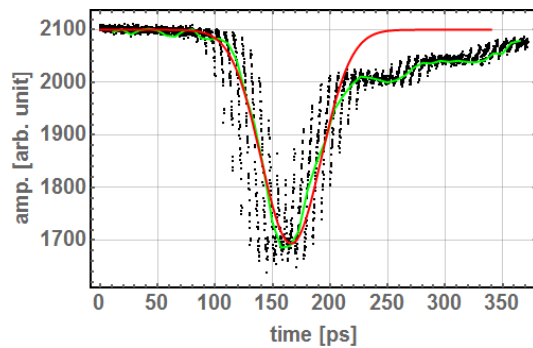


Figure 7: Preliminary test result of frequency beating scheme in the KIT pico-sampler.

legs. The test of a linear-phase response low-pass filter will be performed. A new button-type BPM design is finalized to mitigate unwanted effects caused by complex reflections and trapped modes in an insulator. It will be fabricated and installed at BESSY II next year. Other devices are still in the evaluation phase.

## REFERENCES

- [1] Helmholtz-Zentrum Berlin news and press releases, [https://www.helmholtz-berlin.de/zentrum/zukunft/vsr/index\\_en.html](https://www.helmholtz-berlin.de/zentrum/zukunft/vsr/index_en.html).
- [2] P. Schnizer, *et al.*, “Status of the BESSY VSR Project”, in *Proceedings of IPAC’18*, Vancouver, Canada, 2018, pp. 4138–4141. doi:10.18429/JACoW-IPAC2018-THPMF038
- [3] A. Jankowiak, J. Knobloch, *et al.*, “Technical Design Study BESSY VSR”, Helmholtz-Zentrum Berlin, 2015, doi:10.5442/R0001.
- [4] G. Schiwietz, *et al.*, “Development of the electron-beam diagnostics for the future BESSY-VSR storage ring”, in *Proceedings of IPAC’18*, Vancouver, Canada, 2018, pp. 2110–2113. doi:10.18429/JACoW-IPAC2018-WEPAK011
- [5] M. Koopmans, P. Goslawski, J.-G. Hwang, M. Ries, M. Ruprecht, A. Schällicke, “Status of a Double Slit Interferometer for Transverse Beam Size Measurements at BESSY II”, in *Proceedings of IPAC’17*, Copenhagen, Denmark, 2017, pp. 149–152. doi:10.18429/JACoW-IPAC2017-MOPAB032
- [6] M. Koopmans, P. Goslawski, J.-G. Hwang, A. Jankowiak, M. Ries, A. Schällicke, G. Schiwietz, “Applications of the interferometric beam size monitor at BESSY II”, in *Proceedings of IPAC’18*, Vancouver, Canada, 2018, pp. 2103–2106. doi:10.18429/JACoW-IPAC2018-WEPAK009
- [7] M. Ries, *et al.*, “Transverse Resonance Island Buckets at the MLS and BESSY II”, in *Proceedings of IPAC’15*, Richmond, USA, 2015, pp. 138–140. doi:10.18429/JACoW-IPAC2015-MOPWA021
- [8] P. Goslawski, *et al.*, “Resonance Island Experiments at BESSY II for User Applications”, in *Proceedings of IPAC’16*, Busan, Korea, 2016, pp. 3427–3430. doi:10.18429/JACoW-IPAC2016-THPMR017
- [9] F. Kramer, P. Goslawski, A. Jankowiak, M. Ries, M. Ruprecht, A. Schällicke, “Characterisation of the Second Stable Orbit Generated by Transverse Resonance Island Buckets (TRIBs)”, in *Proceedings of IPAC’18*, Vancouver, Canada, 2018, pp. 1656–1659. doi:10.18429/JACoW-IPAC2018-TUPML052
- [10] T. Mertens, T. Atkinson, F. Glöckner, A. Jankowiak, M. Ries, A. Tsakanian, “Impact of RF Coupler Kicks on Beam Dynamics in BESSY VSR”, in *Proceedings of IPAC’18*, Vancouver, Canada, 2018, pp. 3182–3184. doi:10.18429/JACoW-IPAC2018-THPAF084
- [11] J.-G. Hwang, G. Schiwietz, A. Schällicke, M. Ries, V. Dürr, D. Wolk, “Development of a new button beam-position monitor for BESSY VSR”, presented at *IBIC’18*, Shanghai, China, this conference.
- [12] T. Atkinson, T. Flisgen, P. Goslawski, J.-G. Hwang, T. Mertens and M. Ries, “VSR injector upgrade at BESSY II”, in *Proceedings of IPAC’18*, Vancouver, Canada, 2018, pp. 4110–4113. doi:10.18429/JACoW-IPAC2018-THPMF030
- [13] M. Caselle, “KAPTURE-2 – A picosecond sampling system for individual THz pulses with high repetition rate”, TWEPP2016, Karlsruhe (2016).

# THERMAL COEFFICIENT OF DELAY MEASUREMENT OF THE NEW PHASE STABLE OPTICAL FIBER \*

Jiaji Liu†, Xinpeng Ma, Guoxi Pei, Institute of High Energy Physics Chinese Academy of Sciences, Beijing, China

## Abstract

The Thermal Coefficient of Delay (TCD) is an essential parameter of optical fiber which determines a fiber's phase transfer stability due to temperature variation. The TCD of a new phase stable single mode optical fiber (YPSOC) from Yangtze Optical Fibre and Cable Company (YOFC) is measured. The radio frequency (RF) signal is modulated to optical wave by a laser module which is transmitted through the 400-meter long YPSOC to be measured. The returned optical wave is demodulated to RF signal by the photodetector. A phase detector and a data acquisition module (DAQ) are used to acquire the phase difference between the forward and returned signals. Two temperature-stabilized cabinets are designed to maintain and control the ambient temperature of the measurement system. The TCD of less than 10 ps/km/K at room temperature is obtained. YPSOC and the measurement platform can be applied on signal transmission or measurement system that need to compensate the temperature drift.

## INTRODUCTION

In the long-distance optical wave transmission system, the optical path length will change due to the different temperatures on the transmission path, which will introduce phase drift to the RF/digital transmission system. The TCD range of most standard single mode fibers (SMFs) is from 33.4 to 42.7 ps/km/K.

But, The TCD of phase stable optical fiber (PSOF) by Furukawa is below 5 ps/km/K [1]. And the strong tether fiber optic cable (STFOC) from Linden Photonics is nearly as good as PSOF, its TCD is below 7 ps/km/K [2].

Using this kind of phase stable optical fiber instead of a conventional one will reduce the delay change of the stable RF transmission system.

## TESTED CABLE

The phase stable optical fiber is generally composed of standard optical fiber and negative expansion coefficient materials, therefore it has a good temperature performance and tensile strength. YPSOC is coated with liquid crystal polymer (LCP). A purpose of LCP coating is to make the temperature dependence of transmission delay time small [1]. YPSOC has a 250 μm tight buffered cable core, followed by a tight buffered LCP coating and a soft outer jacket (Fig. 1) [3].

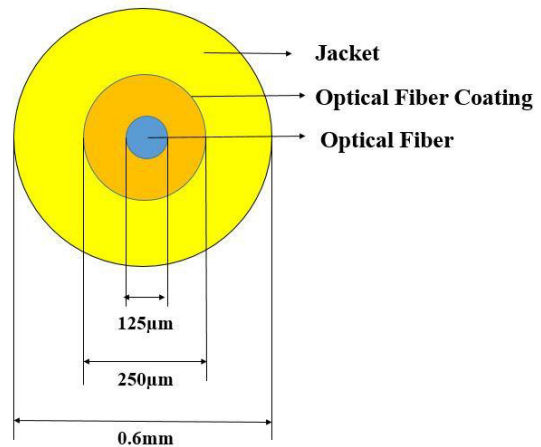


Figure 1: Cross sectional view of YPSOC.

## MEASURE CONCEPT

There has several methods to measure the TCD of a fiber. For example, the TCD of a fiber which is coupled with jacket can be calculated by a formula. But it is complex and difficult to calculate TCD by using this formula [4].

On the other hand, an electronic and optical system can be used to measure the TCD by changing the ambient temperature of the fiber and detecting the time shift. This method is simple and operational. So, the TCD of a fiber can be calculated by the following formula.

$$\text{TCD} = \frac{\text{Delay shift}}{\text{Temperature change} * \text{Fiber Path}} \quad (1)$$

A TCD measurement system based on the second method is designed. The layout of the fiber measurement system is shown in Fig. 2. The black lines are RF signal path and the green lines are optical wave path. The RF signal is sent to the power splitter from an analog signal generator, and transmitted to the laser module and the phase detector. The optical wave (1552 nm) from the laser module is propagated to the receiver through the optical circulator and the 400-meter long YPSOC, then retroreflected by a Faraday rotation mirror (FRM) at the end of the fiber. The round trip optical wave goes through the same fiber. The retroreflected optical wave is converted to RF signal by the photodetector, and transmitted to the phase detector through the amplifier, then compared with the local RF signal. Since the delay through fiber and other RF components is temperature dependent, RF and optical components are temperature stabilized to  $\pm 0.01$  °C.

† liujj@ihep.ac.cn

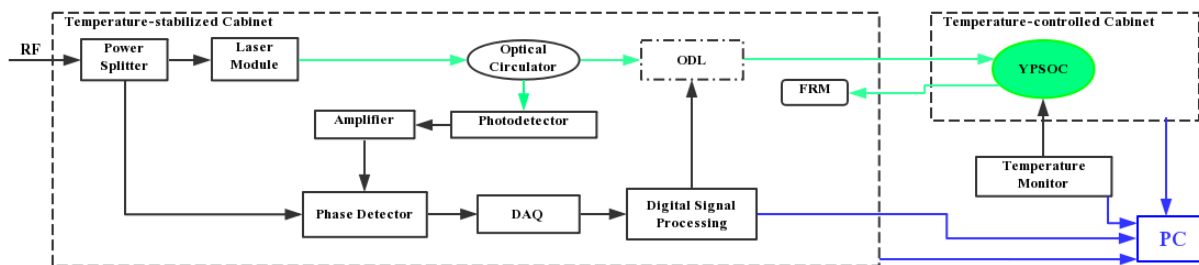


Figure 2: The layout of the fiber measurement system.

The fiber cable can be set in another temperature-controlled box, in order to change the ambient temperature of the fiber manually. A temperature probe is pasted on the fiber and connected to a temperature monitor to obtain the accurate ambient temperature of the fiber.

## PHASE DETECTOR TEST

The phase detector unit is based on the Analog Devices HMC439 IC, its measurement stability is determined by temperature stability and low noise power supply. Its corresponding phase detection range is  $-180^{\circ}\sim180^{\circ}$ . The phase detector's coefficient of the delay and phase detector output is measured with the system shown in Fig. 2. A motorized optical fiber delay line (ODL) is used to change the delay of the system, its variable delay ranges from 0 to 560 ps, but a FRM is inserted at the end of the fiber, so the range of the total delay could be from 0 to 1220 ps.

Measurement of the phase detector is repeated three times, the delay change vs. phase detector output curve is obtained as shown in Fig. 3. The linear fitted result shows that the phase resolution of this phase detector is 2.5 mV/ps.

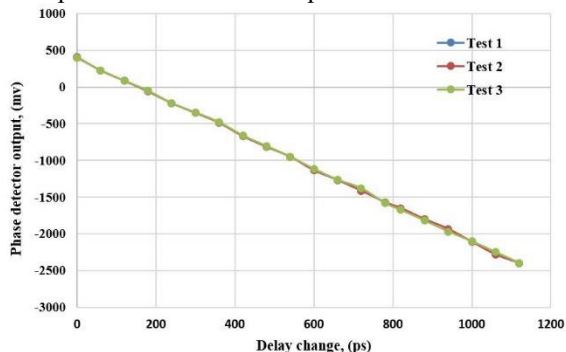


Figure 3: The fitted curve of delay change and phase detector output.

## PHOTODETECTOR TEST

An important parameter with photodiode detection of RF is amplitude-to-phase conversion. If the average optical power varies, the photodiode junction capacitance will be modulated because of the changes in carrier density, then resulting in a shift of RF phase [5]. The amplitude-to-phase response of an EOT's  $>12.5$  GHz Photodetector is measured twice. An optical attenuator is used to change the input optical power of the photodetector, and the phase detector

is used to detect the time shift between the local RF signal and the output RF signal of the photodetector.

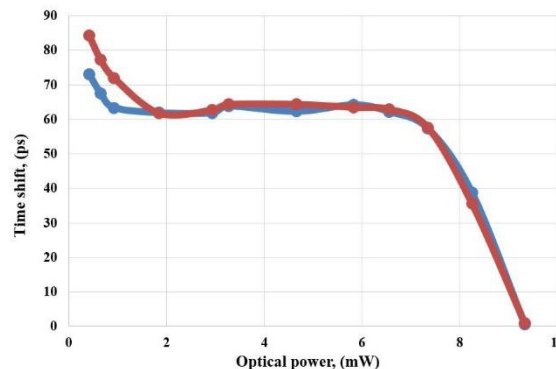


Figure 4: Photodetected phase of 500 MHz RF vs. incident optical power, for an EOT's Photodetector.

In Fig. 4, time shift is stabilized when incident optical power of the photodetector is between 2 mW~7 mW.

## TEMPERATURE-CONTROLLED CABINET DESIGN

The Peltier cooling units are used to stabilize the temperature of all the key components of the measurement system such like laser module, amplifier, photodetector, fiber jumpers, phase detector and ODL. Also the fiber under test is enclosed into a temperature-controlled cabinet to change its ambient temperature. The temperature stability is within  $\pm0.01^{\circ}\text{C}$ .

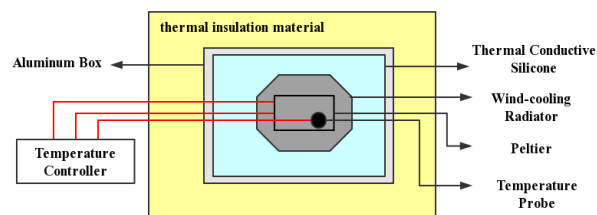


Figure 5: The layout of temperature-controlled cabinet.

We fabricated two temperature-controlled cabinets for the transmitter and the tested fiber. The layout of temperature-controlled cabinet is shown in Fig. 5. The outside of the box is made by thermal insulation material to isolate the heat change. The inside of the each box is made by aluminium to keep the controlled temperature at whole area. The temperature stability is shown in Fig. 6.



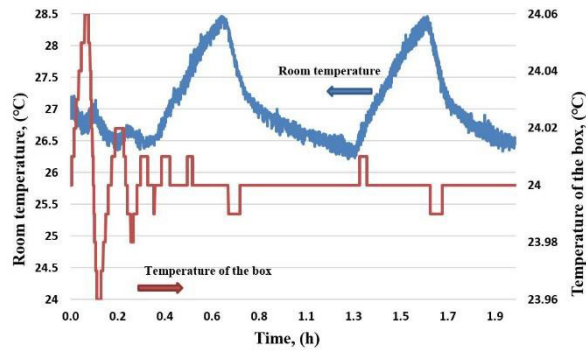


Figure 6: Temperature stability measurement of the temperature control box.

The blue line shows the room temperature, which changes about  $\pm 1$  °C. The red line shows the temperature of the temperature control box, which keeps the temperature about  $\pm 0.01$  °C over 1.5 hours. The achieved temperature stability depends on the room temperature, the heat generated by the component and the ability of the cooling system. The system could keep the temperature stability less than  $\pm 0.02$  °C for a long time measurement.

## MEASUREMENT RESULT

After 8.5 hours of testing, the ambient temperature of fiber and the phase delay curves are shown in Fig. 7. The temperature vs. delay curve is shown in Fig. 8, as the temperature changes from 17.2 °C to 45.6 °C, the delay totally shifts 166ps. Because the optical wave passes the optical fiber twice, the path length of the optical wave transmitting through the optical fiber is 800 m. So, the average TCD of YPSOC is 7.3 ps/km/K (temperature between 17.2 and 45.6 °C).

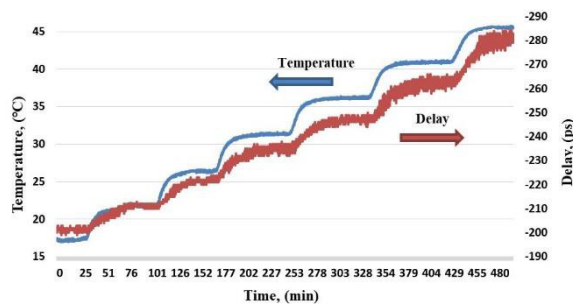


Figure 7: Ambient temperature of the fiber versus the phase delay.

In order to calculate the TCD of the fiber at different temperatures, the corresponding curve slope is required at different temperatures, this slope value is the TCD at this temperature. As the temperature-dependent TCD curve shown in Fig. 9, the fiber's TCD ranges from 5 to 10.5 ps/km/K and grows as the temperature increases as the temperature ranges from 17.2 to 45.6 °C.

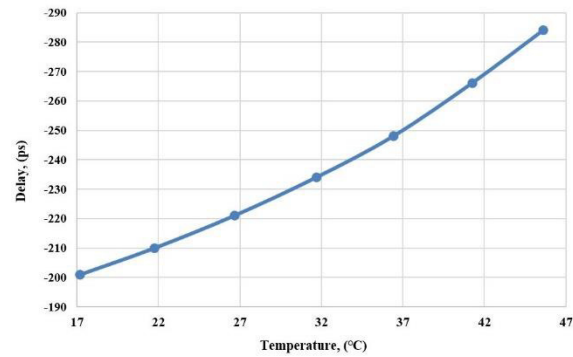


Figure 8: Curve of phase delay vs. temperature change.

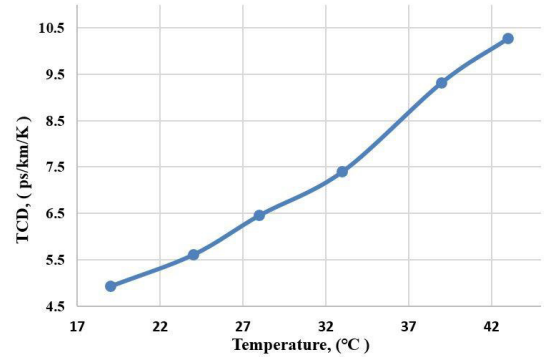


Figure 9: TCD of Yangtze's fiber curve with temperature.

## CONCLUSION

The TCD of YPSOC ranges from 5 to 10.5 ps/km/K (average 7.3 ps/km/K) under the usual operating temperature (17.2 °C~45.6 °C). The measurement result matches the TCD specification provided by YOFC, and YPSOC will be used for the stable phase reference line of BEPC-II and HEPS in the future.

## REFERENCES

- [1] *Specification of Phase Stabilized Optical Fiber Cord with Connector (APC)*, Furukawa Electric, Tokyo, Japan, Sep. 2015, pp. 5.
- [2] M. Bousonville *et al.*, "New phase stable optical fiber", in *Proc. BIW'2012*, Newport News, VA, USA, Apr. 2012, pp. 101-103.
- [3] Yangtze Optical Fiber Company, private communication, Aug. 2018.
- [4] Kashyap, *et al.*, Inventor, "Temperature Desensitization of Delay in Optical Fibres", Patent Authority and No., Apr. 08, 1990.
- [5] R. B. Wilcox *et al.*, "Phase Stable RF-over-fiber Transmission using Heterodyne Interferometry", in *Proc. NOFEC's2010*, San Diego, CA, Mar. 2010.  
doi : 10.1364/NF0EC.2010.JThA38

# BEAM PHASE MEASUREMENT SYSTEM IN CSNS LINAC

Peng Li<sup>#, 1</sup>, Wei Peng<sup>2</sup>, Fang Li<sup>1</sup>, Jun Peng<sup>1</sup>, Ming Meng<sup>1</sup>, Taoguang Xu<sup>1</sup>  
<sup>1</sup> Institute of High Energy Physics (IHEP), Chinese Academy of Sciences (CAS),  
 523803, Dongguan, China  
<sup>2</sup> 38th Institute of China Electronics Technology Group Corporation (CETC-38),  
 230088, Hefei, China

## Abstract

We developed beam phase measurement system ourselves in CSNS (China Spallation Neutron Source). The resolution of the system is less than  $0.1^\circ$  and the accuracy is less than  $1^\circ$ . It played a key role in CSNS Linac commissioning especially in RFQ and DTL commissioning. Further we measured the beam energy by TOF (Time of Flight) method base on this system. The energy accuracy is less than 0.1 MeV.

## INTRODUCTION

The CSNS accelerator consists of an 80MeV H- Linac, a 1.6 GeV Rapid Cycling Synchrotron (RCS) and related beam transport line. There are three beam transport line in Linac: Low Energy Beam Transport line (LEBT) after the 50 keV H- Ion Source, Medium Energy Beam Transport line (MEBT) after the 3MeV Radio Frequency Quadrupole (RFQ), Lianc to Ring Beam Transport line (LRBT) after Drift Tube Linac (DTL). Beam is transported to Target after it be accelerated to 1.6GeV in RCS [1]. The layout of the CSNS Linac is shown in Fig. 1.

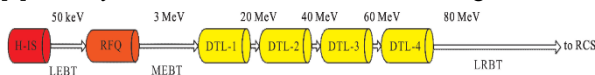


Figure 1. Layout of CSNS Linac.

The repeat period of H- beam macro-pulse is 40ms and pulse width is about 500 $\mu$ s. The radio frequency of beam is 324 MHz and the beam micro-pulse duty ratio is about 30%.

## BEAM PHASE MEASUREMENT SYSTEM

FCT sensors are used as beam phase detectors [2] which were produced by Bergoz company. FCT sensor has a rapid signal rise time, which is shorter than 200 ps so it's good for 324 MHz signal's measurement. And the output of FCT sensor signal also has the 324 MHz time structure [3].

The electronics are researched and developed by IHEP and CETC-38 together in China. There are two sets beam phase measurement systems in CSNS Linac and each set has 8 channels for FCT output signals.

Sub-sampling technology has been adopted to realize the electronics. The ADC sample clock is just 100 MHz shown in Fig. 2. Each channel's phase output is the difference between FCT output signal phase and a reference signal phase. The reference signal is a 324 MHz sine wave signal which from the same RF frequency source with beam. Non-coherent digital IQ

demodulation technology and CORDIC algorithm are used for phase calculation in FPGA. The schematic is shown in Fig. 3.

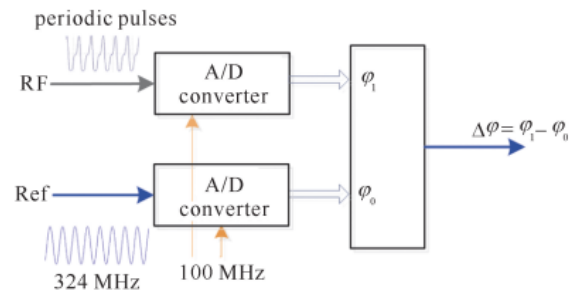


Figure 2. Principle of phase measurement.

The electronics phase resolution is less than  $0.1^\circ$  and the phase non-uniformity between channels limited in  $\pm 0.2^\circ$ . The amplitude accuracy is better than 1% and the phase accuracy is better than  $0.3^\circ$ . We had test the whole system for more than 7 days online with a precise signal generator and find its accuracy is better than  $1^\circ$ .

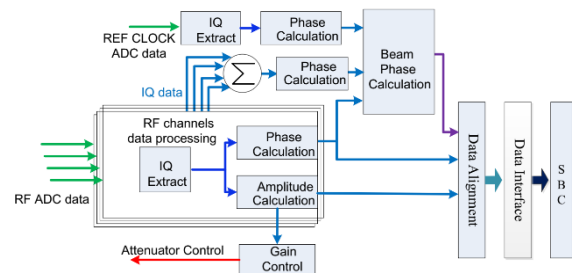


Figure 3: Schematic in FPGA.

The beam phase measurement system played a key role in CSNS Linac commissioning especially in RFQ and DTL commissioning. The RFQ and DTL cavity power phase varied after several days' shutdown or other accident problems. The beam phase measurement system would be running in such a situation.

## BEAM ENERGY MEASUREMENT

Beam energy could be calculated by TOF method meanwhile [4]. The distance between FCT sensors are known after they were installed easily. The beam flight time between FCT sensors is computed by phase difference indirectly. Then the beam velocity and energy could be calculated.

There are 5 FCT sensors and 1 set electronics could be used to compute beam energy after beam pass through RFQ, Buncher-1, Buncher-2 in CSNS Linac MEBT. See Fig 4.

<sup>#</sup>lipeng@ihep.ac.cn

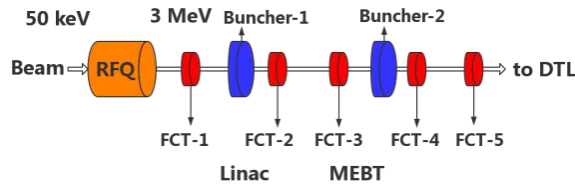


Figure 4: CSNS Linac MEBT layout.

And there are 8 FCT sensors and 1 set electronics be used to compute beam energy after beam pass through 4 DTL cavities and Debuncher. See Fig 5.

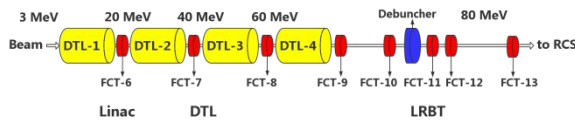


Figure 5: CSNS Linac DTL and LRBT layout.

Due to the distance between FCT sensors and beam theory energy is known. The approximate beam flight time could be estimated. And the exact time is computed by the phase difference:

$$t = \left( \frac{\varphi_2 - \varphi_1}{360} + N \right) \times T \quad (1)$$

$T$  is the RF frequency of beam, here  $T = 1/324$  MHz, and the  $N$  is the period number estimated by the theory energy. We could adjust it manually in practice. So it is an indirect method to measure beam energy.

Any two FCT sensors could be calculated an energy number using Eq. (1) when you confirm beam was not be accelerated or decelerated between them. Apparently the different combinations would get different results. So how can we know which result is right? I have two principles: 1, each combination should be consistent with others. For example,  $N$  is 25 when you choose FCT-1 and FCT-2,  $N$  is 20 when you choose FCT-1 and FCT-3, therefore  $N$  only could be 45 when you choose FCT-1 and FCT-3. You cannot adjust it to 46 or 44 in calculation even if the result seems closer to theory energy. The all combination results display uniformity once you applied the correct  $N$  parameter. 2, The farther of distance between FCTs, the more accurate result you got. The result of FCT-1 and FCT-3 is more accurate than the result of FCT-1 and FCT-2.

Of course, you can measure the time between FCT sensors using a high precision oscilloscope directly. But the error would be very large when flight time is long.

The energy measurement precision of the indirect method in TOF depends on the period number  $N$ . The resolution using our beam phase measurement is less than 0.01 MeV, the accuracy is about 0.02 MeV in any fixed combination, and the accuracy is 0.1 MeV after take all combinations into account. One reason is the inconsistency among FCT sensors and according electronics channels were not been completely eliminated. Table 1 list the beam energy measurement result in CSNS Linac experiment.

Table 1: The Beam Energy Measurement Result in CSNS Linac Experiment

Energy[MeV]	Theory	Measured	Deviation
<b>RFQ</b>	3.0258	3.0284	+0.08%
<b>DTL-1</b>	21.67	21.73	+0.28%
<b>DTL-2</b>	41.42	41.54	+0.29%
<b>DTL-3</b>	61.07	61.36	+0.47%
<b>DTL-4</b>	80.09	80.34	+0.31%

## CONCLUSION

The beam phase measurement systems have been running well since January 2016. It outputs accurate phase result in RFQ and DTL commissioning. On the other side about beam energy measurement, it takes a long time and many times experiments to ascertain the efficiency of the indirect TOF method. Then I got the two principles to determine the estimated period number  $N$  and checked by different FCT sensors' combination. Finally, the measured beam energy result is authentic and helpful for commissioning.

## REFERENCES

- [1] Sheng Wang, J. Peng, H.F.Ouyang, S.N. Fu, "Beam Commissioning Plan for CSNS Accelerators", *Proceedings of HB2012*
- [2] Ikegami M, Kondo Y, Ueno A., "RF tuning schemes for J-PARC DTL and SDDL", *Proceedings of 2<sup>nd</sup> International Linear Accelerator Conference (LINAC 2004)*, 2004, pp:414-416.
- [3] <http://www.bergoz.com>, Bergoz Instrumentation, Fast Current transformer User's manual
- [4] W. Le Coz, C. Doutressoulles, C. Jamet, et al. "Measurement and control of the beam energy for the SPIRAL2 accelerator", *Proceedings of IBIC2013*, Oxford, UK, Sep. 2013, pp:897-899

## INTRODUCTION

Superconducting linac based FELs (Free Electron Lasers) require control of the main RF phase relative to beam arrival time at a very precise level. At FLASH [1] and the E-XFEL (European X-ray FEL) [2], the LLRF (Low Level Radio Frequency) system is responsible for regulation of the RF fields [3]. A “vector-sum” method is applied to control the beam phase. The field vector of each single cavity is measured and then the field vector-sum of up to 32 cavities is calculated. A klystron feeds up to 4 modules with high power 1.3 GHz fields. Each module contains eight superconducting nine cell cavities. Figure 1 shows a schematic view of the LLRF control system [4]. The vector-sum has to be stabilized in amplitude and phase to a given set point. [5]. The stability of the RF amplitude and phase is required to be below 0.01% and 0.01° RMS respectively for both FLASH and the E-XFEL. The control system acts onto the vector-sum and keeps it constant, while each single cavity field within the vector-sum can fluctuate.

A new method based on HOM (Higher Order Modes) to determine the beam phase was developed [6]. When an electron bunch transverses a superconducting cavity, HOMs are excited, which carry the beam phase information. Two couplers located at each side of the TESLA cavity were specially designed to damp and extract the HOM signals. The power leakage of the accelerating field is also picked up by the HOM couplers. These fields can

be used to determine the beam phase with respect to the accelerating RF fields. The monopole modes are most suited for beam phase measurement since they are not affected by beam offset. In this paper, we choose the 2<sup>nd</sup> monopole mode in TM011 band and built a scope based setup. This HOM-BPhM system is an on-line direct beam phase measurement with respect to the RF.

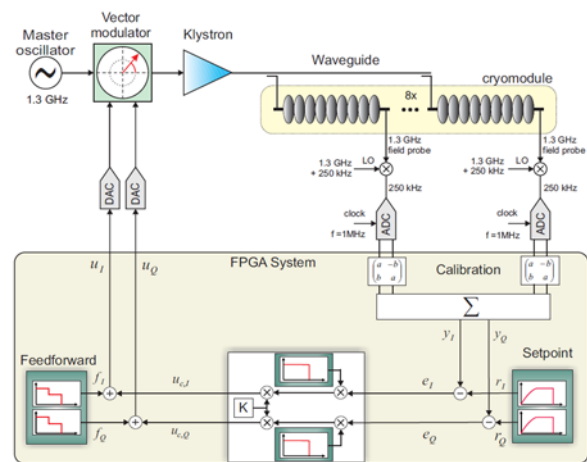


Figure 1: Schematic view of the current LLRF control system consists of analogue and digital sections [4].

In this paper, we first introduce the principle of the HOM-BPhM and then present the result of the long term measurements.

## PRINCIPLE OF HOMBPHM

### Beam Phase Concept

The electric field of each single cavity picked up with probe antennas give the vector-sum [7]. It is assumed that all cavities have the same physical behaviour, which means that the transient field induced by the beam has the same absolute value in each cavity [8]. The calibration is based on measuring this transient in amplitude and phase of each cavity and then calculating the ratio of the single cavity field to the vector-sum.

For maximum acceleration, the RF field should reach its maximum when the beam passes through the centre of the cavity. We define the beam phase according to the time difference between two instants: when the beam passes the cavity AND when the accelerating gradient in the cavity is maximum. The point of maximal accelerating voltage is called “on-crest”, see Fig. 2 [8]. In ACC1 (the first accelerating module in FLASH), and similarly at the E-XFEL, the beam is accelerated “off-crest” to induce a bunch

<sup>†</sup> junhao.wei@desy.de.



energy profile to meet the requirement for longitudinal compression in the bunch compressor section [8].

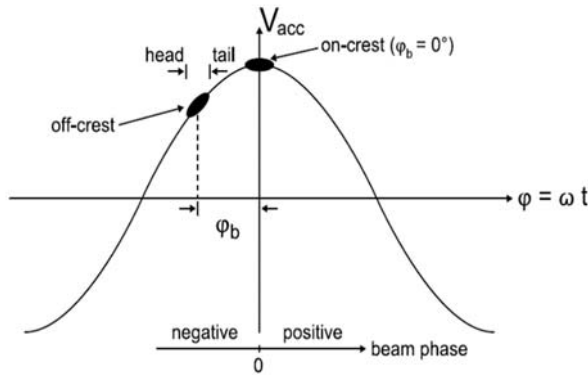


Figure 2: Schematic of beam phase, “on-crest” and “off-crest” concept [3].

The disadvantage of the vector-sum is that the single cavities are not individually controlled. The actual situation in each cavity is underdetermined.

During the facility operation, the RF field from the klystron is usually far stronger than beam excited fields, therefore the probe phase basically indicates the RF phase. It is difficult to separate the beam phase information from the probe detected signal. However, the coupler signal contains both the accelerating mode and the HOMs. This provides an approach to calculate the beam phase directly with respect to the RF phase from one measurement.

### Signal Process

The 9-cell TESLA cavity contains one power input coupler, one pick-up probe antenna and two HOM couplers. The probe detects the 1.3 GHz electric field inside the cavity and the couplers at each side of the cavity provide two HOM signals (HOM1 and HOM2).

Figure 3 shows the diagram of the HOM-BPhM setup [9]. Only one channel is shown. The signal comes from the two HOM couplers on one cavity via RF cables to the measurement rack. A power splitter divides each signal in two. Each of them is then filtered individually, one centred at approximately 1.3 GHz with 100 MHz bandwidth, and the other one at approximately 2.4 GHz with 190 MHz bandwidth. Next, the two filtered signals are combined together to feed into a Tektronix oscilloscope, which has a 20 GS/s sampling rate with a 6 GHz bandwidth. One PC serves as a TCP/IP client connects the scope and the other one as a server for recording data from control system.

As we known, any periodic signal can be decomposed into a Fourier series of simple oscillating functions. In our case, the signal  $x(t)$  can be written as:

$$x(t) = a_0 + \sum_{n=1}^N (a_n \cos(\omega_n t) + b_n \sin(\omega_n t)), \quad (1)$$

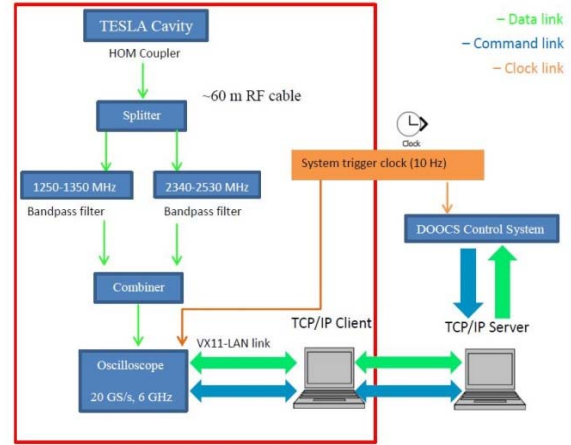


Figure 3: Block diagram of beam phase measurement setup. The figure shows one of the 2 channels from the two HOM couplers of one cavity.

where  $\omega_n = 2\pi f/N$  is the angular frequency,  $a_0$  is the signal offset and the Fourier coefficients  $a_n$  and  $b_n$  are computed as follows:

$$a_n = \frac{2}{T} \int_0^T x(t) \cos(\omega_n t) dt$$

$$b_n = \frac{2}{T} \int_0^T x(t) \sin(\omega_n t) dt \quad (2)$$

For the  $n^{\text{th}}$  HOM mode, the mode amplitude and mode phase can be calculated from its Fourier coefficients:

$$A_n = \sqrt{a_n^2 + b_n^2}; \varphi_n = \arctan 2(a_n, b_n). \quad (3)$$

The phase of each mode can be calculated with Eq. (3). Also, according to the definition in the previous section, the beam phase with respect to the accelerating mode can be written as:

$$\varphi_{beam} = \varphi_0 - \omega_0 \cdot \sum_n \frac{w_n \varphi_n}{\omega_n}, \quad (4)$$

where  $\varphi_0$  and  $\omega_0$  are the phase and angle frequency of RF at 1.3 GHz,  $w_n$  is the weight factor of mode  $n$  according to its power. However, the phase we obtained is not the correct one, due to the different phase of the signals after passing through the cables.

The spectra of the HOM signals excited by one bunch in cavity 1, ACC1, are shown in Fig. 4. The accelerating mode at 1.3 GHz from the klystron is the strongest mode, and the 8<sup>th</sup> and 9<sup>th</sup> modes among the TM011 band modes are excited stronger than the others, because of their higher  $R/Q$ . Therefore, these two modes are chosen to be used to determine the beam phase.

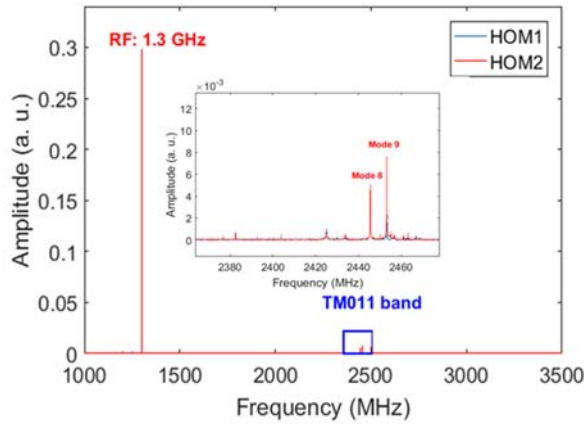


Figure 4: Measured spectra of signals HOM1 and HOM2 from the 2 couplers. Inset: spectra of TM011 mode band. The frequency step is 50 kHz.

## LONG TERM HOMBPHM MONITORING

### Signal Analysis

The HOM-BPhM has been used over longer periods of time to measure simultaneously the signals from the two couplers of one cavity. Figure 5 shows the beam phase obtained with different HOM modes measured from HOM1 and HOM2. The data was measured during 24 hours on August 17th. During the measurement, the RF phase was relatively stable.

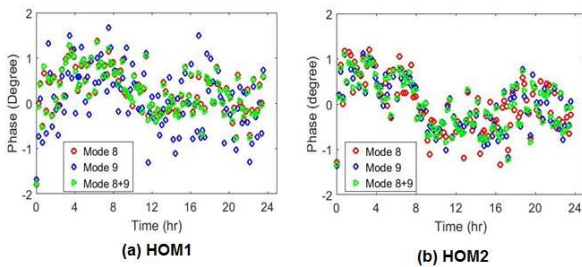


Figure 5: Beam phase measurement by using mode 8 (red), mode 9 (blue) and both modes (green) from HOM (a) and HOM2 (b).

In Fig. 4, the amplitude of mode 9 from HOM1 is smaller than of mode 8, thus it is affected more easily by noise. Also the beam phase measured with mode 9 from HOM1 has the worst RMS value in Fig. 5. The beam phase resolution calculated from coupler1 and coupler2, based on the difference of the two HOMs signals, is  $0.30^\circ$  for mode 8,  $0.43^\circ$  for mode 9 and  $0.27^\circ$  when using both. We obtain the best resolution by using the information of both modes.

A good knowledge of the mode frequencies is important for the phase determination (see eq. (4)). In order to investigate the effect caused by the error of the mode frequency in the phase measurement, the frequencies used for phase calculation are shifted from -50 kHz to 50 kHz with a 1 kHz step. The centre frequency measured by a Real-time Spectrum Analyser (RSA) is 2.445481 GHz for mode 8

and 2.455319 GHz for mode 9. Figure 6 shows the dependence of the phase resolution on the mode frequency shift.

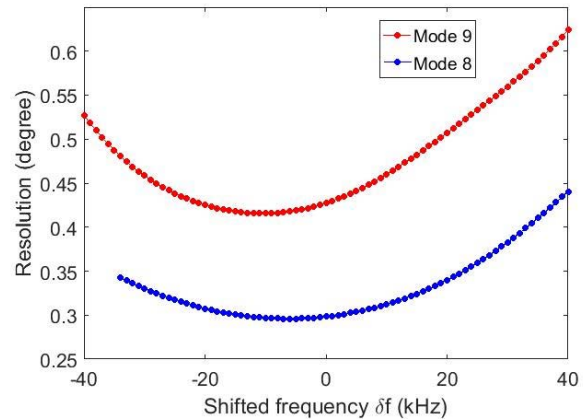


Figure 6: Resolution dependence on the frequency shift of modes 8 and 9 with a step of 1 kHz.

When the frequencies used in Eq. (4) are shifted far away from the actual mode frequencies, the resolution becomes larger. Also, the centre frequencies given by the RSA are not at the minimum resolution points. This means there is an error in the measured mode frequency. On the other hand, when the frequency error is small, the resolution is affected only slightly.

### Long Term Phase Measurement

From August 1<sup>st</sup> to 21<sup>st</sup> we measured the beam phase in cavity 1 of ACC1 at FLASH with some interruptions. Each time, the beam phase was monitored continuously for 2 to 3 days. After removing the invalid data caused by the facility commissioning, we obtained about 7500 effective measurements, shown in Fig. 7. In order to more intuitively present the relationship between the HOM phases, the probe phase and the “Vector-Sum” (VS) phase, we subtract the VS phase from the HOM phases and the probe phase, and then shifted them to zero (for the first measurements), as shown in Fig. 8. The VS calibration curve gives the value of recalibrated zero VS phase.

As we can see from the two figures, the HOM and probe phases initially have a similar evolution as the VS phase, but drift away over time. The VS calibration procedure can eliminate the phase drift and bring the RF phase in cavity one close to the VS phase. Small differences between the HOM-based measured beam phases and the probe RF phase were observed, which can be due to the beam phase jitter and non-synchronous data taking. The RMS error of the HOM-BPhM over the whole period is  $0.41^\circ$ . According to previous simulations [9], the resolution of the monitor depends crucially on the Signal-Noise Rate (SNR) in the system. In our system a 10 dB SNR is present, and is expected to be improved by the electronics now under design [10].

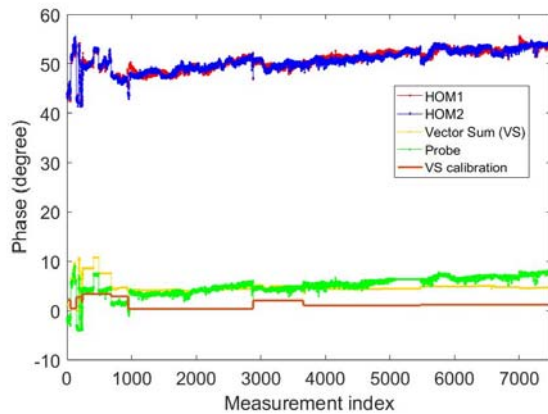


Figure 7: Long term phase measurement at FLASH. The HOM1 and HOM2 phases were measured in cavity 1 in ACC1 at FLASH with the HOM-BPhM system. The VS phase, probe phase and VS calibration phase were recorded from the control system.

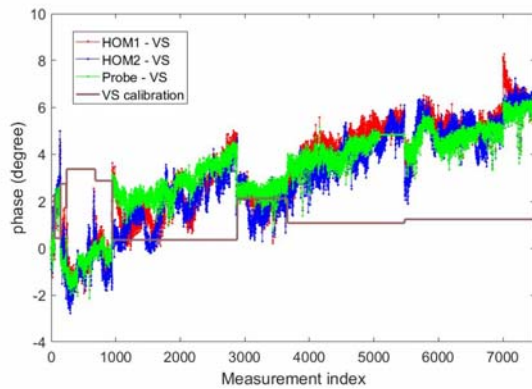


Figure 8: Phase differences of the HOM phases and probe phase with respect to the VS phase.

## SUMMARY

In this paper, we present long-term HOM-based beam phase measurements in cavity 1 of the ACC1 module at FLASH. A scope based setup has been used.

The HOM phase and the probe phase are comparable. The biggest difference between the HOM phase and the probe phase is about 2°. The RMS error of the beam phase difference between HOM1 and HOM2 observed is 0.41°. This is mainly caused by the strong noise from the data acquisition system. An electronics based on direct sampling, now under development, is expected to improve the resolution.

## REFERENCES

- [1] M. Vogt *et al.*, “Status of the Soft X-ray Free Electron Laser FLASH”, in *Proc. IPAC’17*, Copenhagen Denmark, May 2017, pp. 2628-2630. doi:10.18429/JACoW-IPAC2017-WEPA025
- [2] R. Abela *et al.*, “The European X-Ray Free-Electron Laser Technical Design Report”, DESY, Hamburg, Germany, Rep. DESY 2006-097, 2007.
- [3] T. Schilcher, “Vector Sum Control of Pulsed Accelerating Fields in Lorentz Force Detuned Superconducting Cavities”, PhD thesis, Hamburg University, Germany, 1998.
- [4] C. Schmidt, “RF System Modeling and Controller Design for the European XFEL”, PhD thesis, Hamburg University, Germany, 2010.
- [5] M. Hoffmann, “Development of a multichannel RF field detector for the Low-Level RF control of the Free-Electron Laser at Hamburg”, PhD thesis, Hamburg University, Germany, 2008.
- [6] S. Molloy *et al.*, “High Precision Superconducting Cavity Diagnostics with Higher Order Mode Measurements”, *Phys. Rev. ST Accel. Beams*, vol. 9, p. 112802, Nov. 2006.
- [7] B. Aune *et al.*, “Superconducting TESLA Cavities”, *Phys. Rev. ST Accel. Beams*, vol. 3, p. 092001, Sep. 2000.
- [8] A. Brandt, “Development of a Finite State Machine for the Automated Operation of the LLRF Control at FLASH”, PhD thesis, Hamburg University, Germany, 2007.
- [9] L. Shi, “Higher-Order-Mode Based Beam Phase and Beam Position Measurements in Superconducting Accelerating Cavities at the European XFEL”, PhD thesis, University of Manchester, UK, 2017.
- [10] S. Jabłoński, N. Baboi, U. Mavrič, and H. Schlarb, “RF Electronics for the Measurement of Beam Induced Higher Order Modes (HOM) Implemented in the MicroTCA.4 Form Factor”, in *Proc. IPAC’18*, Vancouver, BC, Canada, May 2016, pp. 1916-1918. doi:10.18429/JACoW-IPAC2018-WEPA046

# DIFFERENTIAL EVOLUTION GENETIC ALGORITHM FOR BEAM BUNCH TEMPORAL RECONSTRUCTION\*

D. Wu, D. X. Xiao, J. X. Wang<sup>†</sup>

Institute of Applied Electronics, China Academy of Engineering Physics, Mianyang, 621900, China

## Abstract

Coherent radiation, such as coherent transition radiation, coherent diffraction radiation, coherent synchrotron radiation, etc, can be used to measure the longitudinal distribution of the electron beam bunch of any length, as long as the coherent radiation spectrum can be measured. In many cases, the Kramers-Krönig relationship is used to reconstruct the temporal distribution of the beam from the coherent radiation spectrum. However, the extrapolation of the low frequency will introduce the uncertainty of the reconstruction. In this paper, an algorithm of differential evolution (DE) for temporal reconstruction is discussed. The DE reconstruction works well for the complex and ultrashort distribution. It will be an effective tool to accurately measure the femtosecond bunch temporal structure.

## INTRODUCTION

During the past decades, many methods were developed to measure ultrashort electron beam bunch length, such as streak camera [1], RF zero-phasing [2], deflecting cavity [3], electro-optic sampling [4] and coherent radiation [5–7]. Coherent radiation, such as coherent transition radiation, coherent diffraction radiation, coherent synchrotron radiation, etc, can be used to measure the longitudinal distribution of the electron beam bunch of any length, as long as the coherent radiation spectrum can be measured. When the electron bunch length become as short as a few femtosecond nowadays, the coherent radiation method becomes the best length-measurement tool.

However, the coherent radiation measurement is to record the spectrum of the radiation, which loses the phase information. To reconstruct the longitudinal distribution, the phase information must be reconstructed first. For a long time, Kramers-Krönig (KK) relation was invited to retrieve the phase information. Unfortunately, there are at least three disadvantages of the KK relation. Firstly, extrapolation in the low frequency band will bring uncertainty to reconstruction. Secondly, KK relation is less accurate when time domain distribution is complicated. Thirdly, KK relation costs longer calculation time.

GrEedy Sparse PhAse Retrieval (GESPAR) method was presented by Y. Shechtman and Y. C. Eldar in 2014 [8, 9]. And then it has rapidly gained great applications in coherent imaging, signal processing, macromolecular imaging, and

5G communication[10–12]. GESPAR treats phase reconstruction as a nonlinear least squares problem, and assumes that the time domain signal is composed of a finite number of specific distributions.

In this paper, we invite the Differential evolution (DE) genetic algorithm to solve the nonlinear least squares problem. And the reconstruction with or without the GESPAR assumption is presented, respectively. At last, a temporal reconstruction with DE algorithm is shown from the signal measured on the Chengdu THz FEL (CTFEL) [13] facility.

## RECONSTRUCTION ALGORITHM

### Phase Retrieval with Nonlinear Least Squares

Assuming  $\rho(t)$  is the original time signal, whose frequency signal is  $\hat{\rho}(\nu) = F(\rho(t)) = |\hat{g}(\nu)|e^{-\phi(\nu)}$ , where  $F$  represents the Fourier transform,  $|\hat{g}(\nu)|$  is the amplitude and  $\phi(\nu)$  is the phase.

Four the nonlinear least squares consideration, the objective is to minimize the function  $f = \|\hat{\rho}_G^2 - |\hat{g}|^2\|$ , where  $\hat{\rho}_G$  is the  $G$ -th alternative signal. The flow-chart is shown in Fig. 1.

According to the Fourier transform relationship, we can normalize any segment of the time domain signal to the signal in the (0,1) time period. If the setting unit is 1 s, the corresponding frequency domain unit interval is 1 Hz, for example. And similarly, 1 ps in time domain corresponds 1 THz in frequency domain. This is the reasons why the coherent radiation can measure any short bunch length as long as the frequency signal can be recorded correctly.

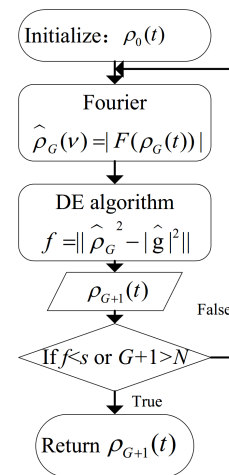


Figure 1: Phase retrieval flow chart with nonlinear least squares.

\* Work supported by China National Key Scientific Instrument and Equipment Development Project (2011YQ130018), National Natural Science Foundation of China with grant (11475159, 11505173, 11505174, 11575264, 11605190 and 11105019)

<sup>†</sup> jianxinwang1026@163.com



## DE Algorithm

Differential evolution (DE) algorithm is a heuristic global optimization based on population, works on Darwin's concept of survival of the fittest[14, 15]. DE and other evolutionary algorithms are often used to solve the beam dynamic optimization[16–19]

DE starts with a population of  $NP$  candidate solutions, which may be represented as  $X_{i,G}$ ,  $i = 1, 2, \dots, NP$ , where  $i$  index denotes the population and  $G$  denotes the generation to which the population belongs. DE uses mutation, crossover and selection to solve problems, which are shown in Fig. 2.

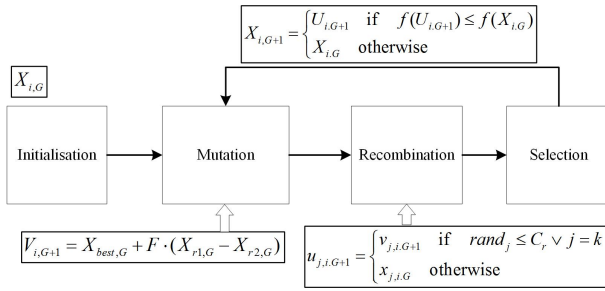


Figure 2: DE flow chart.

The mutation operator is the prime operator of DE. In this paper, a so-called ‘best-strategy-type-1’ is used [20], where  $F \in [0, 1]$  is the control parameter.  $r_i \in \{1, \dots, NP\}$  is a random selection and  $r_1 \neq r_2$ . The operator recombination and selection are also shown in Fig. 2 The crossover rate  $C_r \in [0, 1]$  is the other control parameter of DE.

## RECONSTRUCTION SIMULATION

### All Random Reconstruction

Firstly, the alternative signal is considered to be all random points in the time domain (0,1) with interval of 0.01. The original signal is set as:

$$\rho = \frac{\exp[-(t^4 - 0.07)^2]}{0.00053} + \frac{\exp[-(t^2 - 0.7)^2]}{0.00352} - \frac{\exp(t - 0.2)^2}{0.002}$$

This is a 100-dimensional nonlinear extremum problem. The calculation cost will be very large with general method. But with DE algorithm, about 20 generations evolution take only 1 minute. The speed would much faster when the interval goes larger and the dimension goes down.

The evolution process is shown in Fig. 3. Generation 1 gives all the random points firstly set. When the evolution goes to generation 100, the prototype of the original signal begins to appear. When it goes to generation 3000, the reconstructed signal is much alike to the original one. The main information of the two big peaks have been retrieved mostly, but the third peak has not been reconstructed properly.

### Sparsity-Based Retrieval

The Sparsity-based method is also considered to reduce the dimension obviously. The dictionary can be made of

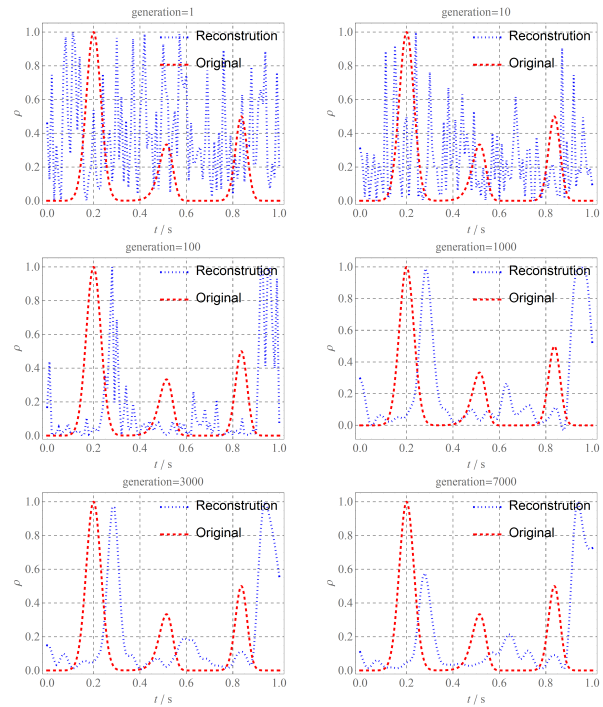


Figure 3: All random reconstruction.

any distribution function, such as Gaussian, flattop, etc, as shown in Eqs. (2) and (3), where  $\varepsilon$  is the step function.

$$\rho_{\text{Gaussian},i}(t) = a_i \exp\left[-\frac{(t - b_i)^2}{c_i}\right] \quad (2)$$

$$\rho_{\text{Flattop},i}(t) = a_i |\varepsilon(t - b_i) - \varepsilon(t - c_i)| \quad (3)$$

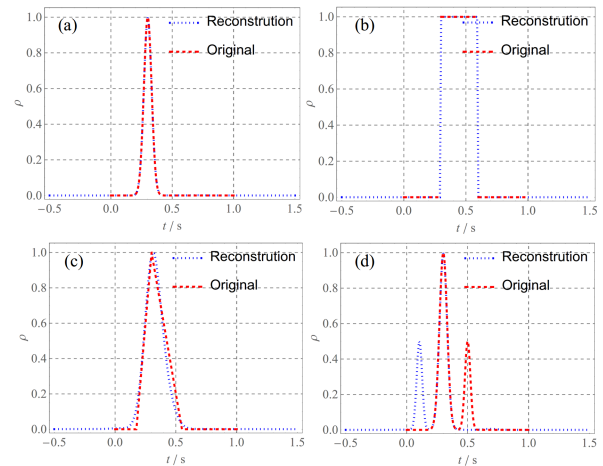


Figure 4: Sparsity-based retrieval with DE algorithm.

Some examples of the DE sparsity-based retrieval are shown in Fig. 4. The original distribution (red curve) are selected as (a) Gaussian, (b) rectangle, (c) triangle and (d) two-peak Gaussian, respectively. The blue curve is the

reconstruction one. For the dimension has been reduced less than 30, the calculation goes much fast than the all-random method. All the results have been achieved within generation 20 and cost less than 1 minute. The performance of the sparsity-based retrieval is much more powerful than the all-random one when the original signals are not too complicated.

## CTR EXPERIMENT RESULTS

An experiment of a picosecond electron beam bunch measurement has been carried out on the Chengdu THz free electron laser (CTFEL) facility. A self-made Martin-Puplett interferometer is applied to get the auto-correlation curve of the coherent transition radiation (CTR) when the electron beam passing through a golden foil (as shown in Fig. 5). The electron energy is about 8 MeV. The charge is 100 pC. The RMS bunch length is estimated as 2 ps by Astra code.

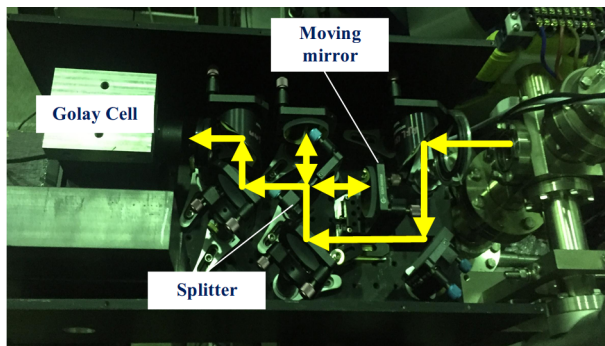


Figure 5: Experiment setup of the self-made Martin-Puplett interferometer.

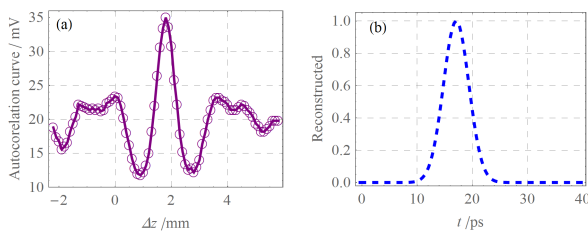


Figure 6: Auto-correlation curve and the DE reconstruction of the beam longitudinal distribution.

The auto-correlation curve is shown in Fig. 6 (a). The baseline is set as 20 mV. Then the Fourier transform and single electron transition radiation are considered and the coherent spectrum has been calculated. From the coherent spectrum, sparsity-based DE retrieval reconstructs the beam distribution, as shown in Fig. 6 (b). This retrieval uses the single Gaussian assumption, whose result agrees well with the KK relation. However, when using multi-peak assumption, the DE algorithm gives more information. as shown in Fig. 7.

In Fig. 7 (a), The retrieval gives two peaks at last. The distance between these peaks are about 11.4 ps, and the RMS

of the main peak is about 2.2 ps. In Fig. 7 (b), the curve gives the result of the photocathode drive laser longitudinal distribution measured by a streak camera. Not surprisingly, the drive laser has two peaks, too. The distance between these peaks are about 30 ps, and the RMS of the main peak is about 5.7 ps. Consider the compression ratio of the accelerator system, the peak distance from the drive laser would become as:  $30 \times 2.2 / 5.7 = 11.6$  ps, which is very close to the retrieval result.

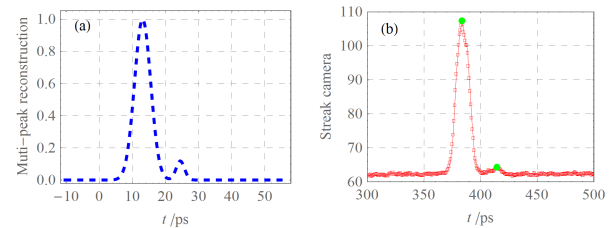


Figure 7: Result of multi-peak assumption (a) and the photocathode drive laser longitudinal distribution measured by a streak camera (b).

## SUMMARY

This paper has briefly introduced the application of differential evolution algorithm to reconstruct the phase information of the coherent radiation for ultrashort beam length measurement. The DE algorithm with all random assumption has the ability to reconstruct any distribution but has a large cost of time. The sparsity-base DE algorithm can solve the problem in most cases and goes much faster. One coherent transition radiation experiment has been carried on the Chengdu THz free electron laser facility. The DE algorithm agree well with the Kramers-Krönig relation and the laser distribution measurement result.

## REFERENCES

- [1] K. Honkavaara, P. Piot, S. Schreiber, and D. Sertore, "Bunch length measurements at the tesla test facility using a streak camera," in *PAC'01*, 2001, pp. 2341–2343.
- [2] W. Graves *et al.*, "Ultrashort electron bunch length measurements at duvfel," in *PAC'01*, vol. 3, 2001, pp. 2224–2226.
- [3] R. Akre, P. Emma, P. Krejcik, and L. Bentson, "Bunch length measurements using a transverse rf deflecting structure in the slac linac," Tech. Rep., 2002.
- [4] S. Casalbuoni, H. Schlarb, B. Schmidt, B. Steffen, P. Schmuser, and A. Winter, "Numerical studies on the electro-optic sampling of relativistic electron bunches," in *PAC'05*, 2005, pp. 3070–3072.
- [5] S. Casalbuoni, B. Schmidt, P. Schmuser, and B. Steffen, "Far-infrared transition and diffraction radiation," DESY, Tech. Rep., 2005.
- [6] V. Blackmore *et al.*, "First measurements of the longitudinal bunch profile of a 28.5 gev beam using coherent smith-purcell radiation," *Physical Review Special Topics-Accelerators and Beams*, vol. 12, no. 3, p. 032 803, 2009.

- [7] S. Korbly, A. Kesar, R. Temkin, and J. Brownell, "Measurement of subpicosecond bunch lengths using coherent smith-purcell radiation," *Physical Review Special Topics-Accelerators and Beams*, vol. 9, no. 2, p. 022 802, 2006.
- [8] Y. Shechtman, A. Beck, and Y. C. Eldar, "Gesparg: Efficient phase retrieval of sparse signals," *IEEE transactions on signal processing*, vol. 62, no. 4, pp. 928–938, 2014.
- [9] Y. C. Eldar, P. Sidorenko, D. G. Mixon, S. Barel, and O. Cohen, "Sparse phase retrieval from short-time fourier measurements," *IEEE Signal Processing Letters*, vol. 22, no. 5, pp. 638–642, 2015.
- [10] Y. Shechtman, Y. C. Eldar, O. Cohen, H. N. Chapman, J. Miao, and M. Segev, "Phase retrieval with application to optical imaging: A contemporary overview," *IEEE Signal Processing Magazine*, vol. 32, no. 3, pp. 87–109, May 2015, issn: 1053-5888. doi: 10.1109/MSP.2014.2352673.
- [11] M. Mutzafi, Y. Shechtman, Y. C. Eldar, O. Cohen, and M. Segev, "Sparsity-based ankylography for recovering 3d molecular structures from single-shot 2d scattered light intensity," *Nature communications*, vol. 6, p. 7950, 2015.
- [12] P. Sidorenko *et al.*, "Sparsity-based super-resolved coherent diffraction imaging of one-dimensional objects," *Nature Communications*, vol. 6, p. 8209, 2015.
- [13] D. Wu *et al.*, "First Lasing of the CAEP THz FEL Facility Driven by a Superconducting Accelerator," in *Proc. 9th International Particle Accelerator Conference (IPAC'18), Vancouver, BC, Canada, April 29-May 4, 2018*, (Vancouver, BC, Canada), ser. International Particle Accelerator Conference, <https://doi.org/10.18429/JACoW-IPAC2018-TUPMF044>, Geneva, Switzerland: JACoW Publishing, Jun. 2018, pp. 1349–1352, ISBN: 978-3-95450-184-7. doi: doi: 10.18429/JACoW-IPAC2018-TUPMF044. <http://jacow.org/ipac2018/papers/tupmf044.pdf>
- [14] R. Storn and K. Price, "Differential evolution—a simple and efficient heuristic for global optimization over continuous spaces," *Journal of global optimization*, vol. 11, no. 4, pp. 341–359, 1997.
- [15] M. Ali, M. Pant, and A. Abraham, "A simplex differential evolution algorithm: Development and applications," *Transactions of the Institute of Measurement and Control*, vol. 34, no. 6, pp. 691–704, 2012.
- [16] I. Bazarov and C. Sinclair, "Multivariate optimization of a high brightness dc gun photoinjector," *Physical Review Special Topics - Accelerators and Beams*, vol. 8, no. 3, p. 034 202, Mar. 2005, issn: 1098-4402. doi: 10.1103/PhysRevSTAB.8.034202. <http://link.aps.org/doi/10.1103/PhysRevSTAB.8.034202>
- [17] J. Qiang, Y. Chao, C. Mitchell, S. Paret, and R. Ryne, "A parallel multi-objective differential evolution algorithm for photoinjector beam dynamics optimization," in *Proceedings of IPAC'13*, 2013, pp. 1031–1033.
- [18] Y. Zhang and D. Zhou, "Application of differential evolution algorithm in future collider optimization," in *7th International Particle Accelerator Conference (IPAC'16), Busan, Korea, May 8-13, 2016*, JACOW, Geneva, Switzerland, 2016, pp. 1025–1027.
- [19] L. Y. Zhou *et al.*, "Design of an x-band photocathode rf gun for tsinghua thomson scattering x-ray source," in *IPAC'17*, 2017, pp. 1025–1027.
- [20] W. Gong, A. Fialho, and Z. Cai, "Adaptive strategy selection in differential evolution," in *Proceedings of the 12th annual conference on Genetic and evolutionary computation*, ACM, 2010, pp. 409–416.

# ELECTRO-OPTIC MODULATOR BASED BEAM ARRIVAL TIME MONITOR FOR SXFEL\*

X.Q. Liu†, Y.B. Leng, R.X. Yuan, L.W. Lai, L.F. Hua, N. Zhang,  
Shanghai Institute of Applied Physics, Chinese Academy of Sciences, Shanghai, China

## Abstract

Beam arrival time monitor (BAM) is an important tool to investigate the temporal characteristic of electron bunch in free electron laser (FEL) like Shanghai soft X-ray Free Electron Laser (SXFEL). Since the timing jitter of electron bunch will affect the FEL's stability and the resolution of time-resolved experiment at FELs, it is necessary to precisely measure the electron bunch arrival time so as to reduce the timing jitter of the electron bunch with beam based feedback. The beam arrival time monitor based on electro-optic modulator (EOM) is already planned and will be developed and tested at SXFEL in the next three years. Here the design and preliminary results of the EOM based beam arrival time monitor will be introduced in this paper.

## INTRODUCTION

As China's first X-ray free electron laser (FEL) facility, SXFEL has finished the infrastructure and installation, right now is under commissioning. The main parameters of SXFEL are listed in table 1.

Table 1: Main Parameters of SXFEL

parameter	value
Wavelength	3-9 nm
length	~300m
FEL principle	HGHG, EEHG
Beam energy	840 MeV
Peak current	500A
Normalized emittance	1.5mm.rad
Bunch length(FWHM)	500 fs

The SXFEL is a test facility for various external seeding modes, such as HGHG and EEHG. External seeding lasers are required for the generation of fully coherent radiation pulse. For seeded FEL, large timing jitter and drift of the electron bunch will affect the synchronization between the electron bunch and seed laser, then consequently reduce the stability of the output radiation. To reduce the timing jitter of the electron bunch with beam based feedback, it is necessary to precisely measure the electron bunch arrival time at different locations through the entire FEL facility. The Beam arrival time monitor (BAM) based on phase cavity and RF phase detecting technology has already been tested at SXFEL and obtained the 67.7 fs arrival time resolution [1], while efforts are ongoing to improve the resolution. Meanwhile, to achieve better bunch arrival time res-

olution, the electro-optic modulator (EOM) based beam arrival time monitor scheme originated from DESY [2-3] is also planned for SXFEL and will be developed and tested at SXFEL in the next three years. In this paper, we present the design of the EOM based beam arrival time monitor for SXFEL, as well some recent progress.

## DESIGN OF THE BEAM ARRIVAL TIME MONITOR

Figure 1 shows the schematic diagram of the BAM for SXFEL. The BAM consists of three parts, the beam pick-up, the BAM frond-end and back-end. The beam pick-up is located in tunnel to extract the transient RF signal generated by the driving electron bunch. The BAM frond-end also placed in tunnel is used to transform the shifting of RF signal's first zero-crossing, which stands for the arrival time of the electron bunch, into intensity variation of a reference optical pulse. The BAM back-end placed outside the tunnel is used to detect the amplitude of the optical pulse and derive the electron bunch arrival time information.

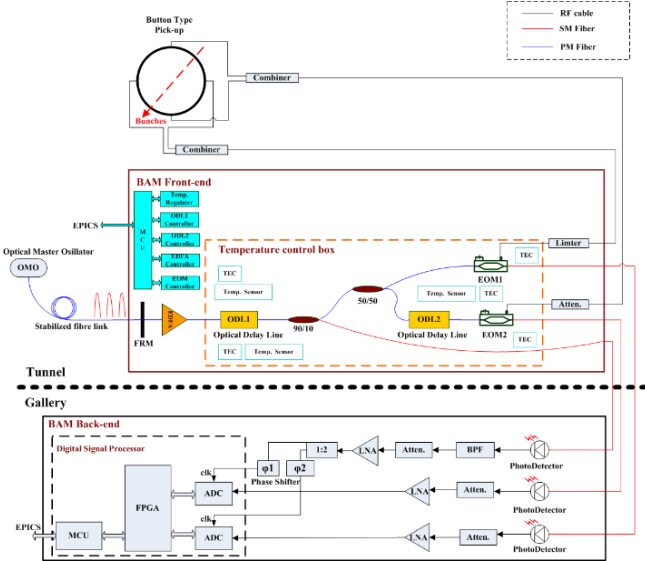


Figure 1: Schematic diagram of the BAM for SXFEL.

## Operation Principle

As shown in Fig.1, the optical master oscillator (OMO) is a mode-locked fibre laser with 1550 nm wavelength and 238 MHz repetition rate. The ultra-stable femtosecond optical pulse emitted from OMO transmits over the stabilized fibre link to the remote BAM station and serves as the optical reference signal for BAM. The reference optical pulse enters the BAM front-end and a faraday rotator mirror (FRM) reflects part of it back to help stabilize the phase of the reference optical pulse. The rest optical pulse passes

\* Work supported by the National Key Research and Development Program of China (Grant No. 2016YFA0401990, 2016YFA0401903).  
† liuxiaoqing@sinap.ac.cn



through the FRM is amplified by an erbium doped fibre amplifier (EDFA) to proper power level and then passes through one optical delay line (ODL). A 10:90 optical splitter placed behind the ODL divides the optical pulse into two parts, the smaller part will be used as a sampling clock of the BAM back-end, while the other part is again divided into two parts equally by a 50:50 optical splitter and then sent to two EOMs.

EOM is the core component of BAM since it can encode the arrival time of the electron bunch to the intensity variation of the reference optical pulse. Figure 2 shows the transmission characteristics curve of the EOM. By setting proper DC bias voltage for EOM, the output optical intensity will be proportional to the external driving voltage of EOM. Therefore, as shown in Fig.3, for reference optical pulse which transmits through the EOM, its intensity will be modulated by the beam pick-up signal applied on RF port of EOM. Since beam pick-up signal is a transient signal, only the exact optical pulse which coincides with the pick-up signal in EOM will be modulated by it. The first zero-crossing of the beam pick-up signal stands for the arrival time for the centre of the electron bunch. By adjusting the delay of the reference optical pulse, the optical pulse will coincide with that zero-crossing. Then the intensity of the modulated optical pulse will change with the temporal position of the zero-crossing and therefore change with the arrival time of the subsequent bunch. The intensity-to-time conversion factor can be acquired by scanning the delay of the reference optical pulse and detecting the corresponding intensity variation, which is accomplished in calibration procedure. By detecting the intensity of the modulated optical pulse, with the calculated intensity-to-time conversion factor, the bunch arrival time respects to the reference optical signal can be derived.

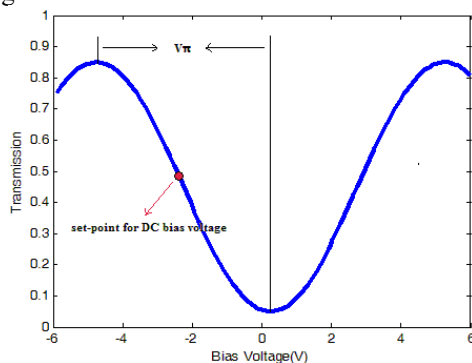


Figure 2: Transmission characteristics curve of the EOM.

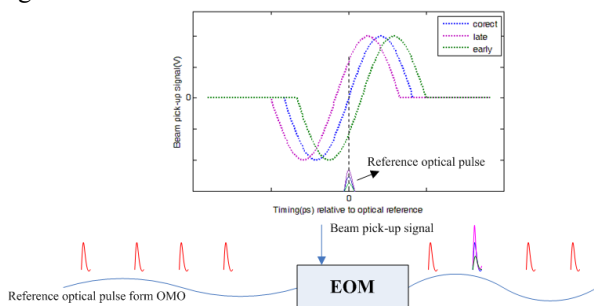


Figure 3: Illustration of the principle for detecting electron bunch arrival time by electro-optical modulation.

As shown in Fig.1, the button type beam pick-up has two pairs of electrodes and they are located in horizontal and vertical directions, respectively. To reduce the orbit-dependency effect, and acquire steeper slope around the zero-crossing as well, signals coupled from oppositely placed electrode-pair are combined in a RF combiner. The combined signal for horizontal electrodes is sent through a voltage limiter and transported to EOM1 to obtain femto-second level arrival time resolution. While combined signal for vertical electrodes is sent through a power attenuator and transported to EOM2 to assure large dynamic range of several hundred picoseconds. The ODL1 is used for adjusting the delay of the reference optical pulse until the optical pulse coincides with the first zero-crossing of the driving signal in EOM1. To make sure the reference optical pulse also coincides with the first zero-crossing of the driving signal in EOM2, another ODL2 is inserted to eliminate the phase difference between them due to different optical and electrical path length. The modulated optical pulses from EOM1 and EOM2, as well as the aforementioned optical pulse used for clock extracting, are transmitted through three optical fibres to the BAM back-end placed outside the tunnel. BAM back-end employs three high speed photodiodes to convert the optical signals to electrical signals. The converted signal used for clock successively passes a band pass filter (BPF), an attenuator, a low noise amplifier (LNA) to extract the 476 MHz clock signal with proper power level for high speed ADCs. While the other two electrical signals converted from output optical pulse of EOMs are sent to two high speed ADCs for digitization. To match with the ADC saturation voltage, LNA and attenuation are used to adjust the amplitude of ADC input signal. Since the frequency of ADC sampling clock is twice of the repetition rate of the electrical pulse signal, the peak and baseline of the pulse signal can be sampled simultaneously. Meanwhile, two phase shifters are used to adjust the delay of ADC sampling clock, which assures ADC can correctly sample the peak of the pulse signals. The two digitized signals are then processed in FPGA to detect their pulse peak and therefore derive the electron bunch arrival time.

### BAM Front-End

BAM front-end which is made up of different optical components, is a crucial module of BAM since it is where the electro-optical modulation takes place. As the electro-optical crystal material like LiNbO<sub>3</sub> in EOM has birefringent effect, the performance of EOM is sensitive to the polarization state of the incident light. To assure stable polarization state, all the optical components used in BAM front-end are planned to adopt polarization maintaining (PM) fibre components. This is practicable because the optical fibre used in stabilized fibre link for SXFEL is also PM fibre, meanwhile, commercial PM fibre components such as EDFA, ODL and EOM needed by BAM front-end are easy to find. Since fibre components are sensitive to environmental fluctuation due to temperature and humidity changes, a temperature control module and proper thermal



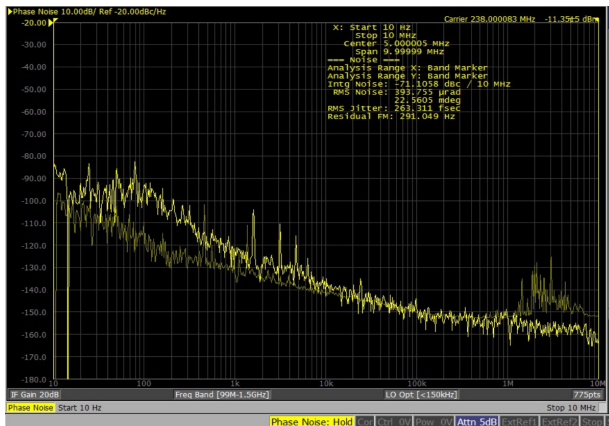


Figure 7: Absolute timing jitter of the extracted 238 MHz clock.

## SUMMARY

We report the design of beam arrival time monitor based on EOM for SXFEL, as well as the recent progress. At present, we have finished the design of BAM. Components used in BAM are under purchasing procedure and are supposed to be ready in this year. The first BAM prototype will be developed for SXFEL and we hope to obtain preliminary test results by the end of 2019.

## REFERENCES

- [1] S. S. Cao *et al.*, “Beam arrival time measurement at SXFEL”, in *Proc. IBIC’17*, Grand Rapids, MI, USA, Aug. 2017, TUPCC18, pp193-195.
- [2] F. Löhl, *et al.* “Electron bunch timing with femtosecond precision in a superconducting free-electron laser” [J]. *Physical Review Letters*, 2010, 104(14):144801.
- [3] F. Löhl, *et al.* in *Proceedings of European Particle Accelerator Conference (EPAC06)*, Edinburgh, Scotland, 2006, p. 2781.
- [4] L. W. Lai *et al.*, “Design and performance of digital BPM processor for DCLS and SXFEL”, in *Proc. IPAC’17*, Copenhagen, Denmark, May 2017, MOPAB092, pp338-340.

# DEVELOPMENT OF BAM ELECTRONICS IN PAL-XFEL

D.C. Shin<sup>\*</sup>, C.-K. Min, G.J. Kim, C.B. Kim, H.-S. Kang, J. Hong<sup>†</sup>, PAL, Pohang, Korea

## Abstract

We describe the electronics for electron bunch arrival time monitor (BAM) with a less than 10 femtosecond resolution, which was developed in 2017 and is currently in use at PAL-XFEL. When electron bunches go through an S-band monopole cavity, about 1 us long RF signal can be obtained to compare with a low phase noise RF reference. The differential phase jitter corresponds to the arrival time jitter of electron bunches. RF front-end (F/E) which converts the S-band pickup signal to intermediate frequency (IF) signal, is the essential part of a good time resolution. The digitizer and the signal processor of the BAM electronics are installed in an MTCA platform. This paper presents the design scheme, test results of the BAM electronics and future improvement plans.

## INTRODUCTION

In the tunnel of PAL-XFEL, 10 BAM pickups are installed. The pickup is made of S-band monopole cavity type. The resonance frequency is 2826 MHz, which have the offset of  $\approx 30$  MHz from our reference, 2856 MHz to remove a dark contribution. More details on the BAM pickup are described in Ref. [1].

BAM electronics consists of RF F/E unit for the frequency conversion of the pickup signal to an IF signal and main IOC for digitizing and processing the signal. RF F/E was designed as non-platform type (e.g. pizza-box type) and main IOC was implemented on the MTCA.4 platform.

The prototype of the BAM electronics, which is developed in 2017, has been tested at both the injector and the main-dump sites.

Table 1 shows the main specifications of the BAM electronics.

Table 1: Specification of the BAM Electronics

Parameter	Value	Unit
Phase Measurement Resolution	$\leq 10$	fs
Repetition Rate for Operation	$\geq 60$	Hz
Input RF Frequency	2826	MHz
REF Frequency	2856	MHz
Sampling Frequency	238	MHz
Platform	MTCA.4	

## ELECTRONICS

The block diagram of the BAM electronics is shown in Fig. 1.

<sup>\*</sup> dcshin@postech.ac.kr  
<sup>†</sup> npwinner@postech.ac.kr.

The signals induced from the pickup are transmitted to the RF F/E via cables with good phase stability for temperature. The BAM pickup signals are converted to IF signals of about 30 MHz using a mixer.

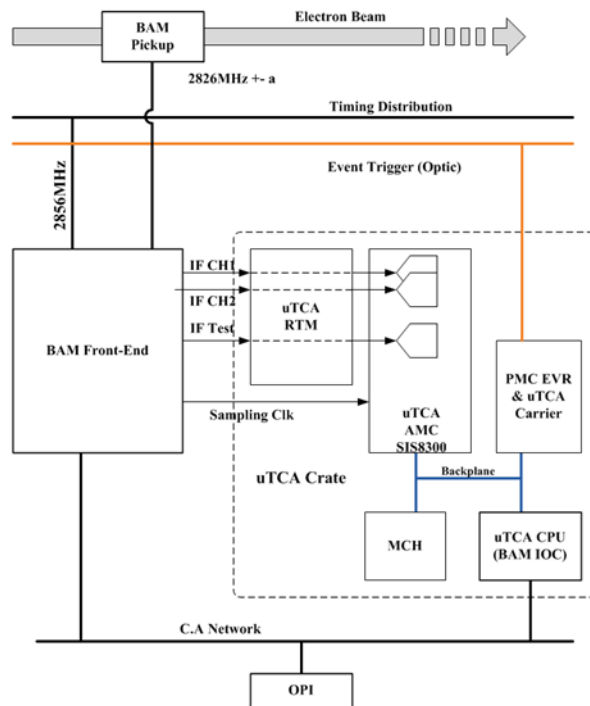


Figure 1: BAM electronics block diagram.

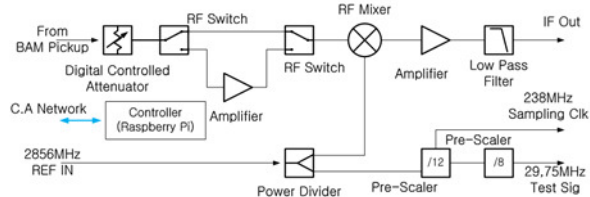


Figure 2: Block diagram of the RF F/E.

Figure 2 shows the RF F/E block diagram. A digital con-trolled attenuator is installed at the input, and is fol-lowed by a switch bank. In a high charge mode, the switch is bypassed and in a low charge mode, the signal is passed through the amplifier for power matching. The frequency down-converted signal using the reference in the mixer go through the IF amplifier and the low pass filter [2].

For the digitizer, a synchronized 238 MHz sampling clock, the 12<sup>th</sup> sub-harmonic of the reference, is generated in the RF F/E. The jitter of the sampling signal has to be small because it affects the signal noise ratio (SNR) of the system. We used HMC905LP3E and HMC794LP3E pre-scaler chips from Analog Device Inc. The total jitter of the 238 MHz sampling clock measured using a signal-



analyzer is about 16 fs. Table 2 below shows the phase noise value at each offset frequency.

Table 2: Phase Noise of the Sampling Clock

Phase Noise	Offset
-115 dBc/Hz	100 Hz
-143 dBc/Hz	1 KHz
-155 dBc/Hz	10 KHz
-160 dBc/Hz	100 KHz
-163 dBc/Hz	1 MHz

Figure 3 shows the installation of the BAM electronics. The upper crate is the main IOC, MTCA crate, which is equipped with a digitizer and a processor cards. There are five digitizer cards. The most rightward one is for BAM and the remaining four digitizers are for beam position monitors (BPMs). To reduce costs, BAM and BPM electronics share the whole system except the digitizer.



Figure 3: Photograph of the BAM Electronics; MTCA Crate on the top and RF F/E on the bottom.

## DIGITAL SIGNAL PROCESSING

The block diagram shown in Fig. 4 illustrates the basic concept of phase processing. A digital down-converter (DDC) generates complex samples by multiplying the digitized IF signal from the ADC with a generated cosine and sine signals from a numerically controlled oscillator (NCO). The SIG\_I and SIG\_Q signals can then be filtered to remove unwanted frequency components (especially the sum frequency component). The digital filter type is a

16-Tap FIR filter. MATLAB Filter Design & Analysis Tool program was used to calculate the filter coefficients.

When the frequency of the NCO is equal to the frequency of the IF, the difference frequency component at the output of the multiplier becomes zero, and only the amplitude component of the I-Q signal remains. The phase can be calculated by the equation arc-tangent [Q/I] function. More detail of the calculation process is described in Ref. [1].

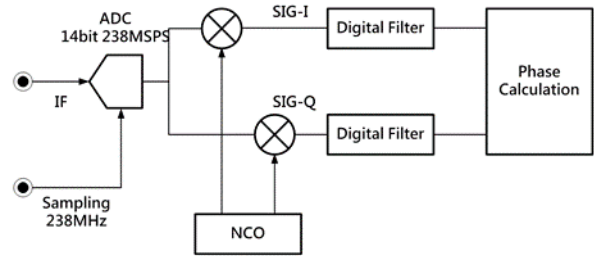


Figure 4: Data processing flow.

The resolution of BAM electronics is closely related to the SNR of the system. Figure 5 shows the simulation result of the relationship between SNR and the BAM phase resolution. The target specification of the prototype was less than 10 fs, and for this, the SNR of the electronics should be at least better than 65 dB [3].

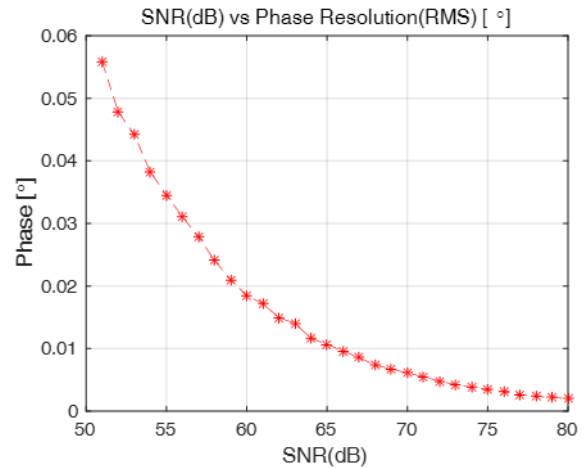


Figure 5: Simulated BAM resolution estimation with the SNR.

Table 3: RF F/E and ADC Gain & NF

Component	Gain (dB)	NF (dB)
Injector site Cable Loss	-3.5	3.5
Controlled Attenuator	Controlled	Controlled
RF SW1	-1.5	1.5
RF SW2	-1.5	1.5
Mixer	-9.0	9.0
Amp	18.0	5
Filter	-0.3	0.3
ADC	0	28.87

Table 3 shows the gain and noise figure (NF) of the RF F/E and the ADC. The SNR is calculated based on this. The ADC used in the SIS8300-LX50 is AD9643-250 and according to the datasheet, the SNR is typical 72 dB for the IF 30 MHz, VIN -1 dBFS and sampling 250 MSPS. Based on these conditions, NF value of the ADC is 28.87 dB for the Nyquist-Bandwidth [4, 5]. Although the NF varies with the value of the controlled attenuator, the SNR of the electronics remains almost constant value of 71 dB at the high charge (100 pC or more) conditions. This is because when the attenuator is adjusted according to the magnitude of the pickup power, the change of the NF due to the adjustment of attenuator is almost equal to the change of the pickup power. ADC jitter is also an important factor affecting SNR.

$$t_{jitter} = \sqrt{(t_{jitter.sampling})^2 + (t_{jitter.Aperture\ ADC})^2}$$

$$SNR_{jitter}[dBc] = -20 \cdot \log_{10}(2\pi \cdot f_{IN} \cdot t_{jitter})$$

The total jitter of the 238 MHz sampling clock is about 16 fs and the aperture jitter of the ADC is typical 0.1 ps according to the datasheet. SNR due to jitter is more than 90 dB at 30 MHz IF [6]. Therefore it is considered that the jitter does not affect the system SNR. Since the SNR of the electronics is 71 dB, electronics seems to meet the resolution performance of less than 10 fs.

### TEST RESULT

Figure 6 shows the correlation of phase between BAM channel-1 and channel-2 measured on the injector site for one hour.

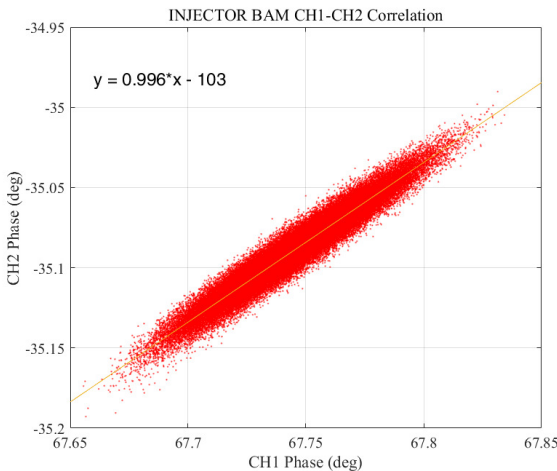


Figure 6: Correlation of phase between two channels measured on the injector site. The BAM output phases are from two different ports of the same pickup cavity and processed independently. Since the measurement value of each channel includes the jitter from the electron beam arrival time, the resolution of only electronics can be obtained by the difference in

the phase values obtained by operating on each channel for the same electron bunch. Figure 7 shows the resolution measurement results of the electronics itself with the elimination of the jitter component of the electron bunch. These values represent the standard deviation value for 100 pulses of the difference between channel-1 and channel-2. The average jitter was about 5.8 fs. Figure 8 shows the phase variation of the electronics for 2.5 days. RF F/E generates a 29.75 MHz continuous wave signal, which is used as a debugging signal, and an input to the extra digitizer channel. We can see that there was a phase change of about 0.06 degrees for 2.5 days.

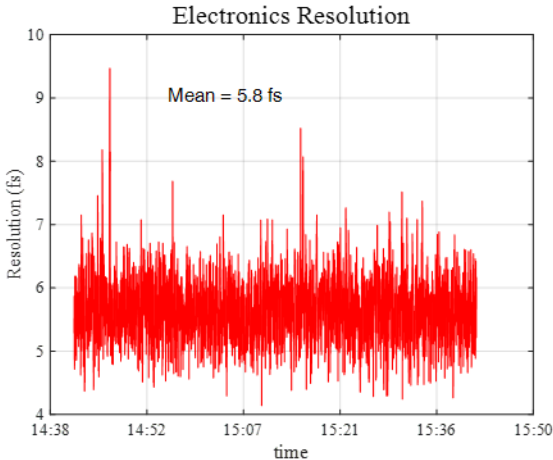


Figure 7: BAM electronics resolution over 100 pulses for 1 hour at 200 pC.

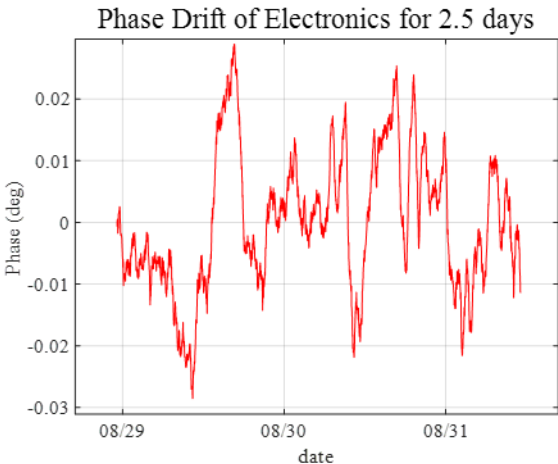


Figure 8: Phase drift of the electronics for 2.5 days.

### SUMMARY

BAM electronics satisfied the goal 10 fs resolution performance and showed similar characteristics to the simulation results. Based on the above design, one additional electronics will be built in 2019 and will be installed in the injector and the hard X-ray main dump site.

On the other hand, there is a phase drift problem due to the temperature change. We are trying to improve this problem through feedback control.

## REFERENCES

- [1] J. Hong *et al.*, “Bunch arrival time monitor for PAL-XFEL”, in *Proc. IBIC2014*, Monterey, CA, USA, Sep. 2014, paper MOPD19, pp. 191-194.
- [2] J. Frisch, “Beam arrival time monitor”, in *Proc. IBIC2015*, Melbourne, Australia, Sep. 2015, paper TUALA01, pp. 256-262.
- [3] J. Hong *et al.*, “Bunch arrival time monitor test at PAL-XFEL ITF”, in *Proc. IPAC2016*, Busan, Korea, May. 2016, paper MOPMB058, pp. 223-225.
- [4] Texas Instrument, Application Report, “Signal chain noise figure analysis”, <http://www.ti.com/lit/an/slaa652/slaa652.pdf>
- [5] Analog Device, Tutorials, “ADC noise figure-an often misunderstood and misinterpreted specification”, <ftp://ftp.analog.com/pub/cft1/ADI%20Classics/Tutorials/MT-006.pdf>
- [6] Texas Instrument, Tech Note, “Clock jitter analysed in the time domain, Part 1”, <http://www.ti.com/lit/an/slyt379/slyt379.pdf>

# MICROBUNCHING INSTABILITY MONITOR FOR X-RAY FREE ELECTRON LASER

C. Kim\*, J.H. Ko, G. Kim, H.-S. Kang, and I.S. Ko  
 Pohang Accelerator Laboratory, POSTECH, Pohang 790-834, Korea

## Abstract

A direct method was developed to measure the microbunching instability in the X-ray Free Electron Laser (XFEL). The microbunching instability comes from the interaction between the electron beam and the coherent synchrotron radiation (CSR), and the FEL intensity can be affected significantly by the microbunching instability. Until now, however, no effective method had been introduced to monitor the microbunching instability, and we tried to install a CCD camera to monitor the microbunching instability after the bunch compressor. The measurement result showed that the microbunching instability can be monitored by the CCD camera, and more interesting features of the microbunching instability were revealed from it.

## INTRODUCTION

When an electron beam passes through an undulator, the spontaneous synchrotron radiation is generated and it can interact back with the electron beam again. The interaction makes the beam energy modulation on the scale of the resonant wavelength from the energy exchange between the radiation electric field and the oscillating motion of the electron beam to the transverse direction [1]. The undulator is a dispersive device and the energy modulation is changed into a longitudinal density modulation which is called a microbunching. The microbunching enhances the coherence of the radiation and increases the radiation intensity to develop a collective instability [2, 3]. The scale of the microbunching is much shorter than that of the bunch length and the microbunching instability grows up until the maximum bunching is achieved if the undulator length is long enough. In short, the microbunching instability is the working principle of Self-Amplified Spontaneous Emission (SASE) [4–6].

In the Free Electron Linac (FEL), bunch compressors are used to enhance the performance of the FEL by reducing the bunch length for high current and high brightness. A relativistic electron bunch can have an energy chirp while passing through the off crest of the linac RF phase before the bunch compressor, and lower energy electrons move to the front of the electron bunch and higher energy ones go back. Inside the bunch compressor, the electron beam passes through a strong dispersive section, and higher energy electrons follow a shorter trajectory and lower energy ones travel a longer trajectory. Because of the path length difference, the high energy electrons at the back of the electron bunch catch up with the lower energy ones in the front, and the bunch length decreases. In this process, it is important not

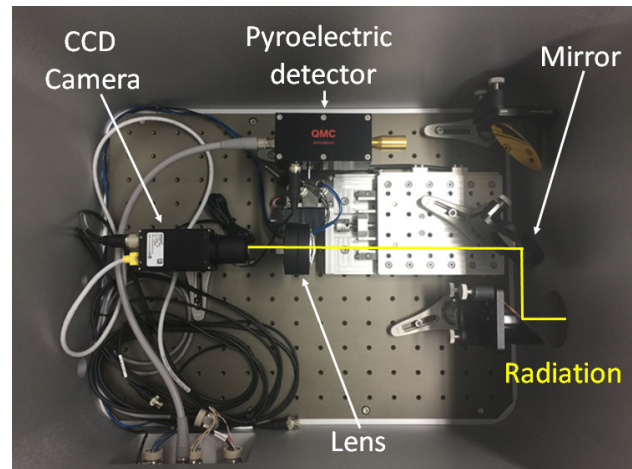


Figure 1: Experimental setup of the Coherent Radiation Monitor of PAL-XFEL.

to increase the energy spread or the transverse emittance beyond tolerances during the bunch compression.

Like an undulator, the bunch compressor is a dispersive device and synchrotron radiation can be generated from bending magnets. This means that the microbunching can be generated in the linac bunch compressor. Especially, Coherent Synchrotron Radiation (CSR) can be a source of the beam density modulation at wavelengths small compared to the bunch length. The effect of microbunching from CSR has been observed in computer simulations of the bunch compressor designed for the Linac Coherent Light Source (LCLS) [7], and in the bunch compressor simulation of the TESLA Test Facility [8]. Analytical studies of the CSR effects in bunch compressors also have been published in literature [9].

In this paper, we introduce a direct method to monitor the microbunching instability. A visible CCD camera is installed to measure the intensity of the coherent radiation after the bunch compressor. The measurement result shows that strong visible radiation is observed after the bunch compressor and the CCD camera can be used as a microbunching monitor without any beam interruption.

## COHERENT RADIATION MONITOR

X-ray Free Electron Laser of Pohang Accelerator Laboratory (PAL-XFEL) is a hard X-ray FEL to produce 0.1 nm wavelength photon [10]. From a photo-cathode RF gun, an electron beam is generated with 5 MeV energy and 150 pC charge by using an Ultra-Violet (UV) laser pulse of 3 ps pulse width. The electron beam is accelerated to 10 GeV energy by using S-band (2856 MHz) RF structures in the

\* chbkim@postech.ac.kr



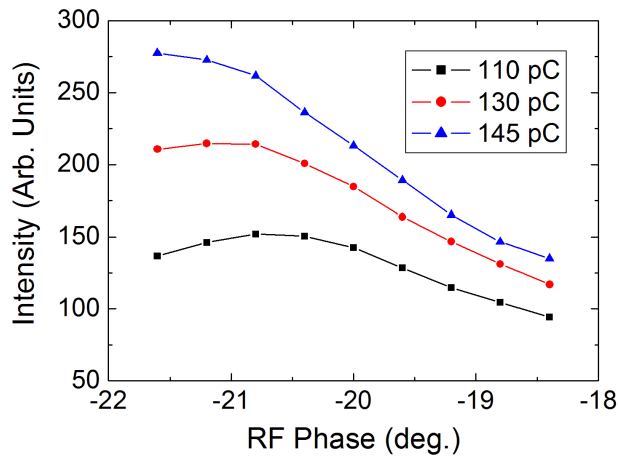


Figure 2: Intensity measurement results of the pyroelectric detector as a function of the linac RF phase before the second bunch compressor.

linac of which length is 780 m. In addition to acceleration, the electron bunch length is reduced down to 50 fs in full width at half maximum after two bunch compressors and 3 kA peak current is obtained at the linac end. The electron beam from the gun passes through two acceleration columns (L0) and reaches the energy of 130 MeV. The electron beam is accelerated to 0.36 GeV with the first linac section (L1) and the bunch length is compressed to 1.3 ps by using the first bunch compressor. After that, the electron beam is accelerated to 2.5 GeV energy with the second linac section (L2). The second linac is connected to the second bunch compressor and the bunch length is reduced to 50 fs. The fully compressed beam is accelerated to 10 GeV energy by using the rest of the linac. The electron beam comes into the undulator section after passing through a beam transport line and generates a hard X-ray pulse.

The intensity of the FEL radiation strongly depends on the bunch length with a given number of electron charges. Thus, the monitoring of the bunch length is a critical issue in the XFEL beam diagnostics. When the electron beam passes through the bunch compressor, radiation can be obtained after the bending magnet. Moreover, Coherent radiation can be obtained if the electron beam which emits the radiation is shorter than the radiation wavelength. After dipole magnets of the bunch compressor, the trajectory of the accelerated electron beam is bent and coherent synchrotron radiation (CSR) is generated. At the edge of the dipole magnet, the electron beam generates another coherent radiation which is called the coherent edge radiation (CER) [11]. Because the radiation intensity is inversely proportional to the bunch length, the bunch length can be estimated by measuring the radiation intensity. A coherent radiation monitor (CRM) is widely used after the bunch compressor for the bunch length monitoring [12]. The CRM shows the relative bunch length and a calibration is needed by using a transverse deflecting cavity which can measure the absolute bunch length.

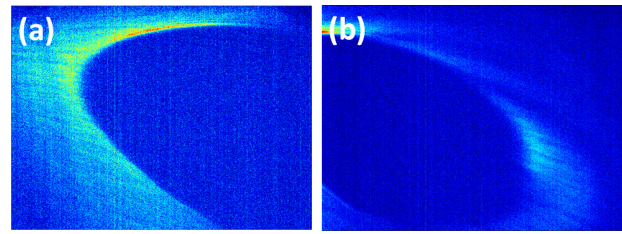


Figure 3: Images of the CCD camera when the mirror moves in the CRM chamber.

The experimental setup of the CRM is shown in Fig. 1. CSR and CER are reflected to a detector by using a gold-coated mirror with a center hole of 10 mm diameter for the electron bunch to pass through, and coherent diffraction radiation (CDR) can be generated when the electron beam passes through the mirror hole. Coherent radiation is guided into the low vacuum chamber by using the gold-coated mirror with a center hole. The low vacuum chamber is controlled under  $10^{-1}$  torr of the air pressure and sealed with a CF-4.5-inch diamond window to reduce the attenuation of radiation intensity. In the low vacuum chamber, THz radiation is focused to a pyroelectric detector by using two parabolic mirrors. The parabolic mirror has 50.8 mm diameter and the gold-coated surface with more than 94% reflection from the terahertz to the visible range. The pyroelectric detector is installed in the focal point of the parabolic mirror to obtain the maximum signal strength. The pyroelectric detector measures the intensity of the terahertz radiation in the range from 0.1 THz to 20 THz and is suitable for the bunch length monitor considering 1.3 ps ( $= 0.77$  THz) bunch length after the first bunch compressor.

## MEASUREMENT RESULTS

After the second bunch compressor, the bunch length of the electron beam is reduced down to 50 fs ( $= 20$  THz), which is twenty times shorter than the wavelength of the 1 THz, and the radiation becomes coherent one which makes saturation of the pyroelectric detector. In Fig. 2, the bunch length is increased as the L2 RF phase goes from  $-22^\circ$  to  $-18^\circ$ . The L0 and the L1 phase are fixed to  $0^\circ$  and  $-11^\circ$ , respectively. Note that the measurement result is saturated when the L2 phase is near to  $-21^\circ$ .

We installed a visible CCD camera to measure the visible radiation intensity to avoid the saturation problem [13]. The nominal bunch length of 50 fs ( $= 15 \mu\text{m}$ ) is longer than the visible wavelength (400 - 700 nm) and the electron beam energy (2.5 GeV) is high enough to generate the visible synchrotron radiation. The CCD camera setup consists of a moving stage, an aluminum coated mirror, and an uncoated focusing lens with a 50.8 mm diameter as shown in Fig. 1. To guide the visible radiation to the CCD camera, we moved the mirror on the moving stage and obtained the transverse image of visible coherent radiation. Figure 3a and 3b show images of the CCD camera as the mirror moves to the chamber wall in Fig. 1. The center hole boundary of

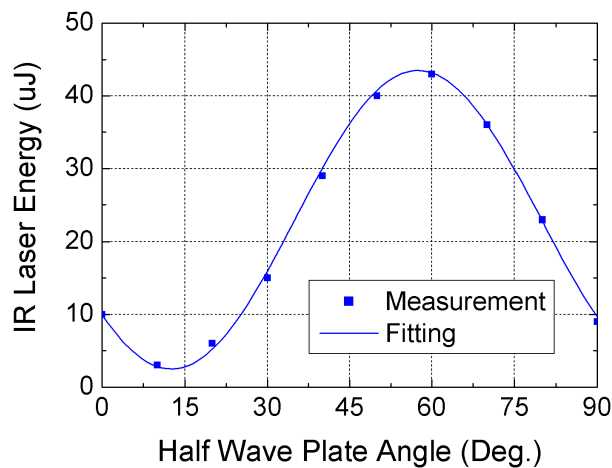


Figure 4: Half-wave-plate angle and IR laser energy relation of the laser heater.

the gold-coated mirror is clearly shown in the CCD camera image. An important thing was that the intensity of the visible radiation was surprisingly strong when the bunch length was near to the minimum.

In PAL-XFEL, a laser heater was installed to reduce the microbunching instability [14]. The laser heater minimizes the microbunching instability growth by controlling the uncorrelated energy spread of the electron beam. In our experiments, the IR laser beam-size was fixed and the IR laser energy of the laser heater was changed from 0  $\mu\text{J}$  to 40  $\mu\text{J}$  by using a half-wave plate. Figure 4 shows the measurement result of the IR laser energy with different angles of the half-wave plate. Figure 5 shows CCD camera images when the laser heater is on and off. The L0, the L1, and the L2 phase are  $0^\circ$ ,  $-11^\circ$ , and  $-21^\circ$ , respectively. The visible radiation intensity is changed with the different IR laser energy. In addition, we also measured the pyroelectric detector intensity with the same IR laser energy. The CSR intensity is decreased as the IR laser energy is increased while the pyroelectric detector intensity does not show any change. This means that the CSR can be used for a monitor of the microbunching instability. After the bunch compressor, the electron beam can produce coherent radiation when the bunch length is shorter than the radiation wavelength. In addition, if the length of the structure, such as the microbunching, in the electron beam is shorter than the radiation wavelength, one can obtain coherent radiation with a strong intensity [15].

## SUMMARY

In PAL-XFEL, the CRMs are installed after the bunch compressors for the bunch length measurement. However, a saturation problem was noticed in the pyroelectric detector

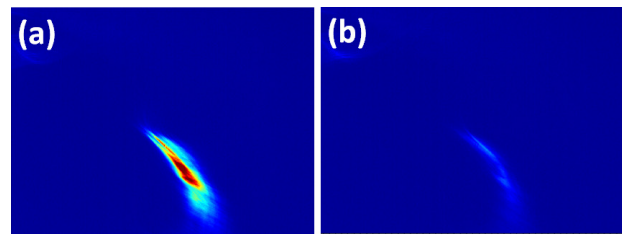


Figure 5: Images of the CCD camera when IR laser energies of the laser heater are (a) 0.55  $\mu\text{J}$ , (b) 23.6  $\mu\text{J}$ .

of the CRM when the bunch length is near to the minimum. To solve the problem, a CCD camera was installed in the CRM chamber, and surprisingly strong radiation was noticed in the visible wavelength with the CCD camera. This strong radiation indicated that the microbunching happened in the electron bunch and it was confirmed from the measurement result with the laser heater.

## REFERENCES

- [1] J. Madey, J. Appl. Phys. **42**, 1906 (1971).
- [2] A.M. Kondratenko and E.L. Saldin, Part. Accel. **10**, 1980 (1980).
- [3] R. Bonifacio, C. Pellegrini, and L.M. Narducci, Opt. Commun. **50**, 373 (1984).
- [4] J. Feldhaus, E.L. Saldin, et al., Nucl. Instrum. Methods Phys. Res. Sect. A **393**, 162 (1997).
- [5] E.L. Saldin, E.A. Schneidmiller, M.V. Yurkov, Optics Communications **212**, 377 (2002).
- [6] J.B. Rosenzweig, D. Alesini, et al., Nucl. Instrum. Methods Phys. Res. Sect. A **593**, 39 (2008).
- [7] The LCLS Design Study Group, SLAC Report No. SLAC-R-521, 1998.
- [8] T. Limberg, P. Piot, and E.A. Schneidmiller, Nucl. Instrum. Methods Phys. Res. Sect. A **475**, 353 (2001).
- [9] E. L. Saldin, E. A. Schneidmiller, and M.V. Yurkov, Nucl. Instrum. Methods Phys. Res. Sect. A **483**, 516 (2002).
- [10] H.-S. Kang et al., Nat. Photon. **11**, 708 (2017).
- [11] J. Wu, P. Emma, in Proceedings of LINAC2006 (Knoxville, Tennessee, USA, 2006), 277.
- [12] H. Loos, T. Borden, et al., in Proceedings of PAC2007 (New Mexico, USA, 2007), 4189.
- [13] J.H. Ko et al., Rev. Sci. Instrum., **89**, 063302 (2018)
- [14] J.H. Lee, J.H. Han, et al., Nucl. Instrum. Methods Phys. Res. Sect. A **843**, 39 (2017).
- [15] C.J. Hirschmugl, M. Sagurton and G.P. Williams, Phys. Rev. A **44**, 1316 (1991).

# DEVELOPMENT, FABRICATION AND LABORATORY TESTS OF BUNCH SHAPE MONITORS FOR ESS LINAC

S. Gavrilov<sup>†1,2</sup>, A. Feschenko<sup>1</sup>, D. Chermoshentsev<sup>1,2</sup>

<sup>1</sup>Institute for Nuclear Research of the Russian Academy of Sciences, Troitsk, Moscow, Russia

<sup>2</sup>Moscow Institute of Physics and Technology, Moscow, Russia

## Abstract

Two Bunch Shape Monitors have been developed and fabricated in INR RAS for European Spallation Source linac. To fulfil the requirements of a 4 ps phase resolution the symmetric  $\lambda$ -type RF-deflector based on a parallel wire line with capacitive plates has been selected. Additional steering magnet to correct incline of the focused electron beam is also used. Limitations due to a space charge of the analysed beam and due to external magnetic fields are discussed. Laboratory tests of the monitors are described.

## INTRODUCTION

Bunch Shape Monitors (BSMs) are intended for the measurements of a longitudinal distribution of particles in bunches of the accelerated proton beam in ESS: the first BSM will be installed in MEBT at 3.6 MeV, and the second one – between the normal conducting and the superconducting parts of the linac at 90 MeV.

The operation principle of BSM, developed in INR RAS, is based on the technique of a coherent transformation of a temporal bunch structure into a spatial charge distribution of low energy secondary electrons through a transverse RF-scanning [1] and is clear from Fig. 1.

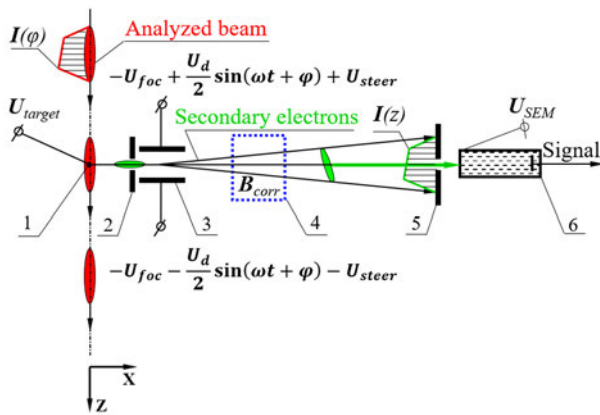


Figure 1: BSM scheme: 1 – tungsten wire target, 2 – inlet collimator, 3 – RF-deflector combined with electrostatic lens, 4 – correcting magnet, 5 – outlet collimator, 6 – secondary electron multiplier.

The series of the analysed beam bunches crosses the wire target 1 which is at a high negative potential about -10 kV. Interaction of the beam with the target results in emission of low energy secondary electrons, which characteristics of importance for bunch shape measurements are practically independent of beam energy, so the monitors are fabricated in practically the same design (Fig. 2), except for the beam aperture size.

<sup>†</sup> s.gavrilov@gmail.com

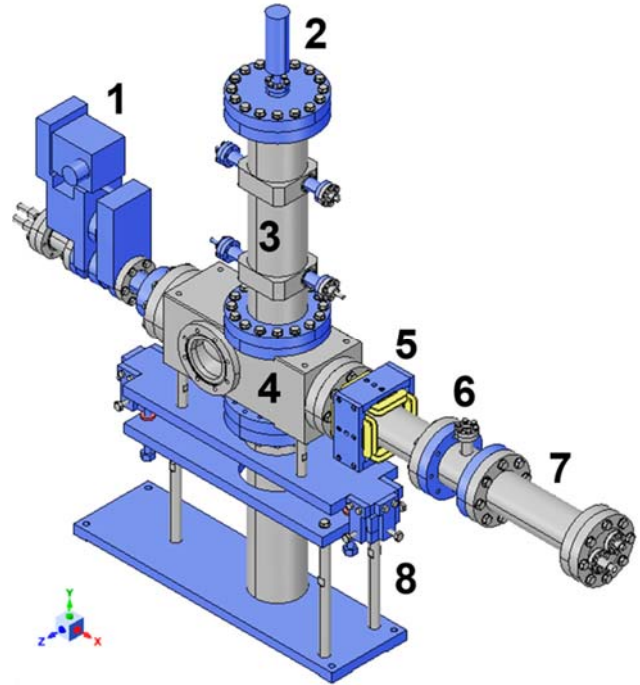


Figure 2: ESS BSM design: 1 – target actuator, 2 – tuner, 3 – RF-deflector, 4 – BSM box, 5 – quadrupole + dipole correcting magnet, 6 – viewport for optical control of e-beam, 7 – SEM-detector, 8 – support with 3D-adjustment.

The electrons are accelerated by electrostatic field and move almost radially away from the target. A fraction of the electrons passes through the inlet collimator 2 and enters the RF-deflector 3, where electric field is a superposition of electrostatic focusing and steering fields and RF-deflecting field with a frequency equal to the RF-field frequency in the linac: 352.2 MHz.

Passed electrons are scanned by the RF-field and an intensity of electrons passed through the outlet collimator 5 represents a fixed point of the longitudinal phase distribution of the primary beam. Other points can be obtained by changing the phase of the deflecting field with respect to the RF-reference. If the phase of the deflecting field is adjusted in a wide range, then the bunch can be observed twice per the period of the deflecting field.

By adjusting the steering voltage, one can change the measured phase position of the observed bunches and obtain the periodicity of bunches to be exactly equal to  $\pi$ . If the bunch duration is larger than  $\pi$ , the intensities corresponding the phase points differed by  $\pi$  are superimposed and the results of bunch shape measurements become wrong.



## MAGNETIC SHIELD AND CORRECTOR

Both monitors will be installed in a close vicinity of magnetic elements (quadrupole and corrector) with strong fringe fields. A magnetic shield is foreseen to provide a non-distorted e-beam transport inside the monitor.

The shield represents a sectional jacket made of 2 mm low-carbon steel. Additionally, the interior surfaces are covered with a 160  $\mu\text{m}$  foil made of an amorphous cobalt-iron alloy with high  $\mu_r$ . Figure 3 shows the effect of the BSM shield on the fringe field of a dipole corrector located close to the monitor. Even better results can be obtained if additional 2 mm low-carbon steel plate screens are added upstream and downstream of BSM – the remnant fields decrease to the level less, than the Earth’s magnetic field, and their influence will be negligible.

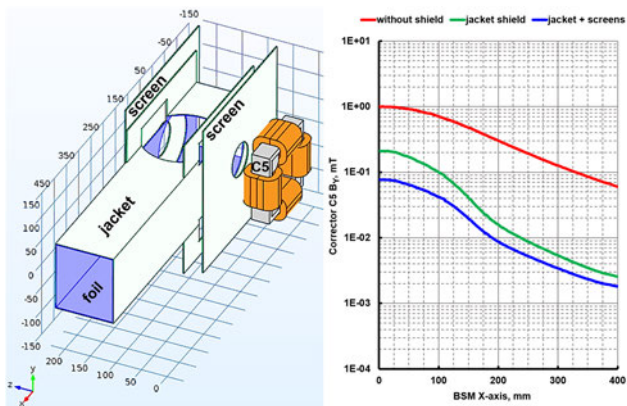


Figure 3: BSM shield layout and an example of dipole corrector  $B_y$  distribution along BSM X-axis.

An influence of remnant moderate static magnetic fields inside the standard shield as well as unavoidable misalignments can be compensated by adjusting the steering voltage  $U_{steer}$  in Z-direction and by a special magnetic corrector in other directions. The correcting magnet with the combination of dipole and quadrupole fields (Fig. 4a) is implemented. The dipole field moves the electron beam along Y-axis. The quadrupole field enables to adjust the tilt of the e-beam in YZ-plane (Fig. 4b).

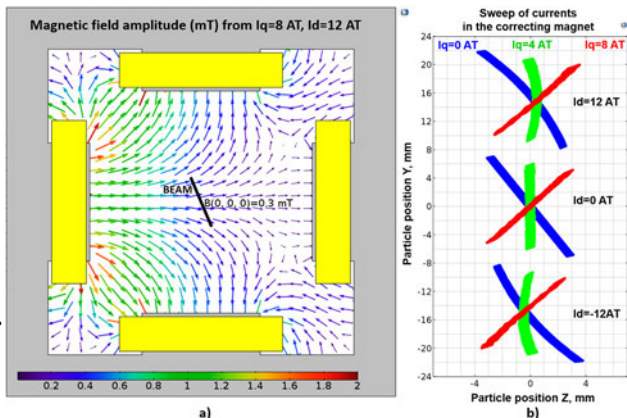


Figure 4: (a) Magnetic corrector with fields superposition. (b) E-beam in the plane of the outlet collimator for different quadrupole  $I_q$  and dipole  $I_d$  coil currents (Ampere·Turns).

## RF-DEFLECTOR

Typically, BSM deflectors are RF cavities based on parallel wire lines with capacitive plates. To improve the uniformity of both deflecting and focusing fields in Y direction, thus improving phase resolution, the  $\lambda$ -type symmetric cavity has been selected for ESS BSMs (Fig. 5).

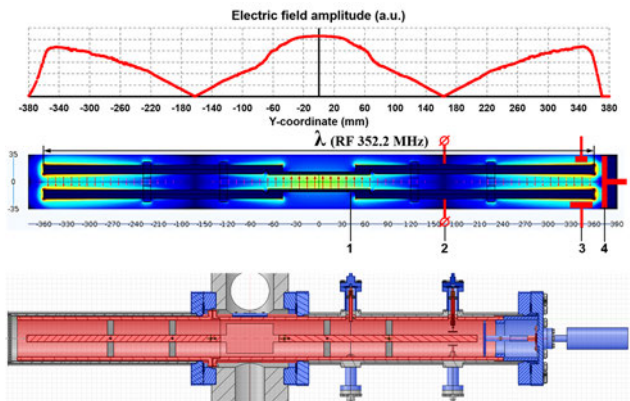


Figure 5: Electric field distribution and cut planes for the symmetric  $\lambda$ -type RF-deflector of ESS BSM.

The electrodes with deflecting plates 1 are supported by ceramic insulators. Focusing potentials are applied to the electrodes with spring contacts 2 at zero field point. Capacitive adjustable couplers 3 are used to drive the cavity and to pick up the RF signal. Fine tuning within the range of about  $\pm 1$  MHz is made from outside the vacuum with capacitive tuner 4 via manual actuator.

## PHASE RESOLUTION AND ACCURACY

The symmetric deflector and the magnetic corrector provide an electron beam completely fitted with the 0.5 mm outlet collimator. Figure 6 shows the e-beams at the outlet collimator for three  $\delta$ -function analysed bunches with the interval of  $0.5^\circ$  (352.2 MHz).

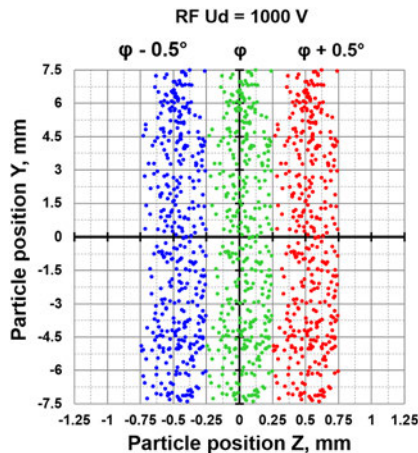


Figure 6: Transverse cross-sections of the e-beam in the plane of the outlet collimator for different phases of deflecting field with the step  $0.5^\circ$  at 352.2 MHz.

The double RMS size of the simulated focused beams equals  $2\sigma_z=0.25$  mm, so in principle the size of the slit can be decreased to 0.25 mm, that provides the resolution  $\Delta\phi_0=0.21^\circ$ . However it was not done due to two reasons.



The first reason is decreasing of intensity of the detected electron beam. The second one is presence of one more crucial component of the phase resolution – time dispersion (delay) of secondary electron emission.

The value of the delay time is not known exactly. The theoretical value for metals is estimated to be about 0.01 ps [2]. The experimental attempts to measure the time dispersion give the upper limit of this value equal to  $(4 \pm 2)$  ps [3] rather than a real one. We assume the delay time of the emission to be uniformly distributed within the range of 0–6 ps, so the double RMS delay equals 3.46 ps, which is equivalent to  $\Delta\phi_{SEE} = 0.44^\circ$  for 352.2 MHz and the resulting phase resolution becomes  $0.48^\circ$ , that corresponds to 0.57 mm collimator.

Estimations described above were done with the assumption of a zero-intensity analysed beam, while a space charge of the real beam can strongly influence the secondary electrons trajectories. Besides a finite phase resolution, which smoothes measured distributions, there is a so-called phase reading error (accuracy). Due to the latter the measured phase coordinate along the bunch does not correspond to a real one because of electron energy modulation and the measured bunch shape becomes distorted. The methods of taking into account the space charge of the analyzed beam are described in [4]. The results of simulations with different beam currents for BSM at MEBT are presented in Fig. 7.

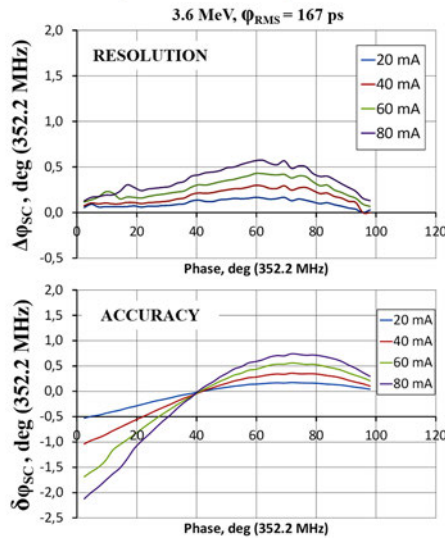


Figure 7: Space charge effects for various beam currents.

The phase resolution and the phase reading error are given as functions of a longitudinal coordinate along the bunch. The bunch head is at the left side in the figures. The electron emitted at the head of the bunch is firstly accelerated by the charge with positive X coordinate and then decelerated. The net effect appears to be decelerating. The electrons emitted at the bunch center or at the bunch tail are also firstly accelerated and then decelerated. However, for these electrons the decelerating effect becomes smaller compared with the bunch head because the moving bunch leaves the area. For bunches with 90 MeV energy and 16.4 ps rms duration space charge effects become five times smaller.

## LABORATORY TESTS

After complete design and fabrication process BSMs have been assembled (Fig. 8), pumped, tuned and tested for proper operation of all systems: vacuum, RF, high voltage, electronics and control system. Electron beam optics was also tested with the help of thermal electrons: heating the wire target, it is possible to observe through the viewport the thermal electron beam on the phosphor covering the front surface of the outlet collimator.



Figure 8: Photo of assembled BSM with the magnetic shield and symmetric RF-deflector.

## CONCLUSION

Two Bunch Shape Monitors have been developed for ESS linac. The symmetric RF-deflector has been fabricated for the first time to improve the uniformity of electric fields. The special magnetic shield for protection against external fringe magnetic fields and correcting magnet with the combination of dipole and quadrupole fields for compensation of remnant magnetostatic fields and misalignments of BSM elements have been implemented.

The estimation of BSM phase resolution for zero beam intensity of  $0.5^\circ$  for 325.2 MHz (4 ps) has been done in real 3D-geometry with inlet-outlet collimators of 0.5 mm, supposing the parameters for energy and time dispersion of secondary emission are known. Space charge effects can increase the upper limit of the phase resolution up to  $0.7^\circ$  and reduce the accuracy of bunch shape measurements in MEBT, but practically do not influence the resolution and the accuracy for 90 MeV beam.

## REFERENCES

- [1] A. Feschenko, "Technique and instrumentation for bunch shape measurements", in *Proc. RUPAC'12*, Saint-Petersburg, Russia, Oct. 2012, pp. 181-185.
- [2] I. M. Bronstein and B. S. Fraiman, *Secondary Electron Emission*, Moscow, Russia: Nauka, 1969 (in Russian).
- [3] E. Ernst, H. Von Foerster, "Time dispersion of secondary electron emission", *J. of Appl. Phys.*, vol. 26, no. 6, pp. 781-782, 1955.
- [4] A. Feschenko and V. Moiseev, "Peculiarities of bunch shape measurements of high intensity ion beams", in *Proc. IPAC'10*, 2010, pp. 1065–1067.

# DEVELOPMENT OF LONGITUDINAL BEAM PROFILE DIAGNOSTICS FOR BEAM-BEAM EFFECTS STUDY AT VEPP-2000

M. Timoshenko\*, V. Borin, V. Dorokhov, O. Meshkov, Yu. Rogovsky, D. Schwartz, Yu. Zharinov  
 BINP SB RAS, Novosibirsk, Russia

## Abstract

The comprehensive development of beam longitudinal profile measurement systems based on stroboscopic optical dissector has started at VEPP-2000 electron-positron collider complex. The dissector was setted and commissioned at booster ring BEP that was deeply upgraded (2013-2015) to achieve top energy of 1 GeV. Bunch lengthening with current was studied at BEP with its new RF-cavity. In addition the method of synchrotron frequency measurement by dissector was applied. After dissector checkouts at BEP the similar studies were carried out with a single beam at VEPP-2000 storage ring in parallel with streak-camera measurements. Good agreement of results was observed. Series of single-turn longitudinal and vertical bunch profiles snapshots was made by streak-camera with respect to delay after counter beam injection. The unexpected longitudinal beam dynamics was observed for intensities above the beam-beam threshold. These studies together with beam-beam coherent oscillations spectra seen by pickups are of a great interest for understanding of flip-flop phenomenon which establish a fundamental luminosity limit at VEPP-2000 operating with round beams.

## INTRODUCTION

The VEPP-2000 is a collider complex which main parts are electron-positron booster BEP and collider VEPP-2000 with two detectors CMD-3 and SND [1]. After modernization BEP energy range began to be from 200 MeV to 1 GeV. It and BEP parameters are described in [2]. The experiments at the collider VEPP-2000 has become possible in this energy range without acceleration.

To achieve luminosity project value  $10^{32} \text{ cm}^{-2} \text{ s}^{-1}$  the comprehensive beam monitoring system is required. There was no longitudinal beam distribution monitoring system. Its observation gave more full understanding of colliding beams nature.

## MEASUREMENT SYSTEM AT BEP

Electron and positron booster BEP are needed for portioned storing of particles supplied by Injection complex VEPP-5 [3] at 395 MeV energy. After storing enough intensity of beams following accelerating (changing beam energy) and injection at collider VEPP-2000 occur. At the accelerating regime BEP work at the energy range from 200 MeV to 1 GeV. Operating with different sort of particle is possible due to polarity reverse of magnet systems.

BEP synchrotron radiation spectrum contains optical range and its spectrum power maximum is around 30 nm. Beam motion is strictly periodical. These factors allow to use synchrotron radiation in optical diagnostic system. BEP have several outputs of synchrotron radiation but all are used. For these reason one of it was upgraded.

The system of longitudinal charge distribution of beam (dissector) was set and tested at BEP at first.

## Optical Table Modernization

The task of modernization conclude in to save current beam transverse position monitor (CCD-camera) functional. For realization it and duplicating light of synchrotron radiation semitransparent mirror was setted in optical table tract. Yellow part of table and mirrors at the Fig. 1 is added in the modernization.

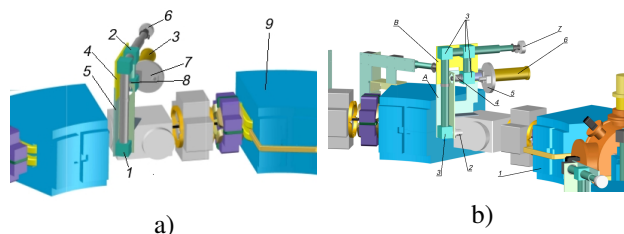


Figure 1: Concept of modernization. Optical table before modernization a), and b) — after modernization.

1— bending magnet, 2— sync. rad. output, 3— cubes with moving mirrors, 4— calibration light source, 5— light filters, 6— dissector, 7— CCD-camera.

## Alignment of Optical Table

After production necessary details and realization of optical table concept it was aligned outside BEP room with using portable CCD-cameras. The task was to pointing and focusing precisely simulation of synchrotron radiation light on the places where the real devices (CCD-camera and dissector) should be setted.

After preliminary alignment the optical table with both devices was installed to BEP synchrotron radiation output Fig. 2 and the final tuning was completed with very low intensity beam (around 100  $\mu\text{A}$ ) in the BEP.

## DISSECTOR

Dissector is a optical stroboscopic device. One of the way of applying it is registration longitudinal distribution of beam charge in a circular accelerators where the beam motion is strictly periodical. The synchrotron radiation light

\* email address: tim94max@gmail.com

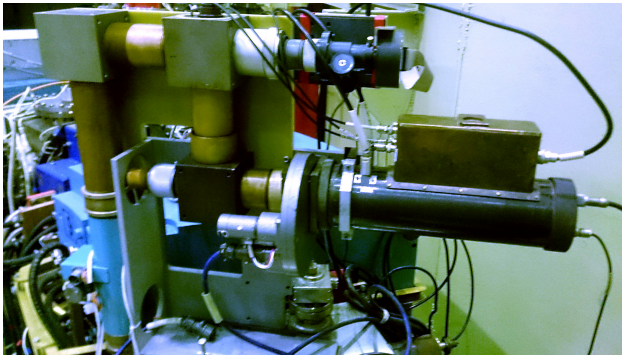


Figure 2: Optical table on the BEP

from beam is focused and pointed at the dissector photo-cathode by optical table systems of mirrors and lenses.

### Operation Principles

Dissector is the vacuum tube consisting of mean components:

- image section
- slit
- multiplier section

Behind photo-cathode in the image section focusing, accelerating and deflecting of photo-electrons take place.

Photo-electron cloud emitted from photo-cathode is focused and accelerated by potential differences between a slit plane, photo-cathode and focusing electrode. Then the cloud transform to narrow electron beam.

Photo-electrons beam can be deflected by electrostatic fields between pair of deflection plates. Sum of two voltages are applied to the plates. One of them is sinusoidal *RF sweep voltage* and other is *scan voltage*. RF sweep voltage forms photo-electron image which duplicates temporal distribution of synchrotron radiation light pulse created by circulated beam in accelerator. Scan voltages slowly shifts the image across the slit consistently cutting different narrow part of image from turn to turn of beam.

After transitions over the slit photo-electrons are multiplied by system of dynodes and form output signal at anode of multiplier.

Calibration of dissector is implemented by calibration source of permanent light. Scaling factor and estimation of resolution can be found.

Final formula of input pulse duration is

$$\Delta l = \frac{D\sqrt{t^2 - t_0^2}}{q T_s}, \quad (1)$$

where  $D = 2R$  — average diameter of accelerator,  $q$  — ratio RF sweep frequency to revolution frequency,  $t_0$  — width of dissector apparatus function,  $t$  — output electrical pulse duration.

You can look for description of dissector principles and calibration more detailed in [4, 5].

For dissector installed at the BEP resolution is 26 ps (or 0.8 cm in spacial dimension).

### The Dissector Used at BINP

As the dissector, electron-optical converter LI-602 is used.

The voltage divider of multiplier is compactly realized in adapter 2. The oscillatory RF-circuit 5 is necessary because transporting clear sinusoidal harmonic signal with high amplitude through long wire without distortion is impossible task. Furthermore electrical breakdowns in the wire connectors take place. The signal with low amplitude ( $\sim 50$  V) is generated at circuit and there signal with high amplitude ( $\sim 1$  kV) is swung and applied to deflection plates.

Parameters of LI-602: Voltage slit — photo-cathode 10 kV; Voltage slit — focusing electrode  $10 \pm 1$  kV; Max. voltage at deflection plates 2.5 kV; Max. spectrum sensitivity 440 – 470 nm; Multiplier voltage  $-1.5 - -2.0$  kV; Slit width 50 mkm.

### BEAM LENGTH

For dissector testing the model of potential well distortion has been selected. The nature of this process is in process of introduction between bunches and accelerator vacuum chamber and all its components (RF-cavity, bellows and other). In this model it was considered that energy spread change insignificantly versus beam intensity.

Distribution of bunch charge is Gaussian for electron-positron accelerators. The bunch length is dispersion of this distribution and is defined in [6] by following formula:

$$\left(\frac{\sigma}{\sigma_0}\right)^3 + \left(\frac{\sigma}{\sigma_0}\right) = -A \cdot \Im\left(\frac{Z}{n}\right)_{\text{eff}}, \quad A = \frac{(2\pi R)^3 I_b}{3h\sigma_0^3 U_0 \cos \phi_s}. \quad (2)$$

### Software

For measurements by dissector it was necessary to develop software. This program has developed at C++ language in QT — cross-platform application framework and widget toolkit. This program allows to operator of VEPP-2000 complex calibrate dissector and observe results of measurements. Program read data from ADC, operate it and calculate bunch length and also visualize results of calculating values of length and of longitudinal bunch profile registration.

Layout of it is showed at Fig. 3 where there are examples of beam profile and history of length measurements with decreasing of beam intensity.

In realization of program we uses library GSL for automatic fitting of data by Gaussian function and bunch length calculating. Also there is length averaging over time periods and writing them to VCAS — system of data storage at VEPP-2000 complex [7].

### MEASUREMENTS AT THE BEP

Three identical dissector measuring systems have been installed at the VEPP-2000 complex. One of them has been installed on the booster BEP and two others have been installed on the VEPP-2000 collider singly for electron and positron beams.



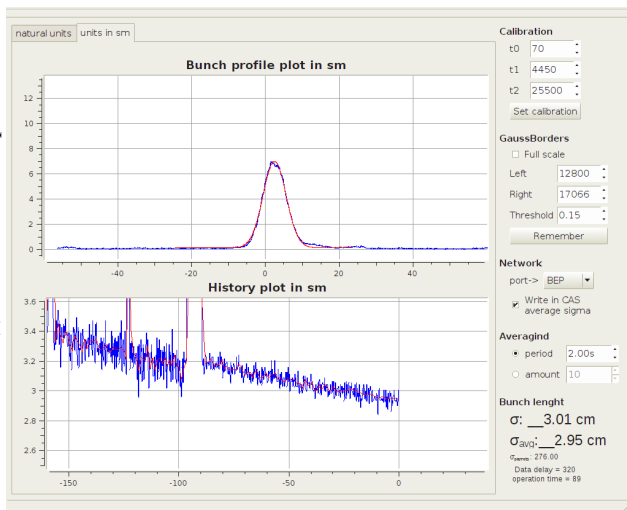


Figure 3: User interface of program

The complex tests of dissector have been done at BEP. Measurements at the BEP:

- Measurement of normalized synchrotron frequency ( $\nu_{s0}$ ) with low intensity of bunch versus RF-cavity voltage has been done (Fig. 4).
- Measurement of bunch length ( $\sigma_0$ ) with low intensity of bunch versus RF-cavity voltage (Fig. 5).
- Measurement of bunch length  $\sigma$  versus its intensity with different values of RF-cavity voltage (Fig. 6).

Bunch intensity in the first two measurements is less 100 mA and we consider that at this intensity measuring synchrotron frequency was  $\Omega_{s0} = \nu_{s0} f_0$  ( $f_0$  — revolution frequency) and bunch length was  $\sigma_0$  (at "null" intensity).

Method of measuring of synchrotron frequency is concluded in switching-off the scan voltage. Then the photoelectron image inside dissector on the slit plane is static but small synchrotron oscillation of bunch causes output signal modulation. In this process distribution slope of photoelectron image should be located opposite slit for better sensitivity. There is function of oscillogram saving by the software and synchrotron frequency is less than ADC speed (around 0.04 MHz versus 2 MHz). These factors allows to make this measurements.

All results are presented at following plots. Theoretical curves are calculated with using known formulas for synchrotron frequency and equilibrium bunch length and also using calculated project parameters of BEP. At the each step little deviations of project parameters are admitted and are corrected according to fitting.

## MEASUREMENTS AT THE VEPP-2000 COLLIDER

We has made one series of measurement of bunch length versus bunch intensity by dissector and streak-camera at the same time. The measuring has been done at 387.5 MeV energy which is energy of last approach for experiments at CMD-3 and SND detectors.

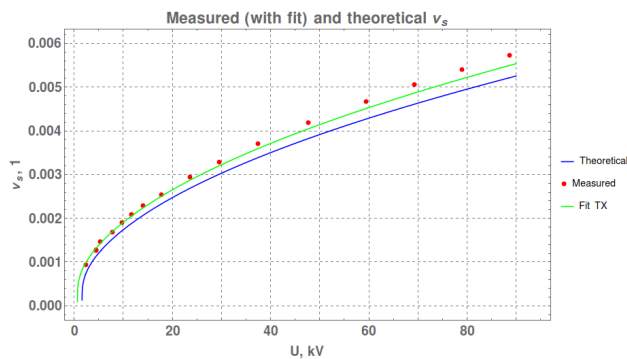


Figure 4:  $\nu_{s0}(U)$

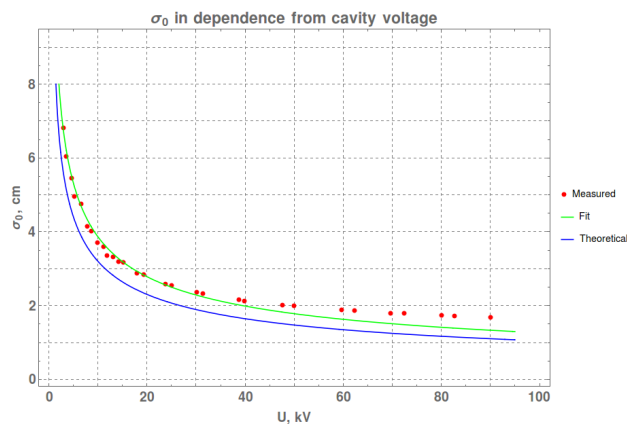


Figure 5:  $\sigma_0(U)$

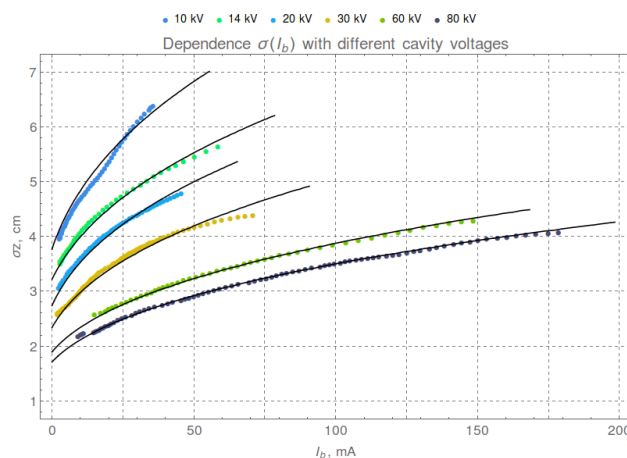


Figure 6:  $\sigma(I_b)$

## Streak-camera

Streak-camera is useful for observing of dynamical processes through making single-turn snapshot of bunch charge profile in plane ZS (longitudinal and vertical coordinates). The distributions of charge can be obtained by snapshot post-processing.

Principles of streak-camera are similar to dissector and the detailed description you can see in [8]. There are photocathode and deflection plates as in the dissector but instead of multiplier section streak-camera has phosphoric screen



and CCD-camera behind it for registration image on screen made by photo-electrons.

Results of it is dependence showed at the following plot at Fig. 7 where the agreement is observed.

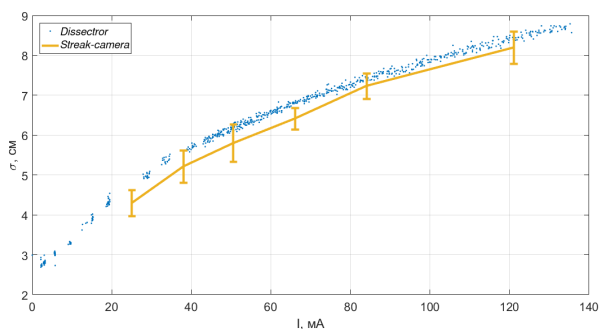


Figure 7:  $\sigma_z(I_b)$

### Injection Process Observed by Streak-camera

The number of measurements was made for the observation of the injection processes for the single bunch and for colliding bunches over subsequent 20-80 turns.

Vertical oscillation and size increasing are observed for single electron bunch with bunch intensity  $I_b$  40 mA. Longitudinal shifts are connected with instability of streak-camera starts.

Unexpected results have been obtained at snapshots with different combination of conditions. The snapshots of electron bunch have been made at different turn after injection from the BEP and different intensities of electron and positron bunches ( $I_{e^-}$  and  $I_{e^+}$ ). The head of electron bunch is on the left side of snapshot.

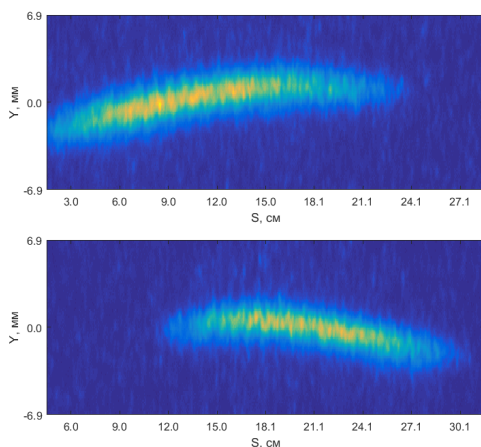


Figure 8: 40th turn,  $I_{e^-} = 66$  mA,  $I_{e^+} = 45$  mA (up), 80th turn,  $I_{e^-} = 50$  mA,  $I_{e^+} = 40$  mA (down).

Injection of the positron bunch has occurred when the electron bunch has circulated (Fig. 8). Almost total loss of injecting positron bunch took place and the intensity of the electron beam did not change significantly.

Injection of the electron bunch has occurred when the positron bunch circulated (Fig. 9). The same problem that the injecting bunch is lost took place.

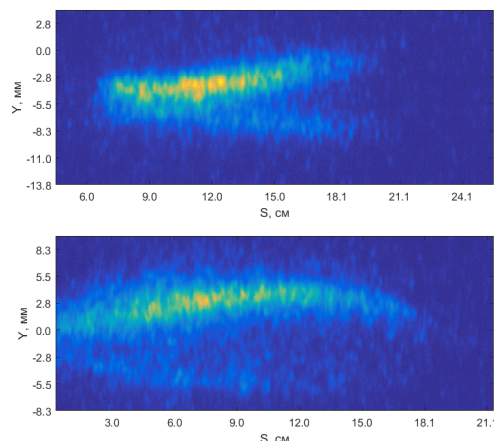


Figure 9: 40th turn,  $I_{e^-} = 30$  mA,  $I_{e^+} = 66$  mA (up), 60th turn,  $I_{e^-} = 30$  mA,  $I_{e^+} = 64$  mA (down).

At the figures we can see vertical tilt of electron bunch influenced interaction with injected positron bunch. After around 40 turns the slope changes its direction. Electron bunch separates to two parts influenced interaction with circulated positron bunch. The current series of measurements is limited by capabilities of time synchronization impulse system.

## CONCLUSION

In work season 2017-2018 the longitudinal beam profile diagnostic get comprehensive development. Dissector has been installed at the BEP. For this task optical table at the synchrotron radiation output has been upgraded and aligned. Two more identical dissectors has been installed to VEPP-2000 collider. All dissectors has been calibrated. For using them the special software has been developed. After that these systems has been commissioned by operators of complex VEPP-2000. Also the streak-camera has been installed at VEPP-2000 collider.

Results of joint measurements of bunch length by dissector and streak-camera at the VEPP-2000 collider and comprehensive measurements of bunch length in the BEP in model of potential well distortion show that work of dissector is correct.

Some interesting snapshots of bunch profile showed that streak-camera is very useful device for studying of processes near injection.

## REFERENCES

- [1] D. Schwartz, D. Berkaev *et al.*, “Recent beam-beam effects and luminosity at VEPP-2000”, in *Proc. 5th International Particle Accelerator Conference (IPAC’14)*, Dresden, Germany, June 2014, pp. 924–927.  
doi:10.18429/JACoW-IPAC2014-TU0BA03
- [2] D. Schwartz, D. Berkaev *et al.*, “Booster of electron positron (BEP) upgrade to 1 GeV”, in *Proc. 5th International Particle Accelerator Conference (IPAC’14)*, Dresden, Germany, June 2014, pp. 102–104.  
doi:10.18429/JACoW-IPAC2014-MOPR0018
- [3] Yu. Maltseva, A. Andrianov *et al.*, “VEPP-5 injection complex: new possibilities for BINP electron-positron colliders”, in *Proc. 9th International Particle Accelerator Conference (IPAC’18)*, Vancouver, BC, Canada, Apr. 2018, pp. 371–373.  
doi:10.18429/JACoW-IPAC2018-MOPMK011
- [4] E. I. Zinin and O. I. Meshkov, “Optical dissector for longitudinal beam profile measurement”, *Journal of Instrumentation*, vol. 10, p. 10024, Oct. 2015, doi:10.1088/1748-0221/10/10/P10024
- [5] O. I. Meshkov, E. I. Zinin *et al.*, “Development, calibration and application of new-generation dissector with picosecond temporal resolution”, in *Proc. 7th International Particle Accelerator Conference (IPAC’16)*, Busan, Korea, May 2016, pp. 251–254. doi:10.18429/JACoW-IPAC2016-MOPMR013
- [6] B. Zotter, “The effective coupling impedance for bunched beam instabilities”, CERN, Geneva, Switzerland, Rep. CERN-ISR-TH-78-16, Jul. 1978.
- [7] A. Senchenko, D. Berkaev *et al.*, “VEPP-2000 collider control system”, in *Proc. 9th International Workshop on Personal Computers and Particle Accelerator Controls (PCaPAC’12)*, Kolkata, India, 2012, Dec. 2012, paper FRCB04, pp. 263–274.
- [8] A. Chao and M. Tigner, *Handbook of accelerator physics and engineering*. 2nd Printing. Singapore: Mainland Press, 1999.

# RESULTS FROM THE CERN LINAC4 LONGITUDINAL BUNCH SHAPE MONITOR

J. Tan<sup>†</sup>, G. Bellodi, CERN, Geneva, Switzerland  
A. Feschenko, S. Gavrilov, Institute for Nuclear Research, Moscow, Russia

## Abstract

The CERN Linac4 has been successfully commissioned to its nominal energy and will provide 160 MeV H<sup>-</sup> ions for charge-exchange injection into the Proton Synchrotron Booster (PSB) from 2020. A complete set of beam diagnostic devices has been installed along the accelerating structures and the transfer line for safe and efficient operation. This includes two longitudinal Bunch Shape Monitors (BSM) developed by the Institute for Nuclear Research (INR, Moscow). Setting-up the RF cavities of Linac4 involves beam loading observations, time-of-flight measurements and reconstruction of the longitudinal emittance from phase profile measurements. In this paper the BSM is presented along with some results obtained during accelerator commissioning, including a comparison with phase measurements performed using the Beam Position Monitor (BPM) system.

## INTRODUCTION

The Linac4 [1] is an 80 m-long, normal-conducting, pulsed, linear accelerator, providing a 160 MeV H<sup>-</sup> ion beam every 1.2 s. A block diagram of the machine is shown in Figure 1. It will replace the ageing 50 MeV proton Linac2 as the injector of the PSB in 2020. The motivation for this upgrade is twofold: firstly to overcome the present space charge limitation at PSB injection, doubling the intensity within the same transverse emittance; secondly to minimise beam loss at PSB injection. The latter requirement is achieved with a charge exchange injection, an adequate chopping scheme and longitudinal phase space painting for high intensity beams.



Figure 1: Linac4 schematic layout.

The beam instrumentation specifications [2, 3] along the accelerator and its transfer line must cover the challenging operational parameters summarized in Table 1.

Table 1: Linac4 Parameters and Achievements To Date

Parameters	Design target	Achieved
Peak current in the linac	40 mA	24 mA
Routine current in the linac	40 mA	20 mA
Transv. Emittance at 160 MeV	0.4 $\pi$ .mm.mrad	0.3 $\pi$ .mm.mrad
Energy at PSB injection	160 MeV	160 MeV
Pulse length / rep. rate	400 $\mu$ s / 1 Hz	up to 600 $\mu$ s/1Hz

<sup>†</sup> jocelyn.tan@cern.ch

The achieved performance during the Linac4 commissioning stages from 45 keV to 160 MeV are presented in [4, 5, 6, 7]. Here we present results of longitudinal beam profile measurements performed with the BSMs located in the transfer line, including a comparison with phase measurements performed using the BPM system.

## BEAM PHASE PROFILE DIAGNOSTICS

### Bunch Shape Monitor

The BSM principle of operation is explained with Figure 2 and is described in detail elsewhere (see for example [8]). In brief, its operation is based on transforming the longitudinal structure of the beam under study into a transverse distribution of low energy secondary electrons.

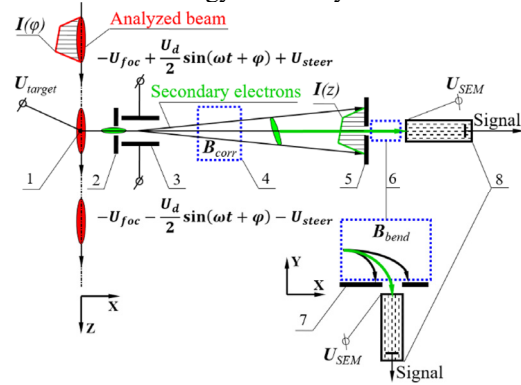


Figure 2: BSM principle: 1-wire target, 2-input collimator, 3- rf deflector combined with electrostatic lens, 4-corrector magnet, 5 and 7- collimators, 6-bending magnet, 8-electron multiplier.

This is achieved by placing a wire target in the beam, which emits secondary electrons in proportion to the instantaneous H<sup>-</sup> intensity. These electrons are accelerated with a HV applied to the target and converted to a transverse distribution using an RF deflection, from which a specific slice is selected for detection using a collimator. The RF deflector operates at the accelerator frequency  $f_{RF}$  of 352.2 MHz. For a fixed setting of the RF deflecting phase with respect to the accelerator reference, the intensity of the secondary electrons passing the collimator and detected with the electron multiplier corresponds to the H<sup>-</sup> intensity at a specific point of the longitudinal charge distribution of the beam under study. The whole distribution is obtained by scanning the phase of the RF deflecting field through a complete half period. The bending magnet is tuned to select only electrons with an energy corresponding to acceleration from the target potential, and is used to remove any influence from electrons detached from H<sup>-</sup> ions

in the target. For each profile, the phase range of the measurements is  $180^\circ$ , with a resolution close to  $1^\circ$ . The phase scan provides one longitudinal point per beam pulse. Nevertheless, the BSM signal is sampled every  $\mu s$  thus providing the longitudinal distribution within the beam pulse. As the complete measurement is performed over many beam pulses, the reproducibility of beam parameters from pulse to pulse is assumed.

Two monitors are currently installed in the transfer line at the end of Linac4, their distance with respect to the last PIMS ( $\pi$  Mode Structure) cavity being respectively 5.55 m and 35 m. When the Linac4 is connected to the PSB in 2020, the final position of the 2<sup>nd</sup> monitor will be at 63.5 m.

### Beam Position Monitor

The beam trajectory measurement system was designed to provide the absolute beam position, the relative beam intensity and the mean beam energy via time-of-flight (TOF) measurements between BPMs. It consists of a set of 42 BPMs, with 15 units installed between the Linac4 RF modules and 27 units spread along the 177 m-long transfer lines to the PSB. Compactness, good linearity and sensitivity to the bunching frequency were the main criteria for selecting shorted striplines pick-ups as the basic sensor [9].

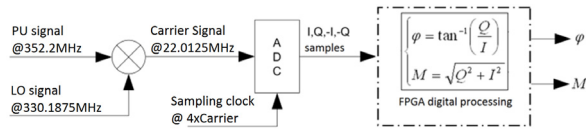


Figure 3: I/Q schematic with  $f_{LO} = f_{RF} \cdot 15/16$ .

The “I/Q method” [10] as represented in Figure 3, is applied for signal processing. The analog signal from the BPM is filtered to obtain the first RF harmonic which then undergoes down-mixing with a Local Oscillator (LO). The resulting intermediate frequency (IF) is sampled at four times the IF so as to acquire data  $\pi/2$  apart. Averaging of I and Q samples over one IF period is performed for noise filtering. From standard trigonometric functions, one then obtains the magnitude M and the relative beam phase for each electrode, as a function of time with a granularity of  $1/f_{IF} = 45$  ns. The position is computed from the difference in magnitude between two facing electrodes and normalisation with their sum, while the beam intensity is proportional to the magnitude sum of all electrodes.

The strong variation of the BPM sensitivity with bunch velocity (due to the changing energy) along the linac is taken into account during the processing. Table 2 lists the specifications and the present performance.

Table 2: BPM Specifications vs. Achieved Performance

Parameters	Specifications	Achieved
Position resolution [mm]	0.1	0.006
Position accuracy [mm]	0.4	0.1
Phase [°]	0.5	0.1
Intensity [mA]	0.5	0.1

## MEASUREMENTS

In addition to the determination of longitudinal emittance for optimum RF module settings [11], the BSM has been extensively used to assess qualitatively or quantitatively the longitudinal distribution over the working range of the cavity, as well as for different chopping frequencies. A first comparison with BPMs phase is included.

### Momentum Spread Measurement for Nominal Settings at 160 MeV

Figure 4 shows the results of bunch shape measurements with the two BSMs obtained for nominal accelerator settings. The longitudinal phase distribution of the pulse is obtained by integrating all phase profiles over time. In order to minimize errors in the rms size estimate, a 2% cut off level is set as represented by the red lines in Figure 4.

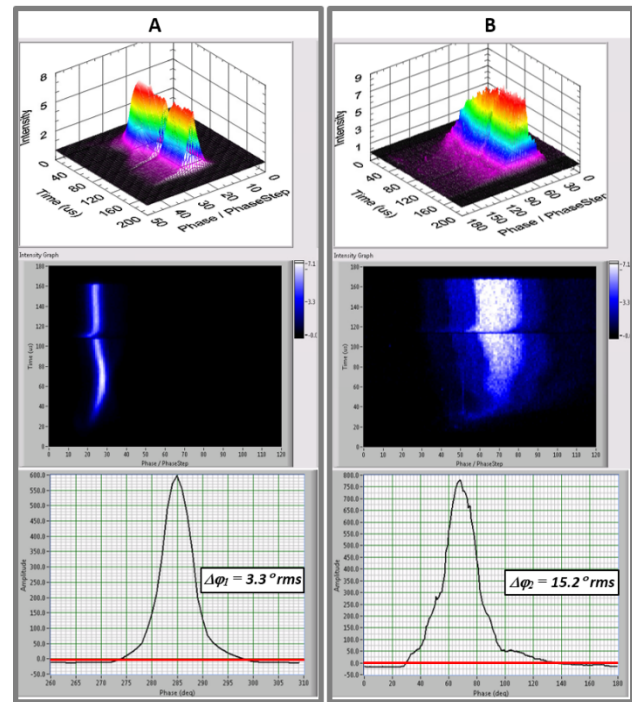


Figure 4: Evolution of the longitudinal bunch profile within the beam pulse observed with the first BSM (A) at the exit of the linac and the second BSM (B) in the transfer line. The phase unit is in degree at 352.2 MHz.

The rms bunch lengths at the first and the second BSMs are  $\sigma_1 = 26$  ps and  $\sigma_2 = 120$  ps respectively. The measurements were performed for a low beam current of 5.6 mA. In this case a momentum spread in the beam can be estimated using simple considerations. Two particles with a momentum difference of  $\Delta p/p$  after drifting a distance  $L$  will be separated longitudinally by the phase interval in degree:

$$\Delta\varphi = \frac{360L}{\lambda\beta\gamma^2} \cdot \Delta p/p$$

Here  $\beta$  and  $\gamma$  are relativistic factors, and  $\lambda$  is the RF wavelength. Substituting  $\Delta\varphi_2 = 15.2^\circ$  measured by the 2<sup>nd</sup> BSM, one can estimate the rms  $\Delta p/p = 7.3 \times 10^{-4}$ .



The simulations performed for a beam current of 62.5 mA [12], show much faster growth of the rms bunch length from 18 ps at the BSM#1 to 140 ps at BSM#2 location and give smaller momentum spread of  $6.7 \times 10^{-4}$  at BSM#2. The larger experimentally estimated momentum spread above is consistent with the wider initial bunch length found at the Linac4 exit.

### Variation of Chopping Pattern

Figure 5 shows the evolution of the bunch shape within the beam pulse for three chopping patterns, for a 140  $\mu$ s-long pulse with optimum cavity settings. The measurement conditions are summarised in Table 3.

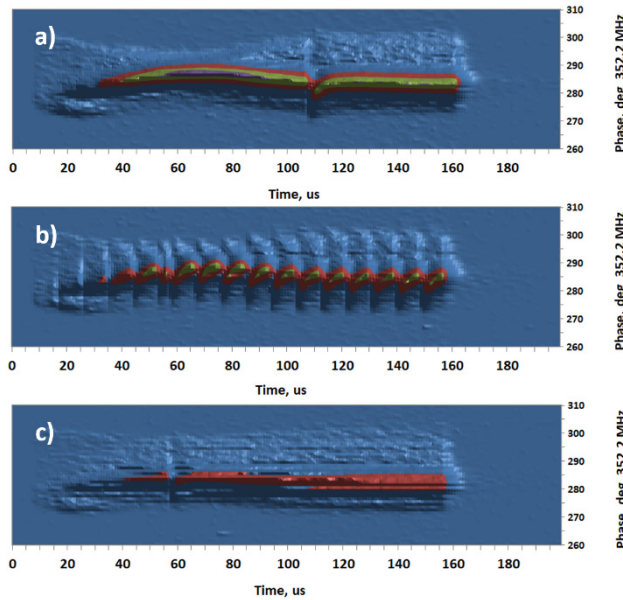


Figure 5: Bunch shape behaviour within the beam pulse for three chopping patterns.

Table 3: Chopper Settings and Rms Bunch Lengths  $\sigma$

Parameters	Fig. 5a)	Fig. 5b)	Fig. 5c)
Av. Current [mA]	17	15	11
Chopper ON [ $\mu$ s]	0	1	0.325
Chopper OFF [ $\mu$ s]	100	8	0.625
Duty cycle [%]	100	89	62.5
$\sigma$ from BSM [ps]	26	28.4	27.6

Fig 5a) shows the pulse structure acquired with the chopper off, while in Fig 5b) the chopped beam structure is clearly visible. The plot in Fig 5c) corresponds to a chopping frequency of 1.05 MHz, very close to the nominal LHC chopping pattern at 0.99 MHz. The BMS specification for a low noise acquisition imposes a relatively low amplifier bandwidth of a few hundred kHz after the electron multiplier which, when combined with the BMS signal sampling at 1 MHz means that one cannot detect the chopping frequency. Nevertheless, the effect of the chopping pattern is small, as can be seen from Table 3 where the rms bunch length is only slightly increased when measuring a chopped beam.

### Phase and Power Scan of PIMS11-12 Cavities

During the commissioning steps of the linac and later for machine operation, the essential technique for emittance reconstruction is based on analytic calculations with transfer matrices and beam profile measurements. This working principle is valid and applied for both transverse and longitudinal planes [11]. In the latter case, phase or amplitude of an RF cavity is varied to modify the beam phase spread which is measured by a BSM downstream. With at least three measurements, a matrix inversion calculation gives the initial longitudinal Twiss parameters at the cavity input. Furthermore, a phase shift of a longitudinal profile can be interpreted by a change of transit time, or an energy gain  $\Delta E$  given by [13]

$$\Delta E = \frac{\Delta P}{I}$$

with  $\Delta P$  as the difference in RF power, and  $I$  as the beam current at a downstream current monitor. This simple and precise method is applied to determine the energy gain through a cavity by beam loading measurement.

The PIMS structure consists of 12 modules powered in pairs. Phase measurements of the PIMS11-12 modules were performed for a beam current of 14 mA with a 200  $\mu$ s beam pulse duration. A nominal accelerating voltage of 4.1 MV was used. The dependence of the average bunch position (phase with respect to the main RF clock), as measured by the BSM, on the phase of the accelerating field in PIMS11-12 is shown in Figure 6. The phase spread of the measured function is  $290.6^\circ$  which in time domain corresponds to a swing of 2.29 ns in the beam transit time between the cavity and the BSM.

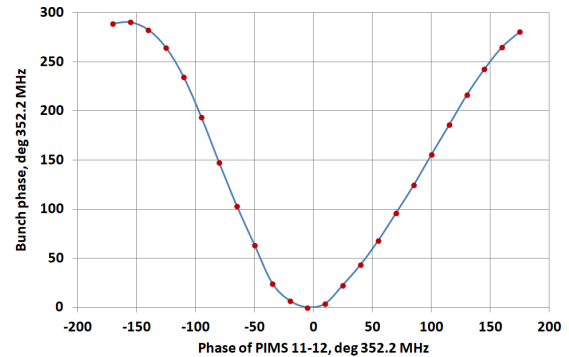


Figure 6: Dependence of average bunch position on the phase of the field in PIMS11-12. The phase spread of the measured function is  $290.6^\circ$  (vertical axis). This is equivalent to 2.29 ns of beam transit time swing.

Bunch lengths have been measured for various amplitudes of PIMS11-12 voltage with nominal settings of PIMS1-10. The initial accelerating voltage of PIMS11-12 was the nominal 4.1 MV. The integrated longitudinal profile over the entire beam pulse measured for several RF power levels are presented in Figure 7. Although the results show a slightly higher profile at 3.1 MV, the rms bunch length here is 6% larger than the nominal one, rising up to

12% at 0.3 MV. As for the phase scan, the beam transit time swing induced by the power scan is 1.03 ns.

Besides the longitudinal emittance reconstruction, the BSM profiles obtained by phase and power scans can be used to set both the amplitude and phase of the accelerating field by comparing with theoretical functions. For a better understanding of the accelerator it should be interesting to associate RF settings from the BSM with those from BPMs via TOF [14].

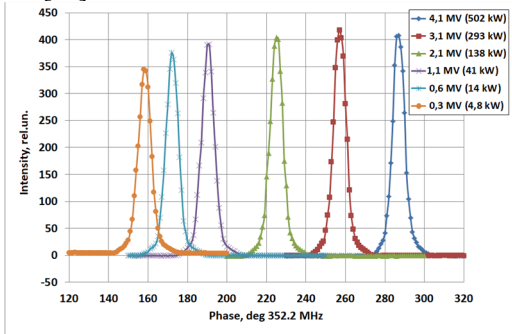


Figure 7: Integrated longitudinal distributions for different accelerating voltages in PIMS11-12. The phase spread (on the horizontal axis) of the peak distribution is 128.5 °. This is equivalent to 1.03 ns of beam transit time swing.

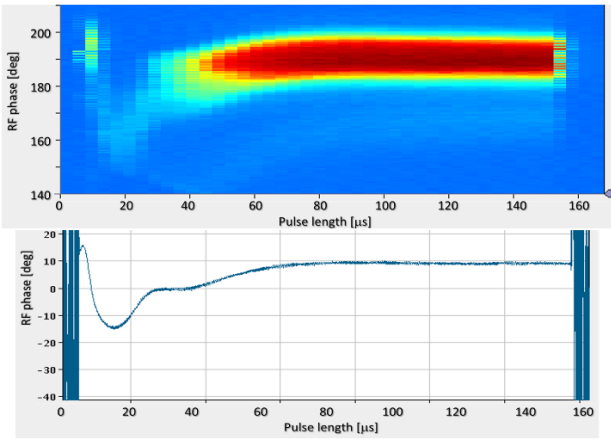


Figure 8: Beam phases in the Linac4 transfer line. Top plot was acquired with the BMS#1. Bottom plot was taken with a nearby BPM.

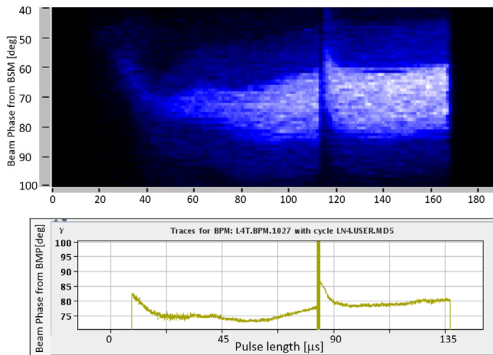


Figure 9: Beam phases in the Linac4 transfer line under different machine settings. Top plot was acquired with the BMS#2. Bottom plot was taken with a nearby BPM.

## Beam Phase Comparison with the BPMs

Longitudinal bunch position measurements taken by the BSM were compared to those from a beam position monitor pick-up located ~1 m away. Figure 8 shows the acquisition of a 150 μs-long pulse with BSM#1 and its neighbouring BPM. Figure 9 shows similar plots taken by BSM#2 and a neighbouring BPM upstream under different machine settings, where the pulse was shortened to 130 μs. For each case, one observes a good agreement for the time evolution of the beam phase.

Since the phase information from the stripline pick-ups relies on the function  $\tan^{-1}$  (see Figure 3), only the non-integer part (modulo  $\pi$ ) of the total phase is known. Furthermore the argument  $Q/I$  does not contain information on the particle distribution of the H<sup>-</sup> bunches. The phase distribution measured in a single shot by a pick-up is equivalent to the peak distribution of the longitudinal bunch length measured by the BSM, which requires a fine phase scan taking about 50 shots. The BSM is therefore used for phase spread measurements and longitudinal emittance reconstruction, while the BPM phase curve can quickly spot shortcomings in, for example, the cavity beam loading feedback system.

## CONCLUSION

The Bunch Shape Monitor has been extensively used for all the commissioning stages of the Linac4 from 3 MeV to 160 MeV, and to explore and optimise the final settings of the machine. This instrument is complementary to the Beam Position Monitors that are able to give the average time structure of the beam phase in a single shot. Both monitors will be useful after the connection of the Linac4 to the PSB, to validate the new transfer line optics at 160 MeV, for setting up the longitudinal painting scheme for high intensity users, and for optimisation during routine operation.

## ACKNOWLEDGEMENTS

The authors would like to thank J.B. Lallement, A. Lombardi and the BE-OP team for their strong support. U. Raich who was in charge of the BSMs is warmly acknowledged for his genuine contribution. Finally, our special thanks to the INR team, namely Y. Kiselev, V. Gaydash and Y. Gotovtsev for their fruitful collaboration and help in the commissioning of the BSM.

## REFERENCES

- [1] F. Gerigk, M. Vretenar (eds.), “Linac4 technical design report”, CERN-AB-2006-084, Dec. 2006
- [2] K. Hanke and A. Lombardi, “Beam measurements for Linac4 and its transfer lines”, CERN L4-B-ES-0002, Nov. 2010
- [3] F. Roncarolo *et al.*, “Overview of the CERN Linac4 beam instrumentation”, in *Proc. LINAC 2010*, Tsukuba, Japan, Sep. 2010, paper THP007, pp. 770-772.
- [4] F. Zocca *et al.*, “Beam diagnostics measurements at 3 MeV of the Linac4 H<sup>-</sup> beam at CERN”, in *Proc. IPAC 2014*, Dresden, Germany, June 2014, pp. 3694-3696,

doi.org/10.18429/JACoW-IPAC2014-THPME179

- [5] A. Lombardi, “Commissioning of the low-energy part of Linac4”, in *Proc. LINAC 2014*, Geneva, Switzerland, Aug.-Sep. 2014, paper MOIOA02, pp.6-10.
- [6] U. Raich *et al.*, “Beam instrumentation performance during commissioning of CERN’s Linac4 to 50 MeV and 100 MeV”, in *Proc. IPAC 2016*, Busan, Korea, May 2016, pp. 293-295, doi.org/10.18429/JACoW-IPAC2016-MOPMR026
- [7] F. Roncarolo *et al.*, “Beam Instrumentation for the CERN Linac4 and PSB Half Sector Test”, in *Proc. IPAC 2017*, Copenhagen, Denmark, May 2017, pp. 408-411, doi.org/10.18429/JACoW-IPAC2017-MOPAB120
- [8] A. Feschenko, “Technique and instrumentation for bunch shape measurements”, in *Proc. RUPAC 2012*, Saint-Petersburg, Russia, September 2012, paper FRXOR01, pp.181-185.
- [9] J. Tan, M. Ludwig, L. Søby, M. Sordet and M. Wendt, “Commissioning of the CERN Linac4 BPM system with 50 MeV proton beams”, in *Proc. IPAC 2013*, Shanghai, China, June 2013, paper MOPWA037, pp. 750-752.
- [10] T. Schilcher, “RF applications in digital processing”, in *Proc. of CERN Acc. School*, CERN-2008-003, Sigtuna, Sweden, May-June 2007, pp. 249-283.
- [11] V. A. Dimov, J.B. Lallement, A. M. Lombardi and R. Gaur, “Emittance reconstruction techniques in presence of space charge applied during the Linac4 beam commissioning”, in *Proc. HB2016*, Malmö, Sweden, July 2016, paper WEPM1Y01, pp. 433-438.
- [12] L. Hein and A. Lombardi, “Update of the Linac4-PSB Transfer Line”, CERN sLHC-Project-Note-0028, Dec. 2010.
- [13] A. Lombardi, “The Linac4 project”, in *Proc. HB2016*, Malmö, Sweden, July 2016, paper MOAM2P20, pp. 1-5.
- [14] M. Bozzolan and J.B. Lallement, “BPM time of flight measurements for setting-up the RF cavities of the CERN Linac4”, to be published in *Proc. LINAC 2018*, Beijing, China, Sep. 2018

# FIRST RESULTS FROM THE BUNCH ARRIVAL-TIME MONITORS AT SwissFEL

V. Arsov<sup>†</sup>, P. Chevtsov, M. Dach, S. Hunziker, M. Kaiser, D. Llorente, A. Romann, V. Schlott, M. Stadler, D. M. Treyer, Paul Scherrer Institut, 5232 Villigen PSI, Switzerland

## Abstract

Two Bunch Arrival-Time Monitors (BAMs) based on fiber optical Mach-Zehnder intensity modulators have been commissioned at SwissFEL. Both operate simultaneously up to 100 Hz with a resolution <5 fs at 200 pC. We have developed concepts and tested hardware, which enhance the BAM commissioning and user operation.

## INTRODUCTION

Two Bunch Arrival-Time Monitors (BAMs) based on fiber optical Mach-Zehnder intensity modulators [1], operating simultaneously up to 100 Hz with a resolution <5 fs at 200 pC, have been commissioned at SwissFEL. They derive their high stability from a pulsed optical reference distribution system in which the length of the single-mode optical fibers is stabilized for drift and jitter. For commissioning, instead of using a balanced optical cross-correlator as a phase detector we use a technically less demanding approach based on low drift and jitter laser-to-RF direct conversion, which delivers few tens of fs stability [2, 3]. In order that all BAMs measure simultaneously, it is necessary that a reference laser (OMO) pulse overlaps with the bunch at the given location. In addition, an integer number of pulses should fit in the link. To meet the above two requirements during commissioning multiple timing scans of the OMO pulses should be made. A complete scan may require a time-shift over an entire pulse train period, i.e., 7 ns. To speed up commissioning and allow adding of further BAM stations we have developed a concept for fast OMO pulse timing scan.

## BAM REFERENCE DISTRIBUTION AND READOUT

### *BAM Optical Master Oscillator (OMO2)*

The core of the SwissFEL reference distribution is a mode-locked laser oscillator (Origami 15, NKT Photonics) with pulse repetition rate of 142.8 MHz, phase-locked to a stable microwave reference at 2998.8 MHz (SMA100A, Rohde & Schwarz), which is locked to a 10 MHz Rb standard (FS725, SRS) [4]. All machine relevant frequencies are derived via harmonic extraction and delivered to the remote locations by single-mode fiber optical links, stabilized according to the client's specific requirements. Among others, BAM has the most stringent stability requirements for sub-10 fs drift, which is achieved via balanced optical cross-correlation [1]. In the general case the fiber optical link

length is arbitrary and does not necessarily provide an overlap of a reference OMO pulse with the electron bunch. To secure a timing overlap, it is necessary to phase shift the OMO pulses over a pulse train period. Since at SwissFEL the OMO is the source of the entire reference distribution, such shifting will not effectively result in an overlap with the bunch, because the effect is a common mode. The alternative is either to have an optical delay line for each individual pulsed link, or to use a second OMO dedicated only for BAM commissioning (OMO2). We chose the second approach (Fig. 1). As in the case of the machine OMO, the one for BAM is locked to the same stable microwave reference. In addition, there is a bucket synchronization at 1.9833 MHz (super period). The advantage is, that any machine component with corresponding bucket synchronization, e.g., the gun and the experimental lasers, have also a common timing origin. The bucket synchronization is obtained by phase locking of one of the 3 GHz slopes to the slope of the super period at the zero crossing. The overlap is achieved with an IQ modulator (aka. vector modulator, shortly VM), which has a 12 bit DAC.

### *BAM Pulsed Optical Front End*

The pulsed link synchronization used for BAM commissioning is based on low drift stabilized phase detector [2, 3]. The set-up is all-fiber and the phase detection principle doesn't require a dispersion compensation. The good drift stability (~10 fs pk-pk) is achieved by temperature stabilization of the basic components within the package, proper choice of the working point of the two photo diodes (2651E, Emcore), as well as careful balance of the forward and backward branches and the corresponding optical pulse powers. Dispersion compensation to reduce the pulse width to ~250 fs is nevertheless made to preserve the BAM resolution. A combination of a piezo-stretcher (PZ2, Optiphase) and a delay stage (MDL-02, General Photonics) is used to compensate for jitter and drift (Fig. 1). The naked fibers are housed in a hermetic package to minimize the environmental influence. The system is located in the temperature and humidity regulated synchronization (T&S) room.

### *BAM Readout Electronics*

The BAM photoreceiver, the 7-slot VME crate with the pulse-forming front-end and readout cards are located in a separate 19" rack in the technical gallery (Fig. 1).

**Photoreceiver.** The device is an in-house development with three channels - "fine" BAM, "coarse" BAM and ADC clock. The photodiodes (2651E, Emcore) have 3 GHz bandwidth. The optical pulses for the two BAM-

<sup>†</sup> vladimir.arsov@psi.ch



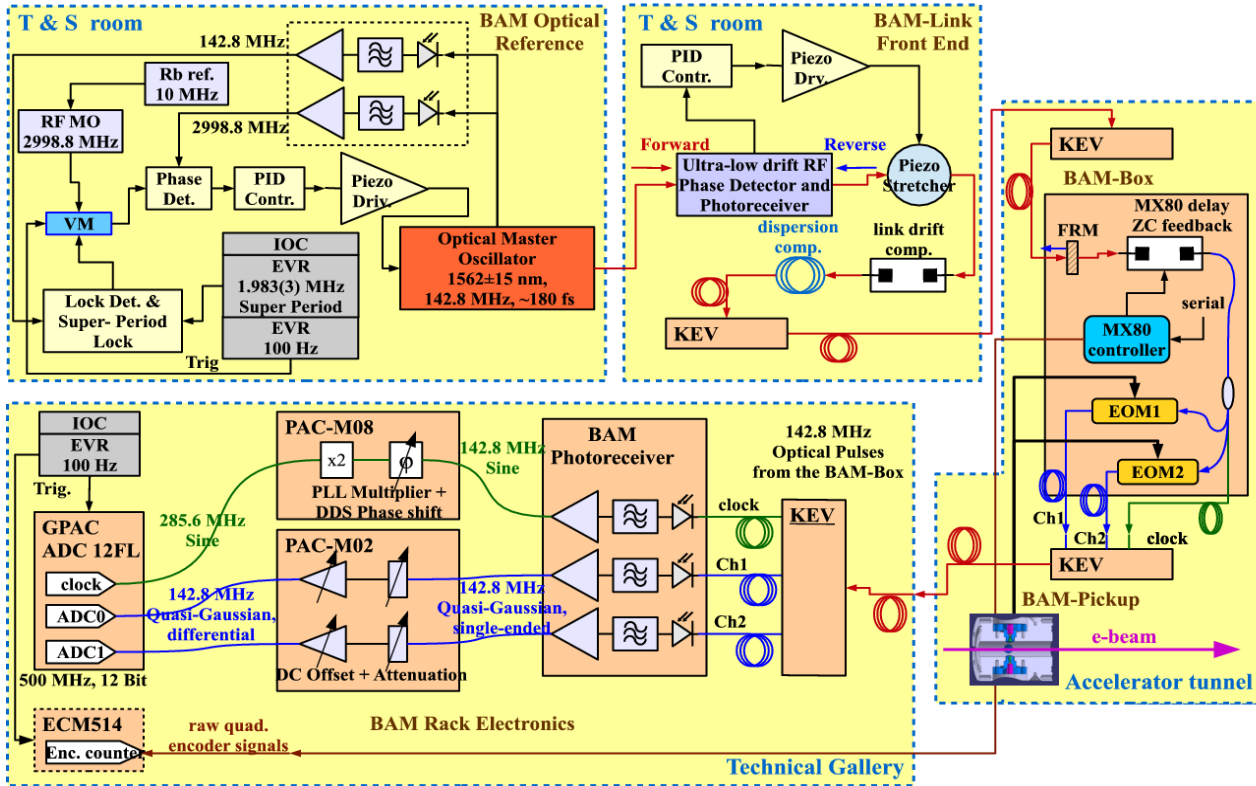


Figure 1: BAM pulsed optical reference and readout.

channels are Gauss-filtered to obtain flat tops and minimal pulse-to-pulse cross-talk at 142.8 MHz. This reduces the ADC sampling jitter sensitivity and improves the BAM resolution. The optical clock at 142.8 MHz has a sine shape. The photodiodes are operated close to saturation at  $\sim 1.5$  mW. The output stage is a broadband trans-impedance amplifier with typical outputs of  $\sim 0.7$  V pk-pk.

The triple photoreceiver is followed by a triple amplifier stage with flexible user adjustable input levels. The typical output is  $\sim 3$  V pk-pk single-ended signal.

**PAC-M02.** The PSI Analogue Carrier Board (PAC) is developed in house for diagnostics applications. It allows plugging of up to four mezzanine-boards, each with two channels. It supports up to 8 remotely controlled DACs, stabilized low-noise supply voltages and four differential digital I/Os.

The PAC-M02 mezzanine board is used for photoreceiver signal conditioning and is controlled from the PAC DACs. At the input of each of the two channels there is a digital step attenuator (DAT-31A-PP+, Mini-Circuits) providing attenuation with 0.5 dB steps. At maximum signal the input to the ADC is 2 V pk-pk. The following step contains single-ended differential amplifier with 700 MHz bandwidth. Its purpose is to DC-shift the signal baseline, so that to fully utilize the ADC dynamic range, thus improving the BAM resolution.

**PAC-M08** is a full DDS clock phase shifter, used to provide stable and adjustable clock signal with 425 fs timing resolution for the GPAC ADC. It has two outputs for 142.8 MHz and 285.6 MHz. The absolute phase is not

recoverable. The design includes a VCXO (KVG V-7213-LF-571.2MHz), locked to the 142.8 MHz reference by a narrow band PLL (ADF4106). The phase shifting is done by a DDS Chip (AD9912). A separate diode multiplier is used for the 285.6 MHz output, which has a substantially lower added jitter ( $<60$  fs) than the one integrated in the DDS chip. The integrated timing jitter of the 285.6 MHz output used for the BAM clock is  $<240$  fs in the bandwidth of 10 Hz-10 MHz, which is sufficiently low for sampling of the photoreceiver pulses.

The much better phase step accuracy (425 fs) and low added phase noise achieved with the PAC-M08 clock shifter improves substantially the BAM resolution, which was earlier limited by the ability to effectively sample the OMO amplitudes at the peak and not at the slope.

**GPAC.** BAM uses the Generic PSI ADC Carrier board (GPAC), originally developed for the European XFEL button BPM [5]. The firmware is modified and kept generic for most of the diagnostics applications. The specific BAM-processing, e.g., normalization of the waveforms, detection of the sample number with the first modulation (electron bunch interaction), bunch ID stamping, calculation of the laser amplitude jitter, is done at the IOC side. The ADCs (KAD5512P-50, Intersil) are 12 bit, 500 MSa/s. The sampling clock is at 285.6 MHz, provided by the PAC-M08 card, allowing sampling of one peak and one baseline points for multiple OMO pulses. Digitized is not the form of a single pulse, but multiple OMO pulse amplitudes, which are then normalized by dividing each next one by the amplitude of the previous pulse [1]. This allows simultaneous detection of two

bunches, as well as multiple pulses preceding the bunch modulation and thus measure *in situ* the amplitude jitter, which contains the shot-to-shot measurement error and which limits the BAM resolution. Since the clock signals are generated from the same optical pulse train as the BAM signals, the sampling is independent on phase shifts, e.g., caused by the delay stage for zero-crossing (ZC) feedback. The GPAC is triggered by the event receiver. The firmware provides a VME bus interrupt for the IOC and allows data processing between the events at 100 Hz.

**ECM514** is an encoder counting VME card for readout of incremental encoder signals. It is triggered by the event receiver. The positions are read in two 32 bit registers - "live" and "latched". The card allows bunch synchronous position read-out of the linear servo motor MX80 in the BAM-Box used for ZC feedback (Fig. 1). The EPICS communication with MX80 is serial, but the controller outputs the raw quad encoder signals, which are counted bunch synchronously by the "latched" register. The processing is done on the IOC side. With each trigger the last motor position is kept and passed to the IOC, where a bunch ID is assigned, together with the processed ADC traces.

**Event receiver.** The EVR-VME-330 (Micro Research Finland) event receiver is served by the machine timing event master. Two events are dedicated for BAM - EV10 with 3.0 ms delay and EV12 with 5.7 ms delay with respect to the sequence start (EV38). EV10 is used for masking, i.e., when this event is active, the hardware triggers for the subsequent events, e.g., EV12 are suppressed (Fig. 2). This feature, developed initially for the MPS, is used to initiate triggers simultaneously to remote IOCs, e.g., the one for the VM in the T&S room and the BAM IOC in the technical gallery.

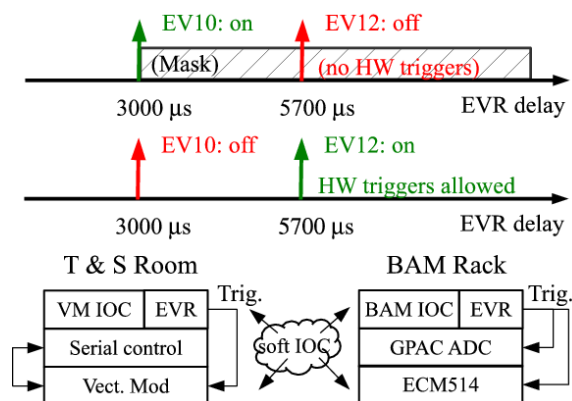


Figure 2: Trigger masking and synchronization.

**I/O Controller,** type IFC1210 VME from IOxOS Technologies [6], runs real-time Linux and is responsible for the EPICS record processing and linking with the machine network. The 100 Hz communication with the rest of the VME boards (GPAC, PAC, ECM) is done through the VME bus. Data processing is done sequentially through the VME interrupt generated by the GPAC card and includes normalization of the raw ADC waveforms, extraction of the BAM relevant data (see

subsection GPAC), MX80 encoder position readout, bunch-ID stamping and structured waveform processing for client applications.

## FAST TIMING SCAN CONCEPT

The "fast" scan refers to a method for bunch synchronous delay-shifting of the OMO pulses over a large interval with a high resolution. The goal is to establish an overlap between the OMO pulse and the electron bunch. Such scans provide information on the BAM pickup transients, e.g., charge or orbit dependence. The method enhances commissioning by speeding up the work on matching the zero crossings of the "fine" and "coarse" channels of a single BAM station, as well as the zero-crossing overlap for all BAMs. It provides also a rough estimate of the BAM resolution.

The method uses the VM in the OMO2 reference path as an actuator (Fig. 1). Up to 7 BAM stations can be included simultaneously in a single run.

The VM is primarily used for super-period lock. It communicates with EPICS over a slow serial port. To allow fast bunch synchronous scans at up to 100 Hz step rate the VM hardware and firmware were modified to support triggering by the event receiver. In VM triggered mode its phase advances by a predefined step on receiving of an external trigger pulse. The 100 Hz scan is much slower than the bandwidth of the OMO2 PLL, therefore the laser remains in lock, but its phase is effectively delayed relative to the origin determined by the bucket synchronization.

A technical challenge was to provide simultaneous trigger start of the VM IOC in the synchronization room and the BAM IOC in the technical gallery. The solution was provided by the trigger masking concept (Fig. 2). The remote clients are normally triggered by the BAM EV12. The trigger masking allows a preceding event, i.e., EV10, when active, to suppress the EV12 controlled triggers for the given client. The trigger sequence by event masking is managed by the fast scan EPICS soft IOC server. During the scan the serial communication with the VM is temporarily interrupted to prevent loss of phase steps.

On the BAM crate side, there is a buffer, which stores the GPAC ADC traces for each individual trigger and a trigger counter. For practical reasons the buffer size is 7170 elements, allowing storage of two ADC traces with 1024 elements (normalized trace). The mechanism allows scans from 0 to 7 ns with 1 ps step or within arbitrarily smaller interval with >80 fs step size. The interval limits are adjusted automatically to the user defined step size, so that the maximum buffer size of 7170 elements is not exceeded.

At the end of the scan the serial communication with the VM is restored and the final VM position is compared to the expected one for the given counter and step size. A warning message is given, if scan steps were lost.

The fast scan tool is fully automated and accessible from the SwissFEL BAM-expert launcher. A typical fast scan with 1 ps step size over a pulse train period lasts

~70 s at 100 Hz and ~12 min at 10 Hz. For comparison, the Matlab VM scan tool used during the Test Injector phase some years ago required 1.5-2 hours.

The buffered traces are stored in Matlab binary files. They can be displayed as a function of the phase delay either during the scan for an arbitrary sample number (online monitoring of the scan quality), or saved for post processing, e.g., with a dedicated expert user tool for slope fitting, which is also accessible from the launcher.

## EXPERIMENTAL RESULTS

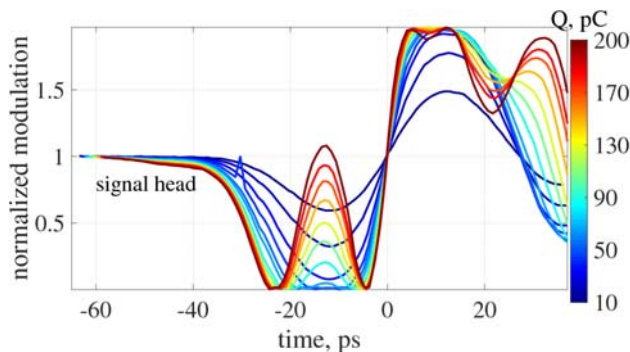


Figure 3: Normalized modulation as a function of the OMO pulse delay at different bunch charges.

The fast scan method was applied to measure the BAM pickup response at different charges (Fig. 3). Used is the 16 mm beam pipe diameter BAM-Pickup at the laser heater [7]. The results are similar to the ones measured earlier at the SwissFEL Test Injector (unpublished). The displayed waveforms are not the pickup voltages, but the normalized modulation of that single OMO pulse, which has interacted with the electron bunch, displayed as a function of the OMO pulse delay. The curves on Fig. 3 have been shifted at post processing to overlap the zero crossings. For high charge a typical "over-rotation" is observed. At higher coupling efficiency the pickup-voltage is higher than the EOM half-wave voltage, which leads to non-linear response and eventually swap to the adjacent EOM slope. The BAM measurement is made in the linear part of the EOM slope (near quadrature) and near the zero-crossing of the pickup-transient.

The quality of the pickup response is defined with the slew rate and the modulation depth. The latter is the ability to achieve 100 % modulation. At the pickup zero crossing the laser amplitudes are in quadrature (normalized modulation equal to 1). At higher amplitudes of the pickup transient the modulation becomes 100 % (normalized modulation equal to 0). The modulation depth is 100 % for a large range of bunch charges between 40 pC and 200 pC, and the dependence is flat (Fig. 4).

The BAM resolution is determined as a the product of the pickup slope [fs/% modulation] and laser amplitude jitter of the multiple laser pulses preceding the electron bunch modulation [% modulation]. Thus the resolution depends not only on the pickup response, but also on the noise of the entire reference distribution chain, BAM-Box and acquisition electronics. The amplitude jitter of the

reference laser pulses is measured shot-to-shot simultaneously with the arrival-times for bunches 1 and 2 and is in the order of 0.15 %. The slew rate was measured with delay stage calibration close to the zero crossing.

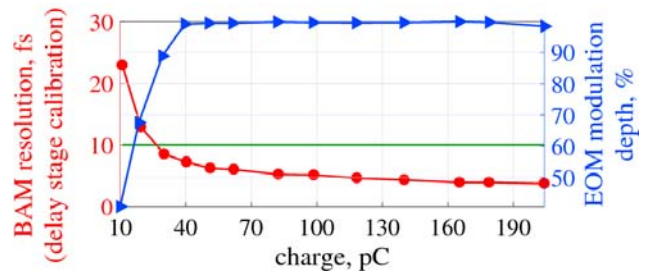


Figure 4: BAM resolution and EOM modulation depth as a function of the bunch charge.

For the 16 mm pickup the resolution is below 10 fs for the charge range 30 -200 pC. For lower charges the coupling efficiency is not sufficient. The improved electronics (photoreceiver, clock phase shifter, ADC input signal conditioning) contributed substantially to the improvement of the BAM resolution. For the BAMs after the undulators, 8 mm pickups are installed [7]. For those, twice as high coupling efficiency and better resolution at low charges is expected.

## CONCLUSION

We have developed concepts for fast timing scan of the reference laser pulses over a larger interval with <80 fs accuracy using a VM in the synchronization path of the laser. Depending on the machine repetition rate the method shortens the time to obtain an overlap between the laser pulse and the electron bunch from initially more than an hour to a few minutes. The technique can be of practical interest not only for BAM, but also for the experimental lasers, where an overlap between the pump and the FEL beams is required. The advantage of the method is that no free space delay stages are involved, which avoids beam pointing instabilities and drifts.

## REFERENCES

- [1] F. Loehl, "Optical synchronization of a free-electron laser with femtosecond precision", DESY, Hamburg, Germany, Rep. DESY-THESIS-2009-31, 2009.
- [2] S. Hunziker *et al.*, "Ultra-low Drift and Jitter Laser-to-RF Direct Conversion Unit", IRUVX Report, WP8, Industrialization, 2011.
- [3] V. Arsov, M. Dehler, S. Hunziker, M. Kaiser, and V. Schlott, "First results from the bunch arrival-time monitor at the SwissFEL Test Injector Facility", in *Proc. IBIC'13*, Oxford, UK, paper MOAL4, pp. 8-11, 2013.
- [4] S. Hunziker *et al.*, "Reference distribution and synchronization system for SwissFEL: concept and first results", in *Proc. IBIC'14*, Monterey, CA, USA, paper MOCZB2, pp. 29-33, 2014.
- [5] W. Koprek, B. Keil, and G. Marinkovic, "Overview of applications and synergies of a generic FPGA-based beam diagnostics electronics platform at SwissFEL", in *Proc.*

*IBIC'15*, Melbourne, Australia, pp. 165-169, 2015.  
doi.org/10.18429/JACoW-IBIC2015-MOPB050

Australia, pp. 1169-1172, 2015. doi:10.18429/JACoW-  
ICALEPCS2015-FRA3003

[6] M. Janousch *et al.*, “Overview and status of the SwissFEL  
project at PSI”, in *Proc. ICALEPCS'15*, Melbourne,

[7] V. Arsov *et al.*, “Design and commissioning of the bunch  
arrival-time monitor for SwissFEL”, in *Proc. IBIC'17*,  
Grand Rapids, MI, USA, pp. 182-186, 2017.  
doi.org/10.18429/JACoW-IBIC2017-TUPCC15



# PHOTON BEAM IMAGER AT SOLEIL

M. Labat\*, J. Da Silva, N. Hubert, F. Lepage,  
Synchrotron SOLEIL - L'Orme des Merisiers, [91 191] Gif-sur-Yvette, France

## Abstract

In one of the long straight sections of SOLEIL is installed a pair of canted in-vacuum undulators for the ANATOMIX and NANOSCOPIUM beamlines. Since the upstream undulator radiation can potentially damage the downstream undulator magnets, an accurate survey of the respective alignment of the two devices is mandatory. An XBPM has been initially installed for this purpose in the beamline frontend. For redundancy and further analysis, an X-ray imager was then designed and added just downstream the XBPM. It is made of a diamond plate that can be inserted into the upstream beamline frontend at low current. We present the commissioning of this new device together with its first results in operation.

## INTRODUCTION

The SOLEIL synchrotron light source is now in operation since 2006 [1]. The storage ring consists of 16 cells, with 24 straight sections of variable lengths, for undulator insertion. In one of the long straight sections, the so-called SDL13, have been installed two horizontal canted undulators [2]. Both undulators are in-vacuum undulators with periods of 20 mm initially, and 18 mm since 2018. The upstream undulator delivers hard X-rays to the NANOSCOPIUM beamline, for nanoscale imaging experiments. The downstream undulator delivers hard X-rays too, to the ANATOMIX beamline dedicated to tomography experiments. The two beamlines are designed to be operated simultaneously.

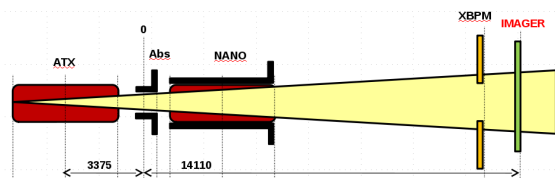


Figure 1: SDL13 (Long Straight Section in cell 13) layout. 0: middle of the straight section. ATX: ANATOMIX and NANO: NANOSCOPIUM undulators. Distances given in mm.

The horizontal canting angle in between the undulators is 6.5 mrad while both insertion devices are separated by about 7 m. Therefore, as illustrated in Fig. 1, the upstream undulator radiation passes through the downstream undulator before reaching the beamline. In nominal operation, both upstream and downstream undulator gaps are set at 5.5 mm, which is found of the order of the vertical aperture of the upstream undulator radiation inside the downstream undulator. In this initial layout, the upstream undulator can seriously damage the downstream undulator magnets.

\* marie.labat@synchrotron-soleil.fr

This is the reason why an absorber has been installed in 2016 in order to shadow the NANOSCOPIUM undulator magnets from the ANATOMIX undulator radiation. The schematic of this absorber, with respect to the electron and ANATOMIX photon beams is presented in Fig. 2. It is a piece of copper with an asymmetric 90 degrees U-shape. Its vertical aperture is 2.8 mm and its geometry was studied in detail in order not to jeopardize the performance of the storage ring in terms of collective effect induced instabilities, beam losses, injection efficiency and beam life time. It can be retracted when needed, thanks to a remote controlled pneumatic translation.

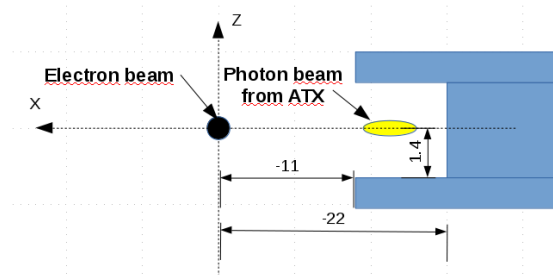


Figure 2: Schematic of the absorber installed in the middle of the SDL13.

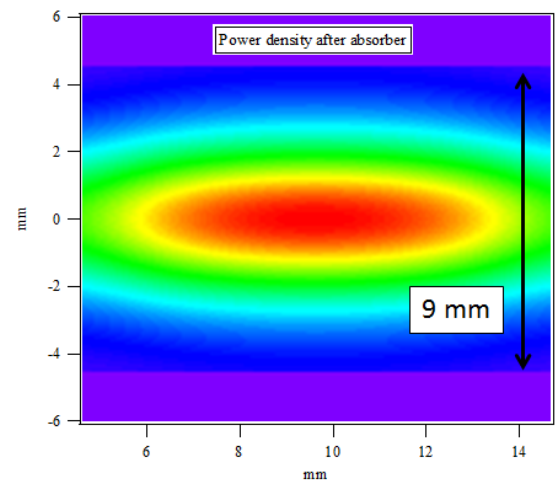
If the upstream undulator, the absorber and the downstream undulator are properly aligned, the safety of all equipments is guaranteed. But any drift from the nominal setting (slab distortion, large temperature variations, human intervention, undulator offset adjustment, storage ring girders re-alignment, misteering of the beam, etc...) can have dramatic consequences. This is why a careful survey of the relative alignment of those three critical equipments is required.

At the first stage of this two canted-undulators project, a double XBPM was installed in the double beamline front end [3]. It enables the simultaneous measurement of the NANOSCOPIUM and ANATOMIX photon beam positions at the exit of the straight section. A couple of years later, it has been decided to give a redundancy to this diagnostic, using an X-ray imager. This paper presents the design, commissioning and operation of this imager.

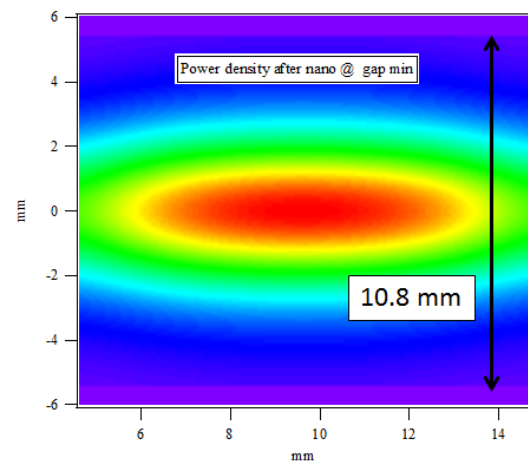
## IMAGER DESIGN

### Specifications

The imager specifications were the following: (i) Image the ANATOMIX X-ray photon beam in the beamline frontend, (ii) Image the shadow created by the absorber on the ANATOMIX radiation pattern, (iii) Image the shadow (or its absence) created by the NANOSCOPIUM undulator on the



(a) With absorber, without NANOSCOPIUM undulator.



(b) Without absorber, with NANOSCOPIUM undulator.

Figure 4: ANATOMIX radiation pattern simulated with SRW at the imager location (a) with the absorber inserted, (b) without absorber but with the NANOSCOPIUM undulator closed at 5.5 mm.

Looking at the ANATOMIX radiation pattern, the shadow corresponds to a step in intensity from the illuminated zone to the shadowed zone by 10 units for a maximum intensity at the radiation centroid of 120 (see Fig. 5). For an accurate measurement of this step location, the imaging system dynamic range should therefore be larger than 1000.

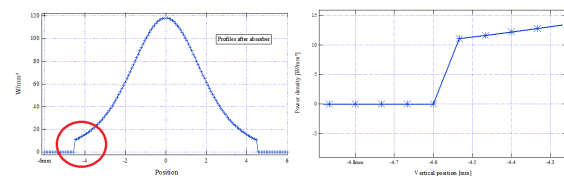


Figure 5: Vertical profile of the ANATOMIX radiation at the imager location. SRW simulation.

Additional thermal simulations were done to give the maximum current sustainable by the diamond: 20 mA.

## The Imager Components

A dedicated vacuum chamber was inserted in the beam-line frontend to house the imager vacuum components. It is installed right after the XBPM vacuum chamber. This vacuum chamber allows the insertion of a diamond disk on ANATOMIX radiation path, not on NANOSCOPIUM radiation path.

The diamond disk is made of CVD diamond and was realized by Diamond Materials. It is a 36 mm diameter disk, tilted by 40° degrees to allow its imaging from the outside of the vacuum chamber. It was brazed on a copper ring for heat evacuation with a meniscus for thermal dilatation under operation. A 30 microns silver coating was added to increase the thermal conductivity. A 3D picture of the diamond disk is shown in Fig. 6.

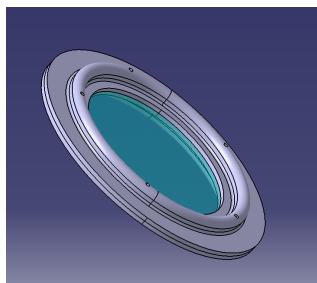


Figure 6: 3D view of the diamond disk brazed on its copper ring.

The diamond is water cooled. The water flows around the diamond disk inside the copper ring for an optimized heat exchange. The cooling system is shown in Fig. 7.

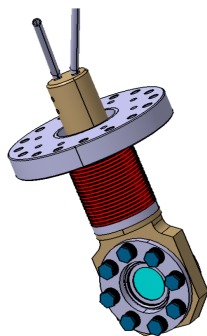


Figure 7: 3D view of the diamond cooling system.

The diamond mounted in its cooling system can be inserted/extracted remotely thanks to a pneumatic jack shown in Fig. 8. The insertion is achieved in the horizontal plane and for machine security reasons, it is by default extracted thanks to two springs.

Finally, the imaging system consists of a commercial objective (RICOH FL-BC7528-9M with a CVO extender 1.5X) and of a CMOS camera (ACE Series acA1920-50gm camera). The imaging is achieved through a lead glass viewport located on the top of the vacuum chamber. The imaging system together with the whole imager are shown in Fig. 9.

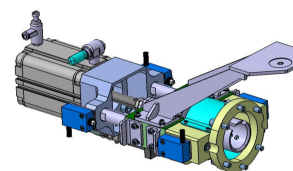


Figure 8: 3D view of the diamond insertion stage.

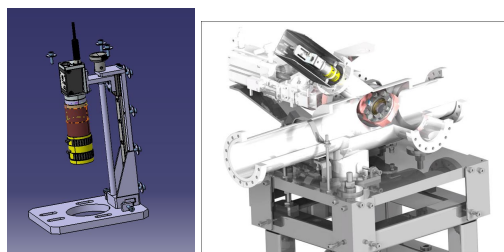


Figure 9: 3D view of the imaging system (left) and of the whole imager (right).

## IMAGER COMMISSIONING

The imager was installed in August 2017. A picture of the system installed is shown in Fig. 10.

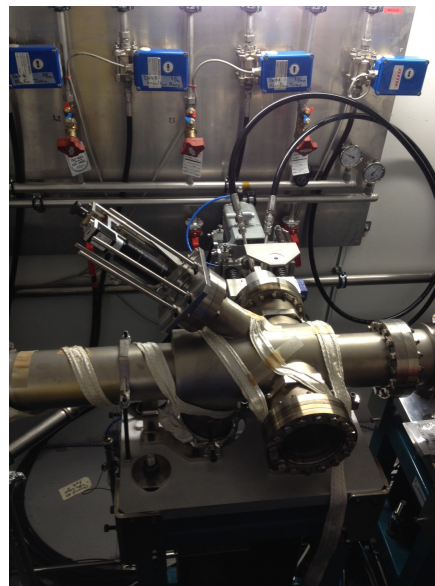


Figure 10: Picture of the imager installed on the SDL13 beamline frontend.

The first step of the commissioning consisted in centering in the horizontal and vertical directions the imaging system, to position the diamond center at the center of the camera sensor. This was achieved manually, using precision screws on the imaging system mechanics. The second step consisted in adjusting the focussing of the imaging system to reach the highest resolution. The diamond imperfections were used for that, manually adjusting the objective setting. The ANATOMIX pattern was successfully observed at the very first trial as shown in Fig. 11, and the photon flux was large enough already at 6 mA. However, it revealed that to visu-

alize the shadowing from NANOSCOPIUM undulator or from the absorber, it was necessary to saturate the centre of the image. We even sometimes add a numerical mask at the center of the image to help the metrology.

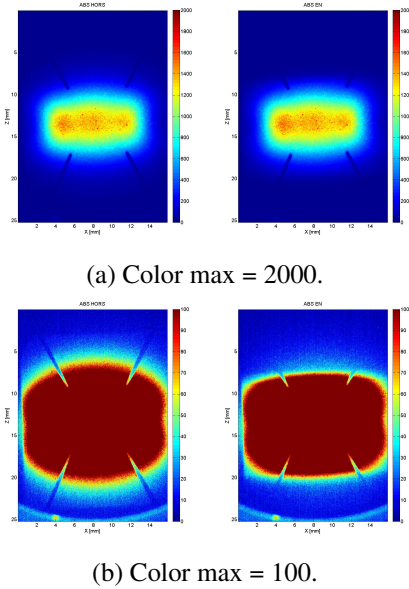


Figure 11: ANATOMIX radiation patterns recorded with the imager with two different color scales. Left images are absorber extracted while right images are absorber inserted.

### IMAGER OPERATION

The imager is in operation since October 2017. It is used in routine to check several aspects of the SDL13. At the beginning of each week of operation, the imager and the XBPM measurements are recorded while closing the NANOSCOPIUM undulator gap to check that the signal is hardly decreased and therefore that NANOSCOPIUM undulator remains in the shadow of the absorber. Each time the absorber or the undulator are moved, and after each shutdown, both diagnostics measurements are also recorded versus the electron beam vertical position in the ANATOMIX undulator (making bumps in the undulator, see Fig. 12) and versus the NANOSCOPIUM undulator offset. Those three systematic measurements enable a reliable check of the relative alignment of the ANATOMIX undulator, the absorber and the NANOSCOPIUM undulator. Up to now, XBPM and

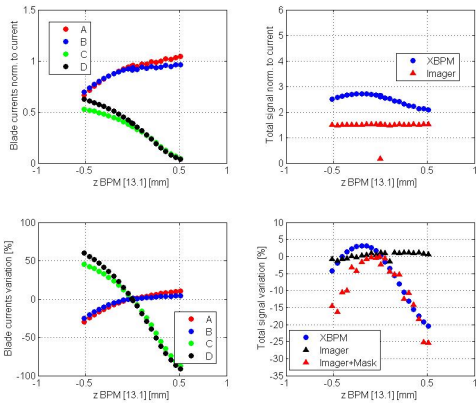


Figure 12: XBPM and imager records versus electron beam vertical position in the ANATOMIX undulator. Absorber is inserted and NANOSCOPIUM gap is opened.

imager measurements have been found in good agreement and helped solving misalignment issues.

### CONCLUSION

For the survey of the SDL13 alignment and consequent safety of its equipment, an imager has been designed, commissioned and installed in the beamline frontend. This imager provides with a redundant diagnostic with respect to the pre-existing double XBPM. The understanding of its images is sometimes more easy than the understanding of the XBPM position measurements, due to the presence of the absorber in between the two insertion devices.

### REFERENCES

- [1] L. S. Nadolski *et al.*, “Progress status for the 10 year old SOLEIL synchrotron radiation facility”, in *Proceedings of IPAC2017*, Copenhagen, Denmark, (2017).
- [2] L. S. Nadolski *et al.*, “Operating simultaneously two in-vacuum canted undulators in synchrotron SOLEIL”, in *Proceedings of IPAC2017*, Copenhagen, Denmark, 851-854 (2017).
- [3] N. Hubert *et al.*, “Design of a new blade type XBPM”, in *Proceedings of IBIC2014*, Monterey, CA, USA, 687-690 (2014).
- [4] O. Chubar, *Proceedings of SPIE - The International Society for Optical Engineering*. 9209. 920907. doi:10.1117/12.2062100



# DEVELOPMENT OF A YAG/OTR MONITOR FOR BEAM HALO DIAGNOSTICS\*

R. Yang<sup>†</sup>, P. Bambade, S. Wallon, LAL, CNRS/IN2P3, Université Paris-Saclay, Orsay, France  
T. Naito, A. Aryshev, N. Terunuma, KEK, Tsukuba, Japan  
M. Bergamaschi, CERN, Geneva, Switzerland

## Abstract

To investigate the mechanisms of beam halo formation and its dynamics, a YAG/OTR monitor has been developed and tested at the KEK-ATF. The monitor has four ceramic Ce:YAG screens for the visualization of the beam core and beam halo and an OTR target to provide complementary beam core measurements. A high dynamic range ( $>10^5$ ) and a high resolution ( $<10\ \mu\text{m}$ ) have been demonstrated experimentally. Measurements of beam halo using this monitor are consistent with previous results and theoretical modeling, and have allowed further progress in the characterization of the driving mechanisms.

## INTRODUCTION

Beam halo is one of the critical issues limiting the performance and causing component damage and activation for the future linear or circular accelerator. Understanding halo formation and distribution is not only a crucial topic of accelerator physics but also of great importance for the mitigation of the unwanted background induced by halo particles, e.g., through an efficient collimation system. To uncover the physical origins of beam halo and how to suppress it, powerful diagnostics with extremely high dynamic range and sensitivity are required. Direct measurements of halo are considered for most accelerators, requiring a dynamic range of at least  $10^5$  and a capability to simultaneously measure core and halo, in order to appropriately probe theoretical predictions of beam halo [1–3].

As a successful test facility for the R&D of ILC, the Accelerator Test Facility (ATF) at KEK has provided an excellent opportunity to investigate the mechanisms of halo formation and demonstrate the necessary diagnostics [4,5]. Its nominal beam energy and beam intensity are 1.3 GeV and  $0.1 \times 10^{10}$ – $1 \times 10^{10}$  e/pulse, respectively. To achieve a sufficient dynamic range for halo measurements, a set of diamond sensor (DS) detectors have been developed and installed at ATF2 [6,7], which is an extraction line built to address the feasibility of focusing electron beams to nanometer (nm) scale vertical size, and provide a beam orbit stability at the nm level at the virtual interaction point. After a reconstruction of measured profiles, the effective dynamic range of the DS detector has been found to be around  $10^5$ . Furthermore, the transverse beam profile and its vacuum dependence observed using these DS detectors clearly indicate the correlation between vertical beam halo and beam-gas scattering (BGS) [8]. However, the saturation of charge collection inside the DS bulk

and the deformations of DS waveforms have severely limited the performances and applications of the DS detectors [9]. To obtain a simultaneous diagnostics and confirm the observations given by the DS detector, a new YAG/OTR monitor has been developed and installed.

In this paper, the design of the YAG/OTR monitor toward the desired dynamic range and resolution are described, followed by performance tests with beam. Comparisons of beam halo measured by the DS detector and the YAG/OTR monitors are presented, which are in good agreement. Further foreseen applications and improvements of the YAG/OTR monitor are also discussed.

## DEVICE CONFIGURATION

The favorable scintillating properties, mechanical rigidity and radiation hardness have made the scintillator material an excellent candidate for direct two-dimensional (2D) imaging devices, widely used for diagnostics of energetic particles and photons. Previous investigations have indicated that the Ce:YAG has a high photon yield (around  $2 \times 10^4$  photons/MeV) and a fast decay time ( $<1\ \mu\text{s}$ ), which are suitable for halo diagnostics [10,11]. Meanwhile, beam profile measurements using the OTR are saturation-free and can provide complementary diagnostics for dense beam core. Considering the practical beam parameters at ATF2, a YAG/OTR system has to satisfy two requirements: a dynamic range of more than  $1 \times 10^5$  and a spatial resolution of less than  $10\ \mu\text{m}$ .

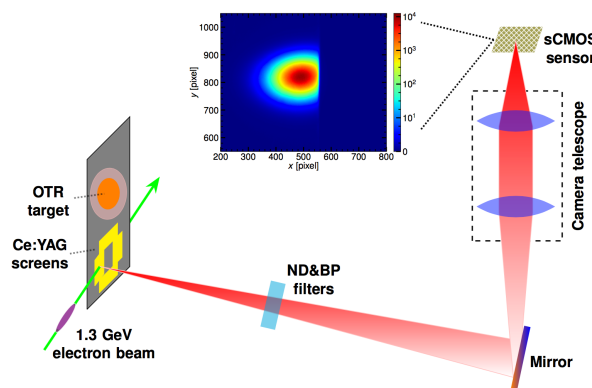


Figure 1: Schematic of the YAG/OTR monitor.

The YAG/OTR monitor mainly consists of four ceramic 0.5 mol% Ce:YAG screens and an OTR target on the same holder, a microscope lens (TS-93006/TS-93022 Sugito Co.), a 16-bit scientific Complementary Metal Oxide Semiconductor (sCMOS) camera (PCO.EDGE 4.2 L) with a low noise

\* Work supported by MSCA-RISE E-JADE project (grant number 645479)

<sup>†</sup> ryang@lal.in2p3.fr

level and neutral-density (ND)/band-pass (BP) filters [12], as shown in Fig. 1. The scintillation light and OTR are extracted through a fused silica viewport with an indium seal to preserve a low vacuum pressure and then focused on the sCMOS sensor via an optical lens. To suppress the "blooming" effect due to the intense light from the beam core, a YAG screen has been split into four small pieces and assembled with a central quadrilateral opening ( $4 \times 2.4 \text{ mm}^2$ ). The size of each YAG pad is  $4 \times 5 \times 0.1 \text{ mm}^3$ . For measurements of beam halo, the central opening allows core particles to pass through without striking the screen and emitting fluorescence light. Besides, an aluminum Kapton  $2 \mu\text{m}$  thick OTR target has been seated in a titanium conical receptacle with an exposed screen diameter of 7 mm. The YAG screens are placed at  $45^\circ$  to the beam trajectory, and the observation is perpendicular to their surfaces, at  $135^\circ$ , horizontally. To probe the backward OTR with the same observation system, the OTR target is placed at  $22.5^\circ$ . In addition, a rectangular opening that is broader than the gap between YAG screens has been drilled on the holder in order to prevent the reflections from the surface of the holder (which has been found to blur the image significantly).

The holder to accommodate the screens is actuated by a four-dimensional manipulator ( $\vec{x}$ ,  $\vec{y}$ ,  $\vec{z}$  and the rotation around  $\vec{z}$ -axis). The backlash and readout accuracies of this manipulator have been calibrated to be around  $13.5 \mu\text{m}$  and less than  $0.2 \mu\text{m}$ , respectively. To control the manipulator remotely, an interface has been developed in Python. Moreover, two dedicated softwares have been developed for data acquisition and adjustment of the camera position along with attached optical objective.

## DYNAMIC RANGE

The lower limit of the dynamic range is mainly determined by the photon yield (PhY) of the YAG screen, the photon collection efficiency and the background noise level. On the other hand, the upper limit is related to the scintillation saturation, which can in principle be corrected by using also the OTR to image the dense beam core. The  $0.5 \text{ mol}\%$  ceramic Ce:YAG manufactured by Konoshima Chemical Company, Ltd., Japan has been used [13]. The scintillating light spectrum is centered near  $525 \text{ nm}$  with a transparency above  $80\%$ , and the PhY has been measured to be about  $2 \times 10^4 \text{ photon/MeV}$ . The energy deposition inside the YAG has been evaluated to be around  $0.1 \text{ MeV/e}$  based on the ESTAR stopping power database [14], and through a Monte Carlo simulation with the MCNPX code [15]. Then, the photon emission efficiency can be further estimated to be about  $2000\text{--}2500 \text{ photon/e}$ . Assuming the scintillation light is mainly in a range from  $500 \text{ nm}$  to  $600 \text{ nm}$ , the transmission of light through the viewport and the optical lenses is around  $85\%$  and the effective observation angle is  $6.2 \text{ mrad}$  for a magnification factor of 3, the photon collection efficiency is expected to be about  $0.32\text{--}0.4 \text{ photon/e}$ . Notice that the reduction of the observation angle due to the refraction of the exiting scintillation light has been taken into account [16].

The sCMOS camera is placed at  $30 \text{ mm}$  above the beam line in order to suppress the background from upstream. However, the background noise from the sCMOS sensor is unavoidable and is relevant to the temperature of the sensor ( $10^\circ \text{C}$  thanks to the cooling system), the shutter mode and the exposure time. In rolling shutter mode, measurements exhibit a non-uniform distribution of pixel noise level and rms background noise less than 1 digital count for an exposure time of  $10 \text{ ms}$ , as shown in Fig. 2. One may notice that the readout has a constant offset which has been designed to ensure a low readout noise. For the absolute readout versus the number of incident photons, such an offset can be determined experimentally and then subtracted. After removing this offset, the residual readout noise/deviation is about  $0.5 \text{ count/pixel}$ , which is corresponding to  $0.33 \text{ photon/pixel}$  taking into account a quantum efficiency of  $70\%$  and a A/D conversion of  $0.46 \text{ e/count}$ .

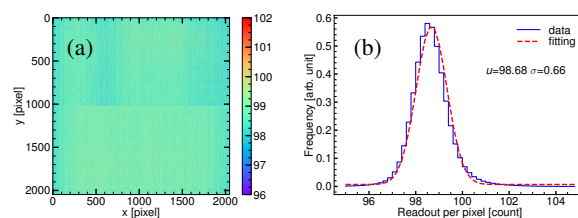


Figure 2: Background image (a) and its histogram (b).

To ensure reliable detection of halo particles, a signal-to-noise of more than three is necessary. Following this, the minimum number of incident photon per pixel should be larger than one, which means a minimum particle density of four electrons over one-pixel size on the YAG screen.

The maximum particle density without scintillation saturation depends on the concentration of Ce ions and can be analytically estimated as

$$\rho_{e,\max} = \frac{\rho_{\text{Ce}}}{\beta n_{\text{eh}} E_d} \quad (1)$$

where  $\rho_{\text{Ce}}$  is the density of the doped Ce ions,  $\beta$  the transport efficiency,  $n_{\text{eh}}$  the density of produced e-h pair and  $E_d$  the energy deposition. An upper limit for the saturation threshold is calculated as  $100 \text{ fC}/\mu\text{m}^2$ . However, it has to be confirmed through experimental measurements. Focusing the beam vertically using a quadrupole (QD20) upstream, the saturation threshold could be extrapolated from the maximum particle density on the YAG screen when the total photon collection/production begins to decrease. For a beam intensity of  $3 \times 10^9 \text{ e/pulse}$ , the flux of YAG scintillation light tends to be constant ( $1.2 \times 10^9$ ) when the beams are large enough and then the photon collection reduces when focusing the beam down to  $40 \mu\text{m}$ , as shown in Fig. 3. During the transition from saturation-free to saturation, a lower limit for the saturation threshold was found to be  $16\text{--}18 \text{ fC}/\mu\text{m}^2$ .

Furthermore, for a magnification factor of 2.5, the effective particle density is estimated to be  $4\text{--}4.8 \times 10^5 \text{ e/pixel}$  in the absence of scintillation saturation. The maximum

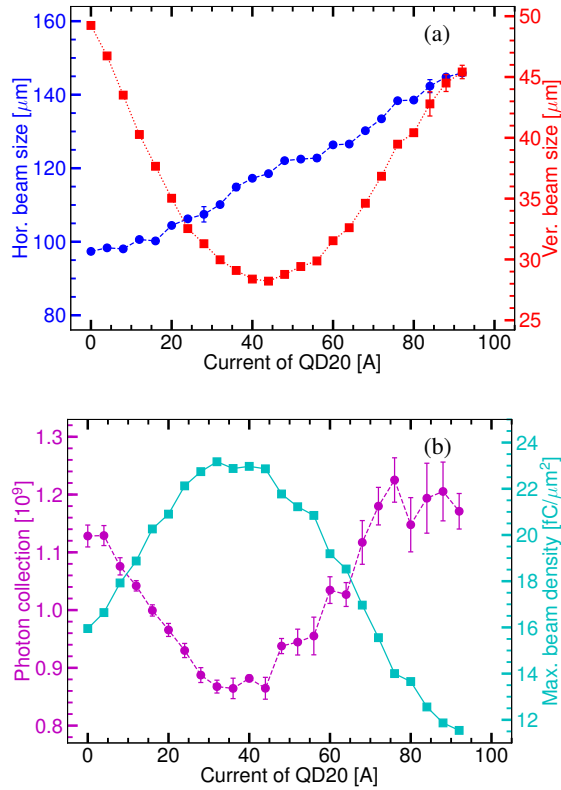


Figure 3: Vertical and horizontal beam sizes (a) and the number of incident photons on the camera sensor (b) as a function of the QD20 current.

readout of the measured 2D beam profiles is about  $2 \times 10^5$ , which also indicates an effective dynamic range of about  $1 \times 10^5$ , as shown in Fig. 4. Moreover, the dynamic range can be further extended by combining the images from OTR screen (core) and YAG screens (halo) with a valid algorithm.

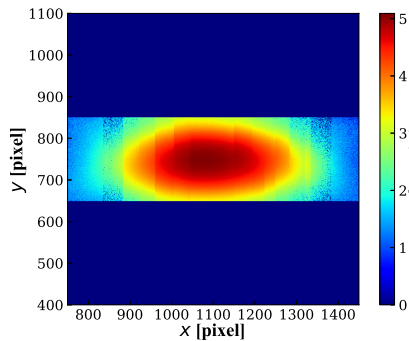


Figure 4: 2D beam profile without scintillation saturation measured by YAG screens.

## SPATIAL RESOLUTION

The nominal vertical and horizontal beam sizes at the YAG/OTR monitor are less than 30 μm and more than

100 μm, respectively. To avoid the scintillation saturation, the vertical beam size is normally enlarged, e.g., to be larger than 50 μm, using the QD20 quadrupole. The spatial resolution of the YAG screen is mainly determined by the optical diffraction limitation, the finite thickness of the screen, the pixel size and the saturation effect. Without the scintillation saturation, the vertical resolution is given by

$$\sigma_{\text{res},y} = \sqrt{\sigma_{\text{diff}}^2 + \sigma_f^2 + \sigma_{\text{px}}^2} \quad (2)$$

where  $\sigma_{\text{diff}}$  is the resolution associated to the optical diffraction,  $\sigma_f$  the resolution related to the thickness of the scintillator and  $\sigma_{\text{px}}$  the pixel size. Assuming a magnification factor of 3, the vertical resolution is estimated to be about 2.08 μm. The horizontal resolution is however degraded by the overlap of scintillation light emitted from different depths. Numerical simulations suggest that the measured beams sizes are significantly larger than what they should be only when the real beam sizes decrease to below 50 μm and 100 μm, vertically and horizontally, respectively. On the other hand, the resolution for measurements using the OTR screen is mainly determined by the optical diffraction and can be characterized by the rms of the point spread function [17]. For the light in the 450–700 nm range, the resolution for OTR measurements is found to be around 5.4–8.4 μm.

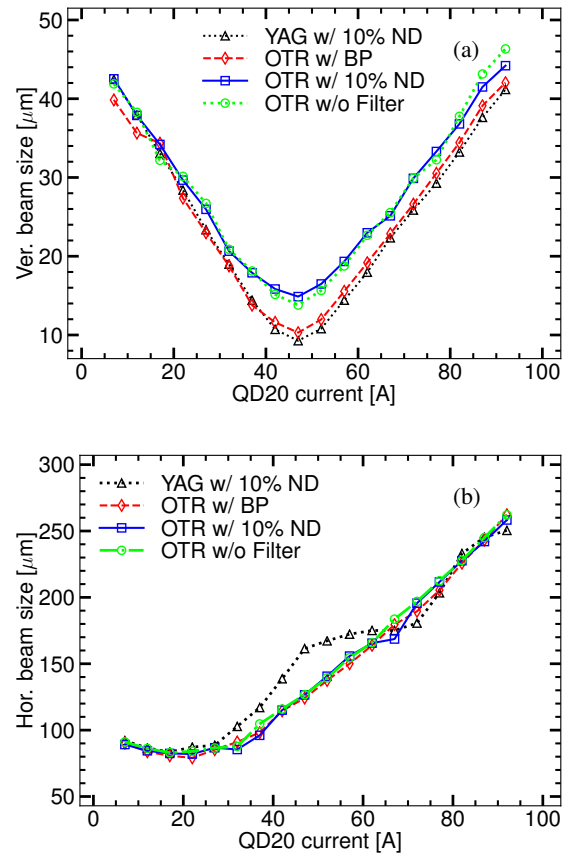


Figure 5: Evolution of vertical (a) and horizontal (b) beam size as a function of QD20 current.

Focusing the beam with the QD20 quadrupole, the minimum vertical beam size has been found to be around  $9.3\text{ }\mu\text{m}$  using the YAG screen, with either a 10% ND filter or a  $550\pm 10\text{ nm}$  BP filter, and about  $10.2\text{ }\mu\text{m}$  from the OTR image with the same BP filter, as shown in Fig. 5 (a). Besides, enlargement of the horizontal beam size measured by the YAG screen due to the scintillation saturation was clearly observed when the vertical beam size was smaller than  $25\text{ }\mu\text{m}$ , as shown in Fig. 5 (b). From these measurements, we could conclude that the resolution of the YAG/OTR monitor is below  $10\text{ }\mu\text{m}$ , vertically, and accomplishes our design goals.

## HALO MEASUREMENTS

Considering the configuration of four YAG pads, measurements of the vertical or horizontal distributions are performed in the following way. Taking the vertical case as an example, the holder is firstly adjusted to obtain an image of the bottom halo particles, where the scintillation light is weak and the influence from the beam core is negligible. Then, part of the image below a "boundary", which is about  $50\text{--}100\text{ }\mu\text{m}$  beneath the edge of the YAG pad, is recorded as an effective slice of the whole beam profile. Subsequently, the bottom YAG pad is moved up to get images of more halo particles. A new "boundary" is then determined, and the part between the previous and new "boundaries" is taken and combined with the existing slices. Repeat such process until entering the core region where the 10% or 1% ND filters will be inserted to attenuate the light intensity and then one moves to the top YAG pad to acquire the upper half profile. The full beam profile is eventually assembled by integrating all the slices after subtracting a common background noise/offset. The reconstructed 2D beam distribution indicates a dynamic range of  $1\times 10^5$ , as shown in Fig. 4. However, the projection of the obtained 2D profile is only valid along the scanning direction.

Halo measurements were performed for various vacuum pressures of the damping ring and compared with the theoretical predictions in the presence of BGS. Good agreement between measurements and predictions are observed for the vertical beam halo but not the horizontal one, as shown in Fig. 6. They are consistent with the measurements using the DS detector, and further confirm the previous experimental observations and the conclusion that the vertical beam halo is dominated by the BGS process.

## CONCLUSION

A high dynamic-range YAG/OTR monitor has been designed and constructed for precise beam halo diagnostics at ATF2. This monitor consists of four ceramic 0.5 mol% Ce:YAG screens and an OTR target on a holder, and an observation system. The analytical and experimental evaluations have suggested that the background noise is less than one photon per pixel, and a lower limit of the scintillation saturation threshold is about  $16\text{--}18\text{ fC}/\mu\text{m}^2$ . The effective dynamic range for 2D beam profiles measured using the YAG screens has been demonstrated to be more than  $1\times 10^5$ ,

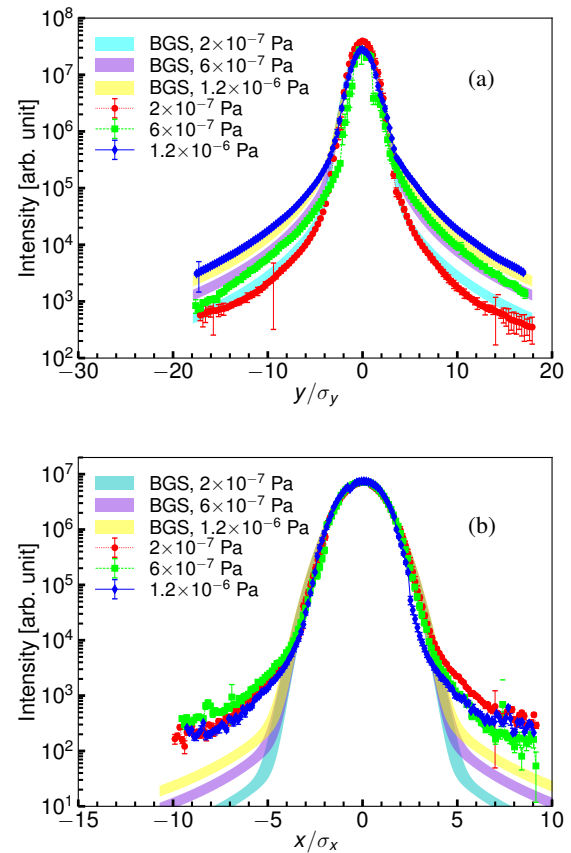


Figure 6: Vertical (a) and horizontal (b) beam profiles measured by YAG screens. Notice that the distributions are normalized to rms beam sizes in order to compare with the theoretical predictions.

which is sufficient for beam halo studies. Besides, the spatial resolution of this monitor is less than  $10\text{ }\mu\text{m}$  for both the YAG screen and OTR target, satisfying our the design goals.

Measurements of vertical and horizontal beam halo for different vacuum pressures of the damping ring have been performed following a dedicated profile scanning method, and are found to be consistent with previous observations. Furthermore, to extend the dynamic range of the YAG/OTR monitor, the combination of images from the YAG screens and OTR is under investigation.

## ACKNOWLEDGEMENTS

The authors would like to express their gratitude to the ATF collaboration and to the staff and engineers of ATF. We wish to thank T. Lefèvre for the support of the sCMOS camera and Z. Hu for his help with the MCNPX simulation.

## REFERENCES

- [1] K. Wittenburg, "Beam halo and bunch purity monitoring," *CERN Accelerator School 2009-005*, pp. 557–580, 2009.
- [2] T. Mitsuhashi, "Beam halo observation by coronagraph," in *Proc. 7th European Workshop on Beam Diagnostics and In-*



- strumentation for Particle Accelerators (DIPAC2005)*, Lyon, France, Jun. 2005, paper ITMM03, pp. 7–11.
- [3] H. D. Zhang *et al.*, "Beam halo imaging with a digital optical mask," *Phys. Rev. ST Accel. Beams* 15(7): 072803, 2012.
- [4] K. Kubo *et al.*, "Extremely low vertical-emittance beam in the Accelerator Test Facility at KEK," *Phy. Rev. Lett* 88(9): 194801, 2002.
- [5] G. R. White *et al.*, "Experimental validation of a novel compact focusing scheme for future energy-frontier linear lepton colliders," *Phy. Rev. Lett.* 112(3): 034802, 2014.
- [6] B. Grishanov *et al.*, "ATF2 proposal," 2005.
- [7] S. Liu *et al.*, "In vacuum diamond sensor scanner for beam halo measurements in the beam line at the KEK Accelerator Test Facility," *Nucl. Instrum. Meth. A* 832 (2016): 231–242.
- [8] R. Yang *et al.*, "Evaluation of beam halo from beam-gas scattering at the KEK Accelerator Test Facility," *Phys. Rev. Accel. and Beams* 21(5): 051001, 2018.
- [9] R. Yang, "Diagnostics and characterization of beam halo at the KEK Accelerator Test Facility," Ph.D. thesis, Université Paris-Saclay, Orsay, France, 2018.
- [10] M. Moszyński *et al.*, "Properties of the YAG: Ce scintillator," *Nucl. Instrum. Meth. A* 345(3): 461–467, 1994.
- [11] T. Naito and T. Mitsuhashi, "Beam halo measurement utilizing YAG: Ce screen," in *Proc. 4th International Beam Instrumentation Conference (IBIC2015)*, Melbourne, Australia, Sep. 2015, pp. 373–376.
- [12] <https://www.pco.de/scmos-cameras/pcoedge-42/>
- [13] T. Yanagida *et al.*, "Evaluation of properties of YAG (Ce) ceramic scintillators," *IEEE transactions on nuclear science*, 52(5): 1836–1841, 2005.
- [14] M.J. Berger, "ESTAR, PSTAR, and ASTAR: Computer programs for calculating stopping-power and range tables for electrons, protons, and helium ions," 1992.
- [15] L. S. Waters, "MCNPX user's manual," Los Alamos National Laboratory, 2002.
- [16] A. Murokh *et al.*, "Limitations on the resolution of YAG: CE beam profile monitor for high brightness electron beam," *The Physics of High Brightness Beams*, pp. 564–580, 2000. [https://doi.org/10.1142/9789812792181\\_0038](https://doi.org/10.1142/9789812792181_0038)
- [17] P. Karataev *et al.*, "First Observation of the Point Spread Function of Optical Transition Radiation", *Phy. Rev. Lett.* 107(17): 174801, 2011.

# FIRST PROTOTYPE OF A CORONAGRAPH-BASED HALO MONITOR FOR bERLinPro\*

Ji-Gwang Hwang<sup>†</sup> and Jens Kuszynski,

Helmholtz-Zentrum Berlin für Materialien und Energie GmbH (HZB), Berlin, Germany

## Abstract

Since particle losses by beam halo induced by space charge force and scattering of trapped ions are critical issues for superconducting-linac based high power machines such as bERLinPro, a halo monitor is demanded to monitor and control particle distribution at the level of  $10^{-4} \sim 10^{-5}$  of the core intensity. A coronagraph-based halo monitor was adopted and the first prototype has been designed as a demonstrator system aimed at resolving a halo-core contrast in the  $10^{-3}$  to  $10^{-4}$  range. This monitor was tested at BESSY II with various operation modes such as Transverse Resonance Island Buckets (TRIBs) and Pulse-Picking by Resonant Excitation (PPRE). We show our design parameters, experimental criterion, and experimental results.

## INTRODUCTION

The Berlin Energy Recovery Linac Prototype (bERLinPro) project was launched at the Helmholtz-Zentrum Berlin (HZB) to demonstrate and establish technologies for energy recovery linac (ERL) based accelerators for a future light source [1, 2]. The bERLinPro will provide electron beams up to 50 MeV in the recirculation loop with several operation modes such as a single pulse mode with various repetition rates, bursting mode, and 50 MHz and 1.3 GHz continuous waves (CW) modes [3]. The bERLinPro injector, consisting of a photocathode 1.4-cell superconducting radio frequency (SRF) gun, followed by three 2-cell booster SRF cavities, generates high-quality electron beams with an energy of 6.5 MeV. The beam is transported to the main linac module and accelerated by three 7-cell SRF cavities up to 50 MeV energy [4]. The design layout is shown in Fig. 1.

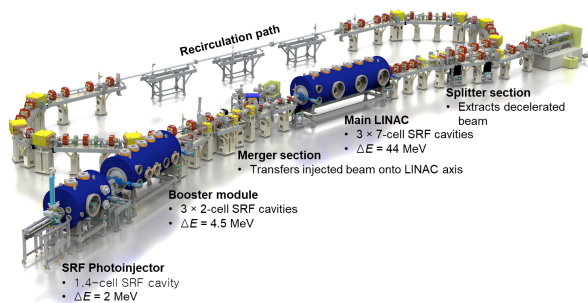


Figure 1: Layout of bERLinPro having accelerating structures of 1.4-cell SRF gun, three 2-cell SRF booster cavities, and three 7-cell SRF cavities for generation of high-quality and high-power electron beams [5].

\* Work supported by German Bundesministerium für Bildung und Forschung, Land Berlin and grants of Helmholtz Association.

<sup>†</sup> ji-gwang.hwang@helmholtz-berlin.de

The construction of a building and basic infrastructure was completed in 2017 so that the installation of accelerator components has begun. As the first stage, the installation of the vacuum system of a “Banana” section, which includes the entire low energy beam path from the gun to the high power beam dump. The 5 mA SRF gun (Gun1) and the cryomodule of the booster cavities as well as a diagnostics line, is ongoing [6].

## HALO MONITOR TEST SETUP

A total of five synchrotron light based electron beam diagnostics for measuring a beam halo distribution, and temporal and spatial distribution will be installed in the recirculator of the bERLinPro. Due to the heat capacity of a cryogenics, it is not allowed to provide an additional power load of more than 50 W on the cryomodule for main SRF cavities by small beam losses from halo particles, which corresponds to  $10^{-5}$  level of maximum beam power. Since a halo monitor is a crucial diagnostic for minimizing uncontrolled beam losses by halo particles by adjusting the optics at the upstream of the first arc section, it stimulates the development of the beam halo monitor with the contrast ratio of  $10^{-5}$ .

For the observation of the halo distribution with the contrast of  $10^{-5}$  to the beam core, various monitors such as a wire-scanner monitor, diamond detector, the optical monitor based on a digital micromirror device (DMD), and coronagraph-based halo monitor were compared and analyzed. Finally, the coronagraph-based halo monitor is preferred since this technique can observe the full 2-D halo distribution without any disturbance to the beam and it has already been demonstrated at the KEK Photon Factory to achieve a  $6 \times 10^{-7}$  ratio for the background to peak intensity [7, 8]. The design study of the coronagraph-based halo monitor with a Lyot-stop technique, which produces the image of an entrance pupil using re-diffraction optics to remove the majority of diffraction fringes, is performed using a Fourier-optics interpretation which is equivalent to the classical optics approach using Fourier transforms, in which the waveform is regarded as made up of a superposition of plane waves [9].

The beam-halo monitor will be installed on the first dipole of the first arc section because this dipole has a relatively small dispersion, which does not disturb the horizontal beam distribution. Since the full energy operation of the bERLinPro is scheduled for 2020, a preliminary test is performed at a diagnostics beam line of BESSY II. The diagnostics beam line of BESSY II provides multi-platform for research and development of various synchrotron light based monitors [10, 11]. The beam line has a distance of  $15.5 \pm 0.5$  m

from a source point. The picture of the coronagraph-based halo monitor installed at the BESSY II diagnostics beamline is shown in Fig. 2.

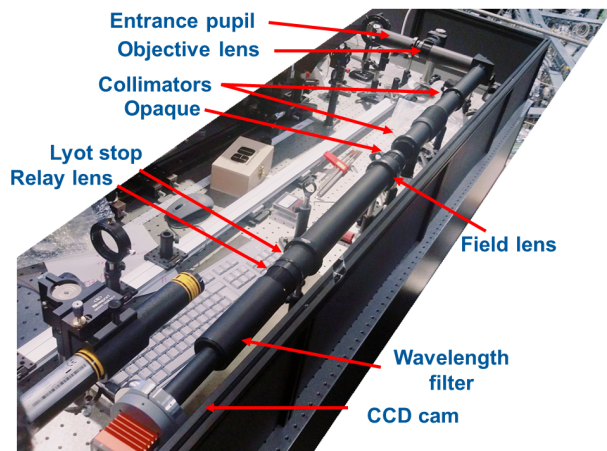


Figure 2: Picture of coronagraph-based halo monitor setup at BESSY II diagnostics beamline.

The coronagraph-based halo monitor consists of an objective lens (first lens) to produce a real beam image, several intermediate collimators, opaque disk to block a high-intensity core, field lens (second lens) to produce re-diffraction fringes, Lyot stop to remove the majority of diffraction fringes, and relay lens (third lens) to make the image for a charge-coupled device (CCD) camera. The square entrance pupil with the opening of 25 mm was adopted. The opaques were printed by a 3D printer with an irregular reflection surface, for various size from 150  $\mu\text{m}$  to 580  $\mu\text{m}$  with a fabrication error of 0.1 mm. All the lenses have a diameter of 2 inches with a quality of 40-20 (scratch-dig) and all elements such as an entrance pupil, lenses, and collimators are installed in 2-inch lens tube to prevent ambient light. The CCD camera used for imaging is a Prosilica GT1920 from Allied Vision. Since the strong distortion of the front-end mirror of the beam line is recognized in the vertical direction from other experiments, all measurements are performed in the horizontal plane.

## PRELIMINARY TEST AT BESSY II

Since July 2015 the BESSY II storage ring has been providing a new bunch filling pattern in Top-Up mode, namely, standard user mode. This consists of a Hybrid (Chopper) bunch of 4 mA in the center of a 200 ns wide dark gap, followed by a pulse-picking by resonant excitation (PPRE) bunch for the single bunch science driven user community, the standard multibunch mode each of 1 mA current separated by 2 ns, and slicing bunches deliver photons daily to the ultrafast experiments at the Femtoslicing facility [12, 13]. In addition to the standard user mode, the BESSY II storage ring provides various sophisticated filling patterns such as a high current single bunch mode, a few bunch mode of 4 bunches, and low-alpha multibunch hybrid mode for time-resolved studies. The low-alpha mode is modified a

momentum compaction factor to smaller values by a special setting of the electron optics of the storage ring. Since the beam size in the low-alpha mode is larger than the standard mode and the beam distribution is expected to be close to the Gaussian distribution, the measurement with various opaque sizes was carried out. The result is shown in Fig. 3.

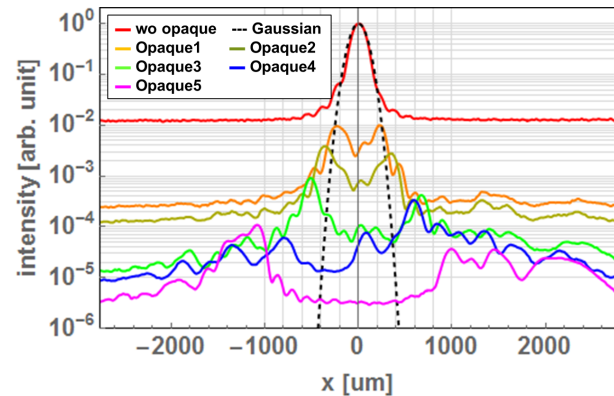


Figure 3: Measured result of beam halo with various opaque disks in the low-alpha mode of BESSY II. Transverse magnification is about 1/14.5 and all data normalized by the exposure time of CCD camera.

As shown in Fig. 3, the measured beam halo distribution is qualitatively close to Gaussian distribution up to  $10^{-3}$  contrast to the beam core. Due to diffraction noise, it is difficult to measure the practical halo distribution at  $10^{-4}$  contrast to the beam core. The polishing quality of the objective lens limits the measurement because the background noise from the Mie-scattering effect due to the dig and scratch on the lens surface is  $3 \times 10^{-4}$  for a 200  $\mu\text{m}$  dig [14].

With the standard user mode, which has the PPRE bunch, the measurement of beam halo was performed to verify the performance of the monitor. Because the PPRE bunch has a 1.2 % (3/250 mA) of total beam current in the ring as well as relatively larger beam size than the 1 mA standard multibunch, so it has the same characteristics as beam halo. The result is shown in Fig. 4.

As shown in Fig. 4, the measured beam size is smaller than the beam size in the low-alpha mode, and the particle distribution deviates greatly from the Gaussian distribution at  $10^{-2}$  contrast to the beam core. Furthermore, the result of numerical simulation using Elegant code show qualitative agreement with the measurement [15, 16].

In order to ensure the performance limitation of the beam halo monitor, it is worthwhile to measure the beam located off the section of strong diffraction noise area. Since 2017 BESSY II provides a special setting of the magnetic lattice generating a second stable orbit using transverse resonance island buckets (TRIBs) [17, 18]. This special operation mode allows the beam separation in the horizontal plane as well as the manipulation option of bunch filling in the second orbit. The outer laying TRIBs bunch is beyond the diffraction noise. By using the halo monitor, we observed coincidentally the diffused particles from a core orbit to the second stable



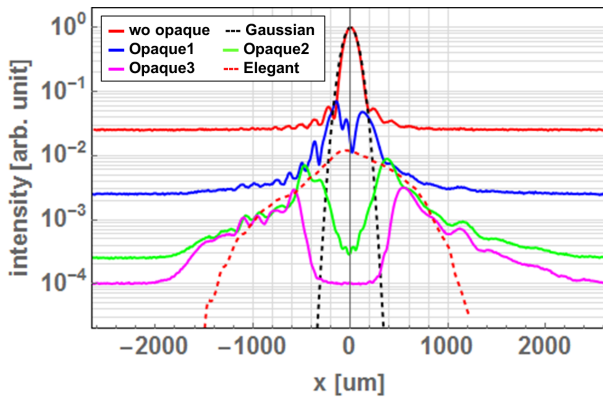


Figure 4: Measured result of beam halo with various opaque disks in the standard user mode of BESSY II. Transverse magnification is same as in Fig. 3 and all data normalized by the exposure time of CCD camera.

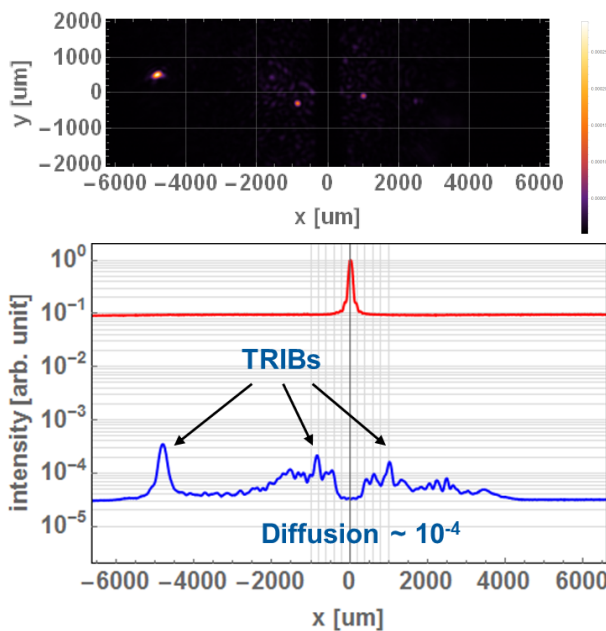


Figure 5: Image of the diffused beam at the second stable orbit measured in the TRIBs operation with the opaque disk. Transverse magnification is same as in Fig. 3.

orbit during the commissioning of TRIBs. The measurement result of the diffused beam at the second stable orbit is shown in Fig. 5.

As shown in Fig. 5, the three TRIBs bunches are clearly distinguishable and the beam intensity is in good agreement with the values measured in the user beam line with comparable detectors. From this measurement, the halo monitor can be used potentially for continuous monitoring of the bunch in the second stable orbit during TRIBs operation.

## SUMMARY

The halo monitor is one of the most crucial diagnostics for high power accelerators such as the bERLinPro to control uncontrolled beam losses in the machine. The preliminary test

of the coronagraph-based halo monitor is performed at the diagnostics beam line of BESSY II with various operation modes. The measurement results show that the monitor can measure the halo at the contrast ratio of  $10^{-3} \sim 10^{-4}$ . The halo monitor can be used potentially for continuous monitoring of the bunch in the second stable orbit during TRIBs operation. The performance to date is limited by the polishing quality of the objective lens since the background noise from the Mie-scattering effect due to the dig and scratch on the lens surface is  $3 \times 10^{-4}$  for a 200  $\mu\text{m}$  dig [14]. We will purchase a high-quality lens to improve the performance of the monitor. The preparation of the mechanical design will be performed to install the monitor into the bERLinPro diagnostics line.

## ACKNOWLEDGEMENT

The authors wish to express their gratitude to P. Goslawski and M. Reis for their valuable discussion and encourage for the experiments in BESSY II.

## REFERENCES

- [1] B. Kuske, N. Paulick, A. Jankowiak, J. Knobloch eds., "bERLinPro Conceptual design report", Helmholtz-Zentrum Berlin, 2015, [https://www.helmholtz-berlin.de/media/media/grossgeraete/beschleunigerphysik/berlinpro\\_MAB/BPro\\_in\\_detail/Publications/bERLinPro\\_CDR.pdf](https://www.helmholtz-berlin.de/media/media/grossgeraete/beschleunigerphysik/berlinpro_MAB/BPro_in_detail/Publications/bERLinPro_CDR.pdf).
- [2] A. Jankowiak, *et al.*, "BERLinPro - A Compact Demonstrator ERL for High Current and Low Emittance Beams", in *Proceedings of LINAC'10*, Tsukuba, Japan, 2010, pp. 407–409.
- [3] M. Abo-Bakr, *et al.*, "Progress Report of the Berlin Energy Recovery Project BERLinPro", in *Proceedings of IPAC'15*, Richmond, USA, 2015, pp. 1438–1439. doi:10.18429/JACoW-IPAC2015-TUPWA018
- [4] M. Abo-Bakr, *et al.*, "Status Report of the Berlin Energy Recovery Linac Project BERLinPro", in *Proceedings of IPAC'16*, Busan, Korea, 2016, pp. 1827–1828. doi:10.18429/JACoW-IPAC2016-TUPW034
- [5] J. Knobloch, *et al.*, *Proceedings of the 56th ICFA Advanced Beam Dynamics Workshop on Energy Recovery Linacs*, New York, USA, MOPBTH006 (2015).
- [6] M. Abo-Bakr, *et al.*, "Status Report of the Berlin Energy Recovery Linac Project BERLinPro", in *Proceedings of IPAC'18*, Vancouver, Canada, 2018, pp. 4127–4130. doi:10.18429/JACoW-IPAC2018-THPMF034
- [7] T. Mitsuhashi, "Beam Halo Observation by Coronagraph", in *Proceedings of DIPAC'05*, Lyon, France, 2005, pp. 7–11.
- [8] T. Mitsuhashi, E. Bravin, F. Roncarolo, G. Trad, "First Observation of the LHC Beam Halo Using a Synchrotron Radiation Coronagraph", in *Proceedings of IPAC'17*, Copenhagen, Denmark, 2017, pp. 1244–1247. doi:10.18429/JACoW-IPAC2017-TU0AB2
- [9] Ji-Gwang Hwang and Jens Kuszynski, "Coronagraph based beam halo monitor development for bERLinPro", in *Proceedings of IPAC'17*, Copenhagen, Denmark, 2017, pp. 355–358. doi:10.18429/JACoW-IPAC2017-MOPAB098



- [10] M. Koopmans, P. Goslawski, J.-G. Hwang, M. Ries, M. Ruprecht, A. Schälicke, “Status of a Double Slit Interferometer for Transverse Beam Size Measurements at BESSY II”, in *Proceedings of IPAC’17*, Copenhagen, Denmark, 2017, pp. 149–152. doi:10.18429/JACoW-IPAC2017-MOPAB032
- [11] G. Schiwietz, *et al.*, “Development of the electron-beam diagnostics for the future BESSY-VSR storage ring”, in *Proceedings of IPAC’18*, Vancouver, Canada, 2018, pp. 2110–2113. doi:10.18429/JACoW-IPAC2018-WEPAK011
- [12] Helmholtz-Zentrum Berlin news and press releases, [https://www.helmholtz-berlin.de/pubbin/news\\_seite?nid=14265&sprache=en&typoid=49888](https://www.helmholtz-berlin.de/pubbin/news_seite?nid=14265&sprache=en&typoid=49888).
- [13] T. Atkinson, *et al.*, “Status and Prospects of the BESSY II Injector System”, in *Proceedings of IPAC’16*, Busan, Korea, 2016, pp. 2826–2828. doi:10.18429/JACoW-IPAC2016-WEPOW007
- [14] T. Mitsuhashi, *et al.*, “Design of Coronagraph for the Observation of Beam Halo at LHC”, in *Proceedings of IBIC’15*, Melbourne, Australia, 2015, pp. 288–292. doi:10.18429/JACoW-IBIC2015-TUCLA03
- [15] M. Borland, *Elegant: a flexible SDDS-compliant code for accelerator simulation.*, Advanced Photon Source LS-287 (2000).
- [16] J.-G. Hwang, *et al.*, “Numerical analysis of excitation property of pulse icking by resonant excitation at BESSY II”, in *Proceedings of IPAC’18*, Vancouver, Canada, 2018, pp. 4131–4133. doi:10.18429/JACoW-IPAC2018-THPMF035
- [17] P. Goslawski, *et al.*, “Resonance Island Experiments at BESSY II for User Applications”, in *Proceedings of IPAC’16*, Busan, Korea, 2016, pp. 3427–3430. doi:10.18429/JACoW-IPAC2016-THPMR017
- [18] P. Goslawski, *et al.*, “Transverse Resonance Island Buckets as Bunch Separation Scheme”, in *Proceedings of IPAC’17*, Copenhagen, Denmark, 2017, pp. 3059–3062. doi:10.18429/JACoW-IPAC2017-WEPIK057

# COMPARISON OF YAG SCREENS AND LYSO SCREENS AT PITZ

R. Niemczyk\*, P. Boonpornprasert, Y. Chen, J. Good, M. Gross, H. Huck, I. Isaev, D. Kalantaryan, C. Koschitzki, M. Krasilnikov, X. Li, O. Lishilin, G. Loisch, D. Melkumyan, A. Oppelt, H. Qian, Y. Renier, F. Stephan, Q. Zhao<sup>†</sup>,

Deutsches Elektronen-Synchrotron DESY, 15738 Zeuthen, Germany  
W. Hillert, University Hamburg, 22761 Hamburg, Germany

## Abstract

The Photo Injector Test facility at DESY in Zeuthen (PITZ) is dedicated to the development of high-brightness electron sources for free-electron lasers. At PITZ, to measure the emittance of space-charge-dominated beams, the slit scan technique is used. For slice emittance measurements a transverse deflecting structure (TDS) is employed. The electron beam distribution is measured by means of scintillator screens. Both the TDS and the slit mask reduce the signal strength, giving stringent requirements on the sensitivity of the screens. At PITZ, high-sensitivity Ce:LYSO screens have been installed at the same screen stations as the standard Ce:YAG screens to solve low-intensity issues. A comparison of both screens is presented.

## INTRODUCTION

Scintillator screens are used to measure the beam distribution and position in particle accelerators. At the Photo-Injector Test Facility at DESY in Zeuthen (PITZ) cerium-doped ytterbium aluminium garnet (Ce:YAG) powder is used as standard screen material [1]. However, advanced electron beam diagnostics require precise measurements of the electron distribution with rather low charge density and, therefore, with low signal intensity from the detector.

Measurement of properties like the slice emittance, the longitudinal phase space [2] or the projected emittance of low-charged beams need a significant increase of the signal strength, especially during time-resolved measurements with the transverse deflecting structure (TDS). The TDS, developed by the Institute for Nuclear Research (INR RAS, Moscow, Russia) in collaboration with DESY, only allows to streak up to three consecutive electron bunches [3].

For a correct reconstruction of the beam distribution the screen and imaging system have to have a high homogeneity, a good signal linearity, a high spatial resolution and a high signal-to-noise ratio. In order to perform a cross-check with the existing system, several high-sensitivity cerium-doped lutetium yttrium orthosilicate (Ce:LYSO) screens were installed at the same screen station as Ce:YAG screens. The same TV read-out system was used for the image analysis.

In this paper, both the screen homogeneity and linearity in terms of light production are measured for both Ce:LYSO and Ce:YAG screens. Additionally, the beam size measurement uncertainty caused by screen non-uniformity is simulated.

At PITZ, the electron beam comes in bunch trains with a repetition rate of 10 Hz [4]. The number of electron pulses per train can be increased to up to 600 pulses at 1  $\mu$ s bunch spacing [5]. For each measurement, ten beam images, i.e. images from ten consecutive bunch trains, and ten background images were taken. The images from the bunch trains were averaged in the postprocessing, after the averaged background was subtracted.

## LARGE-SCALE SCREEN HOMOGENEITY

To estimate the screen homogeneity, the electron beam has been steered to nine different positions on the screen. At each beam position, the Ce:YAG and Ce:LYSO screen image was taken. At the screen station the two different screen types were inserted into the beam path and the screen image was taken by one single camera for both screens, i.e. camera gain and imaging from screen to camera was the same. Camera gain and exposure time were kept the same for both screen images. The sum of pixels<sup>1</sup> inside a squared frame with an edge length of 123 pixels around the beam centroid is calculated as measure for the beam intensity. The observation camera has 1024  $\times$  1360 pixels [6]. It was used

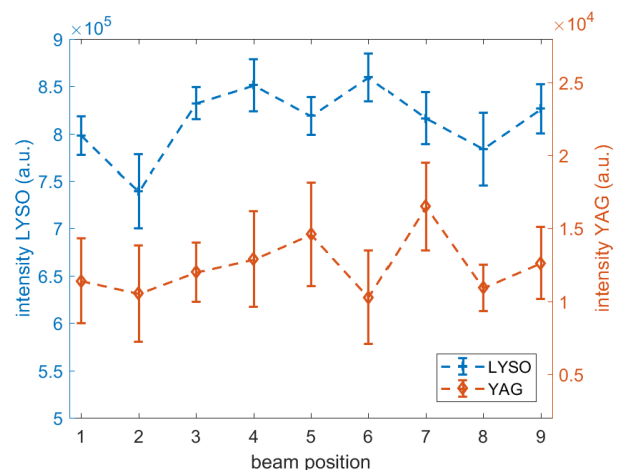


Figure 1: Intensity and rms intensity jitter for Ce:LYSO (blue) and Ce:YAG (orange) screens. The area of interest is square, with an edge length of 123 pixel (of the 512  $\times$  680-wide images) for both screen materials. The AOI is centred around the beam centroid position, i.e. the AOI has a different position at each beam position.

\* raffael.niemczyk@desy.de

<sup>†</sup> On leave from IMP/CAS, Lanzhou, China

<sup>1</sup> Sum of pixel fillings inside the area of interest

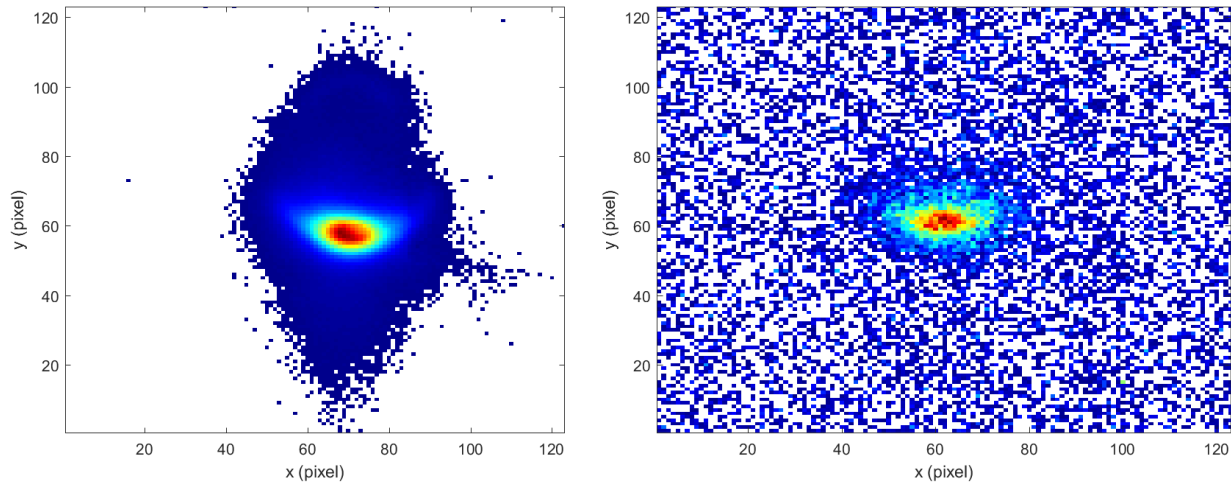


Figure 2: Background-subtracted and averaged beam image at the beam position 3 on the Ce:LYSO screen (left) and the Ce:YAG screen (right). It clearly shows, that the signal-to-noise ratio is higher on the Ce:LYSO screen. The colourmap was set to range from 0 to the maximum value on each screen individually, i.e. negative pixel values are shown white as well.

in a  $2 \times 2$ -binned setting, i.e. the obtained images have a size of  $512 \times 680$  pixels.

During the measurement the electron momentum was 23 MeV/c and the bunch charge was set to  $Q = 30$  pC. Figure 1 shows the measured intensities at nine different beam positions on both screen materials. The beam positions were chosen in a way, that the centroid position differs by  $\sim 60$  pixels to the previous one, either horizontally or vertically. The averaged intensity from the Ce:LYSO screen is almost 70 times higher than the averaged intensity from the Ce:YAG screen. The error bars show the rms intensity jitter of the ten single images taken at each beam position. Inside the area of interest (AOI) the rms intensity change among the nine locations is 4.3 % for Ce:LYSO screen and 19.8 % for the Ce:YAG screen, indicating a better global uniformity of the Ce:LYSO screen. A direct comparison of beam images on the two screen materials at the same beam position is given in Fig. 2. The image shows the ten-times-averaged screen image, after the averaged background has been subtracted.

## LINEARITY WITH BUNCH CHARGE

Additionally to the screen homogeneity, the linearity of the light yield versus the charge was verified. The charge was set by changing the transmission of a variable, optical attenuator of the photocathode laser which generates the electrons. The laser transmission was set to 100 % and was stepwise reduced, yielding bunch charges between 129 pC and 1 pC, measured with a faraday cup. During the measurement, the beam focussing and steering remained unchanged. The electron momentum during the measurement was 19 MeV/c. Figure 3 shows the light intensity on both screen materials. The intensity of both screens shows good linearity with bunch charge density increase, even though the charge is very small compared to the typical bunch charge of  $Q = 500$  pC. The linearity was only tested for small charges

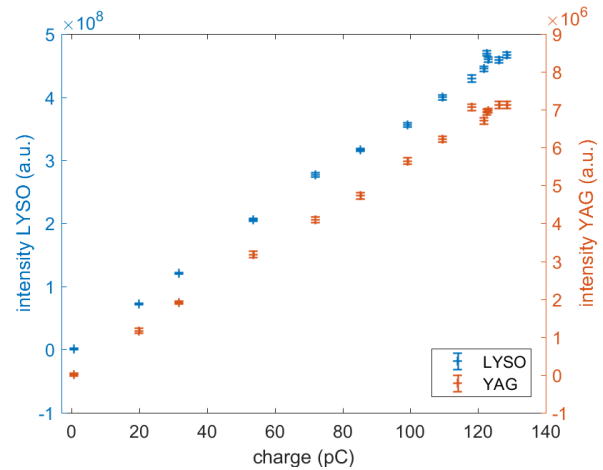


Figure 3: Beam intensity against bunch charge for Ce:LYSO and Ce:YAG screens. Both show a high linearity.

to avoid signal saturation of the Ce:LYSO screen. Figure 4 shows the charge density for the applied charges. The beams size  $\sigma_x \sigma_y$  was calculated for each applied charge at each screen material individually. The error bars shown arise from the uncertainty in the charge measurement.

## SYSTEMATIC ERRORS FROM SCREEN INHOMOGENEITY

Due to screen inhomogeneity, the rms beam size calculation might be spoiled, depending on the original beam size. To estimate the systematic error arising from screen inhomogeneity, the following simulation was done. A 2D Gaussian beam with an rms width in the range of 3 pixels to 15.5 pixels was used. Pixelwise, a uniformly distributed screen efficiency modulation was added to the uniform screen. The screen efficiency modulation amplitude ranged between 0

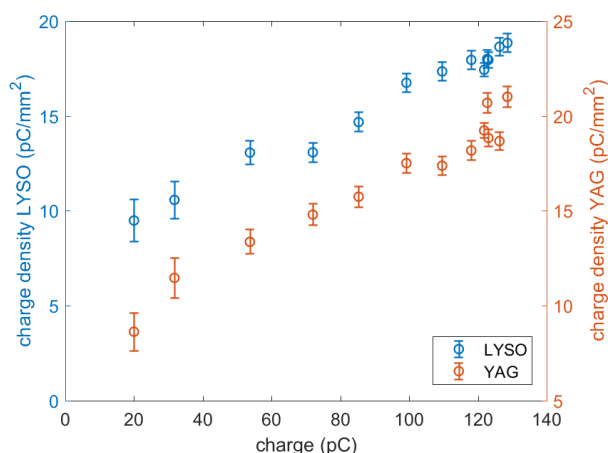


Figure 4: Charge density versus bunch charge. The beam size was calculated from the signal on the Ce:LYSO screen (blue, left axis) and the Ce:YAG screen (orange, right axis).

and 100 %. The obtained image was projected on one axis and the rms size was calculated. This was done 10 000 times for every beam size and each screen modulation amplitude. The standard deviation of the calculated beam sizes, divided by the original beam size, is shown in Fig. 5 for all original beam sizes and noise amplitudes. It shows, that even for the inhomogeneous screens, i.e. the one with more than 80 % modulation of the screen signal from the beam distribution, the beam size uncertainty stays below 2.5 % for the smallest beam sizes, which are only a few pixel wide. In a real experiment beam sizes which are ~10 pixel or bigger are favourable, to ensure a good resolution of the beam, see Fig. 2. For these conditions the beam size uncertainty drops below 1 %.

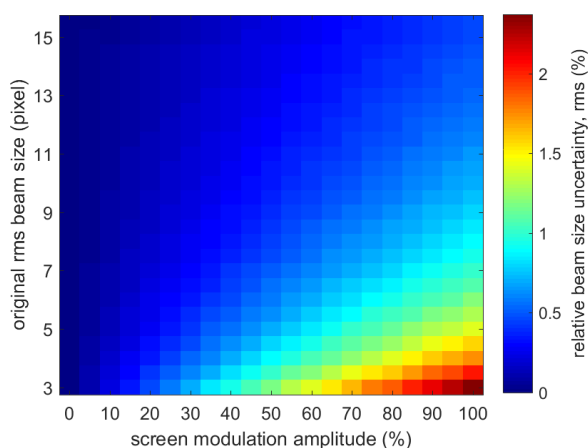


Figure 5: Systematic error in the calculation of the beam size in dependence of the original beam size (vertical axis) and the modulation amplitude of the uniformly distributed noise (horizontal axis). Even for the strongest noise and the smallest considered beam sizes, the uncertainty stays below 2.5 %.

## CONCLUSION

The comparison states that the light sensitivity of the newly installed Ce:LYSO screens is significantly higher than the one of the Ce:YAG screens, which are in use at PITZ, by a factor of 70, see Figs. 1 and 3. The Ce:LYSO screens will help solving intensity problems which will arise in measurements of the slice emittance with a slit mask or other low-intensity measurements, in which the beam is distributed on a wide screen area or the bunch charge is small, e.g. during electron diffraction experiments [7]. However, possible degradation of the signal processing due to imaging errors or camera readout errors might worsen the beam distribution reconstruction. Rough estimations of the screen noise shows, that the growth of systematic error due to uncertainty in the beam size calculation is on the order of 2.5 % or below, depending on the original beam sizes, see Fig. 5.

## REFERENCES

- [1] S. Rimjaem *et al.*, “Comparison of Different Radiators used to Measure the Transverse Characteristics of Low Energy Electron Beams at PITZ”, in *Proc. DIPAC’11*, Hamburg, Germany, May 2011, p. 428.
- [2] M. Gross *et al.*, “Observation of the Self-Modulation Instability via Time-Resolved Measurements, Phys. Rev. Lett., vol. 120, p. 144802, 2018.
- [3] H. Huck *et al.*, “Progress on the PITZ TDS”, in *Proc. IBIC’16*, Barcelona, Spain, May 2016, p. 744.
- [4] J. Baehr *et al.*, “Diagnostics for the Photo Injector Test Facility in DESY Zeuthen”, in *Proc. DIPAC’01*, Grenoble, France, May 2001, p. 154.
- [5] S. Y. Mironov *et al.*, “Spatio-temporal shaping of photocathode laser pulses for linear electron accelerators”, *Physics-Uspekhi* vol. 60, p. 1039, 2017.
- [6] Website Allied Vision, <https://www.alliedvision.com/de/support/technische-dokumentation/prosilica-gt-dokumentation.html>
- [7] H. Qian *et al.*, “Investigation of High Repetition Rate Femtosecond Electron Diffraction at PITZ”, in *Proc. IPAC’17*, Copenhagen, Denmark, May 2017, p. 3727. doi:10.18429/JACoW-IPAC2017-THPAB017



# TIME-SYNCHRONOUS MEASUREMENTS OF TRANSIENT BEAM DYNAMICS AT SPEAR3\*

Q. Lin<sup>†</sup> and Z. Sun, Donghua University, Shanghai, China  
J. Corbett, D. Martin and K. Tian, SLAC, Menlo Park, CA

## Abstract

Multi-bunch beam instabilities can often be controlled with high-speed digital bunch-by-bunch feedback systems. The detected motion is based on charge centroid measurements that, for short bunches, cannot resolve intrabunch charge dynamics. To compliment the BxB data, we installed a fast-gated camera with a rotating mirror to sweep visible-light synchrotron radiation across the camera CCD. The SR measurements present a complimentary view of the motion. For this work we generated transient beam events in SPEAR3 using the BxB feedback system and synchronously observed the motion on the camera. Results are presented for a high-order multibunch beam instability and for single bunch drive-damp experiments.

## INTRODUCTION

SPEAR3 routinely uses a transverse bunch-by-bunch (BxB) feedback system [1] for high current User operations and to study storage ring beam dynamics [2]. The BxB system detects the dipole moment  $q \cdot \Delta x$  for each bunch on each turn where  $q$  is the bunch charge and  $\Delta x$  is the displacement of the bunch centroid. The data is digitally processed with sufficient bandwidth to control the motion of each bunch independently. To date, the SPEAR3 BxB feedback system has been used to control multibunch instabilities, study beam dynamics during resonant drive events and for bunch cleaning. Although BxB feedback systems measure every bunch on every turn, for short bunches the measurement system cannot resolve coherent intrabunch motion or charge decoherence.

To compliment the BxB feedback system we synchronized a fast-gated camera equipped with a rotating mirror to sweep an image of the visible light synchrotron radiation (SR) across the camera CCD. The original idea to “streak” the optical SR beam using a deflecting mirror was developed at KEK [3], applied at PEP-II to measure fast-beam dump dynamics [4], and then used at both SPEAR3 [5] and ANKA [6] to diagnose the bunch bursting in low-alpha mode. For the applications reported here, we time-synchronized the optical SR measurements with the BxB acquisition system to provide complimentary diagnostics during transient beam motion.

At SPEAR3, a high-order multibunch instability can

develop in the vertical plane due to resonances in an in-vacuum insertion chamber (IVUN) chamber [7]. The instability occurs at discrete gap settings where electromagnetic “pillbox” modes in the vacuum chamber couple to transverse beam modes. On a shot-to-shot basis, the motion of individual bunches evolves differently in time, often with complex profiles. Using the rotating mirror to streak the optical SR beam image, an integrated time profile containing the motion of all bunches can be captured.

Similarly, to diagnose single bunch motion, the BxB system or a standard turn-by-turn BPM processor can record driven betatron oscillations for dynamic aperture studies, bunch cleaning or resonant excitation tests for short-pulse x-ray production. Since the bunch charge can decohere in phase space it is important to measure the transverse beam profile using visible-light synchrotron radiation to identify (a) the onset of charge decoherence, and (b) the impact of decoherence on the physical process under investigation.

## EXPERIMENTAL CONFIGURATION

For normal User operations SPEAR3 stores 500 mA beam current with charge distributed in 4 discrete bunch trains plus an isolated timing bunch for pump/probe experiments. Top-up injection occurs every 5 minutes with charge deposited at a 10 Hz rate into single, targeted bunches. A 10 Hz TTL pulse train triggers the injection kickers and provides a convenient signal to use for synchronized diagnostics.

In order to study transient beam dynamics, the timing system was configured to select solitary injection pulses from the 10 Hz pulse train to initiate grow/damp or drive/damp events. The same pulse is used to trigger multiple, synchronous diagnostics. The synchronized diagnostic systems include BxB data acquisition, turn-by-turn BPM processors and visible SR diagnostics.

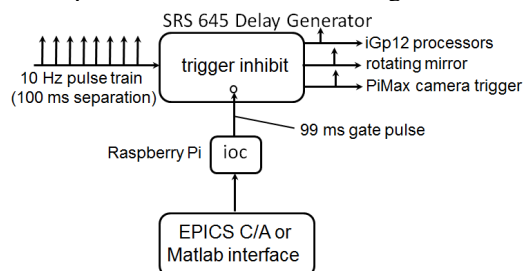


Figure 1: Schematic of the synchronous diagnostic timing system. A Raspberry Pi under EPICS control selects a single, time-isolated trigger.

\*Work supported by the China Scholarship Council and the US Department of Energy Contract DE-AC03-76SF00515, Office of Basic Energy Sciences.

<sup>†</sup>linqi1207@sina.com, zhsun@dhu.edu.cn

## Timing Synchronization

Synchronized measurements using BPM processors and a Roper PiMax camera [8] require both timing accuracy and calibration. For synchronization, a single gate inhibit pulse to an SRS645 delay generator allows timing triggers to pass for parallel diagnostic systems [9]. Individual channel delay times take into account differences in transmission line propagation, electronic latency and photon beam time-of-flight. As illustrated in Fig. 1, the event sequence is initiated by using a trigger inhibit “gate” pulse from a Raspberry Pi configured with EPICS Channel Access [9]. The Raspberry Pi was selected for low cost, ease of implementation and independence from the main control system. At the top level, a Matlab-based graphical control interface [2] (or any C/A client) can instruct the Pi to issue the gate pulse.

Trigger to the iGp12 feedback processors can initiate transient beam events in the form of multibunch grow/damp instabilities or single-bunch drive/damp experiments. The BxB processors also save bunch-by-bunch, turn-by-turn data records in the SRAM memory. (Standard “turn by-turn” BPM processors integrate over all bunches for one revolution period [10]). The PiMax trigger is redistributed in the SR diagnostics room to initiate both the rotating mirror and the camera exposure. The exact PiMax camera exposure sequence is set in software [8]. Beam events of interest are then stored in timestamped files for post processing.

Currently only “single shot” events are captured by the BPM processors and PiMax camera for a given beam transient. It is also possible to trigger the PiMax with a pulse train to capture discrete segments of the beam transient by periodically gating the photocathode [4, 5]. An example of time-gating on a single bunch for a single pass is shown below.

## Optical SR measurement system

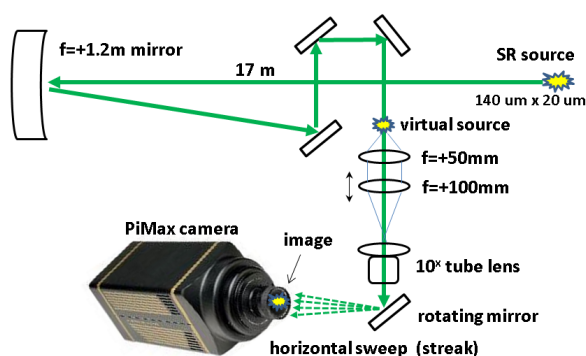


Figure 2: Optical transport line with  $10\times$  tube lens and rotating mirror.

At SPEAR3 the visible SR beam measurement systems use light extracted by a Rh-coated beam pick-off mirror under ring vacuum. The SR beam propagates unfocused to a dedicated optical bench. As shown in Fig. 2, the light travels approximately 17 m to an  $f=+1.2\text{m}$  concave focusing mirror which effectively forms the light-

collecting objective of a Herschel-type telescope [11]. The virtual source is de-magnified by a factor of 14 but is diffraction limited with a point spread function to about  $75\text{ }\mu\text{m rms}$  [12].

To measure transient beam events, we need to project vertical electron beam motion at the SR source point from of order  $100\text{ }\mu\text{m}$  to few mm onto the camera CCD. As seen in Fig. 2 the optical magnification system consists of a  $2\times$  infinite conjugation lens system followed by a commercial  $10\times$  infinity-corrected tube lens [13] yielding a net magnification of  $M_{\text{total}} = 2 \times 10 / 14 \sim 1.5$ . Note that increasing the optical magnification does not improve the signal/noise ratio and tends to spread the photon flux over more pixels leading to a reduction in image brightness. The PiMax images are therefore plotted in log scale to enhance lower intensities. Beam rotation elements, colour filters and polarizers can be inserted between the  $2\times$  telescope lenses. For the experiments reported here rotationally symmetric optics were used for equal magnification in both planes.

For practical reasons the  $10\times$  tube lens was fixed at a stationary position to image the beam onto the camera CCD with fine focus adjustments made by moving the  $f=+100\text{ mm}$  lens under a micrometre control. After reflection from the rotating mirror, the “rest” position of the SR beam is to the left of the camera CCD to avoid saturating the sensor prior to the mirror sweep. Depending on the measurement, the trigger time and mirror sweep speed are adjusted to streak the SR beam image across the CCD at the desired rate [14] and the camera gain and exposure time set accordingly.

## Camera Image Calibration

For transverse beam motion both the BxB and turn-by-turn BPM processors have known amplitude calibration factors in terms of mm/count. The PiMax calibration is more complicated because the calculation of optical magnification factors and mirror sweep speed are difficult to determine in terms of mm/pixel and ms/pixel, respectively. In order to measure the calibration factors empirically, we impulsively deflected the electron beam with the horizontal beam injection kickers to a known amplitude with known time intervals between kicks. Figure 3 illustrates how a Dove prism installed in the optical beam path is used to align the horizontal beam motion with the vertical camera axis.

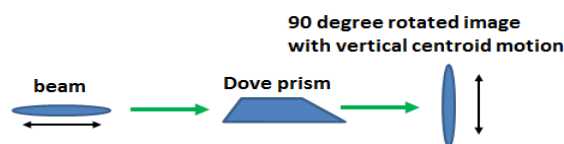


Figure 3: Dove prism rotates the horizontal SR beam axis into the vertical plane.

As shown in Fig. 4-a, the PiMax time axis was calibrated with the three injection kickers pulsed at 1 ms, 3 ms and 6 ms. The kick amplitudes were reduced by 50% to keep the beam within the dynamic aperture and the

horizontal BxB feedback was ON to increase the betatron damping rate.

The injection kicker pulses were measured with a turn-by-turn BPM processor and then lined up with the PiMax image. Referring to Fig. 4, the calibration process yields a scale factor of 0.0083 ms/pixel. The 3 ms time interval between kicker K2 and K3, for instance, corresponds to about 360 pixels.

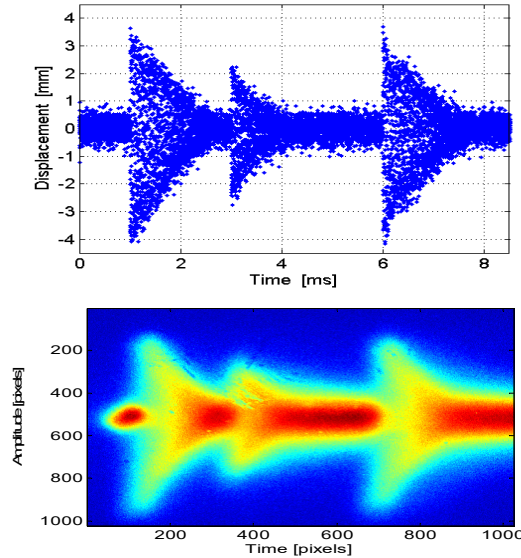


Figure 4: a) horizontal turn-by-turn BPM response and b) calibration image acquired by the PiMax.

As shown in Fig. 4-b, the  $\pm 4$  mm beam displacement recorded by a turn-by-turn BPM processor was used to calibrate the vertical camera axis (amplitude). Scaling by the ratio of horizontal betafuncions between the BPM location and the PiMax SR source point, we have,  $\Delta x = \pm 4 \text{ mm} * \sqrt{1.86/3.0} = \pm 3.15 \text{ mm}$  on the camera [9]. The vertical span of the displacement on the PiMax camera is  $\pm 400$  pixels leading to a calibration factor of 0.0079 mm/px. As a cross-check, the image of the stationary horizontal beam on the camera CCD is  $1.5 * 140 \mu\text{m} / 7.9 * 10^{-3} = 26 \text{ px rms}$  which is consistent with Fig. 4.

For vertical beam measurements the Dove prism was removed and the same calibration factors applied. The action required to obtain an equivalent vertical amplitude must be scaled by the ratio of visible light source point betafuncions  $f = \sqrt{\beta_x / \beta_y} = 2.8$  [9].

## SYNCHRONOUS MEASUREMENTS

Instabilities arise in storage rings when electromagnetic forces resulting from the overlap between the beam spectrum and the vacuum chamber impedance cause a positive feedback loop that grows faster than synchrotron radiation damping. The source and strength of the beam impedance can be studied using grow/damp measurements whereby the BxB feedback is momentarily

switched off and on. Data stored in the BxB memory buffers yields the time evolution of each bunch centroid but cannot resolve charge decoherence. Instead, visible light images representing slices in phase space can be acquired simultaneously to complement the data. Drive/damp events can also be imaged to measure changes in transverse beam profile. This class of experiments is important for bunch cleaning and resonant crabbing research.

## Multibunch Beam Instability

Similar to the mechanism for SASE build-up in an FEL, SPEAR3 is subject to a high-order vertical multibunch instability where the growth process is inherently startup-from-noise. In this case, the beam interacts with resonant pillbox modes trapped in a small-gap IVUN chamber [7]. The statistical nature of the process leads to small variances in the instability onset time and growth rate and rather large variances in the oscillation envelopes for individual bunches. Figure 5-a, for example, shows turn-by-turn data recorded by the iGp12 processor for a single bunch as it executes complex envelop modulations during the damping phase of a grow/damp measurement. The modulations are believed to be caused by beating between different characteristic frequencies of the motion.

Figure 5-b shows the same grow/damp event synchronously measured on the PiMax camera. For this case the camera trigger was delayed by 7 ms to allow time for instability to startup from noise. Typical of most multibunch instability events in SPEAR3, the motion of individual bunches varies during a single measurement or from shot to shot whereas the shape of the envelop for the integrated SR camera image is more stable. For the event shown in Fig. 5, the camera image indicates a peak-to-peak amplitude of about  $\pm 4$  mm at the SR source point. For this measurement the betatron amplitude of many bunches saturated the ADC's in the iGp12 BxB processor.

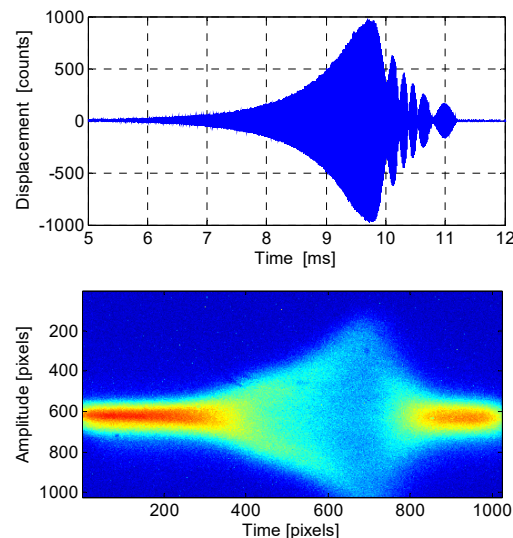


Figure 5: High-order multibunch instability showing a) oscillation envelop for bunch 1, and b) synchronous PiMax image with rotating mirror.



## Single Bunch Drive Studies

For single bunch studies the BxB system or turn-by-turn BPM processors can again be used to measure bunch centroid data with the rotating mirror camera system recording the SR image in time.

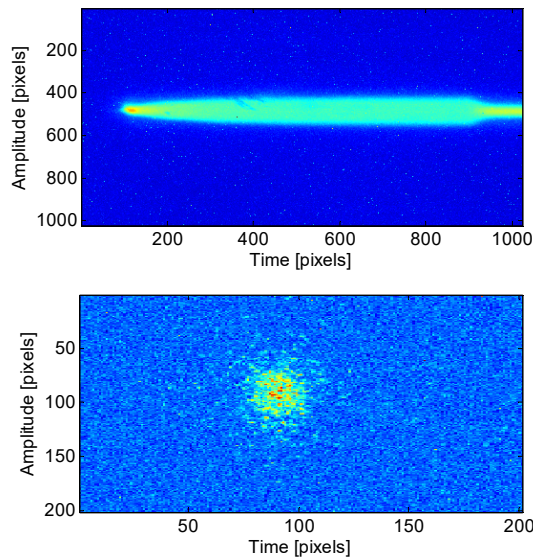


Figure 6: a) rotating mirror image of single-bunch drive-damp test with b) single turn cross-section.

As a preliminary test of resonant drive capability in SPEAR3, the iGp12 feedback processor was configured to excite a vertical betatron oscillation on a single bunch using a built-in phase-locked loop feature that tracks tune shift with amplitude. Both the drive signal and SRAM were synchronously triggered along with the PiMax camera and rotating mirror. As seen in Fig. 6-a, the SR image recorded on the PiMax shows the motion saturates to a sinusoidal steady state after about 3-4 ms.

Using the calibration factor of 0.008 mm/px, the measured amplitude is about 400  $\mu\text{m}$  pk-pk. The one-turn image seen in Fig. 6-b was measured at time  $t = 4$  ms and indicates no distortion in the x-y plane at low oscillation amplitude.

SPEAR3 will soon install high power BxB drive amplifiers that will excite the bunch in fewer turns or to higher amplitude for bunch cleaning. Synchronous SR imaging measurements will be continued to study decoherence with the new amplifiers. Since the bunch is executing driven betatron oscillations, multiple turns can be also captured in a single imaging frame.

## SUMMARY

Synchronously triggered diagnostic systems in storage rings provide correlated data acquisition that helps to understand chamber impedance, beam dynamics and lattice non-linearities. In particular, by synchronizing a fast-gated camera with a rotating mirror with the BxB feedback processor we can study transient beam events from different perspectives. This paper gives preliminary measurements of both grow/damp and drive/damp beam

transients that reveal different features of the motion. In the future we plan to further study multibunch instabilities caused by new IVUN chambers. For applications such as resonant crabbing it is important to measure charge decoherence of the bunch since the duration of the ultrashort x-ray pulse depends critically on the time evolution of charge distribution. Mechanisms leading to amplitude saturation and non-linear charge decoherence within the bunch will be investigated.

## ACKNOWLEDGMENTS

The authors would like to thank S. Berry, P.J. Boussina, L. Campos, D. Teytelman, T. Dunn, S. Condamoor, C. Ramirez, C. Takacs, J. Safranek, S. Wallters and the SPEAR3 operations staff for technical assistance.

## REFERENCES

- [1] DIMTEL, Inc., San Jose, CA, [www.dimtel.com](http://www.dimtel.com).
- [2] K. Tian, *et al.*, "Transverse bunch-by-bunch feedback at SPEAR3 with a graphical user interface", in *Proc. of IPAC'18*, Vancouver, CA, May 2018.
- [3] T. Mitsuhashi, private communication.
- [4] A.S. Fisher, *et al.*, "Turn-by-turn imaging of the beam profile in PEP-II", *BIW 2006*, Batavia, I, (2006).
- [5] W. Cheng, *et al.*, "Fast gated camera measurements in SPEAR3", in *Proc. of PAC'09*, Vancouver, Canada, 2009.
- [6] B. Kehrer, *et al.*, "Simultaneous Detection of Longitudinal and Transverse Bunch Signals at ANKA", *Proc. IPAC16*, Busan, Korea, May 2016.
- [7] K. Tian, J. Sebek and J.L. Vargas, "Investigation of transverse beam instability induced by an IVUN at SPEAR3", *IBIC16*, Barcelona, Spain, 2016.
- [8] Roper PiMax, [www.roperscientific.de](http://www.roperscientific.de)
- [9] Q. Lin, *et al.*, "Time-Synchronized Beam Diagnostics at SPEAR3", in *Proc. of IPAC'18*, Vancouver, CA May 2018.
- [10] S. Condamoor, *et al.*, "Machine studies with Libera Instruments at the SLAC SPEAR3 Accelerators", presented at *IBIC'18*, Sep. 2018, this conference.
- [11] C. Li, "Characterization of field polarization and spatial coherence in a diffraction-limited visible light synchrotron radiation beam", PhD Thesis, SLAC Report 1083, 2017.
- [12] A. Hoffmann, "The Physics of Synchrotron Radiation, Cambridge University Press, 2007.
- [13] <https://www.edmundoptics.com/p/10x-mitutoyo-plan-apo-infinity-corrected-long-wd-objective/6623/>
- [14] SRS DS345, <http://www.thinksrs.com>



# WIRE SCANNER MEASUREMENTS AT THE PAL-XFEL\*

G.J. Kim<sup>†</sup>, B. Oh, D.C. Shin, C.B. Kim, H.-S. Kang  
Pohang Accelerator Laboratory, Gyeongbuk 37673, Korea

## Abstract

The PAL-XFEL, an X-ray Free electron laser user facility based on a 10 GeV normal conducting linear accelerator, has been operational at Pohang, South Korea. The wire scanners are installed for transverse beam profile measurement at the Linac and the Hard X-ray undulator section. The wire scanner is a useful device for emittance measurements in the Hard X-ray undulator section. In this paper, we describe the details of the wire scanner and the results of the measurements.

## INTRODUCTION

In order to operate an accelerator more stably and efficiently, it is necessary to adjust the operation conditions of the apparatus to the designed conditions. In order to perform this operation, it is important to obtain the accurate emittance of the electron beam by the transverse beam size measurement. At the PAL-XFEL are installed 54 screen monitors and 13 wire scanners for beam profile measurement. As shown in Fig. 1 the wire scanner is mainly located at the end of the linear accelerator and the undulator section. This is used to measure the emittance to optimize the FEL generation condition for the undulator section. The wire material is a 34  $\mu\text{m}$  thick carbon wire suitable for the undulator line because it generates lower radiation when it is hit by electron beam [1]. This paper describes device configuration and beam commissioning results using wire scanner.

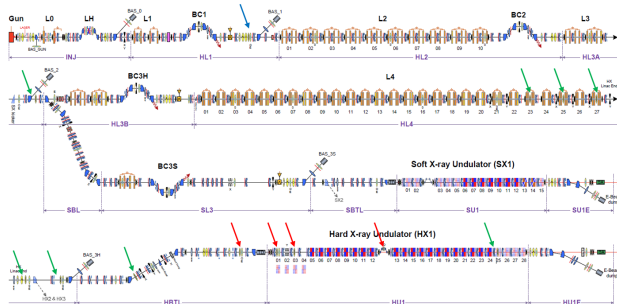


Figure 1: The layout of the PAL-XFEL. The arrows shows the location of the wire scanner. And the red arrow indicates the location of the device where the 34  $\mu\text{m}$  carbon wire is installed.

## HARDWARE FEATURES

The wire scanner measurement system consists of a motion stage and a radiation measuring device. The motion device is used to adjust the position of the wire causing the

interference with the electron beam. The radiation measuring device measure the amount of energy loss caused by the interference of the electron beam with the wire.

## Motion Stage

The wire scanner assembly is mounted on its 45° motion stage with linear motor. As shown in Fig. 2(a), the wire card is equipped with three wires (x, y, u) and an RF shielding tube. It has been reported that the position of the electron beam changes due to the changing of the magnetic field from the linear motor [1]. The linear motor is equipped with an ironless linear motor which is designed not to have attractive force. The wire material is based on the tungsten and carbon wire was selected to minimize the radiation damage to the undulator magnet. The wire scanner with carbon 34  $\mu\text{m}$  wire is installed between after the dogleg section and the last undulator.

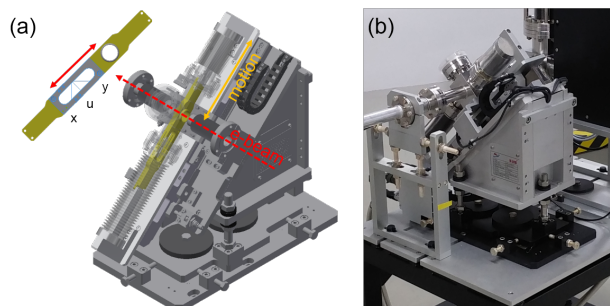


Figure 2: The wire scanner mounted on its motion stage. (a) The 3D modeling of the wire card and motion stage, (b) Installation of the wire scanner.

## Beam Loss Monitor (BLM)

The Beam loss detectors are based on the idea of using optical fibers as a Cherenkov light radiator. The optical fiber used as the radiator is a plastic scintillating fiber of BCF-20 with 250  $\mu\text{m}$  diameter which has 492 nm peak emission wavelength and 2.7 ns decay time [2]. The fiber is shielded from external light and connected directly to the PMT. It was installed by direct winding to the chamber as shown in Fig. 3(a) to measure the generated signal. The photomultiplier tubes (PMT) module uses the Hamamatsu H10722-110 as show in Fig. 3(b). It has 230–700 nm spectral response range with voltage output. As shown in the figure, a certain space is required for installation of optical fiber-based BLM. Because of the limited installation space of the undulator section, the wire scanner was measured using the BLM for Undulators [3].

\* Work supported by MSIP, Korea.

<sup>†</sup> gyujin\_kim@postech.ac.kr

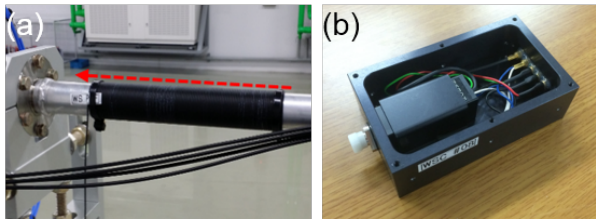


Figure 3: The beam loss detector with optical fiber. (a) fiber wrapped around the chamber, (b) PMT and housing.

### CONTROL SYSTEM

As shown in the Fig. 4, the control system is required to control the power and gain of the PMT as well as the position of the motor, and is configured to acquire the beam loss and beam position value for the measurement. And also the beam loss signal and position value are acquired and controlled based on EPICS and beam synchronous acquisition (BSA) which is working on event timing system. The BLM and BPM IOC's are operated on a timing system based platform. The beam position value that is acquired during the measurement is used to correct the position jitter.

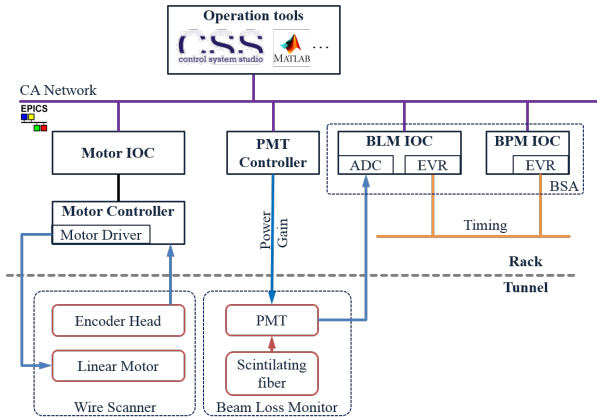


Figure 4: Control layout for wire scanner measurement.

The MATLAB program is used to measure the beam profile with a wire scanner as shown in the Fig. 5. This program is modified for PAL-XFEL, which was used in LCLS.

### BEAM MEASUREMENTS

#### Results from Commissioning

In order to find the optimal BLM installation position which is based on optical fiber, the intensity of the signal according to the position was measured. It can be seen from the Fig. 6 that a relatively large signal is detected around 35 and 90 m irrespective of the position of the device. This position was found to be located behind a bipolar electromagnet which is used to change the trajectory of the electron beam.

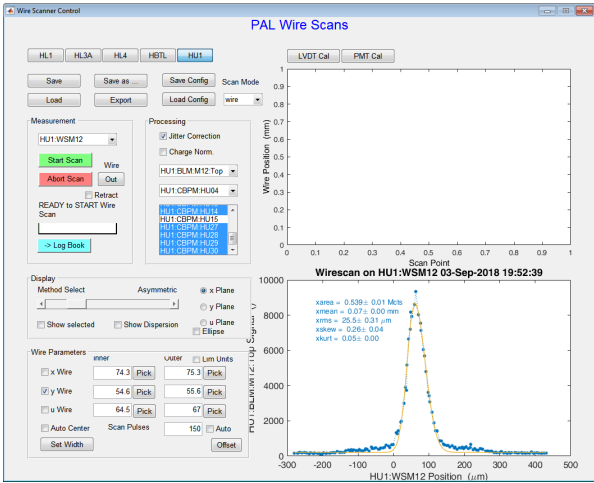


Figure 5: Wire scanner measurement GUI.

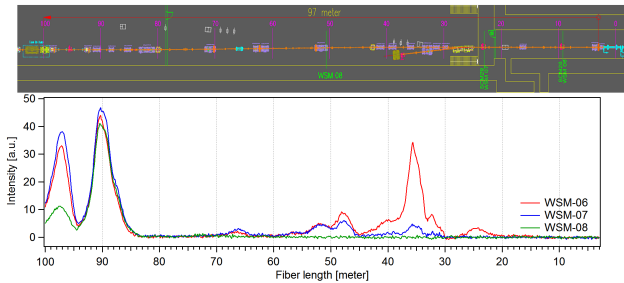


Figure 6: The beam loss intensity distribution along distance at the end of Linac.

#### Results from Machine Tuning

If the beam becomes unstable during the measurement process, it is subjected to a correction process using the electron beam position in the measurement. Figure 7 shows the results before and after correction with beam position. It shows that there is a 10 % error in beam size before correction.

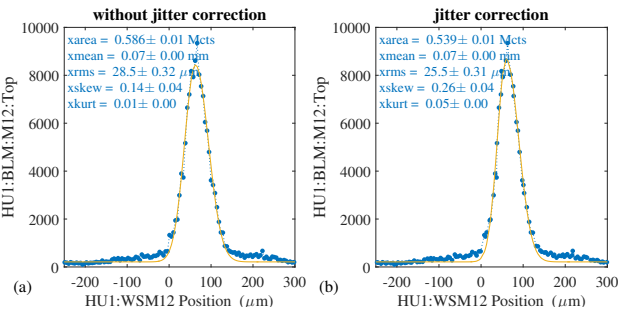


Figure 7: The results of the wire scanner measurement depend on the beam position jitter correction. Beam profile (a) without jitter correction, and (b) with jitter correction.

The wire scanner measurement is used to measure the emittance of the undulator section and to optimize the undulator section. Figure 8 shows the result of the beam size

and emittance measurements with five wire scanners in the undulator section.

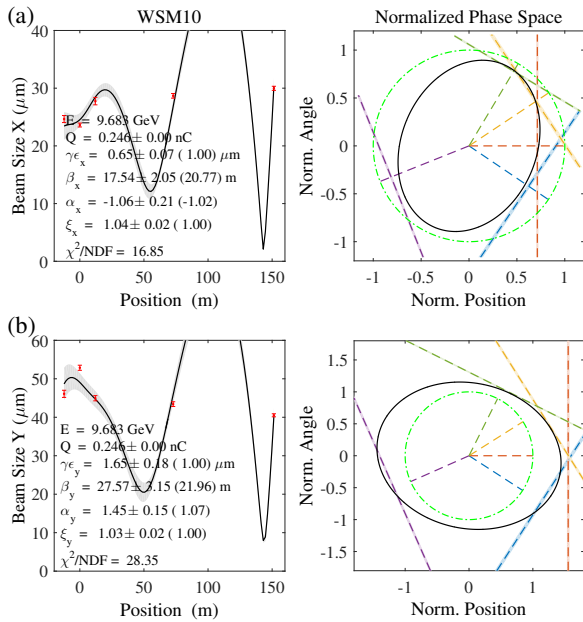


Figure 8: The emittance measurement using five wire-scanners. (a) X-plane, (b) Y-plane.

## SUMMARY

The emittance measurements results with five wire scanners in the undulator section is used for matching of the e-beam to the design lattice by using quadrupoles. The wire scanner is very useful device for diagnosing and optimizing the equipment in the PAL-XFEL.

## ACKNOWLEDGEMENTS

We would like to thank H. Loos for applying the measurement program.

## REFERENCES

- [1] H. Loos, "LCLS Beam Diagnostics", in *Proc. IBIC'14*, Monterey, CA, USA, Sep. 2014, paper WEIXB1, pp. 475–485.
- [2] <http://www.crystals.saint-gobain.com/>
- [3] H. Yang, D. C. Shin, "Beam loss monitor for undulators in PAL-XFEL", in *Proc. FEL'17*, Santa Fe, NM, USA, Sep. 2017, paper WEP044, pp. 503–506.

# GRATING SCANNER FOR MEASUREMENT OF MICRON-SIZE BEAM PROFILES\*

L. G. Sukhikh<sup>†</sup>, A. P. Potylitsyn, S. A. Stokov, Tomsk Polytechnic University, 634050, Tomsk, Russia  
 G. Kube, K. Wittenburg, Deutsches Elektronen Synchrotron DESY, 22607, Hamburg, Germany

## Abstract

Wire scanners are widely used for transverse beam size diagnostics. The minimum detectable beam size is affected by the diameter of a single wire that is of about 4 microns. Sub-micron beam sizes have to be resolved due to development of modern electron accelerators and future linear electron-positron colliders. In this report we propose to use a set of gold stripes with varying period (gap) on a Si substrate. By moving this scanner across the beam one could measure the Bremsstrahlung yield vs. the coordinate, resulting in an oscillating dependence. The visibility of the resulting image allows defining the beam sizes in the range of 0.5–1.5  $\mu\text{m}$  for the proposed scanner parameters.

## INTRODUCTION

Wire scanners are widely used for diagnostics of transverse beam size in the modern electron accelerators. The wire crosses the beam resulting in the bremsstrahlung generation and loss electrons generation. Measuring dependence of high energy photon or loss electron yield on wire coordinate one could obtain transverse beam profile projection. The minimal detectable beam size is affected by the diameter of a single wire. The smallest carbon or tungsten wires used so far have diameters of about 4  $\mu\text{m}$ . If the beam size measured is comparable with the wire diameter is significantly affects the measured profile and should be taken into account. In case of smaller beam sizes one could meet the situation that measured “beam” profile contains only wire diameter. With the development of modern electron accelerators and the demands from future linear electron-positron colliders, micron and sub-micron beam sizes have to be resolved with sub-micron or better resolution. For this purpose a new generation of wire scanners should be developed and tested.

One of the possible methods to increase the resolution of the wire scanners is to decrease its size. The minimal diameter of single free-hanging wire ( $\approx 4 \mu\text{m}$ ) is limited by the mechanical stress. However, one could consider wires with smaller size (units of microns or even sub-microns) on a substrate. In Ref. [1] authors proposed to use thin gold stripes of rectangular shape (1  $\mu\text{m}$  or 2  $\mu\text{m}$  width and 3  $\mu\text{m}$  height) on  $\text{Si}_3\text{N}_4$  membrane used as a substrate. In this case authors of Ref. [1] expect to increase beam size measurement resolution and to be able to resolve sub-micron beams. However, one of the paybacks while using small size

wires is the limited dynamic range of the measurable beam sizes.

In this report we propose another arrangement of gold stripes on Si substrate. We propose to form a grating scanner from a set of gold stripes with variable distance between them. In this report we present the preliminary Geant4 simulations of such a grating scanner with varying gaps that show the possibility to measure beam sizes in the range of 0.5–1.5  $\mu\text{m}$ .

## GRATING SCANNER WITH VARYING GAPS

The scheme of the grating scanner with varying gap is shown in Fig. 1. The scanner considered in this report consists of eleven rectangular gold stripes on Si substrate of 50  $\mu\text{m}$  thickness. The height of the gold stripes was equal to 10  $\mu\text{m}$ . During the simulation we considered two stripe widths, namely  $a = 1 \mu\text{m}$  or  $a = 3 \mu\text{m}$ . The distance between stripes is non-equal and varies in the range of 0.25–3  $\mu\text{m}$ .

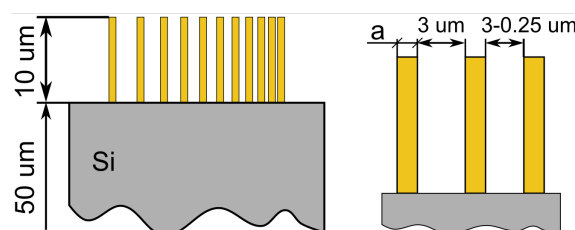


Figure 1: Schematic view of grating scanner with varying gaps.

The basic idea of beam size measurement using proposed scanner is the following. The electron beam interacts with the scanner while moving the scanner across the beam. Amount of the generated photons (or loss electrons) depends on which part of the scanner directly interacted with the beam. If the beam size is small comparing with the gap size the beam interacts either with a gold stripe and the substrate resulting in the maximal bremsstrahlung yield or with the substrate only resulting in the minimal (background) photon yield. In this case the dependence of the photon yield on the grating coordinate is oscillatory. When beam size is much larger than the gap size, the beam interacts with several stripes resulting in monotonic dependence of the photon yield on grating coordinate. The schematic view of beam interacting with the scanner is shown in Fig. 2.

The wire scanner with varying gaps was simulated using Geant4 [2]. The simulation scheme is shown in Fig. 3. The electron beam with electron energy  $E_e = 1.25 \text{ GeV}$  and

\* Work supported by Russian Ministry of Science and Higher Education, Program “Nauka” grant #3.1903.2017 and TPU Competitiveness enhancement Program

<sup>†</sup> sukhikh@tpu.ru



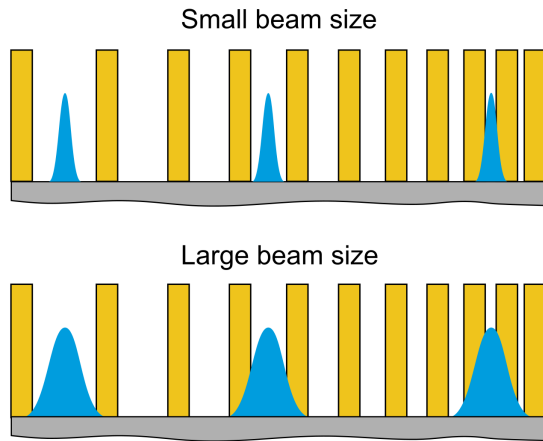


Figure 2: Schematic view of grating scanner with varying gaps interacting with small and large beams.

Gaussian transverse profile (rms  $\sigma_e = 0.5\text{--}3\text{ }\mu\text{m}$ ) interacted with the scanner resulting in bremsstrahlung generation that were counted by the photon counter. The primary electron beam was turned away by the bending magnet. The grating was moved in transverse ( $x$ ) direction with the step  $0.1\text{ }\mu\text{m}$ . The dependence of the registered number of photons on transverse position was simulated.

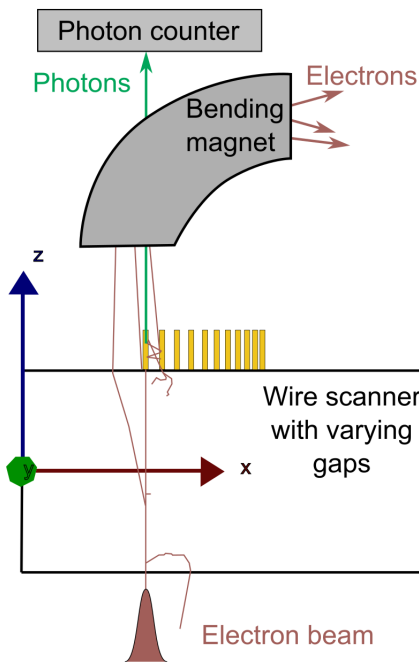


Figure 3: Schematic view of Geant4 simulation geometry.

Figure 4 shows an example of the Geant4 simulation results. Row a) shows dependence of the photon yield on grating scanner coordinate for stripe width equal to  $1\text{ }\mu\text{m}$ . Row b) shows the same for stripe width equal to  $3\text{ }\mu\text{m}$ .

In Figure 4 one can see that visibility (ratio between minimum and maximum) depends both on the coordinate and on the beam size. The photon yield increases with decrease of the the gap size but at the same moment the visibility de-

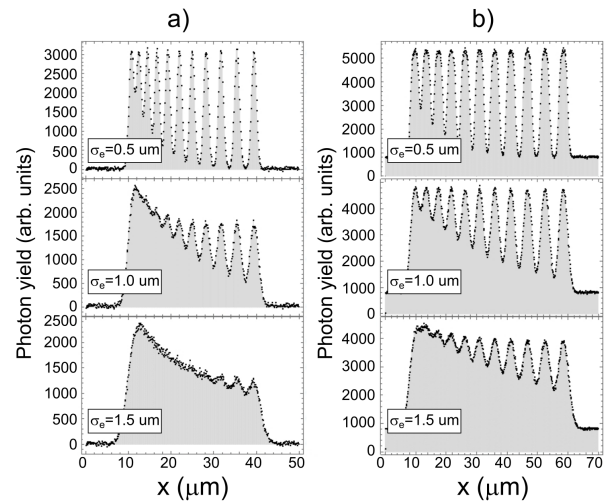


Figure 4: Grating size scans simulated by Geant4 for different beam sizes. Row a) - stripe width is equal to  $1\text{ }\mu\text{m}$ , row b) - stripe width is equal to  $3\text{ }\mu\text{m}$ .

creases. One can also see that the influence of background from the substrate is not significant and signal-to-noise ratio is of about 3–4.

In order to obtain the beam size from the scan the following procedure was developed. For each period of the scan the position of the photon yield minimum and maximum was found as it is shown in Fig. 5.

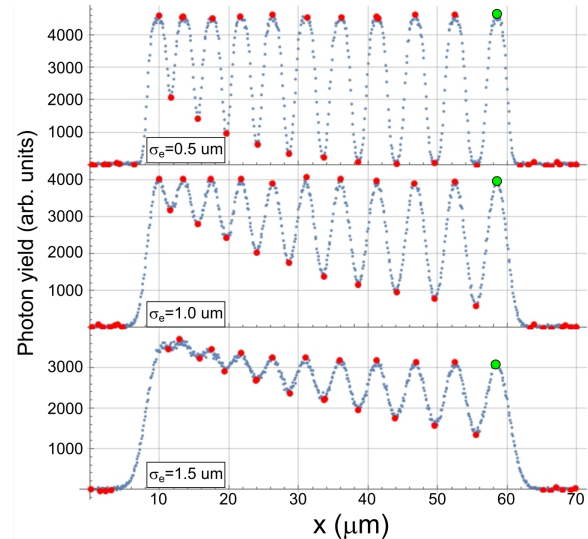


Figure 5: Grating size scans simulated by Geant4 for different beam sizes for stripe width is equal to  $3\text{ }\mu\text{m}$ . Red dots - positions of the minima and maxima, green dot - position of the maximum used for normalization.

The ratio of each minimum to the right maximum (green dots in Fig. 5) was plotted vs. the transverse coordinate (see Fig. 6). The obtained dependence could be fitted by the following function:

$$R(x) = A_0 \exp[-x/x_0], \quad (1)$$

where  $A_0$  and  $x_0$  are the free fit parameters.

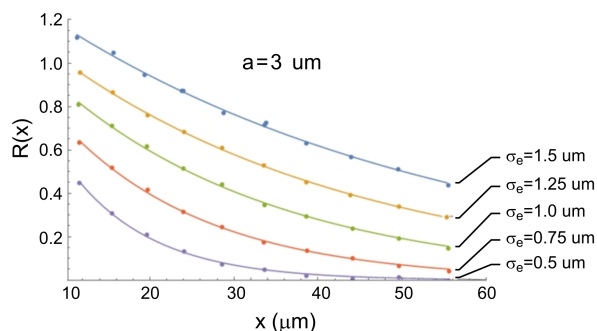


Figure 6: Dependence of the minima to the maximum ratio on transverse coordinate for different beam sizes. Stripe width is equal to 3  $\mu\text{m}$ .

Figure 7 shows the dependence of the fit parameter  $x_0$  on the beam size used during the simulation. One can see that the dependence is linear both for 1  $\mu\text{m}$  stripes and 3  $\mu\text{m}$  ones. From Fig. 7 one can see that due to linear dependence of  $x_0$  fit parameter on beam size  $\sigma_e$  one could obtain actual beam size from the dependence of photon yield on grating shift (see Fig. 4)

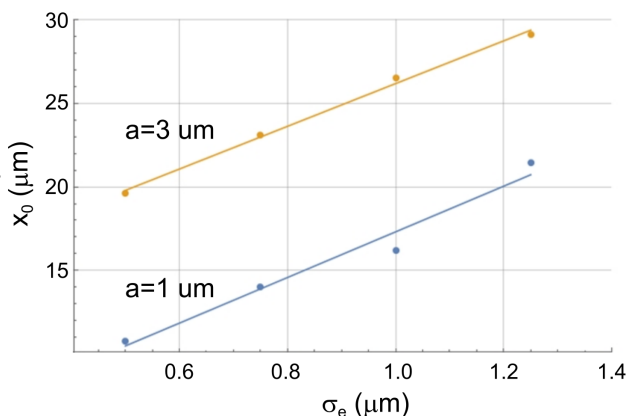


Figure 7: Dependence of the fit parameter  $x_0$  on the beam size  $\sigma_e$  used during the simulation and linear fit. Blue - stripe width is equal to 1  $\mu\text{m}$ , Yellow - stripe width is equal to 3  $\mu\text{m}$ .

## CONCLUSION

New type of wire scanner with varying gaps is proposed and simulated using Geant4. Scanning of the Gaussian beam with such type of a scanner allows to measure beam sizes in the wide range. In the simulated case one could measure beam sizes in the range 0.5–1.5  $\mu\text{m}$  with sub-micron resolution. The scanning range could be increased if one increases stripe width and amount of stripes. In this report gold stripes of 10  $\mu\text{m}$  height on 50  $\mu\text{m}$  Si substrate were simulated resulting in the good signal-to-noise ratio. In order to check the feasibility of the proposed scanner the experimental verification is needed.

## REFERENCES

- [1] S. Borrelli, G. L. Orlandi, M. Bednarzik, C. David, E. Ferrari, V. A. Guzenko, C. Ozkan-Loch, E. Prat, and R. Ischebeck, "Generation and measurement of sub-micrometer relativistic electron beams", *arXiv:1804.04252v1 [physics.acc-ph]*, 11 Apr. 2018.
- [2] J. Allison *et al.*, "Recent developments in Geant4", *Nuclear Instruments and Methods A*, vol. 835, pp. 186–225, 2016.

# SPATIAL RESOLUTION IMPROVEMENT OF OTR MONITORS BY OFF-AXIS LIGHT COLLECTION

A. Potylitsyn<sup>1,†</sup>, L. Sukhikh<sup>1</sup>, G. Kube<sup>2</sup>, A. Novokshonov<sup>1,2</sup>

<sup>1</sup>Tomsk Polytechnic University, 30, Lenin St., Tomsk, 634050, Russia

<sup>2</sup>Deutsches Elektronen-Synchrotron (DESY), Hamburg, Germany

## Abstract

The spatial resolution of an OTR monitor, widely used for electron beam profile diagnostics, is determined by the resolution of the optical system and by the Point Spread Function (PSF) representing the single electron image. In the image plane, the PSF has a typical lobe-shape distribution with an inter-peak distance depending on wavelength and lens aperture ratio [1]. For a beam with a transverse rms size smaller than the distance, the reconstruction of the beam profile has several difficulties [2, 3]. We propose to reduce the PSF contribution and to improve the spatial resolution of an OTR monitor simply by rotating the lens optical axis with respect to the specular reflection direction. If the difference between the rotational angle and the lens aperture is much larger than the inverse Lorentz factor, the PSF has a Gaussian-like distribution which matches practically with the Airy distribution. Thus the resolution depends on wavelength and lens aperture. In principle, for lens apertures in the order of 0.1 rad such an approach should allow to measure beam sizes comparable to the wavelength of observation, using a simple deconvolution procedure for the measured image and the PSF.

## INTRODUCTION

Transverse beam size measurements based on optical transition radiation (OTR) are a widely used technique and OTR monitor stations are operated at most modern electron linacs [4, 5]. For electron energies higher than 50 MeV the OTR intensity collected by a conventional optics system with numerical aperture of  $\theta_m \sim 0.1$  rad achieves  $N_{ph} \sim 10^{-3}$  photons per electron in the band width  $\Delta\lambda / \lambda \sim 0.05$ .

The spatial resolution of a transverse beam size monitor based on OTR is determined by the so-called Point Spread Function (PSF) or, in other words, by the response of the monitor optical system to a point charge crossing the target. With knowledge of the PSF, in principle it is possible to reconstruct beam size and beam shape from an electron bunch passing through the target applying a deconvolution algorithm to the measured OTR image.

The PSF has a double-lobe structure which is defined by the radiation wavelength  $\lambda$ , the acceptance angle or numerical aperture of the optical system  $\theta_m$ , and the alignment accuracy. For the condition of ideal

imaging the OTR monitor resolution determined by so-called diffraction limit can be expressed as

$$R = 1,12 \frac{\lambda M}{\theta_m}. \quad (1)$$

Here  $M$  denotes the magnification factor of the optical system.

For beams with micrometer/submicrometer sizes such an optical system provides PSF dominated regime and one should apply a spectral treatment of the data in order to extract a real beam size [6].

We propose optical schemes for OTR monitors with off-axis light collection in order to avoid a two-lobe structure of the PSF and improve its spatial resolution.

## CALCULATIONS OF OTR PSF DISTRIBUTIONS

Under ultra-relativistic approximation the particle Coulomb field can be sufficiently described by its transverse components and it is possible to write down the OTR field in the lens plane in analogy with wave scattering at a finite size conducting screen:

$$E_{x,y}^L(X_L, Y_L) = \text{const} \int_{S_T} dX_T dY_T \left\{ \frac{\cos \varphi_T}{\sin \varphi_T} \right\} K_1 \left( \frac{k}{\beta\gamma} R_T \right) \times \exp \left[ i \frac{k}{2a} (X_T^2 + Y_T^2) \right] \exp \left[ -i \frac{k}{a} (X_L X_T + Y_L Y_T) \right]. \quad (2)$$

Here  $R_T = \sqrt{X_T^2 + Y_T^2}$ ,  $(X_T, Y_T)$  and  $(X_L, Y_L)$  are the coordinates of target surface and lens plane,  $a$  is the distance between target and lens,  $S_T$  is the target surface area,  $\left\{ \frac{\cos \varphi_T}{\sin \varphi_T} \right\} = \frac{1}{\sqrt{X_T^2 + Y_T^2}} \left\{ \frac{X_T}{Y_T} \right\}$ ,  $K_1(x)$  is the

MacDonald function of the first order,  $k = 2\pi / \lambda$ .

The OTR fields in the image plane using thin lens approximation can be written in the following way after integration over the lens aperture  $S_L$ :

$$E_{x,y}^D(X_D, Y_D) = \text{const} \int_{S_L} dX_L dY_L E_{x,y}^L(X_L, Y_L) \times \exp \left[ -i \frac{k}{b} (X_L X_D + Y_L Y_D) \right]. \quad (3)$$

$b$  is the distance between lens and detector. Inserting Eq. (2) in the last expression and performing 4-fold

<sup>†</sup> email: potylitsyn@tpu.ru

integration, one can obtain the OTR fields and, subsequently, PSF distribution [7, 8]:

$$\frac{d^2 W}{\hbar d\omega d\Omega} = \text{const} \left( |E_x^D|^2 + |E_y^D|^2 \right) = \text{const} \left( \frac{d^2 W_x^D}{\hbar d\omega d\Omega} + \frac{d^2 W_y^D}{\hbar d\omega d\Omega} \right). \quad (4)$$

Figure 1 shows PSF distributions calculated for the following parameters:  $\lambda = 0.5 \text{ um}$ ;  $\gamma = 2000$ ;  $a = b = 500 \text{ mm}$ ; the lens diameter  $d_L = 100 \text{ mm}$  (green curve) and  $d_L = 50 \text{ mm}$  (blue curve).

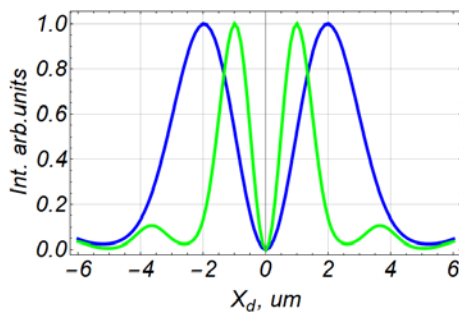


Figure 1: PSF distributions for horizontal polarization component  $d^2 W_x^D / \hbar d\omega d\Omega$  for  $y_D = 0$ .

## METHODS FOR IMPROVEMENT OF THE OTR SPATIAL RESOLUTION

Basis of the first method is the installation of a mask in front of the lens with appropriate size at a position which is asymmetric with respect to the optical axis. If mask size and position are selected in a proper way it is possible to block one of the lobes of the horizontal angular OTR distribution. In this case information is extracted only from the second lobe in the lens plane or in the  $k_x - k_y$  phase space. Due to the properties of the Fourier transformation the output in the  $X_D - Y_D$  plane (i.e. the detector plane) will also have a single maximum distribution.

For such asymmetric geometry the PSF distribution can be calculated from the above mentioned expressions (1)–(3) with integration in (2) over the open part of the lens (Fig. 2).

The single maximum PSF in this case can be approximated by a Gaussian distribution and the rms size of this PSF is much smaller than the diffraction limit Eq. (1):  $\sigma = 2.1 \text{ um}$ ,  $R = 5.6 \text{ um}$ .

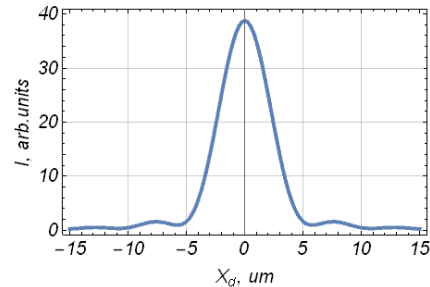
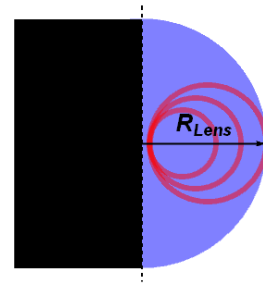


Figure 2: Scheme of the lens screening by an off-axis mask (up) and PSF distribution calculated for this case (down). Parameters:  $\lambda = 0.5 \text{ um}$ ;  $\gamma = 1000$ ;  $a = b = 500 \text{ mm}$ ;  $\theta_m = 0.1$ .

The second method to improve the spatial resolution of an OTR monitor has the same purpose to create a PSF with a single maximum. Again, the OTR horizontal polarization component will be considered in the following. However, in this case the idea is to displace the imaging lens asymmetrically as depicted in Figs. 3 and 4.

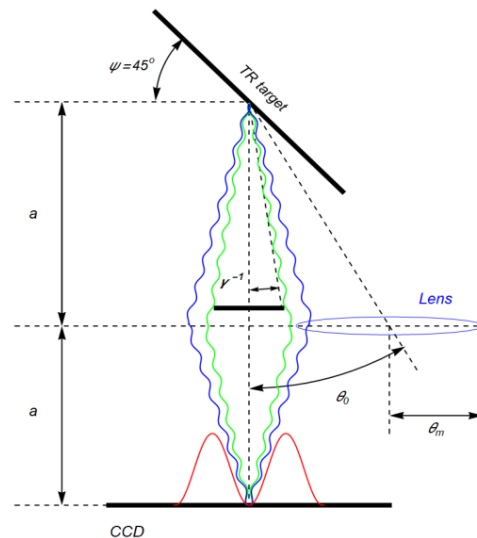


Figure 3: Scheme of the asymmetric lens displacement.



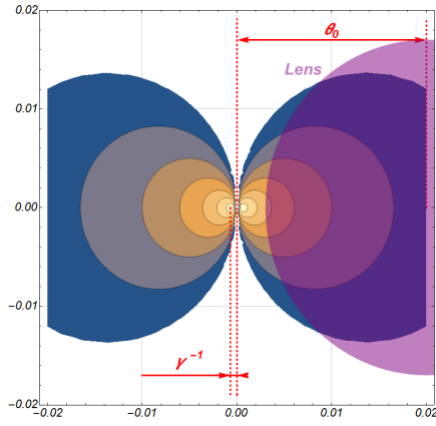


Figure 4: Scheme of the asymmetric light collection.

If the lens optical axis is disoriented with respect to the specular reflection direction from the OTR target at an angle of  $\theta_0$  with  $\theta_0 - \theta_m \gg \gamma^{-1}$  the OTR light will be collected from the outside region of the OTR lobe-shape distribution.

Results of such PSF calculations using asymmetric light collection geometries are presented in Fig. 5 for  $\theta_m = 0.1$  rad (green points) and  $\theta_m = 0.05$  rad (red points). The remaining parameters for the calculation are the same as before.

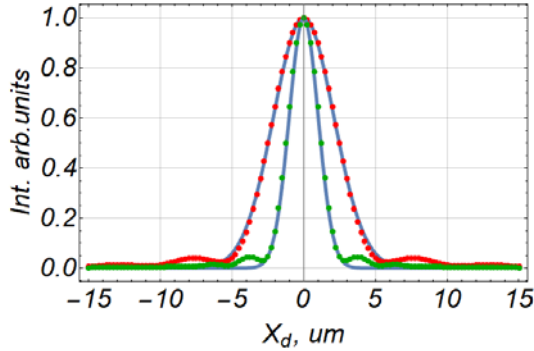


Figure 5: Calculated PSF distributions for an asymmetric lens aperture (red points  $\theta_{0x} = 0.11$ ;  $\theta_{0y} = 0$   $\theta_m = 0.05$  – red points);  $\theta_{0x} = 0.11$ ,  $\theta_m = 0.1$  (green points) and Gaussian fits for them.

Approximating the central maximum by a Gaussian distribution results in an rms value of  $\sigma_1 = 1.01$   $\mu\text{m}$  for the first case and  $\sigma_2 = 2.02$   $\mu\text{m}$  for the second one.

## CONCLUSIONS

In the report we have showed that an off-axis mask screening of the imaging lens or an asymmetric light collection geometry caused by a displacement of the imaging lens both result in light collection from only one lobe of a linearly polarized OTR intensity distribu-

tion. As consequence, the PSF possesses also a single maximum in the image plane.

In the following PSF distributions calculated for asymmetric OTR light collection (see Fig. 2 and Fig. 5) will be compared with the well-known Airy distribution, describing the PSF of an isotropic emitting point source [9]. It is expressed as

$$AF(R_D) = (I_1(\alpha R_D) / \alpha R_D)^2, \quad (5)$$

with  $I_2(x)$  the first order Bessel function and

$$\alpha = 2\pi\theta_m / \lambda, \quad \alpha = 2\pi\theta_m / \lambda, \quad R_D = \sqrt{X_D^2 + Y_D^2}.$$

In Fig. 6 the Airy distribution for  $\lambda = 0.5$   $\mu\text{m}$ ,  $\theta_m = 0.1$ ,  $Y_D = 0$  and the PSF are shown.

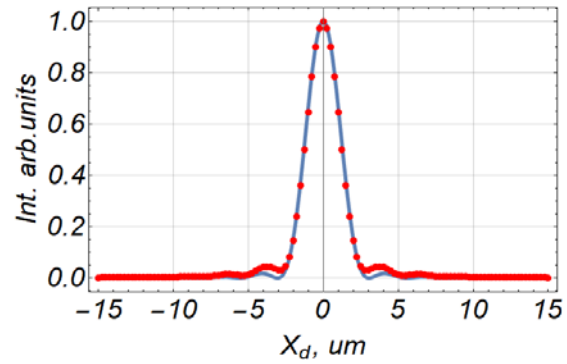


Figure 6: Airy functions for  $y_d = 0$ ;  $\lambda = 0.5$   $\mu\text{m}$ ;  $\theta_m = 0.1$  rad (blue curve) and the PSF calculated for  $\theta_{0x} = 0.11$ ,  $\theta_m = 0.1$ , red dots (see Fig. 5).

One can conclude that the proposed asymmetric light collection scheme provides a spatial resolution practically coinciding with the one for an ideal isotropic source.

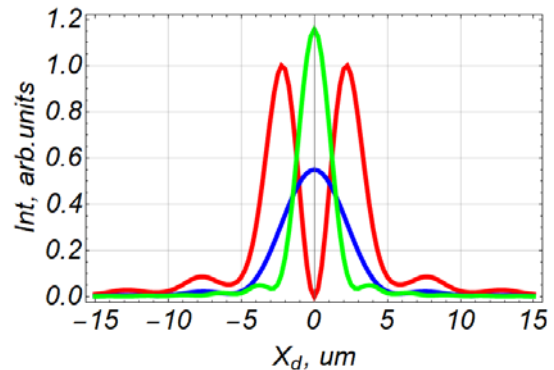


Figure 7: Comparison of calculated OTR PSF functions for conventional light collection (red line), for 50% screening of the lens aperture (blue line) and for off-axis light collection (green line)

Figure 7 compares calculated OTR PSF functions for three different cases, (i) for standard imaging without using a mask (red line), (ii) for blocking the lens aperture by an asymmetric mask (blue line), and (iii) for

off-axis light collection (green line). All PSF functions were calculated for the same set of parameters ( $\gamma = 1000$ ,  $\lambda = 0.5$  um,  $\theta_m = 0.1$ ). As one can see from this comparison, the PSF for the off-axis light collection has the narrowest shape and possesses only a single maximum in contrast to the PSF for standard OTR imaging which exhibits a double-lobe shape.

Drawback of asymmetric OTR observation geometries however is a decrease in the overall intensity. In the ultra-relativistic approximation (which is valid for  $\gamma \geq 1000$  with accuracy better than 1%) it is possible to estimate the OTR photon yield for the cases under consideration using the formula

$$\Delta N_{ph} = \frac{\alpha}{\pi^2} \frac{\Delta\lambda}{\lambda} \int_{\Delta\Omega} \frac{\theta_x^2 + \theta_y^2}{(\gamma^2 + \theta_x^2 + \theta_y^2)} d\theta_x d\theta_y. \quad (6)$$

In the following the yield of the OTR horizontal polarization component is estimated (which is described by the first term in the bracket in Eq. (4)). For the screened geometry presented in Fig. 2 and an optical bandpass filter with  $\Delta\lambda/\lambda = 5\%$  and the same aperture ( $\theta_m = 0.1$ ), the photon yield amounts to  $\Delta N_{ph} \approx 2.4 \cdot 10^{-4}$  ph /  $e^-$ . This corresponds to an intensity level of about 25% of the unpolarized OTR using a conventional imaging scheme without screening. Performing the similar calculation for the case of asymmetric light collection and a rotation of the lens optical axis at an angle of 0.11 and the same aperture, one obtains  $\Delta N_{ph} \approx 1.4 \cdot 10^{-4}$  ph /  $e^-$ .

We believe that the proposed technique allows to achieve a submicron resolution for a transverse beam profile diagnostics which is well above the spatial resolution of the conventional OTR monitor.

## ACKNOWLEDGEMENT

The work was partly supported by the program “Nauka” of the Russian Ministry of Education and Science, grant # 3.1903.2017 and by the TPU Competitiveness Enhancement Program

## REFERENCES

- [1] M. Castellano and V. Verzilov, “Spatial resolution in optical transition radiation beam diagnostics”, *Phys. Rev. ST Accel. Beams*, vol. 1, p. 062801. 1998, doi: 1103/PhysRevAccelBeams.18.120198.
- [2] K. Kruchinin, S. T. Boogert, P. Karataev, *et al.*, in *Proc. 2<sup>nd</sup> Int. Beam Instrumentation Conf (IBIC'13)*, 16-19 Sep., Oxford, UK, p. 615.
- [3] L. G. Sukhikh, A. P. Potylitsyn, and G. Kube, “Simulation of transition radiation based beam imaging from tilted targets”, *Phys. Rev. Accel. Beams*, vol. 20, p. 032802, 2017.
- [4] A. H. Lumpkin, B. X. Yang, W. J. Berg, M. White, J. W. Lewellen, and S. V. Milton, “Optical techniques for electron-beam characterizations on the APS SASE FEL project”, *Nucl. Instrum. Meth. A.*, vol. 429, pp. 336-340, 1999. doi: 0.1016/S0168-9002(99)00373-3.
- [5] E. Chiadroni, M. Castellano, A. Cianchi, K. Honkavaara, and G. Kube, “Effects of transverse electron beam size on transition radiation angular distribution”, *Nucl. Instrum. and Methods A*, vol. 673, pp. 56-63, 2012. doi:10.1016/j.nima.2012.01.011
- [6] K. Kruchinin, A. Aryshev, P. Karataev, *et al.*, “Submicrometer transverse beam size diagnostics using optical transition radiation”, *Journal of Physics: Conference Series*, vol. 517, p. 012011, 2014. doi:0.1088/1742-6596/517/1/012011
- [7] A.P. Potylitsyn, “Image of Optical Diffraction Radiation (ODR) Source and Spatial Resolution of ODR Beam Profile Monitor”, *Advanced Radiation Sources and Applications, NATO Science Series II: Mathematics, Physics and Chemistry*, Springer, N.Y., vol. 199, pp. 149–163, 2006, doi.org:10.1007/1-40203450-4\_12
- [8] G. Kube, “Imaging with Optical Transition Radiation, Transverse Beam Diagnostics for the XFEL”, DESY, Hamburg, Germany, Rep. TESLA-FEL 2008-01.

# DESIGN AND IMPLEMENTATION OF NON-INVASIVE PROFILE MONITORS FOR THE ESS LEBT

C.A. Thomas\*, T. Grandsaert, H. Kocevar,  
O. Midttun, N. Milas, R. Miyamoto, T. Shea,  
European Spallation Source ERIC, Lund, Sweden

## Abstract

Non-invasive Profile Monitors are designed and distributed along the ESS Linac. In the Low Energy Beam Transport (LEBT), a specific one has been designed to be primarily a beam position monitor. Its main requirement is to measure the beam position with 100  $\mu\text{m}$  accuracy, and in addition it provides the beam profile and size. This performance have been shown to be possible and remains to be demonstrated experimentally. The instrument is also potentially capable of measuring the angle of the beam and its divergence. In this paper we will study the accuracy of such a measurement as function of the instrument image quality.

## INTRODUCTION

Non-invasive Profile Monitors [1–3] (NPMs) have been designed at European Spallation Source for the measurement of the beam profile at high power [4]. They are distributed from the LEBT to the last section before the target. We call NPM a transverse profile monitor based on the interaction of the residual gas with the beam of charged particles. There are two principle which the NPMs are based on. One is performing an image of the beam induced gas fluorescence [1], and the other is performing a profile of the beam induced gas ionisation [3].

However, in the LEBT, the main role of the NPM is to measure the position of the beam with respect to the reference beam axis [5]. The required position accuracy is shown to be better than 50  $\mu\text{m}$ , and it is assured by the alignment of the optical axis of the NPM in the general coordinate system in which the whole accelerator is defined. The measurement principle the NPM for the LEBT is based on imaging the gas fluorescence excited by the proton beam. The interaction of the beam with the vacuum residual gas has a same probability along the particle trajectory. Therefore, the fluorescence emission is uniform along the particle path. When projected on the image plane by an optic assembly, the image represents the trajectory of the particle, projected along the optical axis. As a result, the image from the NPM represents the beam profile along the beam trajectory, and projected along one of the transverse axis. Thus, it contains information on the beam position and angle, the size and divergence. Measurement on the image may retrieve this information, and it could be used for beam tuning applications.

In the following we will show how we model an NPM image, using beam parameters, and how the retrieval of

these parameters from image processing and analysis can be affected by the image quality.

## BEAM PROPERTIES FROM NPM IMAGE

A typical NPM image can be modeled taking into account the beam parameters, the optics parameters and the noise of the camera. Such an image can be seen in Fig. 1.

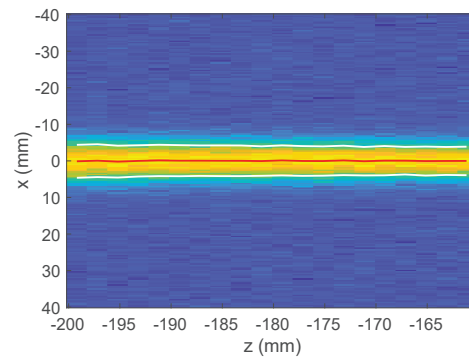


Figure 1: Model of an NPM image with ESS LEBT beam parameters. The white lines represents the beam size along the trajectory, and the red line the centre of mass, as retrieved by a Gaussian fitting algorithm. SNR = 20.

To produce this image, we have used the beam transport model of the LEBT. The transport equations are given:

$$\beta_z = \beta_0 - 2\alpha_0 z + \gamma_0 z^2 \quad (1)$$

$$\alpha_z = \alpha_0 - \gamma_0 z \quad (2)$$

$$\gamma_z = (1 + \alpha_z^2)/\beta_z \quad (3)$$

$$\sigma_x = \sqrt{\beta_z \varepsilon} \quad (4)$$

$$\sigma'_x = \sqrt{\varepsilon \gamma_z} \quad (5)$$

$$c_x = a_1 z + a_0 \quad (6)$$

in which  $z$  is the beam longitudinal propagation coordinate;  $\varepsilon = 16.8 \cdot 10^{-6}$  m.rad, the beam geometrical emittance;  $\beta_z$ ,  $\alpha_z$ ,  $\gamma_z$ , the beam Twiss parameters at the coordinate  $z$ ;  $\beta_0 = 0.11$  m,  $\alpha_0 = 1.02$ ,  $\gamma_0 = 18.54 \text{ m}^{-1}$ , the Twiss parameter at the beamwaist at the exit of the LEBT;  $\sigma_x$  the beam size, and  $\sigma'_x$  the beam divergence;  $c_x$  is the beam centroid;  $a_i$  are the coefficient for the first order polynomial describing the kick angle of the beam.

Using Eqs. 5 and 6, one can compute the beam profile along the propagation axis, assuming for instance a Gaussian distribution.

\* cyrille.thomas@ess.se

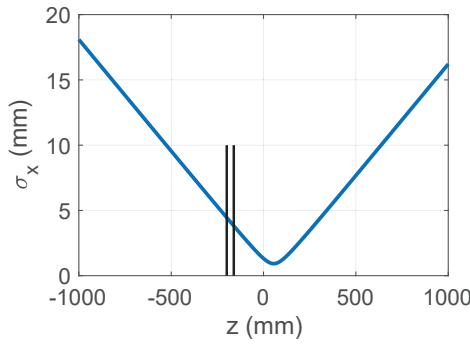


Figure 2: Beam Size along the path using Eqs. 1 to 5. The vertical lines show the field of view of the NPM.

The coordinates of one of the NPMs in the LEBT is at  $z = -180$  mm from the beamwaist in the LEBT extraction cone. The result of the calculation of the beam size along the path is shown in Fig. 2.

To generate the image shown in Fig. 1, we have generated Gaussian profiles, in which the r.m.s. size is given by Eq. 4 and the centre of mass is given by Eq. 6.

## IMAGE QUALITY AND MEASUREMENT UNCERTAINTY

The quality of the measurement of the beam parameters can be affected by several aspects from the instrument. In first place, the beam size and position can be affected by the resolution of the system. The position accuracy depends on the quality of the optical axis alignment; the precision of the position depends on the accuracy in knowing the image magnification. This has been reported in [5]. We will not discuss it in this paper.

All cameras produce an image, in which the light intensity is digitized. The image has an offset background, and the intensity is linear over a range defined by the digital scale. The linearity of the sensor response is critical to retrieve the beam profile. This can be measured and is given by camera manufacturers in the EMVA 1288<sup>1</sup> standard associated report. Most cameras, whether CCD or CMOS are relatively linear within better than 1%, which guarantees the profiles to be proportional to the beam profiles.

The other important camera property that may be critical is the total noise of the sensor. In order to model the noise, we generated images with added random noise, uniformly distributed over the image.

The expression to generate the image is then given by:

$$Im(x, z) = Nrandn(x, z) + I_0 e^{-\frac{(x-c_x(z))^2}{2\sigma_x(z)^2}} \quad (7)$$

This describes a Gaussian distribution in the axis  $x$ , which has a r.m.s size,  $\sigma_x$  and centre position,  $c_x$ , depending on the position  $z$ . The noise is generated using a random normal distribution, with an arbitrary offset equal to 50 and a typical width of 1. This noise distribution can model many ones

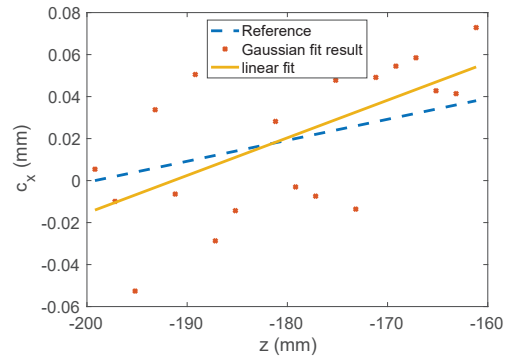


Figure 3: Kick angle of the beam as measured on the Fig. 1 generated image.

as measured on cameras like for instance the one selected for the NPM in the LEBT. The intensity scale of the image ranges over 12 bits.

In order to model the performance of the measurement of the beam size and centre of mass along the beam path we use Eq. 7, varying the intensity  $I_0$  in a range from 1 to 1000 counts. The distribution of the noise is kept at  $\sigma_{noise} = 1$  counts. This defines the signal to noise ratio:  $SNR = I_0/\sigma_{noise}$ .

## Angle Measurement Uncertainty

The beam is modeled so that it receives a kick and its centre moves along a trajectory defined by the kick angle. In the simulation, the kick angle varies from -26mrad to 26mrad. For each selected kick angle, 1000 images are produced with newly generated noise.

For each image, as shown in Fig. 1, a Gaussian fit is performed over 20 lines along 40 mm of propagation axis. The result of the fit gives the centre and size of the beam along the trajectory  $z$ .

A linear polynomial fit is performed on the centres to find out the kick angle. Figure 3 shows the beam centre trajectory as measured by the Gaussian fit. It is compared to the reference beam trajectory. The line generated by the linear polynomial fitting the centre trajectory is also shown. The SNR on the image is 50. The statistical angular measurement error is  $\Delta\theta \approx 0.5$  mrad.

The result of the simulation for a given SNR can be seen in Fig. 4. Here the SNR=100. The left axis shows the mean value of the measured angle, plotted against the reference kick angle. The error between the mean measured angle and the reference is less than 0.1%. On the right axis, the standard deviation over 1000 measured kick angles is reported. This corresponds to the statistical error of the measurement. The average error in this case is  $\Delta\theta = 0.26$  mrad.

Figure 5 summarises the results obtained for the kick angle statistical error vs. SNR. The statistical error in this particular case, where the beam size corresponds to  $\approx 10$  pixels, seems to be less than 1 mrad for SNR larger than 25.

<sup>1</sup> <https://www.emva.org/standards-technology/emva-1288/>



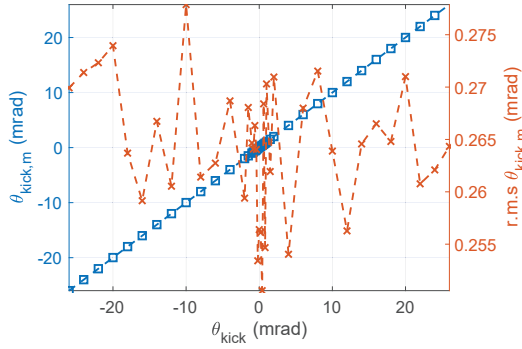


Figure 4: Kick angle and error on a measurement for an image with SNR = 100.

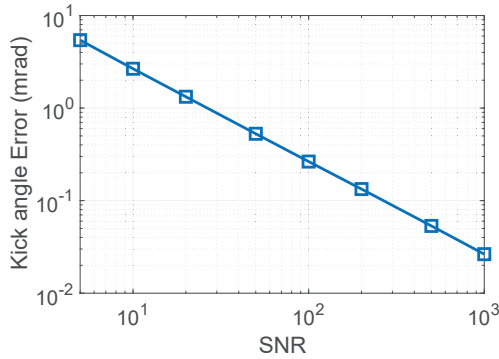


Figure 5: Kick angle statistical error as function of the SNR.

### Beam Size Trajectory Uncertainty

The beam size can be measured along the trajectory. The beam size statistical uncertainty is computed by the standard deviation of the set of measurements compared to the reference beam size. The Fig. 6 shows the standard deviation of the measured beam size,  $\Delta\sigma_x = \left\langle (\sigma_x - \sigma_{x,ref})^2 \right\rangle^{1/2} / \sigma_{x,ref}$ , relative to the reference beam size,  $\sigma_{x,ref}$ , and as function of the SNR. The statistical error on the measurement of the beam size is smaller than 3% for SNR larger than 10.

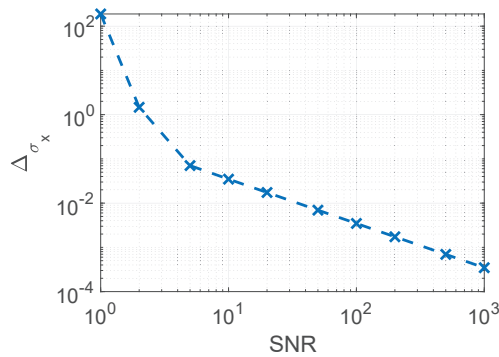


Figure 6: Standard deviation of the beam size measurement as function of the SNR and relative to the beam size.

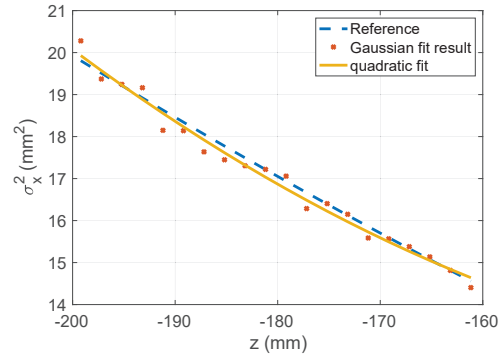


Figure 7: Square of the beam size as measured on the Fig. 1 generated image.

The beam size square is expected to be a quadratic function of  $z$ , as defined by Eqs. 1 and 4. The Gaussian variance values trajectory of each image is fitted by a second order polynomial, expressed as  $\sigma_x^2 = a_0 + a_1z + a_2z^2$ . The coefficients  $a_i$  given by the result of the fit can be compared to the reference as given by Eqs. 1 and 4.

An example of such a fit is shown in the Fig. 7. It presents the beam size square trajectory as fitted by a Gaussian, and compared to the reference. The fitting second order polynomial is also shown.

The mean values of the quadratic polynomial coefficients is shown in the Fig. 8 as function of the SNR. The deviation of the coefficients from their reference,  $\varepsilon\beta_0$ ,  $\varepsilon\alpha_0$  and  $\varepsilon\gamma_0$ , is rather large for values of the SNR smaller than 5. However, for SNR larger than 5, the relative error is less than 5%, and for SNR larger than 20 it is less than 0.5%.

The standard deviation of the quadratic coefficients measurement is shown in the Fig. 9. The plot shows the standard deviation over the set of measurements,  $\langle a_i^2 \rangle^{1/2}$ , divided by the mean values,  $\langle a_i \rangle$ . Relative spreads much smaller than unity can be seen for insignificant noise figure, typically SNR > 500. The noise has a strong impact on the variance of the measurement of the quadratic fit coefficient. This is not a surprise. The position of the NPM is far from the beam waist, where the parabola has a very small curvature. Thus, statistical deviation in the beam size measurement that is larger than the curvature impacts strongly the result of the quadratic fit.

## CONCLUDING REMARKS

The measurement of the images performed by an NPM based on residual gas fluorescence could be used to measure beam position and angle. The angle of the beam can be measured with high precision. In the example studied, for SNR > 25, the statistical error is expected to be less than 1 mrad. The accuracy of the measurement also depends on the fiducialisation of the NPM. As shown in [5] the accuracy of the position can be better than 50  $\mu\text{m}$ .

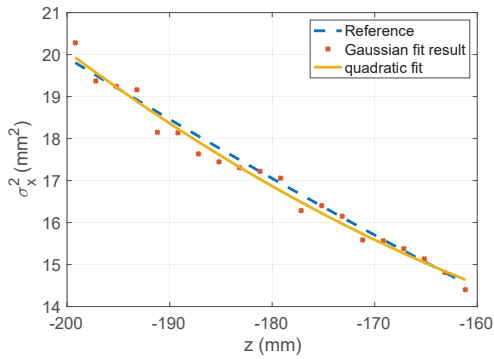


Figure 8: Mean values of the quadratic fit coefficients. Each curves is compared to their reference, as given by the Eq. 1 and 4.

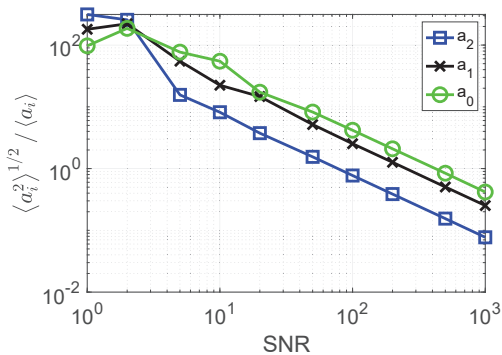


Figure 9: Relative error for the fit of the beam size square.

The beam size can also be retrieved from measurement on the image. The precision of the measurement is better than 3% for SNR larger than 10.

The beam size square trajectory can be measured on the NPM image. However, at the location of the second NPM

in the LEBT studied here, the uncertainty on the parabolic fit is highly dependent on the noise in the image. With SNR larger than 500, the fit return the parabola coefficients within the same order of magnitude. But the average value fall within few percents for SNR larger than 5.

The measurement of the beam size trajectory could also provide more information on the lattice. The Twiss parameters could be retrieved in principle, but it is not discussed in this paper. The measurement however can provide some qualitative information during the commissioning of the accelerator.

The verification of the measurements of the beam and beam size trajectories using an NPM is expected to be done while commissioning of the NPM for the LEBT.

## REFERENCES

- [1] D.P. Sandoval. Fluorescence-Based Video Profile Beam Diagnostics: Theory and Experience. In *BIW*, Santa Fe, New Mexico, USA, 1993.
- [2] P Forck and A Bank. Residual Gas Fluorescence for Profile Measurements at the GSI UNILAC. In *EPAC*, 2002.
- [3] W. H. DeLuca. Beam detection using residual gas ionization. *IEEE Transactions on Nuclear Science*, 16(3):813–822, June 1969.
- [4] B Cheymol, C Bohme, A Jansson, H Hassanzadegan, I Dolenc Kittelmann, T Shea, and L Tchelidze. Overview of the european spallation source warm linac beam instrumentation. In *Proc. of International Beam Instrumentation Conference (IBIC'13)*, International Beam Instrumentation Conference, pages 346–348, Geneva, Switzerland, Sept. 2013. JACoW.
- [5] C.A. Thomas et al. Design and Implementation of Non-Invasive Profile Monitors for the ESS LEBT. In *Proc. of International Beam Instrumentation Conference (IBIC'16)*, Barcelona, Spain, Sept. 13-18, 2016, number 5 in International Beam Instrumentation Conference, pages 552–555, Geneva, Switzerland, Feb. 2017. JACoW. doi:10.18429/JACoW-IBIC2016-TUPG80.

# BEAM-GAS IMAGING MEASUREMENTS AT LHCb

G. Coombs\*, CERN, Geneva, Switzerland and University of Glasgow, Glasgow, United Kingdom  
M. Ferro-Luzzi, R. Matev, CERN, Geneva, Switzerland  
on behalf of the LHCb Collaboration

## Abstract

The LHCb detector is one of the four large particle physics experiments situated around the LHC ring. The excellent spatial resolution of the experiment's vertex locator (VELO) and tracking system allows the accurate reconstruction of interactions between the LHC beam and either residual or injected gas molecules. These reconstructed beam-gas interactions gives LHCb the ability, unique among experiments, to measure the shape and the longitudinal distribution of the beams. Analysis methods were originally developed for the purpose of absolute luminosity calibration, achieving an unprecedented precision of 1.2% in Run I. They have since been extended and applied for online beam-profile monitoring that is continuously published to the LHC, for dedicated cross-calibration with other LHC beam profile monitors and for studies of the dynamic vacuum effects due to the proximity of the VELO subdetector to the beam. In this paper, we give an overview of the LHCb experience with beam-gas imaging techniques, we present recent results on the outlined topics and we summarise the developments that are being pursued for the ultimate understanding of the Run II measurements.

## INTRODUCTION

The Beam-Gas Imaging technique in use at LHCb is unique among particle physics experiments in allowing the independent measurement of charged particle beam profiles of colliding beams. Its principal application is to provide measurements for the precise luminosity calibrations necessary for absolute cross-section determination [1] but it also permits a variety of additional beam diagnostic measurements. This technique was first developed and put to use during Run I of the LHC (from 2009–2013) when a record precision for the luminosity measurement at a bunched beam hadron collider was achieved [2]. This paper presents the technique's current use at LHCb and a set of additional applications developed during Run II.

## THE LHCb DETECTOR

LHCb is a flavour physics experiment designed to observe the decays of  $b$  and  $c$  quarks produced in the high energy hadronic collisions taking place at the LHC [3]. The relatively long lifetimes of the decay products produced by these interactions necessitate a precise measurement of both primary and secondary decay vertices. This is achievable due to the excellent spatial resolution of the detector's tracking system, most notably the VELO subdetector. A schematic

diagram of the full detector layout, including the various subdetectors, can be seen in Fig. 1.

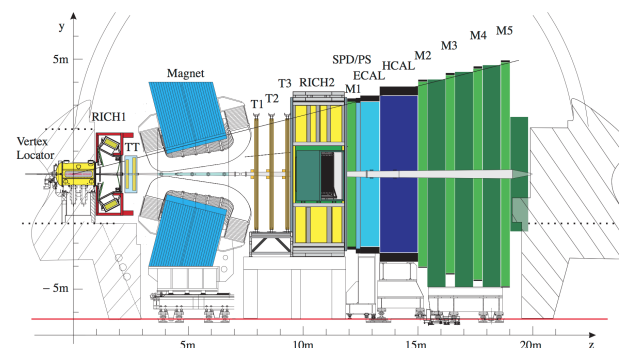


Figure 1: A side view of the LHCb detector showing the various subdetectors that make up the full experiment. The VELO is shown on the far left and the downstream tracking system is made up of the Trigger Tracker (TT), located before the magnet, and the tracking stations T1–T3, located after the magnet [3].

## BEAM-GAS IMAGING

The VELO subdetector can also be used for the precise reconstruction of inelastic interactions between the high-energy proton beam and gas molecules within the LHCb interaction region. These reconstructed beam-gas vertices can then be used to measure the properties of the colliding beams such as their profiles, sizes or crossing angle.

## Reconstruction

The reconstruction of these vertices uses hits in the VELO's 21 silicon strip  $r$ - $\phi$  sensor modules to form tracks which are then combined to find vertices using LHCb's pattern-matching algorithms [4]. A selection based on the vertex track multiplicity and spatial coordinates is applied in order to enhance the sample of beam-gas vertices. Vertices are required to have at least five constituent tracks and to fall within the longitudinal range of the VELO acceptance ( $\pm 1500$  mm). There is an additional radial cut of 4 mm to exclude any secondary interactions with the detector material. The directionality of the constituent tracks is then used to assign vertices to a given beam with a requirement that vertices assigned to beam 1(2) have all tracks in the forward(backward) direction. Forward tracks are defined as those tracks moving from the interaction point towards the LHCb magnet, i.e. from left to right in Fig. 1.

\* george.rufus.coombs@cern.ch

## Gas Injection

While beam-gas interactions do take place during the nominal running of the LHC their rate is very low. In order to obtain enough vertices for a precise profile measurement in a reasonable period of time a gas injection system was developed to temporarily increase the gas pressure in the beam pipe near LHCb. Noble gas species are used for the injection to avoid damaging the NEG coating of the LHC beam pipe, with helium, neon and argon having been employed to date. This gas injection technique increases the beam-gas interaction rate by more than an order of magnitude, as can be seen from Fig. 2. The full description of this system is detailed in [2].

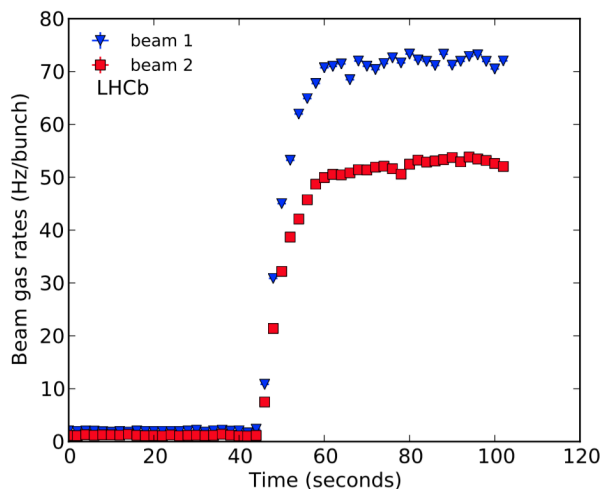


Figure 2: The effect of neon gas injection on the beam-gas interaction rate observed by LHCb during one fill of the LHC [1].

## Beam Profile Measurements

In order to accurately estimate the transverse beam profile, it is first necessary to measure the trajectory of the beam, typically coming at an angle, and subsequently correct the observed vertex distributions. The beam slopes and positions are calculated from a linear fit to the observed distributions of each beam in the  $zx$  and  $zy$  planes. An example of such a fit is shown in Fig. 3. The corrected profile can then be fitted with an appropriate model. For beam width measurements that are used to compare with other LHC instrumentation a simple Gaussian shape is used for consistency. To achieve the ultimate precision for luminosity calibrations, luminous region vertex distributions are added in global fit and the beam shape is modelled with a sum of Gaussian functions, as detailed in [2].

## Detector Resolution

Another quantity that must be corrected for when determining the beam profile is the finite resolution of the detector as the observed vertex position distribution is a convolution of the true beam distribution with the resolution function.

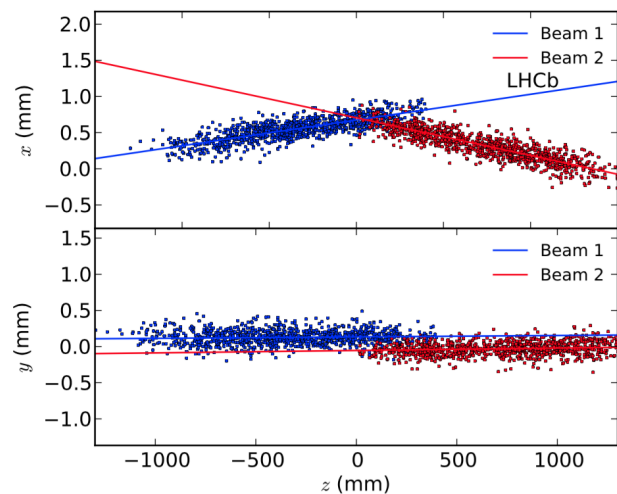


Figure 3: Positions of beam gas vertices in the  $zx$  and  $zy$  planes with the lines showing the fits to the slopes of the two beams. The offset between the two beams in  $y$  is also clearly visible. Figure taken from [1].

A data-driven method of measuring the resolution is used where the tracks used to reconstruct each vertex are divided up randomly into two nearly equal groups and then a new vertex is refitted from each group. The distribution of the difference in spatial position between the two resultant vertices is taken as an estimate of the resolution function. The transverse position resolution for beam-gas vertices is found to be of the order  $20\mu\text{m}$  to  $80\mu\text{m}$ , depending on the vertex track multiplicity and longitudinal position, while the nominal beam size at LHCb is about  $30\mu\text{m}$ . For dedicated luminosity calibration data taking the beam size is increased in order to reduce the relative importance of the resolution.

## Cross-Calibration

In October 2016 a machine development (MD) session was dedicated to the cross-calibration of the various emittance measuring devices around the LHC ring. Bunches of markedly different emittances were injected into the LHC and their emittances measured by each piece of instrumentation. This allowed an in depth study of possible systematic biases in the beam-gas imaging measurement. This effort was detailed thoroughly in references [5, 6].

## GHOST AND SATELLITE CHARGES

The term ghost charge refers to any charge found outside the nominally filled 25 ns bunch slots around the LHC ring. Satellite charges are those charges sitting within a filled bunch slot but outside the central 2.5 ns RF bucket of that slot. Both sets of charges are picked up by the LHC direct current current transformers (DCCTs) but do not contribute to the collisions seen by the LHC experiments. It is thus necessary to measure the fraction of these charges in order to correct the precise total charge from the DCCTs, which is used for normalisation in luminosity calibrations. The size



of this correction varies from the percent (typical with ion beams) to the per mille level (typical during nominal proton physics) in Run II.

LHCb can measure the fraction of ghost charges by counting the number of beam-gas interactions observed during empty-empty crossings, where both slots are nominally empty. Counts are normalised to absolute charge using data from beam-empty crossings, where one of the two beams contains a nominally filled bunch with a known intensity. Both satellite and ghost charges are visible to the LHC longitudinal density monitor (BSRL), which makes use of the synchrotron light emitted by the circulating particles in a dedicated undulator to measure the longitudinal charge distribution [7, 8].

The importance of having an independent measurement to cross-check the BSRL results was demonstrated in November 2017 during the 2.5 TeV low-energy run of the LHC. As can be seen in Fig. 4 the BSRL measurement of the ghost charge fraction appears to decrease throughout the fill while the LHCb measurement increases. This is suspected to be caused by de-bunching of the LHC beam, as also seen in another low energy fill in 2015 [9]. This causes charges to be pushed outside the buckets defined by the LHC RF system. This de-bunched charge is seen as a background by the BSRL and subtracted from its measurement as part of a baseline correction. From the LHCb point of view, however, these charges still produce beam-gas interactions and thus add to the total ghost charge fraction. The difference between the DCCT and FBCT total charge values confirms the trend seen by LHCb. This provides a cross-check as any circulating de-bunched beam will be seen by the DCCT direct current measurement but not by the time-gated FBCT measurement. The uncorrected BSRL data also show an upward trend throughout the fill and their absolute offset was confirmed to be in agreement with the standby signal from the detector in the absence of beam.

## Time Profile

In order to investigate this suspected de-bunching of the beam a new technique was implemented to produce the first LHCb measurement of the time profile within a 25 ns bunch slot. This technique makes use of drift time measurements from LHCb's Outer Tracker (OT) to assign time coordinates to reconstructed vertices. Due to the asymmetric geometry of the LHCb detector it is only possible to make measurements for LHC beam 1.

The OT is a gaseous detector forming the outer section of the three downstream tracking stations T1–T3. These stations contain just under 100 modules with each module made up of two staggered layers of drift tubes. The arrival times of ionization clusters produced by charged particles are measured with respect to the beam crossing time (from the LHC clock) and then digitised for each 25 ns slot. This digitised value is given in units of 0.4 ns, as the 25 ns window is encoded with 6 bits. As of Run II these time values are now calibrated in real-time as described in Ref. [10]. The improved drift-time resolution of the OT hits in Run II allows

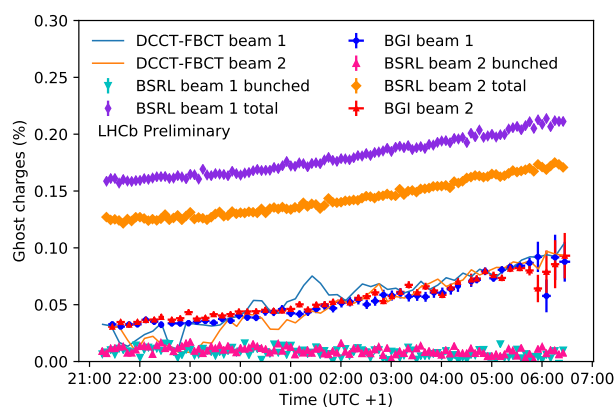


Figure 4: The evolution of the ghost charge fraction throughout LHC fill no. 6380 as measured with the LHCb BGI method and the LHC BSRL instrument. The BSRL values are shown with (bunched) and without (total) the background subtraction. The difference between the DCCT and FBCT total charge measurements, normalised to the earliest LHCb data points for each beam, is shown as a cross-check.

timing information to be assigned to tracks and vertices. Drift time residuals are calculated as the difference between the measured hit drift time and the prediction from the fitted track position. The time value for a single track can then be defined as the weighted average of the drift time residuals from the hits making up the track. The time value for a vertex is finally calculated as the weighted average of the track times of all tracks associated with that vertex.

The standard LHCb reconstruction expects interactions to occur within the narrow window of the luminous region time distribution with a spread of 0.25 ns. Therefore, the observation of the larger time deviations across the 25 ns slot, associated with ghost charges, requires a modification of the reconstruction chain, where various windows related to OT hit timing are relaxed. In addition, the fitted track trajectory, and hence the drift time residuals, is biased by the assumed zero time origin of the interaction, which in turn leads to a bias in the measured track time. To overcome this, multiple reconstructions of each event are performed, each time shifting all OT hit times by a constant in steps of 2.5 ns covering the full 25 ns slot. The reconstructed event with the best global fit quality of all tracks containing OT hits is retained. The value of the applied shift is then summed with the measured residual to give the time value. Using beam-gas interactions from beam-empty crossings, which have a narrow, centred time distribution, we find a vertex time resolution on the order of 0.5 ns.

The first such measurement can be seen in Fig. 5, presenting data from two distinct time periods during the 2017 LHC 2.5 TeV calibration session. The vertex time values relative to the central bucket are shown integrated across all empty-empty crossings for the two time periods. The data from the later time period shows an increase in the ghost charge across all buckets and the 2.5 ns spacing observed

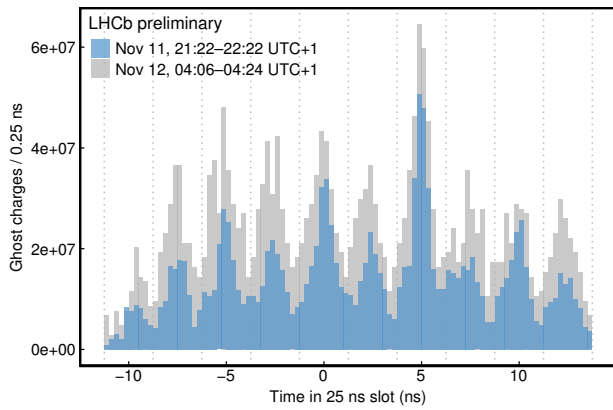


Figure 5: Distribution of measured vertex time for interactions of beam 1 with the gas in the range  $-11.25$  ns to  $13.75$  ns, integrated over all empty-empty crossings, for two time periods during LHC fill no. 6380.

between peaks in each case gives a hint of the de-bunching taking place during this fill. Under nominal LHC operation, at 6.5 TeV, the 200 MHz RF structure of SPS is preserved and the bunch trains provided by the injector chain to the LHC show peaks in their longitudinal charge distribution every 5 ns [11]. However, due to suboptimal RF set up during 2.5 TeV operation, charge seems to leak out of this 5 ns structure and collect in the stable 2.5 ns buckets of the LHC's 400 MHz RF. Our present understanding of the time resolution limits our ability to distinguish potential de-bunched charge sitting between RF buckets from a simple overlap of adjacent peaks. We also need to understand to what extent the trigger and reconstruction efficiency of these measurements reduces at the trailing and leading edges of the bunch slot where the detector timing is not optimal.

## DYNAMIC VACUUM EFFECTS

Beam-induced dynamic vacuum effects are well documented at LHCb with a five fold increase in the vacuum pressure observed under the influence of 1380 bunches of  $2 \times 10^{14}$  protons [12]. It has been proposed that this effect could be enhanced by the movement of the RF foil that isolates the VELO detector modules, which approaches to within 5 mm of the collision point after the declaration of stable beams. If this is the case the effect could become more important in the context of the new VELO design for the LHCb upgrade [13] and as the LHC moves to High Luminosity conditions.

In order to investigate a possible effect, the change in the observed rate of beam-gas interactions inside and outside the volume between the two RF boxes, before and after the VELO closing was measured. To achieve this without biasing the measurement through the change in geometric acceptance due to movement of the VELO, it is necessary to make use of LHCb's downstream tracking system for the vertex reconstruction (see Fig. 1). These tracking stations are normally used in conjunction with the VELO tracks to

form what are known as long tracks. Here, however, we reconstruct beam-gas vertices using only the downstream stations, achieving a transverse resolution of 1.9 mm in  $x$ , 1.3 mm in  $y$  and a longitudinal resolution of  $\sigma_z = 11$  cm.

This proposed effect would cause a beam-intensity dependent pressure differential between the residual gas inside and outside the VELO. Vertices are classified as inside or outside the VELO based on the position of the VELO edges as measured in Ref. [14]. Margins of  $\pm 2\sigma_z$  are used to avoid cross-feed between the samples, resulting in  $[-13, 53]$  cm ( $[-200, -57] \cup [97, 200]$  cm) for the inside (outside) range. A radial cut of 4 mm is applied in order to limit contamination from material interactions. The longitudinal variation of the vertex reconstruction efficiency,  $\rho$ , is estimated when the VELO is open as the ratio of the rates of beam-gas vertices in the two fiducial regions,  $R_{in|open}/R_{out|open}$ . Finally, after the VELO is closed the beam-gas vertex rates are used to estimate the pressure inside relative to outside,  $p_{in}/p_{out} = R_{in|closed}/R_{out|closed}/\rho$ , thus avoiding the need of a precise baseline pressure measurement.

The outlined method is applied in two separate LHC fills of differing beam intensities. At a lower intensity data come from LHC fill no. 6012 with 57 bunches per beam and at the higher intensity from LHC fill no. 6245 with 1916 bunches per beam. Under high intensity conditions only vertices from bunches crossing the opposing beam's abort gap are used in order to eliminate contamination from ghost charge  $p$ - $p$  collisions. The data at low intensity is used as a control sample, assuming the effect there is small with respect to a potential effect at high intensity.

The longitudinal variation of the reconstruction efficiency,  $\rho$ , is measured with the data from the two fills and the difference of 8% is conservatively taken as a systematic uncertainty. Varying the boundaries of the fiducial volumes has a negligible impact on the result. A preliminary relative pressure change,  $p_{in}/p_{out}$ , of  $1.21 \pm 0.02 \pm 0.08$  ( $1.04 \pm 0.04 \pm 0.08$ ) is observed at high (low) intensity, where the first uncertainty is statistical and the second is systematic, indicating a measurable pressure increase with closed VELO at high beam intensity.

## CONCLUSIONS

The BGI technique continues to be a powerful tool for beam diagnostic measurements at the LHC. A set of new applications of this technique developed during Run II are described along with their first results. LHCb's ability to measure the temporal charge distribution of an LHC beam at the nanosecond scale is demonstrated and a first study of dynamic vacuum effects caused by the VELO RF foil is presented.

## ACKNOWLEDGEMENTS

Our thanks and gratitude go to our colleagues from the CERN BE-BI group for their instrumentation expertise and especially to Marcus Palm for his kind help in understanding the BSRL measurements.

## REFERENCES

- [1] LHCb collaboration, R. Aaij *et al.*, “Precision luminosity measurements at LHCb”, JINST 9, P12005, 2014.
- [2] C. Barschel, “Precision luminosity measurements at LHCb with beam-gas imaging”, Ph.D. thesis, RWTH Aachen University, 2014.
- [3] LHCb collaboration, A. A. Alves Jr. *et al.*, “The LHCb detector at the LHC”, JINST 3, S08005, 2008.
- [4] M. Kucharczyk, P. Morawski, and M. Witek, “Primary Vertex Reconstruction at LHCb”, LHCb-PUB-2014-044.
- [5] T. Hadavizadeh *et al.*, “Transverse Emittance Measurements Using LHCb’s Beam-Gas Interactions”, Proceedings of IPAC2017, Copenhagen, Denmark
- [6] R. Alemany-Fernandez *et al.*, “Comparison of Transverse Emittance Measurements in the LHC”, Proceedings of IPAC2017, Copenhagen, Denmark
- [7] A. Alici *et al.*, “Study of the LHC ghost charge and satellite bunches for luminosity calibration”, CERN-ATS-Note-2012-029 PERF, BCN WG Note 4, 2012
- [8] M. Palm *et al.*, “Near-Saturation Single-Photon Avalanche Diode Afterpulse and Sensitivity Correction Scheme for the LHC Longitudinal Density Monitor”, 3rd International Beam Instrumentation Conference, Monterey, California, 2014
- [9] M. Rihl, “Development of a non-destructive beam-profile monitor based on scintillating fibre planes and SIPMs” Ph.D. thesis, Vienna Technical University, 2018
- [10] P. d’Argent *et al.*, “Improved performance of the LHCb Outer Tracker in LHC Run 2”, JINST 12, P11016, 2018
- [11] A. Boccardi *et al.*, “LHC Luminosity calibration using the Longitudinal Density Monitor”, CERN-ATS-Note-2013-034 TECH, 2013
- [12] R. Aaij *et al.*, “Performance of the LHCb Vertex Locator”, JINST 9, P09007, 2014
- [13] LHCb Collaboration, “LHCb VELO Upgrade Technical Design Report”, CERN-LHCC-2013-021, 2013
- [14] M. Alexander *et al.*, “Mapping the material in the LHCb vertex locator using secondary hadronic interactions”, JINST 13, P06008, 2018

# RECENT RESULTS ON NON-INVASIVE BEAM SIZE MEASUREMENT METHODS BASED ON POLARIZATION RADIATION

L. Bobb, Diamond Light Source, Oxfordshire, UK

M. Bergamaschi, R. Jones, R. Kieffer, T. Lefevre, S. Mazzoni<sup>†</sup>, F. Roncarolo, CERN, Geneva, CH  
M. Billing, J. Conway, M. Forster, Y. Padilla Fuentes, J. Shanks, S. Wang, L. Ying, Cornell University, Ithaca, USA

P. Karataev, K. Lekomtsev, JAI at Royal Holloway University of London, Egham, UK

A. Aryshev, N. Terunuma, KEK, Tsukuba, Japan

V.V. Bleko, A. S. Konkov, A. P. Potylitsyn, Tomsk Polytechnic University, Tomsk, Russia

## Abstract

We present recent results on non-invasive beam profile measurement techniques based on Diffraction Radiation (DR) and Cherenkov Diffraction Radiation (ChDR). Both methods exploit the analysis of broadband electromagnetic radiation resulting from polarization currents produced in, or at the boundary of, a medium in close proximity of a charged particle beam. To increase the resolution of DR, measurements were performed in the UV range at a wavelength of 250 nm. With such configurations, sensitivity to the beam size of a 1.2 GeV electron beam below 10  $\mu\text{m}$  was observed at the Accelerator Test Facility (ATF) at KEK, Japan. In the case of the ChDR, a proof of principle study was carried out at the Cornell Electron Storage Ring (CESR) where beam profiles were measured in 2017 on a 5.3 GeV positron beam. At the time of writing an experiment to measure the resolution limit of ChDR has been launched at ATF where smaller beam sizes are available. We will present experimental results and discuss the application of such techniques for future accelerators.

## INTRODUCTION

Non-invasive beam profile measurement techniques offer the advantage of providing beam size information without inserting an object in the beam path, as is required in more traditional methods such as profile measurement using wire scanners, Optical Transition Radiation (OTR) or scintillation screens. There are two main reasons for choosing such methods: being capable of measuring high intensity beams that would destroy any interceptive devices and avoiding any blow-up in emittance due to the interaction of the particles with material. Non interceptive methods can therefore allow a continuous monitoring of the transverse beam size during machine operation. This is the case of the proposed Compact Linear Collider (CLIC), where charge densities up to  $10^8 \text{ nC/cm}^2$  can be reached in the main beam [1], a value that is approximately 100 times higher than the damage limit of the best thermal resistant materials such as Be or SiC.

We report here on the status of two projects that aim at studying Diffraction radiation (DR) and Cherenkov Diffraction Radiation (ChDR) as candidates for non-invasive

beam profile measurement techniques. In DR, beam size information is obtained through the analysis of the far-field angular distribution of light produced when the beam passes through a narrow slit in a metallic screen [2]. In ChDR, light is produced at the boundary of a dielectric material (eg: fused silica) close to the beam path. Notwithstanding the differences in terms of geometry and properties of the emitted radiation, DR and ChDR are based on a similar physical mechanism, that of emission by polarisation currents induced at the surface of a medium [3] by the electromagnetic field of a relativistic particle. This electromagnetic field can be considered as quasi-transverse one, with an effective field radius given by

$$l = \gamma \lambda / 2\pi \quad (1)$$

where  $\gamma$  is the Lorentz factor and  $\lambda$  the wavelength of observation. As a consequence, measurement methods based on DR / ChDR work when the impact parameter  $h$  of the target (the half aperture of a slit in the case of DR, the distance between beam path and crystal edge for ChDR) satisfies the condition  $h \leq l$ . If we consider the visible spectrum (e. g.  $\lambda = 500 \text{ nm}$ ) and relativistic electrons at 1 GeV ( $\gamma \cong 2000$ ), we will obtain an appreciable DR/ChDR emission for  $h \leq 160 \mu\text{m}$ , a condition that can be attained and controlled experimentally.

While DR is a more established technique, the first proposal using it for beam diagnostics dating back to 1998 [4], ChDR can still be considered to be at a proof of concept stage. We will therefore report on these two separately throughout this paper.

## STATUS OF DR EXPERIMENT AT ATF2

A DR setup was installed in 2016 in the extraction line of the Accelerator Test Facility 2 (ATF2) in KEK. A description of the instrument and target can be found in [5]. In the course of 2017, the instrument has been upgraded to its final configuration (see Fig. 1).

<sup>†</sup> email: stefano.mazzoni@cern.ch



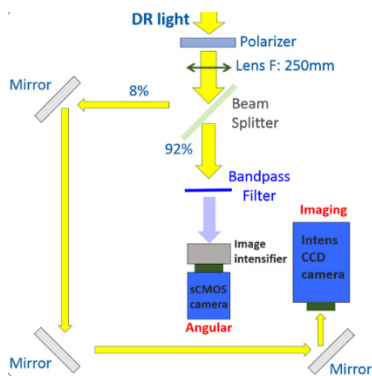


Figure 1: Sketch of the DR setup at ATF2.

DR is produced when the beam passes through a slit with a vertical aperture ranging from 50 to 200  $\mu\text{m}$  and is emitted in the direction of the extraction viewport at an angle of  $40^\circ$  with respect to the beam. After passing through a motorised polariser positioned just outside the extraction viewport, DR is split into two separate optical lines. The “imaging” line creates a 1:3.6 magnified image of the slit onto a gated intensified camera (pco DICAM Pro with GaAs photocathode) which is used for monitoring and alignment purposes. This line is also used to check the position and shape of the beam on an OTR screen and to ensure that the beam is properly centred in the DR slit. The “Angular” line records the far-field DR signal. Far-field conditions are achieved by placing the sensor (a pco Edge 4.2 LT sCMOS coupled to a Hamamatsu C9547 gated image intensifier unit) at the back focal plane of a 2” diameter, 250 mm focus plano-convex lens (LA4538 from Thorlabs). A filter wheel equipped with bandpass filters is positioned between the lens and intensified camera, hosting visible ( $400 \pm 10 \text{ nm}$ ,  $400 \pm 40 \text{ nm}$ ,  $600 \pm 40 \text{ nm}$ ) and UV ( $250 \pm 40$ ,  $230 \pm 10$ ) bandpass filters. The intensified camera is mounted on a motorised stage to compensate for the variation of back focal length as a function of the wavelength of observation.

Beam size measurement using DR is based on the correlation between the visibility (defined as  $V = I_{\min}/I_{\max}$ ) of the projected vertical polarisation component (PVPC) of the angular distribution of intensity of DR with the transverse beam profile [6]. In the left hand side of Fig. 2 we show the vertically polarised signal with the characteristic main lobes and side fringes typical of DR. The PVPC is obtained by integrating the image between the two vertical red lines. The result, plotted on the right side of Fig. 2, shows the  $I_{\min}$  and  $I_{\max}$  used to calculate the visibility. As the intensity of the peaks is not equal,  $I_{\max}$  is calculated as the average value of the two main peaks.

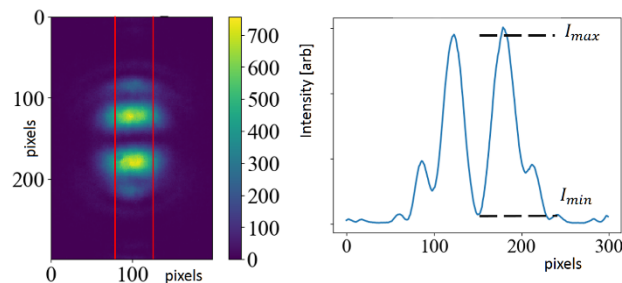


Figure 2: Vertically polarised DR pattern at  $400 \pm 40 \text{ nm}$  (left) and corresponding PVPC (right).

With the present setup we took data at ATF2 during shifts in November 2017 and February 2018. In order to improve the resolution, measurements were performed in the UV range at 250 nm. Figure 3 shows the PVPC visibility of DR acquired with a slit width of  $49.7 \mu\text{m}$ . A  $100.0 \mu\text{m}$  wide mask was used to cut out the synchrotron radiation contribution. The expected vertical beam size ( $\sigma$ ) measured with the imaging line and an OTR screen placed at the same position of the slit is  $5 \mu\text{m}$ .

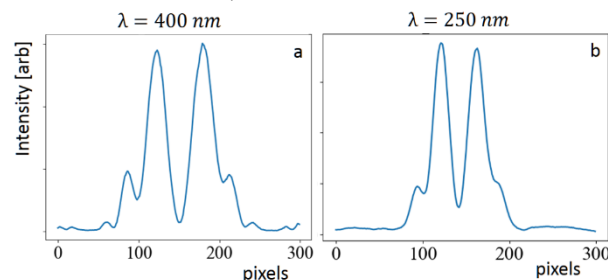


Figure 3: PVPC at 400 nm (a) and at 250 nm (b) using a  $49.7 \mu\text{m}$  slit for a transverse beam size of  $5 \mu\text{m}$

It can be seen that the signal at 250 nm has a larger visibility, with  $V_{250} = 0.145 \pm 0.013$  (statistical) and  $V_{400} = 0.05 \pm 0.013$ . The latter is close to the noise floor, with  $I_{\min}$  is basically at the same level of the image background. DR at 400 nm is therefore not sensitive to such small beam sizes, as a change of beam size will not produce a change in visibility. This is not the case for 250 nm, where a non-zero visibility is observed for a beam size below  $10 \mu\text{m}$  [7].

## STATUS OF CHDR STUDIES

The first observation of incoherent ChDR was performed at CESR with a 5.3 GeV positron bunch of up to 2.5 nC, corresponding to a circulating beam current of 1 mA [8], in an experiment aimed at measuring the light yield in the visible range as a function of the impact parameter defined in eq. 1. The radiator used is a triangular prism made of high purity fused silica (see Fig. 4) mounted on a rotation stage to keep it parallel to the beam path so as to have a constant value of the impact parameter along its length. The side facing the beam is 2 cm long.

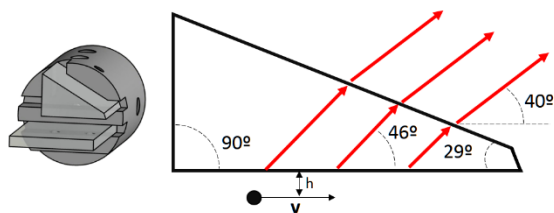


Figure 4: Section of the fused silica prism used in the ChDR setup at CESR.

The target was designed to send the ChDR to an optical system composed of a polariser, a bandpass filter at  $600 \pm 10$  nm and a 500 mm plano-convex lens. This forms the image of the radiator face (beam side) onto a Proxision proxikit gated intensifier with multialkali photocathode coupled to an AVT Manta 145G CCD camera.

The total absolute photon yield of ChDR has been measured as a function of the impact parameter [8]. As expected from polarization radiation theory, the light intensity increases exponentially for smaller impact parameters. At  $h = 1$  mm, the yield produced by the 2 cm-long radiator at a wavelength of  $600 \pm 10$  nm corresponds to  $0.8 \times 10^{-3}$  photons per turn per particle, which is in good agreement with theoretical predictions [8]. This would bring the photon intensity radiated in the entire wavelength range of 200–2000 nm to 0.1 photon per turn per particle for the same impact parameter. This number is comparable to the light intensity generated by backward transition radiation and exceeds, by at least one order of magnitude, the light intensity emitted by DR from a conducting slit of similar aperture. This relatively large yield coupled to the non-invasive nature of ChDR opens the possibility of its use as a beam profile or position monitor.

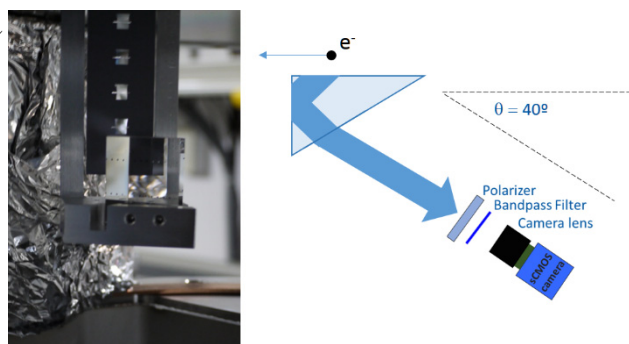


Figure 5: The ChDR prism radiator as seen from the camera (left) and a sketch of the setup (right).

With this motivation, in May 2018 the DR setup at ATF2 described in the previous section was modified to perform ChDR measurement. The extremely small, sub-micron [9] beam size that can be achieved at ATF2 is ideal to measure the ultimate resolution of ChDR and to compare it with predictions from ongoing theoretical work. The modification at ATF2 involved adding a fused silica triangular prism similar to the one of Fig. 4 at the bottom of the DR slit holder (see Fig 5). The target shape is such that ChDR is sent through a viewport positioned at  $40^\circ$  with respect to

the beam path. The ChDR then goes through a polariser and a bandpass filter before being recorded with the DR sCMOS camera described in the previous section with a 2x extended hyperspectral 60 mm macro lens from Jenoptik.

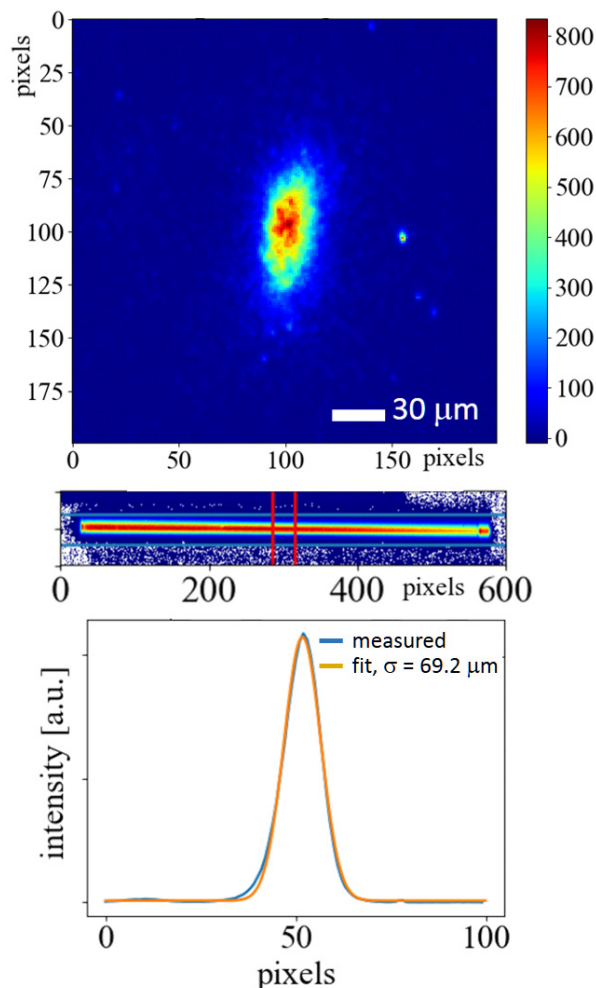


Figure 6: Preliminary ChDR beam size measurements: OTR beam profile (top), ChDR radiator image (middle), vertical beam profile (bottom).

With this setup, the vertical transverse beam profile was capable of being measured using the ChDR signal. The beam was configured to have the smallest possible horizontal beam size, of the order of a few tens of micrometres. Such a configuration allows the impact parameter to be defined with minimum uncertainty, as the transverse size of the beam is small compared with its average distance from the target edge. This means that the results can be better compared with theoretical predictions for photon yield and the ChDR intensity profile at the target surface.

In our case, at the minimum impact parameter  $h_{min} \cong 250$   $\mu\text{m}$ , we obtain a maximum uncertainty of 12 % ( $\sigma$ ). When the instrument is properly aligned and set-up, the vertical polarisation component of the ChDR beam is clearly visible across the side of the crystal facing the beam (see centre image of Figure 6). It can be seen that the width of the ChDR signal has a slight dependence on the transverse position across the target.

This is due to a combination of factors that are currently still under investigation, including a residual angle between the crystal face and the beam trajectory, the depth of field of the imaging system and possible off-axis aberrations of the optical systems. From the analysis of the central part of the crystal (between the two vertical red lines in the central image of Figure 6) a vertical beam profile with  $\sigma = 69.2 \mu\text{m}$  is measured. This is in good agreement with an OTR based measurement performed under the same beam conditions, which gave an rms beam profile of  $67.22 \pm 1.36 \mu\text{m}$ . While a detailed analysis of the results is still ongoing, this preliminary result already shows that the ChDR technique is capable of measuring beams as small as  $70 \mu\text{m}$ .

## CONCLUSIONS

An overview of recent results with non-invasive transverse beam profile measurement techniques based on DR and ChDR has been presented. In the case of DR, sensitivity to below  $10 \mu\text{m}$  ( $\sigma$ ) beam has been demonstrated when observing in the UV regime below  $250 \mu\text{m}$ . Notwithstanding this remarkable performance, DR still requires some effort in the measurement preparation (centering of the beam in the target slit) and data analysis. In addition, DR is quite sensitive to parasitic light (typically synchrotron radiation) that can affect the visibility. For these reasons, additional studies should be dedicated to the optimisation of DR for operational use.

The application of ChDR to beam size measurement is a very recent idea, with this paper presenting the very first results on small  $< 100 \mu\text{m}$  beam. ChDR has the advantage of a relatively large light yield in the visible range, a simple experimental setup and a target geometry that requires a relatively uncomplicated alignment when compared to DR. Being a recent technique, ChDR still requires a number of studies to understand its theoretical resolution limit and any additional experimental or instrumental factors that might limit it. To this purpose, the instrument currently installed at ATF2 will be modified for future high resolution studies with micron sized beams

## REFERENCES

- [1] M Aicheler, P. Burrows, M. Draper, T. Garvey, P. Lebrun, K. Peach, N. Phinney, H. Schmickler, D. Schulte and N. Toge, *A Multi-TeV Linear Collider Based on CLIC Technology: CLIC Conceptual Design Report*. Geneva, CH: CERN, 2012
- [2] R. B. Fiorito *et al.*, “Diffraction Radiation Diagnostics for Moderate to High Energy Charged Particle Beams”, *Nucl. Instr. Meth.*, vol. B173, pp. 67-82, 2001, doi: 10.1016/S0168-583X(00)00066-5
- [3] D. V. Karlovets *et al.*, “Diffraction radiation from a finite-conductivity screen”, *JETP Lett.*, vol. 90, p. 326, 2009, doi: 10.1134/S0021364009170032
- [4] M. Castellano, “A new non-intersecting beam size diagnostics using diffraction radiation from a slit”, *Nucl. Instr. Meth.*, vol. A394, pp. 275-280, 1997, doi: 10.1016/S0168-9002(97)00570-6
- [5] M. Bergamaschi *et al.*, “Diffraction Radiation for Non-Invasive, High-Resolution Beam Size Measurements in Future Linear Colliders”, in *Proc. 8th Int. Particle Accelerator Conf. (IPAC'17)*, Copenhagen, Denmark, May 2017, p. 381, doi: 10.18429/JACoW-IPAC2017-MOPAB111
- [6] P. Karataev *et al.*, “Beam-Size Measurement with Optical Diffraction Radiation at KEK Accelerator Test Facility”, *Phys. Rev. Lett.*, vol. 93, p. 244802, 2004, doi: 10.1103/PhysRevLett.93.244802
- [7] M. Bergamaschi *et al.* “Non invasive micron-scale particle beam size measurement using Optical Diffraction Radiation in the ultra violet wavelength range”, manuscript in preparation
- [8] R. Kieffer *et al.*, “Direct Observation of Incoherent Cherenkov Diffraction Radiation in the Visible Range”, *Phys. Rev. Lett.*, vol. 121, p. 054802, 2018, doi: 10.1103/PhysRevLett.121.054802
- [9] K. Kruchinin *et al.*, “Sub-micrometer transverse beam size diagnostics using optical transition radiation”, *J. Phys: Conf. Ser.*, vol. 517, p. 012011, 2014, doi:10.1103/PhysRevAccelBeams.18.120198



# A MULTIPURPOSE SCINTILLATING FIBRE BEAM MONITOR FOR THE MEASUREMENT OF SECONDARY BEAMS AT CERN

I. Ortega Ruiz\*, L. Fosse, J. Franchi, A. Frassier, J. Fullerton, J. Kral, J. Lauener, T. Schneider, J. Spanggaard, G. Tranquille, CERN, 1211 Geneva, Switzerland

## Abstract

A scintillating fibre beam monitor has been developed at CERN for the measurement of low energy and low intensity secondary beams. This monitor can track the passage of individual particles up to intensities of  $10^7$  particles per second per  $\text{mm}^2$ , over an active area of  $\sim 20 \text{ cm} \times 20 \text{ cm}$ , and with a spatial resolution of 1 mm. Thanks to an external trigger system, the achieved detection efficiency is  $\sim 95\%$  and the noise level is kept below  $10^{-4}$  events/second. The simple design of this monitor avoids the common production difficulties of scintillating fibre detectors and makes its maintenance easier, when compared to other tracking detectors, due to the absence of gas or cooling. Using special electronics, a version of the monitor can also be used for time-of-flight measurements, achieving a time resolution of 900 ps. Thanks to its versatility, the monitor will perform several functions when measuring the secondary beams of the CERN Neutrino Platform: beam profile measurement, magnetic momentum spectrometry, particle identification through time-of-flight, and trigger generation for the experiments.

## INTRODUCTION

The Experimental Areas at CERN deliver beams of secondary particles that are used by many experiments related to high-energy physics research and R&D in particle detectors and accelerator technology. These beams are composed of hadrons and leptons that are delivered over a wide range of energies (1 GeV/c to 450 GeV/c), and intensities ( $10^2$  to  $10^7$  particles per second per  $\text{mm}^2$ ). The profile and position of these beams have been measured for decades with Multi-Wire Proportional Chambers and Delay Wire Chambers. However, these detectors are ageing, which compromises their performance, and they cannot fulfil the requirements of a new experimental area, the Neutrino Platform, since it requires large area monitors capable of detecting individual particles [1, 2].

For these reasons, the Beam Instrumentation group at CERN has investigated a new scintillating fibre beam monitor, whose first prototype was successfully tested with beam as reported in [3, 4]. This article describes the second prototype, which has the code name XBPF (eXperimental Beam Profile Fibre monitor), and the beam tests that have validated its production for the Neutrino Platform. Twelve monitors will be commissioned in this facility at the end of August 2018, at the same time as the new beam lines.

\* inaki.ortega@cern.ch

## XBPF AND XBTF

The XBPF for the Neutrino Platform is composed of 192 scintillating fibres Kuraray SCSF-78 of 1 mm thickness and square cross section. The fibres are packed together along one plane, forming the active area of the detector that stands in front of the beam (Fig. 1). The light from every fibre is read-out on one end by an individual Silicon Photomultiplier (SiPM) from Hamamatsu (model S13360-1350) that allows one to know which fibre has been activated and subsequently to reconstruct the track of the particle from multiple monitors. A mirror glued on the non read-out end of the fibre reflects back the light travelling in that direction along the fibre, thus increasing the total light signal reaching the photomultiplier.

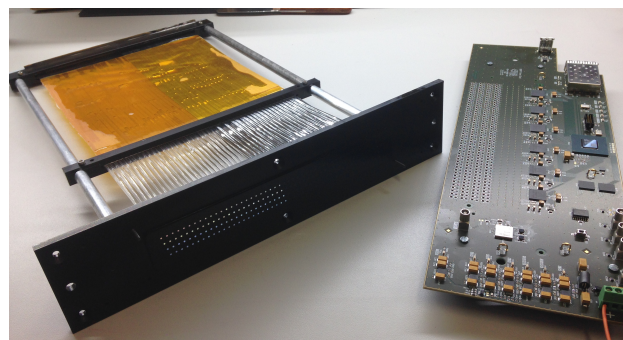


Figure 1: XBPF on the left, and front-end board with the 192 SiPMs on the right.

There exists a second version of the monitor, the XBTF (eXperimental Beam Trigger Fibre monitor), that is used to produce a fast trigger for the XBPF and for the neutrino experiments. In this monitor the fibres are grouped together into two bundles to be read-out by two Photo Multiplier Tubes (PMT) H11934-200 from Hamamatsu. These PMT have a very low dark count rate, at the level of a few Hz, and also have a low transit time spread (300 ps), which makes them suitable for Time-of-Flight applications.

Both the XBPF and XBTF have been designed to be vacuum compatible, which removes the need for vacuum windows, so helping to reduce the material budget of the beam line. The photo detectors are located outside vacuum, with the fibres exiting via a feed-through based on an innovative gluing technique that guarantees the necessary leak tightness. The vacuum tank of the new detectors has a modular design that allows it to host any desired combination of XBPF and XBTF, chosen to optimise the functionality of the beam line (Fig. 2).



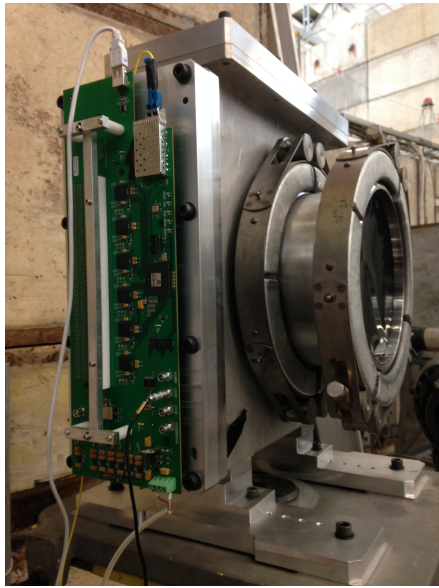


Figure 2: Vacuum tank of the XBPF during installation, with a front-end electronics board in place.

## READOUT ELECTRONICS

The electronics architecture of the XBPF and XBTF is shown in Fig. 3. For the XBTF trigger, the acquisition chain is very simple. The analogue signals from the PMT travel directly over a coaxial cable to a rack in the experimental hall, where they are processed by a NIM discriminator and a logic module. This logic module creates a coincidence of several trigger modules in the beam line and the resulting signal is sent to the XBPF profile monitors and the neutrino experiments with the aim of triggering their acquisition.

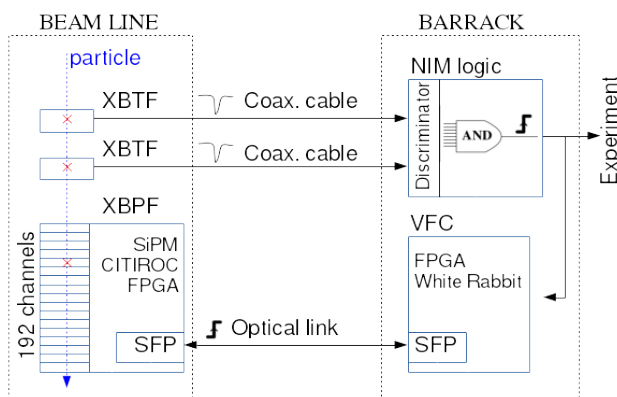


Figure 3: Electronics architecture of the XBPF and XBTF.

The XBPF electronics are divided into a front-end board, plugged directly on the monitor, and a back-end board grouped in a central acquisition chassis in the experimental hall. The front-end board has the following main components:

- 192 SiPM that detect the light generated by the fibres.
- Hamamatsu C11204 power supply, which powers up the SiPM and also features a temperature compensation

feedback system in order to maintain a stable gain in the photodetectors.

- 6 CITIROC ASIC [5] that process the analogue signals from the SiPM. These chips convert the 192 SiPM signals to digital signals in parallel, via configurable discriminators. It also features additional functionalities, such as fine tuning of the SiPM voltage and adjustable pre-amplification of the input signals.
- Xilinx FPGA Artix 7 that configures CITIROC slow control, reads the CITIROC digital output, packages the data, and sends it out in a 10 MHz data stream to a Gbit transceiver.
- SFP module with Gbit transceiver to transfer the data via optical fibre to the back-end.

The back-end module is the VFC, a VME general purpose digital acquisition board developed by the CERN Beam Instrumentation group [6]. This board is fully compatible with White Rabbit, which is an Ethernet-based network for sub-nanosecond accuracy timing distribution [7]. The Neutrino Platform experiments use this technology as their general timing distribution network and the beam instrumentation was required to be compatible.

The main functions of the VFC are to decode the Gbit stream coming from the front-end, to send control data to the front-end, and to create and store the event structure. The data stream from the front-end includes both the information from real particles and the noise from the SiPM, which can be at a rate of several kHz when considering all 192 channels. In order to suppress the noise events, the VFC also receives a trigger signal from the XBTF and only records the events coinciding with that signal.

The acquisition and control software of the XBPF is based on the CERN FESA architecture [8]. Every recorded event has the information of the status of the 192 fibres (hit, no-hit), plus a timestamp of when the event occurred.

## Time-of-Flight

It is possible to use the fast signals of the XBTF to measure the Time-of-Flight (ToF) of the particles from one trigger to another. This feature is very interesting, since it allows the particle composition of the beam to be determined. The figure of merit in a ToF system is the time resolution, which is given by the cumulative effect of the time spread of the following processes:

- Light creation process in the fibre.
- Different path lengths of photons inside the fibre.
- Transit time spread of electrons in the PMT.
- Time walk of the discriminator.
- Resolution of the Time-to-Digital Converter (TDC).

The analogue signals from the PMT are discriminated by a Constant Fraction Discriminator (CAEN N842) as this type of discriminator minimises the jitter of the signals [9]. The discriminated digital signals then go to a special TDC, the FMC-TDC developed at CERN, which has a resolution of 81 ps and is White Rabbit compatible. The model of CFD used, however, is not ideal since it has a long time walk (400 ps), when compared to other discriminators in the market. It also produces NIM signals that must be converted to TTL logic level before being sent to the TDC, increasing therefore the time jitter of the system.

## BEAM TESTS OF THE XBPF

Two XBPF and two XBTF were tested during two weeks in November 2017 in the East Area experimental facility at CERN. The beam conditions were chosen to be similar to the future Neutrino Platform: beams of low momentum (1 GeV/c to 6 GeV/c) and intensities between  $10^3$  and  $10^5$  particles per second.

As can be seen in Fig. 4, two tanks were installed separated by 14 m, hosting one XBPF and one XBTF each. The XBPF in the upstream tank measured the horizontal profile of the beam and the XBPF in the downstream tank, the vertical profile. The trigger signal was created from the coincidence of both XBTF. The upstream tank was installed close to two standard monitors: a delay wire chamber (DWC) for profile reconstruction and a scintillator paddle (SCINT) for intensity measurements. This allowed direct comparisons with the XBPF to be made.

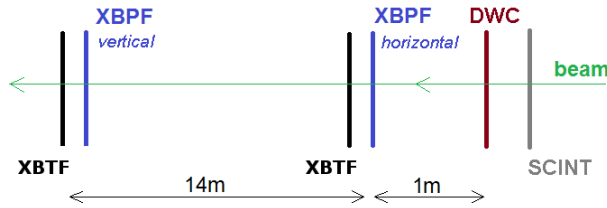


Figure 4: Schematic of the East Area beam test layout.

## Results and Discussion

A direct comparison of the DWC and XBPF profiles immediately shows that the latter produces more accurate profiles (Fig. 5).

Since the information from all fibres is recorded for a given event, it is possible to study performance characteristics of the detector, such as the efficiency or the multiplicity. Multiplicity occurs when multiple fibres are activated during the sampling time of the electronics (100 ns) such that they are recorded in the same event. Figure 6 shows an example of such a fibre-hit analysis.

The efficiency (which can be easily calculated from the number of multiplicity 0 events - a trigger giving no hits in the XBPF) was measured systematically for many different beam conditions for both the upstream and downstream

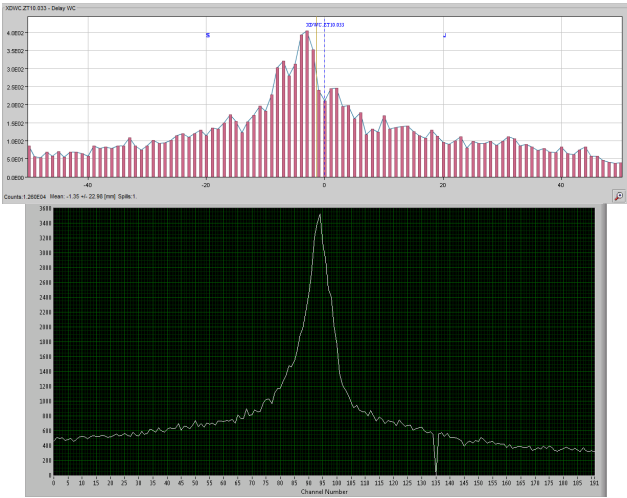


Figure 5: Example of a horizontal profile of a  $-6$  GeV/c pion beam of  $I = 1.5 \times 10^5$  particles measured by the DWC (above) and the XBPF (below).

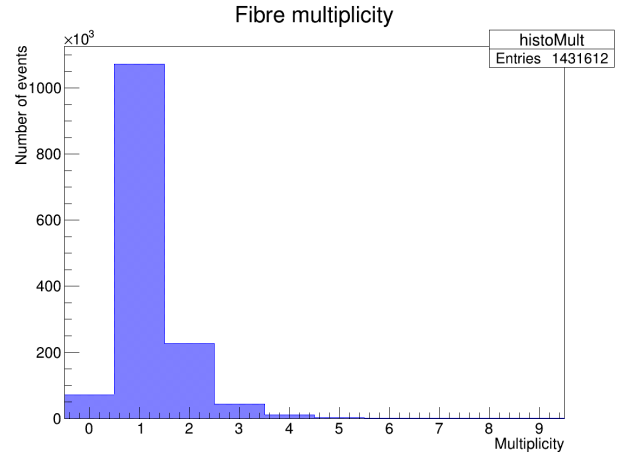


Figure 6: Example of fibre-hit analysis for a beam of  $-6$  GeV/c pions.

XBPF:

$$\epsilon_{\text{upstream}} = 93.8 \pm 2.8\% \quad (1)$$

$$\epsilon_{\text{downstream}} = 84.0 \pm 7.9\% \quad (2)$$

The lower efficiency of the downstream detector could be explained by a non-ideal configuration of the system. Unfortunately, this analysis was only completed after the end of the beam tests and therefore this issue was identified too late. Subsequent measurements performed with the XBPF working as a cosmic ray telescope in the laboratory (Fig. 7), however, have allowed optimum configuration values to be found. With such optimisation, the measured efficiency is:

$$\epsilon_{\text{telescope}} = 94.9 \pm 0.8\% \quad (3)$$

Fibre multiplicity during the beam tests ranged from 4.2% to 39%, and were lower for focused beams. The most plausible explanation is therefore that multiplicity is mainly caused

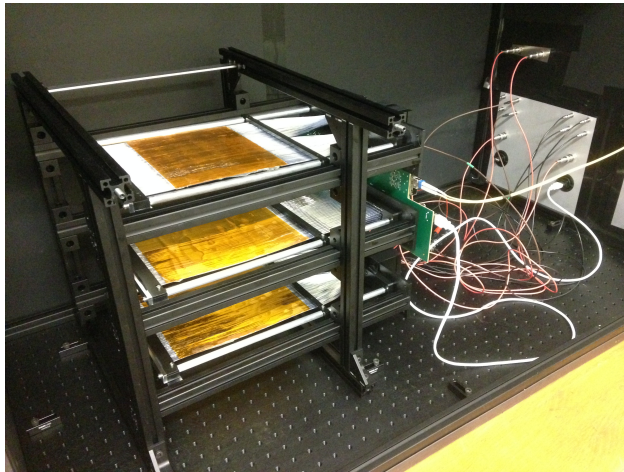


Figure 7: The XBPF working as a cosmic ray telescope.

by particles that impact the detector with large angles, activating two adjacent fibres. Measurements with the cosmic ray telescope and a Monte Carlo simulation have helped to confirm that the majority of multiplicity-two events are caused by such particles. The remaining multiplicity events are believed to be caused by particle showers arriving within the sampling time of the electronics.

The performance of the upstream XBTF could be measured more accurately thanks to having access to the adjacent scintillator paddle signal. By placing the paddle in coincidence with the downstream XBTF, it was possible to measure the particle flow through the upstream XBTF, and consequently measure its efficiency. After tuning the threshold of the discriminator, the efficiency was measured to be:

$$\varepsilon_{\text{XBTF}} = 94.0 \pm 0.1\% \quad (4)$$

Figure 8 shows an example of time-of-flight measurement for a 2 GeV/c beam containing a mixture of pions and protons. The measured time resolution of the ToF system was:

$$\sigma_t \sim 900 \text{ ps} \quad (5)$$

Thanks to this time resolution, it was possible to identify, within a short distance of 14 m, the pions and protons from 0.5 GeV/c to 2.5 GeV/c, with a statistical significance of  $4\sigma$ .

## CONCLUSION AND OUTLOOK

The XBPF has shown an excellent performance in the recent East Area tests and in the cosmic ray telescope setup. It has tracked, particle by particle, secondary beams and cosmic rays up to intensities of  $10^5$  particles per second over a wide range of energies. Furthermore, with the addition of a suitable TDC, the XBTF has been shown to be capable of measuring the time of flight of beam particles with a time resolution of 900 ps.

A modification of the VFC firmware is currently being investigated to allow the triggering of the acquisition by putting two XBPF planes in coincidence. This cross-trigger

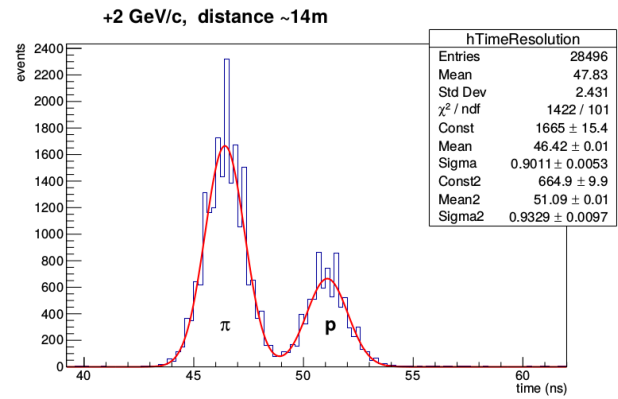


Figure 8: Time-of-flight measured for a 2 GeV/c pion-proton beam over a distance of 14 m.

mode would avoid requiring the XBTF, meaning that a pair of horizontal and vertical XBPF would be sufficient to accurately measure the beam.

The use of different constant fraction discriminators for the ToF system is also under investigation, which could lead to a possible improvement of the time resolution for the Neutrino Platform experiments.

## ACKNOWLEDGEMENTS

The authors would like to thank Wilfried Devauchelle for his invaluable help during the design, production, installation, and commissioning of the new monitor, and also Matthias Raudonis for his investigations in the cross-trigger acquisition mode of the XBPF.

## REFERENCES

- [1] N. Charitonidis, I. Efthymiopoulos, and Y. Karyotakis, "Beam performance and instrumentation studies for the protodune-dp experiment of cenf," *arXiv preprint arXiv:1607.07612*, 2016.
- [2] N. Charitonidis, I. Efthymiopoulos, and Y. Karyotakis, "Addendum to ats note cern-acc-note-2016-0052," CERN, Tech. Rep., 2016.
- [3] I. Ortega Ruiz, G. Tranquille, J. Spanggaard, A. Bay, and G. Haefeli, "Jacow: A scintillating fibre beam profile monitor for the experimental areas of the sps at cern," 2017.
- [4] I. Ortega Ruiz, "Accurate profile measurement of the low intensity secondary beams in the cern experimental areas," PhD thesis, Ecole Polytechnique, Lausanne, 2018.
- [5] J. Fleury *et al.*, "Petiroc and citiroc: Front-end asics for sipm read-out and tof applications," *J. Instrum.*, vol. 9, 2014.
- [6] A. Boccardi, M. Barros Marin, T. Levens, B. Szuk, W. Viganò, and C. Zamantzas, "A modular approach to acquisition systems for future cern beam instrumentation developments," *CERN*, 2015.
- [7] J. Serrano *et al.*, "The white rabbit project," *CERN*, 2013.
- [8] A. Guerrero, J. Gras, S. Jackson, J. Nougaret, M. Arruat, and M. Ludwig, "Cern front-end software architecture for accelerator controls," Tech. Rep., 2003.
- [9] D. Gedcke and W. McDonald, "Design of the constant fraction of pulse height trigger for optimum time resolution," *Nuclear Instruments and Methods*, vol. 58, no. 2, pp. 253–260, 1968.



# DEVELOPMENT OF A BEAM-GAS CURTAIN PROFILE MONITOR FOR THE HIGH LUMINOSITY UPGRADE OF THE LHC

R. Veness, M. Ady, N. S. Chritin, J. Glutting, T. Marriott-Dodington, O. R. Jones, R. Kersevan,  
S. Mazzoni, A. Rossi, G. Schneider, CERN, Geneva, Switzerland

P. Forck, S. Udrea, GSI, Darmstadt, Germany

A. Salehilashkajani, C. P. Welsch, H. D. Zhang, Cockcroft Institute and University of Liverpool,  
Warrington, UK

P. Smakulski, Wrocław University of Science and Technology, Wrocław, Poland

## Abstract

High luminosity upgrades to the LHC at CERN and future high-energy frontier machines will require a new generation of minimally invasive profile measurement instruments.

Production of a dense, focussed gas target allows beam-gas fluorescence to be exploited as an observable, giving an instrument suitable for installation even in regions of high magnetic field.

This paper describes the development of a device based on these principles that would be suitable for operation in the LHC. It focusses on mechanisms for the production of a homogeneous gas curtain, the selection of an appropriate working gas and the optical fluorescence detection system.

## INTRODUCTION

High-Luminosity LHC (HL-LHC) is under construction as an upgrade to the LHC at CERN [1], planned for commissioning from 2026. The upgrade to the LHC and its injectors will lead to a significant increase in beam intensity. Even the small amount expected to appear as a beam halo will contain significant energy, which must be constantly cleaned to avoid unacceptable losses on the collimation system. The principal technical solution under study for this purpose is a ‘hollow electron lens’ (HEL) [2] which uses a hollow cylindrical electron beam, constrained by a superconducting solenoid which is passed concentrically around the circulating proton beam over some 3 m of beamline.

Monitoring the concentricity of these two beams during operation will require simultaneous, minimally-invasive, transverse profile measurement of both proton and hollow electron beams. In addition, this measurement must be in close proximity to the solenoid field constraining the electron beam, preventing the collection of charged particles as an observable.

An instrument is being developed to image fluorescence generated by the interaction between these beams and a thin, supersonic, gas curtain [3,4,5]. By tilting this ‘Beam Gas Curtain’ (BGC) with respect to the beam axis, a 2-D image of both beams can be obtained in much the same way as for a traditional solid screen beam observation system.

The instrument consists of the following main components:

- a gas generation stage consisting of a supersonic gas nozzle followed by three skimmers which select and shape the gas jet.
- an interaction chamber where the 0.45-7 TeV proton beam and 10 keV electron beam interact with the gas jet.
- an optical system for image generation
- an exhaust chamber which pumps the residual gas jet and contains gas jet diagnostics.

There are a number of key developments required for this instrument. It is important to select a working gas that is compatible with the NEG-coated, LHC ultra-high vacuum system, whilst still producing an adequate fluorescence signal from the interaction of both keV electrons and TeV protons, preferably from the spectral line of a neutral atom or molecule to avoid image distortion from electric and magnetic fields. It is also necessary to study the production of a dense supersonic gas curtain whilst minimising the background gas load to the vacuum system, and to develop a radiation-hard imaging system that is efficient for both the electron and proton excited fluorescence signals.

## WORKING GASES

As working gases, Nitrogen ( $N_2$ ) and Neon (Ne) were initially considered [3,6], with estimations made on their cross-sections for relevant transitions at the energies of interest (see Table 2). However, recent considerations regarding vacuum compatibility at CERN lead to the conclusion that  $N_2$  is less desirable than Neon and that a further alternative is Argon (Ar). A literature study was therefore conducted on the fluorescence of Ar and  $Ar^+$  due to excitation by electrons and protons. Whilst a large amount of data is available for fluorescence cross-sections for relatively low-energy ( $E_k \leq 1$  keV) electrons impinging on Ar, there is no relevant data for high-energy electrons or protons. According to measurements by [7] for excitation by  $\leq 250$  eV electrons, the most prominent lines are at 750.4 nm for Ar and 476.5 nm for  $Ar^+$ . However, high intensity lines at 751.5 nm (Ar) and 454.5 nm ( $Ar^+$ ) can also be considered. For extrapolating to higher electron energies the model presented for Ne in [6] has been used for Ar, while for  $Ar^+$  a



relativistic reformulation of the model from [8,9] has been applied. In both cases data extending to 1 keV from [10] and [11] has also been used. In the case of protons the principle of equal velocities is applied to estimate the cross-sections, i.e.  $\sigma_p(7 \text{ TeV}) = \sigma_e(3.8 \text{ GeV})$ . The resulting cross-sections are included in Table 2.

## OPTICS AND INTEGRATION TIME

Fluorescence cross-sections have to be considered in conjunction with the optical system and the image-intensified camera used for photon detection. A prototype of the set-up to be used on the HEL has been designed and commissioned at GSI [6] and subsequently installed on a test set-up at the Cockcroft Institute, where first tests show promising results. Here we present estimations of the average integration times required for the detection of one photon based on the experience gained and the parameters of Table 1. Note that for working at the large solid angle given in Table 1 a Scheimpflug geometry, see e.g. [12], is envisaged to mitigate issues related to the extremely short depth of field.

The resulting single photon integration times ( $\langle t_i \rangle_{\text{MCP}}$ ) for 10 keV electrons and 7 TeV protons are given in Table 2. By multiplying these times with the number of photons needed for a proper image an estimate of the exposure times can be obtained. Considering the small transverse size of the proton beam it is expected that the detection of a few hundred photons should be sufficient to assess its po-

sition and shape. The electron beam, however, is distributed over a much larger area, and it is therefore estimated that  $\sim 10^4$  photons need to be detected for the same purpose. Total integration times of the order of 1 s are thus expected for Ne or Ar as working gases, while in case of N<sub>2</sub> some 10 ms should be adequate. The use of nitrogen, however, has several disadvantages. Firstly, there are compatibility issues with the LHC vacuum system and secondly the relevant emission is only due to the molecular ion. The upper excited level has a relatively long lifetime (60 ns), which may lead to appreciable distortions in the image due to the drift of the ion in the solenoid's magnetic field and strong electromagnetic field of the beams [13].

Table 1: Parameters for Integration Time Estimation

curtain density $n$	$2.5 \cdot 10^{10} \text{ cm}^{-3}$
curtain thickness $d$	0.5 mm
optics transmission $T$	0.85
filter transmission $T_f$	0.8
solid angle $\Omega$	$40\pi \cdot 10^{-4} \text{ sr}$
photocathode efficiency $\eta_{\text{pc}}$	$\lambda$ -dependent [6]
MCP efficiency $\eta_{\text{MCP}}$	0.75
average proton current $I_p$	1 A
DC electron current $I_e$	5 A

Table 2: Average integration time  $\langle t_i \rangle_{\text{MCP}}$  for the detection of one emitted photon and total estimated integration time for the three working gases considered, using the parameters defined in Table 1.

Projectile	Emitter	$\lambda$ [nm]	$\sigma$ [cm <sup>2</sup> ]	$I$ [A]	$\eta_{\text{pc}}$	Estimated Integration time [s]	
						Single photon $\langle t_i \rangle_{\text{MCP}}$	Total protons: $10^2$ photons electrons: $10^4$ photons
electron	N <sub>2</sub> <sup>+</sup>	391.4	$9.1 \cdot 10^{-19}$	5	0.19	$2.9 \cdot 10^{-7}$	0.003
proton	N <sub>2</sub> <sup>+</sup>	391.4	$3.7 \cdot 10^{-20}$	1	0.19	$3.6 \cdot 10^{-5}$	0.004
electron	Ne	585.4	$1.4 \cdot 10^{-20}$	5	0.09	$4.0 \cdot 10^{-5}$	0.4
proton	Ne	585.4	$4.7 \cdot 10^{-22}$	1	0.09	$5.9 \cdot 10^{-3}$	0.59
electron	Ar	750.4 & 751.5	$7.4 \cdot 10^{-20}$	5	0.02	$3.4 \cdot 10^{-5}$	0.34
proton	Ar	750.4 & 751.5	$3.3 \cdot 10^{-21}$	1	0.02	$3.8 \cdot 10^{-3}$	0.38
electron	Ar <sup>+</sup>	454.5 & 476.5	$9.9 \cdot 10^{-21}$	5	0.20	$2.5 \cdot 10^{-5}$	0.25
proton	Ar <sup>+</sup>	454.5 & 476.5	$1.7 \cdot 10^{-21}$	1	0.20	$7.4 \cdot 10^{-4}$	0.074

## GAS JET SIMULATIONS

Formation of the gas stream in the nozzle and subsequent selection and shaping in the skimmers define the gas curtain density at the interaction point with the beam. A predictive design of the BGC gas jet requires simulation of a

continuous gas flow with a pressure range of 14 orders of magnitude, from the gas nozzle at 10 bar to the LHC machine vacuum at  $10^{-10}$  mbar.

A hybrid simulation approach to this problem has been taken using Computational Fluid Dynamics (CFD) and Test-Particle Monte Carlo (TPMC). The upstream part, from the supersonic nozzle up to the first skimmer opening,

has been solved by assuming viscous flow, using CFD. Downstream of the first skimmer a quasi-molecular flow was assumed and the TPMC solver was used. Determination of the transition between the numerical simulation domains was based on the Knudsen number method [14].

### Viscous Flow Regime

A set of numerical simulations has been performed in the upstream part in order to maximise the flow rate through the system by maximising the density and axial velocity flow component of the gas before the first skimmer. During the analysis, two nozzle shapes were tested and compared with each other: the ‘convergent-divergent’ nozzle (CD) and a ‘simple geometry’ (SG) nozzle with constant diameter. The main parameters under test were the distance between the nozzle throat and the first skimmer opening (see Fig. 1), and the nozzle inlet pressure.

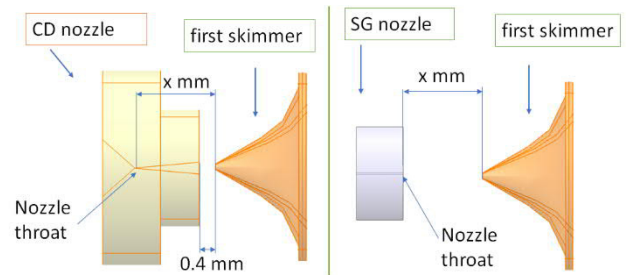


Figure 1: Nozzle and first skimmer as used in the simulations, with  $x$  the variable distance between the nozzle throat and the opening of the first skimmer.

For the simulations presented here, the throat diameter of the supersonic nozzle was set to  $30\text{ }\mu\text{m}$ . In Fig. 2 the number density and average velocity on the cross-sectional surface of the first skimmer are presented. The simulations show that the CD nozzle gives a significantly better efficiency for gas transport through the first skimmer compared to the SG nozzle. The development of CD nozzles will therefore be prioritised for this project.

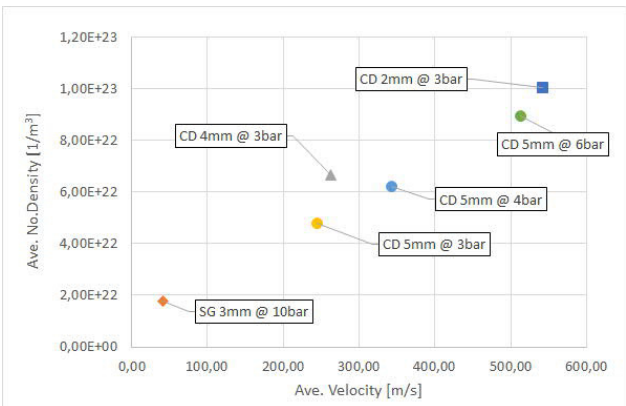


Figure 2: Comparison between nozzle geometries for different nozzle throat to skimmer distances (mm) and inlet pressures (bar).

The flow parameters on the virtual interface of the first skimmer opening were treated as a boundary conditions for the TPMC solver.

All computations were performed using the ANSYS CFX<sup>®</sup> software and the SST turbulence model. Steady-state calculations for the 2D axis-symmetric numerical domain were iterated until reaching an RMS residual level below  $10^{-6}$ .

### Molecular Flow Regime

The low-pressure calculations were performed with the Test-Particle Monte Carlo (TPMC) simulator Molflow+, developed at CERN. A virtual interface at the first skimmer opening was used to generate the gas, so that the flux and direction of particles corresponded to the CFD calculation result at that location. This method predicts an interaction point gas curtain density of  $1.2 \times 10^{10}/\text{cm}^3$ , in line with the analytic result in Table 1.

The computed density in all volumes of the system show a well-delimited gas jet in the centre, comprising particles passing the skimmers without any collision, and a background that originates from gas particles bouncing off the skimmers. Simulations suggest the need to pump away these rebounding particles at every skimming stage, to prevent them effusing through the skimmers and increasing the background in the next volume. Every stage therefore has its own pump and a separating cone installed between the volumes (see Fig. 3).

Simulation-led optimisation also suggested the installation of a baffle structure between the beam interaction location and the gas jet exhaust pump. It allows the collimated gas jet to pass through but reduces particle rebound from the tilted turbo-molecular pump (at the end) back to the interaction chamber.

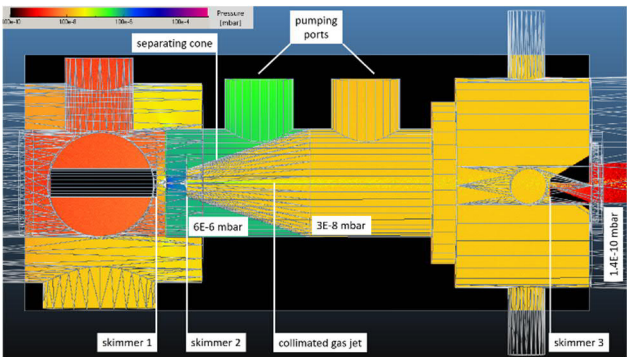


Figure 3: TPMC model showing main components and corresponding pressures.

### TESTS IN PROGRESS

A dedicated design of the gas jet system for the LHC environment has been assembled at the Cockcroft Institute [4]. The design incorporates several new aspects to allow for faster component changes and better performance. This includes turbo-molecular pumps with higher pumping speed for a quick pump-down after a vacuum component change, a dedicated interaction chamber, a higher current

electron-gun to save testing time by reducing the integration time, and an improved imaging system to increase the signal to noise ratio.

Measurements show that a misalignment of only 30  $\mu\text{m}$  in the nozzle and first two skimmers will cause a decrease of 10% in the measurable gas jet signal. The nozzle and first two skimmers have therefore been designed to be aligned in the laboratory using a laser alignment system as a single unit within 30  $\mu\text{m}$  of the ideal axis.

The initial experimental goals for this setup are: to test pumping performance; optimise the gas jet to background pressure ratio; to compare different nozzle and skimmer geometries; to gain operational experience with different candidate gases. Initial tests use a nitrogen gas jet for electron beam profile detection. The next steps will be changing the geometry of the nozzle and skimmer assembly to achieve a higher gas jet density. This system can run in parallel with an older gas jet experiment that was already used to demonstrate the operational principles [6].

## DESIGN FOR LHC INSTALLATION

The BGC design must be adapted from the test system set-up at the Cockcroft Institute for operation on the LHC (Fig. 4). This poses a number of challenges.

The system must not perturb regular LHC physics operation. It is therefore being designed to be fully isolated from the rest of the machine vacuum system using three all-metal gate valves. When closed, only the interaction chamber will be exposed to the LHC vacuum. This allows the use of positive displacement pumps such as turbo-molecular pumps which have a high pumping speed for inert gases. Beam impedance concerns are addressed by using a copper shielded sleeve with regular slots for vacuum conductance.

The distance between the gas nozzle and interaction point must be compatible with the LHC tunnel dimensions. In addition, the final instrument will be required to fit into the 200 mm longitudinal gap between the HEL solenoid cryostats.

The background pressure in the interaction chamber must be as low as possible. The volume between each skimmer as well as the interaction and exhaust chambers will therefore be pumped separately. In total five volumes will require positive displacement pumps. The final number of pumps could be reduced by sharing backing pumps and using only a primary pump between the nozzle and first skimmer.

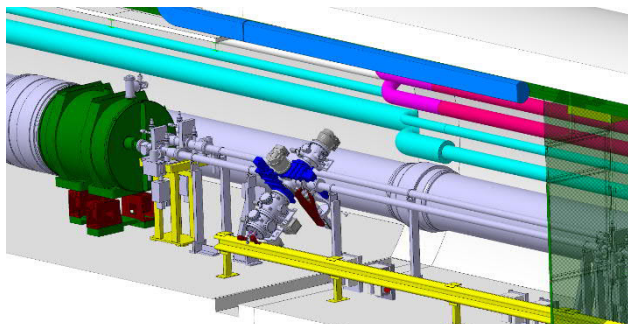


Figure 4 : Preliminary integration model of the BGC instrument in the LHC

## STATUS AND NEXT STEPS

Neon is currently the gas species which seems to provide the best balance of integration time, low excited-state lifetime and vacuum compatibility for use in this application, with Argon as a useful fall-back solution. Simulations show that a practical optical system design can deliver a useable signal with such gases within a matter of seconds.

Viscous and molecular flow simulations have been combined to produce a working tool for optimisation of the gas jet system and associated LHC vacuum components.

Tests are in progress with a newly designed experimental bench to validate the gas selection, optics and gas jet geometry. In parallel, design and integration of an instrument for installation in the LHC is in progress.

A test set-up is also currently installed in the LHC to verify the fluorescence predictions based on the theoretically estimated cross-sections and to assess the background due to the LHC environment. The next step will be to test a prototype instrument both on high-intensity electron beams and in the LHC.

## ACKNOWLEDGEMENTS

The authors would like to thank The Hi Lumi project and the Science and Technology Facilities Council of the UK for supporting this project via a CERN collaboration agreement. Thanks also to Ahmed Cherif from CERN EN-MME for nozzle production support.

## REFERENCES

- [1] <http://hilumilhc.web.cern.ch/>
- [2] S.Redaeli *et al.* "Plans for deployment of hollow electron lenses at the LHC for enhanced beam collimation" in *Proc. IPAC'15*, Richmond, VA, USA, paper WEBB1.
- [3] S. Udrea, *et al.*, "Preparatory Work for a Fluorescence based Profile Monitor for an Electron Lens", in *Proc. IBIC'16*, Barcelona, Spain, September 2016, paper TUPG73, p. 528.
- [4] H.D. Zhang *et al.*, "A supersonic gas jet-based beam profile monitor using fluorescence for HL-LHC", in *Proc. IPAC'18*, Vancouver, BC, Canada. Doi:10.18429/JACoW-IPAC2018-WBPAF034
- [5] V.Tzoganis *et al.*, "A non-invasive beam profile monitor for charged particle beams", *Applied Physics Letters*, vol. 104 (20), p. 204104, 2014
- [6] S. Udrea *et al.*, "Development of a Fluorescence based Gas Sheet Profile Monitor for use with Electron Lenses: Optical System Design and Preparatory Experiments", in *Proc. IBIC'17*, Grand Rapids, MI, USA, August 2017, paper WEPCC08, p. 359.
- [7] J.B. Boffard, B. Chiaro, T. Weber, and C.C. Lin, "Electron-Impact Excitation of Argon: Optical Emission Cross Sections in the Range of 300–2500 nm", *Atom. Dat. and Nucl. Dat. Tables*, vol. 93, p. 831, 2007.
- [8] J.M. Ajello, G.K. James, B.O. Franklin, and D.E. Shemansky, "Medium-Resolution Studies of Extreme Ultraviolet Emission from N<sub>2</sub> by Electron Impact: Vibrational Perturbations and Cross Sections of the c'<sub>4</sub><sup>1</sup>Σ<sub>u</sub><sup>+</sup> and b'<sup>1</sup>Σ<sub>g</sub><sup>+</sup> States", *Phys. Rev. A*, vol. 40, p. 3524, 1989.

- [9] D.E. Shemansky, J.M. Ajello, D.T. Hall, and B. Franklin, "Vacuum Ultraviolet Studies of Electron Impact of Helium: Excitation of He  $n^1P_o$  Rydberg Series and Ionization-Excitation of He<sup>+</sup>  $nl$  Rydberg Series", *The Astrophys. J.*, vol. 296, p. 774, 1985.
- [10] S. Tsurubuchi, T. Miyazaki, and K. Motohashi, "Electron-impact emission cross sections of Ar", *J. Phys. B: At. Mol. Opt. Phys.*, vol. 29, p. 1785, 1996.
- [11] S. Tsurubuchi, "Emission Cross Sections of Ar<sup>+</sup> Measured in a Wide Range of Electron Impact Energies", *J. Phys. Soc. Japan*, vol. 66, p. 3070, 1997.
- [12] Ch. Wiebers *et al.*, "Scintillating Screen Monitors for Transverse Electron Beam Profile Diagnostics at the European XFEL", in *Proc. IBIC'13*, Oxford, UK, September 2013, paper WEPF03, p. 807.
- [13] D. Vilsmeier, P. Forck, M. Sapinski, "A modular Application for IPM Simulations", in *Proc. IBIC'17*, Grand Rapids, MI, USA, August 2017, paper WEPCC07, p. 355.
- [14] La F. Torre, S. Kenjereš, J-L. Moerel and C.R. Kleijn, "Hybrid simulations of rarefied supersonic gas flows in micro-nozzles", *Comput. Fluids* 49 (2011) 312–22



# PERFORMANCE OF A REFLECTIVE MICROSCOPE OBJECTIVE IN AN X-RAY PINHOLE CAMERA

L. Bobb \*, G. Rehm, Diamond Light Source, Oxfordshire, U.K.

## Abstract

X-ray pinhole cameras are used to measure the transverse beam profile of the electron beam in the storage ring from which the emittance is calculated. As improvements to the accelerator lattice reduce the beam emittance, e.g. with upgrades to fourth generation synchrotron light sources, likewise the beam size will be reduced such that micron and sub-micron scale resolution is required for beam size measurement. Therefore the spatial resolution of the pinhole camera imaging system must be improved accordingly. Here, the performance of a reflective microscope objective is compared to the high quality refractive lens which is currently in use to image the scintillator screen to the camera. The modulation transfer functions for each system have been assessed and will be discussed.

## INTRODUCTION

There are three pinhole cameras in operation at Diamond Light Source: two of these systems continuously monitor the beam size [1] for vertical emittance feedback [2], whilst the third pinhole camera is installed on the Diagnostics X-ray beamline for research and development.

All of the pinhole cameras share a common layout in the storage ring as shown in Fig. 1. For each pinhole camera, synchrotron radiation from a bending magnet passes from vacuum to air through a 1 mm thick aluminium window. The spectrum has a photon energy range from 15 keV to approximately 60 keV and a peak at 25 keV. The X-rays then pass through the  $\approx 24 \mu\text{m}$  pinhole aperture which is formed using a stacked arrangement of tungsten blades separated by chemically etched shims [3,4]. The pinhole assembly is kept under nitrogen to prevent oxidation.

The first image plane is located at the scintillator screen which converts X-rays to visible photons. This image is relayed from the scintillator screen to the camera via a lens. The total path length is approximately 15 m.

The source-to-screen magnification is approximately 2.5. The horizontal beam size of the electron beam  $\sigma_x$  is  $\approx 50 \mu\text{m}$ , therefore the horizontal beam size imaged at the scintillator screen is  $\approx 125 \mu\text{m}$ . The electron beam profile which is approximated by a Gaussian extends much further than  $\pm 1\sigma_x$ , thus the field of view of the relay lens should be roughly an order of magnitude greater than the imaged beam size, in this case preferably 1 mm.

Rather than direct X-ray detection using an expensive detector, scintillator screens are incorporated to convert X-rays to visible photons which can be detected using machine vision CCD or CMOS cameras. In order to have a reasonable exposure time ( $< 100 \text{ ms}$ ), a sufficient intensity per pixel

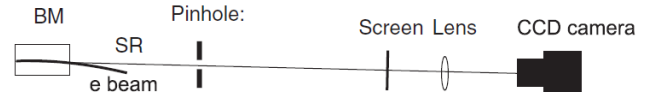


Figure 1: Schematic of the pinhole camera system [1]. A folding mirror is also typically included downstream of the scintillator such that the refractive lens and camera may be located away from the X-ray beam.

(i.e. light yield) to form an image above noise is required. This dictates the lower bound on the scintillator thickness for a given optical setup. The upper bound is determined by the spatial resolution that is required for imaging the electron beam. In some cases direct X-ray detection is necessary [5].

For pinhole cameras at third generation synchrotron light sources, the scintillator thickness is in the 100 to 500  $\mu\text{m}$  range [1, 6]. Due to the limited information provided in the technical specifications from manufacturers, a series of experiments to compare and characterise different scintillator materials have been conducted largely by G. Kube *et al.* [7, 8]. These results have shown that although there is some variation of the spatial resolution for different materials, reducing the thickness of the scintillator provides the greatest improvement in spatial resolution [9].

The Point Spread Function (PSF) describes the spatial resolution of an imaging system. For pinhole cameras each optical element contributes to the overall PSF of the imaging system [3]. Using a Gaussian approximation the overall PSF may be represented as

$$\sigma_{\text{PSF}}^2 = \sigma_{\text{pinhole}}^2 + \sigma_{\text{camera}}^2 \quad (1)$$

with

$$\sigma_{\text{pinhole}}^2 = \sigma_{\text{diffraction}}^2 + \sigma_{\text{aperture}}^2 \quad (2)$$

and

$$\sigma_{\text{camera}}^2 = \sigma_{\text{screen}}^2 + \sigma_{\text{lens}}^2 + \sigma_{\text{sensor}}^2 \quad (3)$$

where the subscripts denote the sources of the PSF contributions [4]. The PSF contribution associated with imaging the scintillator screen denoted  $\sigma_{\text{camera}}$  may be measured using a knife-edge and uniform illumination. The PSF contribution from the pinhole denoted  $\sigma_{\text{pinhole}}$  may be calculated provided the aperture size is known [1].

The overall PSF is dominated by the contribution due to pinhole aperture size  $\sigma_{\text{pinhole}}$  and the contribution from the scintillator screen  $\sigma_{\text{screen}}$ . Investigations are under way to minimise  $\sigma_{\text{pinhole}}$  by improving the control of the pinhole aperture size using alternative fabrication methods such that the optimal size is used given the X-ray spectrum [4, 10].

\* lorraine.bobb@diamond.ac.uk

In this paper we focus on minimising  $\sigma_{\text{screen}}$  which is primarily dependent upon the scintillator thickness. Reducing the scintillator thickness causes a reduction in the light yield. Therefore we propose to replace the refractive lens with a microscope objective which has a significantly larger numerical aperture (NA). Given that the working distance of microscope objectives is small ( $< 40$  mm), the optic must be placed in the path of the X-ray beam. For this reason, a refractive microscope objective is avoided since radiation damage will cause browning of the glass over time. Instead a reflective microscope objective is implemented. In the following sections, the spatial resolution of the reflective microscope objective imager is compared to the refractive lens imager.

## EXPERIMENTAL SETUP

### In the Lab

A schematic overview for each imager as tested in the lab is shown in Figs. 2 and 3. The test target is a negative USAF 1951 target which was backlit with a diffused white light source. Using the test target, the magnification and modulation transfer function (MTF) of each imager were measured.

In the refractive lens setup, a Schneider-Kreuznach Componon-S 2.8/50 lens is used to image the object plane (test target) to a FireWire Point Grey FLEA2 camera. This camera has an ICX204 CCD sensor with an absolute sensitivity threshold of 30 photons. The absolute sensitivity threshold may be approximated as the ratio between the dark noise and the quantum efficiency. This lens is well suited for 1:1 macro imaging. The technical specification of the refractive lens is summarised in Table 1.

From the MTF reported by the manufacturer, the refractive lens has the best spatial resolution when the iris aperture is at a minimum such that the f-number  $f/\# = 8$  [11]. Given that

$$f/\# \approx \frac{1}{2NA} \quad (4)$$

the NA of the refractive lens is 0.06.

The technical specification of the reflective microscope objective is given in Table 1. The objective is coupled to a GigE Manta G319B camera which has an IMX265 CMOS sensor and absolute sensitivity threshold of 5 photons.

### In the Tunnel

For testing with the X-ray pinhole camera and measurement of the PSF, both the refractive and reflective imagers were installed side by side on a translation stage in the tunnel such that they could be remotely inserted into the X-ray beam path. This ensures that the PSF contribution from the pinhole  $\sigma_{\text{pinhole}}$  is constant.

A 25  $\mu\text{m}$  LuAg:Ce scintillator screen was installed on the reflective microscope objective imager and a 200  $\mu\text{m}$  LuAg:Ce screen was installed on the refractive imager. Using XOP [13] to calculate the normalised power absorbed

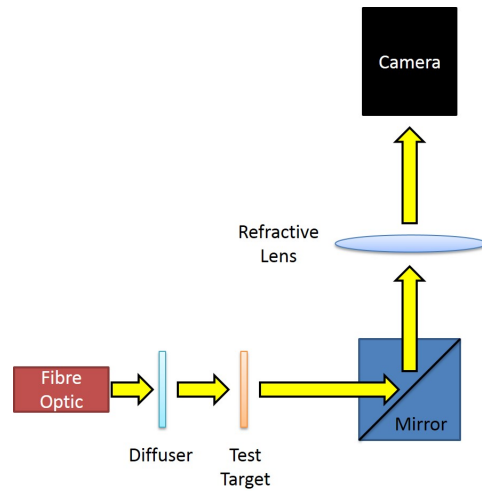


Figure 2: Schematic of the refractive imager.

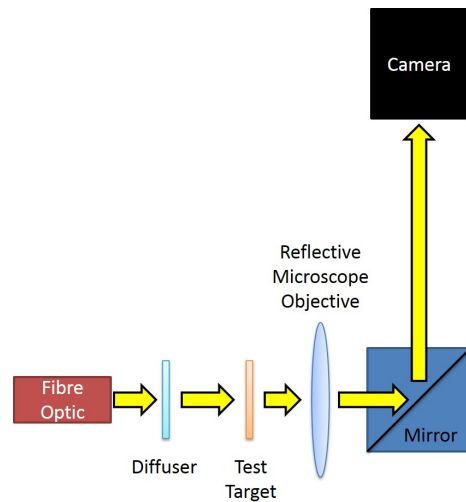


Figure 3: Schematic of the reflective microscope objective imager.

as a function of scintillator thickness, it is estimated that the light yield from the 25  $\mu\text{m}$  is a factor of 3 less than that from the 200  $\mu\text{m}$  LuAg:Ce screen.

The numerical aperture of the reflective microscope objective is a factor of 6.7 larger than the refractive lens. The absolute sensitivity threshold of the Manta G319B camera in the reflective objective imager is 6 times more sensitive to incident photons in comparison to the FLEA2 camera in the refractive imager.

## MODULATION TRANSFER FUNCTION

The MTF (or spatial frequency response) is the magnitude response of the optical system to sinusoids of different spatial frequencies [14]. Using the back illuminated setups shown in Figs. 2 and 3, images of a negative USAF 1951 target were acquired. A diffuser is used to ensure uniform illumination of the target. The test target is rotated relative to the pixels of the camera sensor such that the MTF may be obtained using the

Table 1: Technical specifications of the Schneider Componon-S 2.8/50 refractive lens and Newport 50105-01 reflective microscope objective [11, 12] where an asterisk indicates calculated values.

Parameter	Refractive lens	Reflective microscope objective
F-number	2.8 to 8	1.25*
Numerical Aperture	0.18 to 0.06*	0.4
Focal length	50.2 mm	160 mm (back) 13 mm (effective)
Working Distance	-	24 mm
Magnification	1	15
Transmission	400 - 700 nm	200 - 1000 nm

slanted-edge method [15]. The QuickMTF program [16] was used for the image analysis. The results were then exported to MATLAB.

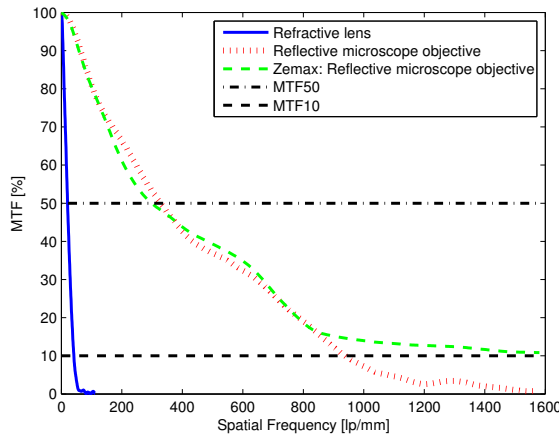


Figure 4: Comparison of the measured MTF of the refractive lens and the reflective microscope objective. Also plotted is the expected MTF from Zemax for a similar microscope objective from Thorlabs.

In order to compare the refractive lens and the reflective microscope objective the screen-to-camera magnification must be taken into account. Using the test target the magnifications of the refractive lens and reflective microscope objective were measured to be 1.04 and 14.7 respectively. Although not shown here, it was verified that the different camera sensors had a negligible impact on the measured MTF. The pixel size of the camera sensor determines the Nyquist frequency.

In Fig. 4 the MTFs of the imagers at the object plane (scintillator screen) are shown. As expected the microscope objective outperforms the refractive lens. If the resolution threshold is taken at MTF10, the maximum resolvable spatial frequencies for the refractive lens and reflective microscope objective are 42 lp/mm and 936 lp/mm respectively. In addition, the MTF from a similar microscope objective from Thorlabs for which a Zemax file was available is in good agreement with the measurement.

## POINT SPREAD FUNCTION MEASUREMENT

Readers are referred to the “PSF measurement using the Touschek lifetime” section described in [4]. A summary of this method will be described here.

For a Touschek dominated beam (e.g. 400 bunches and 200 mA), the vertical beam size is approximately proportional to the beam lifetime  $\tau$  (or condition). In this case the measured vertical beam size is

$$\sigma_M = \sqrt{(k\tau)^2 + \sigma_{PSF}^2} \quad (5)$$

where  $k$  is a scaling factor which relates to the lattice parameters at the source point.

After performing a LOCO on the storage ring to ensure the machine is in agreement with the accelerator model, the skew quads were adjusted using the VEFB controls to gradually change the vertical beam size. During this scan, for each beam size three images with corresponding beam conditions were recorded on pinhole camera 3. The first scan, denoted CAL 1, had the reflective microscope imager in the beam path. The second scan, denoted CAL 2, had the refractive imager in the beam path.

To obtain the measured vertical beam size from each image, the transverse profile was fitted with a 2D Gaussian and scaled using the measured source-to-screen and screen-to-camera magnifications. These magnifications were measured by remotely displacing the pinhole and imager respectively and observing the change in centroid position of the X-ray beam. The measured source-to-screen magnification was 2.47. The measured screen-to-camera magnifications were 1 (refractive imager) and 11 (reflective microscope imager). A least squares fit using Eq. 5 with  $k$  and  $\sigma_{PSF}$  as free parameters was then applied to each dataset

To monitor the stability of the machine and check the reproducibility of the calibration method, data was also acquired from pinhole cameras 1 and 2. Since no changes were made to these systems, the measured  $k$  and  $\sigma_{PSF}$  obtained from each calibration should not change between calibrations.

The calibration datasets from the three pinhole cameras are shown in Fig. 5. For each dataset, the results of the fit are reported in Table 2. Note that comparisons between the pinhole cameras should not be made. This is due to the

Table 2: Results of the PSF measurement for each pinhole camera.

Pinhole camera	CAL 1		CAL 2	
	$k$ [ $\mu\text{m}/\text{mA}/\text{h}$ ]	$\sigma_{PSF}$ [ $\mu\text{m}$ ]	$k$ [ $\mu\text{m}/\text{mA}/\text{h}$ ]	$\sigma_{PSF}$ [ $\mu\text{m}$ ]
1	0.026	7.8	0.026	8.6
2	0.031	7.2	0.031	7.5
3	0.025	7.4	0.026	10.9
	Reflective microscope imager		Refractive lens imager	

differences in the optical elements of each pinhole camera, such that the PSF contributions shown in Eq. 1 are unique to each system. Furthermore, 200  $\mu\text{m}$  Prelude420 (LYSO:Ce) scintillator screens, rather than LuAG:Ce, are installed on pinhole cameras 1 and 2. Remote focussing of the refractive lens is also available on pinholes 1 and 2, but is not present on pinhole 3. Thus comparisons should only be made between the two calibrations of each pinhole camera.

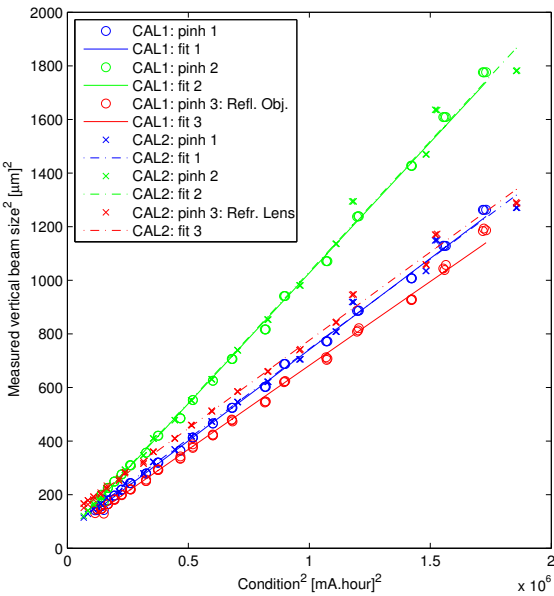


Figure 5: Results of the two calibrations for the three pinhole cameras. On pinhole camera 3, the reflective microscope imager and refractive lens imager were in operation for calibrations 1 and 2 respectively.

In Table 2 it is seen that the parameter  $k$  is reproducible to 0.001 precision for all three pinhole cameras. This indicates that the machine parameters were stable throughout the calibration period. Each calibration takes approximately 1 hour since it takes a few minutes for the reading of the beam lifetime to stabilise at each vertical beam size of the scan.

The PSF measurements from pinhole 3 show that an improvement of 30 % is achieved by replacing the 200  $\mu\text{m}$  screen and refractive lens, with a 25  $\mu\text{m}$  screen and reflective microscope objective. Averaging the difference of the PSF

measurements for pinhole cameras 1 and 2 shows that the average error on  $\sigma_{PSF}$  is 0.5  $\mu\text{m}$ .

Similar exposure times, typically tens of milliseconds, were used on the FLEA2 and Manta cameras to ensure each image contained roughly the same error from beam jitter. The gain was not changed during the calibration scans. At maximum camera gain the photon yield from the 25  $\mu\text{m}$  screen was sufficient to operate the Manta camera in the reflective imager setup with an exposure time < 10 ms.

Further improvements to the spatial resolution could be achieved by using a thinner (< 25  $\mu\text{m}$ ) scintillator screen since the photon flux was more than sufficient given the large numerical aperture of the reflective imager. Additionally, it is known that the depth of field scales inversely with numerical aperture. Thus a scintillator with thickness  $\leq 10 \mu\text{m}$  would be more suitable.

## CONCLUSION

The spatial resolution of pinhole cameras must be improved for operation in future light sources. Although the fundamental limitation arises from the pinhole aperture itself, another important contribution to the overall point spread function comes from the scintillator screen. Depending upon budget and given a large source-to-screen magnification, direct imaging of the X-ray beam would inherently remove this point spread function contribution however, such detectors are significantly more expensive and tend to have a large pixel size. Instead, the results presented in this paper show that a thin scintillator screen coupled with a reflective microscope objective which has a large numerical aperture can provide a significant reduction to the overall PSF of the pinhole camera whilst maintaining the frame rates needed for online feedback.

## REFERENCES

- [1] C. Thomas et al., “X-ray pinhole camera resolution and emittance measurement”, *Phys. Rev. ST Accel. Beams* 13, 022805, (2010).
- [2] I.P.S. Martin et al., “Operating the Diamond Storage Ring with Reduced Vertical Emittance”, *Proc. of IPAC2013, Shanghai, China*, MOPEA071.
- [3] P. Elleaume et al., “Measuring Beam Sizes and Ultra-Small Electron Emittances Using an X-ray Pinhole Camera”, *J. Synchrotron Rad.*, (1995). 2, 209-214.



- [4] L.M. Bobb et al., “Performance Evaluation of Molybdenum Blades in an X-ray Pinhole Camera”, Proc. of IBIC2016, Barcelona, Spain, WEPG63.
- [5] B. Yang et al., “High Energy X-ray Pinhole Camera for High Resolution Electron Beam Size Measurements”, Proc. of IBIC2016, Barcelona, Spain, TUPG66.
- [6] F. Ewald et al., “Vertical Emittance Measurement at the ESRF”, Proc. of DIPAC2011, Hamburg, Germany, MOPD61.
- [7] G. Kube et al., “Inorganic Scintillators for Particle Beam Profile Diagnostics of Highly Brilliant and Highly Energetic Electron Beams”, Proc. of IPAC2012, New Orleans, Louisiana, USA, WEOA02.
- [8] G. Kube et al., “Resolution Studies of Inorganic Scintillation Screens for High Energy and High Brilliance Electron Beams”, Proc. of IPAC2010, Kyoto, Japan, MOPD088.
- [9] G. Kube, “High Resolution Scintillating Screens for Measurements of few Micrometer Beams”, Topical Workshop on Emittance Measurements for Light Sources and FELs, ALBA, 2018.
- [10] L.M. Bobb et al., “Beam Size Measurement Using High Aspect Ratio LIGA Apertures in an X-ray Pinhole Camera”, Proc. of IPAC2017, Copenhagen, Denmark, MOPAB132.
- [11] Schneider-Kreuznach, Componon-S 2.8/50, <http://www.schneiderkreuznach.com/en/industrial-solutions/lenses-and-accessories/products/unifoc-system/v-mount-macro-lenses/componon-s-2850/>
- [12] Newport Reflective Microscope Objectives, <https://www.newport.com/f/reflective-microscope-objectives>
- [13] XOP, <http://www.esrf.eu/Instrumentation/software/data-analysis/xop2.4>
- [14] G.D. Boreman, “Modulation Transfer Function in Optical and Electro-Optical Systems”, SPIE Press, Bellingham, WA (2001).
- [15] E. Buhr et al., “Simple method for modulation transfer function determination of digital imaging detectors from edge images”, Proc. SPIE 5030, Medical Imaging 2003: Physics of Medical Imaging, 877.
- [16] QuickMTF, <http://www.quickmtf.com/>

# EXPERIMENTAL SETUP OF APODIZATION TECHNIQUES FOR BEAM DIAGNOSTICS PERFORMED AT ELBE

B. Freeman, J. Gubeli, and K. Jordan, Jefferson Lab, Newport News, VA, USA  
P. Evtushenko, HZDR, Dresden, Germany

## Abstract

The ELBE (Electron Linac for beams with high Brilliance and low Emittance) facility in Dresden, Germany is a multi-purpose user facility, which is also used for accelerator R&D purposes. The beam line was setup for transverse beam profile measurements, where the imaging system includes a series of three apodizers and five circular apertures. Both of which could be changed remotely during beam operation, through automated LabVIEW routines. The bunch structure and charge were varied to collect a series of images that were acquired automatically, and then stored for later analysis. Over 12,000 images were captured and then analyzed using software written at Jefferson Lab that runs ImageJ as its main image processing library.

## INTRODUCTION

Large Dynamic Range (LDR) diagnostics are becoming increasingly important for high current and high beam power accelerators. Machines where a transverse and longitudinal match must be computed to control the beam optics, a lower average beam current is typically used. When setup is believed to be complete the beam current and duty cycle are usually increased. It has been the experience at the JLab machines, both CEBAF and the FEL [1], in its operation, that the best of setups are just not good enough initially to transport the beam at the requested beam power, without beam losses. The setup, either in the transverse or longitudinal plane must be revisited to sustain the beam power requested by the users. The reason for this, is the inability of the available diagnostics to detect beam tails and beam halo ahead of the machine protection system [1]. The operational impact of this can be significant and has caused some to investigate ways of improving the ability to setup, and to investigate diagnostics that could see the tails and halo during setup.

The smallest point that can be resolved in an optical system is defined by its point spread function (PSF). It is a function of the angular acceptance of the aperture. In the Fourier optics, it is the Fourier transform of the pupil function. When light is collected through the aperture, diffraction effects limit the smallest resolvable spot. To improve the dynamic range of the system, which is defined by ( *Peak/Noise* ), apodizers have been suggested to decrease diffraction in the image plane and drive the noise level down even farther. Apodizers have been used in astronomy, when observing stars which are tiny point sources of light. An apodizer is a Gaussian spatial filter, which limits the amount of light that can enter the image plane by decreasing the transmission of light radial out from the center of the filter. The transmission

profile of the filter is defined by

$$T(r, \sigma) = T_0 e^{-\left(\frac{r}{\sigma\sqrt{2}}\right)^2} \quad (1)$$

where  $T_0 = 97\% \pm 1\%$  [2].

Three apodizers were ordered, all were made on a fused silica substrate. Two of the apodizers were made using a half tone dot method. Which means they were constructed with 10  $\mu\text{m}$  pixels that have an increasing density radially by the relation Equation 1. The pixel density changes the amount of light that is transmitted through the filter. The two half tone gaussian profiles were made such that  $\sigma = 6 \text{ mm} \pm 0.3 \text{ mm}$ , and  $\sigma = 12 \text{ mm} \pm 0.3 \text{ mm}$ . The third apodizer was constructed using a reflective coating with increasing density radially outward from  $r = 0$  at the center of the filter, with  $\sigma = 12 \text{ mm} \pm 0.3 \text{ mm}$  [2].

## EXPERIMENTAL SETUP

The ELBE (Electron Linac for beams with high Brilliance and low Emittance) facility in Dresden, Germany was chosen because of the many configurations possible. The facility is a multipurpose user facility which can also be used for R&D applications. The electron beam at ELBE was setup to allow for several different bunch charges, at different micro-pulse frequencies. The overall purpose of the experiment was to put the Gaussian apodizers to the test, with a large range of various light intensities. The experimental setup was set up to automate the process of varying the apodizers, a series of 5 circular apertures, exposure times, and camera gains.

### Mechanical Setup

A Large Dynamic Range Diagnostic Station (LDRDS) was used in this experiment to profile the electron beam. The LDRDS consists of a six inch cross with two beam intercepting devices and two six-inch conflat flange viewports. One device is a stepper motor driven linear shaft with a two wire fork (wire scanner). The fork is orientated at 45 degrees to the beam along two axes with the wires set horizontally and vertically along the beamline. This fork angle is set to allow any optical transition radiation from the wires, as they pass through the electron beam, to be directed out one of the viewports. This fork is electrically isolated from the chamber and connected to an SMA feedthrough. The lead-screw, gear box and stepper motor combination has a linear resolution of 127 nm ( $\frac{1}{2}$  step) and a maximum linear speed of 1.27 mm/second.

The second device is a two-stage pneumatically driven linear stage. The center shaft is rigidly attached to a slide on two linear ball bushing bearings to produce a very repeatable insertion position. A ball bearing is used as a coupling

between the pneumatic shaft and the stage to eliminate off-axis stage force. The ball bearing is kept in place by two constant force springs. In the experiment setup, the end of the center shaft supports a viewer flag as well as a beam shield to reduce beamline impedance. The viewer flag consists of a polished 50.8 mm diameter, 0.1 mm thick YAG:Ce crystal with an AR coating on both sides centered at 550 nm. The YAG:Ce is held normal to the beam with a polished aluminum mirror behind it at 45 degrees to the beam. This arrangement allows the back of the crystal to be imaged though the second viewport. The LDRDS is installed in the radiation physics user beamline at ELBE, Figure 1.

### Optical Setup

An object telecentric optical design was used to image the YAG:Ce crystal. Three achromatic lenses were used in the design to create a combined magnification of  $-1/3$ . The sensor used for this experiment is a JAI's Fusion Series AD-081GE [3]

it is a 2-CCD High Dynamic Range progressive scan camera. This GigE Vision interface camera features two independently controlled CCDs that can be combined to double the dynamic range over a standard CCD. The AD-081GE has a  $1024 \times 768$   $4.65 \mu\text{m}$  pixel array which allowed us to image a  $10.6 \text{ mm} \times 14.2 \text{ mm}$  object.

Two mirrors were used in the optical design to both jog around an existing obstruction and to move the camera off axis to the secondary electron shower generated at the viewer flag. An Edmund Optics motorized five position filter wheel was placed at the field stop location of the first lens. Loaded in this filter wheel were five circular apertures with diameters set to a half angle field of view of one to five degrees in 1 degree steps. A rotary motorized stage that supported three apodizers was placed between the second and third lens. A 3D CAD model of the setup can be seen in Figure 2 and physical devices as seen in Figure 3.

## AUTOMATION

### LabVIEW

LabVIEW was chosen as the controls and interface platform for this experiment. One nice feature of LabVIEW, along with its ease of interfacing equipment through various methods and in creating Graphical User Interfaces, is that it has a Vision Development Module and a Vision Acquisition Software package. These packages made interfacing the GigE camera nearly trivial. Three standalone LabVIEW applications were written to control the filter wheel, the rotary stage (which allowed for apodizer change out), and the GigE camera.

The application for this experiment contained a state machine that calls on these three hardware applications and ensures the completion of tasks in the proper order. The application was developed to capture and save images from one or both sensors after verifying that the optic line and camera sensors were set correctly. The variables for each image save were the selection of an aperture, an apodizer, a

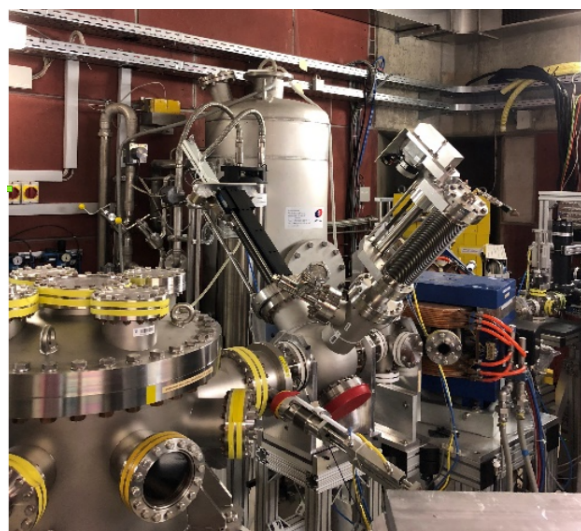


Figure 1: Large Dynamic Range Diagnostic Station (LDRDS) as positioned at ELBE.

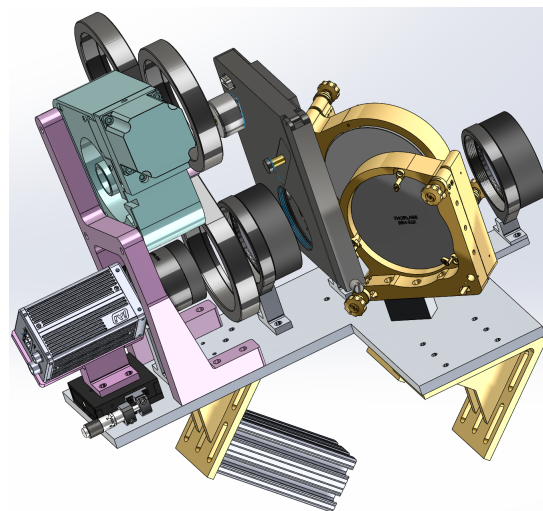


Figure 2: CAD drawing of the optical setup.

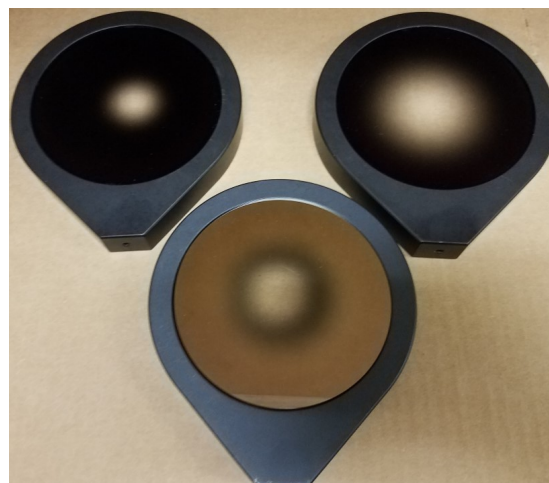


Figure 3: Apodizers installed in mechanical holders.



sensor gain setting and a sensor exposure time. To ensure that we didn't waste valuable beam time at ELBE, the application was developed to execute quickly and to be very flexible. The application would read a four column recipe from a text file and continue to capture and save images until each line was executed. To allow for the quickest run time, the recipe was written as a series of nested loops with the outer loop being the slowest to complete.

For this experiment, these loops were of three exposure times (inner loop), twelve gain settings, five apertures and three apodizers (outer loop). For each electron beam setup, the run script would capture 540 images in less than six minutes.

## Image Analysis

Over 12,000 images were collected from the automated Lab View routines. They were saved to disk and taken back to Jefferson Lab for image analysis. Image analysis was done using a series of perl scripts and software that has been in development for sometime at Jefferson Lab. The software is a pure Java based library, which leans heavily on the ImageJ application. ImageJ is an open source application that was developed by a special for the National Institutes of Health (NIH) for medical imaging analysis. It has a wide variety of features, including the processing of many popular image formats in 8, 16, 24, or 32 bit image formats [4].

The images analyzed were in the format of 16 bit png files. First, the images were organized by aperture, gain, electron beam charge, and exposure time. The software was setup up to process the horizontal and vertical profiles, and then fit a Gaussian function to each of the profiles. After the profiles are written to a file, another script generates a plot for each set of apodizers and then the signal to noise ratio (SNR) in decibels (dB) was computed for each of the image profiles. A set is defined as, all three apodizers for the same camera gain, beam parameters, and each of the apertures. If one of the profiles had  $R^2 \leq 0.90$ , where  $R^2$  is the goodness of fit, the set was rejected. Then the set of apodizers were compared to one another. The over all goal of this calculation is to be able to see which apodizer statistically does the best at reducing the background in the image while allowing the peak signal to be transmitted through. In theory if the transmission profile for the  $\sigma = 6$  mm apodizer is half as much as the  $\sigma = 12$  mm.

## RESULTS

We still have a considerable amount of images to process to better characterize the apodizers and especially in terms of the images size at the apodizer. We have processed the SNR of 12,417 images and have compare the results of the three apodizers. The  $\sigma = 12$  mm reflective apodizer had by far the best SNR for all the image sets. In the horizontal profiles it had the best SNR by 96.5% with 8.6% of the sets rejected for one of the profiles having a poor Gaussian fit. Similarly in the vertical profiles it had the better SNR by 94.4% with 8.8% sets rejected. Some processing was done

in comparing the effects of the aperture sizes and therefore the image size on the apodizer. As expected, the center line pixel intensity profiles of each of the apodizers were near identical with the small angular acceptance aperture. The SNR in these sets of images were within fractions of dB of each other. As the angular acceptance increased, the more the SNR deviated.

Another interesting, but perhaps not surprising observation was that for small angles of angular acceptance of the apertures, the profiles almost were on top of each other. The SNR of the three in these sets of images were within fractions of dB. The  $\sigma = 12$  mm apodizer still won in most cases, although a marginal win. As more light is collected through the aperture, the more the diffraction will affect the image quality. As the angular acceptance increased, the more the SNR deviated.

Figures 4 and 5 represents an example of the plots generated. All three profiles for the three apodizers are shown on the same plot for a particular data set. Figure 4(a) shows the all three of the profiles for the first aperture, which has 1 degree of angular acceptance. Figure 4(b) shows the images used to generate the plot. The images are very close in profile and appearance. Figure 5 shows the same data set, but the 5th aperture was used, which has 5 degrees of angular acceptance. One can easily see that there are more variations in the images in Figure 5(b) than the images in Figure 4(b).

## IMPROVEMENTS

Some improvements to the system and data collection could be made to improve the process, and ability to further analyze the images. For one, an image should have been captured for each set with no apodizer inserted. This would have provided the ability to compare the affect of having an apodizer or not. Based on the data, it may not matter for small angles of light acceptance. For larger angles of light acceptance it may have mattered greatly. Second, there was no way to verify that image was hitting  $r = 0$ , where  $r$  is the point from the center of the apodizer the image rays are focused in the plane of the apodizer. For instance, if the focal point was  $r = 12$  mm on the  $\sigma = 12$  mm apodizer the transmission intensity would drop by roughly half.

Since the goal of this particular experimental was not to measure the dynamic range improvement minimal background images were captured. A background image could have been collected for each of setting, aperture, and apodizer. With the background images and the unapodized image it would have been possible to calculate the improvement in dynamic range of the system. However, the electron beam would have to be turned off to capture the background images, and this would have complicated the setup and software, delaying the data collection process. Finally, the camera that was used was a dual sensor CCD GiGE camera. The two gains could be setup an images collected with both sensors to combine the images for further dynamic range improvement [5].



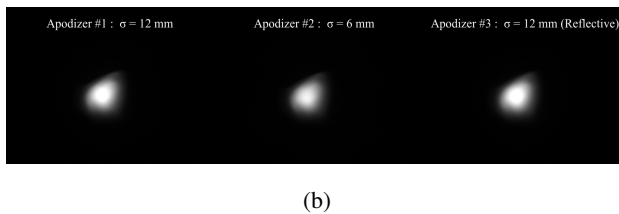
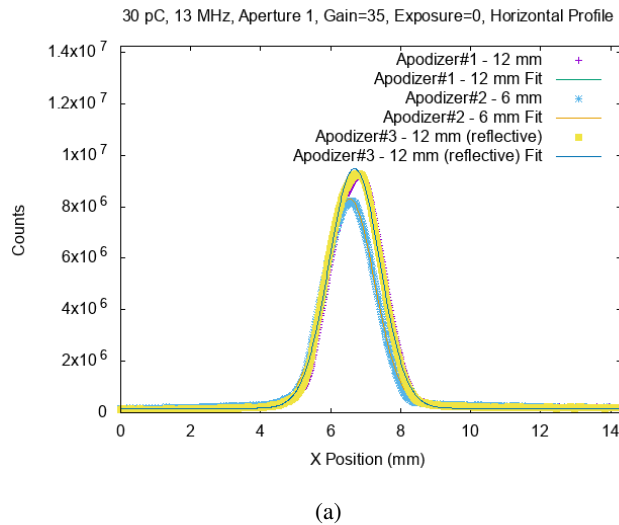


Figure 4: (a) Plot of Aperture #1 (1 degree of angular acceptance), all three apodizers. (b) Images used to generate above plot. Apodizers are  $\sigma = 12$  mm, 6 mm, and 12 mm Reflective from left to right for same data set.

The apodizer transmission profile could have been measured ahead of time to characterize the transmission profile. The optical system could have been designed with beam splitters to image the same image on different sensors. Along, with the aforementioned improvements to the overall data collection another experiment will be planned to fully analyze the improvements that apodization can provide.

## ACKNOWLEDGMENTS

Two days of beam time were used. The beam line setup and experiment went exceptionally well. A very big thanks to the staff at ELBE for helping to make this happen. This material is based upon work supported by the U.S. Department of Energy, Office of Science, Office of Nuclear Physics under contract DE-AC05-06OR23177.

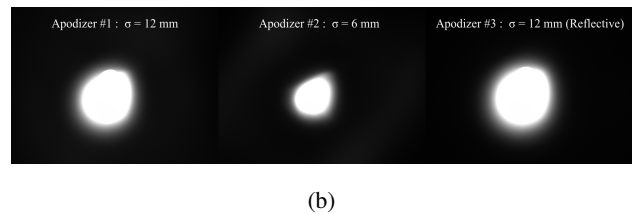
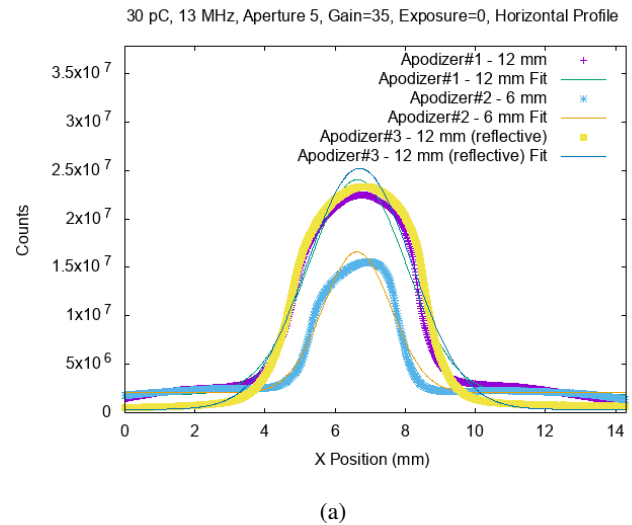


Figure 5: (a) Plot of Aperture #5 (5 degrees of angular acceptance), all three apodizers. (b) Images used to generate above plot. Apodizers are  $\sigma = 12$  mm, 6 mm, and 12 mm Reflective from left to right for same data set.

## REFERENCES

- [1] P. Evtushenko. Large dynamic range beam diagnostics for high average current electron linacs. *International Particle Accelerator Conference (IPAC) 2014 Proceedings*, pages 1900–1901, 2014.
- [2] P. Evtushenko. Jefferson lab specification 02122014-01, 2014.
- [3] JAI. Fusion series camera information. <https://www.jai.com/products/ad-081-ge>.
- [4] Wayne Rasband. Imagej users guide. <https://imagej.nih.gov/ij/>, 2012.
- [5] P. Evtushenko and D. Douglas. "high dynamic range beam imaging with two simultaneously sampling ccds". *International Beam Instrumentation Conference (IBIC) 2012 Proceedings*, pages 263–264, 2012.

# TRANSVERSE BEAM EMITTANCE MEASUREMENTS WITH MULTI-SLIT AND MOVING-SLIT DEVICES FOR LEREC\*

C. Liu<sup>#</sup>, A. Fedotov, D. Gassner, X. Gu, D. Kayran, J. Kewisch, T. Miller, M. Minty, V. Ptitsyn, S. Seletskiy, A. Sukhanov, D. Weiss, Brookhaven National Laboratory, Upton, U.S.A.

A. Fuchs, Ward Melville High School, Setauket- East Setauket, U.S.A.

## Abstract

Low Energy RHIC electron cooling (LEReC) is the first bunched electron cooler, designed to cool low energy ion beams at RHIC. The beam quality, including the transverse beam emittance, is critical for the success of cooling. The transverse electron beam emittance was characterized with a multi-slit and moving-slit device at various locations in the beamline. The beam emittance measurement and analysis are presented in this report.

## INTRODUCTION

LEReC [1], a linear electron accelerator (Figure 1), is designed to cool RHIC ion beams and therefore improve luminosities at beam energies below 10 GeV/n [2]. Electron bunches are generated by a 400 kV DC electron photocathode gun; these bunches then go through a chain of cavities, which includes a 1.2/1.6 MeV 704 MHz superconducting booster cavity, a 2.1 GHz normal-conducting copper cavity to linearize beam energy chirp, a 704 MHz normal-conducting cavity to reduce energy spread of individual bunches and a 9 MHz normal-conducting cavity to reduce energy droop along bunch train due to beam loading. Each electron macro-bunch, consisting of 30 micro-bunches of 40 ps length at 704 MHz repetition frequency, will overlap with a RHIC ion bunch at 9 MHz frequency. The electron beam first propagates with the ion beam in one of the RHIC rings (Yellow) collinearly with the same speed, then turns around and propagates with the ion beam in the other RHIC ring (Blue). With extremely small energy spread ( $5E-4$ ), the electron beam reduces the ion beam energy spread when interacting with it by coulomb friction force. The design electron beam current is 30-55 mA for beam energy 1.6-2.6 MeV, with bunch charge of 130-200 pC and normalized emittance  $<2.5 \mu\text{m}$  [1].

Matching the electron beam transverse emittance to that of the ion beam is crucial for cooling. With low energy and high bunch charge, the electron beam emittance is dominated by space charge effect. Therefore, emittance measurement devices made of slit/slits [3] were chosen in the LEReC accelerator to measure beam emittance along the beamline. The multi-slit and moving-slit sample several transverse slices of the beam which then project to downstream profile monitors. The space charge effect is substantially reduced due to reduction of charge density by the sampling of the slit/slits.

## MATERIAL AND METHOD FOR BEAM EMITTANCE MEASUREMENT

A multi-slit device (Figure 2) [4], installed after the Booster cavity with a YAG profile monitor 2 m downstream, measures beam emittance in the DC gun test line. There are 10 horizontal and 10 vertical slits on the same mask, respectively for vertical and horizontal beam emittance measurement. The slit width is  $150 \mu\text{m}$ , with slit spacing  $1.346 \text{ mm}$ . The mask was made of Tungsten plate of  $1.5 \text{ mm}$  thickness. The multi-slit mask is thick enough to stop most of the electrons at  $1.6 \text{ MeV}$  beam energy. This is designed to avoid background on the downstream profile monitor due to scattered electrons.

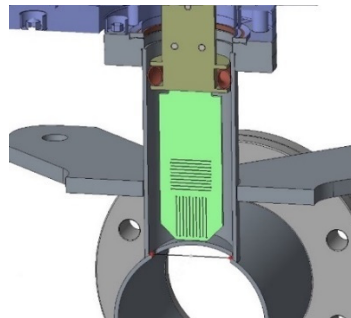


Figure 2: Drawing of multi-slit device at retracted position, with vertical slits at the bottom and horizontal slits at the top part of the mask.

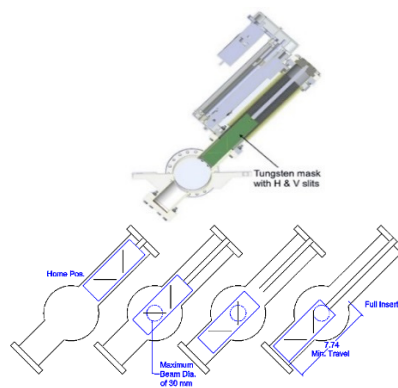


Figure 3: Schematics of moving-slit device. The image on top shows the assembly and the orientation, with a view along the beam path. The lower image illustrates the sampling process, first horizontal and then vertical with the mask driven in by a stepper motor.

\*The work was performed under Contract No. DE-SC0012704 with the U.S. Department of Energy.  
<sup>#</sup> cliu1@bnl.gov

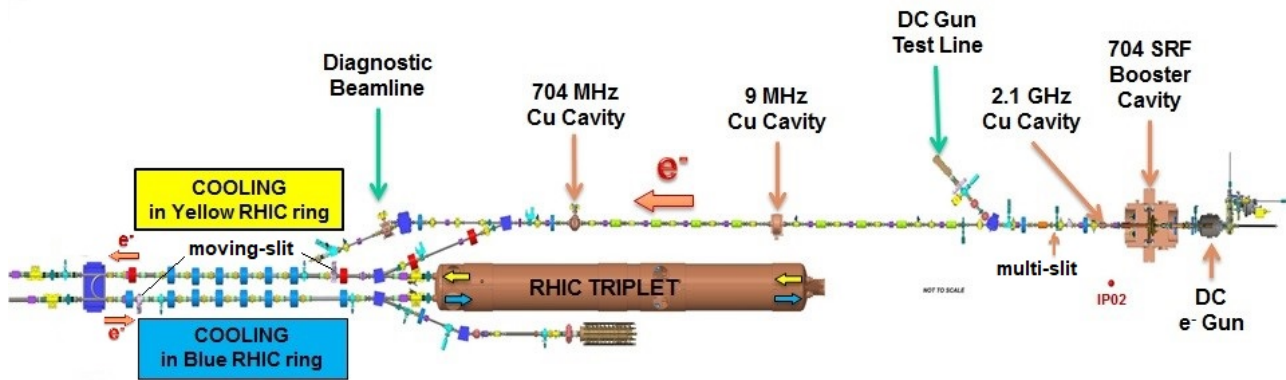


Figure 1: Schematics of Low Energy RHIC electron Cooling accelerator. Low energy electron beam is transported through beamline with solenoids, merged to cooling section in Yellow RHIC ring first, turned around and merged to cooling section in Blue RHIC ring to cool ion beams in both rings.

Two moving-slit devices (Figure 3), placed after the first merging dipole magnet in Yellow RHIC ring and the 180-degree dipole magnet, measure the beam emittance in the cooling sections. The moving-slit, driven by a step motor into the beam path at a 45-degree angle, samples horizontal beam slices and then vertical slices. Up to 40 beam slices can be generated by each scan on the downstream YAG profile monitor for horizontal and vertical measurements. The slit width is 150  $\mu\text{m}$ . The distance from the moving-slit to the downstream profile monitor is 2 m and there are no magnetic elements between the moving-slit and the downstream profile monitor. The potential advantage of this device is to sample more transverse slices for better precision emittance measurement.

## MEASUREMENT RESULTS AND ANALYSIS

The emittance measurement with the multi-slit in the DC gun test line is presented here. Multiple beam slices, sampled from the beam by the multi-slit, propagate in a drift space to the downstream profile monitor. The beam slices would expand in the drift space, with length designed based on model parameters, but not overlap with each other on the downstream profile monitor. The width of each beam slice on the profile monitor represents the divergence of each beam slice. The recorded profile was projected to horizontal or vertical plane. The projection was fitted to a multi-Gaussian distribution, providing information of the amplitudes and RMS width of the peaks. Then the beam emittance was calculated based on the fitting results [5]. With 32 pC bunch charge, the geometrical horizontal beam emittance was measured to be  $0.512 \pm 0.015 \mu\text{m}$ . The image processing and emittance calculation was performed by an in-house program called imageViewer [6].

Beam charge dependence of beam emittance (Figure 6) has been studied with the multi-slit device. The single bunch charge was scanned from 13 to 32 pC by varying the laser intensity for these measurements. The solenoid between the multi-slit and downstream profile monitor was

turned off during the measurements. These beam emittance measurements for different bunch charge were taken with the same optics setting. In the future, these measurements will be performed while changing the beam optics accordingly. By doing this, beam emittance growth due to non-optimal beam optics can be avoided.

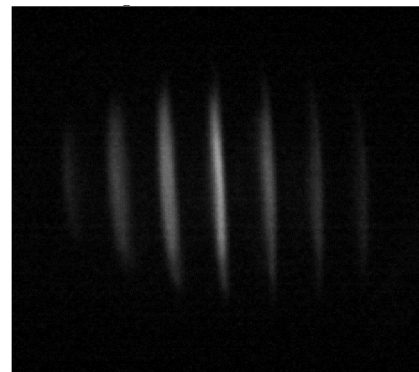


Figure 4: Images taken on the downstream profile monitor with vertical slits of the multi-slit inserted in the beam path.

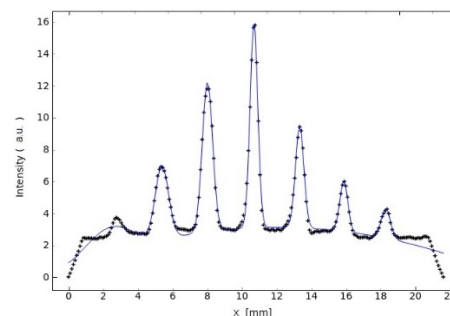


Figure 5: Multiple peak intensity distribution (data points in stars), generated by projecting image of beam slices (Figure 4) along the slice image direction, and its multi-Gaussian peak fitting (solid curve).

Beam emittance measurement results with multi-slit showed a strong dependence on the number of beam slices used in the emittance calculation. With smaller bunch

charge, the outer slices will be excluded by imageViewer if their intensity is comparable to noise level. These beam slices have larger slice emittance than the center ones. Therefore, their accidental exclusion resulted in smaller beam emittance number and larger error bar at lowest bunch charge (Figure 6).

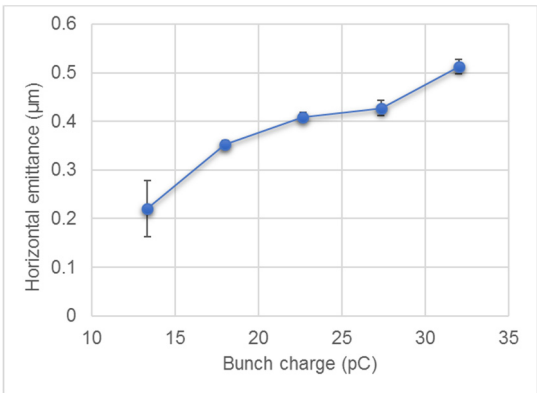


Figure 6: Bunch charge dependence of the horizontal beam emittance measured with multi-slit device. The error bars show the statistic measurement errors.

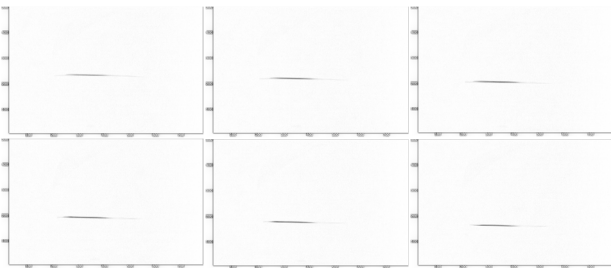


Figure 7: Selected individual beam slice images taken on the profile monitor while sampling the beam with moving horizontal slit.

The preliminary results from commissioning of the moving-slit are presented here. Multiple profiles on the downstream profile monitor (Figure 7) have been taken while the moving-slit was driven through the beam path. The projection of these profiles were combined (Figure 8) to show the samples from the beam. With the same algorithm [5], the emittance was calculated based on the fitting parameters of these peaks. The advantages of moving-slit emittance measurement are that the method produces a greater number of beam slices than with multi-slit device and these slices do not interfere with each other.

It was found that the system is very sensitive to beam orbit. Not only should the beam be centered on the BPM near the moving-slit, but also on the profile monitor. Initial tuning of beam orbit along the moving-slit device is necessary before starting the scanning begins. Due to residual beam offsets, a programmable scanning range was implemented. It is also suspected that beam scraping, which would also affect measured profiles, happened upstream. Therefore, beam optics tuning for good transmission is crucial as well.

One problem associated with the moving-slit device is that the space between the slit and the downstream profile

monitor is short (2 m). The spacing was limited by the available drift space from one solenoid to the next. With a short drift space, the beam slice will not diverge enough on the profile monitor which results in less precision in the measurement of the beam divergence.

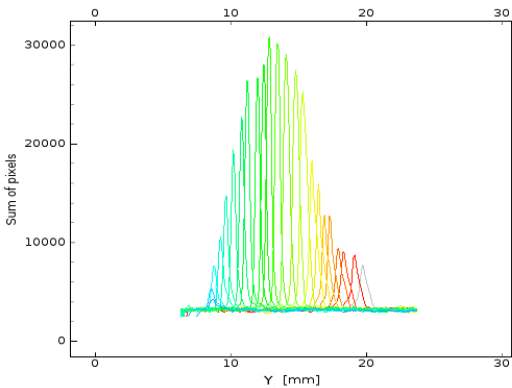


Figure 8: Combination of projection of (~30) individual beam slices, taken at each step while scanning the horizontal slit through the beam. The measured geometrical vertical RMS emittance is 0.49 μm.

Slanted beam slices have been observed in beam emittance measurements in the Yellow cooling section intermittently. This has not been understood and further investigation is needed. It is suspected that there is leakage magnetic field from solenoids, either the one upstream of the slit, or the ones in the Blue cooling section close to the moving-slit measurement device.

## SUMMARY AND OUTLOOK

In this report, the emittance measurement devices, measurement methodology, measurement results and analysis were reported. We obtained reasonable measurement results with the multi-slit device. The preliminary results from commissioning the moving-slit are also presented in this report.

The work reported here provides a perspective for future work on beam emittance measurement. Beam emittance will be characterized as a function of beam currents and beam optics configuration. The dependence of beam emittance on the beam position in the booster cavity will be investigated as well. The final goal is to measure the electron beam emittance at design bunch charge and match it with that of the ion beam.

## REFERENCES

- [1] A. Fedotov *et al.*, “Accelerator physics design requirements and challenges of RF based electron cooler LEReC.”, in *Proc. of NA-PAC’16*, Chicago, IL, USA, 2016, paper WEA4CO05, <https://doi.org/10.18429/JACoW-NAPAC2016-WEA4CO05>
- [2] C. Montag, “RHIC as a low energy collider.” 9<sup>th</sup> International Workshop on Critical Point and Onset of Deconfinement, p041 (2015).



- [3] M. Zhang, “Emittance formula for slits and pepper-pot measurement.” No. FNAL-TM--1988. *Fermi National Accelerator Lab.*, 1996.
- [4] T. Miller *et al.*, “LEReC instrumentation design & construction.”, in *Proc. of IBIC'16*, Barcelona, Spain, 2016, paper TUPG35.
- [5] C. Liu *et al.*, “Design and simulation of emittance measurement with multi-slit for LEReC.”, in *Proc of NA-PAC'16*, Chicago, IL, USA, 2016, <https://doi.org/10.18429/JACoW-NAPAC2016-WEPOB68>.
- [6] A. Sukhanov,  
<https://github.com/ASukhanov/Imagin>



## MEASUREMENT PROCEDURE

Two vertical and two horizontal copper scraper plates are installed in dispersion free regions of the synchrotron. Both plates of each pair are on opposite sides of the vacuum chamber while being at the same longitudinal position. The scraper plates are moved one by one into the path of the circulating beam while measuring the beam intensity losses with a direct current transformer (CTS). The scrapers can be moved with variable speed, with the typical speed being 0.02 m/s.

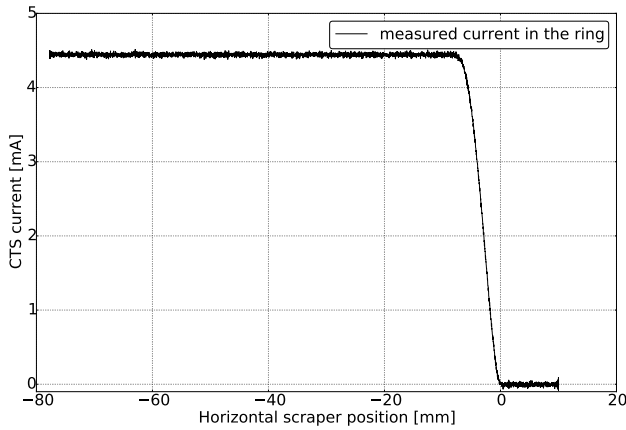


Figure 1: Measured CTS signal for a 400 MeV/n carbon ion beam with degrader 100 % at flattop when moving the horizontal scraper from negative x positions into the beam path.

## ANALYSIS PROCEDURE

To calculate the emittance one can use the well known relationship:

$$\epsilon = \frac{\sigma_{\text{RMS,beam}}^2}{\beta_{\text{twiss}}} \quad (1)$$

where the  $\beta$ -function can be assumed from optics calculations. The RMS beam size relates to the RMS of the particle betatron amplitude distribution according to [8]:

$$\frac{\sigma_{\text{betatron}}^2}{\sigma_{\text{beam}}^2} = 2 \quad (2)$$

By calculating the numerical derivative of the signal curve shown in Fig. 1 one immediately obtains the betatron amplitude distribution of the particles as seen in Fig. 2.

### Analysis Workflow

The analysis procedure follows these steps:

1. Map the beam current signal to the corresponding scraper position
2. Apply a moving average smoothing to the signal
3. Estimate the beam center

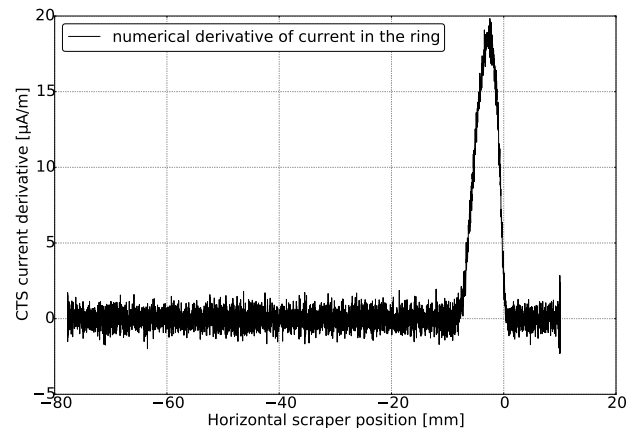


Figure 2: Numerical derivative of the signal shown in Fig. 1 after applying a moving average smoothing with a factor 50 to the signal.

4. Calculate the numerical derivative of the signal
5. Compute the RMS of the obtained betatron amplitude distribution and with Eqs. 1 and 2 calculate the geometric emittance

### Estimation of the Beam Center

While a common approach to estimate the beam center is to scrape twice from opposite sides, it was a goal for this analysis procedure, to be able to create a robust possibility to calculate the transverse emittance from a single measurement as well. This has the advantages of being less prone to errors stemming from cycle-to-cycle fluctuations and allowing the usage of partially incomplete data sets. Especially the second part allows the effective use of limited shift time, as well as enabling the transverse synchrotron emittance to be measured as part of recurrent automatic quality assurance measurements, where the data analysis will be performed at a later point in time.

Multiple ways have been implemented to calculate the beam center from the CTS signal (Fig. 1):

**Curve Fit** If one assumes a Gaussian beam profile in a non-dispersive region, the beam current signal can be analytically described by a function of the form:

$$\frac{I(x)}{I_0} = \left(1 - \exp\left(-\frac{(x - x_0)^2}{2\beta\epsilon}\right)\right) \Theta(x - x_0) \quad (3)$$

with the Heavyside-function  $\Theta$  and the center of the beam  $x_0$ . Since  $\beta$  and the order of magnitude of  $\epsilon$  are assumed to be known, fitting Eq. 3 to the beam current signal gives quite reliable estimations of the beam center, as shown in Fig. 3. The first scraper position at which the measured current gets negative is usually a good initial value for the  $x_0$  variable in the curve fit.

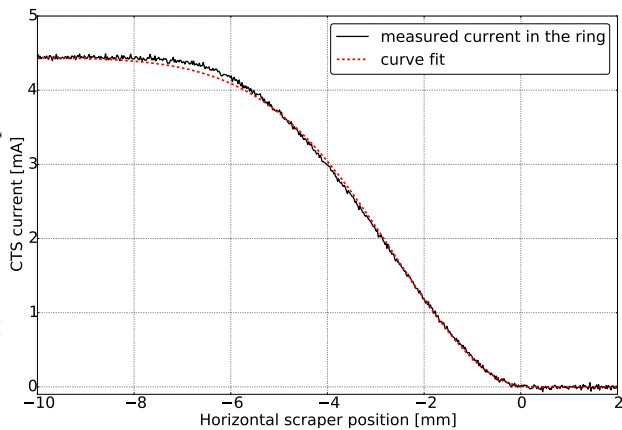


Figure 3: Function from Eq. 3 fitted to the signal from Fig. 1.

**Flank Detection** A more basic algorithm to compute the beam center was also implemented, which checks whether a number of consecutive points are above a threshold defined by the standard deviation of the signal noise. If that is the case the rising flank of the signal has been detected, which should coincide with the beam center.

### Reconstruction of the Positional Distribution

One way to reconstruct the positional distribution of the particles from the betatron amplitude distribution is by assigning uniformly distributed angles to “particles” and modulating them with the cosine like betatron motion. The resulting distribution can give a quick optical feedback, albeit not being relevant for the emittance computation.

An example for a positional distribution calculated in this way can be seen in Fig. 4.

## SIMULATIONS

The simulations to characterize the behavior of the analysis were completely done in Python 3.4. The simulation code was built directly into the analysis program and can therefore be also used as a testing tool for future releases of the whole *PACMAN* framework.

The simulations were carried out with normally distributed particles, created using the `numpy.random` module [9] with the following parameters:

Table 2: Simulation Parameters

Parameter	Value
Number of particles	$10^5$
Input emittance	$0.66 - 1.43 \pi \text{ mm mrad}$
$\beta$ (at scraper)	8.758 m
$\alpha$ (at scraper)	-0.131 rads
Noise $\sigma$ (degrader 10)	0.05
Noise $\sigma$ (no degrader)	0.005

### Accuracy of the Emittance Reconstruction without Noise

When reconstructing the transverse emittance with the parameters in Table 2, the results shown in Table 3 were obtained, showing a very good accuracy of the algorithm. For each input emittance the simulations were run 10 times.

Table 3: Relative errors in reconstruction for the ideal case simulation with no noise. Geometric emittances given in  $\pi \text{ mm mrad}$ .

$\epsilon$	reconstructed $\epsilon$	relative error [%]
0.66	$0.662 \pm 0.005$	$0.35 \pm 0.71$
1.045	$1.049 \pm 0.009$	$0.47 \pm 0.85$
1.43	$1.435 \pm 0.009$	$0.38 \pm 0.63$

### Accuracy of the Emittance Reconstruction with Varying Noise

The noise on the beam current signal is simulated as being normally distributed, with a standard deviation given in Table 2. The values for the noise standard deviation were derived from real measurement data.

Table 4: Relative errors in reconstruction for no degrader and degrader 10 %. Geometric emittances given in  $\pi \text{ mm mrad}$ .

	$\epsilon$	reconstructed $\epsilon$	relative error [%]
no deg.	0.66	$0.679 \pm 0.006$	$2.81 \pm 0.95$
	1.045	$1.069 \pm 0.074$	$2.31 \pm 0.71$
	1.43	$1.459 \pm 0.014$	$2 \pm 0.93$
deg. 10	0.66	$0.699 \pm 0.031$	$5.97 \pm 4.64$
	1.045	$1.071 \pm 0.048$	$2.44 \pm 4.63$
	1.43	$1.492 \pm 0.074$	$4.34 \pm 5.15$

What can be immediately seen from the results shown in Table 4 and Fig. 5 is, that the repeatability decreases significantly with worse signal to noise ratio, while the average error does not increase as much.

## MEASUREMENT RESULTS

The improved analysis procedure has already been put to use during the commissioning of carbon ions as well as in the analysis of repetitive proton quality assurance measurements.

In Table 5 measurement results for the carbon ion beam are summarized which show very good agreement with the design value of  $0.7482 \pi \text{ mm mrad}$ .

## CONCLUSION

The improved emittance analysis procedure tool at MedAustron allows completely automatic and robust reconstruction of the transverse synchrotron emittance from scraping measurements, even when only scraping from one



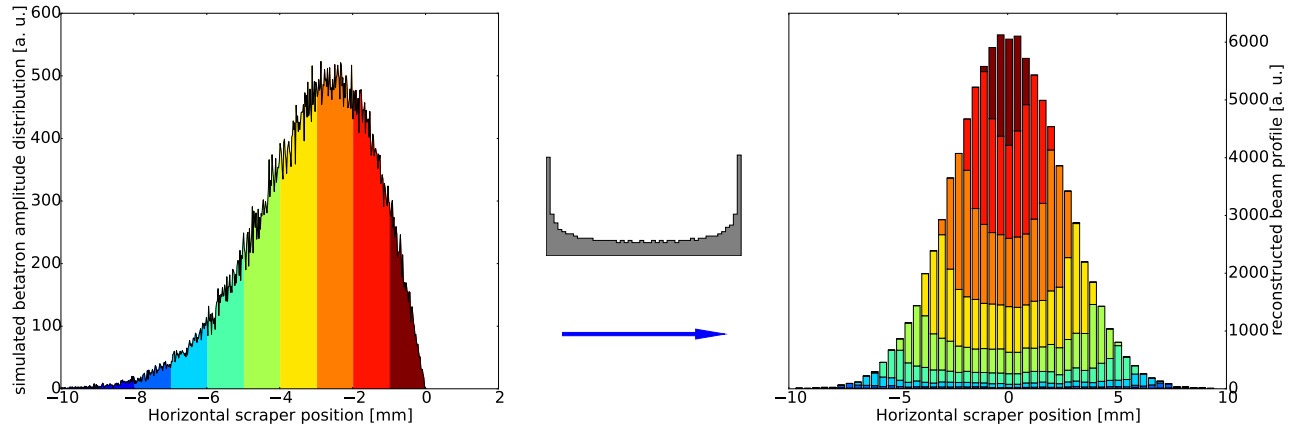


Figure 4: The betatron amplitude distribution (left) is modulated with a cosine distribution (center) to obtain the symmetrical particle position distribution (right).

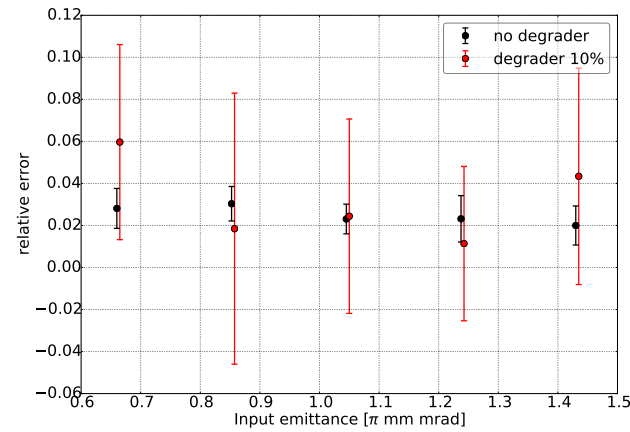


Figure 5: Relative emittance reconstruction error for two different degrader settings.

Table 5: Normalized horizontal emittance results of the still under commissioning carbon beam for the lowest and highest extraction energy in  $\pi$  mm mrad.

degrader	120 MeV/n	400 MeV/n
100 %	0.74	0.81
50 %	0.71	0.74
20 %	0.69	0.74
10 %	0.63	0.76

side. Simulations show that the tool can reliably reconstruct the emittance with average relative errors of less than 1 %. The analysis accuracy is at the moment strongly dependent on the relative noise level of the measured signal, which should be further investigated to mitigate the possible errors introduced. The tool has already been put to use during commissioning and repetitive quality assurance measurements

and could show that the emittance for the carbon ion beam under commissioning is within 10 % of the design value.

## ACKNOWLEDGEMENTS

The authors would like to acknowledge the support of all members of MedAustron's Therapy Accelerator Division, without whose dedication and support these results would not have been possible.

## REFERENCES

- [1] P. J. Bryant *et al.*, FRX01A, EPAC98 (1998).
- [2] G. Magrin *et al.*, "The path to the Italian national centre for ion therapy", ISBN 978-88-95522-44-9, TERA Foundation (2010).
- [3] C. Kurfürst *et al.*, "Status of the MedAustron commissioning with protons and carbon ions", in *Proc. IPAC2018*, 2018, paper TUPAF004.
- [4] T. Kulenkampff *et al.*, "Extraction commissioning for MedAustron proton operation", in *Proc. IPAC2016*, 2016, paper TUPMR036.
- [5] Python, <https://www.python.org/>.
- [6] A. Wastl, T. Kulenkampff, S. Nowak, and A. Garonna, "PAC-MAN - The MedAustron measurement data analysis framework", in *Proc. IPAC2016*, 2016, paper WEPOR045.
- [7] A. Wastl, M. Hager, and M. Regodic, "Operational applications - A software framework used for the commissioning of the MedAustron accelerator", in *Proc. IPAC2015*, 2015, paper MOPHA002.
- [8] C. Carli, A. Jansson, M. Lindroos, and H. Schönauer, "A comparative study of profile and scraping methods for emittance measurements in the PS booster", *Part. Accel.*, vol. 63, pp. 255–277, 2000.
- [9] Numpy, <https://www.numpy.org/>.

# SETUP FOR BEAM PROFILE MEASUREMENTS USING OPTICAL TRANSITION RADIATION\*

J. Pforr<sup>†</sup>, M. Arnold, T. Bahlo, L. Jürgensen, N. Pietralla, A. Rost,  
TU Darmstadt, Darmstadt, Germany  
F. Hug, Johannes Gutenberg-Universität Mainz, Mainz, Germany

## Abstract

The S-DALINAC is a thrice-recirculating, superconducting linear electron accelerator at TU Darmstadt. It can provide beams of electrons with energies of up to 130 MeV and currents of up to 20  $\mu$ A. The accelerator performance was improved by an extension of the beam diagnostics, as this increases the reproducibility of the machine settings. In addition, the installation of several beam profile measurement stations is planned, which should be operational down to a beam current of 100 nA, as this current is used for beam tuning. Combining these devices with a quadrupole scan also allows for emittance measurements. The beam profile measurements shall be done based on optical transition radiation (OTR), resulting from the penetration of relativistic electrons from vacuum into a metal target. The radiation can be detected using standard cameras that provide information on the two-dimensional particle distribution. This contribution will address the layout of the measurement stations and a first test measurement will be presented.

## NEW DIAGNOSTIC STATIONS AT THE S-DALINAC

The current layout of the S-DALINAC is shown in Fig. 1. The electron beam coming from one of the two sources can be accelerated in the superconducting injector to up to 10 MeV beam energy [1]. After the injector the beam can be used at the DHIPS (Darmstadt High Intensity Photon Setup) experimental area [2] or be bent into the main linac. The electrons can pass the main linac up to four times due to the three existing recirculations [3] and are afterwards extracted to the experimental hall with a maximum energy of 130 MeV.

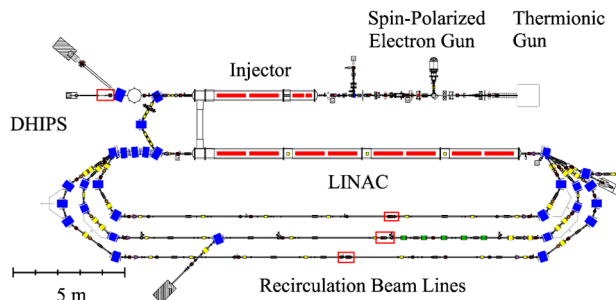


Figure 1: Layout of the S-DALINAC with three recirculation beam lines. The red boxes denote the positions of the planned diagnostic stations.

In order to enable an emittance measurement after each acceleration, there are several diagnostic stations necessary. One is located behind the superconducting injector and further diagnostic stations are planned in the straight sections of each recirculation beam line. The positions were chosen such that quadrupoles are available for an emittance measurement based on a quadrupole scan. In addition, the diagnostic stations consist of an OTR target and CMOS cameras (FLIR BFLY-PGE-31S4M-C) which detect the radiation. This type of camera was chosen for various reasons as a high resolution and framerate. Of special importance is the possibility to adjust many camera parameters, e.g. the exposure time and gain, remotely, which results in a high flexibility. As these cameras have to be protected from radiation damage, the target is supposed to be observed via a mirror in order to allow for better shielding.

## OPTICAL TRANSITION RADIATION

Transition radiation is emitted when a relativistic charged particle crosses the boundary between two media with different permittivity, as the electric field has to rearrange at the boundary. This radiation was predicted in 1947 by Ginzburg and Frank [4], and after pioneering work by Wartski [5] it has been established as a tool for electron beam diagnostics. The emission of OTR is directed in two cones with opening angle of  $1/\gamma$ , as depicted in Fig. 2, where the metal target is inclined with  $45^\circ$  with respect to the electron beam. The radiated power for an electron with Lorentz factor  $\gamma \gg 1$  can be described by [6]

$$W_1(\theta) = \frac{e^2}{4\pi^3\epsilon_0 c} \frac{\beta^2 \sin^2 \theta}{(1 - \beta^2 \cos^2 \theta)^2}$$

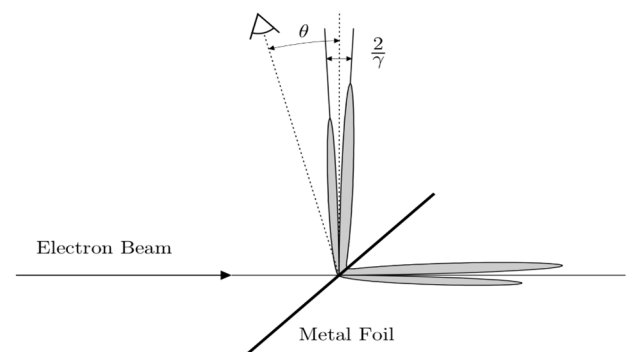


Figure 2: The directional dependence of the intensity of OTR light that is emitted by a metal foil with  $45^\circ$  angle to the electron beam [7].

\* Work supported by DFG through GRK 2128.

<sup>†</sup> jppforr@ikp.tu-darmstadt.de

where  $W_1 = d^2W/d\omega d\Omega$  is the spectral distribution of the energy and  $\beta = v/c$  the particle velocity. Additionally, for further considerations concerning the most suited target materials, it shall be noted that the total intensity of the radiation is proportional to both  $\gamma$  and the plasma frequency, which is the natural frequency of electron oscillation in a metal, of the target material [8].

## TARGET DESIGN

For the target design, different aspects have to be taken into account. As the OTR intensity is proportional to the target plasma frequency, this is an important parameter for the choice of the target material. The plasma frequencies of some metals are summarized in Table 1.

Table 1: Plasma Frequencies of Common Materials [9].

Material	Plasma Frequency [eV]
Aluminium	15
Nickel	9.45
Gold	5.8
Silver	3.735

Due to the high plasma frequency of aluminium, this material is favoured for the OTR targets. Another issue, however, is the target flatness. Due to the directed nature of OTR, any surface modulation will also translate into an intensity modulation in the image. Therefore, not only pure aluminium targets are considered, but also targets which consist of a  $\mu\text{m}$ -thin aluminium layer deposited on a kapton (polyimide) foil. As the kapton can be stretched, a flat surface is easier to achieve. In order to realise the stretching of the target foil, a target holder was designed that keeps the target under tension. The resulting diameter of the target foil is 25 mm, the thickness is mainly determined by thermal properties. The temperature change of the target foil is described semi-empirically by [10]

$$\frac{\Delta T(r, t)}{\Delta t} = \frac{1}{c_p \rho} \left[ \frac{dE}{dx} \rho \exp\left(-\frac{r^2}{2\sigma^2}\right) N(t) - k \nabla^2 T(r, t) - \frac{2\epsilon \sigma_s}{\delta} (T(r, t)^4 - T_0^4) \right]$$

where  $dE/dx$  denotes the stopping power,  $N(t)$  the (possibly time-dependent) particle flux,  $k$  the thermal conductivity,  $\epsilon$  the emissivity and  $\delta$  the target thickness. It shall be noted that in this equation the assumption of a spatial gaussian distribution of the beam was made. The obvious consequence for the target design is that thin targets are advantageous for thermal aspects. For further considerations, the properties of aluminium and kapton are summarized in Tab. 2. From these quantities we can conclude that aluminium can conduct heat better, but emits less energy than kapton by thermal radiation. In order to investigate the relevance of these effects, a simulation of the thermal behaviour of the target was conducted.

Table 2: Thermal Properties of Aluminium and Kapton

	Aluminium	Kapton
Density [g/cm <sup>3</sup> ]	2.7	1.4
Thermal conductivity [W/(Km)]	250	0.2
Emissivity	0.04	0.24

## THERMAL SIMULATIONS

This simulation of the thermal target properties is supposed to give a rough estimate of the heating of both, an aluminium and a kapton target. It was conducted with CST MPhysics Studio [11]. At first, the total deposited power had to be estimated for an expected target thickness of 10  $\mu\text{m}$ . Considering the stopping power only the energy deposition by collisions is relevant [12], which has only a slight energy-dependence, so typical values of the stopping power were used. The resulting power for the maximum beam current of 20  $\mu\text{A}$  results to 0.06 W for kapton and 0.10 W for aluminium. While these values seem small, a uniformly distributed beam spot with a radius of 0.5 mm results in a heated volume of only  $8\text{e-}3 \text{ mm}^3$ , so a significant heating has to be expected. In the model, the target foil was surrounded by an aluminium target holder, which is similar to a heat reservoir due to the thickness of 4 mm. The outer boundaries of this target holder were isothermal. The results for a pure aluminium target and a kapton target are

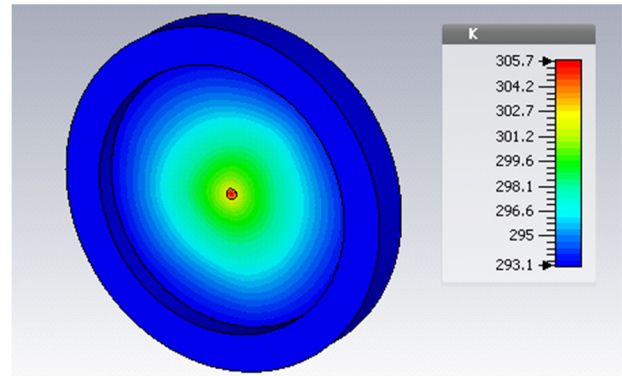


Figure 3: The temperature distribution of an aluminium target for 20  $\mu\text{A}$ . Simulated with CST [11].

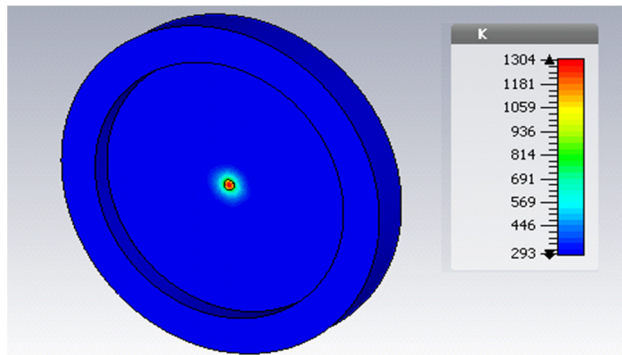


Figure 4: The temperature distribution of a kapton target for 20  $\mu\text{A}$ . Simulated with CST [11].

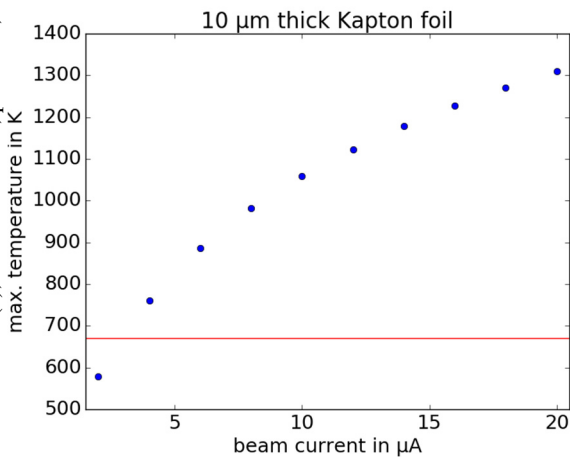


Figure 5: The maximum temperature of a kapton target for various beam currents. The red line denotes 400°C, which we consider the maximum reasonable temperature. This is no strict limit, however, thermal aging takes place and destroying the target must be avoided. Simulated with CST [11].

shown in Fig. 3 and Fig. 4 respectively. It is noticeable that the heat is distributed over a large volume in aluminium due to the high thermal conductivity, while there is only a small heated spot on the kapton target. Consequently, the aluminium target is hardly warmed up, while the kapton target reaches a temperature of 1300 K, which would destroy the kapton. For that reason, for the kapton target a beam current limit has to be found. Therefore, the dependency of the maximum temperature from the beam current was investigated. The results are summarized in Fig. 5. The calculations show that only beam currents of a few  $\mu\text{A}$  are possible without destroying the kapton target. For smaller beamspots this limit would be reduced even further, so a safety margin is necessary as long as the actual beam spot size is unknown. However, the demonstration measurements described in the next section show that a beam size measurement can be conducted at low beam current and energy with sufficient image brightness.

## DEMONSTRATION MEASUREMENT

To demonstrate the applicability of this technique, in Dec. '17 a first emittance measurement with an OTR target was conducted [13]. The target is located behind the superconducting injector, where the beam energy was 5.2 MeV in this beamtime. We used beam currents of  $\sim 100$  nA, as the target image was sufficiently bright, but not saturated. Fig. 6 shows one example image. Despite the fact that the beamspot does not have a 2D-gaussian shape, the horizontal and vertical projections allowed an easy evaluation. After a background subtraction and a calibration of the image size, the beam size could be determined by a gaussian fit. This allowed to determine the emittances, which are on the order of 0.1 mm mrad with typical uncertainties of less than 10 % [13].

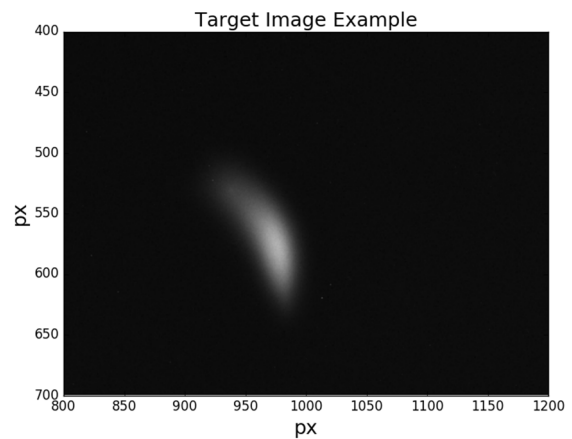


Figure 6: Section of an OTR target image example.

## CONCLUSION AND OUTLOOK

The design considerations of OTR targets for an emittance measurement setup at the S-DALINAC show different options. One option would be to construct targets based on a Kapton foil with a small layer of aluminium added. In this case, the targets can not stand the full beam current of 20  $\mu\text{A}$  but can be used for low current operation (e.g. during beam tuning). On the other hand, pure aluminium targets can withstand the maximum beam current, however, their flatness is problematic. Therefore, the production of kapton-based targets has started. Apart from that, the design of the optics setup and shielding for the camera is ongoing work. Currently, it is planned to conduct an emittance measurement later this year.

## REFERENCES

- [1] Norbert Pietralla, "The Institute of Nuclear Physics at the TU Darmstadt", *Nuclear Physics News*, vol. 28, no. 2, pp. 4-11, 2018, DOI: 10.1080/10619127.2018.1463013
- [2] K. Sonnabend *et al.*, "The Darmstadt High-Intensity Photon Setup (DHIPS) at the S-DALINAC", *Nucl. Instr. Meth.*, vol. 640, pp. 6-12, 2011.
- [3] M. Arnold *et al.*, "Construction and Status of the Thrice Recirculating S-DALINAC", in *Proc. 8th Int. Particle Accelerator Conf. (IPAC'18)*, Copenhagen, Denmark, May 2017, paper TUPAB030, pp. 1384-1387, <https://doi.org/10.18429/JACoW-IPAC2017-TUPAB030>
- [4] V. L. Ginzburg and I. M. Frank, "Radiation of a uniformly moving electron crossing a boundary between two media", *JETP* 16, p. 15, 1946.
- [5] L. Wartski, S. Roland, J. Lasalle, M. Bolore, G. Filippi, *Jour. Appl. Phys.*, Vol. 46, 1975, 3644, doi: 10.1063/1.322092
- [6] V. L. Ginzburg and V. N. Tsytovich, "Several problems of the theory of transition radiation and transition scattering", *Phys. Rep.* 49, pp. 1-89, 1979.
- [7] H. Loos, "Bestimmung der longitudinalen Struktur der Elektronenbunche im Strahl von supraleitenden Beschleunigern", Ph.D. thesis, Phys. Dept., TU Darmstadt, Darmstadt, Germany, 2001.



- [8] S. Döbert *et al.*, “Beam Diagnostics using Transition Radiation”, in *Proc. Workshop on RF Superconductivity*, Gif-sur-Yvette, France, Oct. 1995, pp. 719-722.
- [9] D. Langley, R. A. Coutu Jr., L. A. Starman, and S. Rogers, “Optical Metamaterials for Photonics Applications”, *Proc. SPIE – The International Society of Optical Engineering*, vol. 7468, 2009.
- [10] E. Bravin, T. Lefèvre and C. Vermare, “OTR Studies for the High Charge CTF3 Beam”, *Proc. Particle Accelerator Conference (PAC)*, Portland, Oregon, USA, May 2003, pp. 2464-2466.
- [11] Dassault Systèmes: CST – Computer Simulation Technology GmbH: CST Studio Suite. Version 2016, <http://www.cst.com/>.
- [12] E. Bravin, “Thermal analysis of OTR screens for CTF3”, CTF3 Note 019, 2001.
- [13] F. Hug, M. Arnold, T. Bahlo, J. Pforr, and N. Pietralla, “Beam Based Alignment of SRF Cavities in an Electron Injector Linac”, *Proc. 9<sup>th</sup> Int. Particle Accelerator Conf. (IPAC '18)*, Vancouver, Canada, May 2018, paper THPMF064, pp. 4219-4222.

# THE EUROPEAN XFEL WIRE SCANNER SYSTEM

T. Lensch\*, S. Liu, M. Scholz, Deutsches Elektronen Synchrotron, DESY, Hamburg, Germany

## Abstract

The European-XFEL (E-XFEL) is an X-ray Free Electron Laser facility located in Hamburg (Germany). The superconducting accelerator for up to 17.5 GeV electrons will provide photons simultaneously to several user stations. Currently 12 Wire Scanner units are used to image transverse beam profiles in the high energy sections. These scanners provide a slow scan mode which is currently used to measure beam emittance and beam halo distributions. When operating with long bunch trains (>100 bunches) also fast scans are planned to measure beam sizes in an almost nondestructive manner. Scattered electrons can be detected with regular Beam Loss Monitors (BLM) as well as dedicated wire scanner detectors. Latter are installed in different variants at certain positions in the machine. Further developments are ongoing to optimize the sensitivity of the detectors to be able to measure both, beam halo and beam cores within the same measurement with the same detector. This paper describes the current status of the system and examples of different slow scan measurements.

## INTRODUCTION

At the E-XFEL there are about 60 screen stations installed. Twelve of these screen stations are additionally equipped with wire scanner motion units. These wire scanner units are placed in groups of three upstream of the collimation section and upstream of the three SASE undulator systems. Each wire scanner unit consists of two motorized forks (horizontal and vertical plane). Each fork is driven by a separate linear motor [1]. This 90° configuration of motors helps to avoid vibration influences. The wire position is measured with a linear ruler (Heidenhain) which has a resolution of 0.5 μm. The motion unit is integrated by a custom front end electronic into the MTCA.4 [2] environment. A set of three 90° tungsten wires (50, 30 and 20 μm) and two crossed 60° wires (10 μm) are mounted on each titanium fork (see Fig. 1).

Figure 2 shows a wire scanner motion unit installed upstream of the collimation section. Different detector setups as well as regular Beam Loss Monitors (BLM) downstream of the wire scanner motion units are used for detection of scattered particles. Figure 3 shows a simplified overview of installed wire scanner stations and detectors.

## DETECTORS

### Dedicated Wire Scanner Detectors

Several dedicated wire scanner detectors (WSD) for scattered electrons have been developed and installed downstream of each set of motion units. They are based on photomultipliers (PMTs) of type Philips XP2243B. These fast,

\* timmy.lensch@desy.de

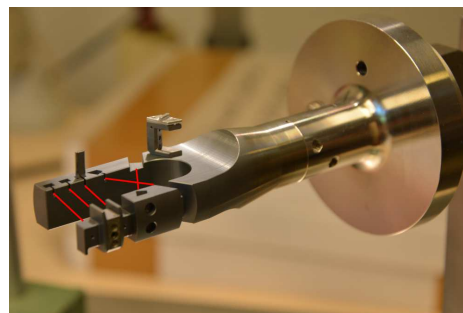


Figure 1: Titanium fork with tungsten wires which are indicated by red lines. From left to right: 50-30-20 μm, crossed wires 10 μm.

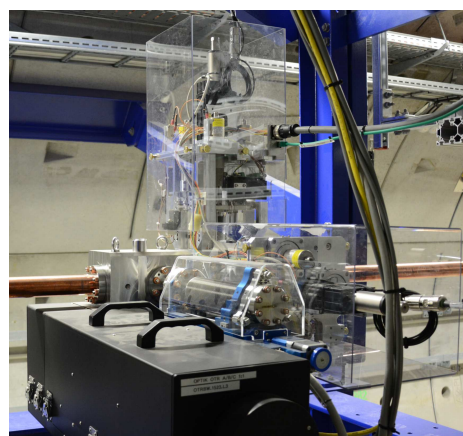


Figure 2: Wire scanner motion unit upstream SASE3 undulators. In the foreground a black optic box and a screen mover are visible.

red sensitive 6-stage tubes are well known from FLASH and HERA wire scanners for years. Currently two types of setups are installed. Plastic scintillating fibers (length: 4 m, diameter: 2 mm) optically coupled to the PMTs are wrapped around the beam pipe to be close to the beam showers. In order to gain more signal, paddles (made of NE110) with larger size compared to fiber detectors have been optically adapted to PMTs of the same type (Philips XP2243B). Measurements show that these paddle based detectors are much more sensitive and can be used better for measurements with low losses (i.e. study of beam halo distribution).

### Regular BLMs

About 470 Beam Loss Monitors (BLM) are installed at the E-XFEL. They are used for machine protection and dark current measurement [3]. For detection of scattered electrons each of these BLMs can be used for the wire scanner analysis, too. Due to the non-linearity of these BLMs they cannot be used at a time for both beam halo and beam core

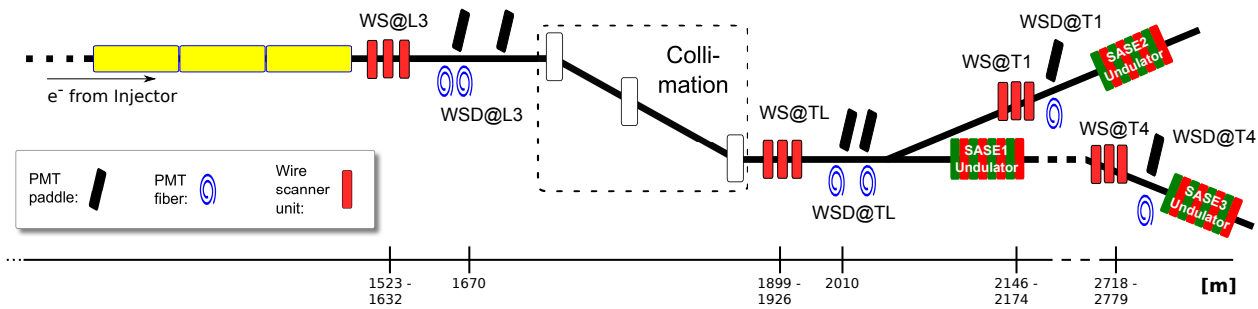


Figure 3: Simplified overview of 12 wire scanner units and detectors. Upstream and downstream collimation section two paddle and two fiber PMTs are installed. Upstream SASE2 and SASE3 undulators only one paddle and one fiber PMT is installed about 20 m downstream of the last wire scanner respectively. Regular BLMs are installed all over the machine at certain positions.

measurements. Therefore a combination of BLMs and dedicated detectors for wire scanners (for beam core) could be used [4]. Figure 4 shows different PMTs installed in the E-XFEL.

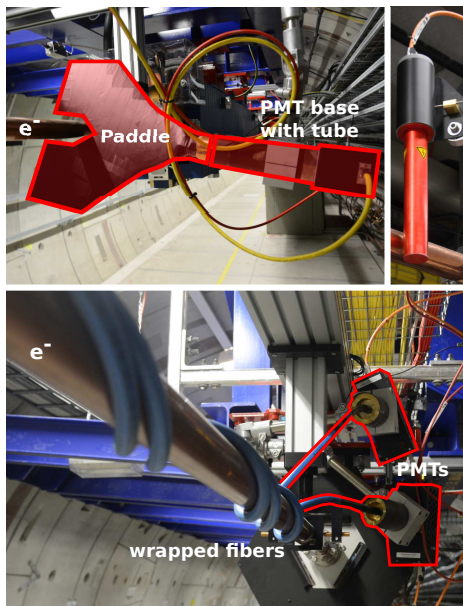


Figure 4: Different detectors in the tunnel: paddle applied to PMT (top left, highlighted red), regular BLM (top right) and two blue hoses with fibers wrapped around beam pipe and connected to PMTs (bottom, surrounded red).

### WSD Readout

Read out of the WSD signals is also based on MTCA.4 components. An in-house developed RTM<sup>1</sup> implements front end electronics for signal conditioning and controlling of a high voltage power supply. The RTM is connected to a commercial Struck AMC<sup>2</sup> ADC SIS8300-L2D [5] with custom firmware. One pair of AMC and RTM can handle two PMT channels and control one external high voltage power supply (company iseg, 2 channels, 2 kV, 6 mA, ripple <2 mVss typ.).

<sup>1</sup> Rear Transition Module

<sup>2</sup> Advanced Mezzanine Card

### SLOW SCAN MODE

A slow scan is performed by moving the fork with a continuous motion from a predefined start position for a desired length and number of points. During running motion at each macro pulse the wire position and the detector signal is saved and displayed. Figure 5 shows the GUI with three wire scanner units upstream collimation section. This GUI is mainly used for further developments of Wire Scanner device and middle layer servers and debugging of installed units. High level software connects to these servers performing emittance measurements during optics matching or to study beam halo distribution. For safety reasons slow scans are only allowed if the machine is running in single bunch mode to not destroy the wires. Therefore the wire scanner motion unit limits the number of bunches by a hard wired connection to the Machine Protection System [6].

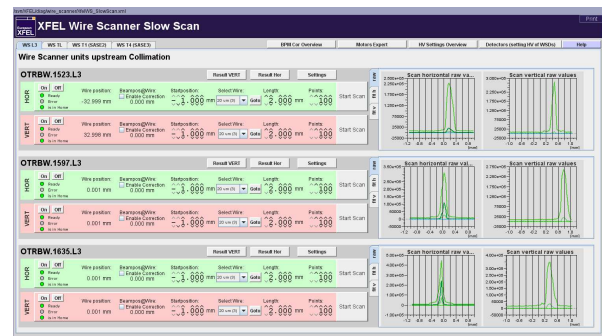


Figure 5: Graphical user interface for slow scan parameters and results for a set of 3 Wire Scanner motion units upstream collimation section. Plots on the right show performed scans with wire position (x axis) and several PMT signals (y axis) for horizontal and vertical plane.

### MEASURE BEAM OPTICS MATCHING

Wire scanners are currently often used to measure the beam optics matching and emittance. Three wires in combination with two different beam optics (quadrupole magnet settings) were used in the measurement that is presented in Fig. 6. Thus six different beam sizes in both planes can be used to calculated the particle distribution in the respective transverse phase spaces at a position upstream the wires.

The measured beam optics parameters can then be compared with the design values and, in case of larger deviations, be corrected [7].

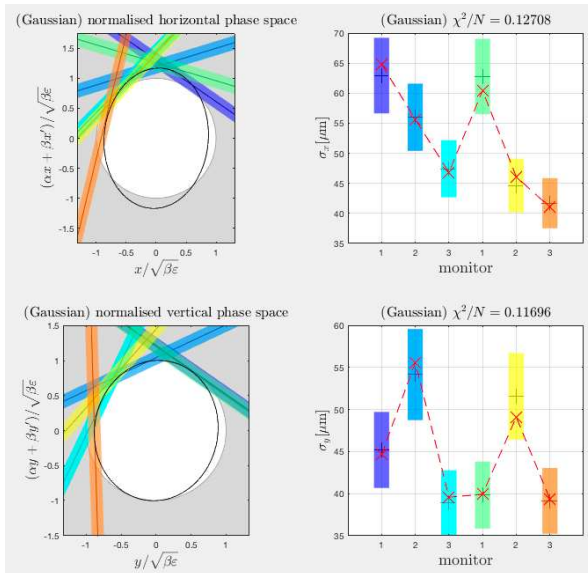


Figure 6: Results from a beam optics and emittance measurement downstream the linac of the E-XFEL using 3 wire stations and 2 different beam optics in between. The plots on the left hand side show the transverse phase spaces normalized to the design beam optics parameters at a position (called the beam optics reference position) upstream the wires. The plots on the right hand side show the measured beam sizes for all six measurements. Both upper plots represent the measurement in the horizontal plane while the lower plots present the results from the vertical plane. The reconstructed phase space ellipses are shown in the phase space plots as black lines. The white circles represent a perfectly matched beam with an emittance of 1 mm mrad.

## MEASURE BEAM HALO DISTRIBUTION

Upstream of SASE 3 undulators wire scanner measurements have been performed during radiation tests. As the scintillating paddle applied to WSD is much more sensitive it is used for beam halo detection. WSD with scintillating fiber is used for beam core measurement. Figure 7 shows the fiber signal (beam core) scaled by factor 500 to overlap with the paddle measured beam halo (beam pipe center at 23 mm) [8].

## SUMMARY AND OUTLOOK

A wire scanner system of 12 scanners and corresponding detectors have been installed at certain positions at the E-XFEL. Slow scans have been performed with these scanners for beam halo and emittance measurements and beam optics matching with reasonable results. Additional detector developments are on going to be more flexible with an adjustable

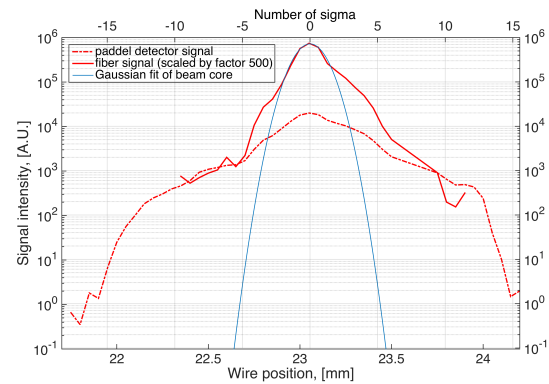


Figure 7: Beam Halo Measurement: fiber detector compared to paddle detector. The fiber detector signal is scaled by a factor 500 to overlap with the paddle measured beam halo.

electrical attenuation of the PMT signal and a variable intensity of light applied to the paddle PMTs. Besides that another type of 15-stage and more handy tube is planned to be installed and investigated. Furthermore an automated adjustment of high voltage settings for the dedicated wire scanner detectors is going to be implemented. Further work will be dedicated to the implementation of fast scan functionality, which is essential for the multi-bunch (>100 bunches) operation.

## ACKNOWLEDGEMENTS

We thank A. Delfs, V. Gharibyan, I. Krouptchenkov, D. Lipka, D. Noelle, M. Pelzer, P. Smirnov, H. Tiessen, M. Werner, K. Wittenburg, A. Ziegler for wire scanner design and installation; O. Hensler for software development.

## REFERENCES

- [1] T. Lensch, "Wire Scanner Installation into the MicroTCA Environment for the European XFEL", in *Proc. IBIC'14*, Monterey, CA, USA, paper MOPF13
- [2] <https://www.picmg.org/openstandards/microtca>
- [3] T. Wamsat, "The European XFEL Beam Loss Monitor System", presented at IBIC2018, Shanghai, China, paper WEOB03, this conference
- [4] S. Liu, "First Beam Halo Measurements using Wire Scanners at European XFEL", in *Proc. FEL'17*, Santa Fe, NM, USA. doi:10.18429/JACoW-FEL2017-TUP003
- [5] <http://www.struck.de/sis8300-12.html>
- [6] S. Karstensen *et al.*, "XFEL machine protection system (MPS) based on UTCA", in *Proc. RT2014*, Nara, Japan
- [7] E. Prat *et al.*, "Four-dimensional transverse beam matrix measurement using the multiple-quadrupole scan technique", *Phys. Rev. ST Accel. Beams* 17, 052801, 2014
- [8] S. Liu *et al.*, "Study of Possible Beam Losses After Post-Linac Collimation at European XFEL", in *Proc. IPAC'18*, Vancouver, Canada. doi:10.18429/JACoW-IPAC2018-THPMF022



# THE NEW DIAGNOSTIC SUITE FOR THE ECHO ENABLED HARMONIC GENERATION EXPERIMENT AT FERMI.

M. Veronese\*, A. Abrami, E. Allaria, M. Bossi, I. Cudin, M. Danailov, R. De Monte, F. Giacuzzo, S. Grulja, G. Kurdi, P. Rebernik Ribic, R. Sauro, G. Strangolino and M. Ferianis, Elettra-Sincrotrone Trieste S.C.p.A., S.S. 14 km 163,5 in AREA Science Park, 34149 Trieste, Italy

## Abstract

The Echo Enabled Harmonic Generation (EEHG) experiment has been implemented on the FEL2 line of the FERMI FEL at Elettra (Italy). The main purpose is to validate the expected performance improvements at short wavelengths before a dedicated major upgrade is deployed. This paper describes the new diagnostics and the operational experience with them during the EEHG experiment. By means of a multi position vacuum vertical manipulator, different optical components are positioned on the electron and seed laser path. Both transverse and longitudinal measurements are performed. A YAG:Ce screen (e beam) and a terbium doped UV scintillator (laser) are imaged on a dedicated CMOS camera. For the temporal alignment, an OTR screen and a scattering surface are used to steer radiation from the e-beam and laser, onto a fast photodetector. Also coherent OTR radiation, due to micro-bunching, is acquired by means of a PbSe photodetector. Finally, for the normal EEHG operation, the laser beam is injected on the electron beam axis by means of a UV reflecting mirror. The results of the installed diagnostics commissioning are here presented.

## INTRODUCTION

One the most recent advances in Free Electron laser design is the so called Echo Enabled Harmonic Generation [1]. In this scheme the electron beam is modulated by two external lasers, compared to High Gain Harmonic Generation (HGHG) [2] where one seed laser is used and to Self Amplified Spontaneous Emission (SASE) [3] which has no external seeding and is based on amplification of shot noise microbunching. Recently microbunching at the 75th harmonic has been observed using a seed laser at 2400 nm [4]. In HGHG the external seed laser couples to electron beam in the modulator undulator to produce a bunched current distribution, then the electron beam pass through the radiator undulators and lasing occurs. The HGHG emission has a quicker built up compared to SASE. HGHG pulses have a high spectral purity and stability and can be fully coherent and transform limited [5]. The main limitation of HGHG at short wavelengths is its sensitivity to quality of the electron beam in terms of phase distortions [6]. EEHG can potentially decrease the sensitivity of the FEL to the electron beam quality and thus ease the operation of the FEL at short wavelengths. Moreover since in EEHG there is no FEL first stage, the beam does not undergo properties degradation due to first stage and so there is no need to use the fresh bunch

technique [7] typical of HGHG multiple cascade FELs. This means that potentially the compression can be increased allowing for higher peak current. An EEHG experiment has been proposed [8] and installed in the FERMI FEL2, to validate the expected improvements. The experiment is aiming at comparing FEL operations in EEHG mode and in standard two stage HGHG with an electron beam energy ranging from 1.1 GeV to 1.5 GeV for wavelength in the 20 to 4 nm spectral range. Finally a new manipulator and diagnostics have been installed in the delay line and are the subject of this paper.

## EEHG LAYOUT

The experiment has been setup in the FEL2 line of the FERMI FEL. FEL2 is a two stage cascade HGHG FEL usually operated in fresh bunch mode. The upgrade for the experiment involves the installation of a new modulator for the second stage of FEL2, a new laser line delivering up to 50 microJoules pulses at 260 nm with duration around 150 fs. The magnetic delay line magnet will be repositioned and a new power supply capable of 750 Amp has been installed allowing to reach R56 above 2 mm. The EEHG modulator undulator has variable gap, linear polarization and a period of 11 cm to fit the laser wavelength of 260nm. Figure 1 shows

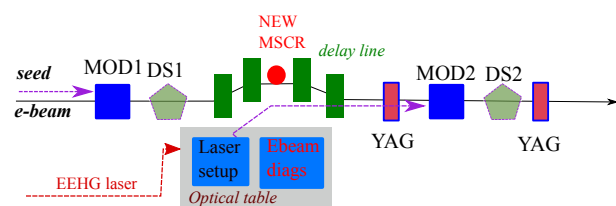


Figure 1: Layout of EEHG experiment at FERMI.

a pictorial layout of the EEHG experiment. The seed laser of the first stage is called 'seed1' and the first stage radiators are not depicted since they are not needed for EEHG and have been set at gaps fully open during the measurements. MOD1 is the first stage modulator and DS1 is the first dispersive section. The magnetic delay line is depicted as a series and green rectangles and is used as the main big R56 needed for EEHG. In the middle of it the new vacuum manipulator has been installed. On the lower part a gray rectangle depicts the optical table that houses all the laser setup that controls the steering, the compression and the third harmonic conversion to generate the 'seed2' UV laser. On the same table we also installed all the motorized actuators and detectors that compose the new diagnostics. Downstream this area we can see in Fig. 1 the YAG:Ce screens are depicted as red rectangles.

\* marco.veronese@elettra.eu

They are used for the transverse alignment of the seed laser vs the electron beam. The new modulator MOD2 is a blue rectangle and DS2 pentagon depicts the second dispersive section. Downstream of it the standard FEL2 radiators are converting current modulation in FEL pulses.

## DIAGNOSTICS CONFIGURATIONS

The new diagnostic suite has been requested to provide several configurations that are depicted in Fig. 2 in a simplified form. The first request is to house the UV mirror needed for injection of seed2. The second is to be able to provide imaging of the seed2 laser on the same plane of the mirror for alignment and reference purposes. The third is to provide electron beam imaging for all the 30 mm range of transverse displacement possible by change the delay line current from 0 to 750 Amp. The fourth is to provide coarse longitudinal alignment of seed2 vs the electron beam. The final request was to provide microbunching measurements by CTR power measurements in the infrared.

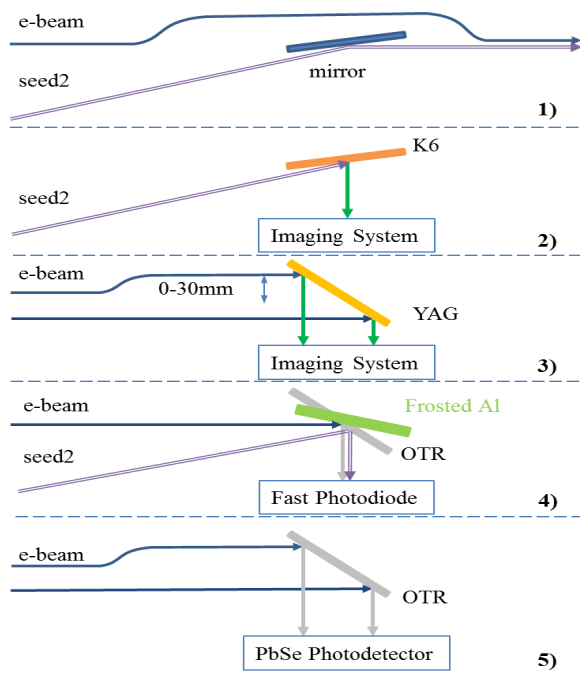


Figure 2: Diagnostics configurations.

## DIAGNOSTICS LAYOUT

This diagnostics upgrade involves a new vacuum chamber for the delay line for the injection of the seed2 laser at 20 deg, the installation of a new motorized manipulator and optimal geometry for the extraction of diagnostics related radiations. The manipulator is located at the center of the FEL2 magnetic delay line. The manipulator is required to have high stability and angular reproducibility. It is equipped with a UV high reflectivity dielectric mirror, a scintillator to image

the seed2 laser, a frosted aluminum plate for coarse temporal alignment and an OTR screen for the same purpose as well as for the purpose of microbunching measurements and finally a YAG:Ce scintillator for electron beam transverse profile measurements.

## MANIPULATOR AND VACUUM COMPONENTS

The manipulator chamber is equipped with a commercial Pfeiffer vacuum manipulator with 150 mm travel. This manipulator has been chosen for the stiff construction while having small lateral footprint to comply with the limited space between the second and the third magnet of the delay line. The manipulator has been customized equipping it with a Renishaw digital encoders (Tonic) with 0.1 micron resolution. The second customization also includes precision holes for dowel pins in the vacuum chamber and in the manipulator to provide a highly reproducible installation in case of need for mirror replacement. The manipulator is shown in Fig. 3. The different angle and the targets size involved lead to a complex design of rod leaving so little material in some parts that we were forced to use stainless steel to provide the required robustness. The angular reproducibility of the steering angle over a full travel repositioning of the manipulator has been measured to be of 70 nrad by imaging the seed2 laser on the downstream IUFEL YAG screens. The lateral displacement of the full travel is of about 5 microns. The vertical position accuracy is less than 1 micron in closed loop. The extraction window is orthogonal to the electron beam propagation direction for diagnostics. As consequence of the multiple requirements it has been chosen of CF63 size and CaF2 has been used to provide transmission up to a wavelength of 10 microns. Figure 4 shows a picture of the

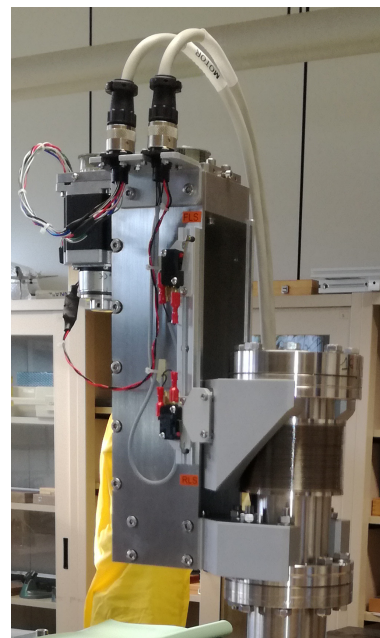


Figure 3: Vacuum manipulator.

manipulator rod oriented orthogonally to the electron beam. The uppermost component is the UV high reflectivity dielectric mirror axis. Moving downwards we find the Metrolux K6 scintillator for seed2 imaging, the frosted aluminum plate used to scatter the seed2 making easier the alignment and less dangerous for the photodiode the high energy laser. Then we find the 1 micron aluminum tensioned foil from Luxel that acts as OTR screen. Finally at the bottom of the rod we installed the YAG:Ce scintillator with a chromium precision recticle deposited on it for calibration purposes.



Figure 4: Vacuum components installed on the manipulator.

## OPTICA TABLE SETUP

Since all radiations leave the vacuum from the same view-port but have different source points and multiple measurements are requested we have devised the setup shown in Fig. 5. At 100 mm from the window we installed a XY motorized translation stage with 100 mm horizontal travel and 50 mm vertical travel. It is equipped with a fast photodiode for temporal coarse alignment and a IR slow photo detector for microbunching measurements. The fast photo detector is Hamamatsu G4176 connected to a 6 GHz Tektronics digital oscilloscope via a bias tee and AIRCOM PLUS low attenuation coaxial cables. The arrival time of the electron beam is marked by the position of the photo detector signal generated by optical transition radiation emitted by the OTR. The seed2 temporal arrival time is obtained by the signal detected on the photo detector after the laser scattered from the frosted aluminum target installed on the manipulator rod. About 50 mm horizontal travel of the XY stage are left available as free path without obstacles to allow imaging of the Metrolux and Crytur scintillators. Imaging of both scintillators is achieved with a single device installed on a 50 mm motorized translations stage. Electron beam imaging can be performed both on OTR and YAG:Ce target. The targets are of 56 mm wide to allow for a field of view of 30 mm needed to be able to make measurements in the

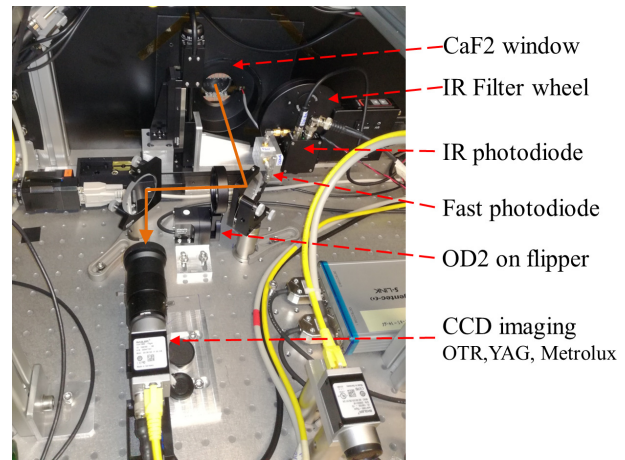


Figure 5: Layout of optical components and detectors.

full range of the delay line. The imaging systems consists of a 75mm focal length lens coupled to a 1/2 inch Basler acA1300-75gm CMOS camera. The working distance providing the 30mm horizontal field of view is of 550 mm. The iris is set to f11 to maximize the depth of field without compromising the resolution. But even in such a configuration the depth of field it is not enough to have the full FOV in focus so the camera is installed on a 50 mm translation stage that is used to change the focus when the electron beam hits a lateral part of the screens. To increase the contrast we have installed behind the YAG a white peek frame. Finally to compensate for the difference of intensity between OTR (as shown in Fig. 6), YAG and Metrolux scintillator an optical density 2 visible neutral density filter has been installed on a remotely controlled flipper on the optical path. Laser beam

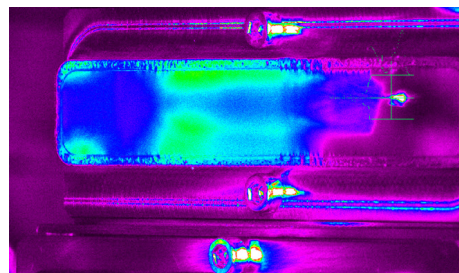


Figure 6: Electron beam imaging on OTR screen.

imaging is important to check the alignment and to guarantee the correct superposition of electron beam and seed2. In the EEHG setup it is done in three positions. The first is the Metrolux scintillator installed in vacuum on the manipulator rod. The second is 1.7 m downstream of the manipulator on the YAG:Ce scintillator of the closest IUFEL screen. The last measurement point is at 6.2 m from the manipulator on the next IUFEL screen. Figure 7 shows the EEHG laser spot on the Metrolux scintillator as imaged by the optical system installed on the table. The same optical system also provides the imaging of the electron beam on the YAG:Ce screen.



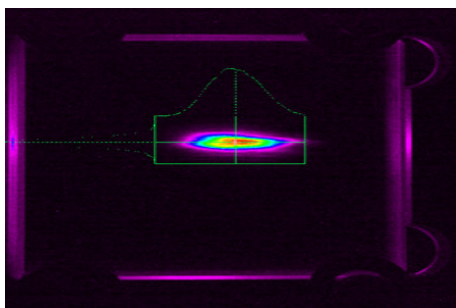


Figure 7: Seed2 laser spot imaging on Metrolux scintillator.

## MICROBUNCHING

Microbunching is crucial aspect influencing the final performances of the FEL especially for the FEL2 short wavelength FEL. For this reason we have equipped this diagnostic station with a system for measuring the coherent transition radiation (CTR) due to microbunching. To have more detailed information of microbunching as a function of other machine parameters such as the laser heater power, the compression, and the magnetic delay line current instead of having just a power measurement we have installed a device capable of providing spectral information. The device is installed on XY stage and consists of a filter wheel and an infrared detector. The filter wheel is equipped with infrared band pass filters with 0.5 microns bandwidth (Thorlabs linch FB series) and a central wavelength of 1.75, 2.25, 2.75, 3.25 and 3.75 microns. The detector is a PbSe photo detector (Thorlabs PDA20H) whose responsivity spans the wavelength range from 1.5 to 4.5 microns. The signal of the photo detector is acquired with a digital oscilloscope. Figure 8 show intensity data as a function of the filter wavelength for a value of the delay line of 300 A and different values of the Laser heater energy. The data are normalized to detector responsivity and then to the signal without filters scaled by an average of the responsivity. As could be expected increasing the laser heater energy causes a reduction of the intensity of CTR. The spectral selectivity of the device also allows to see that the intensity is higher a shorter wavelengths. Moreover as the laser energy is increased the heating seems to be of unequally efficient depending on the wavelength. Recoding curves as the one in Fig. 8 one can have reference data and identify relative variations on long term operation of the machine.

## CONCLUSIONS

The instrumentation installed has performed reliably both in terms of EEHG laser injection system as well as laser and electron beam diagnostics. In particular the microbunch-

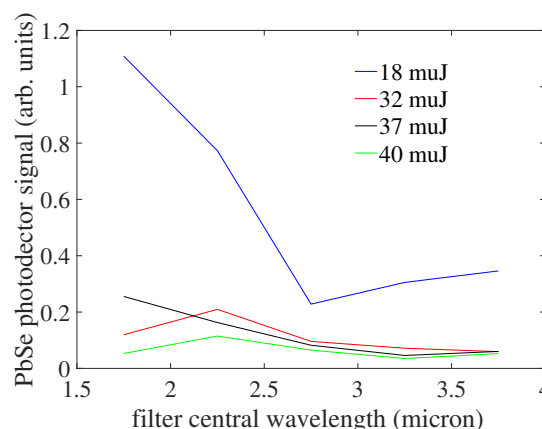


Figure 8: Spectral distribution of microbunching intensity as a function of laser heater energy.

ing CTR has allowed to characterized the IR range spectral range and to provide a relative reference to be used for future comparisons as a simple and direct way to establish the presence and the magnitude of microbunching in the electron beam. We are currently considering ways to extend the spectral range of this diagnostics both to the longer and shorter wavelengths to provide a more complete understanding of the spectral distribution of microbunching.

## ACKNOWLEDGEMENTS

The authors would like to thank: A.Demidovich, P.Cinquegrana, M.Tudor, P.Sigalotti, and D.Vivoda for their support during set-up and operation of the EEHG diagnostics.

## REFERENCES

- [1] Stupakov, G., Phys. Rev. Lett. v. 102, pg. 74801, (2009).
- [2] Yu, L.H. Phys. Rev. A, v. 44, pg. 5178–5193, (1991)
- [3] Bonifacio, R.; Pellegrini, C.; Narducci, Opt. Commun.,v. 50, pg. 373–378 (1984).
- [4] Hemsing, E. *et al.* Nat. Photon. 2016, 10, 512–515.
- [5] E. Allaria *et al.*, The FERMI free-electron lasers, Journal of Synchrotron Radiation 22, 485 (2015)
- [6] E. Allaria Proceedings of SPIE - The International Society for Optical Engineering 10237, 102370F (2017)
- [7] Yu, L.-H.; Ben-Zvi, Nucl. Instrum. Methods Phys. Res. Sect. A Accel. Spectrometers Detect. Assoc. Equip., v. 393, pg 96–99, (1997)
- [8] Rebernik Ribič, P. *et al.*, Photonics, Volume 4, pg. 19 (2017)



# OPTICAL SYSTEM OF BEAM INDUCED FLUORESCENCE MONITOR TOWARD MW BEAM POWER AT THE J-PARC NEUTRINO BEAMLINE

S. Cao\*, M. Friend, K. Sakashita, High Energy Accelerator Research Organization (KEK), Tsukuba, Japan  
M. Hartz<sup>1</sup>, Kavli IPMU (WPI), University of Tokyo, Tokyo, Japan  
<sup>1</sup>also at TRIUMF, Vancouver, Canada  
A. Nakamura, Okayama University, Okayama, Japan

## Abstract

A Beam Induced Fluorescence (BIF) monitor is being developed as an essential part of the monitor update toward MW beam power operation at the J-PARC neutrino beamline. By measuring the fluorescence light from proton-gas interactions, the BIF monitor will be used as a continuous and non-destructive diagnostic tool for monitoring the proton beam profile spill-by-spill, with position and width precision on the order of 200  $\mu\text{m}$ . The main challenge lies in collecting a sufficient amount of fluorescence light for the beam profile reconstruction while controlling the beam-induced noise with the current beamline configuration. A study is presented with a particular focus on the optical system under development, which allows us to transport fluorescence light away from the high radiation environment near the proton beamline and detect the optical signal with a Multi-Pixel Photon-Counter-based fast readout.

## J-PARC NEUTRINO BEAMLINE: TOWARD MW BEAM

The J-PARC complex [1] is serving as a producer of the most intense neutrino beam in the world to one of the world-leading neutrino oscillation experiment, Tokai-to-Kamioka (T2K) [2]. A J-PARC neutrino beamline is designed to guide protons extracted from Main Ring (MR), bend 80.7° toward the T2K far detector, Super-Kamiokande, before bombarding onto a graphite target in order to producing charged pions and kaons which are then decayed into  $\nu_\mu$  (or  $\bar{\nu}_\mu$ ) in flight. Recent results from T2K experiment shows that the CP conserving values of CP violation phase, which is presented in the leptonic mixing matrix, fall outside of  $2\sigma$  of confidence and credible intervals of measured range [3]. To further study CP violation in the leptonic sector, increasing the neutrino beam power is essential and play a role as the main driver for the neutrino intensity frontier. Since the start of user operation in 2010, the MR beam power has been increased steady and operated stably in 485 kW with an intensity of  $2.5 \times 10^{14}$  protons-per-pulse (ppp) at a repetition cycle of 2.48 s in 2018. Toward MW beam power, J-PARC aims to reduce the repetition cycle to 1.3 s and increase the beam intensity up to  $3.2 \times 10^{14}$  ppp by 2026.

To realize MW beam, beam loss handling and continuous monitoring the beam profile with high precision are crucial. Description of the beam loss and beam profile monitors in J-PARC neutrino beamline can be found elsewhere [2].

\* cvson@post.kek.jp

Among these monitors, Segmented Secondary Emission Monitors (SSEM), which are used to monitor the beam profile including the beam center and beam width, are considered critically requiring an upgrade toward MW beam due to limitations discussed in the next section.

## CURRENT BEAM PROFILE MONITOR AND THEIR LIMIT

In general, to measure the proton beam profile, material is inserted into the beamline. In J-PARC neutrino beamline, there is a suite of nineteen SSEMs, each of monitor consists of two 5- $\mu\text{m}$ -thick Titanium (Ti) foils stripped vertically and horizontally along with a Ti foil of same thickness between them. The strip width is about from 2 cm to 5 cm, depending on the beam size at the installed position. Precision of the SSEM measurement on the beam width can be achieved up to 200  $\mu\text{m}$ . However this method leads to 0.005% beam loss per SSEM. Due to this large amount of loss, only the most downstream SSEM is used continuously during normal operation, while others are inserted occasionally into the beamline for operation only during beam tuning periods. A Wire Secondary Emission Monitor (WSEM) has been developed with the same principle as the SSEM but using wires instead of strips to mitigate the beam loss. With WSEM, the beam loss can be reduced by factor of ten. However, continuous monitoring by a WSEM is still questionable, since even 0.0005% beam loss can cause serious problems, specifically the irradiation and damage of beamline components and a residual dose increase which makes maintenance become difficult. Thus, it is crucial to develop a non-destructive (or minimally destructive) beam profile monitor for the future operation of J-PARC at MW beam power.

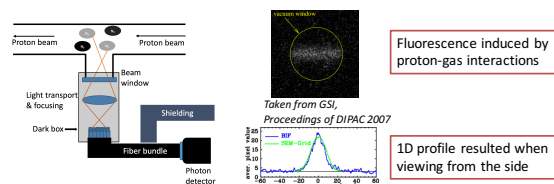


Figure 1: A BIF schematics has been built in the J-PARC neutrino beamline.

## BIF MONITOR: PRINCIPLE AND A WORKABLE CONCEPT

In general, a BIF monitor makes uses of the fluorescence induced by proton beam interactions with gas in the beamline.

The measured transverse profile of the fluorescence light should match with the transverse proton beam profile.

### Specification of the J-PARC Neutrino Beamline

A BIF monitor is under development at the J-PARC neutrino beamline [4] with some requirements to meet the strict conditions in the beamline. First, gas needs to be injected with a gas injection system, since in normal operation, the residual gas level in the beamline is only  $10^{-6}$  Pa, which can not produce enough fluorescence light for observation. Second, a method for dealing with the space charge effect, which is due to the very large transverse field of the proton beam itself, needs to be considered to mitigate or correct the distortion of the beam profile reconstructed from fluorescence of ions which can move in the field. One feasible solution for this is to use a fast readout system, for example using Multi-Pixel Photon Counters (MPPC) as photosensors. The 10-ns-level time resolution of MPPCs allows us to study the profile distortion caused by the space charge effect. Finally, operation in a high radiation environment should be considered for each detection component. For instance, MPPCs are not radiation-hard. Consequently MPPCs should be operated in the sub-tunnel where the radiation level is significantly suppressed by concrete shielded walls. As a result, an optical fiber transport system, which is used to guide the light from the beamline to the sub-tunnel, needs to be used and must be radiation-hard. Fig. 1 shows a workable schematic of the BIF monitor in the J-PARC neutrino beamline.

### A Workable Concept of BIF Monitor

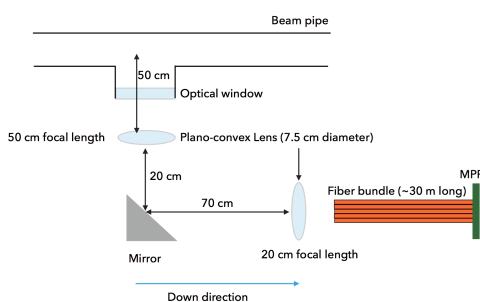


Figure 2: A workable concept for a light transport and focusing system with a fast readout using MPPCs. A 45° downward-mounted mirror is needed to direct light from beamline level to the floor before transporting it to the sub-tunnel using optical fibers.

For the beam profile measurement, the number of fluorescence photons recorded by the BIF photosensor is the key factor. The detected number of photons is proportional to the number of incident protons per spill, number of photons produced per each proton and the overall detection efficiency, as expressed in Eq. 1

$$N_{\gamma}^{\text{det}} = N_p \times N_{\gamma}^p \times \epsilon_{\text{all}}. \quad (1)$$

For this study, one thousand photons detected is used as our target for the optical system development. For the J-PARC beam, the number of incident protons per spill,  $N_p$  is set to be  $2.5 \times 10^{14}$  protons. For  $N_2$  [5], which is tentatively selected as our injected gas, number of photons produced per proton, assuming a signal integrated over 2 cm in the beam axis, is calculated to be  $N_{\gamma}^p = 1.25 \times 10^{-5} \times P_{\text{gas}}$ , where  $P_{\text{gas}}$  is the gas pressure at the BIF interaction point. The overall detection efficiency is calculated based on a feasible configuration, shown in Fig. 2, to be  $\epsilon_{\text{all}} = 4.1 - 7.1 \times 10^{-5}$  which consists of multiple sub-factors: (i) an acceptance and efficiency of lenses and mirror of  $0.99 \times 10^{-3}$  which dominated by the geometrical acceptance of the first lens, (ii) a fiber collection efficiency of 0.22–0.38, (iii) a 40-m fiber transmission efficiency of 0.66, (iv) a fiber-to-MPPC coupling transmission of 0.95, and (v) a MPPC photon detection efficiency of 0.3. These factors are either verified experimentally or derived from the manufacturer spec sheet. As a result, to achieve  $10^3$  photons with the estimated detection efficiency, gas at the monitoring point needs to be at a pressure of  $5.6 - 9.8 \times 10^{-3}$  Pa. This level of gas pressure localization is a benchmark for the gas injection system which is under development. Figure 3 shows a COMSOL simulation of a gas system designed to achieve  $10^{-2}$  Pa near the beam view ports while maintaining an average vacuum level of  $10^{-4}$  Pa at the ion pumps and  $10^{-6}$  Pa at the superconducting magnet section entrance. To achieve this state,  $2 \times 10^{-7}$  kg/s  $N_2$  gas is injected with an 0.5% of duty factor. The gas non-uniformity, which can make the observed beam profile distorted, is also studied, and simulations show that a fluctuation in gas density smaller than 5% can be achieved. Studies with the test vacuum chambers are underway in order to understand the gas flow dependence on the chamber shape and benchmark the gas system simulation.

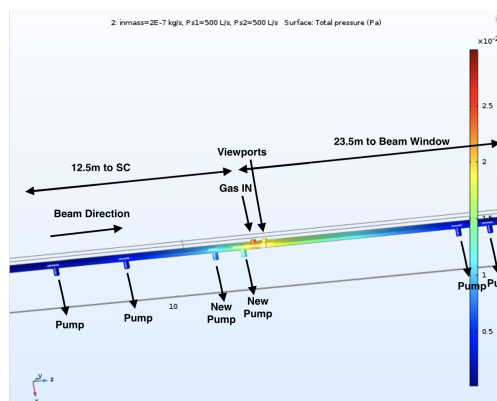


Figure 3: COMSOL simulation of a gas system design.

### Monte Carlo Simulation of the Optical System

The optical system is simulated with the GEANT 4 optical photon simulation tool in order to validate our calculation. Almost all components of the optical system shown in Fig. 2 are included. Optical characteristics of the beam window and lenses are set to the manufacturer specification. The

mirror reflectance is set to 90%. Optical fibers are simulated but with a 40 cm length. The photon inefficiencies at both fiber ends are considered, but the fiber attenuation is not simulated. This factor can be absorbed by reducing the number of photons generated. The gas pressure profile, proton-gas interactions, space charge effects and the photosensors are not included in the simulation, but will be considered in the future.

Assuming the gas pressure and detection and fiber transport efficiency described above, a total of  $5 \times 10^6$  photons with 390 nm wavelength (mimicing light production from N<sub>2</sub> gas) are simulated with the X-view centered at 0 while the Y-view center is varied from -10 mm to 10 mm. The beam width is set to 2 mm ( $1 \sigma$ ) for both X and Y-view. Figure 4 shows the fiber layout and the light pattern collected at the photosensor plane. A total of 978 photons are collected in the case of the centered beam. This is equivalent to  $2 \times 10^4$  acceptance and efficiency, agreeing with our calculation.

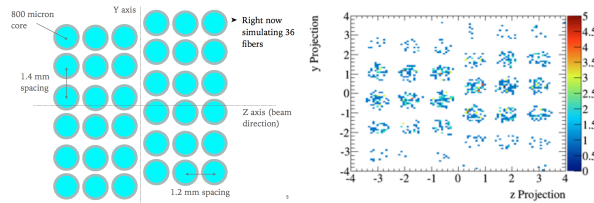


Figure 4: A studied fiber collection layout (left) and photon pattern at the photosensor plane (right).

By integrating the photons along the z-axis, i.e. proton beam axis, we can reconstruct the beam profile in the y-axis as shown in Fig. 5. Further studies are conducted by varying

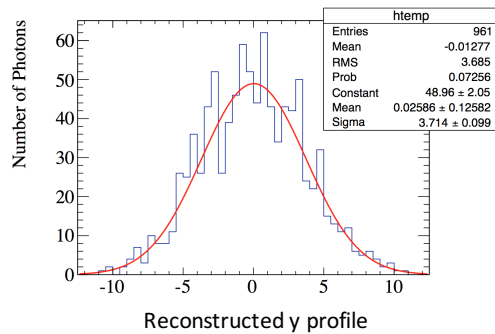


Figure 5: Reconstruction of the y-view beam profile.

the position of the y-view center. Figure 6 shows good linearity of the reconstructed values of the y-view center to the true value.

### Other Option for Light Detection

In addition to developing an optical system with MPPCs as the baseline option, another option, which uses a Microchannel Plate (MCP) gated image intensifier coupled to a radiation-hard Charged Injection Device (CID) camera by a fiber taper, is being considered. This option gives better

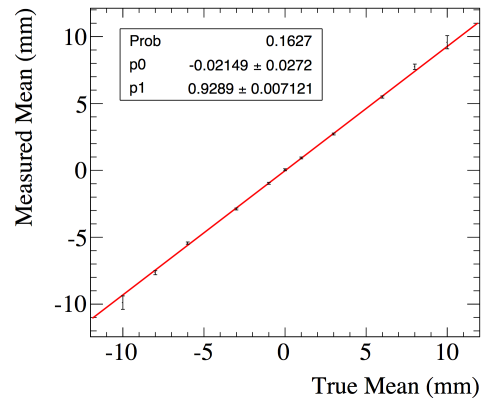


Figure 6: Reconstructed mean of y centers vs. true inputs.

position resolution than the optical fiber array. While it is tested that a CID camera can withstand the high radiation environment near the beamline, MCP survival in such conditions needs to be confirmed. Also the gain of a single stage MCP is just  $\sim 5 \times 10^3$ , much smaller than the  $10^6$  gain of MPPCs. Thus, to get enough photons for beam profile reconstruction, a dual stage MCP should be used. Another issue is that the minimum MCP gate time of 30 ns makes it difficult to mitigate any slow background component. With a CID camera, each integrated spill is stored, and any distortion by space charge effects should be corrected by other measurements or simulation.

## OPTICAL SYSTEM INSTALLATION & BEAM-INDUCED NOISE STUDY

### Optical System Design and Installation

During the J-PARC beam operation from October 2017 to May 2018, an optical transport and focusing system was designed and installed in the J-PARC neutrino beamline, in order to study the beam-induced noise and mechanic feasibility of the system as shown in Fig. 7. For the fiber-to-



Figure 7: Optic system with frame installed in J-PARC neutrino beam line with front view (left) and inside with two lenses and 45° downward-mounted mirror (right).

MPPC coupling, a design is developed as shown in Fig. 8, allowing us to insert and remove the fiber easily without using glue. For the last week of J-PARC beam operation,



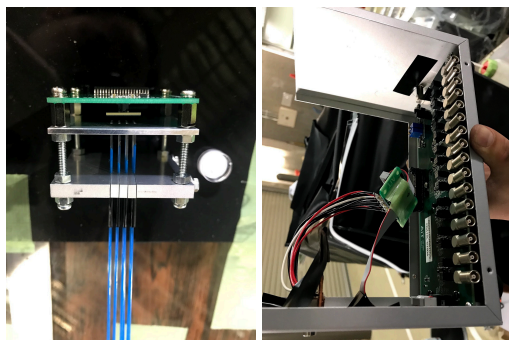


Figure 8: Fiber-to-MPPC coupling structure (left) and multi-channel amplifier board housing (right).

the system was connected to the beamline DAQ, allowing us to study the beam-induced noise in correlation with other beam monitors.

### Beam-Induced Noise Study

To study the beam-induced noise, 40-m long silica fibers with both 400  $\mu\text{m}$  and 800  $\mu\text{m}$  diameter cores were installed near the beam line. The numerical aperture of the fibers is 0.39. For studies shown in this section, a Hamamatsu S13361-3050AE-04 4x4 MPPC array is used with the 16 channel amplifier board, PBA16L-G750A, developed by AiT Instruments. The waveform is recorded by a newly developed Flash Analog-to-Digital Converter (FADC) named CAVALIER (250 MHz sampling), noise from single spill is shown in Fig. 9. The average waveform from  $\sim 1000$  spills is shown in Fig. 10. The data are taken with a black-cap

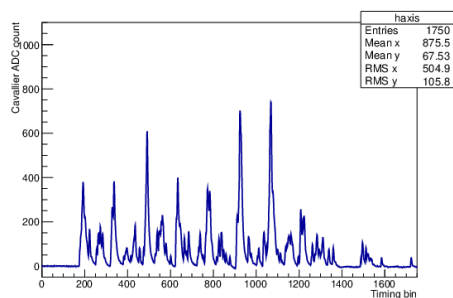


Figure 9: ADC distribution of single beam spill.

covering the beamline end of the fiber. In other words, the observed signal here is from fiber itself when the proton beam passes through the beamline. An eight-peak noise structure corresponds to the eight bunches of the proton beam. It is observed that the noise has two parts: peak (or fast) noise and slow noise. While the peak noise is suspected to be from Cherenkov or scintillation light in the fiber, the slow noise may be from neutrons which may come from backscattering from the target. An effort to shield the background with concrete and polyethylene shows a visible reduction of the slow noise but not of the peak noise. By using the data recorded at various beam intensities, we find that the noise is proportional to the beam intensity and has a strong correlation to the beam loss recorded by a nearby Beam

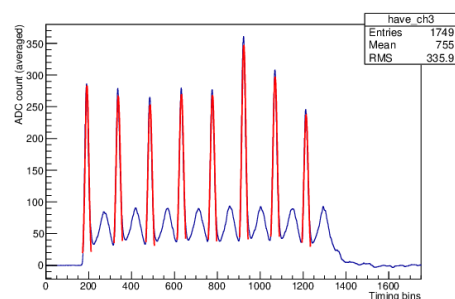


Figure 10: Averaged ADC distribution of  $\sim 1000$  spills. Red are with Gaussian fit on the found peaks of distribution.

Loss Monitor (BLM), as shown in Fig. 11. At 480kW beam operation, the integrated charge of this noise is equivalent to  $\sim 160$  photoelectrons per beam spill for the peak noise and around the same level for the slow noise. A simulation study concludes that the un-subtracted noise level should be kept lower than around 20 photoelectrons per spill. Thus, to realize the BIF monitor, it is important to understand and suppress this beam-induced noise.

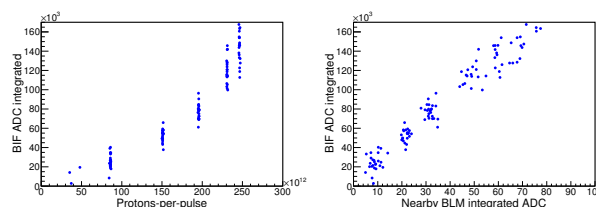


Figure 11: Dependence of noise to the beam intensity (left) and strong correlation of noise to the beam loss (right)

## SUMMARY AND PROSPECT

In summary, a concept of a BIF monitor as an upgrade option for monitoring the future MW beam at J-PARC is introduced. A BIF optical system has been designed and installed in the J-PARC neutrino beamline. Noise induced by the proton beam is observed with silica-core optical fibers. There are on-going efforts to understand and suppress this noise. We plan to build a full working prototype of the BIF optical system in 2018. The next target is to observe real BIF signal by injecting gas into the beamline.

## ACKNOWLEDGEMENT

This work was supported by the JSPS KAKENHI grant system (Grant No. 16H06288).

## REFERENCES

- [1] Y. Yamazaki *et al.*, KEK-REPORT-2002-13.
- [2] K. Abe *et al.*, Nucl. Instrum. Meth. A **659**, 106 (2011)
- [3] K. Abe *et al.*, arXiv:1807.07891 [hep-ex].
- [4] M. Friend *et al.*, doi:10.18429/JACoW-IBIC2016-WEPC66
- [5] J. Bosser *et al.*, Nucl. Instrum. Meth. A **492**, 74 (2002)



# DESIGN AND TEST RESULTS OF A DOUBLE-SLIT EMITTANCE METER AT XiPAF

M. W. Wang<sup>1</sup>, Q. Z. Xing, S. X. Zheng<sup>†</sup>, X. L. Guan, W. H. Huang, X. W. Wang

Key Laboratory of Particle & Radiation Imaging (Tsinghua University), Beijing 100084, China;  
Laboratory for Advanced Radiation Sources and Application, Tsinghua University, Beijing 100084, China; Department of Engineering Physics, Tsinghua University, Beijing 100084, China

Z. M. Wang, D. Wang, C. Y. Wei, M. T. Qiu,<sup>1</sup> also at State Key Laboratory of Intense Pulsed Radiation Simulation and Effect (Northwest Institute of Nuclear Technology), Xi'an 710024, China

## Abstract

Xi'an 200 MeV Proton Application Facility (XiPAF) is composed of a linac injector, a 200-MeV synchrotron and a high energy transport line. To study the beam dynamics along the beam line, a double-slit emittance meter is used to measure the beam phase space in the linac. To have knowledge of the phase space upstream of the emittance meter, an inverse transport method is proposed in the presence of space charge. The design and preliminary test results of the emittance meter are presented in this paper.

## INTRODUCTION

XiPAF (Xi'an 200 MeV Proton Application Facility), a proton radiation facility, consists of a linac injector, a medium energy transport line (MEBT), a synchrotron ring, a high energy transport line (HEBT) and a target [1]. The linac is composed of a low energy beam transport line (LEBT), a four-vane type RFQ and an alvarez-type DTL. During commissioning, knowledge of beam phase spaces at the LEBT output, RFQ output and DTL output are critical for beam matching. Especially at XiPAF, there is no matching section between RFQ and DTL [2]. The beam parameters of the linac are shown in Table 1. Due to the large energy range, the conventional electric scanner is not applicable. A double-slit type emittance meter is used to measure beam transverse phase spaces. Due to the small beam size and large divergence, it's usually hard to measure the beam phase spaces at the exit of the RFQ and DTL directly. Therefore, it's essential to deduce the beam phase spaces at the exits from the measured beam phase space downstream. The transportation is commonly achieved by transport matrix with assumption of linear particle motion. Whereas, the method is ineffective when the space charge effect is significant. A method, using the PIC code rather than transport matrix to simulate the particle motion, is proposed to transport the beam phase space from downstream to upstream with space charge effects. With this method, the knowledge of beam phase space distribution along the beam line can be obtained from the measured phase space at the position of the emittance meter. This paper shows the design and test results of the emittance meter.

Table 1: Main Beam Parameters of XiPAF Linac

Parameter	Value	Unit
Species	H <sup>-</sup>	\
Beam energy	0.05~7	MeV
Peak current	3~10	mA
Pulse length	10~1000	μs
Repetition rate	0.5	Hz

## DESIGN

Figure 1 shows the operation principle of the double-slit emittance meter. The emittance meter contains two slits: the position slit and angle slit. The width of the position slit determines the position resolution. The width of the angle slit and drift distance determine the angle resolution. The smaller the slits, the higher the resolution, but lower signal amplitude.

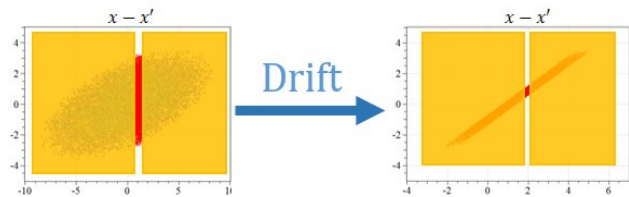


Figure 1: Operation principle of the double-slit emittance meter.

Due to the space limitation, the maximum drift distance is 247 mm. Figure 2 shows the signal amplitude as a function of slit widths. The widths of the two slits at XiPAF are 0.2 mm and 0.1 mm, respectively. Then the maximum current signal is 31.6 μA, and position and angle measurement resolution are 0.2 mm and 0.4 mrad, respectively. The current signal is measured by a Faraday cup mounted behind the angle slit.

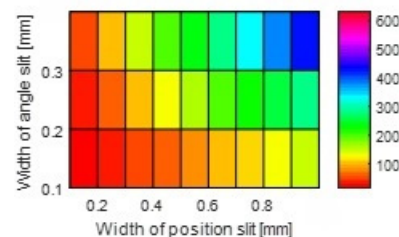


Figure 2: Signal amplitude as a function of slit widths.

<sup>†</sup>zhengsx@mail.tsinghua.edu.cn

# MECHANICS

The majority of the beam will be blocked by the position slit, bringing heat loading. Taking copper as the material of the slit, the maximum temperature is only 410 K, therefore water cooling is unnecessary. The range of 7 MeV H<sup>+</sup> in copper is 133.6  $\mu\text{m}$ . Thus, the minimal thickness of the slits should be large than the value. The parameters of the emittance meter are shown in Table 2. Each slit is formed by two copper sheets. Since the thickness of the slit decreases the acceptance of angle [3], the trapezoidal shape of slit is adopted, as shown in Fig. 3.

Table 2: Parameters of the Emittance Meter

Parameter	Value	Unit
Material	Copper	-
Width of slit	0.2/0.1	mm
Thickness of slit	3/1	mm
Distance between slits	247	mm



Figure 3: Position slit geometry.

# CONTROL AND ACQUISITION

Linear motion of each slit is achieved by server motors, which have a moving repeatability of 5  $\mu\text{m}$ . The beam current acquired by the Faraday cup is transformed to a moderate voltage signal by an I-V converter at the front end. The NI-PXIe system is used to control the motors and acquire signals. The PXIe 6356 card samples the voltage signal at a rate of 1 MHz, and the motors are controlled by calling the dynamic link library (DLL). A GUI, which achieves automatic emittance measurement, is shown in Fig. 4.

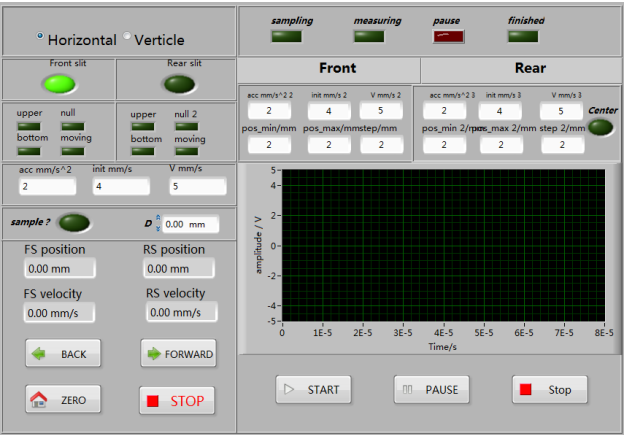


Figure 4: Control interface of the emittance meter.

# EXPERIMENTAL RESULTS

The emittance meter was installed downstream of the RFQ at Tsinghua University to measure the beam phase space and test its performance. The experimental setup is shown in Fig. 5. To eliminate the effect of secondary emission electrons on the current measurement, a minus biasing voltage is added. The measurement results are shown in Fig. 6. The measurement speed is about 1 step per second, and the total time for one plane is about 30 minutes.

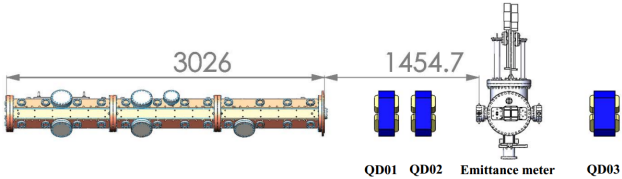


Figure 5: Layout of the experiment.

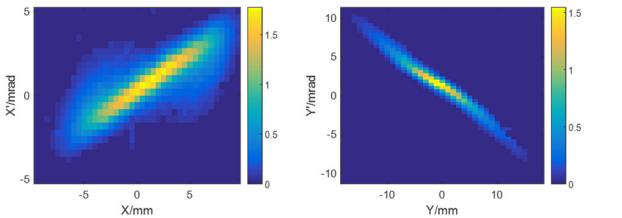


Figure 6: Measured beam phase space in horizontal plane (left) and vertical plane (right).

# PHASE SPACE INVERSE TRANSPORT

As shown in Fig. 5, the emittance meter is not installed at the RFQ exit directly, inverse transportation is needed to deduce the beam phase space at the RFQ exit. A method similar to reconstruct beam phase space from multiple profiles in presence of space charge [4] is proposed. The detailed procedures are as following:

1. Generate a large uniform-distributed multi-particle beam in both transverse planes as the initial solution. As for the longitudinal distribution, the physically designed distribution is used.
2. Beam motion from the RFQ exit to the location of the emittance meter is simulated with a PIC code, Tracwin [5].
3. Simulation results are compared with the measured phase spaces pixel by pixel. A weight is given to each particle according to the measured signal at this pixel and the number of particles falling into it. The particles falling outside the measured phase space are weighted as zero.
4. Normalize the weights defined in step 3 to keep a constant particle number. Then redistribute the initial distribution with the weights.
5. Restart the iteration until the simulation result converges to the measurement result.

The reconstructed beam phase spaces at the RFQ exit are shown in Fig. 7, and Fig. 8 shows the simulated phase space at the location of the emittance meter with the

Content from this work may be used under the terms of the CC BY 3.0 licence (© 2018). Any distribution of this work must maintain attribution to the author(s), title of the work, publisher, and DOI.

reconstructed phase space at the RFQ output as input. Comparison of twiss parameters are shown in Table 3. The reconstructed results are well coincident with the measured results.

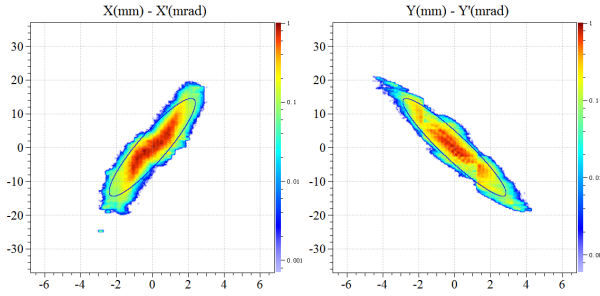


Figure 7: Reconstructed beam phases at the RFQ exit.

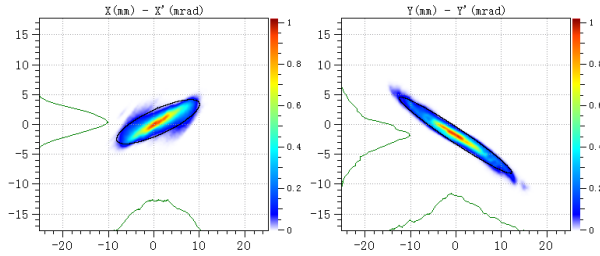


Figure 8: Simulated beam phase spaces at the position of the emittance meter using the reconstructed phase space as input.

Table 3: Comparison of Twiss Parameters of Measured and Simulated Phase Space

	$\alpha_x$	$\beta_x$ [m]	$\epsilon_{xn}rms$ [ $\mu m$ ]	$\alpha_y$	$\beta_y$ [m]	$\epsilon_{yn}rms$ [ $\mu m$ ]
Measured	-1.2	3.9	0.34	4.6	9.1	0.30
Simulated	-1.3	4.0	0.33	4.3	8.6	0.29

To verify the reconstructed result further, phase spaces are measured again with adjusting the current of the quadrupole QD02 from 67.7A to 77.7A. The beam space at emittance meter is also simulated with the new currents setting, still using the reconstructed phase space at the RFQ exit as input. The results by the simulation and measurement are shown in Fig. 9 and Fig. 10. They are also well agreed, verifying the effectiveness of the reconstruction method.

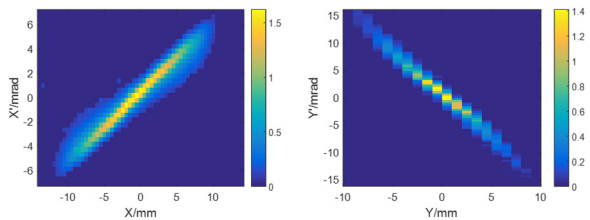


Figure 9: Measured phase space with QD02=77.7 A.

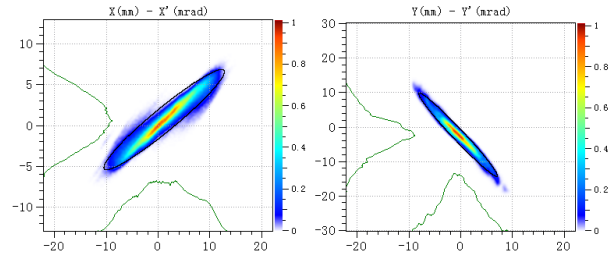


Figure 10: Simulated phase space with QD02=77.7 A.

## CONCLUSION

In this paper, a double-slit emittance meter used for beam emittance measurement at XiPAF linac is introduced. The instrument has a position resolution of 0.2 mm and an angle resolution of 0.4 mrad. About 30 minutes is needed for the measurement of one transverse plane for a moderate measurement range. An emittance reconstruction method has been proposed to transport beam phase space from downstream to upstream in the presence of space charge. The method has been successfully applied at Tsinghua University, and it will be adopted in the coming commissioning of XiPAF.

## REFERENCES

- [1] H.Q.Yao, *et al.*, “Design of the 230MeV Proton Accelerator for Xi'an Proton Application Facility”. in *Proc. HB'16*, Malmö, Sweden, 2016, pp. 55-58.
- [2] Q.Z.Xing, *et al.*, “Development Progress of the 7MeV Linac Injector for the 200MeV Synchrotron of Xi'an Proton Application Facility”. in *Proc. IPAC'17*, Copenhagen, Denmark, 2017, pp. 2336-2338.
- [3] B.Cheymol, Development of beam transverse profile and emittance monitors for the CERN LINAC4[D]. Université Blaise Pascal-Clermont-Ferrand II, 2011.
- [4] V. Dimov *et al.*, “Emittance Reconstruction Techniques in Presence of Space Charge Applied During the Linac4 Beam Commissioning”, in *Proc. HB'16*, Malmö, Sweden, 2016, pp. 433-438.
- [5] TraceWIN code, <http://irfu.cea.fr/en/Phoce/388> Page/index.php?id=780. Accessed 17 May 2018.

# MACHINE LEARNING APPLIED TO PREDICT TRANSVERSE OSCILLATION AT SSRF \*

B. Gao, Y.B. Leng<sup>†</sup>, Y.M. Zhou<sup>1</sup>, J. Chen

Shanghai Institute of Applied Physics, Chinese Academy of Sciences, 201800 Shanghai, China

<sup>1</sup>also at University of Chinese Academy of Sciences, 100049 Beijing, China

## Abstract

A fast beam size diagnostic system has been developed at SSRF storage ring for turn-by-turn and bunch-by-bunch beam transverse oscillation study. This system is based on visible synchrotron radiation direct imaging system. Currently, this system already has good experimental results. However, this system still has some limitations, the resolution is subject to the point spread function; and the speed of the online data processing is limited by the complex Gaussian fitting algorithm. In order to realize the online fast data processing, we present a technique that applied machine learning tools to predict transverse beam size. Using this technique at SSRF storage ring, we report mean squared errors below 4  $\mu\text{m}$  for prediction of the horizontal beam size.

## INTRODUCTION

Research of bunch-by-bunch beam diagnostics at the Beam Instrumentation (BI) group of SSRF (Shanghai Synchrotron Radiation Facility) has been started from the year of 2012 [1]. We also have focusing on the development of a six-dimensional bunch-by-bunch diagnostics system (published on this conference).

With the bunch-by-bunch diagnostics tool, further transverse and longitudinal instability information can be observed. Additionally, it is an excellent tool for machine impedance and wake-field investigations. Moreover, every bunch is the basic unit of the beam physics research, and the motion information of every bunch will be largely approximate to its natural properties.

The six-dimensional bunch-by-bunch diagnostics system consists of the beam position parameters (two dimensions), beam transverse size (two dimensions), beam longitudinal parameters (two dimensions). With this bunch-by-bunch diagnostics system, it is able to build a fast abnormal intelligent trigger system. The layout of the whole system is shown as Fig. 1: The bunch-by-bunch transverse position was implemented with a resolution of 10  $\mu\text{m}$  and was based on the bunch-by-bunch signal processor and delta over sum algorithm [4, 5]. A two-frequency system was employed for the bunch-by-bunch beam length measurement with large dynamic range of 30 pC–6 nC, and a resolution of less than 0.5 ps calibrated by the Streak Camera [6, 7]. For the bunch longitudinal phase measurement, we used the rise edge detection method to detect the button BPM signal, which could reach the resolution of approximately 1 ps [8]. The bunch-by-bunch beam size system is based on

SR (synchrotron radiation) light with a PMT (photomultiplier tubes) detector and Gaussian fitting algorithm [3].

## Motivation

Previous section shows the whole six-dimension bunch-by-bunch diagnostics system and the fast intelligent trigger system. Fast trigger system relies on the online data processing.

In this paper, we will focus on the transverse oscillations. The transverse oscillations and transverse emittance enlargement will lead to machine instabilities. The precise bunch-by-bunch transverse position and size measurement is critical in machine abnormality studies and improvements.

A bunch-by-bunch beam size measurement system has been developed at SSRF. This system is capable of measuring bunches within a separation of 2 ns [2, 3]. However, this system still has some limitations, the speed of online data processing is limited by its complex algorithm. Fortunately, simple bunch-by-bunch diagnostics such as electron bunch monitors (beam position, beam current) can in principle work at the repetition rate. In order to establish a fast abnormal intelligent trigger system, it is necessary to obtain the bunch-by-bunch data online.

Machine learning methods have been widely used in various fields. In this paper, the machine learning technique was applied to observe transverse oscillation. We prefer to use simple bunch-by-bunch diagnostics monitors to predict the result of complex bunch-by-bunch beam size monitors.

We have developed a machine learning tool to predict beam transverse size using beam position and charge as input. Using this technique at SSRF storage ring, we report mean squared errors below 4  $\mu\text{m}$  for prediction of the horizontal beam size.

## CORRELATION BETWEEN DIFFERENT PARAMETERS

Beam charge, position, and size are the main parameters which can be used to characterise the transverse oscillation of the bunch. All of these parameters are related to the transverse oscillation. In order to realize the technique that using beam position and charge as input to predict beam size, correlation analysis between those parameters is indeed.

Correlation analysis between those bunch parameters has been started at SSRF.

In steady state of the storage ring, the transverse oscillation of the bunch is not obvious. Fortunately, the injection events can introduce obvious oscillation. Hence, we investigated the relationship between beam intensity and bunch

\* Work supported by National Science Foundation of China (No. 11375255)

<sup>†</sup> leng@sinap.ac.cn



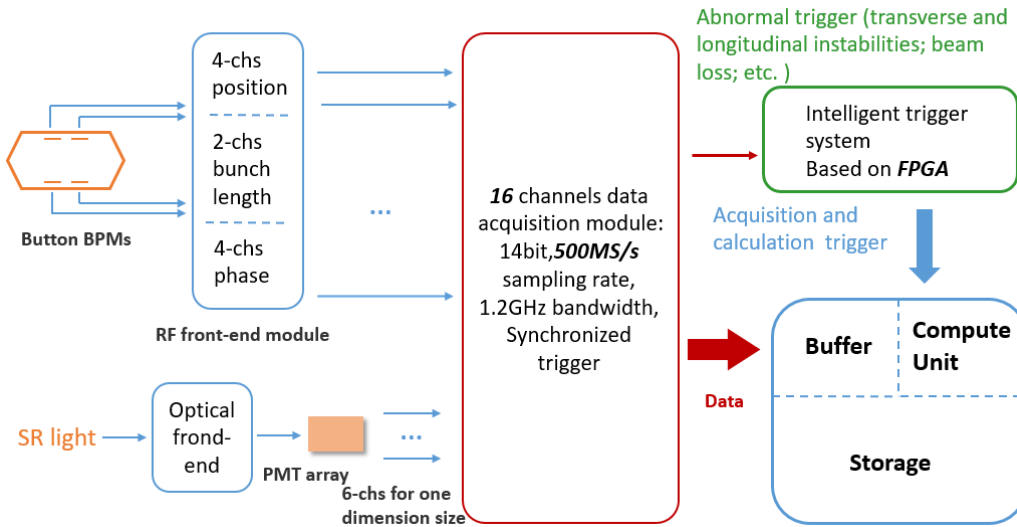


Figure 1: System layout of the six-dimension bunch-by-bunch beam diagnostic system and fast abnormal intelligent trigger system at SSRF.

size, and the relationship between bunch position and bunch size before and after injection events.

The following two figures show the relationship between the beam charge and the size, and between the position and the beam horizontal size [3].

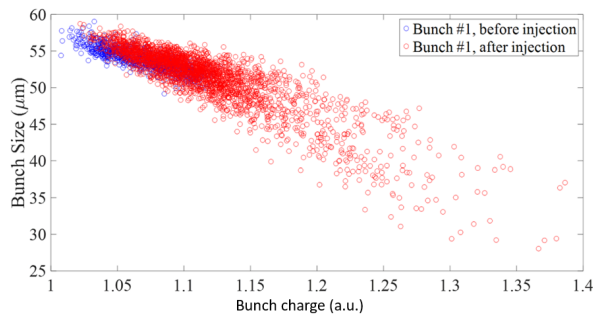


Figure 2: Correlation results between bunch size and bunch charge.

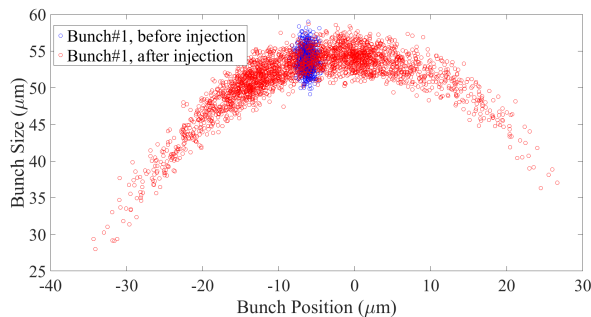


Figure 3: Correlation results between bunch size and center position.

The correlation results show that it is possible to develop a machine learning tool to predict beam transverse size using beam position and charge as input. In the next sections, the machine learning model and the result of the prediction will be presented.

## MODEL TRAINING

The proposed technique based on machine learning for the prediction of transverse beam size is summarized in Fig. 4:

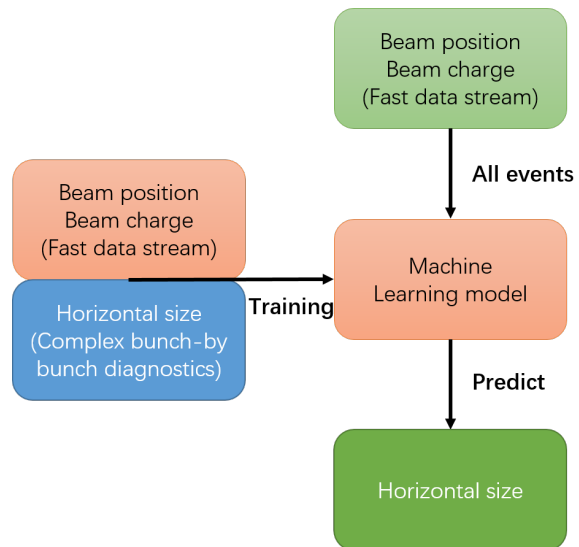


Figure 4: Schematic of the technique based on machine learning to predict transverse beam size.

In this application, the prediction relies on a fast simple bunch-by-bunch data (beam position and charge) for all events, and the offline beam size data obtained from complex bunch-by-bunch beam size monitor for a small fraction of



- diation Facility”, *Nuclear Science and Techniques*, 2018, 29: 1-9.
- [4] Y. Yang, Y.B. Leng, Y.B. Yan, *et al.*, “Development of the bunch-by-bunch beam position acquisition system based on BEEcube”, *Nucl.Sci.Tech.*, 27, 47, 2016.
- [5] Y.B. Leng, Y. Yang, N. Zhang, in *Proceedings of 2nd International Beam Instrumentation Conference*, Oxford, UK, 2013, pp. 746–748
- [6] L.W. Duan, Y.B. Leng, R.X. Yuan, *et al.*, “Injection transient study using a two-frequency bunch length measurement system at the SSRF”, *Nucl. Sci. Tech.*, 28, 93, 2017.
- [7] H.J. Chen, L.W. Duan, Y.B. Leng, *et al.*, in *Proceedings of 6th International Beam Instrumentation Conference*, Grand Rapids, MI, USA, 2017.
- [8] Y.M. Zhou, Y.B. Leng, H.J. Chen, *et al.*, in *Proceedings of 8th International Particle Accelerator Conference*, Copenhagen, Denmark, 2017, pp. 341–344.

# DESIGN AND RADIATION SIMULATION OF THE SCINTILLATING SCREEN DETECTOR FOR PROTON THERAPY FACILITY

P. Tian, Q.S. Chen, K.Tang, J.Q. Li, K.J. Fan\*

State Key Laboratory of Advanced Electromagnetic Engineering and Technology, Huazhong University of Science and Technology, Wuhan 430074, Hubei, China

## Abstract

A proton therapy facility based on a superconducting cyclotron is under construction in Huazhong University of Science and Technology (HUST). In order to achieve precise treatment or dose distribution, the beam current would vary from 0.4 nA to 500 nA, in which case conventional non-intercepting instruments would fail due to their low sensitivity. So we propose to use a retractable scintillating screen to measure beam position and beam profile. In this paper, a comprehensive description of our new designed screen monitor is presented, including the choice of material of the screen, optical calibration and simulation of radiation protection. According to the off-line test, the resolution of the screen monitor can reach 0.13 mm/pixel.

## INTRODUCTION

Huazhong University of Science and Technology (HUST) has planned to construct a proton therapy facility based on an isochronous superconducting cyclotron, from which 250 MeV proton beam is extracted. The layout of HUST proton therapy facility (HUST-PTF) is shown in Fig.1, with the basic specifications listed in Table 1.

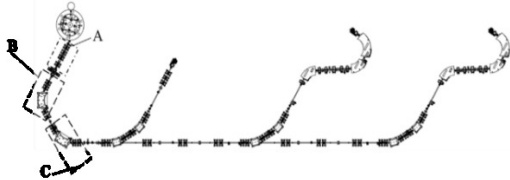


Figure 1: Layout of HUST proton therapy facility.

Table 1: Basic Beam Parameters of HUST-PTF

Phase	Energy/MeV	Current/nA
A	250	60-250
B	70-240	1-15
C	70-240	0.4-5

As the beam current is at the level of nanoampere, conventional non-intercepting instruments, such as inductive beam position monitors (BPMs), will fail to obtain effective beam signals without enough signal-to-noise ratio. Ionization chamber (IC) is popular for this kind of application, but it is too expensive to deploy IC all along the beamline. So we propose to use a relatively simple and economical instrument, scintillation screen, to measure beam position and profile.

The mechanical structure of the scintillation screen is shown in Fig.2. The CCD camera is located on the opposite side to the actuator, which is an air-driving type for the consideration of radiation damage.

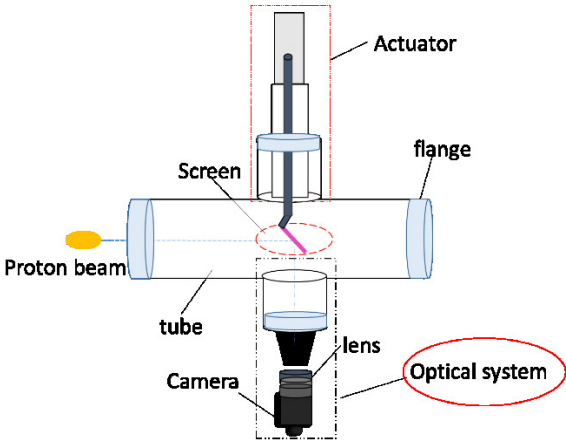


Figure 2: Scheme of retractable scintillator screen setup.

## OPTIMIZATION OF SCREEN

Intercepting scintillation screens determine two-dimensional beam images and are frequently used for transverse profile measurements in beam transfer lines. High precision of profile and position measurements is important for controlling the spatial distribution of the beam [1]. For good luminescent screens, there are several key properties, including high efficiency of energy conversion, large dynamic range and good linearity between particles and light output, high radiation hardness and so on. Based on Refs. [2-4], the linearity of three common scintillators, separately YAG, P43, Al<sub>2</sub>O<sub>3</sub>:Cr are satisfied here when the current is 0.4nA. As for the photon yield related to energy deposition, P43 can produce higher number of photons. Figure 3 shows the different energy depositions of the three materials with thickness of 1 mm calculated by SRIM [5]. The luminescence intensity of the fluorescent screen with Al<sub>2</sub>O<sub>3</sub>:Cr was calculated by Eqs. (1) and (2) below

$$Y = \frac{\eta \times \Delta E \times n}{E_0} \tag{1}$$

with  $\eta$  the energy conversion efficiency,  $\Delta E$  the energy loss of a particle,  $n$  the number of particles,  $E_0$  the energy of the visible photon 3eV, thus yielding  $Y$  the number of the visible photons [6]. For particles of the beam,  $n$  is given by:

$$i = \frac{ne}{t} \tag{2}$$

with beam current  $i$ ,  $e$  the charge of the proton, and  $t$  the width of the beam. Supposing the light output efficiency 0.2%, when beam current is 0.4 nA, the number of photon yield is  $6.42 \times 10^{11}$  /s, which is adequate for the CCD camera, with each pixel absorbing at least 1000-2000 photons [7].

\* Work supported by national key R&D program, 2016YFC0105303.  
† email address: kjfan@hust.edu.cn



Because of the advantage of the higher ability of radiation hardness, the easier access and lower cost of the  $\text{Al}_2\text{O}_3\text{:Cr}$  than the other two materials,  $\text{Al}_2\text{O}_3\text{:Cr}$  has been given the priority in our design.

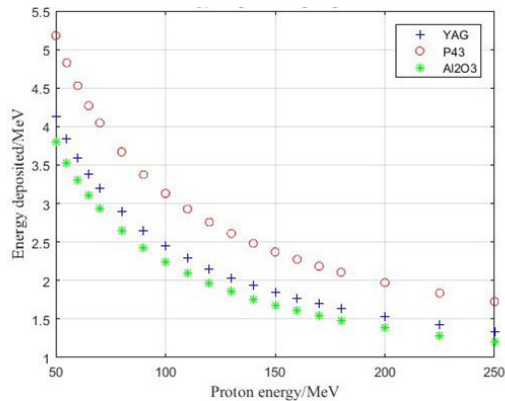


Figure 3: Fluorescent screen (1mm  $\text{Al}_2\text{O}_3\text{:Cr}$ , P43 and 1 mm YAG) with different beam energy).

As to the thickness of the screen, the resolution, heat production, scattering and other influences should be considered. The thinner the screen is, the better spatial resolution the setup will have. On the contrary, the light output will decrease. Referring to prior experiences [8, 9], the thickness of 1 mm was taken into account with the result of Bragg peak with 70MeV proton, shown in Fig. 4. The distance of 1 mm is far away from the Bragg peak, which is acceptable for the design.

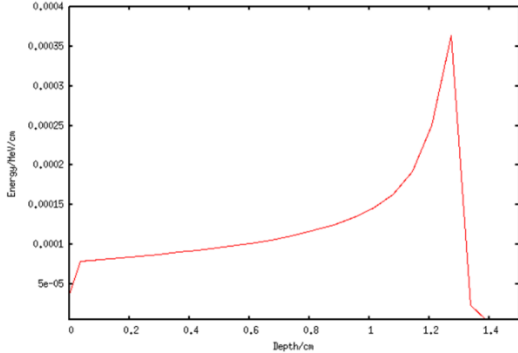


Figure 4: Bragg peak of  $\text{Al}_2\text{O}_3\text{:Cr}$  with 70MeV proton.

CALIBRATION

At present, the scintillating screen detector has been completed, with 1/2" CCD chip, 12-bit resolution, and monochrome, mounted with a distance of 200 mm with respect to the screen slightly below the optic axis. The camera was equipped with a Montex lens of 16 mm focal length. Figure 5 shows the off-line calibration field diagram of the setup. We used the five off-line pictures [one of them shown in Fig. 6(a)] to calculate the resolution and magnification, by using MATLAB to read and identify the pixel coordinates of the four vertices of square and cross, shown in Fig. 6(b). The number of pixels of each side (Table.2, Table.3) and the position of the central point of the cross are calculated, thus obtaining magnification, image resolution of the optical system and the accuracy of

the repeated location. The two calibration results of square and cross can be used for cross validation.

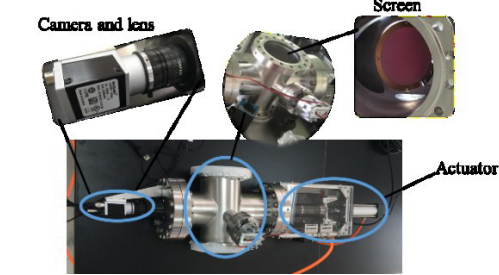


Figure 5: Off-line calibration of the setup.

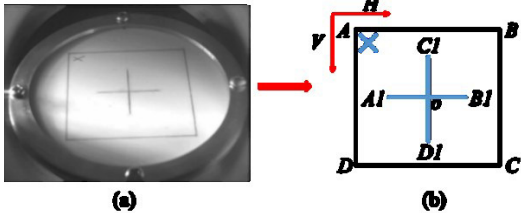


Figure 6: (a) One of the five off-line pictures; (b) Off-line calibration sketch map.

Table 2: Calibration in Square

Order	AB pixel	CD pixel	BC pixel	AD pixel
1	296	334	220	221
2	294	334	218	220
3	293	334	220	221
4	294	334	220	221
5	295	335	219	221
average	294.4	334.2	219.4	220.8
magnification	0.07771		0.07700	
resolution/(mm/pixel)			0.13	

Table 3: Calibration in Cross

Order	A1B1/pixel	C1D1/pixel
1	161	114
2	160	113
3	161	112
4	160	113
5	160	112
average	160.4	112.8
magnification	0.07953	0.07910
resolution/(mm/pixel)	0.13	

According to statistics, the repeated positioning accuracy and the resolution of the system induced from the data are respectively 0.0637mm and 0.13mm/pixel.

RADIATION CALCULATION

Semiconductor devices like CCD operating in a radiation field may undergo degradation due to total dose effect of ionization and displacement damage effect. The ionizing dose effects involve electron-hole pair production, and displacement damage effects coming from the nonionizing processes. Such degradation may cause the deformation of the image captured by CCD for the structure of metal-dielectric semiconductor will become

Content from this work may be used under the terms of the CC BY 3.0 licence (© 2018). Any distribution of this work must maintain attribution to the author(s), title of the work, publisher, and DOI.

sensitive to ionizing radiation [10, 11]. The dose and flux of the sensitive area are calculated using Monte Carlo software, FLUKA and Geant4 [12, 13], to estimate the radiation level the camera can accept. Figure 7 shows the model in FLUKA (same as in Geant4) and the calculated radiation field of the setup. The number of analog particles is  $3 \times 10^7$ .

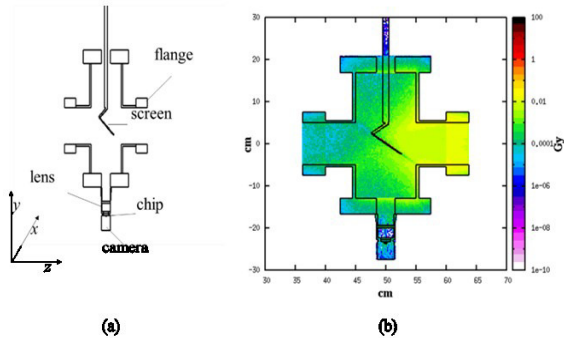


Figure 7: (a) The model in FLUKA; (b) Radiation field of the setup shown on y-z plane, the color band show the different level of dose distributed in the setup.

The dose of the chip simulated at 200 mm away from the screen is very low, on the order of  $10^{-10}$ Gy. Under the condition of the energy 250 MeV and the current 500 nA, the cumulative absorbed dose is 154.65 Gy per year. While at the distance of 230 mm, the chip received a dose of 1.44 Gy per year, which is 0.5% of the tolerated dose. The dose absorbed by the chip at different locations from the screen varies from the distance, shown in Fig. 8, indicating that the smallest dose with distance of 230 mm.

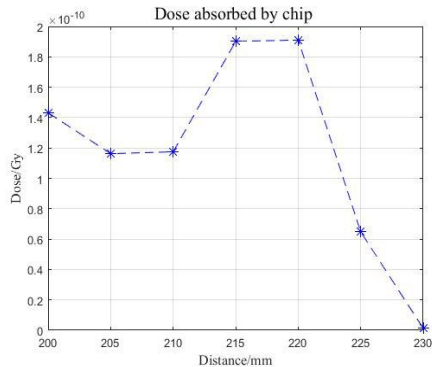


Figure 8: Dose in chip with different distance from screen.

Table 4: Flux Calculated from Geant4 and FLUKA

Flux(particles/cm <sup>2</sup> )	GEANT4	FLUKA
proton	$1.0269 \times 10^5$	$4.6893 \times 10^5$
neutron	$1.3041 \times 10^7$	$1.8951 \times 10^7$

The flux of the two simulation software match well with each other (see Table.4), and both are lower than the tolerated range, respectively  $10^{10}$  protons/cm<sup>2</sup> and  $10^{12}$  neutrons/cm<sup>2</sup>.

### CONCLUSION

The intercepting method of scintillating screen has the advantages of simplicity and low cost, performing well in low beam current condition. The off-line calibration results

of the optical system of the finished setup are fit for the measurement. The radiation dose absorbed by the chip within one year simulated by using FLUKA indicates that the camera needs periodic replacement within one year of operation. The number of particle fluxes through the chip simulated by FLUKA and Geant4 are very close, which reveals that the radiation level is relatively low. There is another choice of placing the camera at 230 mm to avoid more radiation, which will however enlarge the space, may be considered. As to the radiation shielding, various protective materials will be tested later to estimate the effects when using them.

### REFERENCES

- [1] A. Lieberwirth, W. Ensinger, P. Forck et al., “TEST OF THE IMAGING PROPERTIES OF INORGANIC SCINTILLATION SCREENS USING FAST AND SLOW EXTRACTED ION BEAMS,” in *Proc. IBIC’16*, Barcelona, Spain, Sep. 2016, pp. 516-519, doi:10.18429/JACoW-IBIC2016-TUPG70
- [2] Forck P, “Lecture Notes on Beam Instrumentation and Diagnostics,” *JUAS, Darmstadt*, Germany, Jan. – Mar. 2011.
- [3] Krishnakumar, Renuka, “Scintillation Screen Materials for Beam Profile Measurements of High Energy Ion Beams,” Ph.D. thesis, Dept., Technische Universität, Darmstadt, 2016.
- [4] A. Lieberwirth, W. Ensinger, P. Forck, and B. Walasek-Höhne, “Response of Scintillating Screen to Fast and Slow Extracted Ion Beams, in *Proc. IBIC’13*, Oxford, UK, Sep. 2013, paper TUPF21, PP. 553-554.
- [5] SRIM, <http://www.srim.org/>.
- [6] A. Eempicki, “The physics of inorganic scintillators,” *J. Appl. Spec.*, vol. 62, No. 4, 1995.
- [7] M. Turner, B.Biskup, S.Burger et al, “The two-screen measurement setup to indirectly measure proton beam self-modulation in AWAKE”, *J. Nuclear Instruments and Methods in Physics Research A*, 2017.
- [8] B. K. Scheidt, “UPGRADE OF THE ESRF FLUORESCENT SCREEN MONITORS”, in *Proc. DIPAC’03*, Mainz, Germany, May 2003, paper PM14, pp. 125-127.
- [9] G. Kube, C. Behrens, “RESOLUTION STUDIES OF INORGANIC SCINTILLATION SCREENS FOR HIGH ENERGY AND HIGH BRILLIANCE ELECTRON BEAMS”, in *Proc. DIPAC’10*, Kyoto, Japan, 2010, paper MOPD088, pp. 906-908.
- [10] G. R. Hopkinson, J. Dale, and P. W. Marshall, “Proton Effects in Charge-Coupled Devices,” *IEEE Trans. Nucl. Sci.*, vol. 43, NO. 2, 614, 1996.
- [11] S. Hutchins, M. Facchini, E. Tsoulou, “RADIATION TESTS ON SOLID STATE CAMERAS FOR INSTRUMENTATION,” in *Proc. DIPAC’05*, Lyon, France 2005, paper CTWA02, PP.315-317.
- [12] Andrew Welton, “Absorbed Dose and Dose Equivalent Calculations for Modeling Effective Dose”, NASA Johnson Space Center; Houston, TX, United States, JSC-CN-21442, Jan 01, 2010.
- [13] Geant4, <http://geant4.slac.stanford.edu/>.

# X-RAY PINHOLE CAMERA IN THE DIAGNOSTICS BEAMLINE BL7B AT PLS-II

J. Ko<sup>1†</sup>, J. Y. Huang<sup>1</sup>, M. Yoon<sup>2</sup>, K. Kim<sup>1</sup>, B-H. Oh<sup>1</sup>, D-T. Kim<sup>1</sup>, D. Lee<sup>1</sup>, J. Yu<sup>1</sup>, and S. Shin<sup>1</sup>

<sup>1</sup>Pohang Accelerator Laboratory, POSTECH, Pohang, Gyungbuk 37673, KOREA

<sup>2</sup>Department of Physics, POSTECH, Pohang, Gyungbuk 37673, KOREA

## Abstract

The beam diagnostics beamline BL7B using synchrotron radiation with 8.6 keV critical photon energy from bending magnet has been used to measure the electron-beam size and photon-beam profile on real-time basis. After the completion of the PLS-II, the Compound Refractive Lens (CRL) system was implemented in the optical hutch at BL7B to measure the electron-beam size from X-ray imaging. But we could not have a good image due to short available optical path caused by limited space of the optical hutch. To solve this problem a pinhole camera is implemented in the front-end of BL7B in return for the beamline extension. The progresses on the new x-ray imaging system are introduced in this paper.

## INTRODUCTION

After the completion of the PLS-II project [1] to upgrade PLS [2] on March 21, 2012, Pohang Light Source II (PLS-II) is now in full operation. As a result of the upgrade, the PLS beam energy increased from 2.5 GeV to 3.0 GeV, and the stored beam current increased from 200 mA to 400 mA. The emittance is improved from 18.9 nm at 2.5 GeV to 5.8 nm at 3 GeV while the PLS storage ring tunnel structure remains unchanged. In addition, the top-up mode operation is used to stabilize the stored electron beam orbit and the synchrotron radiation flux.

Currently, a total of 31 beamlines including 18 insertion device beamlines are in PLS-II operation for user service. Figure 1 shows the beamline overview of PLS-II. Two multipole wiggler beamlines, three elliptically polarizing undulator beamlines, one planar undulator, twelve in-vacuum undulator beamlines and thirteen bending beamlines have been operated for surface science, magnetic spectroscopy, material science, X-ray scattering, XAFS, MX, SAXS, imaging and lithography [3]. In addition to these beamlines, diagnostics beamline BL7B using bending radiation source have been used to measure photon beam stability, electron beam size and real time photon beam profile.

## Beamline Overview

The specifications of bending radiation in PLS-II for beam diagnostics beamline BL7B are introduced in Table 1. Bending radiation source is the combined function dipole magnet with 1800 mm length. The central field is 1.46 T and is superposed with the focusing field gradient of -0.4 T/m [4]. The beam size at source point is 60  $\mu\text{m} \times 30 \mu\text{m}$  (H  $\times$  V) and beam divergence at source point is 120

$\mu\text{rad} \times 2 \mu\text{rad}$  (H  $\times$  V). With 3 GeV and 400 mA stored electron beam, photon flux at the critical energy of 8.7 keV is  $1.28 \times 10^{12}$  when measured at 15 m from the source point with 1 mm horizontal acceptance.

Unlike typical PLS-II beamline which consists of optical hutch and experimental hutch, beam diagnostics beamline BL7B have only optical hutch and share the optical hutch with the nearby insertion device beamline. Beam diagnostics beamline BL7B do not have the best situation for X-ray imaging due to short optical path length due to limited space, because all optical components are implemented within optical hutch.

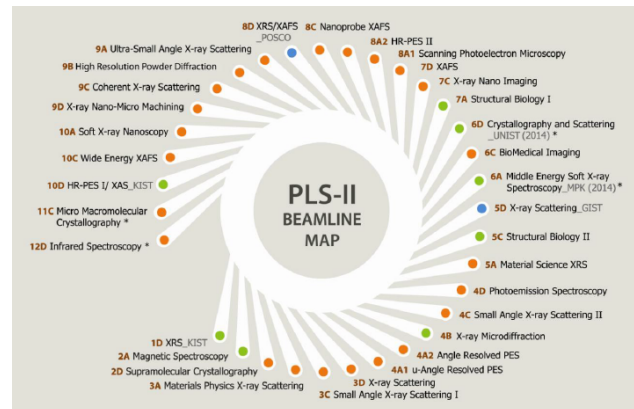


Figure 1: PLS-II beamline map. Here A and C are insertion device beamline, and B and D are bending beamline.

Table 1: The Specifications of Bending Radiation in PLS-II for Beam Diagnostics Beamline BL7B

Parameter	Value	Unit
Electron beam energy	3	GeV
Electron beam emittance	5.8	nm
# of bending magnets	24	
Length of bending magnet	1.8	M
Field / Gradient	1.46/-0.4	(T)/(T/m)
Crit. Photon energy	8.73	keV
Source size (H/V)	60 / 30	$\mu\text{m}$
Source divergence	120 / 2	$\mu\text{rad}$

## Photon Beam Stability

In order to measure photon beam stability in beam diagnostics beamline BL7B, the most common PBPM [5], that is a simple structure equipped with two blades, is implemented before beam line optics. Figure 2 shows long term slow photon beam motion during 8 days user operation.

<sup>†</sup> kopearl@postech.ac.kr



The photon beam motion are described in vertical phase space using two PBPMs in BL7B. By the contribution of slow orbit feedback system and stable thermal loading from top-up operation, long term (8 days) photon beam motion at 13 m from source is within rms  $7\mu\text{m}$  in Fig. 2.

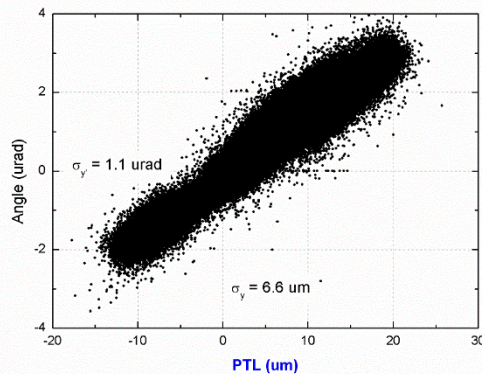


Figure 2: Long term photon beam central motion of PBPM installed at 13 m from the source.

## CRL IMAGING SYSTEM

The Compound Refractive Lens (CRL) were implemented in the beam diagnostics beamline to measure the electron-beam size and real time beam profile from X-ray imaging. Figure 3 shows a schematic diagram of the beam-line layout. The beamline consist of two PBPMs, channel-cut DCM, CRL, Scintillation crystal and tele- $\mu$ -scope. The total length is around 17 m from source to CCD.

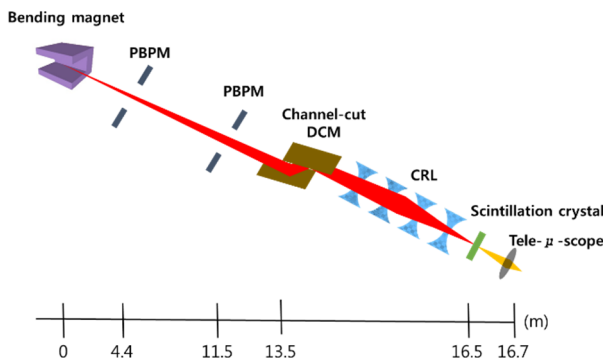


Figure 3: Optical layout of the beamline BL7B.

X-rays are monochromated ( $\Delta E / E \approx 10^{-4}$ ) using a silicon (111) channel cut monochromator located 13.5 m from the source. In order to focus the divergent X-rays, 14 pieces of beryllium parabolic CRLs of diameter  $50\mu\text{m}$ , positioned just downstream of monochromator, are employed. At that position, the FWHM beam size is  $2.1\text{ mm} \times 0.7\text{ mm}$ . The focal length of each CRL is 2.1 m at 21 keV.

Figure 4 (a) shows image formed on YAG screen for 7 keV X-ray through  $200\mu\text{m}$  diameter 6 piece CRL system. Normal image has not formed and different images appear on the edge in the figure. This is background effect of high

energy X-ray on scintillation crystal after passing through channel-cut DCM and CRL substrate. Therefore, 21 keV 3<sup>rd</sup> harmonic energy as high energy is considered with  $50\mu\text{m}$  diameter 14 piece CRL system. As a result, clear image has formed as shown in Fig. 4 (b).

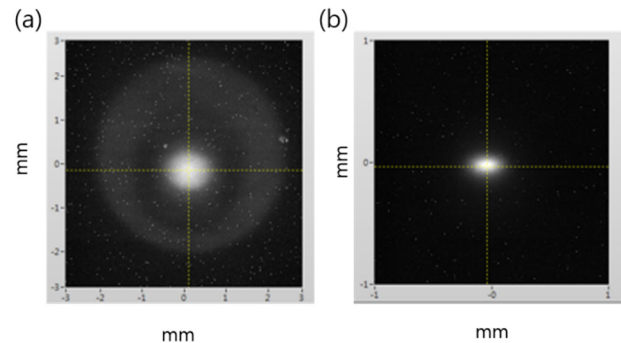


Figure 4: Image on YAG screen. (a) 7 keV and  $200\mu\text{m}$  CRL. (b) 21 keV and  $50\mu\text{m}$  CRL.

However, compared with the measured beam size  $83\mu\text{m}$  and  $25\mu\text{m}$  (horizontal and vertical) from interferometer that is the conventional method via imaging of the visible synchrotron radiation, the beam size from CRL image is measured as  $125\mu\text{m}$  and  $85\mu\text{m}$  for horizontal plane and vertical plane, respectively.

Various causes of beam size measurement error can be deduced as;

- Beam oscillation effect: Measurement error by beam oscillation is inferred with the trend of measured beam size along the shorter exposure time of CCD. Therefore, the measurement with 200 Hz fast acquisition is needed to avoid main oscillation frequencies of storage ring (30 Hz, 60 Hz, 120 Hz, 180 Hz). But the sensitivity is getting worse along shorter acquisition time and at most 10 Hz is highest repetition rate for the measurement. However, measured beam sizes at 10 Hz acquisition are 10 percent smaller than beam sizes measured at 1 Hz for each plane.
- Screen on larger image plane: Mis-position of screen at larger image plane due to limited adjustment range of scintillation crystal.
- Large image demagnification: diffraction error of telescope and measurement error by scintillation crystal thickness enlarge measured beam sizes, since demagnification of x-ray imaging is very large as 0.21 and beam image size on scintillation crystal is at least  $5\mu\text{m}$

However, these causes cannot make that big imaging error. One possible reason of large imaging is the deviation of focal length by fabrication error of CRLs. Although we needed to investigate on this more rigorously, the available optical space for finding the final focus was not enough. Therefore, to solve this problem, the CRL system was dis-assembled and instead a new pinhole camera was installed in the front-end of BL7B.



## PINHOLE IMAGING SYSTEM

A classical pinhole camera set-up has been built at BL7B to measure the electron-beam size and photon-beam profile on real-time basis. From each source point, one ray passes through the pinhole (if it is infinitesimally small) forming an inverted image of the source [6]. A layout of the apparatus is shown in Fig. 5.

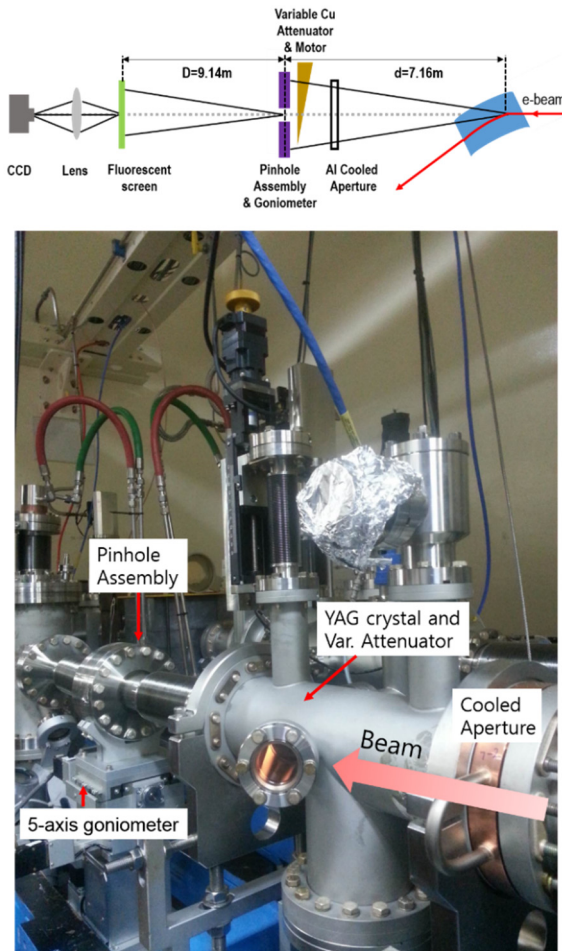


Figure 5: Schematic of the pinhole camera apparatus and system components in front-end.

The X-ray source is the synchrotron radiation coming from the electron beam at the entrance of a bending magnet. The X-rays exit the storage ring vacuum through a 3 mm thick Al window. The pinhole is 1 m downstream of the window and 7.16 m downstream of the source point. After passing through the pinhole, the X-rays strike a fluorescent screen located 9.14m downstream of the pinhole (magnification 1:1.3). Finally, the visible light is imaged with a CCD camera.

The pinhole is quite simple and easy to fabricate. There are actually 5 x 5 rectangular pinholes of various sizes. They are formed using a grid of flat and parallel carbide tungsten plates separated by tungsten wires (Fig. 6). The pinhole assembly is remotely moveable with five degrees

of freedom: horizontal (x) translation, vertical (z) translation, rotation around the x, y, and z axes. For the pinhole, one can choose among five horizontal (50, 40, 35, 25, 20  $\mu\text{m}$ ) and five vertical (40, 35, 25, 20, 16  $\mu\text{m}$ ) sizes. The 500 x 500  $\mu\text{m}$  pinhole is used for alignment purposes. Note that the nonzero penetration of hard X-rays (critical photon energy of 8.73 keV) in tungsten requires the use of a thick pinhole. We are using a 5 mm thick carbide tungsten to block the penetration of high energy x-rays sufficiently. Because of the thickness of the pinhole one should view it like a tunnel rather than a simple hole. With the smallest size aperture, the tunnel presents an aspect ratio of 300 which requires a precise angular adjustment to place it parallel to the incoming X-ray beam. Note that a non-parallelism of the beam with the tunnel axis results in an effective reduction of the aperture.

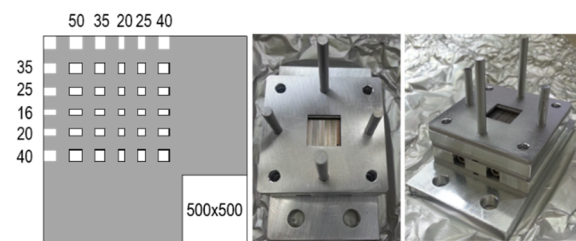


Figure 6: An array of 5 x 5 rectangular pinholes is made with tungsten plates and tungsten wires. The wide pinhole is used for alignment purposes and the small pinholes are used during the measurement.

To acquire and measure the size of the source we image the screen with a tele- $\mu$ -scope and CCD. Figure 7 shows an image formed on fluorescent screen (CdWO<sub>4</sub>) through a 40 x 20  $\mu\text{m}$  pinhole and a two-dimensional Gaussian fitting profiles.

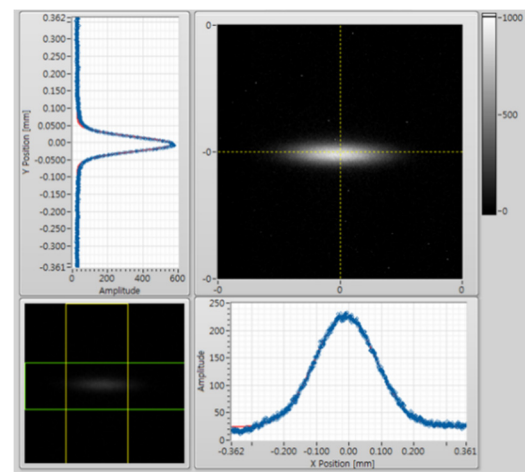


Figure 7: Image on fluorescent screen (CdWO<sub>4</sub>) through a 40 x 20  $\mu\text{m}$  pinhole and a two-dimensional Gaussian fitting profiles.

Compared with the measured beam size 83  $\mu\text{m}$  and 25  $\mu\text{m}$  (horizontal and vertical) from interferometer, the beam

size from pinhole camera image is measured as 95  $\mu\text{m}$  and 21  $\mu\text{m}$  for horizontal plane and vertical plane, respectively.

The performance of the measurement of the transverse electron beam size is given by the width of the point spread function (PSF) of the X-ray pinhole camera [7]. The image formed on the camera is the convolution of several independent contributions including beam size, pinhole size, fluorescent screen and CCD. Let us call  $\Sigma$  the r.m.s. Gaussian size of the acquired image and assume the source and the PSF's to be Gaussian. Then  $\Sigma$  can be expressed as follow:

$$\Sigma = \left[ (S \cdot C_{mag})^2 + S_{aper}^2 + S_{diff}^2 + S_{scr}^2 + S_{CCD}^2 \right]^{1/2} = \left[ \left( S \frac{D}{d} \right)^2 + S_{sys}^2 \right]^{1/2}, \quad (1)$$

where  $S$  is the r.m.s. size of the image of the photon emitted by electron beam at the source point,  $S_{aper}$  is the geometrical contribution introduced by the finite size of the pinhole,  $S_{diff}$  is the diffraction contribution by the small pinhole,  $S_{scr}$  is the screen spatial resolution,  $S_{CCD}$  is the spread induced by the camera, which includes pixel size, lens aberration and depth of focus through the finite thickness of the screen and aperture of the lens and  $S_{sys}$  is effective PSF of the whole pinhole system.  $C_{mag}$  is the magnification factor of the pinhole camera.  $d$  is the distance from source point to pinhole.  $D$  is the distance from pinhole to screen.

To determine the width of system PSF for the pinhole camera a beam based calibration method has been developed in the SSRF storage ring [7]. By varying the beam size  $S$  at the source point and measuring image size  $\Sigma$ , the practical  $S_{sys}$  can be derived from equation (1) using least-square fitting method. The beam size of source point was changed by modifying the power supply current  $I_{Q5}$  of the 5th set of quadrupoles. And the beam size could be described as follow:

$$S_i^2 = \beta_i \epsilon_i + (\eta_i \sigma_\epsilon)^2, \quad (2)$$

where  $S_i$  is the beam size in the horizontal or vertical plane respectively ( $i = x, y$ ), and  $\beta_i$  and  $\eta_i$  are the betatron and dispersion functions at the source point and in the corresponding plane; and  $\epsilon_i$  and  $\sigma_\epsilon$  are the emittance and the relative energy spread of the electron beam.

Figure 8 shows the beam-size according to the pinhole-size. We need to find some correlation between pinhole-size and beam-size in order to verify the usability and reliability of pinhole camera. And then a machine study will also follow to determine the PSF for the pinhole camera described above.

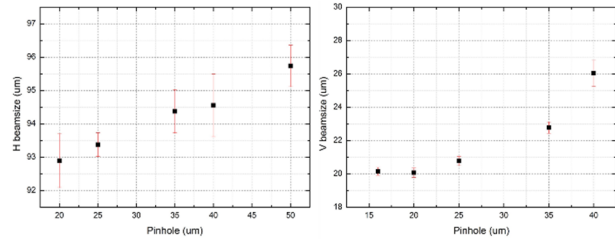


Figure 8: The beam-size according to the pinhole-size for horizontal plane and vertical plane, respectively.

## CONCLUSION

The beam diagnostics beamline BL7B takes the important role to provide the information on photon beam condition in PLS-II. Especially, an X-ray pinhole camera has been installed in BL7B and the electron-beam size and photon-beam profile on real-time basis are measured. To optimize the pinhole imaging system, further investigation based on beam based calibration is necessary.

## ACKNOWLEDGEMENTS

This research was supported by the Converging Research Center Program through the Ministry of Science, ICT and Future Planning, Korea (NRF-2014M3C1A8048817) and the Basic Science Research Program through the National Research Foundation of Korea (NRF-2015R1D1A1A01060049).

## REFERENCES

- [1] S. Shin et al., J. Instrum. 8, P01019 (2013).
- [2] S. H. Shin, M. Yoon and E.-S. Kim, J. Korean Phys. Soc. 49, 1591 (2006).
- [3] See “<http://pal.posech.ac.kr/paleng/Menu.pal?method=menu-View&pagecode=paleng&top=2&sub=3&sub2=1&sub3=0>” for the information of PLS-II beamline.
- [4] S. Shin et al., J. Instrum. 8, P08008 (2013).
- [5] Changbum Kim et al., J. Korean Phys. Soc. 66, 167 (2015).
- [6] P. Elleaume, C. Fortgang, C. Penel, *et al*, Measuring beam sizes and ultra-small electron emittances using an X-ray pinhole camera, J. Synchrotron Rad. 2 (1995), 209–214
- [7] Y.B. Leng, G.Q. Huang, M.Z. Zhang et al., The beam-based calibration of an X-ray pinhole camera at SSRF. Chin. Phys. C 36, 80–83 (2012)

# SELECTION OF WIRES FOR THE NEW GENERATION OF FAST WIRE SCANNERS AT CERN

A. Mariet, R. Veness, CERN, 1211 Geneva, Switzerland

## Abstract

A new generation of fast wire scanners is being produced as part of the LHC Injector Upgrade (LIU) project at CERN. The LIU beam parameters imply that these wire scanners will need to operate with significantly brighter beams. This requires wire scanner systems with micron level accuracy and wires with a considerably increased tolerance to beam damage. This paper presents the method of selection of such wires in terms of material choice and geometry. It also reports on studies with novel materials with a potential to further extend the reach of wire scanners for high brightness beams.

## INTRODUCTION

### Instrument Principle

Wire-scanners are devices used to measure the transverse beam density profile by moving a thin wire across the particle beam. The interaction between the beam and the wire creates secondary particle showers with an intensity proportional to the number of particles crossing the wire.

These secondary particles are intercepted by a scintillator, positioned downstream of the wire, coupled to a photomultiplier which amplifies the resulting signal. The acquisition of the wire position and the signal intensity are combined to reconstruct the transverse beam density profile.

The LHC Injector Upgrade (LIU) project at CERN [1] is increasing beam brightness across the LHC injector chain (Proton Synchrotron Booster (PSB), Proton Synchrotron (PS) and Super Proton Synchrotron (SPS)), to produce smaller, higher intensity beams.

Due to this higher brightness, the principal wire failure mode is expected to be due to the fast increase of temperature leading to melting or surface sublimation. The loss of matter weakens the wire until failure occurs [2].

In order to minimise this issue, the new fast beam wire-scanner (BWS) developed at CERN for LIU (see Fig. 1) has increased the linear velocity of the wire to  $20 \text{ m.s}^{-1}$ , such that the wire remains in the beam for much less time [3]. The downside to this, however, is that for very small beams a signal is only produced for a few points along the profile.

### Wire Research Development

Wire-scanners were first used in 1964 in Oxford and Heidelberg [4], as robust and direct profile measurement instruments. They have since evolved along with accelerator technology, and remain one of the fundamental instruments for measuring the beam profile in most particle accelerators.

Different wire materials and geometries have been used throughout this time. Among the first were steel, tantalum and beryllium, followed later by carbon, quartz, tungsten

and titanium, as well as copper-beryllium alloys and silicon carbide. The advantages and disadvantages of some of these materials will be investigated in this paper. In addition, the geometry of the wire has an important role to play. Existing wires used at CERN have diameters from 7 to 34  $\mu\text{m}$ , and are either single or multi strand (see Table 1).

Table 1: Rotational Wire-scanner Configuration

Ring	PSB	PS	SPS
Wire configuration	12x 7	12x 7	1x 34
Equivalent diameter [ $\mu\text{m}$ ]	24	24	34
Wire length [mm]	120	153	153
Forks length [mm]	150	183	183

The other important parameter in wire scanner design is the scan speed. This parameter defines the time needed by the wire to cross the beam and is directly related to the number of useful data points taken per scan. This combination of material, geometry and scanning speed must satisfy three main criteria:

- Maximal measurement resolution
- Sufficient interaction to generate a signal
- Maximal lifetime of the wire

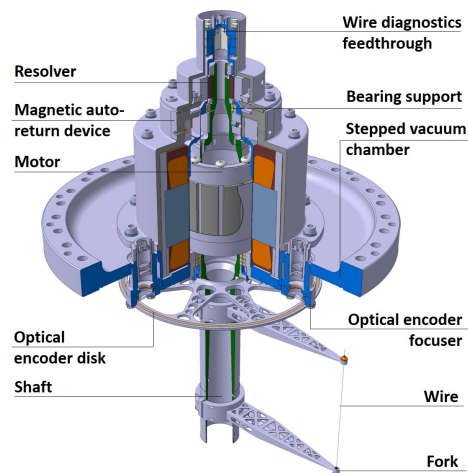


Figure 1: New Fast Beam Wire Scanner for LIU

## MATERIAL SELECTION FOR MECHANICAL PROPERTIES

### Wire Pre-Load

The pre-tension load is a key factor to determine the maximal wire deflection during movement of the scanner movement and hence the limiting resolution of the measurement. Table 2 compiles parameters, the ultimate tensile strength



( $\sigma_{ult}$ ) and the bulk density ( $\rho$ ) for different candidate materials and gives the maximum pre-tension load ( $F_{pmax}$ ) before failure. Clearly, larger cross sections of the same material allow for higher pre-tension loads.

Table 2: Maximum Preload Allowed for Minimal Deflection Calculation

	$\sigma_{ult}$ [MPa]	$\rho$ [kg.m <sup>-3</sup> ]	$F_{pmax}$ [N]	
			(24 $\mu$ m)	(34 $\mu$ m)
Be	550	1800	0.25	0.5
C	900	1800	0.41	0.81
Ti	460	4510	0.21	0.41
Fe	800	7840	0.36	0.73
Cu	220	8960	0.1	0.2
W	1920	19300	0.87	1.74

If the ultimate tensile strength ( $\sigma_{ult}$ ) were the only parameter to evaluate, tungsten would be the best choice due to its high pre-tension load with carbon and steel over a factor two worse.

### Deflection under Constant Angular Acceleration

Rotational wire-scanners accelerate to their nominal beam crossing velocity in  $\frac{1}{4}$  of a turn. Hence the wire undergoes rapid angular acceleration. This can be modelled by a linear wave equation for a vibrating wire subjected to the centrifugal force produced by a rotation of angular velocity  $\omega$ . Considering the attachment points of the wire ( $x = 0, y = 0$ ) and ( $x = L, y = 0$ ) are at a distance  $R$  (length of the forks) from the axis of rotation, the equation of motion in the rotating frame can be written as:

$$\frac{\partial^2 y(x, t)}{\partial t^2} = \frac{F_p}{\lambda} \frac{\partial^2 y(x, t)}{\partial x^2} + \omega^2 y(x, t) + \omega^2 R \quad (1)$$

where  $x$  is the position along the wire,  $y$  is the displacement of the wire from the nominal position (which depends on the  $x$ -position and the time  $t$ ),  $F_p$  is the uniform pre-tension,  $\lambda$  the linear mass density of the wire material,  $L$  the length of the wire, and  $R$  the distance from the wire axis to the shaft axis (i.e. fork length).

Considering the case where  $\omega$  is constant, the solution to equation Eq. (1) can be written explicitly as:

$$y(x, t) = y_{stat}(x) + \sum_{n=1}^{\infty} A_n \cos(\omega_n t) \sin\left(\frac{n\pi x}{L}\right) \quad (2)$$

where  $y_{stat}$  is the deformation function of the stationary state and  $A_n$  the Fourier coefficients of the vibrations around this stationary state.

In our case this stationary state describes the steady state shape of the wire without vibration. It is determined by the equation:

$$\frac{\partial^2 y(x)}{\partial x^2} + \frac{\lambda}{F_p} \omega^2 y(x) + \frac{\lambda}{F_p} \omega^2 R = 0 \quad (3)$$

Let us define a parameter  $\alpha = f_m \times f_g$  where  $f_m = \sqrt{\frac{\rho}{\sigma_{ult}}}$  and  $f_g = \frac{v}{R}$  are material and geometrical functions respectively, with  $v$  defining the scan speed. We remark that  $\alpha$  is independent of the wire diameter. This leads to

$$\frac{\partial^2 y(x)}{\partial x^2} + \alpha^2 y(x) + \alpha^2 R = 0 \quad (4)$$

The solution can be then expressed as

$$y_{stat}(x) = 2R \frac{\sin\left(\frac{\alpha x}{2}\right) \sin\left(\frac{\alpha(L-x)}{2}\right)}{\cos\left(\frac{\alpha L}{2}\right)} \quad (5)$$

The maximal deflection, located in the middle of the wire, can be shown to be written as

$$y_{max} = 2R \frac{\sin^2\left(\frac{\alpha L}{4}\right)}{\cos\left(\frac{\alpha L}{2}\right)} \quad (6)$$

As shown in Fig. 2, the pre-tension is an important parameter, which determines the maximum deflection obtained for a given material.

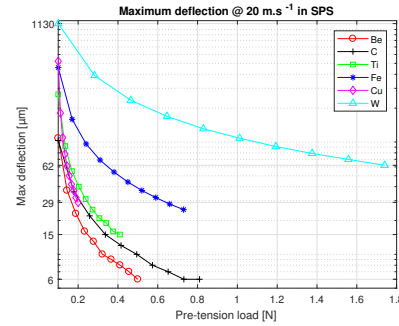


Figure 2: Maximum deflection for SPS @20 m.s<sup>-1</sup>.

Hence materials with a high UTS and a low density will tend to have the lowest deflection during the scan.

Assuming the maximum pre-tension loads for each material, the maximum deflections obtained for the PS and SPS configurations are shown in Fig. 3. For the PSB complex the values decrease by about 30%.

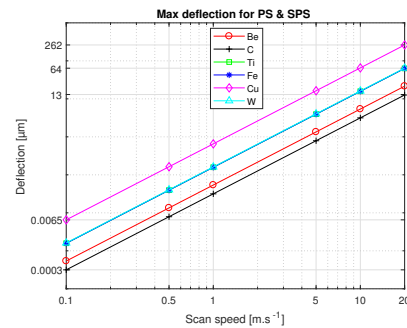


Figure 3: Deflection for PS & SPS at max pre-tension load.

Considering that beam sizes in the injectors range from a few hundred microns to several millimetres, the maximum



deflection of the wire during the scan must remain a fraction of this value. Copper is excluded as it has the highest deflection due to a poor combination of low UTS and high density. Despite its high UTS, tungsten also results in large deflections due to a high density, as does iron and titanium. We are therefore left with beryllium and carbon as the two best potential candidates.

### Vibration of the Wire due to Acceleration

The harmonic frequencies of a vibrating string are defining by  $f_{nstring} = \frac{n}{2L} \sqrt{\left(\frac{F_p}{\lambda}\right)}$ . Considering the rotation of the wire around the axis with angular frequency  $\omega$ , these wire vibration frequencies are modified because of the inertial load and can be expressed for the first mode as:

$$f_w = \frac{1}{2\pi} \sqrt{\left(\frac{F_p}{\lambda} \frac{n^2 \pi^2}{L^2} - \omega^2\right)} \quad (7)$$

The resulting vibration frequencies are independent of R but dependent on the pre-load, the density of the wire, the length between the two forks and the angular rotation frequency. The first mode for each material is summarised in Table 3.

Table 3: First Harmonic Frequencies

	Harmonic frequencies [kHz]					
	Be	C	Ti	Fe	Cu	W
PSB	17.9	23.4	10.4	10.4	5.1	10.3
PS & SPS	14.7	19.2	8.6	8.6	4.2	8.5

The stationary state solution (Fig. 3) shows an amplitude of deflection in the range  $3e-4$  to  $262 \mu\text{m}$ . In reality this value will be a combination of the steady state and the vibration, which depends on the speed profile, i.e. the acceleration function applied to the fork-wire system to bring it across the beam.

Two cases are considered: the ‘nominal’ profile with a slow constant acceleration up to  $133 \text{ rad s}^{-1}$  and the limiting case of a ‘step function’ increase in angular velocity of the shaft.

A slow, constant acceleration combined with a high pre-tension leads to smaller amplitude wire vibrations around the ‘stationary state’ deflection value. This is shown in Fig.4.

However, if the step function acceleration is applied (a situation which can be approached in case of control system failure), the wire amplitude can approach the stationary state value with a risk a breakage, as per Fig. 5.

Due to the deformation, the wire is subjected to an increase in internal stress, leading to a stretching of the wire. The new length can be written as

$$L_d = \int_0^L \sqrt{1 + \left(\frac{dy_{stat}(x)}{dx}\right)^2} dx \quad (8)$$

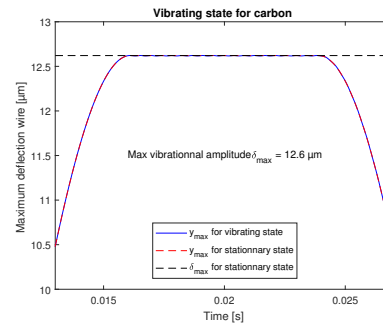


Figure 4: Carbon vibrating state for nominal speed profile.

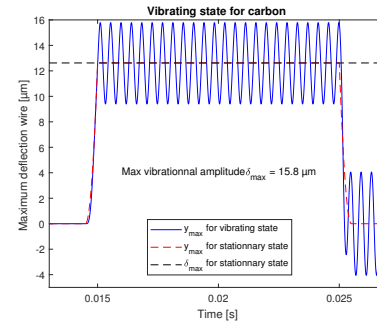


Figure 5: Carbon vibrating state for a sudden switch.

Considering the case with the maximal allowed pre-tension load, and a scan velocity of  $20 \text{ ms}^{-1}$ , the maximum deformation reached is  $261 \mu\text{m}$  for copper in the SPS (Fig. 3). This value leads to an elongation of  $0.8 \mu\text{m}$  (on  $153 \text{ mm}$  length) which is insignificant for an additional load. The stress inside the wire during the rotation is therefore the same as that in the initial state and only depends on the pre-load  $F_p$ .

Mechanical analysis shows that indeed, carbon and beryllium are the best candidates thanks to their low density and their high UTS. The main issue with beryllium is its lower melting temperature of  $1560 \text{ K}$  compared to  $4095 \text{ K}$  for the carbon fibre sublimation temperature. For carbon, there is a significant difference in mechanical properties for different strands, with the small  $7 \mu\text{m}$  carbon fibres having a 70% higher UTS than the  $34 \mu\text{m}$ . This is the reason why  $7 \mu\text{m}$  carbon fibre bundles are used for PSB.

## RESOLUTION OF A SCAN

The LIU-BWS has been designed for precision at high scanning speeds and to minimise damage to the wire material. However, in order to reconstruct profiles for a given bunch, at least three measurement points per beam sigma are required. As the beams are accelerated through the injector chain, the transverse beam size decreases and the circumference of the accelerator, and hence revolution time, increases. This is summarised in Table 4 [1].

For a given bunch (with a length assumed to be small compared to the revolution time) the number of points per

Table 4: Beam Parameters

	PSB	PS	SPS
Energy [GeV]	1.4	25	450
$\sigma_x$ (horizontal) [ $\mu\text{m}$ ]	1570	800	200
$\sigma_y$ (vertical) [ $\mu\text{m}$ ]	1200	500	300
$t_{rev}$ [ $\mu\text{s}$ ]	1.01	2.29	23.1

sigma is defined as

$$n_{pps} = \frac{\sigma_{x/y}}{v_{scan} t_{rev}} \quad (9)$$

Figure 6 summarises the transverse separation between measurement points for the different machines. Both the PSB and PS have large enough beams to resolve the profile with a good accuracy even at the highest speed with the acquisition never dropping below 10 points per sigma.

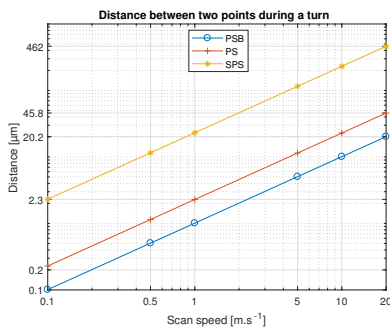


Figure 6: Wire movement per turn against scan speed.

However, to obtain at least three measurement points per sigma for the SPS at top energy, the scan speed has to be reduced to a maximum of  $2.8 \text{ m.s}^{-1}$  horizontally and  $4.3 \text{ m.s}^{-1}$  vertically. Such low speeds are currently obtained using precision linear scanners, but they can only be used with low intensity beams.

## WIRE DAMAGE

It is well known that wires are destroyed by overheating, with recent examples during test in the SPS.

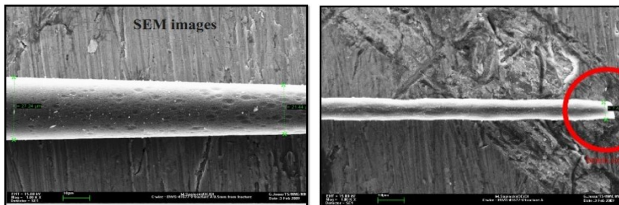


Figure 7: Impacted carbon wires.

Figure 7 shows micrographs of the visible impacts and sublimated damage for carbon in the SPS. The beam momentum was  $400 \text{ GeV/c}$  and intensity reached  $N_p = 2.4 \times 10^{13}$  protons with a longitudinal beam size of  $570 \mu\text{m}$  and transverse beam size of  $730 \mu\text{m}$  for a scan velocity of  $0.5 \text{ m.s}^{-1}$ . Only

the core remains illustrating the limitation of the current materials [2]. A solution to this would be to use a material with similar mechanical and thermal properties to carbon filament, but will have a lower mass density so that the wire absorbs less energy during a scan. Such materials, in the form of long strand carbon nano-tubes (CNT) (Fig. 8), are now becoming available on the market. The first picture shows the wire and the strips rolled onto themselves. The second picture details the inside of the strips, composed of CNT. Characterisation of physical and mechanical properties as well as performance with beam are currently underway at CERN.

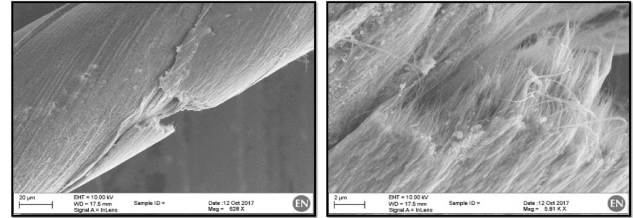


Figure 8: New CNT wire structure.

## SUMMARY AND CONCLUSIONS

Wire-scanners for the high intensity circular accelerators at CERN use carbon wires due to their combination of low density, high ultimate tensile strength and very high sublimation temperature.

We have shown that these wires are also compatible when using high pre-loads with the high resolution needed for the new generation of LIU scanners in the PSB and PS in terms of mechanical deflection and vibration.

However, fundamental material limits are reached for such a wire in the SPS, preventing high-resolution scans of full intensity beams at top energy. Alternative wire materials are therefore actively being studied to push this limit to higher intensity.

## ACKNOWLEDGEMENTS

Thanks to F. Roncarolo, J. Blasco, and A. Marin from CERN and M. Sapinski from GSI for their helpful discussions.

Thanks to M. Meyer from CERN for the CNT micrographs.

## REFERENCES

- [1] <https://espace.cern.ch/liu-project/>
- [2] M. Sapinski, B. Dehning, A. Guerrero, J. Koopman, and E. Metral, "Carbon fiber damage in accelerator beam", CERN, Geneva, Switzerland, 2009.
- [3] R. Veness *et al.*, "Installation and test of pre-series wire scanners for the LHC injectors upgrade project at CERN", in *Proc. IPAC2017*, Copenhagen, Denmark, paper MOPAB121.
- [4] K. Wittenburg, "Presentation on wire scanners state of the art", in *Proc. DIPAC'01*, ESRF, Grenoble, p. 231.

# LOW VS HIGH LEVEL PROGRAMMING FOR FPGA

Jan Marjanovic\*, Deutsches Elektronen-Synchrotron DESY, Hamburg, Germany

## Abstract

From their introduction in the eighties, Field-Programmable Gate Arrays (FPGAs) have grown in size and performance for several orders of magnitude. As the FPGA capabilities have grown, so have the designs. It seems that current tools and languages (VHDL and (System)Verilog) do not match the complexity required for advanced digital signal processing (DSP) systems usually found in experimental physics applications. In the last couple of years several commercial High-Level Synthesis (HLS) tools have emerged, providing a new method to implement FPGA designs, or at least some parts of it. By providing a higher level of abstraction, new tools offer a possibility to express algorithms in a way which is closer to the mathematical description. Such implementation is understood by a broader range of people, and thus minimizes the documentation and communication issues. Several examples of DSP algorithms relevant for beam instrumentation will be presented. Implementations of these algorithms with different HLS tools and traditional implementation in VHDL will be compared.

## INTRODUCTION

According to [1], FPGAs have reached its fourth age. After the "Age of Invention", "Age of Expansion" and "Age of Accumulation" there are devices with enough capacity to include the entire system on a single chip [2]. Although the need to efficiently use the resources provided by the FPGA is still present, the main challenges are managing the complexity of the design and integration of 3rd party IP cores (e.g. DDR3/4 memory controllers, PCIe blocks, DMAs, 1 and 10 Gigabit Ethernet MAC, processors, DSP blocks...).

Numerous approaches to provide a higher level of abstraction were and are presented, mostly by academia, but also by the commercial vendors. One tool which successfully made a transition from an academic tool [3] to a tool in FPGA engineer's toolbox is Xilinx Vivado HLS.

Several studies of HLS vs RTL can be found in the literature. Vendors of the tools are compelled to present their tools in the nicest way [4] or with usually simplified examples. Some of the studies are also quite general [5] or the examples are simplified versions of the problems from experimental physics [6]. In some cases comparison is valuable but only partially relevant for experimental physics applications [7–9].

The framework described in [10] provides a method to develop applications in Matlab for certain MicroTCA boards. Vivado HLS is also used in 10G and 40G Ethernet accelerators, described in [11], and for two real-time data acquisition applications (crystal identification and timestamp sorting),

described in [12]. Recently, Vivado HLS was used for the development of hls4ml [13], a machine learning framework for particle physics.

In the rest of the paper, three examples of modules relevant for experimental physics will be presented. Implementations in VHDL and C++ targeting Vivado HLS are presented side-by-side. Interesting snippets of the code are presented to highlight the differences in the two languages, and to give the reader a possibility to compare the readability of the code for himself or herself. Number of lines of code (reported by `cloc`[14]), resource usage and minimal clock period ( $= 1/f_{max}$ ) for both implementations are also reported.

There are several reasons to base the evaluation on Vivado HLS:

- Author has considerable experience both with Xilinx FPGAs in general and with related tools (Vivado, Vivado HLS)
- Xilinx FPGAs are heavily used at DESY and on MicroTCA AMC boards
- The created IP integrates nicely with the rest of the IPs in Xilinx ecosystem
- Vivado HLS is significantly cheaper than other HLS software suites; therefore it is very likely that industrial partners will have access to it

The latest version available at the time of the writing, Vivado HLS 2018.2, was used for the examples in this paper.

Several other High-Level Synthesis software suites exists, such as Intel HLS Compiler, LabVIEW FPGA, Mathworks HDL Coder, Cadence Status, Mentor Graphics Catapult, and Synopsys Symphony C Compiler. Some open-source tools, such as Panda Bamboo and LegUp are also available. These tools were not considered for this paper.

## EXAMPLES

To better illustrate the differences, the advantages and the shortcomings of both methods, three examples will be compared. The examples are presented in the order of complexity, simplest first.

The first example, linearization function, requires high throughput, but it is in its core quite simple - each sample is processed on its own; there are no dependencies between the samples. The scheduler has an easy task pipelining the operations.

The second example, two-dimensional mean and standard deviation is slightly more complex; because the samples need to be accumulated together, scheduler needs some help from the designer to be able to pipeline the operations.

The third example, IIR filter is a well studied topic in digital signal processing [15]. In the case presented here,

\* jan.marjanovic@desy.de

we require that the filter can process one sample per clock cycle, which would demonstrate whether the HLS compiler is able to schedule the operations to satisfy this requirement.

### Example 1: Linearization Module

In the following section, we look at the linearization transfer function, providing harmonic spur suppression in data acquisition system for DFMC-DSx00.

The ADC on DFMC-DSx00 is capable of producing 12-bit samples at maximum rate of 800 MSPS. To simplify the timing closure for the DSP modules in the system, the data from ADC is parallelized into 4 lanes, running at 200 MHz. The output from the ADC interface core is a 128-bit wide AXI4-Stream interface. The interface for DSx00 is shown in Figure 1.

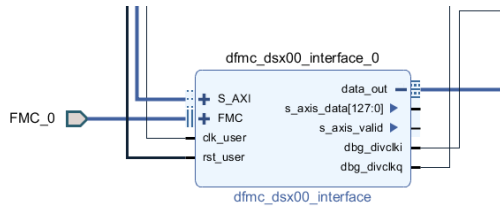


Figure 1: DFMC-DSx00 interface module on KCU105 evaluation board.

The linearization module needs to connect to the ADC interface module on the AXI4-Stream interface; it shall provide an AXI4-Stream slave port. The linearization module shall also provide the output values on an AXI4-Stream master port, which can be attached either to AXI DMA or some other DSP module (e.g. decimation module) in the final application.

The core of the linearization module is a 2nd order polynomial to be evaluated for each of the acquired samples from the ADC.

The transfer function can be described as:

$$y[n] = \sum_{i=0}^N a_i x^i[n], N = 2$$

where  $a_i$  are statically determined coefficients.

One can immediately notice the simplicity of this approach. Only the current sample is considered at each point, which means that problem is trivially pipelineable.

The top function for this module accepts an array of 8 12-bit numbers as input and it outputs an array of 8 12-bit numbers. By providing the output of the same size as the input, the use of this module is transparent for the downstream DSP modules and the software. The module also provides a bypass for the linearization polynomial, which is useful for evaluating the effects of the linearization process in the real system.

The main body of the core consist of just one simple for loop to apply the `linearize()` function on each lane (8 lanes in total). Depending on the value of `bypass` variable,

the output is either direct assignment from the input or the return value of `linearize()` function. A compiler directive is used to replicate (or `unroll`) each instance of the loop to match the output data format from the upstream module.

At the core of the `linearize()` function is the implementation of Horner's Rule [16].

Presented in Listing 1 is the core of the linearization function, when implemented at Register-Transfer Level abstraction level in VHDL. The implementation uses `ieee.fixed_pkg` library to handle the fixed point numbers. From this code listing it can be observed that the design intent gets obscured by the pipelining needed to achieve a high operating frequency ( $f_{max}$ ).

Listing 1: Core of the linearization module, implemented in VHDL

```
proc_stage: process (clk)
begin
    if rising_edge(clk) then
        -- multiply stage
        if stage_valid(2*i) = '1' then
            stage_out(2*i) <= resize(
                arg => to_sfixed(in_data_prev(2*i),
                                in_data'left,
                                in_data'right)
                    * stage_in(2*i),
                size_res => stage_out(0)
            );
        end if;

        -- addition stage
        if stage_valid(2*i+1) = '1' then
            stage_out(2*i+1) <= resize(
                arg => C_COEFS(i) + stage_in(2*i+1),
                size_res => stage_out(0)
            );
        end if;
    end if;
end if;
end process;
```

On the other hand, Listing 2 shows that the implementation in C++ is much shorter, and the main arithmetic operations are also clearly visible.

Listing 2: Core of the linearization module, implemented in C++ for Vivado HLS

```
output_t linearize(input_t in) {
    internal_t tmp = 0;
    for (int i = COEFFS_LEN-1; i >= 0; i--) {
        tmp = COEFFS[i] + in * tmp;
    }
    return tmp;
}
```

Coefficients for this experiment are (2.2854652782872233, 0.9962862193648518, -2.506094726425692e-03).

Both implementations were synthesized and implemented for Xilinx KCU105 Evaluation Kit with XCKU040-2FFVA1156E device. Shown in Figure 2 is the result of the automatic pipelining of the `linearize()` function. The compiler (scheduler) has decided to use one clock cycle for each of the multiplication and one clock cycle for the



Table 1: Comparison Between Implementations of 2nd Order Polynomial in HLS vs RTL

resource	HLS (in C++)	RTL (in VHDL)
CLB	221	314
LUT	461	1081
FF	884	938
DSP	16	24
latency	6	6
interval	1	1
clk period	3.903 ns	4.954 ns
lines of code	52	170

addition. This helps satisfy the specified constraint for initialization interval of 1 and results in optimal utilization of DSP48E2 blocks.

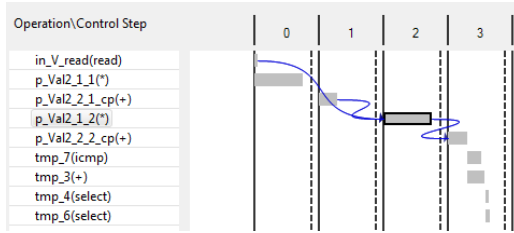


Figure 2: Report from Vivado HLS on implementation.

Shown in the Table 1 are the results of the implementation. Because the HLS compiler takes advantage of the constant propagation, the resource usage is lower compared to the hand-coded VHDL implementation. Vivado HLS was able to remove bits (and corresponding registers and wires) which were determined to be 0 for all inputs.

### Example 2: Two-Dimensional Mean and Standard Deviation

The next investigated example will be an implementation of algorithm to determine the center (or mean) and size (or standard deviation) of two-dimensional Gaussian distribution. This module is used together with GigE Vision core on DAMC-TCK7 AMC board. An example of distribution, with annotated mean and standard deviation is shown in Figure 3.

Before we start investigating the implementation, several algorithms for calculation of standard deviation should be considered.

The naive implementation involves two passes, in the first one the mean of the dataset is determined, and in the second one the standard deviation is calculated, by using the mean value calculated in the first step.

The obvious downside of this algorithm is the need to visit each sample twice, which would mean that some memory is

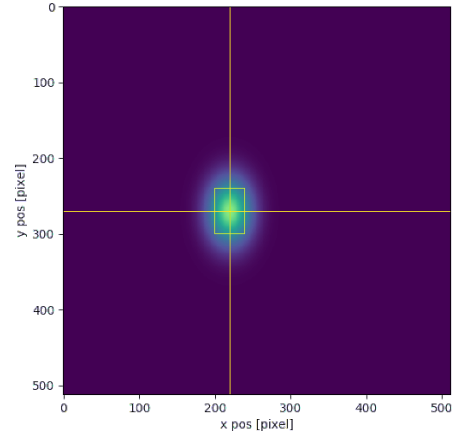


Figure 3: 2D Gaussian distribution; mean and standard deviation are annotated on the image.

required and the mean and the standard deviation cannot be calculated on-the-fly.

The algorithm proposed in [17] only requires one pass through the samples. It also provides better precision when using floating point numbers, but since our implementation will be implemented in integers this property is not relevant in this case.

Based on the equation (15) in [17], for each step a mean needs to be calculated according to the following formula:

$$M_k = M_{k-1} + (x_k - M_{k-1})/k$$

where  $k$  is the iteration count.

Because the division in FPGA usually takes several clock cycles and the algorithm is iterative in its nature (previously calculated values are required to calculate new values), this algorithm is not very suitable for implementation in FPGA.

To obtain an algorithm which mostly relies on multiplication and addition, two operations which map nicely to DSP48E1/2 primitives found in Xilinx FPGAs, the naive formula can be rewritten as:

$$\sigma^2 = \frac{1}{N} \sum x_i^2 - \mu^2$$

It can be noted that for each sample only the multiplication and summation is required, and division is only performed twice at the end of the entire frame.

The code for this module can be found in ANNEX A.

From the function signature of the top function `two_dim_stddev()`, it can be seen that the module accepts stream of data and provides the mean and the standard deviation both in X and Y direction. From the compiler directives at the beginning of the function it can be noted that the input is of type AXI-Stream, while the parameters are made available on the AXI4-Lite interface.

The main body of the function is composed of four for loops. The outermost two loops (`loop_x` and `loop_y`) traverse the frame in X and Y dimension. The innermost two loops are there to interleave the addition and multiplication

Table 2: Report of the Utilization of Resources From Implementation of Two-Dimensional Standard Deviation and Mean in Vivado HLS

Resource	HLS (in C++)	RTL (in VHDL)
slice	764	-
LUT	1714	-
FF	2507	-
DSP	18	-
BRAM	14	-
SRL	38	-
latency	65663 <sup>1</sup>	-
interval	65663	-
clk period	3.095 ns	-

operations on several accumulators, thus resolving the dependency through an operation as described in [18].

The results of the implementation of the algorithm in Vivado HLS are shown in Table 2. The VHDL module for comparison is unfortunately not provided.

### Example 3: IIR Filter

The final example presented in this paper is a 2nd order IIR filter. The implementation in Vivado HLS will be compared to the VHDL implementation from FPGA Firmware Framework for MTCA.4 AMC Modules [19], used in LLRF at DESY. The module ENT\_IIR\_TDF1\_02 is a highly-optimized IIR filter, implemented in Transposed-Direct-Form-I to take full advantage of DSP48E1 modules. Figure 4 shows how 5 DSP48E1 are used to implement the filter in the VHDL implementation (each DSP48E1 is configured to calculate the result in the form of  $B * (D - A) + C$ ).

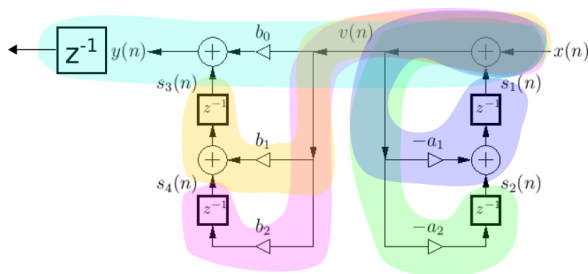


Figure 4: Filter implementation architecture in ENT\_IIR\_TDF1\_02.

The C++ code for this module can be found in ANNEX B. The core of the implementation is a class BiQuadFilter

<sup>1</sup> = 128 clock cycles (4 pixels on a parallel interface) \* 512 lines + 32 clock cycles to initialize variables + 11 clock cycles to flush the multiply-and-accumulate pipeline + 24 clock cycles to gather the accumulators + 48 clock cycles to perform the divisions + 7 clock cycles to calculate the square root + 5 clock cycles used to shift the data from and to pipelines.

Table 3: Comparison Between Implementations of 2nd Order IIR Filter in HLS vs RTL

Resource	HLS (in C++)	RTL (in VHDL)
CLB	32	16
LUT	156	0
FF	147	149
DSP	5	5
BRAM	0	0
SRL	0	0
latency	4	4
interval	1	1
clk period	4.704 ns	4.732 ns
lines of code	60	246

which provides operator() to calculate the next sample. The sizes of variables are tuned to use the maximal width of the DSP48E2 module.

For comparison, both VHDL implement and RTL implementation were compiled for XCKU040-FFVA1152-2 FPGA. The VHDL implementation was packaged with Vivado IP Packager and synthesized (with -mode out\_of\_context) and implemented on the FPGA.

Presented in Table 3 are the results of both implementation. The VHDL implementation is just slightly more optimized in resources, on the other hand the implementation in C++ is much shorter (in terms of lines of code) and the code is easier to read.

This example relies heavily on DSP48E1/2 modules. In the latest versions of Vivado HLS an undocumented library (dsp\_builtins.h) was added with intrinsics targeting DSP48E1/2 module. Usage of these intrinsics could be another way of implementing this example.

## CONCLUSION AND OUTLOOK

Three examples of algorithm implementations in C++ for Vivado HLS were presented. The examples presented here illustrate some quite challenging algorithms with demanding requirements. All examples were able to handle one or more samples per clock cycle, which requires careful organization of operations to allow for pipelining of the operations. It can be seen that Vivado HLS provides a useful alternative even in these challenging examples.

When the requirements are not so stringent, the usage of Vivado HLS provides even more significant improvement in productivity compared to the RTL workflow. This is specially true when the algorithms need to operate on floating-point numbers, since the operations on floating-point numbers usually take several clock cycles and scheduling those can be a non-trivial task.

Vivado HLS seems to be a useful tool to speed up the development. Because of peculiarity of FPGAs, Vivado

HLS cannot turn any C or C++ code into an FPGA module, the code needs to be written in a certain dialect of C or C++ (i.e. no memory allocation, careful selection of mathematic operations and variable types, handling the state to allow for pipelining, ...). Familiarity with the device primitives, such as multiply-and-add block DSP48E1/2, is also an advantage.

Some authors argue that C-like languages are a poor choice for High-Level Synthesis [20] and propose HLS compilers from functional languages, such as Haskell [21]. High-Level Synthesis remains an interesting field of research, where new ideas are still proposed and existing tools are still improved. Because of the decent Quality of Result and improved productivity, it can be expected that HLS workflow will become more and more popular.

## ACKNOWLEDGEMENTS

I would like to thank Sven Stubbe (DESY) for the help with the examples and for productive discussions about High-Level Synthesis.

## REFERENCES

- [1] S. M. Trimberger, "Three ages of FPGAs: A retrospective on the first thirty years of fpga technology," *Proceedings of the IEEE*, vol. 103, no. 3, pp. 318–331, Mar. 2015, issn: 0018-9219. doi: 10.1109/JPROC.2015.2392104.
- [2] R. Sass and A. G. Schmidt, *Embedded Systems Design with Platform FPGAs: Principles and Practices*, 1st. San Francisco, CA, USA: Morgan Kaufmann Publishers Inc., 2010, isbn: 9780080921785, 9780123743336.
- [3] J. Cong, B. Liu, S. Neuendorffer, J. Noguera, K. Vissers, and Z. Zhang, "High-Level Synthesis for FPGAs: From prototyping to deployment," *IEEE Transactions on Computer-Aided Design of Integrated Circuits and Systems*, vol. 30, no. 4, pp. 473–491, Apr. 2011, issn: 0278-0070. doi: 10.1109/TCAD.2011.2110592.
- [4] F. Sijstermans and J. Li, "Working smarter, not harder: NVIDIA closes design complexity gap with High-Level Synthesis," <http://go.mentor.com/4N9cP>
- [5] R. Nane *et al.*, "A survey and evaluation of FPGA High-Level Synthesis tools," *IEEE Transactions on Computer-Aided Design of Integrated Circuits and Systems*, vol. 35, no. 10, pp. 1591–1604, Oct. 2016, issn: 0278-0070. doi: 10.1109/TCAD.2015.2513673.
- [6] Z. Jin, H. Finkel, K. Yoshii, and F. Cappello, "Evaluation of the FIR example using Xilinx Vivado High-Level Synthesis compiler," Jul. 2017. doi: 10.2172/1375449.
- [7] Z. Zhao and J. C. Hoe, "Using Vivado-HLS for structural design: A NoC case study," in *FPGA*, 2017.
- [8] J. R. G. Ordaz and D. Koch, "On the HLS design of bit-level operations and custom data types," in *FSP 2017; Fourth International Workshop on FPGAs for Software Programmers*, Sep. 2017, pp. 1–8.
- [9] F. Winterstein, S. Bayliss, and G. A. Constantinides, "High-level synthesis of dynamic data structures: A case study using Vivado HLS," in *2013 International Conference on Field-Programmable Technology (FPT)*, Dec. 2013, pp. 362–365. doi: 10.1109/FPT.2013.6718388.
- [10] P. Prędkie, M. Heuer, Ł. Butkowski, K. Przygoda, H. Schlarb, and A. Napieralski, "Rapid-X - an FPGA development toolset using a custom Simulink library for MTCA.4 modules," *IEEE Transactions on Nuclear Science*, vol. 62, no. 3, pp. 940–946, Jun. 2015, issn: 0018-9499. doi: 10.1109/TNS.2015.2413673.
- [11] E. Schubert and U. Langenbach, "FPGA-based hardware accelerators for 10/40 GbE TCP/IP and other protocols," in *4th MicroTCA Workshop for Industry and Research*.
- [12] T. Marc-André, "Two FPGA Case Studies Comparing High Level Synthesis and Manual HDL for HEP applications," 2018. arXiv: 1806.10672 [physics.ins-det].
- [13] J. Duarte *et al.*, "Fast inference of deep neural networks in FPGAs for particle physics," *Journal of Instrumentation*, vol. 13, no. 07, P07027, 2018. <http://stacks.iop.org/1748-0221/13/i=07/a=P07027>
- [14] *CLOC - count lines of code*. <https://github.com/AIDaniel/cloc>
- [15] J. O. Smith, *Introduction to digital filters with audio applications*, online book, accessed (date accessed). <http://ccrma.stanford.edu/~jos/filters/>
- [16] S. Xu, S. A. Fahmy, and I. V. McLoughlin, "Square-rich fixed point polynomial evaluation on FPGAs," in *Proceedings of the 2014 ACM/SIGDA International Symposium on Field-programmable Gate Arrays*, ser. FPGA '14, Monterey, California, USA: ACM, 2014, pp. 99–108, isbn: 978-1-4503-2671-1. doi: 10.1145/2554688.2554779. <http://doi.acm.org/10.1145/2554688.2554779>
- [17] D. E. Knuth, *The Art of Computer Programming, Volume 2 (3rd Ed.): Seminumerical Algorithms*. Boston, MA, USA: Addison-Wesley Longman Publishing Co., Inc., 1997, isbn: 0-201-89684-2.
- [18] J. Hrica, "XAPP599 floating-point design with vivado HLS," 2012. [https://www.xilinx.com/support/documentation/application\\_notes/xapp599-floating-point-vivado-hls.pdf](https://www.xilinx.com/support/documentation/application_notes/xapp599-floating-point-vivado-hls.pdf)
- [19] L. Butkowski, T. Kozak, P. Prędkie, R. Rybaniec, and B. Yang, "FPGA Firmware Framework for MTCA.4 AMC Modules," in *Proceedings, 15th International Conference on Accelerator and Large Experimental Physics Control Systems (ICALPECS 2015): Melbourne, Australia, October 17-23, 2015*, 2015, WEPGF074. doi: 10.18429/JACoW-ICALPECS2015-WEPGF074.
- [20] S. A. Edwards, "The challenges of synthesizing hardware from C-like languages," *IEEE Design Test of Computers*, vol. 23, no. 5, pp. 375–386, May 2006, issn: 0740-7475. doi: 10.1109/MDT.2006.134.
- [21] K. Zhai, R. Townsend, L. Lairmore, M. A. Kim, and S. A. Edwards, "Hardware synthesis from a recursive functional language," in *2015 International Conference on Hardware/Software Codesign and System Synthesis (CODES+ISSS)*, Oct. 2015, pp. 83–93. doi: 10.1109/CODES+ISSS.2015.7331371.

## ANNEX A: STATISTICS MODULE IMPLEMENTED IN C++ FOR VIVADO HLS

```
#include "two_dim_stdev.hpp"

void two_dim_stdev(
    hls::stream<input_t> &in, int &meanx, int &stdx, int &meany, int &stdy
) {

#pragma HLS INTERFACE ap_ctrl_none port=return
#pragma HLS INTERFACE axis register both port=in
#pragma HLS DATA_PACK variable=in field_level
#pragma HLS INTERFACE s_axilite port=meanx bundle=ctrl
#pragma HLS INTERFACE s_axilite port=stdx bundle=ctrl
#pragma HLS INTERFACE s_axilite port=meany bundle=ctrl
#pragma HLS INTERFACE s_axilite port=stdy bundle=ctrl

    const int N = 512; // frame size
    const int PAR = 4; // number of parallel HW instances for accum

    ap_uint<30> accum[PAR*INPUT_W];
    ap_uint<38> accum_x[PAR*INPUT_W], accum_y[PAR*INPUT_W];
    ap_uint<45> accum_x2[PAR*INPUT_W], accum_y2[PAR*INPUT_W];

    loop_init: for (int i = 0; i < PAR*INPUT_W; i++) {
        accum[i] = 0; accum_x[i] = 0; accum_y[i] = 0;
        accum_x2[i] = 0; accum_y2[i] = 0;
    }

    loop_y: for (int y = 0; y < N; y++) {
        loop_x: for (int x = 0; x < N/PAR/INPUT_W; x++) {
            input_t z[PAR];
            loop_pipe: for (int i=0; i < PAR; i++) {
#pragma HLS PIPELINE II=1
                in >> z[i];
                loop_arr: for (int j = 0; j < INPUT_W; j++) {
                    accum[i] += z[i].arr[j];
                    ap_uint<10> pos_x = (PAR*INPUT_W*x+INPUT_W*i+j);
                    ap_uint<10> pos_y = y;
                    accum_x[i] += pos_x*z[i].arr[j];
                    accum_y[i] += pos_y*z[i].arr[j];
                    accum_x2[i] += pos_x*pos_x*z[i].arr[j];
                    accum_y2[i] += pos_y*pos_y*z[i].arr[j];
                }
            }
        }
    }

    ap_uint<30> accum_tot = 0;
    ap_uint<38> accum_x_tot = 0, accum_y_tot = 0;
    ap_uint<45> accum_x2_tot = 0, accum_y2_tot = 0;

    loop_gather: for (int i=0; i < PAR; i++) {
        accum_tot += accum[i];
        accum_x_tot += accum_x[i]; accum_y_tot += accum_y[i];
        accum_x2_tot += accum_x2[i]; daccum_y2_tot += accum_y2[i];
    }

    meanx = accum_x_tot / accum_tot;
    meany = accum_y_tot / accum_tot;
    ap_int<16> varx = accum_x2_tot / accum_tot - meanx*meanx;
    ap_int<16> vary = accum_y2_tot / accum_tot - meany*meany;
    stdx = hls::sqrt(varx);
    stdy = hls::sqrt(vary);
}
```



## ANNEX B: IIR FILTER MODULE IMPLEMENTED IN C++ FOR VIVADO HLS

```
#include "iir_hls.hpp"

template<int FIX_W, int FIX_I>
class BiquadFilter {
public:
    BiquadFilter (
        ap_fixed<FIX_W, FIX_I> b0,
        ap_fixed<FIX_W, FIX_I> b1,
        ap_fixed<FIX_W, FIX_I> b2,
        ap_fixed<FIX_W, FIX_I> a1,
        ap_fixed<FIX_W, FIX_I> a2) :
        b0(b0), b1(b1), b2(b2), a1(a1), a2(a2) {

    }

    ap_fixed<FIX_W, FIX_I> operator()(ap_fixed<FIX_W, FIX_I> x){
        ap_fixed<25, 9> tmp_s1  = (x+s1) * -a1 + s2;
        ap_fixed<48, 9> tmp_s2  = (x+s1) * -a2      ;
        ap_fixed<48, 9> tmp_s3  = (x+s1) *  b1 + s4;
        ap_fixed<48, 9> tmp_s4  = (x+s1) *  b2      ;
        ap_fixed<FIX_W, FIX_I> y = (x+s1) *  b0 + s3;

        s1 = tmp_s1;
        s2 = tmp_s2;
        s3 = tmp_s3;
        s4 = tmp_s4;

        return y;
    }

private:
    ap_fixed<FIX_W, FIX_I> b0, b1, b2, a1, a2;
    ap_fixed<25, 9> s1;
    ap_fixed<48, 9> s2, s3, s4;
};

void iir_hls (
    ap_fixed<18, 2> coeffs_b0,
    ap_fixed<18, 2> coeffs_b1,
    ap_fixed<18, 2> coeffs_b2,
    ap_fixed<18, 2> coeffs_a1,
    ap_fixed<18, 2> coeffs_a2,
    ap_fixed<18, 2> data_in,
    ap_fixed<18, 2> &data_out
){

#pragma HLS INTERFACE ap_stable port=coeffs_b0
#pragma HLS INTERFACE ap_stable port=coeffs_b1
#pragma HLS INTERFACE ap_stable port=coeffs_b2
#pragma HLS INTERFACE ap_stable port=coeffs_a2
#pragma HLS INTERFACE ap_stable port=coeffs_a1

#pragma HLS INTERFACE ap_vld port=data_in
#pragma HLS INTERFACE ap_ovld register port=data_out
#pragma HLS INTERFACE ap_ctrl_none port=return

#pragma HLS PIPELINE II=1

    static BiquadFilter<18, 2> f0(coeffs_b0, coeffs_b1, coeffs_b2, coeffs_a1, coeffs_a2);

    data_out = f0(data_in);
}
```

# HIGH-SPEED DIRECT SAMPLING FMC FOR BEAM DIAGNOSTIC AND ACCELERATOR PROTECTION APPLICATIONS

J. Zink\*, M. K. Czwalinna, M. Fenner, S. Jablonski, J. Marjanovic, H. Schlarb  
 DESY, Hamburg, Germany

## Abstract

The rapid development, in the field of digitizers is leading to *Analog-to-Digital Converters* (ADC) with ever higher sampling rates. Nowadays many high-speed digitizers for RF applications and radio communication are available, which can sample broadband signals, without the need of down converters. These ADCs fit perfectly into beam instrumentation and diagnostic applications, e.g. Bunch Arrival time Monitor (BAM), klystron life-time management or continuous wave synchronization. To cover all these high-frequency diagnostic applications, DESY has developed a direct sampling FMC digitizer board based on a high-speed ADC with an analog input bandwidth of 2.4 GHz. A high-speed data acquisition system capable of acquiring 2 channels at 500 MS/s will be presented. As first model application of the versatile digitizer board is the coarse bunch arrival time diagnostics in the free electron laser FLASH at DESY.

## INTRODUCTION

Modern linear accelerators require a very high precision *Low-Level-RF* (LLRF) control system. In the *European X-Ray Free Electron Laser* (XFEL) and *Free-Electron-Laser in Hamburg* (FLASH) the LLRF-systems are realized in *Micro Telecommunication Computing Architecture* (MTCA.4). In addition to the control system the accelerators need very high accuracy diagnostic systems to measure, e.g. the beam position, the bunch arrival time, klystron failures, and other accelerator parameters. To reduce the board space and the

different diagnostic applications. It is integrated in the existing MTCA infrastructure and installed on a DESY *Advanced Mezzanine Card* [2] DAMC-FMC25 [3] carrier board. Due to the high input bandwidth of the digitizer, there is no need for a down converter stage in front of the ADC.

## FMC DIGITIZER DFMC-DS500

The core component of the converter board is a dual channel 12-bit RF sampling ADC from Texas Instruments with a sampling rate of 500 MS/s per channel. In *dual edge sampling* (DES) mode the two channels are combined together and the ADC is sampling at 1 GS/s. The minimum guaranteed single channel analog bandwidth is 2.4 GHz. In DES mode the bandwidth is decreased down to 1.2 GHz. Since the manufacturer offers a whole family of compatible ADCs, different variants can be fitted onto the FMC [4].



Figure 1: New DFMC-DS500 digitizer board.

number of components in the system, the authors designed a digitizer board based on an ADC with a maximum sampling rate of 1 GS/s. The new digitizer board (see Fig. 1) in ANSI/VITA 57.1 2010 [1] FMC form factor will be used in

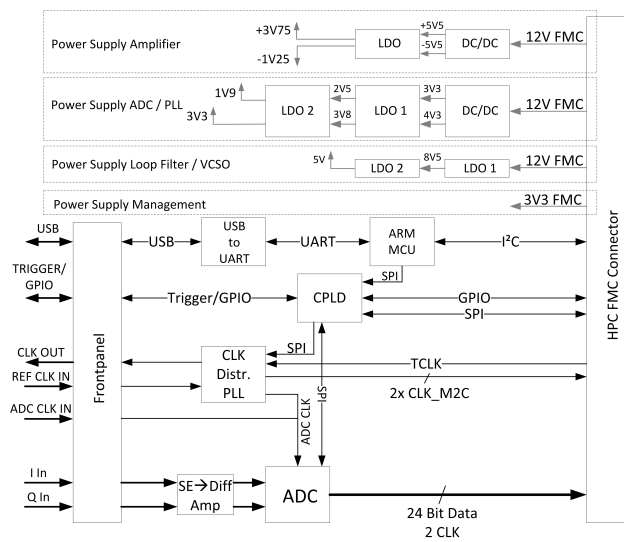


Figure 2: Block diagram of the DFMC-DS500 digitizer.

Figure 2 depicts the block diagram of the digitizer board. The inputs of the ADC are driven by fully differential amplifiers (FDA) [5, 6] with a large-signal bandwidth of 4.8 GHz. These amplifiers act as active baluns and replace the transformers which are normally converting single ended input signals to differential signals. The ADC has two 12-bit wide *low voltage differential signaling* (LVDS) data connections to the carrier card to achieve minimal latency. These lines can be driven with well defined voltage levels independent from the level of the adjust voltage ( $V_{ADJ}$ ) [1].

## Clock Tree

Clocking the ADC can be done in different ways. In addition to a direct clock feed via a front panel connector,

\* johannes.zink@desy.de

there is a *phase-locked loop* (PLL) located on the board which can be locked to an external reference clock or to an on-board high-precision, high-stability 10 MHz reference oscillator.

## Management

An ARM *micro controller unit* (MCU) realizes the management. Main task of the MCU is power management and writing initial configurations into the ADC and the PLL after power on before a *Field Programmable Gate Array* (FPGA) located on the carrier takes over control. To translate several control signals into the  $V_{adj}$  voltage domain a small *Complex Programmable Logic Device* (CPLD) with four input-/output banks is part of the board management.

## DATA ACQUISITION SYSTEM

To evaluate the DFMC-DSx00 FMC mezzanine board, a data acquisition (DAQ) system was developed for Xilinx KCU105 evaluation kit and for DAMC-FMC25 AMC board. The DAQ system consists of firmware (FPGA part) and software. The KCU105 board is plugged in an industrial PC, which provides PCIe interface to the FPGA. Similar arrangement is used for DAMC-FMC25, which provides PCIe interface to an in-crate CPU AMC board.

## Firmware

The main building blocks of the firmware on KCU105 are depicted in the Fig. 3.

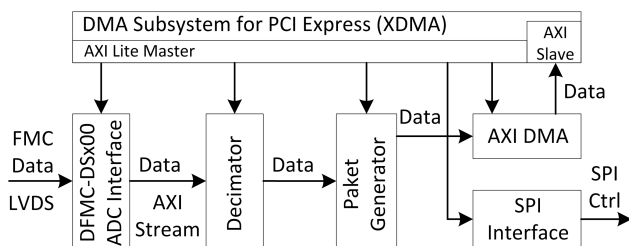


Figure 3: Schematic view of Firmware building block.

**DFMC-DSx00 ADC Interface** The ADC interface is responsible for capturing the data from parallel LVDS bus. This module takes advantage of IDELAY and ISERDES blocks in Xilinx Kintex UltraScale devices. A Built-In Self Test state machine determines the optimal settings of delay chains upon start-up and on user request. The output of the ADC module is 128-bit wide AXI-Stream interface, with four samples in parallel for each channel.

**DFMC-DSx00 SPI Interface** The SPI interface provides communication with components (CPLD, ADC, PLL) on the DFMC-DSx00 mezzanine board. The CPLD provides status information and also the board hardware and firmware version information. The SPI interface can also be forwarded to on-board ADC and on-board PLL, e.g. to retrieve the status information and to change the configuration of the said devices.

**Packet Generator** The packet generator module prepares and packages the data from ADC module in a format, suitable for AXI Direct Memory Access module.

**AXI Direct Memory Access** Xilinx AXI DMA module is used to transfer the data from ADC into on-board DDR4 memory. Attached to the AXI DMA is a small BRAM memory, where the descriptors for the DMA engine are stored. Up to 100 million samples (0.2 second at 500 MS/s) can be stored in the DDR4 memory, providing excellent resolution in frequency domain.

**DMA Subsystem for PCI Express** Xilinx DMA Subsystem for PCI Express is used to provide an access to configuration and status registers in all previously-described modules. It also provides high-throughput DMA access between on-board DDR4 memory and CPU memory.

## Software

Ubuntu 16.04 LTS is running on the industrial PC. A driver is provided by Xilinx to communicate with FPGA registers and with Xilinx DMA Subsystem for PCI Express. On top of the driver a Python library (`dsx00lib`) and a command-line interface (`dsx-cli.py`) were developed. The command-line interface provides several useful commands for evaluating the FMC mezzanine; the most useful feature is the possibility to dump the data into a (compressed) file. Data can be later elaborated with user's software of choice.

## COARSE RF BAM CHANNEL

In FLASH and XFEL accelerators an electro-optical BAM is installed and measures the bunch arrival time. This system has very high accuracy and can determine the arrival time with femtosecond precision [7]. If the BAM is power cycled or a loss of optical synchronisation or large timing jumps of electron bunches occur, the BAM system has to be setup. This procedure is time consuming and requires a specialist. To simplify the setup of the BAM system, a second coarse RF BAM system with picosecond accuracy is planned. This system will provide a coarse bunch arrival time to the optical BAM system to automatically adjust the the optical delay lines [7].

## Beam Pick Up

Figure 4 shows the coarse RF BAM system. The RF BAM system uses the same combined broadband pick up signals like the optical BAM system [8]. By combining two opposite pick up signals together the signal dependence on the bunch transversal position is reduced [7,9]. Before the combined signal is fed into the optical BAM system, a second signal for coarse RF BAM channel is decoupled. Figure 5 depicts the expected waveform and the dependency of the amplitude to the bunch charge. The signal has a high bandwidth of 40 GHz and has a theoretical resolution of 5 - 10 fs [7].

### Analog Front End

A 10 dB coupler produces the signal for the coarse BAM analog front end (AFE). The front end consists of different attenuators, amplifiers and filtering stages. The signal bandwidth and the amplitude is very high and cannot not be directly processed by the DS500 digitizer. Thus in the

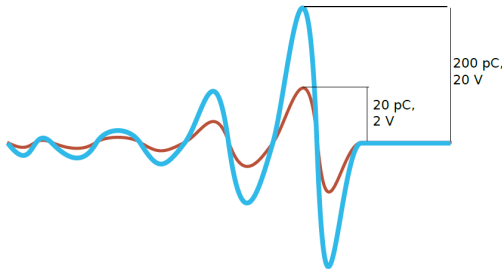


Figure 5: Dependency of the signal amplitude on the bunch charge. The amplitude increases with the bunch charge [7].

first stage the signal is attenuated by 5 dB and filtered. The low pass filter has a cut-off frequency of 2.5 GHz followed by a band pass filter with a center frequency of 2.383 GHz and a band width of 80 MHz. After reducing the bandwidth

to 2.4 GHz the signal is amplified, high pass filtered and attenuated to prevent oscillations between the amplifiers. The digital step attenuator allows to fit the signal level to the full scale range of the ADC. After another amplifier stage there is a power limiter which protects the following ADC and driving stage against excessive overloading.

### Sampling and Processing

Configuring the ADC in dual edge sampling (DES) [10] mode doubles the sampling frequency from 433 MHz to 866 MHz. A reference clock drives the PLL reference input on the DFMC-DS500. Trigger signals coming from the MTCA backplane activate the DAQ on the DAMC-FMC25 and a set of samples is taken by the FPGA. Acquired data can then be processed by the control system and can be used to automatically adjust the electro-optical BAM system for faster setup after machine restart.

### RF BAM Measurement Setup

The final goal of the coarse BAM channel is to determine the bunch arrival time within the range of a few picoseconds. Pick ups at the beam line produce a complex high bandwidth waveform.

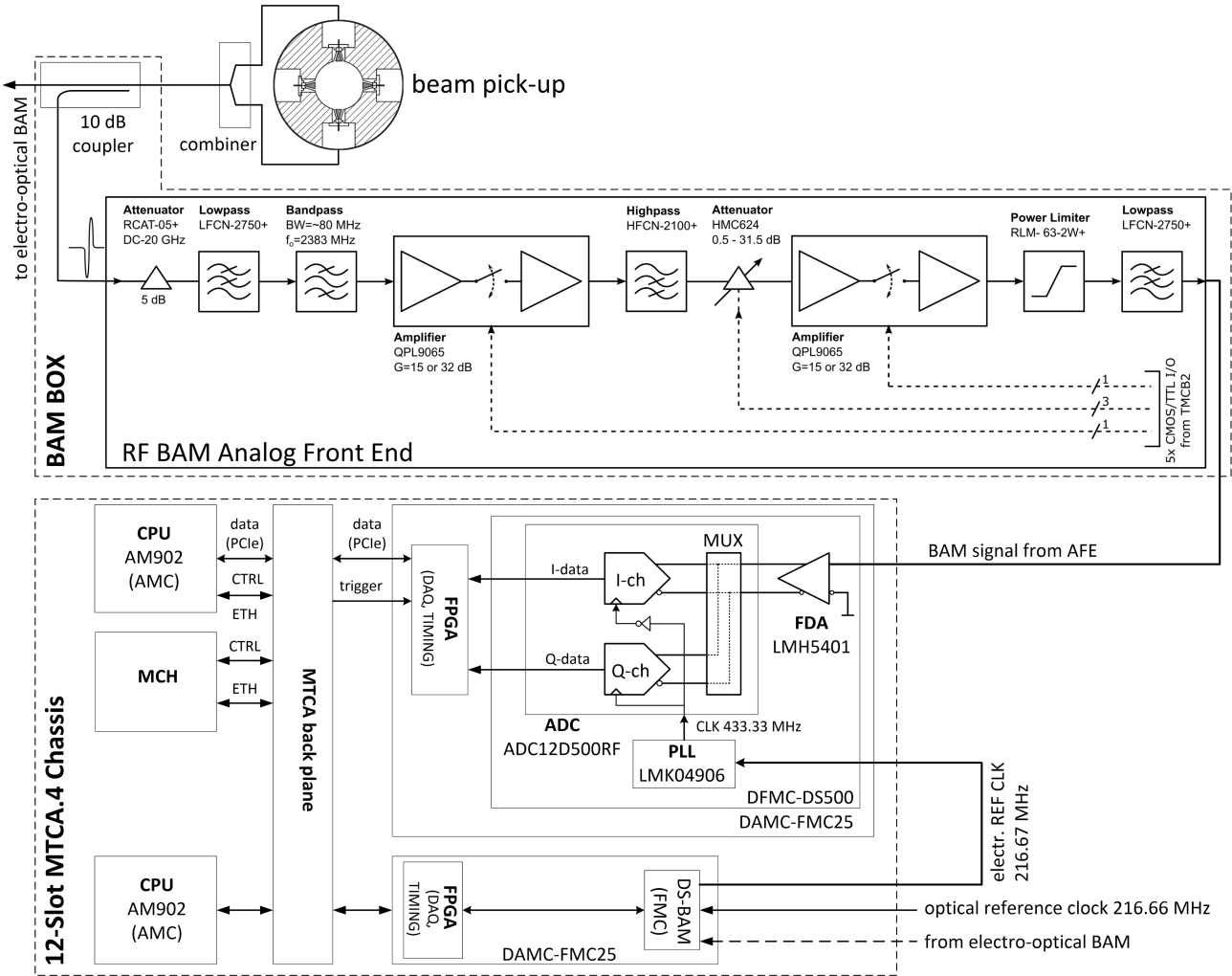


Figure 4: Overview of the coarse RF BAM channel.



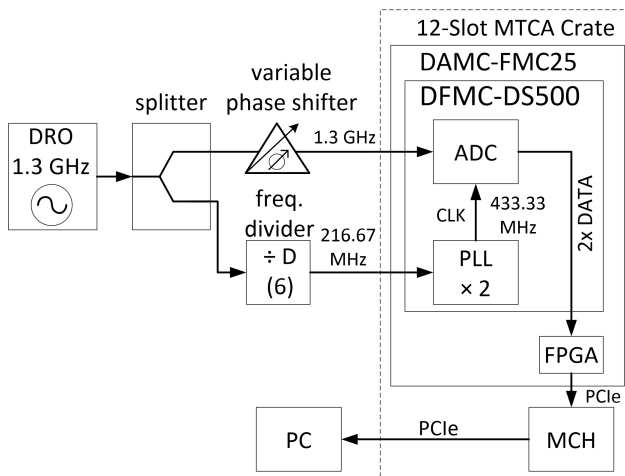


Figure 6: Measurement setup for estimating jitter.

Therefore measurements with 1.3 GHz sine wave were made to evaluate the systems performance under ideal conditions. Figure 6 shows the measurement setup. A *dielectric resonator oscillator* (DRO) was used to produce a clean, stable and accurate sine wave with a frequency of 1.3 GHz. After splitting the signal, one part is fed into a by six clock divider to produce a 216.66 MHz reference clock. The reference clock is doubled by the on board PLL, to provide 433.33 MHz ADC clock. The 1.3 GHz carrier is periodically sampled at the same point and a DC signal is produced. Using the variable phase shifter in between the splitter and ADC allows to shift the amplitude of the sampled DC signal. With this setup the overall jitter of the PLL and the ADC is converted into amplitude noise.

To roughly estimate the timing error of the system the sampled DC was adjusted to zero by shifting the phase of the input signal and 101 batches of 16352 samples were recorded. Figure 7 depicts the PDF of the timing error measured with the DFMC-DS500.

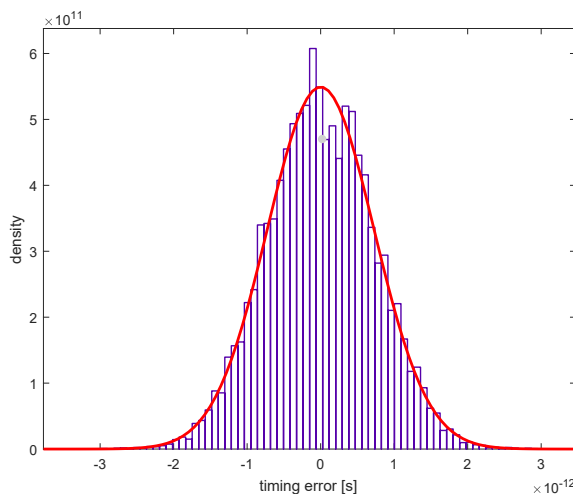


Figure 7: PDF of timing errors.

## CONCLUSION AND OUTLOOK

The measurement data in Figure 7 looks promising concerning coarse RF BAM accuracy. The timing error is 7 ps (peak-to-peak) and 726 fs (RMS). It can be further reduced by averaging the sample values during operation in the accelerator. In the next step, the operation in FLASH will show whether the accuracy can actually be achieved.

The digitizer board, especially the PLL, is not running at the full performance concerning clock jitter and further improvements of the DFMC-DS500 will increase the overall accuracy of the coarse RF BAM system.

## REFERENCES

- [1] *ANSI/VITA 57.1, FPGA Mezzanine Card (FMC) Standard*, 1-885731-49-3, American National Standards Institute, Inc., VMEbus International Trade Association (VITA), PO Box 19658, Fountain Hills, AZ 85269, Feb. 2010
- [2] *Advanced Mezzanine Card Base Specification*, AMC.0 R2.0, PICMG®, PCI Industrial Computer Manufacturers Group, November 15, 2006
- [3] Datasheet AMC-Dual HPC-FMC Carrier, DAMC-FMC25, [https://techlab.desy.de/products/amc/damc\\_fmc25](https://techlab.desy.de/products/amc/damc_fmc25)
- [4] Datasheet ADC12D500RF, <http://www.ti.com/lit/ds/symlink/adc12d500rf.pdf>
- [5] Datasheet LMH5401, <http://www.ti.com/lit/ds/symlink/lmh5401.pdf>
- [6] *Stabilizing Differential Amplifiers as Attenuators*, L. Siebert TIDA-00522 Reference Guide, Texas Instruments Incorporated, August 2016
- [7] M. Viti *et al.*, “The Bunch Arrival Time Monitor at FLASH and European XFEL”, in *Proc. ICALEPCS'17*, Barcelona, Spain, 2017.  
doi:10.18429/JACoW-ICALEPCS2017-TUPHA125
- [8] A. Angelovski *et al.*, “High bandwidth pickup design for bunch arrival-time monitors for free-electron laser”, *Phys. Rev. ST Accel. Beams*, vol. 15, issue 11, pp. 112803, 2012.  
doi:10.1103/PhysRevSTAB.15.112803
- [9] H. Dinter *et al.*, “Prototype of the Improved Electro-Optical Unit for the Bunch Arrival Time Monitors at FLASH and European XFEL”, in *Proc. FEL'15*, Daejeon, Korea, 2015.  
doi:10.18429/JACoW-FEL2015-TUP049
- [10] *Driving the GSPS ADCs in Single-Channel or Dual-Channel Mode for High Bandwidth Applications*, M. Plisch, J. Brinkhurst TIDU175 Texas Instruments Incorporated, July 2012

# PROGRESS ON TRANSVERSE BEAM PROFILE MEASUREMENT USING THE HETERODYNE NEAR FIELD SPECKLES METHOD AT ALBA

S. Mazzone, F. Roncarolo, G. Trad, CERN, Geneva, Switzerland  
B. Paroli, M. Potenza, M. Siano, Università degli Studi di Milano, Milan, Italy  
U. Iriso, C. S. Kamma-Lorger, A. A. Nosych, ALBA, Barcelona, Spain

## Abstract

We present the recent developments of a study aimed at measuring the transverse beam profile using the Heterodyne Near Field Speckles (HNFS) method. The HNFS technique works by illuminating a suspension of Brownian nanoparticles with synchrotron radiation and studying the resulting interference pattern. The transverse coherence of the source, and therefore, under the conditions of validity of the Van Cittert and Zernike theorem, the transverse electron beam size is retrieved from the interference between the transmitted beam and the spherical waves scattered by each nanoparticle. We here describe the fundamentals of this technique, as well as the recent experimental results obtained with 12 keV undulator radiation at the NCD beamline at the ALBA synchrotron. The applicability of such a technique for future accelerators (e.g. CLIC or FCC) is also discussed.

## INTRODUCTION

The HNFS method is a powerful, yet conceptually simple and inexpensive method to measure the transverse coherence properties of a light source. It is described mathematically by the Complex Coherence Factor (CCF):

$$\mu(x_1, x_2) = \frac{\langle E(x_1, t) E^*(x_2, t) \rangle}{[I_1 I_2]^{1/2}} \quad (1)$$

where  $E(x_i, t)$  is the electric field at a given point in space and time,  $I_i = \langle E(x_i, t) E^*(x_i, t) \rangle$  is the intensity of the electric field and  $\langle \dots \rangle$  denotes time averaging. The ability to measure the CCF of a light source is of interest for beam diagnostics as, under the conditions of validity of the Van Cittert and Zernike (VCZ) theorem [1], the CCF is the Fourier transform of the source intensity distribution. As a consequence, when Synchrotron Radiation (SR) is used as the light source, a measurement of its transverse coherence allows the transverse profile of the beam at the emission plane to be retrieved.

The traditional method for measuring the beam size through the CCF is Young's two slit interferometer [2], where SR impinges on a pair of narrow slits forming an interference pattern. In this case, the CCF is retrieved from the visibility  $V$  of the fringes:

$$V \stackrel{\text{def}}{=} \frac{I_{\max} - I_{\min}}{I_{\max} + I_{\min}} = \frac{2\sqrt{I_1 I_2}}{I_1 + I_2} |\mu_{12}| \quad (2)$$

where  $I_i$  is the time averaged intensity at slit  $i$  and  $\mu_{12}$  is a short form for the CCF as defined in Eq. 1. The HNFS

method is an alternative to Young's double slit method that offers some potential advantages. HNFS does not require the almost completely blocking of SR radiation as in the Young's slits configuration, and it does not require the challenging fabrication of narrow slits in a medium that must be opaque to X-rays. While HNFS is known a well-known particle sizing technique, it has never, to our knowledge, been used for beam size monitoring in particle accelerators. We will report of the status of a proof of concept experiment at ALBA to measure beam size using X-ray radiation.

## THE HNFS TECHNIQUE

A typical HNFS setup using X-ray radiation (see Fig. 1) is composed of a suspension of nanoparticles in water positioned at a distance  $z_1$  from the source, which can be a dipole or insertion device. The transmitted and scattered fields propagate for a distance  $z_2$  where they impinge on a YAG scintillator that produces visible light at 550 nm with the same intensity modulations as the incident X-ray radiation. The visible signal is extracted from the X-ray beam path by means of a mirror at 45°. A highly magnified image of the YAG screen is then produced on a sensor by means of a microscope objective.

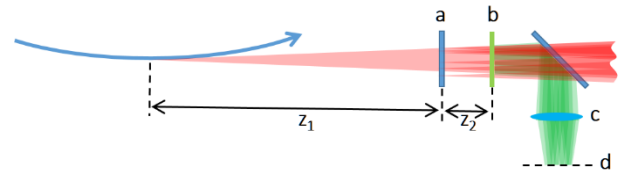


Figure 1: A typical HNFS setup for X-rays (shown in red). a) target composed of a suspension of nanoparticles in water. b) YAG screen with visible light shown in green. c) microscope objective. d) sensor

Heterodyne Near Field Scattering (HNFS) is an interferometric technique where the incident light beam  $E_0$  impinging on the target generates a large number of weak spherical waves ( $E_s, |E_s| \ll |E_0|$ ) that interfere with the transmitted field. The resulting intensity distribution is known as a speckle field and it is recorded onto the scintillator plane at a distance  $z_2$  downstream the scattering sample. The coherence properties of the source are determined from analysis of the stochastic interferogram formed at the scintillator plane with the resulting light intensity distribution given by:

$$I = |E_0 + E_s|^2 = |E_0|^2 + 2\text{Re}[E_0^* E_s] \quad (3)$$

where the multiple scattering term  $|\mathbf{E}_s|^2$  is neglected because of the weak scattering. The second term of Eq. 3 is reminiscent of the CCF (Eq. 1), and represents the sum of the many interference patterns generated by the overlap of the transmitted wave and the weak spherical waves generated by single nanoparticles. However, due to the random position of the nanoparticles, the intensity  $I$  results in a stochastic speckle field where the information about the single interferogram is lost.

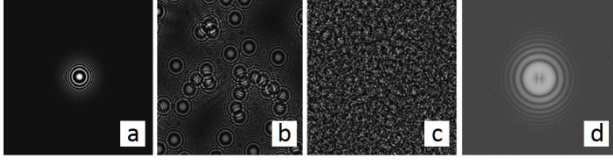


Figure 2. Principle of the HNFS method. The single particle simulated interference pattern (a) is stochastically overlapped for a large (b) and very large (c) number of nanoparticles, resulting in a speckle field. The single particle interferogram is retrieved from the square modulus of the 2D Fourier transform

This can be seen in Fig. 2, where the simulated interference pattern resulting from the interference of a single particle (spherical wave) and a plane wave is shown in (a). When the pattern is overlapped according to the random distribution of a very large number of particles, information about the single interferogram is lost. However, by computing the square modulus of the two-dimensional Fourier transform of the image  $I(q)$ , the square modulus of the CCF can be retrieved in the reciprocal space. It can be shown [3] that in the reciprocal space with coordinates  $q = |\mathbf{q}| = 2k \sin \frac{\vartheta}{2} \approx k\vartheta$  ( $k$  being the radiation wavenumber,  $\vartheta$  the scattering angle):

$$I(q) = |\mu(q)|^2 T(q) H(q) + P(q) \quad (4)$$

where  $T(q)$  is a single particle interferogram,  $H(q)$  combines the Instrument Transfer Function (ITF) – mainly the phosphor and particle form factor (the latter being essentially a constant in our case), and  $P(q)$  the shotnoise and other spurious contributions. Since  $T(q)$  is known theoretically quite precisely and the other terms can be measured, the 2D power spectrum of the image yields the square modulus of the CCF expressed in reciprocal space. The relation between Eq. 4 and Eq. 1 is given by the spatial scaling  $\Delta x(q) = qz_2/k$  [3, 4] (in Eq. 1, we assume that the radiation CCF depends only on  $\Delta x = x_1 - x_2$ ). Then, a simple two dimensional Fourier transform of the square root of  $I(\Delta x(q))$  allows the two dimensional intensity distribution of the source to be recovered.

## THE EXPERIMENTAL SETUP

An HNFS setup has been installed in the NCD-SWEET beamline at ALBA (see Table 1).

Table 1: NCD-SWEET Beamline Parameters

Source type	In vacuum undulator
Period	21.3 mm
Number of periods	92
Gap	5.86 mm
Resonant energy	12.4 KeV
Beam current	150 mA
Bandpass	$3.1 \times 10^{-4}$ (@ 10 keV)
SR source size (RMS)	$131 \times 8 \mu\text{m}^2$ (HxV)

A channel cut silicon monochromator is positioned 22 m away from the centre of the in-vacuum undulator. The sample position can be adjusted to be between 30 and 33 metres from the source, and was fixed at 32.5 m for the measurement here presented. The target is composed of a series of capillaries of 1.5 mm diameter positioned on a motorised stage. The capillaries are filled with a suspension of silica nanoparticles of 500 nm of diameter, with a 10% volume fraction concentration. A reference capillary filled with distilled water without nanoparticles is also present. The scintillator is a YAG:Ce crystal of 0.1 mm thickness, mounted on a long translation stage that allows the distance  $z_2$  (see Fig.1). The measurements here presented were performed at a distance  $z_2 = 252$  mm. The optical system is mounted on the same YAG support and is composed of a 45° mirror, and a 20X microscope objective that forms the image on a Basler scA1300-32gc CCD camera.

## RESULTS AND DISCUSSION

The typical result of a 2D power spectrum obtained through HNFS for a 12.4 keV X-ray beam at NCD-SWEET is shown in Fig. 3. The interference is more prominent along the direction with the larger transverse coherence length (vertical), as expected from theory [4, 5]. This can be understood from the beam shape (smaller size in the vertical direction) and the fact that there exist a Fourier transform relation between the transverse intensity of the source and the far-field transverse coherence. The poor horizontal coherence induces an almost complete lack of single particle interferogram fringes along the corresponding direction, as can be seen in Fig. 3b and 3c. For completeness the horizontal and vertical profile of the shot-noise contribution, can be inferred from the power spectrum of the capillary filled with only distilled water.

Due to limitations in the set-up, it is not possible to access sample-YAG distances smaller than a few cm where we would be sensitive to the phosphor Transfer Function (TF), and where the power spectrum would be perfectly symmetric [5], before coherence effects start to be dominant.

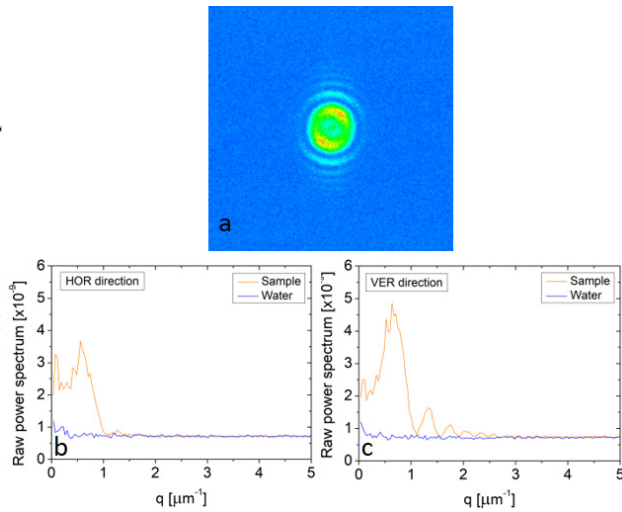


Figure 3: Two dimensional power spectrum of the speckles field (a) with its horizontal (b) and vertical (c) profiles (orange curves).

Surveying the literature [6,7], the transfer function of crystal scintillators is measured to be a negative exponential  $H(q) = H_0 \exp(-q/q_{scint})$ , with  $q_{scint}$  ranging from  $0.6 \mu\text{m}^{-1}$  [6] to  $0.8 \mu\text{m}^{-1}$  [7]. If we assume a similar TF for our YAG phosphor then we can produce corrected plots for different values of  $q_{scint}$  (0.4, 0.5, 0.6, 0.7, 0.8, 0.9, 1.0). Results for values 0.7-1 are reported in Fig. 4 for the vertical direction.

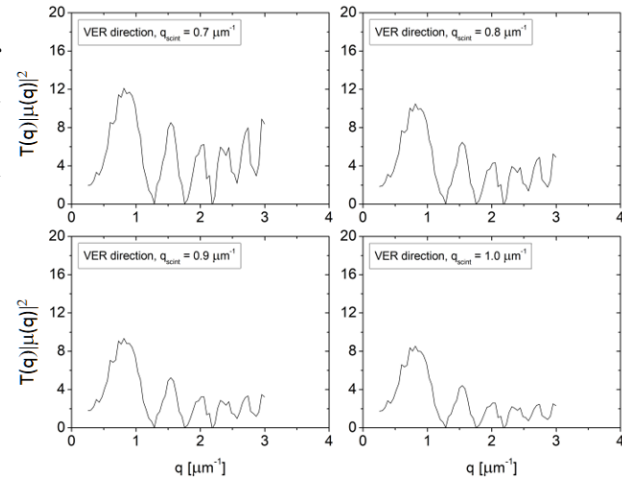


Figure 4: Vertical profiles corrected with an exponential phosphor transfer function  $H(q)$  for four different values of the characteristic exponential decay,  $q_{scint}$ . Horizontal profiles are not shown for brevity

If we had truly measured the  $H(q)$  of the optics, the reduced curves  $T(q)|\mu(q)|^2$  would be normalized to a maximum value of 1 at  $q=0$ . Here, the first Talbot maximum appears at roughly  $q=0.8 \mu\text{m}^{-1}$ , corresponding to a transverse displacement  $\Delta r = qz_2/k = 4 \mu\text{m}$ . This value lies well within the extent of the coherence in the vertical direction, meaning that the corresponding curves  $T(q)|\mu(q)|^2$  along the vertical direction would have a value of 1 in normalized units. The same analysis applies

to horizontal profiles. We thus normalize the corrected horizontal and vertical profiles according to the value of the first Talbot maximum along the vertical direction

$$I_{corr}(q) = \frac{1}{I_0} \frac{I(q)}{H(q)} \propto |\mu(q)|^2 T(q) \quad (5)$$

We do not consider the three power spectra (corresponding to  $q_{scint} = 0.4, 0.5, 0.6$ ) since the normalised coherence function of the radiation exceeds 1, an unphysical result that points to an incorrect value of  $q_{scint}$ .

Let us discuss separately the horizontal and vertical profiles. Fig. 5 shows the normalized horizontal profile  $I_{corr}(q)$ , together with a fitting function which assumes a Gaussian CCF  $\mu(q) = \exp(-q^2/2\sigma^2)$  where  $\sigma$ , expressing the width of  $\mu(q)$  depends on the distance  $z_2$  [5] (252 mm in our case – see Fig. 1). We define the transverse coherence length as

$$\sigma_{coh} = \int_{-\infty}^{+\infty} |\mu(\Delta r)|^2 d\Delta r$$

according to [1], where  $\Delta r$  is a radial transverse displacement from the optical axis defined in the previous paragraph. Under Gaussian approximation,  $\sigma$  can be related to the transverse coherence length of the source as measured at the target plane:

$$\sigma_{coh} = \frac{\sqrt{\pi}}{k} z_2 \sigma \quad (6)$$

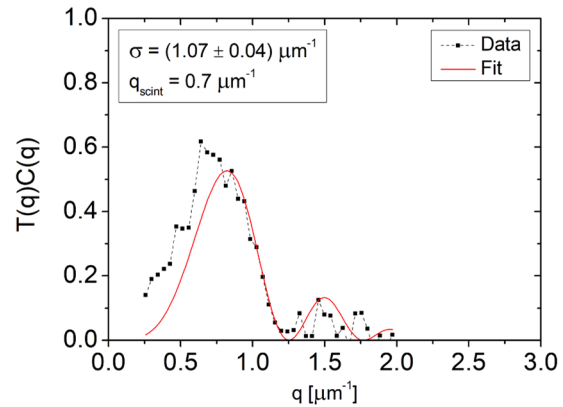


Figure 5: Horizontal profile of  $I_{corr}(q)$  with a  $q_{scint} = 0.7 \mu\text{m}^{-1}$  fitted with the single particle interferogram  $T(q)$  modulated by a Gaussian CCF

In principle, our “manual” data reduction should lead to a value of  $\sigma_{coh}$  which is related to the choice of  $\sigma_{scint}$  used to calculate the corrected intensity. We find however that  $\sigma_{coh}$  shows a very weak dependence on the unknown  $q_{scint}$ , its value changing by only 2% for values of  $q_{scint}$  from 0.7 – 1.0. This means that the envelope of the single particle interferogram fringes along the horizontal direction is entirely dictated by the coherence properties of the source. We therefore consider  $q_{scint} = 0.7 \mu\text{m}^{-1}$ , for which we obtain



$$\sigma_{coh}^h = 7.6 \pm 0.3 \mu\text{m}. \quad (7)$$

This value is in fair agreement with the expected results from simulations assuming perfect resonance conditions and no energy spread effects [4], for which  $\sigma_{coh}^h = 7.1 \mu\text{m}$ . Under the conditions of validity of the VCZ theorem, we finally retrieve the transverse horizontal size of the source as

$$\sigma_{size}^h = \frac{\sqrt{\pi}}{k} \frac{z_1}{\sigma_{coh}^h} = 111 \pm 10 \mu\text{m} \quad (8)$$

which is in fair agreement with the expected value of 131  $\mu\text{m}$ .

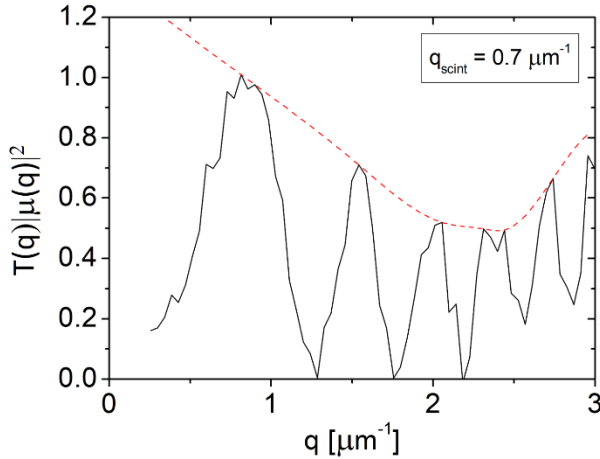


Figure 6: Vertical profile of  $I_{corr}(q)$  for  $q_{scint} = 0.7 \mu\text{m}^{-1}$ .

A similar procedure cannot be applied to the vertical profiles since the envelope of the single particle interferogram is not Gaussian but rather exhibits a sort of echo at  $q=3 \mu\text{m}^{-1}$ , as shown in Fig 6 for the case of  $q_{scint} = 0.7 \mu\text{m}^{-1}$ . Here the dashed red line is drawn simply to guide the eye.

Such a peculiar behavior is not predicted by theory for free-space propagation [4] and might be ascribed to “defective” optics, as was similarly reported in previous observations [3]. In particular it can be caused by the monochromator, whose surface is known to be corrugated. Further measurements are however needed in order to understand this peculiar modulation in the vertical envelope of the Talbot oscillations. Following [3], the coherence function could be given by the overall envelope curve of such echoes. The  $\sigma$  of such curves ranges from 3 to 7  $\mu\text{m}^{-1}$ , corresponding to a transverse beam size  $\sigma_{size}^v$  between 17 and 38  $\mu\text{m}$  in the vertical direction, a range of values that is quite far from the expected 8  $\mu\text{m}$ . This could be due to a poor correction for the phosphor TF, which is expected to influence the vertical power spectrum much more than the horizontal one [5]. Beam energy spread might also affect the coherence properties of SR from an undulator in the vertical direction, as mentioned in [4].

## CONCLUSIONS

We have reported recent measurements of transverse coherence length of a 12.4 keV X-rays beam at the NCD-

SWEET beamline at ALBA. Under the conditions of validity of the VCZ theorem, the transverse beam size of the source was determined. The horizontal beam size is in good agreement with the expected value of 131  $\mu\text{m}$ , while the vertical is affected by large experimental uncertainties that result in a value from 2 to 5 times larger than the expected 8  $\mu\text{m}$ . The cause of such discrepancy is still under investigation, but is believed to be partly related to the approximate knowledge of the phosphor transfer function.

HNFS is still a relatively new technique in accelerator beam diagnostics using X-rays. Our ongoing studies aim to understand its experimental advantages and limitations when compared to the more established two-slit interferometer. In particular, we plan to optimise the HNFS target to produce a high contrast speckles field for an improved measurement of the coherence length and beam size. This could be achieved by using different nanoparticles, or alternatives to a suspension like masks or membranes. Future work also aims at testing HNFS on dipole SR with possible applications on future machines such as the Future Circular Collider.

## REFERENCES

- [1] J. W. Goodman, *Statistical Optics*. New York, NY, USA, John Wiley, 2000
- [2] T. Mitsuhashi, “Beam Profile Measurement by SR Interferometers”, in *Proceedings of the Joint U.S.-CERN-Japan-Russia School on Particle Accelerators*, Montreux, Switzerland, 1998
- [3] M. D. Alaimo, M. A. C. Potenza, M. Manfredda, G. Geloni, M. Sztucki, T. Narayanan, and M. Giglio, “Probing the transverse coherence of an undulator X-ray beam using brownian nanoparticles”, *Phys. Rev. Lett.* Vol. 103, p. 194805, 2009
- [4] M. Siano, B. Paroli, M. A. C. Potenza, U. Iriso, A. A. Nosych, L. Torino, S. Mazzoni “Characterizing temporal coherence radiation with heterodyne near field speckles”, *Phys. Rev. Accel. Beams*, vol. 20, p. 110702, 2017.
- [5] G. Geloni, E. Saldin, E. Schneidmiller, and M. Yurkov, “Transverse coherence properties of X-ray beams in third-generation sources”, *Nucl. Instrum. Methods Phys. Res., Sect. A*, vol 588, p. 463, 2008
- [6] R. Cerbino, L. Peverini, M. A. C. Potenza, A. Robert, P. Bosecke, and M. Giglio, “X-ray scattering information obtained from near-field speckle”, *Nat. Phys.*, vol 4, p. 238 2008, *Supplementary Materials*.
- [7] Y. Kashyap, H. Wang, and K. Sawhney, “Two-dimensional transverse coherence measurements of hard X-ray beams using near-field speckle”, *Phys. Rev. A*, vol. 92, p. 033842 2015.

# INJECTION TRANSIENT STUDY USING 6-DIMENSIONAL BUNCH-BY-BUNCH DIAGNOSTIC SYSTEM AT SSRF \*

Y.M. Zhou<sup>†</sup>, B. Gao, N. Zhang, Y.B. Leng<sup>#</sup>  
 SSRF, SINAP, Shanghai, China

## Abstract

Beam instability often occurs in the accelerator and even causes beam loss. The beam injection transient process provides an important window for the study of beam instability. Measurement of the bunch-by-bunch dynamic parameters of the storage ring is useful for accelerator optimization. A 6-dimensional bunch-by-bunch diagnostic system has been successfully implemented at SSRF. The measurements of transverse position and size and longitudinal phase and length are all completed by the system. Button BPM is used to measure beam position, phase and length, and the synchrotron radiation light is used to beam size measurement. Signals are sampled simultaneously by a multi-channel acquisition system with the same clock and trigger. Different data processing methods are used to extract the 6-dimensional information, where delta-over-sum algorithm for beam position extraction, Gaussian fitting algorithm for beam size extraction, zero-crossing detection algorithm for beam phase extraction and the two-frequency method for bunch length extraction. The system set up and performance will be discussed in more detail in this paper. The application of the injection transient study brings a lot of interesting phenomena and results, which will be discussed as well.

## INTRODUCTION

The Shanghai synchrotron radiation facility (SSRF) is the third synchrotron radiation light source facility in Shanghai China, which can produce broad rates of X-rays for primary scientific research and applications in other domains. The SSRF consists of a 150MeV linear accelerator, a 3.5GeV booster synchrotron and a 3.5GeV storage ring. In the user operation mode, about 500 bunches are stored with 2ns spacing in the storage ring. The harmonic number is 720 with the RF frequency of 499.654MHz [1]. In order to take full advantage of the SSRF, phase-II project is under construction since 2011, 16 beam lines would be built and the electron storage ring would be upgraded. More insertion devices (IDs) with small gaps will be added, which will cause beam instability problems.

For the construction and operation of the machine, if the distribution of high energy particles in three dimensions and the evolution over time can be measured, almost all other parameters can be derived from the above measurements. Therefore, bunch-by-bunch diagnostics is necessary for the bunching beams. Once the diagnostics is realized, it can be used to online monitor the steady or unsteady beam parameters during the user operation mode, which is of great importance for the operation mode optimization and the capture of transient process. At the same time, it is also a useful tool for further analysis of instability, such as

the tremendous change of betatron amplitude and beam size or phase.

In the injection system of the SSRF storage ring, there is a set of beam kickers, which is used to change the momentum of a bunch to meet the injected one [2]. Then, it can change back to the original orbit with the injected bunch. However, due to the imperfect mount, align and configure of the kickers, residual betatron oscillations occurred in the injection system. Therefore, bunches would be affected by the kicker field or the wake-fields from preceding bunches. The bunch-by-bunch diagnostics is a machine research tool for wake field and impedance study.

In recent years, Beam Instrumentation (BI) group at SSRF has also been focusing on the development of bunch-by-bunch diagnostics since 2012. If the bunching beam is assumed to be Gaussian in the three-dimensional space, six spatial parameters ( $(x, y)$  in the transverse position,  $(\sigma_x, \sigma_y)$  in the transverse size,  $(z, \sigma_z)$  in the longitudinal phase and length) can fully describe an independent bunch with the bunch charge. A 6-dimensional (6D) bunch-by-bunch diagnostic system has been set up to measure the parameters simultaneously at SSRF.

## PRINCIPLES

In the acquisition of beam signals, the synchrotron radiation (SR) light is the most ideal signal because it contains all beam information, whereas the button-type beam position monitor (BPM) cannot get the transverse size information. However, it is easy to condition and capture signal for the button BPM signal, and the SR light signal is limited by the bandwidth of the signal conditioning and data acquisition system. So, to realize the 6-dimensional diagnostic system, we use the SR light to obtain the transverse position and size information and use the button BPM to obtain the longitudinal phase and length information or transverse position as well.

### Optical Imaging System

Figure 1 shows the optical direct imaging system in the bunch-by-bunch size system. The concave lens (Lens 1) and convex lens (Lens 2) are used to focus and magnify the light spot, and to adopt the pixel size to the photoelectric detector. The visible light from the SSRF storage ring was separated into two paths through a reflecting mirror: one path was toward the interferometer system for spread function (PSF) calibration, and the other one was toward the bunch-by-bunch size measurement. A diaphragm was used to correct the deformation of the Be mirror. Since the Be mirror deformation mainly occurred in the vertical direction, the measurement of beam vertical size was destroyed. Therefore, we were more concerned with the measurement of beam horizontal size, and the horizontal size result was

about 53μm by the experimental calibration based on the interferometer system [3].

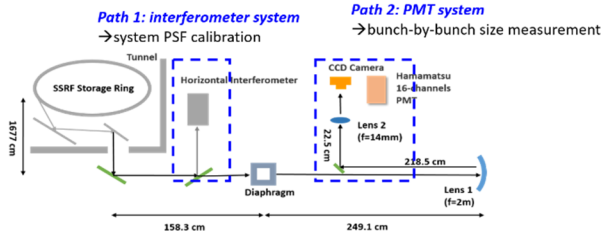


Figure 1: Optical diagram of direct imaging system.

### Button BPM

Since the BPM signal contains all beam information except the transverse size and its signal conditioning and capture is easy, we use it to measure the beam position, phase and length. Figure 2 is the cross section of a button BPM [4]. A line charge at the position  $(\delta, \theta)$  within the probe radius  $a$  and pipe radius  $b$ . The button voltage is produced by the current out of the button and the impedance ( $Z$ ) seen by this current, which can be expressed as:

$$V_b(t) = \frac{\pi a^3 Z}{2\pi b \beta c} \cdot \frac{t - t_0}{\sigma^2} \cdot I_0(t) \cdot F(\delta, \theta). \quad (1)$$

where the current equation is related to longitudinal phase ( $t_0$ ) and length ( $\sigma$ ):

$$I_0(t) = \frac{eN}{\sqrt{2\pi}\sigma} \exp\left(-\frac{(t - t_0)^2}{2\sigma^2}\right). \quad (2)$$

and the position correlation parameters are:

$$\begin{aligned} F(\delta, \theta) &= \frac{a^2 - \delta^2}{a^2 + \delta^2 - 2a\delta \cos \theta} \\ \delta &= \sqrt{x^2 + y^2} \\ \theta_{A,B,C,D} &= \frac{m\pi}{4} - \tan^{-1}\left(\frac{y}{x}\right), (m = 3, 1, 7, 5) \end{aligned} \quad (3)$$

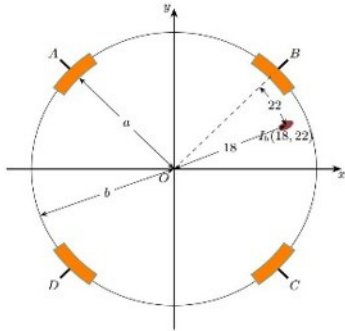


Figure 2: Cross section of button-type BPM.

\*Work supported by National Natural Science Foundation of China (No.11575282 No.11375255 No.11305253)

<sup>†</sup>zhouyimei@sinap.ac.cn

<sup>#</sup>lengyongbin@sinap.ac.cn

### 6D Information Extraction Methods

In our experiments, we used delta-over-sum ( $\Delta/\Sigma$ ) method for transverse position measurement, Gaussian fitting for transverse size measurement, zero-crossing detection method for longitudinal phase measurement and two-frequency method for longitudinal length measurement.

**Delta-over-sum Method** The main method of beam position measurement is the peak sampling of the button BPM signals and calculated by the delta-over-sum algorithm [5]. The equation is as follows:

$$\begin{aligned} x &= k_x \cdot \frac{(V_A(t) + V_D(t)) - (V_B(t) + V_C(t))}{V_A(t) + V_D(t) + V_B(t) + V_C(t)} \\ y &= k_y \cdot \frac{(V_A(t) + V_B(t)) - (V_C(t) + V_D(t))}{V_A(t) + V_D(t) + V_B(t) + V_C(t)} \end{aligned} \quad (4)$$

Among them, the factors ( $k_x, k_y$ ) require online and timely calibration. At the same time, phase drift occurs during the sampling of BPM signals.

**Gaussian Fitting Method** Assuming that the bunch is in Gaussian distribution, we can get four symmetric sampling points from the SR light signal if the channels are adjusted properly (as shown in Fig.3).

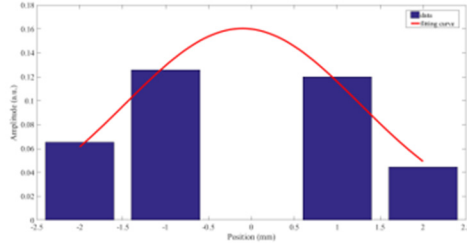


Figure 3: Four-channel sampling signal and Gaussian fitting.

**Zero-crossing Detection Method** The main method of beam phase measurement is the rising-edge sampling of the button BPM signals and calculated by the zero-crossing detection algorithm [6]. Sampling points of the button pickup signal is shown in Fig.4. The longitudinal phase equals the intercept of the time ordinate after linear fitting. To ensure the validity of the algorithm, the longitudinal offset cannot be too larger to prevent the sampling points from exceeding the rising edge threshold.

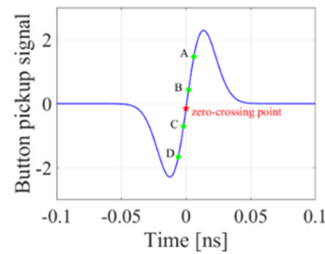


Figure 4: Sampling points of the button pickup signal.

**Two-frequency Method** The main method of measuring beam longitudinal length is two-frequency method [7].

Since enough signal amplitude and RF component limitation, we chose the baseband and 6th harmonic sidebands (about 500MHz and 3GHz) as working frequencies. The bunch length calculation formula is as follows:

$$\sigma = \sqrt{\frac{2}{m_2^2 \omega_0^2 - m_1^2 \omega_0^2} \ln(K_1 \frac{V_1}{V_2} + K_2)} \quad (1)$$

where  $m_2$ ,  $m_1$ ,  $\omega_0$  are theoretically knowable, and the ratio of  $V_1$  to  $V_2$  is measured from the two-frequency system. Due to two channels transfer functions difference and limited bandwidth, two coefficients  $K_1$  and  $K_2$  are introduced into the equation. No theoretical analytic solution for  $K_1$

and  $K_2$  and the two coefficients can be calibrated by Streak Camera

## SYSTEM SETUP

The system framework of the 6D bunch-by-bunch diagnostic system (as shown in Fig.5), which can be used to measure beam transverse size, position, longitudinal phase and length, simultaneously. The data acquisition system is composed of four ADQ digitizers, which has four input channels with a 14-bit ADC, 1.2GHz analogue bandwidth, maximum 1GS/s sampling rate and multi-board synchronization. The synchronous sampling mainly relies on the same clock and trigger from the timing system.

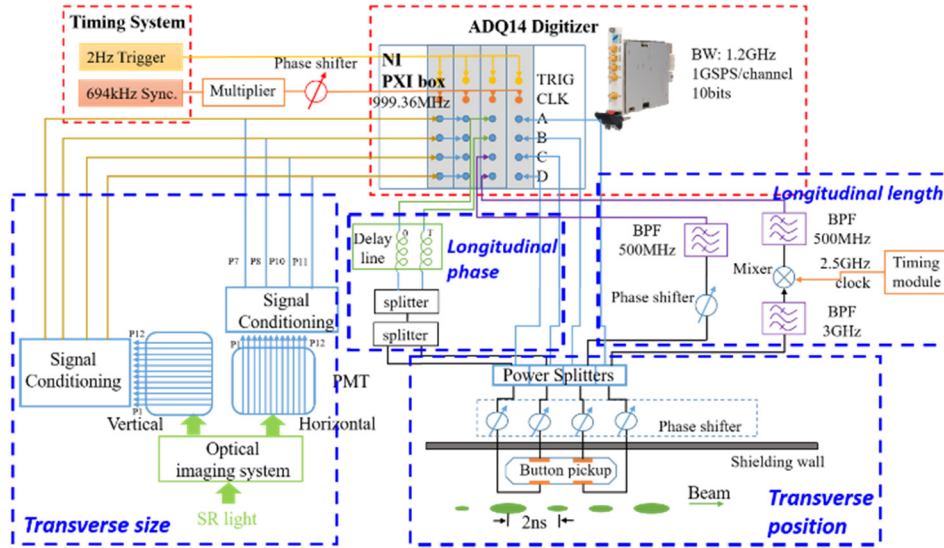


Figure 5: System framework of the 6D bunch-by-bunch diagnostic system.

### Beam Transverse Position Subsystem

Beam transverse position subsystem consists of button BPM, adjusted phase shifters and signal acquisition digitizer. The beam position information is obtained from the Button BPM. And it adds four phase shifters to ensure the phase coherence of the pickup signals. Also, it adds a phase shifter in the clock channel, which is used for phase adjustment of the clock signal to ensure the peak of sampled signals. Meanwhile, in order to facilitate the use of ADQ digitizer, the clock signal is multiplied to 1GHz by the multiplier module.

### Beam Longitudinal Phase Subsystem

Beam longitudinal phase subsystem also consists of button BPM, adjustment phase shifters and signal acquisition digitizer. The beam phase information is obtained from the sum signal of the Button BPMs, which can eliminate the transverse effects. It also has a phase shifter in the clock channel, but the purpose is to ensure the zero-crossing point of the sampled signals. At the same time, the system realizes sampling with the same time interval using four delay lines (typical  $T=100ps$ ).

### Beam Transverse Size Subsystem

SR light signal from the optical imaging system is captured by a high-speed PMT array (Hamamatsu H10515B) with 16 channels of 0.6ns rise time. An analogue front-end board has been designed for fast signal pick-up of photo-multiplier array detector, which converted plug pins to SMA connector. Four amplifiers (Hamamatsu C5594) with wide bandwidth (50k-1.5GHz) and high gain (36dB typ.) are used to condition signals.

### Beam Longitudinal Length Subsystem

The beam signal derived from the button BPM is divided into two channels by a 2-way power splitter. One channel passes through a 500MHz band-pass filter (BPF) as one working frequency. On the other channel, 6-th harmonic frequency is picked up as another working frequency. A mixer with 2.5GHz local oscillator (LO) signal from a timing module is used to output an intermediate frequency of 500MHz from the filtered 3GHz signal.



## PERFORMANCE EVALUATION

### Charge( $Q$ )

The bunch charge can be obtained from the peak value of the button BPM or the SR light. Results from different subsystems are consistent with each other. In the extraction of refilled bunch, the stored bunch is obtained from the averaged charge from all stored bunches. And the refilled bunch charge is equal to the charge after injection minus the charge before injection.

The performance evaluation is based on the daily operation. The total current is 230mA with uniform filling mode.

### Transverse Position ( $x, y$ )

The principal component analysis (PCA) method is used to evaluate the measurement uncertainty of transverse position. Two modes above the noise floor stand for synchrotron oscillation coupled by dispersion. Therefore, the amplitude of noise floor can be used to identify the system resolution. Figure 6 shows the position resolution, which is better than 10 $\mu$ m with 0.6nC.

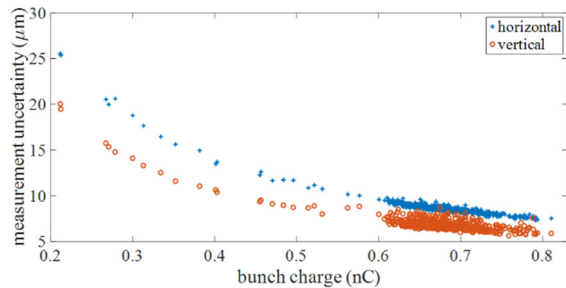


Figure 6: Resolution of the transverse position measurement.

### Longitudinal Phase ( $z$ )

The same method is used to evaluate the longitudinal phase. Figure 7 shows the results of the phase uncertainty. The phase resolution is better than 0.8ps with 0.6nC.

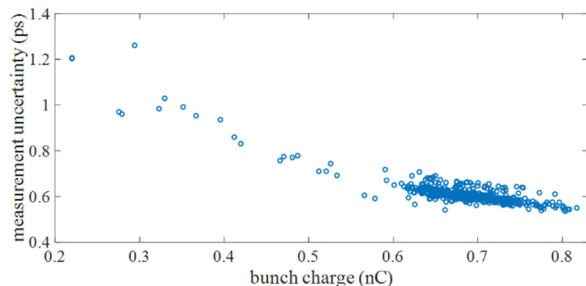


Figure 7: Resolution of the longitudinal phase measurement.

## EXPERIMENTAL RESULTS

An ideal beam experiment involves adjusting the machine parameters, and then compare the measured value with the expected value. It is difficult due to the lack of machine research time. However, the injection transient process is frequently observed in the user operation mode at SSRF. After injection, the injected bunch oscillated

around the stored bunch in the three dimensional space, which induced the damping betatron oscillation due to the timing mismatch of kickers and the damping synchronous oscillation due to the phase mismatch of the refilled charge.

The experiment carried out during the daily operation mode, but the data was captured after injection. The raw data were obtained by the ADQ digitizers simultaneously (as shown in Fig.8). A slight amplitude increase can be seen in the 56-th turns of the position data and then tends to flat after thousands of turns.

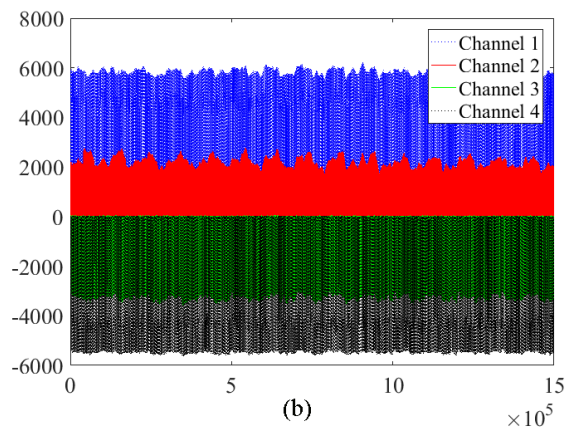
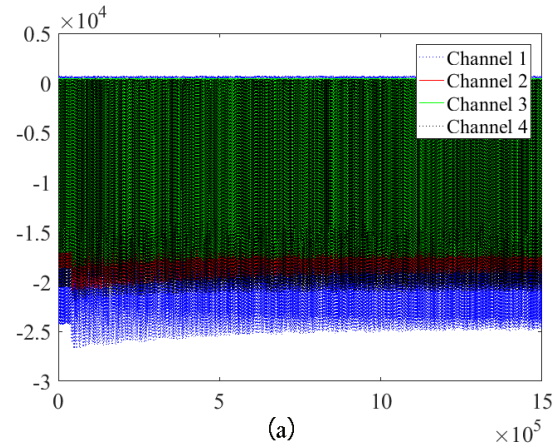


Figure 8: Raw signal data (a) of the beam position measurement (b) of the beam phase measurement.

### Refilled Bunch Position and Phase Extraction

We sampled the negative peak of the BPM signal in the transverse position measurement and sampled four points around the zero-crossing point of the BPM sum signal in the longitudinal phase measurement. Since the bunch length of the stored charge is unchanged during the injection process, we omitted the measurement of longitudinal length and only focus on the four parameters ( $x, y, z, \sigma_x$ ) measurements in the following experiments.

The charge weighted average method is used to extract the transverse position and longitudinal phase of the refilled bunch. After extraction, the horizontal displacement oscillation of the stored bunch and the refilled bunch can be obtained, as shown in Fig.9. An obvious damping betatron oscillation can be seen in the refilled bunch and the maximum oscillated amplitude is almost 10mm.

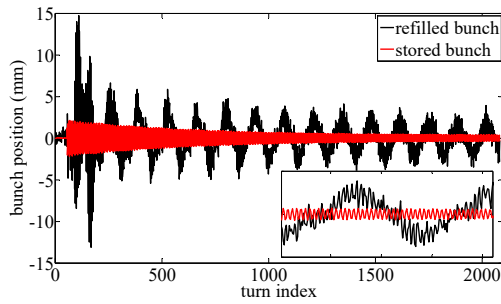


Figure 9: Transverse position extraction of the refilled bunch.

Similar with the refilled bunch position extraction, the refilled bunch phase is shown in Fig.10. The maximum oscillation amplitude is approximately 100ps to 200ps.

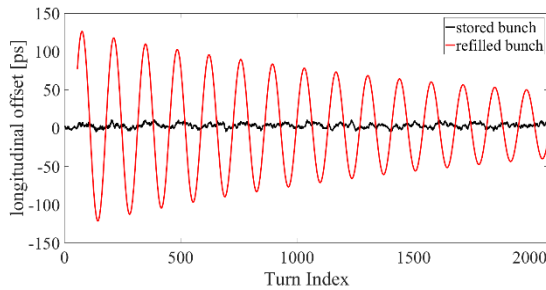


Figure 10: Longitudinal phase extraction of the refilled bunch.

### Impedance and Wake-field Analysis

The betatron oscillation of the bunches was introduced by two sources: the mismatch of the injection kicker field, and the wake-field effects of the previous bunches. The PCA method was used to separate the oscillation modes to more clearly analyse the oscillation of each component. Figure 11 shows the separation results of the beam position, mode-1 expressed as a typical damping oscillation, mainly contributed by the mismatch of the kickers. Mode-2,3,4 are all affected by kicker mismatch and wake-field effects.

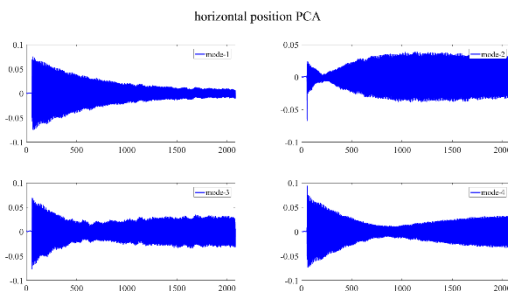


Figure 11: The first four principal components of the oscillation after injection.

Each bunch exhibited different position oscillation amplitude as different contributions from the two parts. As shown in Fig.12, the largest oscillation occurred at bunch #397, whereas the smallest oscillation occurred at bunch #3. The turn-by-turn position oscillation behaviours of these two bunches in the time domain are shown in Fig.13.

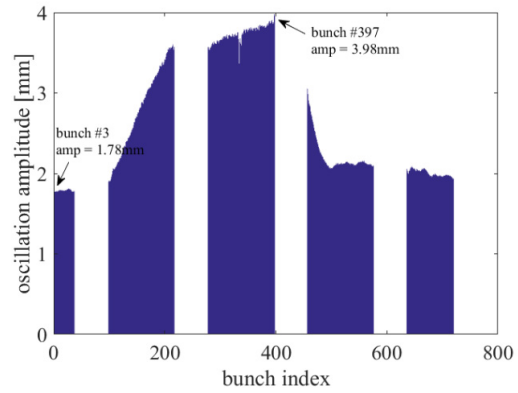


Figure 12: Initial position oscillation amplitude of each bunch.

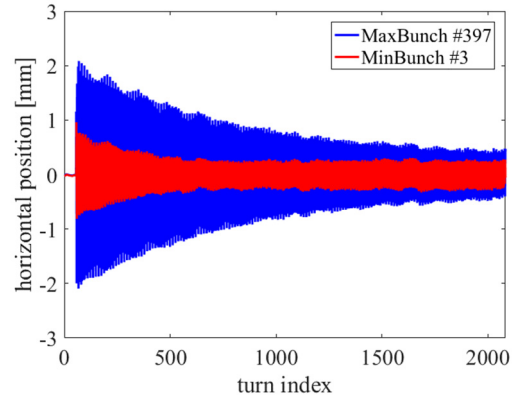


Figure 13: Turn-by-turn position oscillation of bunch #397 and bunch #3 in time domain.

Analysis with the same method, the qualitative bunch size and bunch position results can also be obtained from the transverse size subsystem, as shown in Fig.14. The size results were also the combined effects of the kicker field mismatching and wake-field, and were in good agreement with the position results.

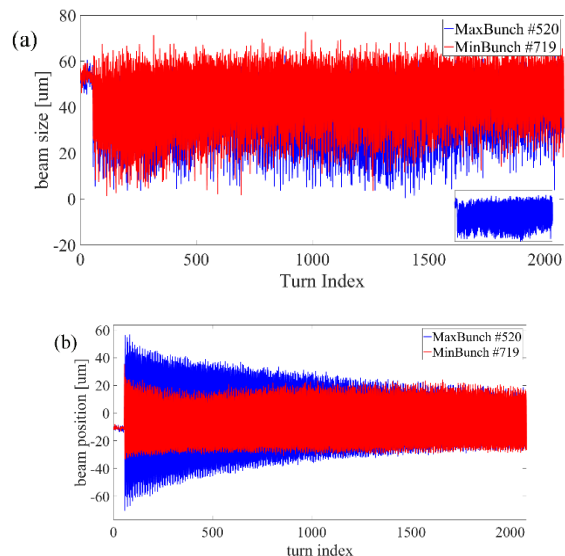


Figure 14: Turn-by-turn position and size oscillation measured by the transverse size subsystem (a) bunch size result, (b) bunch position result.

## CONCLUSIONS

The 6-dimensional diagnostic system with bunch-by-bunch capability is successfully implemented at SSRF. The transverse position and size, and the longitudinal phase and length during the injection transient process are all measured by the system. After the refilled bunch extraction algorithm, transverse position and longitudinal phase of the refilled bunch can be obtained. And the dynamic parameters of the storage ring also can be obtained from the injection transient study. DAQ need to be upgraded and intelligent trigger mode based on FPGA will be implemented. After upgrading, this system will be more useful for physicist to capture bunch-by-bunch data when unstable beam condition shows up.

## REFERENCES

- [1] B.C. Jiang and H.T. Hou, "SIMULATION OF LONGITUDINAL BEAM DYNAMICS WITH THE THIRD HARMONIC CAVITY FOR SSRF PHASE II PROJECT", in *Proc. SAP'14*, Lanzhou, China, Dec. 2014, paper THPMH4, pp. 118-120.
- [2] Z.C. Chen et al., "Wakefield measurement using principal component analysis on bunch-by-bunch information during transient state of injection in a storage ring", *Phys Rev. ST Accel. Beams*, vol. 17, p.112803, Nov. 2014
- [3] H.J. Chen et al., "Bunch-by-bunch beam size measurement during injection at Shanghai Synchrotron Radiation Facility", *Nucl. Sci. Tech.*, vol. 29, no. 79, Jun. 2018.
- [4] Y.B. Yan, PhD Thesis, Research of SSRF BPM data acquisition system and preliminary application, Shanghai Institute of Applied Physics, Chinese Academy of Sciences, 10-15(2009). (in Chinese)
- [5] Y. Yang et al., "Bunch-by-bunch Beam Position and Charge Monitor based on Broadband Scope in SSRF", in *Proc. IPAC'13*, Shanghai, China, May. 2013, paper MOPME054 pp. 595-597
- [6] Y.M. Zhou et al., "Bunch-by-bunch longitudinal phase monitor at SSRF", *Nucl. Sci. Tech.*, vol. 29, no. 113, Aug. 2018.
- [7] L.W. Duan et al., "Injection transient study using a two-frequency bunch length measurement system at the SSRF", *Nucl. Sci. Tech.*, vol. 28, no. 7, Jul. 2017.





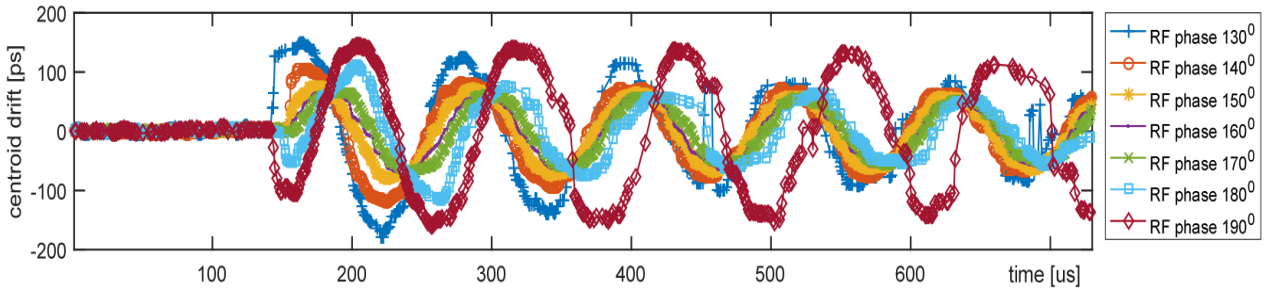


Figure 2: Longitudinal centroid oscillations of a bunch during an injection from Bo to SR with various RF phase mismatch.

Once this timing is set-up, the RF phase is clearly seen with the SC. Figure 1 shows the injection moments observed by the SC for different Bo RF phases. On each of the four images, the horizontal time axis goes from left to right, such that the first  $\sim 150 \mu\text{s}$  correspond to the stored beam circulating in the SR; then an injection occurs and the injected beam starts oscillating. On both top images we can observe two indications of higher RF phase mismatch between the Bo and the SR: the oscillations start with an offset from the stored beam position, and high oscillation amplitudes. On both bottom images the difference in phase is not evident but can be quantitatively measured it using image analysis.

Figure 2 shows tracking of the centroid motion from the different image analysis shown in Fig. 1. The injection phase match can be measured here in two different ways: one is from the maximum amplitude of the oscillations, the second is from the position at which the oscillations start. In both cases the proper RF phase match is found when the Bo RF phase is  $160^\circ$ .

### Energy Offset

Once the injection RF phase has been properly matched, the second step consists of analyzing the energy offset between the Bo and the SR. In stable machine configuration small energy differences between beams in both rings are eventually damped shortly after injection, and the injected beam is stabilized into the equilibrium energy.

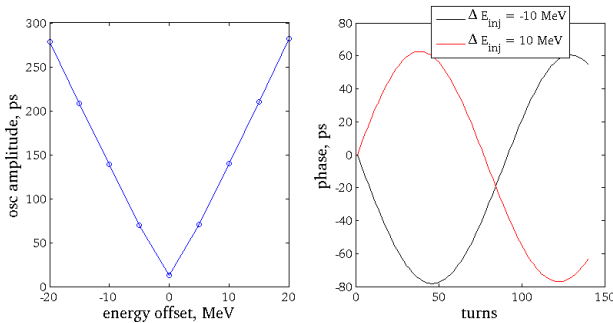


Figure 3: Left: phase mismatch (in ps) for different energy offsets between the Bo and the SR. Right: phase oscillations for energy offset of +10 (black) and -10 MeV (red).

Nevertheless, for a proper phase match, the energy offset can be inferred from the comparison between the injected

beam oscillations produced during the energy damping captured with the SC, and the ones obtained from solving the longitudinal phase/energy equations of motion, which have been performed using the Matlab Accelerator Toolbox (AT).

Figure 3 (left) shows the theoretical maximum phase oscillations for different energy offsets when the Bo and SR phases are properly matched; the right plot shows the oscillations if this offset is positive or negative (first oscillation towards positive or negative phases). In case of ALBA these oscillations have an amplitude of 120 ps and they first go towards positive values. We conclude that the energy offset in this case is +10 MeV. Note that proper care should be taken to properly identify the sign, since the SC image visualization depends on the relative phases.

### INJECTION WITH RF OFF

When an electron beam enters an accelerator where the RF system is turned off, the beam starts to lose energy at every turn and spiral inwards until it eventually gets lost. Its revolution time  $\tau$  changes with time  $t$  according to the relation:

$$\frac{d\tau}{dt} = \frac{\Delta T}{T_0}, \quad (1)$$

where  $T_0$  is the revolution time for beam at nominal energy  $E_0$ . The right part in Eq. (1) can be expressed as a function of energy following the expression:

$$\frac{\Delta T}{T_0} = \alpha \frac{\Delta E}{E_0}, \quad (2)$$

where  $\alpha$  is the momentum compaction factor and  $\Delta E = E - E_0$ . Considering that the beam enters into SR with the energy  $E_0 + \Delta E_{inj}$ , and that every turn it loses the energy  $U_0$ , its energy at turn  $n$  can be expressed as:

$$E = E_0 + \Delta E_{inj} - nU_0. \quad (3)$$

Using  $n = t/T_0$ , Eqs. (1) and (2) can be combined as:

$$\frac{d\tau}{dt} = \frac{\alpha \Delta E_{inj}}{E_0} - \frac{t}{T_0} \frac{\alpha U_0}{E_0}. \quad (4)$$

Integrating both sides of Eq. (4) leads to an analytical expression that describes how the revolution period  $\tau$  changes with time:

$$\tau = \tau_0 + \frac{\alpha \Delta E_{inj}}{E_0} t - \frac{\alpha U_0}{2E_0 T_0} t^2. \quad (5)$$

Note that this expression is basically the same as in [3], but also includes a linear term proportional to  $\Delta E_{inj}$ . As

an example, Fig. 4 shows parabolas described by bunches injected into the ALBA SR with energies equal to corresponding equilibrium energies of  $E_0$  and with fixed offset of  $\Delta E_{inj} = \pm 20$  MeV. The data comes from simulation using the Matlab AT.

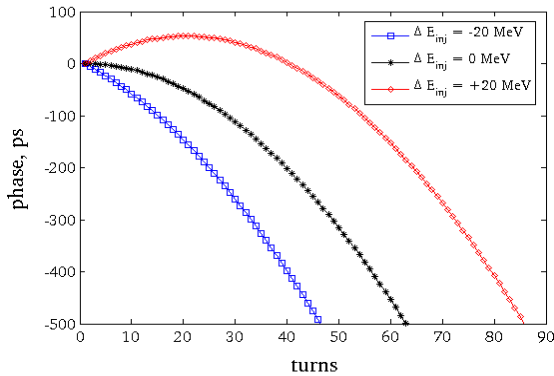


Figure 4: Simulation: bunch phase tracking after injection into SR with RF off for different beam energies.

These simulations show that when the beam is injected with an energy slightly larger than  $E_0$ , it first tends to go towards its new equilibrium orbit, which is seen as if the phase actually increases (parabola goes up). Few turns later it reaches a maximum in its phase, and then it spirals inwards (parabola goes down) until it gets lost. This is described by Eq. (5), from which it can be proved that the time  $\tau_1$  at which this maximum occurs is:

$$\tau_1 = \frac{\Delta E_{inj}}{U_0} \cdot T_0 \quad (6)$$

Note that both Eqs. (5) and (6) give both  $U_0$  and  $\Delta E_{inj}$ , provided that the beam energy  $E_0$  and the momentum compaction factor  $\alpha$  are precisely known.

### Energy Offset and Energy Loss per Turn

An experimental evidence is shown in Fig. 5, corresponding to an injection with RF off and with all SR Insertion Devices (IDs) open. The left and right images correspond to the SC at sweep speeds of 5  $\mu\text{s}/\text{mm}$  and 10  $\mu\text{s}/\text{mm}$  respectively. The yellow line following the streak trace corresponds to a fit using Eq. (5) to the centroid motion. From this analysis, we find that this corresponds to an energy loss of  $U_0=1.03$  MeV (in good agreement with the theoretical values from Table 1), and an injection offset of  $\Delta E_{inj}=18.3$  MeV. This is larger than the values found in the previous section (with RF system on), but it should be mentioned that the two measurements are spaced by 8 months, so the machine conditions were certainly different.

Note that, compared with the measurements of the energy offset with RF system on, this method has the advantage that only one fitting provides both  $U_0$  and  $\Delta E_{inj}$  without the need to rely on additional simulations.

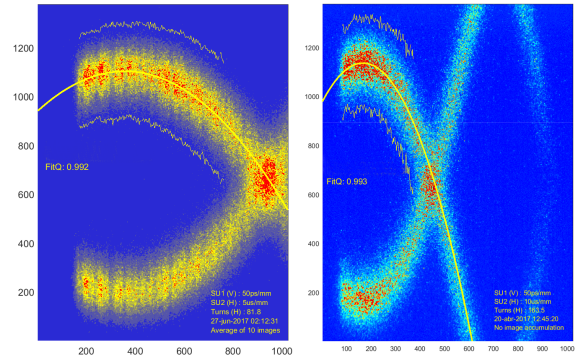


Figure 5: Streak camera acquisition of injection into ALBA SR in multi-bunch mode with RF off and IDs open. Horizontal sweep speeds of SC are 5 (left) and 10  $\mu\text{s}/\text{mm}$  (right).

### Energy Loss for Different Configurations of Insertion Devices

To estimate the precision of this method to calculate the energy loss per turn, the above example has been further tested for different configurations of the IDs, thereby changing the energy loss per turn. Figure 6 shows parabolas, described by beam centroid drifts for three different configurations of the IDs at ALBA:

- IDs closed, SCW on (blue trace, and  $U_0=1.09$  MeV)
- IDs open, SCW on (red trace,  $U_0=1.07$  MeV)
- IDs open, SCW off (green trace,  $U_0=1.03$  MeV)

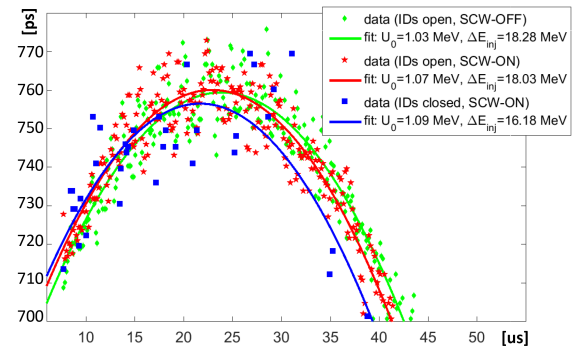


Figure 6: Measurement: Beam spiraling inwards after injection while RF system off, with IDs open, closed, and SCW on/off.

The results agree with theoretical predictions, and we can conclude that we are able to distinguish the losses down to 20 keV/turn. Nevertheless, the calculations are noisy because the SNR for low charge beams is not so good, and not all shots from the injector carry the same charge. As a consequence, we acquire around 10-20 shots for each case, but some of them need to be discarded to reduce bad data.

In order to calibrate this method to calculate the energy loss per turn, we compare the results in Fig. 6 with the ones obtained using the shift of the RF phase and with the theoretical calculations. When the energy loss per turn increases, the RF phase decreases to compensate the loss of energy due to longitudinal focusing. Therefore, by measuring the

RF voltage and the corresponding phase shift, we can infer the energy loss per turn with precision [5]. The method is consistent with the RF measurements if we consider an error bar of 10 keV/turn, as seen in Fig. 7.

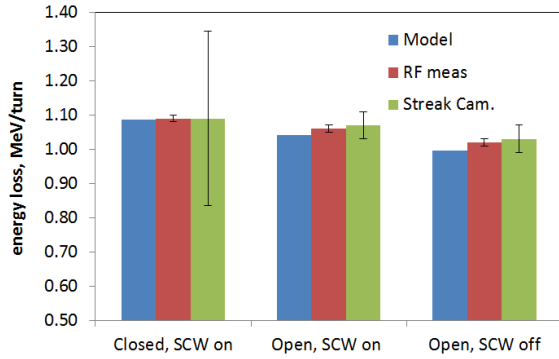


Figure 7: Comparison of the energy loss per turn in three different IDs configurations at ALBA.

## CALCULATION OF MOMENTUM COMPACTION FACTOR

For the case shown in Fig. 5, calculation of the energy loss per turn assumes the theoretical value of momentum compaction factor  $\alpha$ , shown in Table 1. Nevertheless, provided that the energy loss per turn is inferred by other means, the formalism shown in the previous section can be applied to calculate the momentum compaction factor as well.

For instance, we can calculate the energy loss per turn using the RF phase measurements, as shown in Fig. 7. This provides then a tool to infer the momentum compaction factor by leaving  $\Delta E_{inj}$  and  $\alpha$  as free parameters in Eq. (5). Moreover, since this fitting can be done for different status of the IDs, the error bar is further reduced.

Table 2: Momentum compaction factor values for different IDs states at ALBA.  $U_0$  is inferred from RF measurements. On average,  $\alpha = 0.894 \times 10^{-3}$ .

IDs status	$U_0$ , MeV	$\alpha \times 10^3$
Closed, SCW on	1.09	0.8904
Open, SCW on	1.07	0.8957
Open, SCW off	1.03	0.8952

In this case, Table 2 shows results obtained from the three cases described in Fig. 6, from where we conclude that  $\alpha = 0.894 \times 10^{-3} \pm 10\%$  is in good agreement with the theoretical value from Table 1. The error bar stems from the uncertainty in the fit parameters from Fig. 6 correspond to the standard deviation between the three cases.

In order to estimate the reliability of this value, we compare it with the one calculated from the relation between the bunch length  $\sigma_z$  (measured by SC) and the synchrotron tune  $Q_s$  (provided by the bunch-by-bunch system):

$$\sigma_z = \frac{\alpha}{2\pi Q_s f_0} \Delta E / E, \quad (7)$$

where  $f_0$  is the revolution frequency and  $\Delta E / E$  is the beam energy spread (assumed the theoretical one).

Measurements for three different beam intensities at 60, 120 and 180 mA are shown in Fig. 8, where the data is linearly fit with no independent term; the momentum compaction factor measured for beam intensity is shown in the plot. On average  $\alpha = 0.85 \times 10^{-3} \pm 2\%$ , which is very similar to the value obtained with the streak camera.

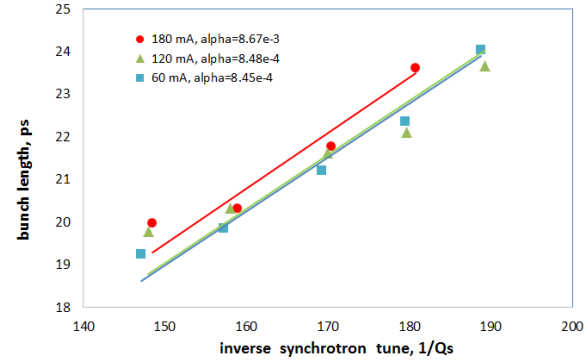


Figure 8: Bunch length measurements at 60, 120 and 180 mA while changing the RF voltage and so varying  $Q_s$ .

## CONCLUSIONS

This work studies the change in the revolution time of a beam injected into the Storage Ring with the RF system off. By analyzing the motion of a beam with the streak camera, we prove that it is possible to measure both the energy loss per turn and the energy offset between the injected beam and the equilibrium energy of the Storage Ring. Furthermore, combining this method with other techniques, we have inferred the momentum compaction factor with good accuracy.

The precision of the results shown in this report is about 10%, and its limitations are related with injection jitters and low SNR of the streak images (produced by low charge beams). Nevertheless, these results are in good agreement with the ones derived by other means.

## REFERENCES

- [1] [www.optronis.com](http://www.optronis.com)
- [2] U. Iriso and F. Fernandez, "Streak Camera Measurements at ALBA: Bunch Length and Energy Matching", in *Proc. of IBIC'12*, Tsukuba, Japan, paper TUPA46, pp. 458, 2012.
- [3] J. M. Byrd and S. De Santis, "Longitudinal injection transients in an electron storage ring", *Phys. Rev. ST Accel. Beams*, vol. 4, pp. 024401, 2001.
- [4] G. Benedetti *et al.*, "Injection into the ALBA Storage Ring", in *Proc. EPAC'08*, Genoa, Italy, paper WEPC068, pp. 2151-2153, 2008.
- [5] B. Bravo *et al.*, "Calibration of the Acceleration Voltage of Six Normal Conducting Cavities at ALBA", in *Proc. IPAC'15*, Richmond, VA, USA, 2015. doi:10.18429/JACoW-IPAC2015-WEPMN049







the applied dose. The alanine dosimeter have to be removed to acquire the integrated dose over the whole time frame. For a punctual online measurement a Multidos radiation probe [3] has been installed next to the setup. The acquired measurement data from that probe has been used to scale the intermediate measurements with the accumulated dose. As a complementary information a temperature probe has been placed on the cable spools to make sure that the cable were not heated up beyond room temperature. Figure 2 shows the final installation of the two samples and the applied diagnostics.

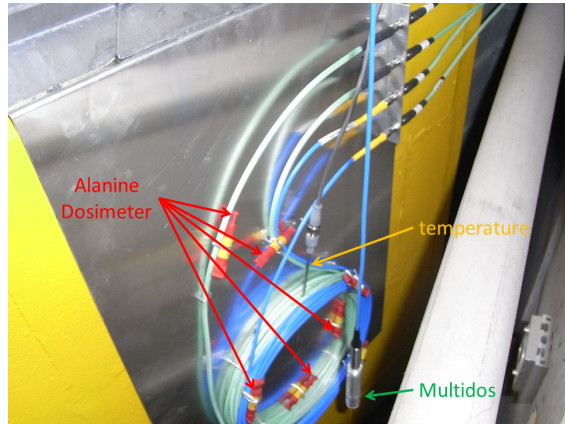


Figure 2: Final long term measurement setup.

The cable samples have been irradiated in the course of five subsequent ELBE user runs from October 2015 till December 2016. Since ELBE is a multi-beamline facility which can usually serve only one end station at a time, the dose has not been applied in a continuous manner but in many different user beam times.

### Measurement Procedure

At the end of every user run, the scattering parameters (S-parameters) have been measured. While S21 and S12 are describing the transmission behavior of a device under test the parameters S11 and S22 are describing the reflection behavior of a sample. Since cables are passive devices, the two reflection and the two transmission coefficients are the same.

The measurements have been performed using a four port vector network analyzer (Rhode & Schwarz ZVA40) that has a bandwidth of 40 GHz.

In order to separate the behavior of the patch cables from the sample cables, the S-parameters have been measured before the carrier plate has been mounted on the back of the beam dump and measured again immediately after the end of the long term run when the plate has been unmounted. This turned out to be important because the used patch cables (CUT2-type) has a characteristic notch in the frequency spectrum that can not be observed in the spectrum of the CUT1.

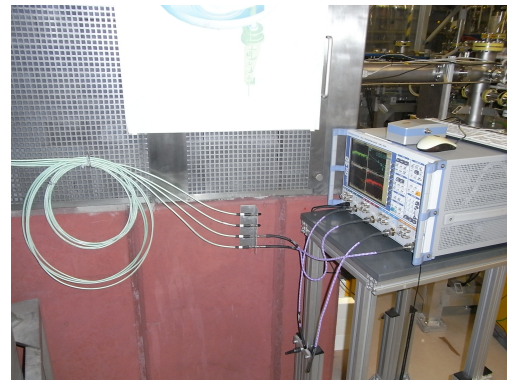


Figure 3: Scattering parameters measurement.

## MEASUREMENT RESULTS

### Long Term Dose Measurement

The long term dose measurement has been performed using the Multidos probe installed in immediate vicinity to the cable samples. Figure 4 shows the integrated dose for the measurement period. The markers in green indicate the individual measurements where the scattering parameters have been acquired and which accumulated dose has been applied to the samples to that point.

The Figures 5 and 6 are showing the results of the S21 measurements for CUT1 and CUT2 up to 40 GHz.

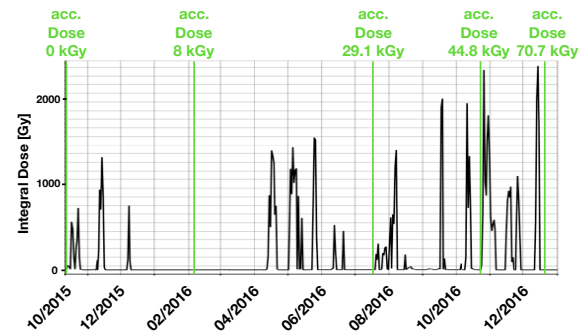


Figure 4: Accumulated dose acquired by a Multidos probe during long term measurement run.

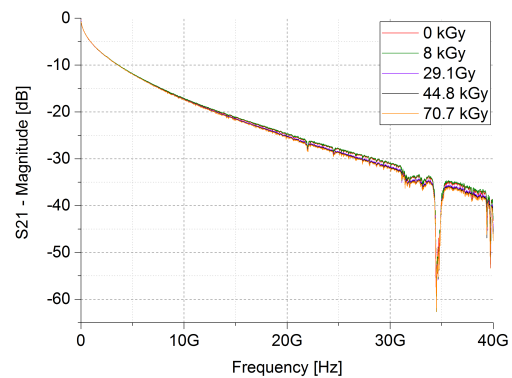


Figure 5: Degradation of 8 m CUT1 (measurements include two 5 m CUT2-type patch cables).

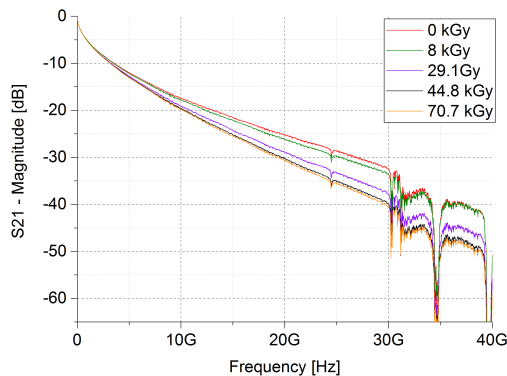


Figure 6: Degradation of 10 m CUT2 (measurements include two 5 m CUT2-type patch cables).

By comparing the degradation of both samples a major difference can be observed. While CUT1 showed a maximum change of the insertion loss of  $-0.8$  dB at a reference point of 20 GHz, CUT2 changed by  $-5.38$  dB. Considering the length difference of both samples the change of insertion loss differs by a factor of 4.3.

### Final Dose Evaluation

The accurate determination of the applied dose has been done after unmounting of the carrier plate and read out of the alanine dosimeter. The acquired dose was dependent on the location of the probe on the plate. Figure 7 shows the distribution of the probes on the sample cables and Table 2 the accumulated dose of every individual probe.

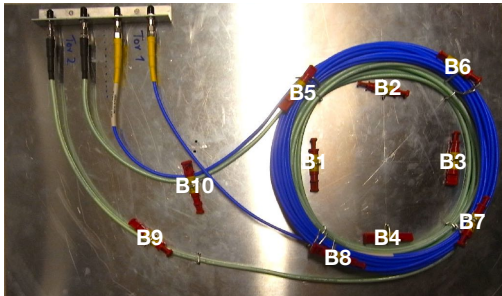


Figure 7: Distribution of Alanine Dosimeter.

Table 2: Final Dose Mapping Behind U100 Beam Dump

Name	Accumulated Dose
B1	64.28 kGy
B2	51.36 kGy
B3	93.85 kGy
B4	83.66 kGy
B5	30.38 kGy
B6	29.52 kGy
B7	57.85 kGy
B8	43.81 kGy
B9	9.40 kGy
B10	13.80 kGy

The measurements in Figures 5 and 6 are dominated by the patch cables that could not be avoided for the in-situ characterization. For a final evaluation the S-parameters have been measured without patch cables and compared to the reference measurement before the samples have been installed in the test setup. A third set of data has been acquired after carefully unwinding the cables.

Figures 8 and 9 are affirming the results of the in-situ measurements. The two samples showed a much different sensitivity to ionizing radiation.

From the cable dimension, metallisation and used dielectric it is possible to calculate the cable performance. Using Equation (1) the frequency dependent insertion loss  $IL(f)$  can be calculated from the resistive loss factor  $K1$  and the dielectric loss factor  $K2$  [4].

$$IL(f) = K1 \cdot \sqrt{f} + K2 \cdot f \quad (1)$$

A Python code was used fit the parameters  $K1$  and  $K2$  from the measured data. The results are presented in Table 3 by applying the non-linear least squares curve\_fit method. With that it can be shown that the main source of degradation was the increasing dielectric loss ( $K2$ ) while the resistive loss ( $K1$ ) barely changed. The high energy photons changed the structure of the dielectric materials and in turn the electrical properties. This is supported by the drop in performance after unwinding the cables. CUT2 showed a much higher sensitivity to mechanical stress than the CUT1.

Table 3: Extracted Loss Factors

	K1	K2
CUT1 before test	0.313	0.0053
CUT1 after test	0.319	0.0099
CUT1 unwound	0.319	0.0099
CUT2 before test	0.249	0.0066
CUT2 after test	0.250	0.0308
CUT2 unwound	0.250	0.0340

Figure 8 is documenting the excellent spectral performance of the CUT1-type cable and indicates that the notches visible in Figure 5 are solely introduced by the applied patch cables.

### CONCLUSION

The measurement setup behind the U100 beam dump at ELBE proofed to be a convenient and robust installation that enables the investigations of radiation induced damage to accelerator parts.

The two cables under test showed a significantly different behavior even though both are made of similar components. The measured differences are subject to further investigations. As a result of the performed calculations it could be shown that the resistive losses are less sensitive to ionizing radiation while the dielectric losses are increasing.

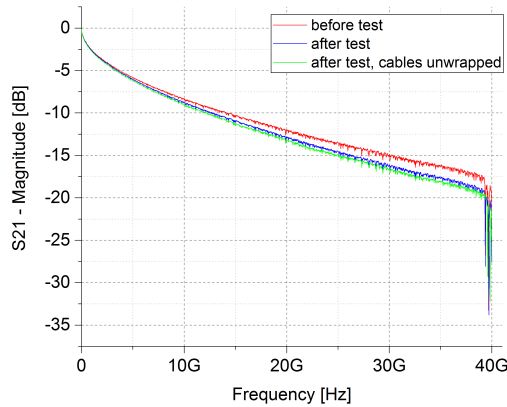


Figure 8: S21 measurements of CUT1 before and after the test mounted on the aluminum plate and unwound after the procedure.

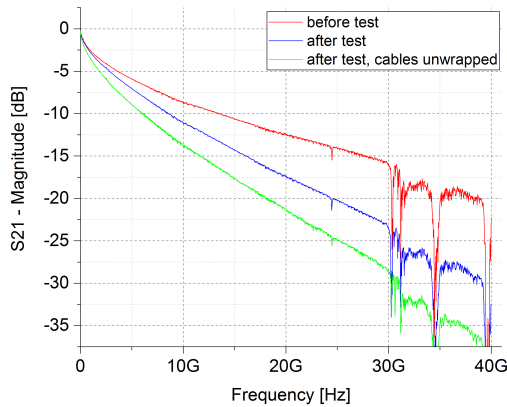


Figure 9: S21 measurements of CUT2 before and after the test mounted on the aluminum plate and unwound after the procedure.

The performed long term study has led to the conclusion that PTFE-based cables can be used in a radiative environment like an linear accelerator with high average current and moderate beam loss. But the cables need to be evaluated before being applied to the machine.

For ELBE the CUT1-type cable is going to be used to transport the broadband pickup signals for the bunch arrival time monitor to the electro-optical modulator.

## ACKNOWLEDGEMENTS

The authors like to thank I. Kösterke for her support concerning all radiation measurement related aspects and M. Freitag and B. Reppe for their support setting up the measurement environment.

## REFERENCES

- [1] A. Angelovski, M. Kuntzsch, and M.K. Czwalińska, *Phys. Rev. ST Accel. Beams* 18 (2015), 012801
- [2] Alanine Dosimeter,  
<https://www.steris-ast.com/tech-tip/comparison-alanine-red-4034-dosimetry-systems/>
- [3] PTW Farmer Ionization Chambers,  
[http://www.ptw.de/farmer\\_chambers0.html](http://www.ptw.de/farmer_chambers0.html)
- [4] M. Kuntzsch and S. Burger, “Degradation of electrical properties of coaxial cables exposed to ionizing radiation”, 2016, Whitepaper, <http://www.testkabel.webseiten.cc/index.php?id=10>





## List of Authors

**Bold** papercodes indicate primary authors; ~~crossed-out~~ papercodes indicate 'no submission'

### — A —

Abbon, P. **WEOC04**  
Abrami, A. **WEPC06**  
Adachi, M. **MOPB08**  
Adamczewski-Musch, J. **TUPC03**  
Adler, L. **WEPC02**  
Ady, M. **WEPB16**  
Allaria, E. **WEPC06**  
Allison, T.L. **TUPA16**  
Altinbas, Z. **TUPA17**  
Alves, H. **TUPA02**  
Anashin, V.S. **MOPA06**  
Aoyagi, H. **TUOB03**  
Arinaga, M. **M00B01, MOPA02**  
Arnold, A. **MOPB04**  
Arnold, M. **MOPB03, WEPC04**  
Arnold, N.D. ~~TUOC02~~  
Arsov, V.R. **WEPA20**  
Aryshev, A. **WEPB02, WEPB14**  
Atkinson, T. **WEPA02**  
Aune, S. **TUPA02**  
Ausset, P. **TUPB03**

### — B —

Baboi, N. **M00B03, TUPB07, WEPA09**  
Bahlo, T. **MOPB03, WEPC04**  
Bambade, P. **MOPA13, TUPC13, WEPB02**  
Bassanese, S. **TUOC01, TUPB13**  
Baud, G. **TUPB14**  
Bekman, I. **TUPC04**  
Bellodi, G. **WEPA19**  
Belloni, F. **WEOC04**  
Beltramelli, J. **TUPA02**  
Ben Abdillah, M. **TUPB03**  
Benedetti, F. **WEOC04**  
Bergamaschi, M. **WEPB02, WEPB14**  
Bertarelli, A. **TUPA15**  
Bertrand, Q. **TUPA02**  
Bey, T. **TUPA02**  
Billing, M.G. **WEPB14**  
Bisegni, C. **MOPB06**  
Blake, R.W. ~~TUOC02~~  
Blanco-García, O.R. **MOPB06**  
Bleko, V.V. **WEPB14**  
Bobb, L. **WEPB14, WEPB18**  
Böhme, C. **MOPA01, TUPC04**  
Bonvicini, G. **M00B01**  
Boonpornprasert, P. **WEPB04**  
Borin, V.M. **WEPA18**  
Bossi, M. **WEPC06**  
Bozzolan, M. **TUPB14**  
Brajnik, G. **TUOC01, TUPB13**

Bravo, B. **THOB02**  
Brill, A.R. ~~TUOC02~~  
Brito Neto, J.L. **WEPA01**  
Brown, D.G. **TUPC13**  
Bruhwel, S. **TUPA16**  
Bruno, D. **TUPA17**  
Bruno, G.B.M. **TUOC03, WEPA01**  
Brutus, J.C.B. **MOPA09, ~~TUOB01~~**  
Bui, H. ~~TUOC02~~  
Burandt, C. **MOPB03**  
Burger, S.J. **THOB03**

### — C —

Cao, L.C. **TUPC10**  
Cao, S.S. **WE0A04**  
Cao, S.S. **TUPC05**  
Cao, S.V. **WEPC08**  
Cargnelutti, M. **TUPB12, TUPB13**  
Carmignani, N. **MOPA17**  
Carra, F. **TUPA15**  
Carwardine, J. ~~TUOC02~~  
Cauchois, A. **MOPA16**  
Cautero, G. **TUOC01**  
Chapman, L.D. **TUOB04**  
Chen, F.Z. **MOPC02**  
Chen, F.Z. **MOPC16, MOPC17, TUPC05**  
Chen, J. **WEPC15, MOPC11**  
Chen, J. **M00C03, MOPC17, TUPB09,**  
**TUPC05, WE0A04**  
Chen, Q.S. **TUPB10, WEPB16**  
Chen, Y. **WEPB04**  
Chen, Y. **TUPA07**  
Chen, Y.C. **MOPA04, MOPC12**  
Chen, Z.C. **MOPC02**  
Chermoshentsev, D.A. **WEPA17**  
Chevtsov, P. **WEPA20**  
Chritin, N. **WEPB16**  
Chubunov, P.A. **MOPA06**  
Chung, Y.S. **M00B02**  
Cleva, S. **TUOC01, TUPB13**  
Coello de Portugal, J.M. **TUOA02, TUOB02**  
Cogan, S. **TUPC07**  
Coiro, O. **MOPB06**  
Combet, M. **TUPA02**  
Condamoor, S. **TUPB12**  
Conway, J.V. **WEPB14**  
Coombs, G.R. **WEPB13**  
Corbett, W.J. **TUPB12, WEPB06**  
Costanzo, M.R. **TUPA17**  
Coulloux, G. **WEOC04**  
Crisp, J.L. **TUPC07**  
Cudin, I. **WEPC06**

7<sup>th</sup> Int. Beam Instrumentation Conf.

ISBN: 978-3-95450-201-1

IBIC2018, Shanghai, China

JACoW Publishing

Czwalinna, M.K.

WE0A03, TH0A02

— D —

Da Silva, J.

WEPB01

Dach, M.

WEPA20

Dallin, L.O.

TU0B04

Danailov, M.B.

WEPC06

Dawson, W.C.

MOPA09

De Franco, A.

WEPC02

De Gersem, H.

MOPC06, MOPC08

De Monte, R.

TU0C01, TUPB13, WEPC06

De Santis, A.

MOPB06

De Santis, S.

M00C04

Decker, G.

TU0C02

Desforge, D.

TUPA02

Dewa, H.

TU0C04

Di Carlo, S.

MOPA13, TUPC13

Dilly, J.

TU0B02

Ding, K.Z.

TUPA07

Ding, L.H.

MOPB13

Ding, Y.K.

TUPA08

Dirksen, P.E.

TUPB01

Dohlus, M.

TUPB05

Dohou, F.

WE0B02

Dolenc Kittelmann, I.

TUPA02

Dong, J.M.

MOPA04

Dorokhov, V.L.

WEPA18

Drees, K.A.

TUPA17

Du, Y.Y.

MOPC10

Du, Z.

WE0B04

Dürr, V.

TUPB04

Duhme, H.T.

M00B03

— E —

Eichinger, M.

TUPA01

El Ajjouri, M.

TUPA03, WE0B02

El Khechen, D.

TUPC13

Emery, L.

TU0C02

Enke, S.

TUPA01

Evtushenko, P.E.

WEPB20

Ewald, F.

WE0C01

— F —

Fan, K.

TUPB10, WEPC16

Farinon, F.

WEPC02

Fedotov, A.V.

TUPA17, WEPB21

Feikes, J.

MOPC03

Feng, Y.C.

MOPA04, MOPC12

Fenner, M.

TH0A02

Ferdinand, R.

TUPB03

Ferianis, M.

WEPC06

Fernandes, M.F.

MOPC06, MOPC08

Ferro-Luzzi, M.

WEPB13

Feschenko, A.

WEPA17, WEPA19

Fisher, A.S.

TUPC13

Fisher, S.A.

TUPA14

Flanagan, J.W.

M00B01, MOPA02, WE0C02

Fletcher, S.

TUPA15

Fol, E.

TU0A02

Forck, P.

MOPB02, MOPC08, WEPB16

Ford, T.M.

TUPC07

Fors, T.

TU0C02

Forster, M.J.

WEPB14

Fosse, L.

WEPB15

Franchi, A.

MOPA17

Franchi, J.

WEPB15

Frank, W.A.

TUPA14

Frassier, A.

WEPB15

Freeman, B.G.

WEPB20

Friend, M.L.

M00B04, MOPB07, WEPC08

Fuchs, A.

WEPB21

Fuentes, Y.L.P.

WEPB14

Fujii, Y.

MOPC18

Fujita, T.

TU0C04

Fukuma, H.

M00B01, MOPA02

Fullerton, J.

WEPB15

Funakoshi, Y.

MOPA13, TUPC13

Furness, T.R.

TUPA15

Furukawa, Y.

TU0B03

Futatsukawa, K.

TUPA04

Fürtinger, M.

TUPA01

— G —

Galatyuk, T.

TUPC03

Gambino, N.

WEPC02

Gao, B.

WEPC15, TH0B01

Gao, F.L.

TUPC12

Gassner, D.M.

MOPA09, TU0B01, TUPA17, WEPB21

Gavrilov, S.A.

MOPA07, WEPA17, WEPA19

Ge, T.

TUPC10

Gentini, L.

TUPA15

Gerth, C.

MOPB02, WE0A03

Gessner, S.J.

TUPB01

Giacuzzo, F.

WEPC06

Glutting, J.

WEPB16

Golm, J.

MOPC06, MOPC08

Good, J.D.

WEPB04

Goslowski, P.

WEPA02

Gougnaud, F.

WE0C04, TUPA02

Grandsaert, T.J.

WEPB12

Grewe, R.

MOPB03

Groß, M.

WEPB04

Grulja, S.

WEPC06

Gu, K.

WE0B04

Gu, X.

TUPA17, WEPB21

Guan, F.P.

TUPC10

Guan, X.

WEPC09

Gubeli, J.

WEPB20

Gubin, V.

MOPA14

Guidoboni, G.

WEPC02

Content from this work may be used under the terms of the CC BY 3.0 licence (© 2018). Any distribution of this work must maintain attribution to the author(s), title of the work, publisher, and DOI.

558

List of Authors

Guillot-Vignot, F. **TUPB01**  
Guo, H.D. **MOPC14, TUPA09**  
Guo, J. **MOPB17**

## — H —

Haider, D.M. **MOPC06, MOPC08**  
Halama, A.J. **MOPA01**  
Hammons, L.R. **TUPA17**  
Hara, T. **TH0A04**  
Harada, K. **MOPB08**  
Harryman, D.M. **TUPA14**  
Hartz, M. **WEPC08**  
Hatakeyama, S. **TUPA04**  
Hauser, J. **MOPB04**  
Hayashi, N. **TUPA04**  
He, J. **MOPC19**  
He, T.H. **WEPA12**  
He, Y. **TUPA08**  
Henry, J. **MOPB17**  
Hensler, O. **MOPB03**  
Hillert, W. **WEPA04**  
Hock, J. **TUPA17**  
Hogan, R.B. **TUPC01**  
Hong, J.H. **WEPA15**  
Hou, S.G. **TUPC10**  
Hu, L.X. **TUPA07**  
Hu, X.J. **WE0B04**  
Hu, Y.Y. **MOPC14, TUPA09**  
Hua, L.F. **WEPA13**  
Huang, J.Y. **WEPC17**  
Huang, L.T. **MOPB09, TUPC12**  
Huang, W.-H. **WEPC09**  
Huang, W.L. **MOPC02, MOPC04**  
Hubert, N. **TUPA03, WE0B02, WEB01**  
Huck, H. **WEPA04**  
Hug, F. **MOPB03, WEPC04**  
Hulsart, R.L. **MOPA09, TU0B01, TUPA17**  
Hunziker, S. **WEPA20**  
Hwang, J.G. **TUPB04, WEPA02, WEB03**

## — I —

Ikeda, H. **MOPB01, MOPA02**  
Inacker, P. **MOPA09, TU0B01, TUPA17**  
Inoue, I. **TH0A04**  
Inubushi, Y. **TH0A04**  
Iriso, U. **MOPB02, WE0C01, TH0A03, TH0B02**  
Isaev, I.I. **WEPA04**  
Ischebeck, R. **MOPB02**  
Ishii, H. **MOPB01, MOPA02**  
Issatov, A. **MOPA06**  
Iwabuchi, S.H. **MOPB01, MOPA02**

## — J —

Jabłoński, S. **TH0A02**

Jamilkowski, J.P. **MOPA09, TUPA17**  
Jankowiak, A. **WEPA02**  
Jehanno, D. **MOPA13, TUPC13**  
Jiang, R. **MOPC02**  
Jing, L. **WE0B04**  
Joannem, T.J. **TUPA02**  
Jones, B. **TUPA14**  
Jones, O.R. **MOPB02, WEB14, WEB16**  
Jordan, K. **WEB20**  
Jürgensen, L.E. **MOPB03, WEPC04**

## — K —

Kaiser, M.G. **WEPA20**  
Kalantaryan, D.K. **WEB04**  
Kallakuri, P.S. **TU0C02**  
Kamerdzhev, V. **MOPA01, TUPC04**  
Kamma-Lorger, C. **TH0A03**  
Kang, H.-S. **WE0A01, WEPA15, WEPA16, WEB09**  
Kang, X.C. **MOPA04, MOPC12**  
Karataev, P. **MOPB16, WEB14**  
Kato, R. **MOPB08**  
Kawamoto, T. **TUPC13**  
Kayran, D. **MOPA09, TUPA17, WEB21**  
Keane, R.T. **TU0C02**  
Kebbiri, M. **TUPA02**  
Kersevan, R. **WEB16**  
Kewisch, J. **TUPA17, WEB21**  
Khojyan, M. **MOPA16**  
Kieffer, R. **WEB14**  
Kim, C. **WE0A01, WEPA15, WEPA16, WEB09**  
Kim, D. **WEPC17**  
Kim, G. **WEPA15, WEPA16, WEB09**  
Kim, G.D. **MOPB02**  
Klehr, F. **MOPA01**  
Klein, R. **MOPC03**  
Klimczok, B. **MOPA01**  
Ko, I.S. **WE0A01, WEPA16**  
Ko, J.H. **WEPA16**  
Ko, J.J. **WEPC17**  
Kocevar, H. **WEB12**  
Konkov, A.S. **WEB14**  
Koopmans, M. **WEPA02**  
Koschitzki, C. **WEB04**  
Koshio, Y. **MOPB04**  
Kral, J. **WEB15**  
Krasilnikov, M. **WEB04**  
Kube, G. **MOPB03, WE0C01, WE0C03, WEB10, WEB11**  
Kubyskyi, V. **MOPA13**  
Kürzeder, T. **MOPB03**  
Kuntzsch, M. **TH0B03**  
Kurdi, G. **WEPC06**  
Kurfürst, C. **TUPA01, WEPC02**  
Kurian, F. **MOPC06, MOPC08**





Mitrofanov, S.V. **MOPA06**  
Mitsubishi, T.M. **WE0C01**  
Mitsuka, G.M. **M00B01, MOPA02**  
Miura, A. **TUPA04**  
Miyamoto, R. **WEPB12**  
Miyao, T. **TUPA04**  
Mols, J.-Ph. **WE0C04**  
Mori, K. **M00B01, MOPA02**  
Mulyani, E. **M00B01**  
Myalski, S. **WEPC02**  
Müller, W.F.O. **MOPC06**

## — N —

Nadot, V. **WE0C04, TUPA02**  
Naito, T. **WEPB02**  
Nakadaira, T. **MOPC18**  
Nakamura, A. **WEPC08**  
Nakamura, N. **MOPB08**  
Nakamura, S. **TUPC13**  
Nakayoshi, K. **M00B04, MOPC18**  
Neubert, R. **MOPC06**  
Neumann, Re. **M00B03**  
Nie, X.J. **M00C02**  
Nie, Y.G. **MOPC12**  
Niedermayer, P. **TUPC04**  
Niemczyk, R. **WEPB04**  
Nölle, D. **TU0A01**  
Norum, W.E. **M00C04**  
Nosych, A.A. **TH0A03, TH0B02**  
Novokshonov, A.I. **WE0C03, WEPB11**

## — O —

Obina, T. **MOPB08**  
Oddo, P. **MOPA09**  
Oh, B.G. **WEPB09**  
Oh, B.H. **WEPC17**  
Oki, T. **TUPC13**  
Oppelt, A. **WEPB04**  
Ortega Ruiz, I. **WEPB15**  
Ottmar, A.V. **MOPA14**

## — P —

Pan, Q. **WEPA12**  
Pang, C.G. **MOPA13, TUPC13**  
Paniccia, M.C. **MOPA09, TU0B01, TUPA17**  
Papaevangelou, T. **TUPA02**  
Paskvan, D.R. **TU0C02**  
Pasquali, M. **TUPA15**  
Pédeau, D. **TUPA03, WE0B02**  
Pei, G. **WEPA06**  
Peier, P. **WE0A03**  
Peinaud, Y. **MOPA13**  
Pekrul, W.E. **TU0B01, TUPA17**  
Peng, J. **WEPA07**  
Peng, W. **WEPA07**

Penirschke, A. **WE0A02**  
Pérez, F. **MOPB02**  
Pertica, A. **TUPA14**  
Petenev, Y. **MOPC03**  
Pforr, J. **MOPB03, WEPC04**  
Pietralla, N. **MOPB03, WEPC04**  
Pietraszko, J. **TUPC03**  
Pietryla, A.F. **TU0C02**  
Pinayev, I. **MOPA09, TU0B01, TUPA17**  
Pivi, M.T.F. **WEPC02**  
Poelker, M. **MOPB17**  
Portmann, G.J. **M00C04**  
Posthuma de Boer, D.W. **TUPA14**  
Potenza, M.A.C. **TH0A03**  
Potylitsyn, A. **WEPB10, WEPB11, WEPB14**  
Pozdeyev, G. **M00C01**  
Pozenel, A. **TUPA01**  
Prasuhn, D. **MOPA01**  
Prudent, J. **MOPA16**  
Ptitsyn, V. **TUPA17, WEPB21**

## — Q —

Qian, H.J. **WEPB04**  
Qian, M.X. **MOPB09**  
Qiu, M.T. **WEPC09**

## — R —

Rebernik Ribič, P. **WEPC06**  
Redaelli, S. **TUPA15**  
Rehm, G. **MOPB16, WEPB18**  
Reimers, K. **TUPC04**  
Renier, Y. **WEPB04**  
Repovž, M. **TUPA01**  
Ries, M. **TUPB04, WEPA02**  
Rimbault, C. **MOPA13**  
Rimmer, R.A. **MOPB17**  
Rogovsky, Yu. A. **WEPA18**  
Romann, A. **WEPA20**  
Roncarolo, F. **WEPB14, TH0A03**  
Rossi, A. **WEPB16**  
Rost, A. **MOPB03, TUPC03, WEPC04**  
Russo, L.M. **TU0C03, WEPA01**  
Rybitskaya, T.V. **MOPA14**

## — S —

Sakashita, K. **M00B04, MOPC18, WEPC08**  
Salehilashkajani, A. **WEPB16**  
Samadi, N. **TU0B04**  
Sapinski, M. **MOPB02**  
Sauro, R. **WEPC06**  
Schälicke, A. **TUPB04, WEPA02**  
Scheidt, K.B. **TUPB02, WE0B01**  
Schiewietz, G. **TUPB04, WEPA02**  
Schlarb, H. **WE0A02, TH0A02**  
Schlott, V. **WE0C01, WEPA20**

7 <sup>th</sup> Int. Beam Instrumentation Conf. ISBN: 978-3-95450-201-1		IBIC2018, Shanghai, China		JACoW Publishing	
Content from this work may be used under the terms of the CC BY 3.0 licence (© 2018). Any distribution of this work must maintain attribution to the author(s), title of the work, publisher, and DOI.	Schmelz, M.	MOPC06, MOPC08	Sun, Z.H.	WEPB06	
	Schmidl, F.	MOPC06, MOPC08	— T —		
	Schmitzer, C.	WEPC02	Takahashi, S.	TU0B03	
	Schneider, Ch.	MOPB04	Takai, R.	MOPB08	
	Schneider, G.	WEPB16	Takano, S.	TU0C04	
	Schneider, T.	WEPB15	Tamashevich, Y.	MOPC03	
	Schoefer, V.	TUPA17	Tan, J.	MOPC06, MOPC08, WEPA19	
	Scholz, M.	WE0C03, WEPC05	Tan, P.	MOPC14, TUPA09	
	Schurig, R.	TH0B03	Tan, Y.E.	TUPC01	
	Schwickert, M.	MOPC06, MOPC08	Tanaka, H.	TH0A04	
	Scola, L.	WE0C04	Tanaka, O. A.	MOPB08	
	Scrivens, R.	TUPB14	Tang, K.	TUPB10, WEPC16	
	Segui, L.	TUPA02	Tanimoto, Y.	MOPB08	
	Seidel, P.	MOPC06, MOPC08	Tavares, D.O.	TU0C03, WEPA01	
	Seletskiy, S.	TUPA17, WEPB21	Tejima, M.	M00B01, MOPA02	
	Seren, N.	TU0C02	Terunuma, N.	WEPB02, WEPB14	
	Shan, L.J.	WEPA12	Than, R.	TUPA17	
	Shang, H.	TU0C02	Thelen, M.	TUPC04	
	Shanks, J.P.	WEPB14	Thieberger, P.	TUPA17	
	Shea, T.J.	TUPA02, WEPB12	Thomas, C.A.	WE0C04, WEPB12	
	Shen, X.	WEPA12	Thornagel, R.	MOPC03	
	Shi, L.	TUPB07, WEPA09	Tian, J.M.	M00C02	
	Shin, D.C.	WEPA15, WEPB09	Tian, K.	WEPB06	
	Shin, S.	WEPC17	Tian, P.	TUPB10, WEPC16	
	Shwartz, D.B.	WEPA18	Timoshenko, M.V.	WEPA18	
	Siano, M.	TH0A03	Titov, A.I.	MOPA07	
	Sieber, T.	MOPC06, MOPC08	Tobiyama, M.	M00B01, MOPA02, TUPC13	
	Silva, H.A.	TU0C03	Tölle, R.	MOPA01	
	Simon, M.	TUPC04	Tomás, R.	TU0A02, TU0B02	
	Skowroński, P.K.	TU0B02	Torino, L.	MOPA17, WE0B01	
	Smakulski, P.	WEPB16	Trad, G.	TH0A03	
	Smart, L.	TUPA17	Tranquille, G.	WEPB15	
	Smirnov, P.A.	M00B03	Traxler, M.	TUPC03	
	Smith, K.S.	TUPA17	Treyer, D.M.	WEPA20	
	Søby, L.	TUPB01, TUPB14	Tsiledakis, G.	TUPA02	
	Song, H.H.	MOPA04, MOPC12	Tsuchiya, K.	MOPB08	
	Song, K.	MOPA04	Tuozzolo, J.E.	MOPA09, TU0B01, TUPA17	
	Song, Y.	TUPA07	Tympel, V.	MOPC06, MOPC08	
	Sorrell, Z.	MOPA09, TU0B01	— U —		
	Spanggaard, J.	WEPB15	Udrea, S.	WEPB16	
	Specka, A.	MOPA16	Uehara, S.	MOPA13, TUPC13	
	Stadler, M.	WEPA20	— V —		
	Stecchi, A.	MOPB06	Valuch, D.	TUPC09	
	Steffen, B.	WE0A03	Varner, G.S.	M00B01	
	Stephan, F.	WEPB04	Veness, R.	WEPB16, WEPC19	
	Stöhlker, T.	MOPC06, MOPC08	Veronese, M.	WEPC06	
	Stolz, R.	MOPC06, MOPC08	Verzilov, V.A.	TUPB01	
	Strangolino, G.	WEPC06	Veseli, S.	TU0C02	
	Strašik, I.	WEPC02	Vidmar, M.	M00A02	
	Strokov, S.A.	WEPB10	Vilcins, S.	TUPB05	
	Sukhanov, A.	WEPB21	Vitoratou, N.	MOPB16	
	Sukhikh, L.G.	WEPB10, WEPB11			
	Suleiman, R.	MOPB17			
	Sullivan, M.K.	TUPC13			
	Sun, B.G.	MOPB09, MOPB10, TUPC12			
	Sun, J.L.	M00C02, MOPA12			

— W —

Wallon, S.	WEPB02
Wallters, S. C.	TUPB12
Wamsat, T.	M00B03, <b>WE0B03</b>
Wang, A.X.	MOPA12, <del>M00C02</del>
Wang, D.	WEPC09
Wang, H.	MOPB17
Wang, J.	<del>TU0C02</del>
Wang, J.	<b>TUPC11</b> , <b>WEPA12</b>
Wang, J.G.	MOPB09, <b>TUPC12</b>
Wang, L.	MOPC10
Wang, M.W.	<b>WEPC09</b>
Wang, Q.	<b>MOPB10</b>
Wang, S.	MOPC04
Wang, S.	WEPB14
Wang, X.W.	WEPC09
Wang, Y.	MOPA04, <b>MOPC12</b>
Wang, Y.	<b>TUPC10</b>
Wang, Z.M.	WEPC09
Wastl, A.	WEPC02
Watanabe, A.	TU0B03
Weber, T.	TH0B03
Wei, C.Y.	WEPC09
Wei, J.H.	MOPB09, <b>TUPB07</b> , <b>TUPC12</b> , <b>WEPA09</b>
Wei, K.	MOPA04
Wei, W.	<del>WE0B04</del>
Weih, S.	MOPB03
Weiss, D.	WEPB21
Welsch, C.P.	MOPC06, <b>WEPB16</b>
Wen, L.P.	<b>TUPC10</b>
Werner, M.	M00B03, <b>TUPB05</b>
Wienands, U.	<b>TUPC13</b>
Wilcox, C.C.	<b>TUPA14</b>
Williamson, J.F.	<b>TUPA15</b>
Wissmann, J.	MOPB03
Wittenburg, K.	MOPB02, <del>WE0C01</del> , <b>WEPB10</b>
Wolk, D.	<b>TUPB04</b>
Woo, H.J.	<b>M00B02</b>
Wu, D.	<b>TUPC11</b> , <b>WEPA12</b>
Wu, F.F.	MOPB09, MOPB10, <b>TUPC12</b>
Wu, J.X.	<del>WE0B04</del>
Wu, T.	MOPC17, <b>TUPC05</b>
Wu, Y.C.	<b>TUPA07</b>

— X —

Xiao, D.X.	<b>TUPC11</b> , <b>WEPA12</b>
Xie, H.M.	<del>WE0B04</del>
Xie, Z.P.	MOPB13, <b>TUPA08</b>
Xing, Q.Z.	WEPC09
Xu, S.	<del>TU0C02</del>
Xu, T.G.	<del>M00C02</del> , MOPA12, MOPC04, <b>WEPA07</b>
Xu, W.	<b>TUPA17</b>
Xu, Z.G.	MOPA04

— Y —

Yabashi, M.	<del>TH0A04</del>
Yamamoto, N.	<b>MOPB08</b>
Yamasu, S.	M00B04
Yan, J.	<b>TUPA16</b>
Yan, J.	<del>WE0B04</del>
Yan, L.G.	<b>TUPC11</b> , <b>WEPA12</b>
Yan, Y.	MOPA04
Yan, Y.B.	<b>MOPC11</b> , MOPC16
Yang, B.X.	<del>TU0C02</del>
Yang, Q.	<b>TUPA07</b>
Yang, R.J.	<b>WEPB02</b>
Yang, T.	<del>M00C02</del>
Yang, Y.L.	MOPB09
Yao, K.	<b>TUPA07</b>
Yin, Y.	MOPA04, MOPC12
Ying, L.Y.	WEPB14
Yoon, M.	WEPC17
Yoshimoto, M.	<b>TUPA04</b>
Yu, C.L.	MOPC11
Yu, J. U.	WEPC17
Yu, L.Y.	M00C03, <b>TUPB09</b> , MOPC11, MOPC17
Yu, Y.C.	MOPC14, <b>TUPA09</b>
Yuan, R.X.	MOPC17, <b>TUPB09</b> , <b>WE0A04</b> , <b>WEPA13</b>

— Z —

Zakosarenko, V.	MOPC08, MOPC06
Zeng, L.	<del>M00C02</del>
Zhang, H.D.	WEPB16
Zhang, L.G.	<b>TUPA09</b>
Zhang, N.	M00C03, <b>MOPB14</b> , MOPC16, <b>WEPA13</b> , <b>TH0B01</b>
Zhang, P.	<b>WEPA12</b>
Zhang, Y.	<del>WE0B04</del>
Zhao, H.	MOPC11
Zhao, Q.T.	WEPB04
Zhao, T.C.	<b>MOPA04</b> , MOPC12
Zhao, Y.	<b>MOPC10</b>
Zhao, Z.	<b>TUPA17</b>
Zhao, Z.L.	MOPA04
Zharinov, Yu.M.	<b>WEPA18</b>
Zheng, S.X.	WEPC09
Zhou, K.	<b>WEPA12</b>
Zhou, T.Y.	MOPB09, <b>TUPC12</b>
Zhou, W.M.	MOPC11, MOPC16
Zhou, Y.M.	MOPB14, <b>WEPC15</b> , <b>TUPC05</b> , <b>TH0B01</b>
Zhu, D.H.	<del>M00C02</del>
Zhu, G.	<del>WE0B04</del>
Zink, J.	<b>TH0A02</b>
Žnidarčič, M.	<b>TUPB13</b>





## *Institutes List*

### **ALBA-CELLS Synchrotron**

Cerdanyola del Vallès, Spain

- Bravo, B.
- Iriso, U.
- Kamma-Lorger, C.
- Nosych, A.A.
- Pérez, F.

### **ANL**

Argonne, Illinois, USA

- Arnold, N.D.
- Blake, R.W.
- Brill, A.R.
- Bui, H.
- Carwardine, J.
- Decker, G.
- Emery, L.
- Fors, T.
- Kallakuri, P.S.
- Keane, R.T.
- Lill, R.M.
- Paskvan, D.R.
- Pietryla, A.F.
- Sereno, N.
- Shang, H.
- Veseli, S.
- Wang, J.
- Wienands, U.
- Xu, S.
- Yang, B.X.

### **AS - ANSTO**

Clayton, Australia

- Hogan, R.B.
- Tan, Y.E.

### **ASIPP**

Hefei, People's Republic of China

- Chen, Y.
- Ding, K.Z.
- Hu, L.X.
- Li, J.
- Song, Y.
- Yang, Q.

### **BINP**

Novosibirsk, Russia

- Dorokhov, V.L.

### **BINP SB RAS**

Novosibirsk, Russia

- Borin, V.M.
- Maltseva, Yu.I.
- Meshkov, O.I.
- Ottmar, A.V.

- Rogovsky, Yu. A.
- Rybitskaya, T.V.
- Schwartz, D.B.
- Timoshenko, M.V.
- Zharinov, Yu.M.

### **BNL**

Upton, Long Island, New York, USA

- Altinbas, Z.
- Bruno, D.
- Brutus, J.C.B.
- Costanzo, M.R.
- Dawson, W.C.
- Drees, K.A.
- Fedotov, A.V.
- Gassner, D.M.
- Gu, X.
- Hammons, L.R.
- Hock, J.
- Hulsart, R.L.
- Inacker, P.
- Jamilkowski, J.P.
- Kayran, D.
- Kewisch, J.
- Litvinenko, V.
- Liu, C.
- Mernick, K.
- Michnoff, R.J.
- Miller, T.A.
- Minty, M.G.
- Oddo, P.
- Paniccia, M.C.
- Pekrul, W.E.
- Pinayev, I.
- Ptitsyn, V.
- Schoefer, V.
- Seletskiy, S.
- Smart, L.
- Smith, K.S.
- Sorrell, Z.
- Sukhanov, A.
- Than, R.
- Thieberger, P.
- Tuozzolo, J.E.
- Weiss, D.
- Xu, W.
- Zhao, Z.

### **CAEP/IAE**

Mianyang, Sichuan, People's Republic of China

- He, T.H.
- Lao, C.L.
- Li, P.
- Liu, J.
- Luo, X.
- Pan, Q.
- Shan, L.J.



## CLS

Saskatoon, Saskatchewan, Canada

- Chapman, L.D.
- Dallin, L.O.

## Cockcroft Institute

Warrington, Cheshire, United Kingdom

- Fernandes, M.F.
- Welsch, C.P.
- Zhang, H.D.

## Cornell University (CLASSE), Cornell Laboratory for Accelerator-Based Sciences and Education

Ithaca, New York, USA

- Billing, M.G.
- Conway, J.V.
- Forster, M.J.
- Fuentes, Y.L.P.
- Shanks, J.P.
- Wang, S.
- Ying, L.Y.

## Dach Consulting GmbH

Brugg, Switzerland

- Dach, M.

## Delta Gamma RF-Expert

Melbourne, Australia

- Burger, S.J.

## DESY

Hamburg, Germany

- Baboi, N.
- Czwalińska, M.K.
- Dohlus, M.
- Duhme, H.T.
- Fenner, M.
- Gerth, C.
- Hensler, O.
- Jabłoński, S.
- Kube, G.
- Lensch, T.
- Lipka, D.
- Liu, S.
- Lorbeer, B.
- Marjanovic, J.
- Marx, M.
- Neumann, Re.
- Nölle, D.
- Novokshonov, A.I.
- Peier, P.
- Schlarb, H.
- Scholz, M.
- Smirnov, P.A.
- Steffen, B.
- Vilcins, S.
- Wamsat, T.

- Werner, M.
- Wittenburg, K.
- Zink, J.

## DESY Zeuthen

Zeuthen, Germany

- Boonpornprasert, P.
- Chen, Y.
- Good, J.D.
- Groß, M.
- Huck, H.
- Isaev, I.I.
- Kalantaryan, D.K.
- Koschitzki, C.
- Krasilnikov, M.
- Li, X.
- Lishilin, O.
- Loisch, G.
- Melkumyan, D.
- Niemczyk, R.
- Oppelt, A.
- Qian, H.J.
- Renier, Y.
- Stephan, F.
- Zhao, Q.T.

## DLS

Oxfordshire, United Kingdom

- Bobb, L.
- Rehm, G.

## DNSC

Dongguan, People's Republic of China

- Meng, M.

## Donghua University

Shanghai, People's Republic of China

- Lin, Q.
- Sun, Z.H.

## EBG MedAustron

Wr. Neustadt, Austria

- Adler, L.
- De Franco, A.
- Eichinger, M.
- Enke, S.
- Farinon, F.
- Fürtinger, M.
- Gambino, N.
- Guidoboni, G.
- Kurfürst, C.
- Myalski, S.
- Pivi, M.T.F.
- Pozenel, A.
- Repovž, M.
- Schmitzer, C.
- Strašák, I.
- Wastl, A.





## HUST

Wuhan, People's Republic of China

- Chen, Q.S.
- Fan, K.
- Guo, H.D.
- Hu, Y.Y.
- Lei, H.
- Li, J.Q.
- Li, X.Y.
- Lin, Y.J.
- Tan, P.
- Tang, K.
- Tian, P.
- Yu, Y.C.
- Zhang, L.G.

## HZB

Berlin, Germany

- Atkinson, T.
- Dürr, V.
- Feikes, J.
- Goslawski, P.
- Hwang, J.G.
- Jankowiak, A.
- Koopmans, M.
- Kuszynski, J.
- Li, J.
- Matveenko, A.N.
- Mertens, T.
- Petenev, Y.
- Ries, M.
- Schälicke, A.
- Schiwietz, G.
- Tamashevich, Y.
- Wolk, D.

## HZDR

Dresden, Germany

- Arnold, A.
- Evtushenko, P.E.
- Hauser, J.
- Kuntzsch, M.
- Michel, P.
- Schneider, Ch.
- Schurig, R.

## I-Tech

Solkan, Slovenia

- Cargnelutti, M.
- Leban, P.
- Žnidarčič, M.

## IBS

Daejeon, Republic of Korea

- Chung, Y.S.
- Kim, G.D.
- Woo, H.J.

## IHEP

Beijing, People's Republic of China

- Du, Y.Y.
- He, J.
- Huang, W.L.
- Li, F.
- Li, P.
- Liu, L.
- Lu, Y.H.
- Ma, L.
- Ma, X.
- Meng, M.
- Nie, X.J.
- Pei, G.
- Tian, J.M.
- Wang, A.X.
- Wang, L.
- Wang, S.
- Xu, T.G.
- Zeng, L.
- Zhao, Y.
- Zhu, D.H.

## IHEP CSNS

Guangdong Province, People's Republic of China

- Huang, W.L.
- Li, F.
- Li, P.
- Nie, X.J.
- Peng, J.
- Sun, J.L.
- Wang, A.X.
- Yang, T.

## IKP

Mainz, Germany

- Hug, F.

## IMP/CAS

Lanzhou, People's Republic of China

- Chen, Y.C.
- Dong, J.M.
- Du, Z.
- Feng, Y.C.
- Gu, K.
- He, Y.
- Hu, X.J.
- Jing, L.
- Kang, X.C.
- Li, M.
- Li, S.
- Li, W.L.
- Li, Y.M.
- Ma, W.N.
- Mao, R.S.
- Nie, Y.G.
- Song, H.H.
- Song, K.
- Wang, Y.

<p>7<sup>th</sup> Int. Beam Instrumentation Conf. ISBN: 978-3-95450-201-1</p> <p>Content from this work may be used under the terms of the CC BY 3.0 licence (© 2018). Any distribution of this work must maintain attribution to the author(s), title of the work, publisher, and DOI.</p>	<ul style="list-style-type: none"> <li>• Wei, K.</li> <li>• Wei, W.</li> <li>• Wu, J.X.</li> <li>• Xie, H.M.</li> <li>• Xie, Z.P.</li> <li>• Xu, Z.G.</li> <li>• Yan, J.</li> <li>• Yan, Y.</li> <li>• Yin, Y.</li> <li>• Zhang, Y.</li> <li>• Zhao, T.C.</li> <li>• Zhao, Z.L.</li> <li>• Zhu, G.</li> </ul>	<p><b>IBIC2018</b>, Shanghai, China</p>	<p>JACoW Publishing</p>
	<p><b>INFN/LNF</b> Frascati, Italy</p> <ul style="list-style-type: none"> <li>• Bisegni, C.</li> <li>• Blanco-García, O.R.</li> <li>• Coiro, O.</li> <li>• De Santis, A.</li> <li>• Michelotti, A.</li> <li>• Milardi, C.</li> <li>• Stecchi, A.</li> </ul>		
	<p><b>Institute of Laser Physics, SB RAS</b> Novosibirsk, Russia</p> <ul style="list-style-type: none"> <li>• Gubin, V.</li> </ul>		
	<p><b>IOQ</b> Jena, Germany</p> <ul style="list-style-type: none"> <li>• Stöhlker, T.</li> </ul>		
	<p><b>IPHT</b> Jena, Germany</p> <ul style="list-style-type: none"> <li>• Schmelz, M.</li> <li>• Stolz, R.</li> <li>• Zakosarenko, V.</li> </ul>		
	<p><b>IPN</b> Orsay, France</p> <ul style="list-style-type: none"> <li>• Ausset, P.</li> <li>• Ben Abdillah, M.</li> </ul>		
	<p><b>ISDE</b> Moscow, Russia</p> <ul style="list-style-type: none"> <li>• Chubunov, P.A.</li> </ul>		
	<p><b>JAEA/J-PARC</b> Tokai-Mura, Naka-Gun, Ibaraki-Ken, Japan</p> <ul style="list-style-type: none"> <li>• Hatakeyama, S.</li> <li>• Hayashi, N.</li> <li>• Miura, A.</li> <li>• Yoshimoto, M.</li> </ul>		
		<p><b>JAI</b> Egham, Surrey, United Kingdom</p> <ul style="list-style-type: none"> <li>• Karataev, P.</li> <li>• Lekomtsev, K.</li> </ul>	
		<p><b>JASRI</b> Hyogo, Japan</p> <ul style="list-style-type: none"> <li>• Dewa, H.</li> <li>• Fujita, T.</li> <li>• Masaki, M.</li> <li>• Takano, S.</li> </ul>	
		<p><b>JASRI/SPRING-8</b> Hyogo, Japan</p> <ul style="list-style-type: none"> <li>• Aoyagi, H.</li> <li>• Furukawa, Y.</li> <li>• Takahashi, S.</li> <li>• Watanabe, A.</li> </ul>	
		<p><b>JINR</b> Dubna, Moscow Region, Russia</p> <ul style="list-style-type: none"> <li>• Mitrofanov, S.V.</li> </ul>	
		<p><b>JINR/FLNR</b> Moscow region, Russia</p> <ul style="list-style-type: none"> <li>• Issatov, A.</li> </ul>	
		<p><b>JLab</b> Newport News, Virginia, USA</p> <ul style="list-style-type: none"> <li>• Allison, T.L.</li> <li>• Bruhwel, S.</li> <li>• Freeman, B.G.</li> <li>• Gubeli, J.</li> <li>• Guo, J.</li> <li>• Henry, J.</li> <li>• Jordan, K.</li> <li>• Lu, W.</li> <li>• Poelker, M.</li> <li>• Rimmer, R.A.</li> <li>• Suleiman, R.</li> <li>• Wang, H.</li> <li>• Yan, J.</li> </ul>	
		<p><b>Kavli IPMU</b> Kashiwa, Japan</p> <ul style="list-style-type: none"> <li>• Hartz, M.</li> </ul>	
		<p><b>KEK</b> Ibaraki, Japan</p> <ul style="list-style-type: none"> <li>• Adachi, M.</li> <li>• Arinaga, M.</li> <li>• Aryshev, A.</li> <li>• Cao, S.V.</li> <li>• Flanagan, J.W.</li> <li>• Friend, M.L.</li> <li>• Fujii, Y.</li> </ul>	

- Fukuma, H.
- Funakoshi, Y.
- Futatsukawa, K.
- Harada, K.
- Ikeda, H.
- Ishii, H.
- Iwabuchi, S.H.
- Kato, R.
- Kawamoto, T.
- Masuzawa, M.
- Mitsuhashi, T.M.
- Mitsuka, G.M.
- Miyao, T.
- Mori, K.
- Naito, T.
- Nakadaira, T.
- Nakamura, N.
- Nakamura, S.
- Nakayoshi, K.
- Obina, T.
- Oki, T.
- Sakashita, K.
- Takai, R.
- Tanaka, O. A.
- Tanimoto, Y.
- Tejima, M.
- Terunuma, N.
- Tobiyama, M.
- Tsuchiya, K.
- Uehara, S.
- Yamamoto, N.

#### Korea University

Seoul, Republic of Korea  
• Kwon, J.W.

#### KPH

Mainz, Germany  
• Hug, F.

#### Laboratory GREYC

Caen, France  
• Ding, L.H.

#### LAL

Orsay, France  
• Bambade, P.  
• Di Carlo, S.  
• Jehanno, D.  
• Kubytskyi, V.  
• Pang, C.G.  
• Peinaud, Y.  
• Rimbault, C.  
• Wallon, S.  
• Yang, R.J.

#### LBNL

Berkeley, California, USA

- De Santis, S.
- Li, D.
- Norum, W.E.
- Portmann, G.J.

#### LLR

Palaiseau, France  
• Cauchois, A.  
• Khojayan, M.  
• Prudent, J.  
• Specka, A.

#### LNLS

Campinas, Brazil  
• Brito Neto, J.L.  
• Bruno, G.B.M.  
• Marques, S.R.  
• Russo, L.M.  
• Silva, H.A.  
• Tavares, D.O.

#### NINT

Shannxi, People's Republic of China  
• Qiu, M.T.  
• Wang, D.  
• Wang, Z.M.  
• Wei, C.Y.

#### Okayama University

Okayama, Japan  
• Nakamura, A.

#### Okayama University, Faculty of Science

Okayama City, Japan  
• Koshio, Y.  
• Yamasu, S.

#### PAL

Pohang, Kyungbuk, Republic of Korea  
• Hong, J.H.  
• Huang, J.Y.  
• Kang, H.-S.  
• Kim, C.  
• Kim, D.  
• Kim, G.  
• Ko, I.S.  
• Ko, J.J.  
• Lee, D.W.  
• Min, C.-K.  
• Oh, B.G.  
• Oh, B.H.  
• Shin, D.C.  
• Shin, S.  
• Yu, J. U.





- Jones, B.
- Pertica, A.
- Posthuma de Boer, D.W.
- Wilcox, C.C.

**Stony Brook University**

Stony Brook, USA

- Litvinenko, V.

**Supracon AG**

Jena, Germany

- Zakosarenko, V.

**TEMF, TU Darmstadt**

Darmstadt, Germany

- De Gersem, H.
- Marsic, N.
- Müller, W.F.O.

**The University of Liverpool**

Liverpool, United Kingdom

- Fernandes, M.F.
- Salehilashkajani, A.
- Welsch, C.P.

**THM**

Friedberg, Germany

- Mattiello, S.
- Penirschke, A.

**Thuringia Observatory Tautenburg**

Tautenburg, Germany

- Neubert, R.

**TPU**

Tomsk, Russia

- Bleko, V.V.
- Konkov, A.S.
- Novokshonov, A.I.
- Potylitsyn, A.
- Stokov, S.A.
- Sukhikh, L.G.

**TRIUMF**

Vancouver, Canada

- Dirksen, P.E.
- Liu, S.
- Verzilov, V.A.

**TU Darmstadt**

Darmstadt, Germany

- Arnold, M.
- Bahlo, T.
- Burandt, C.

- Galatyuk, T.
- Grewe, R.
- Jürgensen, L.E.
- Pforr, J.
- Pietralla, N.
- Rost, A.
- Weih, S.
- Wissmann, J.

**TUB**

Beijing, People's Republic of China

- Guan, X.
- Huang, W.-H.
- Wang, M.W.
- Wang, X.W.
- Xing, Q.Z.
- Zheng, S.X.

**United Rocket and Space Corporation, Institute of Space Device Engineering**

Moscow, Russia

- Anashin, V.S.

**Universita' degli Studi di Milano & INFN**

Milano, Italy

- Potenza, M.A.C.

**University of Hamburg, Institut für Experimentalphysik**

Hamburg, Germany

- Hillert, W.

**University of Hawaii**

Honolulu, USA

- Varner, G.S.

**University of Huddersfield**

Huddersfield, United Kingdom

- Fletcher, S.
- Furness, T.R.
- Williamson, J.F.

**University of Ljubljana, Faculty of Electrical Engineering**

Ljubljana, Slovenia

- Vidmar, M.

**University of Saskatchewan**

Saskatoon, Canada

- Samadi, N.

**Università degli Studi di Milano**

Milano, Italy

- Siano, M.



**USTC/NSRL**

Hefei, Anhui, People's Republic of China

- [Gao, F.L.](#)
- [Huang, L.T.](#)
- [Liu, X.Y.](#)
- [Lu, P.](#)
- [Luo, Q.](#)
- [Qian, M.X.](#)
- [Sun, B.G.](#)
- [Wang, J.G.](#)
- [Wang, Q.](#)
- [Wei, J.H.](#)
- [Wu, F.F.](#)
- [Yang, Y.L.](#)
- [Zhou, T.Y.](#)

**Ward Melville High School**

Setauket- East Setauket, USA

- [Fuchs, A.](#)

**Wayne State University**

Detroit, Michigan, USA

- [Bonvicini, G.](#)

**WRUT**

Wroclaw, Poland

- [Smakulski, P.](#)